

Inertial Sensor Performance Revisited

Christopher Blum, M.Sc.

Vollständiger Abdruck der von der TUM School of Engineering and Design der Technischen Universität München zur Erlangung eines

Doktors der Ingenieurwissenschaften (Dr.-Ing.)

genehmigten Dissertation.

Vorsitz: Prof. Dr.-Ing. Volker Gümmer

Prüfer*innen der Dissertation: 1. Prof. Dr.-Ing. Johann Dambeck
2. Prof. Dr.-Ing. habil. Karla Hiller
3. Prof. Dr.-Ing. Florian Holzapfel

Die Dissertation wurde am 26.09.2022 bei der Technischen Universität München eingereicht und durch die TUM School of Engineering and Design am 07.02.2023 angenommen.

Abstract

In this work, the field of inertial sensor selection, testing, and calibration is revisited.

The question of inertial sensor selection is answered by an analysis of the strapdown inertial navigation's response to initialization and inertial sensor errors. The work presents analytical solutions for the navigation state errors from bias-like and noise-like sensor errors. Graphs allow the simple read-off of acceptable accelerometer and gyroscope errors for the desired navigation performance. The validity of the analytical prediction and its limits are demonstrated using two Monte-Carlo simulation examples. The second part discusses how the sensors can be tested and calibrated in the laboratory to the desired accuracy. Based on comprehensive modeling of laboratory error sources, error budgets for classic inertial sensor test procedures are derived. The error budgets indicate dominant error sources and the achievable sensor accuracy depending on the test procedure. As an alternative to the classic procedures, a Schmidt-Kalman-filter-based test procedure that incorporates models of laboratory errors and sensor noise is discussed.

Kurzfassung

Diese Arbeit stellt eine erneute Betrachtung der Auswahl sowie des Testens und Kalibrierens von Inertialsensoren dar.

Die Frage der Sensorauswahl wird mithilfe einer Analyse der Antworten der Strapdown Trägheitsnavigation auf Initialisierungs- und Sensor-Fehler beantwortet. Die Arbeit zeigt analytische Lösungen für die Navigationszustandsfehler aus bias-like und noise-like Sensorfehlern. Grafiken erlauben das Ablesen der akzeptablen Accelerometer- und Kreisel-Fehler für die gewünschte Navigationsleistung. Die Gültigkeit der analytischen Vorhersagen und ihre Grenzen werden anhand zweier Monte-Carlo Simulationen aufgezeigt.

Im zweiten Teil der Arbeit wird diskutiert, wie die Sensoren im Labor auf die geforderte Genauigkeit hin getestet und kalibriert werden. Anhand einer umfangreichen Modellierung der Fehlereinflüsse im Labor werden Fehlerbudgets für klassische Testprozeduren hergeleitet. Die Fehlerbudgets zeigen die erreichbare Testgenauigkeit und die dominierenden Fehlerquellen in Abhängigkeit von der Testprozedur. Als Alternative zu klassischen Methoden wird eine Testmethode basierend auf einem Schmidt-Kalman-filter diskutiert, der Modelle für die Laborfehler und das Sensorrauschen beinhaltet.

Preface

Significant parts of this thesis were created during my time as a research associate at the Institute of Flight System Dynamics at the Technical University of Munich.

I would first like to thank *Prof. Dr.-Ing. Florian Holzapfel*, head of the Institute of Flight System Dynamics, who placed his trust in me and allowed me to work as a research assistant at his institute. In particular, collaborating on the institute's numerous exciting industrial and research projects proved a valuable experience I would not want to miss. I want to thank *Prof. Holzapfel* for his continuous support of my Ph.D. project in all respects.

Next, my special thanks go to *Prof. Dr.-Ing. Johann Dambeck*, head of the navigation group at the institute. Due to his extraordinary ability to ask crucial questions, this work could come into being at all. I want to thank *Prof. Dambeck* for allowing me to work on this exciting topic and for his continuous support. He always had an open ear and took the time for in-depth technical discussions. Our discussions on technical issues, industry, and professional life will be fondly remembered.

I would like to thank *Prof. Dr.-Ing. Volker Gümmer* for taking over the chair of the examination board and *Prof. Dr.-Ing. Karla Hiller* for her commitment as the second examiner.

Furthermore, I want to thank *Acutronic Switzerland Ltd.* for the kind cooperation with the Institute of Flight System Dynamics. Without this cooperation, this thesis' experimental parts would not have been possible.

Further thanks go to the colleagues at the Institute of Flight System Dynamics. In particular, I want to thank *Monica Kleinloth-Gross* for supporting all organizational matters and keeping the institute operational. I want to thank *Lars Peter, Philip Spiegel, Christoph Göttlicher* and *Chong Wang*. Working with you was a great experience. My special thanks go to the fellow inmates of room MW3615, *Christoph Krause* and *Andreas Kleser*, for the excellent working atmosphere and the numerous technical and non-technical discussions. It has been a joy and honor to work with you.

I sincerely thank my parents for supporting my education and studies. Finally, I want to thank *Julia*, who supported, motivated, and above all, put up with me for years.

Darmstadt, September 2022

Contents

- 1. Introduction** **1**
- 1.1. Motivation 1
- 1.2. Scope of this Thesis 4
- 1.3. State of the Art 6
 - 1.3.1. Inertial Navigation Error Propagation 6
 - 1.3.2. Laboratory Testing of Inertial Sensors 7
- 1.4. Contributions 10
- 1.5. Outline 11

- 2. Preliminaries** **13**
- 2.1. Inertial Sensor Errors 13
 - 2.1.1. Sensor Error Types 13
 - 2.1.2. Inertial Sensor Grades 15
 - 2.1.3. Sensor Error Models 17
- 2.2. Inertial and Integrated Navigation 19
 - 2.2.1. Reference Frames 19
 - 2.2.2. Strapdown Inertial Navigation Principles 22
 - 2.2.3. Integrated Navigation and Data Fusion 25
- 2.3. Signal Analysis and Sensor Noise 28
 - 2.3.1. Power Spectral Density 28
 - 2.3.2. Allan Variance 29
 - 2.3.3. Sensor Noise Processes 31
 - 2.3.4. Confidence Intervals 34

- 3. Strapdown Inertial Navigation Error Propagation** **39**
- 3.1. Introduction 39
- 3.2. Stationary Alignment Errors 40
 - 3.2.1. General 40
 - 3.2.2. Derivation of the Alignment Errors 41
 - 3.2.3. Alignment Uncertainty 43
- 3.3. Strapdown Navigation Error Propagation 47
 - 3.3.1. Navigation Error Dynamics 47
 - 3.3.2. Response to Constant Errors 57
 - 3.3.3. Response to White Noise Sensor Errors 85

3.3.4.	Response to Colored Noise Sensor Errors	95
3.4.	Navigation Performance Prediction	119
3.4.1.	Alignment Uncertainty Charts	119
3.4.2.	A Primer on Positioning Accuracy Measures	122
3.4.3.	Position Uncertainty Charts	126
3.4.4.	Quantitative Performance Prediction Schemes	143
3.5.	Validation of the Predicted Navigation Performance	147
3.5.1.	General	147
3.5.2.	Case 1: General Aviation Aircraft	147
3.5.3.	Case 2: Transatlantic Flight	152
3.6.	Short- and Medium-Term Approximations	157
3.6.1.	Spherical and Non-Rotating Earth	157
3.6.2.	Flat and Non-Rotating Earth	160
3.6.3.	Comparison and Summary	162
4.	Inertial Sensor Laboratory Testing	169
4.1.	Introduction	169
4.2.	Inertial Laboratory Modeling	169
4.2.1.	General Inertial Laboratory Kinematic Model	169
4.2.2.	Ideal Inertial Laboratory Model	173
4.2.3.	IMU Reference Signal Linearized Error Sensitivity	176
4.2.4.	Earth Centered Inertial Frame Approximations	180
4.2.5.	Local Gravity	185
4.2.6.	Laboratory Location	192
4.2.7.	Test Pad and Laboratory Alignment	193
4.2.8.	Test Pad Motion	194
4.2.9.	Rate Table Errors	202
4.2.10.	Summary	227
4.3.	Averaging over Noise Processes	229
4.4.	Laboratory Testing Error Budget	244
4.4.1.	Introduction	244
4.4.2.	Single Position Static Tests	246
4.4.3.	Reversal Position Static Tests	261
4.4.4.	Scale Factor Test-Series	275
4.4.5.	Rate Table Six-Position Tests	294
4.5.	Kalman Filter Based Sensor Testing	316
4.5.1.	KF Design and Modeling	316
4.5.2.	Observability and Trajectory Design	326
4.5.3.	Examples	331

5. Conclusion	345
5.1. Summary	345
5.2. Achievements beyond State-of-the-Art	351
5.3. Outlook	354
Appendices	355
A. Mathematical and mechanical preliminaries	357
A.1. Cross-product building matrix	357
A.2. Time derivative of rotation matrices	357
B. Conversion of Random Walk Measures	359
C. Selected Laplace transformations	361
D. Solutions to the Linearized Error Dynamics	365
D.1. Step Responses	365
D.1.1. Position Errors from Initialization Errors	365
D.1.2. Position Errors from Initial Alignment Errors	367
D.1.3. Position Errors from Sensor Biases	369
D.1.4. Velocity Errors from Initialization Errors	371
D.1.5. Velocity Errors from Initial Alignment Errors	373
D.1.6. Velocity Errors from Sensor Biases	375
D.1.7. Orientation Errors from Initialization Errors	377
D.1.8. Orientation Errors from Initial Alignment Errors	380
D.1.9. Orientation Errors from Sensor Biases	383
D.2. Impulse Responses	389
D.2.1. Position Errors Impulse Responses to Sensor Errors	389
D.2.2. Velocity Errors Impulse Responses to Sensor Errors	392
D.2.3. Orientation Errors Impulse Responses to Sensor Errors	395
E. Validation of the Linearized Error Dynamics	401
E.1. System Response to Initialization Errors	401
E.2. Position Uncertainty from Sensor Noise	416
F. Inertial Laboratory Error Sensitivities	425
G. Overview of IEEE Test Procedures	437
H. Error Sensitivities in Sensor Testing	441
I. Scale Factor Test Series Error Budgets	451
I.1. Test Scenario I	452

I.2. Test Scenario II	454
J. Kalman Filter Noise Models	457
References	461

List of Figures

1.1. Estimated worldwide production volume for military UAVs from 2013 to 2022.	2
1.2. This work in the field of tension between sensor manufacturer and system manufacturer.	3
1.3. Overview of navigation error prediction and compensation at design, production and operation.	5
1.4. Structure of this thesis.	12
2.1. Deterministic sensor error types.	14
2.2. Sensor axis misalignment.	14
2.3. Stochastic sensor errors.	15
2.4. Gyroscope technologies and grades.	16
2.5. Accelerometer technologies and grades.	16
2.6. Geodetic latitude and longitude in the ECEF frame.	21
2.7. General strapdown inertial navigation mechanisation scheme.	23
2.8. General concept of an integrated navigation architecture based on the error state Kalman Filter.	28
2.9. Sensor noise processes in the Allan variance analysis.	34
2.10. Confidence intervals of the overlapping Allan variance estimation for various sensor noise types.	36
3.1. Outline of the Inertial Navigation Error Analysis Chapter.	39
3.2. Earth curvature radii compared to the local spherical approximation.	52
3.3. Velocity influence on the strapdown error dynamics.	56
3.4. Example specific forces measurements of typical aircraft trajectories.	56
3.5. Periods of the linearized strapdown error dynamics.	59
3.6. Block diagram of the vertical fixed, linearized strapdown error dynamics for neglected vehicle motion.	60
3.7. East position error from unit-step initial position and velocity errors.	63
3.8. Development of the horizontal position covariance from initial velocity errors.	64
3.9. Position error from unit-step initial alignment errors.	65
3.10. Development of the horizontal position covariance from uncorrelated initial pitch, roll and yaw alignment error.	66
3.11. Development of the horizontal position covariance from correlated initial pitch, roll and yaw alignment error.	67

3.12. Position error responses to unit-step IMU bias-like errors.	69
3.13. Development of the horizontal position covariance from isotropic accelerometer gyroscope bias-like errors.	70
3.14. North velocity error from unit-step initial position and velocity errors.	71
3.15. East velocity error from unit-step initial position and velocity errors.	72
3.16. Velocity errors from unit-step initial alignment errors.	73
3.17. Velocity error responses to unit-step IMU bias-like errors.	74
3.18. Yaw angle error from unit-step initialization errors.	75
3.19. Attitude angle errors from unit-step initialization errors.	76
3.20. Orientation angle error from unit-step initialization errors.	77
3.21. Development of the attitude covariance over time from 1° (1σ) initial alignment error.	79
3.22. Yaw angle error from unit-step IMU bias-like errors.	80
3.23. Attitude angle error from unit-step IMU bias-like errors.	82
3.24. Development of the attitude covariance over time from $1^\circ/\text{h}$ (1σ) gyro bias and 5 mg (1σ) accelerometer bias.	83
3.25. Position error variance from unit noise-density white Gaussian noise IMU errors.	89
3.26. Development of the horizontal position covariance from isotropic accelerometer and gyroscope white Gaussian noise.	90
3.27. Velocity error variance from unit noise-density white Gaussian noise IMU errors.	91
3.28. Yaw error variance from unit noise-density white Gaussian noise IMU errors. .	92
3.29. Attitude error variance from unit noise-density white Gaussian noise IMU errors.	93
3.30. Development of the attitude covariance from isotropic accelerometer and gyro- scope white Gaussian noise.	94
3.31. Position error variance from quantization noise IMU errors normalized to the quantization noise coefficient Q and $\tau_0 = 1 \text{ s}$	97
3.32. Velocity error variance from quantization noise IMU errors normalized to the quantization noise coefficient Q and $\tau_0 = 1 \text{ s}$	98
3.33. Attitude error variance from quantization noise IMU errors normalized to the quantization noise coefficient Q and $\tau_0 = 1 \text{ s}$	99
3.34. Heading error variance from quantization noise IMU errors normalized to the quantization noise coefficient Q and $\tau_0 = 1 \text{ s}$	100
3.35. Comparison of ideal cutoff and low-pass filter approximation of bias instability noise for a cut-off frequency $f_c = 0.1 \text{ Hz}$	102
3.36. Position error variance from bias instability IMU errors normalized to the bias instability coefficient B	103
3.37. Velocity error variance from bias instability IMU errors normalized to the bias instability coefficient B	104
3.38. Attitude error variance from bias instability IMU errors normalized to the bias instability coefficient B	105

3.39. Heading error variance from bias instability IMU errors normalized to the bias instability coefficient B	106
3.40. Position error variance from rate random walk IMU errors normalized for the rate random walk coefficient K	108
3.41. Velocity error variance from rate random walk IMU errors normalized for the rate random walk coefficient K	109
3.42. Heading error variance from rate random walk IMU errors normalized for the rate random walk coefficient K	110
3.43. Attitude error variance from rate random walk IMU errors normalized for the rate random walk coefficient K	111
3.44. Position error variance from rate and acceleration ramp IMU errors normalized to the bias instability coefficient B	113
3.45. Velocity error variance from rate and acceleration ramp IMU errors normalized to the bias instability coefficient B	114
3.46. Attitude error from rate and acceleration ramp IMU errors normalized to the bias instability coefficient B	115
3.47. Heading error from rate and acceleration ramp IMU errors normalized to the bias instability coefficient B	116
3.48. Impulse response of the latitude error from angular rate error input $\delta\omega_{ib,e}$. . .	117
3.49. Attitude alignment accuracy from inertial sensor residual errors during alignment.	119
3.50. Azimuth alignment accuracy from inertial sensor residual errors during alignment.	120
3.51. Azimuth alignment accuracy from inertial sensor residual errors during alignment.	121
3.52. Position accuracy measures for circular and ellipsoidal covariance matrices. . .	123
3.53. Statistical interpretation of the DRMS and 2DRMS value.	125
3.54. Example cumulative maximum error vs. error.	126
3.55. Time to 10 NM 2DRMS position uncertainty from initial velocity errors.	128
3.56. Time to 1 NM 2DRMS position uncertainty from initial velocity errors.	129
3.57. Time to 10 m 2DRMS position uncertainty from initial velocity errors.	130
3.58. Time to 10 NM 2DRMS position uncertainty from initial alignment errors. . . .	132
3.59. Time to 1 NM 2DRMS position uncertainty from initial alignment errors. . . .	133
3.60. Time to 10 m 2DRMS position uncertainty from initial alignment errors.	134
3.61. Time to 10 NM 2DRMS position uncertainty from IMU bias-like errors.	136
3.62. Time to 1 NM 2DRMS position uncertainty from IMU bias-like errors.	137
3.63. Time to 10 m 2DRMS position uncertainty from IMU bias-like errors.	138
3.64. Time to 10 NM 2DRMS position uncertainty from IMU white Gaussian noise. .	140
3.65. Time to 1 NM 2DRMS position uncertainty from IMU white Gaussian noise. .	141
3.66. Time to 10 m 2DRMS position uncertainty from IMU white Gaussian noise. . .	142

3.67. Workflow of the Monte Carlo simulation to validate the navigation performance prediction schemes.	148
3.68. Visualization of the simulated general aviation flightpath. The red circle demarks the start of the trajectory, the blue cross the end.	148
3.69. Comparison of simulation results and predicted errors of the position and velocity for the simulated general aviation scenario.	150
3.70. Comparison of simulation results and predicted errors of the orientation angles for the simulated general aviation scenario.	151
3.71. Departure trajectory and heading of the transatlantic example flight.	153
3.72. Comparison of simulation results and predicted errors of the position and velocity for the simulated transatlantic flight scenario.	154
3.73. Comparison of simulation results and predicted errors of the orientation angles for the simulated transatlantic flight scenario.	155
3.74. Comparison of different approximations for the north position error from initialization errors.	164
3.75. Comparison of different approximations for the north position error from inertial measurement errors.	165
3.76. Comparison of different approximations for the roll angle error.	166
4.1. Kinematic chain of the inertial laboratory.	171
4.2. Definition of reference frames used in the inertial laboratory kinematic model.	174
4.3. Celestial and terrestrial motion of the Earth's rotation axis.	182
4.4. Difference between the Earth's angular rate vector in the e-Frame as defined by the WGS84 and the ones derived from the IERS EOP observations and models.	183
4.5. Deviations from the WGS84 normal gravity from the standard gravity value.	186
4.6. Global free air gravity anomalies as modeled in the EGM2008.	187
4.7. Earth's surface, geoid and reference ellipsoid with the normal gravity γ and true gravity g	188
4.8. Deflection from the vertical as modeled in the EGM2008.	189
4.9. Tidal acceleration at the Institute of Flight System dynamics according to the tidal scheme of Longman.	190
4.10. Seismic surface waves.	195
4.11. Overview of translatory and rotatory seismic background noise spectra.	197
4.12. Schematic illustration of a passively isolated and an actively stabilized test pad.	200
4.13. Rotatory motion of the test pad due to surface wave excitation.	200
4.14. Example frequency response of the test pad to indirect excitation from surface waves.	200
4.15. Rate table axes orientation and displacement errors.	202
4.16. Axis rocking $\delta\alpha$ and displacement δr from bearing deflections.	207
4.17. Surface waviness of different bearing technologies.	208

4.18. Frequency response of the linearized bearing dynamics.	209
4.19. Amplitude spectrum of the bearing wobble model for different rotation rates.	211
4.20. Exemplary rate table servo loop scheme.	221
4.21. Example of simulated inductosyn measurement errors.	222
4.22. Variance of signal cluster means.	229
4.23. Allan variance with dead-time of bias instability noise for varying cut-off frequencies.	234
4.24. Allan-covariance of the first five clusters of bias instability noise.	239
4.25. Static testing of an IFOS-500 IMU on a measurement plate.	246
4.26. Inertial sensor orientation at static testing.	247
4.27. Allan deviation of the reference environmental background noise and typical sensor noise processes.	250
4.28. Bias determination in the presence of rate random walk noise.	258
4.29. Positions for static reveal measurements.	261
4.30. Two-position static test gyroscope error variance from sensor noise.	264
4.31. Two-position static test accelerometer error variance from sensor noise.	265
4.32. Non-linear input-output relation and hysteresis.	275
4.33. Scale-factor test series gyroscope error variance from sensor noise.	279
4.34. IFOS-500 IMU mounted to a three-axis rate table.	281
4.35. Possible instrument configurations for gyroscope scale factor testing.	282
4.36. Angular rate error from axis tilt. Comparison of the contributions of Earth angular rate and nominal rotation rates with the tilt angle Θ	286
4.37. Six-position testing of an inertial sensor using a three-axis positioning and rate table.	294
4.38. Six position test sensor error variance from sensor noise.	300
4.39. General concept of Kalman Filter based laboratory calibration.	316
4.40. Laboratory sensor calibration using a Schmidt-Kalman filter.	319
4.41. Flicker noise approximation using filter cascade.	320
4.42. Example of the sensor's input angular rates for a constant-rate multi-axes rate table motion.	331
4.43. Estimation results for the outer axis constant rate test case.	334
4.44. Estimation results for the middle axis constant rate test case.	335
4.45. Estimation results for the outer and middle axis constant rate test case.	336
4.46. Estimation results for the all axes constant rate test case.	337
4.47. Estimation results for the scale factor test series.	339
4.48. Estimation results for the six-position test series.	340
4.49. Estimation errors for varying time delay between rate table and sensor signals.	341
5.1. Summary of gyroscope error model terms and test procedures covered in this thesis.	349

5.2. Summary of accelerometer error model terms and test procedures covered in this thesis.	350
5.3. This work's contributions in the context of the development processes.	353
E.1. North position errors of linearized step response and numerical simulation. . .	403
E.2. East position errors of linearized step response and numerical simulation. . . .	405
E.3. North velocity errors of linearized step response and numerical simulation. . .	407
E.4. East velocity errors of linearized step response and numerical simulation. . . .	409
E.5. Roll angle errors of linearized step response and numerical simulation.	411
E.6. Pitch angle errors of linearized step response and numerical simulation.	413
E.7. Yaw angle errors of linearized step response and numerical simulation.	415
E.8. Analytical north position error variance for White Gaussian Noise (WGN) compared to Monte Carlo simulatio.	417
E.9. Analytical east position error variance for WGN compared to Monte Carlo simulation.	418
E.10. Analytical north velocity error variance for WGN compared to Monte Carlo simulatio.	419
E.11. Analytical east velocity error variance for WGN compared to Monte Carlo simulation.	420
E.12. Roll angle error variance for WGN compared to Monte Carlo simulation. . . .	421
E.13. Pitch angle error variance for WGN compared to Monte Carlo simulation. . . .	422
E.14. Yaw angle error variance for WGN compared to Monte Carlo simulation. . . .	423

List of Tables

1.1. List of IEEE standards on Inertial Sensor specification and testing.	8
2.1. Error terms in the IEEE model equations for gyroscopes.	18
2.2. Definition of the ECI Frame.	20
2.3. Definition of the ECEF Frame.	21
2.4. Defining parameters of the WGS84 model.	21
2.5. Definition of the NED Frame.	22
2.6. Definition of the Body Fixed Frame.	22
2.7. Typical sensor noise processes from the IEEE standards.	33
2.8. Correction factors for Allan variance confidence intervals.	34
2.9. Approximations of the overlapping Allan variance equivalent degrees of freedom.	35
3.1. System matrix of the linearized strapdown error dynamics.	50
3.2. Latitude dependency of the strapdown error step responses.	84
3.3. Maximum mission time that allows for neglecting the gyro bias instability for different sensor grades.	117
3.4. Typical horizontal position accuracy measures.	122
3.5. Position Uncertainty Prediction Scheme.	144
3.6. Velocity Uncertainty Prediction Scheme.	145
3.7. Orientation Uncertainty Prediction Scheme.	146
3.8. Parameters of the general aviation aircraft scenario.	147
3.9. Specification of the input errors for the general aviation aircraft scenario simu- lation.	149
3.10. Dynamics of the commercial transatlantic flight scenario.	152
3.11. Specification of the input errors for the transatlantic flight scenario simulation.	152
3.12. Medium term analytical solutions to the strapdown error dynamics for position and velocity errors.	158
3.13. Medium term analytical solutions to the strapdown error dynamics for orienta- tion errors.	159
3.14. Short term analytical solutions to the strapdown error dynamics.	161
3.15. Comparison of approximations of the strapdown error dynamics.	163
4.1. Maximum tidal accelerations on the Earth's surface due to celestial bodies.	190
4.2. Fundamental frequencies of rolling element bearings.	209

4.3. Bearing vibration frequencies from waviness.	210
4.4. Summary of error parameters in the laboratory model.	228
4.5. Variances of power-law sensor noise processes.	233
4.6. Overview of basic test procedures.	244
4.7. Errors of sensor noise process parameters from reference background noise from a least-squares fit of the static test input errors.	251
4.8. Gyro static testing bias error budget.	258
4.9. Accelerometer static testing bias error budget.	260
4.10. Reversal measurement gyro test scale factor estimation error budget.	266
4.11. Reversal measurement gyro test axis misalignment M_{xy} estimation error budget.	267
4.12. Reversal measurement gyro test axis misalignment M_{xz} estimation error budget.	268
4.13. Reversal measurement gyro test bias estimation error budget.	269
4.14. Reversal measurement accelerometer test scale factor estimation error budget.	271
4.15. Reversal measurement accelerometer test axis misalignment M_{xy} estimation error budget.	272
4.16. Reversal measurement accelerometer test axis misalignment M_{xz} estimation error budget.	273
4.17. Reversal measurement accelerometer test bias estimation error budget.	274
4.18. Error sensitivities in scale factor test scenarios.	285
4.19. Scale-factor test rate series considered in the error budgets.	288
4.20. Gyro scale factor test series scale factor error budget.	289
4.21. Gyro scale factor test series bias error budget for scenario I.	290
4.22. Rate table six-position gyro test scale factor estimation error budget.	302
4.23. Rate table six-position gyro test axis misalignment M_{xy} estimation error budget.	304
4.24. Rate table six-position gyro test axis misalignment M_{xz} estimation error budget.	305
4.25. Rate table six-position gyro test bias estimation error budget.	307
4.26. Rate table six-position accelerometer test scale factor estimation error budget. .	310
4.27. Rate table six-position accelerometer test axis misalignment M_{xy} estimation error budget.	312
4.28. Rate table six-position accelerometer test axis misalignment M_{xz} estimation error budget.	313
4.29. Rate table six-position accelerometer test bias estimation error budget.	314
4.30. Observability of sensor errors for different rate table motions.	329
4.31. Sensor noise parameters for the KF-based sensor testing examples.	331
4.32. Laboratory model parameters for the Kalman Filter based sensor testing examples.	332
4.33. Initialisation for Kalman Filter based sensor testing examples.	332
4.34. Comparison of KF-based testing with classical test procedures.	338
5.1. Overview of the resulting navigation errors from initialization and sensor errors.	346
B.1. Conversion of Angular Random Walk Measures.	359

B.2. Conversion of Velocity Random Walk Measures.	360
C.1. Selected Laplace transforms	361
D.1. Latitude error step responses to position and velocity initialization errors. . . .	365
D.2. Longitude error step responses to position and velocity initialization errors. . .	366
D.3. Latitude error step responses to initial alignment errors.	367
D.4. Longitude error step responses to initial alignment errors.	368
D.5. Latitude error step responses to Inertial Measurement Unit (IMU) biases. . . .	369
D.6. Longitude error step responses to IMU biases.	370
D.7. North velocity error step responses to position and velocity initialization errors.	371
D.8. East velocity error step responses to position and velocity initialization errors. .	372
D.9. North velocity error step responses to initial alignment errors.	373
D.10. East velocity error step responses to initial alignment errors.	374
D.11. North velocity error step responses to IMU biases.	375
D.12. East velocity error step responses to IMU biases.	376
D.13. Roll angle error step responses to position and velocity initialization errors. . .	377
D.14. Pitch angle error step responses to position and velocity initialization errors. .	378
D.15. Yaw angle error step responses to position and velocity initialization errors. . .	379
D.16. Roll angle error step responses to initial alignment errors.	380
D.17. Pitch angle error step responses to initial alignment errors.	381
D.18. Yaw angle error step responses to initial alignment errors.	382
D.19. Roll angle error step responses to accelerometer biases.	383
D.20. Roll angle error step responses to gyroscope biases.	384
D.21. Pitch angle error step responses to accelerometer biases.	385
D.22. Pitch angle error step responses to gyroscope biases.	386
D.23. Yaw angle error step responses to accelerometer biases.	387
D.24. Yaw angle error step responses to gyroscope biases.	388
D.25. Latitude error pulse responses to accelerometer errors.	389
D.26. Latitude error impulse responses to gyroscope errors.	390
D.27. Longitude error impulse responses to accelerometer errors.	390
D.28. Longitude error impulse responses to gyroscope errors.	391
D.29. North velocity error impulse responses to accelerometer errors.	392
D.30. North velocity error impulse responses to gyroscope errors.	393
D.31. East velocity error impulse responses to accelerometer errors.	393
D.32. East velocity error impulse responses to gyroscope errors.	394
D.33. Roll angle error impulse responses to accelerometer errors.	395
D.34. Roll angle error impulse responses to gyroscope errors.	396
D.35. Pitch angle error impulse responses to accelerometer errors.	397
D.36. Pitch angle error impulse responses to gyroscope errors.	398
D.37. Yaw angle error pulse responses to accelerometer errors.	399

D.38. Yaw angle error pulse responses to gyroscope errors.	400
F.1. Earth angular rate.	425
F.2. Local gravity.	425
F.3. Rotation of the local NED reference frame with respect to the ECEF frame.	426
F.4. Rotation of the test pad with respect to the local reference frame.	427
F.5. Position of the test pad with respect to the local reference frame.	428
F.6. Rotation of the outer gimbal with respect to the test pad.	429
F.7. Position of the outer gimbal with respect to the test pad.	430
F.8. Rotation of the middle gimbal with respect to the outer gimbal.	431
F.9. Position of the middle gimbal with respect to the outer gimbal.	432
F.10. Rotation of the inner gimbal with respect to the middle gimbal.	433
F.11. Position of the inner gimbal with respect to the middle gimbal.	434
F.12. Rotation and orientation of the UUT.	435
F.13. Position of the UUT with respect to the inner gimbal.	436
G.1. IEEE test procedures related to the gyroscope accuracy.	438
G.2. IEEE accelerometer test procedures related to the accelerometer accuracy.	439
H.1. Error sensitivities of the gyroscope x-axis input during the six-position test.	442
H.2. Error sensitivities of the gyroscope y-axis input during the six-position test.	443
H.3. Error sensitivities of the gyroscope z-axis input during the six-position test.	444
H.4. Error sensitivities of the accelerometer x-axis input during the six-position test.	445
H.4. Error sensitivities of the accelerometer x-axis input during the six-position test, continued.	446
H.5. Error sensitivities of the accelerometer y-axis input during the six-position test.	447
H.5. Error sensitivities of the accelerometer y-axis input during the six-position test, continued.	448
H.6. Error sensitivities of the accelerometer z-axis input during the six-position test.	449
H.6. Error sensitivities of the accelerometer z-axis input during the six-position test, continued.	450
I.1. Gyro scale factor test series scale factor error budget for scenario I.	452
I.2. Gyro scale factor test series bias error budget for scenario I.	453
I.3. Gyro scale factor test series scale factor error budget for scenario II.	454
I.4. Gyro scale factor test series bias error budget for scenario II.	455
J.1. Test pad angular rates reference model approximation.	458
J.2. Test pad tilt angles reference model approximation.	459
J.3. Test pad acceleration reference model approximation.	460

List of Results

1. Inertial Navigation Error Propagation	118
2. Navigation Performance Prediction	156
3. Short- and Medium-Term Approximations of the Strapdown Error Dynamics . . .	167
4. Sensor Noise Identification.	256
5. Bias Determination from Single-Position Static Tests.	259
6. Reversal Position Static Tests	274
7. Gyroscope Scale-Factor Tests	293
8. Six-Position Testing	315
9. Kalman Filter-Based Testing	343

List of Examples

1. Rate table axis wobble in the PSD of a three-axis gyro measurement.	213
2. Rate table axis wobble in the PSD of a three-axis accelerometer measurement. . .	214
3. Power spectral density of rate table position and rate measurements.	224
4. Allan variance analysis of IFOS-500 IMU.	253
5. Dynamic Allan variance of IFOS-500 IMU noise.	254
6. Spectrogram of IFOS-500 IMU noise.	255
7. The effect of gyroscope drift on the scale factor estimation	280
8. Comparison of Scale-factor test scenarios	291
9. IMU 500 Scale Factor Estimation	292
10. IMU 500 Six-Position Test	306

List of Algorithms

1. Conventional Kalman filter	25
2. Extended Kalman filter	26
3. Schmidt-Kalman Filter	27
4. Welch's power spectral density estimator.	30
5. Overlapping Allan variance estimator.	31

List of Models

1. Earth rotation error modeling.	184
2. Gravity error modeling.	191
3. Local leveled reference frame errors.	192
4. Laboratory alignment errors.	194
5. Test pad motion.	201
6. Static rate table errors.	206
7. Rate table axis wobble modeling.	215
8. Rate table deformation und load model.	218
9. Rate table thermal expansion model.	220
10. Rate table positioning and rate error models.	226
11. Quantization Noise	319
12. Angular/Velocity Random Walk	320
13. Bias Instability	321
14. Rate/Acceleration Random Walk	322
15. Oscillating Errors	323
16. Random Constant Errors	324
17. Testpad Motion Model	325
18. Axis Wobble	325
19. Rate Table Positioning and Rate Error	326

List of symbols

Scalars

η	Normal deflection of the local gravity vector.	$h_{n,m}(t)$	Step response of output state n to input state m in the time domain.
$f_{b,d}$	Specific forces in local down direction.	λ	Geodetic longitude.
$f_{b,e}$	Specific forces in local east direction.	$\omega_{ib,d}$	Angular rate of the body with respect to the inertial frame in local down direction.
$f_{b,n}$	Specific forces in local north direction.	$\omega_{ib,e}$	Angular rate of the body with respect to the inertial frame in local east direction.
$f_{b,x}$	Specific forces in body fixed x-direction.	$\omega_{ib,n}$	Angular rate of the body with respect to the inertial frame in local north direction.
$f_{b,y}$	Specific forces in body fixed y-direction.	$\omega_{ib,x}$	Angular rate of the body with respect to the inertial frame in body-fixed x-direction.
$f_{b,z}$	Specific forces in body fixed z-direction.	$\omega_{ib,y}$	Angular rate of the body with respect to the inertial frame in body-fixed y-direction.
f_s	Sample rate.	$\omega_{ib,z}$	Angular rate of the body with respect to the inertial frame in body-fixed z-direction.
g_0	Standard Earth gravity.	ω_{ie}	Nominal Earth angular rate.
$G_{n,m}(s)$	Pulse response of output state n to input state m in the Laplace domain.	Φ	Roll Euler angle.
$g_{n,m}(t)$	Pulse response of output state n to input state m in the time domain.	ϕ	Geodetic latitude.
h	Geodetic altitude.	Ψ	Yaw Euler angle.
$H_{n,m}(s)$	Step response of output state n to input state m in the Laplace domain.	r_M	Local meridional radius of the Earth's curvature.

r_N	Local normal radius of the Earth's curvature.		
σ_n	Standard deviation of state n .	v_e	Velocity in east direction.
σ_n^2	Variance of state n .	v_n	Velocity in north direction.
t	Time.	x_d	Local position in down direction, negative altitude error.
τ_s	Sample time.	x_e	Local position in east direction.
t_e	End time of signal.	x_n	Local position in north direction.
Θ	Pitch Euler angle.	ξ	Meridional deflection of the local gravity vector.
v_d	Velocity in down direction, neg-		

Vectors

\mathbf{f}_b	Vector of specific forces.	ω_{wv}	Angular rate of the middle gimbal with respect to the outer gimbal.
$\boldsymbol{\gamma}$	Local gravity vector.		
ω_{ie}	Vector of angular rates of the NED frame with respect to the Earth fixed frame (transport rate).	$\boldsymbol{\Psi}_{nb}$	Vector of Euler rotation angles from the body fixed frame to the NED frame.
ω_{ib}	Vector of angular rates of the body with respect to the inertial frame.	$\boldsymbol{\Psi}_{n\hat{n}}$	Vector of Euler angles from idealized to true local NED frame.
ω_{ie}	Vector of angular rates of the Earth fixed frame with respect to the inertial frame.	$\boldsymbol{\Psi}_{p\hat{p}}$	Vector of Euler angles from idealized to true test-pad-frame.
ω_{np}	Angular rate of the test pad with respect to the local NED frame.	$\boldsymbol{\Psi}_{u\hat{u}}$	Vector of Euler angles from idealized to true inner gimbal frame.
ω_{pw}	Angular rate of the outer gimbal with respect to the test pad.	$\boldsymbol{\Psi}_{v\hat{v}}$	Vector of Euler angles from idealized to true middle gimbal frame.
ω_{ub}	Angular rate of the sensor body with respect to the inner gimbal.	$\boldsymbol{\Psi}_{w\hat{w}}$	Vector of Euler angles from idealized to true outer gimbal frame.
ω_{vu}	Angular rate of the inner gimbal with respect to the middle gimbal.	\mathbf{v}_n	Vector of the velocity in the local NED reference frame.

Matrices

I	Identity matrix.	R_{bu}	Rotation matrix from the inner gimbal's to the sensor's body fixed frame.
M	Mass moment of inertia.	R_{nb}	Rotation matrix from the body fixed frame to the NED frame.
Ω_{en}	Skew symmetric matrix of the angular rates of the NED frame with respect to the Earth fixed frame.	R_{ne}	Rotation matrix from the Earth fixed frame to the NED frame.
Ω_{ib}	Skew symmetric matrix of the angular rates of the body with respect to the inertial frame.	R_{pn}	Rotation matrix from the local NED frame to the test pad's frame.
Ω_{ie}	Skew symmetric matrix of the angular rates of the Earth fixed frame with respect to the inertial frame.	R_{uv}	Rotation matrix from the middle gimbal's to the inner gimbal's frame.
P	State covariance matrix.	R_{vw}	Rotation matrix from the outer gimbal's to the middle gimbal's frame.
Q	Measurement covariance matrix.	R_{wp}	Rotation matrix from the test pad to the outer gimbal's frame.

Others

δ	Error state .	z̃	Measured state .
		ẑ	Ideal / estimated state .

Chapter 1.

Introduction

1.1. Motivation

This thesis discusses the effects of sensor errors in strapdown inertial navigation and the laboratory test and calibration of these errors. Inertial navigation and the corresponding sensors are a mature technology that has been widely used since the 1950s, with its roots in the early 20th century. Likewise, the research on the propagation of sensor errors and the test of inertial sensors have a long history and could be considered as *completed*. Still, two trends in navigation technology and applications justify, in the author's opinion, a revisit of the effects and testing of inertial sensor errors.

The Development of Extremely Accurate Inertial Sensors

By providing a global source for timing and positioning, the [Global Navigation Satellite Systems](#) became the prime navigation source in civil and military applications. Still, some applications and environments do not allow the use of [GNSS](#) as its signals cannot be received indoors or underwater. Additionally, the vulnerability of [GNSS](#) to intentional disturbances has been observed in conflict situations [1]. The need for [GNSS](#)-independent precision positioning and timing sources is widely acknowledged and led to several development programs on inertial sensors and mobile atomic clocks based on quantum technology:

- The U.S. Department of Defense started multiple programs to develop future inertial sensors as part of their [PNT](#) strategy, including the *Adaptable Navigation Systems (ANS)* and the *Quantum-Assisted Sensing and Readout (QUaSAR)* programs [2].
- The *UK Quantum Technology Hub in Sensors and Metrology* shall boost the development of quantum inertial sensors as part of the UK National Quantum Technologies Programme. UK plans to provide funding of GBP 270 million on quantum technologies [3].
- The *European Union Quantum Manifest* lists the development of a hand-held quantum navigator providing less than 1 mm/day drift within the next ten years as a research goal. EU planned to spend EUR 1 billion on quantum technologies within the Horizon 2020 framework [4].

- The People’s Republic of China lists quantum navigation as a high-priority research target within its thirteenth Five-Year Science and Technology Innovation Plan [5].

The prospective inertial sensors are expected to provide new levels of accuracy, e.g., a cold atom gyroscope with a drift of $10^{-5} \text{ }^\circ \text{ h}^{-1}$ [6]. Such sensor accuracies might allow free-inertial navigation for durations never seen before. This justifies a review of the inertial navigation error propagation for very long times. Furthermore, the calibration and validation of such sensors pose strict requirements on the test laboratory and environment.

Novel Applications and the Urge for Low-cost Sensors

The second trend appears on the opposite side of the inertial sensor accuracy scale, namely in low-cost systems. The growing global market for [Unmanned Aerial Vehicles](#) is expected to reach USD 37 billion in 2025, including USD 11 billion in military, USD 16 billion in commercial and USD 4 billion in consumer applications [7]. As illustrated in [Figure 1.1](#), the segment of mini-UAVs shows the highest growth rates in the military sector. The same accounts for the civil market, where the size and costs of the [UAVs](#) are often very limited. The rapidly increasing number of small [UAVs](#) leads to increasing demand for small, lightweight, and low-cost inertial sensors and systems for both control and navigation.

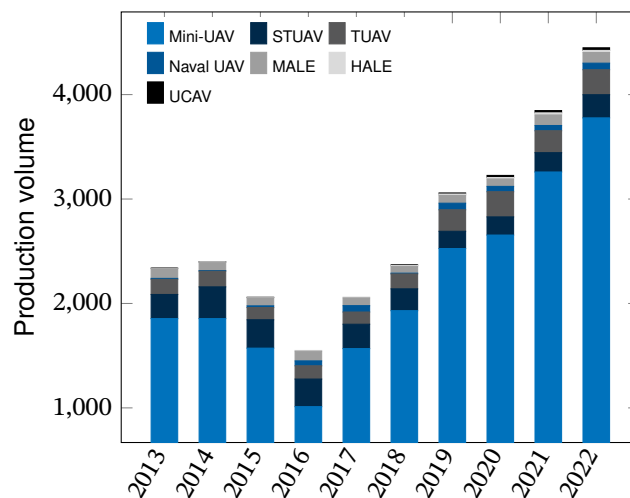


Figure 1.1.: Estimated worldwide production volume for military UAVs from 2013 to 2022 [8].

This growing market comes with a large number of systems to be designed. The need for low-cost components drives a shift from the classical aerospace inertial sensors toward the mass market, e.g., automotive products. Furthermore, modern applications do not necessarily fit well into the established concept of *sensor grades* based on the sensors’ military heritage. Instead, understanding how the required sensor accuracy depends on the navigation requirements is needed to select suitable sensors for a given application. The same accounts for the testing and calibration of inertial sensors. Traditional aerospace sensors are thoroughly tested using high-accuracy equipment, but whether such an effort is justified for every sensor’s accuracy

must be questioned. Test procedures and equipment adapted to the desired sensor accuracy may provide cost savings appreciated by these new applications and markets.

Thus, this thesis aims to promote a better understanding between the sensor and system manufacturers. As depicted in Figure 1.2, the topics covered in this work affect both parties linked through the sensor selection process, procurement, (customized) calibration, and acceptance testing on both sides.

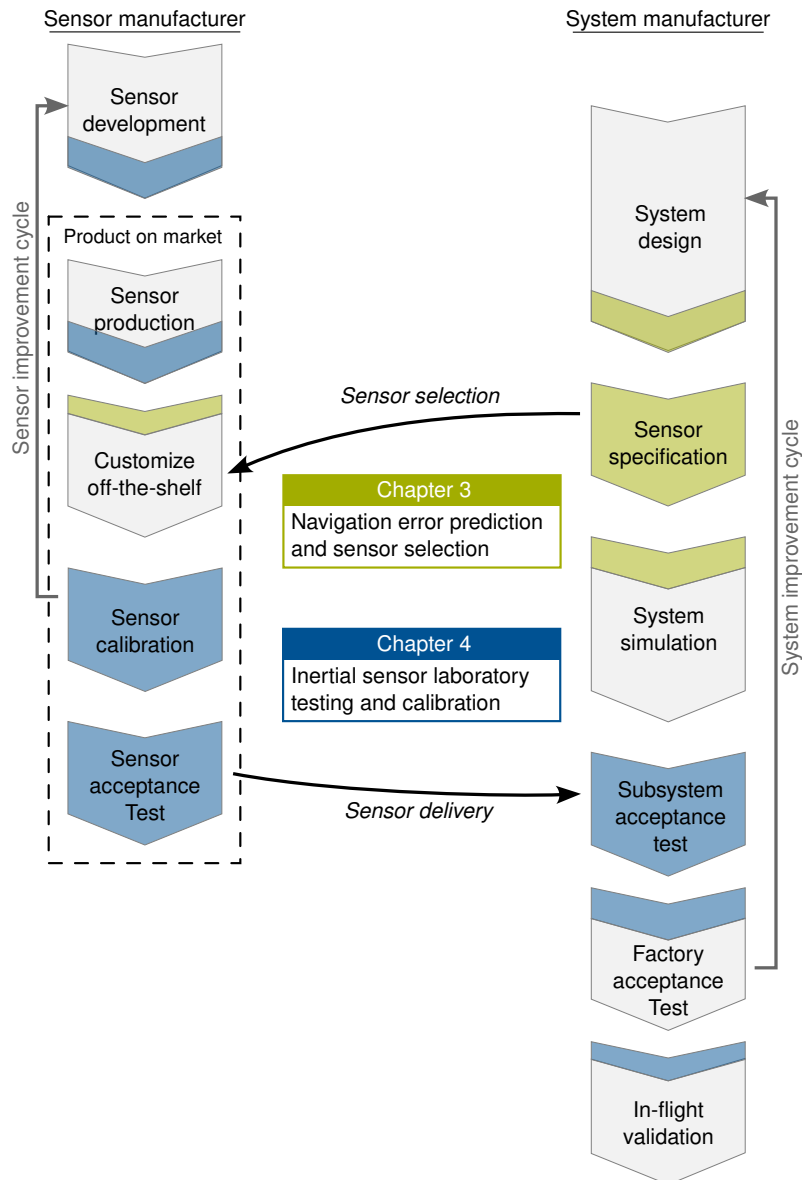


Figure 1.2.: This work in the field of tension between sensor manufacturer and system manufacturer.

In an early stage of system development, the sensor requirements must be specified from the system's navigation requirements. These requirements are used to select typically market-available sensors that may undergo customization, e.g., adaption of the packaging or specific calibration. Chapter 3 presents an analytical navigation error prediction that supports the process of a sensor requirement specification.

The sensor manufacturer, on the other side, requires multiple forms of laboratory sensor testing and calibration at nearly every stage of the sensor's life cycle, but especially during the calibration and acceptance testing of produced sensors. This sensor calibration usually requires highly accurate laboratories. The requirements for the laboratory's accuracy for a desired sensor calibration accuracy are discussed in [Chapter 4](#). Complementary to the sensor manufacturer's tests, the system manufacturer performs sensor tests, typically at the subsystem level. However, these tests are performed at less depth and accuracy than the manufacturer's sensor calibration.

This work shall also help to improve mutual understanding between the sensor manufacturers and system designers.

1.2. Scope of this Thesis

This thesis aims to review the topic of inertial sensor performance, testing, and calibration. In doing so, the work focuses on answering the following two fundamental questions:

1. **How can the required inertial sensor accuracy be derived from the navigation requirements?**

Selecting suitable inertial sensors is crucial in designing inertial and integrated navigation systems and applications. This requires knowledge about how different sensor errors are propagated within the inertial navigation algorithms. Based on these propagation equations, the acceptable sensor errors can be determined for the desired navigation requirement, e.g., position error after a given time. This thesis aims to develop long-term analytical solutions to the error dynamics and provide easy-to-use methods for assessing the required sensor accuracy. These methods are not meant to replace the final validation of operational performance using high-detail models and Monte Carlo simulations but to support the definition of sensor requirements in an early development phase.

2. **How can the required sensor accuracy be tested in the laboratory?**

The determination of inertial sensor errors under specified conditions is the basis for the verification of sensor accuracy. Since calibration compensates for deterministic errors found during testing at varying conditions, it is just an application of the tests' results. This thesis focuses on deriving error budgets for inertial sensor testing in the laboratory. They allow the requirements on laboratory instruments and environmental conditions to be determined from the desired sensor accuracy.

[Figure 1.3](#) illustrates the placement of this work's main chapters within the design, production, and operation of an inertial and integrated navigation system. The graphic shows the limits of the analytical navigation error propagation from [Chapter 3](#) compared to a covariance propagation or even a Monte-Carlo simulation. The stationary analytical error prediction is widely independent of the trajectory and requires only a rough knowledge of the latitude and

assumptions on typical maneuvers for the dynamic-dependent errors. In contrast, the simulation requires complete trajectories representative of the desired application. Monte-Carlo simulation is used in this work to validate the analytically predicted results.

Furthermore, the graphic illustrates the limits of sensor error compensation at the laboratory and the compensation of navigation errors in-flight. The accuracy of classical laboratory testing and calibration procedures is discussed in Chapter 4. The chapter concludes with the design of a Kalman Filter-based sensor error estimation, which can also be used to validate the classical test procedures due to its generality.

Due to the trajectory-dependency and usually limited aiding accuracy, the in-flight calibration represents a possibility but is not a guarantee for navigation error compensation. This emphasizes the importance of good sensor design (e.g., error repeatability) and laboratory calibration.

		Inertial sensor specification and selection		IEEE sensor error models		Production	Operation		
		Navigation error prediction		Accel	Gyro	Sensor error reduction	Nav error reduction		
		Stationary analytical	Dynamic simulation	PA [12]	MEMS [12]	RLG [9]	FOG [10]	CVG [11]	Laboratory calibration
	Trajectory dependency	<i>lineariz. point, (maneuvers)</i>	<i>representative trajectory req.</i>						<i>defines error observability</i>
Initialis. errors	Initial position	<i>within linearization assumptions</i>	<i>without further assumptions</i>						<i>compensation</i>
	Initial velocity								
	Initial orientation								
Sensor Errors	Dynamic-independent	Bias-like	Fixed bias	<i>lump-sum, based on linearization and further assumptions</i>	<i>assumptions on environmental conditions</i>	.	.	<i>identification and compensation*</i>	<i>estimation and compensation</i>
			Temperature sens.			.	.		
			T. gradient sens.			.	.		
			T. rate sens.			.	.		
			T. grad. rate sens.			.	.		
	Vibration sens.	.	.						
	BB noise sens.			.	<i>identification</i>				
	Struct. resonance			.					
	Dynamic-dependent	Noise-like	Quantization	<i>within linearization assumptions</i>	<i>without further assumptions</i>	.	.	<i>stochastic characterization</i>	<i>consideration but no compensation</i>
			Angle/Vel. RW			.	.		
Bias instability			.			.			
Rate/Acc. RW	.	.							
Rate/Acc. ramp	.	.							
Dynamic-dependent		Misalignment	<i>lump-sum bias-like for stationary conditions only</i>	<i>assumptions on environmental conditions</i>	.	.	<i>identification and compensation*</i>	<i>estimation and compensation - observability depends on trajectory</i>	
		SF nonlinearity			.	.			
		SF error			.	.			
		SF temp. sens.			.	.			
SF T. grad. sens.	.	.							
Accel. sens.			.	<i>identification</i>					
		Chapter 3 App. A - E		validation			Chapter 4 App. F - J		validation

*compensation of repeatable errors

Figure 1.3.: Overview of navigation error prediction and compensation at design, production and operation.

1.3. State of the Art

1.3.1. Inertial Navigation Error Propagation

The analysis of the inertial navigation algorithms is as old as the algorithms themselves. It is well known that the inherent integration of the measured accelerations and angular rates causes inertial navigation systems' navigation states (e.g., position) to drift with time. Due to the interaction of the different states, the errors of the navigation states are subject to complex dynamics that shape the propagation of initialization and sensor errors. A typical inertial navigation performance requirement is the maximum position error after a given time of unaided inertial navigation. For many applications, the free inertial position error propagation also defines the maximum acceptable GNSS outage time.

The general concepts of Inertial Navigation System (INS) error propagation are well covered by standard text books like [13, Ch. 5.5 and 5.6], [14, Ch. 12], [15, Ch. 5], [16, Ch. 5] [17, Ch. 7.3]. Due to their dominant role, these works and this thesis only cover strapdown inertial navigation systems ¹. A comprehensive treatment of analytical solutions to the navigation error dynamics can be found in [20, Ch. 13]. Still, above mentioned works only provide short- and medium-term approximations for the error dynamics by neglecting the Earth's angular rate and coupling between the horizontal channels. Although the proposed solutions are called "long term" solutions within the works, their validity is stated as either "up to about 4 hours" [13, p. 155] [14, p. 374], "much less than 24 hours [...] a couple of hours" [15, p. 161] or only two hours [20, p. 13-1].

The existence of other error dynamics, namely a 24-hour oscillation and the Foucault oscillation, is acknowledged but left to numerical analysis [14, p. 346] or neglected [15, p. 163]. An approximate solution to bias-like sensor errors and initialization errors that incorporates the Earth's angular rate is given in [17, Chapter 7.4]. An approximation-free solution to the strapdown equations of motion is given in [21, pp. 43–53], but lacks a solution for the strapdown error equations and is given in the hard-to-understand e-frame representation.

For the prospect quantum inertial navigators, the available solutions to the error dynamics that are valid for several hours are insufficient. Furthermore, the publications on the error dynamics focus on the position error, neglecting the orientation and velocity states. Within this work, a long-term analytical solution to the strapdown error dynamics is derived that incorporates the effects of the Foucault and 24 hours oscillations for all navigation states.

The analytical treatment of the strapdown error dynamics allows a deep insight into the propagation of sensor errors and results in simple-to-use results. Thus it is very suitable to derive basic statements and to support the sensor selection at an early system design phase. However, the analytical approach is based on approximations and neglects the trajectory-dependent errors. Additionally, many characteristics of the real system, like computational errors, are hard to model analytically. The validation of a system's navigation performances

¹An error analysis for platform inertial systems can be found in [18, Ch. 5.4] and [19, Ch. 8].

thus requires numerical simulations [14, pp. 360–362] and ultimately real-world tests.

1.3.2. Laboratory Testing of Inertial Sensors

1.3.2.1. Tests

In their life, inertial sensors are subjected to several tests. In general, these examinations serve two different purposes:

- **Characterization** tests are used to determine the sensor's behavior in various situations. This means, in particular, investigating various errors, i.e., the deviation from the ideal sensor behavior. These tests are used to verify the sensor's performance against the requirements. Additionally, behavioral and failure models of the sensor can be created for simulations of the entire system. The characterization includes deterministic and non-deterministic (stochastic) sensor errors, from which the deterministic ones can be compensated while the stochastic ones can only be characterized.
- **Calibration** uses the results of the characterization tests to identify deterministic and reproducible errors in the sensor output. These errors can then be compensated by inverting the deterministic sensor error behavior in the sensors electronics respectively digital controller.

Both objectives, characterization, and calibration are performed within different types of tests that include:

- **Qualification tests** ensure the feasibility of a sensor design and that the sensor's performance meets a customer's requirements [22, p. 242]. These tests are the most rigorous to determine the sensor's behavior in various conditions fully [14, p. 220]. Here, the statistics of sensor errors are also examined in detail to select the most critical parameters for acceptance testing and calibration.
- **Acceptance tests** is performed during manufacturing to ensure that the sensor meets the customer's requirements. The tests check a set of selected parameters known to scatter throughout the production. These tests also include the calibration of sensor errors known to vary throughout the production. Acceptance tests may be performed on a single-sensor level or for production batches [14, p. 220]. They are also performed after the maintenance of (high-class) sensors [22, p. 242].
- **Reliability tests** are used to determine the long-term behavior of the sensor. They are performed for random production samples to determine the, e.g., mean time between failures in nominal operation [22, p. 243]. Reliability tests can also include examinations of aging processes, which is the change of sensor characteristics with time. Changes in the sensor characteristics due to aging may be compensated by a regular re-calibration at the manufacturer.

The actual test layout is very diverse and depends on the planned application, the sensor technology, and the manufacturer's philosophy.

1.3.2.2. Standards and Procedures

Since 1969 the *Gyro and Accelerometer Panel of the IEEE Aerospace and Electronic Systems Society* has published multiple standards to guide its members on the specification and testing of inertial sensors (see Table 1.1). With Std. 522 [23] the *Institute of Electrical and Electronics Engineers (IEEE)* provides a comprehensive terminology of inertial sensor technologies, including precise terms and definitions of technologies, specification parameters, and effects. This thesis follows the IEEE terminology where applicable.

Table 1.1.: List of IEEE standards on Inertial Sensor specification and testing.

IEEE Std.	Init. pub. year	Scope
292, 293	1969	Spring-restrained Rate Gyroscopes
517	1974	Rate-Integrating Gyroscopes
529	1980	Strapdown application of Rate-Integrating Gyroscopes
528	1984	Inertial Sensor Terminology
671	1985	Non-gyroscopic Inertial Angular Sensors
813	1988	Dynamically Tuned Gyroscopes
952	1997	Interferometric Fiber-Optic Gyroscopes
1293	1998	Non-Gyroscopic Accelerometers
1431	2004	Coriolis Vibratory Gyroscopes
1554	2005	Recommended Practices for Inertial Sensor Testing
647	2006	Laser Gyroscopes
836	2009	Centrifuge Testing of Accelerometers
2007	2014	General Sensor Performance Parameter Definitions

The major part of the applicable standards consists of *Standard Specification Format Guides and Test Procedures* for the different inertial sensor technologies [9, 11, 12, 10, 24, 25]. These standards define error models for each technology that contain the most critical parameters. The standards include the laboratory test procedures to determine these parameters and a format template for publishing the sensor's specification. A general summary of best practices for inertial sensor testing is given in IEEE Std. 1554 [26]. In addition to hints on test planning and documentation, this standard briefly describes typical inertial sensor testing instruments and their general use. This includes a discussion of rate tables, centrifuges, vibration and shock equipment, and the required data acquisition setup. The standard concludes with a brief discussion of environmental (e.g., geophysical) effects and the required surveying and calibration of an inertial test facility.

Independent of the available standards, there are many publications on inertial sensor calibration and testing. Trends in this field of research are test procedures for low-cost equipment, and the application of novel approaches for sensor error determination, e.g., using machine

learning. A review of 22 current sensor calibration methods is given in [27].

1.3.2.3. Inertial Sensor Test Facilities and Instruments

The development of accurate inertial sensors for navigation starting from the 1950s created the need for high-accuracy testing and calibration facilities. Most publications within cited within this section date back to the 1960s and 1970s. The latest publications provide limited insight into the current state of the art, which is expected given the military significance of inertial navigation.

Test instruments like rate tables and dividing heads are well within the scope of mechanical and precision engineering. The few publications explicitly covering the design of inertial sensor testing equipment consequently focus on the construction aspects to provide the desired positioning accuracy and rate stability, e.g., [28]. However, they do not discuss how these requirements relate to the desired test accuracy.

In the development of increasingly accurate inertial sensors, the design and verification of a sufficiently stable (vibration-less) laboratory environment posed a new problem to the sensor developers. To decouple the inertial test instruments from environmental disturbances like seismic vibrations, the instruments (e.g., rate tables) are mounted to an isolated test pad. During the late 1960s, the design of a test pad that provides high tilt stability and isolates from seismic motions became an important goal for the manufacturers and users which led to various publications in the field of *test pad stability* which was later also called *geokinetics*. Actions were coordinated within the *Test Pad Stability Subcommittee* of the *AIAA Technical Committee on Guidance and Control*.

Publications include the design of specific testing facilities, for example at the [USAF Academy](#) [29], at the [Martin Company](#)² [30] and at the [Central Inertial and GPS Test Facility \(CIGTF\)](#) [31]. These designs aim at reducing environmental vibratory accelerations to below the 10^{-5} g range by using passive isolation [31, 30, 29]. The targeted orientation and tilt stability of these examples are in the range of 0.5 to 5 asec [31, 30] and partly achieved by active hydraulic stabilization [29]. A special design example for extreme low vibrational noise is a laboratory in a former salt mine, 350 m below the ground, where the natural noise floor is in the already range of only 10^{-6} g [32]. The possibly detrimental effects of dynamical test instruments (e.g., shakers) on nearby calibration facilities was demonstrated in [33]. Further publications reevaluate and review the achieved stability, e.g. for the [CIGTF](#) [34]. Later generations of inertial sensor test facilities target for a vibration level below 10^{-9} g [35].

In addition to the specific designs, general design considerations and guidelines for passively isolated stable test pads are subject to multiple publications. The effect of surface vibrations and tilts on the test pier design is discussed in [36, 37, 38]. Based on a long-term survey of eight inertial testing facilities, Berg identifies multiple criteria for a stable test site concerning the type of land and the thermal and mechanical isolation [38]. The known seismic vibration

²today Lockheed-Martin Corporation

sources are generally characterized in [39]. Still, the frequency spectrum of test pad motions was only analyzed after the advent of digital Fourier analysis systems in the 1970s [34].

While best practices and design rules for inertial sensor test facilities are well documented in general, there are few publications to investigate the effects of the test pad motion on the final test or calibration results. The limitations on inertial sensor testing that arise from platform vibrations have been investigated by Weinstock in 1966 [40]. Based on measurements of the seismic disturbances at the NASA Inertial Test Facility, Cambridge, MA, Weinstock derives the resulting errors in gyroscope drift rate test results. Still, the study is limited to mechanical gyroscopes, and the conclusions are based on the predicted gyroscope's accuracy in the late 1960s.

To the author's knowledge, no study goes beyond single aspects and provides a comprehensive error budget for sensor testing. This shall be given within this work.

1.4. Contributions

As pointed out above, this field of research has been covered throughout the history of inertial and integrated navigation. Still, in the author's opinion, this thesis contributes to the field in the following aspects:

1. Strap-down Inertial Navigation Error Propagation

This thesis adds further details to the propagation of initialization and inertial sensor errors into navigation errors. In literature, discussions of the error dynamics are limited to medium-term solutions up to 4 h and position errors. This thesis derives the long-term error dynamics for the entire set of navigation states consistently. This also includes the propagation of colored inertial sensor noise processes, in contrast to the white noise assumption that is usually taken. Furthermore, the correlation of the resulting navigation errors is considered.

Based on these results, methods for predicting navigation errors from inertial sensor errors and vice versa are presented. Charts allow the simple reading of the maximum inertial sensor error for a specified navigation error.

2. Inertial Sensor Laboratory Testing

This thesis systematically analyses the error propagation within the inertial sensor testing. The analysis includes a comprehensive list of error sources and corresponding mathematical models. Based on the models, error budgets for the fundamental inertial sensor test procedures are derived. These can be used to determine the achievable sensor accuracy for an existing laboratory setup and to identify the critical performance factors when designing a new facility.

An observability analysis for a comprehensive set of inertial sensor error terms supports the design of rate-table trajectories and procedures for identifying complex sensor error models.

Finally, a Kalman filter-based sensor testing algorithm is developed. By incorporating models for the sensor's noise and the laboratory errors, the algorithm provides a consistent estimation of the accuracy of the sensor error estimation. Combined with a suitable rate table trajectory, this can provide a *one-click* sensor test solution, that estimates complex sensor error models without requiring operator intervention.

A detailed listing of the contributions can be found in [Section 5.2](#).

1.5. Outline

The structure of this thesis is illustrated in [Figure 1.4](#). After a brief introduction, the basics of inertial sensors, navigation, and signal analysis are presented in [Chapter 2](#).

The central part begins with an analytical derivation of the propagation of inertial sensor errors into the orientation errors during stationary alignment ([Section 3.2](#)). Based on the strap-down equations, the linearized navigation error dynamics are derived, and analytical equations for the system's response to initialization and sensor errors are presented in [Section 3.3](#). These equations are finally simplified in [Section 3.6](#) to yield short- and medium-term approximations of the error propagation. The results of the error propagation analysis are then used to create tables and graphics that allow the prediction of the inertial navigation performance from sensor errors ([Section 3.4](#)). Vice-versa, the charts will determine the acceptable sensor errors for a specified navigation performance. Finally, the prediction equations and schemes are validated by two examples of Monte Carlo simulations in [Section 3.5](#).

Following the inertial sensor requirements specification, the sensor errors must be demonstrated in a manufacturer's or system integrator's laboratory. The testing of inertial sensors in the laboratory is discussed in [Chapter 4](#). A mathematical model of the inertial laboratory and its error sources is derived in [Section 4.2](#). These models are then used to create error budgets for the typical sensor test procedures in [Section 4.4](#). This is adjoined by an analytical treatment of averaging over sensor noise processes ([Section 4.3](#)). Finally, [Section 4.5](#) describes how a Kalman-filter-based sensor test procedure is designed and validated with numerical simulations.

This thesis concludes with a summary of the findings and the significant contributions in [Chapter 5](#). The work is adjoined by a comprehensive appendix that includes additional material, like the complete analytical equations for the navigation error response and simulations for their validation. All appendices are linked at the appropriate place in the main text.

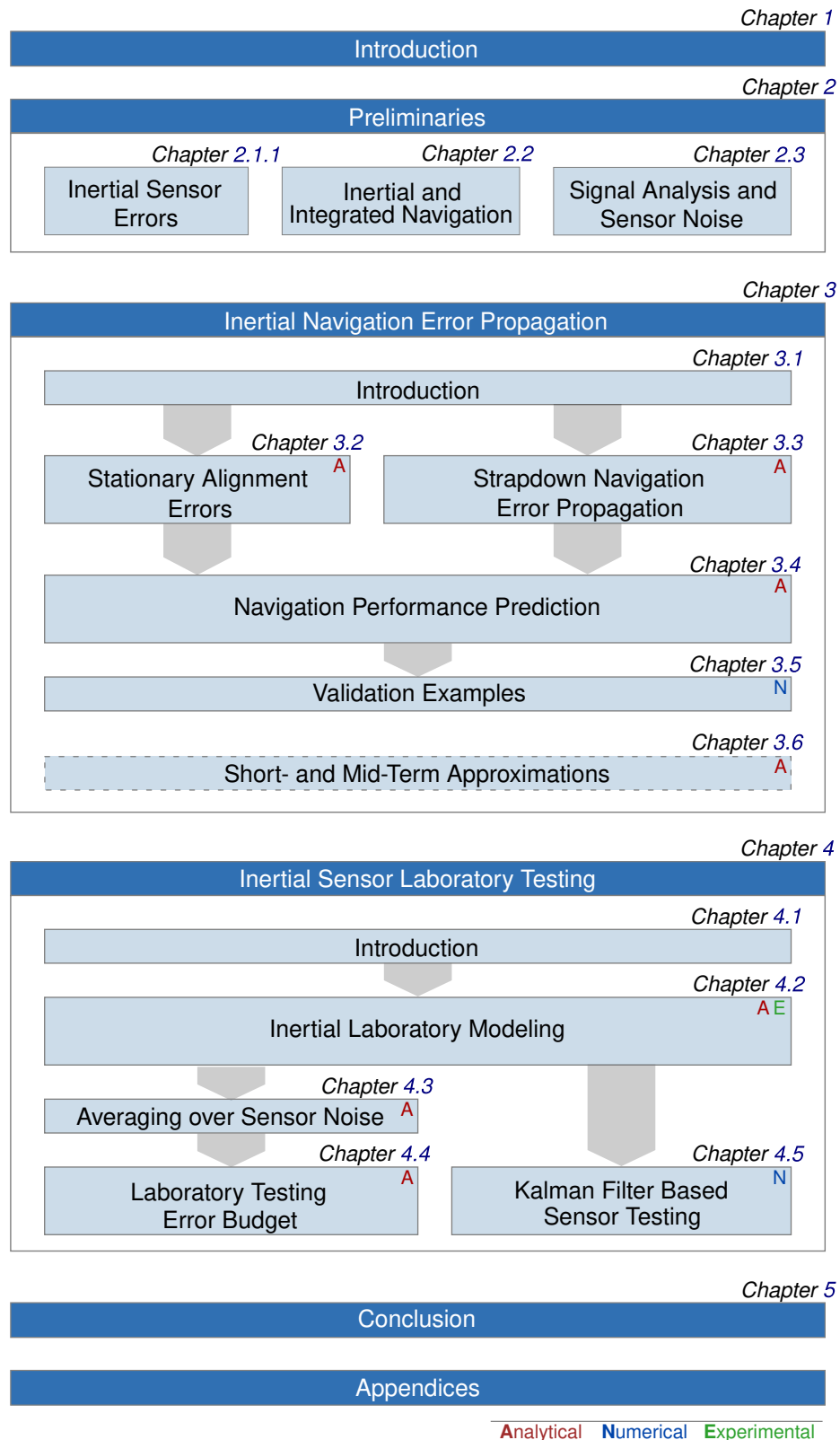


Figure 1.4.: Structure of this thesis.

Chapter 2.

Preliminaries

2.1. Inertial Sensor Errors

2.1.1. Sensor Error Types

This work addresses the effects of sensor errors on inertial navigation performance and the calibration of these same errors. In the context of this work, sensor errors are a deviation of the measured output from the actual input. Sensor failures are considered errors in this context only if they lead to a change in the input-output behavior.

Deterministic sensor errors have to be distinguished from stochastic ones. The deterministic errors are predictable and repeatable, meaning they are a sensor's constant property. This is not limited to constant errors in the input-output relationship but includes sensitivities to motion along the non-input axes and environmental conditions. The typical deterministic sensor errors include:

- **Bias-like Errors** are additive errors on the sensor output that are independent of the input signal, as illustrated in [Figure 2.1a](#). In the IEEE standards [23] bias-like errors are summarized as *systematic drift*. In addition to a constant component (*g-independent bias*), sensor biases can also display sensitivities to environmental conditions (e.g. temperature) and motion (e.g. accelerations, vibrations, etc.) [12, 41, 11]. Even if the bias is constant during operation, it may change from run to run [13, p. 152] and must also be considered as a stochastic error, depending on the context.
- **Scale-Factor Errors** describe deviations from the sensor's ideal static input-output mapping. In the most simple form, this is just a constant error in the linear scale factor ([Figure 2.1b](#)) but can also include asymmetries ([Figure 2.1c](#)), hysteresis effects or any other non-linear relationship ([Figure 2.1d](#)) between input and output of the sensor [22, pp. 26–28]. Just as the bias, also the scale factor can be sensitive to both environmental conditions and motion [12, 41, 11]. In the wide sense, also a *dead band* ([Figure 2.1e](#)) or input range limits ([Figure 2.1f](#)) could be considered as a non-linear scale factor error.
- **Misalignment** is a deviation of the sensor's input (or sensitive) axis orientation from its reference or nominal orientation, as illustrated in [Figure 2.2](#). A misaligned sensor axis

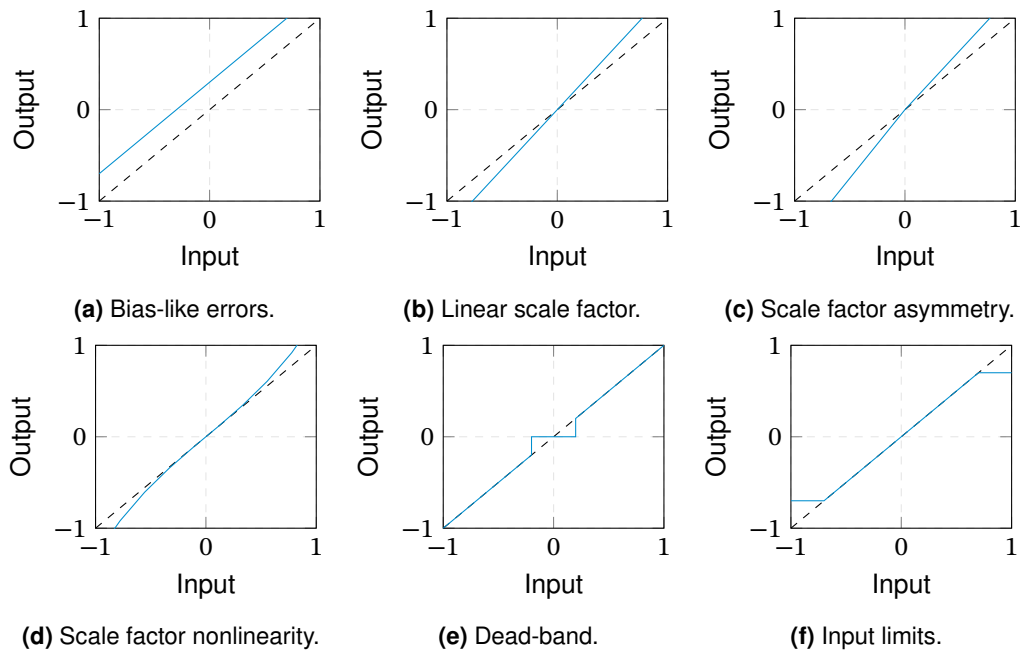


Figure 2.1.: Deterministic sensor error types. The dashed line indicates an ideal sensor input-output mapping, while the solid line represents the erroneous mapping.

will pick up fractions of another axis' signal, therefore it is also called *cross-coupling* [14, p. 154] or more precisely *cross-axis sensitivity*.

The distinction between bias-like errors and scale factor respectively misalignment errors is not always clear-cut: For stationary conditions, e.g., straight and level flight or coordinated turn, the dynamic-dependent errors from scale factor errors and misalignment are constant and can be considered bias-like.

Labeling a sensor error as deterministic implies that it can be, once identified, easily compensated. Deterministic errors are widely compensated during factory calibration, but the identification and thus compensation of sensor errors is only possible within certain limits. The derivation of these limits is precisely the focus of [Chapter 4](#).

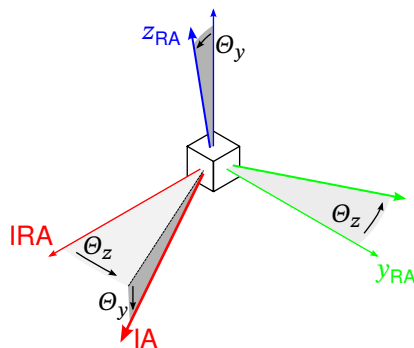


Figure 2.2.: Sensor axis misalignment. The orientation of the sensor's true input axis (IA) deviates from its nominal reference input axis (IRA).

In addition to the deterministic errors, a sensor's output is also subject to stochastic errors. Due to their random nature, stochastic errors cannot be identified and calibrated but are only described by their statistics. The most essential stochastic errors are:

- **Sensor Noise** or *random drift* is an additive random error on the sensors output and like the bias it is independent of the input [22, p. 31]. Sensor noise is a combination of different stochastic processes that can include both high-frequency noise (Figure 2.3b) and low-frequency fluctuations (Figure 2.3c) like in-run variations of the bias. The typical stochastic processes used to model sensor noise are presented in Subsection 2.3.3.
- **Day-to-Day variation** is a variation of the sensor's characteristics from run to run. The most famous example of day-to-day variation is the *turn-on bias* whose variation is much higher than the bias-variation during operation [22, p. 33].

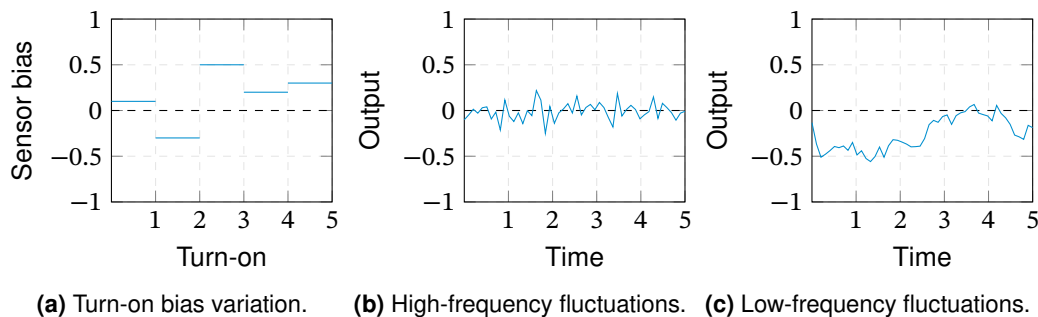


Figure 2.3.: Stochastic sensor errors.

In addition to categorizing the sensor errors as deterministic and stochastic, they can also be grouped by their dependency on the platform dynamics, respectively, the trajectory. While scale factor and misalignment are always dynamic-dependent, the sensor noise is typically dynamic-independent. Bias-like errors include dynamic-dependent (e.g., acceleration sensitivities) and independent (e.g., static bias) errors.

Above discussed errors represent only the basic sensor error types. Each of these errors is composed of various error sources, depending on the measuring principle and technology of the sensor. The following sections will discuss the typical sensor technologies' errors and respective error models.

2.1.2. Inertial Sensor Grades

It is a common practice to assign inertial sensors to a *sensor grade* based on their accuracy. Although there is no universal definition of the different sensor grades, the classical grades are based on the typical application of the associated sensors.

Especially for inertial sensors with low accuracy, there is no uniform definition of sensor grades. On the other hand, the definitions are more precise for the higher grades. Here, the military origins of inertial sensor technology can be seen in the traditional sensor grades and

their names. While there is no agreement on the various grades' names, it is also unclear where the boundaries of the individual grades lie. Most authors agree to define the sensor grades based on the critical performance parameters **scale factor (SF)** error, and sensor bias [13, 42], sometimes also supported by the sensor's noise [43]. Specifically, the critical performance parameters are the residual errors or the in-run variation of SF and bias, often denoted as SF stability and bias stability. The definition of sensor grades used within this work is illustrated in Figure 2.4 and Figure 2.5. Based on the famous bubble charts of G. Schmidt [44], the charts are extended with today's sensor technologies and their respective region key performance parameters.

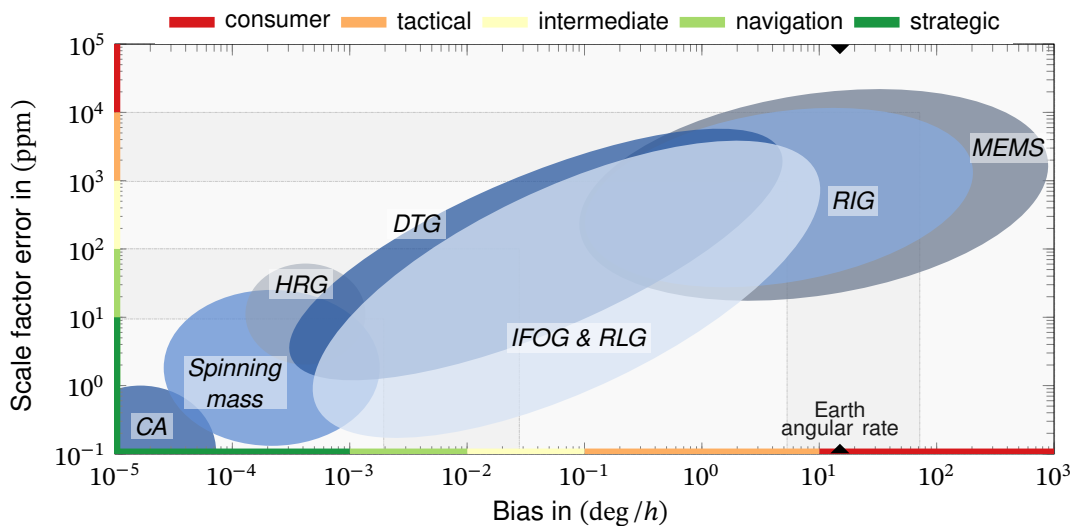


Figure 2.4.: Gyroscope technologies and grades. Derived from [44].

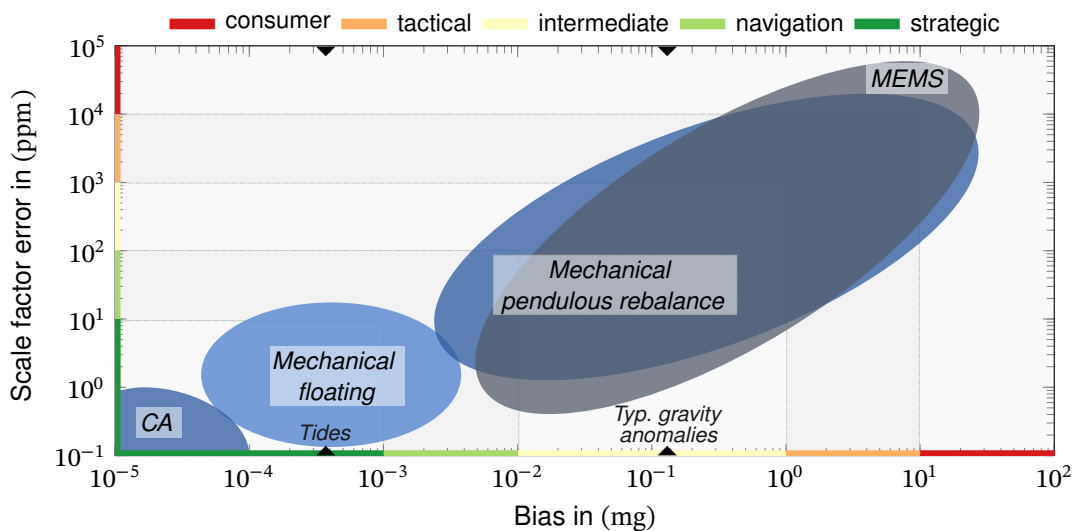


Figure 2.5.: Accelerometer technologies and grades. Derived from [44].

It should be emphasized that the concept of sensor grades and the attribution of sensors and

sensor technologies to applications is only indicative. However, it provides valuable guidance in the first step of selecting inertial sensors for a given application.

2.1.3. Sensor Error Models

Sensor error models or measurement models provide a mathematical description of how the sensor's output relates to the sensor's input. The IEEE standards on inertial sensor specification and testing (see Table 1.1) provide model equations for today's relevant sensor technologies. For Fibre-optic Gyroscope (FOG), Coriolis Vibratory Gyroscope (CVG) and Ring Laser Gyroscope (RLG) the IEEE model equations have the form [25, 9, 12]:

$$\tilde{\omega}_{ib} = S_0 U = \frac{I + E + D}{1 + 10^{-6}\epsilon_k} \quad (2.1)$$

The indicated rate $\tilde{\omega}_{ib}$ is expressed as the product of the nominal scale factor S_0 and the sensor's readout U , which can be, e.g., a voltage or a digital value. In this model, ϵ_k denotes the composite scale factor errors. The input is split into three different terms I , E , and D .

The *inertial input* term I represents the ideal sensor input, as well as the cross-coupling to other input axes caused by the misalignment of the sensor axis [25]:

$$I = \omega_{ib,x} + \omega_{ib,y} \sin \Theta_z - \omega_{ib,z} \sin \Theta_y \quad (2.2)$$

The bias-like errors from environmental influences are summarized in the term E , called *environmentally sensitive terms*:

$$E = D_T \Delta T + \dots \quad (2.3)$$

The *drift terms* D summarizes the (in-run) fixed bias D_F and the drift from sensor noise D_R [12, 9]:

$$D = D_F + D_R + \dots \quad (2.4)$$

In the standard on CVGs, environmental sensitivities D are merged into the drift terms D , which seems reasonable as both represent drift. The standards name the most relevant error terms and sensitivities but do not claim completeness. A summary of the listed terms and sensitivities is given in Table 2.1.

Note that these model equations are a phenomenological error model only; they do not require knowledge of the physical effects that cause these errors. In addition to that, they are kind of static models and do not consider the sensor's dynamics. In contrast to that, the models for the Dynamically Tuned Gyroscope (DTG) [45] and mechanical Single Degree of Freedom Gyroscope (SDFG) [24] are dynamic models that trace back errors to mechanical properties, e.g., rotor unbalance. However, these technologies are no longer considered here due to their sporadic use today.

An error model of similar structure is provided in IEEE Std. 836 [41] for (mainly pendulous)

Table 2.1.: Error terms in the IEEE model equations for gyroscopes.

IEEE Std.		647 [9] RLG	952 [12] FOG	1431 [11] CVG
Misalignment	Θ_y, Θ_z	✓	✓	✓
Scale factor error				
Nonlinearity	$f(\omega)$	✓	✓	
Scale factor error	ϵ_{K0}			✓
Temperature sensitivity	$\epsilon_T \cdot \Delta T$	✓	✓	✓
Temperature gradient sensitivity	$\epsilon_{\nabla T} \cdot \nabla T$	✓		
Acceleration sensitivity	$S_a \cdot a$			✓
Drift				
Temperature sensitivity	$D_T \cdot \Delta T$	✓	✓	✓
Temperature gradient sensitivity	$D_{\nabla T} \cdot \nabla T$	✓		✓
Temperature rate sensitivity	$D_{\dot{T}} \cdot \dot{T}$		✓	✓
Temperature gradient rate sensitivity	$D_{\nabla \dot{T}} \cdot \frac{d\nabla T}{dt}$		✓	
Vibration coning sensitivity	$D_c \cdot a_{V,R}$			✓
Vibration difference freq. sensitivity	$D_{\Delta F} \cdot a_{V,\Delta F}$			✓
Vibration drive freq. sensitivity	$D_D \cdot a_{V,D}$			✓
Vibration pickoff freq. sensitivity	$D_P \cdot a_{V,P}$			✓
Structure resonance sensitivity	$D_{SR} \cdot a_{V,SR}$			✓
Acceleration sensitivity	$D_a \cdot a$			✓
Cross-axis vibration sensitivity	$D_{RI} \cdot a_{V,OF}(\omega_y + \omega_z)$			✓
Broadband noise sensitivity	$D_{RBB} \cdot a_{V,BB}$			✓
Fixed bias	D_F	✓	✓	✓
Angle random walk	$D_{R,N}$	✓	✓	✓
Bias instability	$D_{R,B}$	✓	✓	✓
Rate random walk	$D_{R,K}$	✓	✓	✓
Rate ramp	$D_{R,R}$	✓	✓	✓
Quantization noise	D_Q	✓	✓	✓

accelerometers:

$$a_s = \frac{E}{K_1} = K_0 + a_i + K_2 a_i^2 + K_3 a_i^3 + K_{ip} a_i a_p + K_{io} a_i a_o + K_{op} a_o a_p + \delta_o a_p - \delta_p a_o \quad (2.5)$$

where a_i denotes the acceleration along the nominal input axis, a_p along the pendulous axis and a_o along the remaining right-handed coordinate axis. In this model, the scale factor nonlinearity is explicitly modeled as a third order polynomial and there is also a sensitivity to mixed acceleration terms. In contrast to the gyro models, the misalignment is described by the sensitivities δ_o, δ_p directly, not the misalignment angles. Furthermore, the standard [41] suggests extending the model equation by high order terms of cross-coupling and asymmetries.

While the IEEE standards provide a reference model and naming conventions, a more straightforward formulation is typically used. In the formulation suggested in [14, p. 254], the scale factor error explicitly effects only the nominal input:

$$\tilde{\omega}_{ib,x} = (1 + S_{G,x})\omega_{ib,x} + M_{G,y}\omega_{ib,y} + M_{G,z}\omega_{ib,z} + B_{G,f} + B_{G,x}a_x + B_{G,z}a_z + B_{G,xz}a_y a_z + \nu_{G,x} \quad (2.6)$$

$$\tilde{f}_b = (1 + S_{A,x})f_{b,x} + M_{A,y}f_{b,y} + M_{A,z}f_{b,z} + B_{A,f} + B_{A,v}f_{b,x}f_{b,y} + \nu_{A,x} \quad (2.7)$$

In this formulation the bias-like and cross-sensitivity errors implicitly contain the linear scale factor error around zero. In [14, p. 254], it is suggested to express S_x as a polynomial in ω , respectively f_b , to model a non-linear scale factor. However, this would still ignore the effect of a non-linear scale factor on the bias-like errors. The different sensor noise processes are summarized into the noise terms ν . Again, above equations can of course be extended and adapted to a sensor's specific sensitivities, as summarized in Table 2.1.

2.2. Inertial and Integrated Navigation

2.2.1. Reference Frames

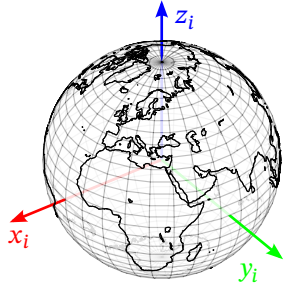
Mathematical models of inertial navigation and the laboratory calibration of inertial sensors require defining a set of reference frames. The utilized coordinate systems follow the definitions of ISO-1151 [46] and ANSI/AIAA R-004 [47], which are the well-accepted standard in the navigation community [13, 14, 21, 15].

2.2.1.1. Earth Centered Inertial (ECI) Frame i

The inertial frame is a Cartesian coordinate system located at the Earth's center of mass, thus called *Earth Centered Inertial* (ECI) frame. Its z -axis is aligned to the Earth's nominal rotation axis, pointing to true north. Different definitions are available for the x -axis. The typical choice is to align the x -axis to the direction from the Earth to the sun at the (Northern Hemisphere) vernal equinox [13]. The y -axis is chosen to complete a right-handed coordinate frame. As

(Earth-based) inertial navigation is typically not performed relative to the inertial frame, the actual direction of the x -axis has no effect in practice. The definition of this ECI-frame is summarized in Table 2.2.

Table 2.2.: Definition of the ECI Frame.

	Origin	Center of mass of Earth and atmosphere
	Rotation	<i>Non rotating</i>
	Axes x_i	Direction from the Earth to the sun at vernal equinox
	y_i	Completes a right-handed Cartesian frame
	z_i	Along the Earth's rotation axis, pointing north

Comparison to the International Celestial Reference Frame (ICRF) The International Celestial Reference Frame is a quasi-inertial frame defined by the International Astronomical Union (IAU). Its orientation is ideally fixed to a set of extragalactic radio sources. Due to the considerable distance of these objects, primarily quasars, their motion may be neglected [48]. This results in a very stable reference frame with a noise floor of 40 asec and axis stability of 10 asec for the latest version called ICRF2 [49].

While the ECI-frame is based on the assumption that the Earth's rotation axis is fixed relative to space, the axis performs a precessing and nutating motion relative to the ICRF. Additionally, the Earth's angular rate about this axis changes slightly with time. The *quality* of the inertial reference frame assumption is discussed in Subsection 4.2.4.

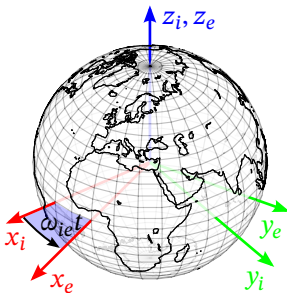
2.2.1.2. Earth Centered Earth Fixed (ECEF) Frame e

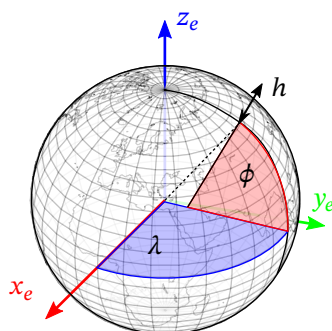
As the name implies, the ECEF is again located at the Earth's center of mass (incl. the atmosphere). Furthermore, it is fixed to the Earth's surface. This causes the frame to rotate about the Earth's spin axis, which coincides with the frame's z_e axis. The x_e points from the frame's origin to the intersection of the prime meridian with the equatorial plane. This definition is summarized in Table 2.3.

In navigation, a position relative to the Earth's surface is usually expressed in the geodetic latitude ϕ , longitude λ , and altitude h . As illustrated in Figure 2.6, the geodetic latitude is defined as the intersection angle of the local normal of the reference ellipsoid with the equatorial plane. The geodetic longitude is defined as the angle to the prime meridian. Altitude is defined as the normal distance to the reference ellipsoid.

This thesis uses the World Geodetic System 1984 (WGS84) model to describe the Earth's ideal ellipsoidal shape, gravity, and rotation. The defining parameters of the WGS84 reference ellipsoid are summarized in Table 2.4.

Table 2.3.: Definition of the ECEF Frame.

	Origin	Center of mass of Earth and atmosphere
	Rotation	Constant rotation at ω_{ie} about z_e
	Axes x_e	From the origin to the intersection of the prime meridian and equator.
	y_e	Completes a right-handed Cartesian frame
	z_e	Along the Earth's rotation axis, pointing north

**Figure 2.6.:** Geodetic latitude and longitude in the ECEF frame.

2.2.1.3. Local North-East-Down (NED) or Navigation Frame n

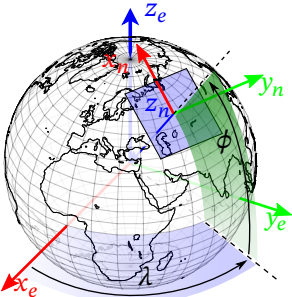
The local north-east-down frame (also local navigation frame) is aligned to the Earth's local curvature. The x_n is a tangent to the local reference ellipsoid pointing to the true north. The z_n axis is aligned to the local normal of the reference ellipsoid, and the y_e forms a right-handed Cartesian frame and points to the East. The NED-frame moves with the vehicle and is typically used to describe a vehicle's velocity and orientation relative to the local ground.

An alternative local frame is the East-North-Up (ENU) frame (here with index l), which just switches the order of the x and y axis to form a right-handed system with the x_l axes pointing up.

Table 2.4.: Defining parameters of the WGS84 model [50].

symbol	parameter	value
a	semi-major axis	6 378 137.0 m
$1/f$	flattening	298.257223563
GM	gravitational constant	$3986004.418 \pm 0.008 \cdot 10^8 \text{ m}^3/\text{s}^2$
ω_{ie}	angular velocity	$7292115 \cdot 10^{-11} \text{ rad/s}$

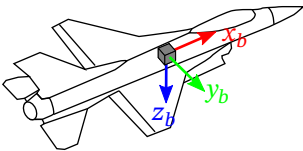
Table 2.5.: Definition of the NED Frame.

	Origin	Arbitrary reference point, often identical to the b -frame's origin
	Rotation	Transport rate to keep the frame aligned
	Axes	x_n Tangent to the reference ellipsoid, pointing to true north
		y_n Completes a right-handed Cartesian frame, pointing to the east
		z_n Normal to the reference ellipsoid, pointing down

2.2.1.4. Body Fixed Frame b

The body-fixed frame represents the navigating vehicle itself. Its orientation and origin are fixed to the vehicle, with the x_b axis typically pointing to the nose, the y_b to the right wing, and the z_b axis pointing to the belly of an aircraft. As inertial sensors and navigation systems are mounted to the aircraft, their measurements are taken in a body-fixed frame. Note that the sensor's body-fixed frame does not necessarily match the aircraft's body-fixed frame. As this thesis focuses on inertial sensors and navigation systems and not on the surrounding vehicle, the b -frame refers to

Table 2.6.: Definition of the Body Fixed Frame.

	Origin	Arbitrary reference point of the vehicle or sensor
	Rotation	Vehicle's rotation
	Axes	x_b Pointing to the front of the vehicle
		y_b Completes a right-handed Cartesian frame
		z_b Pointing to the bottom of the vehicle

2.2.2. Strapdown Inertial Navigation Principles

The basic idea of inertial navigation is the integration of angular rate and acceleration measurements to attitude angles, velocities, and ultimately, a position estimate. While early navigation systems used a mechanical, gimballed platform (*stabilized platform*) to align the accelerometers with the desired reference frame, the progress of microcomputers allowed the shift from the mechanical rotation of the sensors to a rotation of the accelerometer measurements in software where all sensors are fixed to the vehicle's body (*strapped down*) [14, p. 13].

The general structure of a strapdown inertial navigation algorithm or mechanization is depicted in Figure 2.7. Based on the initial attitude estimate (see alignment, Section 3.2), the gyroscope's angular rate measurements are used to determine the current attitude relative to the selected reference frame. This information is used to transform the accelerometer measurements from the body fixed into just that reference frame. A position-dependent gravity model is used to compensate for the local gravity in the measured accelerations. After correcting

for accelerations that arise from a rotating reference frame, the acceleration is integrated into a velocity and position. Again, this requires knowledge of the initial velocity and position.

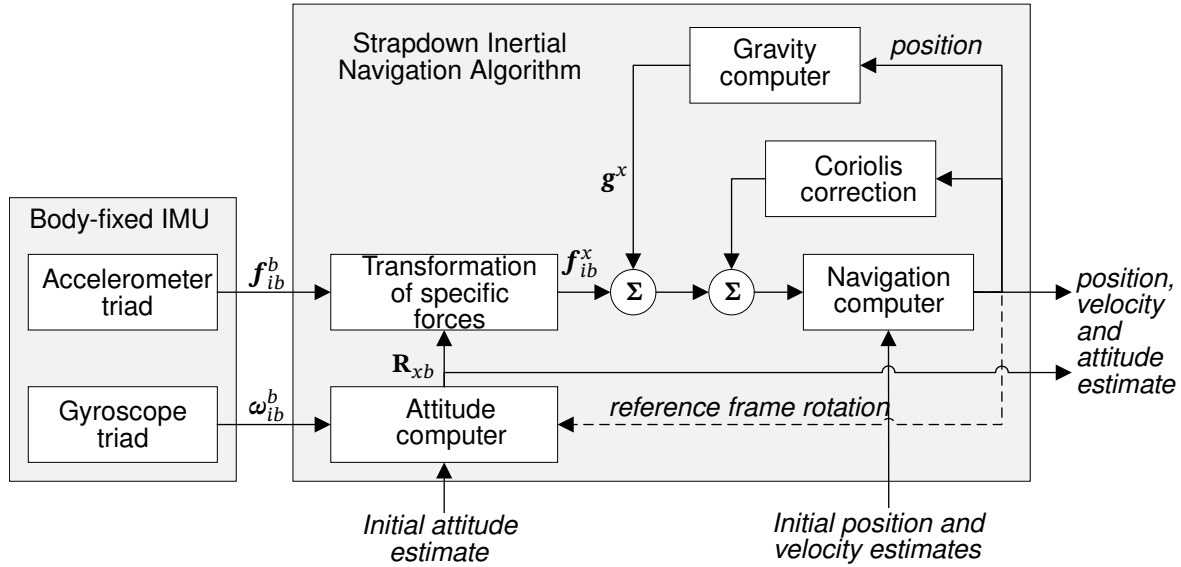


Figure 2.7.: General strapdown inertial navigation mechanization scheme. Adapted from [14, p. 26].

The following section will present basic strapdown inertial navigation mechanizations and their corresponding **Ordinary Differential Equation (ODE)**. Here, the focus is not on practical implementation but on providing an accessible basis for the subsequent navigation error analysis and integrated navigation. For implementation and practical questions, like time-integration and discretization, quaternion attitude representation, and all Earth navigation, the reader may refer to [15], [14] or [13]. For accessibility, only non-integrating sensor output (accelerations and rates) is considered for the strapdown error analysis. Strapdown algorithms for direct use of integrated sensor outputs are described in, e.g., [13] and [51].

2.2.2.1. Strapdown Equations in the Earth-fixed frame

If the Earth-fixed reference frame (e -frame) is selected, the position is given as the integral of the velocity relative to the Earth-fixed frame. As illustrated in Figure 2.7, the measurement of the specific forces is transformed into the e -frame and compensated for the local gravitation as well as Coriolis and centrifugal forces that arise from the rotation of the e -frame relative to the inertial frame. This yields the following strapdown **ODEs** for position \mathbf{x}_e , velocity \mathbf{v}_e and orientation \mathbf{R}_{eb} [15, p. 126]:

$$\dot{\mathbf{x}}_e = \mathbf{v}_e \quad (2.8)$$

$$\dot{\mathbf{v}}_e = \mathbf{R}_{eb}\mathbf{f}_b - 2\boldsymbol{\Omega}_{ie}\mathbf{v}_e + \mathbf{g}_e(\mathbf{x}_e) - \boldsymbol{\Omega}_{ie}\boldsymbol{\Omega}_{ie}\mathbf{x}_e \quad (2.9)$$

$$\dot{\mathbf{R}}_{eb} = \mathbf{R}_{eb}\boldsymbol{\Omega}_{ib} - \boldsymbol{\Omega}_{ie}\mathbf{R}_{eb} \quad (2.10)$$

with the rotation matrix from the b - to e -frame \mathbf{R}_{eb} , the specific forces \mathbf{f}_b and the skew symmetric matrices $\mathbf{\Omega}$ of the respective angular rate vectors $\boldsymbol{\omega}$

The gravitation term $\mathbf{g}_e(\mathbf{x}_e)$ and centrifugal forces term $\mathbf{\Omega}_{ie}\mathbf{\Omega}_{ie}\mathbf{x}_e$ can be combined into the local gravity term [14, p. 27]:

$$\boldsymbol{\gamma}_e(\mathbf{x}_e) = \mathbf{g}_e(\mathbf{x}_e) - \mathbf{\Omega}_{ie}\mathbf{\Omega}_{ie}\mathbf{x}_e \quad (2.11)$$

Here, the Earth's angular rate is assumed constant and the WGS84 reference value of $\omega_{ie} = 7.292115 \cdot 10^{-5}$ rad/s is used.

2.2.2.2. Strapdown Equations in the local navigation frame

As velocity and position information in the e -frame is rather hard to interpret, a more accessible representation is desired. When choosing a local leveled North-East-Down frame, the position change can be easily expressed in the geodetic coordinates latitude, longitude and altitude [15, p. 129]:

$$\dot{\boldsymbol{\lambda}} = \begin{bmatrix} \dot{\phi} \\ \dot{\lambda} \\ \dot{h} \end{bmatrix} = \begin{bmatrix} \frac{v_n}{R_M(\phi)+h} \\ \frac{v_e}{(R_N(\phi)+h)\cos(\phi)} \\ -v_d \end{bmatrix} = \mathbf{D}(\phi, h)^{-1}\mathbf{v}_n \quad (2.12)$$

The choice of a moving local leveled reference frame yields the additional transport rate $\boldsymbol{\omega}_{en}$ term in the velocity and orientation ODE [15, pp. 129–130]:

$$\dot{\mathbf{v}}_n = \mathbf{R}_{nb}\mathbf{f}_b - (2\mathbf{R}_{ne}\mathbf{\Omega}_{ie}\mathbf{R}_{en} + \mathbf{\Omega}_{en})\mathbf{v}_n + \boldsymbol{\gamma}_n(\phi, \lambda, h) \quad (2.13)$$

$$\dot{\mathbf{R}}_{nb} = \mathbf{R}_{nb}\mathbf{\Omega}_{ib} - \mathbf{\Omega}_{in}\mathbf{R}_{nb} \quad (2.14)$$

with the local gravity

$$\boldsymbol{\gamma}_n(\phi, \lambda, h) = \mathbf{g}_n(\phi, \lambda, h) - \mathbf{R}_{ne}\mathbf{\Omega}_{ie}\mathbf{\Omega}_{ie}\mathbf{x}_e(\phi, \lambda, h) \quad (2.15)$$

The rotation matrix from the Earth-fixed frame to the local leveled frame is given by

$$\mathbf{R}_{ne} = \begin{bmatrix} -\sin \phi \cos \lambda & -\sin \phi \sin \lambda & \cos \phi \\ \sin \lambda & \cos \lambda & 0 \\ -\cos \phi \cos \lambda & -\cos \phi \sin \lambda & -\sin \phi \end{bmatrix} \quad (2.16)$$

and the corresponding transport rate in the navigation frame is given by:

$$\boldsymbol{\omega}_{en} = \begin{bmatrix} \dot{\lambda} \cos \phi & -\dot{\phi} & -\dot{\lambda} \sin \phi \end{bmatrix} \quad (2.17)$$

From (2.12), it is evident that this mechanization reaches a singularity near the poles. One possible solution to this problem is the introduction of an additional moving reference frame, the so-called Wander-Azimuth mechanization. A description of this concept can be found in [15, pp. 131–134], [13, pp. 180–182] and [52]. Still, for accessibility, only the n-frame mechanization is analyzed within this thesis.

2.2.3. Integrated Navigation and Data Fusion

2.2.3.1. Kalman Filtering

”Kalman filtering is an optimal state estimation process applied to a dynamic system that involves random perturbations” [53, p. xi]. In fact, the **Kalman filter (KF)** is a minimum variance estimator for a time-discrete linear state-space system

$$\mathbf{x}_{k+1} = \mathbf{\Phi}_k \mathbf{x}_k + \mathbf{G}_k \mathbf{u}_k + \mathbf{\Gamma}_k \mathbf{v}_k \quad (2.18)$$

$$\mathbf{y}_k = \mathbf{H}_k \mathbf{x}_k + \mathbf{D}_k \mathbf{u}_k + \boldsymbol{\eta}_k \quad (2.19)$$

with a deterministic input \mathbf{u}_k , process noise \mathbf{v}_k and measurement noise $\boldsymbol{\eta}_k$. Both noise components are independent zero-mean **WGN** sequences, defined by their respective covariance matrices \mathbf{Q}_k and \mathbf{R}_k [53, pp. 26–27]. The **KF** thus combines knowledge from the dynamic system and the measurements $\tilde{\mathbf{y}}$ to determine a stochastically optimal estimate of the system states $\hat{\mathbf{x}}$, and thus a *Data Fusion*.

In general, the **KF** and its variants consist of a *prediction* step, which propagates the states and covariance estimates in time, and the *correction* step, which uses the measurements to update the state estimates in a stochastically optimal way. The conventional **KF** equations for above linear state space system are given in **Algorithm 1**.

Algorithm 1: Conventional Kalman filter

The conventional Kalman Filter equations, initially published in [54], are given in the modern formulation taken from [53, p. 25].

System	$\mathbf{x}_{k+1} = \mathbf{\Phi}_k \mathbf{x}_k + \mathbf{G}_k \mathbf{u}_k + \mathbf{\Gamma}_k \mathbf{v}_k$ $\mathbf{y}_k = \mathbf{H}_k \mathbf{x}_k + \mathbf{D}_k \mathbf{u}_k + \boldsymbol{\eta}_k$	$\mathbf{v}_k = \text{WGN}(0, \mathbf{Q}_k)$ $\boldsymbol{\eta}_k = \text{WGN}(0, \mathbf{R}_k)$ $\mathbb{E}[\mathbf{v}_k \boldsymbol{\eta}_l^\top] = \mathbf{0} \quad \forall k, l$
State prediction	$\hat{\mathbf{x}}_{k+1} = \mathbf{\Phi}_k \hat{\mathbf{x}}_k + \mathbf{G}_k \mathbf{u}_k$	
Cov. prediction	$\mathbf{P}_{k+1} = \mathbf{\Phi}_k \mathbf{P}_k \mathbf{\Phi}_k^\top + \mathbf{\Gamma}_k \mathbf{Q}_k \mathbf{\Gamma}_k^\top$	
Kalman Gain	$\mathbf{K}_k = \mathbf{P}_k \mathbf{H}_k^\top [\mathbf{H}_k \mathbf{P}_k \mathbf{H}_k^\top + \mathbf{R}_k]^{-1}$	
State correction	$\hat{\mathbf{x}}_k^+ = \hat{\mathbf{x}}_k^- + \mathbf{K}_k (\tilde{\mathbf{y}}_k - \mathbf{H}_k \hat{\mathbf{x}}_k^-)$	
Cov. correction	$\mathbf{P}_k^+ = [\mathbf{I} - \mathbf{K}_k \mathbf{H}_k] \mathbf{P}_k^-$	

Many dynamic systems, and also strapdown inertial navigation, cannot be modeled as linear state-space system, but have non-linear propagation and measurement equations:

$$\mathbf{x}_{k+1} = \mathbf{f}_k(\mathbf{x}_k, \mathbf{u}_k, \mathbf{v}_k) \quad (2.20)$$

$$\mathbf{y}_k = \mathbf{h}_k(\mathbf{x}_k, \mathbf{u}_k, \boldsymbol{\eta}_k) \quad (2.21)$$

The Extended Kalman Filter is a variant of the conventional Kalman Filter suited for slightly non-linear systems. It is based on using the linearization of the non-linear propagation and measurement equations for the covariance calculations and the direct non-linear equations for the state estimates. The Extended Kalman Filter equations are summarized in [Algorithm 2](#).

The state-space system in (2.18) can be easily augmented with additional states to model noise processes. These noise processes are driven by WGN and allow the modeling of time-correlated noise, e.g., sensor noise, for both measurement and process noise in the Kalman Filter. Typically, the noise processes are mutually independent, which means there is no correlation between the corresponding noise process states. Furthermore, noise states often shall not be estimated, but only the effect of the noise shall be incorporated into the estimation. Under these assumptions, the particular structure of the system allows a separation of the system into an estimation system that contains the states to be estimated and multiple noise systems that can be propagated independently of the estimation system. For these systems, only its covariance matrix and the cross-correlation to the estimation states are propagated and eventually updated during the correction step. The equations for the Schmidt-Kalman filter are summarized in [Algorithm 3](#).

Algorithm 2: Extended Kalman filter

The idea of the Extended Kalman Filter can be traced back to [55]. The below formulation of the equations is taken from [53, pp. 115–116].

System	$\mathbf{x}_{k+1} = \mathbf{f}_k(\mathbf{x}_k, \mathbf{u}_k, \mathbf{v}_k)$ $\mathbf{y}_k = \mathbf{h}_k(\mathbf{x}_k, \mathbf{u}_k, \boldsymbol{\eta}_k)$	$\mathbf{v}_k = \text{WGN}(0, \mathbf{Q}_k)$ $\boldsymbol{\eta}_k = \text{WGN}(0, \mathbf{Q}_k)$ $\mathbb{E}[\mathbf{v}_k \boldsymbol{\eta}_l^\top] = \mathbf{0} \quad \forall k, l$
State prediction	$\hat{\mathbf{x}}_{k+1} = \mathbf{f}_k(\mathbf{x}_k, \mathbf{u}_k, \mathbf{v}_k)$	
Cov. prediction	$\mathbf{P}_{k+1} = \left(\frac{\partial \mathbf{f}_k}{\partial \mathbf{x}_k} \right) \mathbf{P}_k \left(\frac{\partial \mathbf{f}_k}{\partial \mathbf{x}_k} \right)^\top + \left(\frac{\partial \mathbf{f}_k}{\partial \mathbf{u}_k} \right) \mathbf{Q}_k \left(\frac{\partial \mathbf{f}_k}{\partial \mathbf{u}_k} \right)^\top$	
Kalman Gain	$\mathbf{K}_k = \mathbf{P}_k^- \left(\frac{\partial \mathbf{h}_k}{\partial \mathbf{x}_k} \right)^\top \left[\left(\frac{\partial \mathbf{h}_k}{\partial \mathbf{x}_k} \right) \mathbf{P}_k^- \left(\frac{\partial \mathbf{h}_k}{\partial \mathbf{x}_k} \right)^\top + \mathbf{R}_k \right]^{-1}$	
State correction	$\hat{\mathbf{x}}_k^+ = \hat{\mathbf{x}}_k^- + \mathbf{K}_k (\tilde{\mathbf{y}}_k - \mathbf{h}(\hat{\mathbf{x}}_k^-, \mathbf{u}_k))$	
Cov. correction	$\mathbf{P}_k^+ = \left[\mathbf{I} - \mathbf{K}_k \left(\frac{\partial \mathbf{h}_k}{\partial \mathbf{x}_k} \right) \right] \mathbf{P}_k^-$	

Algorithm 3: Schmidt-Kalman Filter

In the Schmidt-Kalman filter, measurement and sensor noise are modeled as separate and mutually independent noise processes. For each process, the cross-covariance to the estimated states is propagated and updated together with the estimation state correction. There are no states for the noise processes, and their noise covariances are not updated.

The Schmidt-Kalman filter equations, originally published in [56, pp. 333–334], are here given in the formulation from [57, pp. 208–209]:

Process noise $i = 1 \dots n$

$$\begin{aligned} \text{System} \quad \mathbf{x}_{v_i,k+1} &= \mathbf{\Phi}_{v_i,k} \mathbf{x}_{v_i,k} + \mathbf{\Gamma}_{v_i,k} \mathbf{q}_{v_i,k} & \mathbf{q}_{v_i,k} &= \text{WGN}(0, \mathbf{Q}_{v_i}) \\ \mathbf{v}_{i,k} &= \mathbf{H}_{v_i,k} \mathbf{x}_{v_i,k} + \mathbf{D}_{v_i,k} \mathbf{q}_{v_i,k} & \mathbb{E}[\mathbf{q}_{v_i,k} \mathbf{q}_{v_j,k}^\top] &= \mathbf{0} \quad \forall i \neq j, k \end{aligned}$$

$$\text{Cov. prediction} \quad \mathbf{P}_{v_i v_i, k+1} = \mathbf{\Phi}_{v_i,k} \mathbf{P}_{v_i v_i, k} \mathbf{\Phi}_{v_i,k}^\top + \mathbf{\Gamma}_{v_i,k} \mathbf{Q}_{v_i v_i, k} \mathbf{\Gamma}_{v_i,k}^\top$$

$$\text{Cross-cov. prediction} \quad \mathbf{P}_{x v_i, k+1} = \mathbf{\Phi}_{x,k} \mathbf{P}_{x v_i, k} \mathbf{\Phi}_{v_i,k}^\top$$

$$\text{Cross-cov. correction} \quad \mathbf{P}_{x v_i, k}^+ = (\mathbf{I} - \mathbf{K}_k \mathbf{H}_k) \mathbf{P}_{x v_i, k}^-$$

Measurement noise $j = 1 \dots m$

$$\begin{aligned} \text{System} \quad \mathbf{x}_{\eta_j, k+1} &= \mathbf{\Phi}_{\eta_j, k} \mathbf{x}_{\eta_j, k} + \mathbf{\Gamma}_{\eta_j, k} \mathbf{q}_{\eta_j, k} & \mathbf{q}_{\eta_j, k} &= \text{WGN}(0, \mathbf{Q}_{\eta_j}) \\ \boldsymbol{\eta}_{i, k} &= \mathbf{H}_{\eta_j, k} \mathbf{x}_{\eta_j, k} + \mathbf{D}_{\eta_j, k} \mathbf{q}_{\eta_j, k} & \mathbb{E}[\mathbf{q}_{\eta_j, k} \mathbf{q}_{\eta_i, k}^\top] &= \mathbf{0} \quad \forall j \neq i, k \\ & & \mathbb{E}[\mathbf{q}_{v_i, k} \mathbf{q}_{\eta_j, l}^\top] &= \mathbf{0} \quad \forall j, i, k, l \end{aligned}$$

$$\text{Cov. prediction} \quad \mathbf{P}_{\eta_j \eta_j, k+1} = \mathbf{\Phi}_{\eta_j, k} \mathbf{P}_{\eta_j \eta_j, k} \mathbf{\Phi}_{\eta_j, k}^\top + \mathbf{\Gamma}_{\eta_j, k} \mathbf{Q}_{\eta_j \eta_j, k} \mathbf{\Gamma}_{\eta_j, k}^\top$$

$$\text{Cross-cov. prediction} \quad \mathbf{P}_{x \eta_j, k+1} = \mathbf{\Phi}_{x, k} \mathbf{P}_{x \eta_j, k} \mathbf{\Phi}_{\eta_j, k}^\top$$

$$\begin{aligned} \text{Cross-cov. correction} \quad \mathbf{P}_{x \eta_j, k}^+ &= (\mathbf{I} - \mathbf{K}_k \mathbf{H}_k) \mathbf{P}_{x \eta_j, k}^- - \mathbf{K}_k \mathbf{H}_{\eta_j, k} \mathbf{P}_{\eta_j \eta_j, k} \quad (\text{for the used meas.}) \\ & \quad (\mathbf{I} - \mathbf{K}_k \mathbf{H}_k) \mathbf{P}_{x \eta_j, k}^- \quad (\text{for the others}) \end{aligned}$$

Estimation system

$$\begin{aligned} \text{System} \quad \mathbf{x}_{k+1} &= \mathbf{\Phi}_k \mathbf{x}_k + \sum_i^m \mathbf{\Gamma}_{i, k} \mathbf{v}_{i, k} \\ \mathbf{y}_k &= \mathbf{H}_k \mathbf{x}_k + \sum_j^n \boldsymbol{\eta}_{j, k} \end{aligned}$$

$$\text{State prediction} \quad \hat{\mathbf{x}}_{k+1} = \mathbf{\Phi}_{x, k} \hat{\mathbf{x}}_k$$

$$\begin{aligned} \text{Cov. prediction} \quad \mathbf{Q}_k &= \sum_{i=1}^n \mathbf{\Gamma}_{i, k} (\mathbf{H}_{v_i, k} \mathbf{P}_{v_i v_i, k} \mathbf{H}_{v_i, k}^\top + \mathbf{D}_{v_i, k} \mathbf{Q}_{v_i v_i, k} \mathbf{D}_{v_i, k}^\top) \mathbf{\Gamma}_{i, k}^\top \\ \mathbf{P}_{xx, k+1} &= \mathbf{\Phi}_{x, k} \mathbf{P}_{xx, k} \mathbf{\Phi}_{x, k}^\top + \mathbf{Q}_k \\ & \quad + \sum_{i=1}^n (\mathbf{\Gamma}_{i, k} \mathbf{H}_{v_i, k} \mathbf{P}_{\eta_i x, k}) \mathbf{\Phi}_k^\top + \mathbf{\Phi}_k \sum_{i=1}^n (\mathbf{P}_{x \eta_i, k} \mathbf{H}_{v_i, k}^\top \mathbf{\Gamma}_{i, k}^\top) \end{aligned}$$

$$\begin{aligned} \text{Kalman Gain} \quad \mathbf{R}_k &= \sum_{j=1}^m (\mathbf{H}_{\eta_j, k} \mathbf{P}_{\eta_j \eta_j, k} \mathbf{H}_{\eta_j, k}^\top + \mathbf{D}_{\eta_j, k} \mathbf{Q}_{\eta_j \eta_j, k} \mathbf{D}_{\eta_j, k}^\top) \\ \mathbf{S}_k &= \mathbf{H}_k \mathbf{P}_{xx, k} \mathbf{H}_k^\top + \mathbf{R}_k \\ & \quad + \sum_{j=1}^m (\mathbf{H}_{\eta_j, k} \mathbf{P}_{\eta_j x, k}^\top) \mathbf{H}_k^\top + \mathbf{H}_k \sum_{j=1}^m (\mathbf{P}_{x \eta_j, k} \mathbf{H}_{\eta_j, k}^\top) \\ \mathbf{K}_k &= (\mathbf{P}_{xx, k} \sum_{j=1}^m \mathbf{P}_{x \eta_j, k} \mathbf{H}_{\eta_j, k}^\top) \mathbf{S}_k^{-1} \end{aligned}$$

$$\text{State correction} \quad \hat{\mathbf{x}}_k^+ = \hat{\mathbf{x}}_k^- + \mathbf{K}_k (\mathbf{y}_k - \mathbf{H}_k \hat{\mathbf{x}}_k^-)$$

$$\text{Cov. correction} \quad \mathbf{P}_{xx, k}^+ = (\mathbf{I} - \mathbf{K}_k \mathbf{H}_k) \mathbf{P}_{xx, k}^- - \mathbf{K}_k \sum_{j=1}^m \mathbf{H}_{\eta_j, k} \mathbf{P}_{\eta_j x, k}$$

2.2.3.2. Integrated Navigation

The pure strapdown inertial navigation, as presented in Subsection 2.2.2 suffers from growing errors due to the integration of sensor errors. The basic idea of integrated navigation is to combine and correct the inertial navigation solution with external aidings in a stochastically consistent way. Ideally, the sources have complementary error characteristics, the high-dynamic but drifting inertial navigation should be combined with a non-drifting but possibly lower update-rate aiding. The most prominent example is the INS/GNSS integration, where GNSS position and velocity measurements are used to correct the inertial navigation solutions' drift [14, pp. 409–410]. The classical integrated navigation concepts use Kalman Filter-based data fusion and its variants to optimally combine inertial navigation with external aidings.

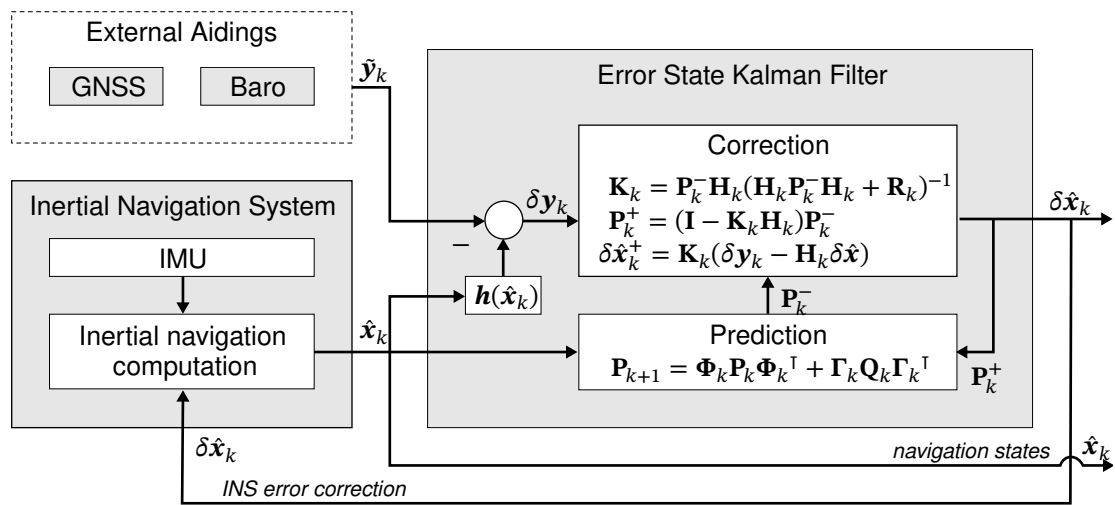


Figure 2.8.: General concept of an integrated navigation architecture based on the error state Kalman Filter.

As illustrated in Figure 2.8, the Kalman Filter is typically not used to directly estimate the navigation states but the errors of the navigation states. Compared to the total navigation states, the strapdown navigation errors have lower dynamics and can be easily linearized. The strapdown-error dynamics is derived and widely discussed in Subsection 3.3.1. The estimated navigation errors are fed back to correct the total navigation states.

2.3. Signal Analysis and Sensor Noise

2.3.1. Power Spectral Density

The power spectral density describes the distribution of power over frequency within the signal. For a (wide-sense) stationary random process, the Power Spectral Density (PSD) $S_x(f)$ is the Fourier transform of the signal's auto-correlation $R_{xx}(\tau)$ [58, p. 721]:

$$S_x(f) = \mathcal{F}\{R_{xx}(\tau)\} \quad (2.22)$$

where the auto-correlation of is typically defined as [59, p. 411]:

$$R_{xx}(\tau) = \int_{-\infty}^{\infty} x(t + \tau)x(\tau)dt \quad (2.23)$$

The PSD is a useful tool to analyze the composition of noise that can be described by a (wide-sense) stationary random process. In practice, all sensor and instrument signals are time-discrete (sampled) and the PSD must be estimated from a finite set of recorded samples. The most basic method to estimate a signal's $x[n]$ PSD is the so called *periodogram*. Using the Fast Fourier Transformation, it can be directly computed for the discrete frequencies f_k of a signal of length N as [58, p. 722]:

$$S_{\text{PER}}(f_k) = \frac{1}{N} \left| \sum_{n=0}^{N-1} x[n]e^{-j2\pi k \frac{n}{N}} \right|^2 \quad \text{with } f_k = \frac{k}{N}, \quad k = 0, 1, \dots, N-1 \quad (2.24)$$

For this simple estimator, the variance of the PSD estimate approximately scales with the squared PSD:

$$\text{Var}[S_{\text{PER}}(f)] \approx S^2(f) \quad (2.25)$$

This variance can be effectively reduced by splitting the signal into equal-length segments and averaging the PSD determined for each segment (Bartlett's method). Further reduction can be achieved if the signal is split into overlapping segments, as suggested by Welch [60]. In contrast to Bartlett's method, Welch's method applies windowing to each segment, and the allowed overlap increases the number of segments and thus reduces the estimate's variance [58, pp. 726–727]. The basic procedure of Welch's method is described in Algorithm 4.

In practice, signal noise is not necessarily a stationary process but may change with time, e.g., due to environmental changes. A simple tool to analyze non-stationary noise is the *spectrogram*, based on the short-time Fourier transformation. Using a sliding window, the signal is split into multiple (overlapping) segments for which the PSD is determined. The window length is a compromise between time resolution (narrow window), and frequency resolution (wide window) [58, pp. 747-748]. The spectrogram is usually plotted as a 2D heatmap with frequency and time on the axes.

2.3.2. Allan Variance

Initially developed for the analysis of the frequency stability of atomic clocks [61], the **Allan Variance (AVAR)** has become a standard procedure for the study of inertial sensor noise [26]. The AVAR is defined as the (sample) variance of the difference of average values of two consecutive signal clusters [62, p. 14]:

$$\sigma_{\text{AV}}^2(\tau) = \frac{1}{2(M-1)} \sum_{i=1}^M [\bar{\omega}_{i+1} - \bar{\omega}_i]^2 \quad (2.26)$$

Algorithm 4: Welch's power spectral density estimator.

In principle Welch's power spectral density estimator consists of the following steps [58, pp. 726–727]:

Signal segmentation	Choose the number of overlapping samples D and split signal into K overlapping segments of length L , so that $N = L + D(K - 1)$: $x_i[n] = x[n + iD]$
Window function	Choose a window function $w[n]$ and determine the window normalization C , e.g. Bartlett window: $w[n] = \frac{2}{L} \left(\frac{L}{2} - \left n - \frac{L-1}{2} \right \right)$, $C = \frac{1}{L} \sum_{n=0}^{L-1} w^2[n]$
Periodograms	Calculate periodogram for each windowed segment i : $S_i(f_k) = \frac{1}{L} \left \sum_{n=0}^{L-1} w[n] x_i[n] e^{-j2\pi k \frac{n}{L}} \right ^2$
Averaging	Average over the periodograms: $S_{\text{Welch}}(f_k) = \frac{1}{CK} \sum_{i=0}^K S_i(f_k)$

where $\overline{\omega}_i$ is the average over the i^{th} signal cluster of length τ . In the context of the **AVAR**, τ is typically denoted *averaging time* [62, p. 2].

Thus, the **AVAR** depends on the length τ of the clusters. The typically used *overlapping Allan variance* utilizes all possible overlapping samples from the available data to increase the confidence intervals of the **AVAR** estimate. The overlapping **AVAR** $\sigma^2(\tau)$ for averaging time τ can be estimated from a sensor's integrated, e.g., angle output Θ as follows [12]:

$$\sigma_{\text{AV}}^2(\tau) = \frac{1}{2\tau^2(N-2m)} \sum_{k=1}^{N-2m} (\Theta[k+2m] - 2\Theta[k+m] + \Theta[k])^2 \quad (2.27)$$

with the cluster size m that relates the averaging time to the sample time τ_0 :

$$\tau = m\tau_0 \quad (2.28)$$

Within this work, the **AVAR** is marked with the subscript AV to distinguish it from the classical variance. For non-integrating sensor output $\omega[k]$, the required $\Theta[k]$ may be determined by numerical integration using, e.g., Euler forward or the trapezoidal integration scheme. The basic method to determine the Allan variance from a given signal is described in **Algorithm 5**.

Generally, the confidence interval of **AVAR** estimates depends on the underlying noise processes. However, a simple approximation is given by $\sigma(\tau)/\sqrt{N}$ for the 1σ (68%) interval [62, p. 37]. If the noise type is known, the above approximation can be improved by applying the appropriate correction factors for the respective noise type. More accurate confidence intervals can be determined from χ^2 statistics. This requires knowledge of the equivalent degrees of

freedom of the χ^2 distribution for each noise type [62, pp. 39–40].

Algorithm 5: Overlapping Allan variance estimator.

Preparation	For frequency-like signals (e.g., angular rates), create phase-like signal by forward-Euler numerical integration: $\Theta[k] = \sum_{i=0}^k \omega[i]\tau_0$
Averaging times	Select averaging times $\tau = m\tau_0$ of interest in the range of $m \in [1, (N-1)/2]$, for a signal of length N . Typically m is limited to $m < N/4$. A (logarithmically) downsampled subset of the possible lengths m may be used to reduce the number of calculations.
Calculation	Calculate the Allan Variance for each cluster length m of interest as [62]: $\sigma_{AV}^2(\tau) = \frac{1}{2\tau^2(N-2m)} \sum_{k=1}^{N-2m} (\Theta[k+2m] - 2\Theta[k+m] + \Theta[k])^2$

The determination of the fully overlapping Allan variance as described in Algorithm 5 has high computational effort of $\Theta(N^3)$ for N sample points. Therefore, many efficient and fast computation algorithms have been suggested, e.g., [63, 64].

The AVAR can be determined from integrating over the PSD and applying a transfer function that represents the clustering and averaging operations [12, p. 63]:

$$\sigma_{AV}^2(\tau) = 4 \int_0^{\infty} S_{\Omega}(f) \frac{\sin^4(\pi f \tau)}{\pi f \tau} df \quad (2.29)$$

Analog to the spectrogram, there is also an extension of the Allan variance to non-stationary noise, called the **Dynamic Allan Variance (DAVAR)** [65]. Furthermore, several other variances, such as the Modified Allan Variance or the Hadamard variance, have been proposed to overcome drawbacks of the classical Allan variance [62, p. 11].

2.3.3. Sensor Noise Processes

Inertial sensor noise is a complex combination of several different noise processes that are usually identified using the PSD and AVAR analysis. Based on these two methods, the IEEE standards on specification and testing of various inertial sensor technologies [9, 41, 26] define a set of typical noise processes that can be found in inertial sensor output:

- **Quantization Noise (QN)** is caused by a quantization of the measurements, which is close to angular respectively velocity white noise. In the context of frequency stability, this corresponds to phase white noise. Quantization noise may be caused by the measurement

principle in optical sensors but is also caused by analog to digital conversion [26]. The scaling coefficient is Q .

- **Angular Random Walk (ARW) / Velocity Random Walk (VRW)** is a white noise signal on the measured angular rates, respectively acceleration. In the context of frequency stability, it is equivalent to frequency white noise. For optical sensors, this can be attributed to spontaneous photon emissions [41]. It is specified by the scaling coefficient N .
- **Bias Instability (BI)** is a slow variation of the sensor's bias. It is a frequency flicker noise with a sharp cutoff at f_c . It is mainly attributed to random flickering within the electronics. Bias instability is parameterized by the scaling B and the cutoff frequency f_c .
- **Rate Random Walk (RRW) / Acceleration Random Walk** is a random walk process on the angular rate respectively acceleration. This is equivalent to white noise on the angular accelerations respectively the acceleration rate of change (jerk). Its scaling coefficient is K .
- **Rate Ramp Noise / Acceleration Ramp Noise** is a linearly increasing drift on the rate output. Rate ramp noise should not be confused with a flicker random-walk in the frequency, although they have the same slope in the Allan variance plot. Its origin is attributed to slow changes in the sensor's characteristics, e.g., a change of the FOG's source intensity [41]. The defining coefficient is R .

Above and further noise processes, like Markov noise or sinusoidal noise, may or may not be observable in the sensor output. This existence and magnitude of the different noise processes is mainly defined by the sensor's measurement principle and its implementation. A summary of the defining PSD and AVAR slopes is given in Table 2.7. Under the assumption that the different noise processes are independent, the combined Allan variance of the sensor's noise is given by the summation over all noise processes:

$$\sigma_{AV}^2(\tau) \approx \frac{3Q^2}{\tau^2} + \frac{N^2}{\tau} + (0.664B)^2 + \frac{K^2\tau}{3} + \frac{R^2\tau^2}{2} + \dots \quad (2.30)$$

From an Allan variance plot, as depicted in Figure 2.9, the defining parameters of the different noise processes can be easily read off. Alternatively, the parameters may be determined from the AVAR by performing a least-squares fit of the reference model equations from Table 2.7. As the variances for higher averaging times are determined from a smaller set of clusters, the estimation error grows with the averaging time. To consider this effect in the parameter identification, a weighted least-squares scheme is suggested in [66]. Further more, equation (2.30) should be adopted to actual AVAR results to prevent adjustment to an inappropriate noise model. Alternatively, a non-negative least-squares algorithm should be used to prevent fitting errors due to negative model coefficients.

Table 2.7.: Typical sensor noise processes from the IEEE standards [41].

Process	Power Spectral Density	Allan Variance
Quantization Noise	$S_Q(f) \approx Q^2 \tau_s (2\pi f)^2$	$\sigma_{AV,Q}^2(\tau) = \frac{3Q^2}{\tau^2}$
Angular Random Walk	$S_N(f) = N^2$	$\sigma_{AV,N}^2(\tau) = \frac{N^2}{\tau}$
Bias Instability	$S_B(f) = \begin{cases} \left(\frac{B^2}{2\pi}\right) \frac{1}{f} & f \leq f_{0,B} \\ 0 & f > f_{0,B} \end{cases}$	$\sigma_{AV,B}^2(\tau) = \frac{2B^2}{\pi} \left[\ln 2 - \frac{\sin^3(x)}{2x^2} (\sin(x) + 4x \cos(x)) + Ci(2x) - Ci(4x) \right], \quad x = \pi f_{0,B} \tau$
Rate Random Walk	$S_K(f) = \frac{K^2}{(2\pi f)^2}$	$\sigma_{AV,K}^2(\tau) = \frac{K^2 \tau}{3}$
Rate Ramp Noise	$S_R(f) = \frac{R^2}{(2\pi f)^3}$	$\sigma_{AV,R}^2(\tau) = \frac{R^2 \tau^2}{2}$

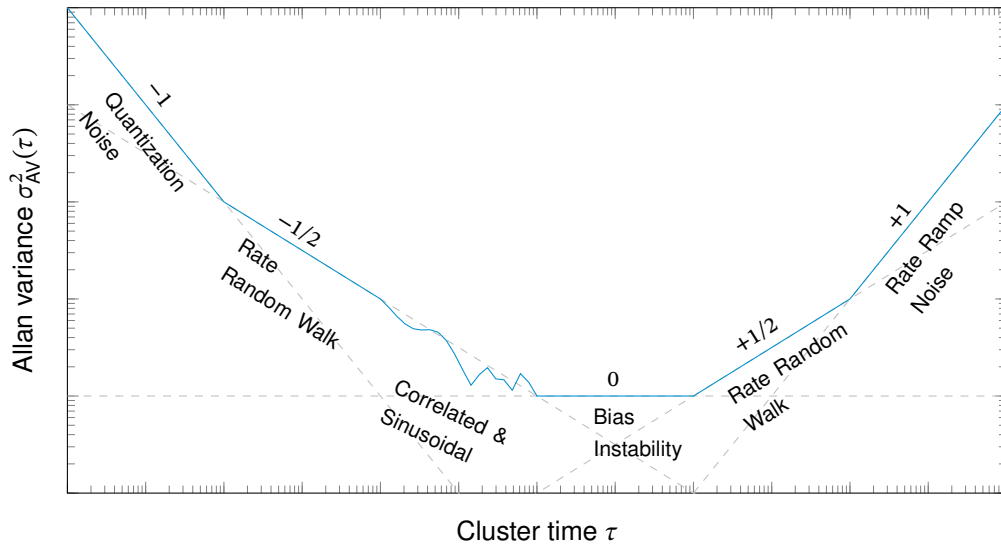


Figure 2.9.: Sensor noise processes in the Allan variance analysis.

2.3.4. Confidence Intervals

As the identification of sensor noise processes is widely based on the *AVAR* estimate, its estimation accuracy is a critical factor for the sensor noise characterization. It is reasonable that the confidence interval scales somehow with the number of points used to determine the *AVAR*. Due to the underlying averaging of multiple estimates, the estimation accuracy of the *AVAR* depends on the time-correlation of the signal. The estimation of the confidence interval thus requires knowledge or at least a guess of the true noise processes.

A very simple approximation of the 68 % confidence interval of the Allan variance estimate is given by [62, p. 37]:

$$C_{68\%} = K_n \frac{\sigma_{AV}(\tau)}{\sqrt{N}} \quad (2.31)$$

with the Allan variance $\sigma_{AV}(\tau)$, the number of data points N and K_n a correction factor to take into account the correlation caused by the noise processes. The correction factors for the typical noise processes are summarized in Table 2.8. Despite the introduction of correction

Table 2.8.: Correction factors for Allan variance confidence intervals [62, p. 37].

Noise process	K_n
Quantization noise	0.99
Angular random walk	0.87
Bias instability	0.77
Rate random walk	0.75

factors, above equation provides only a rough approximation. A more accurate estimate of the confidence intervals can be obtained from the χ^2 statistics. Here, the variance at confidence p

is related to the sample Allan variance $\sigma_{AV}(\tau)$ as [62]:

$$\sigma_p^2 = \sigma_{AV}^2(\tau) \frac{d}{\chi^2(p, d)} \quad (2.32)$$

where d is the **equivalent degrees of freedom (e.d.f)** of the χ^2 distribution, characteristic for the Allan variance calculation and the noise types. A method to determine the exact e.d.f for different noise types is given in [67]. However, since the power-law noise is just an idealization of the true noise, the exact e.d.f provide a slight advantage compared to approximation formulas. A set of empirical formulas for the e.d.f for various noise types from [68] is given in Table 2.9.

Table 2.9.: Approximations of the overlapping Allan variance equivalent degrees of freedom [68] from the number of data points N and the averaging factor $m = \tau/\tau_0$.

Noise process	Equivalent degree of freedom d
Quantization noise	$\frac{(N+1)(N-2m)}{2(N-m)}$
Angular random walk	$\left[\frac{3(N-1)}{2m} - \frac{2(N-2)}{N} \right] \frac{4m^2}{4m^2+5}$
Bias instability	$\frac{2(N-2)^2}{2.3N-4.9}$ for $m=1$ $\frac{4m(N+3m)}{5N^2}$ for $m>1$
Rate random walk	$\left[\frac{N-2}{m} \right] \left[\frac{(N-1)^2 - 3m(N-1) + 4m^2}{(N-3)^2} \right]$

The resulting upper boundaries of the confidence intervals can now be determined from (2.32) and Table 2.9. The variation of the confidence interval with the number of samples is exemplarily depicted in Figure 2.10a. The total number of samples has little effect on the integrating noise types angular random walk, bias instability, and rate random walk. Although the effect on the confidence intervals for quantization noise is relatively high, the confidence intervals for this type of noise are relatively low for a wide range of averaging times. Clearly, the confidence intervals of the integrating noise types converge towards $m = N/2$, where the e.d.f is 1.

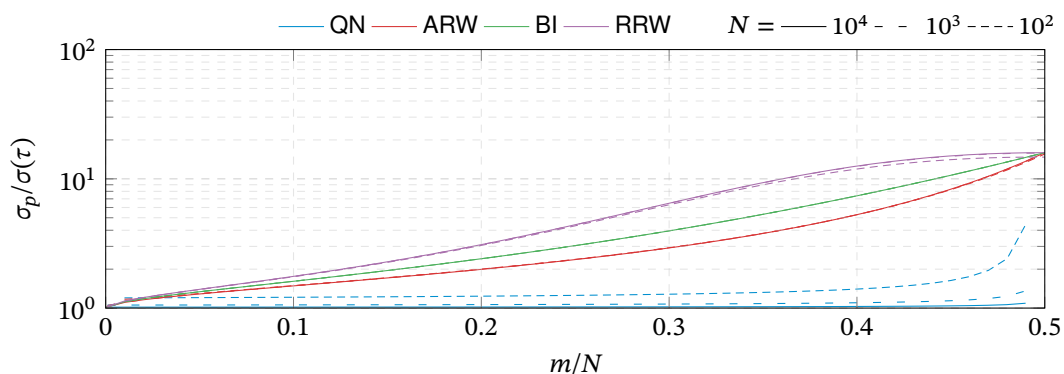
The upper boundary variation with the confidence level is depicted in Figure 2.10b. It can be seen that already for $m/N < 0.25$, at least the magnitude of an Allan Variance estimate is almost certainly correct, i.e., the boundary of the 99% interval is at a maximum ten times the estimated Allan variance. Therefore, Allan variance plots are often cut-off at 1/4 of the total number of recorded samples, especially if no confidence intervals are stated.

The above definitions of the e.d.f are only for single power-law noise processes. Inertial sensor noise, however, consists of multiple noise processes. For such a case, it can be demonstrated that the e.d.f d of the variance estimator is at least the minimum e.d.f d_k of the underlying processes [67]:

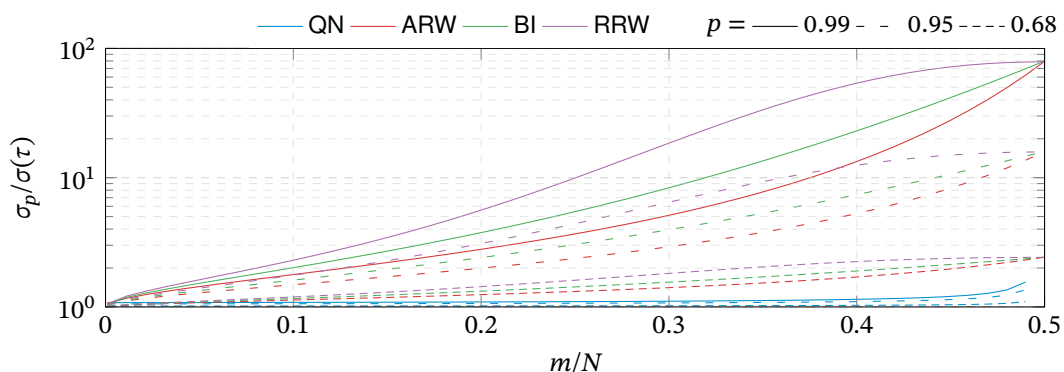
$$d \geq \min_k \{d_k\} \quad (2.33)$$

If the noise types have been identified, e.g., from the slope of the Allan variance plots, the

above equation allows the determination of a worst-case estimate of d . Therefore, the degrees of freedom d_k are calculated for each expected noise type, and the smallest value is used at each τ . The confidence intervals depicted in Example 4 have been determined using this procedure. Alternatively, the power-law noise type at each value of τ can be determined by comparing the Barnes' B_1 function at τ to the appropriate reference values for the respective power-law noise, see [62, p. 44]. Having determined the most representative noise type at each τ , the appropriate e.d.f and the confidence intervals can be determined separately for each τ .



(a) Upper boundary of the 95% confidence interval with respect to $\sigma(\tau)$ with variation of the total number of samples N .



(b) Upper boundary of various confidence intervals with respect to $\sigma(\tau)$ for $N = 1000$.

Figure 2.10.: Confidence intervals of the overlapping Allan variance estimation for various sensor noise types.

The IEEE standards on inertial sensors suggest an alternate equation to determinate "the percentage error" e of the AVAR estimates [10, p. 71]:

$$e = \frac{1}{\sqrt{2\left(\frac{N}{K} - 1\right)}} \quad (2.34)$$

Here, N is the total number of recorded data points, and K is the number of independent clusters used to determine the AVAR at τ . For equal distribution of the clusters it is $K = \frac{N}{m}$. Equation (2.34) does neither include stochastic considerations nor does it incorporate any

information on the noise types. It may therefore be considered as a rough approximation similar to (2.31), only. However, the order magnitude of the total test duration is close to the values read off from the graphs in [Figure 2.10](#) and is, therefore, a handy tool for test design.

Chapter 3.

Strapdown Inertial Navigation Error Propagation

3.1. Introduction

Having defined the navigation requirements, these need to be transferred into the inertial sensor accuracy. The relationship between inertial sensor errors and the resulting navigation performance will be discussed in this chapter. The structure and outline of this chapter is illustrated in Figure 3.1.

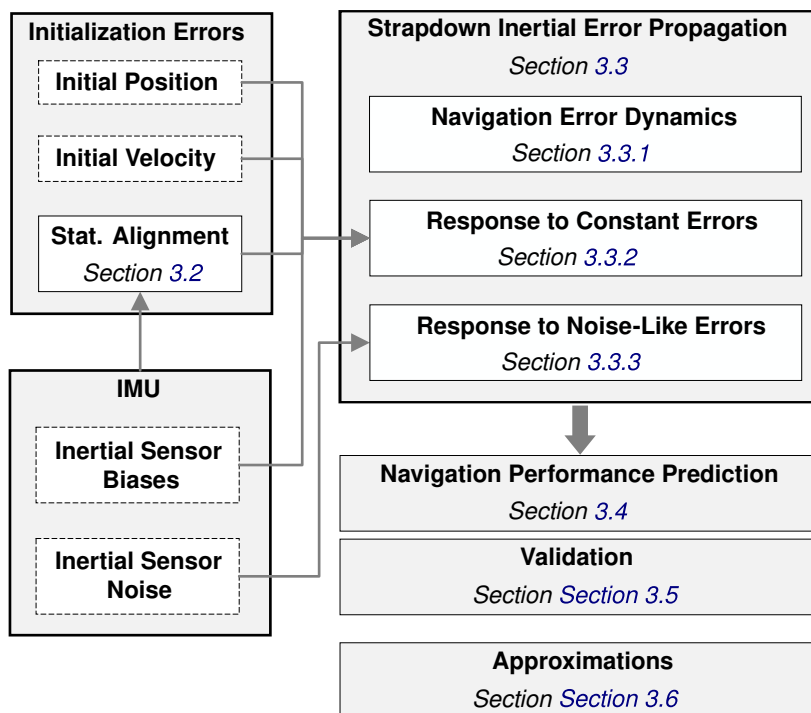


Figure 3.1.: Outline of the Inertial Navigation Error Analysis Chapter.

Following the operation of inertial navigation systems, the chapter starts with analyzing the propagation of sensor errors into the stationary alignment. Subsequently, the propagation of initialization errors and sensor errors is discussed. The resulting navigation errors from initialization and sensor errors are derived and visualized. These results are then used to

create methods for predicting the navigation performance from sensor errors. Ultimately, these methods are validated using two numerical examples.

3.2. Stationary Alignment Errors

Inertial navigation requires an initialization of the navigations states, prior to their propagation. Determining the initial position and velocity requires external aiding, either by additional sensors (e.g., GNSS) or other knowledge about the situation. Such a situation can be, e.g., an aircraft at a known parking position. In contrast, the initial orientation can be determined entirely from the inertial sensors' measurements.

Typically, alignment procedures are distinguished between the autonomous self-aligning techniques and the transfer alignment from a reference to another system [14, pp. 277]. Self-alignment relies only on the IMU measurements and no further aiding or maneuver. The impact of inertial sensor errors on self-alignment accuracy will be analyzed in the following section.

3.2.1. General

Mathematically, the task of self-alignment is to identify the rotation matrix \mathbf{R}_{nb} that describes the vehicle's orientation towards the North-East-Down (NED)-frame from the strapdown equations:

$$\dot{\mathbf{v}}_n = \mathbf{R}_{nb}\mathbf{f}_b - (2\mathbf{R}_{ne}\boldsymbol{\omega}_{ie} + \boldsymbol{\omega}_{en}) \times \mathbf{v}_n + \boldsymbol{\gamma}_n \quad (3.1)$$

$$\dot{\mathbf{R}}_{nb} = \mathbf{R}_{nb}\boldsymbol{\Omega}_{ib} - \boldsymbol{\Omega}_{in}\mathbf{R}_{nb} \quad (3.2)$$

To find a fixed initial orientation, above ODE need to be evaluated at a steady state. Ideally, this is realized by a stationary (non-moving) vehicle. In practice, however, many vehicles are subject to perturbations even during alignment. For example, these can be a ship's motion or vibrations induced from an aircraft's running engines. If perturbations cannot be reduced by isolation or procedures, a Kalman Filter can be used to estimate the attitude in the presence of perturbations [14, p. 286].

It is important to note that even if the perturbation motion is zero in average

$$\frac{1}{t} \int_0^t \dot{\mathbf{v}}_n(\tau) d\tau = 0 \quad (3.3)$$

$$\frac{1}{t} \int_0^t \mathbf{v}_n(\tau) d\tau = 0 \quad (3.4)$$

the non-linearity of the centrifugal forces in (3.1) will not average to zero in general. They will

lead to a bias-like error in the specific force measurement, instead:

$$\boldsymbol{\omega}_{en} \times \mathbf{v}_n = \begin{bmatrix} \frac{v_e}{r_N} \\ -\frac{v_n}{r_M} \\ \frac{v_e}{r_N} \tan \phi \end{bmatrix} \times \begin{bmatrix} v_n \\ v_e \\ v_d \end{bmatrix} = \begin{bmatrix} -\frac{v_n v_d}{r_M} - \frac{v_e^2}{r_N} \tan \phi \\ \frac{v_e v_n}{r_N} \tan \phi - \frac{v_e v_d}{r_N} \\ \frac{v_e^2}{r_N} + \frac{v_n^2}{r_M} \end{bmatrix} \quad (3.5)$$

However, in practice the resulting additional specific forces are rather small due to the scaling with the Earth's radius: perturbations in the range of 1 m s^{-1} lead to an error in the range of 10^{-8} g .

Assuming a steady state, equations (3.1) and (3.2) can be solved for the inertial measurements as a function of the orientation matrix and the reference signals gravity and Earth's angular rate:

$$\mathbf{f}_b = \mathbf{R}_{bn} \boldsymbol{\gamma}_n \quad (3.6)$$

$$\boldsymbol{\omega}_{ib} = \mathbf{R}_{bn} \mathbf{R}_{ne} \boldsymbol{\omega}_{ie} \quad (3.7)$$

From these equations the orientation angles can be determined as trigonometric functions of the stationary IMU outputs:

$$\Phi = \text{atan} \left(\frac{-f_{b,x}}{-f_{b,y}} \right) \quad (3.8)$$

$$\Theta = \text{asin} \left(\frac{f_{b,x}}{\|\mathbf{f}_b\|} \right) \quad (3.9)$$

$$\Psi = \text{atan} \left(\frac{-\omega_{ib,y} \cos \Phi + \omega_{ib,z} \sin \Phi}{\omega_{ib,x} \cos \Phi + \omega_{ib,y} \sin \Phi \sin \Theta + \omega_{ib,z} \cos \Phi \sin \Theta} \right) \quad (3.10)$$

The inertial measurements in these equations are typically averages of the IMU's output. This shall attenuate the sensor's noise and perturbations.

3.2.2. Derivation of the Alignment Errors

To determine the relationship between sensor and model errors and the alignment errors, each parameter is split into its measured value and the error:

$$\tilde{\mathbf{f}}_b + \delta \mathbf{f}_b = \mathbf{R}_{b\tilde{n}} \mathbf{R}_{\tilde{n}n} (\tilde{\boldsymbol{\gamma}}_n + \delta \boldsymbol{\gamma}) \quad (3.11)$$

Note that the inertial sensor errors $\delta \mathbf{f}_b$ and $\delta \boldsymbol{\omega}_{ib}$ are the residual errors after averaging and conditioning (e.g. filtering) the measured IMU outputs.

The errors should be small by definition, which justifies linearization for the error terms. The error rotation matrix $\mathbf{R}_{\tilde{n}n}$ can thus be approximated by the skew-symmetric matrix of the

error rotation angles (see Appendix A):

$$\mathbf{R}_{\tilde{n}n} \approx (\mathbf{I} + \boldsymbol{\Psi}_{n\tilde{n}\times}) \quad (3.12)$$

Applying (3.6) and neglecting 2nd order terms as

$$\tilde{\mathbf{f}}_b + \delta \mathbf{f}_b \approx \mathbf{R}_{b\tilde{n}} (\mathbf{I} + \boldsymbol{\Psi}_{n\tilde{n}\times}) (\tilde{\boldsymbol{\gamma}}_n + \delta \boldsymbol{\gamma}) \quad (3.13)$$

$$\tilde{\mathbf{f}}_b + \delta \mathbf{f}_b \approx \mathbf{R}_{b\tilde{n}} \tilde{\boldsymbol{\gamma}}_n + \mathbf{R}_{b\tilde{n}} \underbrace{(\boldsymbol{\Psi}_{n\tilde{n}\times}) \delta \boldsymbol{\gamma}_n}_{2^{\text{nd}} \text{ order}} + \mathbf{R}_{b\tilde{n}} (\boldsymbol{\Psi}_{n\tilde{n}\times}) \tilde{\boldsymbol{\gamma}}_n + \mathbf{R}_{b\tilde{n}} \delta \boldsymbol{\gamma}_n \quad (3.14)$$

$$\mathbf{R}_{b\tilde{n}}^\top \delta \mathbf{f}_b \approx (\boldsymbol{\Psi}_{n\tilde{n}\times}) \tilde{\boldsymbol{\gamma}}_n + \delta \boldsymbol{\gamma}_n \quad (3.15)$$

$$\mathbf{R}_{b\tilde{n}}^\top \delta \mathbf{f}_b - \delta \boldsymbol{\gamma}_n \approx (\boldsymbol{\Psi}_{n\tilde{n}\times}) \tilde{\boldsymbol{\gamma}}_n \quad (3.16)$$

leads to the following relationship between the orientation errors and the inertial measurement errors and gravity model errors:

$$\mathbf{R}_{b\tilde{n}}^\top \begin{bmatrix} \delta f_{b,x} \\ \delta f_{b,y} \\ \delta f_{b,z} \end{bmatrix} - \begin{bmatrix} \varepsilon g \\ \eta g \\ \Delta g \end{bmatrix} \approx \begin{bmatrix} \delta \Theta \\ -\delta \Phi \\ 0 \end{bmatrix} g \quad (3.17)$$

Here, the local gravity errors are represented by the local gravity anomaly Δg and the deflections from the plumb line ε, η . Expressed in Euler-angles, the rotation matrix is given as:

$$\mathbf{R}_{b\tilde{n}}^\top = \begin{bmatrix} \cos \tilde{\Theta} \cos \tilde{\Psi} & \sin \tilde{\Phi} \sin \tilde{\Theta} \cos \tilde{\Psi} - \cos \tilde{\Phi} \sin \tilde{\Psi} & \cos \tilde{\Phi} \sin \tilde{\Theta} \cos \tilde{\Psi} + \sin \tilde{\Phi} \sin \tilde{\Psi} \\ \cos \tilde{\Theta} \sin \tilde{\Psi} & \sin \tilde{\Phi} \sin \tilde{\Theta} \sin \tilde{\Psi} + \cos \tilde{\Phi} \sin \tilde{\Psi} & \cos \tilde{\Phi} \sin \tilde{\Theta} \sin \tilde{\Psi} - \sin \tilde{\Phi} \cos \tilde{\Psi} \\ -\sin \tilde{\Theta} & \sin \tilde{\Phi} \cos \tilde{\Theta} & \cos \tilde{\Phi} \cos \tilde{\Theta} \end{bmatrix} \quad (3.18)$$

Applying the same procedure to the angular measurements (3.7)

$$\tilde{\boldsymbol{\omega}}_{ib} + \delta \boldsymbol{\omega}_{ib} = \mathbf{R}_{b\tilde{n}} \mathbf{R}_{\tilde{n}n} \mathbf{R}_{ne}(\phi, \lambda) (\tilde{\boldsymbol{\omega}}_{ie} + \delta \boldsymbol{\omega}_{ie}) \quad (3.19)$$

$$\tilde{\boldsymbol{\omega}}_{ib} + \delta \boldsymbol{\omega}_{ib} \approx \mathbf{R}_{b\tilde{n}} (\mathbf{I} + \boldsymbol{\Psi}_{\tilde{n}n\times}) \mathbf{R}_{ne}(\phi, \lambda) (\tilde{\boldsymbol{\omega}}_{ie} + \delta \boldsymbol{\omega}_{ie}) \quad (3.20)$$

$$\tilde{\boldsymbol{\omega}}_{ib} + \delta \boldsymbol{\omega}_{ib} \approx \mathbf{R}_{b\tilde{n}} \mathbf{R}_{ne}(\phi, \lambda) \tilde{\boldsymbol{\omega}}_{ie} + \mathbf{R}_{b\tilde{n}} \mathbf{R}_{ne}(\phi, \lambda) \delta \boldsymbol{\omega}_{ie} + \quad (3.21)$$

$$\mathbf{R}_{b\tilde{n}} (\boldsymbol{\Psi}_{\tilde{n}n\times}) \mathbf{R}_{ne}(\phi, \lambda) \tilde{\boldsymbol{\omega}}_{ie} + \underbrace{\mathbf{R}_{b\tilde{n}} (\boldsymbol{\Psi}_{\tilde{n}n\times}) \mathbf{R}_{ne}(\phi, \lambda) \delta \tilde{\boldsymbol{\omega}}_{ie}}_{2^{\text{nd}} \text{ order}}$$

$$\mathbf{R}_{b\tilde{n}}^\top \delta \boldsymbol{\omega}_{ib} \approx (\boldsymbol{\Psi}_{\tilde{n}n\times}) \mathbf{R}_{ne}(\phi, \lambda) \tilde{\boldsymbol{\omega}}_{ie} + \mathbf{R}_{ne}(\phi, \lambda) \delta \boldsymbol{\omega}_{ie} \quad (3.22)$$

$$\mathbf{R}_{b\tilde{n}}^\top \delta \boldsymbol{\omega}_{ib} - \mathbf{R}_{ne}(\phi, \lambda) \delta \boldsymbol{\omega}_{ie} \approx (\boldsymbol{\Psi}_{\tilde{n}n\times}) \mathbf{R}_{ne}(\phi, \lambda) \tilde{\boldsymbol{\omega}}_{ie} \quad (3.23)$$

ultimately yields:

$$\mathbf{R}_{b\bar{n}}^\top \begin{bmatrix} \delta\omega_{ib,x} \\ \delta\omega_{ib,y} \\ \delta\omega_{ib,z} \end{bmatrix} - \mathbf{R}_{ne}(\phi, \lambda) \begin{bmatrix} \delta\omega_{ie,x} \\ \delta\omega_{ie,y} \\ \delta\omega_{ie,z} \end{bmatrix} \approx \begin{bmatrix} -\delta\Theta \sin \phi \\ \delta\Psi \cos \phi + \delta\Phi \sin \phi \\ -\delta\Theta \cos \phi \end{bmatrix} \omega_{ie} \quad (3.24)$$

with the rotation matrix between the Earth-Centered-Earth-Fixed (ECEF) and NED frames:

$$\mathbf{R}_{ne}(\phi, \lambda) = \begin{bmatrix} -\sin \phi \cos \lambda & -\sin \phi \sin \lambda & \cos \phi \\ -\sin \lambda & \cos \lambda & 0 \\ -\cos \phi \cos \lambda & -\cos \phi \sin \lambda & -\sin \lambda \end{bmatrix} \quad (3.25)$$

Equations (3.17) and (3.24) are solved for the orientation errors to determine the following linear relation to the sensors' and gravity's errors:

$$\underbrace{\begin{bmatrix} \delta\Phi \\ \delta\Theta \\ \delta\Psi \end{bmatrix}}_{\delta\psi} = \mathbf{H}_{SA} \cdot \underbrace{\begin{bmatrix} \delta f_{b,x} & \delta f_{b,y} & \delta f_{b,z} & \delta\omega_{ib,x} & \delta\omega_{ib,y} & \delta\omega_{ib,z} & \varepsilon & \eta & \Delta g & \delta\omega_{ie,x} & \delta\omega_{ie,y} & \delta\omega_{ie,z} \end{bmatrix}^\top}_{\delta\mathbf{u}^\top} \quad (3.26)$$

with

$$\mathbf{H}_{SA}^\top = \begin{bmatrix} \frac{\cos \bar{\Theta} \sin \bar{\Psi}}{\bar{g}} & \frac{\cos \bar{\Theta} \cos \bar{\Psi}}{\bar{g}} & \frac{\cos \bar{\Theta} \sin \bar{\Psi} \tan \phi}{\bar{g}} \\ \frac{\sin \bar{\Phi} \sin \bar{\Theta} \sin \bar{\Psi} + \cos \bar{\Phi} \cos \bar{\Psi}}{\bar{g}} & \frac{\sin \bar{\Phi} \sin \bar{\Theta} \cos \bar{\Psi} - \cos \bar{\Phi} \sin \bar{\Psi}}{\bar{g}} & \frac{(\sin \bar{\Phi} \sin \bar{\Theta} \sin \bar{\Psi} + \cos \bar{\Phi} \cos \bar{\Psi}) \tan \phi}{\bar{g}} \\ \frac{\cos \bar{\Phi} \sin \bar{\Theta} \cos \bar{\Psi} - \sin \bar{\Phi} \cos \bar{\Psi}}{\bar{g}} & \frac{\cos \bar{\Phi} \sin \bar{\Theta} \cos \bar{\Psi} + \sin \bar{\Phi} \sin \bar{\Psi}}{\bar{g}} & \frac{(\cos \bar{\Phi} \sin \bar{\Theta} \cos \bar{\Psi} - \sin \bar{\Phi} \cos \bar{\Psi})}{\bar{g}} \\ 0 & 0 & \frac{\cos \bar{\Theta} \sin \bar{\Psi}}{\bar{\omega}_{ie} \cos \phi} \\ 0 & 0 & \frac{\sin \bar{\Phi} \sin \bar{\Theta} \sin \bar{\Psi} + \sin \bar{\Phi} \cos \bar{\Psi}}{\bar{\omega}_{ie} \cos \phi} \\ 0 & 0 & \frac{\cos \bar{\Phi} \sin \bar{\Theta} \cos \bar{\Psi} - \sin \bar{\Phi} \cos \bar{\Psi}}{\bar{\omega}_{ie} \cos \phi} \\ 0 & -1 & 0 \\ 1 & 0 & \tan \phi \\ 0 & 0 & 0 \\ 0 & 0 & \sin \lambda \\ 0 & 0 & -\cos \lambda \\ 0 & 0 & 0 \end{bmatrix} \quad (3.27)$$

3.2.3. Alignment Uncertainty

The linear relationship (3.26) allows the leap from a deterministic to the probabilistic view of the input and output errors. The uncertainty of the alignment angles can be described by its

covariance matrix $\mathbf{P}_{\delta\psi}$:

$$\mathbf{P}_{\delta\psi} = E[\delta\boldsymbol{\Psi}\delta\boldsymbol{\Psi}^\top] = E[\mathbf{H}_{SA}\delta\mathbf{u}\delta\mathbf{u}^\top\mathbf{H}_{SA}^\top] = \mathbf{H}_{SA}E[\delta\mathbf{u}\delta\mathbf{u}^\top]\mathbf{H}_{SA}^\top = \mathbf{H}_{SA}\mathbf{P}_u\mathbf{H}_{SA}^\top \quad (3.28)$$

In many applications, the vehicles are close to leveled during the self-alignment. For example, runways and taxiways but also ships are fairly leveled, which justifies the following assumption:

Assumption 3.2.1. *The vehicle is sufficiently close to being leveled so that the small-angle approximation applies, and quadratic and higher terms of the pitch and roll angles can be neglected. For attitude angles of less than 5 deg, this approximation results in an error of less than 0.4%.*

Under assumption 3.2.1, matrix \mathbf{H}_{SA} simplifies to:

$$\mathbf{H}_{SA,lvd} = \begin{bmatrix} -\frac{s\bar{\Psi}}{\bar{g}} & -\frac{c\bar{\Psi}}{\bar{g}} & \frac{(\bar{\Phi}-\bar{\Theta})c\bar{\Psi}}{\bar{g}} & 0 & 0 & 0 & 0 & 1 & 0 & 0 & 0 & 0 \\ \frac{c\bar{\Psi}}{\bar{g}} & -\frac{s\bar{\Psi}}{\bar{g}} & \frac{\bar{\Phi}s\bar{\Psi}+\bar{\Theta}c\bar{\Psi}}{\bar{g}} & 0 & 0 & 0 & -1 & 0 & 0 & 0 & 0 & 0 \\ \frac{\bar{g}}{s\bar{\Psi}t\phi} & \frac{\bar{g}}{c\bar{\Psi}t\phi} & \frac{(\bar{\Theta}-\bar{\Phi})c\bar{\Psi}}{\bar{g}} & \frac{s\bar{\Psi}}{\bar{\omega}_{ie}c\phi} & \frac{\bar{\Phi}c\bar{\Psi}}{\bar{\omega}_{ie}c\phi} & \frac{(\bar{\Theta}-\bar{\Phi})c\bar{\Psi}}{\bar{\omega}_{ie}c\phi} & 0 & t\phi & 0 & s\lambda & -c\lambda & 0 \end{bmatrix} \quad (3.29)$$

For readability, the trigonometric functions have been abbreviated as s (sine), c (cosine) and t (tangent). In general, there is no correlation between the different model errors, and the sensor axes are independent. Consequently, the cross-correlation between the different input errors can be neglected:

Assumption 3.2.2. *The inertial sensor and modeling errors during self-alignment are uncorrelated. Thus, the covariance matrix of the input errors \mathbf{P}_u is purely diagonal.*

Under assumptions 3.2.1 and 3.2.2 the input error covariance matrix is diagonal with the residual variance of the error terms as entries:

$$\mathbf{P}_{\delta\mathbf{u}} = \text{diag}\left(\sigma_{\delta f_{b,x}}^2, \sigma_{\delta f_{b,y}}^2, \sigma_{\delta f_{b,z}}^2, \sigma_{\delta\omega_{ib,x}}^2, \sigma_{\delta\omega_{ib,y}}^2, \sigma_{\delta\omega_{ib,z}}^2, \sigma_\varepsilon^2, \sigma_\eta^2, \sigma_{\Delta g}^2, \sigma_{\delta\omega_{ie,x}}^2, \sigma_{\delta\omega_{ie,y}}^2, \sigma_{\delta\omega_{ie,z}}^2\right) \quad (3.30)$$

Using (3.28) and the above input covariance yields the following alignment error covariance

matrix:

$$\mathbf{P}_{\delta\psi, \text{lvd}} = \begin{bmatrix} \sigma_\varepsilon^2 + \frac{\sigma_{\delta f_{b,x}}^2 s^2 \Psi + \sigma_{\delta f_{b,y}}^2 c^2 \Psi}{\bar{g}^2} & \frac{(\sigma_{\delta f_{b,y}}^2 - \sigma_{\delta f_{b,x}}^2) s 2\Psi}{2\bar{g}^2} & \left(\sigma_\varepsilon^2 - \frac{\sigma_{\delta f_{b,x}}^2 s^2 \Psi + \sigma_{\delta f_{b,y}}^2 c^2 \Psi}{\bar{g}^2} \right) t \phi \\ \frac{(\sigma_{\delta f_{b,y}}^2 - \sigma_{\delta f_{b,x}}^2) s 2\Psi}{2\bar{g}^2} & \sigma_\eta^2 + \frac{\sigma_{\delta f_{b,x}}^2 c^2 \Psi + \sigma_{\delta f_{b,y}}^2 s^2 \Psi}{\bar{g}^2} & \frac{(\sigma_{\delta f_{b,x}}^2 - \sigma_{\delta f_{b,y}}^2) s 2\Psi t \phi}{2\bar{g}^2} \\ \left(\sigma_\varepsilon^2 - \frac{\sigma_{\delta f_{b,x}}^2 s^2 \Psi + \sigma_{\delta f_{b,y}}^2 c^2 \Psi}{\bar{g}^2} \right) t \phi & \frac{(\sigma_{\delta f_{b,x}}^2 - \sigma_{\delta f_{b,y}}^2) s 2\Psi t \phi}{2\bar{g}^2} & \begin{aligned} & \sigma_\varepsilon^2 t^2 \phi + \sigma_{\delta \omega_{ie,x}}^2 s^2 \lambda + \sigma_{\delta \omega_{ie,y}}^2 c^2 \lambda \\ & + \frac{\sigma_{\delta \omega_{ib,x}}^2 s^2 \tilde{\Psi} + \sigma_{\delta \omega_{ib,y}}^2 c^2 \tilde{\Psi}}{\tilde{\omega}_{ie}^2 c^2 \phi} \\ & + \frac{(\sigma_{\delta f_{b,y}}^2 c^2 \tilde{\Psi} + \sigma_{\delta f_{b,x}}^2 s^2 \tilde{\Psi}) t^2 \phi}{\bar{g}^2} \end{aligned} \end{bmatrix} \quad (3.31)$$

Usually, an inertial sensor triad consists of equal sensors for each axis. Consequently, all sensor axes share the same error statistics and are thus described by the same variance.

Assumption 3.2.3. *The inertial sensor and model errors are isotropic, which is all axes are described by the same variance:*

- $\sigma_{f_{b,x}}^2 = \sigma_{f_{b,y}}^2 = \sigma_{f_{b,z}}^2 = \sigma_{f_b}^2$
- $\sigma_{\delta \omega_{ib,x}}^2 = \sigma_{\delta \omega_{ib,y}}^2 = \sigma_{\delta \omega_{ib,z}}^2 = \sigma_{\delta \omega_{ib}}^2$
- $\sigma_{\delta \omega_{eb,x}}^2 = \sigma_{\delta \omega_{ie,y}}^2 = \sigma_{\delta \omega_{ie}}^2$

Taking assumption 3.2.3 into account, the alignment covariance becomes independent of the actual azimuth and geodetic longitude and provides a simple to use estimation of the self-alignment accuracy from different error inputs:

$$\mathbf{P}_{\delta\psi, \text{lvd,iso}} = \begin{bmatrix} \sigma_\varepsilon^2 + \frac{\sigma_{\delta f_b}^2}{\bar{g}^2} & 0 & \left(\sigma_\varepsilon^2 - \frac{\sigma_{\delta f_b}^2}{\bar{g}^2} \right) \tan \phi \\ 0 & \sigma_\eta^2 + \frac{\sigma_{\delta f_b}^2}{\bar{g}^2} & 0 \\ \left(\sigma_\varepsilon^2 - \frac{\sigma_{\delta f_b}^2}{\bar{g}^2} \right) \tan \phi & 0 & \sigma_\varepsilon^2 \tan^2 \phi + \sigma_{\delta \omega_{ie}}^2 + \frac{\sigma_{\delta \omega_{ib}}^2}{\tilde{\omega}_{ie}^2 \cos^2 \phi} + \frac{\sigma_{\delta f_b}^2 \tan^2 \phi}{\bar{g}^2} \end{bmatrix} \quad (3.32)$$

The resulting matrix (3.32) is a stochastic extension of the widely known approximations that can be found in textbooks like [14, p. 284]. Additionally, model errors like the gravity deflection and uncertainties of the Earth's nominal angular rate have been introduced.

The covariance matrix provides insight into the correlations between orientation angles and the contributions of different model errors. The initial pitch and roll errors are uncorrelated in the case of isotropic sensor errors. They depend on the accelerometer measurements and gravity deflections only. As leveling aligns to the local gravity, but the orientation is defined relative to the reference ellipsoid, the gravity deflections from the vertical are directly transferred into the pitch, respectively, roll angles errors. The azimuth error is uncorrelated with the pitch angle, but there is a correlation with the roll angle, which increases with the vehicle's geodetic latitude. The azimuth variance itself also increases with latitude.

3.3. Strapdown Navigation Error Propagation

3.3.1. Navigation Error Dynamics

Within this section, the linearized error dynamics of strapdown inertial navigation are derived. Here, the strapdown navigation algorithm in the n -frame is chosen for its vivid interpretation of the states.

In order to derive the error propagation, each navigation state or measurement is split into the measured or modeled state $\tilde{\mathbf{x}}$ and the error $\delta\mathbf{x}$:

$$\mathbf{x} = \tilde{\mathbf{x}} + \delta\mathbf{x} \quad (3.33)$$

Orientation states are split into two consecutive rotations, first to the erroneous orientation and from there to the true orientation or vice versa:

$$\mathbf{R}_{ab} = \mathbf{R}_{a\tilde{b}}\mathbf{R}_{\tilde{b}b} \quad (3.34)$$

$$\mathbf{R}_{ab} = \mathbf{R}_{a\tilde{a}}\mathbf{R}_{\tilde{a}b} \quad (3.35)$$

The position of the error rotation is arbitrary but affects the error dynamics. In this analysis, the second option is used because it eliminates the vehicle's rotational dynamics from the rotational error dynamics.

3.3.1.1. Nonlinear Error Dynamics

Using definition (3.33), the strapdown position ODE (2.12) can be solved for the time-derivative of the position error:

$$\dot{\tilde{\lambda}} + \delta\dot{\lambda} = \mathbf{D}(\tilde{\phi} + \delta\phi, \tilde{h} + \delta h)^{-1} \cdot (\tilde{\mathbf{v}}_n + \delta\mathbf{v}_n) \quad (3.36)$$

$$\delta\dot{\lambda} = \mathbf{D}(\tilde{\phi} + \delta\phi, \tilde{h} + \delta h)^{-1} \cdot (\tilde{\mathbf{v}}_n + \delta\mathbf{v}_n) - \mathbf{D}(\tilde{\phi}, \tilde{h})^{-1} \cdot \tilde{\mathbf{v}}_n \quad (3.37)$$

Applying the same procedure to the velocity ODE (2.13) yields:

$$\begin{aligned} \dot{\tilde{\mathbf{v}}}_n + \delta\dot{\mathbf{v}}_n &= \mathbf{R}_{n\tilde{n}}\mathbf{R}_{\tilde{n}b}(\tilde{\mathbf{f}}_b + \delta\mathbf{f}_b) + \tilde{\boldsymbol{\gamma}}_n(\tilde{\lambda} + \delta\lambda) + \delta\boldsymbol{\gamma}_n \\ &\quad - (2\mathbf{R}_{en}^\top(\tilde{\lambda} + \delta\lambda) \cdot (\tilde{\boldsymbol{\omega}}_{ie} + \delta\boldsymbol{\omega}_{ie}) + \boldsymbol{\omega}_{en}(\tilde{\lambda} + \delta\lambda, \tilde{\mathbf{v}}_n + \delta\mathbf{v}_n)) \times (\tilde{\mathbf{v}}_n + \delta\mathbf{v}_n) \end{aligned} \quad (3.38)$$

$$\begin{aligned} \delta\dot{\mathbf{v}}_n &= (\mathbf{R}_{n\tilde{n}} - \mathbf{I}_{3 \times 3}) \cdot \mathbf{R}_{\tilde{n}b}\tilde{\mathbf{f}}_b + \mathbf{R}_{n\tilde{n}}\mathbf{R}_{\tilde{n}b}\delta\mathbf{f}_b + \tilde{\boldsymbol{\gamma}}_n(\tilde{\lambda} + \delta\lambda) - \tilde{\boldsymbol{\gamma}}_n(\tilde{\lambda}) + \delta\boldsymbol{\gamma}_n \\ &\quad - (2\mathbf{R}_{ne}(\tilde{\lambda} + \delta\lambda) \cdot (\tilde{\boldsymbol{\omega}}_{ie} + \delta\boldsymbol{\omega}_{ie}) + \boldsymbol{\omega}_{en}(\tilde{\lambda} + \delta\lambda, \tilde{\mathbf{v}}_n + \delta\mathbf{v}_n)) \times (\tilde{\mathbf{v}}_n + \delta\mathbf{v}_n) \\ &\quad + (2\mathbf{R}_{ne}(\tilde{\lambda}) \cdot (\tilde{\boldsymbol{\omega}}_{ie} + \delta\boldsymbol{\omega}_{ie}) + \boldsymbol{\omega}_{en}(\tilde{\lambda}, \tilde{\mathbf{v}}_n)) \times \mathbf{v}_n \end{aligned} \quad (3.39)$$

Analogously, the orientation error dynamics is derived from (2.14):

$$\frac{d}{dt}(\mathbf{R}_{n\tilde{n}}\mathbf{R}_{\tilde{n}b}) = \dot{\mathbf{R}}_{n\tilde{n}}\mathbf{R}_{\tilde{n}b} + \mathbf{R}_{n\tilde{n}}\dot{\mathbf{R}}_{\tilde{n}b} \quad (3.40)$$

$$\dot{\mathbf{R}}_{n\tilde{n}} = (\mathbf{R}_{nb}\boldsymbol{\Omega}_{ib} - \boldsymbol{\Omega}_{in}\mathbf{R}_{nb})\mathbf{R}_{\tilde{n}b}^\top - \mathbf{R}_{n\tilde{n}}\dot{\mathbf{R}}_{\tilde{n}b}\mathbf{R}_{\tilde{n}b}^\top \quad (3.41)$$

$$\dot{\mathbf{R}}_{n\bar{n}} = (\mathbf{R}_{nb}\boldsymbol{\Omega}_{ib} - \boldsymbol{\Omega}_{in}\mathbf{R}_{nb})\mathbf{R}_{\bar{n}b}^\top - \mathbf{R}_{n\bar{n}}(\mathbf{R}_{\bar{n}b}\tilde{\boldsymbol{\Omega}}_{ib} - \boldsymbol{\Omega}_{in}\mathbf{R}_{\bar{n}b})\mathbf{R}_{\bar{n}b}^\top \quad (3.42)$$

$$\dot{\mathbf{R}}_{n\bar{n}} = \mathbf{R}_{n\bar{n}}(\mathbf{R}_{\bar{n}b}\delta\boldsymbol{\Omega}_{ib}\mathbf{R}_{\bar{n}b}^\top + \tilde{\boldsymbol{\Omega}}_{in}) - (\tilde{\boldsymbol{\Omega}}_{in} + \delta\boldsymbol{\Omega}_{in})\mathbf{R}_{n\bar{n}} + H.O.T. \quad (3.43)$$

3.3.1.2. Linearized Error Dynamics

System theory provides a wide range of tools for analyzing linear systems, which shall be exploited for investigating the strapdown error dynamics. Parts of the derived error dynamics are already linear regarding the navigation state errors. Other parts can be linearized if the error terms are sufficiently small, which is assumed for the following analysis. Linearization of (3.37) to (3.43) for the error terms at the estimated states $\tilde{\boldsymbol{\lambda}} = [\tilde{\phi} \ \tilde{\lambda} \ \tilde{h}]^\top$, $\tilde{\mathbf{v}}_n$ and $\mathbf{R}_{\bar{n}b}$ and measured respectively modeled inputs $\tilde{\mathbf{f}}_b, \tilde{\boldsymbol{\omega}}_{ib}, \tilde{\boldsymbol{\gamma}}_n, \tilde{\boldsymbol{\omega}}_{ie}$ (all error terms are zero at the linearization point) yields the following error ODEs:

$$\begin{aligned} \delta\dot{\boldsymbol{\lambda}} &\approx \left. \delta\dot{\boldsymbol{\lambda}}(\boldsymbol{\lambda}, \mathbf{v}_n) \right|_{\tilde{\boldsymbol{\lambda}}, \tilde{\mathbf{v}}_n} + \left. \frac{\partial\dot{\boldsymbol{\lambda}}(\boldsymbol{\lambda}, \mathbf{v}_n)}{\partial\delta\boldsymbol{\lambda}} \right|_{\tilde{\boldsymbol{\lambda}}, \tilde{\mathbf{v}}_n} \delta\boldsymbol{\lambda} + \left. \frac{\partial\dot{\boldsymbol{\lambda}}(\boldsymbol{\lambda}, \mathbf{v}_n)}{\partial\delta\mathbf{v}_n^\top} \right|_{\tilde{\boldsymbol{\lambda}}, \tilde{\mathbf{v}}_n} \delta\mathbf{v}_n \\ &\approx \mathbf{D}(\tilde{\boldsymbol{\lambda}})^{-1}\tilde{\mathbf{v}}_n - \mathbf{D}(\tilde{\boldsymbol{\lambda}})^{-1}\tilde{\mathbf{v}}_n + \mathbf{0} \delta\boldsymbol{\lambda} + \mathbf{D}(\tilde{\boldsymbol{\lambda}})^{-1}\delta\mathbf{v}_n \\ &\approx \mathbf{D}(\tilde{\boldsymbol{\lambda}})^{-1}\delta\mathbf{v}_n \end{aligned} \quad (3.44)$$

Using the linear approximation of the error rotation matrix by the skew symmetric of the corresponding angles

$$\mathbf{R}_{n\bar{n}} \approx ((\boldsymbol{\psi}_{n\bar{n}} \times) + \mathbf{I}_{3 \times 3}) \quad (3.45)$$

the linearized ODEs for velocity and orientation errors are determined analogously:

$$\begin{aligned} \delta\dot{\mathbf{v}}_n &\approx \left. \delta\dot{\mathbf{v}}_n(\boldsymbol{\lambda}, \mathbf{v}_n, \mathbf{R}_{nb}, \mathbf{f}_b, \boldsymbol{\gamma}_n) \right|_{\tilde{\boldsymbol{\lambda}}, \tilde{\mathbf{v}}_n, \mathbf{R}_{\bar{n}b}, \tilde{\mathbf{f}}_b, \tilde{\boldsymbol{\gamma}}_n} + \left. \frac{\partial\delta\dot{\mathbf{v}}_n(\boldsymbol{\lambda}, \dots)}{\partial\delta\boldsymbol{\lambda}} \right|_{\tilde{\boldsymbol{\lambda}}, \tilde{\mathbf{v}}_n, \mathbf{R}_{\bar{n}b}, \tilde{\mathbf{f}}_b, \tilde{\boldsymbol{\gamma}}_n} \delta\boldsymbol{\lambda} \\ &\quad + \left. \frac{\partial\delta\dot{\mathbf{v}}_n(\boldsymbol{\lambda}, \dots)}{\partial\delta\mathbf{v}_n} \right|_{\tilde{\boldsymbol{\lambda}}, \tilde{\mathbf{v}}_n, \mathbf{R}_{\bar{n}b}, \tilde{\mathbf{f}}_b, \tilde{\boldsymbol{\gamma}}_n} \delta\mathbf{v}_n + \left. \frac{\partial\delta\dot{\mathbf{v}}_n(\boldsymbol{\lambda}, \dots)}{\partial\boldsymbol{\psi}_{n\bar{n}}} \right|_{\tilde{\boldsymbol{\lambda}}, \tilde{\mathbf{v}}_n, \mathbf{R}_{\bar{n}b}, \tilde{\mathbf{f}}_b, \tilde{\boldsymbol{\gamma}}_n} \boldsymbol{\psi}_{n\bar{n}} \\ &\quad + \left. \frac{\partial\delta\dot{\mathbf{v}}_n(\boldsymbol{\lambda}, \dots)}{\partial\delta\mathbf{f}_b} \right|_{\tilde{\boldsymbol{\lambda}}, \tilde{\mathbf{v}}_n, \mathbf{R}_{\bar{n}b}, \tilde{\mathbf{f}}_b, \tilde{\boldsymbol{\gamma}}_n} \delta\mathbf{f}_b + \left. \frac{\partial\delta\dot{\mathbf{v}}_n(\boldsymbol{\lambda}, \dots)}{\partial\delta\boldsymbol{\gamma}_n} \right|_{\tilde{\boldsymbol{\lambda}}, \tilde{\mathbf{v}}_n, \mathbf{R}_{\bar{n}b}, \tilde{\mathbf{f}}_b, \tilde{\boldsymbol{\gamma}}_n} \delta\boldsymbol{\gamma}_n \\ &\approx \left(\frac{\partial\boldsymbol{\gamma}(\tilde{\boldsymbol{\lambda}})}{\partial\delta\boldsymbol{\lambda}^\top} + \frac{\partial(2\mathbf{R}_{ne}(\tilde{\boldsymbol{\lambda}})\boldsymbol{\omega}_{ie} + \boldsymbol{\omega}_{en}(\tilde{\boldsymbol{\lambda}}, \tilde{\mathbf{v}}_n)) \times \tilde{\mathbf{v}}_n}{\partial\delta\boldsymbol{\lambda}^\top} \right) \delta\boldsymbol{\lambda} \\ &\quad + \frac{\partial(2\mathbf{R}_{ne}(\tilde{\boldsymbol{\lambda}})\boldsymbol{\omega}_{ie} + \boldsymbol{\omega}_{en}(\tilde{\boldsymbol{\lambda}}, \tilde{\mathbf{v}}_n)) \times \tilde{\mathbf{v}}_n}{\partial\delta\mathbf{v}_n^\top} \delta\mathbf{v}_n - (\mathbf{R}_{\bar{n}b}\tilde{\mathbf{f}}_b \times) \delta\boldsymbol{\psi}_{n\bar{n}} \\ &\quad + \mathbf{R}_{\bar{n}b}\delta\mathbf{f}_b + \delta\boldsymbol{\gamma}_n \end{aligned} \quad (3.46)$$

Application of the above approximation (3.45), neglection of the quadratic error terms yields the following orientation ODE:

$$\begin{aligned} \dot{\mathbf{R}}_{n\bar{n}} &\approx \mathbf{R}_{\bar{n}b}\delta\boldsymbol{\Omega}_{ib}\mathbf{R}_{\bar{n}b}^\top + \boldsymbol{\Omega}_{in} + \boldsymbol{\Psi}_{n\bar{n}}\mathbf{R}_{\bar{n}b}\delta\boldsymbol{\Omega}_{ib}\mathbf{R}_{\bar{n}b}^\top + \boldsymbol{\Psi}_{n\bar{n}}\tilde{\boldsymbol{\Omega}}_{in} - \tilde{\boldsymbol{\Omega}}_{ib} - \delta\boldsymbol{\Omega}_{in} \\ &\quad - \tilde{\boldsymbol{\Omega}}_{in}\boldsymbol{\Psi}_{n\bar{n}} - \delta\boldsymbol{\Omega}_{in}\boldsymbol{\Psi}_{n\bar{n}} \\ \dot{\boldsymbol{\Psi}}_{n\bar{n}} &\approx \mathbf{R}_{\bar{n}b}\delta\boldsymbol{\Omega}_{ib}\mathbf{R}_{\bar{n}b}^\top + \boldsymbol{\Psi}_{n\bar{n}}\tilde{\boldsymbol{\Omega}}_{in} - \tilde{\boldsymbol{\Omega}}_{in}\boldsymbol{\Psi}_{n\bar{n}} - \delta\boldsymbol{\Omega}_{in} \end{aligned} \quad (3.47)$$

Using the Jacobi identity of the cross-product

$$\Psi_{n\bar{n}}\Omega_{in} - \Omega_{in}\Psi_{n\bar{n}} = (\Psi_{n\bar{n}}\omega_{in}) \times = -(\Omega_{in}\psi_{n\bar{n}}) \times \quad (3.48)$$

and vectorization of the skew-symmetric matrices yields:

$$\dot{\psi}_{n\bar{n}}(\lambda, \dots) \approx \mathbf{R}_{\bar{n}b}\delta\omega_{ib} - \tilde{\Omega}_{in}(\tilde{\lambda}, \tilde{\mathbf{v}}_n)\psi_{n\bar{n}} - \delta\omega_{in}(\lambda, \mathbf{v}_n) \quad (3.49)$$

which can then be linearized for the errors:

$$\begin{aligned} \dot{\psi}_{n\bar{n}} &\approx \dot{\psi}_{n\bar{n}}(\lambda, \dots) \Big|_{\tilde{\lambda}, \tilde{\mathbf{v}}_n, \mathbf{R}_{\bar{n}b}, \tilde{\omega}_{ib}} + \frac{\partial \dot{\psi}_{n\bar{n}}(\lambda, \dots)}{\partial \psi_{n\bar{n}}^\top} \Big|_{\tilde{\lambda}, \tilde{\mathbf{v}}_n, \mathbf{R}_{\bar{n}b}, \tilde{\omega}_{ib}} \psi_{n\bar{n}} + \frac{\partial \dot{\psi}_{n\bar{n}}(\lambda, \dots)}{\partial \delta\omega_{ib}^\top} \Big|_{\tilde{\lambda}, \tilde{\mathbf{v}}_n, \mathbf{R}_{\bar{n}b}, \tilde{\omega}_{ib}} \delta\omega_{ib} \\ &+ \frac{\partial \dot{\psi}_{n\bar{n}}(\lambda, \dots)}{\partial \delta\lambda^\top} \Big|_{\tilde{\lambda}, \tilde{\mathbf{v}}_n, \mathbf{R}_{\bar{n}b}, \tilde{\omega}_{ib}} \delta\lambda + \frac{\partial \dot{\psi}_{n\bar{n}}(\lambda, \dots)}{\partial \delta\mathbf{v}_n^\top} \Big|_{\tilde{\lambda}, \tilde{\mathbf{v}}_n, \mathbf{R}_{\bar{n}b}, \tilde{\omega}_{ib}} \delta\mathbf{v}_n \\ &\approx -\Omega_{in}(\tilde{\lambda}, \tilde{\mathbf{v}}_n)\psi_{n\bar{n}} + \mathbf{R}_{\bar{n}b}\delta\omega_{ib} - \frac{\partial \omega_{in}(\tilde{\lambda}, \tilde{\mathbf{v}}_n)}{\partial \lambda^\top} \delta\lambda - \frac{\partial \omega_{in}(\tilde{\lambda}, \tilde{\mathbf{v}}_n)}{\partial \mathbf{v}_n^\top} \delta\mathbf{v}_n \end{aligned} \quad (3.50)$$

Based on equations (3.44) to (3.50), the following linear state space system can be formed:

$$\underbrace{\begin{bmatrix} \delta\dot{\lambda} \\ \delta\dot{\phi} \\ \delta\dot{h} \\ \delta\dot{v}_n \\ \delta\dot{v}_e \\ \delta\dot{v}_d \\ \delta\dot{\Phi} \\ \delta\dot{\Theta} \\ \delta\dot{\Psi} \end{bmatrix}}_{\delta\dot{z}} = \underbrace{\begin{bmatrix} \mathbf{A}_{11} & \mathbf{A}_{12} & \mathbf{A}_{13} \\ \mathbf{A}_{21} & \mathbf{A}_{22} & \mathbf{A}_{23} \\ \mathbf{A}_{31} & \mathbf{A}_{32} & \mathbf{A}_{33} \end{bmatrix}}_{\mathbf{A}} \underbrace{\begin{bmatrix} \delta\lambda \\ \delta\phi \\ \delta h \\ \delta v_n \\ \delta v_e \\ \delta v_d \\ \delta\Phi \\ \delta\Theta \\ \delta\Psi \end{bmatrix}}_{\delta z} + \underbrace{\begin{bmatrix} \mathbf{0}_{3\times 3} & \mathbf{0}_{3\times 3} & \mathbf{0}_{3\times 3} \\ \mathbf{R}_{\bar{n}b} & \mathbf{0}_{3\times 3} & \mathbf{I}_{3\times 3} \\ \mathbf{0}_{3\times 3} & \mathbf{R}_{\bar{n}b} & \mathbf{0}_{3\times 3} \end{bmatrix}}_{\mathbf{B}} \underbrace{\begin{bmatrix} \delta f_{b,x} \\ \delta f_{b,y} \\ \delta f_{b,z} \\ \delta\omega_{ib,x} \\ \delta\omega_{ib,y} \\ \delta\omega_{ib,z} \\ \delta\gamma_{n,x} \\ \delta\gamma_{n,y} \\ \delta\gamma_{n,z} \end{bmatrix}}_{\delta u} \quad (3.51)$$

Table 3.1.: System matrix of the linearized strapdown error dynamics.

Position error rate caused by the...	
position error	$\mathbf{A}_{11} = \begin{bmatrix} 0 & 0 & \frac{-\tilde{v}_n}{(R_n(\tilde{\phi})+\tilde{h})^2} \\ \frac{\tilde{v}_e \tan \tilde{\phi}}{(R_n(\tilde{\phi})+\tilde{h}) \cos \tilde{\phi}} & 0 & \frac{-\tilde{v}_e \tan \tilde{\phi}}{(R_n(\tilde{\phi})+\tilde{h})^2 \cos \tilde{\phi}} \\ 0 & 0 & 0 \end{bmatrix}$
velocity error	$\mathbf{A}_{12} = \begin{bmatrix} \frac{1}{R_n(\tilde{\phi})+\tilde{h}} & 0 & 0 \\ 0 & \frac{1}{(R_n(\tilde{\phi})+\tilde{h}) \cos \tilde{\phi}} & 0 \\ 0 & 0 & 0 \end{bmatrix}$
orientation error	$\mathbf{A}_{13} = \mathbf{0}_{3 \times 3}$
Velocity error rate caused by the...	
position error	$\mathbf{A}_{21} = \begin{bmatrix} -2\omega_{ie}\tilde{v}_e \cos \tilde{\phi} - \frac{\tilde{v}_e^2}{(R_n(\tilde{\phi})+\tilde{h}) \cos^2 \tilde{\phi}} & 0 & \frac{\tilde{v}_e^2 \tan \tilde{\phi} - \tilde{v}_n \tilde{v}_d}{(R_n(\tilde{\phi})+\tilde{h})^2} \\ -2\omega_{ie}(\tilde{v}_n \cos \tilde{\phi} - \tilde{v}_d \sin \tilde{\phi}) - \frac{\tilde{v}_n \tilde{v}_e}{(R_n(\tilde{\phi})+\tilde{h}) \cos^2 \tilde{\phi}} & 0 & \frac{-\tilde{v}_e \tilde{v}_n \tan \tilde{\phi} - \tilde{v}_e \tilde{v}_d}{(R_n(\tilde{\phi})+\tilde{h})^2} \\ 2\omega_{ie}\tilde{v}_e \sin \tilde{\phi} + \frac{\partial \gamma(\tilde{\phi}, \tilde{h})}{\partial \phi} & 0 & \frac{\tilde{v}_e^2 + \tilde{v}_d^2}{(R_n(\tilde{\phi})+\tilde{h})^2} + \frac{\partial \gamma(\tilde{\phi}, \tilde{h})}{\partial h} \end{bmatrix}$
velocity error	$\mathbf{A}_{22} = \begin{bmatrix} \frac{\tilde{v}_d}{R_n(\tilde{\phi})+\tilde{h}} & 2\omega_{ie} \sin \tilde{\phi} - \frac{2\tilde{v}_e \tan \tilde{\phi}}{R_n(\tilde{\phi})+\tilde{h}} & \frac{\tilde{v}_n}{R_n(\tilde{\phi})+\tilde{h}} \\ 2\omega_{ie} \sin \tilde{\phi} + \frac{\tilde{v}_e \tan \tilde{\phi}}{R_n(\tilde{\phi})+\tilde{h}} & \frac{\tilde{v}_n \tan \tilde{\phi} + \tilde{v}_d}{R_n(\tilde{\phi})+\tilde{h}} & 2\omega_{ie} \cos \tilde{\phi} + \frac{\tilde{v}_e}{R_n(\tilde{\phi})+\tilde{h}} \\ \frac{-2\tilde{v}_n}{R_n(\tilde{\phi})+\tilde{h}} & -2\omega_{ie} \cos \tilde{\phi} - \frac{-\tilde{v}_e}{R_n(\tilde{\phi})+\tilde{h}} & 0 \end{bmatrix}$
orientation error	$\mathbf{A}_{23} = \begin{bmatrix} 0 & \tilde{f}_{n,z} & -\tilde{f}_{n,y} \\ -\tilde{f}_{n,z} & 0 & \tilde{f}_{n,x} \\ \tilde{f}_{n,y} & -\tilde{f}_{n,x} & 0 \end{bmatrix}$
Orientation error rate caused by the...	
position error	$\mathbf{A}_{31} = \begin{bmatrix} \omega_{ie} \sin \tilde{\phi} & 0 & \frac{\tilde{v}_e}{(R_n(\tilde{\phi})+\tilde{h})^2} \\ 0 & 0 & \frac{-\tilde{v}_n}{(R_n(\tilde{\phi})+\tilde{h})^2} \\ \omega_{ie} \cos \tilde{\phi} + \frac{\tilde{v}_e}{(R_n(\tilde{\phi})+\tilde{h}) \cos^2 \tilde{\phi}} & 0 & \frac{-\tilde{v}_e \tan \tilde{\phi}}{(R_n(\tilde{\phi})+\tilde{h})^2} \end{bmatrix}$
velocity error	$\mathbf{A}_{32} = \begin{bmatrix} 0 & \frac{-1}{R_n(\tilde{\phi})+\tilde{h}} & 0 \\ \frac{1}{R_n(\tilde{\phi})+\tilde{h}} & 0 & 0 \\ 0 & \frac{\tan \tilde{\phi}}{R_n(\tilde{\phi})+\tilde{h}} & 0 \end{bmatrix}$
orientation error	$\mathbf{A}_{33} = \begin{bmatrix} 0 & -\omega_{ie} \sin \tilde{\phi} - \frac{\tilde{v}_e \tan \tilde{\phi}}{R_n(\tilde{\phi})+\tilde{h}} & \frac{\tilde{v}_n \tan \tilde{\phi}}{R_n(\tilde{\phi})+\tilde{h}} \\ \omega_{ie} \sin \tilde{\phi} + \frac{\tilde{v}_e \tan \tilde{\phi}}{R_n(\tilde{\phi})+\tilde{h}} & 0 & \omega_{ie} \cos \tilde{\phi} - \frac{\tilde{v}_e}{R_n(\tilde{\phi})+\tilde{h}} \\ \frac{-\tilde{v}_n}{R_n(\tilde{\phi})+\tilde{h}} & -\omega_{ie} \cos \tilde{\phi} - \frac{\tilde{v}_e}{R_n(\tilde{\phi})+\tilde{h}} & 0 \end{bmatrix}$

The components of the system matrix \mathbf{A} are given in Table 3.1. Similar representations, in different state order or slightly different parametrization, can be obtained from standard literature, e.g. [14, pp. 344–345] and [15, pp. 153–157].

The position error has already been constrained to a few kilometers to justify the linearization of the error dynamics. In this case, the Earth's curvature radii are approximately constant within the envelope of the analysis. The system matrix \mathbf{A} can be further simplified by replacing the local curvature with an average radius. The Gaussian mean radius represents the average radius of all directions χ at latitude ϕ [15, p. 154]:

$$R(\phi) = \frac{1}{2\pi} \int_0^{2\pi} \frac{R_m(\phi)R_n(\phi)}{R_n(\phi) \cos^2 \chi + R_m(\phi) \sin^2 \chi} d\chi = \sqrt{R_m(\phi)R_n(\phi)} \quad (3.52)$$

As illustrated in Figure 3.2, the maximum error between this approximation and the true local radii is less than 0.4%. The system matrix \mathbf{A} then simplifies to:

$$\mathbf{A}_R = \begin{bmatrix} 0 & 0 & \frac{-\bar{v}_n}{(R+h)^2} & \frac{1}{(R+h)} & 0 & 0 & 0 & 0 & 0 \\ \frac{\bar{v}_e \tan \phi}{(R+h) \cos \phi} & 0 & \frac{-\bar{v}_e}{(R+h)^2 \cos \phi} & 0 & \frac{1}{(R+h) \cos \phi} & 0 & 0 & 0 & 0 \\ 0 & 0 & 0 & 0 & 0 & -1 & 0 & 0 & 0 \\ \hline -2\omega_{ie} \bar{v}_e \cos \phi & 0 & \frac{\bar{v}_e^2 \tan \phi - \bar{v}_n \bar{v}_d}{R^2} & \frac{\bar{v}_d}{(R+h)} & \frac{-2\omega_{ie} \sin \phi}{(R+h)} & \frac{\bar{v}_n}{(R+h)} & 0 & \tilde{f}_{n,z} & -\tilde{f}_{n,y} \\ \frac{\bar{v}_e^2}{(R+h) \cos^2 \phi} & 0 & \frac{-\bar{v}_e \bar{v}_n \tan \phi - \bar{v}_e \bar{v}_d}{(R+h)^2} & \frac{2\omega_{ie} \sin \phi}{(R+h)} & \frac{\bar{v}_n \tan \phi + \bar{v}_d}{(R+h)} & 2\omega_{ie} \cos \phi + \frac{\bar{v}_e}{(R+h)} & -\tilde{f}_{n,z} & 0 & \tilde{f}_{n,x} \\ 2\omega_{ie} (\bar{v}_n \cos \phi - \bar{v}_d \sin \phi) & 0 & \frac{\bar{v}_n \bar{v}_e}{(R+h) \cos^2 \phi} & \frac{\bar{v}_e \tan \phi}{(R+h)} & \frac{\bar{v}_n \tan \phi + \bar{v}_d}{(R+h)} & 2\omega_{ie} \cos \phi + \frac{\bar{v}_e}{(R+h)} & -\tilde{f}_{n,z} & 0 & \tilde{f}_{n,x} \\ 2\omega_{ie} \bar{v}_e \sin \phi & 0 & \frac{\bar{v}_e^2 + \bar{v}_d^2}{(R+h)^2} + \frac{\partial \gamma}{\partial h} & \frac{-2\bar{v}_n}{(R+h)} & -2\omega_{ie} \cos \phi - \frac{2\bar{v}_e}{(R+h)} & 0 & \tilde{f}_{n,y} & -\tilde{f}_{n,x} & 0 \\ \hline \omega_{ie} \sin \phi & 0 & \frac{\bar{v}_e}{(R+h)^2} & 0 & \frac{-1}{(R+h)} & 0 & 0 & -\omega_{ie} \sin \phi & \frac{\bar{v}_n}{(R+h)} \\ 0 & 0 & \frac{\bar{v}_n}{(R+h)^2} & \frac{1}{(R+h)} & 0 & 0 & \omega_{ie} \sin \phi & \frac{\bar{v}_e \tan \phi}{(R+h)} & \frac{\bar{v}_n}{(R+h)} \\ \omega_{ie} \cos \phi & 0 & \frac{-\bar{v}_e \tan \phi}{(R+h)^2} & 0 & \frac{\tan \phi}{(R+h)} & 0 & \omega_{ie} \cos \phi & 0 & \omega_{ie} \cos \phi \\ + \frac{\bar{v}_e}{(R+h) \cos^2 \phi} & 0 & \frac{-\bar{v}_e \tan \phi}{(R+h)^2} & 0 & \frac{\tan \phi}{(R+h)} & 0 & + \frac{\bar{v}_e \tan \phi}{(R+h)} & -\omega_{ie} \cos \phi & + \frac{\bar{v}_e}{(R+h)} \\ & & & & & & \frac{-\bar{v}_n}{(R+h)} & + \frac{\bar{v}_e}{(R+h)} & 0 \end{bmatrix} \quad (3.53)$$

3.3.1.3. Vertical Channel Fixed Strapdown Error Propagation

Equation (3.51) fully describes the error dynamics of strapdown inertial navigation for small errors. However, due to the instability of the vertical channel, inertial navigation is used together with an additional vertical aiding source most of the time. This is classically a barometric altimeter for aircraft or, if available GNSS measurements. Such a fix of the vertical channel should be considered in the error propagation to obtain a meaningful representation of the inertial navigation error propagation in practice. Otherwise, the altitude error would exponentially grow, dominating the total position error and rendering the analysis useless.

Independent of the actual method, a vertical aiding should ideally reset the vertical position errors and thus eliminate the instability of the altitude. In this work, the vertical aiding is considered by eliminating the vertical states δh and δv_d . Although the system's vertical error dynamics have been eliminated, there may still be an erroneous altitude δh and height rate δv_d that affects the other error states. These errors are now introduced as input to the system.

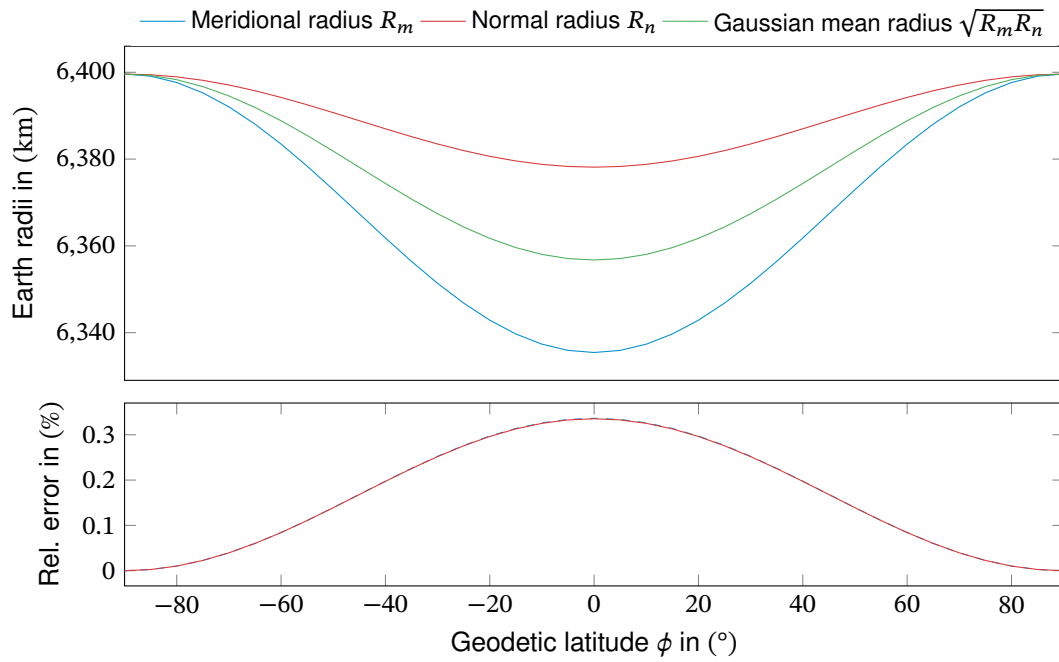


Figure 3.2.: Earth curvature radii compared to the local spherical approximation.

The linear error dynamics for a vertically fixed (index vf) strapdown system is then given as:

$$\underbrace{\begin{bmatrix} \delta\lambda \\ \delta\dot{\phi} \\ \delta\dot{v}_n \\ \delta\dot{v}_e \\ \delta\dot{\Phi} \\ \delta\dot{\Theta} \\ \delta\dot{\Psi} \end{bmatrix}}_{\delta z_{vf}} = \mathbf{A}_{vf} \underbrace{\begin{bmatrix} \delta\lambda \\ \delta\phi \\ \delta v_n \\ \delta v_e \\ \delta\Phi \\ \delta\Theta \\ \delta\Psi \end{bmatrix}}_{\delta z_{vf}} + \mathbf{B}_{vf} \underbrace{\begin{bmatrix} \delta f_{b,x} \\ \delta f_{b,y} \\ \delta f_{b,z} \\ \delta\omega_{ib,x} \\ \delta\omega_{ib,y} \\ \delta\omega_{ib,z} \\ \delta\gamma_n \\ \delta\gamma_e \\ \delta\gamma_d \\ \delta h \\ \delta v_d \end{bmatrix}}_{\delta u_{vf}} \quad (3.54)$$

The system matrix for this reduced system is then given as:

$$\mathbf{A}_{vf} = \begin{bmatrix} 0 & 0 & \frac{1}{R} & 0 & 0 & 0 & 0 \\ \frac{\tilde{v}_e \tan \tilde{\phi}}{(R+h) \cos \tilde{\phi}} & 0 & 0 & \frac{1}{(R+h) \cos \tilde{\phi}} & 0 & 0 & 0 \\ -2\omega_{ie} \tilde{v}_e \cos \tilde{\phi} & 0 & \frac{\tilde{v}_d}{(R+h)} & \frac{-2\omega_{ie} \sin \tilde{\phi}}{(R+h)} & 0 & \tilde{f}_{n,z} & -\tilde{f}_{n,y} \\ \frac{\tilde{v}_e^2}{(R+h) \cos^2 \tilde{\phi}} & 0 & \frac{\tilde{v}_d \tan \tilde{\phi}}{(R+h)} & \frac{\tilde{v}_n \tan \tilde{\phi} + \tilde{v}_d}{(R+h)} & -\tilde{f}_{n,z} & 0 & \tilde{f}_{n,x} \\ 2\omega_{ie}(\tilde{v}_n \cos \tilde{\phi} - \tilde{v}_d \sin \tilde{\phi}) & 0 & \frac{2\omega_{ie} \sin \tilde{\phi}}{(R+h)} & \frac{-1}{(R+h)} & 0 & -\frac{\omega_{ie} \sin \tilde{\phi}}{(R+h)} & \frac{\tilde{v}_n}{(R+h)} \\ + \frac{\tilde{v}_n \tilde{v}_e}{(R+h) \cos^2 \tilde{\phi}} & 0 & + \frac{\tilde{v}_e \tan \tilde{\phi}}{(R+h)} & 0 & \frac{\omega_{ie} \sin \tilde{\phi}}{(R+h)} & 0 & \frac{\omega_{ie} \cos \tilde{\phi}}{(R+h)} \\ \omega_{ie} \sin \tilde{\phi} & 0 & 0 & \frac{-1}{(R+h)} & \frac{\omega_{ie} \sin \tilde{\phi}}{(R+h)} & 0 & \frac{\tilde{v}_e}{(R+h)} \\ 0 & 0 & \frac{1}{(R+h)} & 0 & + \frac{\tilde{v}_e \tan \tilde{\phi}}{(R+h)} & 0 & + \frac{\omega_{ie} \cos \tilde{\phi}}{(R+h)} \\ \frac{\omega_{ie} \cos \tilde{\phi}}{(R+h) \cos^2 \tilde{\phi}} & 0 & 0 & \frac{\tan \tilde{\phi}}{(R+h)} & \frac{-\tilde{v}_n}{(R+h)} & -\frac{\omega_{ie} \cos \tilde{\phi}}{(R+h)} & 0 \end{bmatrix} \quad (3.55)$$

The new input matrix is reduced for the vertical states and extended to incorporate the altitude and height rate errors as inputs. The input matrix for vertically fixed strapdown navigation is thus given as:

$$\mathbf{B}_{vf} = \begin{bmatrix} 0 & 0 & 0 & 0 & 0 & 0 & 0 & 0 & 0 & \frac{-\tilde{v}_n}{(R+h)^2} & 0 \\ 0 & 0 & 0 & 0 & 0 & 0 & 0 & 0 & 0 & \frac{-\tilde{v}_e}{(R+h)^2 \cos \tilde{\phi}} & 0 \\ \tilde{\mathbf{R}}_{\tilde{n}b} & 0 & 0 & 0 & 1 & 0 & 0 & \frac{\tilde{v}_e^2 \tan \tilde{\phi} - \tilde{v}_n \tilde{v}_d}{(R+h)^2} & \frac{\tilde{v}_n}{R} \\ 0 & 0 & 0 & 0 & 0 & 1 & 0 & \frac{-\tilde{v}_e \tilde{v}_n \tan \tilde{\phi} - \tilde{v}_e \tilde{v}_d}{(R+h)^2} & 2\omega_{ie} \cos \tilde{\phi} + \frac{\tilde{v}_e}{(R+h)} \\ 0 & 0 & 0 & 0 & 0 & 0 & 0 & \frac{\tilde{v}_e}{(R+h)^2} & 0 \\ 0 & 0 & 0 & \mathbf{R}_{\tilde{n}b} & 0 & 0 & 0 & \frac{\tilde{v}_n}{(R+h)^2} & 0 \\ 0 & 0 & 0 & 0 & 0 & 0 & 0 & \frac{-\tilde{v}_e \tan \tilde{\phi}}{(R+h)^2} & 0 \end{bmatrix} \quad (3.56)$$

where a reduced rotation matrix $\mathbf{R}_{\tilde{n}b}$ is used:

$$\tilde{\mathbf{R}}_{\tilde{n}b} = \begin{bmatrix} \cos \tilde{\Theta} \cos \tilde{\Psi} & \sin \tilde{\Phi} \sin \tilde{\Theta} \cos \tilde{\Psi} - \cos \tilde{\Phi} \sin \tilde{\Psi} & \cos \tilde{\Phi} \sin \tilde{\Theta} \cos \tilde{\Psi} + \sin \tilde{\Phi} \sin \tilde{\Psi} \\ \cos \tilde{\Theta} \sin \tilde{\Psi} & \sin \tilde{\Phi} \sin \tilde{\Theta} \sin \tilde{\Psi} + \cos \tilde{\Phi} \cos \tilde{\Psi} & \cos \tilde{\Phi} \sin \tilde{\Theta} \sin \tilde{\Psi} - \sin \tilde{\Phi} \cos \tilde{\Psi} \end{bmatrix} \quad (3.57)$$

3.3.1.4. Neglection of the Vehicle Motion

The system and input matrix of the linear strapdown error dynamics (3.54) still depend on the vehicle's current state. This includes a dependency on the vehicle NED-velocity, as well as its orientation \mathbf{R}_{nb} and the corresponding specific forces. This dependency allows an analysis of the strapdown error dynamics for every flight state, velocity, and even direction of flight. However, this is not feasible for a general navigation error analysis. For that, the analysis is

restricted to the most general and representative state.

The linearized system is analyzed at steady zero-velocity and the vehicle is assumed to be aligned to the local NED-frame:

$$v_n = v_e = v_d = 0 \quad (3.58)$$

$$f_{n,x} = f_{n,y} = 0 \quad (3.59)$$

$$f_{n,z} = -g \quad (3.60)$$

$$\mathbf{R}_{\tilde{n}b} = \mathbf{I}_{3 \times 3} \quad (3.61)$$

Under these assumptions, the state space representation of the linear strapdown error dynamics reduces to:

$$\mathbf{A}_{vf,s} = \begin{bmatrix} 0 & 0 & \frac{1}{(R+h)} & 0 & 0 & 0 & 0 \\ 0 & 0 & 0 & \frac{1}{(R+h)\cos\tilde{\phi}} & 0 & 0 & 0 \\ \hline 0 & 0 & 0 & -2\omega_{ie}\sin\tilde{\phi} & 0 & -g & 0 \\ 0 & 0 & 2\omega_{ie}\sin\tilde{\phi} & 0 & g & 0 & 0 \\ \hline \omega_{ie}\sin\tilde{\phi} & 0 & 0 & \frac{-1}{(R+h)} & 0 & -\omega_{ie}\sin\tilde{\phi} & 0 \\ 0 & 0 & \frac{1}{(R+h)} & 0 & \omega_{ie}\sin\tilde{\phi} & 0 & \omega_{ie}\cos\tilde{\phi} \\ \omega_{ie}\cos\tilde{\phi} & 0 & 0 & \frac{\tan\tilde{\phi}}{(R+h)} & 0 & -\omega_{ie}\cos\tilde{\phi} & 0 \end{bmatrix} \quad (3.62)$$

$$\mathbf{B}_{vf,s} = \begin{bmatrix} 0 & 0 & 0 & 0 & 0 & 0 & 0 & 0 & 0 & 0 \\ 0 & 0 & 0 & 0 & 0 & 0 & 0 & 0 & 0 & 0 \\ \hline 1 & 0 & 0 & 0 & 0 & 0 & 1 & 0 & 0 & 0 \\ 0 & 1 & 0 & 0 & 0 & 0 & 0 & 1 & 0 & 2\omega_{ie}\cos\tilde{\phi} \\ \hline 0 & 0 & 0 & 1 & 0 & 0 & 0 & 0 & 0 & 0 \\ 0 & 0 & 0 & 0 & 1 & 0 & 0 & 0 & 0 & 0 \\ 0 & 0 & 0 & 0 & 0 & 1 & 0 & 0 & 0 & 0 \end{bmatrix} \quad (3.63)$$

with the input vector

$$\delta\mathbf{u}_{vf} = [\delta f_{b,n}, \delta f_{b,e}, \delta f_{b,d}, \delta\omega_{ib,n}, \delta\omega_{ib,e}, \delta\omega_{ib,d}, \delta\gamma_n, \delta\gamma_e, \delta\gamma_d, \delta h, \delta v_d]^T \quad (3.64)$$

These assumptions look rather limiting, but they provide a reasonable approximation, especially for the analysis of the error dynamics:

- The velocity-dependent terms of (3.55) are small compared to the other terms. Jekeli argues that velocities of less than 200 m/s may be neglected compared to the Earth angular rate [15, p. 157]. Still, the value of the velocity terms compared to the other

terms is not a sufficient argument. The velocity terms introduce additional couplings between the different error states. These couplings even change the system dynamics of the latitude error from a marginal stable oscillation to an unstable oscillation, as demonstrated in Figure 3.3. A comparison of the system dynamics indicates that this instability is extremely weak, with the result that the influence of the velocity becomes apparent only after about 8 to 10 days of free inertial navigation.

- The choice of the specific forces represents both a stationary aligned vehicle and an aircraft in straight and level flight. Although aircraft experience many different flight states, like take-off, landing, and turns, the specific forces measurements are dominated by the Earth's gravity for typical trajectories (cf. Figure 3.4). Here, the deviation of the specific forces from the assumed straight and level state is less than 0.1 g for most of the time. This assumption does not hold for aerobatic flight and specific military applications, like air-to-air missiles.
- The orientation matrix $\mathbf{R}_{\bar{n}b}$ within the input matrix can be easily neglected by directly choosing the IMU measurements in the n -frame as inputs. Furthermore, equal sensors are typically used within the IMU's sensor triads. The measurement uncertainty is the same in any direction and assumed to be uncorrelated, so the corresponding covariance matrix is rotation-invariant. In this case, the actual orientation $\mathbf{R}_{\bar{n}b}$ does not affect the position uncertainty.

In conclusion, the neglect of the vehicle motion in the strapdown error dynamics yields sufficiently accurate results for many applications. On the contrary, this approximation is insufficient for vehicles with high accelerations (e.g., missiles) and, in the long term, for higher velocities. However, there is hardly any applications that requires days of free inertial navigation at aircraft velocities.

3.3.1.5. Range of Validity for the Linearization

While the approximations of the linearized system have been justified in the above section, the range of validity for the linearization itself has not been discussed yet. For the derivation of the error dynamics, the strapdown differential equations were separated into estimated and error states and subsequently linearized for the error states. With increasing error states, the linearization at the estimated states becomes less representative of the non-linear system. Due to their different nature, the different states must be considered separately:

- In the strapdown equations, the position affects the propagation of the transport rates, the local gravity, the local Earth angular rate, and the propagation of velocities into the position. In the above section, it was argued that the vehicle's velocity and thus the transport rate could be neglected for moderate velocities. Furthermore, gravity errors from an erroneous position affect the vertical channel, which is fixed for this analysis. This leaves the effect of position errors on the local Earth's radii that are used to transfer

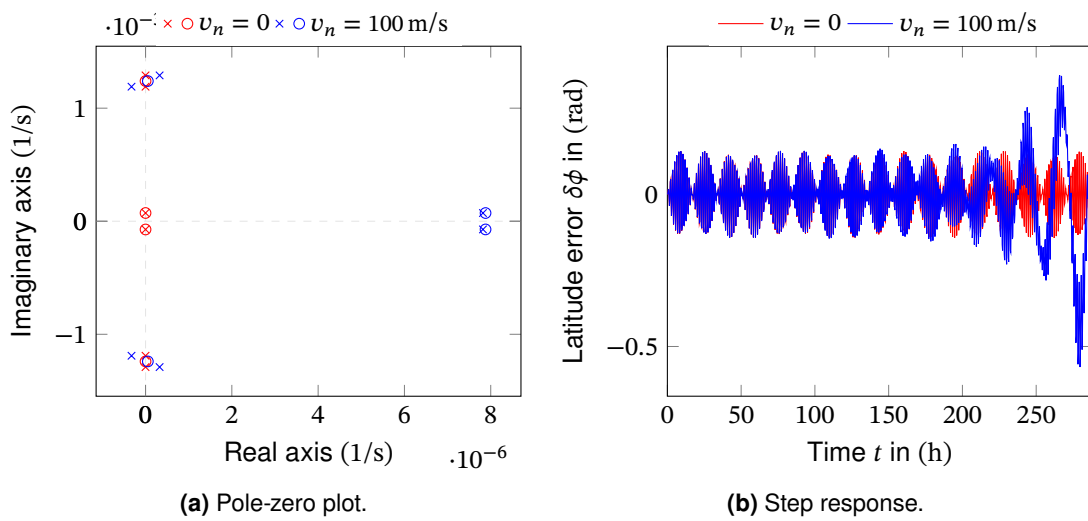
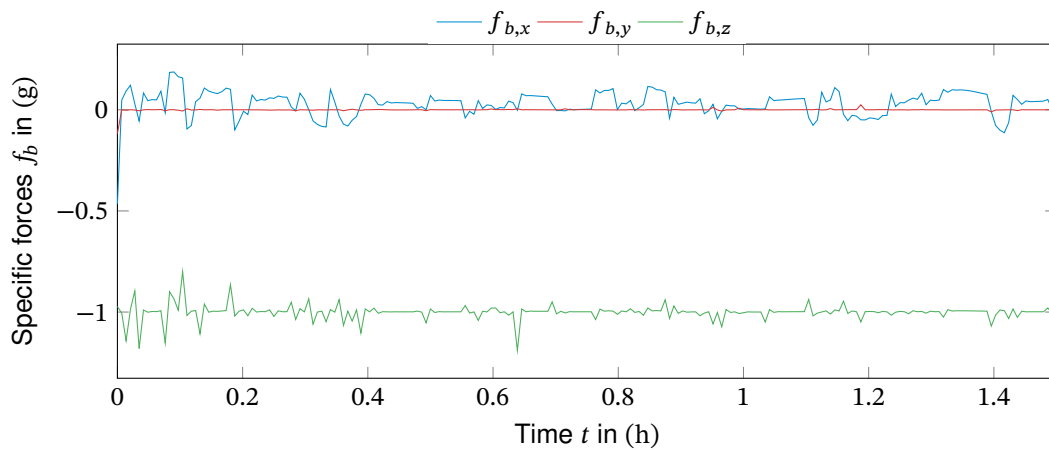
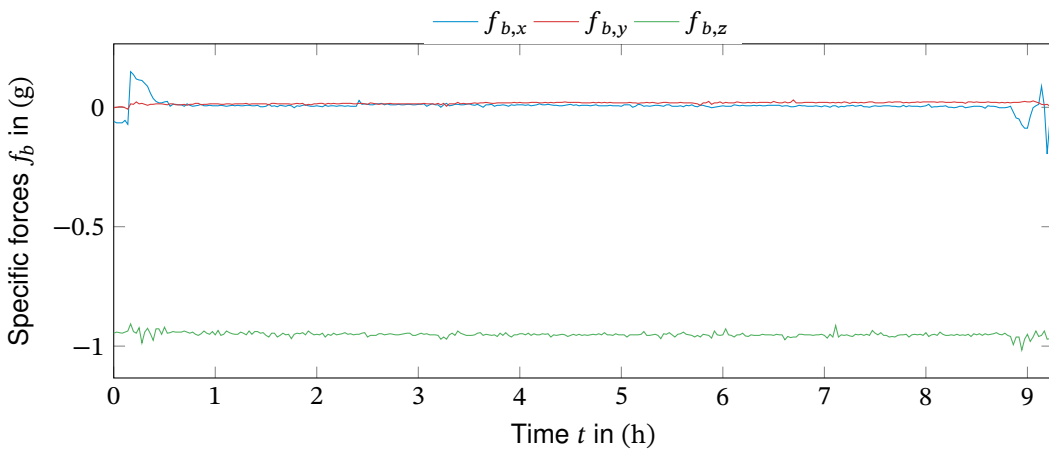


Figure 3.3.: Velocity influence on the strapdown error dynamics: Latitude error from $f_{b,x}$ error for vertical channel fixed, linearized strapdown error dynamics at $\phi = 45^\circ, v_e = 0, \Phi = 0, \Theta = 0, \Psi = 0$.



(a) Simulated flight of a small twin-prop aircraft [69].



(b) Recorded flight data of a transatlantic Boeing 747 cargo flight [70].

Figure 3.4.: Example specific forces measurements of typical aircraft trajectories.

the local velocity (errors) into geodetic position (errors). However, the local Earth radii vary less than 0.5 % over the globe. The linearization of the sine and cosine terms of the latitude dependency of the local components of the Earth's angular rate results in relative errors of less than 1 % for latitude errors below 1° , which corresponds to about 110 km at medium latitudes.

- For the given approximation, the effects of the vehicle's velocity on the system matrix have been neglected for velocities below 200 m/s. Velocity errors are significantly below this threshold and can thus be neglected compared to the already neglected effects of the vehicle's velocity.
- Linearization of the orientation error matrix neglects the orientation sequence of the Euler-angles. The linearization relies on the small-angle approximation of the sine and cosine but also on the neglect of products of sines. For angles below 8° the relative error of the small angle approximation of both sine and cosine is less than 1 %. The neglect of the quadratic sine terms compared to linear sine terms results yields a relative error of less than 1.75 % for angles below 1° .

A comparison of the analytically derived system responses to the results of a non-linear strapdown navigation simulation indicates a good approximation for the above-given thresholds of 100 km position error, 10 m/s velocity errors, and 1° orientation errors. In this case, the relative errors of the navigation state errors are about 1 %, for long simulation times of up to 48 h. For higher errors, such as 1000 km position error, 100 m/s velocity errors, and 10° , resulting system responses are still very similar to the simulation results, but the relative errors reach the 10 % magnitude.

Given the wide validity range of the linearization, the violation of the assumptions of low vehicle velocity and stationary conditions, respectively, straight and level flight seems more significant in practice. However, these assumptions are required for the trajectory-independent performance prediction, performed in an early design phase.

3.3.2. Response to Constant Errors

3.3.2.1. General

Having derived a linear state space representation for the (vertically aided) strapdown error dynamics, the system's response to different error inputs will be investigated in this section. From a system theoretical view, the following two types of errors are a step input to the error dynamics system:

- **Initialization errors** An erroneous initialization for the navigation states, e.g., a residual attitude uncertainty after alignment.
- **Bias-like sensor errors** A bias-like error on the inertial sensor measurements. The

long-term drift of the bias (bias instability) is considered a noise process and thus not considered in this analysis.

For a general linear state space system

$$\dot{\mathbf{z}} = \mathbf{A}\mathbf{z} + \mathbf{B}\mathbf{u} \quad (3.65)$$

$$\mathbf{y} = \mathbf{C}\mathbf{z} + \mathbf{D}\mathbf{u} \quad (3.66)$$

the transfer function that relates the input \mathbf{u} to output \mathbf{y} in the Laplace domain

$$\mathbf{Y}(s) = \mathbf{G}(s)\mathbf{U}(s) \quad (3.67)$$

is given by [71, pp. 144–145]:

$$\mathbf{G}(s) = \mathbf{C}(s\mathbf{I} - \mathbf{A})^{-1}\mathbf{B} + \mathbf{D} \quad (3.68)$$

Transformation of the transfer function $\mathbf{G}(s)$ from the frequency to the time domain yields the pulse response $\mathbf{g}(s)$

$$\mathbf{g}(t) = \mathcal{L}^{-1}\{\mathbf{G}(s)\} \quad (3.69)$$

and a multiplication in the Laplace domain transforms to a convolution of the pulse response with the input signal

$$y(t) = g(t) * u(t) = \int_0^t g(\tau)u(t - \tau)d\tau \quad (3.70)$$

A system's response to a step of constant height u is the integral of the pulse response

$$Y(s) = G(s)\frac{1}{s}U = H(s)U \quad (3.71)$$

$$y(t) = \int_0^t g(\tau)\Theta(t - \tau)d\tau u = \int_0^t g(\tau)d\tau u = h(t)u \quad (3.72)$$

with the Heaviside step function $\Theta(t)$ [72, p. 714]. The input errors are modeled as random constant u from a zero-mean distribution. The zero-mean assumption is justified because a known non-zero-mean of the error would have been easily corrected. The input is only the uncertainty of the actual measurements of initialization values, represented by its variance σ^2 . The uncertainty of the output is then given as:

$$\sigma_y^2(t) = h^2(t)\sigma_u^2 \quad (3.73)$$

This scalar expression for the variance can easily be expanded to the multivariate case:

$$\mathbf{P}_{yy}(t) = \underbrace{\begin{bmatrix} h_{1,1}(t) & \dots & h_{1,m}(t) \\ \vdots & & \vdots \\ h_{n,1}(t) & \dots & h_{n,m}(t) \end{bmatrix}}_{\mathbf{H}} \underbrace{\begin{bmatrix} \sigma_{1,1}^2 & \dots & \sigma_{1,m}^2 \\ \vdots & & \vdots \\ \sigma_{m,1}^2 & \dots & \sigma_{m,m}^2 \end{bmatrix}}_{\mathbf{P}_{uu}} \underbrace{\begin{bmatrix} h_{1,1}(t) & \dots & h_{1,b}(t) \\ \vdots & & \vdots \\ h_{m,1}(t) & \dots & h_{m,b}(t) \end{bmatrix}}_{\mathbf{H}^T} \quad (3.74)$$

Using equation (3.68) the step responses of the vertically fixed strapdown error dynamics (3.54) can be determined. The utilized Laplace transformations are given in Appendix C. The strapdown error dynamics' step responses for all combinations of in- and outputs are given in Appendix D.

The step responses in the frequency domain show up to three different complex conjugate poles, whose natural frequencies are the Earth angular rate ω_{ie} and the two frequencies ω_{s-} and ω_{s+} :

$$\omega_{s-}^2 = 2\omega_{ie}^2 \sin^2 \tilde{\phi} + \omega_s^2 - 2\omega_{ie} \sin \tilde{\phi} \sqrt{\omega_{ie}^2 \sin^2 \tilde{\phi} + \omega_s^2} \quad (3.75)$$

$$\omega_{s+}^2 = 2\omega_{ie}^2 \sin^2 \tilde{\phi} + \omega_s^2 + 2\omega_{ie} \sin \tilde{\phi} \sqrt{\omega_{ie}^2 \sin^2 \tilde{\phi} + \omega_s^2} \quad (3.76)$$

The variation of these frequencies with the geodetic latitude is depicted in Figure 3.5.

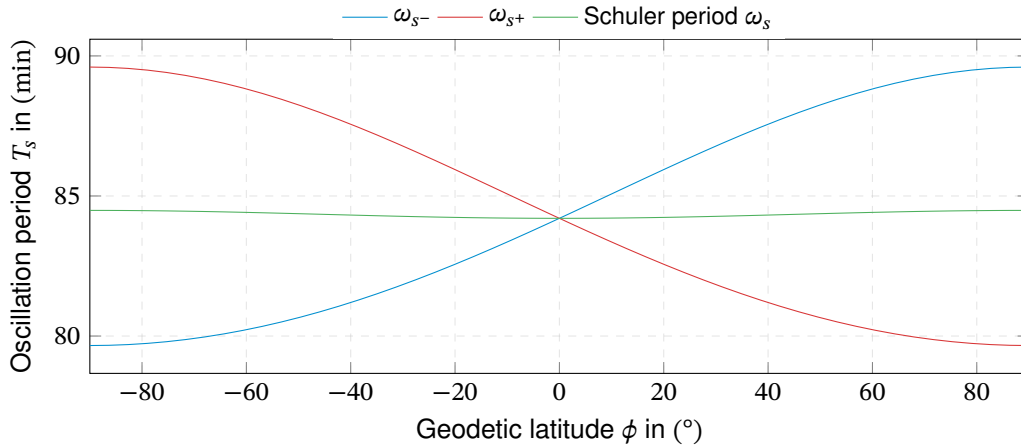


Figure 3.5.: Periods of the linearized strapdown error dynamics.

Note that the rates (3.75) and (3.76) are the full expression of the modified Schuler rates that can be found in literature, e.g. [15, p. 163]:

$$\omega_{s-} \approx \omega_s - \omega_{ie} \sin \tilde{\phi} \quad (3.77)$$

$$\omega_{s+} \approx \omega_s + \omega_{ie} \sin \tilde{\phi} \quad (3.78)$$

Using the trigonometric addition theorem [72, p. 81] the superposition of two equal amplitude oscillations of ω_{s-} and ω_{s+} can be shown yield a Schuler oscillation that is modulated at the

Foucault rate ω_f :

$$\begin{aligned} \sin(\omega_{s_+} t) + \sin(\omega_{s_-} t) &= 2 \sin\left(\frac{(\omega_{s_+} + \omega_{s_-})}{2} t\right) \cos\left(\frac{(\omega_{s_+} - \omega_{s_-})}{2} t\right) \\ &\approx 2 \sin(\omega_s t) \underbrace{\cos(\omega_{ie} \sin \tilde{\phi} t)}_{\omega_f} \end{aligned} \quad (3.79)$$

As observed from Figure 3.5, the modified Schuler rates are symmetric and converge to the non-modified Schuler rate near the equator. For differing amplitudes, the superposition yields more complicated patterns that cannot be rewritten analogously to (3.79). Still, their origin from a Schuler and Foucault oscillation can be recognized in the graphs.

Figure 3.6 depicts the utilized strapdown error dynamics as a block diagram. Like in [14, p. 346], the different oscillation rates can be attributed to different loops in the analyzed error dynamics' structure.

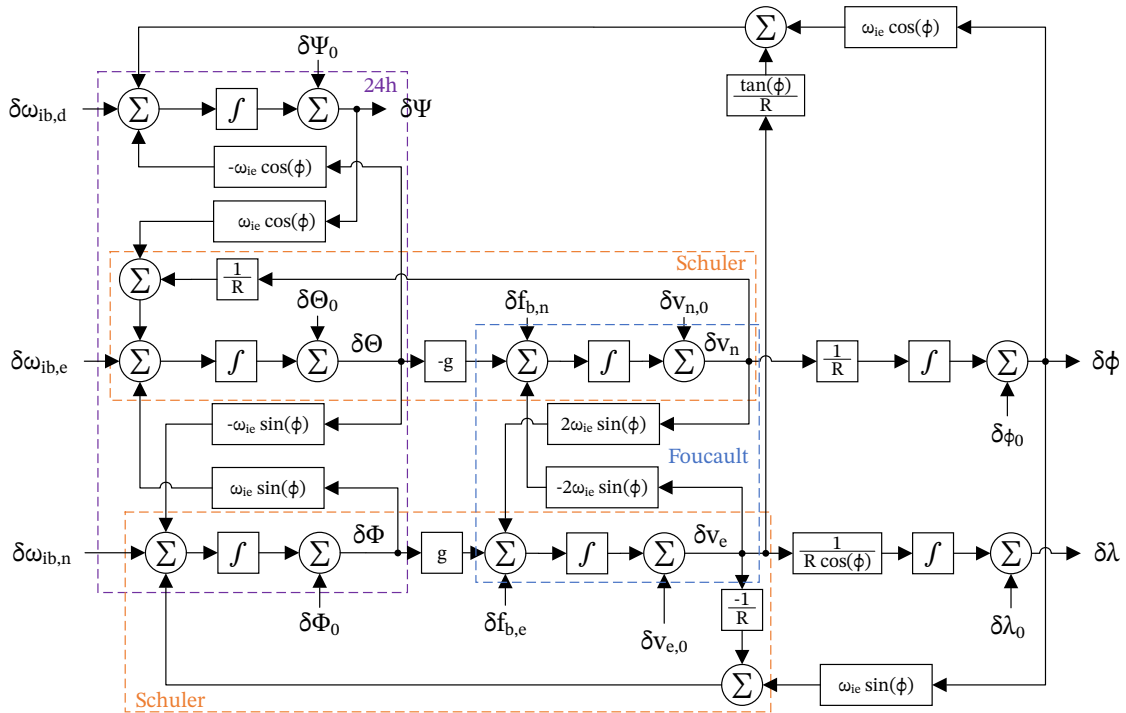


Figure 3.6.: Block diagram of the vertical fixed, linearized strapdown error dynamics for neglected vehicle motion.

These loops are well-known in navigation literature and can be explained by simplified models:

- The **Schuler oscillation**, derived by Maximilian Schuler in 1923 [73], results from an orientation error towards the local gravity vector that yields a re-balancing force. This setup corresponds to a pendulum that ranges from the vehicle to the Earth's center of

gravity, with the resulting angular rate:

$$\omega_s = \sqrt{\frac{g}{R}} \quad (3.80)$$

Neglecting the vehicle's altitude, this pendulum oscillates at the *Schuler period* of 84.4 min [14, p.339].

- The **24-hour oscillation** is the direct result of the Earth's rotation. As the Earth's angular rate is part of the gyroscope measurements, an erroneous attitude results in an erroneous angular rate component of the Earth's rotation in the respective orthogonal gyro axis. Roll and pitch errors oscillate at a period of about 24 h with a phase offset of 90°, which equals a pitch and roll uncertainty that rotates around the yaw axis once per day.
- The **Foucault oscillation** is named after Léon Foucault and his famous Foucault pendulum that was used to demonstrate the Earth's rotation. Like the Foucault pendulum, the interaction of the Earth's rotation with the vehicle's/pendulums velocity results in Coriolis forces [15, p. 163] that drive the Foucault oscillation at:

$$\omega_f = \omega_{ie} \sin \tilde{\phi} \quad (3.81)$$

From an Earth-fixed view, this results in the observed error dynamics at the Foucault rate.

The derived system responses to different error inputs are presented in the following sections. For easy use, the plotted system responses are normalized for a unit-sized input. This can result in very high values of the graphs. Note that these results need to be scaled with the errors to reach realistic magnitudes. Furthermore, it must be ensured that the resulting magnitudes do not exceed the range of validity for the linearization (see [Subsection 3.3.1.5](#)).

3.3.2.2. Position Error from Initial Position and Velocity Errors

The transfer functions and step responses are derived for SI-unit in- and outputs. Still, for vividness, the following graphs have been transformed to north and south position errors using the local radius R approximation:

$$\delta x_n \approx R \delta \phi \quad (3.82)$$

$$\delta x_e \approx R \cos \phi \delta \lambda \quad (3.83)$$

Additionally, all angles have been converted to degrees in the following graphics.

The responses of the latitude and longitude error states to initialization errors of position and velocity are presented in [Table D.1](#) and [Table D.2](#). A graphical presentation of these step responses is given in [Figure 3.7](#). As expected for a rotational ellipsoid Earth shape, an initial longitude error has no effect. An initial error in the latitude, however, excites both latitude

and longitude oscillation with a period of 24 hours. This oscillation is superposed with a Schuler oscillation modulated with the Foucault period. Longitude and latitude responses are phase-shifted by 90° . Initial velocity errors result only in the above-mentioned Schuler oscillation modulated with the Foucault period. Although the altitude is fixed in this model, an initial down velocity error interacting with the Earth's angular rate causes Coriolis forces that ultimately lead to an oscillating position error.

The development of the position error covariance from initial north and east velocity errors is depicted exemplarily in [Figure 3.8](#). The position errors are the integral of the initial velocity errors in each direction and are nearly uncoupled. For isotropic initial velocity errors, this results in a nearly circular covariance ellipse. Since both horizontal position errors oscillate in phase, the covariance ellipse keeps its shape and only oscillates in size.

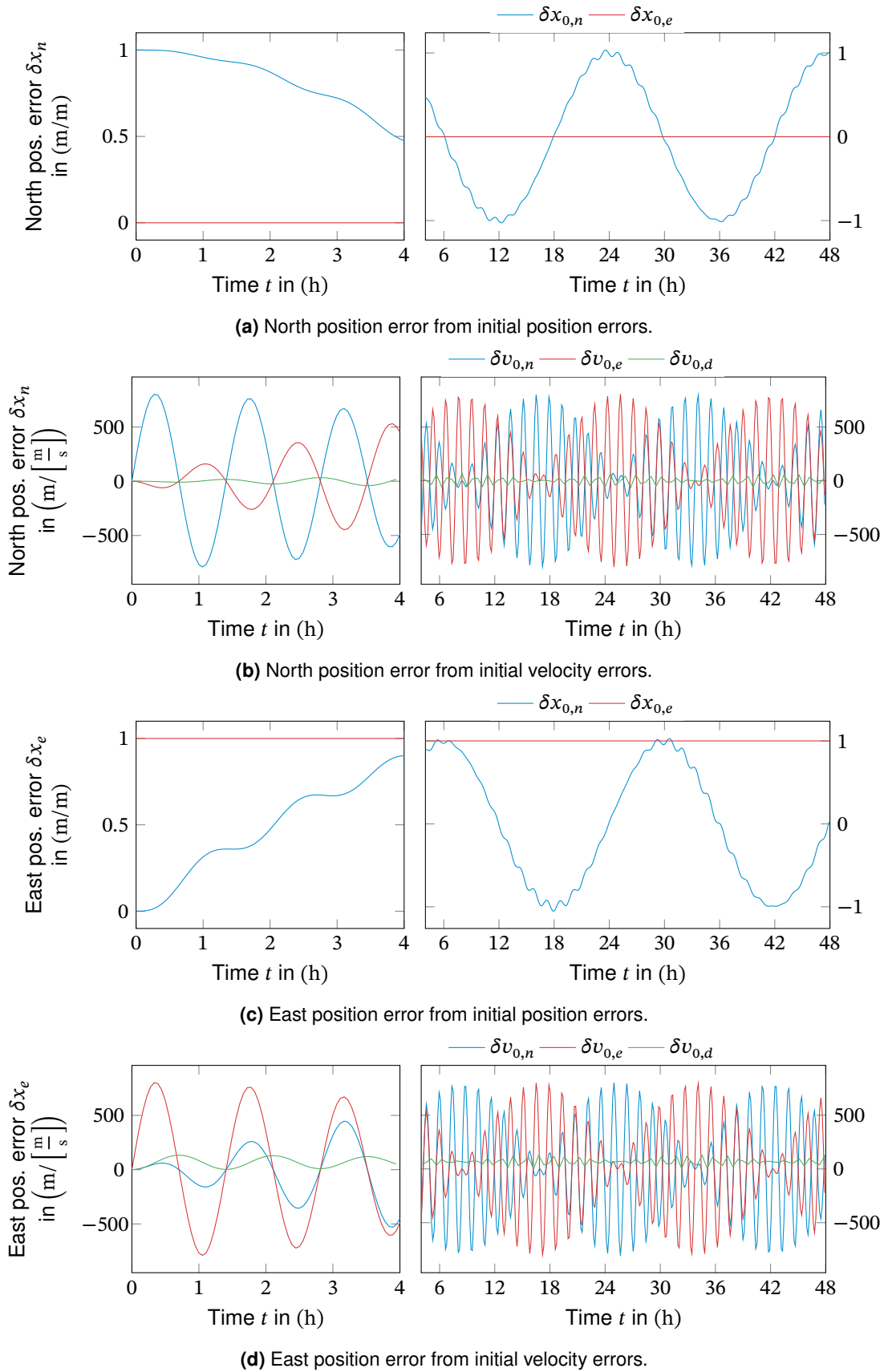


Figure 3.7.: North and east position errors from unit-step initial position and velocity errors at $\phi = 45^\circ$ and $\psi = 0^\circ$.

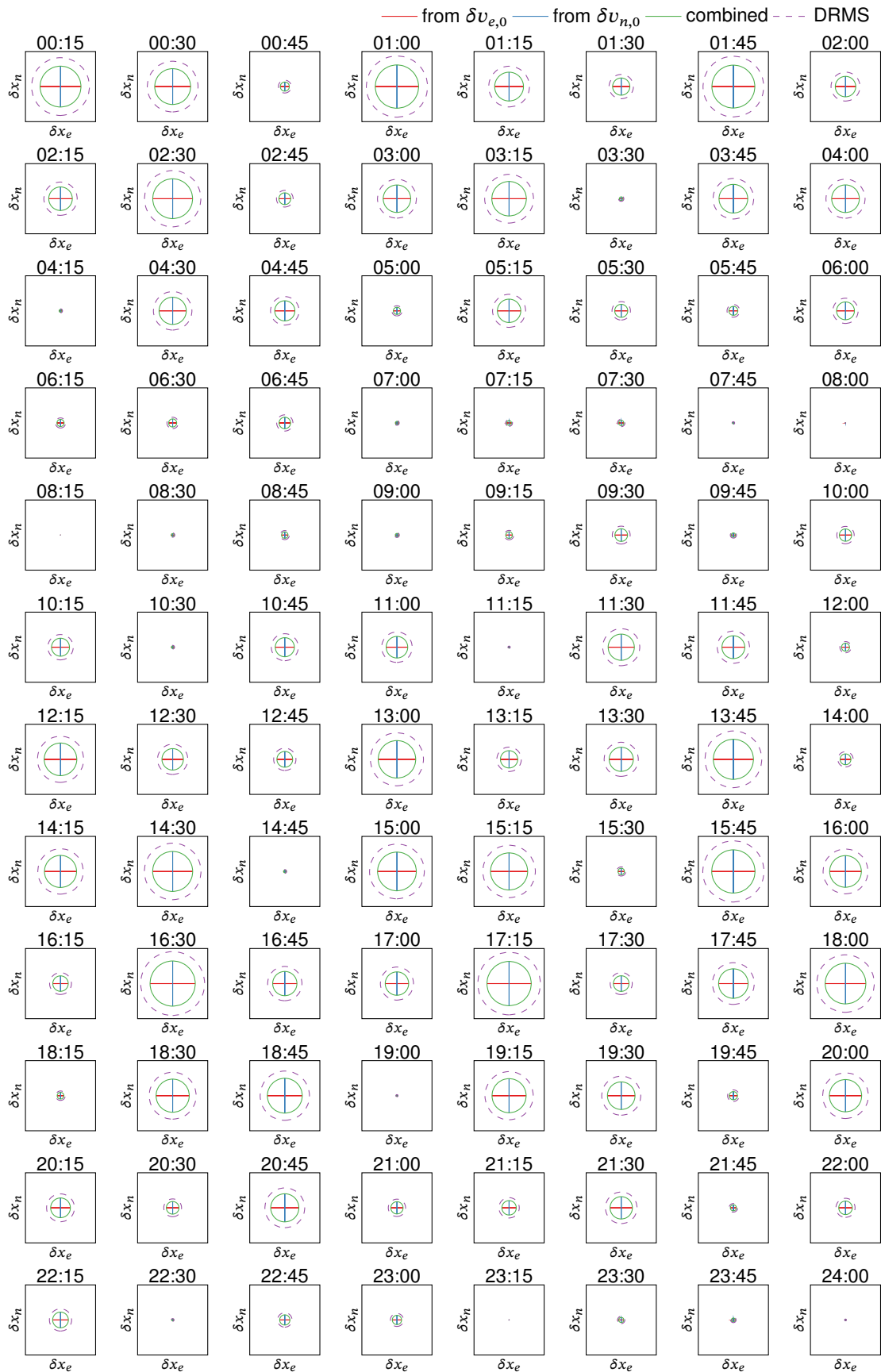


Figure 3.8.: Development of the horizontal position covariance from 0.1 m/s initial velocity errors (1σ) at $\phi = 45^\circ$ and $\psi = 0^\circ$.

3.3.2.3. Position Error from Initial Alignment Errors

The equations for the propagation of initial alignment errors are given in Table D.3 and Table D.4. The system's responses are depicted in Figure 3.9. Both latitude and longitude errors are characterized by a stable 24-hour oscillation, superposed with the Foucault modulated Schuler oscillation. While the Schuler oscillations are a significant part of the system's response to initial leveling errors, the response to initial azimuth errors is dominated by the 24-hour oscillation.

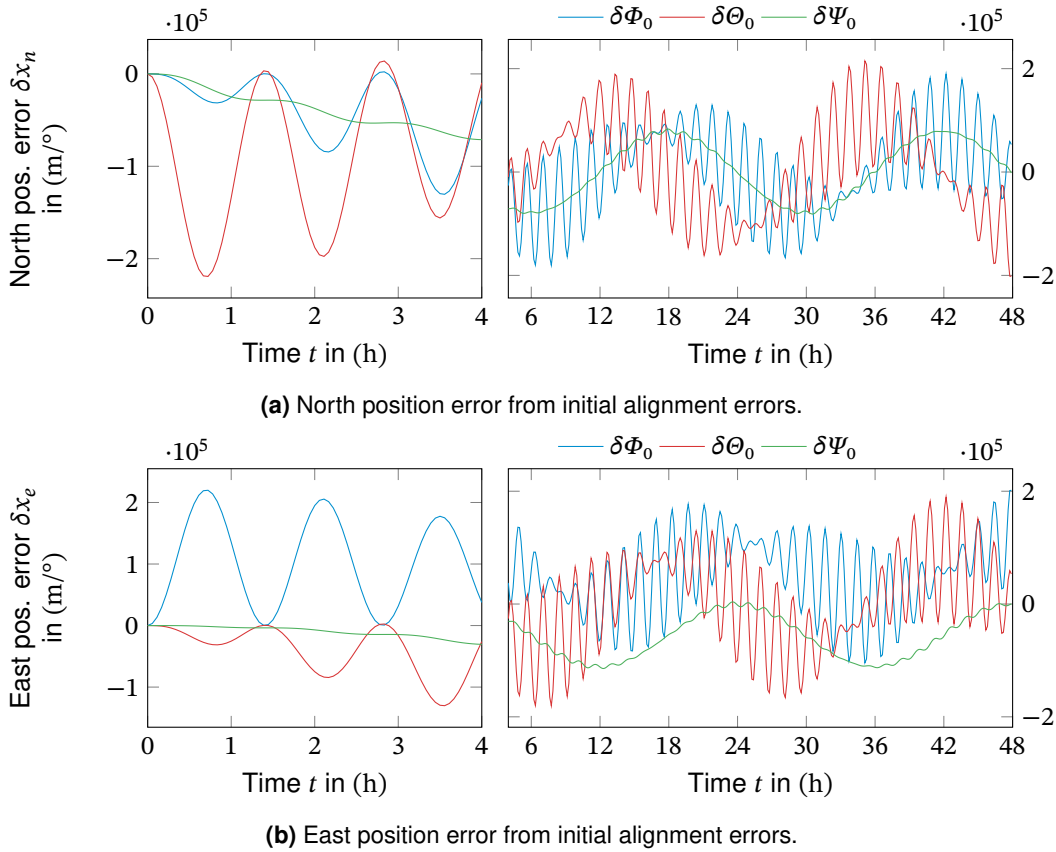


Figure 3.9.: Position error from unit-step initial alignment errors at $\phi = 45^\circ$ and $\psi = 0^\circ$.

The variation of the position covariance from initial alignment errors over time is depicted in Figure 3.10. Here, all alignment angle errors are assumed to be uncorrelated, and the leveling angles, roll, and pitch are supposed to have equal variance. These assumptions are valid for, e.g., gravity-based leveling using accelerometers and heading alignment from another source than the gyroscopes. The position uncertainty is dominated by the initial roll and pitch alignment error. The complex interaction of the responses to initial alignment errors results in a covariance ellipse that rotates with time and switches between elliptical and nearly circular. Still, the maximum size of this ellipse is bound and defined by initial orientation errors.

From equation (3.32), it can be seen that the initial heading alignment is correlated with the roll angle if the azimuth alignment is performed using the gyroscopes. Neglecting the uncertainty of gravity deflections σ_e^2 , (3.32) gives the off-diagonal entry of the covariance matrix

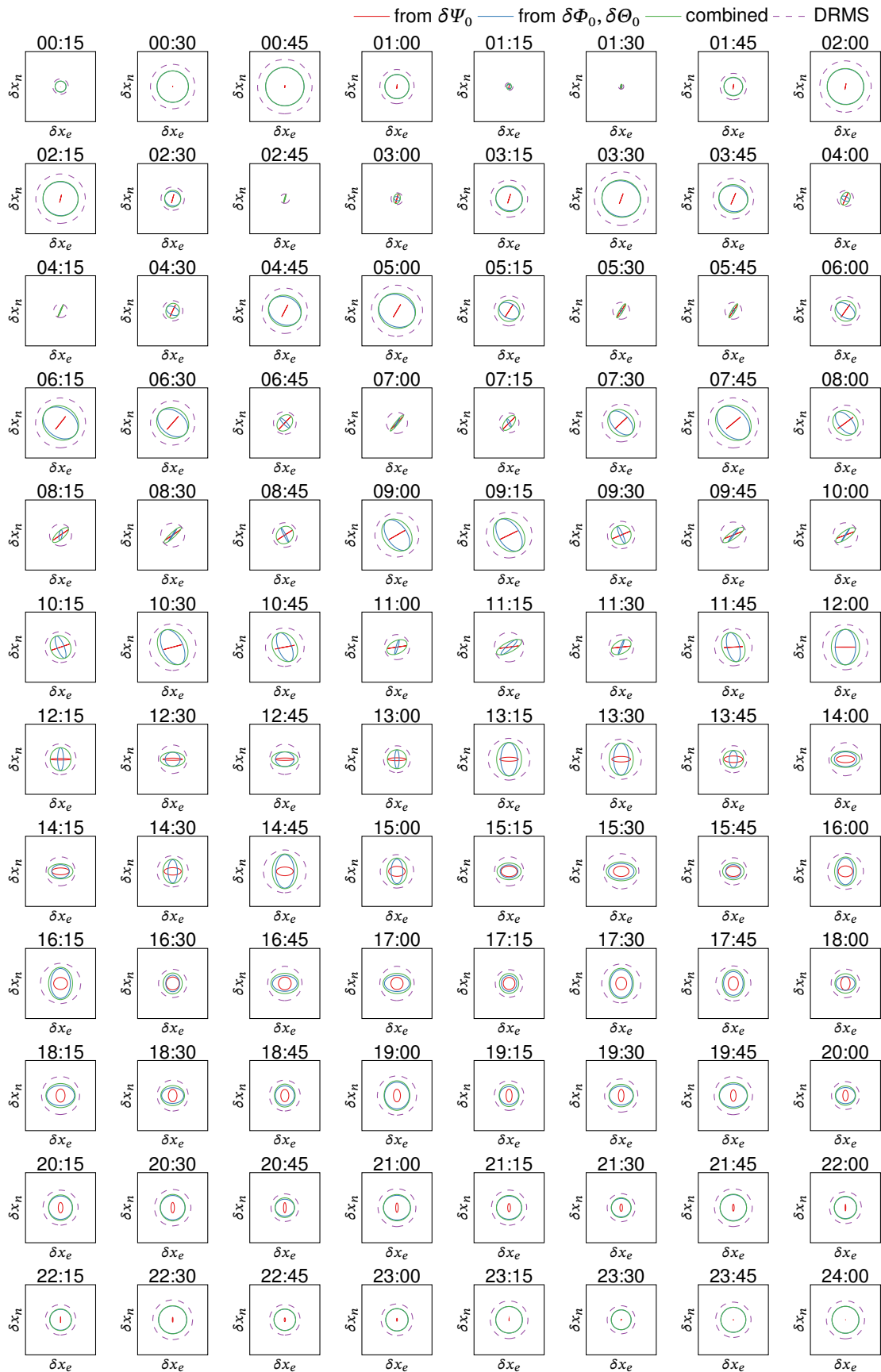


Figure 3.10.: Development of the horizontal position covariance from uncorrelated 0.01° initial pitch and roll (1σ) and 0.01° (1σ) yaw alignment error at $\phi = 45^\circ$ and $\psi = 0^\circ$.



Figure 3.11.: Development of the horizontal position covariance from correlated 0.01° initial pitch and roll (1σ) and 0.01° (1σ) yaw alignment error at $\phi = 45^\circ$ and $\psi = 0^\circ$.

as:

$$P_{\delta\phi\delta\psi} = -\frac{\sigma_{\delta f_b}^2}{\bar{g}^2} \tan \phi = -\sigma_{\delta\phi}^2 \tan \phi \quad (3.84)$$

This can be used to incorporate the correlation arising from the initial roll accuracy $\sigma_{\delta\phi}^2$ using (3.84). The resulting variation of the covariance over time is depicted in Figure 3.11. Clearly this increases the ellipticity of the horizontal position covariance from roll and pitch errors but has little effect on the Distance Root Mean Square (DRMS) values.

3.3.2.4. Position Errors from Bias-like IMU Errors

The responses of position errors to bias-like IMU errors are given in Table D.5 and Table D.6, both in the frequency and time domain.

Accelerometer biases excite latitude and longitude errors to a Schuler oscillation modulated with the Foucault oscillation. In the frequency domain representation, this manifests as two poles symmetrically placed close to the Schuler period ω_s . Note that a north accelerometer bias excites a north error oscillation north of the initial location, while an east accelerometer bias results in a north oscillation with the initial location in the mean. For the longitude errors, the same takes effect. For the vertically fixed strapdown error dynamics, a vertical acceleration error does not effect the position errors.

However, the position errors from gyroscope biases show a more nuanced behavior. A stable 24-hour oscillation dominates the latitude error. This oscillation is superposed by the Foucault modulated Schuler oscillation that has already been observed for the accelerometer biases. For the vertical angular rate biases, this superposed oscillation is hardly observable.

For the longitude error, completely different behavior can be observed. A bias of pitch rate measurement results in a stable oscillation dominated by the Foucault period and some superposed Schuler oscillations. Roll and yaw rate biases lead to a linear error growth superposed with 24-hour oscillation and small Schuler oscillations.

As illustrated in Figure 3.13, the position uncertainty from specific forces bias-like errors is nearly circular, with an oscillating size. As gyroscope biases lead to a linear growth (superposed with oscillations) of the east position error but to a limited oscillation of the north error, the resulting position uncertainty is getting increasingly elliptical with time. The north and east position uncertainty from bias-like IMU-errors are nearly uncorrelated. Due to its unbound growth, the east-position error quickly dominates the total position error.

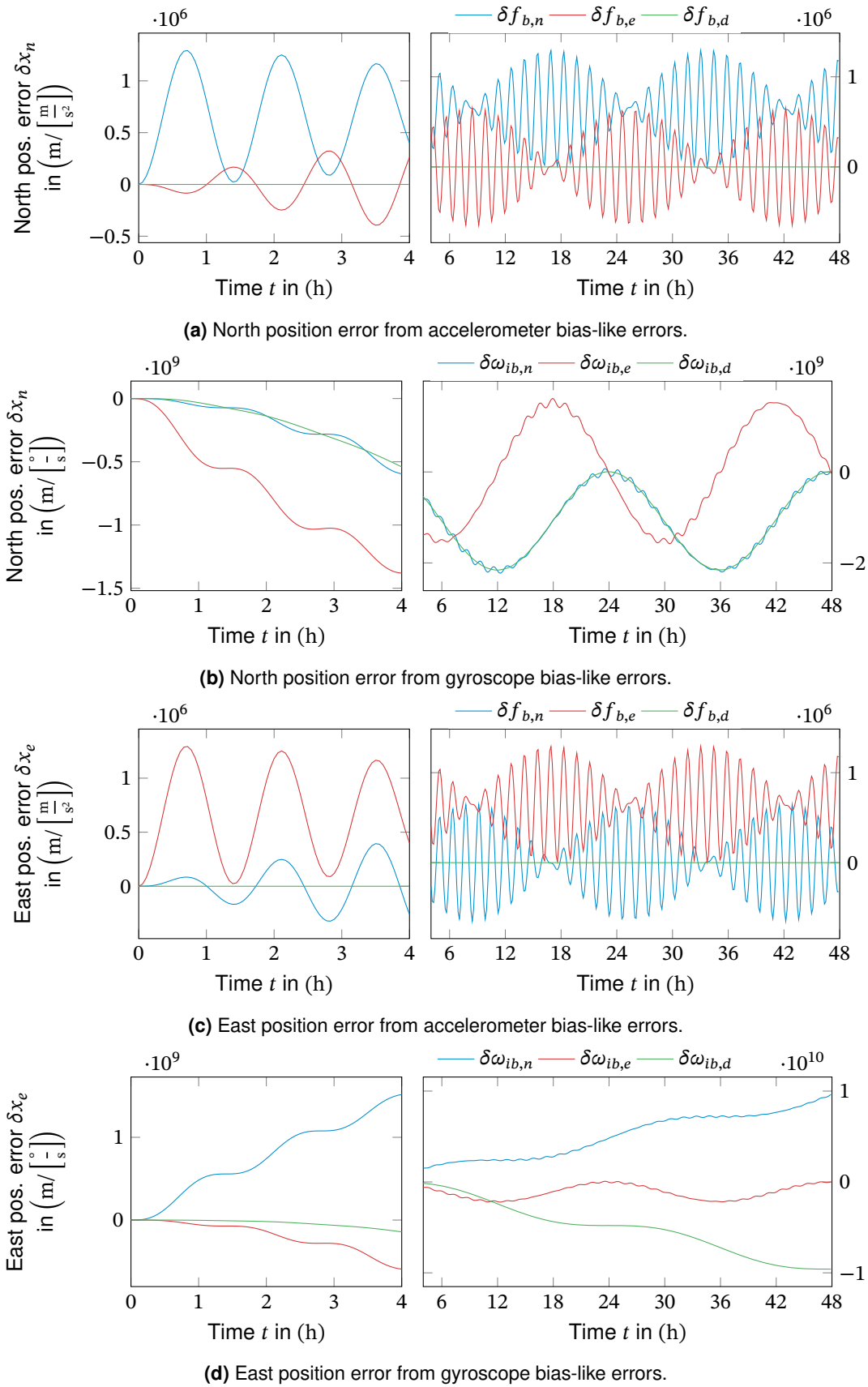


Figure 3.12.: Position error responses to unit-step IMU bias-like errors at $\phi = 45^\circ$ and $\psi = 0^\circ$.

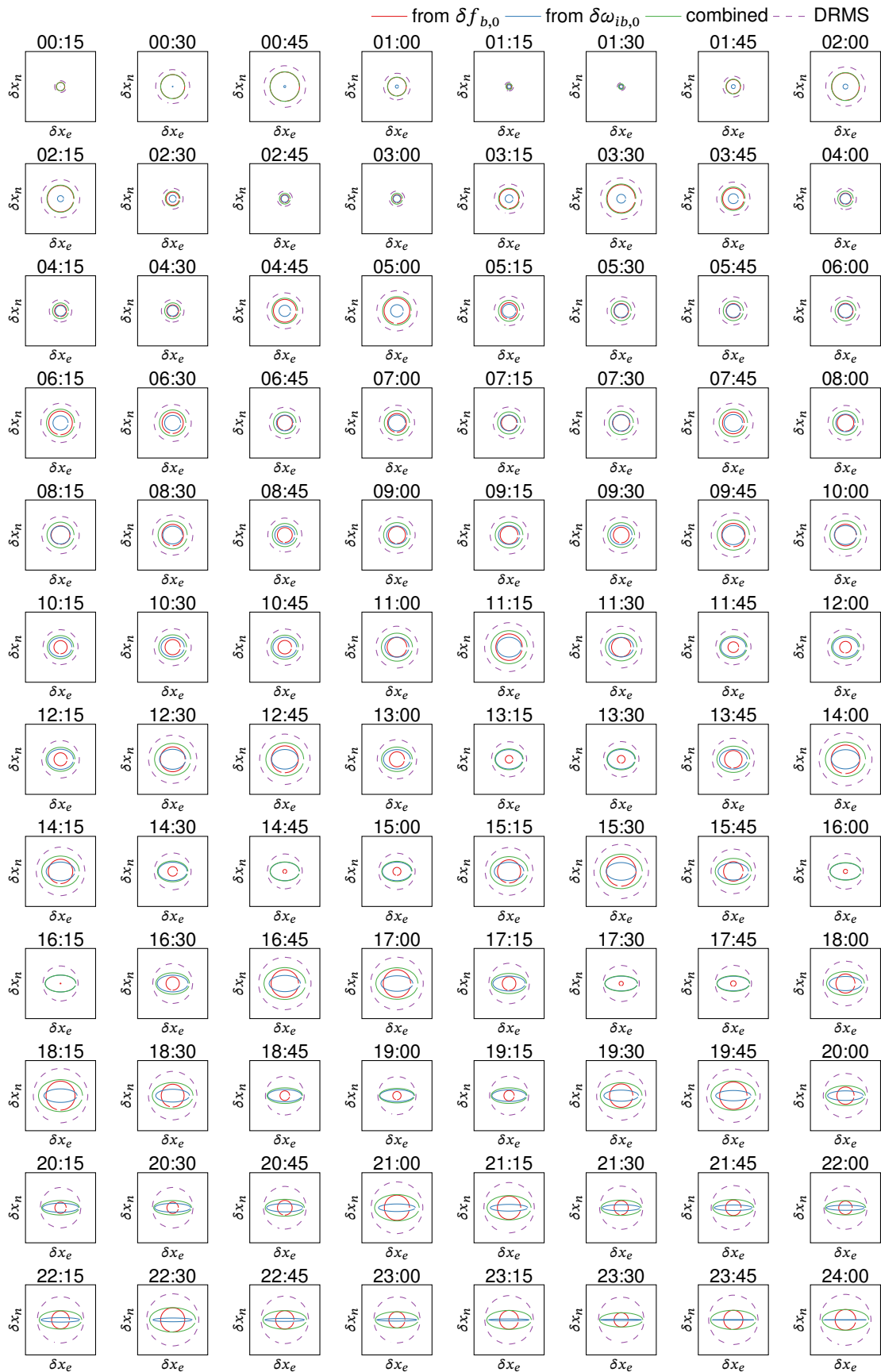


Figure 3.13.: Development of the horizontal position covariance from isotropic 1 mg accelerometer (1σ) and 0.01°h^{-1} (1σ) gyroscope bias-like errors at $\phi = 45^\circ$ and $\psi = 0^\circ$.

3.3.2.5. Velocity Error from Initial Position and Velocity Errors

The velocity errors from initial position and velocity errors are compiled in Table D.7 and Table D.8. The corresponding graphs are depicted in Figure 3.14 and Figure 3.15 for the north respectively east velocity error.

As the velocity errors are the time-derivative of the position errors, the higher frequency oscillations (here, Schuler oscillations) are amplified compared to the slow 24 h oscillations. Analogously to the position errors, an initial east position error has no effect.

The response to initial velocity errors is a Schuler oscillation, modulated at a 34 h Foucault period. The initial velocity sets the maximum amplitude of the system's response. Orthogonal horizontal velocity errors excite an equal-shaped oscillation where the modulation's phase is offset at 90°. A down velocity error (e.g., from baro measurements) has a minor effect on the other velocity errors, even for a vertically aided strapdown algorithm.

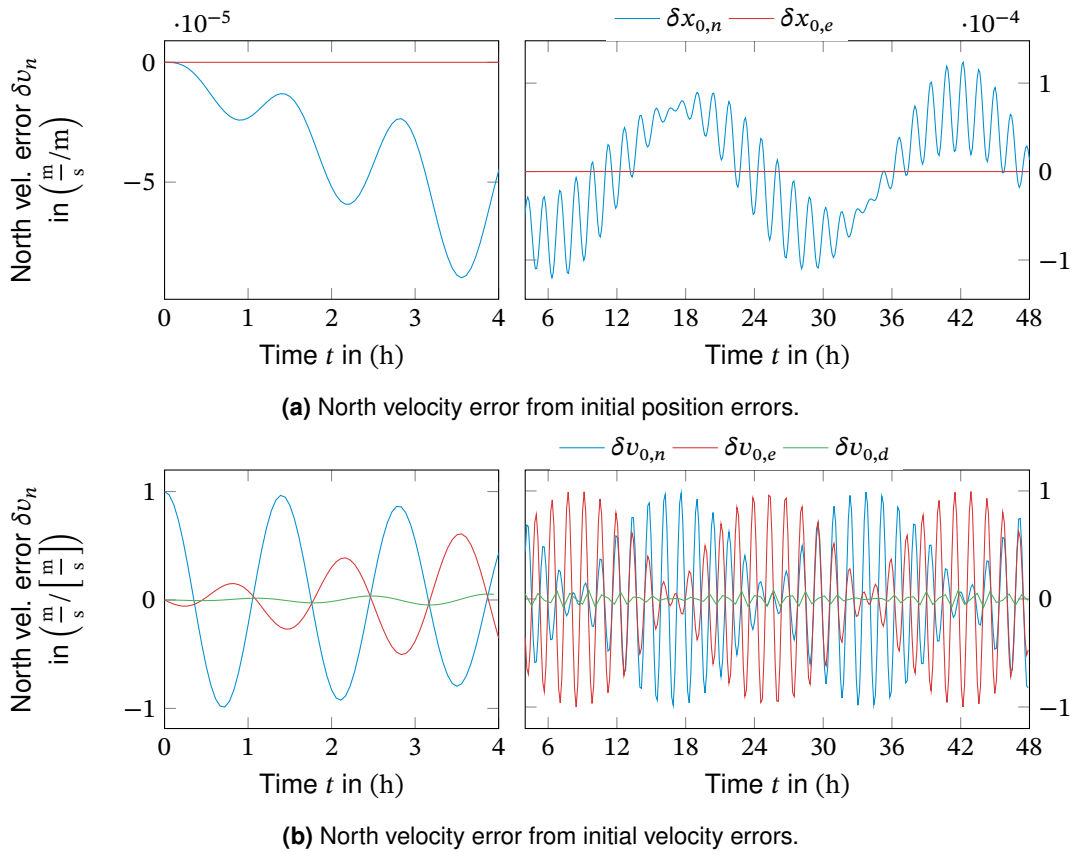
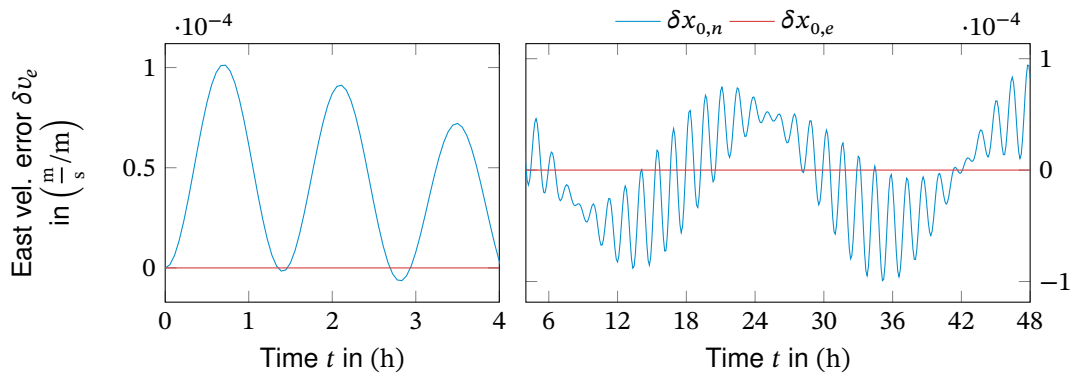
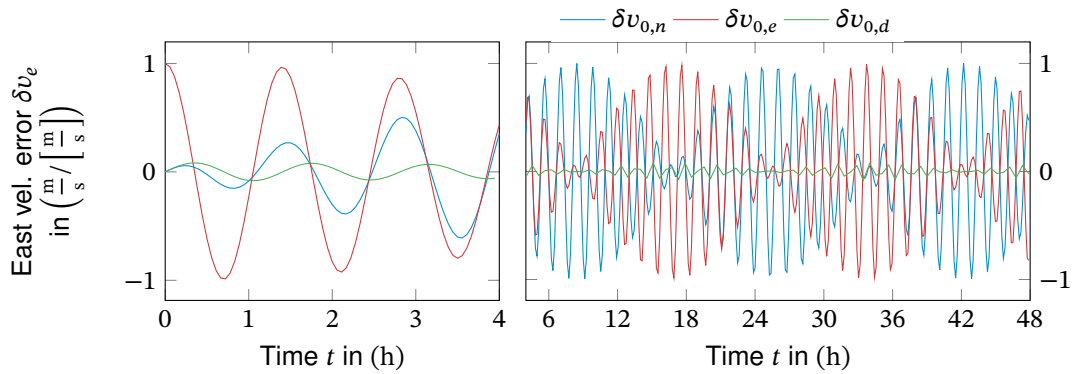


Figure 3.14.: North velocity error from unit-step initial position and velocity errors at $\phi = 45^\circ$ and $\psi = 0^\circ$.



(a) East velocity error from initial position errors.



(b) East velocity error from initial velocity errors.

Figure 3.15.: East velocity error from unit-step initial position and velocity errors at $\phi = 45^\circ$ and $\psi = 0^\circ$.

3.3.2.6. Velocity Error from Initial Alignment Errors

The velocity error response to initial orientation errors is presented in Table D.9 and Table D.10. As depicted in Figure 3.16, an initial roll and pitch error excites both north and east velocity errors to a modulated Schuler oscillation. An initial tilt leads to a fast error growth in that direction (e.g., pitch leads to north error) and a 90° phase-shifted reaction in the perpendicular direction. Similar to the position errors, an initial yaw angle error leads only to a relatively small velocity error dominated by the Foucault oscillation.

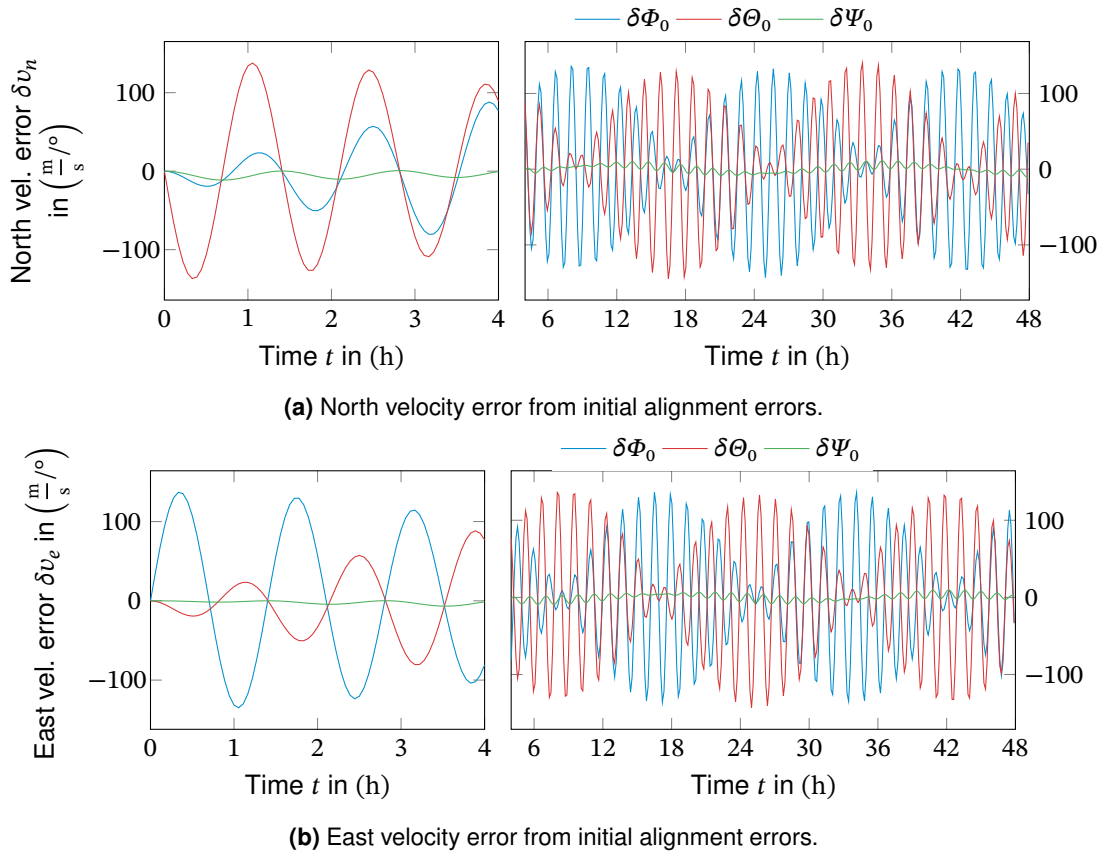
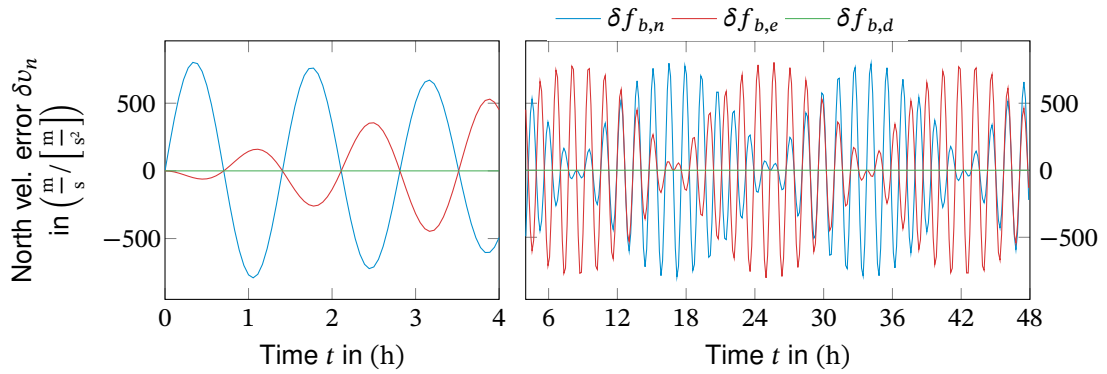


Figure 3.16.: Velocity errors from unit-step initial alignment errors at $\phi = 45^\circ$ and $\psi = 0^\circ$.

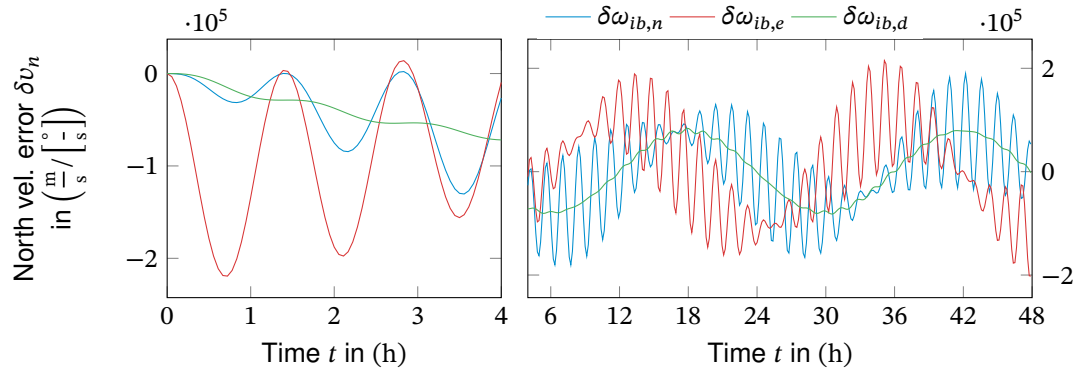
3.3.2.7. Velocity Error from from Bias-like IMU Errors

Table D.11 and Table D.12 list the north and east velocity errors from bias-like IMU measurement errors. A graphical depiction of these step responses is given in Figure 3.17.

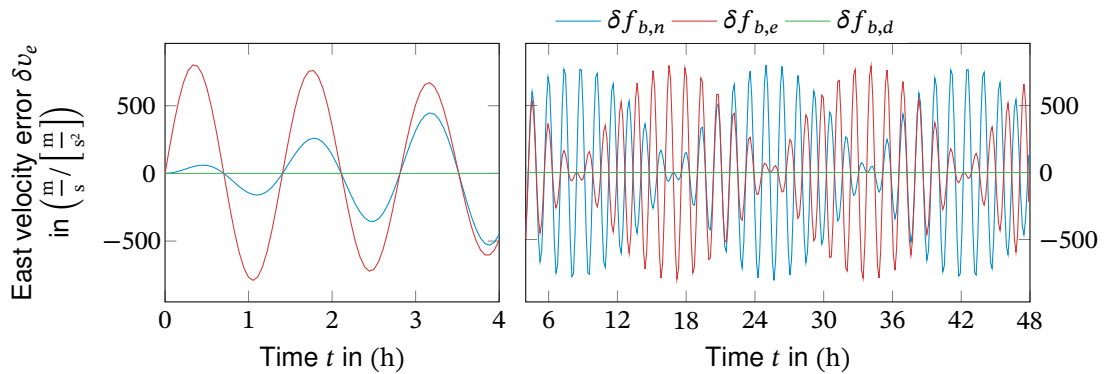
Again, the velocity errors from acceleration biases are described by a Schuler oscillation modulated at the Foucault period of 34 h (for $\phi = 45^\circ$). The responses show the already described phase shift for error inputs on perpendicular axes. Like the position errors, the velocity errors from gyroscope biases are composed of Schuler and Foucault oscillations. While the north velocity describes a symmetrical oscillation around zero, the means of the east velocity errors from $\omega_{ib,n}$ and $\omega_{ib,d}$ are offset.



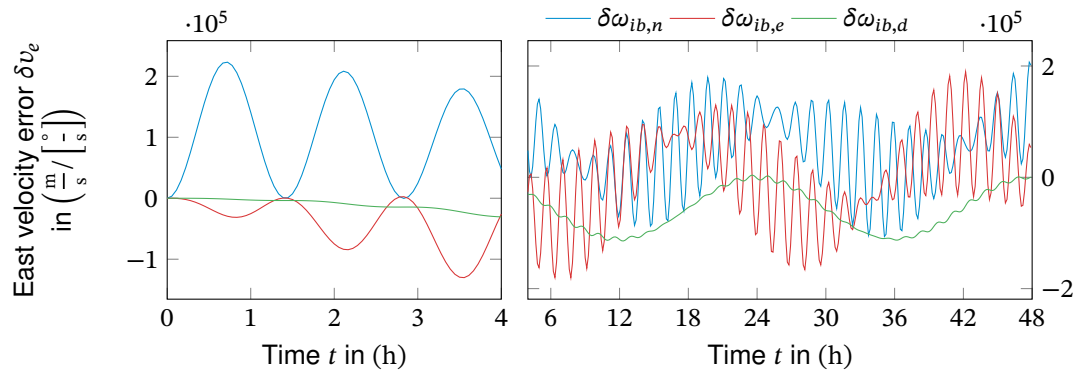
(a) North velocity error from accelerometer bias-like errors.



(b) North velocity error from gyroscope bias-like errors.



(c) East velocity error from accelerometer bias-like errors.



(d) East velocity error from gyroscope bias-like errors.

Figure 3.17.: Velocity error responses to unit-step IMU bias-like errors at $\phi = 45^\circ$ and $\psi = 0^\circ$.

3.3.2.8. Orientation Error from Initial Position and Velocity Errors

The step responses of the orientation errors, roll, pitch and yaw, to initialization errors are listed in Tables D.13, D.14 and D.15. The corresponding plots are presented in Figure 3.18 and Figure 3.19.

Again, an initial longitude error on the reference ellipsoid has no effect. A latitude error, however, excites errors in all three orientation angles: Roll and pitch angles are dominated by the Schuler oscillation modulated with a 24-hour oscillation. In contrast, the yaw angle oscillation is dominated by the 24-hour oscillation. The orientation errors from velocity errors are also dominated by the Schuler oscillation, modulated with the 24 hours oscillation.

Except for the yaw angle error from an initial latitude error, the orientation errors from initialization errors are minimal: An initial latitude error of 1° leads to a maximum roll angle error of 0.04° , an initial horizontal velocity error of 100 m/s leads to a roll angle error of less than 0.001° . Although the yaw angle error is susceptible to initial latitude errors, the error growth is relatively slow, reaching the maximum error after 6 hours.

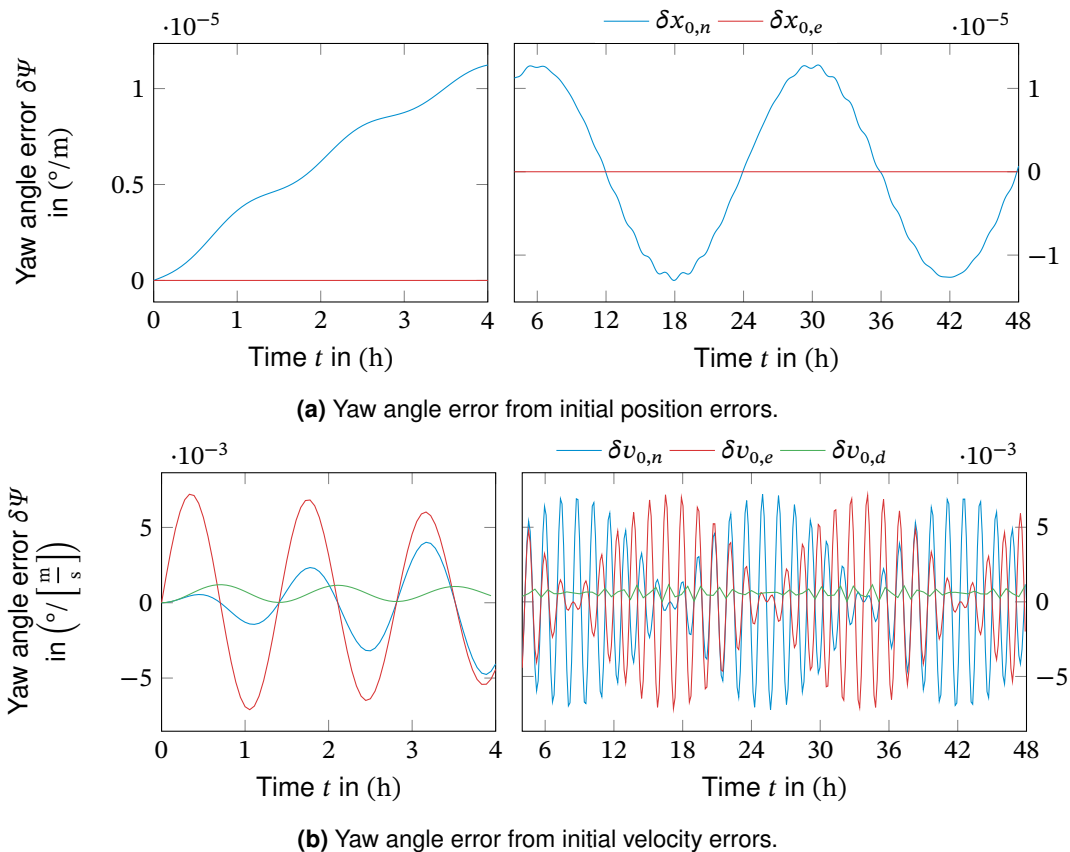


Figure 3.18.: Yaw angle error from unit-step initialization errors at $\phi = 45^\circ$ and $\psi = 0^\circ$.

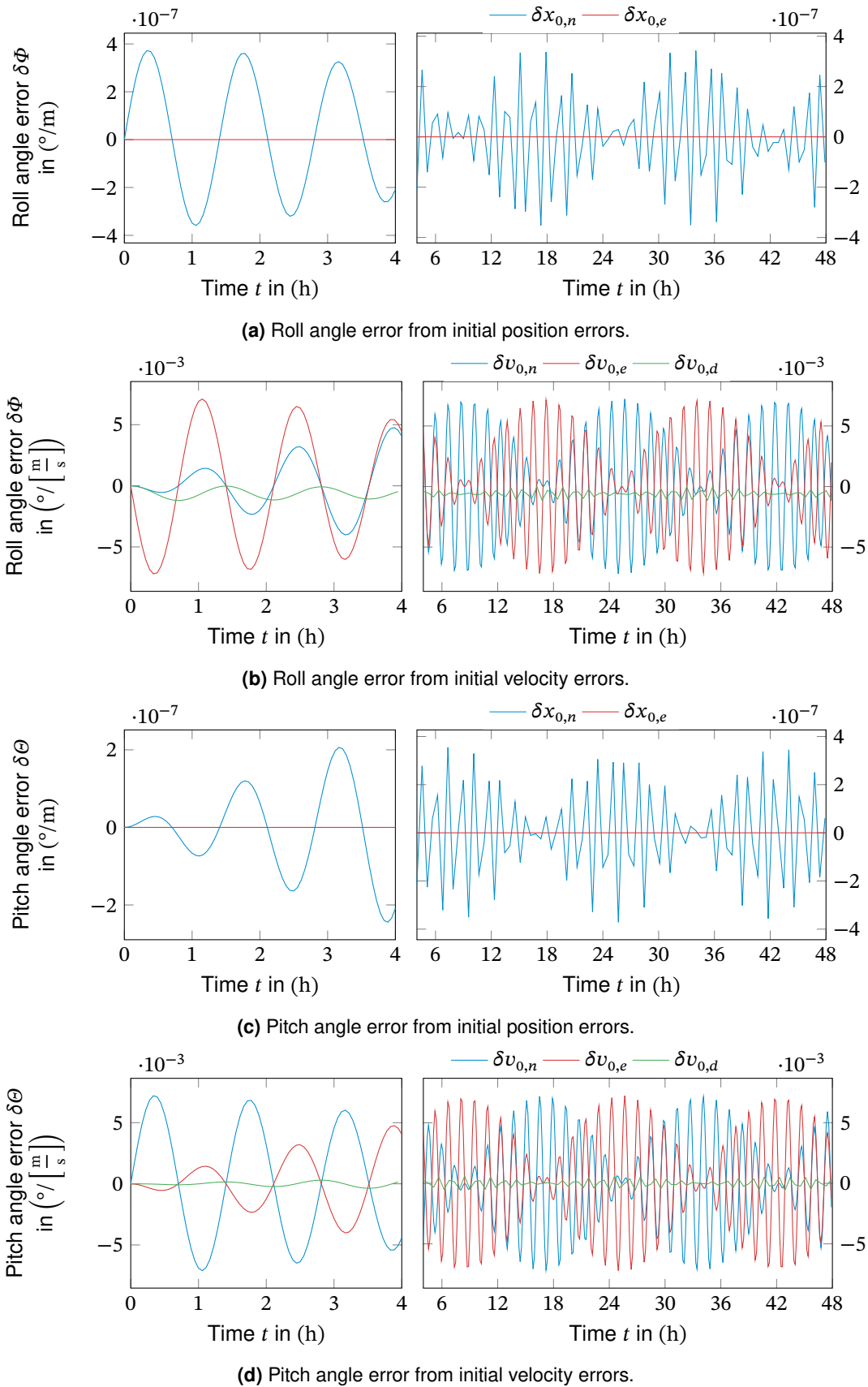


Figure 3.19.: Attitude angle errors from unit-step initialization errors at $\phi = 45^\circ$ and $\psi = 0^\circ$.

3.3.2.9. Orientation Error from Initial Alignment Errors

The step responses of the orientation errors to initial orientation errors (alignment errors) are summarized in Tables D.16, D.17 and D.18. The corresponding plots are presented in Figure 3.20.

An initial displacement of the attitude angles, roll, and pitch lead to a stable Schuler oscillation modulated with the Foucault period. The initial displacement gives the maximum of these oscillations, which ultimately is the residual leveling error after the vehicle's alignment. An initial azimuth error causes only a very small oscillation of the attitude errors.

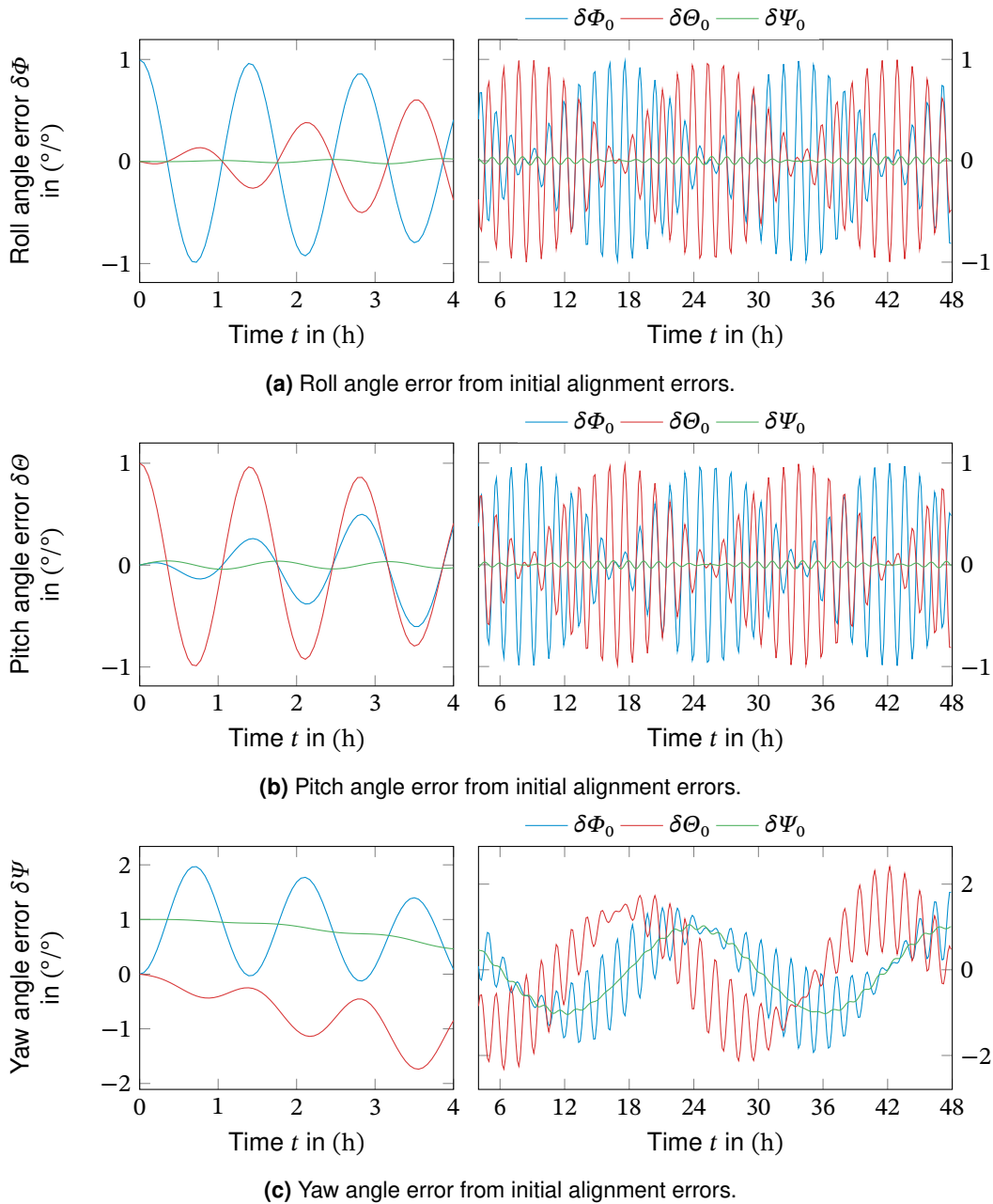


Figure 3.20.: Orientation angle error from unit-step initialization errors at $\phi = 45^\circ$ and $\psi = 0^\circ$.

The azimuth angle error's response to an initial azimuth deflection is a stable 24-hour oscillation with a small superpose Schuler oscillation. Again, the maximum is given by the initial azimuth error. An initial roll or pitch angle error also excites the azimuth error to a 24-hour oscillation, but with a superposed dominant Schuler oscillation. The maximum azimuth error here is about two times the initial leveling errors.

The development of the orientation error covariance from an isotropic initial uncertainty is depicted in [Figure 3.21](#). From an initially isotropic uncertainty, the uncertainty in each direction starts oscillating, where the initial covariance limits the maximum amplitude of the roll and pitch covariance. The azimuth uncertainty, however, reaches a multiple of the initial amplitude and displays a changing correlation with the roll uncertainty. This correlation has already been observed for the stationary alignment ([3.2](#)), but here it is superposed by the dynamics of the different attitude angles.

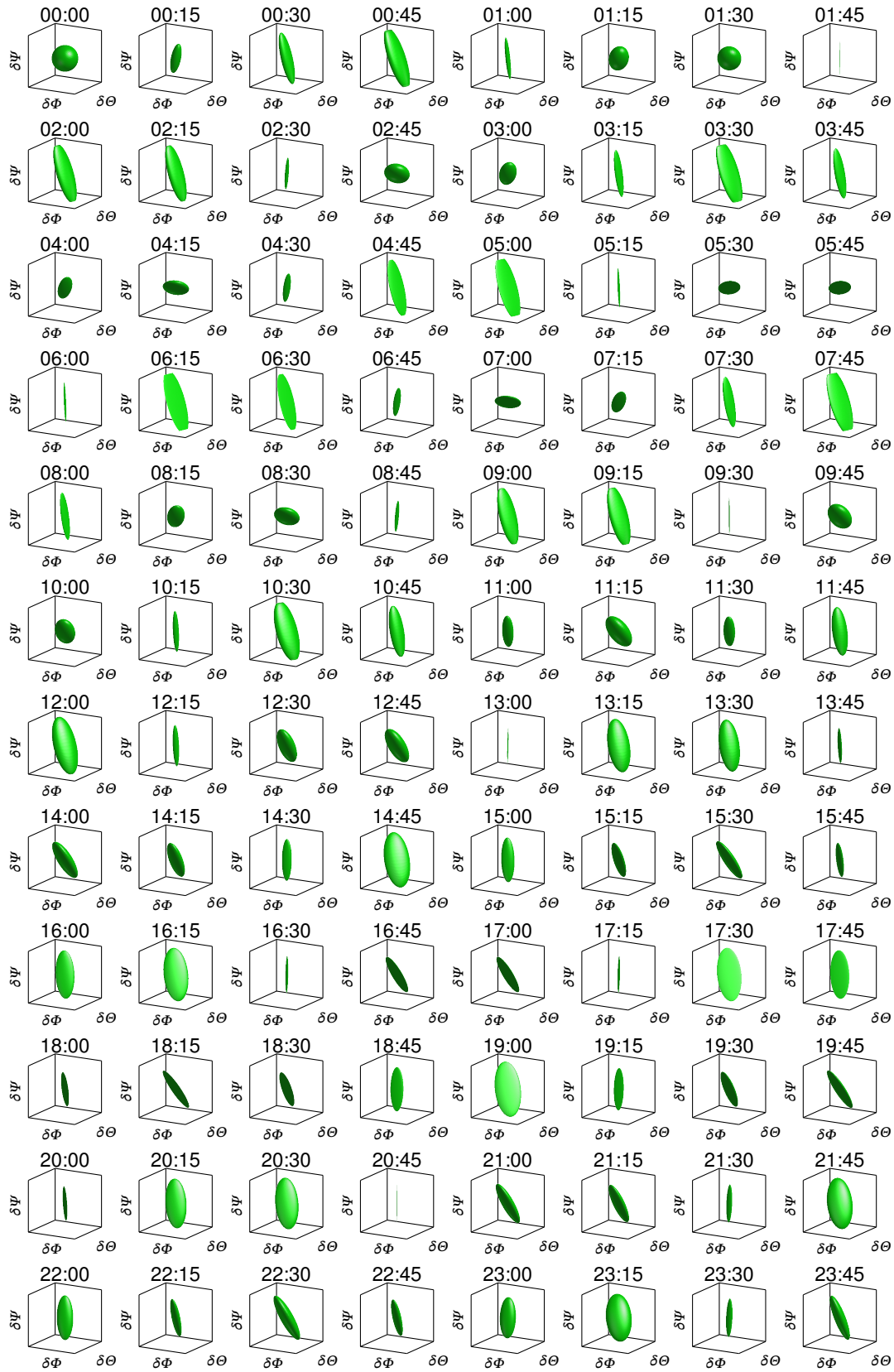


Figure 3.21.: Development of the attitude covariance over time from 1° (1σ) initial alignment error. All axes are equally scaled.

3.3.2.10. Orientation Error from Bias-like IMU Errors

The step responses of the orientation errors to bias-like IMU errors are given in the tables of Subsection D.1.9. A graphical representation of these step responses is given in Figure 3.22 and Figure 3.23.

Again, the roll and pitch angle errors are excited to a Schuler oscillation modulated at the Foucault rate. The vertical accelerometer bias $f_{b,z}$ has no effect in the case of the vertically fixed, initially aligned vehicle. Compared to the horizontal angular rate biases, the vertical angular rate bias has little effect. While the azimuth error from bias-like acceleration errors is a Schuler oscillation modulated by a 24 hours period, the reaction to angular rate bias-like errors is dominated by the 24-hour oscillation with a small superposed Schuler oscillation.

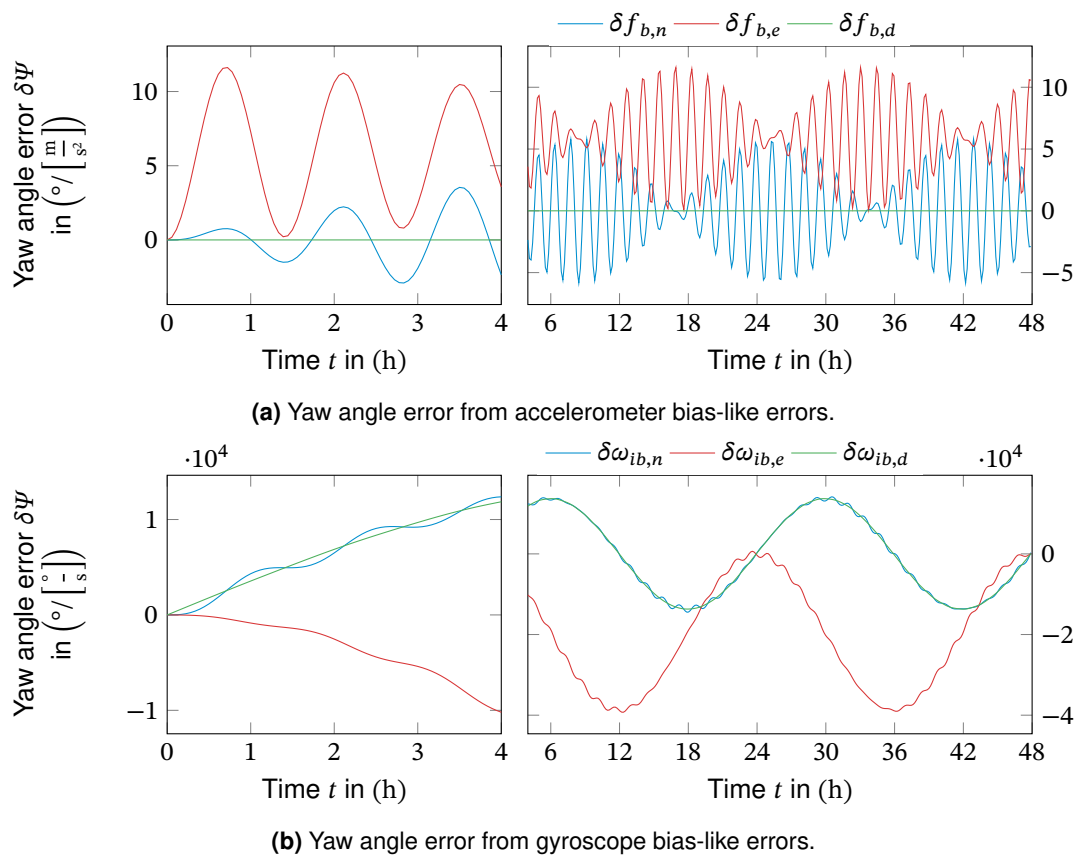


Figure 3.22.: Yaw angle error from unit-step IMU bias-like errors at $\phi = 45^{\circ}$ and $\psi = 0^{\circ}$.

An example of the resulting covariance from different sensor biases is presented in Figure 3.24. The accelerometer biases result mainly in an uncertainty in the pitch and roll angles. An azimuth uncertainty arises only through the correlation between azimuth and roll angle. In the plots, this is represented by the slightly tilted red disk with varying dimensions. The gyroscope biases excite mainly the azimuth uncertainty, represented by the slim blue ellipsoid. In addition to the oscillation in all dimensions, the attitude covariance from gyro biases also rotates around the azimuth axis, resulting from the phase shift between the step responses of the roll and

pitch angle errors.

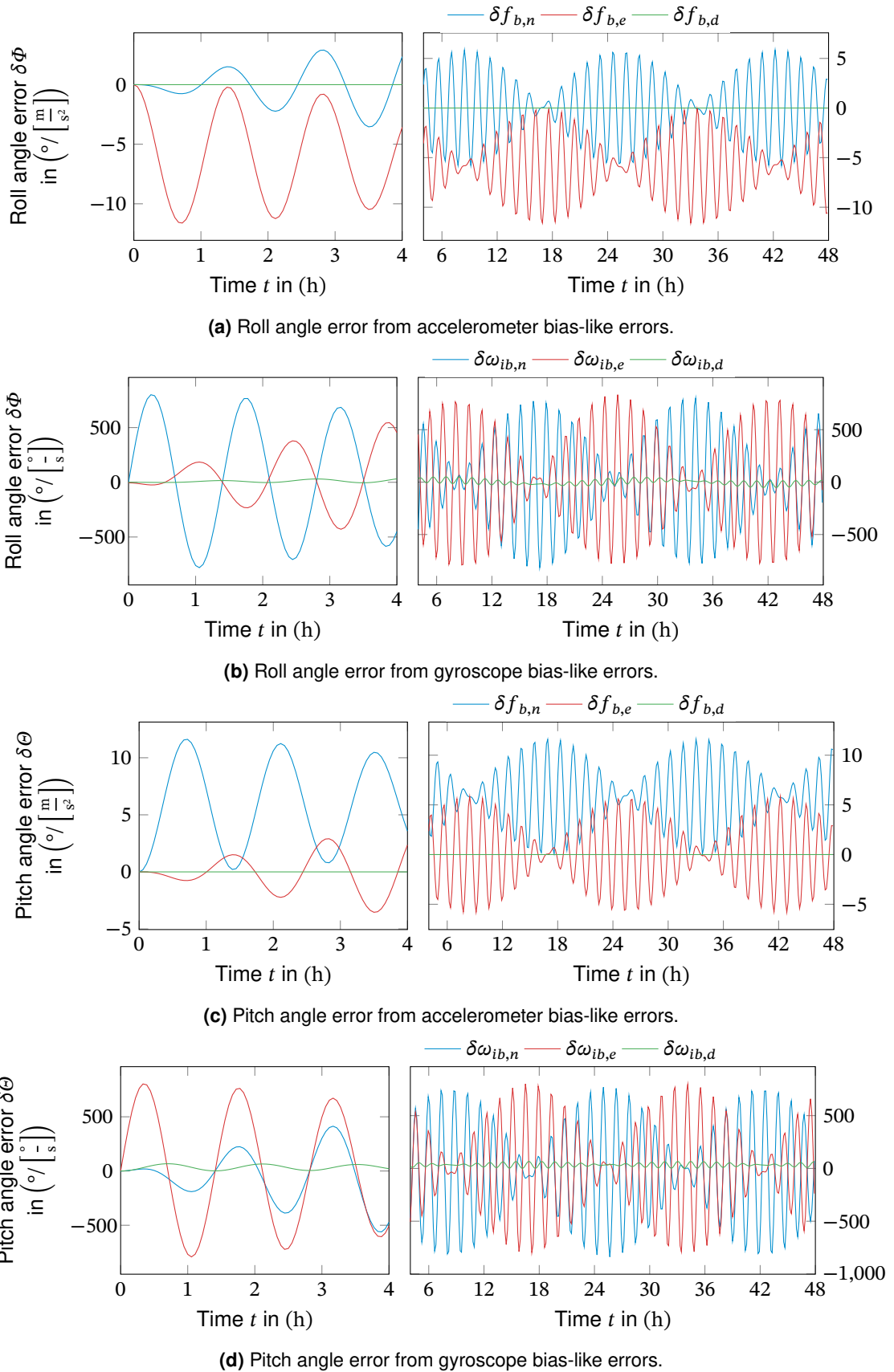


Figure 3.23.: Attitude angle error from unit-step IMU bias-like errors at $\phi = 45^\circ$ and $\psi = 0^\circ$.

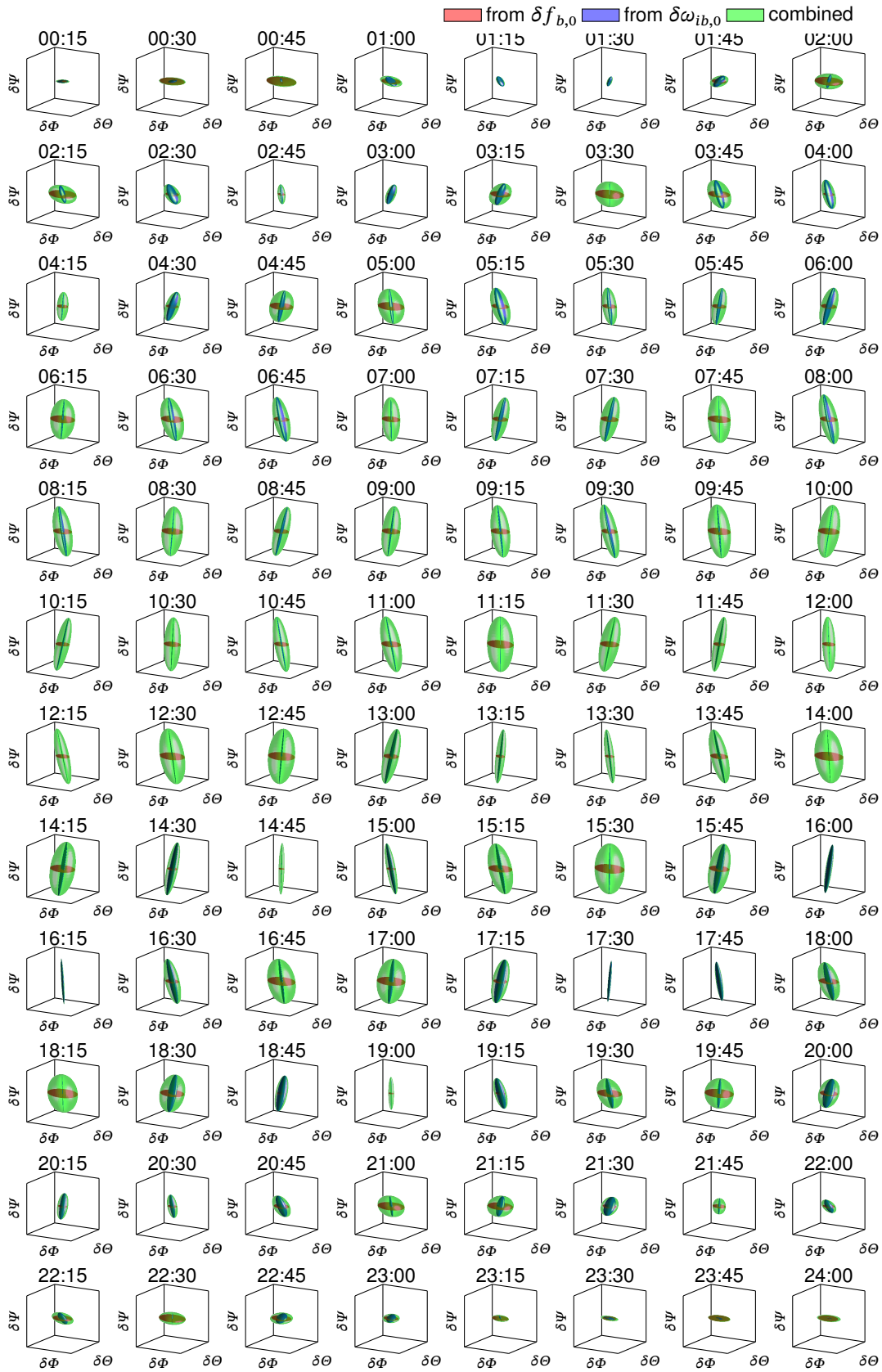


Figure 3.24.: Development of the attitude covariance over time from $1^\circ/\text{h}$ (1σ) gyro bias and 5 mg (1σ) accelerometer bias. Roll and pitch angle axes are equally scaled, while the azimuth axis is depicted at a scale of 0.1 to increase perceptiveness.

3.3.2.11. Latitude dependency

The vehicle's latitude has direct effect on the modulation of the Schuler rate which is represented by (3.75) and (3.76). This is caused by Foucault rate's (3.81) dependency on the latitude. Consequently, the Schuler oscillations display no modulation at the equator, while the modulation frequency grows towards the Earth's angular rate at the poles.

In addition to the Foucault rate, also some of the step responses directly depend on the latitude. The dependencies summarized in Table 3.2 modify the amplitudes of the three underlying oscillations and thus alter both shape and amplitude of the total response. The maximum number of error responses exists at medium latitudes since many responses vanish at the equator or the poles.

Table 3.2.: Latitude dependency of the strapdown error step responses.

input	Output state						
	$\delta\phi$	$\delta\lambda$	δv_n	δv_e	$\delta\Phi$	$\delta\Theta$	$\delta\Psi$
$\delta\phi_0$	$\sin^2\phi$	$\tan\phi$	$\sin^2\phi$	$\tan\phi$	$\sin\phi$	-	$\cos\phi$
$\delta\lambda_0$	-	-	-	-	-	-	-
$\delta v_{n,0}$	-	$\tan\phi$	-	$\tan\phi$	$\sin\phi$	-	$\tan\phi\sin\phi$
$\delta v_{e,0}$	$\sin\phi$	$\sec\phi$	$\sin\phi$	$\sec\phi$	-	$\sin\phi$	$\tan\phi$
$\delta v_{d,0}$	$\sin 2\phi$	-	$\sin 2\phi$	-	$\cos\phi$	$\sin 2\phi$	$\sin\phi$
$\delta\Phi_0$	$\sin\phi$	$\sec\phi$	$\sin\phi$	$\sec\phi$	-	$\sin\phi$	$\tan\phi$
$\delta\Theta_0$	-	$\tan\phi$	-	$\tan\phi$	$\sin\phi$	-	$\cos\phi$
$\delta\Psi_0$	$\cos\phi$	$\sin\phi$	$\cos\phi$	$\sin\phi$	$\sin 2\phi$	$\cos\phi$	$\cos^2\phi$
$\delta f_{b,x}$	-	$\tan\phi$	-	$\tan\phi$	$\sin\phi$	-	$\sin\phi\tan\phi$
$\delta f_{b,y}$	$\sin\phi$	$\sec\phi$	$\sin\phi$	$\sec\phi$	-	$\sin\phi$	$\tan\phi$
$\delta f_{b,z}$	-	-	-	-	-	-	-
$\delta\omega_{ib,x}$	$\sin\phi$	$\sec\phi$	$\sin\phi$	$\sec\phi$	-	$\sin\phi$	$\tan\phi$
$\delta\omega_{ib,y}$	-	$\tan\phi$	-	$\tan\phi$	$\sin\phi$	-	$\cos\phi$
$\delta\omega_{ib,z}$	$\cos\phi$	$\sin\phi$	$\cos\phi$	$\sin\phi$	$\sin 2\phi$	$\cos\phi$	-

3.3.3. Response to White Noise Sensor Errors

3.3.3.1. System Response to White Gaussian Noise

A noise-like error on the inertial sensor measurements continuously excites the error dynamics. In general, noise can be modeled as a stochastic process. The most simple case is white Gaussian noise, fully described by its mean μ and (co)variance σ .

Again, the system's output is determined from the convolution of the system's impulse response and the white Gaussian noise input (see Equation 3.70):

$$u(t) \sim \mathcal{N}(\mu_u, \sigma_u) \quad (3.85)$$

White Gaussian noise is a stationary process. Consequently, the variance is constant over time. The expected value of the system's output is simply the step response scaled by the input's expected value:

$$\mu_y(t) = E[y(t)] = E\left[\int_0^t g(\tau)u(t-\tau)d\tau\right] = \mu_{u,v} \int_0^t g(\tau)d\tau = \mu_{u,v}h(t) \quad (3.86)$$

For the following analysis only zero-mean WGN is considered as noise input, since any non-zero means are already treated as bias-like input. The zero-mean white Gaussian noise input ($\mu_u = 0$) results in a zero-mean output $\mu_y(t) = 0$. By definition, the autocovariance of white noise is zero for any two different evaluation times $\tau \neq \rho$ and the variance σ_u^2 if $\tau = \rho$. In the scalar case, the variance of the output signal at time t due to WGN input of variance expressed as the Angular Random Walk (ARW)/Velocity Random Walk (VRW) coefficient $\sigma_u^2 = N_u^2$ (see Table 2.7) is given as:

$$\begin{aligned} \sigma_y^2(t) &= E[y(t)^2] - \underbrace{\mu_y^2}_{=0} = E\left[\int_0^t g(t-\rho)u(\rho)d\rho \int_0^t g(t-\tau)u(\tau)d\tau\right] \\ &= E\left[\int_0^t \int_0^t g(t-\rho)u(\rho)u(\tau)g(t-\tau)d\rho d\tau\right] \\ &= \int_0^t \int_0^t g(t-\rho) \underbrace{E[u(\rho)u(\tau)]}_{N_u^2 \delta(\rho-\tau)} g(t-\tau)d\rho d\tau \\ &= N_u^2 \int_0^t \int_0^t g(t-\rho)\delta(\rho-\tau)g(t-\tau)d\rho d\tau \\ &= N_u^2 \underbrace{\int_0^t g^2(t-\tau)d\tau}_{k(t)} \end{aligned} \quad (3.87)$$

Again, this expression can be expanded to the multivariate case

$$\mathbf{P}_{yy}(t) = \int_0^t \underbrace{\begin{bmatrix} g_{1,1}(t-\tau) & \dots & g_{1,m}(t-\tau) \\ \vdots & & \vdots \\ g_{n,1}(t-\tau) & \dots & g_{n,m}(t-\tau) \end{bmatrix}}_{\mathbf{G}} \mathbf{N}_{uu} \underbrace{\begin{bmatrix} g_{1,1}(t-\tau) & \dots & g_{1,n}(t-\tau) \\ \vdots & & \vdots \\ g_{m,1}(t-\tau) & \dots & g_{m,n}(t-\tau) \end{bmatrix}}_{\mathbf{G}^T} d\tau \quad (3.88)$$

with the input noise covariance matrix \mathbf{N}_{uu} .

The impulse response functions in frequency and time domain for the linearized strapdown error dynamics (3.55) are listed in Annex D.2. Analog to step responses that have been discussed in the previous section, the impulse responses of the linearized strapdown error dynamics are a superposition of harmonic oscillations at the modified Schuler rates ω_{s+} (3.76), ω_{s-} (3.76) and the Earth angular rate ω_{ie} .

The most general form of these impulse responses in the time domain is one of the functions

$$g_{a,\sin}(t) = a_0 + a_1 t + a_2 \sin(\omega_{s-} t) + a_3 \sin(\omega_{s+} t) + a_4 \sin(\omega_{ie} t) \quad (3.89)$$

$$g_{a,\cos}(t) = a_0 + a_1 t + a_2 \cos(\omega_{s-} t) + a_3 \cos(\omega_{s+} t) + a_4 \cos(\omega_{ie} t) \quad (3.90)$$

where the coefficients a_0 and a_4 are zero for many functions. For these forms, a general analytic solution of the required integral can be given for any combination of sine and cosine based step responses $g_a(t)$ and $g_b(t)$ in equation (3.87).

For two sine-based impulse responses this solution is:

$$\begin{aligned} k(t) &= \int_0^t g_{a,\sin}(t-\tau) g_{b,\sin}(t-\tau) d\tau \\ &= \left(a_0 b_0 + \frac{a_2 b_2 + a_3 b_3 + a_4 b_4}{2} \right) t + (a_0 b_1 + a_1 b_0) t^2 + a_1 b_1 t^3 \\ &\quad - \frac{a_2 b_3 + b_2 a_3}{2(\omega_{s-} + \omega_{s+})} \sin((\omega_{s-} + \omega_{s+})t) - \frac{a_2 b_4 + b_2 a_4}{2(\omega_{s-} + \omega_{ie})} \sin((\omega_{s-} + \omega_{ie})t) \\ &\quad - \frac{a_3 b_4 + b_3 a_4}{2(\omega_{s+} + \omega_{ie})} \sin((\omega_{s+} + \omega_{ie})t) + \frac{a_2 b_3 + b_2 a_3}{2(\omega_{s-} - \omega_{s+})} \sin((\omega_{s-} - \omega_{s+})t) \\ &\quad + \frac{a_2 b_4 + b_2 a_4}{2(\omega_{s-} - \omega_{ie})} \sin((\omega_{s-} - \omega_{ie})t) + \frac{a_3 b_4 + b_3 a_4}{2(\omega_{s+} - \omega_{ie})} \sin((\omega_{s+} - \omega_{ie})t) \\ &\quad - \frac{a_2 b_2}{4\omega_{s-}} \sin(2\omega_{s-} t) - \frac{a_3 b_3}{4\omega_{s+}} \sin(2\omega_{s+} t) - \frac{a_4 b_4}{4\omega_{ie}} \sin(2\omega_{ie} t) \\ &\quad + 2 \frac{a_0 b_2 + b_0 a_2 + (a_1 b_2 + b_1 a_2) t}{\omega_{s-}} \sin\left(\frac{\omega_{s-}}{2} t\right) \\ &\quad + 2 \frac{a_0 b_3 + b_3 a_0 + (a_1 b_3 + b_1 a_3) t}{\omega_{s+}} \sin\left(\frac{\omega_{s+}}{2} t\right) \\ &\quad + 2 \frac{a_0 b_4 + b_4 a_0 + (a_1 b_4 + b_1 a_4) t}{\omega_{ie}} \sin\left(\frac{\omega_{ie}}{2} t\right) \end{aligned} \quad (3.91)$$

For the integral over mixed sine and cosine-based impulse responses, the analytical solution is given as:

$$\begin{aligned}
 k(t) &= \int_0^t g_{a,\sin}(t-\tau)g_{b,\cos}(t-\tau)d\tau \\
 &= b_0 \left(\frac{a_2}{\omega_{s_-}} + \frac{a_3}{\omega_{s_+}} + \frac{a_4}{\omega_{ie}} \right) - \frac{\omega_{s_+} b_2 a_3 - \omega_{s_-} a_2 b_3}{\omega_{s_-}^2 - \omega_{s_+}^2} - \frac{\omega_{ie} b_2 a_4 - \omega_{s_-} a_2 b_4}{\omega_{s_-}^2 - \omega_{ie}^2} - \frac{\omega_{ie} b_3 a_4 - \omega_{s_+} a_3 b_4}{\omega_{s_+}^2 - \omega_{ie}^2} \\
 &\quad + \left(a_0 b_0 + \frac{a_2 b_1}{\omega_{s_-}} + \frac{a_3 b_1}{\omega_{s_+}} + \frac{a_4 b_1}{\omega_{ie}} \right) t + (a_0 b_1 + a_1 b_0) t^2 + a_1 b_1 t^3 \\
 &\quad + \frac{(\omega_{s_+} b_2 a_3 - \omega_{s_-} a_2 b_3) \cos(\omega_{s_-} t) \cos(\omega_{s_+} t) + (\omega_{s_-} b_2 a_3 - \omega_{s_+} a_2 b_3) \sin(\omega_{s_-} t) \sin(\omega_{s_+} t)}{\omega_{s_-}^2 - \omega_{s_+}^2} \\
 &\quad + \frac{(\omega_{ie} b_2 a_4 - \omega_{s_-} a_2 b_4) \cos(\omega_{s_-} t) \cos(\omega_{ie} t) + (\omega_{s_-} b_2 a_4 - \omega_{ie} a_2 b_4) \sin(\omega_{s_-} t) \sin(\omega_{ie} t)}{\omega_{s_-}^2 - \omega_{ie}^2} \\
 &\quad + \frac{(\omega_{ie} b_3 a_4 - \omega_{s_+} a_3 b_4) \cos(\omega_{s_+} t) \cos(\omega_{ie} t) + (\omega_{s_+} b_3 a_4 - \omega_{ie} a_3 b_4) \sin(\omega_{s_+} t) \sin(\omega_{ie} t)}{\omega_{s_+}^2 - \omega_{ie}^2} \\
 &\quad + \frac{a_0 b_2 + a_1 b_2 t}{\omega_{s_-}} \sin(\omega_{s_-} t) + \frac{a_0 b_3 + a_1 b_3 t}{\omega_{s_+}} \sin(\omega_{s_+} t) + \frac{a_0 b_4 + a_1 b_4 t}{\omega_{ie}} \sin(\omega_{ie} t) \\
 &\quad - \frac{a_2 b_0 + a_2 b_1 t}{\omega_{s_-}} \cos(\omega_{s_-} t) - \frac{a_3 b_0 + a_3 b_1 t}{\omega_{s_+}} \cos(\omega_{s_+} t) - \frac{a_4 b_0 + a_4 b_1 t}{\omega_{ie}} \cos(\omega_{ie} t) \\
 &\quad + \frac{a_2 b_2}{2\omega_{s_-}} \sin(\omega_{s_-} t)^2 + \frac{a_3 b_3}{2\omega_{s_+}} \sin(\omega_{s_+} t)^2 + \frac{a_4 b_4}{2\omega_{ie}} \sin(\omega_{ie} t)^2
 \end{aligned} \tag{3.92}$$

The integral over two cosine-based impulse responses is:

$$\begin{aligned}
 k(t) &= \int_0^t g_{a,\cos}(t-\tau)g_{b,\cos}(t-\tau)d\tau \\
 &= \left(a_0 b_0 + \frac{a_2 b_2 + a_3 b_3 + a_4 b_4}{2} \right) t + (a_0 b_1 + a_1 b_0) t^2 + a_1 b_1 t^3 \\
 &\quad + \frac{a_2 b_3 + b_2 a_3}{2(\omega_{s_-} + \omega_{s_+})} \sin((\omega_{s_-} + \omega_{s_+})t) + \frac{a_2 b_4 + b_2 a_4}{2(\omega_{s_-} + \omega_{ie})} \sin((\omega_{s_-} + \omega_{ie})t) \\
 &\quad + \frac{a_3 b_4 + b_3 a_4}{2(\omega_{s_+} + \omega_{ie})} \sin((\omega_{s_+} + \omega_{ie})t) + \frac{a_2 b_3 + b_2 a_3}{2(\omega_{s_-} - \omega_{s_+})} \sin((\omega_{s_-} - \omega_{s_+})t) \\
 &\quad + \frac{a_2 b_4 + b_2 a_4}{2(\omega_{s_-} - \omega_{ie})} \sin((\omega_{s_-} - \omega_{ie})t) + \frac{a_3 b_4 + b_3 a_4}{2(\omega_{s_+} - \omega_{ie})} \sin((\omega_{s_+} - \omega_{ie})t) \\
 &\quad + \frac{a_2 b_2}{4\omega_{s_-}} \sin(2\omega_{s_-} t) + \frac{a_3 b_3}{4\omega_{s_+}} \sin(2\omega_{s_+} t) + \frac{a_4 b_4}{4\omega_{ie}} \sin(2\omega_{ie} t) \\
 &\quad + \frac{a_0 b_2 + b_0 a_2 + (a_1 b_2 + b_1 a_2) t}{\omega_{s_-}} \sin(\omega_{s_-} t) \\
 &\quad + \frac{a_0 b_3 + b_3 a_0 + (a_1 b_3 + b_1 a_3) t}{\omega_{s_+}} \sin(\omega_{s_+} t) \\
 &\quad + \frac{a_0 b_4 + b_4 a_0 + (a_1 b_4 + b_1 a_4) t}{\omega_{ie}} \sin(\omega_{ie} t)
 \end{aligned} \tag{3.93}$$

The error variance from white Gaussian noise on the inertial sensor measurements has been determined using the above expressions. Analog to the previous section, the following graphs have been transformed to north and south position errors, and all angles have been converted to degrees.

3.3.3.2. Position Variance from White Gaussian Sensor Noise

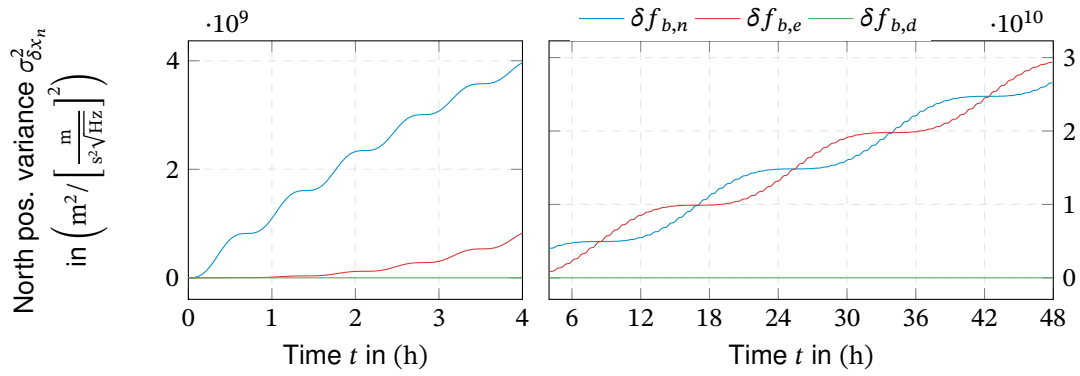
Using the impulse responses from [Table D.25](#) and [Table D.27](#) with equations (3.91) to (3.93), the growth of the position variances is calculated. The resulting error growth is depicted in [Figure 3.25](#).

The variances show a linear growth with superposed oscillations at the Schuler and the 24-hour period. In contrast to the deterministic errors, the position error from sensor noise is not bound. A noise input on the north acceleration measurement leads to initial solid growth of the north position uncertainty compared to the east error and vice versa for east acceleration measurements. As observed before, a down-oriented acceleration measurement does not affect the vertically fixed strapdown propagation. Similar behavior can be observed for position uncertainty from gyroscope white noise. It is worth noting that noise on the vertical angular rate measurement leads to an error growth of the same magnitude as the horizontal gyroscope measurements.

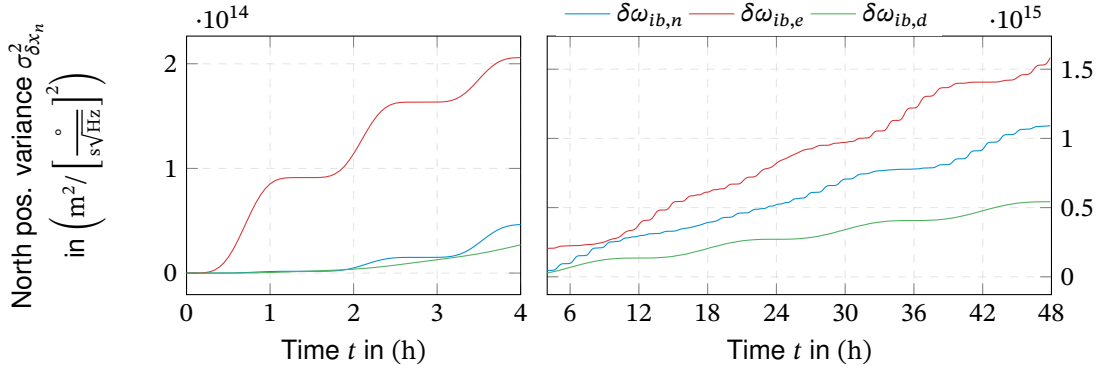
The development of the horizontal position covariance from white Gaussian sensor noise is depicted in [Figure 3.26](#). For isotropic sensor errors, the specific forces noise results in a continuously growing position uncertainty without correlation between the north and east position error (red circle). The gyroscope noise, however, results in a varying correlation between north and east position errors.

3.3.3.3. Velocity Variance from White Gaussian Sensor Noise

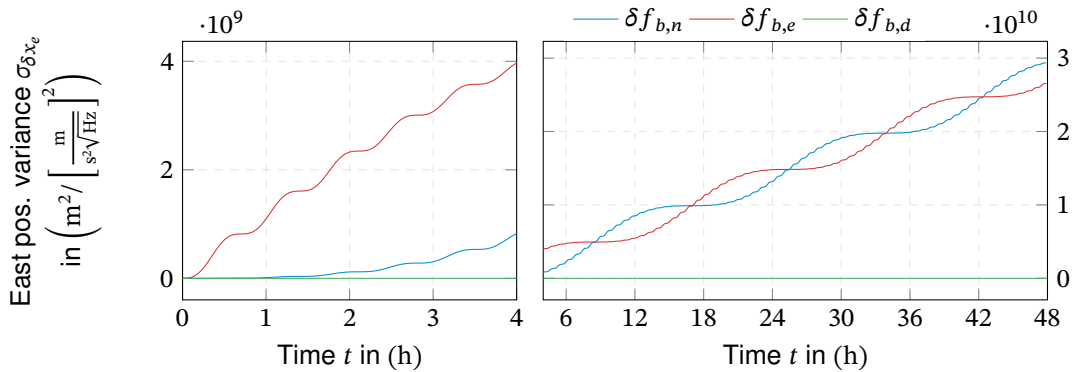
Analogously to the position errors, the velocity variance from sensor noise is determined from the impulse responses tabulated in [Table D.29](#) and [Table D.31](#). The growth of the velocity errors' variances over time is depicted in [Figure 3.27](#). Similar to the position errors, the velocity errors' variances display linear growth, with superposed Schuler and 24-hour oscillations. Although hardly visible, the velocity error variances from $\delta\omega_{ib,d}$ display similar behavior as the other graphs, but at a two magnitudes smaller scale.



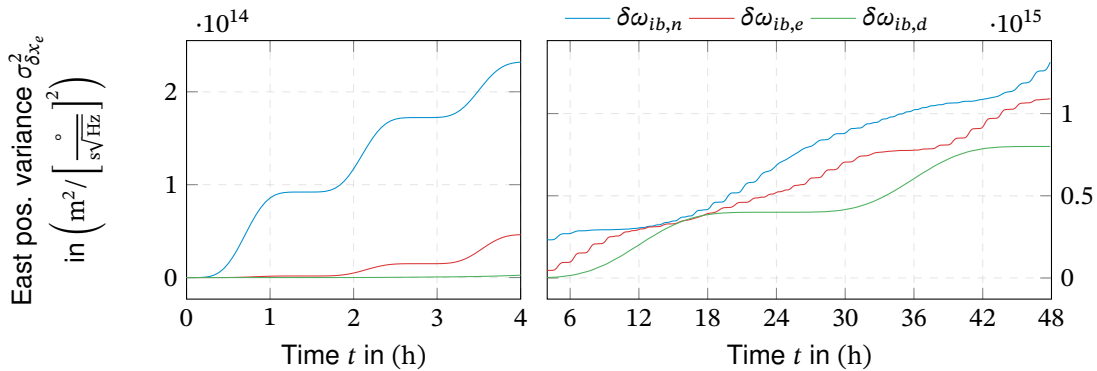
(a) North position error variance from accelerometer velocity random walk input.



(b) North position error variance from gyroscope angle random walk input.



(c) East position error variance from accelerometer velocity random walk input.

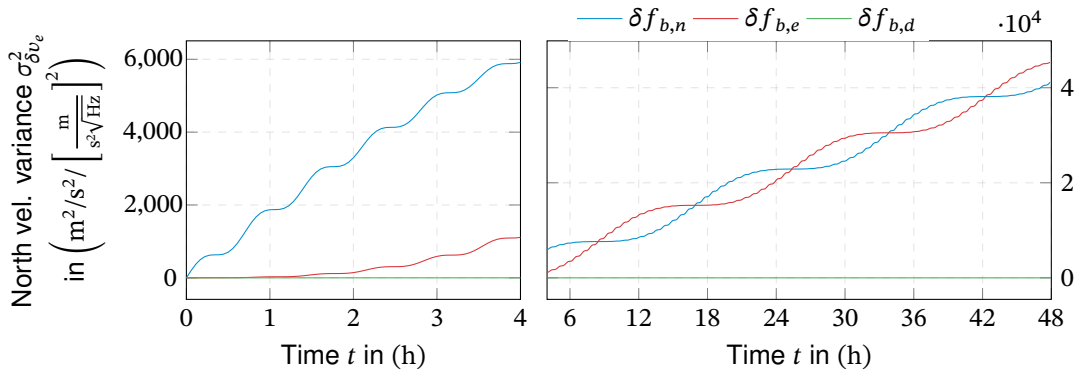


(d) East position error variance from gyroscope angle random walk input.

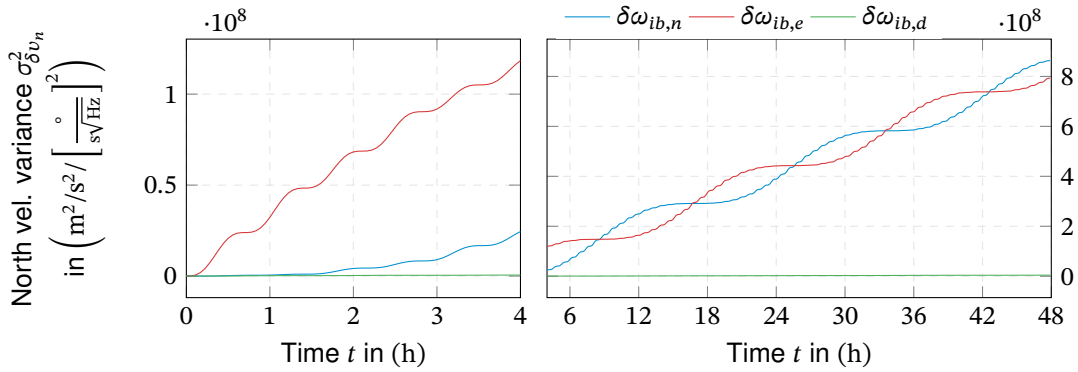
Figure 3.25.: Position error variance from unit noise-density white Gaussian noise IMU errors at $\phi = 45^\circ$ and $\psi = 0^\circ$.



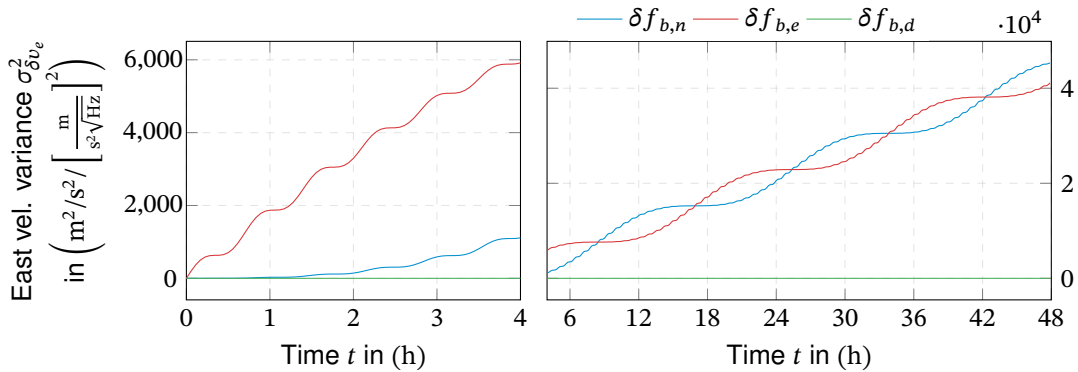
Figure 3.26.: Development of the horizontal position covariance from isotropic $1 \text{ mg}/\sqrt{\text{Hz}}$ accelerometer and $0.0017^\circ/\sqrt{\text{h}}$ gyroscope random walk at $\phi = 45^\circ$ and $\psi = 0^\circ$.



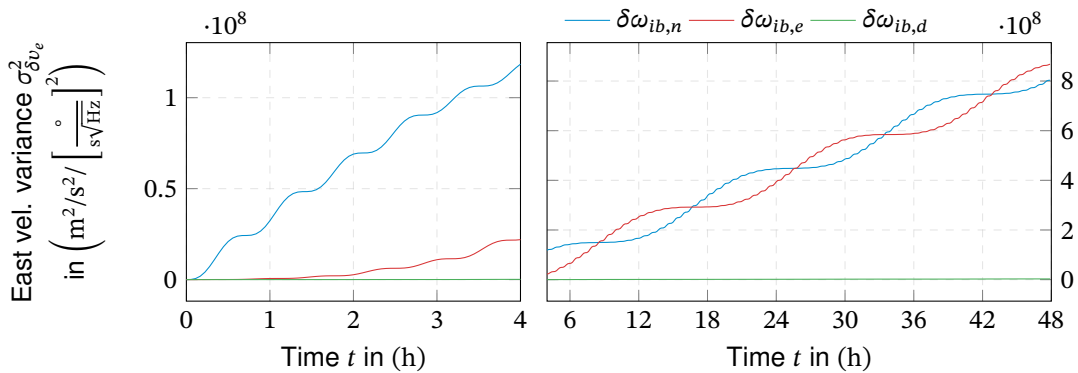
(a) North velocity error variance from accelerometer velocity random walk input.



(b) North velocity error variance from gyroscope angle random walk input.



(c) East velocity error variance from accelerometer velocity random walk input.



(d) East velocity error variance from gyroscope angle random walk input.

Figure 3.27.: Velocity error variance from unit noise-density white Gaussian noise IMU errors at $\phi = 45^\circ$ and $\psi = 0^\circ$.

3.3.3.4. Orientation Variance from White Gaussian Sensor Noise

Analog to the previous section, the orientation angle error variances have been determined from the impulse responses that are given in Table D.33, Table D.35 and Table D.37. The respective plots of the position uncertainty are given in Figure 3.28 and Figure 3.29.

All orientation angles react to accelerometer and gyroscope noise in a very similar way. White noise input on the vertical gyroscope measurement creates low uncertainty on the roll and pitch angle errors compared to the other axes. The yaw angle variance, however, grows similarly fast from vertical gyro noise as from the other sensor axes and, in general, almost twice as fast as the roll and pitch error variance.

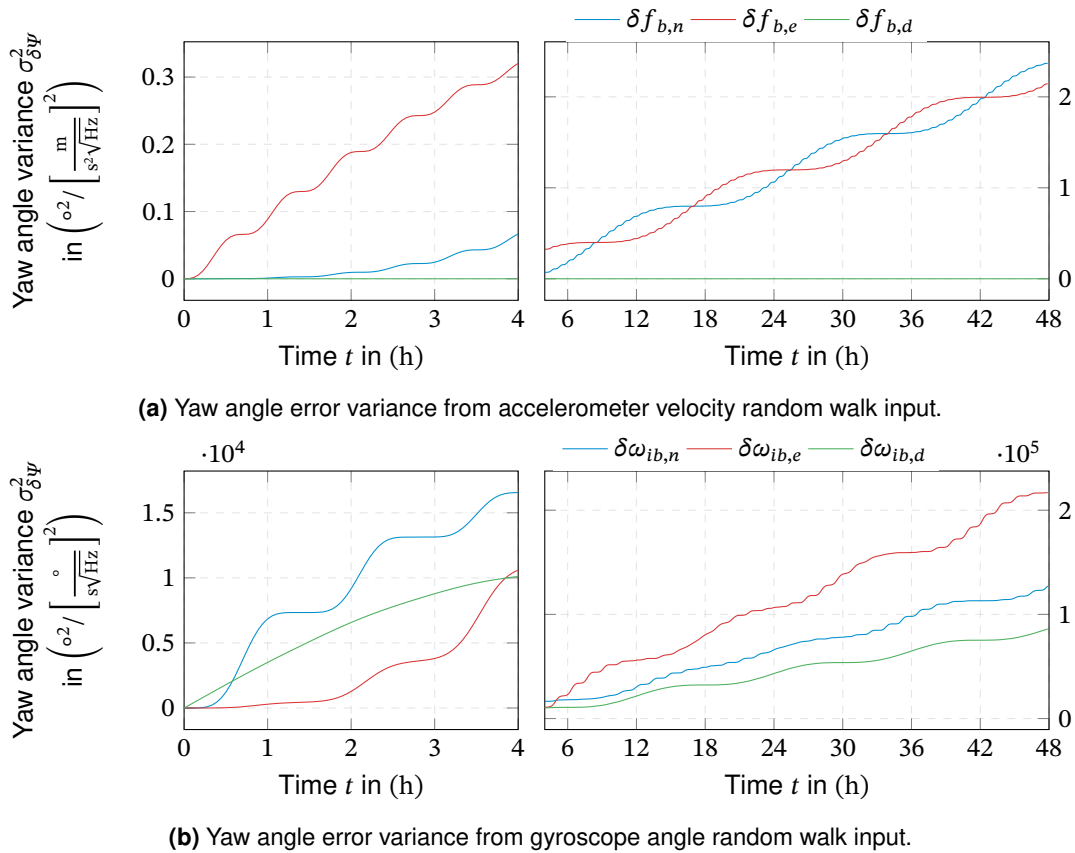


Figure 3.28.: Yaw error variance from unit noise-density white Gaussian noise IMU errors at $\phi = 45^\circ$ and $\psi = 0^\circ$.

The covariance arising from the above-determined responses to White Gaussian noise is depicted in Figure 3.30 for an exemplary set of random walk coefficients. The covariance ellipsoids from accelerometer and gyroscope noise display a primarily linear growth, as expected from Figure 3.29. Roll and pitch errors are nearly uncorrelated, while roll and yaw angles display a constant correlation.

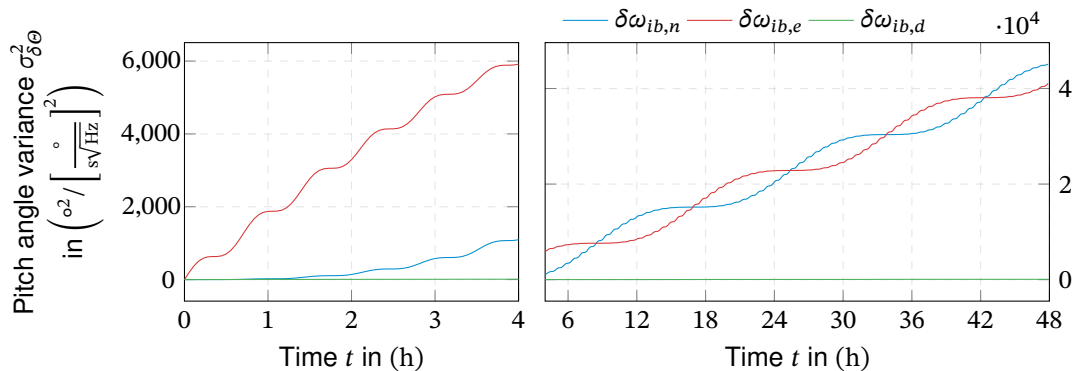
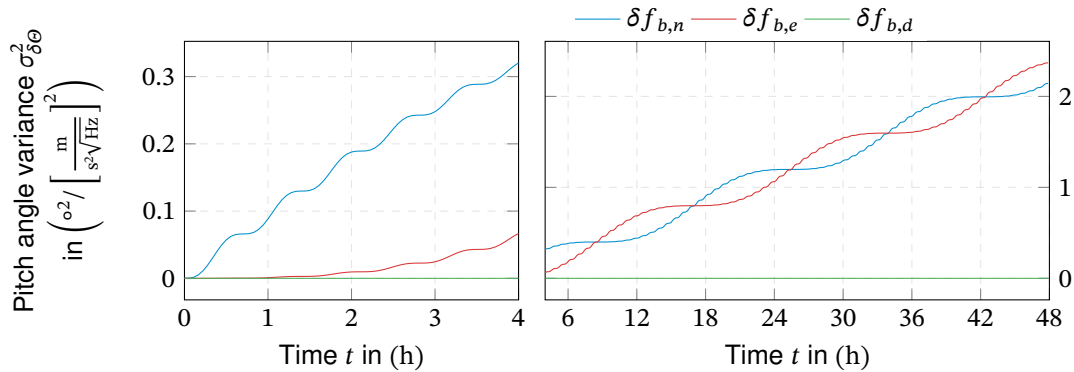
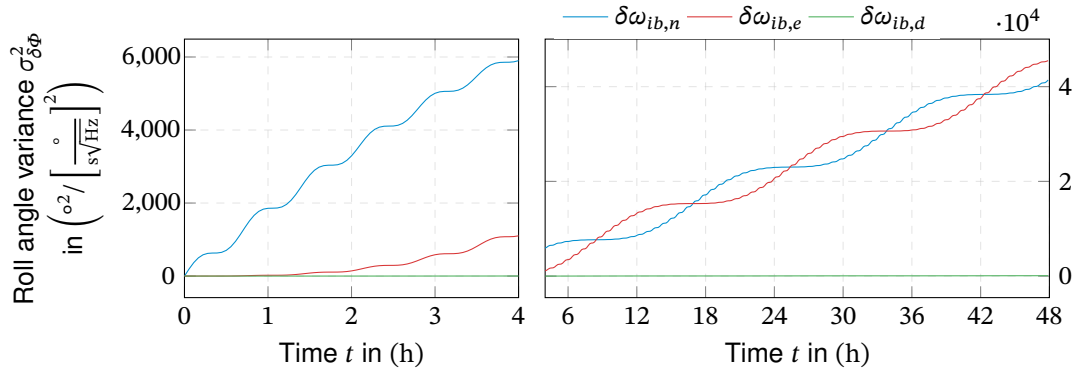
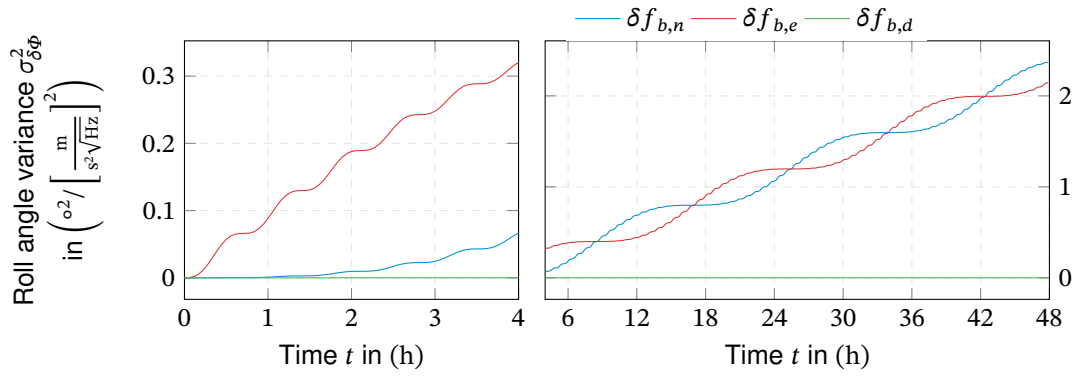


Figure 3.29.: Attitude error variance from unit noise-density white Gaussian noise IMU errors at $\phi = 45^\circ$ and $\psi = 0^\circ$.

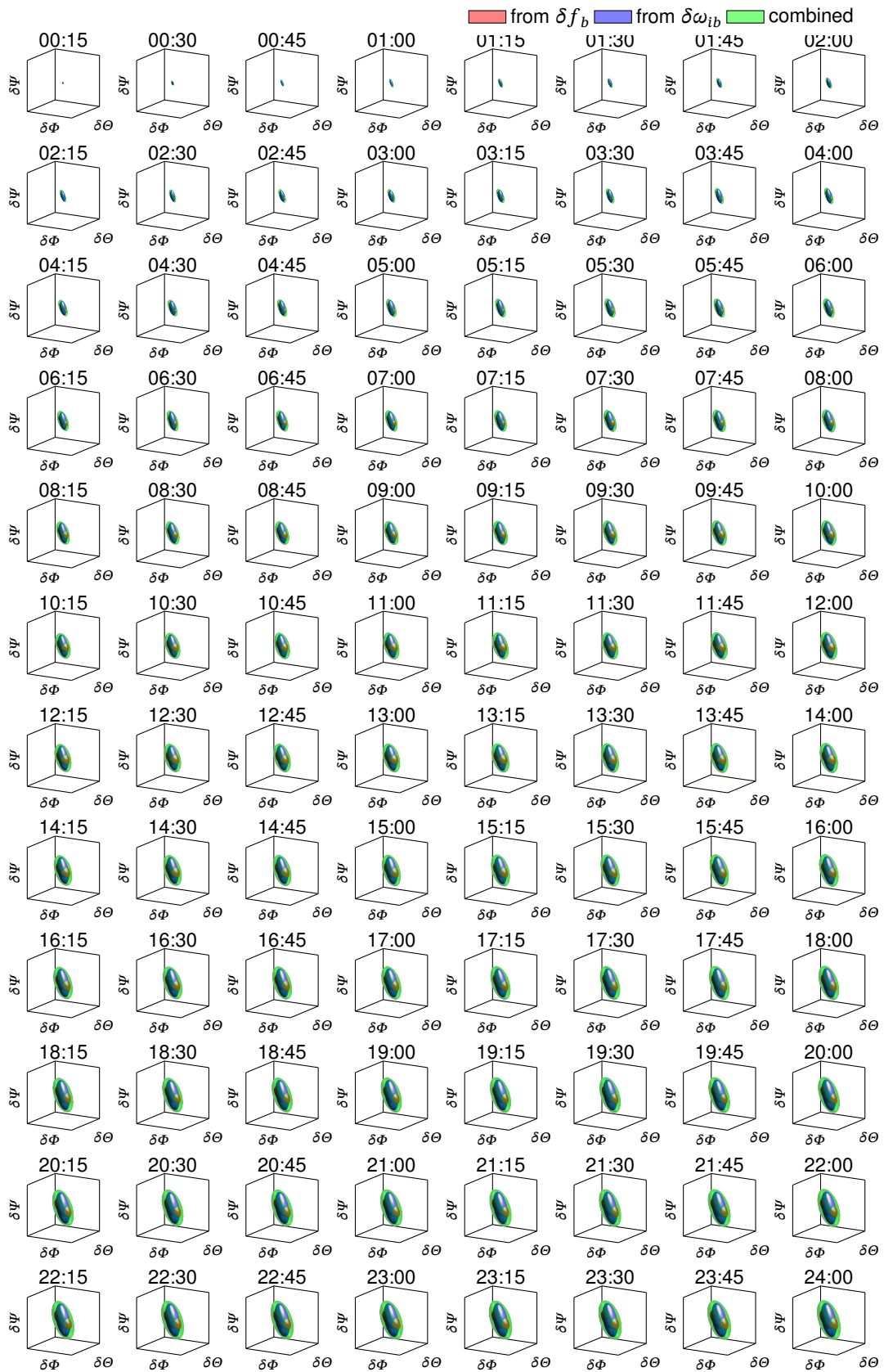


Figure 3.30.: Development of the attitude covariance from isotropic $25 \text{ mg}/\sqrt{\text{Hz}}$ accelerometer and $0.125^\circ/\sqrt{\text{h}}$ gyroscope random walk at $\phi = 45^\circ$ and $\psi = 0^\circ$. All axes are equally scaled.

3.3.4. Response to Colored Noise Sensor Errors

The response to white noise has been demonstrated in the last section. As already pointed out in [Subsection 2.3.3](#), real sensor noise is colored (time-correlated) instead of white. The author has published the following analysis of the colored noise in strapdown inertial navigation in [74].

For consistency with the previous chapter, the published results from [74] are extended by the velocity and orientation errors' responses to colored noise. This analysis sticks to the already presented IEEE conventions ([Table 2.7](#)) to describe the inertial sensor noise processes. A comparison of these conventions with other publications can be found in, e.g., [10, p. 72]. The processes defined for angular rate measurements here can be used analogously for acceleration measurements.

Angular random walk is actually white Gaussian noise in the rates, which has already been discussed in the previous section [3.3.3.1](#). Using a transfer function $G(f)$ that transforms unit-PSD white noise into the respective colored noise, the other sensor noise processes can be modeled. For a (wide-sense) stationary stochastic process, the Wiener-Khinchin theorem states that the PSD of an output signal is the squared magnitude of the system's transfer function times the input's PSD [75, p. 129]:

$$S_y(f) = |G(f)|^2 S_x(f) \quad (3.94)$$

The desired noise processes from [Table 2.7](#) can thus be created from white Gaussian noise if a suitable shaping filter with transfer function $G(s)$ exists. The design of the shaping filter for each noise process and the resulting navigation errors will be discussed in the following.

3.3.4.1. Quantization Noise

Quantization noise is the time-derivative of white noise, which results in a quadratically increasing PSD (violet noise) as defined in [Table 2.7](#). Using the Fourier transform rules [72, p. 1083], the auto-covariance of such noise is given by the second time derivative of the Dirac delta function:

$$E[u(\rho)u(\tau)] = \delta''(\rho - \tau) \quad (3.95)$$

Inserting definition (3.95) into (3.87), the variance of the navigation errors from quantization noise is given by the squared impulse response function $g(t)$ (see [Section D.2](#)):

$$\sigma_Q^2(t) = Q^2 \tau_0 g^2(t) \quad (3.96)$$

As defined in [Table 2.7](#), the quantization noise is not only scaled by the coefficient Q but also by the sample rate. The resulting variances of the navigation errors are presented in [Figure 3.31](#) to [Figure 3.34](#). Due to the time-derivative character of the input noise, the resulting variances differ from the results of the other noise processes.

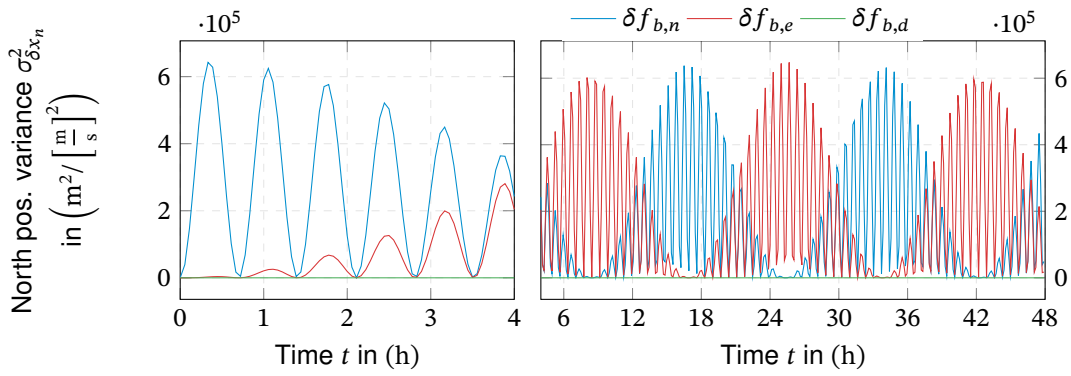
An interesting and counter-intuitive effect can be observed in the velocity and orientation

errors: Some navigation error responses have an initial value of 1 instead of the expected zero initial value. This can be explained by the characteristics of quantization noise, which describes a quantized measurement of the integrated sizes (angle increments and velocity). Consequently, the input noise is already defined in the same level of integration as the output error, e.g., velocity or orientation errors. Of course, the initial value is defined as zero in a time-discrete scenario, and the variance will jump when progressing to the second time step.

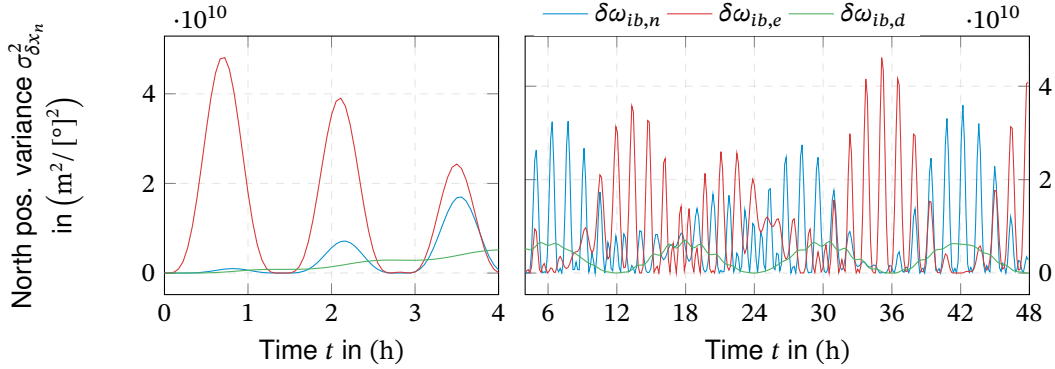
Note that the effect of quantization noise strongly depends on the actual implementation of the strapdown algorithm and the chosen integration scheme. A high-order integration scheme, for example, may require intermediate time steps, and integrating over these intermediate time steps can counter-act the derivative nature of quantization noise and result in a response similar to the response to white noise. This effect has been observed when using a 4th order Runge-Kutta integration scheme that outputs navigation states at half the input rates.

Furthermore, this analysis relies on the assumption of purely stochastic nature of quantization noise which is not necessarily met in practice. A discussion of this problem and a detailed analysis of quantization noise in strapdown inertial navigation is given by Savage in [76]. That work also considers the effect of multi-frequency algorithms and methods to compensate for quantization noise.

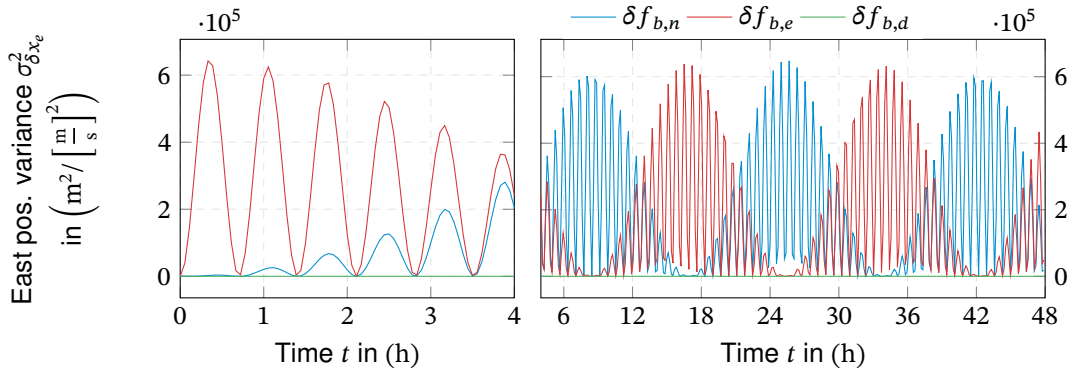
Due to the taken assumptions and the above-discussed dependence on the strapdown implementation, the presented results cannot be considered as general as the results for the other noise types. Especially the boundedness of the presented variance curves is a result of the chosen analysis approach. It must not be taken for granted for any other combination sample-rate and integration scheme, especially in real-world quantization noise.



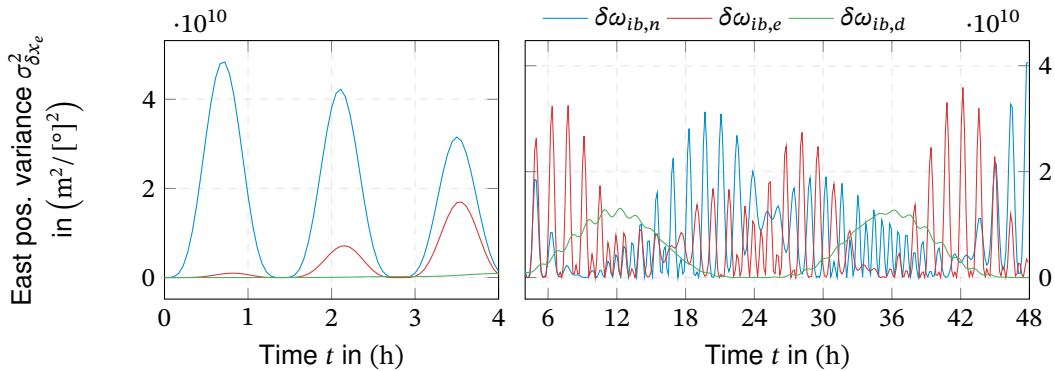
(a) North position error variance from accelerometer quantization noise input.



(b) North position error variance from gyroscope quantization noise input.



(c) East position error variance from accelerometer quantization noise input.



(d) East position error variance from gyroscope quantization noise input.

Figure 3.31.: Position error variance from quantization noise IMU errors normalized to the quantization noise coefficient Q and $\tau_0 = 1$ s at $\phi = 45^\circ$ and $\psi = 0^\circ$.

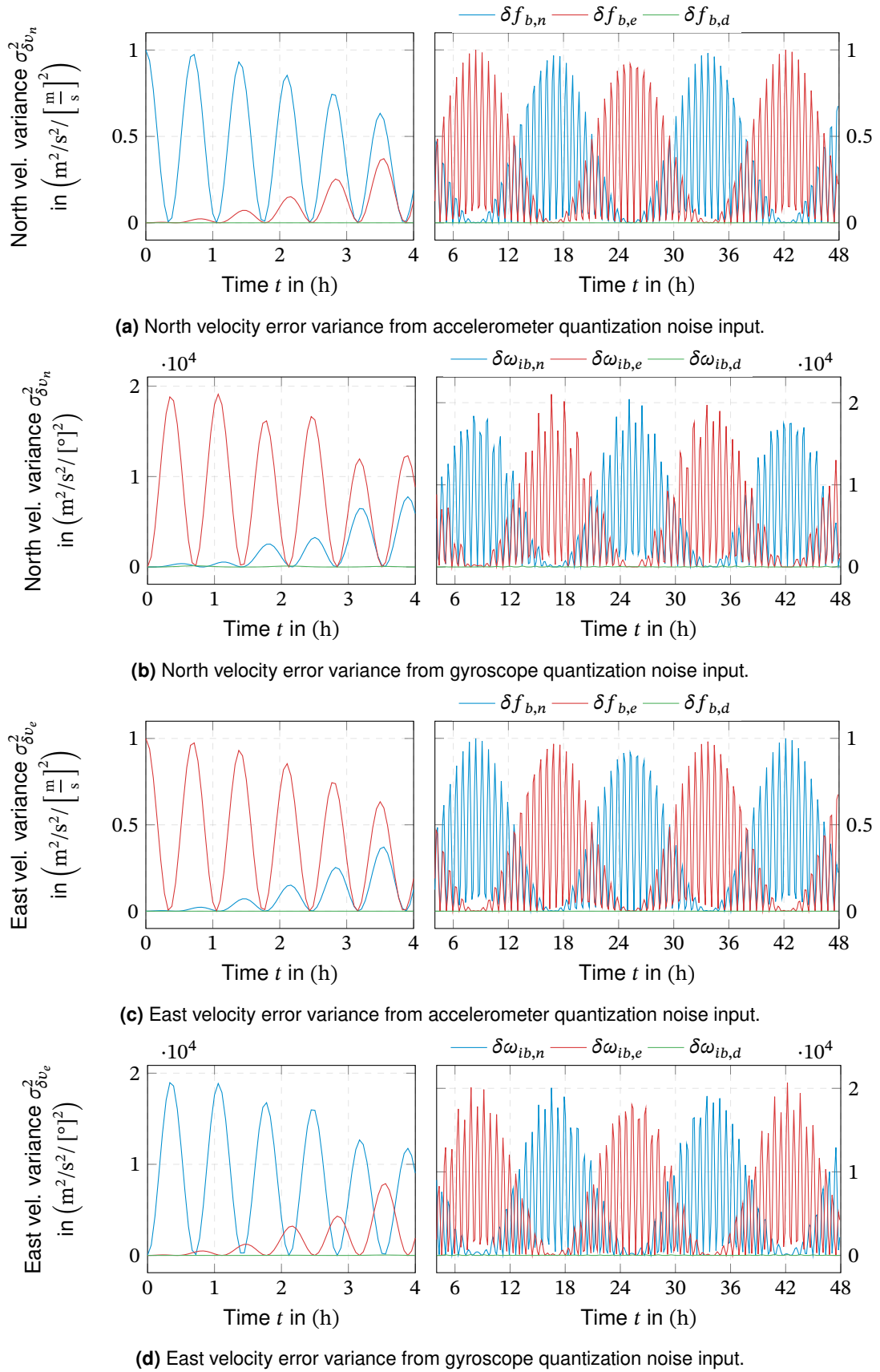
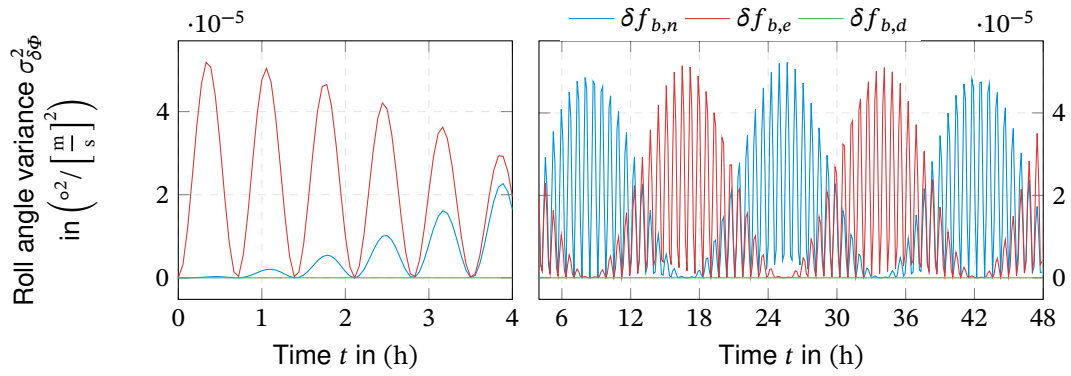
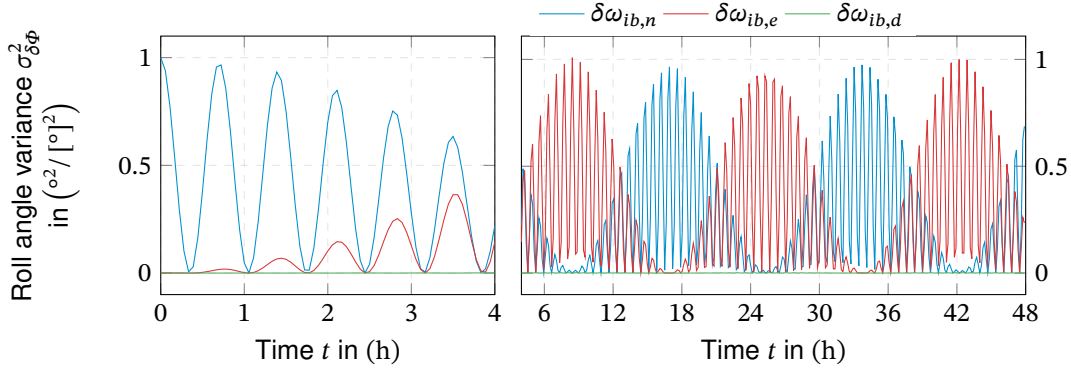


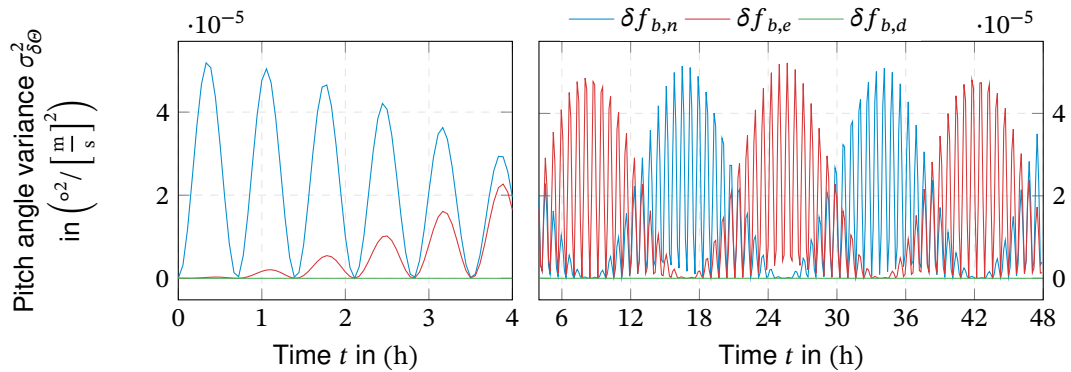
Figure 3.32.: Velocity error variance from quantization noise IMU errors normalized to the quantization noise coefficient Q and $\tau_0 = 1$ s at $\phi = 45^\circ$ and $\psi = 0^\circ$.



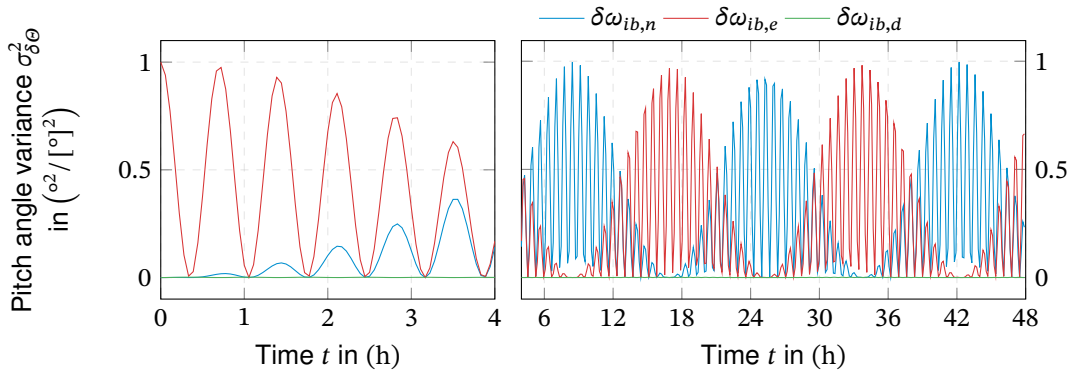
(a) Roll angle error variance from accelerometer quantization noise input.



(b) Roll angle error variance from gyroscope quantization noise input.



(c) Pitch angle error variance from accelerometer quantization noise input.



(d) Pitch angle error variance from gyroscope quantization noise input.

Figure 3.33.: Attitude error variance from quantization noise IMU errors normalized to the quantization noise coefficient Q and $\tau_0 = 1$ s at $\phi = 45^\circ$ and $\psi = 0^\circ$.

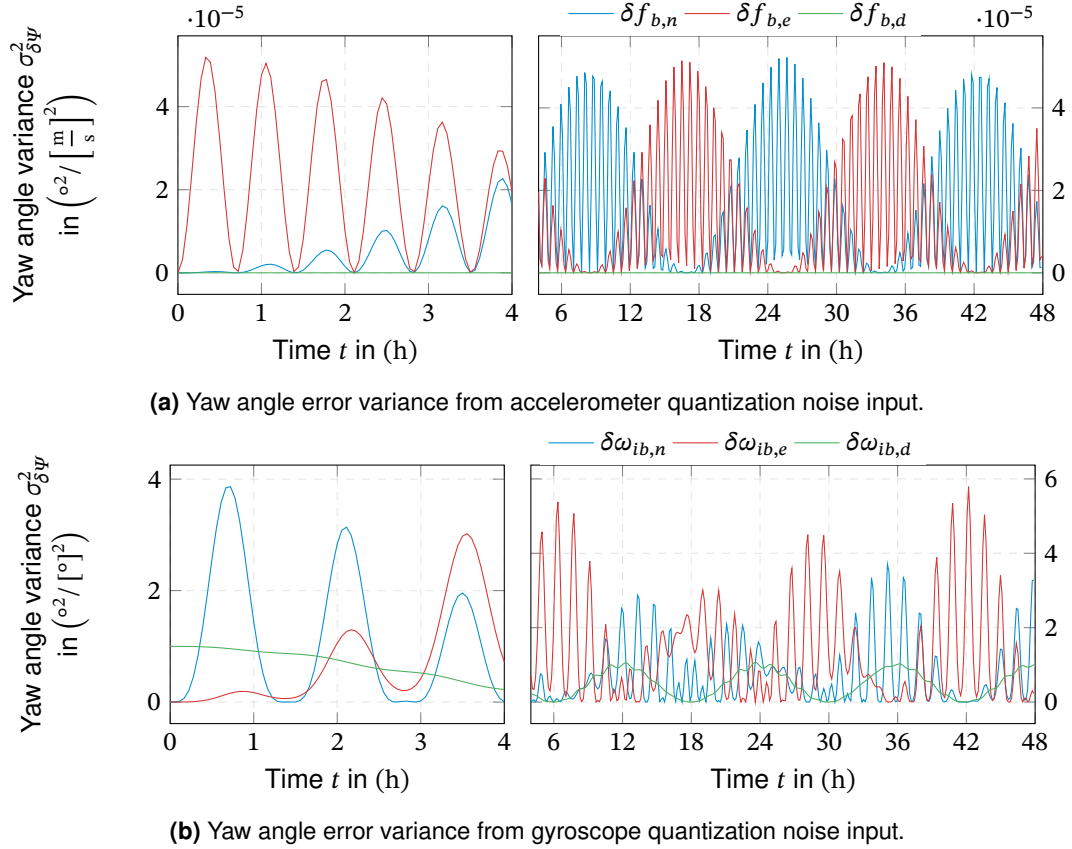


Figure 3.34.: Heading error variance from quantization noise IMU errors normalized to the quantization noise coefficient Q and $\tau_0 = 1$ s at $\phi = 45^\circ$ and $\psi = 0^\circ$.

3.3.4.2. Bias Instability

As described in Table 2.7, bias instability is a flicker noise process with a theoretical sharp cut-off at the frequency f_{co} . Looking at the defining PSD of flicker noise, the transfer function that generates flicker noise from a white noise input can be identified to

$$G_{FN}(s) = \frac{1}{\sqrt{s}} \quad (3.97)$$

This irrational transfer function poses several problems, that have been widely discussed in the context of power law noise generation [77, 78, 79]. Although the transfer function and impulse response for power law noise PSD $S(f) = f^{-\alpha}$ can be given analytically as

$$G(s) = \frac{1}{s^{\alpha/2}} \quad (3.98)$$

$$g(t) = \frac{t^{\alpha/2-1}}{\Gamma(\alpha/2)} \quad (3.99)$$

these impulse responses cannot be used to predict the system's output variance for odd and non-integer values of α , which results in an irrational transfer function [78]. Irrational transfer functions do not correspond to a finite state linear filter [78], consequently they are not fully described by their impulse response (in contrast to LTI systems) and equation (3.70) does not hold anymore. Furthermore, the impulse response for flicker noise ($\alpha = 1$) is undefined at $t = 0$.

Traditionally, flicker noise is approximated by Linear Time-Invariant (LTI) systems, e.g., by a set of multiple linear filters [80]. Still, this ARMA model approach is only a rough approximation. The longer the observation time, the more poles are required to keep the desired level of approximation. The high number of terms required also prevents a practical analytical treatment. Therefore, a different approach will be used within this thesis.

As mentioned before, the continuous-time impulse response does not fully describe the irrational transfer function. However, Kasdin [78] presents a method that creates a discrete-time impulse response accurately representing power-law noise over the entire time range of interest. The impulse response can be determined from the following recursive relation [78]:

$$\begin{aligned} g_{FN}[0] &= 1 \\ g_{FN}[k] &= \left(k - 1 - \frac{\alpha}{2}\right) \frac{g[k-1]}{k} \end{aligned} \quad (3.100)$$

Originally, this impulse response was used to create power law noise in a batch process, by convoluting it with a time-discrete white Gaussian noise input:

$$x[k] = \sum_{l=0}^{k-1} g[k-l]w[l] \quad (3.101)$$

Within this thesis, the impulse response is used to determine the variance of the system's response to flicker noise, respectively bias instability input. First, the flicker noise $g_{FN}[k]$ is convoluted with a simple 1st order low-pass filter impulse response $g_c[k]$ to approximate the bias instability's cutoff:

$$g_{B,in}[k] = \sum_{l=0}^{k-1} g_c[k-l] g_{FN}[l] \quad (3.102)$$

with the bias instability coefficient B and the low-pass filter's impulse response, given by

$$g_c[k] = \tau_0 \frac{e^{-\frac{k\tau_0}{T_c}}}{T_c} \quad (3.103)$$

with the time constant T_c and sample time τ_0 . As illustrated in Figure 3.35, there is only a little difference in the Allan variances for the first-order low-pass and the ideal sharp cutoff. The low-pass approximation shifts the Allan variance plot slightly to higher cluster times.

The resulting bias instability impulse response $g_B[k]$ is then convoluted with the strapdown

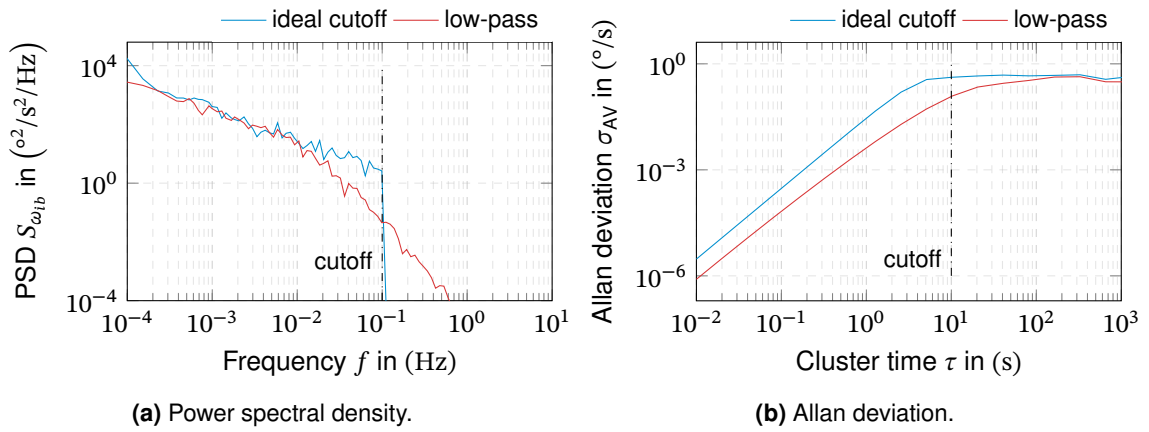


Figure 3.35.: Comparison of ideal cutoff and low-pass filter approximation of bias instability noise for a cut-off frequency $f_c = 0.1$ Hz.

error dynamic's impulse responses $g[k]$:

$$g_B[k] = \sum_{l=0}^{k-1} g[k-l] g_{B,in}[l] \quad (3.104)$$

where $g[k]$ can be obtained from the continuous step response $g(t)$ as:

$$g[k] = \tau_0 g(t) \quad (3.105)$$

Finally, the output's variance is determined as [78]:

$$\sigma_K^2[k] = B^2 \underbrace{\sum_{l=0}^{k-1} g_B[l]^2}_{K[k]} \quad (3.106)$$

This allows the creation of plots analogous to the other noise processes. The strapdown system's output variance normalized for the bias instability coefficient B and a cut-off frequency of $f_c = 1 \cdot 10^{-3}$ Hz is depicted in Figure 3.36 to Figure 3.39. The cut-off frequency f_c has been selected to represent the range of available systems from about $1 \cdot 10^{-2}$ Hz to $1 \cdot 10^{-4}$ Hz [81, 82, 83, 84]. The small effect of the cut-off frequency on the resulting navigation errors is demonstrated in [74].

As expected, the dominance of long-wavelength components in the bias instability transfers into the navigation errors. For most cases, the responses to the respective horizontal sensor inputs are phase-shifted by 90° . An exception is the position errors from gyroscope noise, where the angular rates about the north-pointing and the down-pointing axes yield similar error growth.

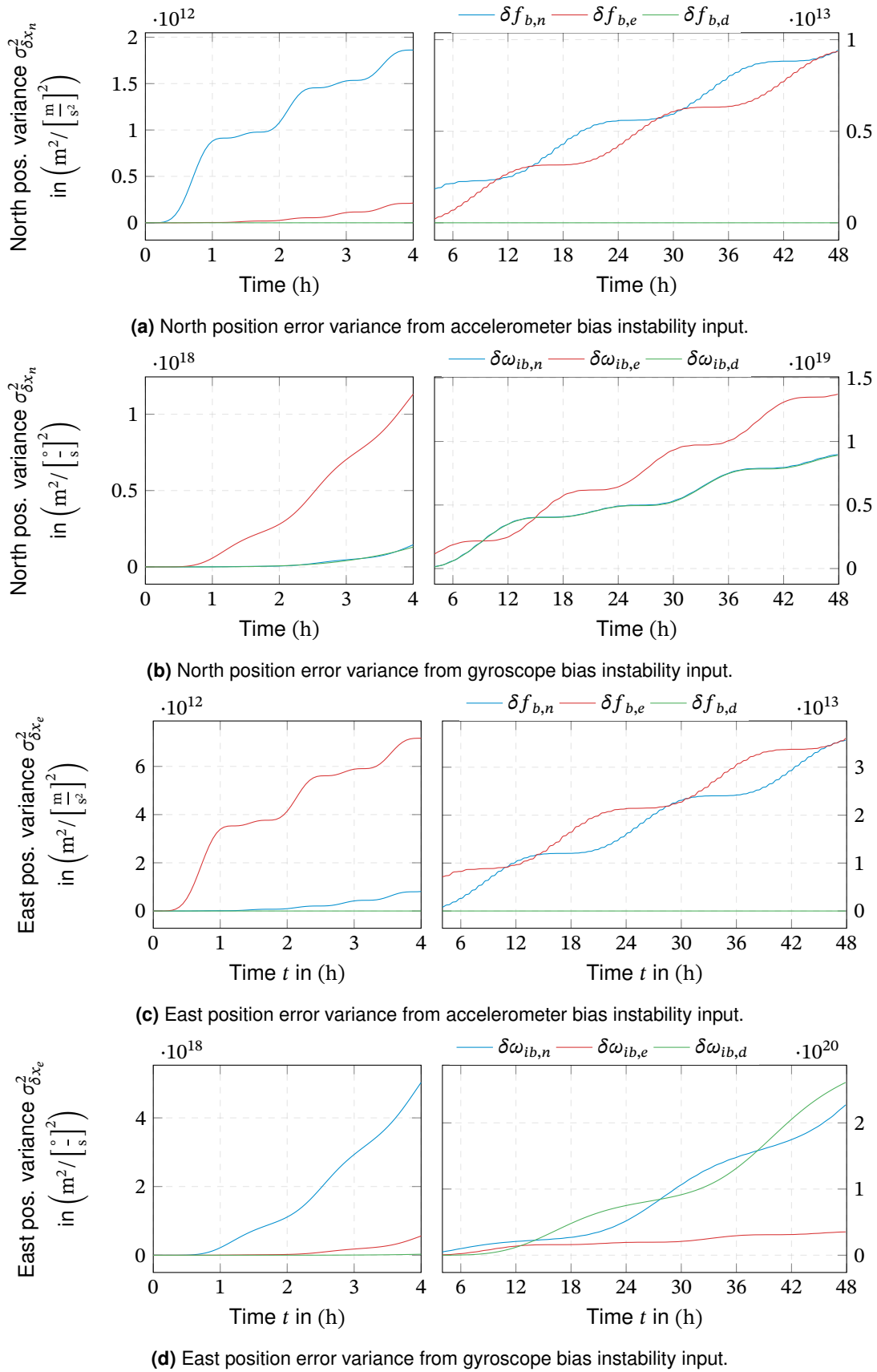


Figure 3.36.: Position error variance from bias instability IMU errors normalized to the bias instability coefficient B and a cutoff time of $T_c = 1000s$ at $\phi = 45^\circ$ and $\psi = 0^\circ$.

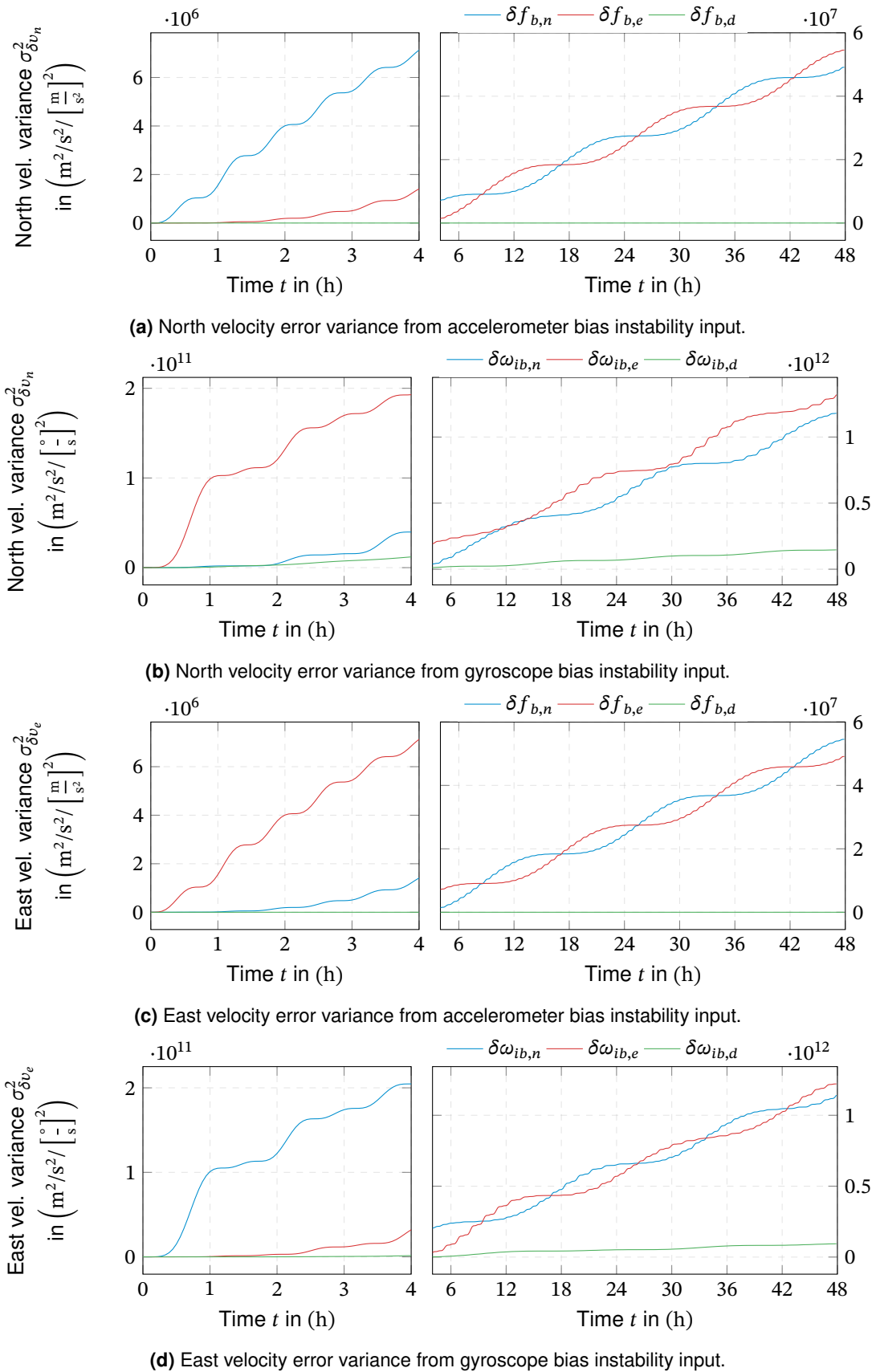
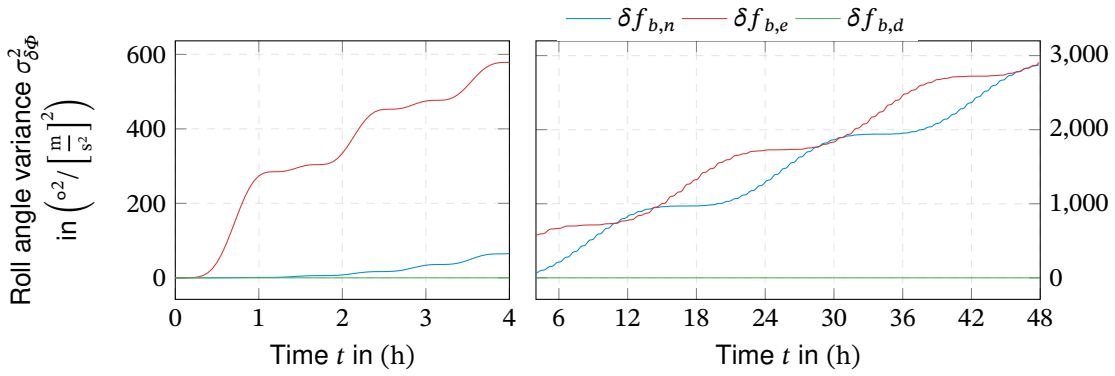
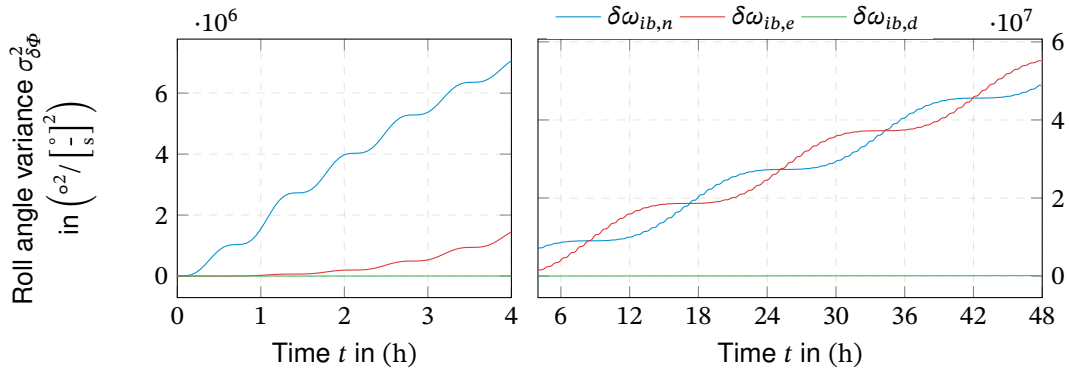


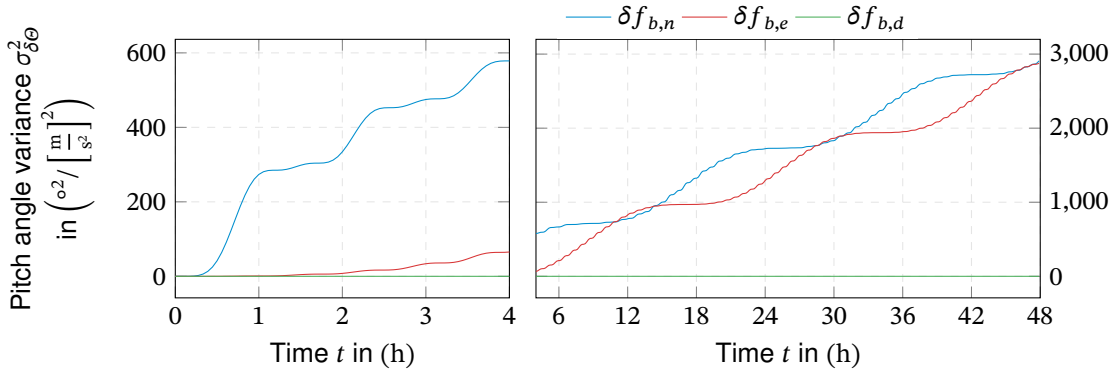
Figure 3.37.: Velocity error variance from bias instability IMU errors normalized to the bias instability coefficient B and a cut-off time of $T_c = 1000s$ at $\phi = 45^\circ$ and $\psi = 0^\circ$.



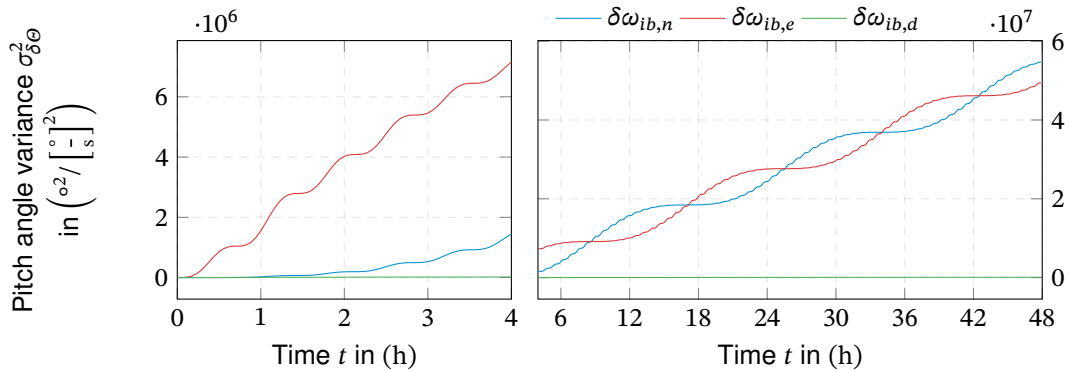
(a) Roll angle error variance from accelerometer bias instability input.



(b) Roll angle error variance from gyroscope bias instability input.

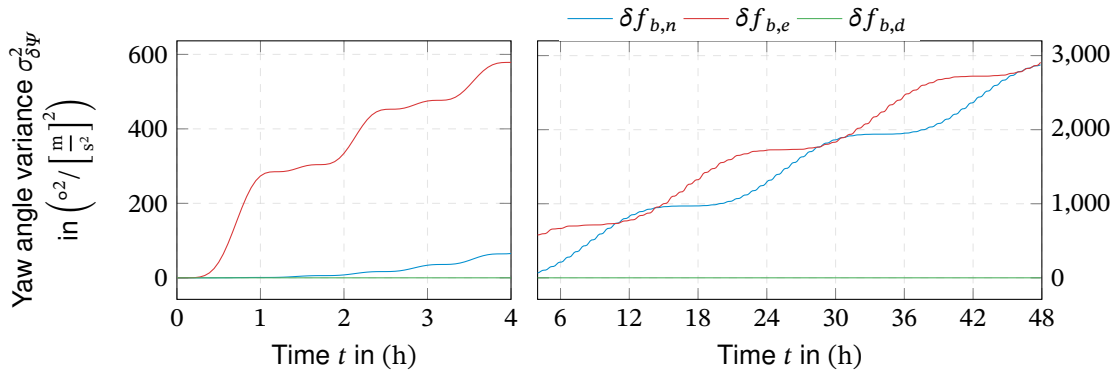


(c) Pitch angle error variance from accelerometer bias instability input.

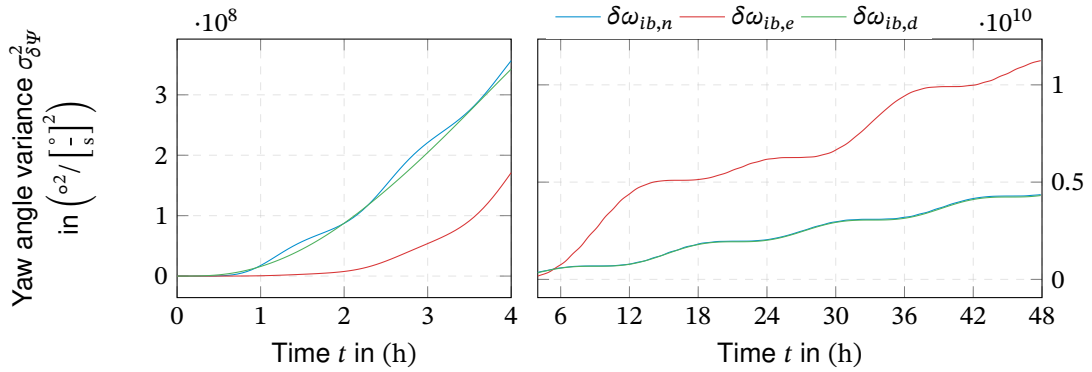


(d) Pitch angle error variance from gyroscope bias instability input.

Figure 3.38.: Attitude error variance from bias instability IMU errors normalized to the bias instability coefficient B and a cut-off time of $T_c = 1000s$ at $\phi = 45^\circ$ and $\psi = 0^\circ$.



(a) Yaw angle error variance from accelerometer bias instability input bias instability input.



(b) Yaw angle error variance from gyroscope bias instability input.

Figure 3.39.: Heading error variance from bias instability IMU errors normalized to the bias instability coefficient B and a cut-off time of $T_c = 1000s$ at $\phi = 45^\circ$ and $\psi = 0^\circ$.

3.3.4.3. Rate and Acceleration Random Walk

For rate random walk, the corresponding transfer function can be easily determined, as the rate random walk signal is integrated white noise. The modified impulse response that represents the system's response to rate random walk yields:

$$G_K(s) = \frac{1}{s}G(s) \quad (3.107)$$

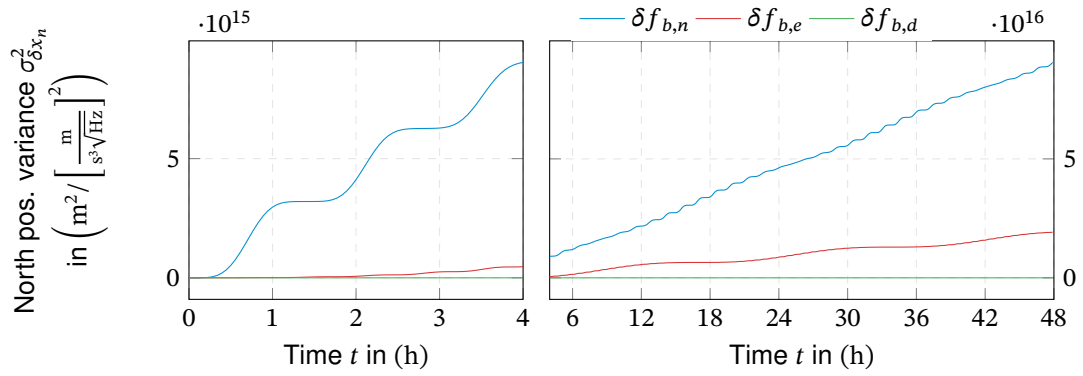
$$g_K(t) = \int_0^t g(\tau)d\tau \quad (3.108)$$

This can be easily calculated analytically from the tabulated impulse responses in Annex D.2. Using (3.91) to (3.93), the variance can be determined analytically:

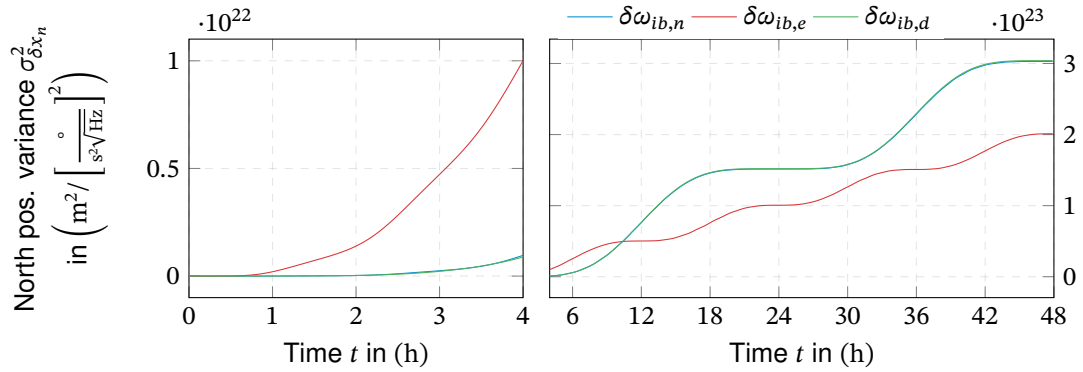
$$\sigma_K^2(t) = K^2 \int_0^t g_K^2(t - \tau)d\tau \quad (3.109)$$

The resulting position error variance from rate and acceleration random walk is depicted in Figure 3.40. From its PSD, it is evident that the lower frequency components dominate rate random walk. The effect of this can be easily observed in the navigation error variances. The resulting curves display a rather long wavelength behavior compared to the white noise case. Interestingly, the introduction of rate random walk noise creates, respectively, increases the divergence of the response to different input axis.

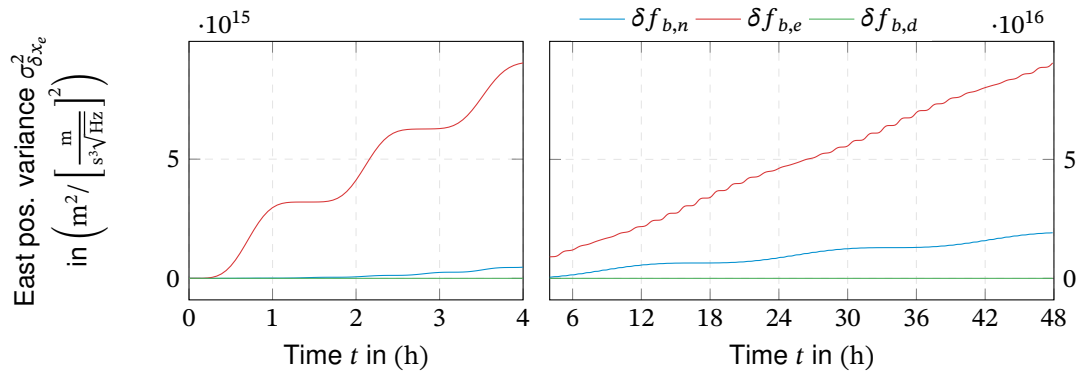
Similar behavior can be observed for the velocity errors, depicted in Figure 3.41. Here, the divergence of responses to excitation of different axes is observed only for the gyro errors. The orientation error responses to the rate and acceleration random walk are presented in Figure 3.42 and Figure 3.43. Again, a divergence of the response to different input axis was introduced for accelerometer noise. The introduction of rate random walk errors mainly affects the yaw angle errors, where the higher-frequency dynamics are attenuated, and the error variances are dominated by the 24 h oscillation superposed on linear growth.



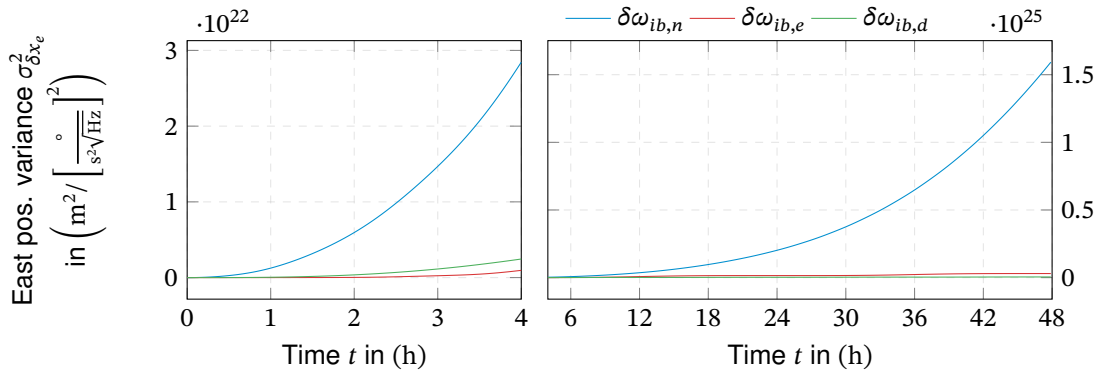
(a) North position error variance from accelerometer acceleration random walk input.



(b) North position error variance from gyroscope rate random walk input.

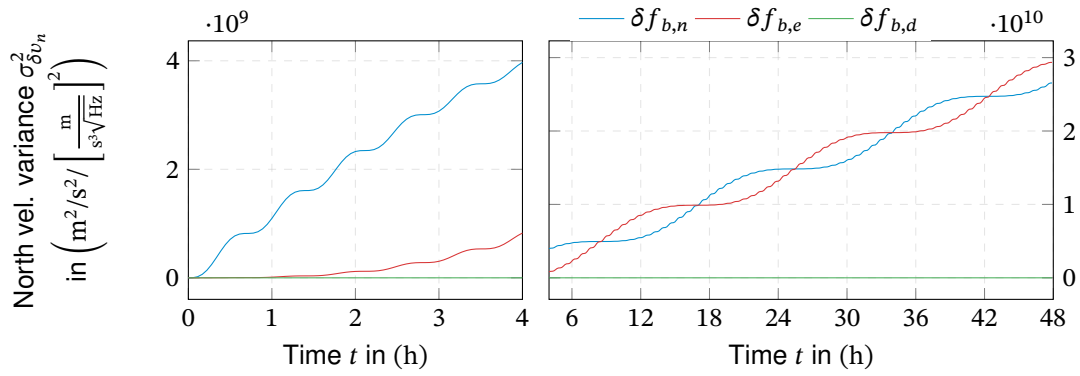


(c) East position error variance from accelerometer acceleration random walk input.

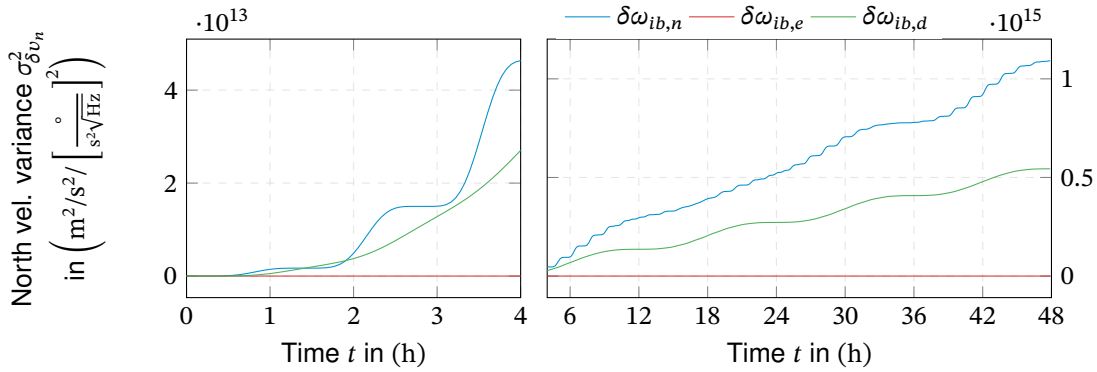


(d) East position error variance from gyroscope rate random walk input.

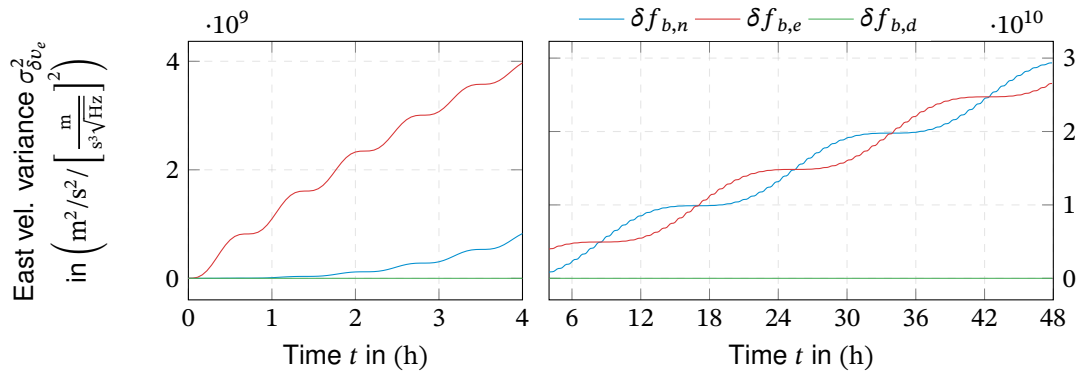
Figure 3.40.: Position error variance from rate random walk IMU errors normalized for the rate random walk coefficient K at $\phi = 45^\circ$ and $\psi = 0^\circ$.



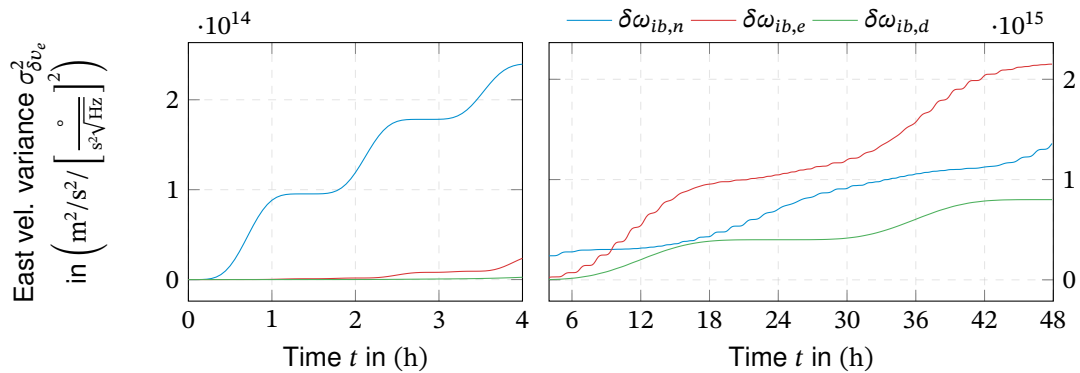
(a) North velocity error variance from accelerometer acceleration random walk input.



(b) North velocity error variance from gyroscope rate random walk input.

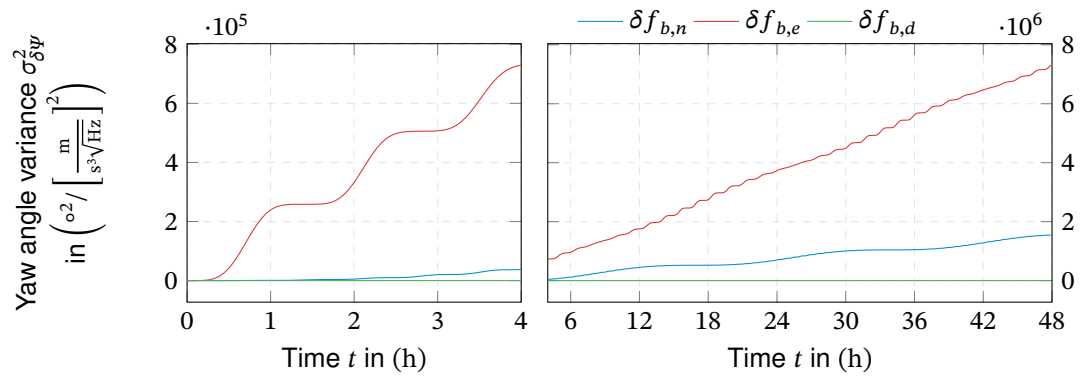


(c) East velocity error variance from accelerometer acceleration random walk input.

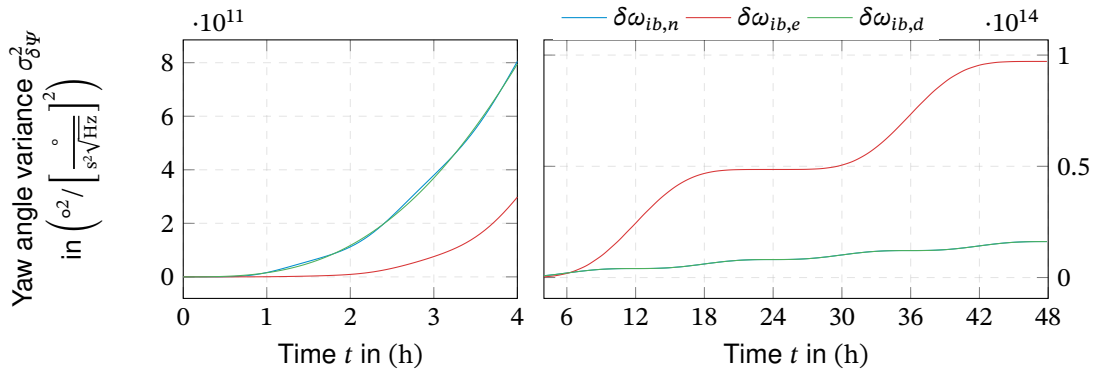


(d) East velocity error variance from gyroscope rate random walk input.

Figure 3.41.: Velocity error variance from rate random walk IMU errors normalized for the rate random walk coefficient K at $\phi = 45^\circ$ and $\psi = 0^\circ$.

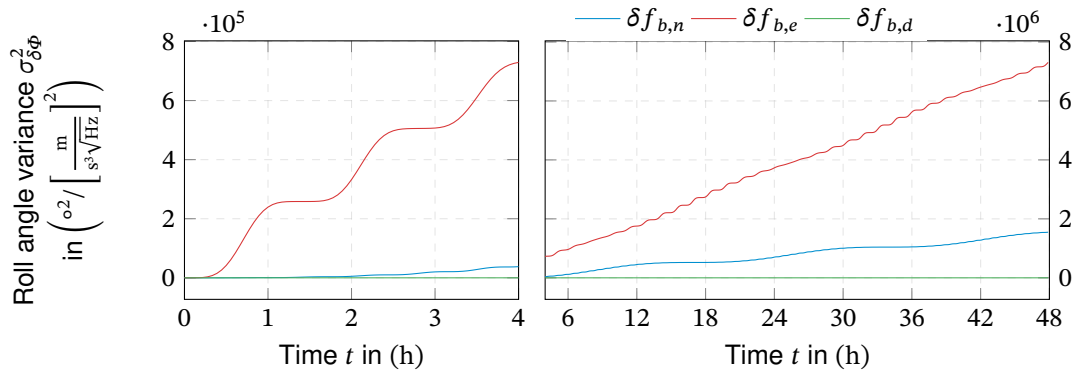


(a) Yaw angle error variance from accelerometer acceleration random walk input.

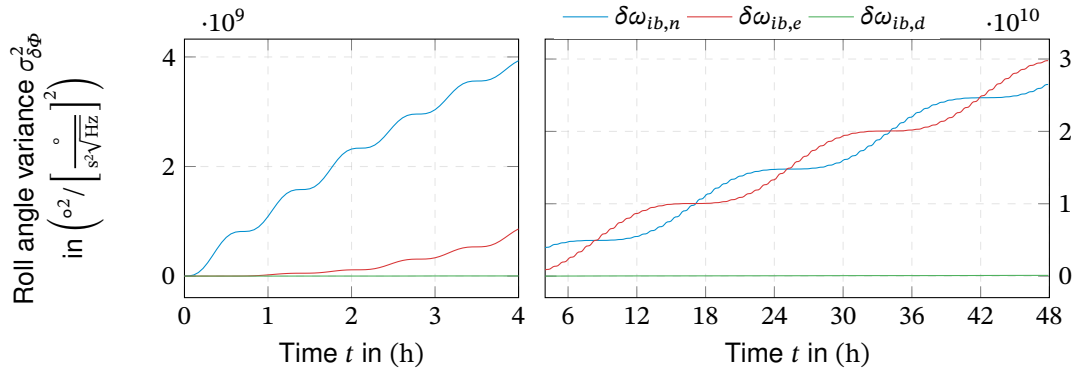


(b) Yaw angle error variance from gyroscope rate random walk input.

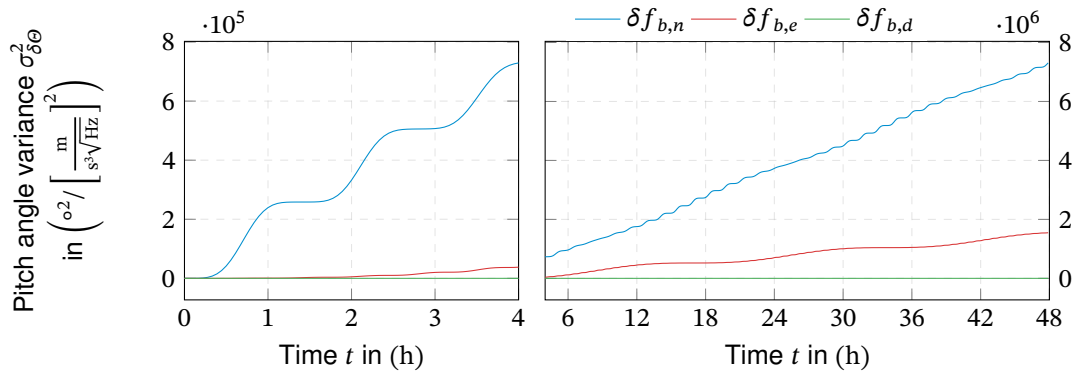
Figure 3.42.: Heading error variance from rate random walk IMU errors normalized for the rate random walk coefficient K at $\phi = 45^\circ$ and $\psi = 0^\circ$.



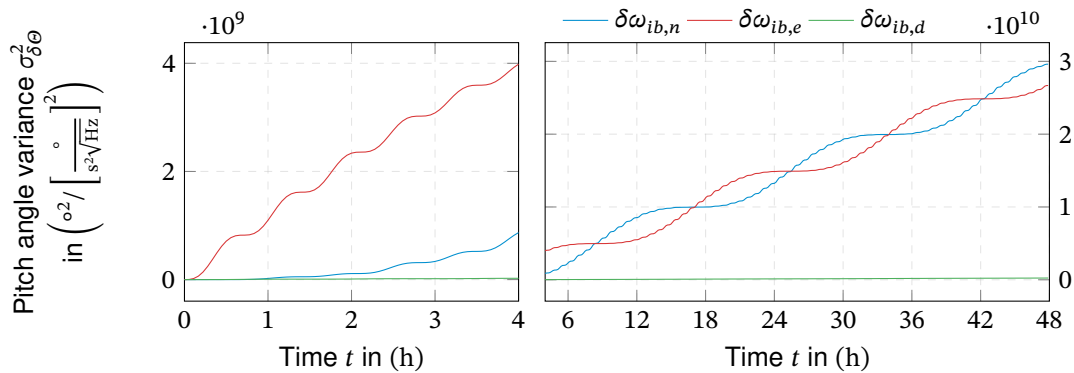
(a) Roll angle error variance from accelerometer acceleration random walk input.



(b) Roll angle error variance from gyroscope rate random walk input.



(c) Pitch angle error variance from accelerometer acceleration random walk input.



(d) Pitch angle error variance from gyroscope rate random walk input.

Figure 3.43.: Attitude error variance from rate random walk IMU errors normalized for the rate random walk coefficient K at $\phi = 45^\circ$ and $\psi = 0^\circ$.

3.3.4.4. Rate Ramp Noise

Following the IEEE standards [10], rate ramp noise is described as a linear growing drift in the rate output for finite but considerably long time:

$$\delta\omega(t) = Rt \quad (3.110)$$

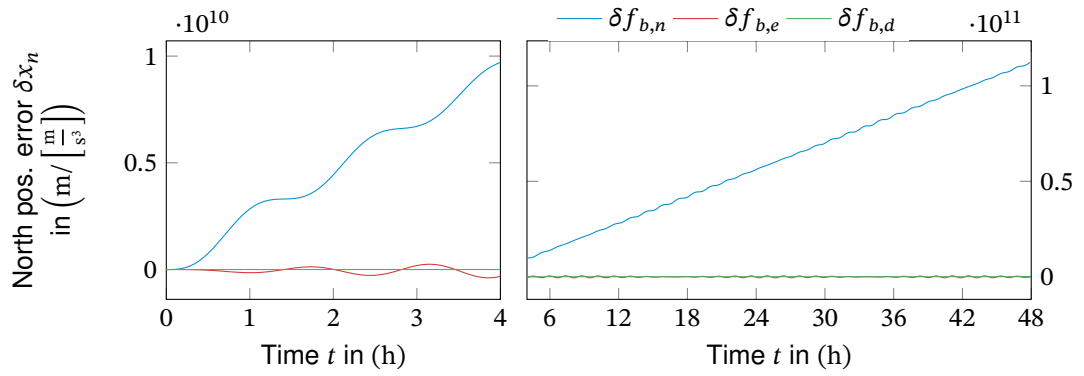
Thus, for a finite time, rate ramp noise is rather deterministic than stochastic and must not be confused with integrated flicker noise that has the same PSD and Allan variance characteristics. Still, it is included within this section to keep consistent with the IEEE standards, where it is also discussed as a component of the sensor's noise. Analogous to (3.71), the system's response to a linearly growing input is determined from the system's transfer function $G(s)$ as

$$Y(s) = G(s)\frac{1}{s^2}R = H(s)\frac{1}{s}R \quad (3.111)$$

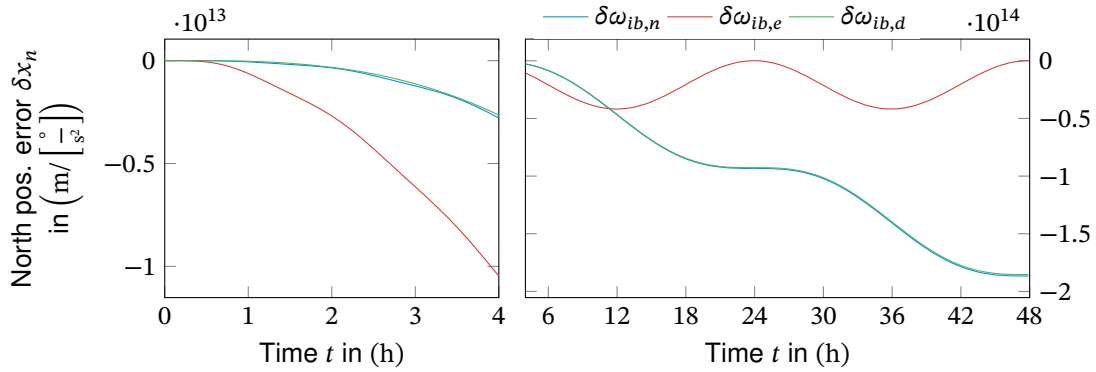
$$y(t) = R \int_0^t h(\tau)d\tau \quad (3.112)$$

which means that the response to linearly growing input is the integral of the system's response to constant errors (Subsection 3.3.2). The resulting navigation errors from ramp-like sensor errors is depicted in Figure 3.44 to Figure 3.47.

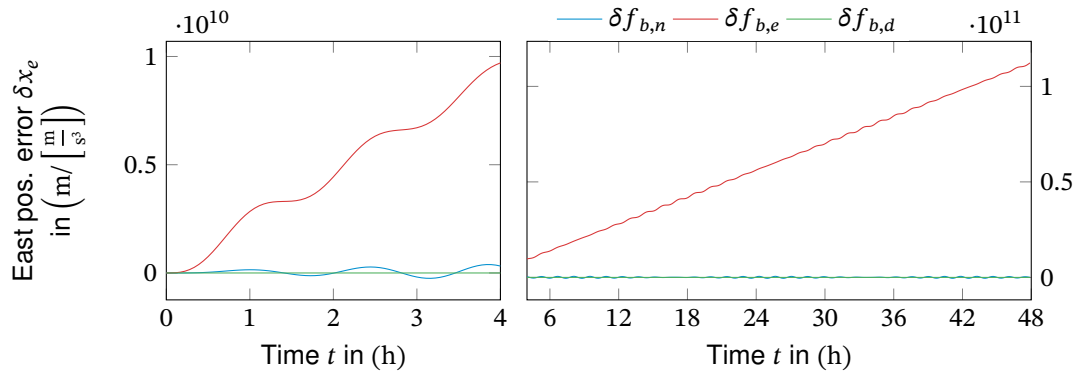
Despite the constantly growing input, many navigation state errors display oscillations within a fixed bound. This accounts for the roll angle errors, independent of the sensor and the north velocity errors, at least for the accelerometer errors. In contrast to that, most position errors grow without bounds. An exception is the position error from a perpendicular specific forces ramp, which results in a bound oscillation, e.g., a north position error from an east-pointing acceleration ramp error.



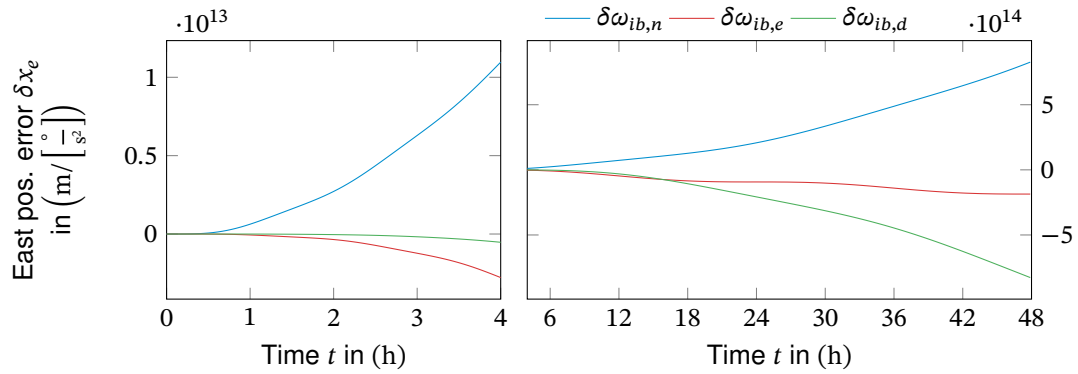
(a) North position error from acceleration ramp errors.



(b) North position error from gyroscope rate ramp errors.



(c) East position error from acceleration ramp errors.



(d) East position error from gyroscope rate ramp errors.

Figure 3.44.: Position error variance from rate and acceleration ramp IMU errors normalized to the ramp slope R at $\phi = 45^\circ$ and $\psi = 0^\circ$.

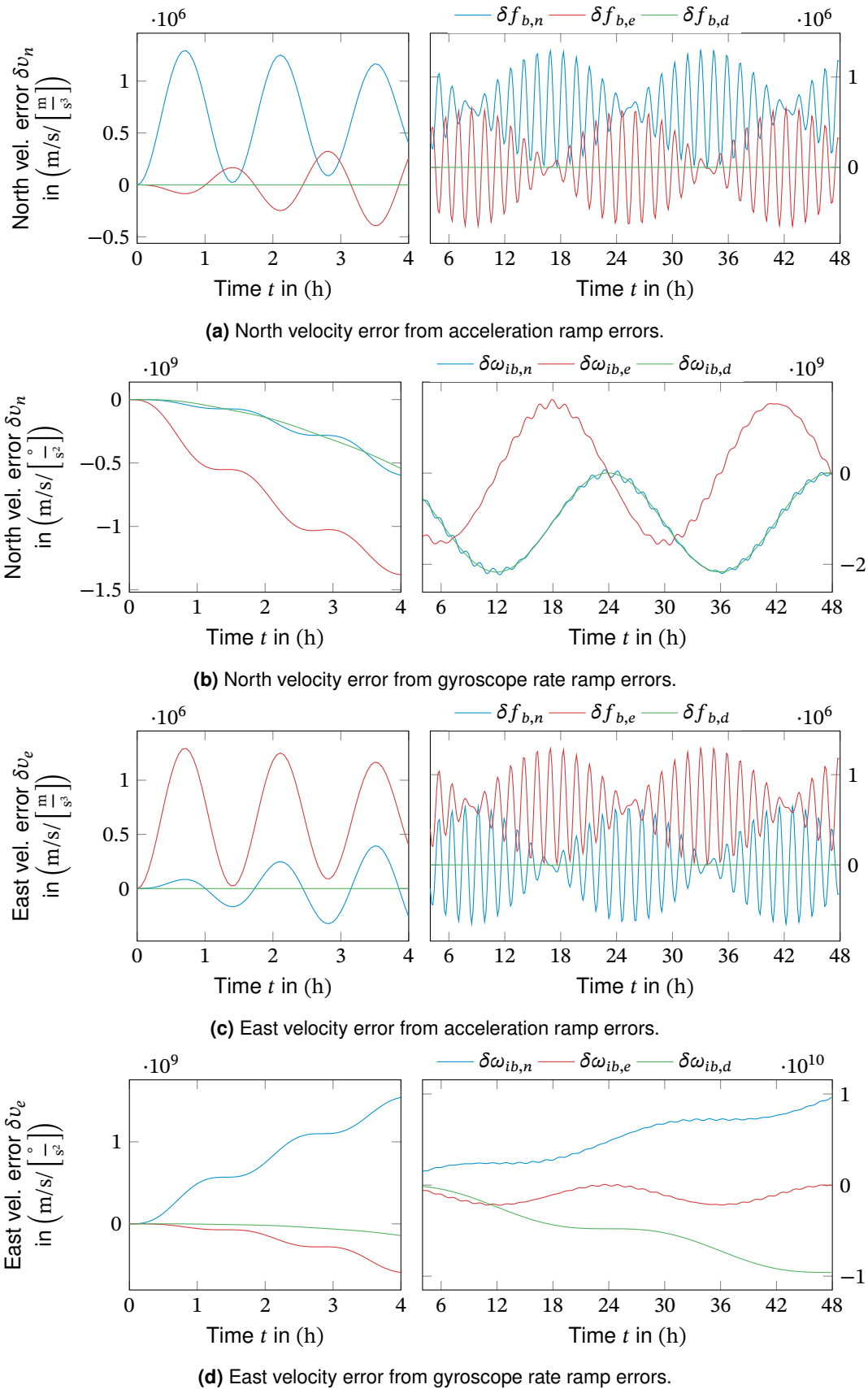


Figure 3.45.: Velocity error variance from rate and acceleration ramp IMU errors normalized to the ramp slope R at $\phi = 45^\circ$ and $\psi = 0^\circ$.

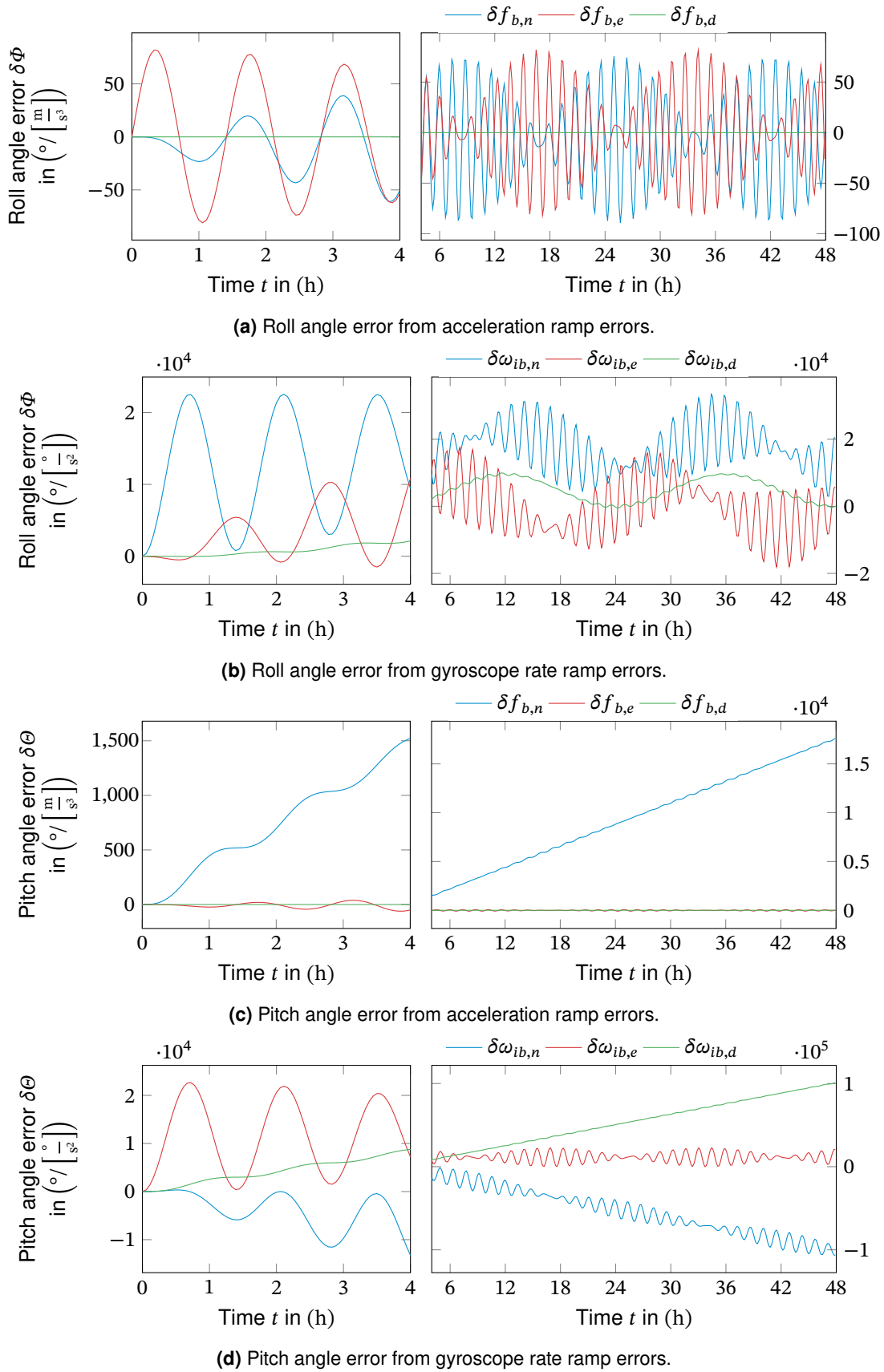


Figure 3.46.: Attitude error from rate and acceleration ramp IMU errors normalized to the ramp slope R at $\phi = 45^\circ$ and $\psi = 0^\circ$.

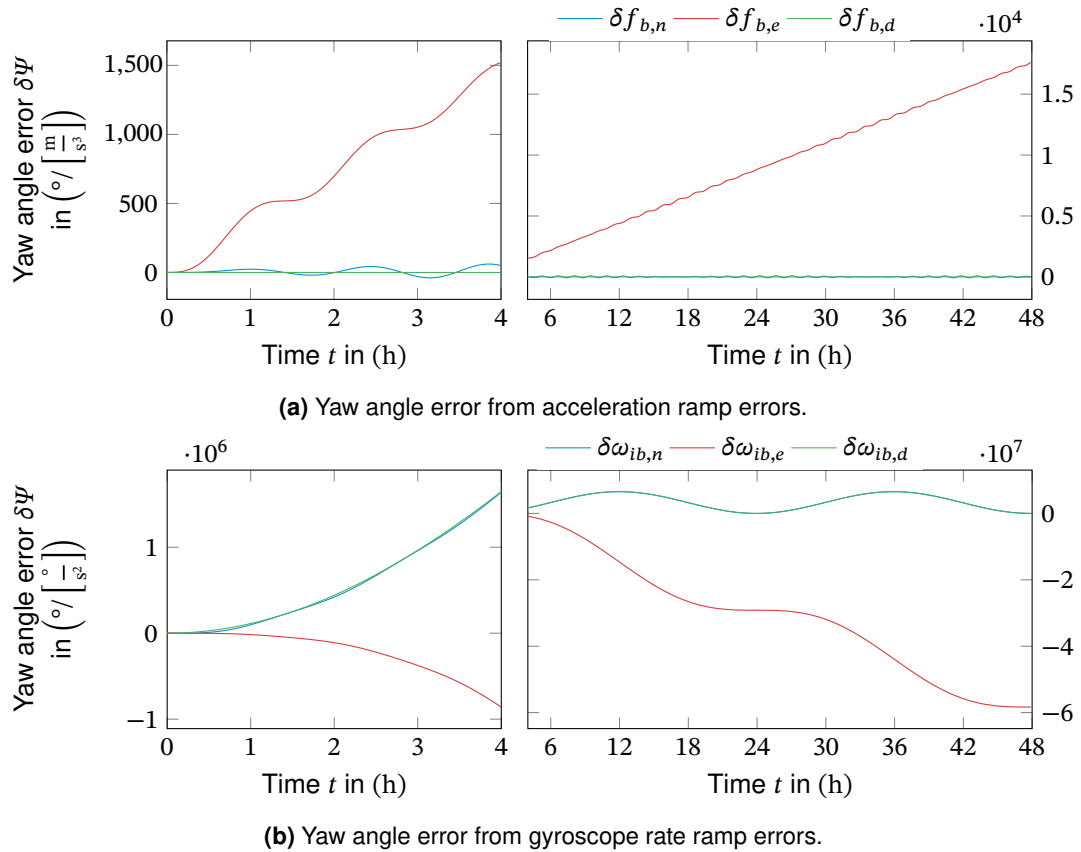


Figure 3.47.: Heading error from rate and acceleration ramp IMU errors normalized to the ramp slope R at $\phi = 45^\circ$ and $\psi = 0^\circ$.

3.3.4.5. Markov Noise

Exponentially correlated noise is created by a first-order Gauss-Markov process driven by white noise. From its defining PSD in [10, p. 69] the corresponding transfer function is easily identified as:

$$G_c(s) = \frac{q_c T_c}{1 + T_c s} \quad (3.113)$$

Using this transfer function, the navigation state error variance can be analyzed analytically. Still, this yields more cumbersome expressions than the responses to white noise input.

The Markov noise input can also be interpreted as low-pass filtering of the system's response to white Gaussian noise input. As the lowest strapdown navigation error dynamics is the Schuler oscillation at about 84 min, the effect of Markov noise can only be distinguished from white Gaussian noise for relatively long correlation times. The result of low-pass filtering the impulse response is exemplarily illustrated in Figure 3.48. From this consideration, the system's response to Markov noise can be anticipated by low-pass filtering the system's response to white noise from Subsection 3.3.3.1.

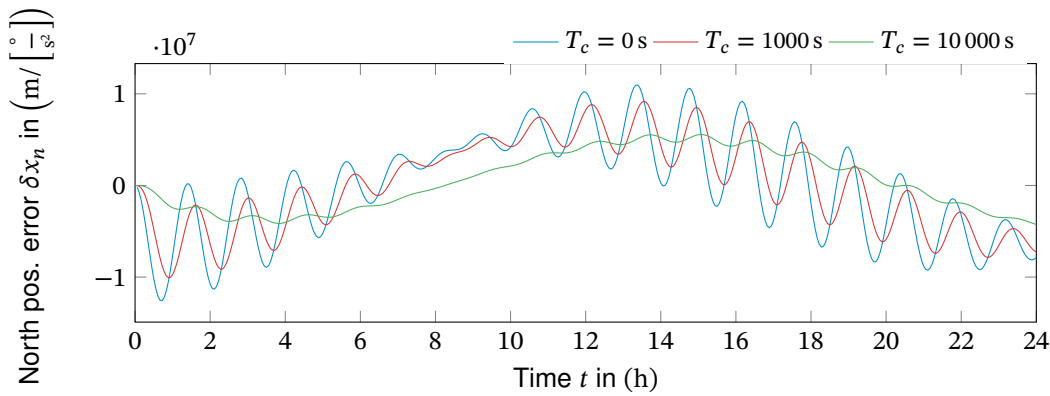


Figure 3.48.: Impulse response of the latitude error from angular rate error input $\delta\omega_{ib,e}$.

3.3.4.6. The Significance of Colored Sensor Noise

From the previous sections, it is apparent that colored sensor noise results in a widely different system response compared to the typically considered white noise input. As the navigation errors grow at different times, the respective contribution of different noise types to the total navigation error varies with time. For short times, the results are typically dominated by the white noise components, while the effect of in-run bias instability becomes prevalent over time. The author has illustrated this behavior for real-world sensor examples in [74].

As pointed out in [74], colored sensor noise can contribute significantly to the navigation errors for real-world sensor specifications. Table 3.3 is reprinted from [74] and exemplarily illustrates the maximum time for which the position error is dominated by the white components of the gyroscopes' noise. The analysis is limited to an angular random walk and in-run bias instability, as these were the two identifiable and dominating noise components.

Table 3.3.: Maximum mission time allows for neglecting the gyro bias instability for different sensor grades. Below the threshold time, the bias instability's contribution to the total position error is less than 1% of the angular random walk's contribution [74].

Grade	Example	Tech.	Noise Parameters			DRMS (1 h) (km)	1% Threshold	
			N $\left(\frac{\circ}{\sqrt{h}}\right)$	B $\left(\frac{\circ}{h}\right)$	T_B (s)		Time (s)	DRMS (m)
Industrial	DMU10 [82]	CVG	0.4	15	500	2800 *	11	0.14
	STIM300 [81]	CVG	0.15	0.5	1000	80	96	12
Tactical	DSP3100 [85]	FOG	0.048	0.072	2000	7	55	0.1
Navigation	GG1320 [86]	RLG	0.0015	0.0024	2000	0.4	245	1.3

* This position error clearly exceeds validity range of the linearized model.

Also, from above examples it can be seen that there is no typical ratio between a sensor's in-run bias instability and the angular/velocity random walk. In fact, this depends on the sensor technology and actual design. However, the trend goes towards better bias-instability

values for higher sensor grades. The optical sensors used for higher sensor grades typically provide a very good in-run stability.

In conclusion, the effect of colored sensor noise cannot be generalized but depends strongly on the planned application (time) and sensor specification. However, the graphs presented in this chapter allow an approximation of the effects of different noise processes from, e.g., a data sheet's noise specification. The results can then be used to assess the significance of the colored noise for the given application. Independent of the above error predictions, a detailed sensor noise model should be used for high-detail simulation. This applies particularly to the performance assurance and demonstration of a navigation system using Monte-Carlo simulations.

Result 1: Inertial Navigation Error Propagation

The derived system responses represent the error growth from initialization errors and sensor errors at static conditions.

The equations and graphs can be used to predict the navigation state errors from the dynamic-independent sensor errors, like sensor bias and noise, but also gravity model errors.

The bias-like dynamic-dependent sensor errors, like scale factors, misalignments, or g-sensitivities, can be considered piecewise for steady conditions (e.g., coordinated turns). However, this requires knowledge of a representative trajectory, typically not available at the early stage of the system design targeted in this chapter.

Comparing the derived system's responses, the following observations were made:

- Noise-like errors result in similar system responses as bias-like and initialization errors. Therefore, sensor noise needs to be considered in the navigation performance prediction.
- The system's responses to colored sensor noise differ from those to white noise. In general, colored sensor noise can not be approximated by an increased white noise input.
- In the long-term, the long-wave noise processes, like bias-instability, rate random walk, and rate ramp, tend to dominate the navigation errors.
- However, it's not possible to name a generally dominant noise process since it depends on the combination of the sensor's actual noise parameters and the application time.

Given the above-described complexity of the propagation of different errors, it is advisable to consider all bias-like and noise-like errors in an early navigation performance prediction, respectively sensor selection.

Furthermore, the derived equations and graphs should be used to assess the significance of colored sensor noise components for a given sensor specification. This is also emphasized by the fact that noise-like errors, in contrast to bias-like errors, can only be considered but not compensated by integrated navigation.

3.4. Navigation Performance Prediction

3.4.1. Alignment Uncertainty Charts

Based on the analysis in Section 3.2, the stationary alignment accuracy from sensor errors shall be visualized. According to the derived alignment covariance matrix (3.28), the attitude uncertainty depends only on the specific forces errors measurement. During stationary alignment, the IMU measurements are usually averaged over time to reduce the effects of sensor noise and environmental disturbances, e.g., vibrations. The alignment accuracy depends on the residual sensor errors after this averaging process, mainly sensor bias and residual errors from averaged noise. The simple relationship between specific forces and attitude (pitch and roll) accuracy is depicted in Figure 3.49 for isotropic accelerometer error statistics. The chart allows the direct read-off of the allowed accelerometer error from the desired attitude accuracy and vice versa. The typical sensor grades are added to indicate the achievable stationary alignment accuracy. To justify the linearization assumption, the plot is limited to 10° attitude error.

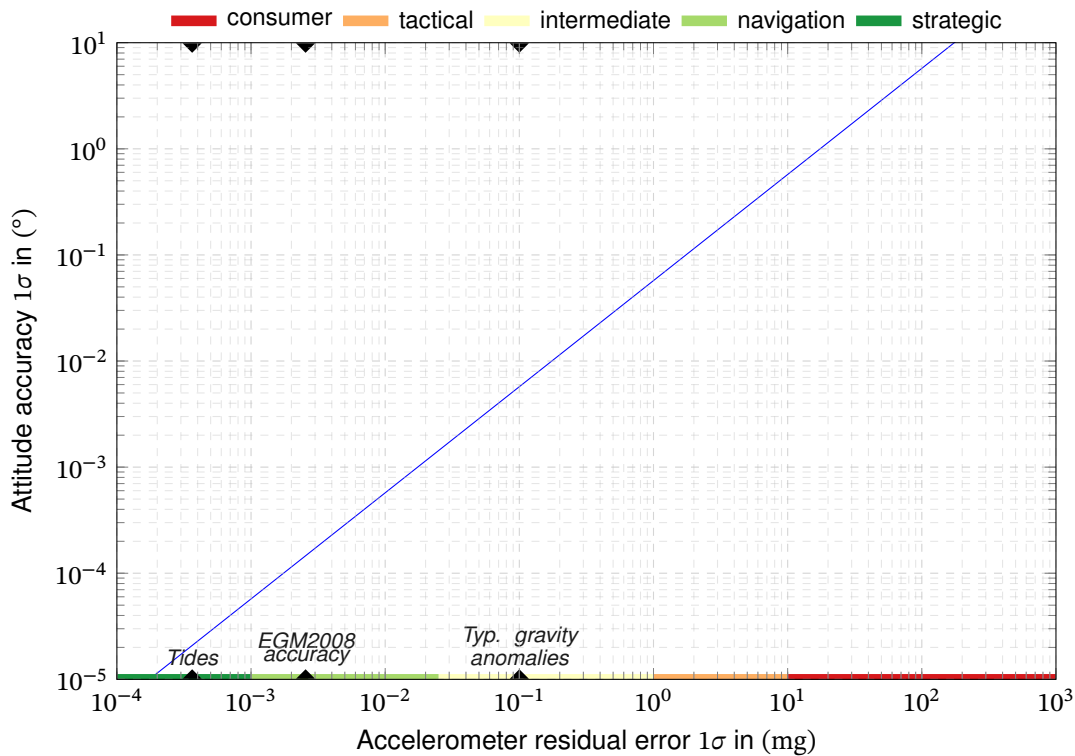


Figure 3.49.: Attitude alignment accuracy from inertial sensor residual errors during alignment.

As discussed in Section 3.2, the azimuth determination requires prior determination of the attitude angles Φ and Θ . Consequently, the azimuth uncertainty depends on both the error of the angular rate measurements and the accelerometer errors. Based on the azimuth variance of (3.32), Figure 3.50 has been created to visualize how accelerometer and gyroscope errors transfer into azimuth accuracy. The parallel bent lines give the different iso-levels of azimuth accuracy. The blue diagonal stripes indicate the share of gyroscope respectively accelerometer

errors of the total azimuth error. A significant deviation from the diagonal center line means that the total error is dominated by either gyroscope or accelerometer errors, and the other sensor is excessively accurate. Note that these optimal ratios only consider the alignment and may be different for other processes of inertial navigation.

The given chart is created for a latitude of 45° , but the latitude dependency is indicated by the dash-dotted line with the angle markers. For changing latitudes, the total graph moves along the line from the 45° marker to the desired latitude, as depicted in Figure 3.51. At the equator, the graph would be shifted indefinitely to the right, indicating that the accelerometer error has no effect anymore. Moving towards the poles, the graph is shifted to the lower left. In this case, the dependency on both accelerometer and gyroscope error increases. For given sensor errors, the resulting azimuth error increases.

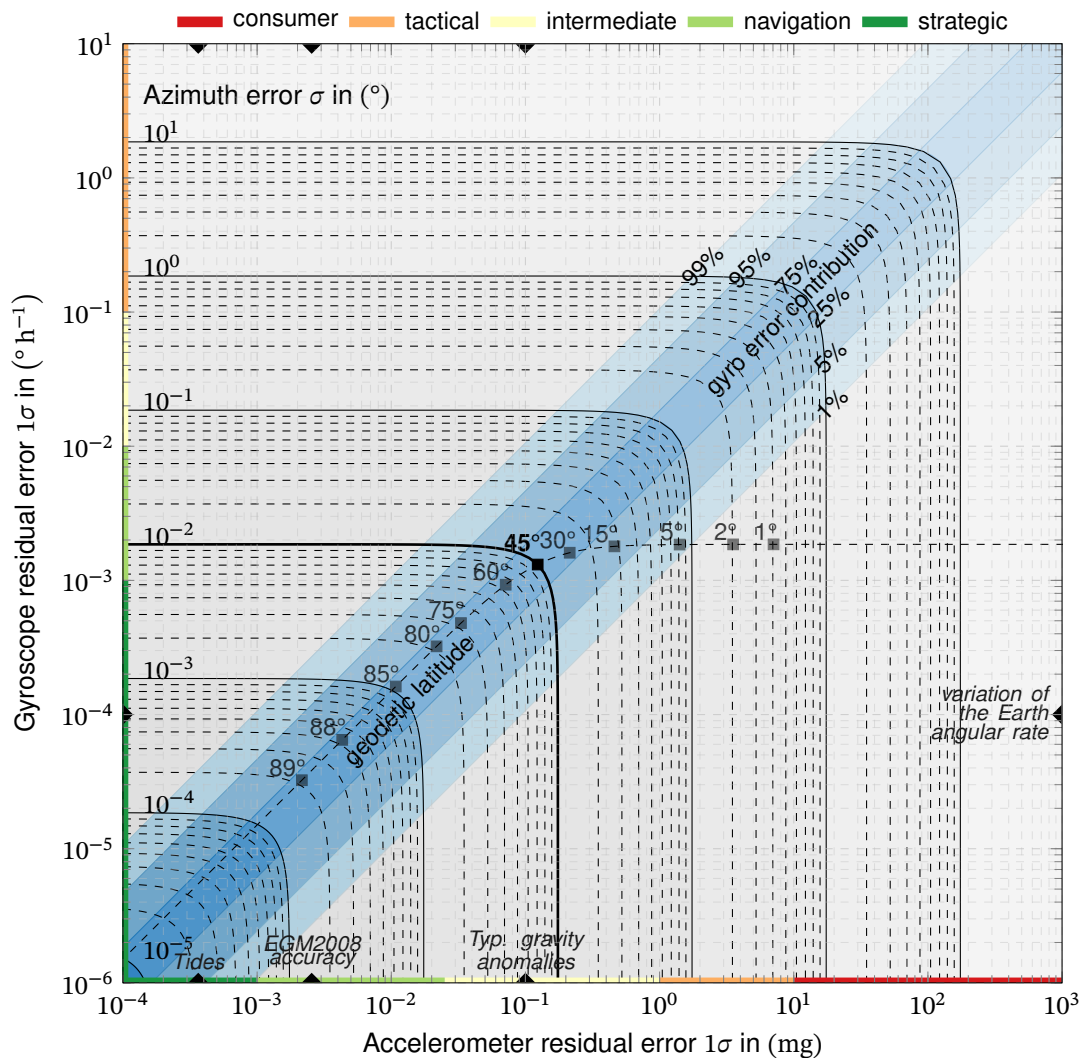
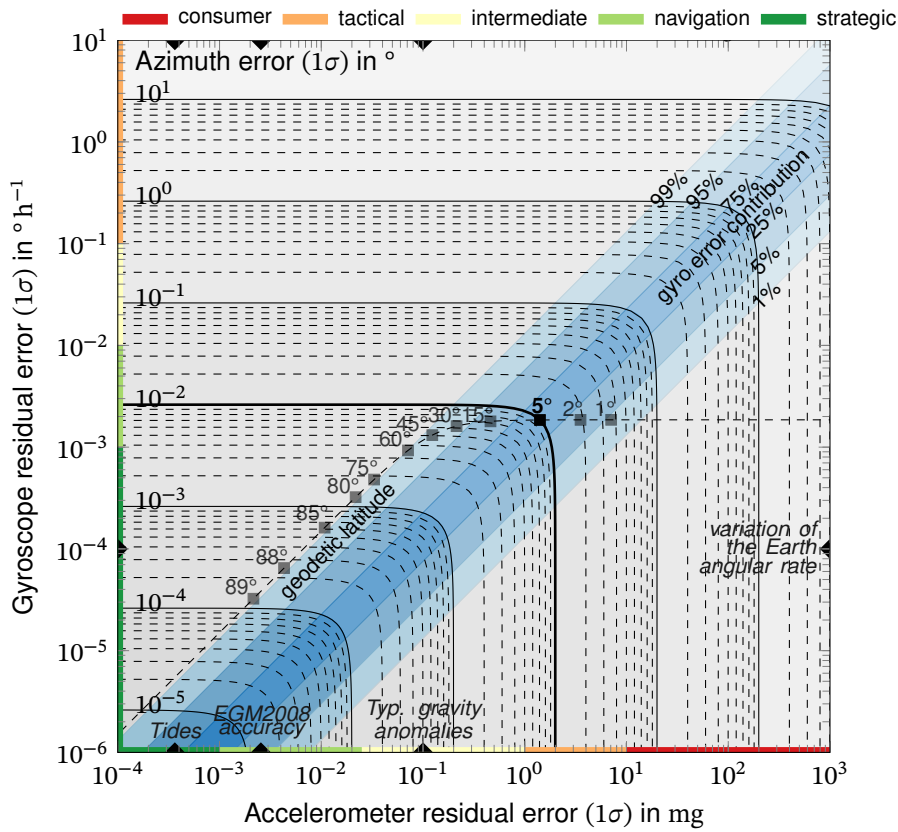
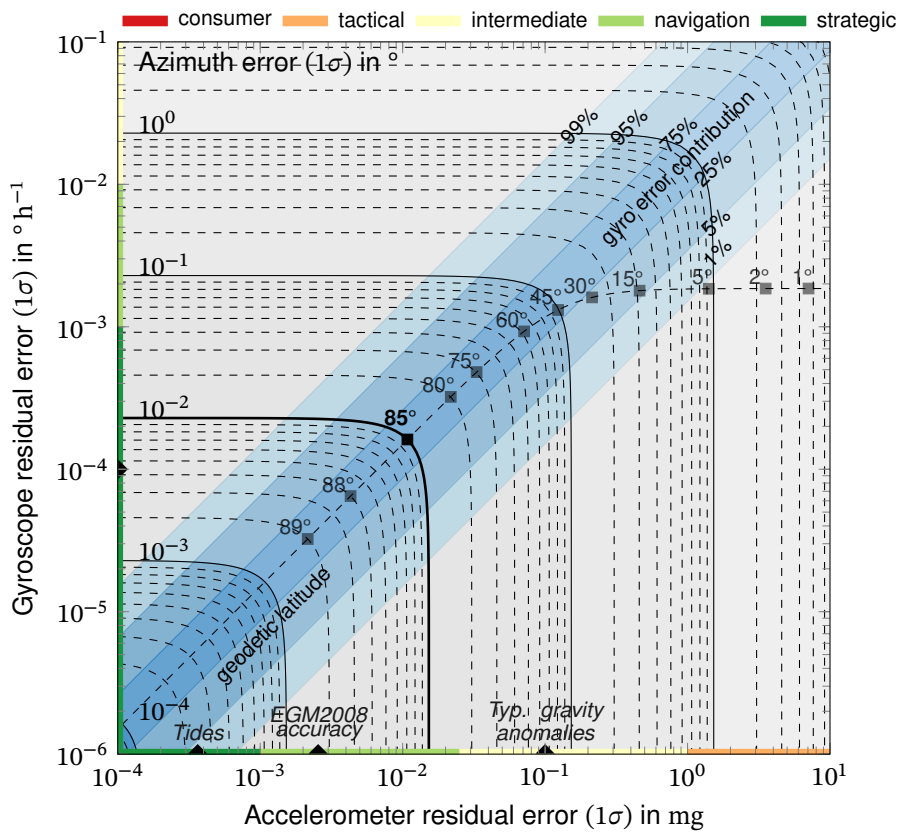


Figure 3.50.: Azimuth alignment accuracy from inertial sensor residual errors during alignment at a geodetic latitude of $\phi = 45^\circ$.



(a) At a geodetic latitude of $\phi = 5^\circ$.



(b) At a geodetic latitude of $\phi = 85^\circ$.

Figure 3.51.: Azimuth alignment accuracy from inertial sensor residual errors during alignment at a geodetic latitude of $\phi = 5^\circ$ and $\phi = 85^\circ$.

3.4.2. A Primer on Positioning Accuracy Measures

3.4.2.1. Typical Position Accuracy Measures

In section 3.3 the covariance matrix of the navigation error states has been derived for various input errors. While the covariance matrix is an exact representation of a multivariate zero-mean Gaussian distribution of the errors, its interpretation is non-trivial. Instead, people tend to expect a simple single number to answer the question *How accurate is this navigation system?*.

For obvious reasons it is not possible to reduce, e.g., a 2d covariance matrix of the position error

$$\mathbf{P} = \begin{bmatrix} P_{xx} & P_{xy} \\ P_{xy} & P_{yy} \end{bmatrix} = \begin{bmatrix} \sigma_x^2 & P_{xy} \\ P_{xy} & \sigma_y^2 \end{bmatrix} \quad (3.114)$$

to a single number without loss of information. Geometrically, this is equivalent to trying to represent a (rotated) ellipse by a simple circle. Still, several scalar measures are used to describe position accuracy in navigation and the satellite navigation industry. A summary of the most typically used measures is given in Table 3.4.

Table 3.4.: Typical horizontal position accuracy measures [87, pp. 42–44], [88], [89].

Abbrev.	Measure	Definition
CEP	Circular Error Probable	Radius of a circle, centered at the true value, that covers 50 % cumulative probability.
R95	Horizontal 95 % accuracy	Radius of a circle, centered at the true value, that covers 95 % cumulative probability.
67 %	Horizontal 67 % accuracy	Radius of a circle, centered at the true value, that covers 67 % cumulative probability.
DRMS / rms ₂	Distance Root Mean Square	Root mean square of horizontal errors.
2DRMS	Twice DRMS	Twice Root mean square of horizontal errors.

The typical accuracy measures from Table 3.4 can be categorized into two groups that will be discussed in the following.

3.4.2.2. Circular Error Probables

Circular Error Probable (CEP) measures give the radius r of a circle around the true value that contains a specified cumulative probability, e.g. $p = 50\%$ for the classical CEP. For a zero-mean 2d Gaussian distribution with covariance matrix \mathbf{P} for a cumulative probability of p is defined by [87, p. 37]

$$\iint_{x^2+y^2 < r^2} \frac{1}{2\pi\sigma_x\sigma_y\sqrt{1-\rho^2}} \exp\left(\frac{-1}{2(1-\rho^2)} \left[\frac{x^2}{\sigma_x^2} - \frac{2\rho xy}{\sigma_x\sigma_y} + \frac{y^2}{\sigma_y^2}\right]\right) dx dy = p \quad (3.115)$$

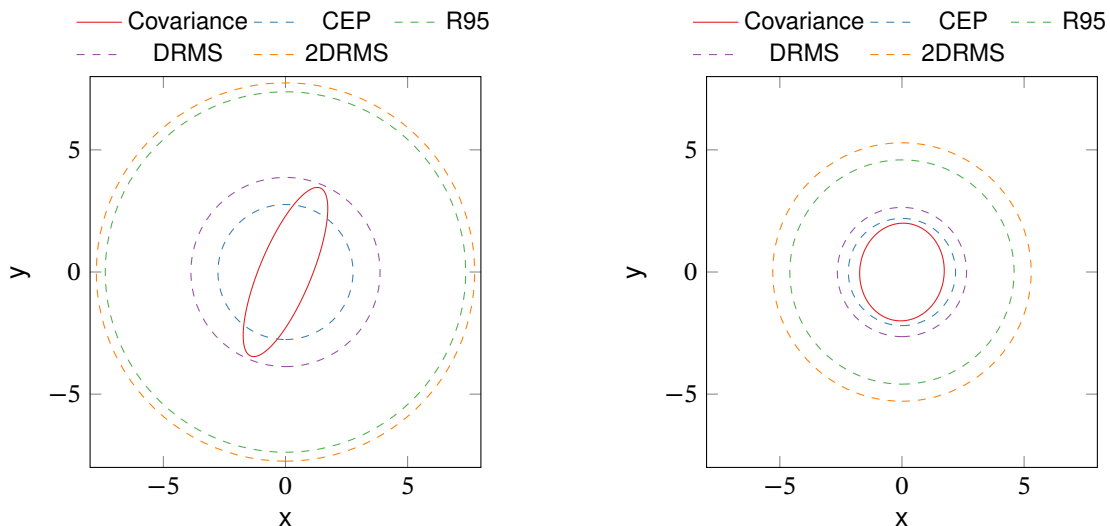
with the correlation coefficient

$$\rho = \frac{P_{xy}}{\sigma_x\sigma_y} \quad (3.116)$$

For the special case of a pure diagonal covariance matrix with equal entries σ and respective $\rho = 0$, the circular radius r can be determined analytically as [87, p. 43]:

$$r = \sigma\sqrt{-2\ln(1-p)} \quad (3.117)$$

Any other case requires numerical integration and root search of the above integral [87, p. 49]. For circular or nearly circular error distributions, the CEP provides a vivid and straightforward measure of accuracy. The classical CEP₅₀, for example, states that 50% of all position measurements lie within a circle of the given radius. Although the statement of a circular error probable can be calculated and will be statistically correct even for an elliptical distribution, the CEP value misleads to the wrong assumption of a circular distribution as illustrated in Figure 3.52.



(a) Highly elliptical $\sigma_x^2 = 3, \sigma_y^2 = 12, \rho = 0.75$.

(b) Nearly circular $\sigma_x^2 = 3, \sigma_y^2 = 4, \rho = 0.0289$.

Figure 3.52.: Position accuracy measures for circular and ellipsoidal covariance matrices.

3.4.2.3. Root Mean Square Measures

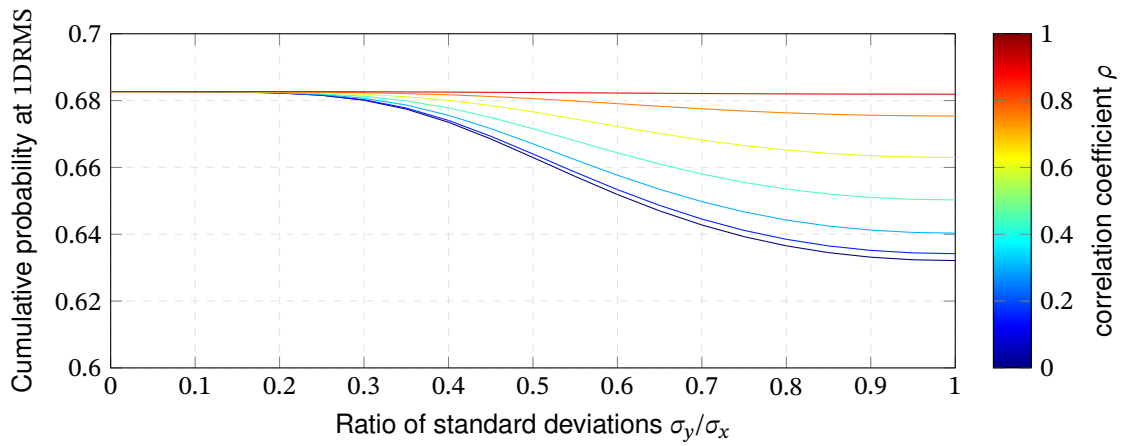
The **Root Mean Square (RMS)** measures (e.g. **DRMS**) represent the mean of the total position errors, e.g. horizontal distances. For a 2D Gaussian distribution, the **DRMS** value can be determined from the covariance matrix as:

$$\text{DRMS} = \sqrt{\sigma_x^2 + \sigma_y^2} \quad (3.118)$$

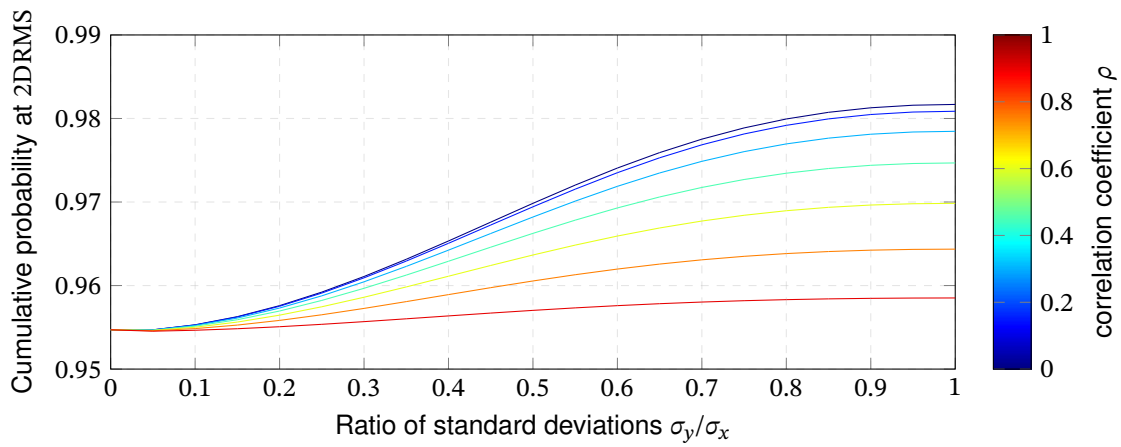
The classical **DRMS** uses only the diagonal elements of the covariance matrix and thus neglects correlations. Compared to the **CEP** measures, the **DRMS** has the advantage of a straightforward calculation. Additionally, the **DRMS** allows the simple addition of multiple error sources as the sum of their resulting position variances, e.g:

$$\text{DRMS} = \sqrt{\sigma_{x,f_b}^2 + \sigma_{x,\omega_{ib}}^2 + \sigma_{y,f_b}^2 + \sigma_{y,\omega_{ib}}^2} \quad (3.119)$$

The major drawback of the **DRMS** measures is the lack of stochastic interpretation. In contrast to the **CEP** measures, the **DRMS** value does not give direct information on the confidence region. The corresponding cumulative probability within a **DRMS** radius circle depends on the shape of the distribution. For a zero-mean 2D Gaussian distribution, this is represented by the (root) diagonal elements σ_y/σ_x and the correlation coefficient ρ . Equation (3.115) has been numerically evaluated for varying covariance matrices. The resulting probability within **DRMS** and **2DRMS** is depicted in **Figure 3.53**. Depending on the covariance matrix, the radius of **DRMS** represents a probability between 63.2 % and 68.3 %. The **2DRMS** value corresponds to a probability between 95.5 % and 98.2 %. Due to the relatively small variations of the cumulative probability, the **DRMS** measure provides a reasonable scalar accuracy measure. Still, the above-mentioned problems of representing the 2D distribution by a single scalar value exist.



(a) Cumulative probability within a 1 DRMS radius circle for varying variance ratios and correlation coefficients.



(b) Cumulative probability within a 2 DRMS radius circle for varying variance ratios and correlation coefficients.

Figure 3.53.: Statistical interpretation of the DRMS and 2DRMS value.

3.4.3. Position Uncertainty Charts

Similar to the stationary alignment accuracy charts, also the position accuracy from sensor and initialization errors shall be visualized. The equations derived in Section 3.3 allow determining the position uncertainty at time t for given sensor and initialization errors. During system design, often, the inverse problem is to be solved:

Which sensor grade is required to guarantee a given maximum position error within a given period?

Or, for a given set of sensors, the problem could be formulated as:

How long can the maximum position error be guaranteed for a given sensor performance?

To answer this question, the following charts have been created. Each chart indicates the time until, e.g., the horizontal position error reaches a given threshold, e.g., 1 NM. As illustrated in section 3.3, the position and orientation errors from constant error inputs oscillate. Still, for the simplified performance prediction, the maximum ever reached error (see Figure 3.54) provides a more meaningful measure of navigation performance. For the creation of the plots, the cumulative maximum of the response is used for each input. Otherwise, the different contributions could cancel out, and the maximum allowed error for one input could grow locally with time. The neglect of these effects leads to conservative (overestimate) of the error growth but ensures a monotonic increasing function.

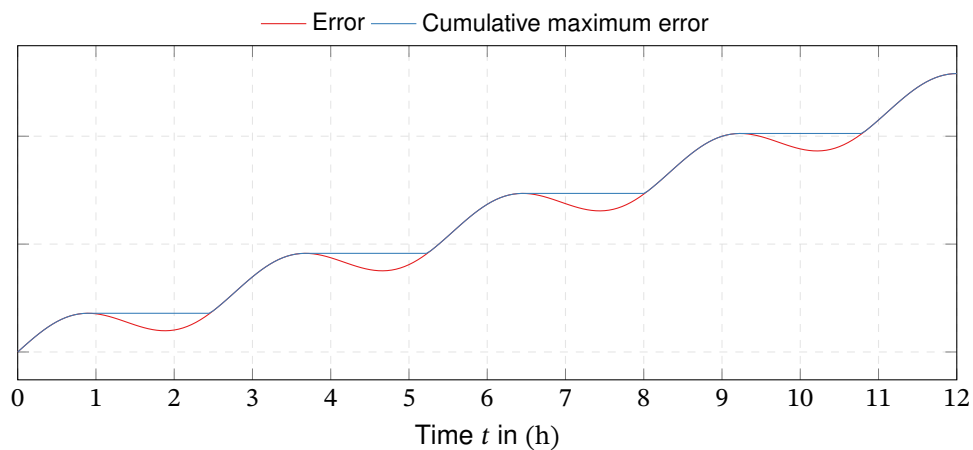


Figure 3.54.: Example cumulative maximum error vs. error.

One basic idea of the created charts is to illustrate the contributions of different error sources. Here, a position uncertainty measure that allows the simple addition of different errors is beneficial. As it represents a confidence radius of at least 95.5 %, 2DRMS is used (see Subsection 3.4.2). The position uncertainty charts are created for three different, representative, Twice Distance Root Mean Square (2DRMS) thresholds:

- 10 NM is the maximum **Total System Error (TSE)**¹ for RNP10 operations, which is the typical requirement for oceanic flights. More strict **Required Navigation Performance (RNP)** operations are usually dominated by **GNSS**-based navigation.
- 1 NM is the industry-standard threshold to describe an inertial navigation system's performance.
- 10 m is a vivid magnitude that represents typical **Navstar Global Positioning System (GPS) Standard Positioning Service (SPS)** accuracy [91, p. 22].

To account for the contribution of the different error inputs, iso-lines for constant contribution ratios of the inputs are given in the following charts. These lines indicate a suitable combination of the different error inputs, e.g., a set of gyroscopes and corresponding accelerometers, so that the total error is not dominated by one of these.

In the following sections the initialization error responses $h_{i,j}$ are taken from [Appendix D](#), where the index i corresponds to the output state and j to the input.

3.4.3.1. Position Uncertainty from Initial Position Errors

The horizontal position uncertainty, represented by the **DRMS** value, is obtained from the step responses of the position error to initial position errors:

$$\text{DRMS}(t) = \sqrt{[h_{1,1}^2(t) + h_{2,1}^2(t)]\sigma_{\delta\phi}} \quad (3.120)$$

As discussed in [Section 3.3](#), the strapdown error dynamics is completely insensitive to longitude errors. Initial latitude errors excite an oscillation whose maximum is given by just that initial error. In conclusion, the initial position errors already define the maximum position errors that arise from these, and there is no need for performance prediction charts.

3.4.3.2. Position Uncertainty from Initial Velocity Errors

The horizontal position error, expressed as **DRMS**, is determined from the step responses as:

$$\text{DRMS}(t) = \sqrt{\text{DRMS}_{\delta v_n}^2(t) + \text{DRMS}_{\delta v_e}^2(t)} \quad (3.121)$$

$$\text{DRMS}_{\delta v_n}^2(t) = [h_{1,3}(t)^2 + h_{2,3}(t)^2] \sigma_{\delta v_n}^2 \quad (3.122)$$

$$\text{DRMS}_{\delta v_e}^2(t) = [h_{1,4}(t)^2 + h_{2,4}(t)^2] \sigma_{\delta v_e}^2 \quad (3.123)$$

Based on above equations, the time to different position error thresholds from initial velocity errors is depicted in [Figure 3.55](#) to [Figure 3.57](#). The diagonal lines indicate fixed ratios of contribution from the two error sources. The maximum position error increases nearly linearly during the first few minutes but is only very slow between 1 h and 24 h. Afterward, the error

¹While **Performance Based Navigation (PBN)** actually sets the requirement for the **TSE**, for RNP10 the **FTE** and **PDE** can be neglected, leaving a 10 NM requirement to the **Navigation System Error (NSE)** [90].

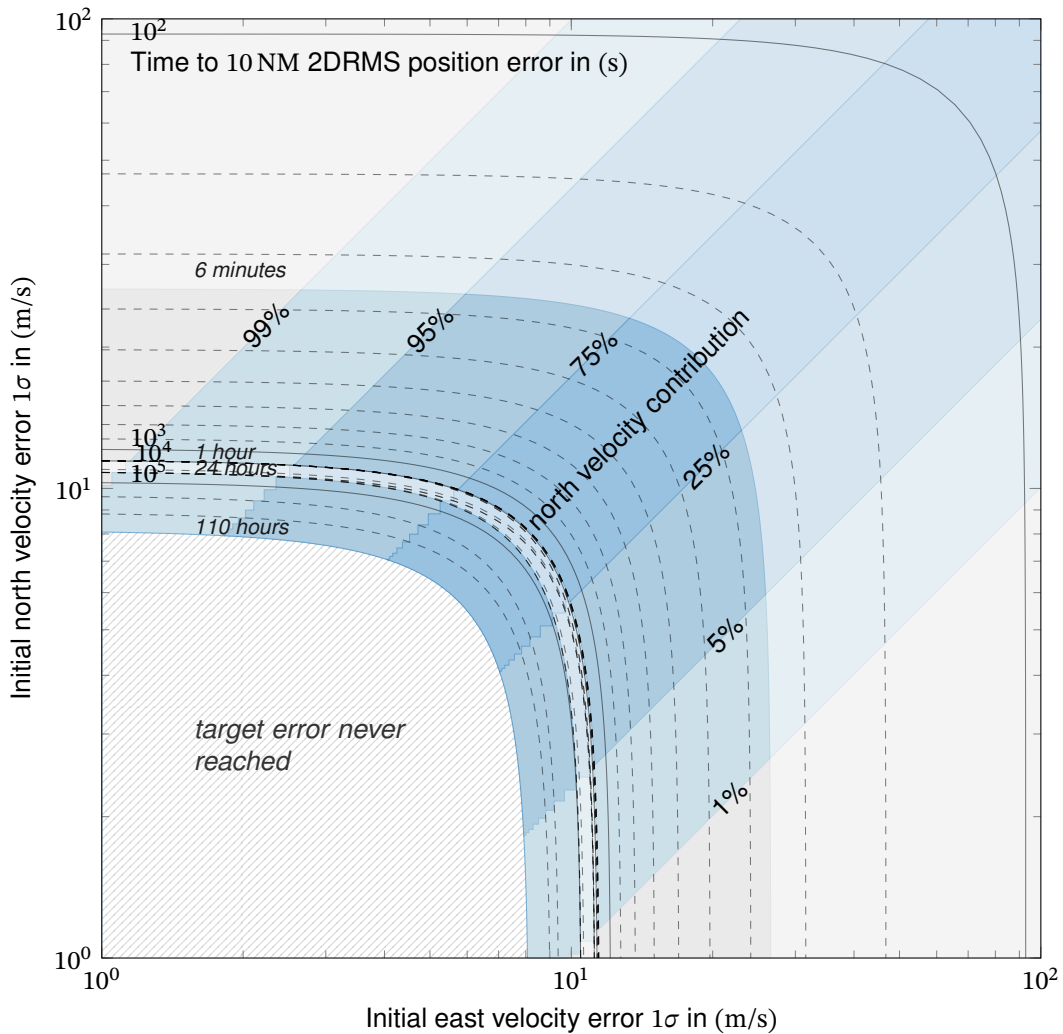


Figure 3.55.: Time to 10 NM 2DRMS position uncertainty from initial velocity errors at $\phi = 45^\circ$.

increases moderately until the maximum position has been reached at around 110 h. This behavior manifests as a distinct thin area in the time iso-lines.

For a threshold of 10 NM, as depicted in Figure 3.55, even large velocity errors of several meters per second lead to position errors within that threshold. As the error dynamics are dominated by the linear growth phase, changing the threshold only shifts the plot's shape towards the lower input errors but does not substantially change its shape. For 10 m 2DRMS threshold, the maximum initial velocity error to stay within that threshold is reduced to several millimeters per second. While the required meters per the second accuracy for 10 NM threshold should not pose any problem in most applications, this millimeters per the second requirement does, especially when initializing on a moving platform, e.g., ships.

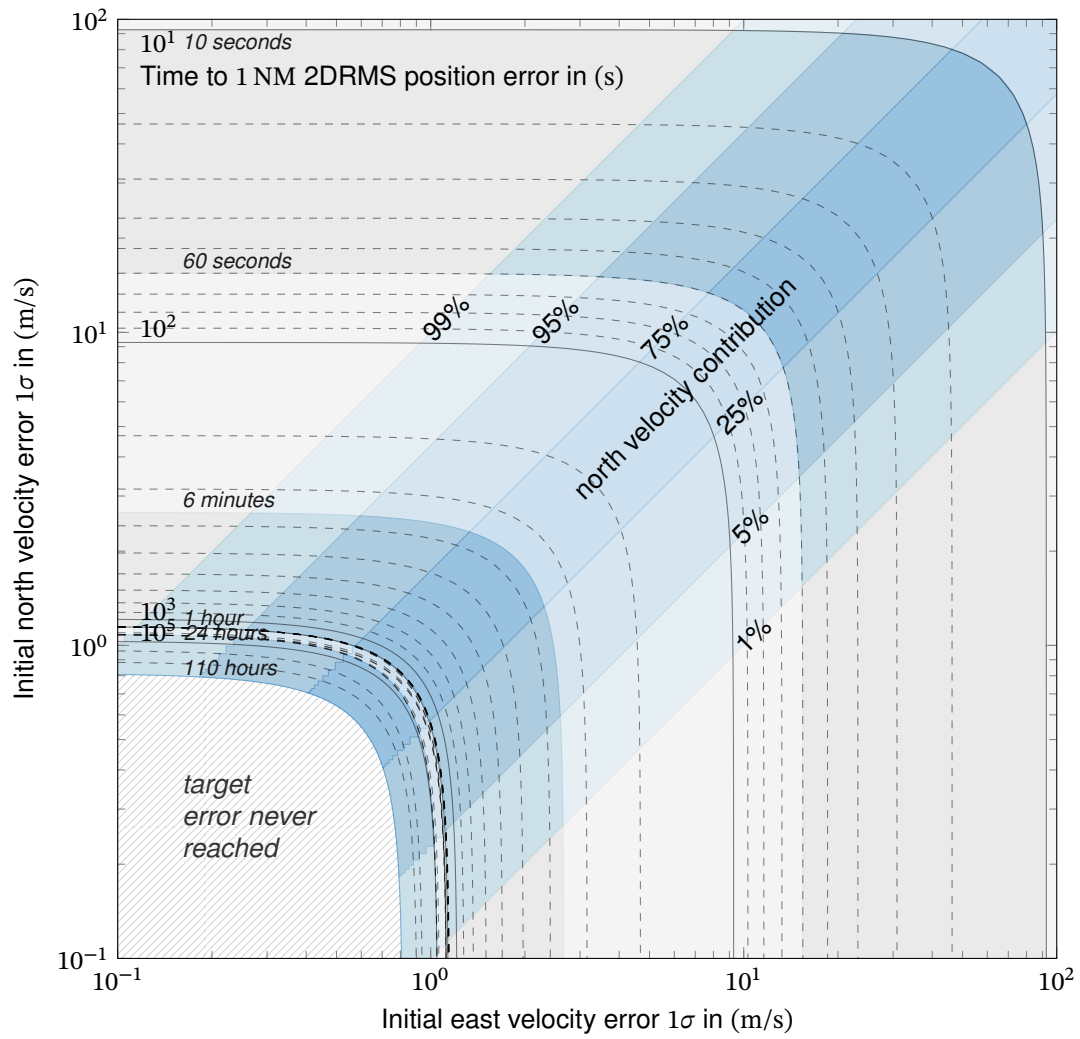


Figure 3.56.: Time to 1 NM 2DRMS position uncertainty from initial velocity errors at $\phi = 45^\circ$.

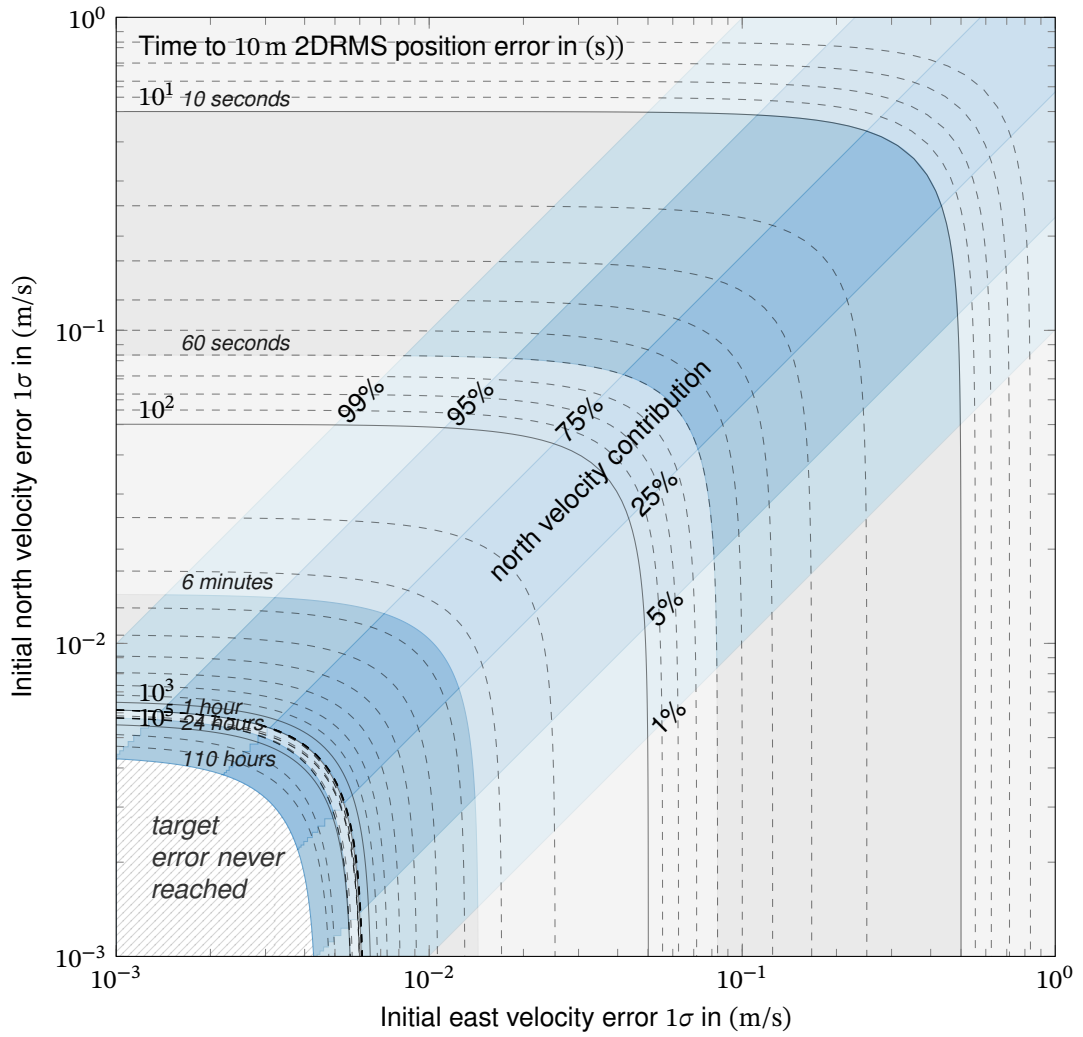


Figure 3.57.: Time to 10 m 2DRMS position uncertainty from initial velocity errors at $\phi = 45^\circ$.

3.4.3.3. Position Uncertainty from Initial Alignment Errors

Using the position error's step responses from [Subsection D.1.2](#), the horizontal position error as **DRMS** is calculated as:

$$\text{DRMS}(t) = \sqrt{\text{DRMS}_{\delta\phi, \delta\theta}^2(t) + \text{DRMS}_{\delta\psi}^2(t)} \quad (3.124)$$

$$\text{DRMS}_{\delta\phi, \delta\theta}^2(t) = [h_{1,5}(t)^2 + h_{2,5}(t)^2] \sigma_{\delta\phi}^2 + [h_{1,6}(t)^2 + h_{2,6}(t)^2] \sigma_{\delta\theta}^2 \quad (3.125)$$

$$\text{DRMS}_{\delta\psi}^2(t) = [h_{1,7}(t)^2 + h_{2,7}(t)^2] \sigma_{\delta\psi}^2 \quad (3.126)$$

Determining the initial pitch and roll angles using gravity alignment relative to the reference frame (WGS84 ellipsoid) is limited by the local gravity's **Deflection of the Vertical (DoV)**. According to the **Earth Gravity Model 2008 (EGM2008)**, the DoV in north-south ξ and east-west η range from -122.3 asec to 104.4 asec with a global **RMS** of 5.4 asec and a global RMS error of around 1 asec [92]. Markers for these limitations have been added to the following plots' pitch and roll alignment axis.

The created charts share a familiar shape that moves within the parameter plane with increasing position error threshold. In each graph, the iso-contribution lines start as a straight line from the upper right (low alignment accuracy) and bend towards the pitch-roll error axis at around half a Schuler period 2500 s. From here, the pitch and roll alignment errors have little influence, and the heading alignment error dominates the position error. From about 27 h, the cumulative maximum position error has been reached, and the position error threshold will not be reached for even lower alignment errors. To ensure the validity of the linearized strapdown error equations, the plot's axes are limited to a maximum alignment error of 10° (1σ).

Intuition would tell that an azimuth error combined with a velocity would lead to linear growth of the position error. While this is true for the motion of a vehicle, it is not true for inertial navigation: The azimuth angle as a component of the rotation matrix \mathbf{R}_{nb} is only used to transform accelerations from the body to the n -frame, not velocities (see (3.43)). Consequently, the following charts are valid, independent of the vehicle's velocity. Overall, the position error is more sensitive to initial pitch and roll errors than azimuth errors.

For a high position error threshold of 10 NM, the time to error from alignment errors is depicted in [Figure 3.58](#). For a leveling uncertainty better than 0.03° (108 asec) and azimuth error better than 0.08° (288 asec), the position threshold is never reached. For an extreme leveling uncertainty of 10° (1σ), the 10 NM **2DRMS** are already reached after 90 s and the azimuth uncertainty has virtually no effect at all.

The equivalent graphics for a **2DRMS** threshold of 1 NM is given in [Figure 3.59](#). Here the maximum alignment errors that lead to 1 NM **2DRMS** are reduced by $1/10$ to around 0.003° (11 asec) for the leveling and 0.008° (29 asec) for the azimuth. For the upper limit pitch and roll errors, however, the position error threshold is already reached at around 28 s.

Finally, the graphics is given for a threshold of 10 m in [Figure 3.60](#). To keep the maximum

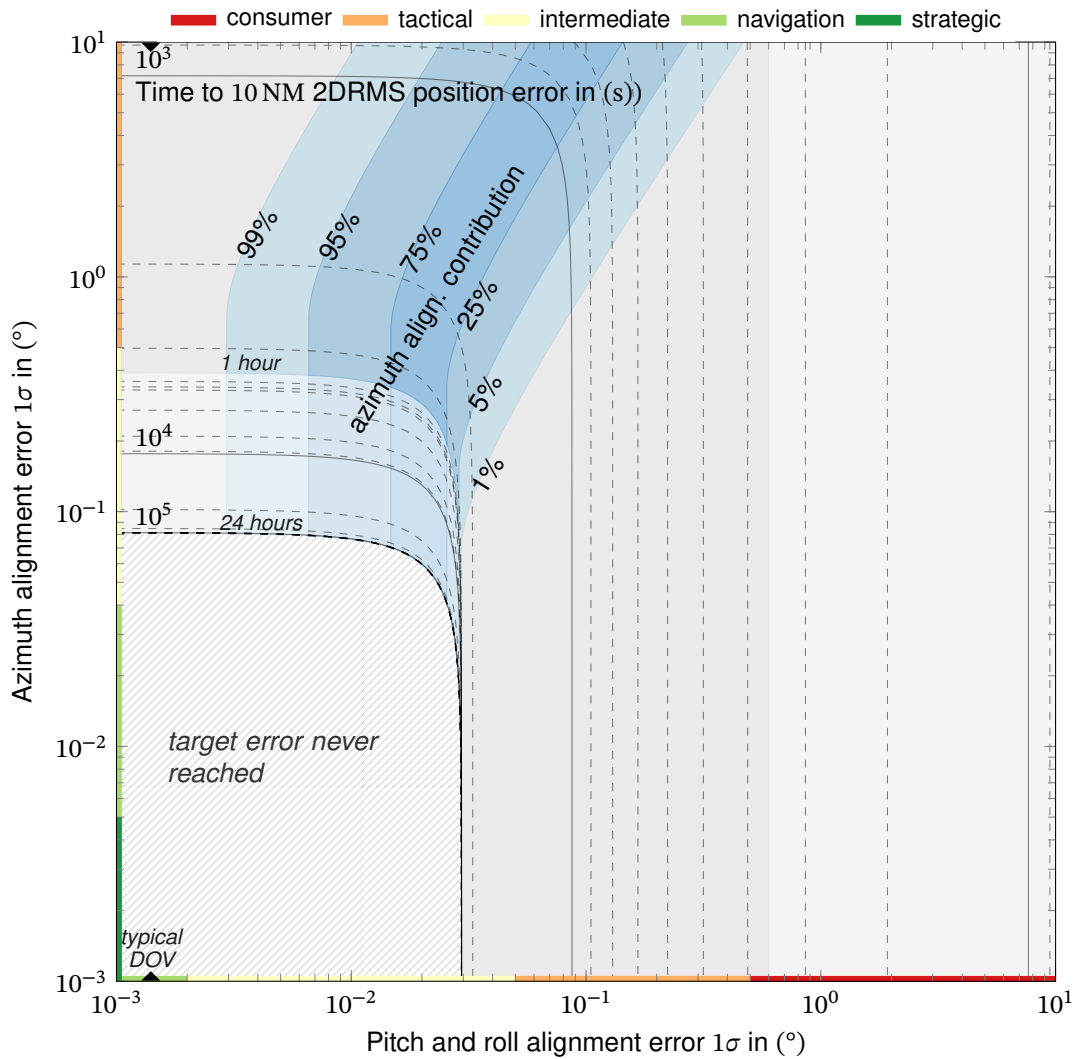


Figure 3.58.: Time to 10 NM 2DRMS position uncertainty from initial alignment errors at $\phi = 45^\circ$.

position error below this very low threshold, extreme alignment accuracy is required: leveling errors better than $1.5 \cdot 10^{-5}^\circ$ (0.05 asec) and azimuth errors below $5 \cdot 10^{-5}^\circ$ (0.18 asec). Such an extreme leveling alignment requires the consideration of the gravity's DoV. Still, as marked in the chart, the uncertainty of typical global gravity models like the [EGM2008](#) is magnitudes higher than the required alignment accuracy. This poses, for example, a problem to the proposed ultra accurate quantum inertial navigation systems that shall have a position drift of only a few meters per day. Alignment to that accuracy level requires additional aiding, e.g., alignment to fixed-stars.

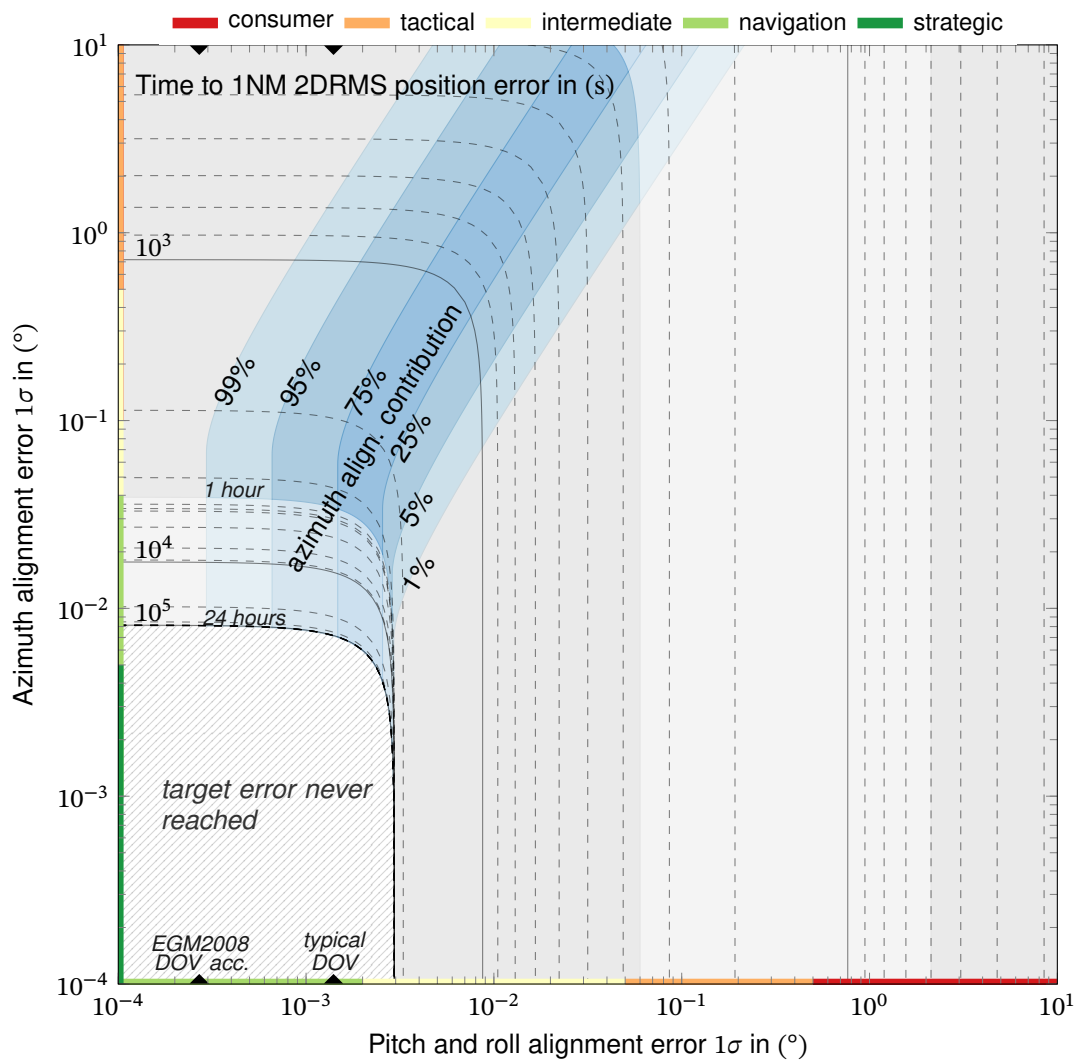


Figure 3.59.: Time to 1 NM 2DRMS position uncertainty from initial alignment errors at $\phi = 45^\circ$.

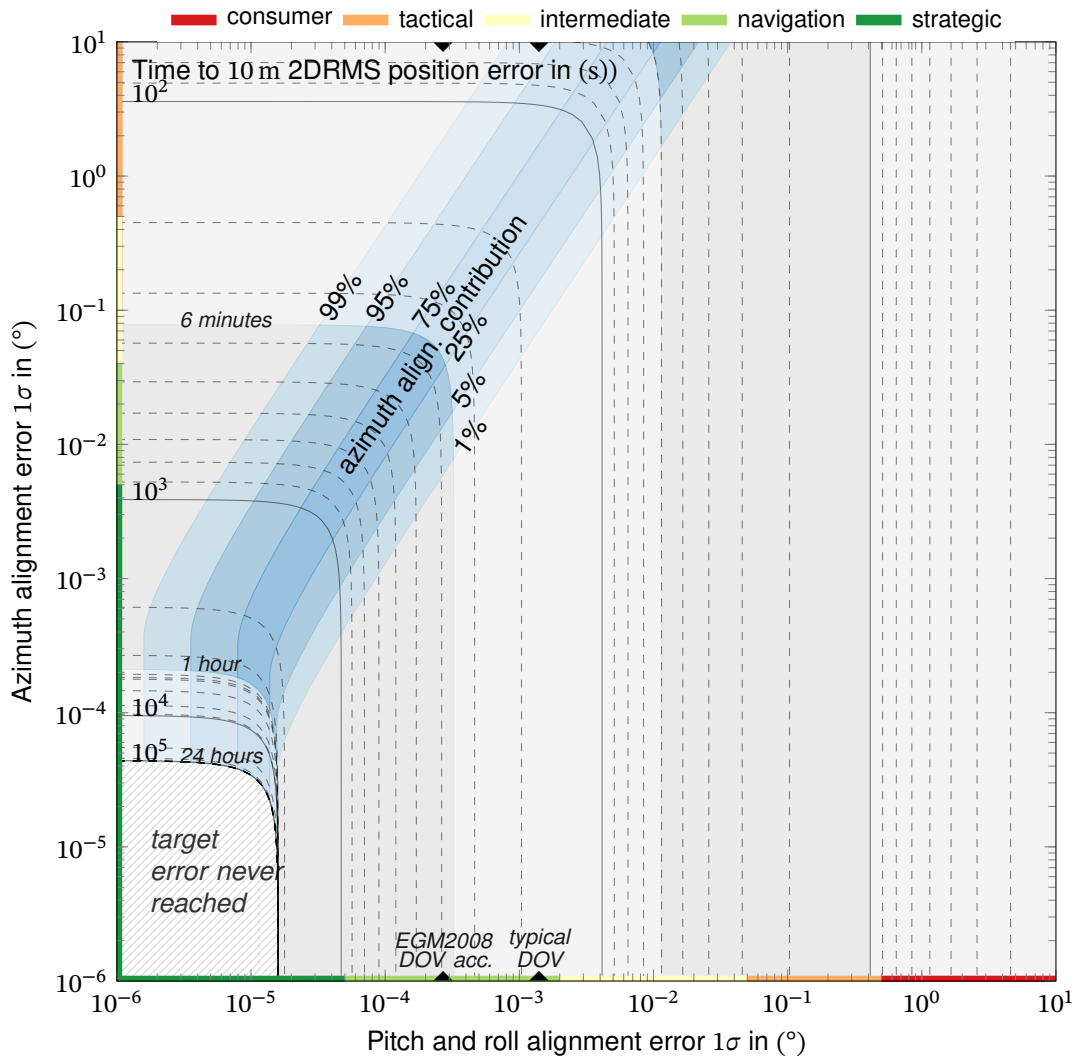


Figure 3.60.: Time to 10 m 2DRMS position uncertainty from initial alignment errors at $\phi = 45^\circ$.

3.4.3.4. Position Uncertainty from IMU bias-like errors

The time to a 2DRMS horizontal position error of the different thresholds is illustrated in the [Figure 3.61](#) to [Figure 3.63](#). The horizontal position error as DRMS from IMU biases has been calculated using the step responses from [Subsection D.1.3](#):

$$\text{DRMS} = \sqrt{\text{DRMS}_{\text{acc}}^2 + \text{DRMS}_{\text{gyro}}^2} \quad (3.127)$$

$$\text{DRMS}_{\text{acc}}^2 = [h_{1,8}^2 + h_{2,8}^2 + h_{1,9}^2 + h_{2,9}^2 + h_{1,10}^2 + h_{2,10}^2] \sigma_{\text{acc}}^2 \quad (3.128)$$

$$\text{DRMS}_{\text{gyro}}^2 = [h_{1,11}^2 + h_{2,11}^2 + h_{1,12}^2 + h_{2,12}^2 + h_{1,13}^2 + h_{2,13}^2] \sigma_{\text{gyro}}^2 \quad (3.129)$$

Note that the sensor bias uncertainty in this context represents a lumped-sum of all residual bias-like errors left after potential compensation, respectively, in-field calibration.

All three charts share a common shape: For short times (upper right), the iso-contribution lines are a straight diagonal that indicates a similar sensitivity of the position error to accelerometer and gyroscope errors. At around half a Schuler period (≈ 2500 s), they bend towards the accelerometer error axis. From this point on, the accelerometer errors have no effect anymore, and the gyroscope errors dominate the position error. The actual location of this bend is different for each graph, so it depends on the targeted error threshold.

Several important indicative model values and limitations have been added to the axes to support the assessment of the sensor error magnitudes. Note that this is slightly inconsistent, as the axes represent sensor bias uncertainties (1σ). The nominal WGS84 Earth angular rate of $7.292\,115 \cdot 10^{-5}$ rad/s [50] and the magnitude of its variation around $1 \cdot 10^{-4}$ °/h [93] have been added to the gyroscope error axis. Additional model thresholds have been added to the accelerometer bias axis. The error between the normal gravity formula (Sogmiliana) and the measured gravity is called gravity anomaly [94, p. 151]. According to the [EGM2008](#), the gravity anomaly ranges from -361.8 mGal to 868.4 mGal with a global RMS of 34.5 mGal [92]. An indicative gravity anomaly value of 100 mGal has been added to the axes. Additionally, the [EGM2008](#)'s typical accuracy of 2.5 mGal has been added to indicate its limitations. For even better accelerometers, even the moon's and sun's tidal forces of about 0.33 mGal [95, p. 127] becomes relevant.

For a large error threshold, here 10 NM as illustrated in [Figure 3.61](#), the threshold is only reached after relatively long times. As stated before, the gyroscope errors dominate in the long term. In this case, this can also be seen in the position of the bend at relatively poor IMU grades. Assuming a sufficiently accurate gyroscope, the graph indicates that even an intermediate grade accelerometer would allow inertial navigation within 10 NM position error at extremely long times like one year.

For a position error threshold of 1 NM (see [Figure 3.62](#)), the characteristic bend moves further towards better gyro and accelerometer grades. As 1 NM is the industry reference for comparing inertial navigation systems, additional sensor grade labels have been added to the corresponding time iso-lines. For the gyroscope errors, these labels match the typical

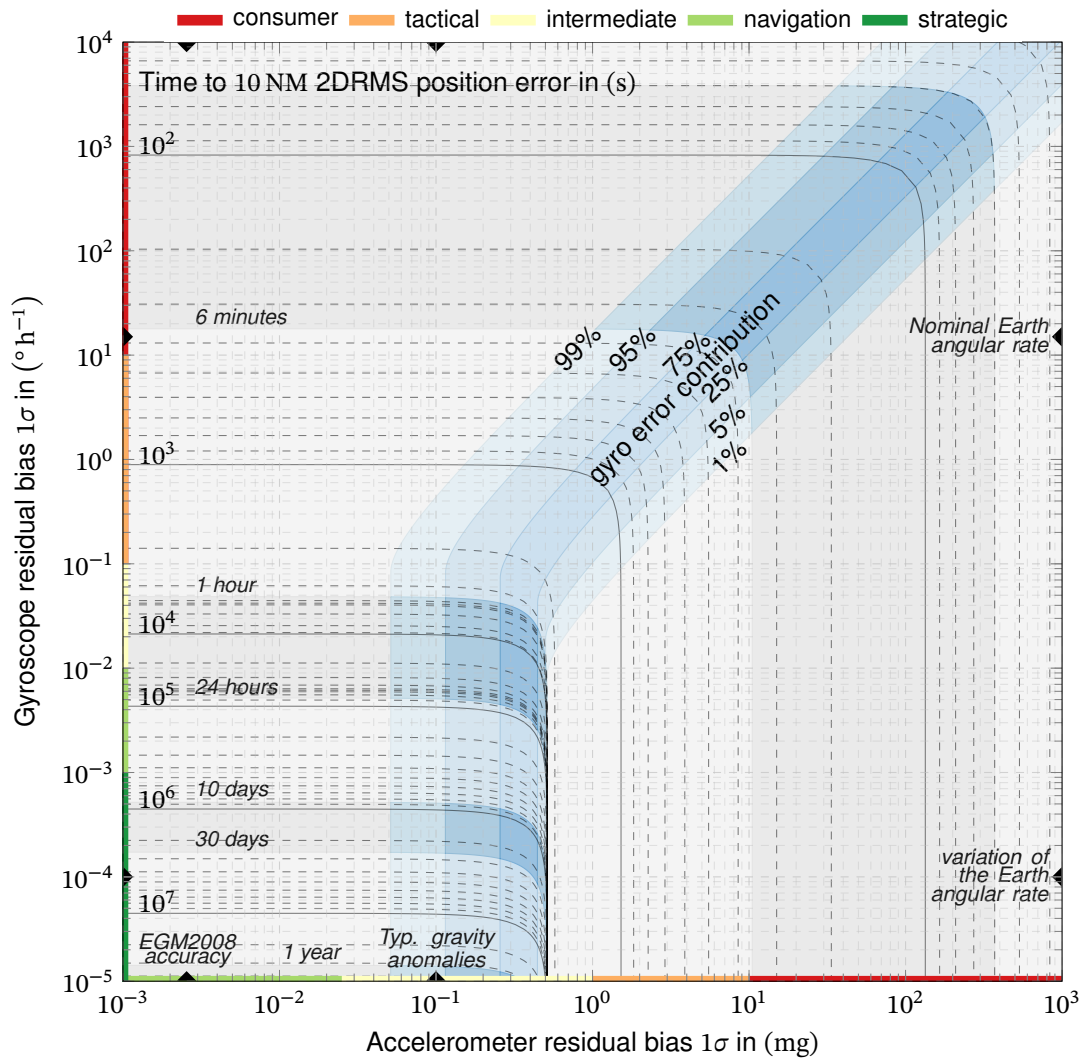


Figure 3.61.: Time to 10 NM 2DRMS position uncertainty from IMU bias-like errors at $\phi = 45^\circ$.

grade definitions quite well, e.g., a 1 NM per hour system fits perfectly within the navigation grade range. However, the typical grade definitions do not match the accelerometer errors. At least for the position error from bias-like errors, the industry definitions seem to overrate the contribution of the accelerometer error. Considering that a stationary vehicle or at least a very low dynamics was assumed within this chapter, the more conservative definition of accelerometer grades may be justified.

The corresponding graph for a position error threshold of 10 m is given in Figure 3.63. For such a small threshold, the characteristic bend at 2500 s is only reached by highly accurate sensors. Consequently, the position error is similarly sensitive to accelerometer and gyroscope errors for a wide range.

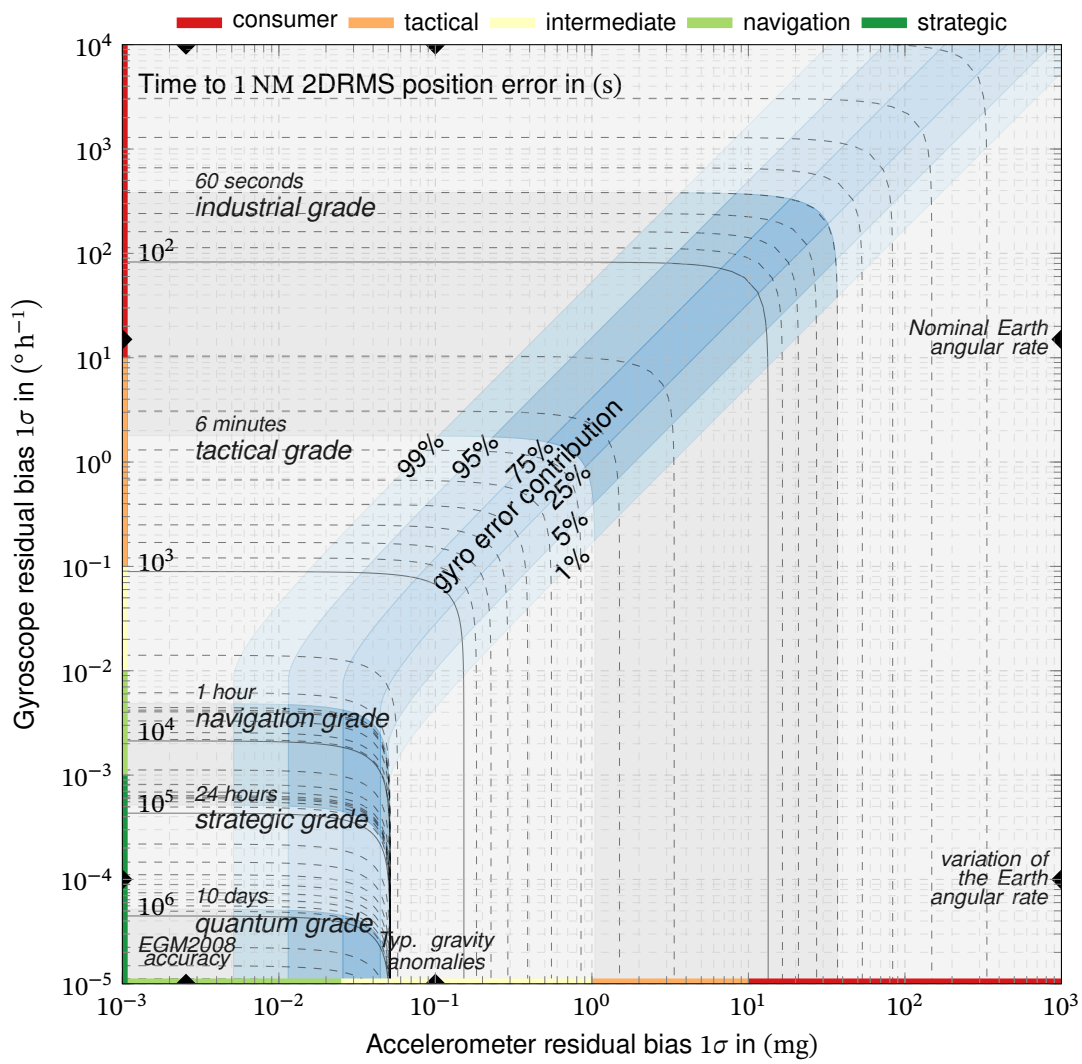


Figure 3.62.: Time to 1 NM 2DRMS position uncertainty from IMU bias-like errors at $\phi = 45^{\circ}$.

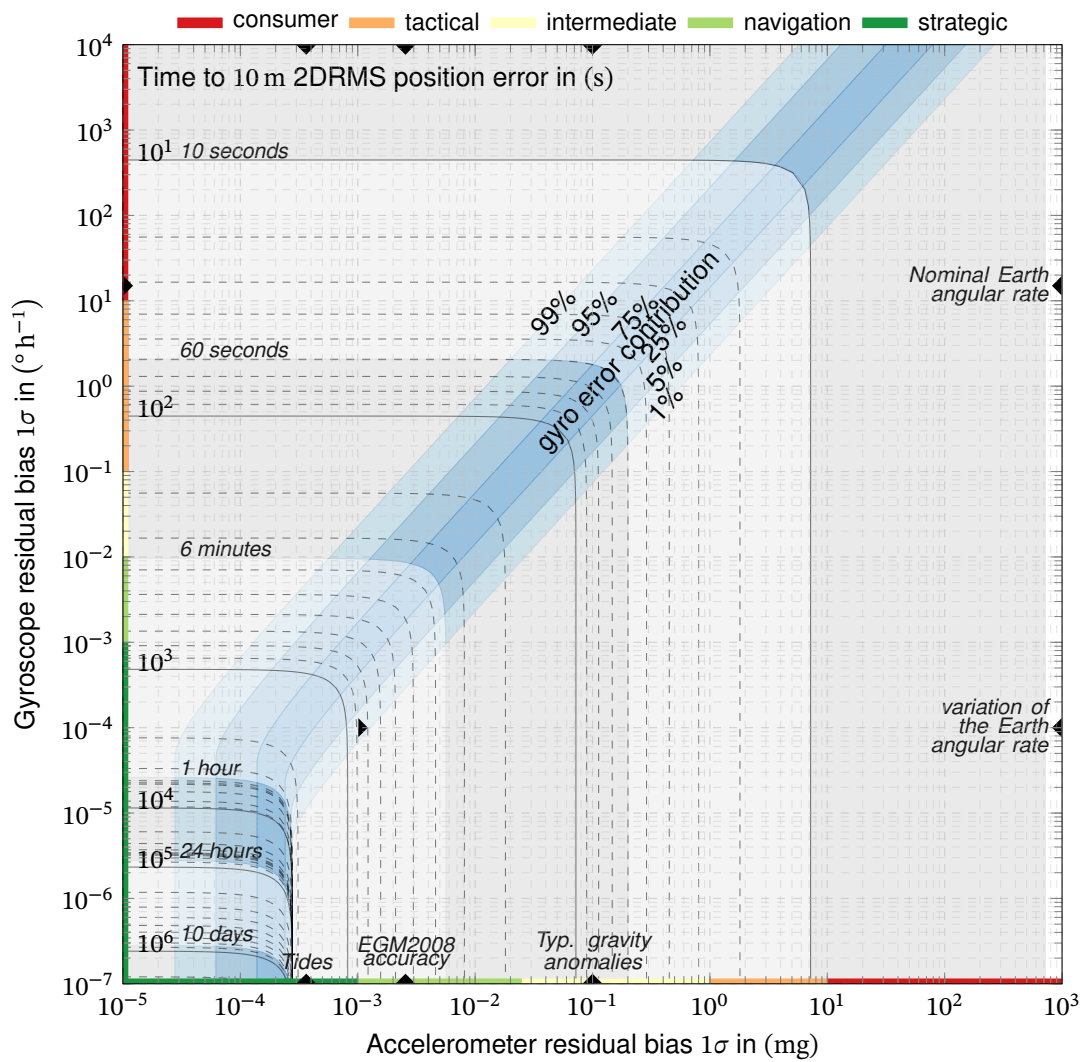


Figure 3.63.: Time to 10 m 2DRMS position uncertainty from IMU bias-like errors at $\phi = 45^{\circ}$.

3.4.3.5. Position Uncertainty from IMU white Gaussian noise

Analogously to the position uncertainty charts for constant errors, the position uncertainty charts are created for WGN input. The analysis focuses on velocity and angular random walk noise, since these are the most prominent noise terms, typically given in data sheets. Using the impulse responses from Section E.2 and the analytical integrals (3.91) to (3.93), the DRMS position uncertainty is determined from:

$$\text{DRMS} = \sqrt{\text{DRMS}_{\text{acc}}^2 + \text{DRMS}_{\text{gyro}}^2} \quad (3.130)$$

$$\text{DRMS}_{\text{acc}}^2 = [k_{1,8} + k_{2,8} + k_{1,9} + k_{2,9} + k_{1,10} + k_{2,10}] \sigma_{\text{acc}}^2 \quad (3.131)$$

$$\text{DRMS}_{\text{gyro}}^2 = [k_{1,11} + k_{2,11} + k_{1,12} + k_{2,12} + k_{1,13} + k_{2,13}] \sigma_{\text{gyro}}^2 \quad (3.132)$$

The time to a given position uncertainty threshold has been visualized for a threshold of 10 NM (Figure 3.64), 1 NM (Figure 3.65) and 10 m (Figure 3.66).

The charts are characterized by a distinct shape of the error contribution iso-lines. For short to medium times of several Schuler periods, the time to the position threshold is dominated by the Schuler oscillations. From about 4 hours, the results are dominated by linear error growth. This behavior is reflected in the change of the slope of the error contribution lines after about one hour.

Looking at the 1 NM plot Figure 3.65, one can see that the grade labels of typical commercially available gyroscopes match the proposed sensor grade definitions of this thesis quite well. However, the market-available accelerometers provide much better noise characteristics than necessary compared to the corresponding gyro performance.

For example, to achieve typical navigation grade performance at 1 NM per hour of drift, a maximum angular random walk of about $0.004^\circ/\sqrt{\text{h}}$ is required, which is met by off-the-shelf navigation grade gyros. For the acceleration sensors, however, only a velocity random walk of $3 \text{ mg}/\sqrt{\text{Hz}}$ is required, which is already achieved by good consumer-grade or poor tactical grade accelerometers. Optical gyroscopes are subject to the shot noise fundamental limit, which sets a theoretical limit to their angular random walk [22, p. 173]. Still, in [96] a FOG with an angular random walk of $38 \cdot 10^{-6}^\circ/\sqrt{\text{h}}$ has been demonstrated. From Figure 3.66, it can be seen that such a low noise would allow a drift of only 10 m in 10 days. In theory, a deployable FOG could achieve $1 \cdot 10^{-6}^\circ/\sqrt{\text{h}}$, while an extremely large RLG of 4 m diameter could achieve even $0.1 \cdot 10^{-6}^\circ/\sqrt{\text{h}}$ [96]. In practice, optical gyroscopes will not get below this threshold, and another sensor technology will be required to improve navigation performance even further.

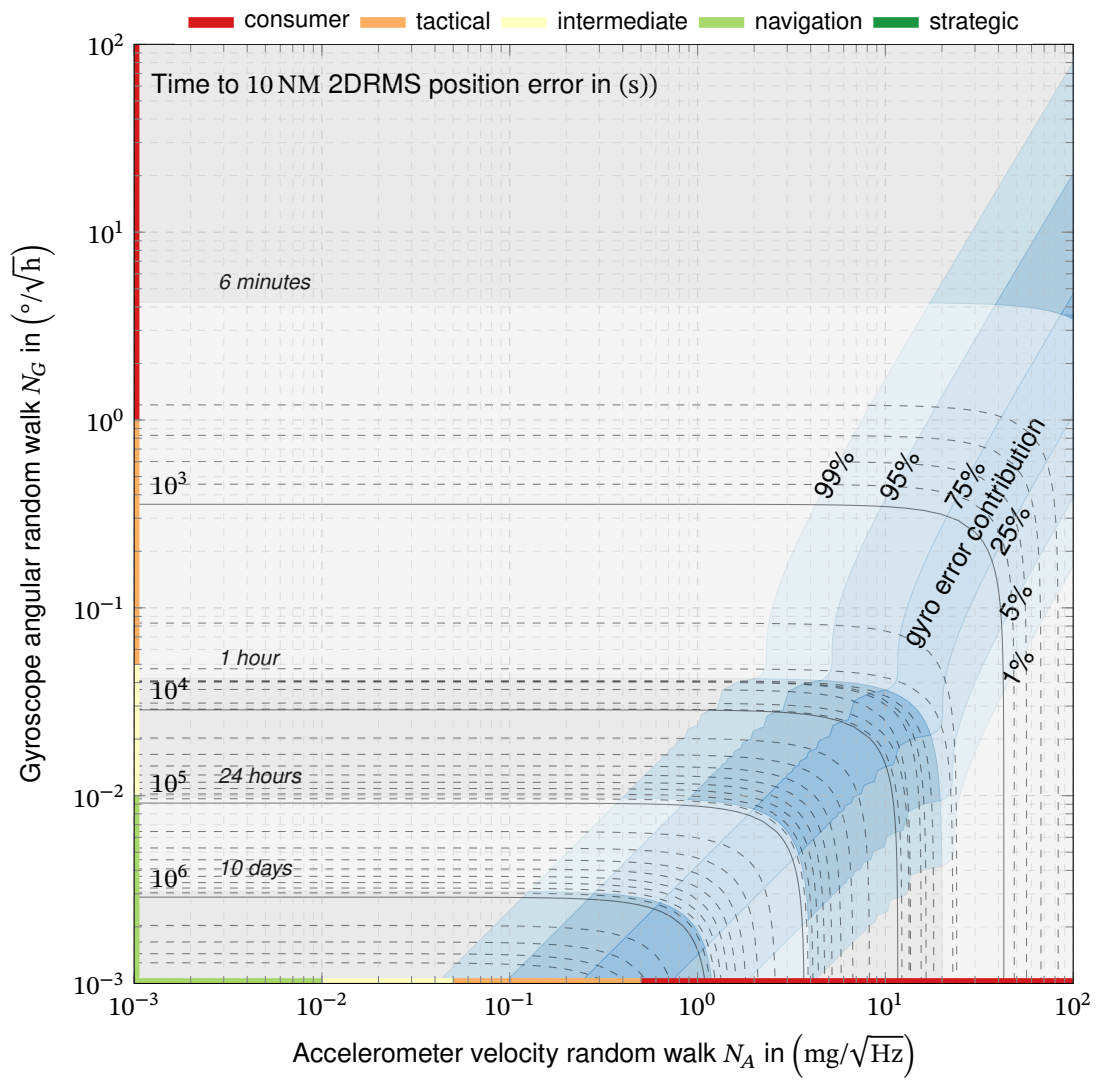


Figure 3.64.: Time to 10 NM 2DRMS position uncertainty from IMU white Gaussian noise at $\phi = 45^\circ$.

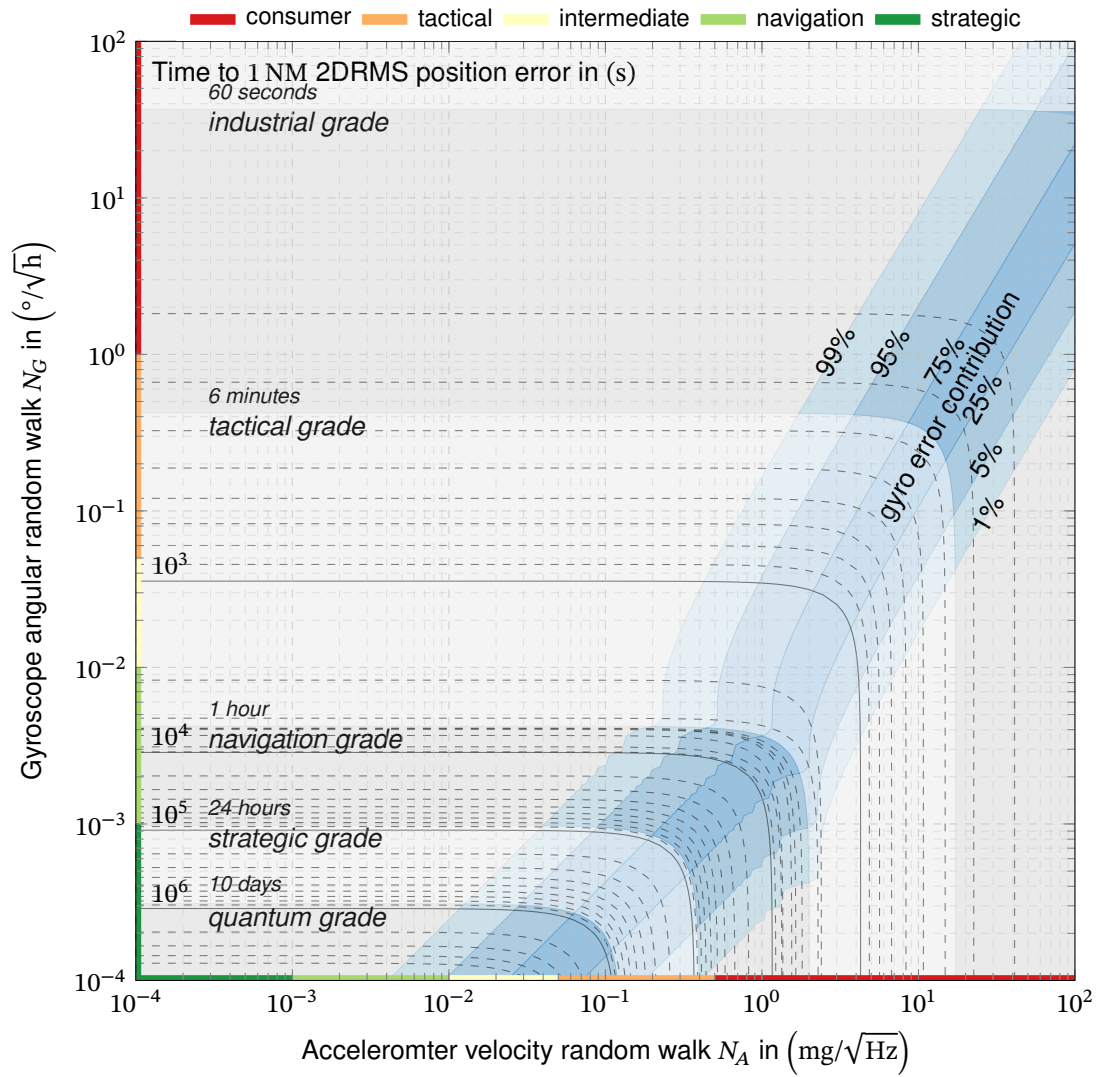


Figure 3.65.: Time to 1 NM 2DRMS position uncertainty from IMU white Gaussian noise at $\phi = 45^\circ$.

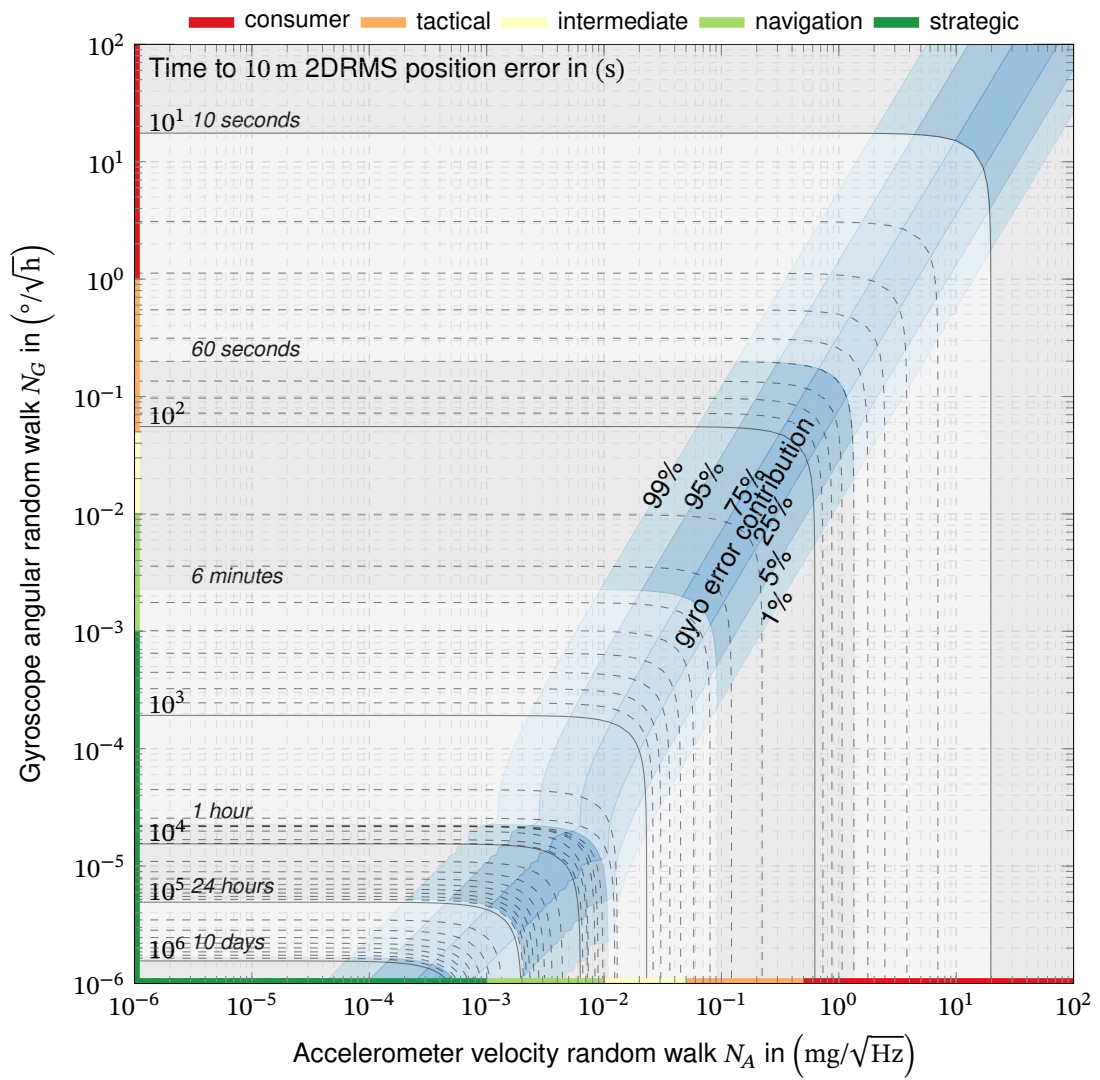


Figure 3.66.: Time to 10 m 2DRMS position uncertainty from IMU white Gaussian noise at $\phi = 45^\circ$.

3.4.4. Quantitative Performance Prediction Schemes

As an alternative to the performance prediction charts above, an error budget for inertial navigation can also be directly built from the tabulated step and impulse responses from Annex D A calculation scheme to determine the north and east position uncertainty as well as the DRMS value at time t is given in Table 3.5.

The error response to the inputs can either be calculated using the tables in Annex D or directly read off from Figure 3.7, Figure 3.9 and Figure 3.12, as well as Figure 3.25. Note that these plots are already scaled north and east position error so that calculations (F) and (G) need to be omitted in that case. It is up to the user whether the actual error at time t is determined or the maximum error reached up to time t .

The orientation uncertainty can be predicted by using Table 3.7. Analog to the position and velocity errors, the sensitivity to the different input errors can be read from Figure 3.18, Figure 3.19, Figure 3.20, Figure 3.22, Figure 3.23 and for noise like errors from Figure 3.28 and Figure 3.29. Due to the underlying linearized error dynamics, this propagation scheme loses its validity for orientation angle standard deviations higher than about 10° .

In contrast to the direct numerical simulation of the scenario, the analytical approach provides insight into each error source's dynamics and contribution. From this, key performance parameters can be easily identified.

Table 3.5.: Position Uncertainty Prediction Scheme.

Error source				Latitude uncertainty			Longitude uncertainty			DRMS		
Description	Symbol	1 σ (A)	Unit	from Annex D	$h(t)$ (B)	$h(t)^2\sigma^2$ (C) = (A) ² (B) ²	from Annex D	$h(t)$ (D)	$h(t)^2\sigma^2$ (E) = (A) ² (D) ²	North var. (F) = (C) _M ²	East var. (G) = (E) _N ² cos ² ϕ	DRMS (H) = $\sqrt{(F) + (G)}$
Init. Latitude	$\delta\phi_0$		rad	$h_{1,1}(t)$			$h_{2,1}(t)$					
Init. Longitude	$\delta\lambda_0$		rad	$h_{1,2}(t)$	0	0	$h_{2,2}(t)$	1				
Init. North Vel.	$\delta v_{n,0}$		m/s	$h_{1,3}(t)$			$h_{2,3}(t)$					
Init. East Vel.	$\delta v_{e,0}$		m/s	$h_{1,4}(t)$			$h_{2,4}(t)$					
Roll Alignment	$\delta\Phi_0$		rad	$h_{1,5}(t)$			$h_{2,5}(t)$					
Pitch Alignment	$\delta\Theta_0$		rad	$h_{1,6}(t)$			$h_{2,6}(t)$					
Yaw Alignment	$\delta\Psi_0$		rad	$h_{1,7}(t)$			$h_{2,7}(t)$					
Accelerometer Bias	$\delta f_{b,n,0}$		m/s ²	$h_{1,8}(t)$			$h_{2,8}(t)$					
	$\delta f_{b,e,0}$		m/s ²	$h_{1,9}(t)$			$h_{2,9}(t)$					
Gyroscope Bias	$\delta\omega_{ib,n,0}$		rad/s	$h_{1,11}(t)$			$h_{2,11}(t)$					
	$\delta\omega_{ib,e,0}$		rad/s	$h_{1,12}(t)$			$h_{2,12}(t)$					
	$\delta\omega_{ib,d,0}$		rad/s	$h_{1,13}(t)$			$h_{2,13}(t)$					
Description	Symbol	N (A)		$\int_0^t g^2(t-\tau)d\tau$ (B)	(C) = (A) ² (B)		$\int_0^t g^2(t-\tau)d\tau$ (D)	(E) = (A) ² (D)	North var. (F) = (C) _M ²	East var. (G) = (E) _N ² cos ² ϕ	DRMS (H) = $\sqrt{(F) + (G)}$	
Velocity Random Walk	$N_{f_{b,n}}$		m/(s ² $\sqrt{\text{Hz}}$)	$g_{1,8}$			$g_{2,8}$					
	$N_{f_{b,e}}$		m/(s ² $\sqrt{\text{Hz}}$)	$g_{1,9}$			$g_{2,9}$					
Angular Random Walk	$N_{\omega_{ib,n}}$		rad/(s $\sqrt{\text{Hz}}$)	$g_{1,11}$			$g_{2,11}$					
	$N_{\omega_{ib,e}}$		rad/(s $\sqrt{\text{Hz}}$)	$g_{1,12}$			$g_{2,12}$					
	$N_{\omega_{ib,d}}$		rad/(s $\sqrt{\text{Hz}}$)	$g_{1,13}$			$g_{2,13}$					
Acceleration Random Walk	$K_{f_{b,n}}$		m/s ² $\sqrt{\text{Hz}}$	$g_{K,1,8}$			$g_{K,2,8}$					
	$K_{f_{b,e}}$		m/s ² $\sqrt{\text{Hz}}$	$g_{K,1,9}$			$g_{K,2,9}$					
Rate Random Walk	$K_{\omega_{ib,n}}$		rad/s $\sqrt{\text{Hz}}$	$g_{K,1,11}$			$g_{K,2,11}$					
	$K_{\omega_{ib,e}}$		rad/s $\sqrt{\text{Hz}}$	$g_{K,1,12}$			$g_{K,2,12}$					
	$K_{\omega_{ib,d}}$		rad/s $\sqrt{\text{Hz}}$	$g_{K,1,13}$			$g_{K,2,13}$					
Accelerometer Bias Instability	B_{f_b}		m/s ²	<i>no analytical solution</i>								
Gyro Bias Instability	$B_{\omega_{ib}}$		rad/s	<i>no analytical solution</i>								
Acceleration Ramp Noise	$R_{f_{b,n}}$		m/s ³	<i>no analytical solution</i>								
Rate Ramp Noise	$R_{\omega_{ib,n}}$		rad/s ²	<i>no analytical solution</i>								
Velocity Quantization Noise	$Q_{f_{b,n}}$		m/s	$g_{Q,1,8}$			$g_{Q,2,8}$					
	$Q_{f_{b,e}}$		m/s	$g_{Q,1,9}$			$g_{Q,2,9}$					
Angular Quantization Noise	$Q_{\omega_{ib,n}}$		rad	$g_{Q,1,11}$			$g_{Q,2,11}$					
	$Q_{\omega_{ib,e}}$		rad	$g_{Q,1,12}$			$g_{Q,2,12}$					
	$Q_{\omega_{ib,d}}$		rad	$g_{Q,1,13}$			$g_{Q,2,13}$					
Σ											-	

Table 3.6.: Velocity Uncertainty Prediction Scheme.

Error source				North velocity uncertainty			East velocity uncertainty			RMS
Description	Symbol	1σ (A)	Unit	from Annex D	$h(t)$ (B)	$h(t)^2\sigma^2$ (C) = (A) ² (B) ²	from Annex D	$h(t)$ (D)	$h(t)^2\sigma^2$ (E) = (A) ² (D) ²	(F) = $\sqrt{(C) + (E)}$
Init. Latitude	$\delta\phi_0$		rad	$h_{3,1}(t)$			$h_{4,1}(t)$			
Init. Longitude	$\delta\lambda_0$		rad	$h_{3,2}(t)$		0	$h_{4,2}(t)$			
Init. North Vel.	$\delta v_{n,0}$		m/s	$h_{3,3}(t) =$			$h_{4,3}(t) =$			
Init. East Vel.	$\delta v_{e,0}$		m/s	$h_{3,4}(t)$			$h_{4,4}(t)$			
Roll Alignment	$\delta\Phi_0$		rad	$h_{3,5}(t)$			$h_{4,5}(t)$			
Pitch Alignment	$\delta\Theta_0$		rad	$h_{3,6}(t)$			$h_{4,6}(t)$			
Yaw Alignment	$\delta\Psi_0$		rad	$h_{3,7}(t)$			$h_{4,7}(t)$			
Accelerometer Bias	$\delta f_{b,n,0}$		m/s ²	$h_{3,8}(t)$			$h_{4,8}(t)$			
	$\delta f_{b,e,0}$		m/s ²	$h_{3,9}(t)$			$h_{4,9}(t)$			
Gyroscope Bias	$\delta\omega_{ib,n,0}$		rad/s	$h_{3,11}(t)$			$h_{4,11}(t)$			
	$\delta\omega_{ib,e,0}$		rad/s	$h_{3,12}(t)$			$h_{4,12}(t)$			
	$\delta\omega_{ib,d,0}$		rad/s	$h_{3,13}(t)$			$h_{4,13}(t)$			
Description	Symbol	N (A)		$\int_0^t g^2(t-\tau)d\tau$ (B)	(C) = (A) ² (B)		$\int_0^t g^2(t-\tau)d\tau$ (D)	(E) = (A) ² (D)	(F) = $\sqrt{(C) + (E)}$	
Velocity Random Walk	$N_{f_{b,n}}$		m/(s ² $\sqrt{\text{Hz}}$)	$g_{3,8}$			$g_{4,8}$			
	$N_{f_{b,e}}$		m/(s ² $\sqrt{\text{Hz}}$)	$g_{3,9}$			$g_{4,9}$			
Angular Random Walk	$N_{\omega_{ib,n}}$		rad/(s $\sqrt{\text{Hz}}$)	$g_{3,11}$			$g_{4,11}$			
	$N_{\omega_{ib,e}}$		rad/(s $\sqrt{\text{Hz}}$)	$g_{3,12}$			$g_{4,12}$			
Acceleration Random Walk	$N_{\omega_{ib,d}}$		rad/(s $\sqrt{\text{Hz}}$)	$g_{3,13}$			$g_{4,13}$			
	$K_{f_{b,n}}$		m/(s ² $\sqrt{\text{Hz}}$)	$g_{3,8}$			$g_{4,8}$			
Rate Random Walk	$K_{f_{b,e}}$		m/s ² $\sqrt{\text{Hz}}$	$g_{K,3,9}$			$g_{K,4,9}$	<y		
	$K_{\omega_{ib,n}}$		rad/s $\sqrt{\text{Hz}}$	$g_{K,3,11}$			$g_{K,4,11}$			
	$K_{\omega_{ib,e}}$		rad/s $\sqrt{\text{Hz}}$	$g_{K,3,12}$			$g_{K,4,12}$			
	$K_{\omega_{ib,d}}$		rad/s $\sqrt{\text{Hz}}$	$g_{K,3,13}$			$g_{K,4,13}$			
Accelerometer Bias Instability	B_{f_b}		m/s ²	<i>no analytical solution</i>						
Gyro Bias Instability	$B_{\omega_{ib}}$		rad/s	<i>no analytical solution</i>						
Acceleration Ramp Noise	R_{f_b}		m/s ³	<i>no analytical solution</i>						
Rate Ramp Noise	$R_{\omega_{ib}}$		rad/s ²	<i>no analytical solution</i>						
Velocity Quantization Noise	$Q_{f_{b,n}}$		m/s	$g_{Q,3,8}$			$g_{Q,4,8}$			
	$Q_{f_{b,e}}$		m/s	$g_{Q,3,9}$			$g_{Q,4,9}$	<y		
Angular Quantization Noise	$Q_{\omega_{ib,n}}$		rad	$g_{Q,3,11}$			$g_{Q,4,11}$			
	$Q_{\omega_{ib,e}}$		rad	$g_{Q,3,12}$			$g_{Q,4,12}$			
	$Q_{\omega_{ib,d}}$		rad	$g_{Q,3,13}$			$g_{Q,4,13}$			
Σ										

Table 3.7.: Orientation Uncertainty Prediction Scheme.

Error source				Roll angle uncertainty			Pitch angle uncertainty			Yaw angle uncertainty		
Description	Symbol	1 σ (A)	Unit	from Annex D	$h(t)$ (B)	$h(t)^2\sigma^2$ (C) = (A) ² (B) ²	from Annex D	$h(t)$ (D)	$h(t)^2\sigma^2$ (E) = (A) ² (D) ²	from Annex D	$h(t)$ (F)	$h(t)^2\sigma^2$ (G) = (A) ² (F) ²
Init. Latitude	$\delta\phi_0$		rad	$h_{5,1}(t)$			$h_{6,1}(t)$			$h_{7,1}(t)$		
Init. Longitude	$\delta\lambda_0$		rad	$h_{5,2}(t)$	0		$h_{6,2}(t)$			$h_{7,2}(t)$		
Init. North Vel.	$\delta v_{n,0}$		m/s	$h_{5,3}(t)$			$h_{6,3}(t)$			$h_{7,3}(t)$		
Init. East Vel.	$\delta v_{e,0}$		m/s	$h_{5,4}(t)$			$h_{6,4}(t)$			$h_{7,4}(t)$		
Roll Alignment	$\delta\Phi_0$		rad	$h_{5,5}(t)$			$h_{6,5}(t)$			$h_{7,5}(t)$		
Pitch Alignment	$\delta\Theta_0$		rad	$h_{5,6}(t)$			$h_{6,6}(t)$			$h_{7,6}(t)$		
Yaw Alignment	$\delta\Psi_0$		rad	$h_{5,7}(t)$			$h_{6,7}(t)$			$h_{7,7}(t)$		
Accelerometer Bias	$\delta f_{b,n,0}$		m/s ²	$h_{5,8}(t)$			$h_{6,8}(t)$			$h_{7,8}(t)$		
	$\delta f_{b,e,0}$		m/s ²	$h_{5,9}(t)$			$h_{6,9}(t)$			$h_{7,9}(t)$		
Gyroscope Bias	$\delta\omega_{ib,n,0}$		rad/s	$h_{5,11}(t)$			$h_{6,11}(t)$			$h_{7,11}(t)$		
	$\delta\omega_{ib,e,0}$		rad/s	$h_{5,12}(t)$			$h_{6,12}(t)$			$h_{7,12}(t)$		
	$\delta\omega_{ib,d,0}$		rad/s	$h_{5,13}(t)$			$h_{6,13}(t)$			$h_{7,13}(t)$		
Description	Symbol	N (A)		$\int_0^t g^2(t-\tau)d\tau$ (B)	(C) = (A) ² (B)		$\int_0^t g^2(t-\tau)d\tau$ (D)	(E) = (A) ² (D)		$\int_0^t g^2(t-\tau)d\tau$ (F)	(G) = (A) ² (F)	
Velocity Random Walk	$N_{f,b,n}$		m/(s ² $\sqrt{\text{Hz}}$)	$g_{5,8}$			$g_{6,8}$			$g_{7,8}$		
	$N_{f,b,e}$		m/(s ² $\sqrt{\text{Hz}}$)	$g_{5,9}$			$g_{6,9}$			$g_{7,9}$		
Angular Random Walk	$N_{\omega_{ib,n}}$		rad/(s $\sqrt{\text{Hz}}$)	$g_{5,11}$			$g_{6,11}$			$g_{7,11}$		
	$N_{\omega_{ib,e}}$		rad/(s $\sqrt{\text{Hz}}$)	$g_{5,12}$			$g_{6,12}$			$g_{7,12}$		
Acceleration Random Walk	$N_{\omega_{ib,d}}$		rad/(s $\sqrt{\text{Hz}}$)	$g_{5,13}$			$g_{6,13}$			$g_{7,13}$		
	$K_{f,b,n}$		m/(s ² $\sqrt{\text{Hz}}$)	$g_{K,5,8}$			$g_{K,6,8}$			$g_{K,7,8}$		
Rate Random Walk	$K_{f,b,e}$		m/(s ² $\sqrt{\text{Hz}}$)	$g_{K,5,9}$			$g_{K,6,9}$			$g_{K,7,9}$		
	$K_{\omega_{ib,n}}$		rad/(s $\sqrt{\text{Hz}}$)	$g_{K,5,11}$			$g_{K,6,11}$			$g_{K,7,11}$		
	$K_{\omega_{ib,e}}$		rad/(s $\sqrt{\text{Hz}}$)	$g_{K,5,12}$			$g_{K,6,12}$			$g_{K,7,12}$		
	$K_{\omega_{ib,d}}$		rad/(s $\sqrt{\text{Hz}}$)	$g_{K,5,13}$			$g_{K,6,13}$			$g_{K,7,13}$		
Accelerometer Bias Instability	$B_{f,b,n}$		m/s ²	<i>no analytical solution</i>								
Gyro Bias Instability	$B_{\omega_{ib,n}}$		rad/s	<i>no analytical solution</i>								
Acceleration Ramp Noise	$R_{f,b,n}$		m/s ³	<i>no analytical solution</i>								
Rate Ramp Noise	$R_{\omega_{ib,n}}$		rad/s ²	<i>no analytical solution</i>								
Velocity Quantization Noise	$Q_{f,b,n}$		m/s	$g_{Q,5,8}$			$g_{Q,6,8}$			$g_{Q,7,8}$		
	$Q_{f,b,e}$		m/s	$g_{Q,5,9}$			$g_{Q,6,9}$			$g_{Q,7,9}$		
Angular Quantization Noise	$Q_{\omega_{ib,n}}$		rad	$g_{Q,5,11}$			$g_{Q,6,11}$			$g_{Q,7,11}$		
	$Q_{\omega_{ib,e}}$		rad	$g_{Q,5,12}$			$g_{Q,6,12}$			$g_{Q,7,12}$		
	$Q_{\omega_{ib,d}}$		rad	$g_{Q,5,13}$			$g_{Q,6,13}$			$g_{Q,7,13}$		
Σ				-			-			-		

3.5. Validation of the Predicted Navigation Performance

3.5.1. General

This section analyzes the validity of the previously derived navigation performance prediction schemes and charts. The accuracy of the separate analytical responses to constant and noise-like errors is demonstrated by comparison to numerical simulation results in Annex E.1 and E.2. Still, these results are based on several assumptions, especially neglecting vehicle motion. The feasibility of these assumptions and the derived performance prediction charts and schemes are analyzed by comparison to Monte Carlo (MC) simulation results for real-world scenarios.

For the simulation, the constant initialization errors and sensor biases are randomized and applied to the reference trajectory. Additionally, noise is added to the error-free IMU measurements. The resulting sensor signals are fed to a vertically fixed strapdown algorithm. Here the propagated attitude is corrected every time step using the reference values. The strapdown equations are integrated numerically using a 4th order Runge-Kutta scheme.

As illustrated in Figure 3.67, the resulting state vector errors for each simulation run are calculated and incorporated into the mean and covariance estimate. Due to memory restrictions, the results of each MC run are not stored, but the stochastic properties are calculated iteratively. Finally, the mean and variance over all MC runs are stored and compared to the analytical prediction for each test case. Of course, analyzing a small set of scenarios and trajectories cannot provide a formal and general proof of feasibility. The validity of the approximations for similar scenarios and applications can be concluded by showing the feasibility of very typical and representative scenarios.

3.5.2. Case 1: General Aviation Aircraft

The first test case is based on a 90-minute long flight of a twin-prop general aviation aircraft. The underlying trajectory and associated ideal inertial sensor measurements have been created using the aerodynamic reference trajectory generation tool-chain developed by Lorenz Görcke [69]. The generated trajectory starts directly in the air and performs several loops over the Bavarian Alps. The flight path is depicted in Figure 3.68. The scenario has a total duration of 5400 s and is sampled at 2000 Hz. The trajectory represents a typical general aviation flight at low to medium dynamics, which is summarized in Table 3.8.

Table 3.8.: Parameters of the general aviation aircraft scenario.

Parameter	Value
Flight duration	01:30:00h
Maximum distance from start	68.92 km
Maximum velocity	92.13 m/s
Maximum acceleration	0.45 g
Maximum angular rates	11.18 °/s

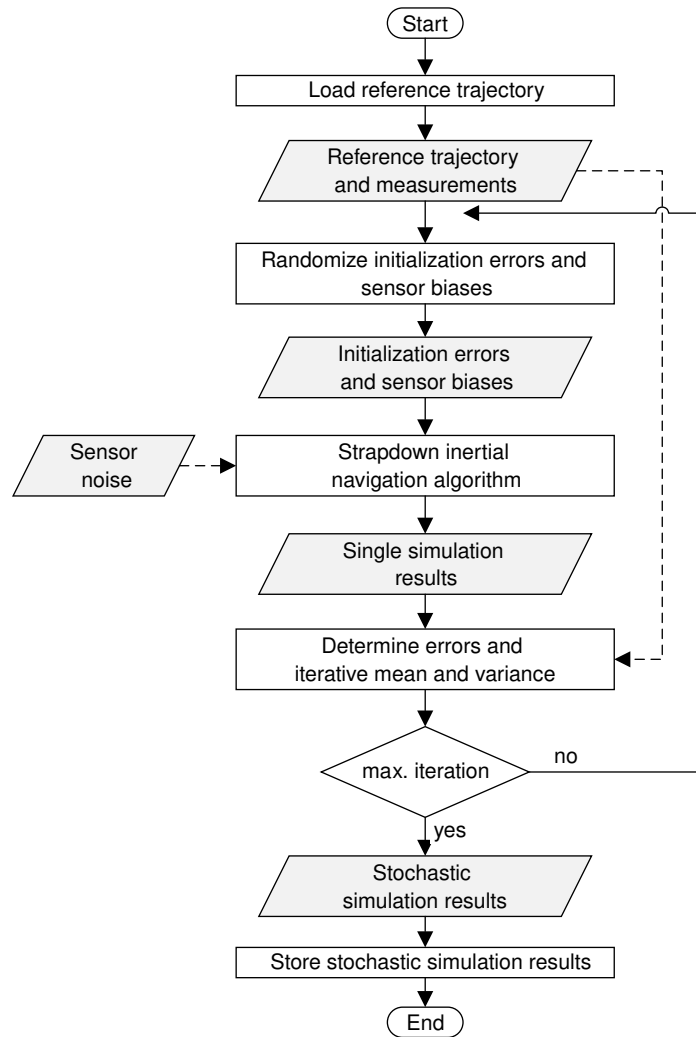


Figure 3.67.: Workflow of the Monte Carlo simulation to validate the navigation performance prediction schemes.

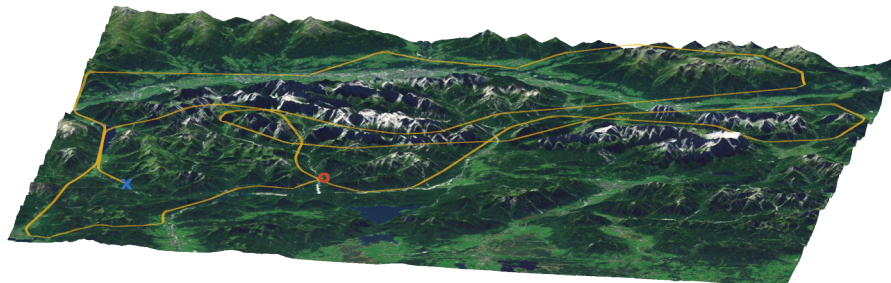


Figure 3.68.: Visualization of the simulated general aviation flightpath. The red circle demarks the start of the trajectory, the blue cross the end.

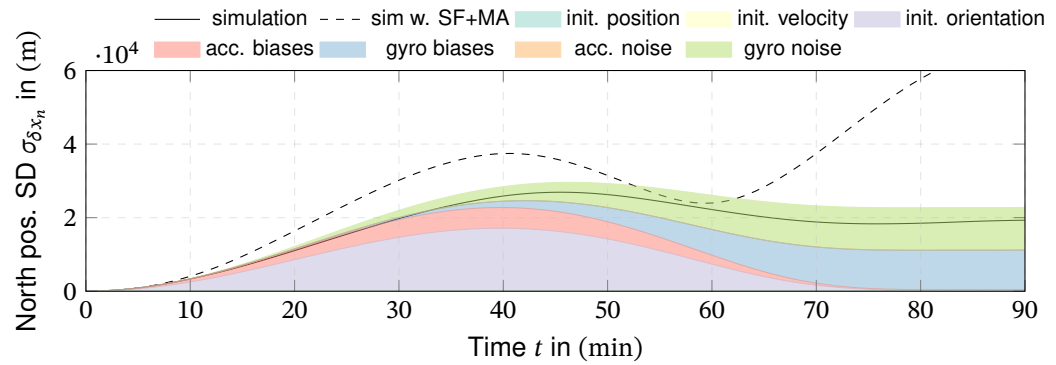
A Monte Carlo simulation with 1000 runs has been performed for this trajectory. Since the analytical prediction schemes do not consider the trajectory-dependent errors from sensor scale factor errors and misalignments, the MC simulation has been performed with and without these errors. The used error parameters are specified in Table 3.9. The analytically predicted navigation state uncertainty is determined from the step and noise responses analogously to 3.4.4. The resulting standard deviations of the navigation state errors are depicted in Figure 3.69 and Figure 3.70.

If SF and misalignment (MA) errors are neglected, the analytical predictions match the simulation results surprisingly well. The analytical solutions match the simulation results in magnitude but also correctly reproduce the error dynamics. Minor deviations can be attributed to the trajectory dependencies that are entirely neglected in the analytical prediction. Consequently, also the prediction cannot represent the effects of SF and MA errors. Although the magnitude of the simulation results with these errors cannot be predicted correctly, the underlying error dynamics can still be observed in the results. For the given test scenario, the scale factor error amplifies the position and velocity errors by a factor of about two. The trajectory dependency can also be observed in the orientation error results, which follow the aircraft's maneuvers.

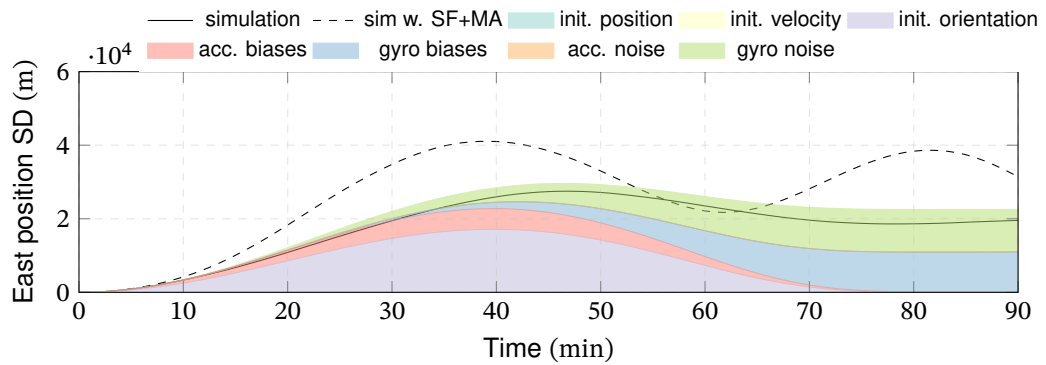
Table 3.9.: Specification of the input errors for the general aviation aircraft scenario simulation.

Parameter		Symbol	Value
Initialization errors (1σ)	Position	$\delta x_{n,0}, \delta x_{e,0}$	10 m
	Velocity	$\delta v_{n,0}, \delta v_{e,0}$	0.1 m/s
	Orientation	$\delta \Phi_0, \delta \Theta_0, \delta \Psi_0$	0.1°
Sensor bias (1σ)	Accelerometer	$\delta f_{b,x,0}, \delta f_{b,y,0}, \delta f_{b,z,0}$	1 mg
	Gyroscopes	$\delta \omega_{ib,x,0}, \delta \omega_{ib,y,0}, \delta \omega_{ib,z,0}$	0.1 °/h
Sensor SF Error (1σ)	Accelerometer	$S_{A,x}, S_{A,y}, S_{A,z}$	1500 ppm
	Gyroscopes	$S_{G,x}, S_{G,y}, S_{G,z}$	1500 ppm
Sensor MA (1σ)	Accelerometer	$M_{A,xy}, M_{A,xz}, M_{A,yx}, M_{A,yz}, \dots$	0.5 mrad
	Gyroscopes	$M_{G,xy}, M_{G,xz}, M_{G,yx}, M_{G,yz}, \dots$	0.5 mrad
Sensor noise	Accelerometer	$N_{acc,x}, N_{acc,y}, N_{acc,z}$	1 mg/ $\sqrt{\text{Hz}}$
	Gyroscope	$N_{gyr,x}, N_{gyr,y}, N_{gyr,z}$	0.1 °/ $\sqrt{\text{h}}$

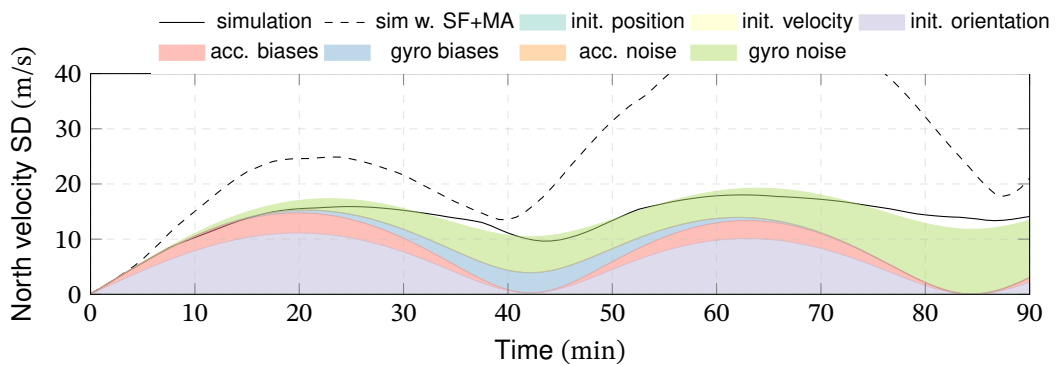
While the analytical prediction scheme yields accurate results, a less complex and faster prediction of the expectable order of magnitude of the errors is often favorable. Such an approach is given the charts of section 3.4.3. Of course, these charts only state the time to a given position error threshold for separate input errors. Due to that representation, the results cannot be easily summed up to incorporate multiple input errors. For this test-case a 2DRMS position error of 1 NM is reached after 4:20 minutes. For the specified sensor noise, a time of approximately 8 min can be read off from Figure 3.65. For the alignment errors Figure 3.59 indicates a time of about 5:00 minutes, for the sensor biases a value of about 6:30 minutes can be read off from Figure 3.62. The worst-case value determined from the charts provides a



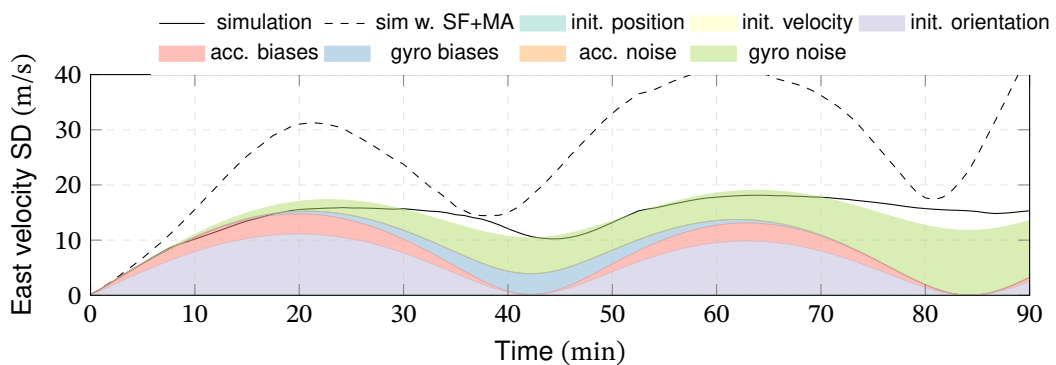
(a) North position.



(b) East position.

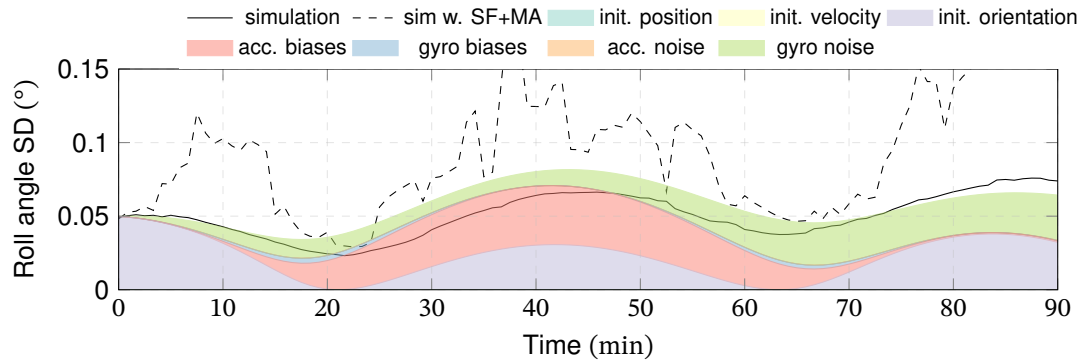


(c) North velocity.

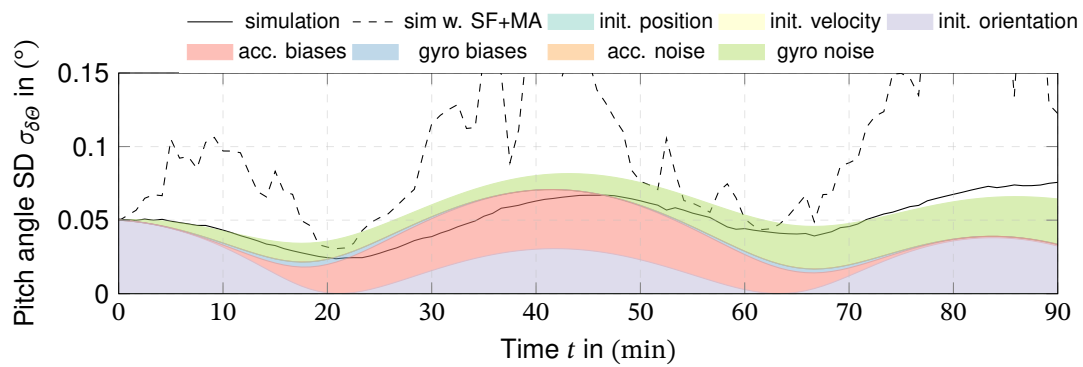


(d) East velocity.

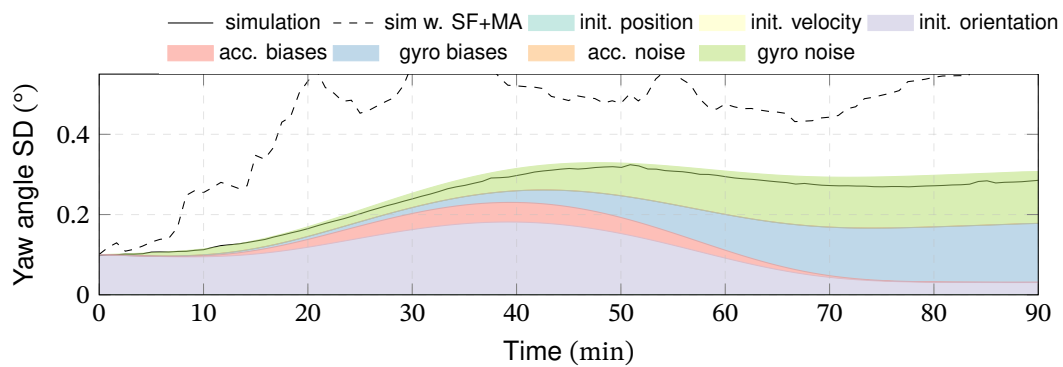
Figure 3.69.: Comparison of simulation results and predicted errors of the position and velocity for the simulated general aviation scenario.



(a) Roll angle.



(b) Pitch angle.



(c) Yaw angle.

Figure 3.70.: Comparison of simulation results and predicted errors of the orientation angles for the simulated general aviation scenario.

reasonable prediction of the magnitude of the error growth, at least for an early design phase.

3.5.3. Case 2: Transatlantic Flight

This test case represents a 9 h flight from Los Angeles to Glasgow. The trajectory and the ideal IMU measurements have been generated by smoothing, interpolating, and re-sampling Quick Access Recorder data of a Boeing 747 flight. The resulting inertial reference data are sampled at 1000 Hz demonstrate a consistency that yields a maximum position error of less than 1 mm for free-inertial integration. The properties of this trajectory are summarized in [Table 3.10](#).

Table 3.10.: Dynamics of the commercial transatlantic flight scenario.

Parameter	Value
Flight duration	09:14:43h
Maximum distance from start	8245.64 km
Maximum velocity	336.59 m/s
Maximum acceleration	1.04 g
Maximum angular rates	3.25 °/s

The error parameters for this simulation (see [Table 3.11](#)) are selected to represent a navigation grade INS. The initialization errors represent GNSS-like position accuracy and initial alignment accuracy according to section 3.2.

Table 3.11.: Specification of the input errors for the transatlantic flight scenario simulation.

Parameter	Symbol	Value	
Initialization errors (1σ)	Position	$\delta x_{n,0}, \delta x_{e,0}$	10 m
	Velocity	$\delta v_{n,0}, \delta v_{e,0}$	0.01 m/s
	Orientation	$\delta \Phi_0, \delta \Theta_0$	0.001°
Sensor bias (1σ)	Accelerometer	$\delta f_{b,x,0}, \delta f_{b,y,0}, \delta f_{b,z,0}$	0.01 mg
	Gyroscopes	$\delta \omega_{ib,x,0}, \delta \omega_{ib,y,0}, \delta \omega_{ib,z,0}$	0.002 °/h
Sensor SF Error (1σ)	Accelerometer	$S_{A,x}, S_{A,y}, S_{A,z}$	10 ppm
	Gyroscopes	$S_{G,x}, S_{G,y}, S_{G,z}$	10 ppm
Sensor MA (1σ)	Accelerometer	$M_{A,xy}, M_{A,xz}, M_{A,yx}, M_{A,yz}, \dots$	10 μ rad
	Gyroscopes	$M_{G,xy}, M_{G,xz}, M_{G,yx}, M_{G,yz}, \dots$	10 μ rad
Sensor noise	Accelerometer	$N_{acc,x}, N_{acc,y}, N_{acc,z}$	0.01 mg/ $\sqrt{\text{Hz}}$
	Gyroscope	$N_{gyr,x}, N_{gyr,y}, N_{gyr,z}$	0.0025 °/ $\sqrt{\text{h}}$

Again separate MC simulations with 1000 runs have been performed with and without SF and MA errors. The simulation results and the analytically predicted standard deviations are depicted in [Figure 3.72](#) and [Figure 3.73](#). Clearly, this scenario violates the assumptions taken in section 3.3.1.4: The aircraft's velocity is more than 300 m/s contributes significantly compared to the Earth's angular rate. However, the assumption of straight and leveled flight is well

fulfilled most of the time.

Similar to the previous test case, the analytical prediction matches the MC simulation results surprisingly well. If the SF and MA errors are neglected, the analytical methods predict the correct magnitude and dynamics for most of the position, velocity, and orientation errors. The east position and the yaw angle error are an exception from this. Starting from about 3 h of flight, these errors deviate from the analytical prediction but begin to converge until the end of the simulation. This may be attributed to the trajectory dependence and the violation of the assumptions taken for linearization.

In contrast to the high-dynamic general aviation case, considering SF and MA in the simulation has only a minor effect on the position and velocity errors. This is caused by two factors: First, the example inertial sensors have very low SF and MA errors of only 10 ppm. For static conditions, the equivalent resulting errors are in the same magnitude as the sensors' biases. Second, the transatlantic flight trajectory is low dynamic. From the visualization of the

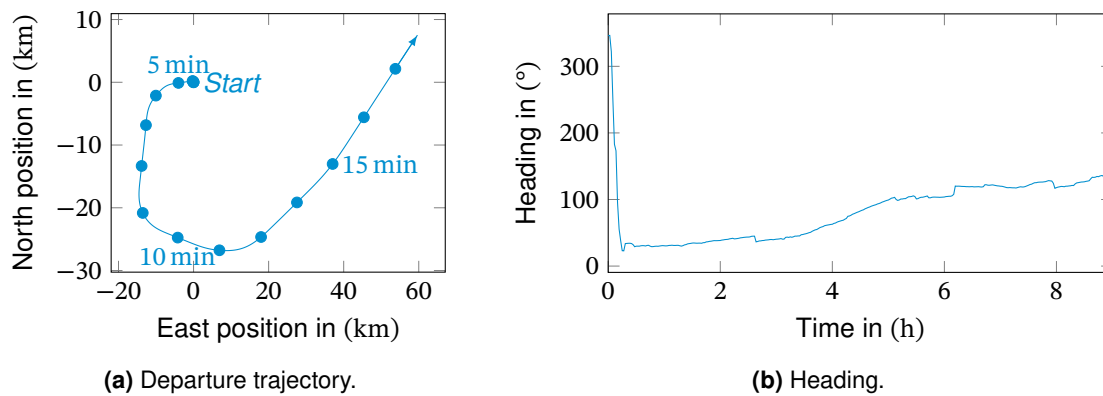
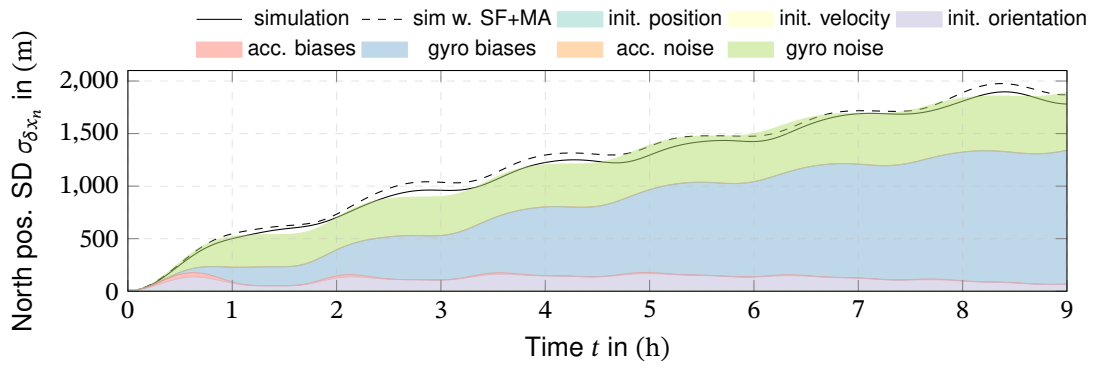
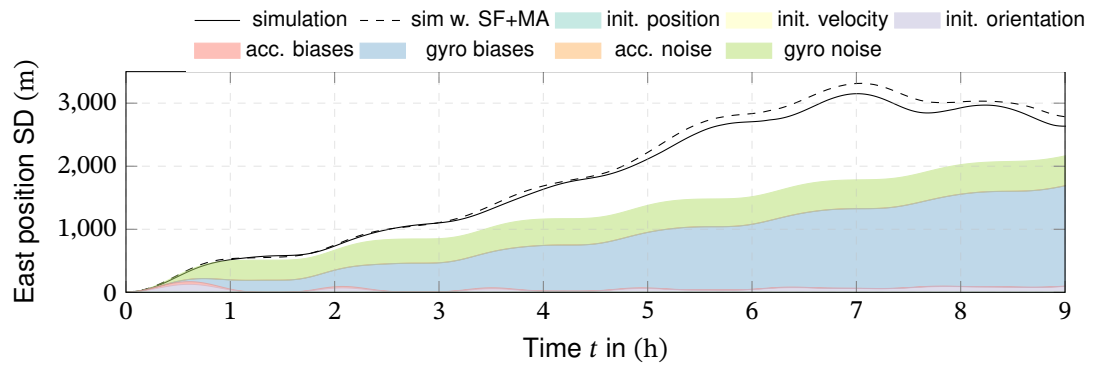


Figure 3.71.: Departure trajectory and heading of the transatlantic example flight.

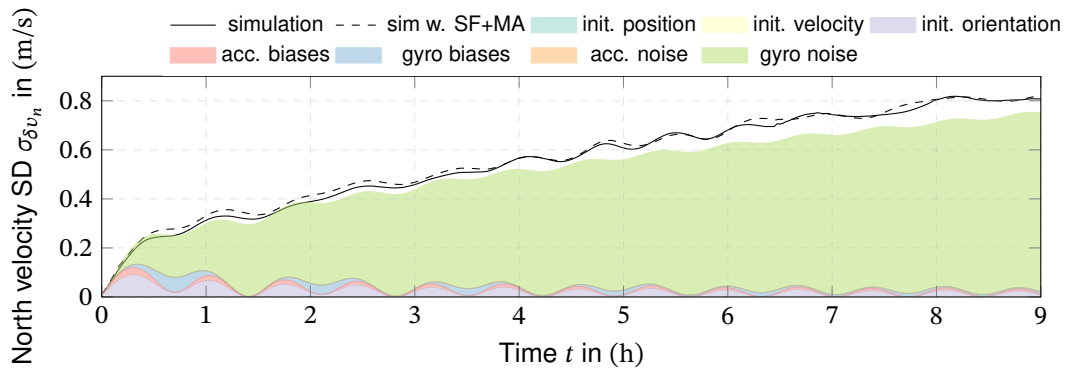
aircraft's trajectory in Figure 3.71, the most dynamic part of the trajectory can be found in just these first 15 min: The aircraft starts towards the west, performs a 230° left-turn, and departs straight to the northeast. Afterward, there are only very few low-dynamic maneuvers. The effects of the relatively high dynamic start can be observed in a step increase of the orientation errors at about 10 min. However, the dynamic-dependent errors introduce far fewer errors than the violation of a static vehicle's assumptions observed in the heading and longitude errors.



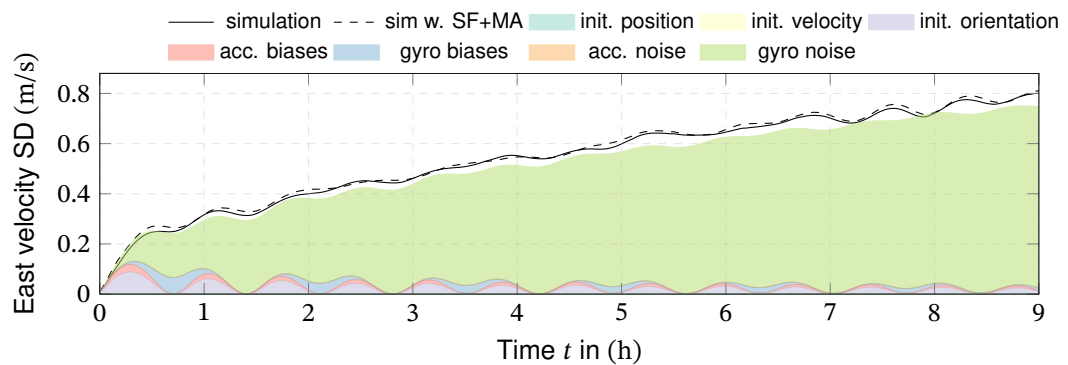
(a) North position.



(b) East position.

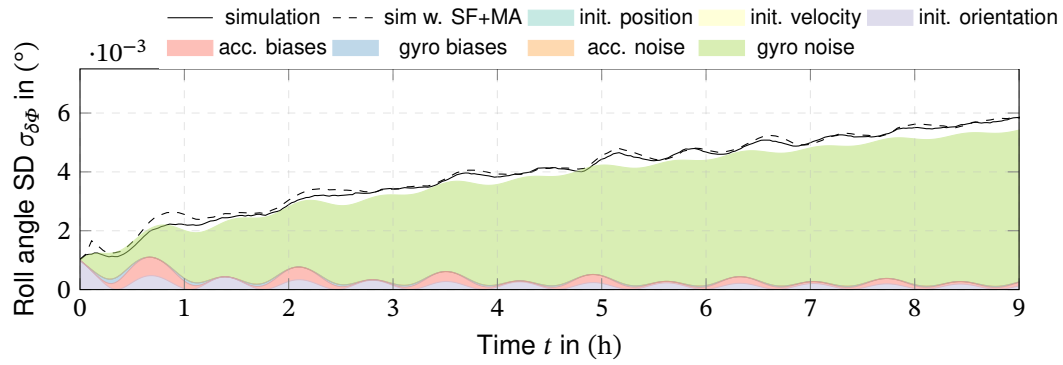


(c) North velocity.

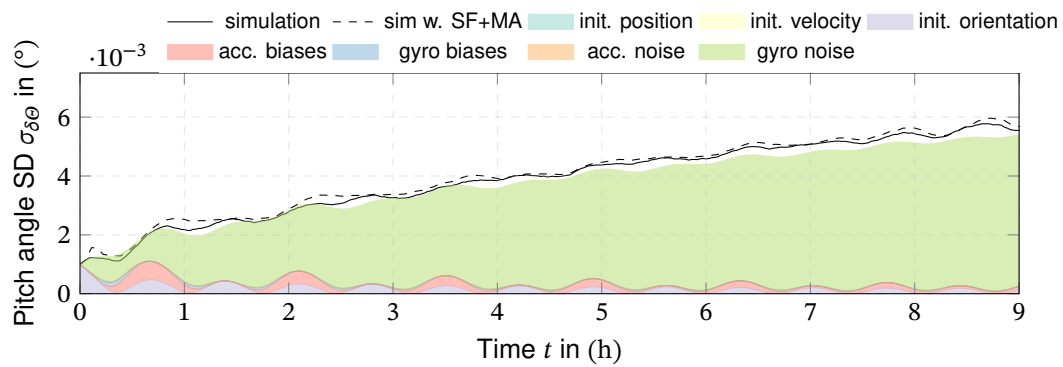


(d) East velocity.

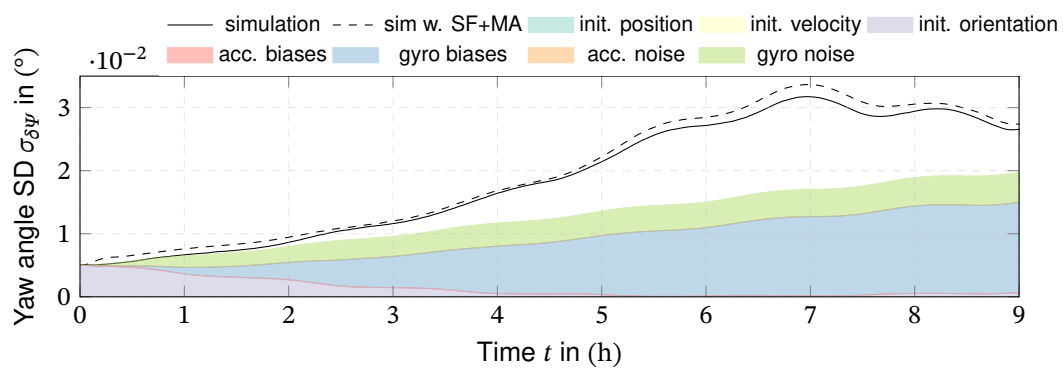
Figure 3.72.: Comparison of simulation results and predicted errors of the position and velocity for the simulated transatlantic flight scenario.



(a) Roll angle.



(b) Pitch angle.



(c) Yaw angle.

Figure 3.73.: Comparison of simulation results and predicted errors of the orientation angles for the simulated transatlantic flight scenario.

Result 2: Navigation Performance Prediction

The prediction charts presented in [Subsection 3.4.3](#) provide an easy-to-use visualization of fundamental relations between sensor performance and navigation errors. The charts allow a simple read-off and thus estimation of the magnitude of the allowed sensor and initialization errors for a given position error requirement.

In contrast, the quantitative calculation schemes provide a tool to predict the growth of any navigation state error from initialization errors, dynamic-independent bias-like sensor errors, and sensor noise. The schemes are best transferred into a computer program to allow the simple variation of the error parameters when creating an error budget.

The validation of the analytically predicted results by comparison with Monte-Carlo strapdown navigation simulation results demonstrated the validity but also the limits of the presented methods:

- The navigation error growth from initialization errors, sensor noise, and dynamic-independent bias-like sensor errors can be predicted by the presented methods at high accuracy.
- Despite the underlying static assumptions and linearizations, the errors are surprisingly well predicted even for trajectories that lead far away from the linearization point.
- Depending on the trajectory's dynamics, the dynamic-dependent sensor errors can contribute significantly to the navigation state errors.
- These dynamic-dependent errors can be considered either by piecewise steady approximation of the trajectory or by a numerical covariance propagation along the trajectory.
- A high-accuracy prediction of the navigation errors, including non-linearities of the strapdown equations and dynamic-dependent sensor errors, requires elaborate Monte-Carlo simulation.

Since the consideration of dynamic-dependent sensor errors and non-linearities of the strapdown-propagation requires the availability of a representative trajectory, the presented methods represent the best prediction of navigation errors available at a very early design phase where no or little trajectory information is at hand.

They set a minimum level of navigation errors to which the effects from the dynamic-dependent sensor errors are added.

3.6. Short- and Medium-Term Approximations

The previous analyses were based on the long-term analytical system responses. In literature and in practice, approximations of the error dynamics are widely used to predict the navigation performance. In the following section, the typical short- and medium-term approximations for all navigation states are derived from the long-term solutions. The results are compared to assess the validity of these approximations.

3.6.1. Spherical and Non-Rotating Earth

Neglecting of the Earth's rotation rate in the state space system (3.62) leads to the strapdown error dynamics for a spherical and non-rotating Earth. The simplified state space system is given written:

$$\delta \dot{\mathbf{z}} = \begin{bmatrix} 0 & 0 & \frac{1}{R+h} & 0 & 0 & 0 & 0 \\ 0 & 0 & 0 & \frac{1}{(R+h)\cos\bar{\phi}} & 0 & 0 & 0 \\ \hline 0 & 0 & 0 & 0 & 0 & -g & 0 \\ 0 & 0 & 0 & 0 & g & 0 & 0 \\ \hline 0 & 0 & 0 & \frac{-1}{R+h} & 0 & 0 & 0 \\ 0 & 0 & \frac{1}{R+h} & 0 & 0 & 0 & 0 \\ 0 & 0 & 0 & \frac{\tan\bar{\phi}}{R+h} & 0 & 0 & 0 \end{bmatrix} \delta \mathbf{z} + \begin{bmatrix} \mathbf{0}_{2 \times 3} & \mathbf{0}_{2 \times 3} & \mathbf{0}_{2 \times 3} & \mathbf{0}_{2 \times 2} \\ \mathbf{I}_{2 \times 3} & \mathbf{0}_{2 \times 3} & \mathbf{I}_{2 \times 3} & \mathbf{0}_{2 \times 2} \\ \hline \mathbf{0}_{3 \times 3} & \mathbf{I}_{3 \times 3} & \mathbf{0}_{3 \times 3} & \mathbf{0}_{3 \times 2} \end{bmatrix} \delta \mathbf{u}_{vf} \quad (3.133)$$

with the state and input vectors

$$\delta \mathbf{z} = [\delta x_n, \delta x_e, \delta v_n, \delta v_e, \delta \Phi, \delta \Theta, \delta \Psi]^T \quad (3.134)$$

$$\delta \mathbf{u}_{vf} = [\delta f_{b,n}, \delta f_{b,e}, \delta f_{b,d}, \delta \omega_{ib,n}, \delta \omega_{ib,e}, \delta \omega_{ib,d}, \delta \gamma_n, \delta \gamma_e, \delta \gamma_d, \delta h, \delta v_d]^T \quad (3.135)$$

The responses to initialization and sensor errors are determined for the above state-space system using the previously described methods. The analytical solution to above error dynamics are given Table 3.12 and Table 3.13.

In contrast to the full error dynamics, this simplified form displays only linear growth and Schuler oscillations but no 24 h and Foucault oscillations. Similar approximations are extensively discussed in [20, Ch. 13]. A brief but more accessible discussion of this mid-term dynamics for bias-like and initialization errors can be found in [14, Ch. 12.4]. In contrast, the tables here provide solutions for all navigation states and analytical responses to colored sensor noise.

Table 3.12.: Medium term analytical solutions to the strapdown error dynamics for position and velocity errors.

	Input	Position error		Velocity error	
		North δx_n	East δx_e	North δv_n	East δv_e
Initialization	$\delta x_{n,0}$	$h_{1,1}(t) = 1$	$h_{2,1}(t) = 0$	$h_{3,1}(t) = 0$	$h_{4,1}(t) = 0$
	$\delta x_{e,0}$	$h_{1,2}(t) = 0$	$h_{2,2}(t) = 1$	$h_{3,2}(t) = 0$	$h_{4,2}(t) = 0$
	$\delta v_{n,0}$	$h_{1,3}(t) = \frac{\sin(\omega_s t)}{\omega_s}$	$h_{2,3}(t) = 0$	$h_{3,3}(t) = \cos(\omega_s t)$	$h_{4,3}(t) = 0$
	$\delta v_{e,0}$	$h_{1,4}(t) = 0$	$h_{2,4}(t) = \frac{\sin(\omega_s t)}{\omega_s}$	$h_{3,4}(t) = 0$	$h_{4,4}(t) = \cos(\omega_s t)$
	$\delta \Phi_0$	$h_{1,5}(t) = 0$	$h_{2,5}(t) = R(1 - \cos(\omega_s t))$	$h_{3,5}(t) = 0$	$h_{4,5}(t) = R\omega_s \sin(\omega_s t)$
	$\delta \Theta_0$	$h_{1,6}(t) = R(\cos(\omega_s t) - 1)$	$h_{2,6}(t) = 0$	$h_{3,6}(t) = -R\omega_s \sin(\omega_s t)$	$h_{4,6}(t) = 0$
Sensor Biases	$\delta \Psi_0$	$h_{1,7}(t) = 0$	$h_{2,7}(t) = 0$	$h_{3,7}(t) = 0$	$h_{4,7}(t) = 0$
	$\delta f_{b,n,0}$	$h_{1,8}(t) = \frac{1}{\omega_s^2}(1 - \cos(\omega_s t))$	$h_{2,8}(t) = 0$	$h_{3,8}(t) = \frac{1}{\omega_s^2} \sin(\omega_s t)$	$h_{4,8}(t) = 0$
	$\delta f_{b,e,0}$	$h_{1,9}(t) = 0$	$h_{2,9}(t) = \frac{1}{\omega_s^2} - \frac{\cos(\omega_s t)}{\omega_s^2}$	$h_{3,9}(t) = 0$	$h_{4,9}(t) = \frac{1}{\omega_s} \sin(\omega_s t)$
	$\delta \omega_{ib,n,0}$	$h_{1,11}(t) = 0$	$h_{2,11}(t) = R\left(t - \frac{\sin(\omega_s t)}{\omega_s}\right)$	$h_{3,11}(t) = 0$	$h_{4,11}(t) = R(1 - \cos(\omega_s t))$
	$\delta \omega_{ib,e,0}$	$h_{1,12}(t) = -R\left(t - \frac{\sin(\omega_s t)}{\omega_s}\right)$	$h_{2,12}(t) = 0$	$h_{3,12}(t) = R(\cos(\omega_s t) - 1)$	$h_{4,12}(t) = 0$
	$\delta \omega_{ib,d,0}$	$h_{1,13}(t) = 0$	$h_{2,13}(t) = 0$	$h_{3,13}(t) = 0$	$h_{4,13}(t) = 0$
Velocity Random Walk	$N_{f,b,n}^2$	$k_{1,8}(t) = \frac{1}{2\omega_s^2}\left(t - \frac{\sin(2\omega_s t)}{2\omega_s}\right)$	$k_{2,8}(t) = 0$	$k_{3,8}(t) = \frac{t}{2} + \frac{\sin(2\omega_s t)}{4\omega_s}$	$k_{4,8}(t) = 0$
	$N_{f,b,e}^2$	$k_{1,9}(t) = 0$	$k_{2,9}(t) = \frac{1}{2\omega_s^2}\left(t - \frac{\sin(2\omega_s t)}{2\omega_s}\right)$	$k_{3,9}(t) = 0$	$k_{4,9}(t) = \frac{t}{2} + \frac{\sin(2\omega_s t)}{4\omega_s}$
Angular Random Walk	$N_{\omega_{ib,n}}^2$	$k_{1,11}(t) = 0$	$k_{2,11}(t) = \frac{3R^2}{2}t - \frac{2R^2 \sin(\omega_s t)}{\omega_s} + \frac{R^2 \sin(2\omega_s t)}{4\omega_s}$	$k_{3,11}(t) = 0$	$k_{4,11}(t) = R^2\left(\frac{\omega_s^2 t}{2} - \frac{\omega_s \sin(2\omega_s t)}{4}\right)$
	$N_{\omega_{ib,e}}^2$	$k_{1,12}(t) = \frac{3R^2}{2}t - \frac{2R^2 \sin(\omega_s t)}{\omega_s} + \frac{R^2 \sin(2\omega_s t)}{4\omega_s}$	$k_{2,12}(t) = 0$	$k_{3,12}(t) = R^2\left(\frac{\omega_s^2 t}{2} - \frac{\omega_s \sin(2\omega_s t)}{4}\right)$	$k_{4,12}(t) = 0$
	$N_{\omega_{ib,d}}^2$	$k_{1,13}(t) = 0$	$k_{2,13}(t) = 0$	$k_{3,13}(t) = 0$	$k_{4,13}(t) = 0$
Acceleration Random Walk	$K_{f,b,n}^2$	$k_{K,1,8}(t) = \frac{1}{2\omega_s^4}\left(t + \frac{\sin(2\omega_s t)}{2\omega_s}\right)$	$k_{K,2,8}(t) = 0$	$k_{K,3,8}(t) = \frac{1}{2\omega_s^2}\left(-t + \frac{\sin(2\omega_s t)}{2\omega_s}\right)$	$k_{K,4,8}(t) = 0$
	$K_{f,b,e}^2$	$k_{K,1,9}(t) = 0$	$k_{K,2,9}(t) = \frac{1}{2\omega_s^4 \cos^2 \phi}\left(t + \frac{\sin(2\omega_s t)}{2\omega_s}\right)$	$k_{K,3,9}(t) = 0$	$k_{K,4,9}(t) = \frac{1}{2\omega_s^2}\left(-t + \frac{\sin(2\omega_s t)}{2\omega_s}\right)$
Rate Random Walk	$K_{\omega_{ib,n}}^2$	$k_{K,1,11}(t) = 0$	$k_{K,2,11}(t) = \frac{R^2}{\cos^2 \phi}\left(\frac{1}{3}t^3 - \frac{1}{4\omega_s^2} \sin(2\omega_s t) - \frac{2}{\omega_s^2} \sin(\omega_s t) + \frac{1}{2\omega_s^2} t + \frac{2}{\omega_s^2} t \cos(\omega_s t)\right)$	$k_{K,3,11}(t) = 0$	$k_{K,4,11}(t) = R^2\left(\frac{t}{2} + \frac{\sin(2\omega_s t)}{4\omega_s}\right)$
	$K_{\omega_{ib,e}}^2$	$k_{K,1,12}(t) = R^2\left(\frac{1}{3}t^3 - \frac{1}{2\omega_s^2} \sin(\omega_s t) \cos(\omega_s t) - \frac{2}{\omega_s^2} \sin(\omega_s t) + \frac{1}{2\omega_s^2} t - \frac{2}{\omega_s^2} t \cos(\omega_s t)\right)$	$k_{K,2,12}(t) = 0$	$k_{K,3,12}(t) = R^2\left(\frac{t}{2} + \frac{\sin(2\omega_s t)}{4\omega_s}\right)$	$k_{K,4,12}(t) = 0$
	$K_{\omega_{ib,d}}^2$	$k_{K,1,13}(t) = 0$	$k_{K,2,13}(t) = 0$	$k_{K,3,13}(t) = 0$	$k_{K,4,13}(t) = 0$
Velocity Quantization Noise	$Q_{f,b,n}^2$	$k_{Q,1,8}(t) = \frac{1}{2}t + \frac{1}{4\omega_s} \sin(2\omega_s t)$	$k_{Q,2,8}(t) = 0$	$k_{Q,3,8}(t) = \frac{\omega_s t}{2} - \frac{\omega_s}{4\omega_s} \sin(2\omega_s t)$	$k_{Q,4,8}(t) = 0$
	$Q_{f,b,e}^2$	$k_{Q,1,9}(t) = 0$	$k_{Q,2,9}(t) = \left(\frac{1}{2}t + \frac{1}{4\omega_s} \sin(2\omega_s t)\right) \frac{1}{\cos^2 \phi}$	$k_{Q,3,9}(t) = 0$	$k_{Q,4,9}(t) = \frac{\omega_s t}{2} - \frac{\omega_s}{4\omega_s} \sin(2\omega_s t)$
Angular Quantization Noise	$Q_{\omega_{ib,n}}^2$	$k_{Q,1,11}(t) = 0$	$k_{Q,2,11}(t) = \frac{R^2}{\cos^2 \phi}\left(\frac{\omega_s}{2}t - \frac{\omega_s}{4} \sin(2\omega_s t)\right)$	$k_{Q,3,11}(t) = 0$	$k_{Q,4,11}(t) = R^2\left(\frac{\omega_s^2 t}{2} + \frac{\omega_s^2}{4} \sin(2\omega_s t)\right)$
	$Q_{\omega_{ib,e}}^2$	$k_{Q,1,12}(t) = R^2\left(\frac{\omega_s}{2}t - \frac{\omega_s}{4} \sin(2\omega_s t)\right)$	$k_{Q,2,12}(t) = 0$	$k_{Q,3,12}(t) = R^2\left(\frac{\omega_s^2 t}{2} + \frac{\omega_s^2}{4} \sin(2\omega_s t)\right)$	$k_{Q,4,12}(t) = 0$
	$Q_{\omega_{ib,d}}^2$	$k_{Q,1,13}(t) = 0$	$k_{Q,2,13}(t) = 0$	$k_{Q,3,13}(t) = 0$	$k_{Q,4,13}(t) = 0$

There is no analytical expression for the navigation errors from bias-instability and rate ramp noise. See section 3.3.4.2 for a numerical solution.

Table 3.13.: Medium term analytical solutions to the strapdown error dynamics for orientation errors.

	Input	Orientation error		
		Roll $\delta\Phi$	Pitch $\delta\Theta$	Yaw $\delta\Psi$
Initialization	$\delta x_{n,0}$	$h_{5,1}(t) = 0$	$h_{6,1}(t) = 0$	$h_{7,1}(t) = 0$
	$\delta x_{e,0}$	$h_{5,2}(t) = 0$	$h_{6,2}(t) = 0$	$h_{7,2}(t) = 0$
	$\delta v_{n,0}$	$h_{5,3}(t) = 0$	$h_{6,3}(t) = \frac{\sin(\omega_s t)}{R\omega_s}$	$h_{7,3}(t) = 0$
	$\delta v_{e,0}$	$h_{5,4}(t) = -\frac{\sin(\omega_s t)}{R\omega_s}$	$h_{6,4}(t) = 0$	$h_{7,4}(t) = \frac{\tan\phi \sin(\omega_s t)}{R\omega_s}$
	$\delta\Phi_0$	$h_{5,5}(t) = \cos(\omega_s t)$	$h_{6,5}(t) = 0$	$h_{7,5}(t) = \tan\phi (1 - \cos(\omega_s t))$
	$\delta\Theta_0$	$h_{5,6}(t) = 0$	$h_{6,6}(t) = \cos(\omega_s t)$	$h_{7,6}(t) = 0$
	$\delta\Psi_0$	$h_{5,7}(t) = 0$	$h_{6,7}(t) = 0$	$h_{7,7}(t) = 1$
Sensor Biases	$\delta f_{b,n,0}$	$h_{5,8}(t) = 0$	$h_{6,8}(t) = \frac{1}{g} - \frac{\cos(\omega_s t)}{g}$	$h_{7,8}(t) = 0$
	$\delta f_{b,e,0}$	$h_{5,9}(t) = \frac{\cos(\omega_s t)}{g} - \frac{1}{g}$	$h_{6,9}(t) = 0$	$h_{7,9}(t) = \frac{\tan\phi}{g} - \frac{\tan\phi \cos(\omega_s t)}{g}$
	$\delta\omega_{ib,n,0}$	$h_{5,11}(t) = \frac{\sin(\omega_s t)}{\omega_s}$	$h_{6,11}(t) = 0$	$h_{7,11}(t) = \tan\phi \left(t - \frac{\sin(\omega_s t)}{\omega_s} \right)$
	$\delta\omega_{ib,e,0}$	$h_{5,12}(t) = 0$	$h_{6,12}(t) = \frac{\sin(\omega_s t)}{\omega_s}$	$h_{7,12}(t) = 0$
	$\delta\omega_{ib,d,0}$	$h_{5,13}(t) = 0$	$h_{6,13}(t) = 0$	$h_{7,13}(t) = t$
Velocity Random Walk	$N_{f_{b,n}}^2$	$k_{5,8}(t) = 0$	$k_{6,8}(t) = \frac{t}{2Rg} - \frac{\sin(2\omega_s t)}{4Rg\omega_s}$	$k_{7,8}(t) = 0$
	$N_{f_{b,e}}^2$	$k_{5,9}(t) = \frac{1}{2Rg} \left(t - \frac{\sin(2\omega_s t)}{2\omega_s} \right)$	$k_{6,9}(t) = 0$	$k_{7,9}(t) = \left(\frac{t}{2Rg} - \frac{\sin(2\omega_s t)}{4Rg\omega_s} \right) \tan^2\phi$
Angular Random Walk	$N_{\omega_{ib,n}}^2$	$k_{5,11}(t) = \frac{t}{2} + \frac{\sin(2\omega_s t)}{4\omega_s}$	$k_{6,11}(t) = 0$	$k_{7,11}(t) = \left(\frac{3}{2}t - \frac{2\sin(\omega_s t)}{\omega_s} + \frac{\sin(2\omega_s t)}{4\omega_s} \right) \tan\phi$
	$N_{\omega_{ib,e}}^2$	$k_{5,12}(t) = 0$	$k_{6,12}(t) = \frac{t}{2} + \frac{\sin(2\omega_s t)}{4\omega_s}$	$k_{7,12}(t) = 0$
	$N_{\omega_{ib,d}}^2$	$k_{5,13}(t) = 0$	$k_{6,13}(t) = 0$	$k_{7,13}(t) = t$
Acceleration Random Walk	$K_{f_{b,n}}^2$	$k_{K,5,8}(t) = 0$	$k_{K,6,8}(t) = \frac{t}{2} + \frac{\sin(2\omega_s t)}{4\omega_s}$	$k_{K,7,8}(t) = 0$
Rate Random Walk	$K_{f_{b,e}}^2$	$k_{K,5,9}(t) = \frac{t}{2} + \frac{\sin(2\omega_s t)}{4\omega_s}$	$k_{K,6,9}(t) = 0$	$k_{K,7,9}(t) = \left(\frac{t}{2} + \frac{\sin(2\omega_s t)}{4\omega_s} \right) \tan^2\phi$
	$K_{\omega_{ib,n}}^2$	$k_{K,5,11}(t) = -\frac{t}{2\omega_s^2} + \frac{\sin(2\omega_s t)}{4\omega_s^3}$	$k_{K,6,11}(t) = 0$	$k_{K,7,11}(t) = \tan^2\phi \left(\frac{1}{3}t^3 - \frac{2}{\omega_s^3} \sin(\omega_s t) + \frac{1}{2\omega_s^2} t - \frac{1}{2\omega_s^3} \cos(\omega_s t) \sin(\omega_s t) + \frac{2}{\omega_s^3} t \cos(\omega_s t) \right)$
	$K_{\omega_{ib,e}}^2$	$k_{K,5,12}(t) = 0$	$k_{K,6,12}(t) = -\frac{t}{2\omega_s^2} - \frac{\sin(2\omega_s t)}{4\omega_s^3}$	$k_{K,7,12}(t) = 0$
Velocity Quantization Noise	$K_{\omega_{ib,d}}^2$	$k_{K,5,13}(t) = 0$	$k_{K,6,13}(t) = 0$	$k_{K,7,13}(t) = \frac{1}{3}t^3$
	$Q_{f_{b,n}}^2$	$k_{Q,5,8}(t) = 0$	$k_{Q,6,8}(t) = \frac{\omega_s^4}{2} t + \frac{\omega_s^3}{4} \sin(2\omega_s t)$	$k_{Q,7,8}(t) = 0$
	$Q_{f_{b,e}}^2$	$k_{Q,5,9}(t) = \frac{\omega_s^4}{2} t + \frac{\omega_s^3}{4} \sin(2\omega_s t)$	$k_{Q,6,9}(t) = 0$	$k_{Q,7,9}(t) = \left(\frac{\omega_s^4}{2} t + \frac{\omega_s^3}{4} \sin(2\omega_s t) \right) \tan^2\phi$
Angular Quantization Noise	$Q_{\omega_{ib,n}}^2$	$k_{Q,5,11}(t) = -\frac{\omega_s^2}{2} t + \frac{\omega_s}{4} \sin(2\omega_s t)$	$k_{Q,6,11}(t) = 0$	$k_{Q,7,11}(t) = \left(\frac{\omega_s^2}{2} t - \frac{\omega_s}{4} \sin(2\omega_s t) \right) \tan^2\phi$
	$Q_{\omega_{ib,e}}^2$	$k_{Q,5,12}(t) = 0$	$k_{Q,6,12}(t) = -\frac{\omega_s^2}{2} t + \frac{\omega_s}{4} \sin(2\omega_s t)$	$k_{Q,7,12}(t) = 0$
	$Q_{\omega_{ib,d}}^2$	$k_{Q,5,13}(t) = 0$	$k_{Q,6,13}(t) = 0$	$k_{Q,7,13}(t) = 0$

There is no analytical expression for the navigation errors from bias-instability and rate ramp noise. See section 3.3.4.2 for a numerical solution.

3.6.2. Flat and Non-Rotating Earth

The state space system (3.133) can be further simplified for a flat and non-rotating Earth. For a flat Earth, latitude and longitude errors are replaced by north- and east position errors which leads to the following state vector:

$$\delta \mathbf{z}_{\text{flat}} = [\delta x_n, \delta x_e, \delta v_n, \delta v_e, \delta \Phi, \delta \Theta, \delta \Psi]^T \quad (3.136)$$

The new system matrix is obtained from (3.133) by replacing latitude and longitude with the north- and east position errors and assuming an infinite Earth radius $R \rightarrow \infty$. This yields the following simple state-space system:

$$\delta \dot{\mathbf{z}}_{\text{flat}} = \begin{bmatrix} 0 & 0 & 1 & 0 & 0 & 0 & 0 \\ 0 & 0 & 0 & 1 & 0 & 0 & 0 \\ \hline 0 & 0 & 0 & 0 & 0 & -g & 0 \\ 0 & 0 & 0 & 0 & g & 0 & 0 \\ \hline 0 & 0 & 0 & 0 & 0 & 0 & 0 \\ 0 & 0 & 0 & 0 & 0 & 0 & 0 \\ 0 & 0 & 0 & 0 & 0 & 0 & 0 \end{bmatrix} \dot{\mathbf{z}}_{\text{flat}} + \begin{bmatrix} \mathbf{0}_{2 \times 3} & \mathbf{0}_{2 \times 3} & \mathbf{0}_{2 \times 3} & \mathbf{0}_{2 \times 2} \\ \hline \mathbf{I}_{2 \times 3} & \mathbf{0}_{2 \times 3} & \mathbf{I}_{2 \times 3} & \mathbf{0}_{2 \times 2} \\ \hline \mathbf{0}_{3 \times 3} & \mathbf{I}_{3 \times 3} & \mathbf{0}_{3 \times 3} & \mathbf{0}_{3 \times 2} \end{bmatrix} \delta \mathbf{u}_{vf} \quad (3.137)$$

These elementary error dynamics are equivalent to free integration of the inputs without cross-couplings. The resulting analytical solutions are summarized in Table 3.14. Similar short-term approximations are well covered in literature, e.g., [14, p. 355]. Again, Table 3.14 completes the equations found in literature to all navigation states and input errors. Due to the complete neglect of the error dynamics, this approximation only represents the navigation error's initial response accurately. Since not even the Schuler-oscillation is represented in the equations, their validity must be limited to a fraction of 84 min. The range of validity of these approximations will be discussed in the next section.

Table 3.14.: Short term analytical solutions to the strapdown error dynamics.

	Input	Position error		Velocity error		Orientation error		
		North δx_n	East δx_e	North δv_n	East δv_e	Roll $\delta\Phi$	Pitch $\delta\Theta$	Yaw $\delta\Psi$
Initialization	$\delta x_{n,0}$	$h_{1,1}(t) = 1$	$h_{2,1}(t) = 0$	$h_{3,1}(t) = 0$	$h_{4,1}(t) = 0$	$h_{5,1}(t) = 0$	$h_{6,1}(t) = 0$	$h_{7,1}(t) = 0$
	$\delta x_{e,0}$	$h_{1,2}(t) = 0$	$h_{2,2}(t) = 1$	$h_{3,2}(t) = 0$	$h_{4,2}(t) = 0$	$h_{5,2}(t) = 0$	$h_{6,2}(t) = 0$	$h_{7,2}(t) = 0$
	$\delta v_{n,0}$	$h_{1,3}(t) = t$	$h_{2,3}(t) = 0$	$h_{3,3}(t) = 1$	$h_{4,3}(t) = 0$	$h_{5,3}(t) = 0$	$h_{6,3}(t) = 0$	$h_{7,3}(t) = 0$
	$\delta v_{e,0}$	$h_{1,4}(t) = 0$	$h_{2,4}(t) = t$	$h_{3,4}(t) = 0$	$h_{4,4}(t) = 1$	$h_{5,4}(t) = 0$	$h_{6,4}(t) = 0$	$h_{7,4}(t) = 0$
	$\delta\Phi_0$	$h_{1,5}(t) = 0$	$h_{2,5}(t) = -\frac{1}{2}gt^2$	$h_{3,5}(t) = 0$	$h_{4,5}(t) = -gt$	$h_{5,5}(t) = 1$	$h_{6,5}(t) = 0$	$h_{7,5}(t) = 0$
	$\delta\Theta_0$	$h_{1,6}(t) = -\frac{1}{2}gt^2$	$h_{2,6}(t) = 0$	$h_{3,6}(t) = -gt$	$h_{4,6}(t) = 0$	$h_{5,6}(t) = 0$	$h_{6,6}(t) = 1$	$h_{7,6}(t) = 0$
	$\delta\Psi_0$	$h_{1,7}(t) = 0$	$h_{2,7}(t) = 0$	$h_{3,7}(t) = 0$	$h_{4,7}(t) = 0$	$h_{5,7}(t) = 0$	$h_{6,7}(t) = 0$	$h_{7,7}(t) = 1$
Sensor Biases	$\delta f_{b,n,0}$	$h_{1,8}(t) = \frac{1}{2}t^2$	$h_{2,8}(t) = 0$	$h_{3,8}(t) = t$	$h_{4,8}(t) = 0$	$h_{5,8}(t) = 0$	$h_{6,8}(t) = 0$	$h_{7,8}(t) = 0$
	$\delta f_{b,e,0}$	$h_{1,9}(t) = 0$	$h_{2,9}(t) = \frac{1}{2}t^2$	$h_{3,9}(t) = 0$	$h_{4,9}(t) = t$	$h_{5,9}(t) = 0$	$h_{6,9}(t) = 0$	$h_{7,9}(t) = 0$
	$\delta\omega_{ib,n,0}$	$h_{1,11}(t) = 0$	$h_{2,11}(t) = -\frac{1}{6}gt^3$	$h_{3,11}(t) = 0$	$h_{4,11}(t) = 0$	$h_{5,11}(t) = t$	$h_{6,11}(t) = 0$	$h_{7,11}(t) = 0$
	$\delta\omega_{ib,e,0}$	$h_{1,12}(t) = -\frac{1}{6}gt^3$	$h_{2,12}(t) = 0$	$h_{3,12}(t) = 0$	$h_{4,12}(t) = 0$	$h_{5,12}(t) = 0$	$h_{6,12}(t) = t$	$h_{7,12}(t) = 0$
	$\delta\omega_{ib,d,0}$	$h_{1,13}(t) = 0$	$h_{2,13}(t) = 0$	$h_{3,13}(t) = 0$	$h_{4,13}(t) = 0$	$h_{5,13}(t) = 0$	$h_{6,13}(t) = 0$	$h_{7,13}(t) = t$
Velocity Random Walk	$N_{f_{b,n}}^2$	$k_{1,8}(t) = \frac{1}{3}t^3$	$k_{2,8}(t) = 0$	$k_{3,8}(t) = t$	$k_{4,8}(t) = 0$	$k_{5,8}(t) = 0$	$k_{6,8}(t) = 0$	$k_{7,8}(t) = 0$
	$N_{f_{b,e}}^2$	$k_{1,9}(t) = 0$	$k_{2,9}(t) = \frac{1}{3}t^3$	$k_{3,9}(t) = 0$	$k_{4,9}(t) = t$	$k_{5,9}(t) = 0$	$k_{6,9}(t) = 0$	$k_{7,9}(t) = 0$
Angular Random Walk	$N_{\omega_{ib,n}}^2$	$k_{1,11}(t) = 0$	$k_{2,11}(t) = \frac{1}{20}g^2t^5$	$k_{3,11}(t) = 0$	$k_{4,11}(t) = \frac{1}{3}t^3$	$k_{5,11}(t) = t$	$k_{6,11}(t) = 0$	$k_{7,11}(t) = 0$
	$N_{\omega_{ib,e}}^2$	$k_{1,12}(t) = \frac{1}{20}g^2t^5$	$k_{2,12}(t) = 0$	$k_{3,12}(t) = \frac{1}{3}t^3$	$k_{4,12}(t) = 0$	$k_{5,12}(t) = 0$	$k_{6,12}(t) = t$	$k_{7,12}(t) = 0$
	$N_{\omega_{ib,d}}^2$	$k_{1,13}(t) = 0$	$k_{2,13}(t) = 0$	$k_{3,13}(t) = 0$	$k_{4,13}(t) = 0$	$k_{5,13}(t) = 0$	$k_{6,13}(t) = 0$	$k_{7,13}(t) = t$
Acceleration Random Walk	$K_{f_{b,n}}^2$	$k_{K,1,8}(t) = \frac{1}{20}t^5$	$k_{K,2,8}(t) = 0$	$k_{K,3,8}(t) = \frac{1}{3}t^3$	$k_{K,4,8}(t) = 0$	$k_{K,5,8}(t) = 0$	$k_{K,6,8}(t) = 0$	$k_{K,7,8}(t) = 0$
	$K_{f_{b,e}}^2$	$k_{K,1,9}(t) = 0$	$k_{K,2,9}(t) = \frac{1}{20}t^5$	$k_{K,3,9}(t) = 0$	$k_{K,4,9}(t) = \frac{1}{3}t^3$	$k_{K,5,9}(t) = 0$	$k_{K,6,9}(t) = 0$	$k_{K,7,9}(t) = 0$
Rate Random Walk	$K_{\omega_{ib,n}}^2$	$k_{K,1,11}(t) = 0$	$k_{K,2,11}(t) = \frac{1}{252}g^2t^7$	$k_{K,3,11}(t) = 0$	$k_{K,4,11}(t) = \frac{1}{20}t^5$	$k_{K,5,11}(t) = \frac{1}{3}t^3$	$k_{K,6,11}(t) = 0$	$k_{K,7,11}(t) = 0$
	$K_{\omega_{ib,e}}^2$	$k_{K,1,12}(t) = \frac{1}{252}g^2t^7$	$k_{K,2,12}(t) = 0$	$k_{K,3,12}(t) = \frac{1}{20}t^5$	$k_{K,4,12}(t) = 0$	$k_{K,5,12}(t) = 0$	$k_{K,6,12}(t) = \frac{1}{3}t^3$	$k_{K,7,12}(t) = 0$
	$K_{\omega_{ib,d}}^2$	$k_{K,1,13}(t) = 0$	$k_{K,2,13}(t) = 0$	$k_{K,3,13}(t) = 0$	$k_{K,4,13}(t) = 0$	$k_{K,5,13}(t) = 0$	$k_{K,6,13}(t) = 0$	$k_{K,7,13}(t) = \frac{1}{3}t^3$
Vel. Quantization Noise	$Q_{f_{b,n}}^2$	$k_{Q,1,8}(t) = \frac{1}{3}t^3$	$k_{Q,2,8}(t) = 0$	$k_{Q,3,8}(t) = 1$	$k_{Q,4,8}(t) = 0$	$k_{Q,5,8}(t) = 0$	$k_{Q,6,8}(t) = 0$	$k_{Q,7,8}(t) = 0$
	$Q_{f_{b,e}}^2$	$k_{Q,1,9}(t) = 0$	$k_{Q,2,9}(t) = t$	$k_{Q,3,9}(t) = 0$	$k_{Q,4,9}(t) = 1$	$k_{Q,5,9}(t) = 0$	$k_{Q,6,9}(t) = 0$	$k_{Q,7,9}(t) = 0$
Angular Quantization Noise	$Q_{\omega_{ib,n}}^2$	$k_{Q,1,11}(t) = 0$	$k_{Q,2,11}(t) = \frac{1}{3}g^2t^3$	$k_{Q,3,11}(t) = 0$	$k_{Q,4,11}(t) = t$	$k_{Q,5,11}(t) = 1$	$k_{Q,6,11}(t) = 0$	$k_{Q,7,11}(t) = 0$
	$Q_{\omega_{ib,e}}^2$	$k_{Q,1,12}(t) = \frac{1}{3}g^2t^3$	$k_{Q,2,12}(t) = 0$	$k_{Q,3,12}(t) = t$	$k_{Q,4,12}(t) = 0$	$k_{Q,5,12}(t) = 0$	$k_{Q,6,12}(t) = 1$	$k_{Q,7,12}(t) = 0$
	$Q_{\omega_{ib,d}}^2$	$k_{Q,1,13}(t) = 0$	$k_{Q,2,13}(t) = 0$	$k_{Q,3,13}(t) = 0$	$k_{Q,4,13}(t) = 0$	$k_{Q,5,13}(t) = 0$	$k_{Q,6,13}(t) = 0$	$k_{Q,7,13}(t) = 1$

3.6.3. Comparison and Summary

The three discussed approximations represent different levels of system complexity. Comparing the different levels of approximation, several differences can be observed:

- The **neglect of error dynamics** in the short- and medium-term approximation. Initial position errors stay constant while orientation and velocity errors are freely integrated in the short term approximations, whereas the medium- and long-term solutions display bound oscillations or linear growth superposed with oscillations. While the medium-term approximations display only the Schuler oscillation, the long-term solutions additionally include the 24 h and Foucault oscillations.
- A **lack of cross-coupling responses** in the short and medium-term approximations. For the short-term approximation, position and orientation errors arise only when directly excited in the direction of the output. For example, a north acceleration error leads only to a north position error. The same is true for the medium-term approximation, except for the yaw angle error that is also sensitive to inputs in the east direction. Further cross-axis responses occur in the long-term solution, e.g., even an acceleration error in the east direction excites a north position error.
- Different **periods of validity** of the approximations. Even where all the approximations display a similar initial response to the input, these responses diverge over time. While the short-term solution shows linear to quadratic error growth, the medium-term solution is a harmonic oscillation (superpose to linear growth in some cases). In the long-term solution, this oscillation is additionally modulated at a 24-hour or Foucault period.

To illustrate the differences in validity between the short-, medium- and long-term solution, some example error responses for the north position and roll angle errors are depicted in [Figure 3.74](#), [Figure 3.75](#) and [Figure 3.76](#). The short-term solution captures the initial response to error inputs quite well. The short-term polynomial solution matches the true harmonic oscillations of the medium and long-term solutions up to around 10 min. After that, the short-term solution displays a substantial divergence from the other approximations. The medium-term solution displays the Schuler oscillations that dominate the long-term solution but lack their amplitude modulation. The change in amplitude becomes relevant after 2 to 4 h. The observed validity periods approve the literature values stated in [14, p. 350], [15, p. 163] and [20, p. 13-1]. The validity of the long-term solution is mainly limited by the neglect of the vehicle motion as discussed in section 3.3.1.4. The resulting properties of the different approximations are summarized in [Table 3.15](#).

Looking at the depicted error growth, it is tempting to say that the short- and medium-term solutions are always more conservative than the long-term solution and, especially the medium-term solution, could be used as a worst-case estimate. However, there are arguments against this assumption:

Table 3.15.: Comparison of approximations of the strapdown error dynamics.

	Short-term	Medium-term	Long-term
Earth shape	flat	spherical	spherical
Earth rotation	-	-	ω_{ie}
Error growth	polynomially	oscillating	mod. oscillating
Periodicity	-	$T_s \approx 84.4$ min	$T_s \approx 84.4$ min, $T_f \approx 34$ h at $\phi = 45^\circ$, $T_{ie} \approx 24$ h
Cross-axis sensitivity	-	azimuth only	extensive
Validity period	< 10 min	< 4 h	< 10 d

1. The short-term solution displays unlimited polynomial growth. This leads to a practically worthless estimation of the true errors that are often limited to medium and long terms.
2. The medium-term solution captures the Schuler oscillation and the maximum of the error quite well. Still, a modulation caused by the Earth's angular rate may change the direction of the error oscillation (see [Figure 3.74c](#)). In that case, the assumed maximum amplitude is correct, but the direction of the error may be diametrically wrong.
3. For some states, the short- and medium-term approximations do not display any response where the long-term solution indeed does. This contradicts the assumed feasibility as a worst-case estimate.

Taking the extremely reduced complexity of the short-term approximations into account, the existence and use of all three approximations are justified. Still, care must be taken to select the suitable approximation and consider its respective limitations.

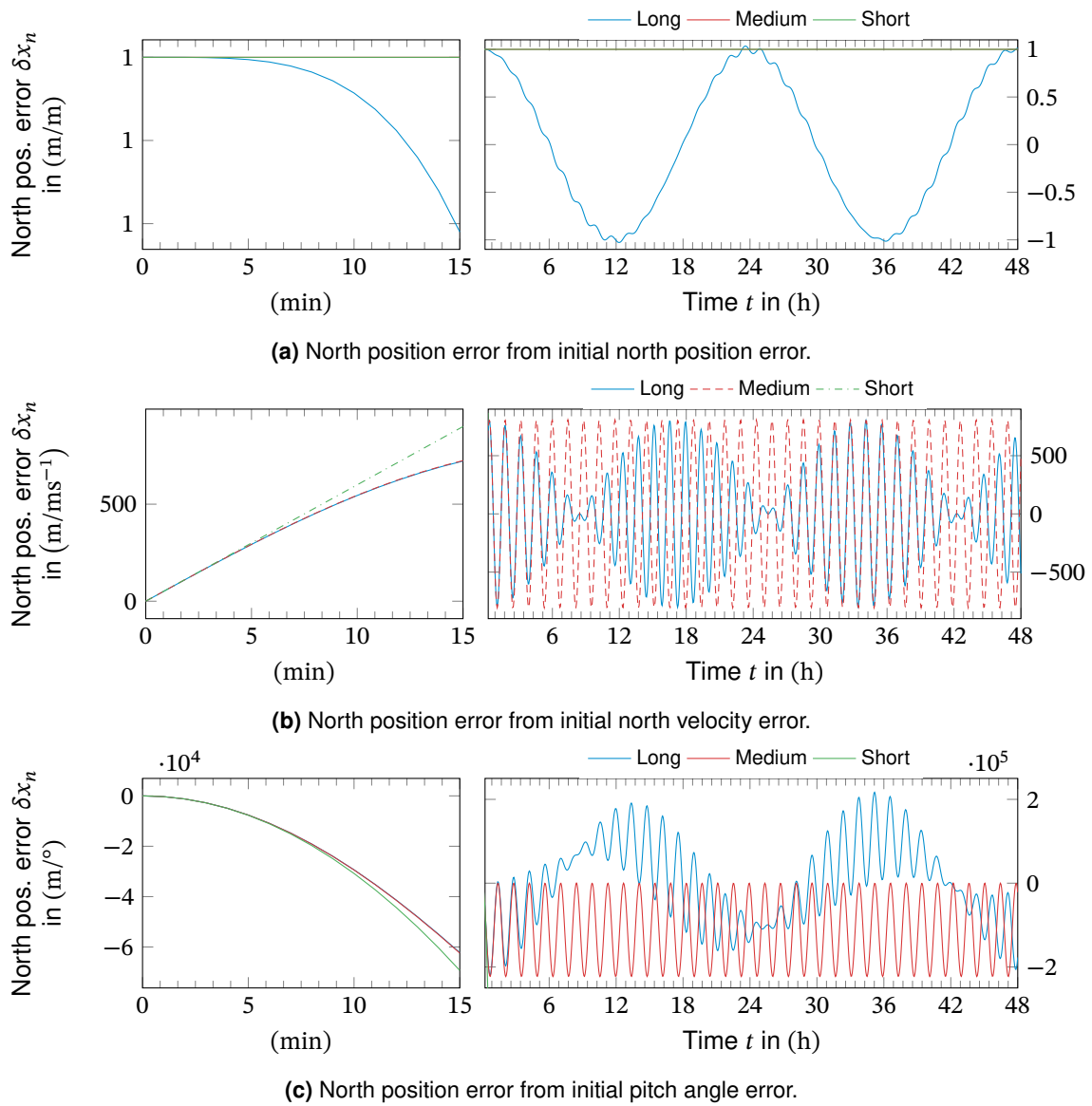


Figure 3.74.: Comparison of different approximations for the north position error from initialization errors.

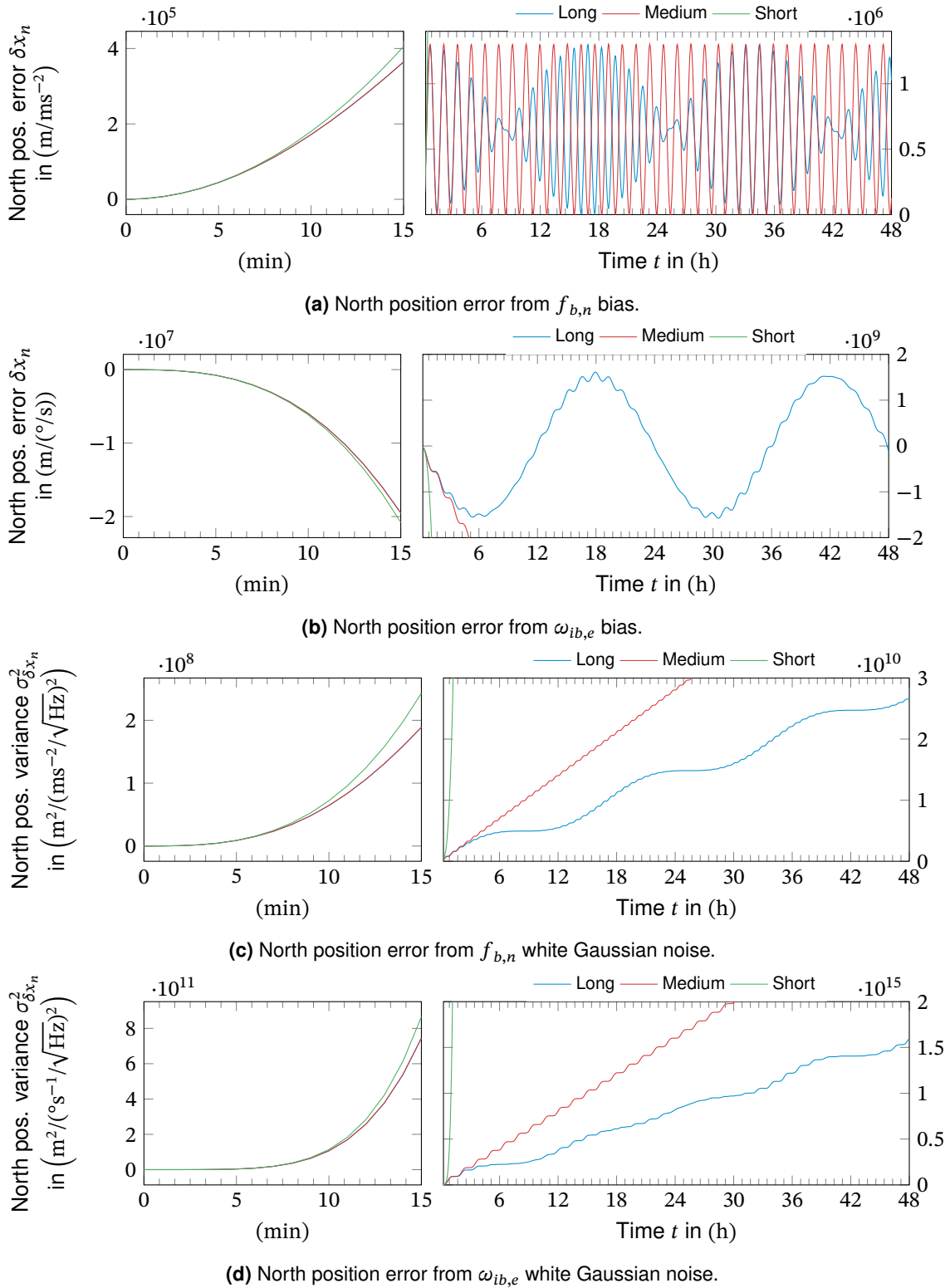


Figure 3.75.: Comparison of different approximations for the north position error from inertial measurement errors.

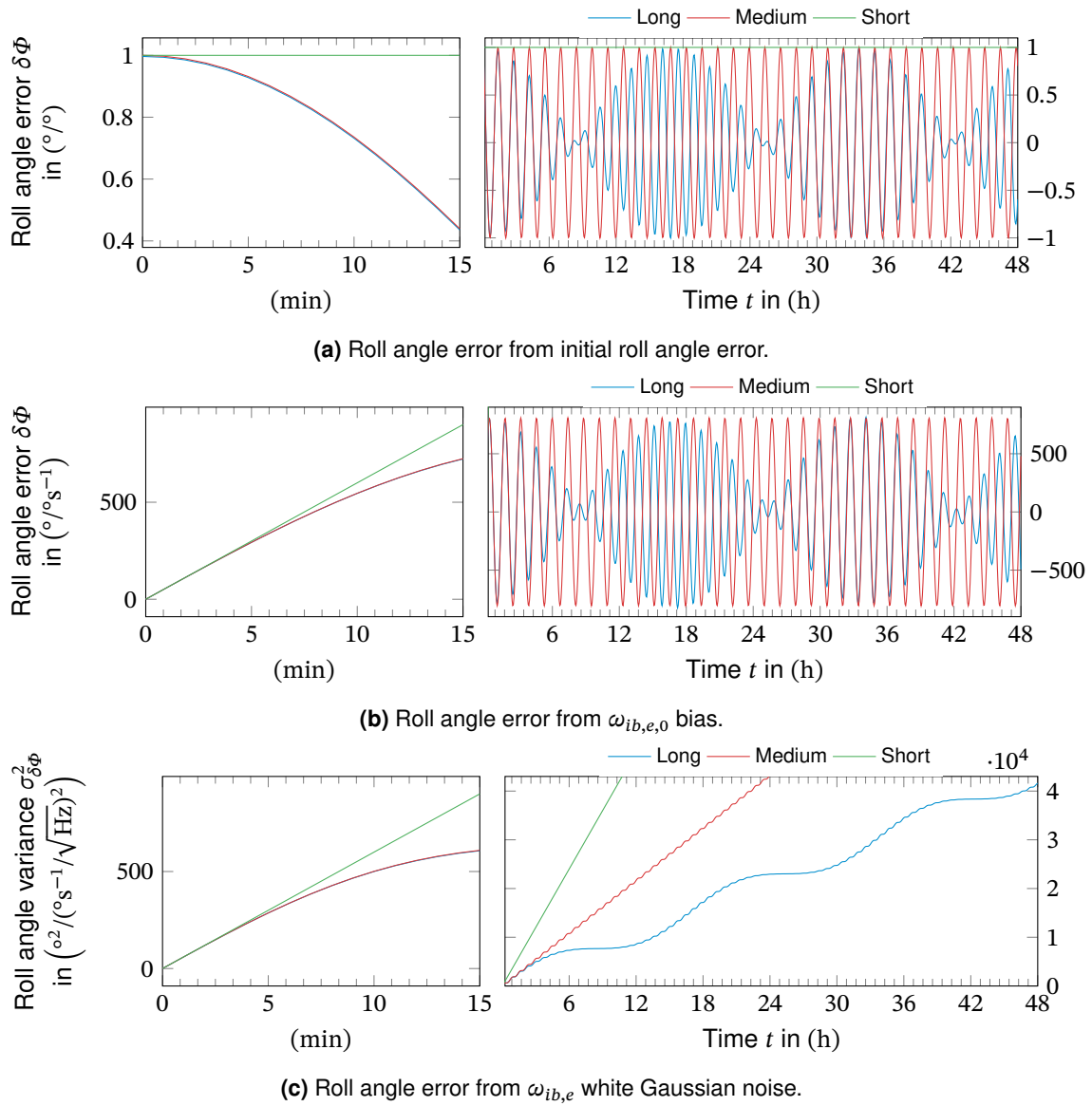


Figure 3.76.: Comparison of different approximations for the roll angle error.

Result 3: Short- and Medium-Term Approximations of the Strapdown Error Dynamics

In this section, the classical short- and medium-term approximations of the strapdown navigation error propagation have been derived from the long-term solutions.

Compared to the long-term solutions, the validity of the approximated solutions was assessed:

- The classical short-term approximation with polynomially error growth provides a good approximation of the navigation error dynamics for up to 10 min.
- The classical medium-term approximation with sinusoidal error growth provides a good approximation of the navigation error dynamics for a few Schuler periods, which is approximately 4 h.
- Although the short and medium-term approximations indicate a higher error growth than the long-term solution, they cannot be used as a worst-case approximation: Both approximations lack system responses that arise from a coupling of the different states and fail to represent sign changes observed in the long-term solutions.

In summary, long-term solutions should be preferred over approximations whenever possible during system design.

However, the short- and medium-term approximations may be feasible to assess the short-time error growth locally in specific situations.

Chapter 4.

Inertial Sensor Laboratory Testing

4.1. Introduction

This chapter focuses on determining the sensor errors as a basis for both sensor *testing* and *calibration*. The chapter starts with deriving a kinematic model for the entire inertial laboratory, including a three-axis rate table. Subsequently, various error sources along the kinematic model are identified, and mathematical models are created. These models are then used to determine the test accuracy in two different approaches: First, error budgets for the typical analytical sensor test procedures are created in [Section 4.4](#). Second, a Kalman-filter-based approach with inherent test accuracy estimation is developed in [Section 4.5](#).

4.2. Inertial Laboratory Modeling

4.2.1. General Inertial Laboratory Kinematic Model

Laboratory calibration and testing of inertial sensors require precise knowledge of the applied reference angular rates and accelerations. This chapter first discusses the mathematical modeling of an ideal inertial laboratory to determine ideal (error-free) sensor measurements for the analysis and numerical simulation of the calibration and testing process. Subsequently, this ideal model is expanded by introducing error terms connected to real-world effects and error sources.

To derive a universal model of an inertial laboratory, a representative laboratory setup is selected:

- The inertial laboratory is placed at a fixed location on Earth. The instruments are placed on a test pad. This can be either passively isolated or actively stabilized.
- For this model, a three-axis rate table is used as a reference. While this is not necessarily a typical test setup, it provides a reasonably general model that can be easily reduced to two-axis and single-axis rate tables or dividing heads by simply fixing the exceeding degrees of freedom.
- The sensor always represents the top of the kinematic chain. Orientation and position of the sensor with respect to the rate table is fixed but can be changed between tests.

Based on this setup, the kinematic chain is developed from an *inertial* reference frame to the sensors reference frame. An overview of this chain and the used reference frames is illustrated in Figure 4.1. Additionally, the definitions of the reference frames are illustrated in Figure 4.2.

4.2.1.1. Angular Rates

Following the kinematic chain, the total angular rate with respect to the inertial frame, given in the sensor's body fixed frame is given as:

$$\boldsymbol{\omega}_{in} = \mathbf{R}_{ne}\boldsymbol{\omega}_{ie} \quad (4.1)$$

$$\boldsymbol{\omega}_{ip} = \mathbf{R}_{pn}\boldsymbol{\omega}_{in} + \boldsymbol{\omega}_{np} \quad (4.2)$$

$$\boldsymbol{\omega}_{iw} = \mathbf{R}_{wp}\boldsymbol{\omega}_{ip} + \boldsymbol{\omega}_{pw} \quad (4.3)$$

$$\boldsymbol{\omega}_{iv} = \mathbf{R}_{vw}\boldsymbol{\omega}_{iw} + \boldsymbol{\omega}_{wv} \quad (4.4)$$

$$\boldsymbol{\omega}_{iu} = \mathbf{R}_{uv}\boldsymbol{\omega}_{iv} + \boldsymbol{\omega}_{vu} \quad (4.5)$$

$$\boldsymbol{\omega}_{ib} = \mathbf{R}_{bu}\boldsymbol{\omega}_{iu} + \boldsymbol{\omega}_{ub} \quad (4.6)$$

with

- $\boldsymbol{\omega}_{ub}$ Angular rate of the sensor body with respect to the inner gimbal.
- $\boldsymbol{\omega}_{vu}$ Angular rate of the inner gimbal with respect to the middle gimbal.
- $\boldsymbol{\omega}_{wv}$ Angular rate of the middle gimbal with respect to the outer gimbal.
- $\boldsymbol{\omega}_{pw}$ Angular rate of the outer gimbal with respect to the test pad.
- $\boldsymbol{\omega}_{np}$ Angular rate of the test pad with respect to the local NED frame.
- $\boldsymbol{\omega}_{ie}$ Angular rate of the ECEF frame with respect to the inertial reference frame.
- \mathbf{R}_{bu} Rotation matrix from the inner gimbal's to the sensor's body fixed frame.
- \mathbf{R}_{uv} Rotation matrix from the middle gimbal's to the inner gimbal's frame.
- \mathbf{R}_{vw} Rotation matrix from the outer gimbal's to the middle gimbal's frame.
- \mathbf{R}_{wp} Rotation matrix from the test pad to the outer gimbal's frame.
- \mathbf{R}_{pn} Rotation matrix from the local NED frame to the test pad's frame.
- \mathbf{R}_{ne} Rotation matrix from the ECEF frame to the local NED frame.

The total angular rate comprises the summed-up angular rates of each rate table gimbal, the test pad motion, and the Earth's angular rate. In general, there may be an angular rate between the inner gimbal and the sensor due to oscillations of the mechanical fixture. However, there is no angular rate between the laboratory's reference location (the NED frame) and the ECEF frame. The laboratory's location is just a reference point, and any laboratory motion will be attributed to the pad's deviation from this reference point.

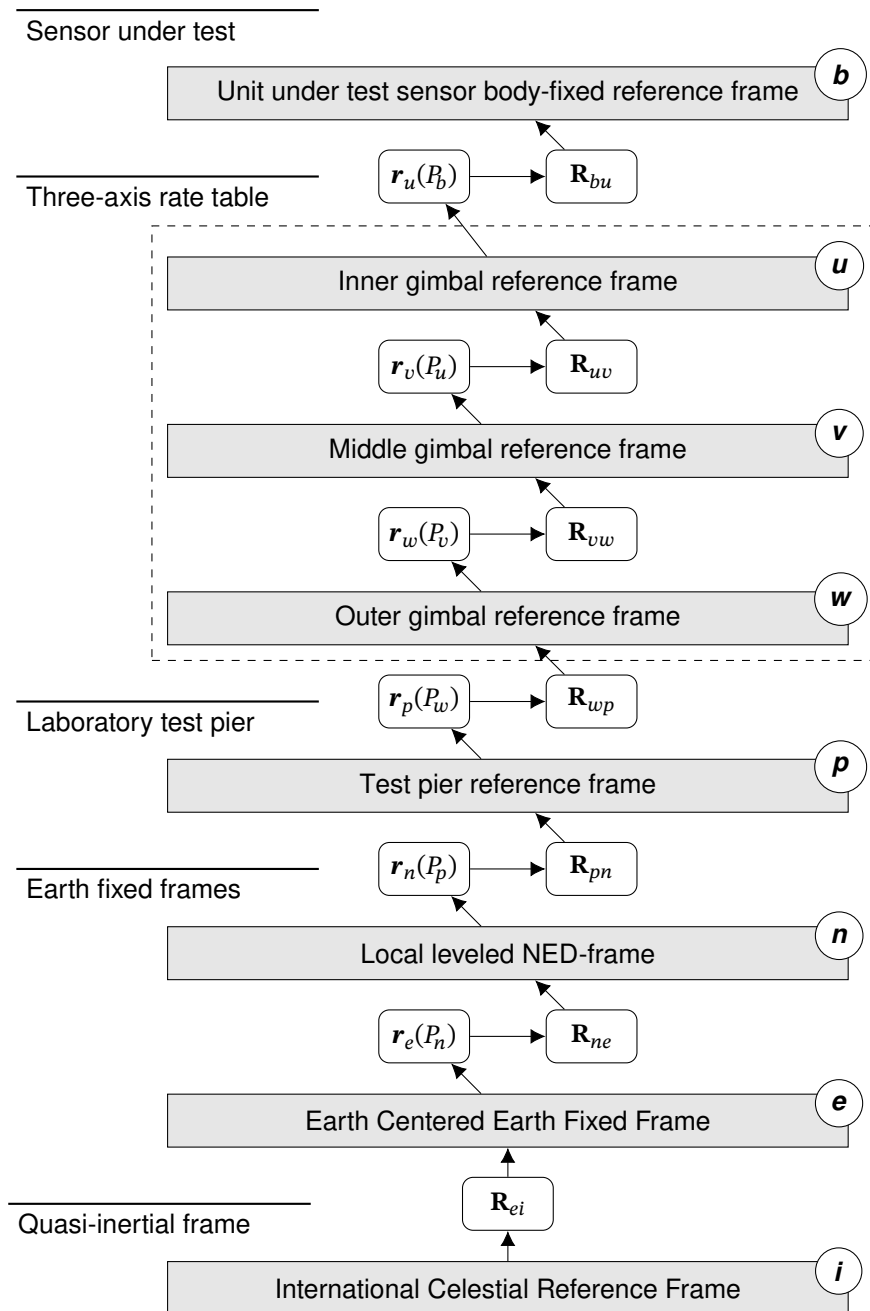


Figure 4.1.: Kinematic chain of the inertial laboratory. The figure illustrates the different translations and rotations from the inertial reference frame to the sensor's body-fixed frame in the laboratory. The three-axis rate table (dashed-box) is selected as a general example and can be easily replaced by the actual setup, like two- or single-axis tables or shakers.

4.2.1.2. Angular Acceleration

Using the classical kinematic relations, the angular acceleration with respect to the inertial frame can be given as:

$$\dot{\omega}_{in} = \mathbf{R}_{ne}\dot{\omega}_{ie} \quad (4.7)$$

$$\dot{\omega}_{ip} = \mathbf{R}_{pn} [\dot{\omega}_{in} + \omega_{in} \times \omega_{np}] + \dot{\omega}_{np} \quad (4.8)$$

$$\dot{\omega}_{iw} = \mathbf{R}_{wp} [\dot{\omega}_{ip} + \omega_{ip} \times \omega_{pw}] + \dot{\omega}_{pw} \quad (4.9)$$

$$\dot{\omega}_{iv} = \mathbf{R}_{vw} [\dot{\omega}_{iw} + \omega_{iw} \times \omega_{wv}] + \dot{\omega}_{wv} \quad (4.10)$$

$$\dot{\omega}_{iu} = \mathbf{R}_{uv} [\dot{\omega}_{iv} + \omega_{iv} \times \omega_{vu}] + \dot{\omega}_{vu} \quad (4.11)$$

$$\dot{\omega}_{ib} = \mathbf{R}_{bu} [\dot{\omega}_{iu} + \omega_{iu} \times \omega_{ub}] + \dot{\omega}_{ub} \quad (4.12)$$

Again, a general model is derived, allowing a non-constant angular rate of the Earth and angular accelerations between all frames of the rate table.

4.2.1.3. Translational Kinematics

The position of the sensor's reference point with respect to the laboratory's reference location is given as:

$$\mathbf{r}_v(P_b) = \mathbf{r}_v(P_u) + \mathbf{R}_{vu}\mathbf{r}_u(P_b) \quad (4.13)$$

$$\mathbf{r}_w(P_b) = \mathbf{r}_w(P_v) + \mathbf{R}_{wv}\mathbf{r}_v(P_b) \quad (4.14)$$

$$\mathbf{r}_p(P_b) = \mathbf{r}_p(P_w) + \mathbf{R}_{pw}\mathbf{r}_w(P_b) \quad (4.15)$$

$$\mathbf{r}_n(P_b) = \mathbf{r}_n(P_p) + \mathbf{R}_{np}\mathbf{r}_p(P_b) \quad (4.16)$$

where

$\mathbf{r}_u(P_b)$ Position of the sensor's reference point with respect to the inner gimbal's frame.

$\mathbf{r}_v(P_u)$ Position of the inner gimbal's origin with respect to the middle gimbal's frame.

$\mathbf{r}_w(P_v)$ Position of the middle gimbal's origin with respect to the outer gimbal's frame.

$\mathbf{r}_p(P_w)$ Position of the outer gimbal's origin with respect to the test pad's frame.

$\mathbf{r}_n(P_p)$ Position of the test pad's origin with respect to the local NED frame.

4.2.1.4. Specific Forces

More critical for inertial sensor testing are the specific forces during testing. Using the Earth's gravity at the sensor's position $\gamma(P_b)$ that already includes the forces caused by the Earth's rotation ω_{ie} , the acceleration along the kinematic chain and the sensor's specific forces are given as:

$$\mathbf{a}_n = 0 \quad (4.17)$$

$$\mathbf{a}_p = \mathbf{R}_{pn} [\boldsymbol{\Omega}_{en} \boldsymbol{\Omega}_{en} \mathbf{r}_n(P_p) + \dot{\boldsymbol{\Omega}}_{en} \mathbf{r}_n(P_p) + 2\boldsymbol{\Omega}_{en} \dot{\mathbf{r}}_n(P_p) + \ddot{\mathbf{r}}_n(P_p) + \mathbf{a}_n] \quad (4.18)$$

$$\mathbf{a}_w = \mathbf{R}_{wp} [\boldsymbol{\Omega}_{ep} \boldsymbol{\Omega}_{ep} \mathbf{r}_p(P_w) + \dot{\boldsymbol{\Omega}}_{ep} \mathbf{r}_p(P_w) + 2\boldsymbol{\Omega}_{ep} \dot{\mathbf{r}}_p(P_w) + \ddot{\mathbf{r}}_p(P_w) + \mathbf{a}_p] \quad (4.19)$$

$$\mathbf{a}_v = \mathbf{R}_{vw} [\boldsymbol{\Omega}_{ew} \boldsymbol{\Omega}_{ew} \mathbf{r}_w(P_v) + \dot{\boldsymbol{\Omega}}_{ew} \mathbf{r}_w(P_v) + 2\boldsymbol{\Omega}_{ew} \dot{\mathbf{r}}_w(P_v) + \ddot{\mathbf{r}}_w(P_v) + \mathbf{a}_w] \quad (4.20)$$

$$\mathbf{a}_u = \mathbf{R}_{uv} [\boldsymbol{\Omega}_{ev} \boldsymbol{\Omega}_{ev} \mathbf{r}_v(P_u) + \dot{\boldsymbol{\Omega}}_{ev} \mathbf{r}_v(P_u) + 2\boldsymbol{\Omega}_{ev} \dot{\mathbf{r}}_v(P_u) + \ddot{\mathbf{r}}_v(P_u) + \mathbf{a}_v] \quad (4.21)$$

$$\mathbf{a}_b = \mathbf{R}_{bu} [\boldsymbol{\Omega}_{eu} \boldsymbol{\Omega}_{eu} \mathbf{r}_u(P_b) + \dot{\boldsymbol{\Omega}}_{eu} \mathbf{r}_u(P_b) + 2\boldsymbol{\Omega}_{eu} \dot{\mathbf{r}}_u(P_b) + \ddot{\mathbf{r}}_u(P_b) + \mathbf{a}_u] \quad (4.22)$$

$$\mathbf{f}_b = \mathbf{a}_b + \mathbf{R}_{bn} \boldsymbol{\gamma}_n(P_b) \quad (4.23)$$

As the local NED-frame is fixed to the ECEF-frame ($\boldsymbol{\omega}_{en} = 0$), the angular rate respectively angular acceleration of the n-Frame is given by:

$$\boldsymbol{\Omega}_{in} = \boldsymbol{\omega}_{in} \times = (\mathbf{R}_{ne} \boldsymbol{\omega}_{ie}) \times \quad (4.24)$$

$$\dot{\boldsymbol{\Omega}}_{in} = \dot{\boldsymbol{\omega}}_{in} \times = (\mathbf{R}_{ne} \dot{\boldsymbol{\omega}}_{ie}) \times \quad (4.25)$$

4.2.2. Ideal Inertial Laboratory Model

In calibration, the sensor's output is always related to the reference sensor input. An ideal model of the inertial laboratory and its equipment is required to determine the reference input from the test instrument's commanded motion (or vice-versa). For an ideal laboratory, several assumptions are taken on the testing equipment as well as the laboratory environment:

- The rate table gimbals and the mechanical fixture of the sensor are perfectly rigid bodies. This eliminates $\hat{\boldsymbol{\omega}}_{ub}$, $\dot{\hat{\boldsymbol{\omega}}}_{ub}$ and $\hat{\mathbf{r}}_u(P_b)$ as well as the rate table translational errors $\hat{\mathbf{r}}_v(P_u)$, $\dot{\hat{\mathbf{r}}}_v(P_u)$ and $\hat{\mathbf{r}}_p(P_w)$.
- The position of the rate table on the test pad is fixed and known. All rotation axes intersect in one single point. The position $\hat{\mathbf{r}}_u(P_b)$ and orientation \mathbf{R}_{bu} of the inertial sensor relative to the inner gimbal's reference frame is known and constant. The translation vectors simplify to:

$$\hat{\mathbf{r}}_p(P_w) = \begin{bmatrix} x_w \\ y_w \\ z_w \end{bmatrix}, \quad \hat{\mathbf{r}}_w(P_v) = \begin{bmatrix} 0 \\ 0 \\ z_v \end{bmatrix}, \quad \hat{\mathbf{r}}_v(P_u) = \begin{bmatrix} 0 \\ 0 \\ 0 \end{bmatrix}, \quad \hat{\mathbf{r}}_u(P_b) = \begin{bmatrix} x_b \\ y_b \\ z_b \end{bmatrix},$$

- The test pad provides a perfectly stable reference that is locally leveled to the reference ellipsoid and has a fixed azimuth. This eliminates $\hat{\boldsymbol{\omega}}_{np}$, $\dot{\hat{\boldsymbol{\omega}}}_{np}$ and $\hat{\mathbf{r}}_n(P_p)$. Further more

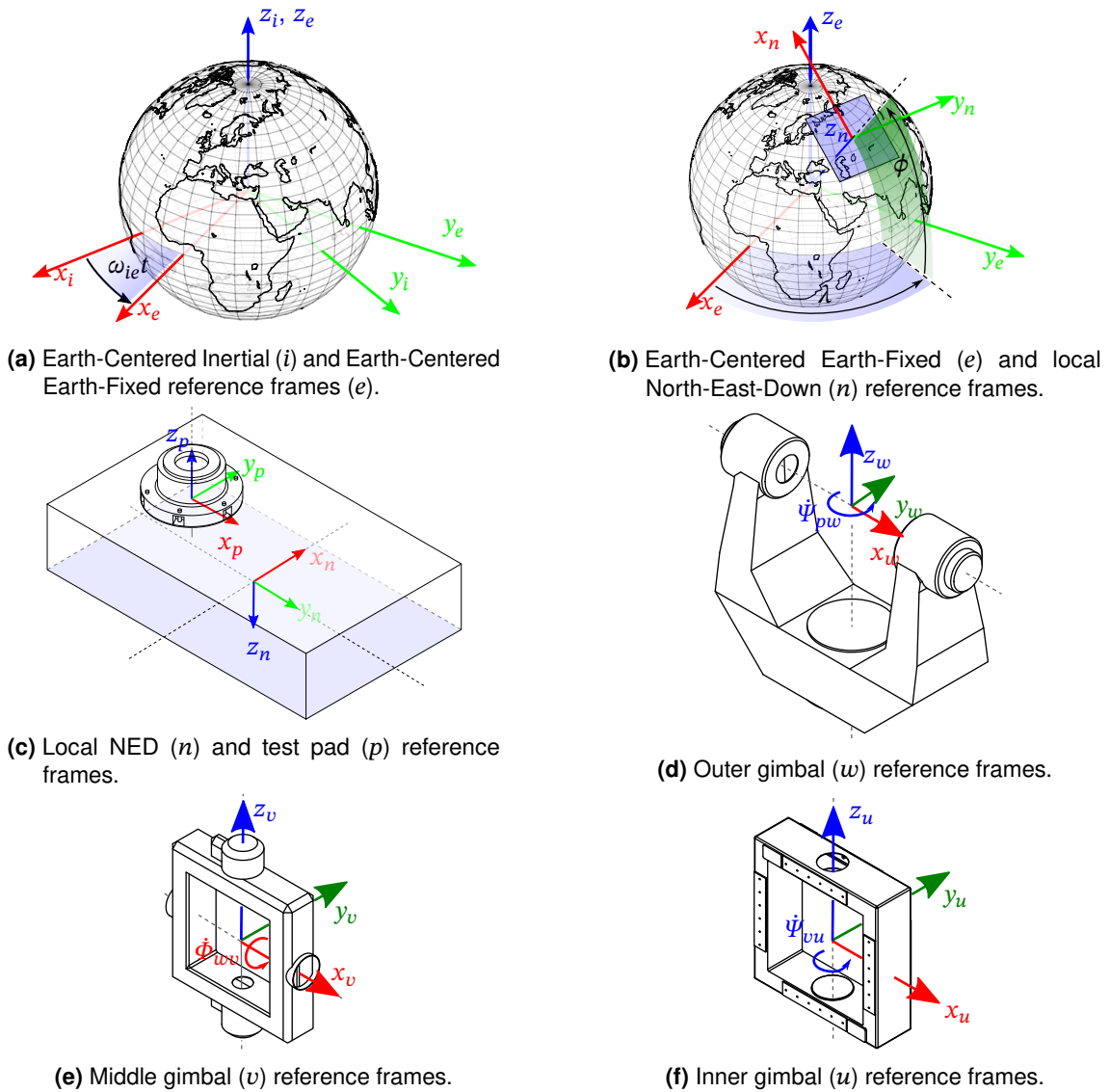


Figure 4.2.: Definition of reference frames used in the inertial laboratory kinematic model. The colored arrows indicate the reference axes and motion of an ideal laboratory.

the rotation between the NED frame and the pad is fixed to

$$\mathbf{R}_{pn} = \begin{bmatrix} 0 & 1 & 0 \\ 1 & 0 & 0 \\ 0 & 0 & -1 \end{bmatrix} \begin{bmatrix} \cos \hat{\psi}_{pn} & -\sin \hat{\psi}_{pn} & 0 \\ \sin \hat{\psi}_{pn} & \cos \hat{\psi}_{pn} & 0 \\ 0 & 0 & 1 \end{bmatrix}.$$

- The rate table is error-free and the rotation follows exactly the ideal rotation axes. The motion of the inner gimbal around its z axis is described by:

$$\mathbf{R}_{uv} = \begin{bmatrix} \cos \hat{\psi}_{uv} & -\sin \hat{\psi}_{uv} & 0 \\ \sin \hat{\psi}_{uv} & \cos \hat{\psi}_{uv} & 0 \\ 0 & 0 & 1 \end{bmatrix}, \quad \hat{\omega}_{vu} = \begin{bmatrix} 0 \\ 0 \\ \dot{\hat{\psi}}_{vu} \end{bmatrix}$$

The middle gimbal ideally rotates around its x -axis. The corresponding rotation matrix and angular rate are:

$$\mathbf{R}_{vw} = \begin{bmatrix} 1 & 0 & 0 \\ 0 & \cos \hat{\phi}_{vw} & \sin \hat{\phi}_{vw} \\ 0 & -\sin \hat{\phi}_{vw} & \cos \hat{\phi}_{vw} \end{bmatrix}, \quad \hat{\omega}_{vw} = \begin{bmatrix} \dot{\hat{\phi}}_{vw} \\ 0 \\ 0 \end{bmatrix}$$

Analogue to the inner gimbal, the outer gimbal performs a rotation around its z axis:

$$\mathbf{R}_{wp} = \begin{bmatrix} \cos \hat{\psi}_{wp} & -\sin \hat{\psi}_{wp} & 0 \\ \sin \hat{\psi}_{wp} & \cos \hat{\psi}_{wp} & 0 \\ 0 & 0 & 1 \end{bmatrix}, \quad \hat{\omega}_{pw} = \begin{bmatrix} 0 \\ 0 \\ \dot{\hat{\psi}}_{pw} \end{bmatrix}$$

- The Earth's angular rate is assumed to be constant, eliminating $\dot{\omega}_{ie}$. The nominal WGS84 Earth's angular rate is assumed, yielding the angular rate vector:

$$\hat{\omega}_{ie} = \begin{bmatrix} 0 \\ 0 \\ \omega_{ie} \end{bmatrix}, \quad \omega_{ie} = 7\,292\,115 \cdot 10^{-11} \text{ rad/s}$$

The above assumptions are, of course, very optimistic. However, this ideal model is often the best estimate for the true motion, as the error's actual manifestation is usually unknown. Under above assumptions the expression for the angular rates (4.6) is reduced to:

$$\hat{\omega}_{ib} = \mathbf{R}_{bu} [\hat{\omega}_{vu} + \mathbf{R}_{vu} [\hat{\omega}_{vw} + \mathbf{R}_{vw} [\hat{\omega}_{pw} + \mathbf{R}_{wp} \mathbf{R}_{pn} \mathbf{R}_{ne} \hat{\omega}_{ie}]]] \quad (4.26)$$

The angular accelerations for an ideal laboratory are determined analogously from (4.12):

$$\begin{aligned}\hat{\omega}_{ib} &= \mathbf{R}_{bu} [\hat{\omega}_{vu} + (\mathbf{R}_{uv}\hat{\omega}_{iv}) \times \hat{\omega}_{vu}] + \\ &\quad \mathbf{R}_{bu}\mathbf{R}_{uv} [\hat{\omega}_{wv} + (\mathbf{R}_{vw}\hat{\omega}_{iw}) \times \hat{\omega}_{wv}] + \\ &\quad \mathbf{R}_{bu}\mathbf{R}_{uv}\mathbf{R}_{vw} [\hat{\omega}_{pw} + (\mathbf{R}_{wp}\hat{\omega}_{ip}) \times \hat{\omega}_{pw}]\end{aligned}\quad (4.27)$$

Application of the idealizations on (4.23) yields:

$$\begin{aligned}\hat{f}_b &= \mathbf{R}_{bu} \left[(\dot{\hat{\Omega}}_{iu} + \hat{\Omega}_{iu}\hat{\Omega}_{iu}) \hat{r}_u(P_b) \right] + \\ &\quad \mathbf{R}_{bu}\mathbf{R}_{uv}\mathbf{R}_{vw} \left[(\dot{\hat{\Omega}}_{iw} + \hat{\Omega}_{iw}\hat{\Omega}_{iw}) \hat{r}_w(P_v) \right] + \\ &\quad \mathbf{R}_{bu}\mathbf{R}_{uv}\mathbf{R}_{vw}\mathbf{R}_{wp} \left[(\dot{\hat{\Omega}}_{ip} + \hat{\Omega}_{ip}\hat{\Omega}_{ip}) \hat{r}_p(P_w) \right] + \\ &\quad \mathbf{R}_{bu}\mathbf{R}_{uv}\mathbf{R}_{vw}\mathbf{R}_{wp}\mathbf{R}_{pn}\hat{g}_n(P_n)\end{aligned}\quad (4.28)$$

In reality, these idealizations do not hold. The following sections will discuss the different error sources and how they corrupt the reference motion.

4.2.3. IMU Reference Signal Linearized Error Sensitivity

The error budget of the inertial laboratory will be based on the linearized sensitivity of the IMU's reference motion ω_{ib} , f_b to different error sources. Therefore, all transformations and motion vectors in equations (4.6), (4.12) and (4.23) are split into an **ideal** (modeled) part and an error part. Errors are grouped into **error states** along the kinematic chain and input **error parameters**. Orientation errors are thereby expressed by a following (multiplying from the left) rotation matrix representing the necessary rotation from the ideal reference frame orientation to its true orientation. Applying above procedure to the angular rate equations (4.6) yields:

$$\hat{\omega}_{in} + \delta\omega_{in} = \mathbf{R}_{n\hat{n}} \mathbf{R}_{\hat{n}e} (\hat{\omega}_{ie} + \delta\omega_{ie}) \quad (4.29)$$

$$\hat{\omega}_{ip} + \delta\omega_{ip} = \mathbf{R}_{p\hat{p}} \mathbf{R}_{\hat{p}n} (\hat{\omega}_{in} + \delta\omega_{in}) + (\hat{\omega}_{np} + \delta\omega_{np}) \quad (4.30)$$

$$\hat{\omega}_{iw} + \delta\omega_{iw} = \mathbf{R}_{w\hat{w}} \mathbf{R}_{\hat{w}p} (\hat{\omega}_{ip} + \delta\omega_{ip}) + (\hat{\omega}_{pw} + \delta\omega_{pw}) \quad (4.31)$$

$$\hat{\omega}_{iv} + \delta\omega_{iv} = \mathbf{R}_{v\hat{v}} \mathbf{R}_{\hat{v}w} (\hat{\omega}_{iw} + \delta\omega_{iw}) + (\hat{\omega}_{wv} + \delta\omega_{wv}) \quad (4.32)$$

$$\hat{\omega}_{iu} + \delta\omega_{iu} = \mathbf{R}_{u\hat{u}} \mathbf{R}_{\hat{u}v} (\hat{\omega}_{iv} + \delta\omega_{iv}) + (\hat{\omega}_{vu} + \delta\omega_{vu}) \quad (4.33)$$

$$\hat{\omega}_{ib} + \delta\omega_{ib} = \mathbf{R}_{b\hat{b}} \mathbf{R}_{\hat{b}u} (\hat{\omega}_{iu} + \delta\omega_{iu}) + (\hat{\omega}_{ub} + \delta\omega_{ub}) \quad (4.34)$$

The angular accelerations (4.12) are separated analogously:

$$\dot{\hat{\omega}}_{in} + \delta\dot{\omega}_{in} = \mathbf{R}_{n\hat{n}} \mathbf{R}_{\hat{n}e} (\dot{\hat{\omega}}_{ie} + \delta\dot{\omega}_{ie}) \quad (4.35)$$

$$\begin{aligned} \hat{\omega}_{ip} + \delta\omega_{ip} &= \mathbf{R}_{p\hat{p}} \mathbf{R}_{\hat{p}n} \left[\left(\hat{\omega}_{in} + \delta\omega_{in} \right) + \left(\hat{\omega}_{in} + \delta\omega_{in} \right) \times \left(\hat{\omega}_{np} + \delta\omega_{np} \right) \right] \\ &\quad + \left(\hat{\omega}_{np} + \delta\omega_{np} \right) \end{aligned} \quad (4.36)$$

$$\begin{aligned} \hat{\omega}_{iw} + \delta\omega_{iw} &= \mathbf{R}_{w\hat{w}} \mathbf{R}_{\hat{w}p} \left[\left(\hat{\omega}_{ip} + \delta\omega_{ip} \right) + \left(\hat{\omega}_{ip} + \delta\omega_{ip} \right) \times \left(\hat{\omega}_{pw} + \delta\omega_{pw} \right) \right] \\ &\quad + \left(\hat{\omega}_{pw} + \delta\omega_{pw} \right) \end{aligned} \quad (4.37)$$

$$\begin{aligned} \hat{\omega}_{iv} + \delta\omega_{iv} &= \mathbf{R}_{v\hat{v}} \mathbf{R}_{\hat{v}w} \left[\left(\hat{\omega}_{iw} + \delta\omega_{iw} \right) + \left(\hat{\omega}_{iw} + \delta\omega_{iw} \right) \times \left(\hat{\omega}_{vw} + \delta\omega_{vw} \right) \right] \\ &\quad + \left(\hat{\omega}_{vw} + \delta\omega_{vw} \right) \end{aligned} \quad (4.38)$$

$$\begin{aligned} \hat{\omega}_{iu} + \delta\omega_{iu} &= \mathbf{R}_{u\hat{u}} \mathbf{R}_{\hat{u}v} \left[\left(\hat{\omega}_{iv} + \delta\omega_{iv} \right) + \left(\hat{\omega}_{iv} + \delta\omega_{iv} \right) \times \left(\hat{\omega}_{vu} + \delta\omega_{vu} \right) \right] \\ &\quad + \left(\hat{\omega}_{vu} + \delta\omega_{vu} \right) \end{aligned} \quad (4.39)$$

$$\begin{aligned} \hat{\omega}_{ib} + \delta\omega_{ib} &= \mathbf{R}_{b\hat{b}} \mathbf{R}_{\hat{b}u} \left[\left(\hat{\omega}_{iu} + \delta\omega_{iu} \right) + \left(\hat{\omega}_{iu} + \delta\omega_{iu} \right) \times \left(\hat{\omega}_{ub} + \delta\omega_{ub} \right) \right] \\ &\quad + \left(\hat{\omega}_{ub} + \delta\omega_{ub} \right) \end{aligned} \quad (4.40)$$

The accelerations and specific forces equations (4.23) are separated in the same way.

$$\begin{aligned} \hat{\mathbf{a}}_p + \delta\mathbf{a}_p &= \mathbf{R}_{p\hat{p}} \mathbf{R}_{\hat{p}n} \left[\left(\hat{\Omega}_{en} + \delta\Omega_{en} \right)^2 \left(\hat{\mathbf{r}}_n(P_p) + \delta\mathbf{r}_n(P_p) \right) \right. \\ &\quad + \left(\hat{\dot{\Omega}}_{en} + \delta\dot{\Omega}_{en} \right) \left(\hat{\mathbf{r}}_n(P_p) + \delta\mathbf{r}_n(P_p) \right) \\ &\quad + 2 \left(\hat{\Omega}_{en} + \delta\Omega_{en} \right) \left(\hat{\dot{\mathbf{r}}}_n(P_p) + \delta\dot{\mathbf{r}}_n(P_p) \right) \\ &\quad \left. + \left(\hat{\ddot{\mathbf{r}}}_n(P_p) + \delta\ddot{\mathbf{r}}_n(P_p) \right) \right] \end{aligned} \quad (4.41)$$

$$\begin{aligned} \hat{\mathbf{a}}_w + \delta\mathbf{a}_w &= \mathbf{R}_{w\hat{w}} \mathbf{R}_{\hat{w}p} \left[\left(\hat{\Omega}_{ep} + \delta\Omega_{ep} \right)^2 \left(\hat{\mathbf{r}}_p(P_w) + \delta\mathbf{r}_p(P_w) \right) \right. \\ &\quad + \left(\hat{\dot{\Omega}}_{ep} + \delta\dot{\Omega}_{ep} \right) \left(\hat{\mathbf{r}}_p(P_w) + \delta\mathbf{r}_p(P_w) \right) \\ &\quad + 2 \left(\hat{\Omega}_{ep} + \delta\Omega_{ep} \right) \left(\hat{\dot{\mathbf{r}}}_p(P_w) + \delta\dot{\mathbf{r}}_p(P_w) \right) \\ &\quad \left. + \left(\hat{\ddot{\mathbf{r}}}_p(P_w) + \delta\ddot{\mathbf{r}}_p(P_w) \right) + \left(\hat{\mathbf{a}}_p + \delta\mathbf{a}_p \right) \right] \end{aligned} \quad (4.42)$$

$$\begin{aligned} \hat{\mathbf{a}}_v + \delta\mathbf{a}_v &= \mathbf{R}_{v\hat{v}} \mathbf{R}_{\hat{v}w} \left[\left(\hat{\Omega}_{ew} + \delta\Omega_{ew} \right)^2 \left(\hat{\mathbf{r}}_w(P_v) + \delta\mathbf{r}_w(P_v) \right) \right. \\ &\quad + \left(\hat{\dot{\Omega}}_{ew} + \delta\dot{\Omega}_{ew} \right) \left(\hat{\mathbf{r}}_w(P_v) + \delta\mathbf{r}_w(P_v) \right) \\ &\quad + 2 \left(\hat{\Omega}_{ew} + \delta\Omega_{ew} \right) \left(\hat{\dot{\mathbf{r}}}_w(P_v) + \delta\dot{\mathbf{r}}_w(P_v) \right) \\ &\quad \left. + \left(\hat{\ddot{\mathbf{r}}}_w(P_v) + \delta\ddot{\mathbf{r}}_w(P_v) \right) + \left(\hat{\mathbf{a}}_w + \delta\mathbf{a}_w \right) \right] \end{aligned} \quad (4.43)$$

$$\begin{aligned}
 \hat{\mathbf{a}}_u + \delta \mathbf{a}_u &= \mathbf{R}_{uu} \mathbf{R}_{uv} \left[\left(\hat{\boldsymbol{\Omega}}_{ev} + \delta \boldsymbol{\Omega}_{ev} \right)^2 \left(\hat{\mathbf{r}}_v(P_u) + \delta \mathbf{r}_v(P_u) \right) \right. \\
 &\quad + \left(\dot{\hat{\boldsymbol{\Omega}}}_{ev} + \delta \dot{\boldsymbol{\Omega}}_{ev} \right) \left(\hat{\mathbf{r}}_v(P_u) + \delta \mathbf{r}_v(P_u) \right) \\
 &\quad + 2 \left(\hat{\boldsymbol{\Omega}}_{ev} + \delta \boldsymbol{\Omega}_{ev} \right) \left(\dot{\hat{\mathbf{r}}}_v(P_u) + \delta \dot{\mathbf{r}}_v(P_u) \right) \\
 &\quad \left. + \left(\ddot{\hat{\mathbf{r}}}_v(P_u) + \delta \ddot{\mathbf{r}}_v(P_u) \right) + \left(\hat{\mathbf{a}}_v + \delta \mathbf{a}_v \right) \right]
 \end{aligned} \tag{4.44}$$

$$\begin{aligned}
 \hat{\mathbf{a}}_b + \delta \mathbf{a}_b &= \mathbf{R}_{bb} \mathbf{R}_{bu} \left[\left(\hat{\boldsymbol{\Omega}}_{eu} + \delta \boldsymbol{\Omega}_{eu} \right)^2 \left(\hat{\mathbf{r}}_u(P_b) + \delta \mathbf{r}_u(P_b) \right) \right. \\
 &\quad + \left(\dot{\hat{\boldsymbol{\Omega}}}_{eu} + \delta \dot{\boldsymbol{\Omega}}_{eu} \right) \left(\hat{\mathbf{r}}_u(P_b) + \delta \mathbf{r}_u(P_b) \right) \\
 &\quad + 2 \left(\hat{\boldsymbol{\Omega}}_{eu} + \delta \boldsymbol{\Omega}_{eu} \right) \left(\dot{\hat{\mathbf{r}}}_u(P_b) + \delta \dot{\mathbf{r}}_u(P_b) \right) \\
 &\quad \left. + \left(\ddot{\hat{\mathbf{r}}}_u(P_b) + \delta \ddot{\mathbf{r}}_u(P_b) \right) + \left(\hat{\mathbf{a}}_u + \delta \mathbf{a}_u \right) \right]
 \end{aligned} \tag{4.45}$$

$$\begin{aligned}
 \hat{\mathbf{f}}_b + \delta \mathbf{f}_b &= \left(\hat{\mathbf{a}}_b + \delta \mathbf{a}_b \right) \\
 &\quad + \mathbf{R}_{bb} \mathbf{R}_{bu} \dots \mathbf{R}_{pp} \mathbf{R}_{pn} \left[\hat{\gamma}_n \left(\hat{\mathbf{r}}_e(P_b) + \delta \mathbf{r}_e(P_b) \right) + \delta \gamma_n \left(\hat{\mathbf{r}}_e(P_b) \right) \right]
 \end{aligned} \tag{4.46}$$

Above equations can be easily solved for the errors of the IMU motion $\delta \omega_{ib}$, $\delta \dot{\omega}_{ib}$, $\delta \mathbf{f}_b$, which are the difference between the ideal reference signal and the true motion. Linearizing (4.34) for the error terms and subtracting the ideal angular rates, yields the linear sensitivities of the angular rate errors along the kinematic chain:

$$\delta \omega_{in} \approx \mathbf{R}_{ne} \delta \omega_{ie} - \left(\mathbf{R}_{ne} \hat{\omega}_{ie} \right) \times \boldsymbol{\psi}_{n\hat{n}} \tag{4.47}$$

$$\delta \omega_{ip} \approx \mathbf{R}_{pn} \delta \omega_{in} - \left(\mathbf{R}_{pn} \hat{\omega}_{in} \right) \times \boldsymbol{\psi}_{p\hat{p}} + \delta \omega_{np} \tag{4.48}$$

$$\delta \omega_{iw} \approx \mathbf{R}_{wp} \delta \omega_{ip} - \left(\mathbf{R}_{wp} \hat{\omega}_{ip} \right) \times \boldsymbol{\psi}_{w\hat{w}} + \delta \omega_{pw} \tag{4.49}$$

$$\delta \omega_{iv} \approx \mathbf{R}_{vp} \delta \omega_{ip} - \left(\mathbf{R}_{vp} \hat{\omega}_{ip} \right) \times \boldsymbol{\psi}_{v\hat{v}} + \delta \omega_{vp} \tag{4.50}$$

$$\delta \omega_{iu} \approx \mathbf{R}_{uv} \delta \omega_{iv} - \left(\mathbf{R}_{uv} \hat{\omega}_{iv} \right) \times \boldsymbol{\psi}_{u\hat{u}} + \delta \omega_{vu} \tag{4.51}$$

$$\delta \omega_{ib} \approx \mathbf{R}_{bu} \delta \omega_{iu} - \left(\mathbf{R}_{bu} \hat{\omega}_{iu} \right) \times \boldsymbol{\psi}_{b\hat{b}} + \delta \omega_{ub} \tag{4.52}$$

The same procedure is applied to the angular accelerations:

$$\delta \dot{\omega}_{in} \approx \mathbf{R}_{ne} \delta \dot{\omega}_{ie} - \left(\mathbf{R}_{ne} \hat{\omega}_{ie} \right) \times \boldsymbol{\psi}_{n\hat{n}} \tag{4.53}$$

$$\begin{aligned}
 \delta \dot{\omega}_{ip} &\approx \mathbf{R}_{pn} \delta \dot{\omega}_{in} + \mathbf{R}_{pn} \hat{\omega}_{in} \times \delta \omega_{np} - \mathbf{R}_{pn} \hat{\omega}_{np} \times \delta \omega_{in} \\
 &\quad - \left(\mathbf{R}_{pn} \left(\dot{\hat{\omega}}_{in} + \hat{\omega}_{in} \times \hat{\omega}_{np} \right) \right) \times \boldsymbol{\psi}_{p\hat{p}} + \delta \dot{\omega}_{np}
 \end{aligned} \tag{4.54}$$

$$\begin{aligned}
 \delta \dot{\omega}_{iw} &\approx \mathbf{R}_{wp} \delta \dot{\omega}_{ip} + \mathbf{R}_{wp} \hat{\omega}_{ip} \times \delta \omega_{pw} - \mathbf{R}_{wp} \hat{\omega}_{pw} \times \delta \omega_{ip} \\
 &\quad - \left(\mathbf{R}_{wp} \left(\dot{\hat{\omega}}_{ip} + \hat{\omega}_{ip} \times \hat{\omega}_{pw} \right) \right) \times \boldsymbol{\psi}_{w\hat{w}} + \delta \dot{\omega}_{pw}
 \end{aligned} \tag{4.55}$$

$$\begin{aligned} \delta\dot{\omega}_{iw} \approx & \mathbf{R}_{\hat{v}w} \delta\dot{\omega}_{iw} + \mathbf{R}_{\hat{v}w} \hat{\omega}_{iw} \times \delta\omega_{wv} - \mathbf{R}_{\hat{v}w} \hat{\omega}_{wv} \times \delta\omega_{iw} \\ & - \left(\mathbf{R}_{\hat{v}w} \left(\dot{\hat{\omega}}_{iw} + \hat{\omega}_{iw} \times \hat{\omega}_{wv} \right) \right) \times \boldsymbol{\psi}_{v\hat{v}} + \delta\dot{\omega}_{wv} \end{aligned} \quad (4.56)$$

$$\begin{aligned} \delta\dot{\omega}_{iu} \approx & \mathbf{R}_{\hat{u}v} \delta\dot{\omega}_{iv} + \mathbf{R}_{\hat{u}v} \hat{\omega}_{iv} \times \delta\omega_{vu} - \mathbf{R}_{\hat{u}v} \hat{\omega}_{vu} \times \delta\omega_{iv} \\ & - \left(\mathbf{R}_{\hat{u}v} \left(\dot{\hat{\omega}}_{iv} + \hat{\omega}_{iv} \times \hat{\omega}_{vu} \right) \right) \times \boldsymbol{\psi}_{u\hat{u}} + \delta\dot{\omega}_{vu} \end{aligned} \quad (4.57)$$

$$\begin{aligned} \delta\dot{\omega}_{ib} \approx & \mathbf{R}_{\hat{b}u} \delta\dot{\omega}_{iu} + \mathbf{R}_{\hat{b}u} \hat{\omega}_{iu} \times \delta\omega_{ub} - \mathbf{R}_{\hat{b}u} \hat{\omega}_{ub} \times \delta\omega_{iu} \\ & - \left(\mathbf{R}_{\hat{b}u} \left(\dot{\hat{\omega}}_{iu} + \hat{\omega}_{iu} \times \hat{\omega}_{ub} \right) \right) \times \boldsymbol{\psi}_{b\hat{b}} + \delta\dot{\omega}_{ub} \end{aligned} \quad (4.58)$$

Similarly, the sensitivity of the specific forces errors are determined to:

$$\begin{aligned} \delta\mathbf{a}_p \approx & \mathbf{R}_{p\hat{n}} \left[\left(\hat{\Omega}_{en}^2 + \dot{\hat{\Omega}}_{en} \right) \delta\mathbf{r}_n(P_p) + 2\hat{\Omega}_{en} \delta\dot{\mathbf{r}}_n(P_p) + \delta\ddot{\mathbf{r}}_n(P_p) \right. \\ & \left. - 2\dot{\hat{\mathbf{r}}}_n(P_p) \times \delta\omega_{en} - 2\hat{\Omega}_{en} \hat{\mathbf{r}}_n(P_p) \times \delta\omega_{en} - \hat{\mathbf{r}}_n(P_p) \times \delta\dot{\omega}_{en} \right] \end{aligned} \quad (4.59)$$

$$\begin{aligned} \delta\mathbf{a}_w \approx & \mathbf{R}_{w\hat{p}} \left[\left(\hat{\Omega}_{ep}^2 + \dot{\hat{\Omega}}_{ep} \right) \delta\mathbf{r}_p(P_w) + 2\hat{\Omega}_{ep} \delta\dot{\mathbf{r}}_p(P_w) + \delta\ddot{\mathbf{r}}_p(P_w) \right. \\ & \left. - 2\dot{\hat{\mathbf{r}}}_p(P_w) \times \delta\omega_{ep} - 2\hat{\Omega}_{ep} \hat{\mathbf{r}}_p(P_w) \times \delta\omega_{ep} - \hat{\mathbf{r}}_p(P_w) \times \delta\dot{\omega}_{ep} + \delta\mathbf{a}_p \right] \\ & - \hat{\mathbf{a}}_p \times \boldsymbol{\psi}_{w\hat{w}} \end{aligned} \quad (4.60)$$

$$\begin{aligned} \delta\mathbf{a}_v \approx & \mathbf{R}_{v\hat{w}} \left[\left(\hat{\Omega}_{ew}^2 + \dot{\hat{\Omega}}_{ew} \right) \delta\mathbf{r}_w(P_v) + 2\hat{\Omega}_{ew} \delta\dot{\mathbf{r}}_w(P_v) + \delta\ddot{\mathbf{r}}_w(P_v) \right. \\ & \left. - 2\dot{\hat{\mathbf{r}}}_w(P_v) \times \delta\omega_{ew} - 2\hat{\Omega}_{ew} \hat{\mathbf{r}}_w(P_v) \times \delta\omega_{ew} - \hat{\mathbf{r}}_w(P_v) \times \delta\dot{\omega}_{ew} + \delta\mathbf{a}_w \right] \\ & - \hat{\mathbf{a}}_w \times \boldsymbol{\psi}_{v\hat{v}} \end{aligned} \quad (4.61)$$

$$\begin{aligned} \delta\mathbf{a}_u \approx & \mathbf{R}_{u\hat{v}} \left[\left(\hat{\Omega}_{ev}^2 + \dot{\hat{\Omega}}_{ev} \right) \delta\mathbf{r}_v(P_u) + 2\hat{\Omega}_{ev} \delta\dot{\mathbf{r}}_v(P_u) + \delta\ddot{\mathbf{r}}_v(P_u) \right. \\ & \left. - 2\dot{\hat{\mathbf{r}}}_v(P_u) \times \delta\omega_{ev} - 2\hat{\Omega}_{ev} \hat{\mathbf{r}}_v(P_u) \times \delta\omega_{ev} - \hat{\mathbf{r}}_v(P_u) \times \delta\dot{\omega}_{ev} + \delta\mathbf{a}_v \right] \\ & - \hat{\mathbf{a}}_v \times \boldsymbol{\psi}_{u\hat{u}} \end{aligned} \quad (4.62)$$

$$\begin{aligned} \delta\mathbf{a}_b \approx & \mathbf{R}_{b\hat{u}} \left[\left(\hat{\Omega}_{eu}^2 + \dot{\hat{\Omega}}_{eu} \right) \delta\mathbf{r}_u(P_b) + 2\hat{\Omega}_{eu} \delta\dot{\mathbf{r}}_u(P_b) + \delta\ddot{\mathbf{r}}_u(P_b) \right. \\ & \left. - 2\dot{\hat{\mathbf{r}}}_u(P_b) \times \delta\omega_{eu} - 2\hat{\Omega}_{eu} \hat{\mathbf{r}}_u(P_b) \times \delta\omega_{eu} - \hat{\mathbf{r}}_u(P_b) \times \delta\dot{\omega}_{eu} + \delta\mathbf{a}_u \right] \\ & - \hat{\mathbf{a}}_u \times \boldsymbol{\psi}_{b\hat{b}} \end{aligned} \quad (4.63)$$

$$\begin{aligned}
 \delta \mathbf{f}_b &\approx \delta \mathbf{a}_b + \mathbf{R}_{\hat{b}u} \mathbf{R}_{\hat{u}v} \mathbf{R}_{\hat{v}w} \mathbf{R}_{\hat{w}p} \mathbf{R}_{\hat{p}n} \left(\delta \boldsymbol{\gamma}_n(\hat{\mathbf{r}}_e(P_b)) + \left. \frac{\partial \hat{\boldsymbol{\gamma}}_n(\mathbf{r}_e)}{\partial \mathbf{r}_e} \right|_{P_b} \delta \mathbf{r}_e(P_b) \right) \\
 &\quad - \left(\mathbf{R}_{\hat{b}u} \mathbf{R}_{\hat{u}v} \mathbf{R}_{\hat{v}w} \mathbf{R}_{\hat{w}p} \mathbf{R}_{\hat{p}n} \hat{\boldsymbol{\gamma}}_n(\hat{\mathbf{r}}_e(P_b)) \right) \times \boldsymbol{\psi}_{b\hat{b}} \\
 &\quad - \mathbf{R}_{\hat{b}u} \left(\mathbf{R}_{\hat{u}v} \mathbf{R}_{\hat{v}w} \mathbf{R}_{\hat{w}p} \mathbf{R}_{\hat{p}n} \hat{\boldsymbol{\gamma}}_n(\hat{\mathbf{r}}_e(P_b)) \right) \times \boldsymbol{\psi}_{u\hat{u}} \\
 &\quad - \mathbf{R}_{\hat{b}u} \mathbf{R}_{\hat{u}v} \left(\mathbf{R}_{\hat{v}w} \mathbf{R}_{\hat{w}p} \mathbf{R}_{\hat{p}n} \hat{\boldsymbol{\gamma}}_n(\hat{\mathbf{r}}_e(P_b)) \right) \times \boldsymbol{\psi}_{v\hat{v}} \\
 &\quad - \mathbf{R}_{\hat{b}u} \mathbf{R}_{\hat{u}v} \mathbf{R}_{\hat{v}w} \left(\mathbf{R}_{\hat{w}p} \mathbf{R}_{\hat{p}n} \hat{\boldsymbol{\gamma}}_n(\hat{\mathbf{r}}_e(P_b)) \right) \times \boldsymbol{\psi}_{w\hat{w}} \\
 &\quad - \mathbf{R}_{\hat{b}u} \mathbf{R}_{\hat{u}v} \mathbf{R}_{\hat{v}w} \mathbf{R}_{\hat{w}p} \left(\mathbf{R}_{\hat{p}n} \hat{\boldsymbol{\gamma}}_n(\hat{\mathbf{r}}_e(P_b)) \right) \times \boldsymbol{\psi}_{p\hat{p}} \\
 &\quad - \mathbf{R}_{\hat{b}u} \mathbf{R}_{\hat{u}v} \mathbf{R}_{\hat{v}w} \mathbf{R}_{\hat{w}p} \mathbf{R}_{\hat{p}n} \left(\hat{\boldsymbol{\gamma}}_n(\hat{\mathbf{r}}_e(P_b)) \right) \times \boldsymbol{\psi}_{n\hat{n}}
 \end{aligned} \tag{4.64}$$

The position error $\delta \mathbf{r}_e(P_b)$ used in the determination of the local gravity has the following sensitivities to the defined error parameters:

$$\begin{aligned}
 \delta \mathbf{r}_e(P_b) &\approx \mathbf{R}_{\hat{n}p} \mathbf{R}_{\hat{p}w} \mathbf{R}_{\hat{w}v} \mathbf{R}_{\hat{v}u} \delta \mathbf{r}_u(P_b) + \mathbf{R}_{\hat{n}p} \mathbf{R}_{\hat{p}w} \mathbf{R}_{\hat{w}v} \delta \mathbf{r}_v(P_u) \\
 &\quad + \mathbf{R}_{\hat{n}p} \mathbf{R}_{\hat{p}w} \delta \mathbf{r}_w(P_v) + \mathbf{R}_{\hat{n}p} \delta \mathbf{r}_p(P_w) + \delta \mathbf{r}_n(P_p) \\
 &\quad + \mathbf{R}_{\hat{n}p} \mathbf{R}_{\hat{p}w} \mathbf{R}_{\hat{w}v} \mathbf{R}_{\hat{v}u} (\hat{\mathbf{r}}_u(P_b)) \times \boldsymbol{\psi}_{u\hat{u}} \\
 &\quad + \mathbf{R}_{\hat{n}p} \mathbf{R}_{\hat{p}w} \mathbf{R}_{\hat{w}v} \left[\hat{\mathbf{r}}_v(P_u) + \mathbf{R}_{\hat{v}u} \hat{\mathbf{r}}_u(P_b) \right] \times \boldsymbol{\psi}_{v\hat{v}} \\
 &\quad + \mathbf{R}_{\hat{n}p} \mathbf{R}_{\hat{p}w} \left[\hat{\mathbf{r}}_w(P_v) + \mathbf{R}_{\hat{w}v} \left[\hat{\mathbf{r}}_v(P_u) + \mathbf{R}_{\hat{v}u} \hat{\mathbf{r}}_u(P_b) \right] \right] \times \boldsymbol{\psi}_{w\hat{w}} \\
 &\quad + \mathbf{R}_{\hat{n}p} \left[\hat{\mathbf{r}}_p(P_w) + \mathbf{R}_{\hat{p}w} \left[\hat{\mathbf{r}}_w(P_v) \right. \right. \\
 &\quad \quad \left. \left. + \mathbf{R}_{\hat{w}v} \left[\hat{\mathbf{r}}_v(P_u) + \mathbf{R}_{\hat{v}u} \hat{\mathbf{r}}_u(P_b) \right] \right] \right] \times \boldsymbol{\psi}_{p\hat{p}} \\
 &\quad + \left[\hat{\mathbf{r}}_n(P_p) + \mathbf{R}_{\hat{n}p} \left[\hat{\mathbf{r}}_p(P_w) \right. \right. \\
 &\quad \quad \left. \left. + \mathbf{R}_{\hat{p}w} \left[\hat{\mathbf{r}}_w(P_v) + \mathbf{R}_{\hat{w}v} \left[\hat{\mathbf{r}}_v(P_u) + \mathbf{R}_{\hat{v}u} \hat{\mathbf{r}}_u(P_b) \right] \right] \right] \right] \times \boldsymbol{\psi}_{n\hat{n}}
 \end{aligned} \tag{4.65}$$

The sensitivities of the kinematic properties $\boldsymbol{\omega}_{ib}$, $\dot{\boldsymbol{\omega}}_{ib}$ and \mathbf{f}_b towards the various error parameters are listed in Appendix F. Using the error sensitivities, the contributions of various error sources to the reference motion can be determined. These deviations from the idealized laboratory model will be discussed in the following.

4.2.4. Earth Centered Inertial Frame Approximations

Inertial sensors measure motion relative to the inertial, which is non-accelerated, space. In inertial navigation, the Earth-Centered Inertial reference frame is used as inertial reference. As illustrated in Figure 4.2a, for this idealization, the inertial frame's z-axis coincides with the Earth's rotation axis and is also the Earth Centered Earth Fixed frame's z-axis. Although these definitions are widely and successfully used in inertial navigation, this model is only a rough approximation of the Earth's actual motion.

The Earth's motion is usually determined from the observation of celestial bodies. Using [Very-Long Baseline Interferometry \(VLBI\)](#) on far-distant radio sources (quasars) allows the determination of the Earth's orientation relative to these. From these measurements, the [International Earth Rotation and Reference Systems Service \(IERS\)](#) derives mathematical models to describe the Earth's rotation, and the change of its orientation [97]. In 2011, the motion of the Earth's rotation axis was measured directly for the first time using a 4 m diameter ring-laser gyroscope [98]. In contrast to [VLBI](#) Earth orientation measurements, ring-lasers provide continuous measurements of the Earth's rotation rate.

The [IERS](#) models describes the Earth's orientation as the transformation between the [Geocentric Celestial Reference System \(GCRS\)](#) and the (Earth fixed) [International Terrestrial Reference System \(ITRS\)](#). The [WGS84](#) reference system shares its origin and axis definition with the [ITRS](#), and its realizations are regularly updated to match the [ITRS](#). Today, the coordinates of [WGS84](#) and [ITRS](#) match about 10 cm. For this analysis, the [ITRS](#) will be used as [ECEF](#) frame. Although the [GCRS](#) moves with the Earth, its orientation relative to the space can be considered fixed. Here, the [GCRS](#) is used as an inertial reference frame, being the best reference known today. The acceleration disturbances arising from the Earth's interaction with the other solar system bodies will be discussed in the [Subsection 4.2.5](#).

This model only considers the orientation of the theoretical Earth fixed reference frame relative to the inertial frame. This section does not cover local disturbances and seismic activities since they are attributed to the test pier motion in [Subsection 4.2.8](#).

According to the [IAU 2000](#) and [IAU 2006](#) resolutions [97], the Earth's orientation relative to the celestial reference frame is described by three sequential rotations

$$\mathbf{R}_{ie} = \mathbf{R}_{ir}(t)\mathbf{R}_{rm}(t)\mathbf{R}_{me}(t) \quad (4.66)$$

where

- $\mathbf{R}_{me}(t)$ describes the so-called **Polar Motion**, which is the motion of the Earth's rotation axis within the Earth's body. This wobble motion consists of a one-year oscillation (*annual wobble*) and a 14-months oscillation, called *Chandler wobble*. The annual wobble is mainly caused by the redistribution of the atmosphere's masses with the seasons [99]. The Chandler wobble is a nutation that arises because the Earth's rotation axis does not match its principal axis of inertia and is excited by atmospheric and oceanic processes [100].
- $\mathbf{R}_{rm}(t)$ describes the **Earth Rotation Angle** around the intermediate polar axis. This angle is a direct function of the Universal Time UT1 determined from [VLBI](#) observation of quasars. In contrast to [International Atomic Time \(TAI\)](#), the UT1 does not evolve continuously but follows the variations of the Earth's angular rate, caused e.g. by gravitational interaction with the moon [101, pp. 293–294]. As UT1 does not include subdaily variations, the effects of ocean tides $\Delta UT1_{oceans}$ and libration $\Delta UT1_{libration}$ have to be

added [97]. These result in a variation of the Earth’s rotation rate at periods of 1 year, 0.5 year, 28 days as well as 14 days [102].

- $\mathbf{R}_{ir}(t)$ describes the so called **Motion of the Celestial Pole**, which is the motion of the rotation axis with respect to the celestial (inertial) reference. This motion consists of a precession and nutation. As illustrated in Figure 4.3a, the precession describes a rotation of the 23.5° tilted rotation axis with a period of about 26 000 years. This motion is superposed with a 18.6 years period nutation. These motions are caused by the gravitational interaction with the sun, moon and the planets [103].

Note that the separation between terrestrial (polar) motion and celestial motion (precession and nutation) is, by convention, based on the periods of the different processes. The required measurements and models to determine above rotation matrices for a given time t are published by the IERS [97].

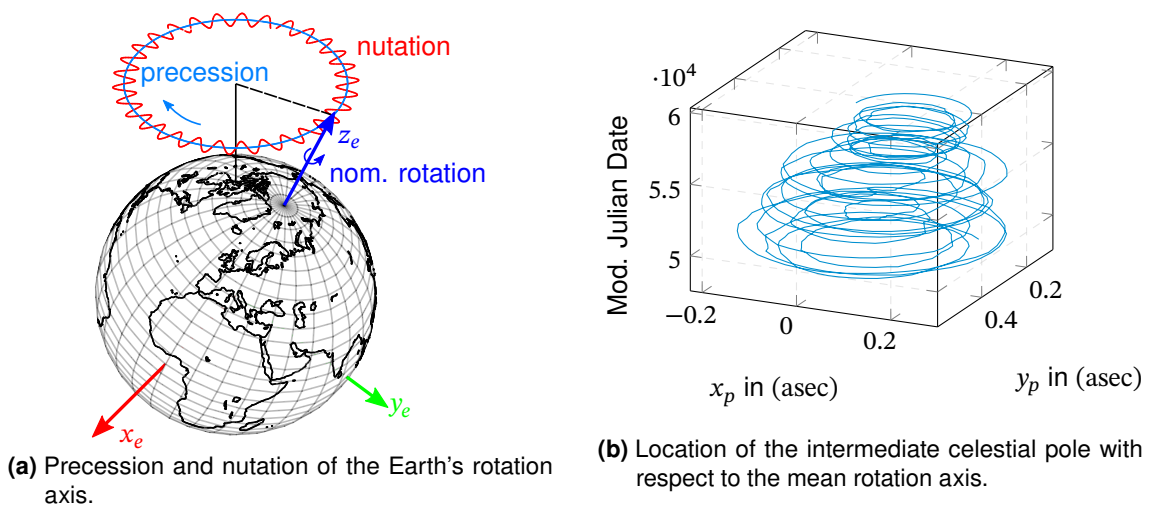


Figure 4.3.: Celestial and terrestrial motion of the Earth’s rotation axis.

Using the IERS Earth orientation data, the orientation and angular rate of the Earth’s surface relative to the inertial space can be determined. Long-term and daily orientation data can be obtained from the IERS website [104]. The error between the basic WGS84 rotation model (constant rotation around z_i) and the angular rate derived from IERS observations over a one-year time scale is given in Figure 4.4. The above-listed processes cause this error. Note that the IERS publishes only daily observations of the orientation. The angular rates have been derived by fourth-order Lagrange interpolation between observations and incorporation of the diurnal and sub-diurnal variations from the Fourier series as modeled in [97]. The accuracy of the utilized EOP observations is stated as about $70 \mu\text{asec}$ for the polar motion and $200 \mu\text{asec}$ for the precession and nutation, as well as $5 \mu\text{s}$ for the length of day corrections [104].

Theoretically, these models would allow highly accurate modeling of the Earth’s angular rate in inertial sensor calibration. However, as there is no continuous rate reference but only daily Earth orientation observation data, the calibration of a sensor bias down to the levels of Earth’s

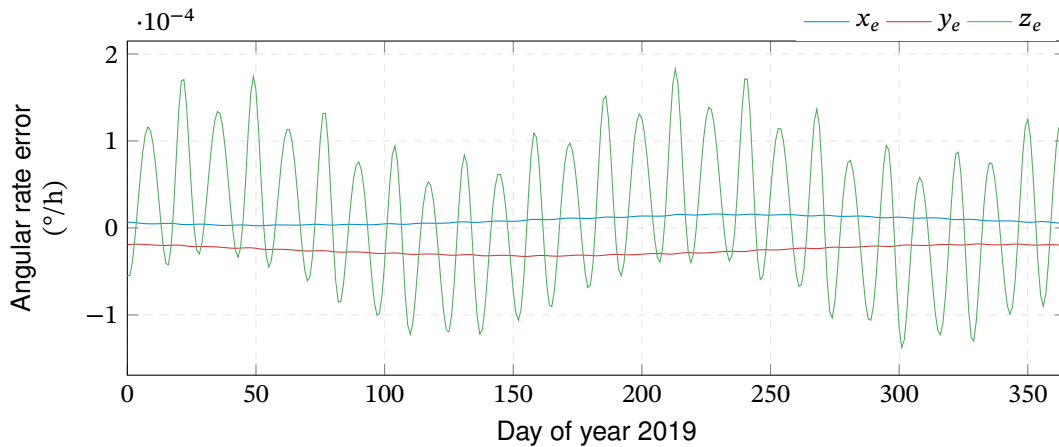


Figure 4.4.: Difference between the Earth's angular rate vector in the e-Frame as defined by the WGS84 and the ones derived from the IERS EOP observations and models.

rotation rate variations would require an integration of the sensor's output at least between two consecutive Earth orientations observations. This may change once direct continuous Earth's angular rate measurements, e.g., from Grossring (G) [105], will be accurate enough to combine them with the VLBI observations into a continuous reference.

Still, even if a theoretical, mobile gyroscope did reach this level of accuracy, a real-time reference or model of the Earth's angular would be required to consider it in the navigation equations and ultimately benefit from such an accuracy. However, this level of accuracy would be required to yield a free-inertial position error of 1 NM in three to four days (see Figure 3.62).

It should be noted that a further increase in accuracy demands would also require the incorporation of relativistic effects. The direct observation of relativistic effects like the Geodetic precession and the Lense-Thierring precession using large ring-lasers on the ground is still the subject of research. These relativistic effects are expected at around $1 \cdot 10^{-9}$ of the Earth's angular rate [93] or around $1.5 \cdot 10^{-8}$ °/h.

Model 1: Earth rotation error modeling.

Description

Variation of the Earth's angular rate, caused by a motion of the Earth's crust and precessing and nutating motion of the Earth's rotation axis.

Parameters

$\delta\omega_{ie}, \delta\dot{\omega}_{ie}$

Sensitivities

Table F.1

Low accuracy level: WGS84

When using the constant Earth angular rate as defined in the [WGS84](#), the angular rate error can be determined by comparing the [WGS84](#) constant to the IERS observations, as depicted in [Figure 4.4](#).

If the [IERS](#) model shall be evaluated, at least the below listed dominating components can be used to describe the auto-correlation and auto-covariance of the errors. Here, the components with periods of multiple years have been summarized into a constant value, representing the mean of the years 2015 to 2020:

Component	Amplitude, °/h	Period, days
$\omega_{ie,x}$	$8.34 \cdot 10^{-6}$	∞
	$5.68 \cdot 10^{-6}$	378.65
	$3.01 \cdot 10^{-7}$	1.08
	$4.09 \cdot 10^{-7}$	0.99
$\omega_{ie,y}$	$-2.60 \cdot 10^{-5}$	∞
	$5.23 \cdot 10^{-6}$	378.65
	$2.96 \cdot 10^{-7}$	1.08
	$3.98 \cdot 10^{-7}$	0.99
$\omega_{ie,z}$	$6.70 \cdot 10^{-6}$	∞
	$2.78 \cdot 10^{-5}$	182.05
	$5.18 \cdot 10^{-5}$	13.65
	$9.65 \cdot 10^{-6}$	9.14

Due to the very long periods of many days, however, it is unlikely that the variations of the Earth's angular rate will be averaged out during a sensor test. For many tests, the uncertainty of the assumed constant rotation speed may also be described as a random constant of magnitude around $1 \cdot 10^{-5}$ °/h, composed of the above described amplitudes.

High accuracy level: IERS

When using the IERS models for the Earth's angular rate, the remaining errors are defined by the accuracy of the IERS models. The accuracy of the daily IERS earth observation parameters is within 0.5 msec [106]. The derived angular rate error can only be roughly approximated as the parameters are daily, discrete measurements. Assuming linear interpolation between two observations, the angular rate error is within the magnitude of $1.15 \cdot 10^{-8}$ °/h, which is already in the range of relativistic effects.

Note that inertial navigation could only benefit from a gyroscope of that accuracy if the real Earth angular rate were known during the in-field application.

4.2.5. Local Gravity

As indicated in (4.28), the local gravity \mathbf{g}_n is the most important specific forces reference in an inertial laboratory (except for centrifuge-testing). The following section will briefly describe the deviations of the Earth's gravity field from the theoretical models. The accuracy limitations of different models will be discussed to motivate a gravimeter survey of the laboratory's location for higher accuracy requirements.

4.2.5.1. Normal Gravity Formula

The most simple gravity model would be a constant $g_0 = 9.80665 \text{ m/s}^2$ pointing downwards on the local reference ellipsoid. Still, even for a theoretical homogeneous ellipsoid, the normal gravity depends on the geodetic latitude ϕ . The theoretical normal gravity on the reference ellipsoid can be analytically determined from Sogmiliana's formula [50]:

$$\gamma(\phi) = \gamma_e \frac{1 + \left(\frac{b\gamma_p}{a\gamma_e} - 1\right) \sin^2 \phi}{1 - e^2 \sin^2 \phi} \quad (4.67)$$

with the value for the **WGS84** reference ellipsoid:

a	6 378 137.0 m	<i>Semi-major axis of the Earth</i>	
b	6 356 752.3141 m	<i>Semi-minor axis of the Earth</i>	
e^2	$6.694\,379\,990\,14 \cdot 10^{-3}$	<i>First eccentricity squared</i>	The normal gravity reduces
γ_e	$9.780\,326\,771\,5 \text{ m/s}^2$	<i>Normal gravity at the equator</i>	
γ_p	$9.832\,186\,368\,5 \text{ m/s}^2$	<i>Normal gravity at the poles</i>	

with the height above the reference ellipsoid. This reduction is typically described the following approximative formula [50]:

$$\gamma(h, \phi) = \gamma(\phi) \left(1 - \frac{2}{a} \left(1 + f + \frac{\omega^2 a^2 b}{GM} - 2f \sin^2 \phi \right) h + \frac{3}{a^2} h^2 \right) \quad (4.68)$$

with

$1/f$	298.257 223 563	<i>Reciprocal of flattening</i>
ω	$7\,292\,115.0 \cdot 10^{-11} \text{ rad/s}$	<i>Earth angular rate</i>
GM	$3\,986\,004.418 \cdot 10^8 \text{ m}^3/\text{s}^2$	<i>Earth's gravitational constant</i>

The error of above formula is less than $1.45 \cdot 10^{-6} \text{ m/s}^2$ up to an altitude of 20 km and significantly better for low altitudes [15, pp. 188–189]. With rising altitude, the gravity vector will be reduced and increasingly tilted towards the equator. The arising north component of the gravity vector can be approximated as [15, p. 189]:

$$\gamma_N(h, \phi) \approx -8.08 \cdot 10^{-6} \frac{\text{m}}{\text{s}^2 \text{km}} h_{km} \sin 2\phi \quad (4.69)$$

The resulting difference between the, latitude dependent, normal gravity $\gamma(\phi)$ and the constant standard gravity g_0 is depicted in Figure 4.5. As the standard gravity has been arbitrarily defined as the gravity around middle latitudes, the maximum deviations occur at the poles and the equator. The maximum deviation is around 2.5 Gal or equivalently 0.26 % of g_0 . Consequently, for very crude requirements (e.g., consumer-grade sensors with scale factor errors in the per-cent region), even the standard gravity g_0 may be a sufficiently accurate reference.

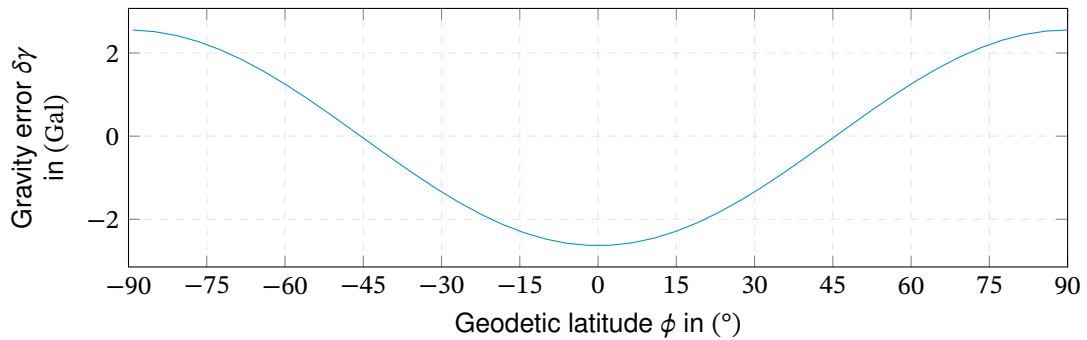


Figure 4.5.: Deviations from the WGS84 normal gravity from the standard gravity value $\gamma(\phi) - g_0$.

Although significantly more accurate than the standard gravity, the normal gravity model does not accurately represent the local gravity. The actual differences will be discussed in the next section.

4.2.5.2. Gravity Anomalies

A gravity anomaly is defined as the difference between the observed and the theoretically predicted gravity at a given point caused by irregularities in the Earth's mass distribution. The theoretical (modeled) gravity on the reference ellipsoid is therefore corrected for planetary, terrain and geological effects, depending on which type of gravity anomaly is investigated [95, pp. 143–144].

While the so-called *free-air gravity anomaly* is unsuitable for most geological problems, it is well suited to illustrate the accuracy of the normal gravity formula. It is defined as the difference between measured g_{obs} and theoretical normal gravity $\gamma(\phi, h)$ at a given point, taking into account the change of gravity with height [95, p. 146]:

$$g_{FAA} = g_{obs} - \gamma(\phi, h) \quad (4.70)$$

The free-air anomalies as modeled in the EGM2008 are globally illustrated in Figure 4.6. The significant gravity anomalies are concentrated but not limited to the mountainous regions and vary from just a few mGal to several hundred mGal. For accuracy requirements of better than about 0.01 % g_0 (for moderate terrain), the gravity anomalies need to be taken into account, either from models (like EGM2008[92] or EIGEN-6C [107]) or ideally from local gravimeter surveying. The global RMS of the EGM2008 gravity anomaly uncertainty, for example, is about

6.6 mGal ($6.7 \cdot 10^{-6} g_0$) (1σ). The propagated uncertainty is part of the EGM2008 and can be evaluated for any point on Earth [92].

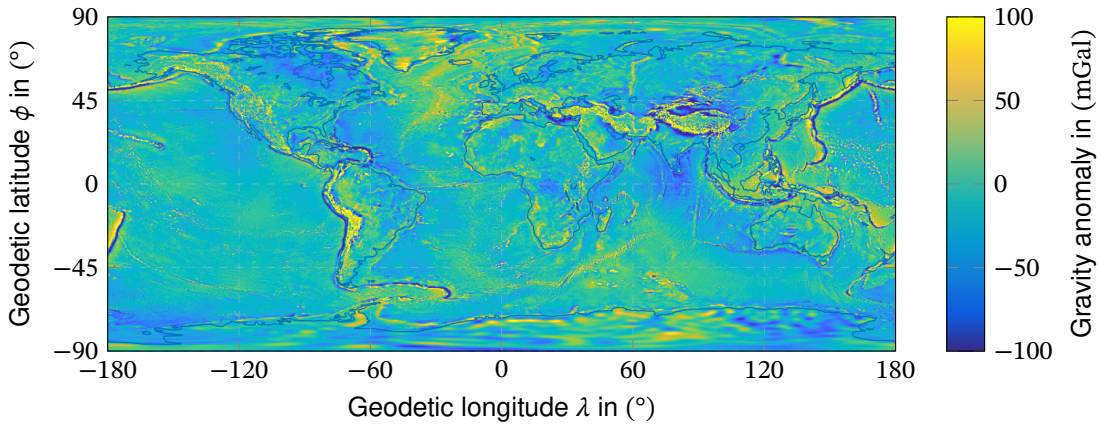


Figure 4.6.: Global free air gravity anomalies as modeled in the EGM2008 [92]. Note that the color scale is cutoff at 100 mGal but the maximum value of the EGM2008 is actually around 966 mGal.

Further increase in the reference accuracy can only be achieved by local gravimeter measurements. These reach accuracy levels of around 0.01 mGal ($1 \cdot 10^{-8} g_0$) for relative gravimeters and around 1 μ Gal ($1 \cdot 10^{-9} g_0$) for absolute gravimeters [95, pp. 97–98].

4.2.5.3. Deflection from the Vertical

The irregularities in the Earth’s mass distribution cause variations in the magnitude of the local gravity vector but also influence its direction. This is described by the tilt of the local gravity vector relative to the local vertical on the reference ellipsoid. Thus deflection from the vertical, see Figure 4.7. This deflection is parameterized by the meridional deflection ξ (north-south) and the deflection from the prime vertical η (east-west). The gravity vector in the local NED-frame can thus be approximated as [15, p. 190]:

$$\mathbf{g}_n = \begin{bmatrix} -\xi g & -\eta g & g \end{bmatrix}^T \quad (4.71)$$

The global deflections from the vertical as determined from the EGM2008 are depicted in Figure 4.8. As with the gravity anomaly, they range from mostly a few arc seconds to multiple tens of arc seconds in rough terrain. The local deflection from the vertical can be determined at very high accuracy using a *zenith camera*. A digital camera is aligned with the local plumb line pointing to the sky. From the observed direction to a known star, the local deflection from the vertical can be determined to an accuracy better than 0.1 asec [108].

The importance of vertical deflection for inertial sensor calibration lies in the alignment of the laboratory. Typically, the inertial test-slab and instruments are aligned to local gravity, as it is a very strong signal and easy to use. Consequently, the laboratory will not be to the reference ellipsoid, and the Earth’s angular rate will be observed under tilt. For high accuracy demands,

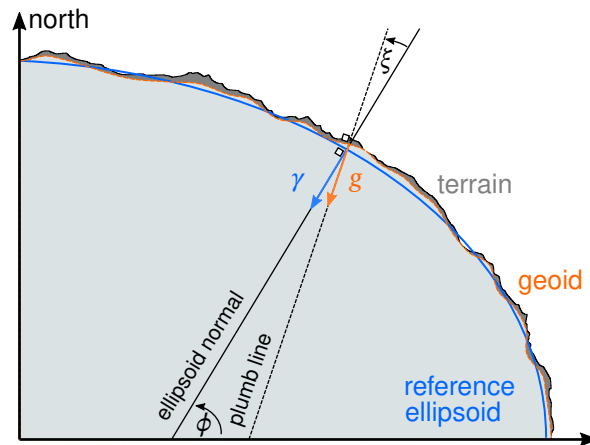


Figure 4.7.: Earth's surface, geoid and reference ellipsoid with the normal gravity γ and true gravity g .

the local deflection from the vertical needs to be surveyed and considered for Earth's angular rate reference.

4.2.5.4. Temporal Variations

In addition to the local variations of the Earth's gravity field, there are also temporal variations caused by variations of the Earth's rotation axis and tides as well as natural and artificial redistribution of masses [95, p. 123].

Pressure variations cause a variation of the mass distribution in the atmosphere and thus effect the local gravity. Typical pressure fluctuations range from less than 1 mbar for atmospheric tides, over around 10 mbar for seasonal variations, up to 60 mbar for cyclonic events [95, p. 126]. These lead to pressure variations at about $20 \mu\text{Gal}$ ($20 \cdot 10^{-8} \text{ m/s}^2$), where relation between local zone pressure variation and gravity variation is approximately given as [109]:

$$\Delta g_{atm} = -0.356 \frac{\mu\text{Gal}}{\text{mbar}} \Delta p \quad (4.72)$$

A more accurate gravity reduction method incorporating three-dimensional atmospheric pressure data is, e.g., given by [110].

Further temporal variations of the local gravity are caused by subsurface mass variations, mainly due to groundwater changes. The typical seasonal changes in water levels cause less than $10 \mu\text{Gal}$ in gravity change. Still, they may also reach a multiple of that in tropical regions with high seasonal rainfall [95, p. 128]. Another measurable mass shift and corresponding change of gravity is the global de-glaciation. The loss of ice masses on Greenland, for example, causes a yearly decrease of local gravity of about $0.5 \mu\text{Gal}$ (2012), accelerating at $0.02 \mu\text{Gal}/\text{year}^2$ [111].

The most crucial temporal change of local gravity is caused by the tidal accelerations of the Moon and Sun. While the gravitational acceleration of, e.g., the Moon and the centrifugal

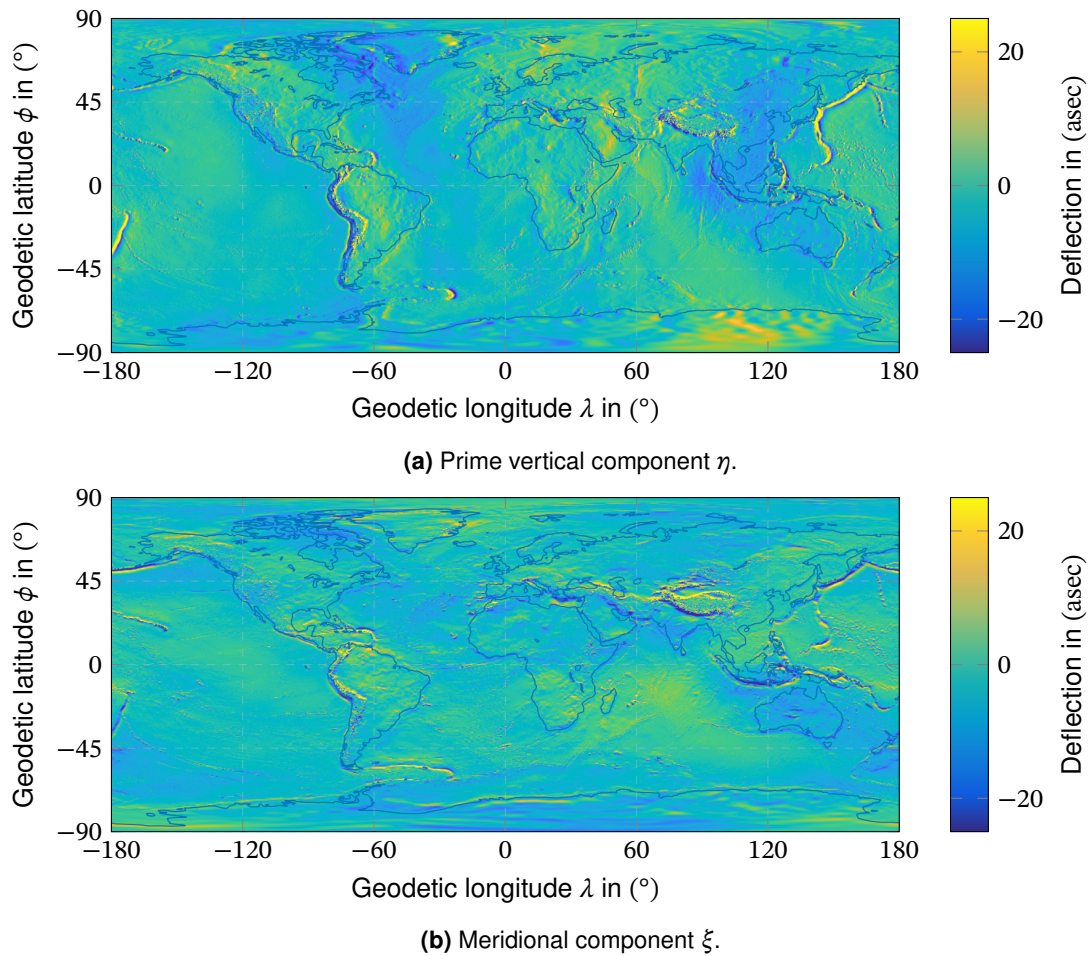


Figure 4.8.: Deflection from the vertical as modeled in the EGM2008 [92]. Note that the color scale is cutoff at 25 asec but the maximum value of the EGM2008 is actually around 100 asec.

acceleration due to Earth's orbital motion cancel out in the Earth's center of mass, there is a residual acceleration on the Earth's surface, called tidal acceleration [112]. This location-dependent tidal acceleration causes a (phase-shifted) elastic deformation of the Earth that causes an amplification of the tidal accelerations of about 16 % compared to the solid-Earth tides. For accuracy requirements better than $10 \mu\text{Gals}$ and less than 500 km from the coast-line, the mass shift due to ocean tides and the surface deflection due to the shifted water loads need to be considered [95, pp. 127–128].

For general purposes, the tidal acceleration can be effectively determined using Longman's program [113]. An example plot of the tidal acceleration at the Institute of Flight System Dynamics, Garching, determined from an implementation of Longman's equations [114] is given in Figure 4.9. The theoretical maximum tidal accelerations by the relevant solar system's celestial bodies are given in Table 4.1. The Moon's and Sun's accelerations are at least $8.5 \cdot 10^3$ times higher than for the next planet, justifying the limitation to just these two influences.

Theoretically determined tidal accelerations typically show a phase shift towards measured tides. This is caused by the local elasticity that is not properly incorporated in the tide models

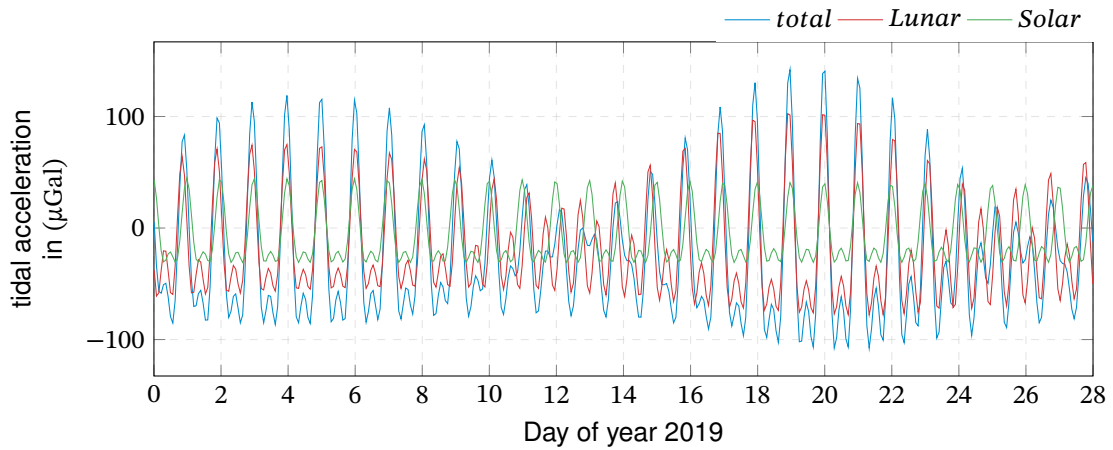


Figure 4.9.: Tidal acceleration at the Institute of Flight System dynamics (48°15'59.03"N 11°40'5.79"E 536m) according to the tidal scheme of Longman.

Table 4.1.: Maximum tidal accelerations on the Earth's surface due to celestial bodies [112].

Body	Max. tidal acceleration
Moon	$1.37 \cdot 10^{-6} \text{ m/s}^2$
Sun	$0.50 \cdot 10^{-6} \text{ m/s}^2$
Mercury	$3.64 \cdot 10^{-13} \text{ m/s}^2$
Venus	$5.88 \cdot 10^{-11} \text{ m/s}^2$
Mars	$1.18 \cdot 10^{-12} \text{ m/s}^2$
Jupiter	$6.54 \cdot 10^{-12} \text{ m/s}^2$
Saturn	$2.36 \cdot 10^{-13} \text{ m/s}^2$
Uranus	$3.67 \cdot 10^{-15} \text{ m/s}^2$
Neptun	$1.06 \cdot 10^{-15} \text{ m/s}^2$
Pluto	$7.61 \cdot 10^{-20} \text{ m/s}^2$

[95, pp. 127–128]. If a gravity reference in the accuracy level of tidal accelerations is required, a continuously measuring tide meter may be beneficial.

Model 2: Gravity error modeling.

Description

Errors of the local gravity models or measurements, deflection from the vertical and temporal variation of the local gravity.

Parameters

$\delta\gamma_n$

Sensitivities

Table F.2

Low accuracy level: gravity model

If the local gravity is determined from a gravity model, the model error can be modeled as a random constant defined by the model's accuracy.

For the [EGM2008](#), there is an error propagation model that allows the determination of the model accuracy for every location on Earth. For most of the Earth's surface, except for high mountains and the south pole, the error of the gravity anomaly is below $1 \cdot 10^{-4} \text{ m/s}^2$ (1σ) and the error of the deflection from the vertical in the order of 1 asec (1σ) [92].

As depicted in [Figure 4.9](#), their base period is about 12 hours and 24 minutes with amplitudes of typically less than $1 \cdot 10^{-6} \text{ m/s}^2$. The temporal variations of gravity thus become only relevant if the gravity error shall be compensated to a level below $1 \cdot 10^{-6} \text{ m/s}^2$.

High accuracy level: gravimeter measurement and tidal correction

If the local gravity is measured during the setup of the inertial laboratory, the residual constant gravity error can be reduced to the level of $1 \cdot 10^{-7} \text{ m/s}^2$ [95, p. 97] where the tidal accelerations become visible. Gravimeter measurements in combination with modern Earth and ocean tide models allow the prediction of tidal accelerations to an accuracy better than $1 \mu\text{Gal}$ ($1 \cdot 10^{-8} \text{ m/s}^2$) [115]. The local deflection from the vertical may be determined to about 0.1 asec [108].

For example, the calculation of the tidal acceleration can be performed at high accuracy with the aid of the ETERNA-X program of the [Bundesamt für Kartographie und Geodäsie \(BKG\)](#) [116].

4.2.6. Laboratory Location

In addition to the gravity's location dependency, the laboratory's location has a direct effect on the rotation from the ECEF to the local NED frame $\mathbf{R}_{ne}(\phi, \lambda)$, see (4.6) and Figure 4.1.

The rotation matrix \mathbf{R}_{ne} , as defined in (2.16), is a rotation around the geodetic latitude ϕ and longitude λ angles. The position accuracy will, therefore, directly effect the accuracy of the rotation. Static location determination using satellite navigation is a trivial task today, yielding impressive accuracy even with low-end hardware. Smartphones, for example, provide an average accuracy of 4.9 m [117], which is close to the GPS SPS nominal performance [118]. Using below first order approximation

$$\Delta\phi = \frac{\Delta x}{R_m + h} \tag{4.73}$$

$$\Delta\lambda = \frac{\Delta x}{(R_n + h) \cos \phi} \tag{4.74}$$

this corresponds to an accuracy of about 0.1 asec in latitude and 0.2 asec in longitude at middle latitudes. Using Precise Point Positioning (PPP) the position accuracy can be driven down to less than 20 cm [119], corresponding to about 10 msec in angle.

Model 3: Local leveled reference frame errors.

Description

Orientation error of the local leveled reference frame, caused by a position uncertainty of the laboratory. The residual orientation errors are modeled as independent zero-mean random constant Gaussians.

Parameters

$\delta\boldsymbol{\Psi}_{n\hat{n}}$

Sensitivities

Table F.3

Low accuracy level: GPS Standard Performance

For standard GPS position accuracy of about 5 m (1σ) the orientation errors of the local NED frame can be described by a standard deviation of:

$$\sigma_{\Delta\phi} \approx 0.16 \text{ asec} \quad \sigma_{\Delta\lambda} \approx 0.16 \text{ asec} \cdot \sec(\phi)$$

High accuracy level: GPS Precise Point Positioning

For a precisely surveyed laboratory location from PPP, the standard deviation of the random constant orientation errors are reduced to about

$$\sigma_{\Delta\phi} \approx 0.0065 \text{ asec} \quad \sigma_{\Delta\lambda} \approx 0.0065 \text{ asec} \cdot \sec(\phi)$$

which can be neglected in virtually any case.

4.2.7. Test Pad and Laboratory Alignment

Testing inertial sensors requires an accurate and stable reference orientation relative to the two natural reference signals, gravity, and the Earth's rotation. Ideally, this reference is identical with the local leveled *NED* frame. This requires both leveling (pitch and roll angle) and a north-alignment (azimuth) of the laboratory's local reference frame.

Note that the orientation of the laboratory's reference frame does not necessarily match the orientation of the concrete test slab. A passive concrete test pad is roughly aligned to the local gravity vector during the casting of the concrete. The precise leveling is then performed for the test instruments, e.g., at the mounting of a rate table or a test plate. Similarly, the test pad's orientation towards the north and its geometry are not of interest for the laboratory alignment, but the test instruments have to provide some reference to the north, either by simple markings or, e.g., the orientation of a horizontal rate table axis.

In the most simple case, the laboratory's reference frame leveling is performed using the local gravity. A simple water level or, more precisely, an inclinometer may be used to align the reference, e.g., the base of the rate table, to the local gravity vector. But as discussed in [Subsection 4.2.5](#), the local gravity vector has a deviation from the ideal vertical on the reference ellipsoid that would form the *z* axis of the *NED* frame. In this case, the leveling accuracy is affected by the inclinometer's measurement accuracy and the local gravity's deflection from the vertical. While precise inclinometers reach an accuracy of about 0.2 asec (e.g., [120]), the typical deflection from the vertical in moderate terrain is in the range of few asec, see [Figure 4.8](#). Using astro-geodetic methods, the laboratory's reference can be aligned to the *WGS84* reference ellipsoid, independent of the local gravity. In this case, leveling accuracies better than 0.1 asec [108] can be reached.

Similarly, the north alignment can be done practically with two methods. First, the true north direction can be determined using a gyrocompass, and second, geodetic survey techniques. Astro-geodetic survey techniques provide accuracies in the region of 2 asec [121], while gyrocompasses typically reach accuracies in the range of about typically $0.5^\circ \text{ sec}(\phi)$ [122], which is around 0.7° for medium latitudes. The use of a magnetic compass is only possible if the orientation of the Earth's local magnetic field is precisely known. As global models like the [World Magnetic Model \(WMM\)](#) do not include local declination anomalies that may exceed 10° [123], a local reference measurement with respect to true north is required.

Model 4: Laboratory alignment errors.

Description

Leveling and north-alignment errors of the laboratory's respectively test-pad's reference frame. The residual orientation errors of the laboratory's reference frame are modeled as independent zero-mean random constant Gaussians.

Parameters

$$\delta \Psi_{pp}$$

Sensitivities

Table F.4

Low accuracy level: Leveling to local gravity

For a low-accuracy approach, using simple gravity leveling and gyro-compassing with typical devices, the standard deviation of the orientation angle errors can be expected in the range of:

$$\sigma_{\delta\phi_{pp}} \approx 2.5 \text{ asec} \quad \sigma_{\delta\theta_{pp}} \approx 2.5 \text{ asec} \quad \sigma_{\delta\psi_{pp}} \approx 0.5^\circ \text{ sec}(\phi)$$

The above values only indicate typical instrument errors and moderate terrain.

High accuracy level: Astro-geodetic alignment

Using high-precision astro-geodetic measurements, the residual alignment errors of the laboratory's reference frame can be reduced to about:

$$\sigma_{\delta\phi_{pp}} \approx 0.2 \text{ asec} \quad \sigma_{\delta\theta_{pp}} \approx 0.2 \text{ asec} \quad \sigma_{\delta\psi_{pp}} \approx 2 \text{ asec}$$

4.2.8. Test Pad Motion

Inertial sensor testing equipment, like rate tables, are typically mounted on isolating test pads (also test pier or test slab). The main task of the test pier is to provide a stable, ideally motion-free, platform by isolating the laboratory from external vibrations. The different external disturbances and two types of test pad realizations will be discussed in the following.

4.2.8.1. External Disturbances

The test pad's stability can be disturbed by direct or indirect excitation. Direct excitations are the forces and moments directly acting on the test pad, e.g., reaction forces and moments caused by the rate table's motion or an operator walking on the test pad. Direct excitation can be easily handled as it is mainly under the operator's control, e.g., by using a false floor on top of the test pad. The reaction moments of the rate tables are well known and can thus be considered.

The indirect excitation, on the other hand, is much harder to handle, as its sources can typically not be affected. Indirect excitation is caused by seismic waves, especially surface waves, that excite the test pad's motion. Surface waves are either pure horizontal translational waves perpendicular to the wave direction (*Low waves*) or a combination of vertical and horizontal translation in the wave direction (*Rayleigh waves*), as illustrated in Figure 4.10 [124].

The actual level of seismic disturbances depends on the location of the laboratory and its environment. However, there have been multiple attempts to determine a representative

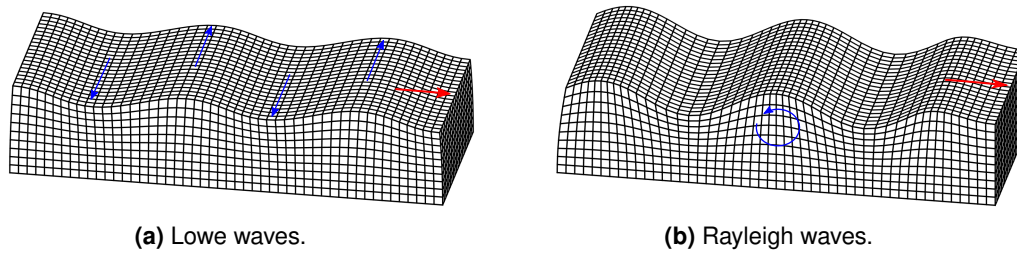


Figure 4.10.: Seismic surface waves. The red arrow indicates the wave direction, while the blue arrows indicate the motion of the particles.

spectrum of disturbances. An early systematic description of the Earth's seismic noise was given by Brune and Oliver in 1959 [125]. Seismic background noise can be considered a stationary process [126] and thus be described by its PSD. The first model explicitly developed for inertial sensor testing was derived by Weinstock in 1966 [40]. The model is mainly based on the seismic background noise observations obtained during the *VELA Uniform* program that targeted the detection and localization of covert nuclear weapon tests. Today's standard model for seismic noise backgrounds was developed by Peterson for the **United States Geological Survey (USGS)** in 1993 [127]. It defines two representative PSD curves, called **New High Noise Model (NHNM)** and **New Low Noise Model (NLNM)**, for high respectively low noise environments. These models are compiled from global observations and are widely accepted in seismology [126]. Another reference spectrum has been determined for developing the LIGO Gravitational-Wave Observatory seismic isolation system [128]. The seismic background noise spectra for various observation stations and networks can also be obtained from the IRIS Web Service [129].

The different PSD curves are summarized in Figure 4.11a. For the dominant Rayleigh waves, the horizontal and vertical amplitudes are similar [126]. Consequently, the presented spectra are representative of both horizontal and vertical acceleration. These reference models do not include direct tidal accelerations. Furthermore, the USGS and the LIGO model do not include artificial noise, as they are determined for locations sufficiently isolated from human activities. In contrast to that, Weinstock's model includes artificial sources. Several measured vibration spectra from urban [130] and industrial [131] environments are added as a reference for artificial noise. These measurements have been transformed from velocity and acceleration amplitudes to acceleration PSD using methods from [126].

Seismic waves do excite not only translatory displacement but also a tilt of the local Earth's surface. Analog to the acceleration, a summary of different tilt PSD curves is presented in Figure 4.11b. Based on different assumptions, Weinstock derived the tilt noise PSD from his reference acceleration spectrum [40]. Also, for the LIGO development, two representative tilt spectra have been derived for calm as well as windy days [128]. The seismic tilt background noise PSD for various observation stations in China has been published by Zhao [132]. The curves for the Xiaomiao and Chengde stations are added as a reference. These spectra have not yet been corrected for the Earth's solid tides. Depending on the actual design, the tidal tilt may

cause a motion of the test pad (e.g., if the pad is actively aligned to local gravity) that needs to be considered. Again, the LIGO model and Zhao's measurements do not account for artificial noise, while Weinstock's model does.

As a reference for artificial excitation, the local surface tilt has been derived from the vertical displacement measurements, assuming an elastic surface wave, see (4.77). The approximated tilts, derived from the measurements of Kamperman [130], and Albert [131] for a wave velocity of $c_s = 250\text{m/s}$, are added to the graph.

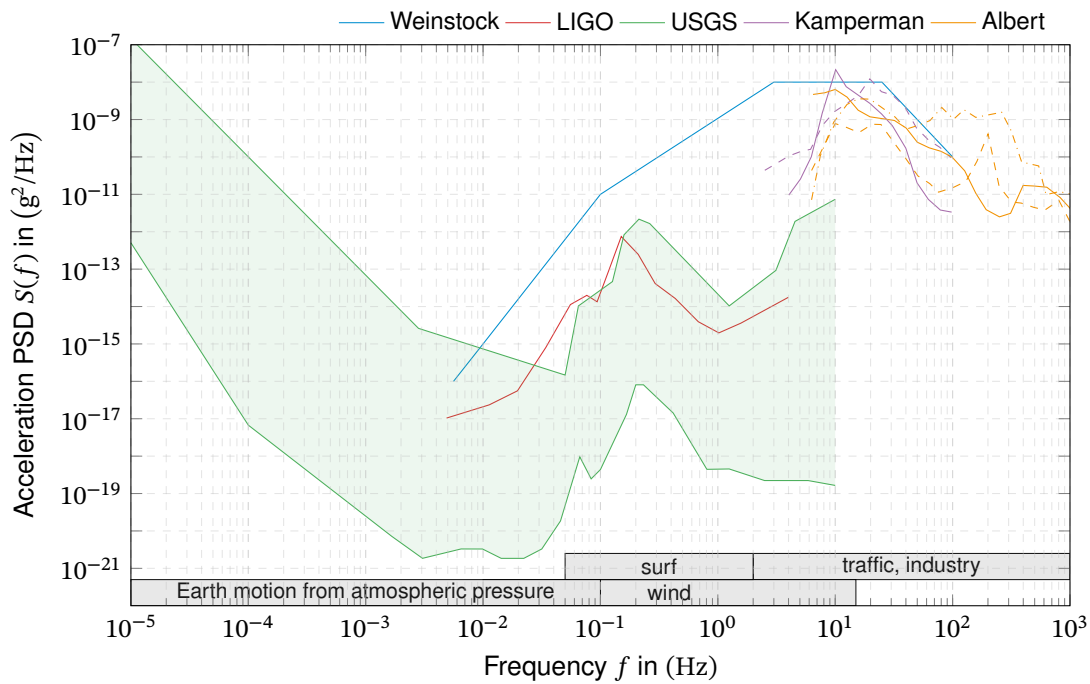
Weinstock's curve seems conservative for low frequencies compared to the other references. However, the curve matches the measured spectra quite well for the high artificial frequencies. As Weinstock's curve is partly based on the same assumptions and measurements as the here-derived tilts, there may be a systematic error caused by the elastic wave model. Furthermore, for high frequencies, the wavelength decreases below the dimensions of the test pad. As illustrated in Figure 4.13, the test pad can no longer follow the surface wave's tangent for small wavelengths.

In general, the reference curves seem to cover both natural and artificial noise quite well. In cases when the actual seismic background is not (yet) known for the test slab's location, a combination of the above-discussed reference models may be used for a first analysis. The natural background noise seems similar worldwide, while the man-made source depends on the actual location. It should be considered that artificial noise can be effectively reduced by choosing a suitable quiet laboratory location. Cultural noise can also be reduced by going deep below the surface, e.g., [32]. Furthermore, high-frequency noise disturbances can be reduced by sub-surface trenches of sheet pile barriers with depths of at least one-third of the surface wavelength [31].

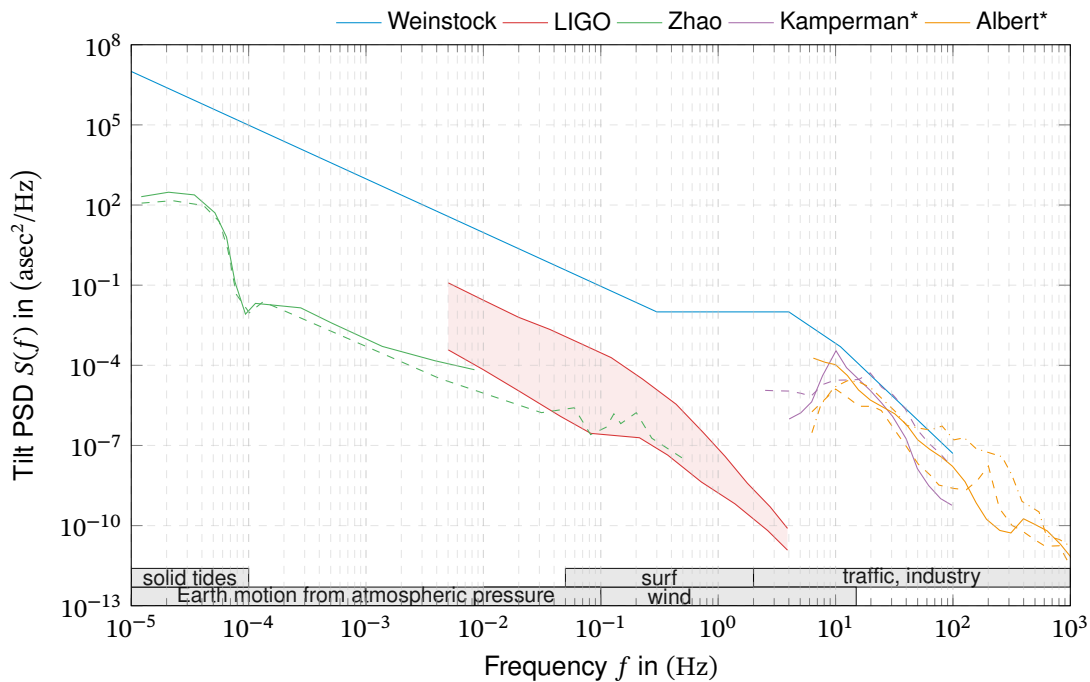
4.2.8.2. Passively Isolated Test Pad

Typically, a passively isolated test pad is just a block of reinforced concrete, more or less freely floating on compacted soil, see Figure 4.12a. The general idea is to have high inertia to reduce its reaction to excitation to an acceptable level. Therefore they are also called *inertia pads*. However, unique forms and designs, including hollowed test slabs and even a 9 to pad suspended from a 7.5 m tower, have been proposed and realized [31]. The research of designing a stable test platform for inertial sensor testing dates back to the early 1960s when increasing sensor accuracy raised concerns about the required laboratory references. These efforts were concentrated in the *Test Pad Stability Subcommittee* (from 1970 *Geokinetics Subcommittee*) of the [American Institute of Aeronautics and Astronautics \(AIAA\)](#) Technical Committee on Guidance and Control [37].

The typical model for a passively isolated test pad is a mass-spring-damper system for each of the six degrees of freedom of the pad [31, 36]. For this simple model, the test pad is modeled as rigid body. This assumption is justified if the slab's bending stiffness is higher than the



(a) Acceleration power spectral density of seismic noise. Modeled reference spectra: USGS New Noise Models [127], Weinstock [40] and LIGO [128]. Measured spectra in urban and industrial environment: Kamperman [130] and Albert [131].



(b) Tilt power spectral density of seismic noise. Modeled reference spectra: Weinstock [40] and LIGO [128]. Measured spectra: Zhao [132]. Tilt derived from acceleration ($c_s = 250m/s$): Kamperman [130] and Albert [131].

Figure 4.11.: Overview of translatory and rotatory seismic background noise power spectral densities.

ground's stiffness [133, p. 192]:

$$\frac{1}{12} \frac{E_f}{M_{E,s}} \left(\frac{h_f}{b_f} \right)^3 \geq 0.1 \quad (4.75)$$

where

- E_f *Elastic modulus of the pad*
- $M_{E,s}$ *Constrained modulus of the soil*
- h_f *Height of the pad*
- b_f *Length of the pad's longest edge*

Furthermore, the test pad is assumed to be not embedded in the ground. Embedding the pad generally leads to a slight increase in spring stiffness and a considerable increase in damping [134], but is not covered by the spring-damper model.

The spring constants K_i and damping coefficients C_i can be determined analytically from the test pad's geometry (equivalent radius from length and width) and the soil characteristics, see, [134]. The relevant soil parameters dynamic shear module G_d , the Poisson's ratio ν , and density ρ need to be determined experimentally for the local environment. On the one hand, the pad can be excited directly by external forces and moments \mathbf{p} , e.g., caused by reaction moments of the rate table accelerations or an operator walking on the test pad. On the other hand, the test pad can also be indirectly excited by a translatory or rotatory displacement of the reference point \mathbf{u}_0 caused by a surface wave. In matrix-vector form, the equation of motion of the rigid test pad yields [134]:

$$\mathbf{M}\ddot{\mathbf{u}}(t) + \mathbf{C}(\dot{\mathbf{u}}(t) - \dot{\mathbf{u}}_0(t)) + \mathbf{K}(\mathbf{u}(t) - \mathbf{u}_0(t)) = \mathbf{p}(t) \quad (4.76)$$

where

- \mathbf{M} *Blockdiagonal matrix of mass and moments of inertia*
- \mathbf{C} *Diagonal matrix of damping coefficients*
- \mathbf{K} *Diagonal matrix of spring constants*
- \mathbf{u} *Column vector of translatory and rotatory displacement*
- \mathbf{u}_0 *Column vector of translatory and rotatory displacement of the reference point*
- \mathbf{p} *Column vector of external forces and moments*

While the Lowe waves only a horizontal motion of the test pad, the Rayleigh wave's vertical excitation will also lead to a rotatory movement of the test pad. If the surface wave's wavelength reaches the dimensions of the test pad, it will follow the wave's tangent, as illustrated in Figure 4.13.

Given that the wave's source is sufficiently far away, the source can be approximated as line-shaped. Using the small-angle approximation the pad's tilt is given by the local spatial

derivative of the surface wave [135]:

$$\theta(t) = \arctan \frac{du(s, t)}{ds} \approx U_0 \frac{2\pi}{\lambda_w} \sin(\omega_w t - \frac{2\pi}{\lambda_w} s) \quad (4.77)$$

This analytical model allows a simple determination of the transfer functions from both indirect excitation $\mathbf{H}_i(s)$ and direct excitation $\mathbf{H}_d(s)$ to the pad's displacement:

$$\mathbf{u}_i(s) = \underbrace{(\mathbf{M}s^2 + \mathbf{C}s + \mathbf{K})^{-1} (\mathbf{C}s + \mathbf{K})}_{\mathbf{G}_i(s)} \mathbf{u}_0(s) \quad (4.78)$$

$$\mathbf{u}_d(s) = \underbrace{(\mathbf{M}s^2 + \mathbf{C}s + \mathbf{K})^{-1}}_{\mathbf{G}_d(s)} \mathbf{p}(s) \quad (4.79)$$

For symmetrical pads, all matrices are diagonal matrices. Consequently, the six degrees of freedom are decoupled and can be treated separately. Example frequency responses to indirect excitation are depicted in Figure 4.14. The general second-order low-pass behavior fits quite well with published measurements for passive test slabs, see [130].

For a known, or at least estimated, disturbance spectrum, the resulting test-pad motion spectrum can be easily determined using the Wiener-Khinchin-theorem (3.94).

Despite the practical usage of the above model, it can only represent the fundamental behavior of the test slab dynamics. In reality, the damping and spring coefficients of the soil are frequency-dependent. This dependency should be taken into account when determining the transfer function. Correction factors for the frequency dependency can be found in [134] for some configurations. However, this and other model inaccuracies should also be covered by a variation study of the model coefficients as suggested in [31].

4.2.8.3. Actively Stabilized Test Pad

In contrast to the passively isolated test pad, an actively stabilized pad provides active control of its leveling and excitation damping. As illustrated in Figure 4.12b, the test pad's orientation is measured and closed loop controlled using actuators. For example, the so-called *iso-pad* at the Frank J. Seiler Research Laboratory at the USAF Academy, Colorado, consists of a 200 to pad of reinforced concrete that is mounted on hydraulic actuators. These actuators are closed-loop controlled from tilt-meter measurements down to 1 msec. Pad motions above 0.1 Hz are observed by additional seismometers and actively damped by electro-magnetic shakers. The design goal of this test pad was an acceleration stability of $1 \cdot 10^{-9} g_0$ up to 20 Hz [35]. The actual transfer function from external and internal excitations highly depends on the actual pad and controller design and cannot be generalized.

It should be noted that such an actively stabilized pad will always be aligned to the local gravity, with the consequences already discussed in Subsection 4.2.5.3. Additional observation of the deflection from the vertical, respectively determination of the astronomic latitude may be required.

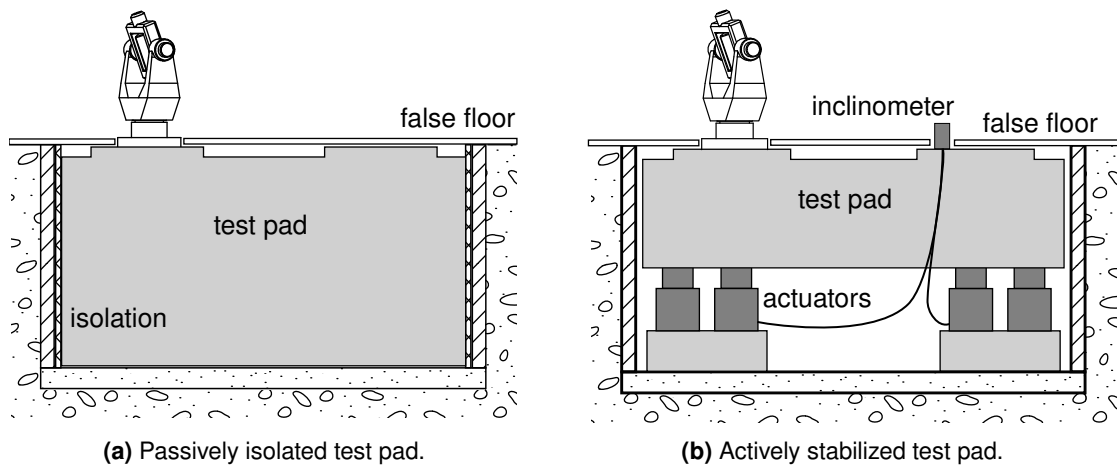


Figure 4.12.: Schematic illustration of a passively isolated and an actively stabilized test pad.

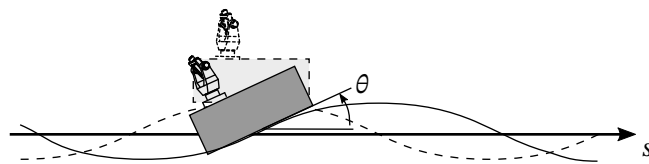


Figure 4.13.: Rotatory motion of the test pad due to surface wave excitation.

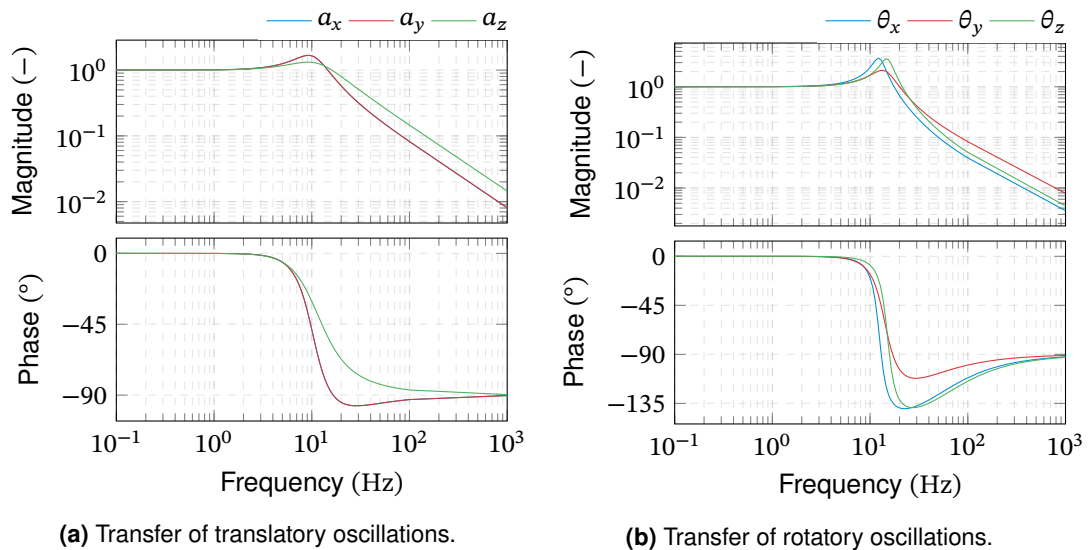


Figure 4.14.: Example frequency response of the test pad to indirect excitation from surface waves. Test pad dimensions are $6 \text{ m} \times 3.2 \text{ m} \times 2 \text{ m}$, with a density of $\rho_F = 2200 \text{ kg/m}^3$. The soil parameters are $\nu = 0.3$, $G_d = 30 \text{ MPa}$ and $\rho_s = 1900 \text{ kg/m}^3$.

Model 5: Test pad motion.

Description

Motion of the test pad with respect to the local reference frame. The orientation errors, angular rates and accelerations are modeled as stochastic processes, characterized by their PSD.

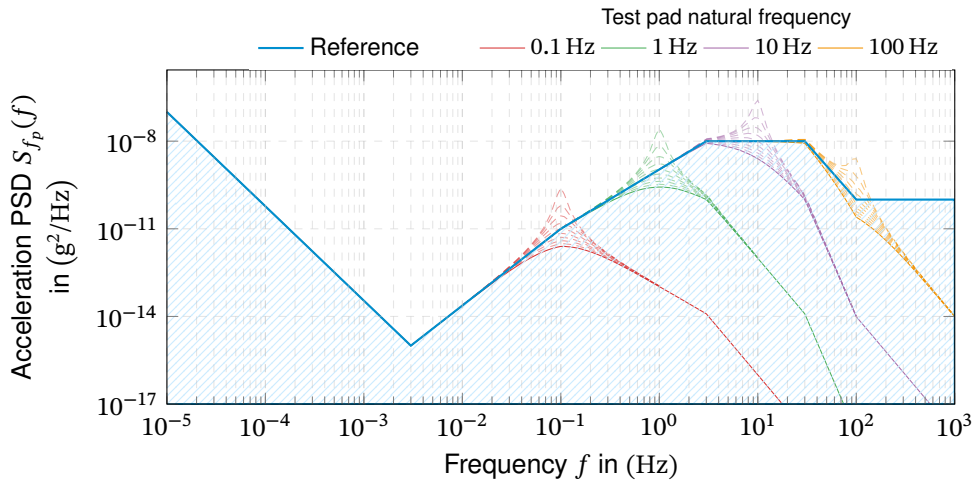
Parameters

$\delta\omega_{np}, \delta\dot{\omega}_{np}, \delta\Psi_{pp}, \delta\dot{r}_n(P_p), \delta\ddot{r}_n(P_p)$

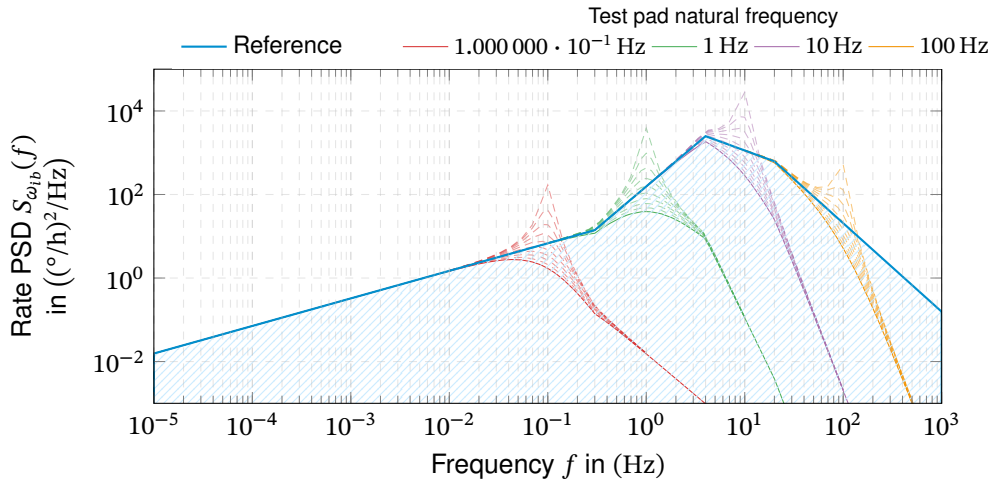
Sensitivities

Table F.4, Table F.5

Reference motion spectrum Based on the presented models in Figure 4.11, a new conservative reference PSD curve over a wider frequency range can be composed. Although the actual local background noise is not isotropic, the reference PSD represents a reasonable approximation for all directions.



(5.a) Acceleration power spectral density.



(5.b) Angular rates power spectral density.

As described in Subsection 4.2.8.1, a passively isolated test pad can be approximated as a mass-spring-damper system whose response is characterized by the damping coefficient at the natural frequency. Variations of the seismic background for different test pads are included in the above graphs. The dashed lines represent different damping ratios, ranging from 0.1 to 1.0 (solid line).

Note that the presented reference PSD curves are only indicative. Their representativeness should be questioned for each testing location, especially for laboratories close to natural (e.g., the shore) and artificial sources.

4.2.9. Rate Table Errors

In Subsection 4.2.1, a three-axis rate table has been chosen as the most general inertial testing instrument. This the model can be easily reduced to two- or single-axis tables and even centrifuges. Thus, the typical errors of a three-axis rate table will be discussed exemplary in this section. After introducing a general error model in the rate table's section of the kinematic chain, the different error sources are discussed and characterized.

4.2.9.1. Rate Table Errors in the Kinematic Chain

Any rate table imperfections add errors to the kinematic chain representing the rate table. As illustrated in Figure 4.15, rate table imperfections introduce orientation errors and displacement errors of the reference frames representing the table's gimbals. Orientation errors are described

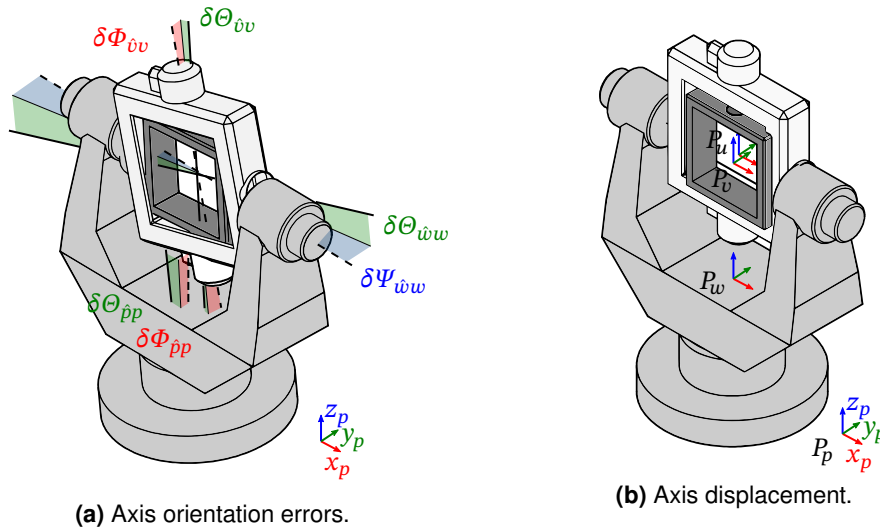


Figure 4.15.: Rate table axes orientation and displacement errors.

by an additional rotation that occurs before the nominal rotation following the kinematic chain towards the inner gimbal. The orientation errors consist of a tilt of the nominal rotation axis described by $\delta\Phi$, $\delta\Theta$ or $\delta\Psi$ and a consecutive error rotation about the nominal axis:

$$\mathbf{R}_{wp} = \underbrace{\mathbf{R}_z(\hat{\Psi}_{wp})}_{\text{nominal rotation } \mathbf{R}_{wp}} \underbrace{\mathbf{R}_z(\delta\Psi_{\hat{p}p})\mathbf{R}_y(\delta\Theta_{\hat{p}})\mathbf{R}_x(\delta\Phi_{\hat{p}p})}_{\text{axis orientation error } \mathbf{R}_{pp}} \quad (4.80)$$

$$\mathbf{R}_{vw} = \underbrace{\mathbf{R}_x(\hat{\Phi}_{vw})}_{\text{nominal rotation } \mathbf{R}_{vw}} \underbrace{\mathbf{R}_x(\delta\Phi_{vw})\mathbf{R}_z(\delta\Psi_{\hat{w}w})\mathbf{R}_y(\delta\Theta_{\hat{w}w})}_{\text{axis orientation error } \mathbf{R}_{ww}} \quad (4.81)$$

$$\mathbf{R}_{uv} = \underbrace{\mathbf{R}_z(\hat{\Psi}_{uv})}_{\text{nominal rotation } \mathbf{R}_{uv}} \underbrace{\mathbf{R}_z(\delta\Psi_{\hat{u}u})\mathbf{R}_y(\delta\Theta_{\hat{u}u})\mathbf{R}_x(\delta\Phi_{\hat{u}u})}_{\text{axis orientation error } \mathbf{R}_{uu}} \quad (4.82)$$

Additionally, there may be orientation errors in the sensor's mounting to the inner gimbal. As there is no nominal rotation but only an arbitrary nominal orientation of the sensor $\mathbf{R}_{b\hat{u}}$,

introducing the orientation errors yield:

$$\mathbf{R}_{bu} = \mathbf{R}_{b\hat{u}} \underbrace{\mathbf{R}_x(\delta\Phi_{\hat{u}u})\mathbf{R}_y(\delta\Theta_{\hat{u}u})\mathbf{R}_z(\delta\Psi_{\hat{u}u})}_{\text{axis orientation error } \mathbf{R}_{\hat{u}u}} \quad (4.83)$$

For a precision instrument like a rate table, the axis orientation errors are in the arc-second range. Consequently, the orientation error matrices can be linearized for the error angles and the order of rotations becomes insignificant:

$$\mathbf{R}_{wp} \approx \begin{bmatrix} \cos \hat{\Psi}_{wp} & -\sin \hat{\Psi}_{wp} & 0 \\ \sin \hat{\Psi}_{wp} & \cos \hat{\Psi}_{wp} & 0 \\ 0 & 0 & 1 \end{bmatrix} \left(\mathbf{I}_{3 \times 3} + \underbrace{\begin{bmatrix} \delta\Phi_{\hat{p}p} \\ \delta\Theta_{\hat{p}p} \\ \delta\Psi_{\hat{p}p} \end{bmatrix}}_{\delta\boldsymbol{\Psi}_{\hat{p}p}} \times \right) \quad (4.84)$$

$$\mathbf{R}_{vw} \approx \begin{bmatrix} 1 & 0 & 0 \\ 0 & \cos \hat{\Phi}_{vw} & -\sin \hat{\Phi}_{vw} \\ 0 & \sin \hat{\Phi}_{vw} & \cos \hat{\Phi}_{vw} \end{bmatrix} \left(\mathbf{I}_{3 \times 3} + \underbrace{\begin{bmatrix} \delta\Phi_{\hat{w}w} \\ \delta\Theta_{\hat{w}w} \\ \delta\Psi_{\hat{w}w} \end{bmatrix}}_{\delta\boldsymbol{\Psi}_{\hat{w}w}} \times \right) \quad (4.85)$$

$$\mathbf{R}_{uw} \approx \begin{bmatrix} \cos \hat{\Psi}_{uw} & -\sin \hat{\Psi}_{uw} & 0 \\ \sin \hat{\Psi}_{uw} & \cos \hat{\Psi}_{uw} & 0 \\ 0 & 0 & 1 \end{bmatrix} \left(\mathbf{I}_{3 \times 3} + \underbrace{\begin{bmatrix} \delta\Phi_{\hat{v}v} \\ \delta\Theta_{\hat{v}v} \\ \delta\Psi_{\hat{v}v} \end{bmatrix}}_{\delta\boldsymbol{\Psi}_{\hat{v}v}} \times \right) \quad (4.86)$$

$$\mathbf{R}_{bu} \approx \mathbf{R}_{b\hat{u}} \left(\mathbf{I}_{3 \times 3} + \underbrace{\begin{bmatrix} \delta\Phi_{\hat{u}u} \\ \delta\Theta_{\hat{u}u} \\ \delta\Psi_{\hat{u}u} \end{bmatrix}}_{\delta\boldsymbol{\Psi}_{\hat{u}u}} \times \right) \quad (4.87)$$

In general, total tilt errors $\delta\Phi$, $\delta\Theta$, $\delta\Psi$ are composed of static errors, errors from axis wobble as well as deformations under load and due to thermal expansion:

$$\delta\boldsymbol{\Phi}(t) = \delta\boldsymbol{\Phi}_{\text{static}} + \delta\boldsymbol{\Phi}_{\text{wobble}}(t) + \delta\boldsymbol{\Phi}_{\text{load}}(t) + \delta\boldsymbol{\Phi}_{\text{thermal}}(t) \quad (4.88)$$

The same accounts for the other tilt errors. In contrast, the errors along the nominal rotation axes result from the measurement and control errors of the axis' servo loop. The orientation errors between the inner gimbal and the sensor's reference frame are only affected by static errors and deformations due to load.

Following above approximations, the angular rates between each two gimbals can be written

as:

$$\boldsymbol{\omega}_{pw} \approx \begin{bmatrix} 0 \\ 0 \\ \dot{\hat{\Psi}}_{wp} \end{bmatrix} + \begin{bmatrix} \cos \hat{\Psi}_{wp} & -\sin \hat{\Psi}_{wp} & 0 \\ \sin \hat{\Psi}_{wp} & \cos \hat{\Psi}_{wp} & 0 \\ 0 & 0 & 1 \end{bmatrix} \begin{bmatrix} \delta \dot{\hat{\Phi}}_{pp} \\ \delta \dot{\hat{\Theta}}_{pp} \\ \delta \dot{\hat{\Psi}}_{pp} \end{bmatrix} \quad (4.89)$$

$$\boldsymbol{\omega}_{wv} \approx \begin{bmatrix} \dot{\hat{\Phi}}_{vw} \\ 0 \\ 0 \end{bmatrix} + \begin{bmatrix} 1 & 0 & 0 \\ 0 & \cos \hat{\Phi}_{vw} & -\sin \hat{\Phi}_{vw} \\ 0 & \sin \hat{\Phi}_{vw} & \cos \hat{\Phi}_{vw} \end{bmatrix} \begin{bmatrix} \delta \dot{\hat{\Phi}}_{vw} \\ \delta \dot{\hat{\Theta}}_{vw} \\ \delta \dot{\hat{\Psi}}_{vw} \end{bmatrix} \quad (4.90)$$

$$\boldsymbol{\omega}_{vu} \approx \begin{bmatrix} 0 \\ 0 \\ \dot{\hat{\Psi}}_{uv} \end{bmatrix} + \begin{bmatrix} \cos \hat{\Psi}_{uv} & -\sin \hat{\Psi}_{uv} & 0 \\ \sin \hat{\Psi}_{uv} & \cos \hat{\Psi}_{uv} & 0 \\ 0 & 0 & 1 \end{bmatrix} \begin{bmatrix} \delta \dot{\hat{\Phi}}_{uv} \\ \delta \dot{\hat{\Theta}}_{uv} \\ \delta \dot{\hat{\Psi}}_{uv} \end{bmatrix} \quad (4.91)$$

$$\boldsymbol{\omega}_{ub} \approx \mathbf{R}_{bu} \begin{bmatrix} \delta \dot{\hat{\Phi}}_{uu} \\ \delta \dot{\hat{\Theta}}_{uu} \\ \delta \dot{\hat{\Psi}}_{uu} \end{bmatrix} \quad (4.92)$$

The translatory errors are simply added to the nominal displacements of the reference frames

$$\mathbf{r}_p(P_w) = \hat{\mathbf{r}}_p(P_w) + \delta \mathbf{r}_p(P_w) \quad (4.93)$$

$$\mathbf{r}_w(P_v) = \hat{\mathbf{r}}_w(P_v) + \delta \mathbf{r}_w(P_v) \quad (4.94)$$

$$\mathbf{r}_v(P_u) = \hat{\mathbf{r}}_v(P_u) + \delta \mathbf{r}_v(P_u) \quad (4.95)$$

$$\mathbf{r}_u(P_b) = \hat{\mathbf{r}}_u(P_b) + \delta \mathbf{r}_u(P_b) \quad (4.96)$$

where the errors, again, are composed of several effects:

$$\delta \mathbf{r}(t) = \delta \mathbf{r}_{\text{static}} + \delta \mathbf{r}_{\text{wobble}}(t) + \delta \mathbf{r}_{\text{load}}(t) + \delta \mathbf{r}_{\text{thermal}}(t) \quad (4.97)$$

The different error sources are modeled and analyzed in the following.

4.2.9.2. Static Axis Errors

For an ideal rate table, all axes are perfectly orthogonal and intersect in a single point. Due to manufacturing imperfections, there is a static orientation error in the table's rotation axes. Analog to that, there is also a constant translatory displacement of the axes. These errors are measured and defined at the static position of the unloaded rate table. Due to their static nature, these errors are modeled as random constant Gaussian variables. In contrast to many other errors, the static errors are not necessarily zero-mean, as imperfections can be measured after the installation but only partially compensated after the manufacturing. In this case, the error's standard deviation is defined by the measurement accuracy of the instruments. If no

measurement is available, the errors are assumed to be zero-mean but with a higher standard deviation representing the typical variations of geometrical errors from manufacturing.

Axis Orientation Errors

The axis orientation errors are usually specified as *non-orthogonality*. Non-orthogonality describes the static angular deviation from orthogonality within the plane defined by two (ideally) crossing rotation axes. These errors are affected by the manufacturing and setup accuracy of the mechanical structure. Within the kinematic chain of a three-axis rate table, the pitch angles of the middle axis $\delta\Theta_{w\hat{w},stat}$ and the inner axis $\delta\Theta_{v\hat{v},stat}$ are described by the non-orthogonality specification. Typical non-orthogonality specifications are in the range of few arc-seconds [136, 137].

There is also a residual static orientation error along the nominal rotation axes $\delta\Psi_{w\hat{w},stat}$, $\delta\Psi_{v\hat{v},stat}$ and $\delta\Psi_{u\hat{u},stat}$. Such an error is typically lower, as it can be compensated comparably easily, e.g., by shifting the rotation angle's offset in software. These errors would be included in the *positioning accuracy* specification of a rate table.

The outer gimbal's vertical rotation axis can be tilted along two angles $\delta\Phi_{p\hat{p},stat}$ and $\delta\Theta_{p\hat{p},stat}$ from its ideal alignment to the laboratory's vertical reference. As this orientation is aligned during the installation of the rate table, it can be assumed that it is performed as well as possible with the used measurement instruments, which justifies a zero-mean assumption and leaves only a standard deviation defined by the measurement accuracy. The same applies to the orientation error of the sensor package with respect to the inner gimbal $\delta\Psi_{b\hat{b},stat}$.

Axis Displacement Errors

The axis displacement is typically not part of the rate table specification. However, it may be assumed to be within the range of mechanical engineering accuracies, which is about 0.5 mm for parts with dimensions in the range of 1 m [138, Table 1]. The static displacement vectors of the rate table's axis and thus reference frames $\delta\mathbf{r}_{p,stat}(P_w)$, $\delta\mathbf{r}_{w,stat}(P_v)$, $\delta\mathbf{r}_{v,stat}(P_u)$ and $\delta\mathbf{r}_{u,stat}(P_b)$ may be modeled as a random constant vector of independent Gaussians with zero-mean.

Model 6: Static rate table errors.

Description

Static orientation errors and displacement of rate table axes caused by manufacturing imperfections. Errors are modeled as independent random constant Gaussians.

Parameters

$\delta\Psi_{w\dot{w}}, \delta\Psi_{v\dot{v}}, \delta\Psi_{u\dot{u}}, \delta\Psi_{b\dot{b}},$
 $\delta\mathbf{r}_p(P_w), \delta\mathbf{r}, \omega(P_v), \delta\mathbf{r}_v(P_u), \delta\mathbf{r}_u(P_b)$

Sensitivities

Table F.6ff, Table F.7ff

Static axis orientation errors

If no measurements of the static rate table errors are available for the used device, the axis orientation and displacement errors may be modeled as independent zero-mean random constant Gaussians with the following standard deviations:

Parameter		Typical Error (1 σ)
Non-orthogonality	$\delta\Theta_{w\dot{w},stat}, \delta\Theta_{v\dot{v},stat}$	5 asec
Positioning Error	$\delta\Psi_{w\dot{w},stat}, \delta\Psi_{v\dot{v},stat}, \delta\Psi_{u\dot{u},stat}$	1.5 asec
Axis displacement	$\delta\mathbf{r}_p(P_w), \delta\mathbf{r}, \omega(P_v), \delta\mathbf{r}_v(P_u), \delta\mathbf{r}_u(P_b)$	0.5 mm

4.2.9.3. Axis Wobble

Axis wobble is a variable tilt of the rotation axis that changes with the rotation angle. This tilt is caused by several effects, both static and dynamic, including:

- The change of the gravity vector during rotation may change the preload and stress conditions in the gimbal and thus in the supporting bearings which effects the stiffness of the bearings.
- Manufacturing imperfections (unroundness, surface waviness, local defects) of the bearing result in variations of the bearing's stiffness with the rotation angle.
- An imbalance of the rotating gimbal causes a harmonic excitation of the bearing's dynamics. The motion of the axis is defined by the bearing's stiffness and damping as well as its geometry.
- When rotating, the passing of manufacturing imperfections also excite the bearing's dynamics.

As illustrated in Figure 4.16, the axis tilt and displacement is caused by a displacement of the axis center within the two supporting bearings:

$$\delta\Phi_{wobble} = \text{atan}\left(\frac{u_{2,y} - u_{1,y}}{l}\right) \approx \frac{u_{2,y} - u_{1,y}}{l} \quad (4.98)$$

$$\delta r_{y,wobble} = \frac{u_{2,y} + u_{1,y}}{2} \quad (4.99)$$

Obviously, the axis wobble is defined by the characteristics of the bearings, which will be briefly described next. The analysis focuses on the two most common bearing types for rate tables, the classical rolling-element bearings and aero-static (gas) bearings.

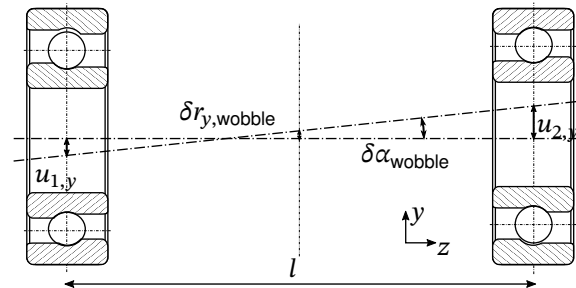


Figure 4.16.: Axis rocking $\delta\alpha$ and displacement δr from bearing deflections.

Bearing Errors

The phenomenon of axis wobble is closely related to the problems of vibration or run-out¹ of bearing-supported rotors which is widely investigated in mechanical engineering and especially precision manufacturing. Since bearings have a finite stiffness, the rotor-bearing system can be modeled as an oscillatable mass-spring-damper system. Unfortunately, the spring stiffness is a non-linear function of the deflection [139, pp. 968–969].

In addition to rotor imbalance, which will be discussed in Subsection 4.2.9.4, the geometrical errors of the bearings are the dominant source of vibrations or run-out [139, pp. 970–971]. These geometrical errors are mainly surface waviness or unroundness of the bearing's inner ring, outer ring, and, if applicable, rolling elements as illustrated in Figure 4.17. The categorization of geometrical errors into unroundness, waviness, and surface roughness are based on the ratio of amplitude and wavelength of the errors [140, p. 14] but will not be considered further here. For rolling element bearings, the geometrical errors change the local compression of the elements and thus lead to a variable stiffness of the bearings as the element revolves along the bearing [141, pp. 101–112]. Similarly, the surface waviness leads to variations of the clearance and thus the supporting gas film thickness in aero-static bearings. This also results in a variation of the local stiffness [142].

In static conditions, this variation of the local stiffness along the circumference leads to a deflection of the rotor's axis from the bearing's center. During rotation, the stiffness variations lead to time-varying forces that excite the rotor-bearing dynamic system to oscillations. The radial deviation from the ideal circular shape of the bearing elements can be expressed by a sum of sine waves along the element's circumference. For rolling element bearings, the

¹the deviation of the rotor axis from its ideal position

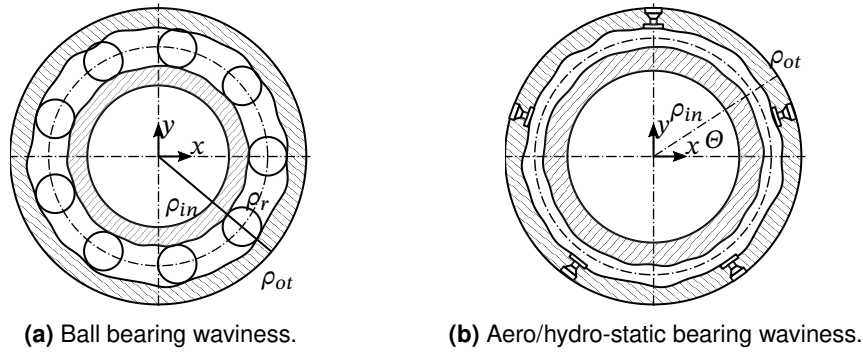


Figure 4.17.: Surface waviness of different bearing technologies.

deviation from the reference circle at the rolling element i is given as [141, p. 103]:

$$\rho^i(t) = \underbrace{\sum_k A_k \cos \left[k \left(\omega_c t + 2\pi \frac{i}{N_r} \right) + \eta_k \right]}_{\text{outer race waviness}} - \underbrace{\sum_k B_k \cos \left[k \left(\omega_i t + 2\pi \frac{i}{N_r} \right) + \psi_k \right]}_{\text{inner race waviness}} + \underbrace{\sum_k 2C_{2k}^i \cos (2k\omega_r t + \theta_{2k}^i)}_{\text{rolling element waviness}} \quad (4.100)$$

The resulting excitation forces are then determined from application of the Hertzian contact theory to each rolling element's compression and subsequent summation over all elements $i = 1 \dots N_r$. It can be demonstrated that only waviness orders of $k = qN_r$ remain after summation for the outer and inner race, while all others vanish [141, p. 104]. The underlying rotation rates of the cage and rolling elements are defined by the bearing's geometry, only. The respective formulas are summarized in Table 4.2.

For aero-static bearings, only the rotor's surface waviness induces a motion of the axis center with the rotation. A perfectly round rotor would stay in a center point defined by the outer journal's waviness but would not display any motion [143]. The variation of the radial clearance can thus be expressed as

$$\rho(t, \zeta) = \sum_k A_k \cos [k(\zeta - \omega_i t) + \eta_k] \quad (4.101)$$

where $\zeta \in [0, 2\pi[$ is the angular coordinate of the rotor surface.

The waviness adds little load for sufficient pre-load, so the Hertzian contact formulas can be linearized [141, p. 107]. Due to the small amplitudes of waviness, the stiffness of aero-static bearings may be linearized [142]. The rotor-bearing system then is represented by a linear mass-spring-damper system with the well-known transfer function [139, ch. 26]: in general, the amplification of the excitation grows from 1 at low frequencies up to a maximum at the critical frequency and finally decreases again for high frequencies. The amplitude and frequency of this maximum depend on rotor mass and the bearing's stiffness and damping. However, typical critical frequencies are in the range of several hundred Hz (see Figure 4.18), while

Table 4.2.: Fundamental frequencies of rolling element bearings [139, p. 994].

Effect	Frequency
Rotation of shaft / inner ring	f_i
Rotation of cage	$f_c = \frac{1}{2}f_i \left(1 - \frac{d_r}{d_m} \cos \phi\right)$
Rotation of the rolling elements	$f_r = 2\frac{d_m}{d_r}f_c \left(1 - \frac{f_c}{f_i}\right)$
Roller passing inner ring defects	$f_{rpi} = N_r (f_i - f_c)$
Roller passing outer ring defects	$f_{rpo} = N_r f_c$

N_r : number of rolling elements, d_r : rolling element diameter,
 d_m : bearing pitch diameter, ϕ : contact angle

the maximum rotation rate of most rate tables is usually around 1 to 2 Hz. For such a low excitation rate, the bearing dynamics can be neglected for aero-static bearings, too [143].

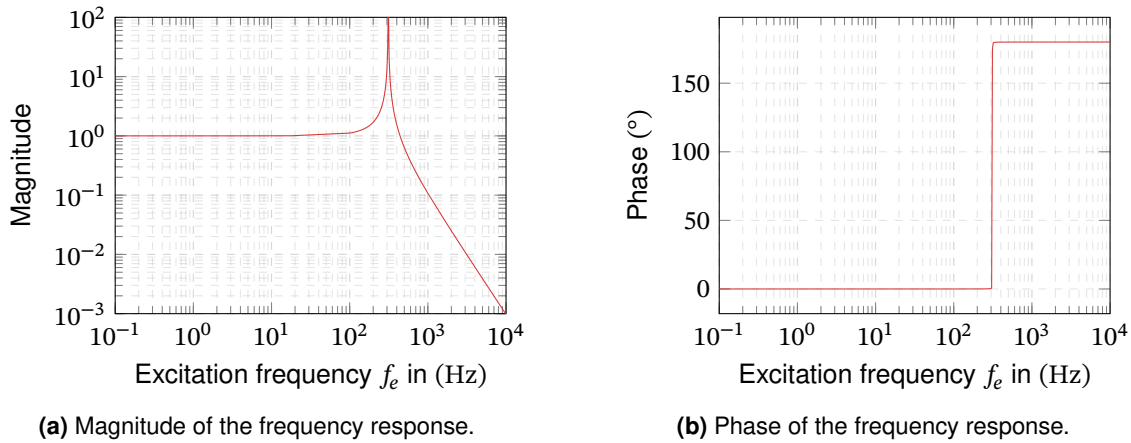


Figure 4.18.: Frequency response of the linearized bearing dynamics. Transfer function has been determined for a simplified linear model in accordance to [139, pp. 1013–1024]. Bearing stiffness $k = 3 \cdot 10^9$ N/m and damping coefficient $c = 1 \cdot 10^4$ Ns/m have been estimated following [144]. Gimbal/rotor mass is $m = 1000$ kg.

For a ball bearing, the different harmonics of the outer and inner races' waviness add to excitation forces with the possible frequencies defined in Table 4.3. A derivation of the excitation forces can be found in [141, p. 109]. As these vibrations cause the axis to wobble, it should, in general, show the same harmonics, and the wobble angle should be of the form:

$$\delta\Phi_{\text{wobble}} = \sum_q \sum_p [A_q \cos(qN_r\omega_c t + \eta_q) + B_{q,p} \cos((qN_r\omega_c + p\omega_i)t + \psi_{q,p})] \quad (4.102)$$

where $q \in \mathcal{N}_0^+$ and $p \in \mathcal{N}_0$. The occurring orders q and p depend on the actual geometrical errors of the bearings and cannot be predicted. Here, the effects of rolling elements waviness is neglected, as they are usually manufactured to a significantly higher accuracy than the rings [141, p. 106]. Although the waviness amplitudes of bearings can be determined at high accuracy in the laboratory [139, p. 981], this does not allow direct conclusions on the rate table's gimbal wobble amplitudes. The amplitudes of the bearing vibrations depend strongly on the

actual assembly conditions, e.g., the actual load. Additionally, the surface waviness's relative phases depend on the installation orientation. Thus, the amplitudes and the order of existing harmonics of the axis wobble have to be determined at the assembled rate table.

Table 4.3.: Bearing vibration frequencies from waviness [139, p.982]

Component	Order	Frequencies
Inner ring	$k = qN_r \pm p$	$qN_r(f_i - f_c) \pm pf_i$
Outer ring	$k = qN_r \pm p$	qN_rf_c
Roller	k (even)	$kf_b \pm pf_c$

In practice, however, the amplitudes and phases of the different harmonics cannot be determined sufficiently accurately to create a deterministic model. Instead, the wobble motion shall be modeled by a stochastic process, defined by its PSD. The tilt is the sum of several harmonic oscillations at frequencies that depend on the axis' angular rate and some constants, like diameters and waviness orders. For such a purely sine-based signal, the PSD and thus the processes' auto-covariance is defined by Dirac impulses at these characteristic frequencies.

Typically, the axis wobble is specified as the maximum tilt variation over one revolution. Specifications are in the range of 2.5 to 5 asec [136] and 0.5 asec for aero-static bearings [28] and usually refer to the RMS of the tilt errors along multiple revolutions. Modeling the wobble amplitudes from just one value requires some relationship between the waviness amplitudes. An exponential decline with the waviness order k is suggested in [145]:

$$A_k = Ae^{-0.05k} \quad (4.103)$$

For a given set of waviness orders, the respective amplitudes can be determined from an RMS value as follows:

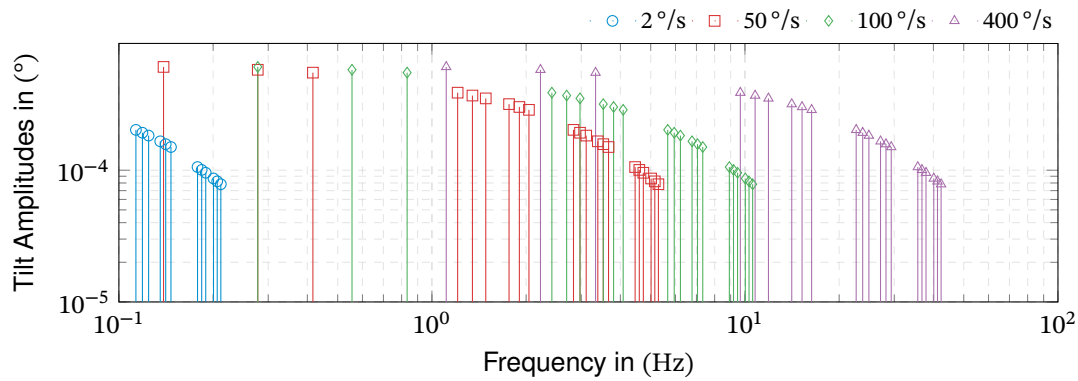
$$A_{q,p} = A_{\text{RMS}} \frac{e^{-0.05(qN_r+p)}}{\sqrt{\sum_p \sum_q e^{-2 \cdot 0.05(qN_r+p)}}} \quad (4.104)$$

In practice, the existing harmonics q and p , are typically unknown. As the amplitudes decline with the order, a rough approximation may simply stick to the first few harmonics, e.g. $q = [0, 1, 2, 3]$, $p = [\pm 1, \pm 2, \pm 3]$ as depicted in Figure 4.19.

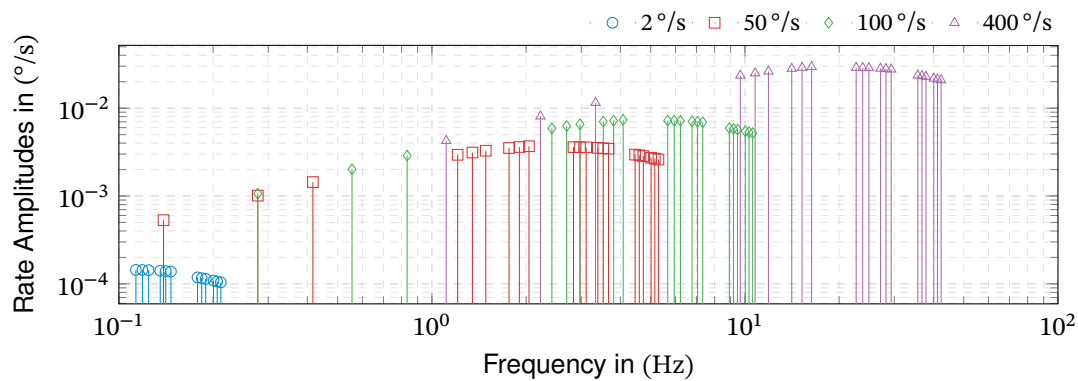
Using (4.98) and (4.99), the linear displacement of the gimbal's center can be approximated from the wobble's tilt as:

$$\delta r_{wbl}(t) = \left(\frac{l}{2}\right) \delta \Phi_{wbl}(t) \quad (4.105)$$

The accelerations can analogously be determined from double time-derivation of the above equation. The validity of the above models will be discussed in the next section.



(a) Tilt angle amplitude spectrum.



(b) Angular rate amplitude spectrum.

Figure 4.19.: Amplitude spectrum of the bearing wobble model for different rotation rates. The model amplitudes follow (4.103) for $A_{\text{RMS}} = 5 \text{ asec}$ and includes the waviness orders $q = [0, 1, 2, 3]$, $p = [\pm 1, \pm 2, \pm 3]$.

Validation

The above-derived stochastic models suggest the existence of clearly defined frequencies in an inertial sensor's measurements about the axes orthogonal to the nominal rotation. A measurement's PSD should consequently contain distinctive peaks at frequencies of Table 4.3. As the wobble angular rates depend linearly on the axis' nominal angular rate, the PSD is expected to scale quadratically when increasing the axis' rate.

This exact phenomenon is observed in measurements obtained during a scale factor test. A FOG IMU IFOS-500 from Fiber Optical Solutions was rotated about its z-axis using the institute's three-axis rate table. The table's inner axis was aligned to local gravity and rotated at different rates. The measurements of all three gyroscope and accelerometer axes was recorded for each rate for 90 min. The PSD of the measurements at $2^\circ/\text{s}$, $50^\circ/\text{s}$, $100^\circ/\text{s}$ and $400^\circ/\text{s}$ is depicted in Example 1 for the gyroscopes and Example 2 for the accelerometers. The sensor's inherent noise floor from a 24 h stationary test is added for reference.

In all depicted test cases, the PSD of the z axis gyroscope displays the characteristic slope of constant input. Only for the very slow rate of $2^\circ/\text{s}$ can some deviation caused by the rate table's controls be observed. The higher the commanded rate, the higher the curve shifts towards

higher powers. For the very low rate of $2^\circ/\text{s}$, the output of the two orthogonal gyro axes cannot be distinguished from the stationary reference. Starting from $50^\circ/\text{s}$ peaks at characteristic frequencies raise from the background noise. Mainly, there are multiples of the axis rotation rate f_i , but also multiples of f_{bpi} and some side-lobes. Further increase of the angular rate raises the amplitude of higher-order harmonics above the background noise level. The amplitudes grow quadratically with the applied angular rate, which fits the predicted behavior. Only the amplitude at the nominal rotation rate $1f_i$ does not grow significantly, as it is dominated by the Earth's angular rate that is picked up by the gyroscope axes that move within the local leveled plane. Additionally, the unbalance of the axis may contribute to this amplitude. Also, with a growing angular rate, the characteristic slope of the constant input rises in the x and y axis measurements. This is caused by a misalignment of the sensor's axes, where the sensors pick up fractions of the rate table's nominal rotation.

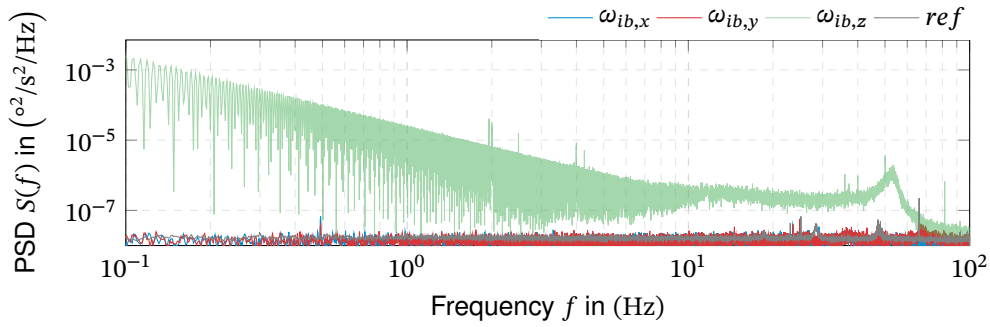
For the accelerometer measurements, depicted in [Example 2](#), the situation is similar. The same characteristic frequencies observed for the gyroscope measurements become visible with growing angular rates. The amplitudes at $1f_i$ are dominated by the pickup of the local gravity caused by a constant misalignment of the rate table's rotation axis. The noise levels representing a constant input grow with f_i^4 , which is caused by centrifugal forces due to an offset of about 1 mm from the rotation axis.

Equation (4.105) suggests a constant relationship between angular and linear accelerations. The experimental data, however, show a higher ratio than expected from (4.105) that additionally declines with growing frequencies. This is probably caused by a frequency-dependent response of the rate table's structure to this excitation. Equation (4.105) provides only a rough estimate for the acceleration levels, but the exact amplitudes should be determined experimentally.

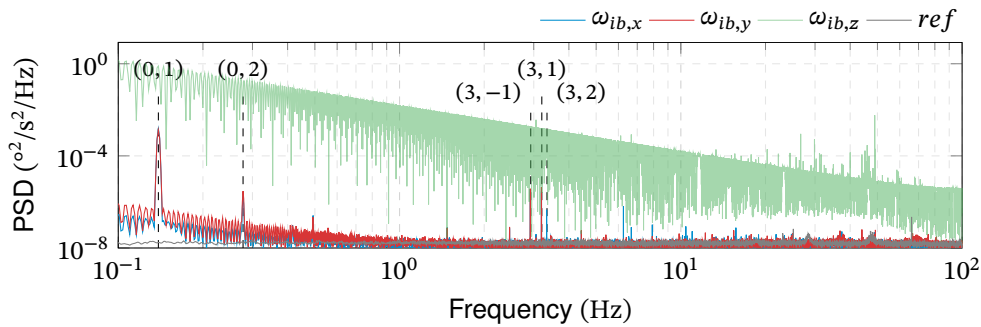
It must be emphasized that the occurring waviness orders and amplitudes are characteristic of this single rate table axis and cannot be generalized. The simple model is only roughly representative of the actual bearing wobble. While the experimental data confirm the dominance of the low order harmonics, here $q = [0, 3]$, $p = [\pm 1, \pm 2, \pm 3]$, not every order exists in the sample data. The suggested decline of the amplitudes with the frequency can only be observed as a general trend. The model cannot predict the existing orders or the corresponding amplitudes exactly. However, it may be used as a worst-case model if there is no further knowledge than, e.g., a wobble [RMS](#) specification. In this case, at least the possible frequencies and thus the time-correlation of the wobble signals are considered, which becomes essential when averaging the sensor's signal. The same accounts for the dependency on the axis' nominal angular rate.

Example 1: Rate table axis wobble in the PSD of a three-axis gyro measurement.

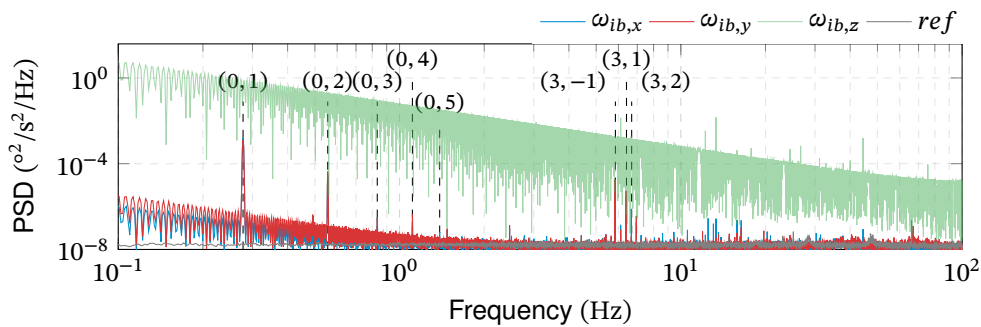
Vertical rotation of a IFOS-500 IMU about the z axis at different rates for each 90 min. PSD is determined using Welch's method, window length 100000 samples, 50% overlap, sample rate 200 Hz. Inner and outer ring vibrations are marked by its components (q, p) respectively (q) , as given in Table 4.3. For reference, the x -axis gyro noise PSD from a stationary 24 h test is depicted.



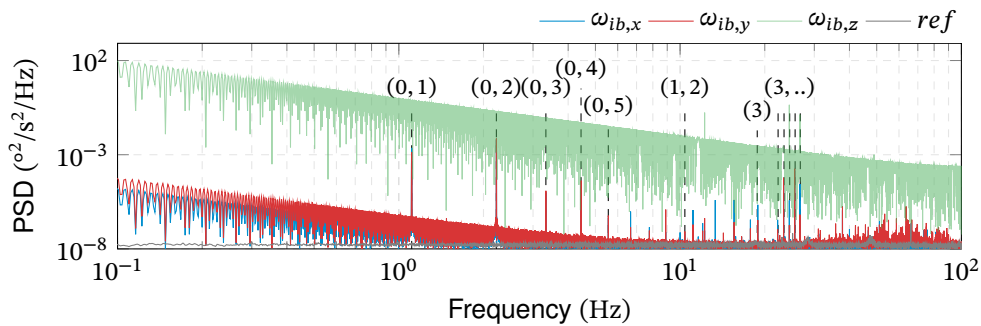
(1.a) Rate table inner axis at $2^\circ/s$



(1.b) Rate table inner axis at $50^\circ/s$



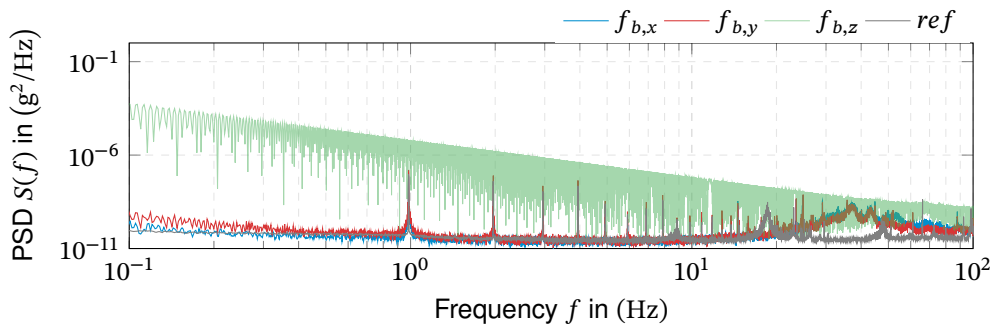
(1.c) Rate table inner axis at $100^\circ/s$



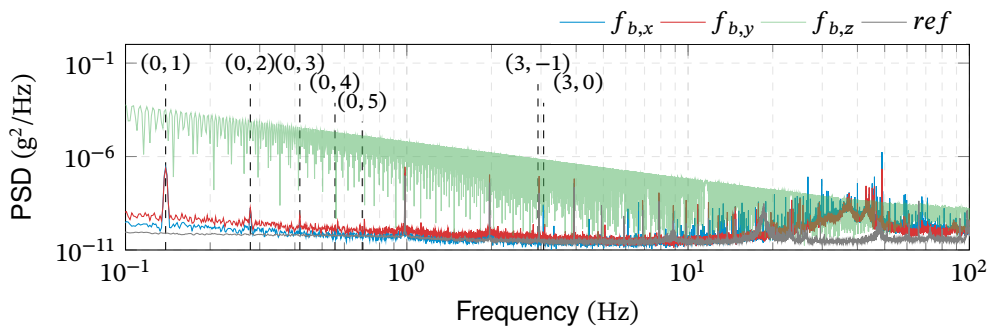
(1.d) Rate table inner axis at $400^\circ/s$

Example 2: Rate table axis wobble in the PSD of a three-axis accelerometer measurement.

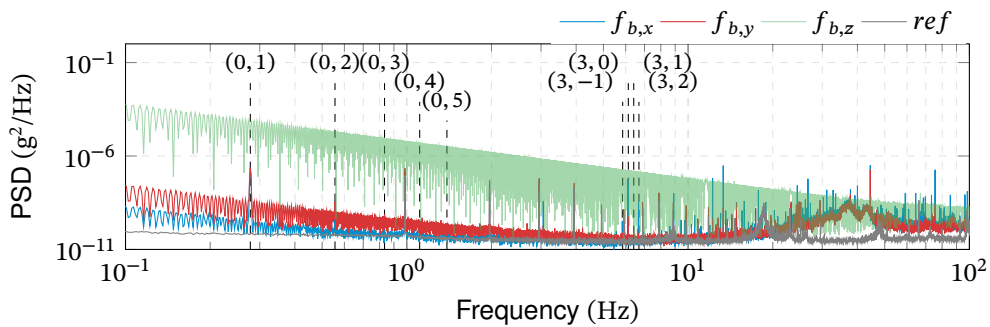
Vertical rotation of a IFOS-500 IMU about the z axis at different rates for each 90 min. PSD is determined using Welch's method, window length 100000 samples, 50% overlap, sample rate 200 Hz. Inner and outer ring vibrations are marked by its components (q, p) respectively (q) , as given in Table 4.3. For reference, the x-axis gyro noise PSD from a stationary 24h test is depicted.



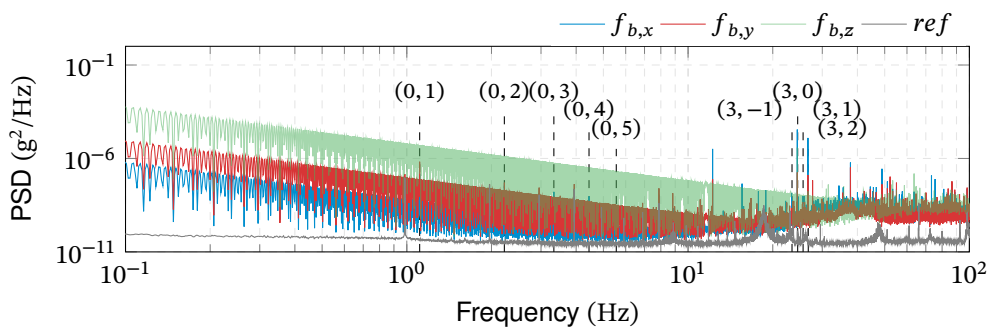
(2.a) Rate table inner axis at 2°/s



(2.b) Rate table inner axis at 50°/s



(2.c) Rate table inner axis at 100°/s



(2.d) Rate table inner axis at 400°/s

Model 7: Rate table axis wobble modeling.**Description**

Axis tilt errors, corresponding displacements and resulting rates and accelerations from bearing imperfections. Wobble effects only the two tilt angles of the axis, not the rotation along the axis itself.

Parameters

$\delta\Phi_{p\hat{p}}, \delta\Theta_{p\hat{p}}, \delta\Theta_{w\hat{w}}, \delta\Psi_{w\hat{w}}, \delta\Theta_{v\hat{v}}, \delta\Psi_{v\hat{v}}$
 $\delta r_{p,x}(P_w), \delta r_{p,y}(P_w), \delta r_{w,y}(P_v), \delta r_{w,z}(P_v)$
 $\delta r_{v,x}(P_u), \delta r_{v,z}(P_u)$

Sensitivities

Table F.6ff, Table F.7ff

Axis wobble model

Rate table axis wobble can be modeled as the sum of harmonic oscillations at frequencies that depend on the axis' rotation rate and the geometry of the bearing:

$$\delta\Phi_{\text{wobble}} = \sum_{q,p} A_{q,p} \cos((qN_r(f_i - f_c) + pf_i)t)$$

The relevant frequencies f_c and f_i can be determined from the axis' rotation rate as summarized in Table 4.2 and Table 4.3. The corresponding axis displacement can be approximated from the bearing distance using (4.105).

Amplitudes and occurring waviness orders q, p can be determined from a PSD analysis of inertial sensor measurements of the respective rate table axis' motion. If experimental data is not available, the existence of the first few waviness orders may be assumed, and the amplitudes may be approximated from (4.104). A typical wobble RMS values are around 2.5 asec.

In both cases, the phase information of the different sine terms is unknown. However, phase information is irrelevant for the statistics, e.g., auto-covariance, required to model the rate uncertainty arising from axis wobble.

4.2.9.4. Deformation under Load

The rate table's structure has only a limited stiffness. External forces and moments thus yield an elastic deformation of the structure and thus orientation and position errors of the different gimbals. Each part of a rate table is usually designed symmetrically to its rotation axis. Therefore, the loads arising from its own mass should only result in a symmetric deformation that does not shift or tilt its center. The structure's deformation is thus dominated by the loads generated by the mechanical parts up the kinematic chain.

The stiffness of the rate table depends on the actual construction, the used materials and geometries. An experimental determination of above's derivatives is rather complex. Alternatively, the derivatives can be determined numerically from the [Computer-Aided Design \(CAD\)](#) model of the rate table using industry standard structural analysis tools.

Typical Stiffness

As stated before, the actual stiffness of a rate table depends on its construction and cannot be generalized. The mechanical structure could be designed arbitrarily stiffly, which is limited by cost and weight in practice.

Using the Euler-Bernoulli beam theory, the deflection of a beam with constant cross-section under load can be approximated. For a beam clamped at the one end and loaded with a force F at the other end, the end's deflection yields [146, p. 144]

$$\Delta z = F_z \frac{l^3}{3EI} = \frac{F_z}{k_z} \quad (4.106)$$

with the beam length l , Young's modulus E , and the second moment of area I . This allows, for example, the approximation of stiffness of the rate table's outer gimbal yoke against vertical forces acting on the middle axis bearings. Assuming a rectangular steel tube of 200 mm \times 200 mm, with a wall thickness of 5 mm and a length of 0.8 m yields:

$$\frac{\partial \delta r_{w,z}(P_v)}{\partial F_{w,z}} = 5.27 \cdot 10^{-9} \frac{\text{m}}{\text{N}} \quad (4.107)$$

This approximation may indicate the general level of stiffness, but of course, the actual values depend on the rate table's structure.

The bearings, however, are [Commercial off-the-shelf \(COTS\)](#) components with a known stiffness range. According to [147, p. 36], the radial stiffness of ball bearings can be approximated as $k_x = d \cdot 5 \cdot 10^6 \text{ N/m}$, where d is the inner diameter in mm. Thus, the radial stiffness is in the range of 10^8 to 10^9 N/m for realistic axis diameters. As the bearing's and the structure's stiffness are connected in series, the total system cannot be more stiff than the least stiff element:

$$\frac{1}{k_{\text{total}}} = \frac{1}{k_{\text{brg}}} + \frac{1}{k_{\text{structure}}} \quad (4.108)$$

Considering this, and the approximation (4.107), a total stiffness in the range of 10^8 N/m can be assumed.

For equal bearing stiffness on both sides of the axis the equivalent rotational stiffness against moments can be determined from the bearing distance l :

$$k_{\Theta} = \frac{k_z l^2}{4} \quad (4.109)$$

For an assumed bearing distance of $l = 0.5$ m, the resulting axis tilt from a moment load is given determined to ($k_z = 1 \cdot 10^8$ N/m):

$$\frac{\partial \delta \Theta_{\dot{w}w}}{\partial M_{w,y}} = 0.033 \frac{\text{asec}}{\text{Nm}} \quad (4.110)$$

Even for an unbalanced load of 10 kg, 10 cm lever-arm and standard gravity, this would yield a tilt of just 0.33 asec. For comparison, a tilt stiffness of $2.4 \cdot 10^{-4} \frac{\text{asec}}{\text{Nm}}$ against the weight force of an unbalanced test package is given for a proposed rate table design in [28]. This value accounts for the structure only and not for the bearings.

Structural Eigenmodes

Varying excitation forces and moments may excite the Eigenmodes of the rate table's structure. Excitation at the Eigenfrequencies (or multiples of that) leads to resonance and thus amplification of the resulting deformations. Again, the Eigenmodes and frequencies, of course, depend on the geometry and materials of the structure and cannot be generalized. Instead, the Eigenmodes have to be determined experimentally or using numerical methods on a virtual model of the system.

An experimental investigation of the two-axis rate table's Eigenfrequencies is given in [35]. Shakers excited an actively stabilized test pad, and the rate table's vibration was measured using multiple mobile seismometers across its structure. Depending on the excitation direction, frequencies of 22 Hz respectively 25 Hz were found for the yoke structure and 31 Hz / 34 Hz for the second gimbal's structure with counter-weights. The experimental results for this 680 kg rate table may be representative of similar devices in structure and mass.

In static operation, the rotation rates are usually too low to excite the Eigenmodes of the rate table. However, an excitation is well possible in dynamic conditions. Notch-filters prevent resonance in the rate table's servo control loops that attenuate the excitation around the structure's Eigenfrequencies. However, excitation of the structure may still arise, e.g., from bearing vibrations and seismic noise.

Model 8: Rate table deformation und load model.

Description

Tilt and displacement of rate table axes respectively reference frames caused by static and dynamic loads.

Parameters

$\delta\Psi_{p\hat{p}}, \delta\Psi_{w\hat{w}}, \delta\Psi_{v\hat{v}}, \delta\Psi_{u\hat{u}}, \delta\Psi_{b\hat{b}}$
 $\delta\mathbf{r}_p(P_w), \delta\mathbf{r}_w(P_v), \delta\mathbf{r}_v(P_u), \delta\mathbf{r}_u(P_b)$

Sensitivities

Table F.6ff, Table F.7ff

Deformation model

Static and, in particular, dynamic loads depend strongly on the commanded rate table motion. Also, the tilt and displacement sensitivity to loads cannot be generalized but depends on the actual construction of the rate table. In general, rate tables are well-balanced precision instruments so that no load except gravity should exist during the typical static test motions.

The bearings dominate the construction's flexibility, so typical values may be used to assess the order of magnitude of a rate table's flexibility. The approximations in this section suggest that the tilt errors from loads are significantly below 0.5 asec for realistic loads. If the loads arise from balancing inaccuracies, the resulting errors may be modeled as zero-mean random constant Gaussians with the standard deviation derived from the imbalance uncertainty.

Considering the challenges of modeling these errors and in comparison to the static and wobble errors of a rate table, it is reasonable to neglect the errors from loads in many cases. Note that this is not justified in high-dynamic operations or extremely unbalanced loads.

4.2.9.5. Thermal Expansion

Analog to the deformations under loads, a detailed analysis of the deformations due to the temperature distributions requires knowledge of the actual rate table design. A design symmetrical to the axes of rotation ensures that a uniform temperature change does not result in an axis tilt. An asymmetrical temperature distribution, however, can be caused by either external or internal heat sources:

- **External heat sources**, like solar radiation, can be considered space-fixed relative to the rate table. A non-rotating rate table will thus be heated from one side. The resulting temperature distribution will cause a deformation of the rate table. For a rotating rate table, the external heat source can be assumed to act on all sides of the rate table, yielding a rotation symmetric temperature distribution about the rotation axis and consequently no tilt. External heat sources can generally be well controlled within a laboratory environment.
- **Internal heat sources**, like the motors and bearings, are body-fixed to the structure. Ultimately, the different heat sources and sinks (convection to the environmental air) will reach an equilibrium and a steady-state temperature distribution, which declines with distance from the heat sources. So, after a warm-up time, there will be constant tilt and displacement caused by the asymmetrical temperature distribution.

Again, without knowledge of a specific rate table design, only a rough approximation of the orientation errors from temperature differences can be given. For a symmetrical and closed structure, like the middle and inner gimbal depicted in Figure 4.15, unbalanced heating from the bearings or motors will not cause a tilt of the axis. For such a design, only the thermal expansion of the outer gimbal's yoke is critical.

For example, the tilt of the middle gimbal can be approximated from the difference in the average temperatures of the two vertical arms of the outer gimbal's yoke $\Delta\bar{T}$. Assuming a coefficient of thermal expansion $\alpha = 1.2 \cdot 10^{-5} \text{ K}^{-1}$ (steel, [148, p. C8]), a yoke width of $l = 1.6 \text{ m}$ and height of $h = 0.8 \text{ m}$ yields:

$$\delta\Theta_{\omega\dot{\omega},\text{thermal}} = \text{atan} \frac{\alpha h \Delta T}{l} \approx \alpha \frac{h}{l} \Delta T \approx 0.56 \frac{\text{asec}}{\text{K}} \Delta T \quad (4.111)$$

The outer gimbal's temperature expansion may serve as a worst case scenario as it has the largest dimensions and thus potentially the highest temperature differences. A constant temperature difference of relevant magnitudes between two sides of the rate table's structure requires a relatively high asymmetric heat input. For example, DeMoore [28] states a tilt of 0.01 asec/W from an unbalanced heat input at the outer axis bearings for his proposed design.

According to [148, p. G.94], the bearing friction torque may be approximated as:

$$M_R = 10^{-7} f_0 \cdot 160 \cdot d_m^3 + f_1 F_1 d_m \quad (4.112)$$

where $f_0 = 2$ and $f_1 = 0.0025$ for angular contact ball bearings and low angular rates. Assuming a mean diameter of $d_m = 80 \text{ mm}$ for the middle axis' bearings, a load of $F_1 = 10 \text{ kN}$ and a maximum rotation rate of $\omega = 360 \text{ deg/s}$ yields a friction power loss of:

$$P_R = M_R \omega \approx 15 \text{ W} \quad (4.113)$$

Assuming further a worst-case dispersion of the friction of about 10 % between the different bearings, yields a maximum heat unbalance of 1.5 W, which results in tilts of about 0.015 asec.

During warm-up, heat sources such as friction and electrical power loss, heat transport, and heat dissipation to the environment contribute to the temperature distribution within the structure. After some time, the temperature distribution converges towards a stationary condition and thus a constant tilt, respectively displacement. Precision testing should be thus performed only after the structure has reached a stationary temperature distribution. The often monitored motor temperatures can be used as an indicator, if a stationary distribution has been reached.

Model 9: Rate table thermal expansion model.

Description

Tilt and displacement of rate table axes respectively reference frames caused by thermal expansion of the structure.

Parameters

$\delta\Psi_{p\hat{p}}, \delta\Psi_{w\hat{w}}, \delta\Psi_{v\hat{v}}, \delta\Psi_{u\hat{u}}, \delta\Psi_{b\hat{b}}$
 $\delta\mathbf{r}_p(P_w), \delta\mathbf{r}_w(P_v), \delta\mathbf{r}_v(P_u), \delta\mathbf{r}_u(P_b)$

Sensitivities

Table F.6ff, Table F.7ff

Thermal expansion model

After a warm-up of the rate table's structure, the axes displacement and tilt can be modeled as a zero-mean random constant Gaussian. From the approximations within this section, it can be suggested that the resulting tilts and displacements are well below 0.1 asec and 0.1 mm. Under nominal operation conditions, the errors from thermal expansion cannot be distinguished from the general static errors of the rate table.

Rate table temperature measurements, such as motor temperatures, should be monitored to ensure no excessive thermal imbalance.

4.2.9.6. Positioning and Rate Errors

The rate table uses a servo loop to control the axes' angular position $\Psi_{pw}, \Phi_{wv}, \Psi_{vu}$ and rates $\dot{\Psi}_{pw}, \dot{\Phi}_{wv}, \dot{\Psi}_{vu}$. Positioning and rate control are based on measurements of the actual angular position of each rate table axes. This is typically achieved using inductive, magnetic, or optical angle encoders. Based on these measurements, the angular rate and acceleration are also estimated and used in the closed-loop position and rate control. A representative single-axis control scheme is depicted in Figure 4.20. The error between the desired and actual axis position is affected by the following sources:

- The **encoder measurement errors** corrupts the angular position measurement used in the control loop. This limits the total positioning accuracy of the axis' servo control.
- **Actuator imperfections**, like cogging torques and electronics noise caused by the servo amplifiers, introduce additional disturbances to the control loop.
- The **controller characteristics** defines the transfer function from commanded angle and rate to the actual angle. The architecture and tuning of the control loop affect the system's dynamic behavior and steady-state accuracy. The implementation of the controller introduces additional errors, like numerical precision and electronics noise at the commanded torque.
- Due to the **flexibility of the mechanical structure**, the gimbal's actual orientation may differ from the angular position of the encoder's and motors' point of attack. This error is independent of the control loop and is modeled as described in Subsection 4.2.9.4.

The different error sources contributing to the closed-loop control errors will be discussed in the following.

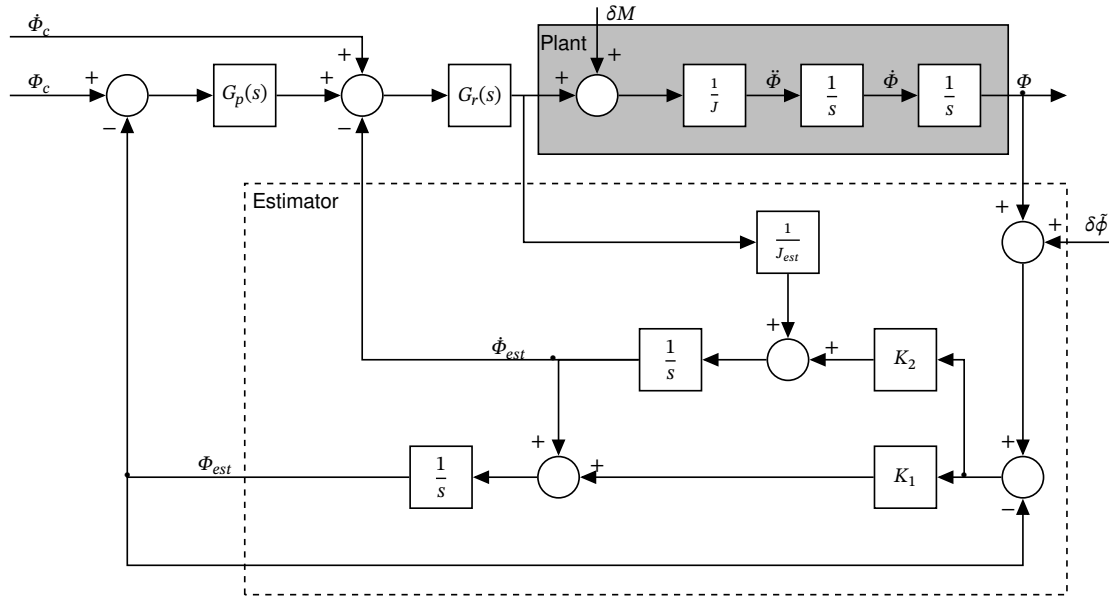


Figure 4.20.: Exemplary rate table servo loop scheme. The close-loop controller tracks the commanded position Φ_c and rate $\dot{\Phi}_c$. Rate and position are estimated from measured positions using a simple two-state observer. Rate table servo control scheme from [28].

Angle Encoder Measurement Errors

The system accuracy of COTS rotary encoders is around 1 asec, for both inductive (e.g. inductosyn [149]) and magnetic or optical (e.g. [150, 151]) encoders.

In detail, the measurement errors display a periodic behavior. Due to their widespread use, the error behavior of inductosyn encoders was intensively analyzed and discussed. The measurement error $\Delta\Phi$ at the mechanical rotation angle Φ is dominated by a once-per revolution harmonics and cyclic errors, defined the number of poles N [152]:

$$\Delta\tilde{\Phi} = a_0 \sin(\Phi + \psi_0) + a_1 \sin(N\Phi + \psi_1) + a_2 \sin\left(\frac{N}{2}\Phi + \psi_1\right) + a_4 \sin(2N\Phi + \psi_4) + \nu_\Phi(t) \quad (4.114)$$

The different phases ϕ_i are unknown but constant. Additional noise ν_Φ is added to account for noise in the driving and pick-off electronics. The once-per-revolution a_0 and the fundamental error a_1 are caused mainly by eccentricity and tilt between the inductosyn's stator and rotor. The other terms are driven by gain drifts in the electronics and non-linearities in the circuits [152].

A simulated example of inductosyn measurement noise is depicted in Figure 4.21. For such an error model, the angle error when moving a significant angle increment can be smaller than for a small increment. Due to that behavior, the measurement error is often described by a coarse position error (large increments) and a fine position error (small increments). Such a description is, for example, used in [28].

The above-given model is also experimentally confirmed in [153]. Due to the primarily

deterministic behavior and the simple error model, the inductosyn errors can be calibrated and compensated very effectively. A potential reduction of the errors down to 0.001 asec by calibration is claimed in [28]. Other authors obtained a residual error of less than 0.1 asec during calibration experiments [154]. Calibration, using error model (4.114) reduces the amplitudes of the different harmonics but does not change the general structure.

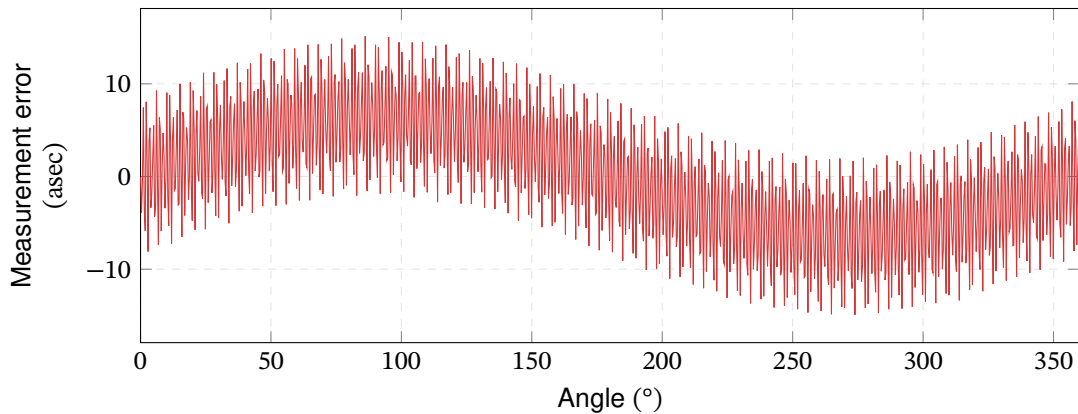


Figure 4.21.: Example of simulated inductosyn measurement errors. The parameters $a_0 = 6.5$ asec, $a_1 = 2.8$ asec, $a_2 = 6.5$ asec, $a_4 = 0.5$ asec are chosen similar to the amplitudes presented in the FFT analysis in [153]. All phases are assumed zero, and zero-mean white Gaussian noise with $\sigma_n = 0.1$ asec has been added.

Typical rotary inductosyn encoders have $N = 720$ poles. If no further information is available, the total measurement error of, e.g., 0.1 asec RMS may be distributed equally to the four amplitudes' variances for a basic approximation.

Actuator Modeling

Due to their simplicity, direct electric drives are today's dominant actuator technology for positioning and rate tables (c.f. [155, 156, 157, 158]). The electric drives may be accompanied or replaced by hydraulic motors for large systems and high dynamics requirements. For electric servo drives, the **Permanent Magnet Synchronous Motor (PMSM)** has become the dominant technology due to its high power density and excellent control dynamics [159, p. 413].

Typical electric motor dynamics have a time constant well below 1 ms and can consequently be neglected compared to the closed-loop servo dynamics. Still, the generated motor torque is subject to disturbances called torque ripple. These are caused by voltage, a respectively current ripple of drive electronics, and so-called cogging. Cogging is caused by the interaction of the rotor's magnets and the stator's slots and leads to a harmonic variation of the torque over the mechanical rotation angle Φ [160]:

$$T_{\text{cogging}} = \sum_{n=1,2,3,\dots}^{\infty} T_n \sin(N_c n \Phi) \quad (4.115)$$

A summary of different analytical and numerical approaches to determine the cogging torque

for certain motor designs can be found in [161]. For typical COTS servo motors, the cogging torque is less than 5%. As the cogging torque is mainly deterministic, it can be effectively compensated using look-up tables or dedicated control schemes. The total torque ripple may be modeled by a combination of deterministic torque cogging and white Gaussian noise ν :

$$T_{\text{ripple}}(t) = T_{\text{cogging}}(\Phi(t)) + \nu(t) \quad (4.116)$$

Closed Loop Position and Rate Error

Using the above-derived models for the sensors and actuators with the basic control structure from Figure 4.20, the transfer function from measurement and actuator errors to the position can be determined:

- For the depicted control scheme, the transfer function from the real angle position to the estimated angular position is given as:

$$\phi_{\text{est}}(s) = \frac{K_1 s + \left(\frac{1}{J_{\text{est}}} K_1 G_r + K_2 \right)}{s^2 + \left(K_1 + \frac{1}{J_{\text{est}} G_r} \right) s + \left(\frac{1}{J_{\text{est}}} (K_1 G_r + G_r G_p) + K_2 \right)} (\phi(s) + \delta\phi(s)) \quad (4.117)$$

- Closing the control loop, even at zero commanded rate, leads to an amplification of the measurement noise and thus to position errors. The transfer functions from actuator and measurement errors to the angular position are determined to:

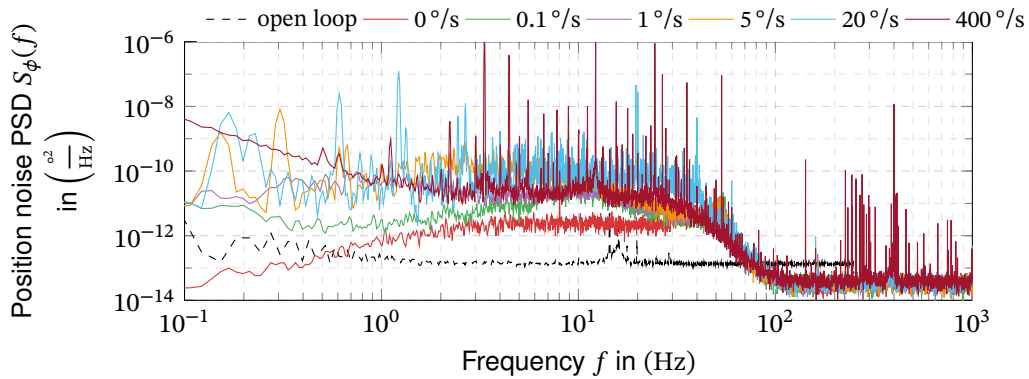
$$\phi(s) = \frac{1}{J} \frac{s^2 + \left(\frac{1}{J_{\text{est}}} G_r + K_1 \right) s + \left(K_2 + \frac{1}{J_{\text{est}}} (K_1 G_r + G_p G_r) \right)}{s^4 + (G_r + K_1) s^3 + \left(K_2 + \frac{G_r (K_1 + G_p)}{J_{\text{est}}} \right) s^2 + \frac{G_r (K_2 + K_1 G_p)}{J} s + \frac{K_2 G_p G_r}{J}} \delta M(s) \quad (4.118)$$

$$\phi(s) = \frac{-1}{J} \frac{(K_2 G_r + K_1 G_p G_r) s + K_2 G_p G_r}{s^4 + (G_r + K_1) s^3 + \left(K_2 + \frac{G_r (K_1 + G_p)}{J_{\text{est}}} \right) s^2 + \frac{G_r (K_2 + K_1 G_p)}{J} s + \frac{K_2 G_p G_r}{J}} \delta\phi(s) \quad (4.119)$$

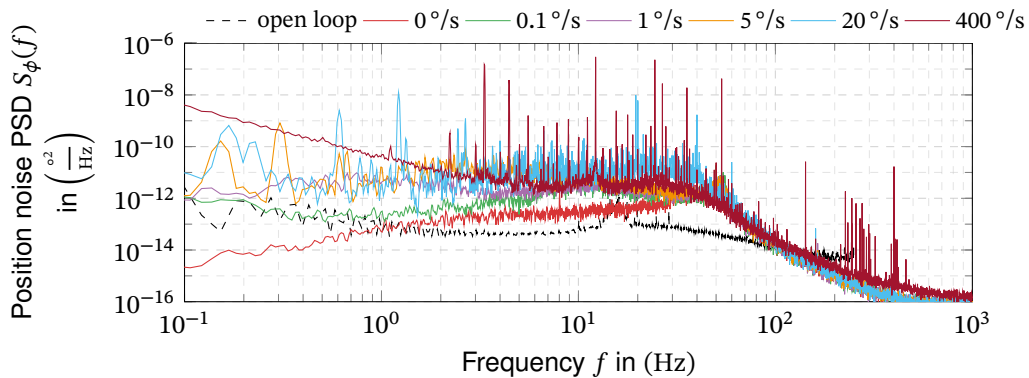
The noise of the rate table's position and rate could be determined from the analytical models above. For a given measurement noise, the servo control's transfer functions can be used to approximate the table's position and rate errors. The actual torque errors, however, cannot be predicted but need to be determined for a given motor experimentally. As the measuring accuracy is better than the actually achieved position, the position and rate errors can be determined from recorded rate table data.

Example 3: Power spectral density of rate table position and rate measurements.

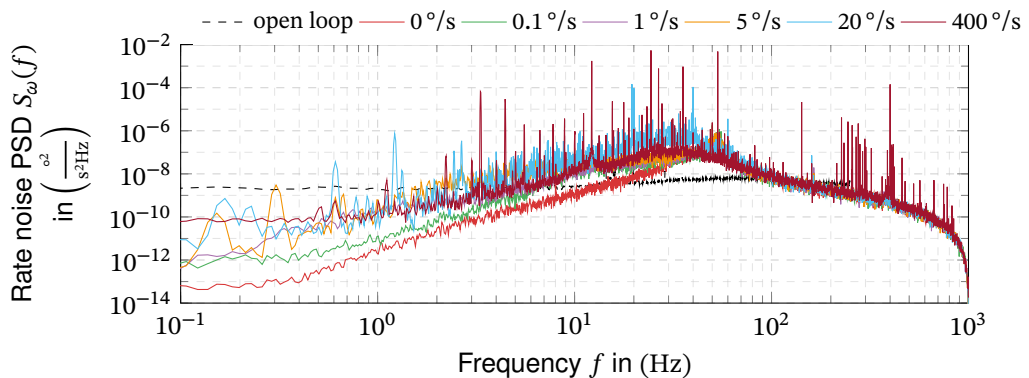
Power spectral density of position and rate noise measurements and estimates at a constant rate. PSD has been determined using Welch's method on 300 s recordings at 2000 Hz sample rate with a window length of 10 000 samples. Position noise has been determined as the error between the measured/estimated position and a least-squares fit.



(3.a) Power spectral density of position measurement noise.



(3.b) Power spectral density of position estimate noise.



(3.c) Power spectral density of rate estimate noise.

Validation

The PSD of recorded data for the position and rate errors of a single rate table axis are depicted in Example 3. The depicted PSD spectra consist of a noise floor and many specific peaks. The shape of the noise floor can be attributed to the servo loop's transfer function. The transfer function of the position and rate observer can be easily recognized by comparing the estimated and the measured position noise PSD.

The position noise can be easily determined by comparing the close-loop (active servo loop) to the open-loop case (just measuring position, no actuators). The resulting position noise is approximately one decade higher than the measurement noise. Consequently, the measurements can be used to estimate the rate table's position noise in closed servo-loop operation.

In constant position, the measurement noise is nearly white (constant PSD). As expected from the transfer function, the observer loop attenuates the higher frequency components, in this example, starting from approximately 30 Hz. For a stationary position, the angle-dependent measurement and actuator errors are constant and cannot be observed in the measurement. A rotation of the axis increases the position noise floor compared to the stationary operation. The angle-dependent measuring and actuator errors add oscillations at specific frequencies. These frequencies clearly are integer multiples of the axis' rotation rate and thus comply to the models (4.114) and (4.115). In accordance with the model, the harmonic frequencies increase with the rotation rate, and the respective amplitudes are subject to the servo loop's transfer function. As Example 3.a is based on position measurements, the curves also include the measurement noise that manifests as a minimum noise level of about $10 \cdot 10^{-13} \text{ } \sigma^2/\text{Hz}$ which can be observed at frequencies above 100 Hz. Although the general behavior matches the model, not all observed details can be explained by the simple model. Possible explanations for these deviations are structural resonances, non-linear effects like bearing friction, and jitter and digitalization errors within the control system. It must be emphasized that the position PSD does not represent the entire position uncertainty in the case of zero-rate. In this case, the measurement errors and motor cogging that can be observed as peaks in the PSD otherwise degrade to a quasi-random-constant error.

In conclusion, the measured PSD spectra confirm above-discussed models. However, the amplitudes and occurring orders caused by measurement and actuator errors cannot be predicted but can only be identified from such a measurement. Using the experimentally determined PSD curve, a model based on a background noise floor and the observed harmonics can be composed for a specific axis and angular rate.

For physically integrating sensors, the average rate stability over multiple revolutions is more relevant than the instantaneous rate errors. The average rate is defined as:

$$\bar{\omega} = \frac{\Delta\Phi}{\Delta t} \quad (4.120)$$

Consequently, the average rate error is driven by the position error $\delta\Phi$ at the start and end of

the test. As the position uncertainty is constant over time, the average rate stability improves with increased test time. Non-integrating sensors, however, are sensitive to the instantaneous rate errors and thus to the angular rate noise as depicted in [Example 3.c](#). At high angular rates, the depicted spectrum contains high peaks at frequencies in the kHz range. This might introduce aliasing effects for non-integrating sensors with low (internal) sampling rates.

Model 10: Rate table positioning and rate error models.

Description

Positioning and rate error along the rate table's nominal rotation axes.

Parameters

$\delta\Psi_{p\hat{p}}, \delta\Phi_{w\hat{w}}, \delta\Psi_{v\hat{v}}$
 $\delta\omega_{pw}, \delta\omega_{wv}, \delta\omega_{vu}$

Sensitivities

[Table F.6ff](#), [Table F.7ff](#)

Positioning error model

Detailed modeling of the positioning and rate error of a rate table axis requires in-depth knowledge of the underlying control design and measurement and actuator errors. All of these errors are highly device-specific and can not be generalized. However, the derived models and [Example 3](#) represent a typical configuration of electric motors and inductive encoders.

If no measurements are available, a very rough worst-case approximation may consist of second-order system response, some oscillations at multiples of the applied angular rates, and the motor's and measurement system's number of poles. Amplitudes may be approximated from [RMS](#) specifications of the position or angular rate errors.

4.2.10. Summary

Based on the partial derivatives of the kinematic chain, the following linear equation describes the contributions of the different error sources to the errors of the reference angular rates and specific forces:

$$\begin{bmatrix} \delta\omega_{ib}(t) \\ \delta f_b(t) \end{bmatrix}_{6 \times 1} = \begin{bmatrix} \frac{\partial \delta\omega_{ib}(t)}{\partial \delta\omega_{ie}} & \frac{\partial \delta f_b(t)}{\partial \delta\omega_{ie}} \\ \frac{\partial \delta\omega_{ib}(t)}{\partial \delta\omega_{ib}(t)} & \frac{\partial \delta f_b(t)}{\partial \delta\omega_{ib}(t)} \\ \frac{\partial \Psi_{n\hat{n}}}{\partial \Psi_{n\hat{n}}} & \frac{\partial \Psi_{n\hat{n}}}{\partial \delta f_b(t)} \\ 0 & \frac{\partial \gamma_n}{\partial \gamma_n} \\ \frac{\partial \delta\omega_{ib}(t)}{\partial \delta\omega_{np}} & \frac{\partial \delta f_b(t)}{\partial \delta\omega_{np}} \\ 0 & \frac{\partial \delta\omega_{np}}{\partial \delta f_b(t)} \\ \frac{\partial \delta\omega_{ib}(t)}{\partial \delta\omega_{ib}(t)} & \frac{\partial \delta f_b(t)}{\partial \delta\omega_{np}} \\ \frac{\partial \Psi_{p\hat{p}}}{\partial \Psi_{p\hat{p}}} & \frac{\partial \Psi_{p\hat{p}}}{\partial \delta f_b(t)} \\ 0 & \frac{\partial \delta f_b(t)}{\partial \delta r_n(P_p)} \\ 0 & \frac{\partial \delta f_b(t)}{\partial \delta \dot{r}_n(P_p)} \\ 0 & \frac{\partial \delta f_b(t)}{\partial \delta \ddot{r}_n(P_p)} \\ \frac{\partial \delta\omega_{ib}(t)}{\partial \delta\omega_{pw}} & \frac{\partial \delta f_b(t)}{\partial \delta\omega_{pw}} \\ 0 & \frac{\partial \delta\omega_{pw}}{\partial \delta f_b(t)} \\ \frac{\partial \delta\omega_{ib}(t)}{\partial \delta\omega_{pw}} & \frac{\partial \delta \dot{\omega}_{pw}}{\partial \delta f_b(t)} \\ \frac{\partial \Psi_{w\hat{w}}}{\partial \Psi_{w\hat{w}}} & \frac{\partial \Psi_{w\hat{w}}}{\partial \delta f_b(t)} \\ 0 & \frac{\partial \delta r_p(P_w)}{\partial \delta f_b(t)} \\ 0 & \frac{\partial \delta f_b(t)}{\partial \delta \dot{r}_p(P_w)} \\ 0 & \frac{\partial \delta f_b(t)}{\partial \delta \ddot{r}_p(P_w)} \\ \frac{\partial \delta\omega_{ib}(t)}{\partial \delta\omega_{wv}} & \frac{\partial \delta f_b(t)}{\partial \delta\omega_{wv}} \\ 0 & \frac{\partial \delta\omega_{wv}}{\partial \delta f_b(t)} \\ \frac{\partial \delta\omega_{ib}(t)}{\partial \delta\omega_{wv}} & \frac{\partial \delta \dot{\omega}_{wv}}{\partial \delta f_b(t)} \\ \frac{\partial \Psi_{v\hat{v}}}{\partial \Psi_{v\hat{v}}} & \frac{\partial \Psi_{v\hat{v}}}{\partial \delta f_b(t)} \\ 0 & \frac{\partial \delta r_w(P_v)}{\partial \delta f_b(t)} \\ 0 & \frac{\partial \delta f_b(t)}{\partial \delta \dot{r}_w(P_v)} \\ 0 & \frac{\partial \delta f_b(t)}{\partial \delta \ddot{r}_w(P_v)} \\ \frac{\partial \delta\omega_{ib}(t)}{\partial \delta\omega_{vu}} & \frac{\partial \delta f_b(t)}{\partial \delta\omega_{vu}} \\ 0 & \frac{\partial \delta\omega_{vu}}{\partial \delta f_b(t)} \\ \frac{\partial \delta\omega_{ib}(t)}{\partial \delta\omega_{vu}} & \frac{\partial \delta \dot{\omega}_{vu}}{\partial \delta f_b(t)} \\ \frac{\partial \Psi_{u\hat{u}}}{\partial \Psi_{u\hat{u}}} & \frac{\partial \Psi_{u\hat{u}}}{\partial \delta f_b(t)} \\ 0 & \frac{\partial \delta f_b(t)}{\partial \delta r_v(P_u)} \\ 0 & \frac{\partial \delta f_b(t)}{\partial \delta \dot{r}_v(P_u)} \\ 0 & \frac{\partial \delta f_b(t)}{\partial \delta \ddot{r}_v(P_u)} \\ \frac{\partial \delta\omega_{ib}(t)}{\partial \delta\omega_{ib}(t)} & \frac{\partial \delta f_b(t)}{\partial \delta f_b(t)} \\ \frac{\partial \Psi_{b\hat{b}}}{\partial \Psi_{b\hat{b}}} & \frac{\partial \Psi_{b\hat{b}}}{\partial \delta f_b(t)} \\ 0 & \frac{\partial \delta r_u(P_b)}{\partial \delta f_b(t)} \\ 0 & \frac{\partial \delta f_b(t)}{\partial \delta \dot{r}_u(P_b)} \\ 0 & \frac{\partial \delta f_b(t)}{\partial \delta \ddot{r}_u(P_b)} \end{bmatrix}_{93 \times 6}^T \begin{bmatrix} \delta\omega_{ie}(t) \\ \delta\Psi_{n\hat{n}}(t) \\ \delta\gamma_n(t) \\ \delta\omega_{np}(t) \\ \delta\dot{\omega}_{np}(t) \\ \delta\Psi_{p\hat{p}}(t) \\ \delta r_n(P_p(t)) \\ \delta \dot{r}_n(P_p(t)) \\ \delta \ddot{r}_n(P_p(t)) \\ \delta\omega_{pw}(t) \\ \delta\dot{\omega}_{pw}(t) \\ \delta\Psi_{w\hat{w}}(t) \\ \delta r_p(P_w(t)) \\ \delta \dot{r}_p(P_w(t)) \\ \delta \ddot{r}_p(P_w(t)) \\ \delta\omega_{wv}(t) \\ \delta\dot{\omega}_{wv}(t) \\ \delta\Psi_{v\hat{v}}(t) \\ \delta r_w(P_v(t)) \\ \delta \dot{r}_w(P_v(t)) \\ \delta \ddot{r}_w(P_v(t)) \\ \delta\omega_{vu}(t) \\ \delta\dot{\omega}_{vu}(t) \\ \delta\Psi_{u\hat{u}}(t) \\ \delta r_v(P_u(t)) \\ \delta \dot{r}_v(P_u(t)) \\ \delta \ddot{r}_v(P_u(t)) \\ \delta\Psi_{b\hat{b}} \\ \delta r_u(P_b(t)) \\ \delta \dot{r}_u(P_b(t)) \\ \delta \ddot{r}_u(P_b(t)) \end{bmatrix}_{93 \times 1} \quad (4.121)$$

The linear sensitivities \mathbf{H} depend on the actual rate table state, which is ideally described by its axes' position, rate and angular acceleration:

$$\mathbf{z}(t) = \left[\Psi_{pw}(t) \quad \dot{\Psi}_{pw}(t) \quad \ddot{\Psi}_{pw}(t) \quad \Phi_{wv}(t) \quad \dot{\Phi}_{wv}(t) \quad \ddot{\Phi}_{wv}(t) \quad \Psi_{vu}(t) \quad \dot{\Psi}_{vu}(t) \quad \ddot{\Psi}_{vu}(t) \right]$$

A summary of the different error terms, grouped by error sources, is given in Table 4.4. The table also lists the respective section in the appendix, where the partial derivatives are analytically given depending on the rate table's state.

Table 4.4.: Summary of error parameters in the laboratory model.

Group	Error parameters	Sensitivities	Error sources
Earth rotation	$\delta\omega_{ie}$	Table F.1	Earth precession, nutation and polar motion
Earth gravity	$\delta\gamma_n$	Table F.2	Gravity anomalies, temporal variations
Lab. Alignment	$\Psi_{n\hat{n}}$	Table F.3	Lab. location, alignment, DoV
Test pad motion	$\delta\omega_{np}, \delta\dot{\omega}_{np}$	Table F.4	Seismic activities, reaction forces
	$\delta\mathbf{r}_n(P_p), \delta\dot{\mathbf{r}}_n(P_p), \delta\ddot{\mathbf{r}}_n(P_p)$	Table F.5	
Outer gimbal	$\delta\omega_{pw}, \delta\dot{\omega}_{pw}, \Psi_{p\hat{p}}$	Table F.6	Mechanical errors, bearings, controls
	$\delta\mathbf{r}_p(P_w), \delta\dot{\mathbf{r}}_p(P_w), \delta\ddot{\mathbf{r}}_p(P_w)$	Table F.7	
Middle gimbal	$\delta\omega_{wv}, \delta\dot{\omega}_{wv}, \Psi_{w\hat{w}}$	Table F.8	Mechanical errors, bearings, controls
	$\delta\mathbf{r}_w(P_v), \delta\dot{\mathbf{r}}_w(P_w), \delta\ddot{\mathbf{r}}_w(P_v)$	Table F.9	
Inner gimbal	$\delta\omega_{vu}, \delta\dot{\omega}_{vu}, \Psi_{v\hat{v}}$	Table F.10	Mechanical errors, bearings, controls
	$\delta\mathbf{r}_v(P_u), \delta\dot{\mathbf{r}}_v(P_u), \delta\ddot{\mathbf{r}}_v(P_u)$	Table F.11	
UUT	$\delta\omega_{ub}, \delta\dot{\omega}_{ub}, \Psi_{u\hat{u}}$	Table F.12	Mechanical errors
	$\delta\mathbf{r}_u(P_b), \delta\dot{\mathbf{r}}_u(P_b), \delta\ddot{\mathbf{r}}_u(P_b)$	Table F.13	

In the following sections, the presented errors models will be applied to the above overall equation to determine the errors respectively uncertainty of the reference angular rates and specific forces for different sensor test scenarios. Here, the test procedures specify the applied rates and position states $\mathbf{z}(t)$ used as a working point in the derived linear error sensitivities.

4.3. Averaging over Noise Processes

Sensor test procedures rely on averaging over the sensor's output while holding a constant input to reduce the effects of external disturbances and sensor noise. Within this work, the various noise-like errors are modeled as a zero-mean wide-sense stationary stochastic process. They are characterized by their auto-correlation, respectively their PSD. This section discusses the effect of averaging on the signal's stochastic moments. As illustrated in Figure 4.22, the sensor's output is split into clusters of equal length τ , and the average of each cluster is calculated. There may be a dead-time between the clusters, so the sampling time T is different from τ . Equations for the mean, different variances, and the correlation between these clusters will be derived.

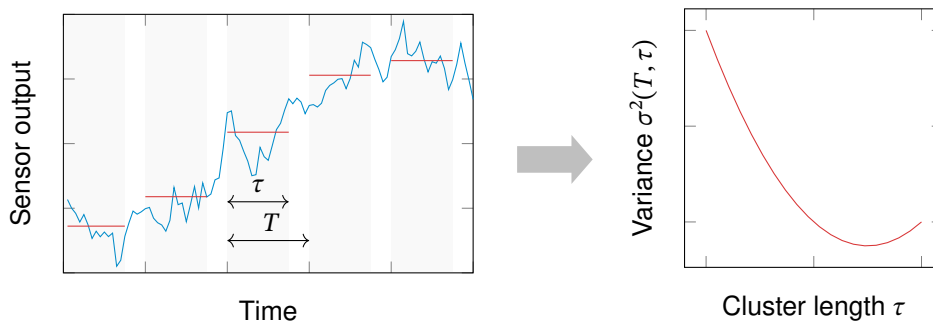


Figure 4.22.: Variance of signal cluster means. The signal is split into clusters of equal length τ and sample time T . In general, the variance depends on both the cluster time τ and sample time T .

4.3.0.1. Variances from Power Spectral Density

The statistical analysis of sensor signal averages is closely related to the study of the frequency stability of atomic clocks, which was significantly advanced by Barnes [162] and Allan [61] in the 1960s. The work on frequency stability can be adapted to inertial sensor noise by acknowledging that the clock's frequency corresponds to the non-integrating sensor's output, e.g., angular rate, and the phase corresponds to the integrated sensor's output, e.g., angle. The derivation of the variances from the wide-sense stationary signal's (two-sided) PSD is based on the Fourier transform pair of PSD $S_y(f)$ and auto-correlation $R_{yy}(\tau)$ [58, p. 721]:

$$S_y(f) = \mathcal{F}\{R_{yy}(\tau)\} \quad (4.122)$$

As the auto-correlation is an even function, it may be determined from the PSD using the cosine transform as [163]:

$$R_{yy}(\tau) = \int_0^{\infty} S_y(f) \cos(2\pi f\tau) df \quad (4.123)$$

The average \bar{y} over a signal $y(t)$ from T to $T + \tau$ can be determined from its integrated signal $x(t)$:

$$\bar{y} = \frac{1}{\tau} \int_T^{T+\tau} y(t) dt = \frac{x(T + \tau) - x(T)}{\tau} \quad (4.124)$$

where the PSD of the integrated and none non-integrated signal are related as:

$$S_x(f) = \frac{1}{(2\pi f)^2} S_y(f) \quad (4.125)$$

Variance

For a zero-mean signal y , the cluster averages and integrated signals are also zero-mean. The variance of the cluster averages can thus be related to the auto-correlation as follows:

$$\begin{aligned} \sigma^2(\tau) = \mathbb{E}[\bar{y}^2] &= \mathbb{E} \left[\left(\frac{x(T + \tau) - x(T)}{\tau} \right)^2 \right] \\ &= \frac{1}{\tau^2} (\mathbb{E}[x(T + \tau)^2] - 2\mathbb{E}[x(T + \tau)x(T)] + \mathbb{E}[x(T)^2]) \\ &= \frac{1}{\tau^2} [2R_{xx}(0) - 2R_{xx}(\tau)] \end{aligned} \quad (4.126)$$

Using equations (4.123) and (4.125), the variance can be determined from the non-integrated signal's PSD as (cf. [163]):

$$\sigma^2(\tau) = \mathbb{E}[\bar{y}^2] = \int_0^\infty S_y(f) \left(\frac{\sin(\pi f \tau)}{\pi f \tau} \right)^2 df \quad (4.127)$$

For a stationary process, the variance does not depend on the time and thus is invariant to the sampling time T . For many noise processes, the above integral does not converge. The following section will demonstrate this problem and its consequences for power-law noise processes.

M-sample Variance

The M -sample variance describes the variance of the cluster means from a set of M clusters of length τ . The clusters are generally not adjacent but may be taken at a sampling period T . Using the integrated signal $x(t)$, the M -sample variance is then given by:

$$\sigma^2(M, T, \tau) = \frac{1}{M-1} \left[\sum_{n=0}^{M-1} \left(\frac{x(nT + \tau) - x(nT)}{\tau} \right)^2 - \frac{1}{M} \left(\sum_{n=0}^{M-1} \frac{x(nT + \tau) - x(nT)}{\tau} \right)^2 \right] \quad (4.128)$$

For the typical case that there is no dead time between the clusters ($T = \tau$), above equation can be transformed to [61]:

$$\sigma^2(M, \tau, \tau) = \frac{2}{(M-1)\tau^2} \left[M(R_{xx}(0) - R_{xx}(\tau)) - \frac{1}{M} (R_{xx}(0) - R_{xx}(M\tau)) \right] \quad (4.129)$$

Again, equations (4.123) and (4.125) are used to replace the auto-correlation with the PSD, which yields [164]:

$$\sigma^2(M, \tau, \tau) = \frac{M}{M-1} \left[\int_0^\infty S_y(f) \left(\frac{\sin(\pi\tau f)}{\pi\tau f} \right)^2 \left(1 - \left(\frac{\sin(M\pi\tau f)}{M \sin(\pi\tau f)} \right)^2 \right) df \right] \quad (4.130)$$

Allan Variance

Being the variance of two adjacent clusters' averages, the Allen variance is a special case of the M -sample variance for $M = 2$. The Allan variance can thus be determined from (4.130) for $M = 2$, and yields (cf. [12]):

$$\sigma_{AV}^2(\tau) = \sigma^2(2, \tau, \tau) = 2 \int_0^\infty S_y(f) \frac{(\sin \pi\tau f)^4}{(\pi\tau f)^2} df \quad (4.131)$$

Considering a dead-time between the sampling, the Allan variance can be derived as:

$$\begin{aligned} \sigma_{AV}^2(T, \tau) &= \mathbb{E} \left[\left(\frac{x(T+\tau) - x(T) - x(\tau) + x(0)}{\tau} \right)^2 \right] \\ &= \frac{1}{\tau^2} [4R_{xx}(0) - 4R_{xx}(T) - 4R_{xx}(\tau) + 2R_{xx}(T+\tau) + 2R_{xx}(T-\tau)] \end{aligned} \quad (4.132)$$

Application of (4.123) and (4.125) yields:

$$\sigma_{AV}^2(T, \tau) = \int_0^\infty S_y(f) \frac{2 \sin(\pi T f)^2 + 2 \sin(\pi\tau f)^2 - \sin(\pi(T-\tau)f)^2 - \sin(\pi(T+\tau)f)^2}{(\pi\tau f)^2} df \quad (4.133)$$

Using trigonometric identities it can be demonstrated that (4.133) and (4.131) are, as expected, equal for $T = \tau$.

Auto-Covariance

Many inertial sensor test procedures use the averaged sensor output from subsequent positions to determine sensor parameters (e.g., scale factor tests). Therefore, the cross-correlation between the cluster averages is essential in determining the sensor parameters. The covariance between two cluster averages that are sampled with time distance T is determined as:

$$\begin{aligned} \mathbb{E}[\bar{y}_T \bar{y}_0] &= \mathbb{E} \left[\frac{x(T+\tau) - x(T)}{\tau} \frac{x(\tau) - x(0)}{\tau} \right] \\ &= \frac{1}{\tau^2} (\mathbb{E}[x(T+\tau)x(\tau)] - \mathbb{E}[x(T+\tau)x(0)] - \mathbb{E}[x(T)x(\tau)] + \mathbb{E}[x(T)x(0)]) \\ &= \frac{1}{\tau^2} (2R_{xx}(T) - R_{xx}(T+\tau) - R_{xx}(T-\tau)) \end{aligned} \quad (4.134)$$

Again equations (4.123) and (4.125) are used to replace the auto-correlation by the PSD, which yields:

$$\mathbb{E}[\bar{y}_T \bar{y}_0] = \int_0^\infty S_y(f) \frac{2 \cos(2\pi f T) - \cos(2\pi f(T + \tau)) - \cos(2\pi f(T - \tau))}{(2\pi f \tau)^2} df \quad (4.135)$$

For a stationary stochastic process y , the stochastic moments do not depend on the time. Thus (4.135) only depends on the distance between two clusters, like the Allan variance. The integrals do not necessarily converge; e.g., for wide-sense stationary processes, the variance of the averaged signal is indeterminate. The following section will demonstrate the problem for certain types of power-law noise processes.

These equations have to be evaluated numerically for an arbitrary noise PSD. Analytical solutions will be given for power-law noise processes in the next section.

4.3.0.2. Variances of Averaged Power-Law Noise Clusters

Analytical equations for the M -sample variance can be given for the typically power-law noise processes observed in inertial sensor noise. Based on Barnes' B_1 function, which is the ratio of the expected values of the M -sample variance to the Allan variance, the M -sample variance for power-law noise processes can be determined as [165]:

$$B_1(M, T, \tau) = \frac{\mathbb{E}[\sigma_y^2(M, T, \tau)]}{\mathbb{E}[\sigma_y^2(2, T, \tau)]} = \frac{\text{M-sample variance}}{\text{Allan variance}} \quad (4.136)$$

$$B_1(M, \tau, \tau) = \frac{M(1 - M^\mu)}{2(M - 1)(1 - 2^\mu)} \quad (4.137)$$

where μ is the slope of the power law noise in the M -sample τ - σ plot. The variance of the power-law noise process can be determined by taking the limit of the M -sample variance:

$$\sigma^2(\tau) = \lim_{M \rightarrow \infty} \sigma^2(M, \tau, \tau) \quad (4.138)$$

Additionally, there is a B_2 function that relates the Allan variance with dead-time between the samples to the classical Allan variance without dead-time [165]:

$$B_2(T, \tau) = \frac{\mathbb{E}[\sigma_y^2(2, T, \tau)]}{\mathbb{E}[\sigma_y^2(2, \tau, \tau)]} = \frac{\text{Allan variance (T between samples)}}{\text{Allan variance (adjacent samples)}} \quad (4.139)$$

For power-law noise, an analytical solution of the B_2 function can be given as [165]:

$$B_2(r, \tau) = \begin{cases} 1 & \text{for } r = 1 \\ \frac{1 + \frac{1}{2} [2(r)^{\mu+2} - (r+1)^{\mu+2} - (r-1)^{\mu+2}]}{2(1 - 2^\mu)} & \text{for } r > 1 \end{cases} \quad (4.140a)$$

$$(4.140b)$$

where r is the ratio of the sample time T and the cluster time τ :

$$r = \frac{T}{\tau} \quad (4.141)$$

The above equations determine the M -sample variance, the Allan variance and the classical variance of the IEEE sensor noise processes. The resulting analytical solutions are given in Table 4.5. The table displays some interesting results that are worth noting:

- Introducing a dead-time ($r > 1$), the Allan variance of quantization noise is reduced, but remains independent of r for $r > 1$. This is also noted in [165].
- For the angular random walk, which is rate white noise, all samples and clusters are uncorrelated. All types of variances are thus equal, independent of the sample time or the number of clusters.
- Starting from the bias instability (represented by flicker noise), the samples are correlated. This causes a dependency on the sample time T and the number of clusters M . The M -sample variance does not converge but grows with the number of samples, and the classical variance is indeterminate.

Table 4.5.: Variances of power-law sensor noise processes.

Noise process	$S(f)$	$\sigma_{AV}^2(\tau)$	$\sigma_{AV}^2(r, \tau), r > 1$	$\sigma^2(M, \tau, \tau)$	$\sigma^2(\tau)$
Quantization noise, Q	$\tau_s(2\pi f)^2 Q^2$	$\frac{3}{\tau^2} Q^2$	$\frac{2}{\tau^2} Q^2$	$2 \frac{M-\frac{1}{M}}{M-1} \frac{1}{\tau^2} Q^2$	$\frac{1}{\tau^2} Q^2$
Angular random walk, N	N^2	$\frac{1}{\tau} N^2$	$\frac{1}{\tau} N^2$	$\frac{1}{\tau} N^2$	$\frac{1}{\tau} N^2$
Flicker Noise ^a , B	$\approx \frac{1}{2\pi f} B^2$	$\approx \frac{2 \ln 2}{\pi} B^2$	see footnote ^b	$\approx \frac{M \ln M}{M-1} \frac{1}{\pi} B^2$	-
Rate random walk, K	$\frac{1}{(2\pi f)^2} K^2$	$\frac{1}{3} \tau K^2$	$\frac{1}{6} (3r-1) \tau K^2$	$\frac{M}{6} \tau K^2$	-
Rate ramp noise, R	$\frac{1}{(2\pi f)^3} R^2$	$\frac{1}{2} \tau^2 R^2$	$\frac{1}{2} r^2 \tau^2 R^2$	$\frac{M(M+1)}{12} \tau^2 R^2$	-

^aapproximating bias instability by neglecting the band-limit

$$b \approx \frac{-2r^2 \ln(r) + (r-1)^2 \ln(r-1) + (r+1)^2 \ln(r+1)}{\ln 16} \frac{2 \ln 2}{\pi} B^2$$

In Table 4.5, the bias instability is approximated by pure flicker noise to fit into the power-law noise framework. By definition, the bias-instability is band-limited flicker noise, which can be considered by adopting the upper integration limit of (4.133) to the cutoff frequency f_0 . This yields the expressions for the classical Allan variance given in the IEEE standards [12]

$$\sigma_{AV,B}^2(\tau) = \frac{2}{\pi} B^2 \left[\ln 2 - \frac{\sin^3(x)}{2x^2} (\sin(x) + 4x \cos(x)) + \text{Ci}(2x) - \text{Ci}(4x) \right], \quad x = \pi f_0 \tau \quad (4.142)$$

and can be extended to this lengthy expression for the bias instability's Allan variance with

dead-time ($r \geq 2$):

$$\begin{aligned} \sigma_{AV,B}^2(r, \tau) = & \frac{1}{2\pi} \left[-2 \ln(\tau) - 2r^2 \ln(r\tau) + (r+1)^2 \ln((r+1)\tau) + (r-1)^2 \ln((r-1)\tau) \right] \\ & + \frac{1}{4\pi x} \left[-2 \sin(2x) - 2r \sin(2rx) + (r+1) \sin(2(r+1)x) \right. \\ & \quad \left. + (r-1) \sin(2(r-1)x) \right] \\ & + \frac{1}{8\pi x^2} \left[2 \cos(2x) + 2 \cos(2rx) - \cos(2(r+1)x) - \cos(2(r-1)x) - 1 \right] \\ & + \frac{1}{2\pi} \left[2 \text{Ci}(2x) + 2r^2 \text{Ci}(2rx) - (r+1)^2 \text{Ci}(2(r+1)x) \right. \\ & \quad \left. - (r-1)^2 \text{Ci}(2(r-1)x) \right] \end{aligned} \quad (4.143)$$

where, $x = \pi f_0 \tau$. Above equations make use of the cosine integral function $\text{Ci}(x)$ [72, p. 460]

$$\text{Ci}(x) = - \int_x^\infty \frac{\cos(t)}{t} dt \quad (4.144)$$

which has no closed form solution and needs to be evaluated numerically. The resulting Allan variance with dead-time for varying r and cut-off frequencies is depicted in Figure 4.23. The cut-off frequency shifts the Allan variance curve along the cluster time axis, while the Allan variance increases with the dead-time ratio r .

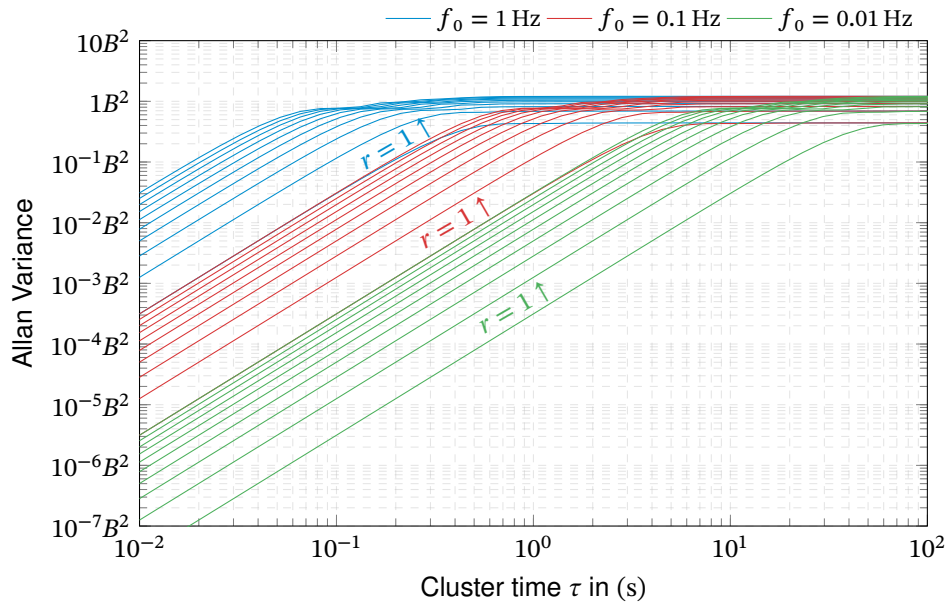


Figure 4.23.: Allan variance with dead-time of bias instability noise for varying cut-off frequencies. The cluster sampling time ratio r increases from 1 (no dead-time) to 10 from the bottom-right to top-left.

The fact that the variance cannot be given for power-law noise with $\alpha \leq 0$ is explained by the fact that these processes are not stationary in the strict sense: The variance of these processes

grows with time. Vividly, one does not know the actual time of a noise's underlying process, so the variance cannot be given. Although one cannot give the process's absolute variance, the drift within the process is well-defined. Therefore, the Allan variance exists even for these processes. The definition of the Allan variance as variance of the average of two (consecutive) signal clusters:

$$\sigma_{AV}^2(T, \tau) = \frac{1}{2} \mathbb{E} [(\bar{y}_r - \bar{y}_0)^2] \quad (4.145)$$

The Allan variance can thus be used to describe the uncertainty of the difference between two cluster averages. As a result, at least the uncertainty of all signal clusters can be related to an arbitrary (e.g., the first in the test sequence) average value. The Allan variance with dead time also describes the variance between non-contiguous clusters. The implications of this will be further discussed in the test procedure analysis.

For a detailed stochastic description, the cross-correlation between two cluster averages is also of interest. This Allan-like covariance of the difference between a cluster average at time r and an arbitrary common cluster average and another the same for a cluster at time j can be derived as:

$$\begin{aligned} P_{AV}(r, j, \tau) &= \frac{1}{2} \mathbb{E} [(\bar{y}_r - \bar{y}_0)(\bar{y}_j - \bar{y}_0)] \\ &= \frac{1}{2} \mathbb{E} \left[\frac{x((r+1)\tau) - x(r\tau) - x(\tau) + x(0)}{\tau} \frac{x((j+1)\tau) - x(j\tau) - x(\tau) + x(0)}{\tau} \right] \\ &= \frac{1}{2\tau^2} \left\{ 2U(\tau) + 2U(r\tau) + 2U(j\tau) + U((r-j+1)\tau) + U((r-j-1)\tau) \right. \\ &\quad \left. - 2U((r-j)\tau) - U((r+1)\tau) - U((r-1)\tau) - U((j+1)\tau) - U((j-1)\tau) \right\} \end{aligned} \quad (4.146)$$

with

$$U(\tau) = 2 [R_{xx}(0) - R_{xx}(\tau)] \quad (4.147)$$

Quantization Noise

Equation (4.146) can be evaluated for the sensor noise types by applying the appropriate functions of U . Using (9) from [61] and the definition from Table 2.7 yields for the quantization noise:

$$U_Q(\tau) = |\tau_s| Q^2 \quad (4.148)$$

$$P_{AV,Q}(r, j, \tau) = \begin{cases} \frac{3}{\tau^2}Q^2 & \text{for } r = j = 1 \\ \frac{2}{\tau^2}Q^2 & \text{for } r = j > 1 \\ \frac{1}{2\tau^2}Q^2 & \text{for } |r - j| = 1 \wedge (j = 1 \vee r = 1) \\ \frac{3}{2\tau^2}Q^2 & \text{for } |r - j| > 1 \wedge (j = 1 \vee r = 1) \\ \frac{1}{2\tau^2}Q^2 & \text{for } |r - j| = 1 \wedge (j > 1 \wedge r > 1) \\ \frac{1}{\tau^2}Q^2 & \text{else} \end{cases} \quad (4.149)$$

Above definitions of the *Allan*-covariances for quantization noise yield a matrix of the following structure:

$$\mathbf{P}_{AV,Q} = \begin{bmatrix} 6 & 2 & 3 & 3 & \dots & 3 & 3 \\ 2 & 4 & 1 & 2 & & 2 & 2 \\ 3 & 1 & 4 & 1 & & 2 & 2 \\ \vdots & & & & \ddots & & \vdots \\ 3 & 2 & 2 & 2 & & 4 & 1 \\ 3 & 2 & 2 & 2 & \dots & 1 & 4 \end{bmatrix} \frac{Q^2}{2\tau^2} \quad (4.150)$$

Note that the above matrix represents the cross-correlation of the difference between two clusters' means with the first cluster's mean, thus a generalization of the Allan variance. It is not the *classical* covariance of the cluster averages, which is given as the following band-diagonal matrix:

$$\mathbf{P}_Q = \begin{bmatrix} 2 & -1 & \dots & 0 & 0 \\ -1 & 2 & & 0 & 0 \\ \vdots & & \ddots & & \vdots \\ 0 & 0 & & 2 & -1 \\ 0 & 0 & \dots & -1 & 2 \end{bmatrix} \frac{Q^2}{\tau^2} \quad (4.151)$$

Angular/Velocity Random Walk

Analog to that, the cross-covariance for the angular random walk can be determined to:

$$U_N(\tau) = \frac{1}{2}|\tau|N^2 \quad (4.152)$$

$$P_{AV,N}(r, j, \tau) = \begin{cases} \frac{1}{\tau}N^2 & \text{for } r = j \\ \frac{1}{2\tau}N^2 & \text{else} \end{cases} \quad (4.153)$$

This definition leads to the following *Allan*-covariance matrix:

$$\mathbf{P}_{AV,N} = \begin{bmatrix} 2 & 1 & 1 & 1 & \dots & 1 & 1 \\ 1 & 2 & 1 & 1 & & 1 & 1 \\ 1 & 1 & 2 & 1 & & 1 & 1 \\ \vdots & & & \ddots & & \vdots & \\ 1 & 1 & 1 & 1 & & 2 & 1 \\ 1 & 1 & 1 & 1 & \dots & 1 & 2 \end{bmatrix} \frac{N^2}{2\tau} \quad (4.154)$$

As stated above, for the angular/velocity random walk, the *classical* covariance of the averaged clusters exists. Since ARW is ideally uncorrelated white noise, the resulting covariance matrix is purely diagonal:

$$\mathbf{P}_N = \begin{bmatrix} 1 & 0 & \dots & 0 & 0 \\ 0 & 1 & & 0 & 0 \\ \vdots & & \ddots & \vdots & \\ 0 & 0 & & 1 & 0 \\ 0 & 0 & \dots & 0 & 1 \end{bmatrix} \frac{N^2}{\tau} \quad (4.155)$$

Bias Instability

The bias instability is again a special case. For pure flicker noise, [61] gives the following equation for $U(\tau)$:

$$U_B(\tau) \approx \lim_{\mu \rightarrow 0^-} \frac{|\tau|^{\mu+2}}{4 - 2^{\mu+2}} \frac{2}{\pi} B^2 \ln(2) \quad (4.156)$$

which takes into account that the flicker noise's covariance diverges in the phase domain. Equation (4.146) has to be evaluated for fixed r and j and (4.156) using l'Hôpital's rule [72, p. 54]. For pure flicker noise, the resulting (cross) Allan variance has no dependency on the cluster length τ .

Using (4.125) with $S_{xx}(f) = (2\pi f)^{-3}$ and the cut-off frequency f_0 as upper integration limit

in (4.146), yields the following lengthy expression for the Allan-covariance:

$$\begin{aligned}
 P_{AV,B}(r, j, \tau) = & \left\{ \frac{1}{4\pi} \left[-2 \ln(\tau) - 2j^2 \ln(j\tau) - 2r^2 \ln(r\tau) + (j-1)^2 \ln((j-1)\tau) + \right. \right. \\
 & + (j+1)^2 \ln((j+1)\tau) + (r-1)^2 \ln((r-1)\tau) \\
 & + (r+1)^2 \ln((r+1)\tau) + 2(j-r)^2 \ln((j-r)\tau) \\
 & - (j-r+1)^2 \ln((j-r+1)\tau) \\
 & \left. - (j-r-1)^2 \ln((j-r-1)\tau) \right] \\
 & + \frac{1}{8\pi x} \left[-2 \sin(2x) - 2j \sin(2jx) \right. \\
 & - 2r \sin(2rx) + (j+1) \sin(2(j+1)x) + (j-1) \sin(2(j-1)x) \\
 & + (r+1) \sin(2(r+1)x) + (r-1) \sin(2(r-1)x) \\
 & + 2(j-r) \sin((j-r)x) - (j-r+1) \sin((j-r+1)x) \\
 & \left. - (j-r-1) \sin((j-r-1)x) \right] \\
 & + \frac{1}{16\pi x^2} \left[2 \cos(2x) + 2 \cos(2jx) + 2 \cos(2rx) - \cos(2(j+1)x) \right. \\
 & - \cos(2(j-1)x) - \cos(2(r+1)x) - \cos(2(r-1)x) \\
 & - 2 \cos(2(j-r)x) + \cos(2(j-r+1)x) + \cos(2(j-r-1)x) - 1 \left. \right] \\
 & + \frac{1}{4\pi} \left[2 \text{Ci}(2x) + j^2 \text{Ci}(2jx) + r^2 \text{Ci}(2rx) - (r+1)^2 \text{Ci}(2(r+1)x) \right. \\
 & - (r-1)^2 \text{Ci}(2(r-1)x) - (j+1)^2 \text{Ci}(2(j+1)x) \\
 & - (j-1)^2 \text{Ci}(2(j-1)x) - 2(j-r)^2 \text{Ci}(2(j-r)x) \\
 & + (j-r+1)^2 \text{Ci}(2(j-r+1)x) \\
 & \left. + (j-r-1)^2 \text{Ci}(2(j-r-1)x) \right] \Big\} B^2, \quad x = \pi f_0 \tau
 \end{aligned} \tag{4.157}$$

Above equation is actually indeterminate for various combinations of r and j , e.g., $r = j$. However, if r and j are set before solving the integral, closed solutions can be obtained. The presented equations have been determined using *Mathematica 11.2* [166], and verified against numerical simulation. The resulting covariance *matrix* for the first five clusters is depicted in [Figure 4.24](#). Just like above equations, the graphs display a non-trivial behavior, but can be summarized to these important observations:

- Both diagonal and off-diagonal elements display a similar dependency on the cluster time τ , respectively $f_0\tau$: The variance grows at approximately +2 in the log-log plot and bends towards a plateau value around the cut-off frequency.
- The Allan-covariance grows with the cluster's distance to the first cluster.
- The Allan-covariance decreases with a growing distance $|r - j|$ between two clusters.

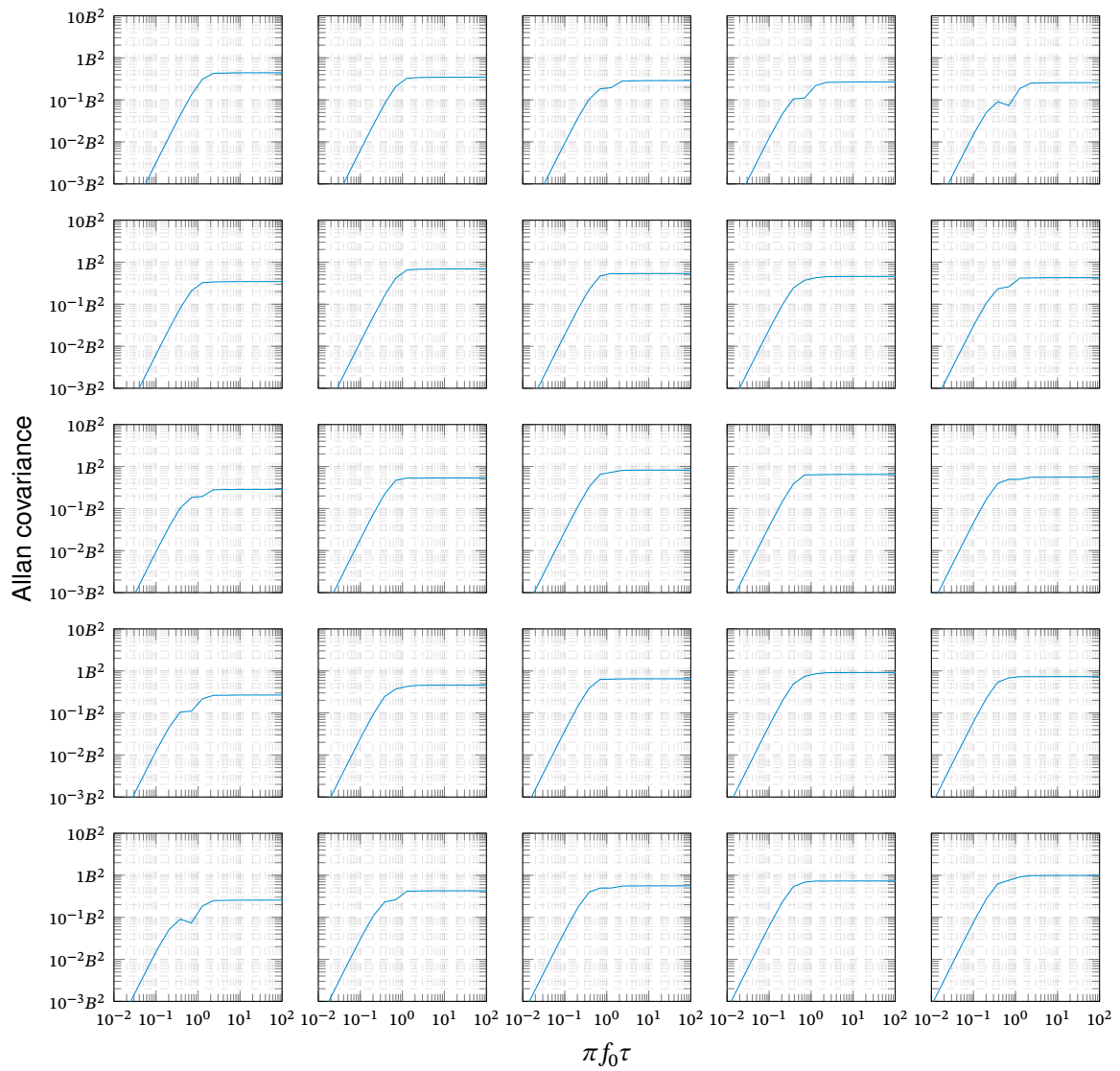


Figure 4.24.: Allan-covariance of the first five clusters of bias instability noise.

Rate/Acceleration Random Walk

Similarly, the cross-covariance of the averaged rate random walk is determined from (23) of [61] for $\mu = 1$:

$$U_K(\tau) = -\frac{|\tau|^3}{4} \frac{1}{3} K^2 \quad (4.158)$$

$$P_{AV,K}(r, j, \tau) = \left(|r-1|^3 + |r+1|^3 + |j-1|^3 + |j+1|^3 - 2|r|^3 - 2|j|^3 + 2|j-r|^3 - |j-r+1|^3 - |r-j+1|^3 - 2 \right) \frac{\tau}{24} K^2 \quad (4.159)$$

An example *Allan*-covariance matrix for the first 5 clusters is given below:

$$\mathbf{P}_{AV,K} = \begin{bmatrix} \frac{1}{3} & \frac{5}{12} & \frac{5}{12} & \frac{5}{12} & \frac{5}{12} \\ \frac{5}{12} & \frac{5}{6} & \frac{11}{12} & \frac{11}{12} & \frac{11}{12} \\ \frac{5}{12} & \frac{11}{12} & \frac{4}{3} & \frac{17}{12} & \frac{17}{12} \\ \frac{5}{12} & \frac{11}{12} & \frac{17}{12} & \frac{11}{6} & \frac{23}{12} \\ \frac{5}{12} & \frac{11}{12} & \frac{17}{12} & \frac{23}{12} & \frac{7}{3} \end{bmatrix} \tau K^2 \quad (4.160)$$

Rate/Acceleration Ramp Noise

Finally, the *Allan*-covariance of rate ramp noise ($\mu = 2$) is determined as follows:

$$U_R(\tau) = -\frac{|\tau|^4}{12} \frac{1}{2} R^2 \quad (4.161)$$

$$P_{AV,R}(r, j, \tau) = \left((r-1)^4 + (r+1)^4 + (j-1)^4 + (j+1)^4 - 2r^4 - 2j^4 + 2(j-r)^4 - (j-r+1)^4 - (r-j+1)^4 - 2 \right) \frac{\tau^2}{48} R^2 \quad (4.162)$$

Again, the *Allan*-covariance matrix for the first 5 clusters is exemplarily given as:

$$\mathbf{P}_{AV,R} = \begin{bmatrix} \frac{1}{2} & 1 & \frac{3}{2} & 2 & \frac{5}{2} \\ 1 & 2 & 3 & 4 & 5 \\ \frac{3}{2} & 3 & \frac{9}{2} & 6 & \frac{15}{2} \\ 2 & 4 & 6 & 8 & 10 \\ \frac{5}{2} & 5 & \frac{15}{2} & 10 & \frac{25}{2} \end{bmatrix} \tau^2 R^2 \quad (4.163)$$

As stated before, the covariance of the cluster means itself cannot be given for the last three noise processes. However, the derived *Allan*-covariance describes the variation of the cluster

means with respect to the first cluster mean. Using this concept, the growing uncertainty of the averaged signal of consecutive signal clusters can be described during sensor testing.

Sinusoidal Noise

In addition to the power-law noise, sinusoidal noise shall be included in this discussion. Sinusoidal noise is characterized by a single frequency sinusoidal signal with random initial phase. Such a noise may be part of the sensor noise [12], but is also often caused by the test instruments (e.g., bearings and actuators of a rate table), see [Subsection 4.2.9](#).

The sinusoidal signal's (single-sided) PSD is determined from the Fourier transformation of a sine signal $y(t) = \Omega \sin(2\pi f_0 t + \phi)$ and yields:

$$S_{\Omega}(f) = \frac{1}{4} \Omega^2 [\delta(f - f_0) + \delta(f + f_0)] \quad (4.164)$$

Using (4.146), the Allan-covariance can be determined to:

$$P_{AV,\Omega}(r, j, \tau) = \Omega^2 \frac{\cos(\pi f_0(r-j)\tau) \sin^2(\pi f_0 \tau) \sin(\pi f_0 j \tau) \sin(\pi f_0 r \tau)}{2(\pi f_0 \tau)^2} \quad (4.165)$$

and the classical covariance between two averaged signal clusters can be determined from (4.135):

$$P_{\Omega}(r, j, \tau) = \Omega^2 \frac{\cos(2\pi f_0(r-j)\tau) \sin^2(\pi f_0 \tau)}{2(\pi f_0 \tau)^2} \quad (4.166)$$

From the above equations, it is obvious that the effects of pure sinusoidal noise can be effectively reduced by increasing the averaging time τ . Furthermore, the variance vanishes if the averaging time is a multiple of the signals period.

The above equations are valid for clusters of the same known frequency but a random phase. During sensor testing, however, the applied angular rates are changed for each position and thus signal cluster. For example, bearing wobble (see [Subsection 4.2.9.3](#)) is modeled as the sum of sines/cosines with random initial phase but known frequencies that depend on the applied angular rate. Although the frequency is changed between the clusters, each cluster inherits the final phase of its previous cluster, respectively, the resulting phase of all clusters between the two considered clusters. The covariance of two such clusters with frequencies f_r and f_j is thus given as:

$$P_{\Omega}(r, j, \tau) = \mathbb{E} \left[\left(\frac{1}{\tau} \int_0^{\tau} \cos(2\pi f_r t + \phi_r) dt \right) \left(\frac{1}{\tau} \int_0^{\tau} \cos(2\pi f_j t + \phi_j) dt \right) \right] \quad (4.167)$$

The phases ϕ_r and ϕ_j represent the phase at the start of each signal cluster and are thus the cumulative phase resulting from all previous clusters:

$$\phi_r = \sum_i^r 2\pi f_i \tau + \phi_0 \quad (4.168)$$

$$\phi_j = \sum_i^j 2\pi f_i \tau + \phi_0 \quad (4.169)$$

Above integrals can be easily solved, and the expected value can be determined for a random initial phase ϕ_0 that is uniformly distributed between 0 and 2π . The analytical solution yields:

$$P_{\Omega}(r, j, \tau) = \Omega^2 \frac{\sin(\pi f_r \tau) \sin(\pi f_j \tau)}{2\pi^2 f_r f_j \tau^2} \cos(\pi f_j \tau - \pi f_r \tau + \phi_j - \phi_r) \quad (4.170)$$

4.3.0.3. The Effect of Kinematics

Finally, the effect of rotation shall be briefly discussed. Depending on the test profile, the various laboratory errors and noise processes do not enter the sensor's output equation directly but are *observed* from a rotating frame. Mathematically, this means a multiplication of the error with a sine respectively cosine function.

Random Constant Errors

If random constant errors are seen from a rotating view, the time-dependency is only introduced by the rotation. As the random constant error e does not depend on time, the signal's expected value and variance are scaled by averaging over the trigonometric functions:

$$y(t) = a \cos(\omega_r t + \phi) e \quad (4.171)$$

$$\bar{y}(\tau) = \frac{1}{\tau} \int_0^{\tau} a \cos(\omega_r t + \phi) e dt \quad (4.172)$$

$$\mathbb{E}[\bar{y}(\tau)] = a \frac{\sin(\omega_r \tau + \phi) - \sin(\phi)}{\omega_r \tau} \mathbb{E}[e] \quad (4.173)$$

$$\text{Var}[\bar{y}(\tau)] = \left(a \frac{\sin(\omega_r \tau + \phi) - \sin(\phi)}{\omega_r \tau} \right)^2 \text{Var}[e] - \mathbb{E}[\bar{y}(\tau)]^2 \quad (4.174)$$

For the typical case of a zero-mean random constant error e , the general (cross-) covariance between averaged signal clusters in a test-series can be given as:

$$P_e(r, j, \tau) = a^2 \frac{\sin(\pi f_r \tau) \sin(\pi f_j \tau)}{2\pi^2 f_r f_j \tau^2} \cos(\pi f_r \tau + \phi_r) \cos(\pi f_j \tau + \phi_j) \text{Var}[e] \quad (4.175)$$

where ϕ_j, ϕ_r are the phases at the start of the respective cluster.

Noise-like Errors

If the (wide-sense) stationary stochastic process $\eta(t)$ is multiplied with a sine or cosine factor, the averaged signal's expected value reduces with the averaging time τ :

$$y(t) = a \cos(\omega_r t + \phi) \eta(t) \quad (4.176)$$

$$\bar{y}(\tau) = \frac{1}{\tau} \int_0^\tau a \cos(\omega_r t + \phi) \eta(t) dt \quad (4.177)$$

$$\mathbb{E}[\bar{y}(\tau)] = \frac{a \sin(\omega_r \tau + \phi) - \sin(\phi)}{\omega_r \tau} \mathbb{E}[\eta] \quad (4.178)$$

The covariance of averaged clusters can be obtained from the PSD of the noise (4.135) by applying the modulation theorem. The multiplication with a cosine or sine factor in the time domain is equivalent to a frequency shift in the frequency domain [72, p. 771]. Using the modulation theorem, the PSD of the signal seen under rotation can be determined from:

$$S_{\eta, \text{rotating}} = \frac{1}{4} \left[S_\eta \left(f + \frac{\omega_r}{2\pi} \right) + S_\eta \left(f - \frac{\omega_r}{2\pi} \right) + 2\sqrt{S_\eta \left(f - \frac{\omega_r}{2\pi} \right) S_\eta \left(f + \frac{\omega_r}{2\pi} \right)} \right] \quad (4.179)$$

This modified PSD is then used to determine the covariance of the cluster averages.

4.4. Laboratory Testing Error Budget

4.4.1. Introduction

This section discusses the effects of the above-derived error sources on the calibration of inertial sensors. A survey of the available IEEE standards on inertial sensor testing (see [Table G.1](#) and [Table G.1](#)) reveals the existence of a set of basic test procedures that is applied to virtually all sensor types. The same accounts for non-IEEE tests, as summarized, e.g., in [167, 168]. While different sensor technologies require attention to their specific problems and error models, the underlying test procedures are very similar and differ only in detail. Although many inertial sensor testing methods exist, they can be boiled down to the three basic tests summarized in [Table 4.6](#).

Table 4.6.: Overview of basic test procedures. The table lists typical instruments and methods that are used in the most basic tests.

	Static Tests	Rate Transfer Tests	Multi-Pose Tests
Description	sensor in known static orientation	variation of reference input	sensor in different orientations and varying inputs
Scope	<ul style="list-style-type: none"> • bias • noise 	<ul style="list-style-type: none"> • scale factor(s) • transfer function 	<ul style="list-style-type: none"> • bias • misalignment • scale factor
Instruments	<ul style="list-style-type: none"> • stable test table 	<ul style="list-style-type: none"> • rate table • centrifuge 	<ul style="list-style-type: none"> • rate table • dividing head
Methods	<ul style="list-style-type: none"> • averaging • PSD, AVAR 	<ul style="list-style-type: none"> • averaging → least squares 	<ul style="list-style-type: none"> • averaging → least squares • Kalman Filtering

These represent the basic test procedures used to test for the sensor performance respectively accuracy. The procedures have to be embedded in an overall testing strategy (see [26]) to determine dependencies from environmental conditions, e.g., temperature or magnetic fields, as well as repeatability and reliability [22, pp. 240–241]. Usually, this means that the essential tests are repeated under varying conditions, and the variation of resulting calibration parameters is analyzed.

Based on the derived linear sensitivities and the error models defined in [Section 4.2](#), the variance of the test target parameters can be determined for varying positions and averaging times τ . For the derivation of the error budgets, the input errors are grouped based on their origin:

- **Earth rotation variations** represent all effects that lead to a temporal variation of the Earth's angular rate vector and thus a deviation from the WGS84 reference rate. Here, no knowledge of the phase of the periodic variations of the angular rate is assumed.

- **Gravity variations** represent the uncertainty caused by temporal variations of the local gravity.
- **Test-pad motion** summarizes all natural and anthropogenic sources of motion of the laboratory's test pad. Here they are modeled by a reference motion model defined in [Model 5](#).
- **Laboratory alignment** represents the alignment errors of the test-pad relative to the [WGS84](#) reference ellipsoid. This includes both leveling of the test pad as well as north-alignment and position errors.
- **Axis non-orthogonality and misalignment** groups all errors that result in (quasi-) constant orientation errors of the rate table axes, like manufacturing and setup errors and stationary temperature expansion errors. This also includes alignment errors of the nominal sensor axis to the rate table's axes.
- **Axis wobble** represents the orientation errors of the rate table axes that depend on the axis' angular position, typically caused by bearing imperfections.
- **Control errors** summarize both position and angular rate errors caused by the measurement errors, servo-loop control, and actuators of the rate table.

This grouping enables the identification of the dominant error sources and thus also the possible starting points for increasing accuracy.

4.4.2. Single Position Static Tests

4.4.2.1. Test Description

Static tests (also tombstone tests [22, p. 249]) are mainly used to examine the noise characteristics of the sensor's output. The sensor is placed on a seismically isolated or stabilized test table for these tests. As the rate table controls introduce additional noise, even in a static condition, the static tests should be performed directly on, e.g., an aligned granite measurement plate as depicted in Figure 4.25. The sensor's output for this static input is recorded and subsequently analyzed, e.g., the sensor noise is characterized using PSD and AVAR. The test duration is varied between less than an hour and multiple days, depending on the sensor grade and planned application [22, p. 249].

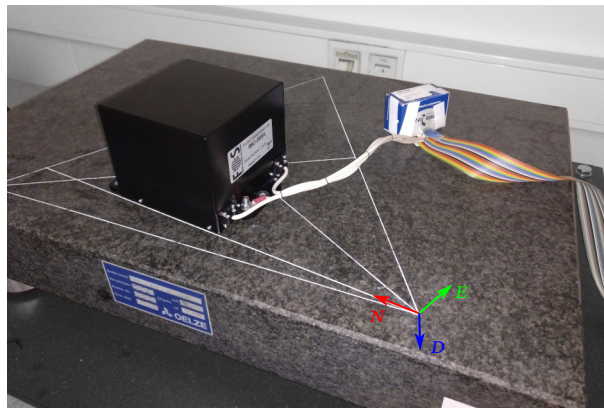


Figure 4.25.: Static testing of an IFOS-500 IMU on a measurement plate in the basement of the Institute of Flight System Dynamics. The measurement plate is aligned to the local gravity vector and provides a reference to true north.

The sensor's input axis may be aligned to the local west-east direction to eliminate the Earth's angular rate or just aligned to the local vertical, see Figure 4.26. If the input axis is horizontally leveled and aligned to the west-east direction (case I), there is ideally zero input signal along the tested gyroscope axis. The ideal accelerometer input is zero in this case. If the input axis is aligned to the local vertical (case II) and measures local gravity and a component of the Earth's angular rate. Whether the test is performed at zero-input (axis aligned east) or at some component of the Earth's angular rate depends on the testing philosophy, e.g., if an effect of the input on the noise characteristics is expected. The zero-input case allows a simple determination of the sensor's bias. However, this requires precise alignment with respect to the local gravity and, more difficult, to the Earth's rotation vector.

4.4.2.2. Static Test Error Model

In the context of the kinematic chain introduced in Subsection 4.2.1, the use of an aligned measurement plate can be represented by mounting the tested sensor directly to the laboratory test pad frame p and neglecting the rate table's components. Under these assumptions, the

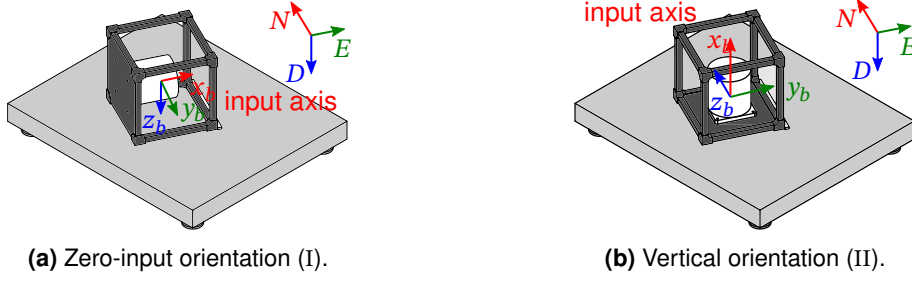


Figure 4.26.: Inertial sensor orientation at static testing. In these scenarios, the sensor's x_b axis is the tested input axis.

ideal sensor input is only the Earth's rotation along the local north and down axis. The ideal angular rates input and its linearized errors are given as:

$$\hat{\omega}_{ib} = \mathbf{R}_{\hat{b}p} \mathbf{R}_{\hat{p}n} \mathbf{R}_{\hat{n}e} \hat{\omega}_{ie} \quad (4.180)$$

$$\begin{aligned} \delta\omega_{ib} = & \mathbf{R}_{\hat{b}u} \mathbf{I}_{\hat{u}p} (\mathbf{I}_{\hat{p}n} \mathbf{R}_{\hat{n}e} \delta\omega_{ie} + \delta\omega_{np}) - (\mathbf{R}_{\hat{b}u} \mathbf{I}_{\hat{u}p} \mathbf{I}_{\hat{p}n} \mathbf{R}_{\hat{n}e} \hat{\omega}_{ie}) \times \boldsymbol{\psi}_{\hat{b}\hat{b}} \\ & - \mathbf{R}_{\hat{b}u} \mathbf{I}_{\hat{u}p} (\mathbf{I}_{\hat{p}n} \mathbf{R}_{\hat{n}e} \hat{\omega}_{ie}) \times \boldsymbol{\psi}_{\hat{p}\hat{p}} - \mathbf{R}_{\hat{b}u} \mathbf{I}_{\hat{u}p} \mathbf{I}_{\hat{p}n} (\mathbf{R}_{\hat{n}e} \hat{\omega}_{ie}) \times \boldsymbol{\psi}_{\hat{n}\hat{n}} \end{aligned} \quad (4.181)$$

Along the tested gyroscope sensor axis, above equations reduce to the following equations for the zero input case I:

$$\hat{\omega}_{ib}^I = 0 \quad (4.182)$$

$$\begin{aligned} \delta\omega_{ib}^I = & -\sin(\lambda) \delta\omega_{ie,x} + \cos(\lambda) \delta\omega_{ie,y} \\ & + \delta\omega_{np,x} + \hat{\omega}_{ie} \cos(\phi) (\delta\Psi_{\hat{b}\hat{b}} + \delta\Psi_{\hat{p}\hat{p}} - \delta\Psi_{\hat{n}\hat{n}}) \\ & - \hat{\omega}_{ie} \sin(\phi) (\delta\Theta_{\hat{b}\hat{b}} + \delta\Theta_{\hat{p}\hat{p}} - \delta\Theta_{\hat{n}\hat{n}}) \end{aligned} \quad (4.183)$$

For the vertically aligned case II, the ideal input and errors along the tested axis are:

$$\hat{\omega}_{ib}^{II} = \hat{\omega}_{ie} \sin(\phi) \quad (4.184)$$

$$\begin{aligned} \delta\omega_{ib}^{II} = & \cos(\phi) \cos(\lambda) \delta\omega_{ie,x} + \cos(\phi) \sin(\lambda) \delta\omega_{ie,y} + \sin(\phi) \omega_{ie,z} \\ & + \delta\omega_{np,z} - \hat{\omega}_{ie} \cos(\phi) (\delta\Phi_{\hat{b}\hat{b}} + \delta\Phi_{\hat{p}\hat{p}} + \delta\Theta_{\hat{n}\hat{n}}) \end{aligned} \quad (4.185)$$

The ideal specific forces input and its linearized errors are determined in the same way:

$$\hat{\mathbf{f}}_b = \mathbf{R}_{\hat{b}p} \mathbf{R}_{\hat{p}n} \hat{\boldsymbol{\gamma}}_n(R_b) \quad (4.186)$$

$$\begin{aligned} \delta\mathbf{f}_b = & \mathbf{R}_{\hat{b}u} \mathbf{I}_{\hat{u}n} \delta\boldsymbol{\gamma}_n + \mathbf{R}_{\hat{b}u} \left[\hat{\boldsymbol{\Omega}}_{iu}^2 + \mathbf{I}_{\hat{u}n} \frac{\partial \hat{\boldsymbol{\gamma}}_n(R_b)}{\partial \mathbf{r}_e} \mathbf{I}_{\hat{n}u} \right] \delta\mathbf{r}_u(R_b) + \mathbf{R}_{\hat{b}u} \mathbf{I}_{\hat{u}p} \boldsymbol{\eta}_{fp} \\ & - (\mathbf{R}_{\hat{b}u} \mathbf{I}_{\hat{u}n} \hat{\boldsymbol{\gamma}}_n(R_b)) \times \boldsymbol{\psi}_{\hat{b}\hat{b}} - \mathbf{R}_{\hat{b}u} [\mathbf{I}_{\hat{u}p} (\mathbf{I}_{\hat{p}n} \hat{\boldsymbol{\gamma}}_n(R_b)) \times] \boldsymbol{\psi}_{\hat{p}\hat{p}} \\ & - \mathbf{R}_{\hat{b}u} [\mathbf{I}_{\hat{u}n} \hat{\boldsymbol{\gamma}}_n(R_b) \times] \boldsymbol{\psi}_{\hat{n}\hat{n}} \end{aligned} \quad (4.187)$$

For the zero input case (I), these equations, again, are reduced to:

$$\hat{f}_b^I = 0 \quad (4.188)$$

$$\begin{aligned} \delta f_b^I = & \delta \gamma_{n,y} - \hat{\gamma}_0 (\delta \Theta_{\hat{b}b} + \delta \Theta_{\hat{p}p} + \delta \Phi_{\hat{n}n}) - \hat{\omega}_{ie}^2 \delta r_{n,y}(P_p) \\ & - \hat{\omega}_{ie} \sin(\phi) \delta \dot{r}_{n,x}(P_p) - \hat{\omega}_{ie} \cos(\phi) \delta \dot{r}_{n,z}(P_p) + \delta \ddot{r}_{n,y}(P_p) \end{aligned} \quad (4.189)$$

and for the vertically aligned case (II) to:

$$\hat{f}_b^{II} = \hat{\gamma}_0 \quad (4.190)$$

$$\begin{aligned} \delta f_b^{II} = & -\delta \gamma_{n,z} + \hat{\omega}_{ie}^2 \sin(\phi) \cos(\phi) \delta r_{n,x}(P_p) + \hat{\omega}_{ie}^2 \cos^2(\phi) \delta r_{n,z}(P_p) \\ & - \hat{\omega}_{ie} \cos(\phi) \delta \dot{r}_{n,y}(P_p) - \delta \ddot{r}_{n,z}(P_p) \end{aligned} \quad (4.191)$$

Clearly, both static gyroscope tests are affected by variations of the Earth's angular rate, test-pad motion and orientation errors of the laboratory and test-pad. Similar accounts to the accelerometer testing, which is of course sensitive to variations of the local gravity instead of the Earth's angular rate.

For the following analyses, a simple but general sensor error is assumed:

$$\tilde{\omega}_{ib} = S(\hat{\omega}_{ib,x} + \delta \omega_{ib,x}) + M_{G,y} \hat{\omega}_{ib,y} + M_{G,z} \hat{\omega}_{ib,z} + b_G + \nu_G \quad (4.192)$$

$$\tilde{f}_b = S(\hat{f}_{b,x} + \delta f_{b,x}) + M_{B,y} \hat{f}_{b,y} + M_{B,z} \hat{f}_{b,z} + b_A + \nu_A \quad (4.193)$$

where $S()$ represents the sensor's scale factor and transfer function. A sensor's transfer function typically shows some form of low-pass behavior, with cut-off frequencies typically higher than the typical environmental disturbances. If there are no resonance effects in the sensor's, neglecting its low-pass behavior and assuming a constant scale factor function provides a worst-case approximation. For the static tests, there is no variation of the inputs. Consequently, the transfer function can be approximated by a single scale factor S_0 , valid for just this input range.

4.4.2.3. Sensor Noise Characterization Errors

Sensor noise is usually analyzed using the PSD and mainly AVAR methods, as discussed in Section 2.3. This section discusses the effect of environmental disturbances on the noise characterization and the uncertainty of the Allan variance estimation.

In preparation for the noise analysis, all constant parts of the sensor's signal are usually removed by subtracting the signal's mean value. This eliminates all constant errors, and leaves only the temporal variation of the Earth's angular rate and gravity, the test-pad motion and the sensor's noise:

$$\tilde{\omega}_{ib} - \overline{\tilde{\omega}_{ib}} = S_0 \cdot (\delta \omega_{ib,x} - \overline{\delta \omega_{ib,x}}) + \nu_G - \overline{\nu_G} \quad (4.194)$$

$$\tilde{f}_b - \overline{\tilde{f}_b} = S_0 \cdot (\delta f_{b,x} - \overline{\delta f_{b,x}}) + \nu_A - \overline{\nu_A} \quad (4.195)$$

The time-varying errors from the input signal and the sensor's noise add up and cannot be separated in the sensor's output. The input errors, respectively, input noise, thus define a minimum noise level in the vicinity of which the intrinsic sensor noise can no longer be distinguished from the disturbances.

Using equation (2.29), the reference PSD curves from Model 5 and the approximations of gravity variation and angular rate variation are transformed to the Allan variances. The resulting Allan deviation curves are depicted in Figure 4.27. For reference, the typical Allan deviation (root Allan variance) (ADEV) curve of sensor noise processes is added to the plot.

The values given in Table 4.7 provide a fundamental order of magnitude of the errors in the noise parameter estimation caused by variations of the sensor's reference input. The seismic background noise mainly affects the AVAR analysis in the frequency spectrum above 1 Hz. Luckily, the shape and magnitude of the background noise AVAR can be effectively modified using an isolated or stabilized test pad. As illustrated in Figure 4.27, a test pad with a natural frequency of about 1 Hz reduces the peak ADEV by about two orders of magnitude. The two test cases, I and II, differ in the sensor orientation and thus the components of the variations of local gravity and the Earth's rotation that are picked up by the sensor. As these variations have periods of multiple hours, they do not interfere with the dominant seismic background in the higher frequencies but cause an increase of the AVAR at long cluster times. The high increase and oscillations of the acceleration ADEV for test case I at averaging times above 100 s is caused by test pad tilt oscillations and the resulting capturing of the local gravity by the ideally horizontally aligned sensor axis.

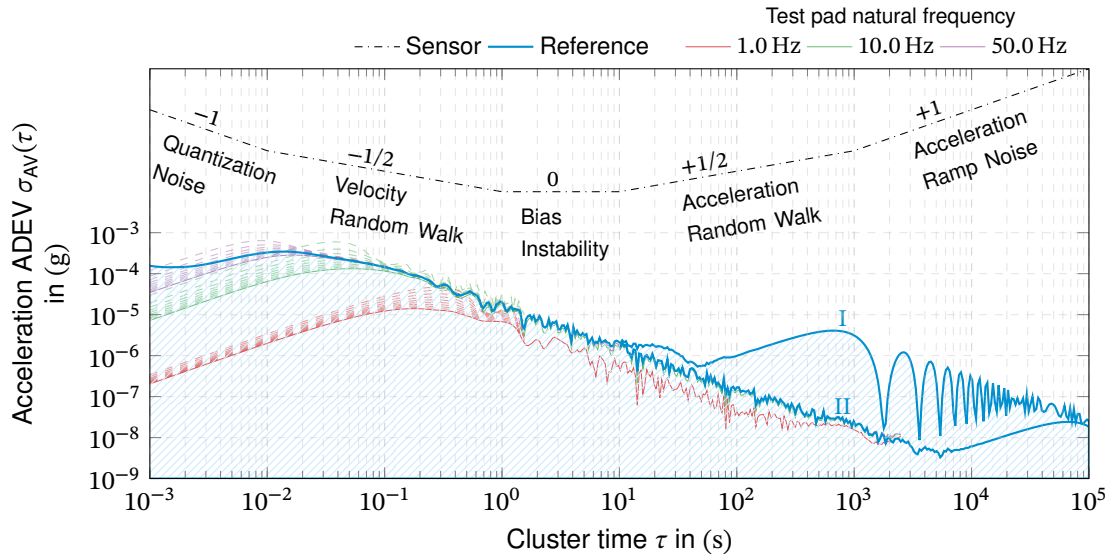
Noise Estimation

The scaling coefficients of the standard sensor noise processes are typically determined from a least-squares fit of the reference noise processes $\sigma_{AV,N}^2(\tau)$, $\sigma_{AV,K}^2(\tau)$, $\sigma_{AV,B}^2(\tau)$ and $\sigma_{AV,Q}^2(\tau)$ (see Table 2.7) to the measured AVAR. Splitting the measured AVAR $\hat{\sigma}_{AV}^2(\tau)$ into the sensor's intrinsic noise AVAR $\hat{\sigma}_{AV}^2(\tau)$ and the parts caused by the disturbances $\delta\sigma_{AV}^2(\tau)$, yields the following system of equations:

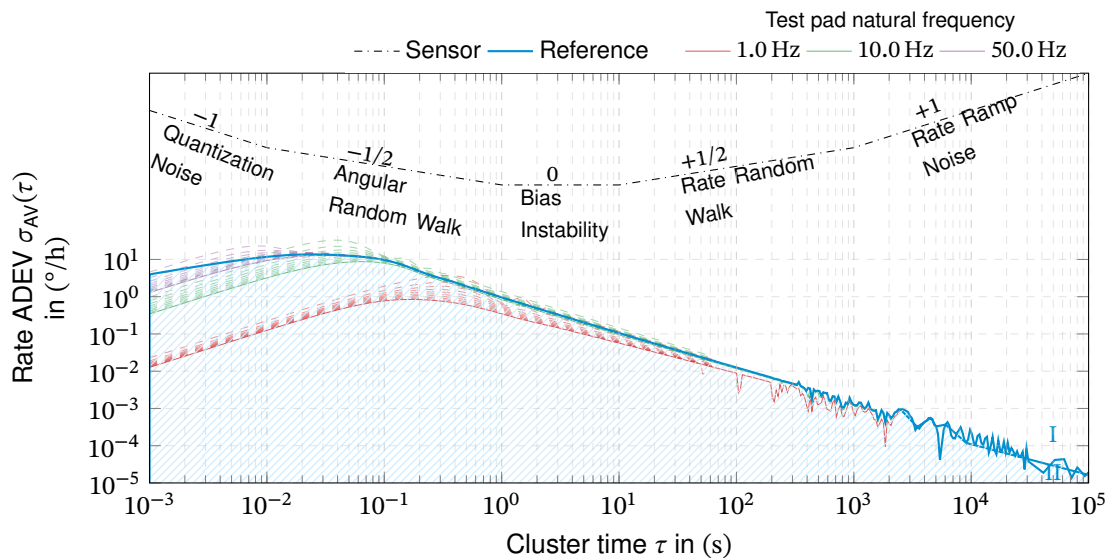
$$\underbrace{\begin{bmatrix} \hat{\sigma}_{AV}^2(\tau_1) + \delta\sigma_{AV}^2(\tau_1) \\ \hat{\sigma}_{AV}^2(\tau_2) + \delta\sigma_{AV}^2(\tau_2) \\ \vdots \\ \hat{\sigma}_{AV}^2(\tau_n) + \delta\sigma_{AV}^2(\tau_n) \end{bmatrix}}_{\hat{\mathbf{y}}} = \underbrace{\begin{bmatrix} \frac{3}{\tau_1^2} & \frac{1}{\tau_1} & (0.664)^2 & \frac{\tau_1}{3} \\ \frac{3}{\tau_2^2} & \frac{1}{\tau_2} & (0.664)^2 & \frac{\tau_2}{3} \\ \vdots & \vdots & \vdots & \vdots \\ \frac{3}{\tau_n^2} & \frac{1}{\tau_n} & (0.664)^2 & \frac{\tau_n}{3} \end{bmatrix}}_{\mathbf{H}} \underbrace{\begin{bmatrix} \hat{Q}^2 + \delta Q^2 \\ \hat{N}^2 + \delta N^2 \\ \hat{B}^2 + \delta B^2 \\ \hat{K}^2 + \delta K^2 \end{bmatrix}}_{\hat{\boldsymbol{\theta}}} \quad (4.196)$$

A least-squares estimate of the noise parameters $\boldsymbol{\theta}$ is determined as [72, p. 781]:

$$\hat{\boldsymbol{\theta}} = (\mathbf{H}^T \mathbf{H})^{-1} \mathbf{H}^T \hat{\mathbf{y}} \quad (4.197)$$



(a) Acceleration Allan deviation.



(b) Angular rates Allan deviation.

Figure 4.27.: Allan deviation of the reference environmental background noise and typical sensor noise processes. The additional curves illustrate the effect of a passively isolated test pad for a range of natural frequencies. The dashed lines represent different damping ratios, ranging from 0.1 to 1.0 (solid line). The two test-cases I and II differ only for high averaging times, which are not affected by the test pad isolation.

or

$$\hat{\Theta} = (\mathbf{H}^T \mathbf{W} \mathbf{H})^{-1} \mathbf{H}^T \mathbf{W} \hat{\mathbf{y}} \quad (4.198)$$

for a weighting \mathbf{W} of data points, as suggested in [66]. Here the AVAR data points are weighted with the number of clusters used to determine the variance to account for the estimation accuracy of each data point. Note that rate or acceleration ramp noise R is a linear drift in the non-integrated sensor output that is typically removed before the Allan variance analysis [10, p. 47], and therefore is not estimated here.

If the sensor's scale factor error and its transfer function are neglected, the sensor's non-constant output is just the sum of the input and the sensor's noise. By estimating the noise parameters from the AVAR of the input errors, $\delta \mathbf{y}$ thus gives the errors $\delta \Theta$ that add to the desired sensor noise parameter estimates Θ :

$$\delta \Theta = (\mathbf{H}^T \mathbf{W} \mathbf{H})^{-1} \mathbf{H}^T \mathbf{W} \delta \mathbf{y} \quad (4.199)$$

Application of the weighted least-squares estimation to the background noise AVAR yields the estimation errors summarized in Table 4.7. Note that, while the noise parameters cannot be negative by definition, the parameter estimation errors can indeed. Although the values are only indicative, they demonstrate that the effect of background noise on the sensor noise parameter estimation is hard to predict. Estimating the noise parameters strongly depends on the choice of the noise model, which should be adapted to the observed AVAR curve. In general, a lower natural frequency of the test pier yields a better reduction of seismic background noise and thus results in lower errors in the parameter estimation. However, resonance amplification for test pad natural frequencies around 10 Hz may lead to increased estimation errors. This can, e.g., be observed at the bias instability δB^2 for both accelerations and angular rates.

Table 4.7.: Errors of sensor noise process parameters from reference background noise from a least-squares fit (see [66]) of the static test input errors. Values are given for different test-pad natural frequencies and a damping ratio of 0.25 is assumed for the test pad.

Error	Unit	No test-pad	Test-pad natural frequency		
			50 Hz	10 Hz	1 Hz
δQ^2	$(^\circ)^2$	$-1.72 \cdot 10^{-4}$	$-2.90 \cdot 10^{-4}$	$-8.63 \cdot 10^{-5}$	$7.34 \cdot 10^{-7}$
δN^2	$(^\circ/\text{h}/\sqrt{\text{Hz}})^2$	$4.01 \cdot 10^{-1}$	$6.64 \cdot 10^{-1}$	$1.46 \cdot 10^{-1}$	$-2.54 \cdot 10^{-3}$
δB^2	$(^\circ/\text{h})^2$	$5.71 \cdot 10^1$	$7.03 \cdot 10^1$	$9.11 \cdot 10^1$	1.31
δK^2	$(^\circ/\text{h}/\sqrt{\text{Hz}})^2$	$-1.48 \cdot 10^{-3}$	$-1.83 \cdot 10^{-3}$	$-2.37 \cdot 10^{-3}$	$-3.14 \cdot 10^{-5}$
δQ^2	$(\text{g s})^2$	$-1.09 \cdot 10^{-13}$	$-2.27 \cdot 10^{-13}$	$-3.16 \cdot 10^{-14}$	$1.84 \cdot 10^{-16}$
δN^2	$(\text{g}/\sqrt{\text{Hz}})^2$	$2.73 \cdot 10^{-10}$	$5.33 \cdot 10^{-10}$	$5.77 \cdot 10^{-11}$	$-6.41 \cdot 10^{-13}$
δB^2	g^2	$2.38 \cdot 10^{-8}$	$3.44 \cdot 10^{-8}$	$2.65 \cdot 10^{-8}$	$3.39 \cdot 10^{-10}$
δK^2	$(\text{g}/\sqrt{\text{Hz}})^2$	$-6.18 \cdot 10^{-13}$	$-8.95 \cdot 10^{-13}$	$-6.89 \cdot 10^{-13}$	$-8.79 \cdot 10^{-15}$

An Allan variance analysis of measurement data is presented in Example 4. In this example, the effect of environmental disturbances can be observed for low cluster times that correspond

to the high frequency artificial seismic noise. These disturbances can also be observed in the corresponding spectrograms in [Example 6](#). Parts of the external disturbances can be easily identified as they change from day to night-time, indicating natural or artificial activities.

The existence and the effect of these time-varying disturbances can be observed in a [DAVAR](#) plot. Such a graph illustrates the variation of the Allan variance with time, similar to a spectrogram. For time-varying disturbances like in [Example 5](#), one can distinguish the difference of the [AVAR](#) for times with and without the disturbances. While this works well for many seismic noise sources related to human culture's day-night cycle, it doesn't help with natural seismic background noise.

Identification of Disturbances

The previous section demonstrated that the sensor noise could not be separated from the external disturbances for a one-position single-axis static test without further assumptions. While gravity variations from Lunar and Solar tides and variations of the Earth's angular rate can be determined from deterministic models and thus compensated, the test pad motion is widely random. This includes both the disturbance frequencies, amplitudes, and transients and directions of, e.g., the surface waves, see [Subsection 4.2.8.1](#).

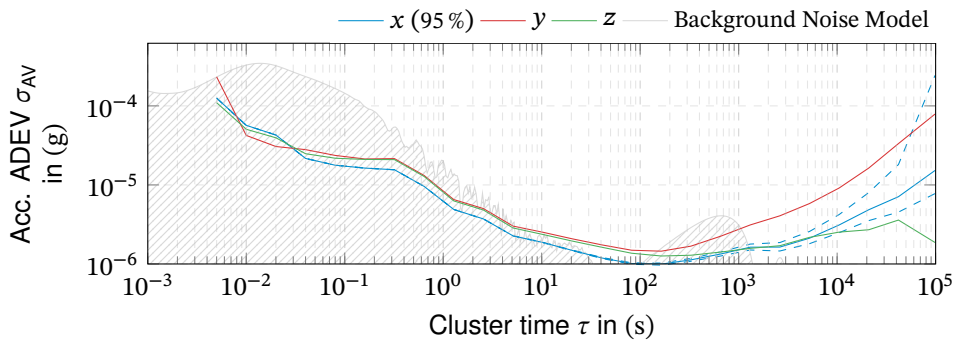
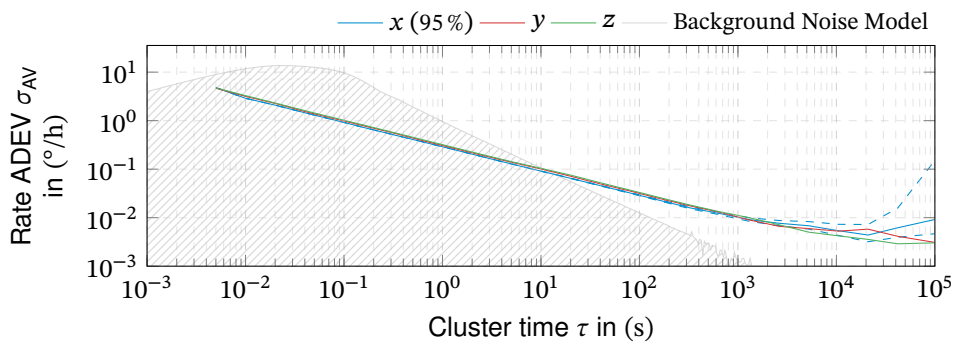
However, the sensor noise can be seen as a body-fixed error, while the external disturbances may be considered *space fixed*. Based on this insight, it should be possible to distinguish between sensor noise and external disturbances by simultaneously using multiple orientations or multiple sensor axes.

In principle, seismic waves can be identified and located by the run-time difference between multiple sensors. This, however, requires sensors with a drift lower than the expected disturbance and sufficient spatial distance between the sensors that allows a resolution of the different run-times. This is not possible with a sensor triad inside an [IMU](#). As described in [Subsection 4.2.8.1](#), surface waves consist of horizontal and vertical components. This suggests a strong correlation exists between the background noise recorded by each sensor axis. The two horizontally aligned axes should sense components of horizontal oscillation. In contrast, the vertical component should sense the vertical component of the surface wave at a constant phase offset to the two horizontal components. Additionally, disturbances should be observable at equal frequencies in the gyroscope and the accelerometer output.

However, a correlation of the sensor's output can also be caused by electronics in the [IMU](#), like a shared power supply. If available, the correlation between the supply voltage and the sensor outputs should be analyzed to exclude this possibility. Although the environmental disturbances are space-fixed, a change of the sensor orientation does not provide sufficient information to separate sensor noise from seismic disturbances. However, identifying space-fixed disturbances is possible if a single source of disturbances is assumed. The mathematical approach to reducing disturbances may be helpful in some instances, but generally, it is more advisable to reduce environmental disturbances in the laboratory.

Example 4: Allan variance analysis of IFOS-500 IMU.

The Allan deviation was determined from 48 h static testing of an IFOS-500 IMU [169] on a measurement plate in the basement of the Institute of Flight System Dynamics. In this test, the sensor's x -axis was pointing down, y to true north, and z to the east. The dashed lines indicate the 95 % confidence interval of the Allan variance estimate.

**(4.a)** Accelerometer noise.**(4.b)** Gyroscope noise.

For high frequencies, or small cluster times, the determined Allan variance ranges into the background noise spectrum, especially for accelerometer measurements. Here, the velocity random walk's slope is corrupted by correlated or sinusoidal noise. This indicates that the Allan variance estimate for low cluster times is affected by environmental disturbances. However, without further knowledge about the true seismic disturbances, it is impossible to tell if the intrinsic sensor noise is lower than determined in the Allan variance analysis. The isolated test pad typically reduces seismic background noise for the very short cluster times below 0.1 s.

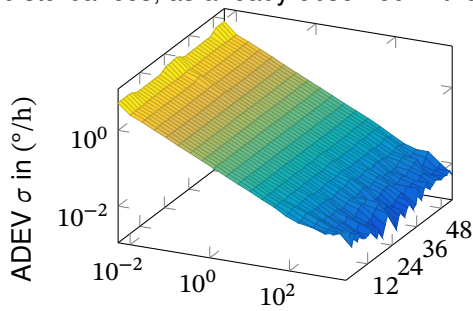
Neglecting the question of validity and the slight variations between the axes, the approximated noise parameters from these measurements are summarized below:

Parameter	Accelerometer	Gyroscope
Quantization noise Q	-	-
Velocity/Angle random walk N	$5 \cdot 10^{-6} \text{ g}/\sqrt{\text{Hz}}$	$5 \cdot 10^{-3} \text{ }^\circ/\sqrt{\text{h}}$
Bias instability B	$1 \cdot 10^{-6} \text{ g}$	$2 \cdot 10^{-3} \text{ }^\circ/\text{h}$
Acceleratom/Rate random walk K	$5 \cdot 10^{-8} \text{ g}/\sqrt{\text{s}}$	-

These results basically agree with those in the manufacturer's data sheet [169].

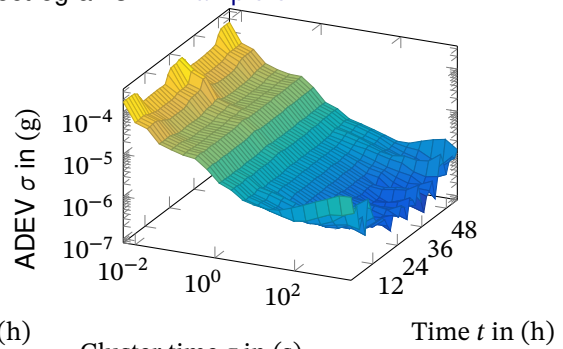
Example 5: Dynamic Allan variance of IFOS-500 IMU noise.

The following graphs depict the Dynamic Allan variance determined from the same data as [Example 4](#). The Allan variance for low cluster times indicates the presence of external disturbances, as already observed in the spectrograms in [Example 6](#).



Cluster time τ in (s)

(5.a) Gyroscope x axis.

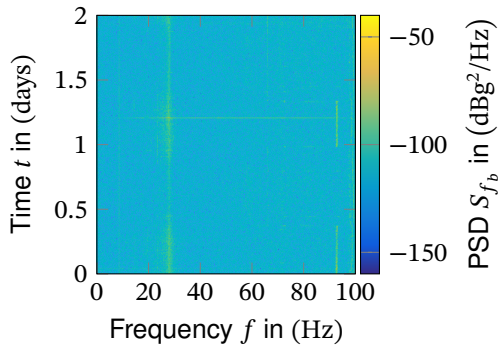


Cluster time τ in (s)

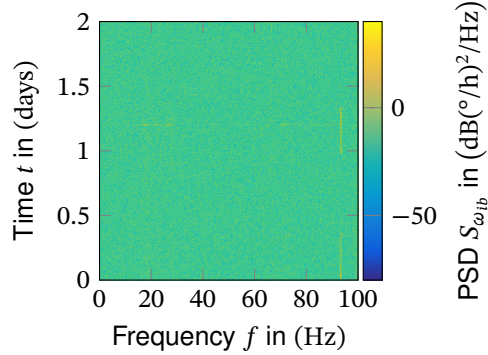
(5.b) Accelerometer x axis.

Example 6: Spectrogram of IFOS-500 IMU noise.

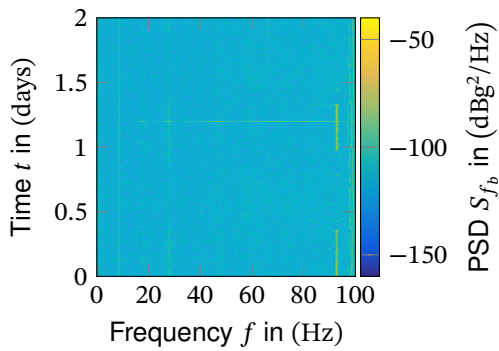
The following spectrograms have been determined from the same data as Example 4. The sensor's x -axis was pointing down, y to true north, and z to the east.



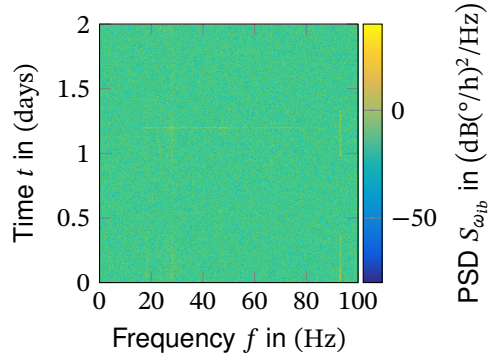
(6.a) Accelerometer x axis.



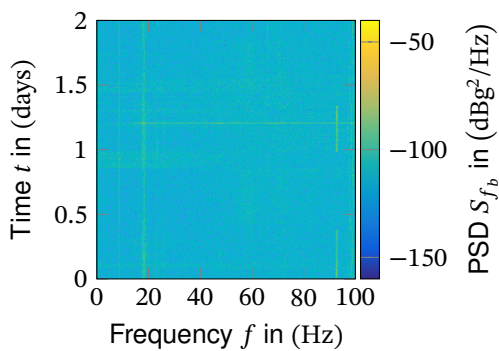
(6.b) Gyroscope x axis.



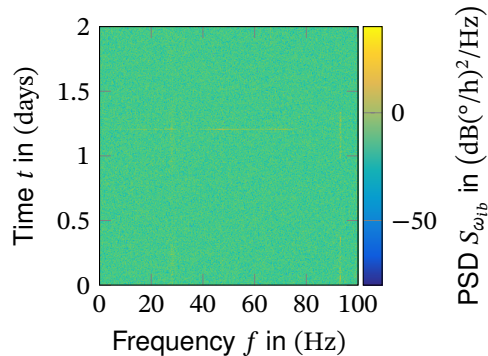
(6.c) Accelerometer y axis.



(6.d) Gyroscope y axis.



(6.e) Accelerometer z axis.



(6.f) Gyroscope z axis.

The environmental disturbances can be observed in these spectrograms at distinct frequencies. The alternating spectrums at night and day times indicate an artificial disturbance, in this case probably building utilities placed in the basement of the institute's building. While the disturbances at around 91 Hz can be observed on all axes, the oscillations around 19 Hz and 22 Hz differ in amplitude between the north and east-oriented axes. This indicates the existence of at least two primary and spatially distributed disturbance sources.

Result 4: Sensor Noise Identification.

The characterization of inertial sensor noise using the Allan variance analysis is performed at constant or even zero input. However, environmental disturbances and model errors add temporal variations to the sensor's input that, in general, cannot be distinguished from the sensor's noise:

- Seismic background noise and temporal variations of gravity and the Earth's rotation limit the accuracy of the parameter identification of sensor noise processes. This is especially true for the frequency range above 1 Hz, which is dominated by man-made vibrations.
- Isolated test pads can reduce the disturbances above about 10 Hz by orders of magnitude. However, the resonance effects of the coupling between test-pad and soil can also slightly worsen the accuracy parameter estimation.
- Sensor noise correlated across multiple axes cannot be separated from environmental disturbances without additional information. Changing the sensor's orientation helps separate (ideally) space-fixed disturbances from IMU fixed noise.
- Man-made disturbances tend to vary with time and can be detected in spectrograms or the dynamic Allan variance. Harmonic disturbances may be removed by signal processing, or actions are taken to reduce the disturbances.

For sensor noise characterization, the environmental disturbances at the test location should be surveilled, and actions should be taken to isolate them from man-made disturbances. Furthermore, the tested sensors' noise signals should be examined for potential environmental disturbances that can be correlated with human activities or natural effects, e.g., weather.

4.4.2.4. Static Bias Testing Error Budget

A sensor's bias is defined as its output at zero input. During static testing, this can be achieved by aligning an accelerometer's input axis perpendicular to the local plumb line or a gyro's input axis to the local east-west direction, as described in scenario I. Averaging over the sensor's signal yields:

$$\overline{\hat{\omega}_{ib}} = S_0 \cdot \overline{\delta\omega_{ib,x}} + M_{G,y} \hat{\omega}_{ie} \sin(\phi) + b_G + \overline{v_G} \quad (4.200)$$

$$\overline{\hat{f}_b} = S_0 \cdot \overline{\delta f_{b,x}} + M_{B,z} \hat{\gamma}_0 + b_A + \overline{v_A} \quad (4.201)$$

Ideally, averaging over the sensor's signal at zero-input simply leaves the sensor's bias b_G respectively b_A . In reality input errors and sensor noise do not entirely average out but leave a residual error. Additionally, the sensor's internal misalignment adds a constant error, which cannot be distinguished from the sensor's bias in the sensor's output from a single static test. Note that the sensor's internal misalignment $M_{G,y}, M_{B,z}$ can be estimated in multi-position tests, eliminating their contribution to the bias estimate. This can be as simple reversal measurement, where the the sensor is rotated about 180° along the tested input axis, see [Subsection 4.4.3](#).

In addition to the input errors, the sensor's intrinsic noise also corrupts the sensor's bias estimation. Having performed the noise characterization from the static tests, the existing noise processes and their sensor output parameters are known. As discussed in [Section 4.3](#), the variance for the bias instability and rate random walk processes is indeterminate. This prevents stating the uncertainty of the bias estimate in the likely presence of these noise processes. The bias determined from an arbitrary cluster thus contains the deterministic parts of the sensor bias and an unknown contribution caused by the low-frequency noise. However, this is more of a theoretical problem as it is not necessary to determine a theoretical bias that is valid at all times. Instead, the mean value just determined from the test data is set as the bias *for the moment*, as it indeed represents the best-fit bias at least for the considered time frame. The principle is illustrated in [Figure 4.28](#). The uncertainty of this bias is then only affected by the other noise processes that have a well-defined variance. The bias estimate is the best possible fit to eliminate the deterministic sensor bias from the sensor's current output for the moment. Still, it will become more and more uncertain with time due to the bias instability and rate random walk processes. Due to in-run drifts and turn-on bias variations, the determined bias is only valid for a single run of the sensor or even just fractions of it, which motivates the online calibration of the sensor's biases.

The contributions of the different error sources to the bias estimate during static sensor testing are illustrated in [Table 4.8](#) for the gyroscopes and [Table 4.9](#) for the accelerometers.

For the gyroscope, the plots indicate that the heading error of the tested sensor axis dominates the error budget. The uncertainty caused by variations of the Earth's rotation rate and direction results in a bias standard deviation of less than $1 \cdot 10^{-5} \text{ }^\circ/\text{h}$ and is hardly affected by averaging. In contrast, the errors from the test-pad motion can be reduced by one order of magnitude by

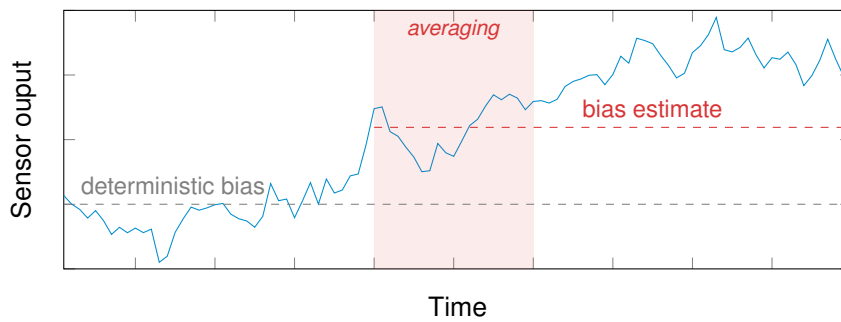


Figure 4.28.: Bias determination in the presence of rate random walk noise. Averaging over a cluster leads to a momentary bias estimate. Vividly, a random walk’s variance grows with time, and the position of the taken samples in the random walk process is unknown. Therefore, the mean of a sample cluster is arbitrarily defined as bias.

Table 4.8.: Gyro static testing bias error budget for varying averaging time. The laboratory is located at $\phi = 45^\circ$

	consumer	tactical	intermediate	navigation	strategic
<p>Earth rotation variations see Subsection 4.2.4</p> <ul style="list-style-type: none"> • using WGS84 as reference • unknown/random time 					
<p>Test-pad motion see Subsection 4.2.8</p> <ul style="list-style-type: none"> • test-pad isolation neglected • isotropic background noise 					
<p>Laboratory alignment see Subsection 4.2.7, Subsection 4.2.6</p> <ul style="list-style-type: none"> • — Leveling error / DoV of 1" (1σ) • - - North alignment error of 0.01° (1σ) 					
<p>Sensor misalignment</p> <ul style="list-style-type: none"> • Alignment error normalized to 1" (1σ) 					

averaging for multiple hours. However, the resulting bias standard deviation is already for short averaging times in the range of $1 \cdot 10^{-4} \text{ }^\circ/\text{h}$. While the leveling errors result in errors below $1 \cdot 10^{-4} \text{ }^\circ/\text{h}$ (1σ), a north alignment error of just 0.01° limits the bias accuracy to worse than $1 \cdot 10^{-3} \text{ }^\circ/\text{h}$ and thus to navigation grade sensors. However, with a better heading alignment, a strategic grade sensor bias uncertainty in the range of $1 \cdot 10^{-4} \text{ }^\circ/\text{h}$ can be achieved and is then limited by the test-pad motion.

In contrast, the error budget for accelerometer static bias tests indicates that a strategic grade level of accuracy can be easily achieved, even for short averaging times. For the analyzed test case, the temporal variations of the local gravity contribute less than $1 \cdot 10^{-7} \text{ g}$ to the bias standard deviation, which can be further reduced by averaging over multiple hours. Similar applies to the test-pad motion. The resulting bias standard deviation is about $1 \cdot 10^{-5} \text{ g}$ and can be further reduced for long averaging times. As expected, heading and consequently north alignment error does not affect the accelerometer bias, but leveling errors are crucial. However, as a leveling accuracy in the range of few asec is not a problem, a bias standard deviation of less than $10 \mu\text{g}$ seems possible for a typical setup.

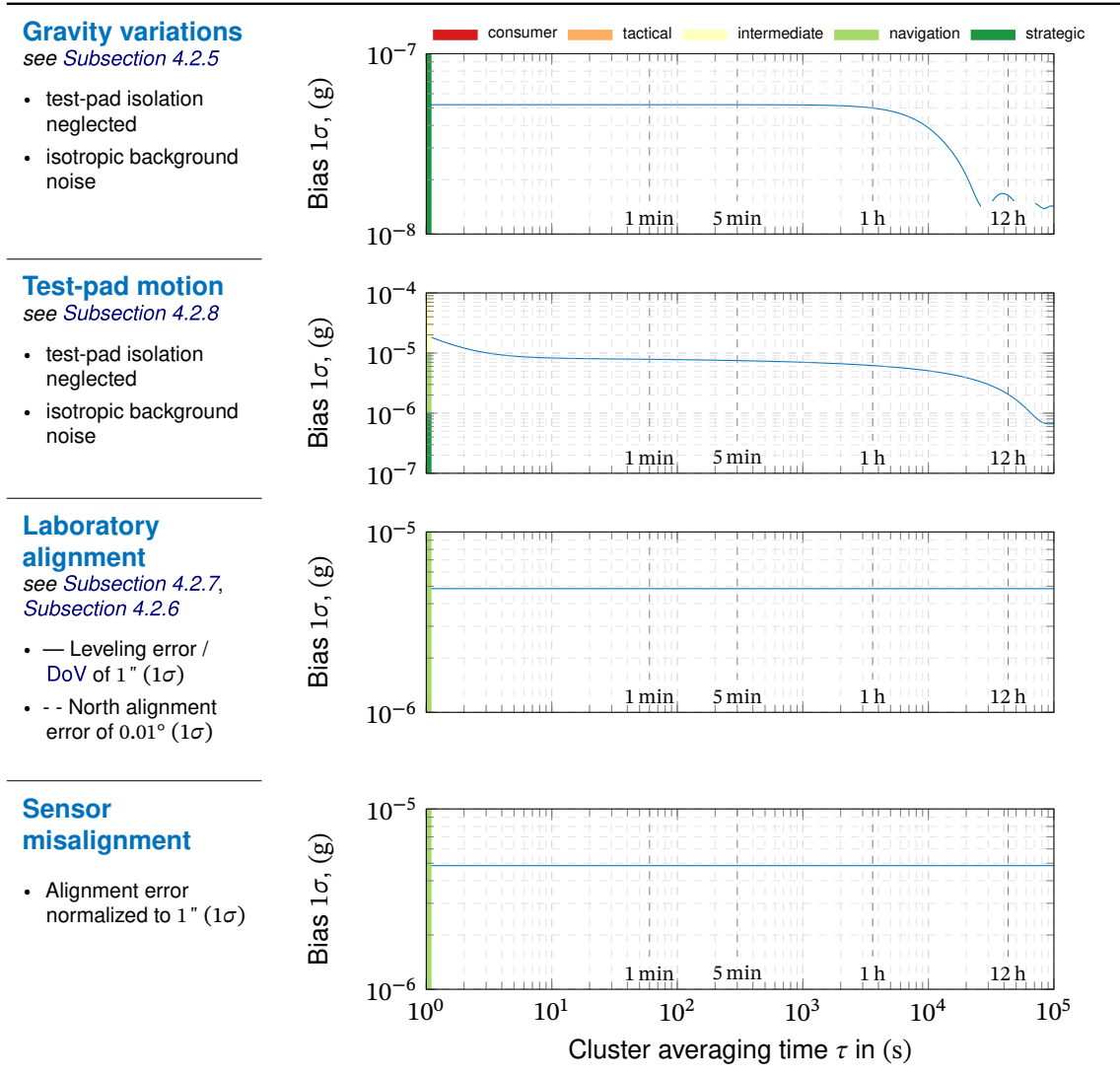
Result 5: Bias Determination from Single-Position Static Tests.

The determination of an inertial sensor's bias from a single-position static test provides the most simple test procedure, but suffers from multiple drawbacks:

- A single static test does not allow the determination of the sensor bias independently of the sensor's internal misalignment.
- Test-pad motion and temporal variations of the Earth's angular rate and gravity represent a lower bound for the estimation accuracy of the sensor bias.
- Accelerometer tests are susceptible to leveling errors, while the north-alignment errors dominate the gyroscope tests.

In total, the single-position test allows the determination of the gyro bias at strategic grade accuracy, while alignment errors and test-pad motions limit the testing of the accelerometer bias to navigation grade accuracy.

Table 4.9.: Accelerometer static testing bias error budget for varying averaging time. The laboratory is located at $\phi = 45^\circ$



4.4.3. Reversal Position Static Tests

As discussed in Subsection 4.4.2.4, a sensor’s bias cannot be determined independently from the sensor’s misalignment in a single position static test. This section demonstrates how a sensor’s linear SF, misalignment angles, and bias can be determined independently from each other by using reversal measurements of the local Earth’s angular rate and gravity as input.

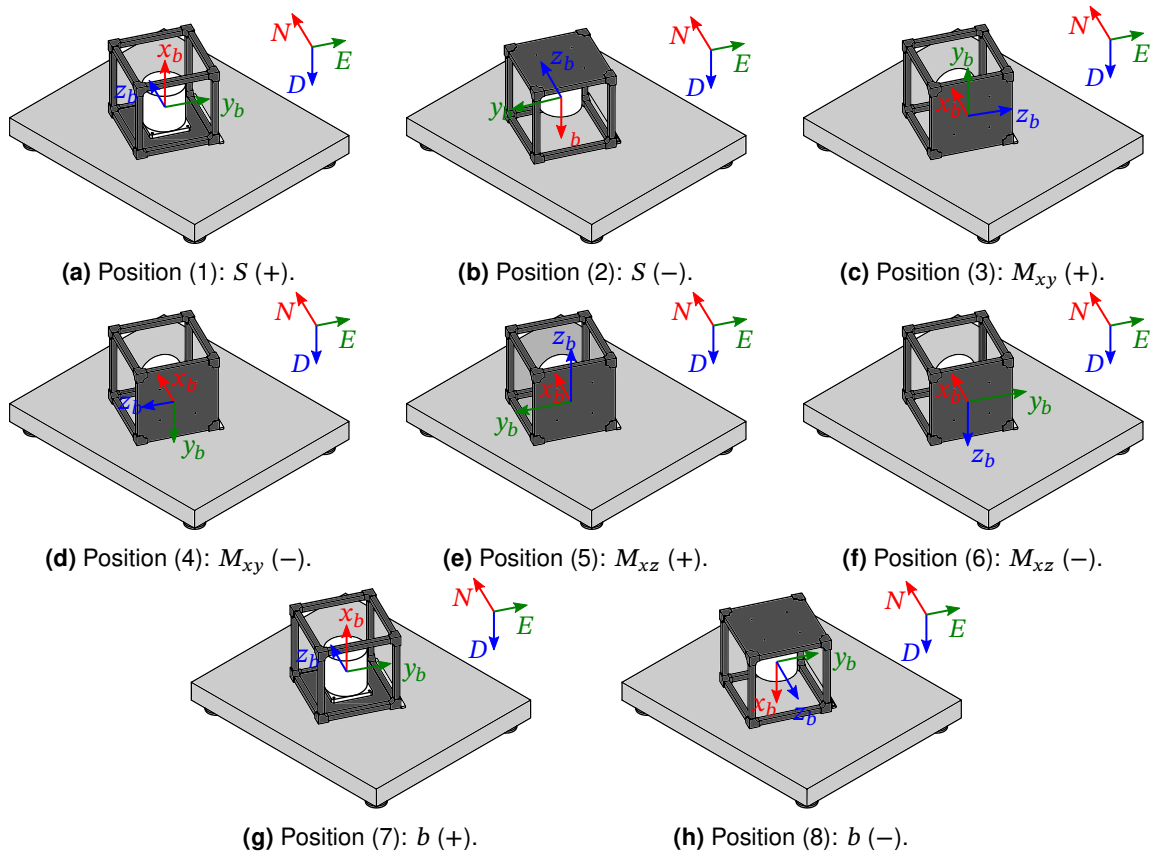


Figure 4.29.: Positions for static reversal measurements.

As depicted in Figure 4.29, two reversal measurements are used to determine the sensor parameters. For the depicted tests, the vertical component of the Earth’s local gravity is used as input and flipped so that the other inputs cancel out. This orientation is suitable for laboratories at latitudes $|\phi| \geq 45^\circ$. For lower latitudes, the local horizontal component of the Earth’s angular rate should be used as a reference input, and the depicted orientations need to be modified accordingly.

4.4.3.1. Test Description and Parameter Estimation

Analogously to Subsection 4.4.2.4, a simple sensor error model with linear scale factor S , misalignments M and additive bias b is used. The analysis will be exemplarily conducted for

the sensors's x -axis:

$$\tilde{\omega}_{ib,x} = S_G \omega_{ib,x} + M_{G,xy} \omega_{ib,y} + M_{G,xz} \omega_{ib,z} + b_G + \nu_G \quad (4.202)$$

$$\tilde{f}_{b,x} = S_A f_{b,x} + M_{A,xy} f_{b,y} + M_{A,xz} f_{b,z} + b_A + \nu_A \quad (4.203)$$

The sensor errors of the above error model can be determined by taking the difference respectively the arithmetic mean of two averaged measurements. For the gyroscope, the SF and misalignment angles are determined as the difference between the two reversal measurements, e.g., (1) and (2), divided by the ideal double input:

$$S_G = \frac{\overline{\tilde{\omega}_{ib,x}^{(1)}} - \overline{\tilde{\omega}_{ib,x}^{(2)}}}{2 \sin(\phi) \overline{\dot{\omega}_{ie}}} \quad M_{G,xy} = \frac{\overline{\tilde{\omega}_{ib,x}^{(3)}} - \overline{\tilde{\omega}_{ib,x}^{(4)}}}{2 \sin(\phi) \overline{\dot{\omega}_{ie}}} \quad M_{G,xz} = \frac{\overline{\tilde{\omega}_{ib,x}^{(5)}} - \overline{\tilde{\omega}_{ib,x}^{(6)}}}{2 \sin(\phi) \overline{\dot{\omega}_{ie}}} \quad (4.204)$$

For the bias estimate, the test orientations are designed to cancel out all nominal inputs when adding the two averaged measurements (7) and (8):

$$b_G = \frac{\overline{\tilde{\omega}_{ib,x}^{(7)}} + \overline{\tilde{\omega}_{ib,x}^{(8)}}}{2} \quad (4.205)$$

Analogously the SF and misalignment of the accelerometer are determined by subtracting two reversal measurements, e.g., (1) and (2):

$$S_A = \frac{\overline{\tilde{f}_{b,x}^{(1)}} - \overline{\tilde{f}_{b,x}^{(2)}}}{2\gamma} \quad M_{A,xy} = \frac{\overline{\tilde{f}_{b,x}^{(3)}} - \overline{\tilde{f}_{b,x}^{(4)}}}{2\gamma} \quad M_{A,xz} = \frac{\overline{\tilde{f}_{b,x}^{(5)}} - \overline{\tilde{f}_{b,x}^{(6)}}}{2\gamma} \quad (4.206)$$

Finally, the accelerometers bias is, again, the arithmetic mean of the signal averages of the two symmetrical positions (7) and (8):

$$b_A = \frac{\overline{\tilde{f}_{b,x}^{(7)}} + \overline{\tilde{f}_{b,x}^{(8)}}}{2} \quad (4.207)$$

Above idealized equations assume that the sensor's noise ν ideally averages to zero during each pose. In reality, the sensor noise does not average to zero but leaves a residual error in the measurements. The effects of input errors and the sensor noise are discussed in the following sections.

4.4.3.2. Effects of Sensor Noise

The two-position tests rely on the subtraction, respectively summation of the sensor output averaged over each position. Hence, the correlation between these two averages becomes essential for the resulting variance of the parameter estimate.

Using the methods described in Subsection 4.3.0.2, the 2×2 covariance matrix of the sensor's noise averaged over each position can be determined for the identified sensor noise processes.

From this covariance matrix, here exemplarily given for position (1) and (2),

$$\mathbf{Q}_{\vec{v}} = \begin{bmatrix} Q^{(1)} & Q^{(1,2)} \\ Q^{(1,2)} & Q^{(2)} \end{bmatrix} \quad (4.208)$$

the resulting scale factor estimation variance for the gyroscope errors caused by the sensor noise can be easily determined to

$$\sigma_{\omega,S}^2 = \frac{Q^{(1)} - 2Q^{(1,2)} + Q^{(2)}}{(2 \sin(\phi) \hat{\omega}_{ie})^2} \quad (4.209)$$

and for the accelerometers it can be determined from:

$$\sigma_{f_b,S}^2 = \frac{Q^{(1)} - 2Q^{(1,2)} + Q^{(2)}}{(2\gamma)^2} \quad (4.210)$$

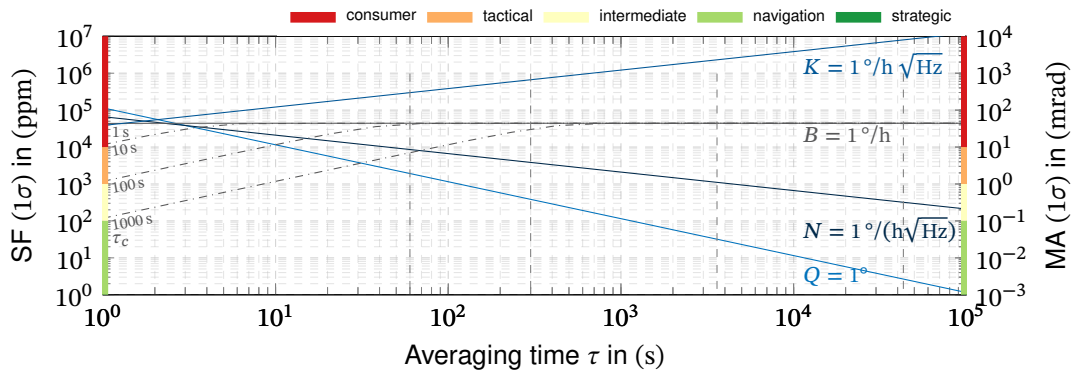
The variance of the misalignment estimates is determined analogously using positions (3) and (4), respectively, (5) and (6). The variance of the bias estimate is determined to:

$$\sigma_S^2 = \frac{Q^{(7)} + 2Q^{(7,8)} + Q^{(8,8)}}{4} \quad (4.211)$$

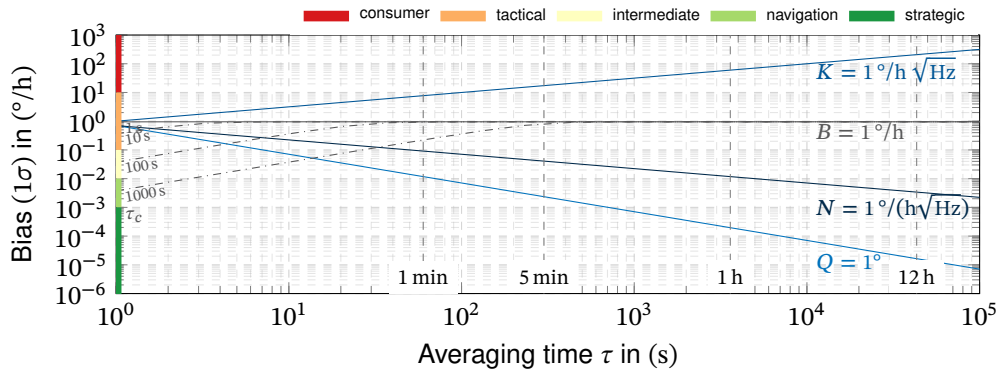
The resulting standard deviation of the parameter estimates with varying averaging time are depicted in [Figure 4.30](#) and [Figure 4.31](#) for the typical sensor noise processes. The resulting plots are normalized for the noise coefficients Q , N , B and K , specified in $^\circ/\text{s}$ respectively mg . The standard deviation of the cluster averages scales linearly with the noise coefficients and can thus easily be scaled to the noise level of interest. In general, the effects of sensor noise can be split into three different groups:

- The errors from quantization noise and angular/velocity random walk are drastically decreased with increasing averaging time. These noise processes can be easily handled and do not pose a practical limit to the sensor error estimation.
- The resulting variance from the bias instability is not affected by averaging for averaging times higher than the bias instabilities time constant. Thus, it limits the estimation accuracy that cannot be overcome.
- Rate/acceleration random walk causes an error that increases with the averaging time. The same applies to a potential rate/acceleration ramp in the sensor's output.

To minimize the effects of sensor noise on the parameter estimation, the averaging time should be selected to minimize the sum of the effects of all noise processes. This is just the cluster time τ at the minimum of the sensor's Allan variance plot, as determined in [Subsection 4.4.2.3](#).



(a) Gyroscope scale factor and misalignment standard deviation.



(b) Gyroscope bias standard deviation.

Figure 4.30.: Two-position static test gyroscope error variance from sensor noise for varying averaging time τ per pose. The plots are scaled for a geodetic latitude of $\phi = 45^\circ$.

4.4.3.3. Gyroscope Test Error Model

The ideal gyroscope input is simply the ideally constant Earth's angular rate $\hat{\omega}_{ie}$, observed from different orientations:

$$\hat{\omega}_{ib}^{(P)} = \mathbf{R}_{bp}^{(P)} \mathbf{I}_{pn} \mathbf{R}_{ne} \hat{\omega}_{ie} \quad (4.212)$$

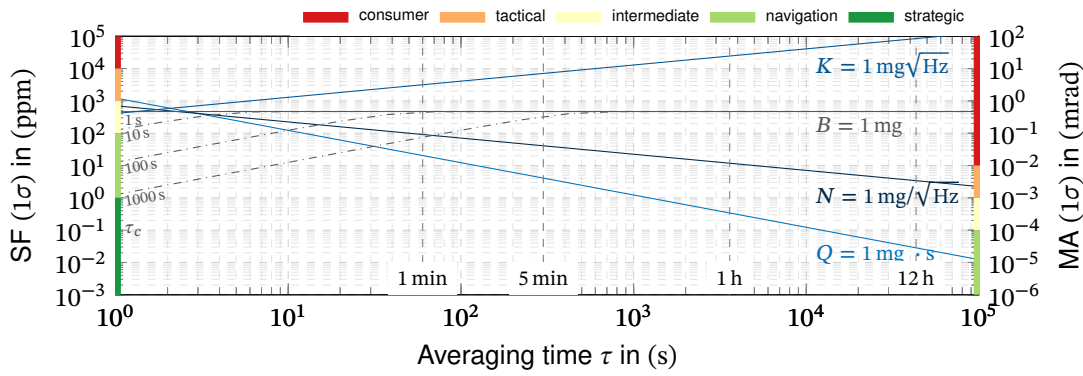
Introduction of error terms and linearization of the nominal input equations for the errors, yields:

$$\begin{aligned} \delta\omega_{ib}^{(P)} = & \mathbf{R}_{bp}^{(P)} (\mathbf{I}_{pn} \mathbf{R}_{ne} \delta\omega_{ie} + \delta\omega_{np}) - [\mathbf{R}_{bp}^{(P)} \mathbf{R}_{pn} \mathbf{R}_{ne} \hat{\omega}_{ie}] \times \psi_{bb} \\ & - \mathbf{R}_{bp}^{(P)} [\mathbf{R}_{pn} \mathbf{R}_{ne} \hat{\omega}_{ie}] \times \psi_{pp} - \mathbf{R}_{bp}^{(P)} \mathbf{R}_{pn} [\mathbf{R}_{ne} \hat{\omega}_{ie}] \times \psi_{nn} \end{aligned} \quad (4.213)$$

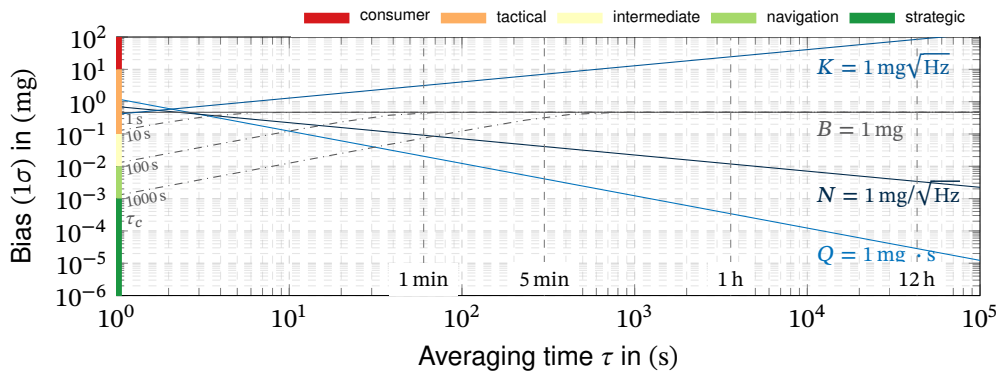
In this scenario, the sensor's input is affected by variations of the Earth's angular rate, test-pad motion and static orientation errors of the test-pad and the sensor.

4.4.3.4. Gyroscope Test Error Budget

Based on the derived error sensitivities and error models from Section 4.2, the error budgets for linear scale factor, misalignment, and bias are determined.



(a) Accelerometer scale factor and misalignment standard deviation.



(b) Accelerometer bias standard deviation.

Figure 4.31.: Two-position static test accelerometer error variance from sensor noise for varying averaging time τ per pose.

The error budget for the SF estimate is depicted in Table 4.10. Due to the change in orientation, the sensor’s alignment to the test plate has no first-order effect. However, this does not hold for the laboratory alignment errors. For the considered averaging times, the Earth’s angular rate variations can be neglected and thus result in a constant uncertainty in the SF estimate. In contrast, the errors from test-pad motion can be reduced by two magnitudes when averaging over multiple hours.

Due to the construction of the misalignment test orientations, the error budgets for the two misalignment angles Table 4.11 and Table 4.12 are equal. Sensor alignment errors are directly transferred into errors of the misalignment estimation, which is reasonable considering that the misalignment represents orientation errors of the axes within the sensor’s package. Laboratory alignment errors, however, are canceled out by the reversal of the sensor’s orientation. The uncertainty of the misalignment estimate from both the variations of the Earth’s angular rate and the test-pad motion increase with the averaging time. However, the test-pad motion decreases when averaging about 10 h. In summary, the misalignment estimates from reversal tests are dominated by sensor alignment errors. The errors introduced by the environment are in the range of $1 \mu\text{rad}$, which would allow testing up to strategic grade sensors.

The gyroscope’s bias estimate displays a similar dependency on the variations of the Earth’s

Table 4.10.: Reversal measurement gyro test scale factor estimation error budget for varying averaging time. The laboratory is located at $\phi = 45^\circ$

Earth rotation variations

see Subsection 4.2.4

- using WGS84 as reference
- unknown/random time

Test-pad motion

see Subsection 4.2.4

- test-pad isolation neglected
- isotropic background noise

Laboratory alignment

see Subsection 4.2.7, Subsection 4.2.6

- — Leveling error / DoV of 1" (1σ)
- - - North alignment error of 0.01° (1σ)

Sensor alignment

- Orientation error of 0.01° (1σ)

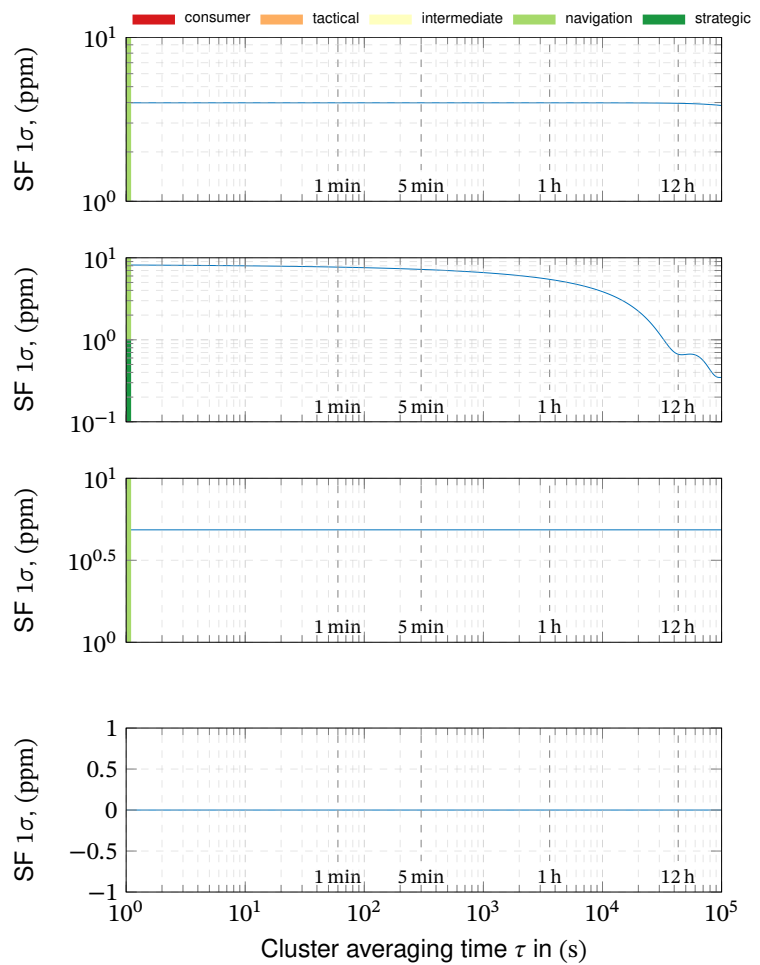


Table 4.11.: Reversal measurement gyro test axis misalignment M_{xy} estimation error budget for varying averaging time. The laboratory is located at $\phi = 45^\circ$

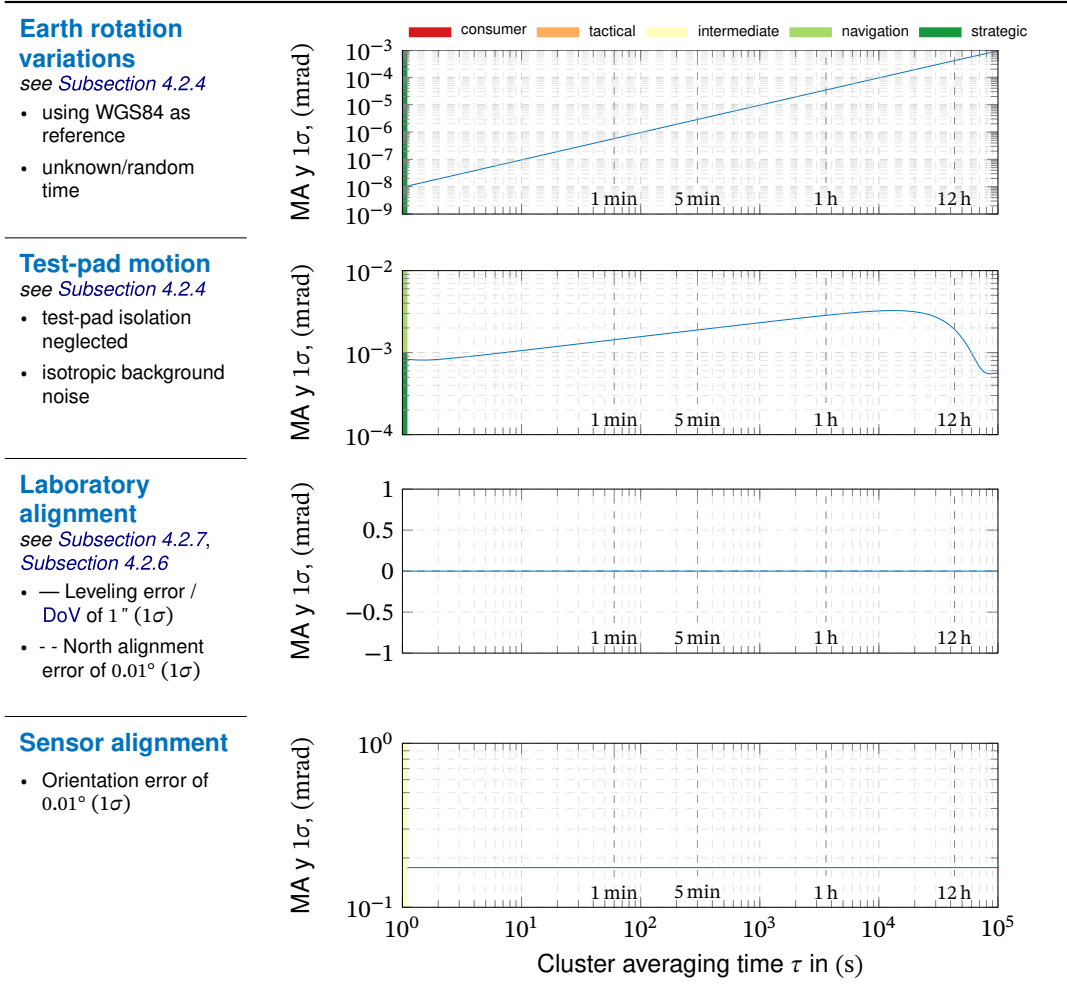
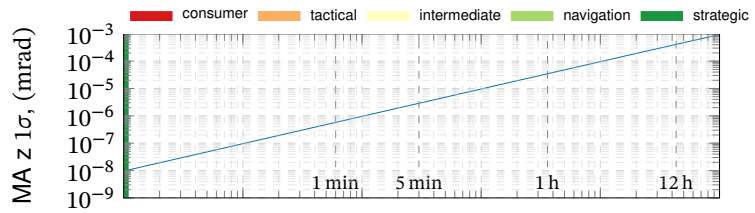


Table 4.12.: Reversal measurement gyro test axis misalignment M_{xz} estimation error budget for varying averaging time. The laboratory is located at $\phi = 45^\circ$

Earth rotation variations

see Subsection 4.2.4

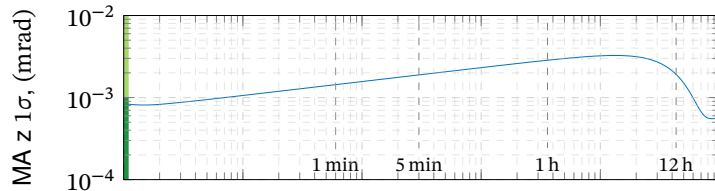
- using WGS84 as reference
- unknown/random time



Test-pad motion

see Subsection 4.2.4

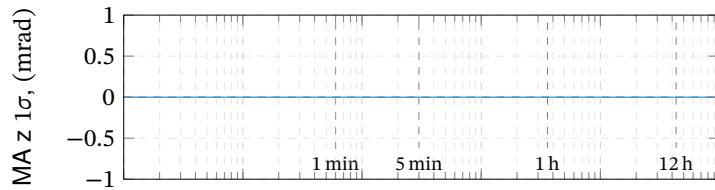
- test-pad isolation neglected
- isotropic background noise



Laboratory alignment

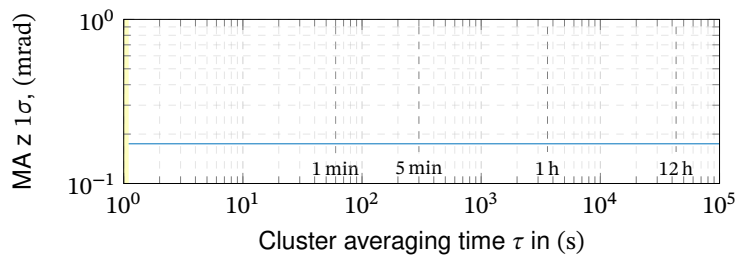
see Subsection 4.2.7, Subsection 4.2.6

- — Leveling error / DoV of 1" (1σ)
- - - North alignment error of 0.01° (1σ)



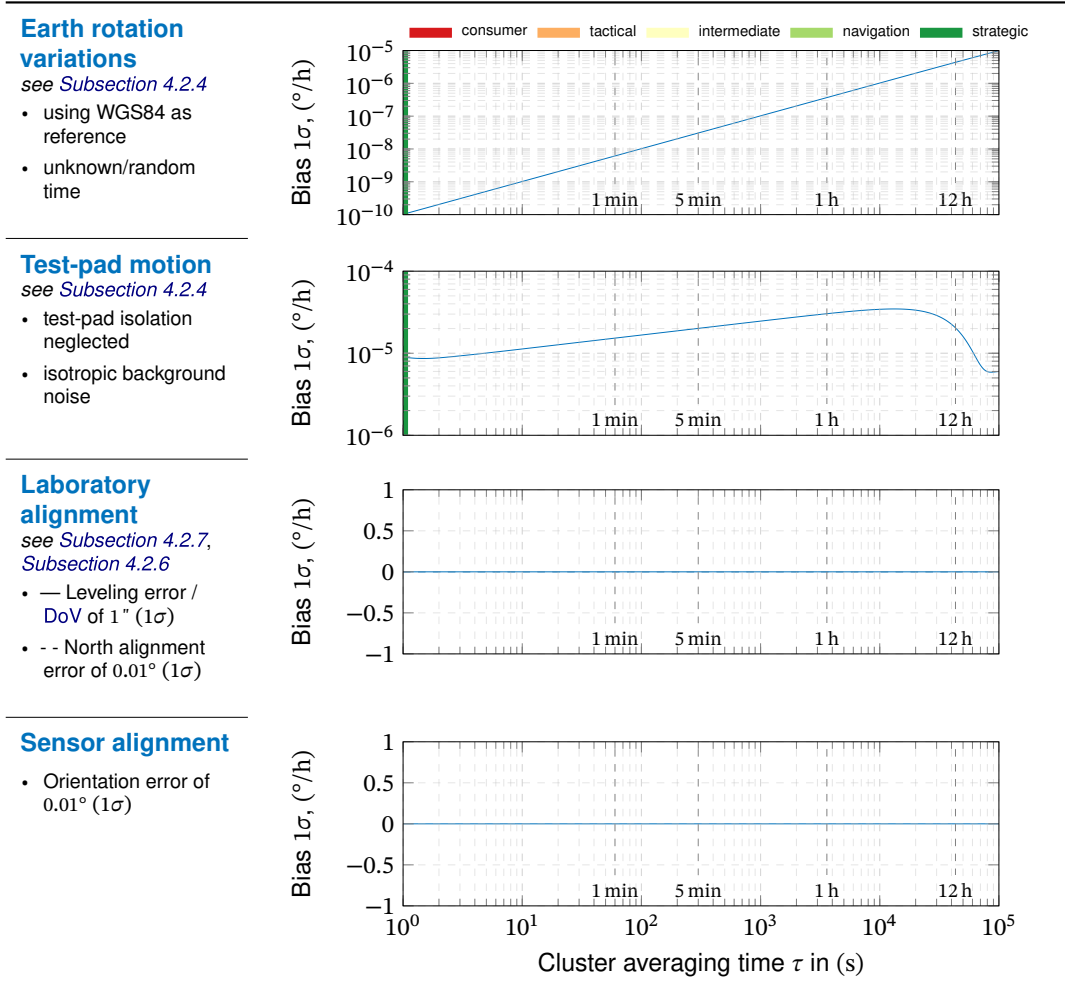
Sensor alignment

- Orientation error of 0.01° (1σ)



angular rates and the test-pad motion. As both local components of the Earth’s angular rate are flipped, sensor alignment and laboratory alignment errors are altogether canceled out. This bias estimate is not only independent of alignment errors but also from the sensor’s internal misalignment. It thus provides a more accurate estimate than the single position test from Subsection 4.4.2.4. However, incorporating two positions increases the effects of the Earth’s angular rate and the test-pad motion.

Table 4.13.: Reversal measurement gyro test bias estimation error budget for varying averaging time. The laboratory is located at $\phi = 45^\circ$



4.4.3.5. Accelerometer Test Error Model

Analogously to the gyroscopes, the accelerometer’s ideal input is simply the local gravity, observed under varying orientations:

$$\hat{\mathbf{f}}_b = \mathbf{R}_{\hat{b}p}^{(P)} \mathbf{I}_{pn} \gamma_n(R_b) \tag{4.214}$$

Linearization of the above ideal input equation for the error terms yields:

$$\begin{aligned}
 \delta \mathbf{f}_b = & \mathbf{R}_{\hat{b}p}^{(P)} \mathbf{I}_{\hat{p}n} \delta \boldsymbol{\gamma}_n - \mathbf{R}_{\hat{b}p}^{(P)} \mathbf{I}_{\hat{p}n} (\hat{\boldsymbol{\gamma}}_n(P_b) \times) \delta \boldsymbol{\Psi}_{n\hat{n}} \\
 & - \mathbf{R}_{\hat{b}p}^{(P)} (\mathbf{I}_{\hat{p}n} \hat{\boldsymbol{\gamma}}_n(P_b)) \times \delta \boldsymbol{\Psi}_{p\hat{p}} - (\mathbf{R}_{\hat{b}p} \mathbf{I}_{\hat{p}n} \hat{\boldsymbol{\gamma}}_n(P_b)) \times \delta \boldsymbol{\Psi}_{b\hat{b}} \\
 & + \mathbf{R}_{\hat{b}p}^{(P)} \mathbf{I}_{\hat{p}n} \hat{\boldsymbol{\Omega}}_{in}^2 \delta \mathbf{r}_n(P_p) + \mathbf{R}_{\hat{b}p}^{(P)} \mathbf{I}_{\hat{p}n} \hat{\boldsymbol{\Omega}}_{in} \delta \dot{\mathbf{r}}_n(P_p) + \mathbf{R}_{\hat{b}n}^{(P)} \delta \ddot{\mathbf{r}}_n(P_p)
 \end{aligned} \tag{4.215}$$

Again, the reference input to the accelerometers is corrupted by variations of the local gravity, test-pad motion and the orientation errors. The last line in the above equation is, in total, represented by the test-pad motion reference models derived in [Subsection 4.2.8](#).

4.4.3.6. Accelerometer Test Error Budget

As the accelerometer tests are performed using the same orientations as the gyroscope tests, the resulting error budgets display a similar overall structure.

The error budget for the accelerometer's linear scale factor is given in [Table 4.14](#). The effects of test-pad motion and variations of the local gravity can be reduced by increasing the averaging time. Already for short averaging times, the achieved SF accuracy is better than 1 ppm. The effects of laboratory and sensor alignment errors are entirely canceled out.

As with the gyroscope tests, the error budgets for the two misalignment angles are equal. The misalignment inaccuracy from test-pad motion can be decreased by averaging. However, the effects of the local gravity variations, mainly due to tides, increase up to about 3 h and display a periodic decrease for higher averaging times. Due to the symmetric poses, the effects of laboratory alignment errors cancel out. Again, the sensor misalignment errors are directly transferred into errors of the misalignment estimates. As with the gyroscope tests, the resulting overall misalignment error from the environmental disturbances is below 1 μ rad.

The error budget for the accelerometer's bias estimate is depicted in [Table 4.17](#). The effects of test-pad motion on the bias estimate are reduced by two orders of magnitude when averaging more than a few minutes. As for the misalignment estimates, the effects from gravity variations increase with averaging times up to 3 h and decrease periodically for longer averaging times. In summary, the errors of the bias estimate from environmental errors are easily below 1 μ g and thus allow the testing of strategic grade sensors. Again, the errors from both laboratory and sensor alignment cancel out, and the bias estimate is also independent of the sensors' internal misalignment errors.

Table 4.14.: Reversal measurement accelerometer test scale factor estimation error budget for varying averaging time. The laboratory is located at $\phi = 45^\circ$

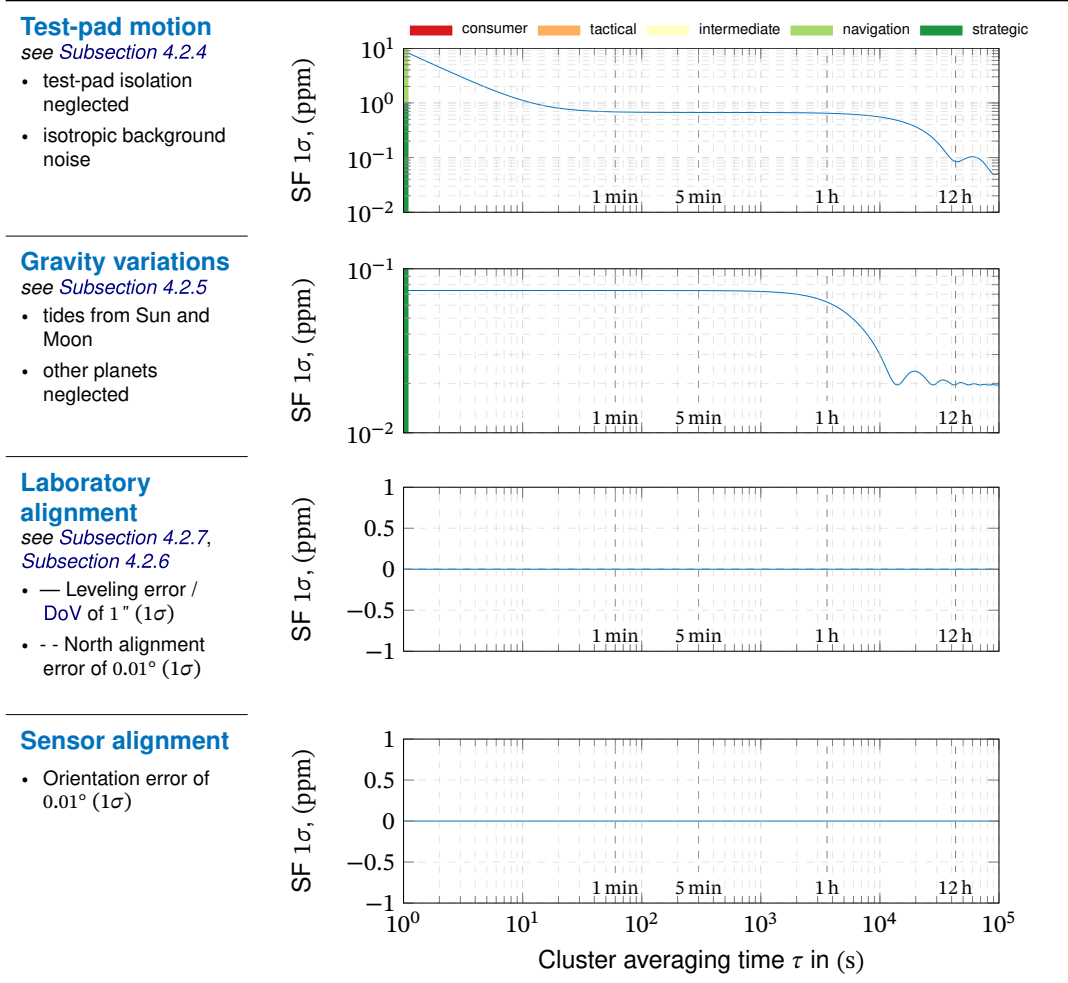
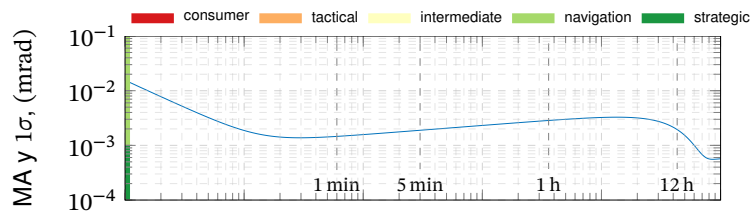


Table 4.15.: Reversal measurement accelerometer test axis misalignment M_{xy} estimation error budget for varying averaging time. The laboratory is located at $\phi = 45^\circ$

Test-pad motion

see Subsection 4.2.4

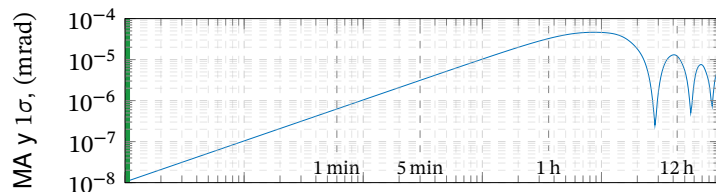
- test-pad isolation neglected
- isotropic background noise



Gravity variations

see Subsection 4.2.5

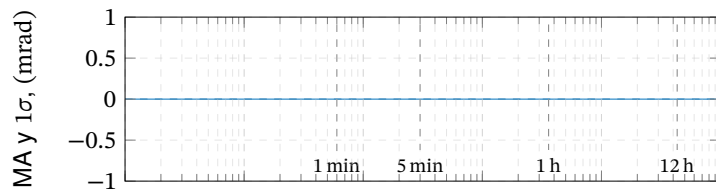
- tides from Sun and Moon
- other planets neglected



Laboratory alignment

see Subsection 4.2.7, Subsection 4.2.6

- — Leveling error / DoV of 1" (1σ)
- - - North alignment error of 0.01° (1σ)



Sensor alignment

- Orientation error of 0.01° (1σ)

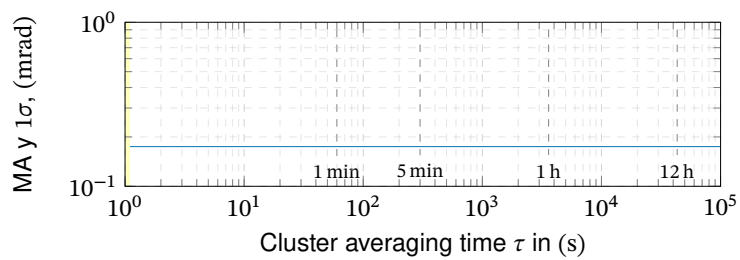


Table 4.16.: Reversal measurement accelerometer test axis misalignment M_{xz} estimation error budget for varying averaging time. The laboratory is located at $\phi = 45^\circ$

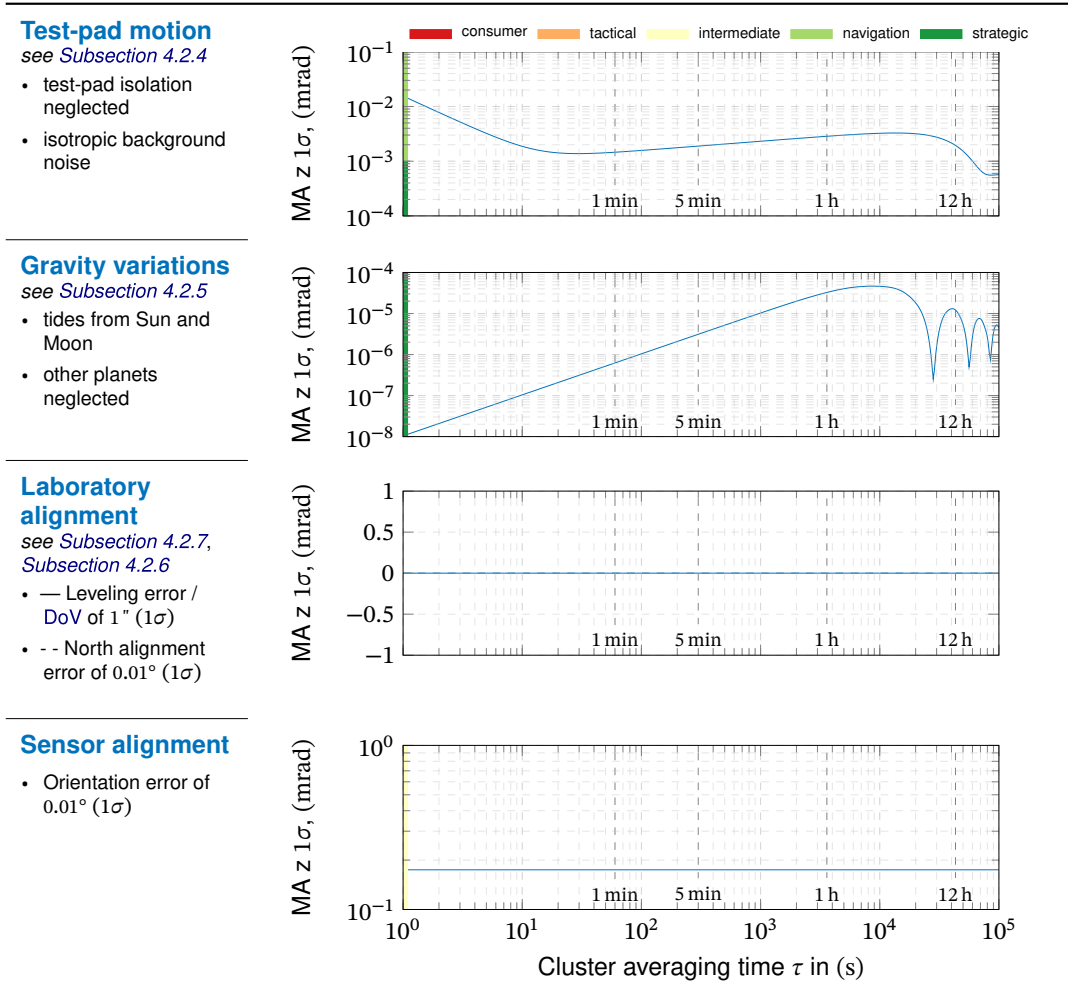


Table 4.17.: Reversal measurement accelerometer test bias estimation error budget for varying averaging time. The laboratory is located at $\phi = 45^\circ$

Test-pad motion

see *Subsection 4.2.4*

- test-pad isolation neglected
- isotropic background noise

Gravity variations

see *Subsection 4.2.5*

- tides from Sun and Moon
- other planets neglected

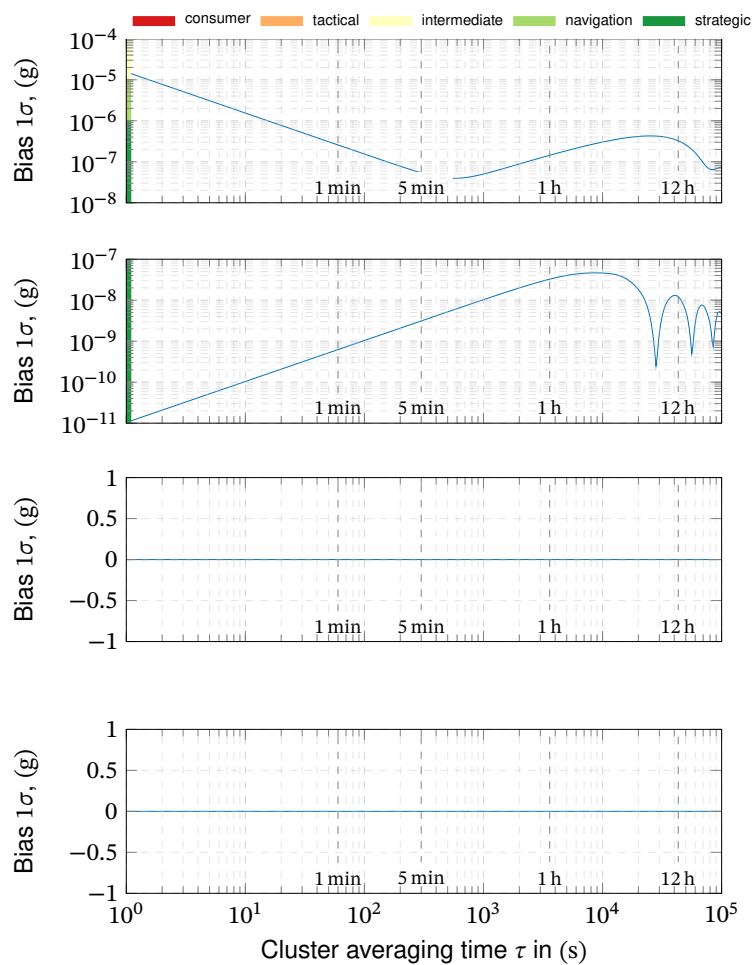
Laboratory alignment

see *Subsection 4.2.7*, *Subsection 4.2.6*

- — Leveling error / DoV of $1''$ (1σ)
- - - North alignment error of 0.01° (1σ)

Sensor alignment

- Orientation error of 0.01° (1σ)



Result 6: Reversal Position Static Tests

Reversal position tests allow the independent determination of a sensor’s linear scale factor, misalignment, and bias. Here, the following observations were made:

- The determination of gyroscope scale factor and misalignment angles from static tests is limited to high accuracy sensors that can use the weak signal of the Earth’s angular rate as reference input. The static tests of the accelerometers do not require a specific sensor grade, as the local gravity is typically a sufficiently strong signal.
- Sensor alignment angles during testing are directly transferred into errors of the sensor’s misalignment estimate.
- To minimize the effects of sensor noise and drift, the averaging time of each position should be set to the global minimum of the sensor’s Allan variance plot.
- The combination of two subsequent measurements yields an increased bias uncertainty from variations of the local gravity and the variations of the Earth’s angular rate.

For the gyroscope, **SF** and **MA** can be tested to strategic grade accuracy, while the bias accuracy reaches navigation grade. Similar results can be achieved for the accelerometers, where the **SF** reaches close to strategic-grade accuracy.

4.4.4. Scale Factor Test-Series

Scale-factor tests, also called rate transfer tests, investigate the relation of the sensor's output to its input over the whole input range. During scale factor tests, the sensors are subjected to a series of different inputs (e.g., angular rates), and the resulting output is recorded. Gyroscope scale factor tests require at least a single-axis rate table. Accelerometer scale factor tests typically require a centrifuge to generate loads of more than 1 g. The input is typically a finite number of points (poses) distributed over the sensor's nominal input range. This test determines the relationship between the static input and the sensor's output, as illustrated in Figure 4.32. In general, there is a non-linear relation between input and output. In the case of hysteresis effects, the scale factor can also depend on the previous inputs [14, p. 226]. Furthermore, the input-output relation is actually frequency-dependent, which is however not considered at the classical scale factor tests. These determine the scale factors at stationary conditions only.

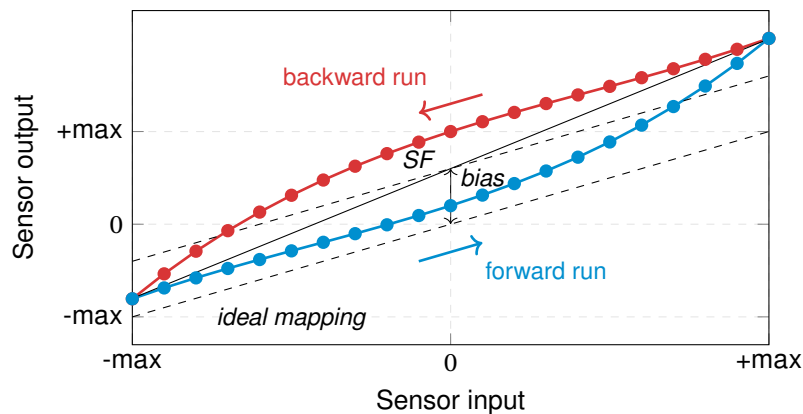


Figure 4.32.: Non-linear input-output relation and hysteresis.

To reduce external disturbances and the effects of sensor noise, each data point in the scale factor test series is determined by holding the constant input for a given time and averaging the sensor's output. Based on the data sets obtained from the scale factor test series, a nominal input-output mapping function is determined by fitting, e.g., a polynomial to the data points. In the most simple form, a simple linear model is used. In this case, the line's slope is the constant scale factor. Asymmetries in the test data may be handled by using different models or at least parameters for positive and negative inputs [22, p. 252].

The residuals of the fitted model are usually used to describe the scale factor errors, in the case of a linear model also called *scale factor linearity error*. This may be specified either as **Root Mean Square Error (RMSE)** or as the maximum error. The different errors for positive and negative inputs may also be used to describe the sensor's residual asymmetry errors. The scale factor tests should be repeated at different environmental conditions, to determine the scale factor's stability and environmental dependency [10, 25, 12].

4.4.4.1. Test Description and Parameter Estimation

The scale factor tests aim at determining an unknown scaling function $s()$ that maps the sensor's input to its output. A simple single-axis measurement model that incorporates the sensor bias b_G , noise ν_G , linear misalignment θ and non-linear scaling function $s(\omega)$, is given as:

$$\tilde{\omega}_{ib} = s(\hat{\omega}_{ib,x} + \delta\omega_{ib,x}) + M_{G,y}\hat{\omega}_{ib,y} + M_{G,z}\hat{\omega}_{ib,z} + b_G + \nu_G \quad (4.216)$$

$$\tilde{f}_b = s(\hat{f}_{b,x} + \delta f_{b,x}) + M_{G,y}\hat{f}_{b,y} + M_{G,z}\hat{f}_{b,z} + b_A + \nu_A \quad (4.217)$$

Above used misalignment terms, M are a linearization of the (non-linear) scale factor function for the off-axis components of the input

$$M_{G,y} = \frac{\partial s(\hat{\omega})}{\partial \hat{\omega}_{ib,y}} \quad M_{G,z} = \frac{\partial s(\hat{\omega})}{\partial \hat{\omega}_{ib,z}} \quad (4.218)$$

as the misalignment of the axis causes a physical pick-off of the signals orthogonal to the nominal input axis. Therefore, these components are also affected by the (non-linear) scale factor function $s()$:

$$\tilde{\omega}_{ib} = s(\hat{\omega}_{ib,x} + \delta\omega_{ib,x} - \sin(\Phi_{\hat{b}b}) \hat{\omega}_{ib,y} + \sin(\Theta_{\hat{b}b}) \hat{\omega}_{ib,z}) + b_G + \nu_G \quad (4.219)$$

$$\tilde{f}_b = s(\hat{f}_{b,x} + \delta f_{b,x} - \sin(\Phi_{\hat{b}b}) \hat{f}_{b,y} + \sin(\Theta_{\hat{b}b}) \hat{f}_{b,z}) + b_A + \nu_A \quad (4.220)$$

In the following analysis, the misalignment errors will be considered in the form of the angles $\Phi_{\hat{b}b}, \Theta_{\hat{b}b}$. Typically, the static input-output mapping function is approximated as a polynomial:

$$s(\omega) = c_p\omega^p + \dots + c_1\omega + c_0 \quad (4.221)$$

For clarity, the following equations refer only to the gyroscope measurements. However, they are equally valid for accelerometer measurements. Note that the sensor bias in (4.219) and (4.220) can either be expressed by c_0 or b_G . The classical approach is to determine the polynomial coefficients from a least-squares-estimate [26]. The scale factor test series returns a set of n equations that link the averaged sensor output $\bar{\omega}_i$ with the (ideal) static inputs $\hat{\omega}_i$ by the polynomial coefficients c_p to c_0 :

$$\underbrace{\begin{bmatrix} \bar{\omega}_1 \\ \bar{\omega}_2 \\ \vdots \\ \bar{\omega}_n \end{bmatrix}}_{\bar{y}} = \underbrace{\begin{bmatrix} \hat{\omega}_1^p & \hat{\omega}_1^{p-1} & \dots & \hat{\omega}_1 & 1 \\ \hat{\omega}_2^p & \hat{\omega}_2^{p-1} & \dots & \hat{\omega}_2 & 1 \\ \vdots & \vdots & & \vdots & \vdots \\ \hat{\omega}_n^p & \hat{\omega}_n^{p-1} & \dots & \hat{\omega}_n & 1 \end{bmatrix}}_{\mathbf{H}} \underbrace{\begin{bmatrix} c_p \\ c_{p-1} \\ \vdots \\ c_1 \\ c_0 \end{bmatrix}}_{\mathbf{c}} + \underbrace{\begin{bmatrix} \bar{\nu}_1 \\ \bar{\nu}_2 \\ \vdots \\ \bar{\nu}_n \end{bmatrix}}_{\bar{v}} \quad (4.222)$$

The standard approach to solving the above over-determined system of equations is the classical least-squares fit, here expressed using the pseudo-inverse of \mathbf{H} [72, p. 781]:

$$\hat{c} = (\mathbf{H}^T \mathbf{H})^{-1} \mathbf{H}^T \hat{\mathbf{y}} \quad (4.223)$$

$$\mathbf{P}_{\hat{c}\hat{c}} = (\mathbf{H}^T \mathbf{H})^{-1} \mathbf{H}^T \mathbf{Q}_{\hat{\mathbf{y}}\hat{\mathbf{y}}} \mathbf{H} (\mathbf{H}^T \mathbf{H})^{-1} \quad (4.224)$$

Such a least-squares estimation of a non-linear static process, however, is only consistent if certain assumptions are met [170, p. 212]:

- The input signal must be exactly measurable, which means \mathbf{H} is error free.
- $\det(\mathbf{H}^T \mathbf{H}) \neq 0$.
- The measurement error of y is stationary and zero-mean.
- The input signals, and consequently \mathbf{H} , are independent of the measurement errors.

The first assumption neglects the sensor's input errors, which are environmental disturbances and rate table errors. This assumption can be justified if the sensor's noise is much higher than the input errors. However, this assumption is not necessarily met for high-accuracy sensors. In this case, an errors-in-variables approach, like total-leas-squares [171], can be used to consider the input uncertainty and thus improve the estimation consistency. Additionally, the input errors are correlated due to the slow noise processes in the environmental disturbances. As the rate table errors may also depend on the commanded angular rate, the magnitude of the input errors may differ for each data point. Furthermore, also the output errors are non-stationary. As discussed before, the variances of, e.g., bias instability noise grows with time, so the cluster averages' uncertainty increases with each position of the scale factor test series.

Although the requirements for a consistent estimation are violated, the classical least-squares estimate is still the standard approach for scale factor (function) estimation [26]. Suppose the scale factor polynomial coefficients are estimated using the classical (and non-weighted) least-squares. In that case, the estimates are not only sub-optimal, but also the covariance estimate (4.224) is too low. Using the linearization of the estimated scale factor function $s(\omega)$, the contribution of the input errors can be included to get an approximation of the parameter estimate's total covariance $\mathbf{P}_{\hat{c}\hat{c}}$:

$$\mathbf{P}_{\hat{c}\hat{c}} = (\mathbf{H}^T \mathbf{H})^{-1} \mathbf{H}^T \left[\mathbf{Q}_{\hat{\mathbf{y}}} + \left(\frac{\partial \hat{\mathbf{y}}}{\partial \omega_{ib}} \right) \Big|_c \mathbf{Q}_{\delta \omega_{ib}} \left(\frac{\partial \hat{\mathbf{y}}}{\partial \omega_{ib}} \right) \Big|_c^T \right] \mathbf{H} (\mathbf{H}^T \mathbf{H})^{-1} \quad (4.225)$$

where $\mathbf{P}_{\hat{\mathbf{y}}}$ is the covariance matrix of the averaged sensor noise and $\mathbf{P}_{\delta \omega_{ib} \delta \omega_{ib}}$ the covariance of the averaged input disturbances for each signal cluster of the scale factor test series.

Before discussing the errors that form above covariance matrices, some relations and dependencies of the least-squares fitting should be noted:

1. **Number of poses.** In the classical least-square estimation with uncorrelated measurement errors for each position, the estimation variance decreases with the number of positions. For realistic sensor noise, however, the cluster averages are correlated.

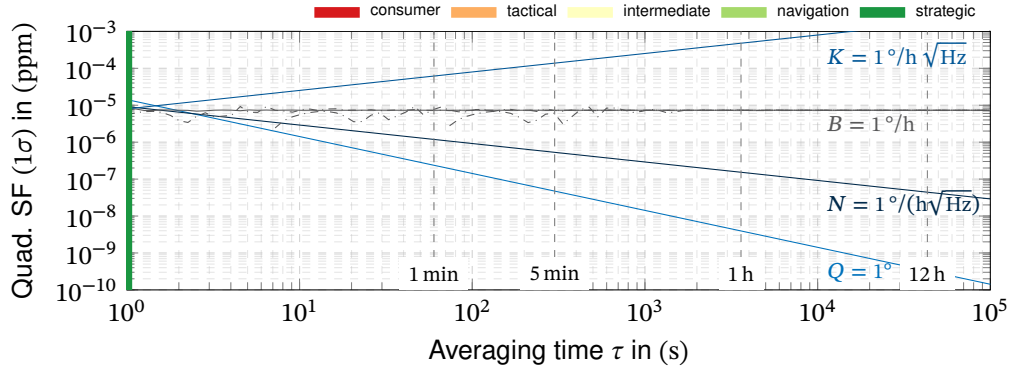
2. **Correlation of cluster means.** The correlation between the position averages affects how the measurement uncertainty is distributed on the scale factor and bias estimates. The higher the correlation, the more the noise resembles a constant error which corrupts the bias estimate, while the scale factor estimate is less affected by the noise. Consequently, a high correlation between the clusters is desired for a scale factor test series. An optimal position length (cluster time) can thus be determined from the minimum of the Allan variance plots, which corresponds to a maximum correlation between the cluster means.
3. **Maximum input rates.** The sensor's measurement noise is assumed to be widely independent of the input. Increasing the input rates of the test positions thus yields an immediate increase in the signal-to-noise ratio and thus the accuracy of the scale factor estimate.

4.4.4.2. Effects of Sensor Noise

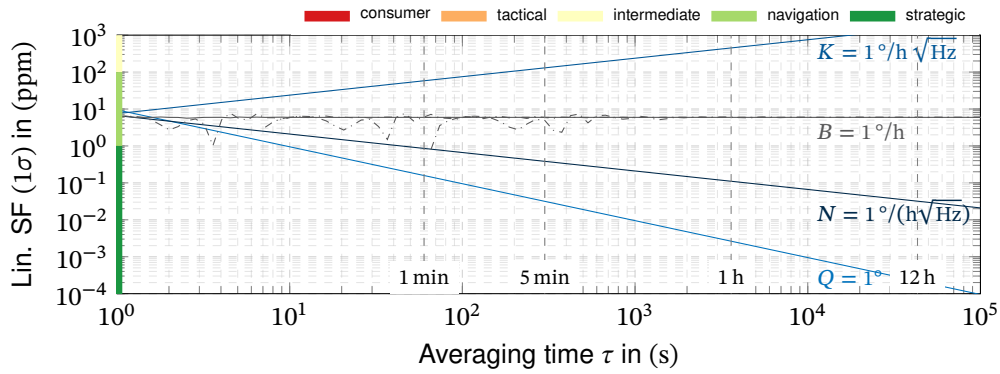
For the scale factor test, the estimation depends on the chosen scale factor polynomial to be estimated and the number and magnitudes of the applied angular rates. A universal error budget for the sensor noise can thus not be given. However, the general effects of sensor noise processes on the estimation accuracy are similar and differ in the scaling only. An example of the effects of sensor noise on a quadratic and linear SF and the bias estimation from a SF test series is depicted in [Figure 4.33](#). The general effect of the different sensor noise processes on the estimation results is very similar to the behavior already discussed for the reversal measurement tests in [Subsection 4.4.3](#). The graphs for the bias estimate are equal to the ones of the static reversal tests. For all parameters, a variation of the effects of the bias instability can be observed for averaging times smaller than the bias instability's time constant. Independent of this ripple, the bias instability poses again the already known limit for the estimation accuracy that cannot be reduced by averaging.

Since the sensor's noise is widely independent of the applied angular rate, the signal-to-noise ratio for the scale factor estimation can be easily improved by increasing the applied angular rates.

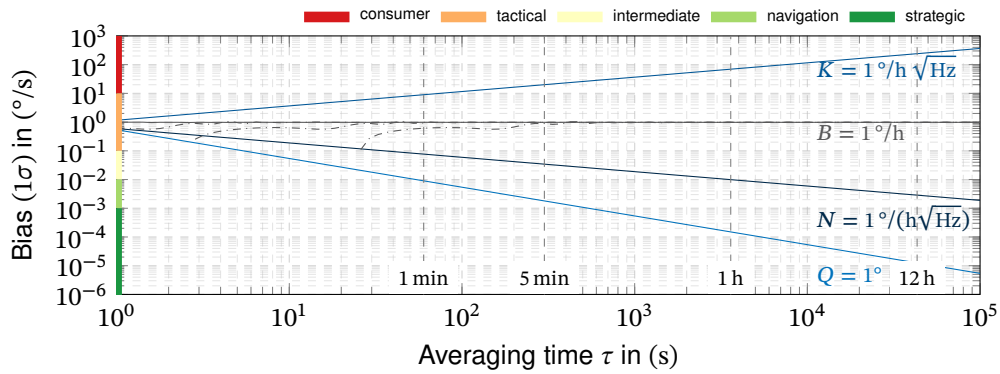
As discussed before, the effect of long-term drift like bias-instability and rate random walk grows with the test duration. This introduces additional bias-like errors to the pose averages that increasingly deviate from the sensor's initial bias and thus disturb the scale factor estimation. This effect can be considered by using the weighted least-squares estimation, where the weighting matrix is the inverse of the cluster's noise covariance matrix. The effect is demonstrated in [Example 7](#).



(a) Gyroscope quadratic scale factor standard deviation.



(b) Gyroscope linear scale factor standard deviation.



(c) Gyroscope bias standard deviation.

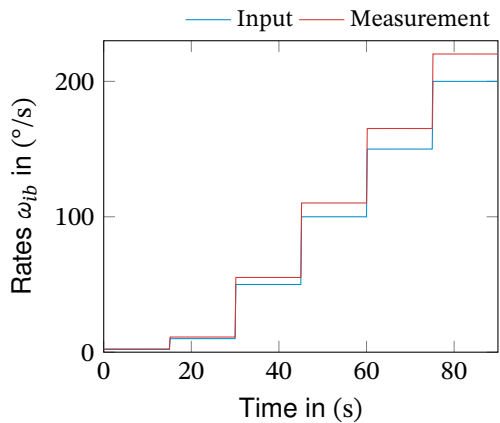
Figure 4.33.: Scale-factor test series gyroscope error variance from sensor noise for varying averaging time τ per pose. The graphs depict an example SF test series with 6 positions at rates of [1, 5, 10, 20, 100, 200] $^{\circ}$ /s.

Example 7: The effect of gyroscope drift on the scale factor estimation

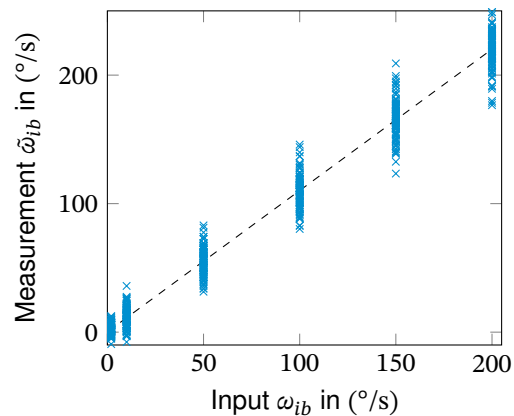
This example illustrates the effect of long-term gyroscope drift on the scale factor test. To demonstrate the effect of long-term drift, the test scenario with an overemphasized long-term drift is created:

Angular rates	[2, 10, 50, 100, 150, 200]°/s	$\Rightarrow \mathbf{Q}_{\bar{y}} = \begin{bmatrix} 1.1 & 2.2 & 3.3 & 4.4 & 5.4 & 6.5 \\ 2.2 & 4.4 & 6.6 & 8.7 & 10.8 & 12.9 \\ 3.3 & 6.6 & 9.9 & 13.1 & 16.2 & 19.4 \\ 4.3 & 8.7 & 13.1 & 17.4 & 21.6 & 25.9 \\ 5.4 & 10.8 & 16.2 & 21.6 & 27.0 & 32.3 \\ 6.5 & 12.9 & 19.4 & 25.9 & 32.3 & 38.8 \end{bmatrix} \text{ (}^\circ/\text{h)}^2$
Cluster time	900 s	
Angular RW	$1 \cdot 10^{-3} \text{ }^\circ/(\sqrt{\text{h}})$	
Bias instability	$1 \text{ }^\circ/\text{h}, T_c = 100 \text{ s}$	
Rate RW	$100 \text{ }^\circ/\text{h}^{3/2}$	
Rate ramp	$1000 \text{ }^\circ/\text{h}^2$	
True SF	1.1	
True bias	$0.2 \text{ }^\circ/\text{s}$	

The resulting input rates and sensor outputs are depicted below. A Monte-Carlo simulation with 1000 runs has been performed to determine the error statistics of the scale factor and bias estimation error. Note that the errors in the scatter plot have been magnified by a factor of 500 to make the variation of the pose averages visible.



(7.a) Input and sample measurement realization.



(7.b) Scale factor estimation.

Using the inverse noise covariance matrix as the weighting matrix, the higher uncertainty of the later positions can be considered in the least-squares estimation. This puts less weight on the last positions and considers the correlation between the position means. The resulting error statistics are given below:

	SF error		Bias error (°/s)	
	Mean	Variance	Mean	Variance
Ordinary least-squares	$1.61 \cdot 10^{-3}$	$2.20 \cdot 10^{-8}$	$6.40 \cdot 10^{-2}$	$1.72 \cdot 10^{-4}$
Weighted least-squares	$1.51 \cdot 10^{-4}$	$8.14 \cdot 10^{-8}$	$-3.55 \cdot 10^{-2}$	$1.31 \cdot 10^{-4}$

Considering the long-term drift increases the estimation consistency of the scale factor by one order of magnitude in this example. This effect increases with the overall test duration and is thus especially relevant if sensors with high long-term drift (e.g., **Micro-Electro-Mechanical System (MEMS)**) shall be tested for long times. The test duration should be chosen at the minimum of the sensor's **AVAR** curve to minimize the variation of the cluster means.

4.4.4.3. Gyroscope Test Error Model

Gyroscope scale factor tests require creating a series of constant angular rates and thus at least a single rate-table axis (scenario I). In the case of a two or three-axis rate table, the additional axes can be used to control the orientation of either the sensor or the rotation axis. Like this, the rotation axis could be oriented so that the sensor's axis is not affected by the Earth's angular rate. Suppose the scale factor tests are performed on a multi-axis rate table. In that case, there are multiple possibilities to create the reference motion: One option is to use the table's inner axis to perform the scale factor rotation series and the other axes to align the input axis perpendicular to the Earth's angular rate and the local gravity (scenario II). In this case, the sensor is subject to a sinusoidal acceleration input that may alter the sensor output in case of an acceleration sensitivity. Therefore, other orientations should be preferred if an acceleration sensitivity is expected.

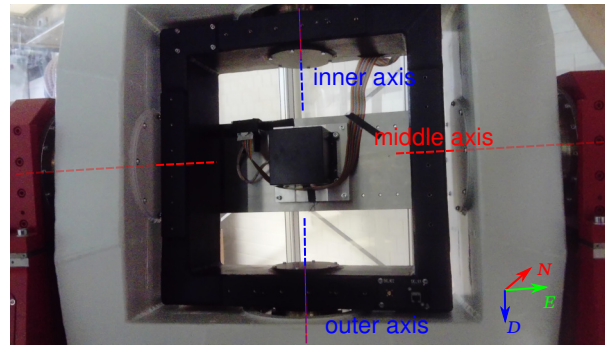


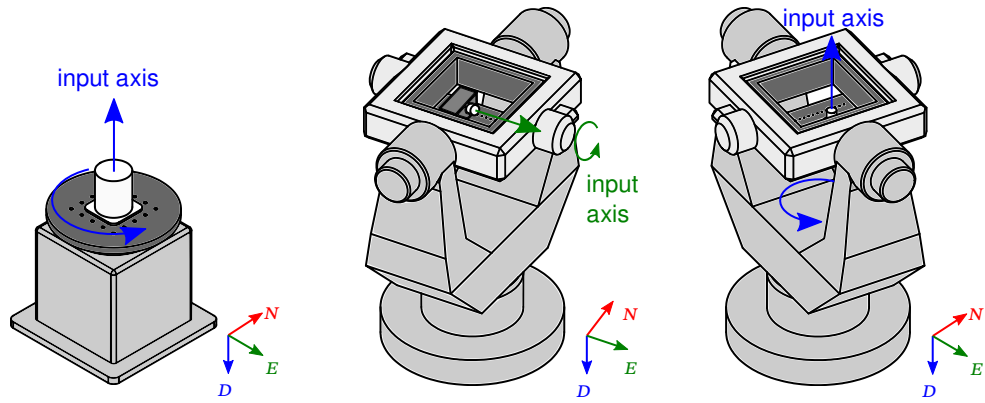
Figure 4.34.: IFOS-500 IMU mounted to a three-axis rate table. The unit's center of measurement (actually of its accelerometer triad) is placed in the intersection point of all three-rotation axes. The rate table's inner and outer axes coincide in the depicted position.

For a three-axis table, the scale factor series may be performed with the table's outer axis. In this case, the sensor's orientation relative to the reference rotation can be easily changed using the two inner axes, eliminating the need for remounting the sensor triad (scenario III). These three options are illustrated in Figure 4.35. The three test setups result in different kinematic chains, errors, and sensitivities.

For the single vertical axis rate table, the kinematics yield the following ideal sensor inputs $\hat{\omega}_{ib}^I$ and linearized input errors $\delta\omega_{ib}^I$:

$$\hat{\omega}_{ib}^I = \mathbf{R}_{bu} (\mathbf{R}_{uv}(t) \mathbf{I}_{vn} \mathbf{R}_{ne} \hat{\omega}_{ie}) + \hat{\omega}_{vu} \quad (4.226)$$

$$\begin{aligned} \delta\omega_{ib}^I = & \mathbf{R}_{bu} \delta\omega_{vu} + \mathbf{R}_{bu} \mathbf{R}_{uv}(t) \mathbf{I}_{vp} (\mathbf{I}_{pn} \mathbf{R}_{ne} \delta\omega_{ie} + \delta\omega_{np}) \\ & - [\mathbf{R}_{bu} (\mathbf{R}_{uv}(t) \mathbf{I}_{vn} \mathbf{R}_{ne} \hat{\omega}_{ie}) + \hat{\omega}_{vu}] \times \psi_{bb} \\ & - \mathbf{R}_{bu} [\mathbf{R}_{uv}(t) \mathbf{I}_{vn} \mathbf{R}_{ne} \hat{\omega}_{ie}] \times \psi_{au} \\ & - \mathbf{R}_{bu} \mathbf{R}_{uv}(t) [\mathbf{I}_{vn} \mathbf{R}_{ne} \hat{\omega}_{ie}] \times \psi_{ov} \\ & - \mathbf{R}_{bu} \mathbf{R}_{uv}(t) \mathbf{I}_{vp} [\mathbf{I}_{pn} \mathbf{R}_{ne} \hat{\omega}_{ie}] \times \psi_{pp} \\ & - \mathbf{R}_{bu} \mathbf{R}_{uv}(t) \mathbf{I}_{vn} [\mathbf{R}_{ne} \hat{\omega}_{ie}] \times \psi_{nn} \end{aligned} \quad (4.227)$$



(a) Single axis rate table, vertically aligned (I). (b) Rotation of the inner axis, axis orientation set (II). (c) Rotation of the outer axis, sensor orientation set (III).

Figure 4.35.: Possible instrument configurations for gyroscope scale factor testing.

For the single axis rate table, the tested sensor axis is aligned with the table's vertical (z_b) axis. The angular rate error input to the sensor axis is thus given as:

$$\hat{\omega}_{ib}^I = \hat{\omega}_{vu} + \hat{\omega}_{ie} \sin \phi \quad (4.228)$$

$$\begin{aligned} \delta\omega_{ib}^I = & \delta\omega_{vu} - \cos(\phi) \cos(\lambda) \delta\omega_{ie,x} - \cos(\phi) \sin(\lambda) \delta\omega_{ie,y} - \sin(\phi) \delta\omega_{ie,z} + \delta\omega_{np,z} \\ & + \cos \Psi_{uv}(t) \hat{\omega}_{ie} \cos \phi (\Theta_{\hat{b}b} + \Theta_{\hat{u}u}) + \sin \Psi_{uv}(t) \hat{\omega}_{ie} \cos \phi (\Phi_{\hat{b}b} + \Phi_{\hat{u}u}) \\ & + \hat{\omega}_{ie} \cos \phi (\Theta_{\hat{v}v} + \Theta_{\hat{p}p} + \Theta_{\hat{n}n}) \end{aligned} \quad (4.229)$$

In case of a three-axis rate table, whose inner axis is aligned to the local west-east direction, the ideal and error angular rates are given as:

$$\hat{\omega}_{ib}^{II} = \mathbf{R}_{\hat{b}u} \left(\mathbf{R}_{\hat{u}v}(t) \underbrace{\mathbf{R}_{\hat{v}w}}_{\mathbf{R}_x(-90^\circ)} \underbrace{\mathbf{R}_{\hat{w}p}}_{\mathbf{R}_z(-90^\circ)} \mathbf{I}_{\hat{p}n} \mathbf{R}_{\hat{n}e} \hat{\omega}_{ie} \right) + \hat{\omega}_{vu} \quad (4.230)$$

$$\begin{aligned} \delta\omega_{ib}^{II} = & \mathbf{R}_{\hat{b}u} \delta\omega_{vu} + \mathbf{R}_{\hat{b}u} \mathbf{R}_{\hat{u}v}(t) \mathbf{R}_{\hat{v}w} \delta\omega_{wv} + \mathbf{R}_{\hat{b}u} \mathbf{R}_{\hat{u}v}(t) \mathbf{R}_{\hat{v}w} \delta\omega_{pw} \\ & + \mathbf{R}_{\hat{b}u} \mathbf{R}_{\hat{u}v}(t) \mathbf{R}_{\hat{v}w} \mathbf{R}_{\hat{w}p} (\mathbf{I}_{\hat{p}n} \mathbf{R}_{\hat{n}e} \delta\omega_{ie} + \delta\omega_{np}) \\ & - [\mathbf{R}_{\hat{b}u} (\mathbf{R}_{\hat{u}v}(t) \mathbf{R}_{\hat{v}w} \mathbf{R}_{\hat{w}p} \mathbf{R}_{\hat{n}e} \hat{\omega}_{ie}) + \hat{\omega}_{vu}] \times \psi_{\hat{b}b} \\ & - \mathbf{R}_{\hat{b}u} [\mathbf{R}_{\hat{u}v}(t) \mathbf{R}_{\hat{v}w} \mathbf{R}_{\hat{w}p} \mathbf{I}_{\hat{p}n} \mathbf{R}_{\hat{n}e} \hat{\omega}_{ie} + \hat{\omega}_{vu}] \times \psi_{\hat{u}u} \\ & - \mathbf{R}_{\hat{b}u} \mathbf{R}_{\hat{u}v}(t) [\mathbf{R}_{\hat{v}w} \mathbf{R}_{\hat{w}p} \mathbf{I}_{\hat{p}n} \mathbf{R}_{\hat{n}e} \hat{\omega}_{ie}] \times \psi_{\hat{v}v} \\ & - \mathbf{R}_{\hat{b}u} \mathbf{R}_{\hat{u}v}(t) \mathbf{R}_{\hat{v}w} [\mathbf{R}_{\hat{w}p} \mathbf{I}_{\hat{p}n} \mathbf{R}_{\hat{n}e} \hat{\omega}_{ie}] \times \psi_{\hat{w}w} \\ & - \mathbf{R}_{\hat{b}u} \mathbf{R}_{\hat{u}v}(t) \mathbf{R}_{\hat{v}w} \mathbf{R}_{\hat{w}p} [\mathbf{I}_{\hat{p}n} \mathbf{R}_{\hat{n}e} \hat{\omega}_{ie}] \times \psi_{\hat{p}p} \\ & - \mathbf{R}_{\hat{b}u} \mathbf{R}_{\hat{u}v}(t) \mathbf{R}_{\hat{v}w} \mathbf{R}_{\hat{w}p} \mathbf{I}_{\hat{p}n} [\mathbf{R}_{\hat{n}e} \hat{\omega}_{ie}] \times \psi_{\hat{n}n} \end{aligned} \quad (4.231)$$

The ideal angular rate and the angular rate error along the tested axis is then determined to:

$$\begin{aligned}
 \hat{\omega}_{ib}^{\text{II}} &= \hat{\omega}_{vu} \\
 \delta\omega_{ib}^{\text{II}} &= \delta\omega_{vu,z} - \sin(\lambda)\delta\omega_{ie,x} + \cos(\lambda)\delta\omega_{ie,y} + \delta\omega_{np,y} \\
 &\quad - \hat{\omega}_{ie} (-\cos\Psi_{uv}(t)\cos\phi - \sin\Psi_{uv}(t)\sin\phi) (\Phi_{\hat{b}b} + \Phi_{\hat{u}u}) \\
 &\quad - \hat{\omega}_{ie} (\sin\Psi_{uv}(t)\cos\phi - \cos\Psi_{uv}(t)\sin\phi) (\Theta_{\hat{b}b} + \Theta_{\hat{u}u}) \\
 &\quad - \hat{\omega}_{ie} \sin\phi (\Phi_{\hat{v}v} + \Phi_{\hat{w}w} - \Theta_{\hat{p}p} - \Phi_{\hat{n}n}) \\
 &\quad - \hat{\omega}_{ie} \cos\phi (\Theta_{\hat{v}v} + \Psi_{\hat{w}w} + \Psi_{\hat{p}p} - \Psi_{\hat{n}n})
 \end{aligned} \tag{4.232}$$

For the third case, a three-axis rate table with the reference rotation created by the outer axis, the ideal and error angular rates yield:

$$\begin{aligned}
 \hat{\omega}_{ib}^{\text{III}} &= \mathbf{R}_{\hat{b}u}\mathbf{I}_{\hat{u}w}(\mathbf{R}_{\hat{w}p}(t)\mathbf{I}_{\hat{p}n}\mathbf{R}_{\hat{n}e}\hat{\omega}_{ie}) + \hat{\omega}_{pw} \\
 \delta\omega_{ib}^{\text{III}} &= \mathbf{R}_{\hat{b}u}\delta\omega_{vu} + \mathbf{R}_{\hat{b}u}\mathbf{R}_{\hat{u}v}\delta\omega_{wv} + \mathbf{R}_{\hat{b}u}\mathbf{R}_{\hat{u}v}\mathbf{R}_{\hat{v}w}\delta\omega_{pw} \\
 &\quad + \mathbf{R}_{\hat{b}u}\mathbf{R}_{\hat{v}w}\mathbf{R}_{\hat{w}p}(t)(\mathbf{I}_{\hat{p}n}\mathbf{R}_{\hat{n}e}\delta\omega_{ie} + \delta\omega_{np}) \\
 &\quad - [\mathbf{R}_{\hat{b}u}\mathbf{R}_{\hat{u}v}\mathbf{R}_{\hat{v}w}(\mathbf{R}_{\hat{w}p}(t)\mathbf{I}_{\hat{p}n}\mathbf{R}_{\hat{n}e}\hat{\omega}_{ie} + \hat{\omega}_{pw})] \times \psi_{\hat{b}b} \\
 &\quad - \mathbf{R}_{\hat{b}u}[\mathbf{R}_{\hat{u}v}\mathbf{R}_{\hat{v}w}(\mathbf{R}_{\hat{w}p}(t)\mathbf{I}_{\hat{p}n}\mathbf{R}_{\hat{n}e}\hat{\omega}_{ie} + \hat{\omega}_{pw})] \times \psi_{\hat{u}u} \\
 &\quad - \mathbf{R}_{\hat{b}u}\mathbf{R}_{\hat{u}v}[\mathbf{R}_{\hat{v}w}(\mathbf{R}_{\hat{w}p}(t)\mathbf{I}_{\hat{p}n}\mathbf{R}_{\hat{n}e}\hat{\omega}_{ie} + \hat{\omega}_{pw})] \times \psi_{\hat{v}v} \\
 &\quad - \mathbf{R}_{\hat{b}u}\mathbf{R}_{\hat{u}v}\mathbf{R}_{\hat{v}w}[\mathbf{R}_{\hat{w}p}(t)\mathbf{I}_{\hat{p}n}\mathbf{R}_{\hat{n}e}\hat{\omega}_{ie} + \hat{\omega}_{pw}] \times \psi_{\hat{w}w} \\
 &\quad - \mathbf{R}_{\hat{b}u}\mathbf{R}_{\hat{u}v}\mathbf{R}_{\hat{v}w}\mathbf{R}_{\hat{w}p}(t)[\mathbf{I}_{\hat{p}n}\mathbf{R}_{\hat{n}e}\hat{\omega}_{ie}] \times \psi_{\hat{p}p} \\
 &\quad - \mathbf{R}_{\hat{b}u}\mathbf{R}_{\hat{u}v}\mathbf{R}_{\hat{v}w}\mathbf{R}_{\hat{w}p}(t)\mathbf{I}_{\hat{p}n}[\mathbf{R}_{\hat{n}e}\hat{\omega}_{ie}] \times \psi_{\hat{n}n}
 \end{aligned} \tag{4.233}$$

In this setup, the two inner gimbals are used to align different sensor axis with the rate table's outer rotation axis. Along the tested sensor axis, these nominal and linearized error angular rates are given as:

$$\hat{\omega}_{ib}^{\text{III}} = \hat{\omega}_{pw} + \hat{\omega}_{ie} \sin\phi \tag{4.235}$$

$$\begin{aligned}
 \delta\omega_{ib}^{\text{III}} &= \delta\omega_{pw,z} + \delta\omega_{vu,z} + \delta\omega_{np,z} \\
 &\quad - \cos(\phi)\cos(\lambda)\delta\omega_{ie,x} - \cos(\phi)\sin(\lambda)\delta\omega_{ie,y} - \sin(\phi)\delta\omega_{ie,z} \\
 &\quad + \sin\Psi_{wp}(t)\hat{\omega}_{ie}\cos\phi(\Theta_{\hat{b}b} + \Theta_{\hat{u}u} + \Theta_{\hat{v}v} + \Theta_{\hat{w}w}) \\
 &\quad + \cos\Psi_{wp}(t)\hat{\omega}_{ie}\cos\phi(\Phi_{\hat{b}b} + \Phi_{\hat{u}u} + \Phi_{\hat{v}v} + \Phi_{\hat{w}w}) \\
 &\quad + \hat{\omega}_{ie}\cos\phi(\Phi_{\hat{p}p} + \Theta_{\hat{n}n})
 \end{aligned} \tag{4.236}$$

Note that the positioning noise of the inner axis $\delta\omega_{vu,z}$ contributes to the sensor's input axis only for the test positions for which the inner gimbal's rotation axis coincides with the outer axis.

A summary of the errors and the linearized error sensitivities for these three setups are given in [Table 4.18](#). Compared to the single-axis device, each additional rate table axis introduces

additional orientation and rate errors. The combination of the error sensitivities and the respective error model leads to three different cases of how the errors affect the averaged angular rate reference used for the scale factor tests:

- Random constant errors observed from a static view. Thus a constant sensitivity is not affected by averaging. These errors directly corrupt the reference angular rate used in the scale factor tests.
- Random constant errors observed from a rotating view are reduced drastically during averaging, see [Subsection 4.3.0.3](#). Averaging over complete revolutions eliminates the effect of these errors.
- Noise-like errors are affected by averaging. In most cases, averaging reduces the signal's variance. However, this is not necessarily the case, as discussed for the wide-sense stationary processes, see [Section 4.3](#). Observation of these errors from a rotating view leads to a faster decrease in the cluster average's variance. In contrast to constant errors, averaging over complete revolutions does not entirely eliminate noise-like errors.

Using the linearized sensitivities and the appropriate error models from [Section 4.2](#) the covariance matrices for each error term can be constructed for the given test scenario, that is, the number of positions, the rates applied, and the duration of each position. As the different errors are uncorrelated, the total covariance matrix of the test's input rates is the sum of the contributing error covariance matrices:

$$\mathbf{P}_{\overline{\delta\omega_{ib}}} = \mathbf{P}_{\overline{\delta\omega_{ie}}} + \mathbf{P}_{\overline{\Theta_{\hat{n}n}}} + \mathbf{P}_{\overline{\Phi_{\hat{n}n}}} + \mathbf{P}_{\overline{\Psi_{\hat{n}n}}} + \dots \quad (4.237)$$

where each error x contributes the covariance matrix of its position averages, including the linearized sensitivities:

$$\mathbf{P}_{\overline{x}} = \begin{bmatrix} P_{\overline{x},0,0} & \dots & P_{\overline{x},0,n} \\ \vdots & \ddots & \vdots \\ P_{\overline{x},n,0} & \dots & P_{\overline{x},n,n} \end{bmatrix} \quad (4.238)$$

with

$$P_{\overline{x},i,j} = \mathbb{E} \left[\left(\frac{1}{T} \int_{iT}^{(i+1)T} \frac{\partial \delta\omega_{ib}(t)}{\partial \delta x} \delta x(t) dt \right) \left(\frac{1}{T} \int_{jT}^{(j+1)T} \frac{\partial \delta\omega_{ib}(t)}{\partial \delta x} \delta x(t) dt \right) \right] \quad (4.239)$$

Validity of Linearization

Looking at the sensitivities in [table 4.18](#), it is noticeable that the linearization hides the effect of orientation errors on the nominal rotation rate. The nominal rotation rate is reduced with the cosine of the orientation error, while the effect of external signals such as the earth rotation rate increases with the sine of the orientation error. From the Taylor series

Table 4.18.: Error sensitivities in scale factor test scenarios.

Error		Linearized sensitivity		
		Case I	Case II	Case III
<i>Earth rotation</i>	$\delta\omega_{ie,x}$	$-\cos(\phi)\cos(\lambda)$	$-\sin(\lambda)$	$-\cos(\phi)\cos(\lambda)$
	$\delta\omega_{ie,y}$	$-\cos(\phi)\sin(\lambda)$	$\cos(\lambda)$	$-\cos(\phi)\sin(\lambda)$
	$\delta\omega_{ie,z}$	$-\sin(\phi)$		$-\sin(\phi)$
<i>NED frame</i>	$\Phi_{\hat{n}n}$		$\hat{\omega}_{ie}\sin(\phi)$	
	$\Theta_{\hat{n}n}$	$\hat{\omega}_{ie}\cos(\phi)$		$\hat{\omega}_{ie}\cos(\phi)$
	$\Psi_{\hat{n}n}$		$\hat{\omega}_{ie}\cos(\phi)$	
<i>Test pad</i>	$\delta\omega_{np,y}$		1	
	$\delta\omega_{np,z}$	1		1
	$\Phi_{\hat{p}p}$			$\hat{\omega}_{ie}\cos(\phi)$
	$\Theta_{\hat{p}p}$	$\hat{\omega}_{ie}\cos(\phi)$	$\hat{\omega}_{ie}\sin(\phi)$	
	$\Psi_{\hat{p}p}$		$-\hat{\omega}_{ie}\cos(\phi)$	
<i>Outer axis</i>	$\delta\omega_{pw,z}$			1
	$\Phi_{\hat{w}w}$		$-\hat{\omega}_{ie}\sin(\phi)$	$\cos(\Psi_{wp}(t))\hat{\omega}_{ie}\cos(\phi)$
	$\Theta_{\hat{w}w}$			$\sin(\Psi_{wp}(t))\hat{\omega}_{ie}\cos(\phi)$
	$\Psi_{\hat{w}w}$		$-\hat{\omega}_{ie}\cos(\phi)$	
<i>Middle axis</i>	$\Phi_{\hat{v}v}$		$-\hat{\omega}_{ie}\sin(\phi)$	$\cos(\Psi_{wp}(t))\hat{\omega}_{ie}\cos(\phi)$
	$\Theta_{\hat{v}v}$	$\hat{\omega}_{ie}\cos(\phi)$	$-\hat{\omega}_{ie}\cos(\phi)$	$\sin(\Psi_{wp}(t))\hat{\omega}_{ie}\cos(\phi)$
<i>Inner axis</i>	$\delta\omega_{vu,z}$	1	1	1
	$\Phi_{\hat{u}u}$	$\sin(\Psi_{uv}(t))\hat{\omega}_{ie}\cos(\phi)$	$\hat{\omega}_{ie}[-\cos(\Psi_{uv}(t))\cos(\phi) - \sin(\Psi_{uv}(t))\sin(\phi)]$	$\cos(\Psi_{wp}(t))\hat{\omega}_{ie}\cos(\phi)$
	$\Theta_{\hat{u}u}$	$\cos(\Psi_{uv}(t))\hat{\omega}_{ie}\cos(\phi) - \cos(\Psi_{uv}(t))\sin(\phi)$	$\hat{\omega}_{ie}[\sin(\Psi_{uv}(t))\cos(\phi)$	$\sin(\Psi_{wp}(t))\hat{\omega}_{ie}\cos(\phi)$
<i>Sensor</i>	$\Phi_{\hat{b}b}$	$\sin(\Psi_{uv}(t))\hat{\omega}_{ie}\cos(\phi)$	$\hat{\omega}_{ie}[-\cos(\Psi_{uv}(t))\cos(\phi) - \sin(\Psi_{uv}(t))\sin(\phi)]$	$\cos(\Psi_{wp}(t))\hat{\omega}_{ie}\cos(\phi)$
	$\Theta_{\hat{b}b}$	$\cos(\Psi_{uv}(t))\hat{\omega}_{ie}\cos(\phi)$	$\hat{\omega}_{ie}[\sin(\Psi_{uv}(t))\cos(\phi) - \cos(\Psi_{uv}(t))\sin(\phi)]$	$\sin(\Psi_{wp}(t))\hat{\omega}_{ie}\cos(\phi)$

development of the trigonometric functions around zero, it is evident that the cosine vanishes due to the linearization.

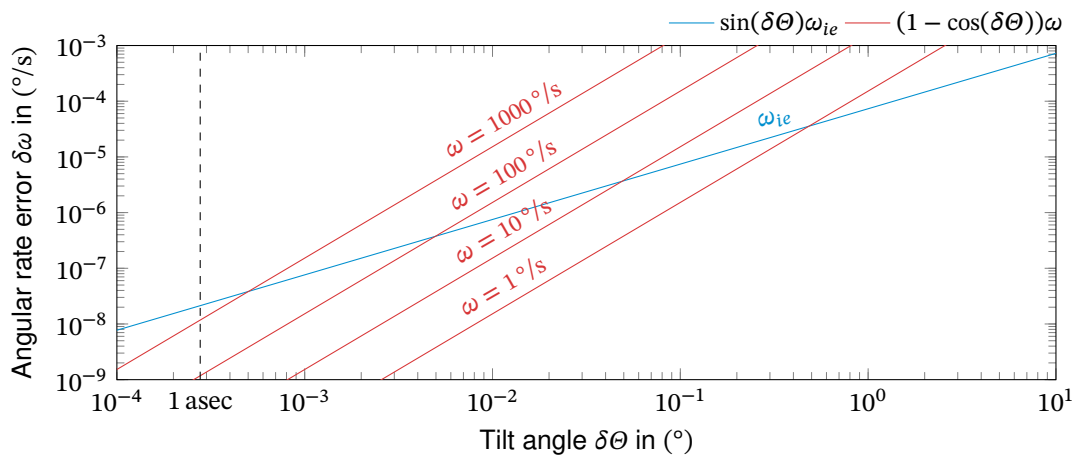


Figure 4.36.: Angular rate error from axis tilt. Comparison of the contributions of Earth angular rate and nominal rotation rates with the tilt angle θ .

Although the cosine decreases one order slower (quadratic) than the sine increases (linear), the nominal rotation rate is typically many times larger than, for example, the Earth rotation rate. Therefore, it can be questioned from which angles the different growths of sine and cosine around zero outweigh the orders of magnitude between the nominal rotation and the Earth's rotation.

The different resulting angular rate errors from a tilt $\delta\theta$ with respect to the nominal input axis are depicted in Figure 4.36. As discussed before, typical orientation errors are in the order of few asec. For axis, angular rates of up to $1000^\circ/\text{s}$ and especially for more realistic rates around $100^\circ/\text{s}$ the decrease of the cosine outweighs the difference in magnitudes between the axis rate and the Earth's angular rate by far. Consequently, the linearization and thus neglecting the effect on the nominal rotation term is well justified for realistic orientation errors.

4.4.4.4. Gyroscope Test Error Budget

Based on the above models of the scale factor test scenarios and the scale factor estimation, the uncertainty of the scale factor estimate can be determined. For the analysis of the scale factor identification, several assumptions are taken:

- The sensor is neither remounted nor turned off between the tests. Not only does this prevent additional handling efforts, but it also prevents the introduction of other errors, like a varying turn-on bias.
- The time to change the input angular rate can be neglected, compared to the averaging times at constant input. Even low angular accelerations of $100^\circ/\text{s}^2$ allow reaching a typical input limit of $400^\circ/\text{s}$ in less than 4 s, while each rate is held for at least several minutes. Of course, only the sensor's output between the acceleration phases should be

averaged and used for the scale factor determination. However, the dead time between adjacent tests can be neglected.

- All positions of constant angular rate are held for the same time. The rationale is that both environmental disturbances and sensor noise are independent of the applied rate. Note that instrument errors of the rate table slightly depend on the angular rate.

The composition of the various error sources and models into an error budget is discussed for test case III. The error budget for the *SF* estimate is given in Table 4.20, for the bias estimate in Table 4.21. The scale factor test series is analyzed for four typical rate series summarized in Table 4.19. The respective error budgets for test cases I and II can be found in Appendix I.

From the error budget in Table 4.20, the *SF* estimation seems rather insensitive to laboratory errors, as even short averaging times yield a *SF* standard deviation below 1 ppm. The long-term variation of the Earth's angular rate increases the *SF* variance with the averaging time. However, the total resulting error is below $1 \cdot 10^{-4}$ ppm for averaging times up to 12 h per applied rate. As constant errors do not contribute to the scale factor, the laboratory alignment has no effect. Averaging reduces the effects of axis non-orthogonality and the control errors by multiple orders of magnitude. The contributions of the axis non-orthogonality can be eliminated by averaging over complete rotations. The same applies to the sensor alignment errors. In summary, the *SF* error is dominated the rate table's ability to generate a stable angular rate. However, the effects of these control errors can also be effectively reduced by averaging.

Comparing the different rate series *a* to *d*, it can be seen that higher rates clearly improve the signal-to-noise ratio of the sensor input and thus reduce the scale factor estimation uncertainty. In practice, the applied angular rate series should be designed to sample the expected scale factor function of the sensor over the entire input range.

In contrast to the *SF* estimation, the bias estimation is hardly affected by choice of the applied rate series. While the errors caused by the variation of the Earth's angular rate are hardly affected by averaging, the effects of test-pad motion can be reduced by multiple orders of magnitude. Leveling errors result in constant contributions to the bias estimate, while the vertical orientation of the sensor axis in test case III makes it insensitive to north alignment errors. Axis non-orthogonality is also hardly affected by averaging and yields a constant lower bound, caused by the static axis orientation errors. Again, the dominating factor is the rate table's control error that results in bias errors around $1^\circ/\text{h}$ (1σ) for short averaging times. This error is effectively reduced by averaging down to a level of $1 \cdot 10^{-3}^\circ/\text{h}$ (1σ) for averaging more than 1 h. From this point on, the accuracy is limited by the constant residual axis position errors of the inner two gimbals that cause an orientation error of the tested sensor axis. Again, the contributions from sensor alignment can be entirely canceled out by averaging over complete revolutions. All in all, the achievable bias estimation accuracy in the scale factor test series is in the range of navigation grade. As the rate table limits the accuracy, one should refer to static tests if higher accuracy is desired.

Three different variants to create the reference motion have been presented in this section

Table 4.19.: Scale-factor test rate series considered in the error budgets.

Series	Applied rates in °/s								Comment
a	1	5	10	20	30	40	50		
b	2	10	20	40	60	80	100		<i>double rates of a)</i>
c	1	5	10	20	100	200			
d	1	5	10	20	100	200	300	400	<i>add higher rates to c)</i>

and [Appendix I](#). The differences in mechanization between the scenarios yield different error contributions. Example error budgets of the three scenarios are presented in [Example 8](#). As expected, the additional rate table axes introduce further errors from axis non-orthogonality, wobble, and position control errors. Due east-west alignment of the input axis in case II, the effect of the variation of the Earth's angular rate is reduced. While the scale factor estimate is insensitive to the constant alignment errors for all cases, a heading error of the horizontally aligned test case II causes an error in the bias estimate. Similar can be observed for axis non-orthogonality errors in test case II. These result in constant error contributions because they only affect the tilt of the Earth's angular rate but not the rate table's rotation.

Although the differences between the total errors of the test cases can be easily spotted, all errors are in the same order of magnitude. Compared to the vertical single-axis rate table, the additional axes of the three-axes table introduce errors that amount to a 12 % higher standard deviation. The horizontal testing (case II) increases the scale factor standard deviation by 57 %. In practice, the test method should be selected according to practical aspects, such as the available hardware and the efforts required to handle it. For example, a vertical rotation axis (scenario I and II) generally does not require azimuth alignment compared to Scenario II, and additional axes (scenario III) do not require manual re-arrangement of a multi-axis sensor unit.

An example of the scale factor test series for an [FOG IMU](#) is presented in [Example 9](#).

Table 4.20.: Gyro scale factor test series scale factor error for scenario III. The laboratory is located at $\phi = 45^\circ$. The applied rate series *a* to *d* are summarized in Table 4.19.

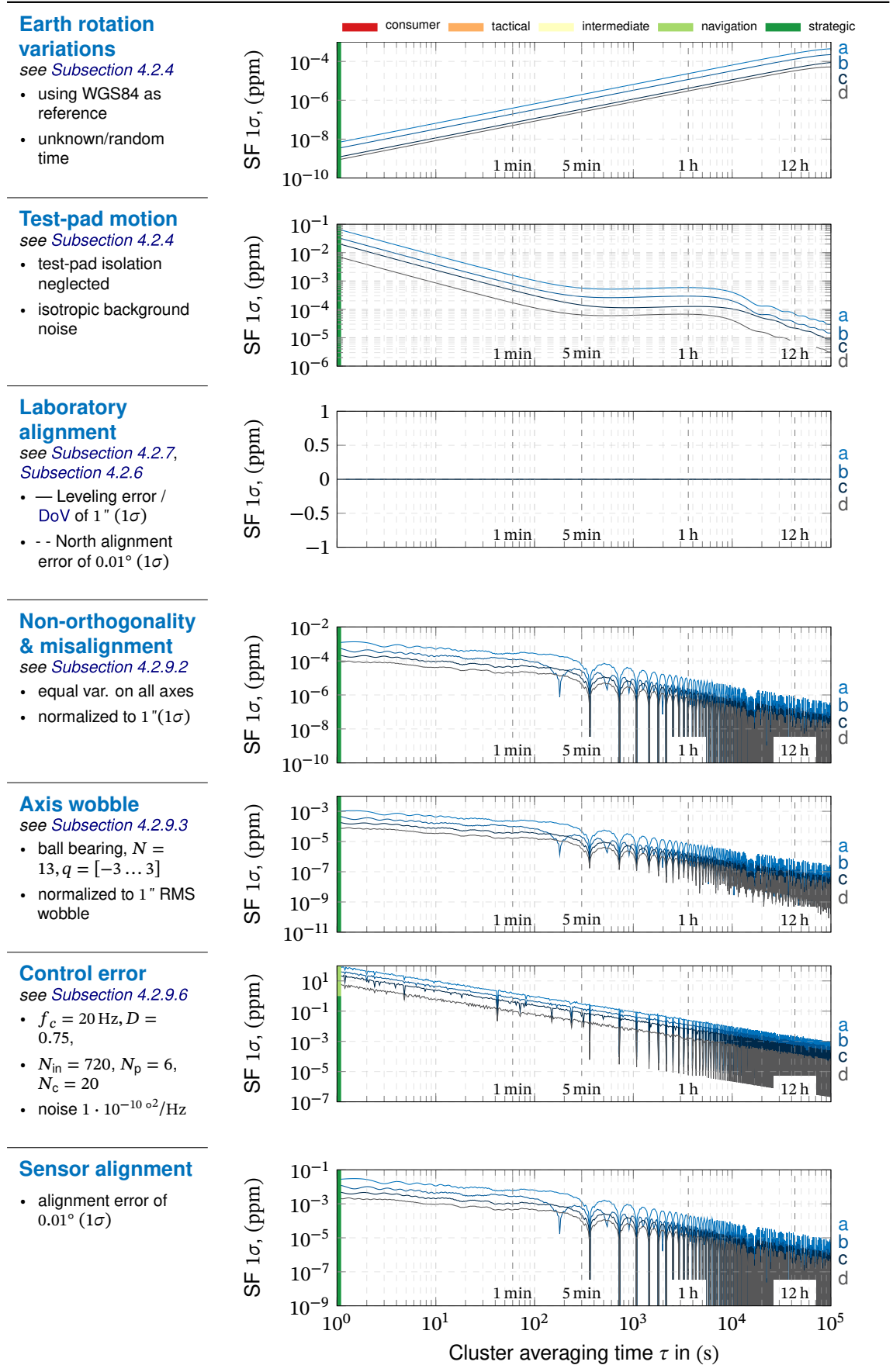


Table 4.21.: Gyro scale factor test series bias error for scenario III. The laboratory is located at $\phi = 45^\circ$. The applied rate series *a* to *d* are summarized in Table 4.19.

Earth rotation variations

see Subsection 4.2.4

- using WGS84 as reference
- unknown/random time

Test-pad motion

see Subsection 4.2.4

- test-pad isolation neglected
- isotropic background noise

Laboratory alignment

see Subsection 4.2.7, Subsection 4.2.6

- — Leveling error / DoV of 1" (1σ)
- -- North alignment error of 0.01° (1σ)

Non-orthogonality & misalignment

see Subsection 4.2.9.2

- equal var. on all axes
- normalized to 1" (1σ)

Axis wobble

see Subsection 4.2.9.3

- ball bearing, $N = 13, q = [-3 \dots 3]$
- normalized to 1" RMS wobble

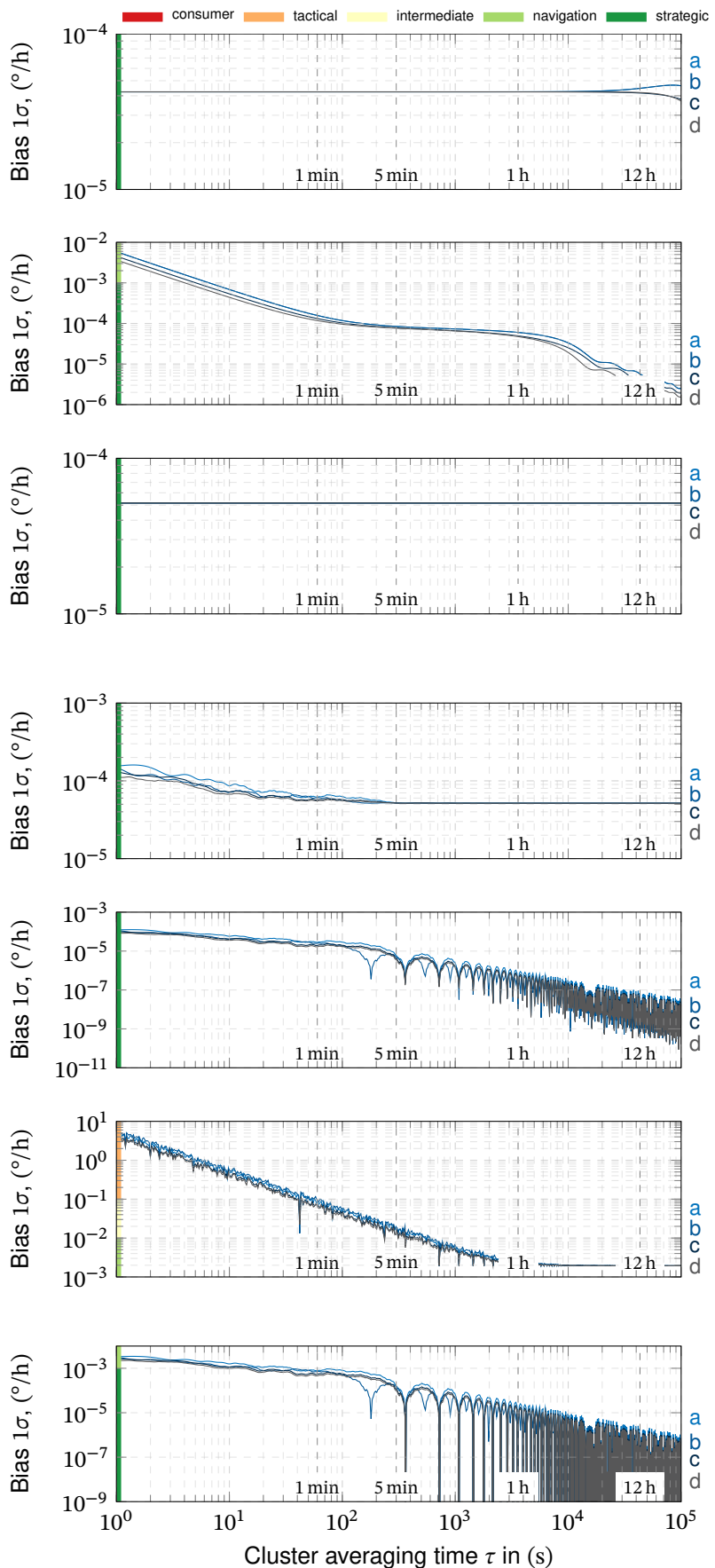
Control error

see Subsection 4.2.9.6

- $f_c = 20 \text{ Hz}, D = 0.75,$
- $N_{in} = 720, N_p = 6, N_c = 20$
- noise $1 \cdot 10^{-10} \text{ } \sigma^2/\text{Hz},$ peaks $1 \cdot 10^{-8} \text{ } \sigma^2/\text{Hz}$

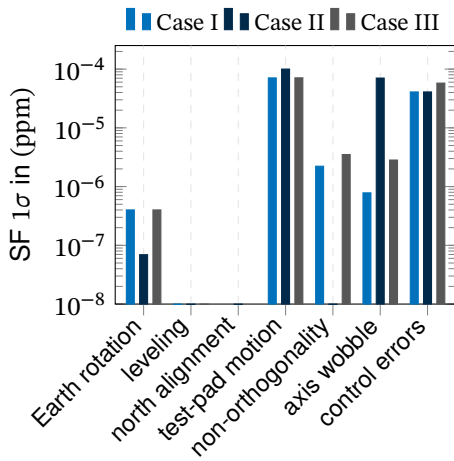
Sensor alignment

- alignment error of 0.01° (1σ)

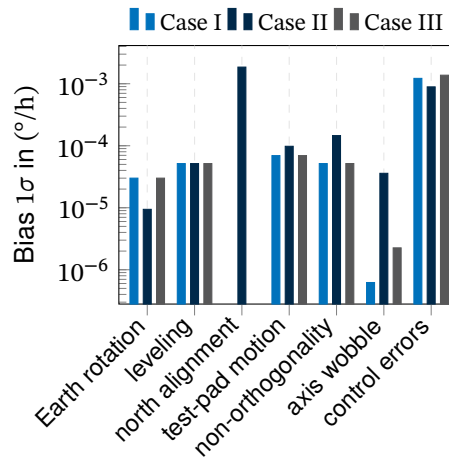


Example 8: Comparison of Scale-factor test scenarios

The effect of the different mechanization of the presented test-scenarios is investigated for the same reference configuration as in Table 4.20. The angular rates are 1, 5, 10, 20, 100, 200, 300°/s with an averaging time of 600 s per applied rate. The analytical determination of the input covariance matrices and ordinary least-squares estimation yields the following variance contributions from different error sources:



(8.a) Scale-factor variance.



(8.b) Bias variance.

A comparison of the total resulting uncertainty of the estimated parameters are given below. For case II and III, also the relative error to the reference case I is given:

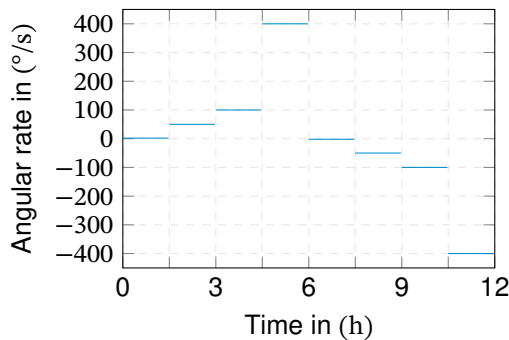
Sensor parameter estimation uncertainty	Case I	Case II	Case III
Scale-factor 1σ in ppm	8.2 · 10 ⁻⁵	1.3 · 10 ⁻⁴ (+57%)	9.2 · 10 ⁻⁵ (+12%)
Bias 1σ in °/h	1.2 · 10 ⁻³	2.1 · 10 ⁻³ (+68%)	1.4 · 10 ⁻³ (+12%)

Example 9: IMU 500 Scale Factor Estimation

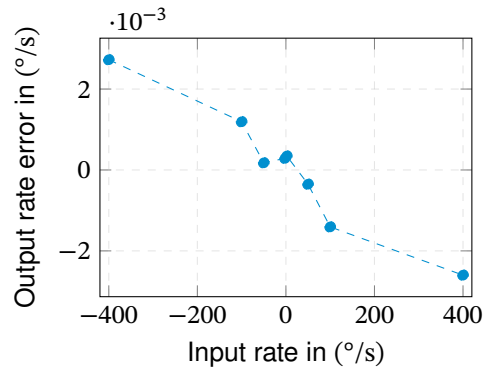
The scale factor tests of the FOG IMU were performed at the inertial laboratory of the Institute of Flight System Dynamics. The laboratory is located at latitude $\phi = 48.2667^\circ$. The sensor test is performed using a three-axis rate table, with vertical orientation of the tested sensor axis, as described in test scenario III. The laboratory is modeled in accordance with the error budgets, however alignment and axis errors are scaled to represent the real setup at the institute:

Laboratory parameters		Sensor noise	
Laboratory alignment	2.5 asec	Angular random walk N	$5 \cdot 10^{-3} \text{ }^\circ/\sqrt{\text{h}}$
Non-orthogonality	5.0 asec	Bias instability B	$2 \cdot 10^{-3} \text{ }^\circ/\text{h}$
Wobble RMS	2.5 asec	<i>determined from Example 4</i>	

As depicted below, the test series consists of the angular rates $\pm[2, 50, 100, 400]^\circ/\text{s}$, which are applied for 5400 s, each. The negative rates series was applied subsequently to the positive rates.



(9.a) Applied angular rates over time.



(9.b) Scale-factor error.

From the laboratory model and the sensor noise parameters, the resulting uncertainty of the SF and bias estimate can be determined. Below, these uncertainties are compared to the parameters that were estimated during the test series:

	Estimate	Sensor noise (1σ)	Laboratory (1σ)
Linear SF Error (ppm)	7.003	$2.065 \cdot 10^{-3}$	$3.539 \cdot 10^{-5}$
Linearity Error RSS	$4.313 \cdot 10^{-3}$		
Bias ($^\circ/\text{h}$)	-1.047	$2.081 \cdot 10^{-3}$	$1.384 \cdot 10^{-3}$

As expected, the errors introduced by the laboratory and the environment are magnitudes lower than the estimated error. For the tested sensor, also the errors from sensor noise are much lower than the observed scale factor error of the sensor. This allows the determination and thus compensation of the sensor's errors at very high accuracy at the time of testing. Still, the variation of these parameters with time and environmental conditions requires the repetition of these tests are different conditions.

Result 7: Gyroscope Scale-Factor Tests

The determination of gyroscope scale factors on a rate table leaves the user with many degrees of freedom. However, the following results are independent of the selected test mechanization, the number of poses, and applied rates:

- Rates and durations should be chosen so that each position consists of complete revolutions. This drastically reduces errors from both misalignments, mounting errors, and axis-bearing errors.
- The choice of a single or multi-axis rate table and vertical or horizontal rotation axis has only a moderate effect on the resulting testing accuracy. The test setup should instead be chosen based on practical aspects, like the available hardware and handling efforts.
- For a typical rate table, the scale factor accuracy is dominated by the axis rate errors. Its effect is about two orders of magnitude higher than the effect of seismic background noise, respectively, the test pad stability. Still, a typical setup reaches a scale factor variance of less than 1 ppm for a few minutes of averaging per position.
- Compared to the sensor noise, the laboratory's errors become relevant for the scale factor estimation, only for navigation grade and better gyroscopes. In these cases, considering input errors in the estimation, e.g., using an error-in-variables approach, improves the estimation consistency.

The gyroscope scale factor can be determined to strategic-grade accuracy for the analyzed laboratory setup. However, the simultaneously determined bias estimate is strongly corrupted by the rate table's dynamic errors and limited to intermediate or close navigation grade accuracy.

4.4.4.5. Accelerometer Testing

For scale factor tests, the accelerometers must be subjected to constant accelerations covering the sensor's entire input range (and possibly beyond). Typical rate tables do not provide the necessary combination of angular rates and lever arms to create accelerations of multiple *g*. Instead, the accelerometer scale factor tests are performed on precision centrifuges. A detailed analysis of error sources and test accuracy for centrifuge testing is given in IEEE Std. 836-2009 [172]. This standard covers both mechanical and instrumentation errors during testing at high detail. Therefore, the scale factor centrifugal testing of accelerometers is not covered in this theses.

The standard [172] does not cover the effects of sensor drift. However, this work's analysis for the gyroscope noise can be applied to accelerometers without loss of validity.

4.4.5. Rate Table Six-Position Tests

In Subsection 4.4.2.4, it was demonstrated that the sensor bias cannot be determined separately from the internal axis misalignment with a single-position static test. This problem can be solved by using two reversal positions for the determination of each error to be determined. In contrast to the reversal position tests, the multi-position tests use the averaged output from multiple, typically six or more, positions to estimate multiple sensor errors simultaneously. The most basic multi-position test aims at determining the linear (low-rate) scale factor, the axis misalignment, and bias.

For this purpose, the sensor is subjected to a series of constant inputs along different axes. Multi-position tests can be performed with different instruments, ranging from simple cube-shaped mountings over rotating heads to multi-axis positioning and rate tables. The general idea of multi-position tests is to use multiple positions to provide sufficient (or more) independent observations to solve the sensor's model equation for the sensor errors. Often, there are more positions (observations) than error terms, so these are typically estimated using least-squares or similar adjustment methods.

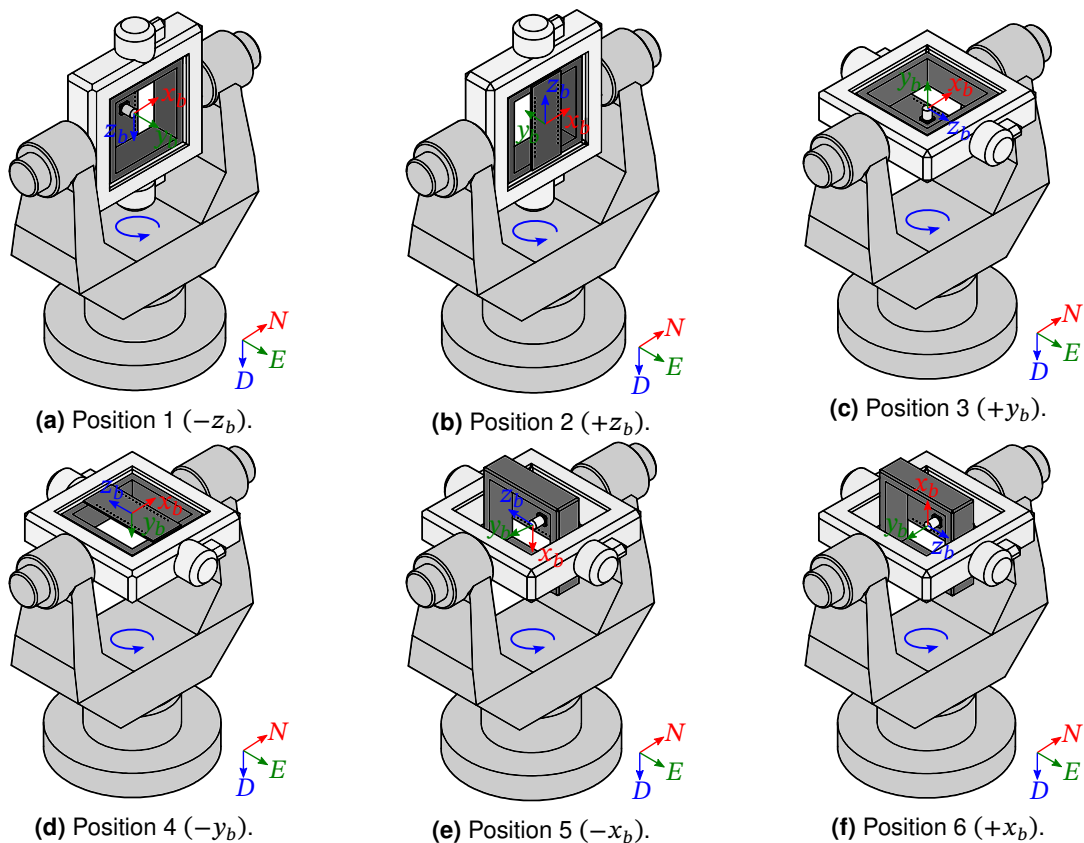


Figure 4.37.: Six-position testing of an inertial sensor using a three-axis positioning and rate table.

Specific multi-position test scenarios for different sensor technologies allow an analytical determination of the sensor errors that include the sensor bias, axis misalignment, and acceleration sensitivities. Examples for such test procedures are the six-pose test for SDFGs

gyroscopes [22, pp. 249–250] or the eight-pose test for DTGs [22, p. 253] and eight-pose stability test described in [14, pp. 223–231]. In the following, the analyses and error budgets will be demonstrated for a simple six-position test, illustrated in Figure 4.37.

4.4.5.1. Test Description and Parameter Estimation

For the example six-position test, the sensor’s orientation relative to the outer axis and the local gravity is changed so that each sensor axis is subjected to both positive and negative input. Accelerometers and gyroscopes share the same positions in this test scheme and can be tested simultaneously. Changing the outer axis rotation direction instead of flipping the sensor’s orientation is not an equivalent approach. First, it does not produce symmetric inputs because of the vertical component of the Earth’s angular rate. Second, such a procedure would not create reversal measurements for the accelerometers.

Using a three-axis rate table, multiple positions can be easily created for all axis of a sensor triad simultaneously, reducing the testing duration and the required handling efforts. A simple error model that includes scale factors, misalignment and biases of a gyroscope-triad is given as:

$$\tilde{\omega}_{ib} = \begin{bmatrix} S_x & M_{xy} & M_{xz} \\ M_{yx} & S_y & M_{yz} \\ M_{zx} & M_{zy} & S_z \end{bmatrix} \omega_{ib} + \mathbf{b}_{G,f} + \boldsymbol{\nu}_G \quad (4.240)$$

At least 4 positions that provide 3 observations each, are required to determine above 12 errors. However, typically, a symmetrical set of 6 positions and a least-squares adjustment are used to estimate the errors. In theory, the Earth’s angular rate vector can be used as an input for the multi-position tests. This however requires a sensor with sufficient accuracy and stability better than the Earth’s rotation, which is only true for navigation grade and better sensors. Multi-position gyroscope tests are therefore performed at rates that are significantly higher than the sensor’s in-run bias instability.

For the symmetric input angular rates scheme depicted in Figure 4.37 six positions result in

the following system of equations for the gyroscope test:

$$\underbrace{\begin{bmatrix} \bar{\omega}_{ib,x}^{(1)} \\ \bar{\omega}_{ib,x}^{(2)} \\ \bar{\omega}_{ib,x}^{(3)} \\ \bar{\omega}_{ib,x}^{(4)} \\ \bar{\omega}_{ib,x}^{(5)} \\ \bar{\omega}_{ib,x}^{(6)} \\ \bar{\omega}_{ib,y}^{(1)} \\ \bar{\omega}_{ib,y}^{(2)} \\ \bar{\omega}_{ib,y}^{(3)} \\ \bar{\omega}_{ib,y}^{(4)} \\ \bar{\omega}_{ib,y}^{(5)} \\ \bar{\omega}_{ib,y}^{(6)} \\ \bar{\omega}_{ib,z}^{(1)} \\ \bar{\omega}_{ib,z}^{(2)} \\ \bar{\omega}_{ib,z}^{(3)} \\ \bar{\omega}_{ib,z}^{(4)} \\ \bar{\omega}_{ib,z}^{(5)} \\ \bar{\omega}_{ib,z}^{(6)} \end{bmatrix}}_{\bar{\mathbf{y}}} = \underbrace{\begin{bmatrix} 0 & 0 & -\bar{\omega} & 1 & 0 & 0 & 0 & 0 & 0 & 0 & 0 & 0 \\ 0 & 0 & +\bar{\omega} & 1 & 0 & 0 & 0 & 0 & 0 & 0 & 0 & 0 \\ 0 & -\bar{\omega} & 0 & 1 & 0 & 0 & 0 & 0 & 0 & 0 & 0 & 0 \\ 0 & +\bar{\omega} & 0 & 1 & 0 & 0 & 0 & 0 & 0 & 0 & 0 & 0 \\ -\bar{\omega} & 0 & 0 & 1 & 0 & 0 & 0 & 0 & 0 & 0 & 0 & 0 \\ +\bar{\omega} & 0 & 0 & 1 & 0 & 0 & 0 & 0 & 0 & 0 & 0 & 0 \\ 0 & 0 & 0 & 0 & 0 & 0 & -\bar{\omega} & 1 & 0 & 0 & 0 & 0 \\ 0 & 0 & 0 & 0 & 0 & 0 & +\bar{\omega} & 1 & 0 & 0 & 0 & 0 \\ 0 & 0 & 0 & 0 & 0 & -\bar{\omega} & 0 & 1 & 0 & 0 & 0 & 0 \\ 0 & 0 & 0 & 0 & 0 & +\bar{\omega} & 0 & 1 & 0 & 0 & 0 & 0 \\ 0 & 0 & 0 & 0 & -\bar{\omega} & 0 & 0 & 1 & 0 & 0 & 0 & 0 \\ 0 & 0 & 0 & 0 & +\bar{\omega} & 0 & 0 & 1 & 0 & 0 & 0 & 0 \\ 0 & 0 & 0 & 0 & 0 & 0 & 0 & 0 & 0 & -\bar{\omega} & 1 & 0 \\ 0 & 0 & 0 & 0 & 0 & 0 & 0 & 0 & 0 & +\bar{\omega} & 1 & 0 \\ 0 & 0 & 0 & 0 & 0 & 0 & 0 & 0 & 0 & -\bar{\omega} & 0 & 1 \\ 0 & 0 & 0 & 0 & 0 & 0 & 0 & 0 & +\bar{\omega} & 0 & 1 & 0 \\ 0 & 0 & 0 & 0 & 0 & 0 & 0 & 0 & -\bar{\omega} & 0 & 0 & 1 \\ 0 & 0 & 0 & 0 & 0 & 0 & 0 & 0 & +\bar{\omega} & 0 & 0 & 1 \end{bmatrix}}_{\mathbf{H}} \underbrace{\begin{bmatrix} S_{G,x} \\ M_{G,xy} \\ M_{G,xz} \\ b_{G,x} \\ M_{G,yx} \\ S_{G,y} \\ M_{G,yz} \\ b_{G,y} \\ M_{G,zx} \\ M_{G,zy} \\ S_{G,z} \\ b_{G,z} \end{bmatrix}}_c + \underbrace{\begin{bmatrix} \bar{v}_{G,x}^{(1)} \\ \bar{v}_{G,x}^{(2)} \\ \bar{v}_{G,x}^{(3)} \\ \bar{v}_{G,x}^{(4)} \\ \bar{v}_{G,x}^{(5)} \\ \bar{v}_{G,x}^{(6)} \\ \bar{v}_{G,y}^{(1)} \\ \bar{v}_{G,y}^{(2)} \\ \bar{v}_{G,y}^{(3)} \\ \bar{v}_{G,y}^{(4)} \\ \bar{v}_{G,y}^{(5)} \\ \bar{v}_{G,y}^{(6)} \\ \bar{v}_{G,z}^{(1)} \\ \bar{v}_{G,z}^{(2)} \\ \bar{v}_{G,z}^{(3)} \\ \bar{v}_{G,z}^{(4)} \\ \bar{v}_{G,z}^{(5)} \\ \bar{v}_{G,z}^{(6)} \end{bmatrix}}_{\bar{\mathbf{v}}} \quad (4.241)$$

In this case, the averaged input rate is the sum of the rate table's outer axis rate $\hat{\omega}_{pw}$ and the local vertical component of the Earth's angular rate:

$$\bar{\omega} = \hat{\omega}_{pw} + \hat{\omega}_{ie} \sin(\phi) \quad (4.242)$$

Analogously to the scale factor estimation in [Subsection 4.4.4.1](#), the least-squares estimation uses the pseudo-inverse of \mathbf{H} and the estimation covariance is determined (4.224). For the example six-position test, the pseudo-inverse is a block diagonal matrix

$$(\mathbf{H}^T \mathbf{H})^{-1} \mathbf{H}^T = \begin{bmatrix} \mathbf{h}^{-1} & \mathbf{0}_{4 \times 6} & \mathbf{0}_{4 \times 6} \\ \mathbf{0}_{4 \times 6} & \mathbf{h}^{-1} & \mathbf{0}_{4 \times 6} \\ \mathbf{0}_{4 \times 6} & \mathbf{0}_{4 \times 6} & \mathbf{h}^{-1} \end{bmatrix} \quad (4.243)$$

with the three equal blocks \mathbf{h}^{-1} :

$$\mathbf{h}^{-1} = \begin{bmatrix} 0 & 0 & 0 & 0 & -\frac{1}{2\bar{\omega}} & \frac{1}{2\bar{\omega}} \\ 0 & 0 & -\frac{1}{2\bar{\omega}} & \frac{1}{2\bar{\omega}} & 0 & 0 \\ -\frac{1}{2\bar{\omega}} & \frac{1}{2\bar{\omega}} & 0 & 0 & 0 & 0 \\ \frac{1}{6} & \frac{1}{6} & \frac{1}{6} & \frac{1}{6} & \frac{1}{6} & \frac{1}{6} \end{bmatrix} \quad (4.244)$$

The estimation matrices for the accelerometers are given by:

$$\mathbf{h}^{-1} = \begin{bmatrix} 0 & 0 & 0 & 0 & -\frac{1}{2\bar{\gamma}} & \frac{1}{2\bar{\gamma}} \\ 0 & 0 & -\frac{1}{2\bar{\gamma}} & \frac{1}{2\bar{\gamma}} & 0 & 0 \\ -\frac{1}{2\bar{\gamma}} & \frac{1}{2\bar{\gamma}} & 0 & 0 & 0 & 0 \\ \frac{1}{6} & \frac{1}{6} & \frac{1}{6} & \frac{1}{6} & \frac{1}{6} & \frac{1}{6} \end{bmatrix} \quad (4.245)$$

Note that this estimation of the scale factor and misalignment angles is equivalent to the classical reversal measurement method specified in the [IEEE](#) standards, e.g., [10, p. 40] and discussed in [Subsection 4.4.3](#). The bias, however, is estimated from all six positions.

4.4.5.2. Effects of Sensor Noise

The sensor noise covariance matrix for the multi-position test is composed of the covariance matrices for the different noise processes, just like for the scale factor tests. In general, the resulting noise covariance matrix $\mathbf{Q}_{\bar{v}}$ is a block diagonal matrix composed of the noise covariance matrices of each sensor axis, as determined in [Subsection 4.4.4.2](#). However, there may also be a correlated fraction of the noise $\mathbf{Q}_{\bar{v},\text{corr}}$ which is caused by a common error source. Such a correlated error on all axes could be caused by a common temperature change (which should be prevented during testing) and voltage oscillations from a shared power supply. The total noise covariance matrix is thus given by the uncorrelated sensor noise block matrices and the correlated noise blocks shared by all axes:

$$\mathbf{Q}_{\bar{v}} = \begin{bmatrix} \mathbf{Q}_{\bar{v},x} + \mathbf{Q}_{\bar{v},\text{corr}} & \mathbf{Q}_{\bar{v},\text{corr}} & \mathbf{Q}_{\bar{v},\text{corr}} \\ \mathbf{Q}_{\bar{v},\text{corr}} & \mathbf{Q}_{\bar{v},y} + \mathbf{Q}_{\bar{v},\text{corr}} & \mathbf{Q}_{\bar{v},\text{corr}} \\ \mathbf{Q}_{\bar{v},\text{corr}} & \mathbf{Q}_{\bar{v},\text{corr}} & \mathbf{Q}_{\bar{v},z} + \mathbf{Q}_{\bar{v},\text{corr}} \end{bmatrix} \quad (4.246)$$

However, due to the block-diagonal structure of the pseudo-inverse (4.243), a possible cross-correlation between the axes' noise does not affect the estimation covariance, and each sensor axis can be analyzed on its own. The variances of the estimated parameters can be analytically determined from the elements of the covariance matrix $\mathbf{Q}_{\bar{v}}$. For the gyroscope the resulting

variance of the parameter estimates are:

$$\sigma_{\omega, S_x}^2 = \frac{1}{4\hat{\omega}^{-2}} \left(Q_{\nu_G, x}^{(5)} - 2Q_{\nu_G, x}^{(5,6)} + Q_{\nu_G, x}^{(6)} \right) \quad (4.247)$$

$$\sigma_{\omega, M_{xy}}^2 = \frac{1}{4\hat{\omega}^{-2}} \left(Q_{\nu_G, x}^{(3)} - 2Q_{\nu_G, x}^{(3,4)} + Q_{\nu_G, x}^{(4)} \right) \quad (4.248)$$

$$\sigma_{\omega, M_{xz}}^2 = \frac{1}{4\hat{\omega}^{-2}} \left(Q_{\nu_G, x}^{(1)} - 2Q_{\nu_G, x}^{(1,2)} + Q_{\nu_G, x}^{(2)} \right) \quad (4.249)$$

$$\sigma_{\omega, b_x}^2 = \frac{1}{36} \sum_{i=1}^6 \sum_{j=1}^6 Q_{\nu_G, x}^{(i,j)} \quad (4.250)$$

The equations for the accelerometer's errors are determined analogously:

$$\sigma_{f_b, S_x}^2 = \frac{1}{4\hat{\gamma}^{-2}} \left(Q_{\nu_A, x}^{(5)} - 2Q_{\nu_A, x}^{(5,6)} + Q_{\nu_A, x}^{(6)} \right) \quad (4.251)$$

$$\sigma_{f_b, M_{xy}}^2 = \frac{1}{4\hat{\gamma}^{-2}} \left(Q_{\nu_A, x}^{(3)} - 2Q_{\nu_A, x}^{(3,4)} + Q_{\nu_A, x}^{(4)} \right) \quad (4.252)$$

$$\sigma_{f_b, M_{xz}}^2 = \frac{1}{4\hat{\gamma}^{-2}} \left(Q_{\nu_A, x}^{(1)} - 2Q_{\nu_A, x}^{(1,2)} + Q_{\nu_A, x}^{(2)} \right) \quad (4.253)$$

$$\sigma_{f_b, b_x}^2 = \frac{1}{36} \sum_{i=1}^6 \sum_{j=1}^6 Q_{\nu_A, x}^{(i,j)} \quad (4.254)$$

The above equations already display the differences between the multi-position tests. In contrast to the scale factor tests where the variance of every pose affects the estimate, in multi-position tests the linear scale factor S_x (4.247) and misalignment M_{xy} (4.248), M_{xz} (4.249) are affected by the respective two reversal input positions, only. The resulting SF and misalignment variance depends on the variation of the output averages of the two positions and therefore decreases with the increasing correlation between the two used reversal positions.

The bias estimate, however, is based on the average of all positions and consequently affected by all position variances and their cross-correlations. The variance of the bias estimate decreases with a decreasing correlation between the positions. Again, due to the bias-instability and rate random walk, the variance of this bias estimate refers to the difference between the estimated bias to a virtual bias valid before the first position (cf. Subsection 4.4.2.4 and Subsection 4.4.4.2).

The effects of the standard sensor noise processes on the variance of the SF, misalignment and bias estimates are depicted in Figure 4.38. Since the standard deviation scales linearly with the noise-defining parameters, they can be scaled from the given normalized plots. Due to the same parameter estimation, the resulting graphs for the SF and misalignment errors Figure 4.38a is very similar to the one for the reversal position tests Figure 4.30a. However, the graphs are shifted due to the increased input rate (here 1 °/s) compared to the Earth's angular rate. The resulting parameter standard deviation scales with $\hat{\omega}^{-1}$ so that the graphs can be shifted for other applied rates (neglecting the contribution of the Earth's angular rate).

The resulting standard deviation of the gyroscope bias estimate is depicted in Figure 4.38b.

In contrast to the gyro SF estimate, the applied angular rate has no effect on the bias estimate.

For the accelerometer, the input and orientations match the static reversal position test discussed in Subsection 4.4.3. Since the SF and misalignment are determined in exactly the same way, the resulting plot in Figure 4.38c is equal to Figure 4.31a. However, the determination of the bias incorporates all six measurements and is independent of the sensor's input.

In summary, the six-position test displays the same general sensitivity to sensor noise as the two-position reversal test: The errors from quantization noise and angular/velocity random walk can be easily reduced by averaging. At the same time, the bias instability poses an accuracy limit that cannot be circumvented by averaging. However, rate/acceleration random walk or even rate ramp noise will cause increasing errors with increased averaging time. Ideally, the averaging time for each pose should be selected close to the minimum of the sensor's Allan variance plot.

4.4.5.3. Gyroscope Test Error Model

The ideal angular rates vector at the tested sensor triad is given by the Earth's angular rate and the rotation rate of the outer axis

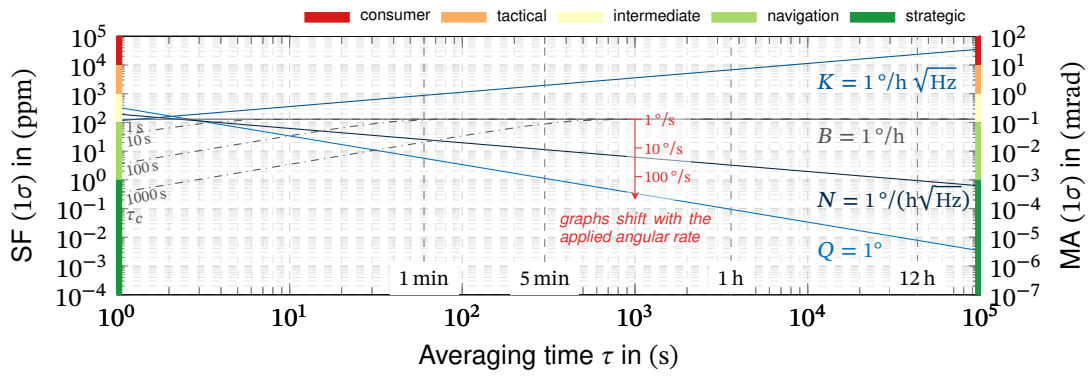
$$\hat{\omega}_{ib}^{(P)} = \mathbf{I}_{\hat{b}u} \mathbf{R}_{\hat{u}v}^{(P)} \mathbf{R}_{\hat{v}w}^{(P)} \left(\mathbf{R}_{\hat{w}p}(t) \mathbf{I}_{pn} \mathbf{R}_{ne} \hat{\omega}_{ie} + \begin{bmatrix} 0 \\ 0 \\ \hat{\omega}_{pw} \end{bmatrix} \right) \quad (4.255)$$

where the two rotations representing the inner and middle gimbals' positions $\mathbf{R}_{\hat{u}v}^{(P)}$ and $\mathbf{R}_{\hat{v}w}^{(P)}$ are constant for each position P . It is assumed that each position is averaged over an integer number of revolutions of the outer axis. In this case, the horizontal components of the Earth's angular rate average out and only the local vertical component is added to the outer axis' rotation rate:

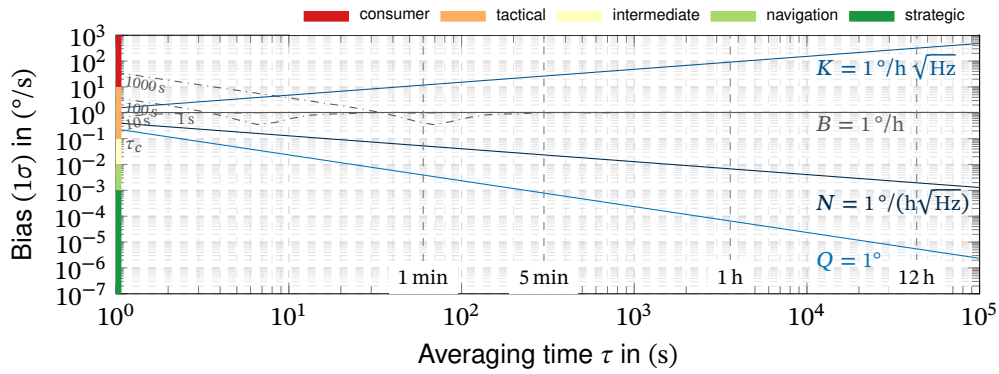
$$\bar{\hat{\omega}} = \hat{\omega}_{ie} \sin(\phi) + \hat{\omega}_{pw} \quad (4.256)$$

Linearization of the kinematic equations for the input errors yields:

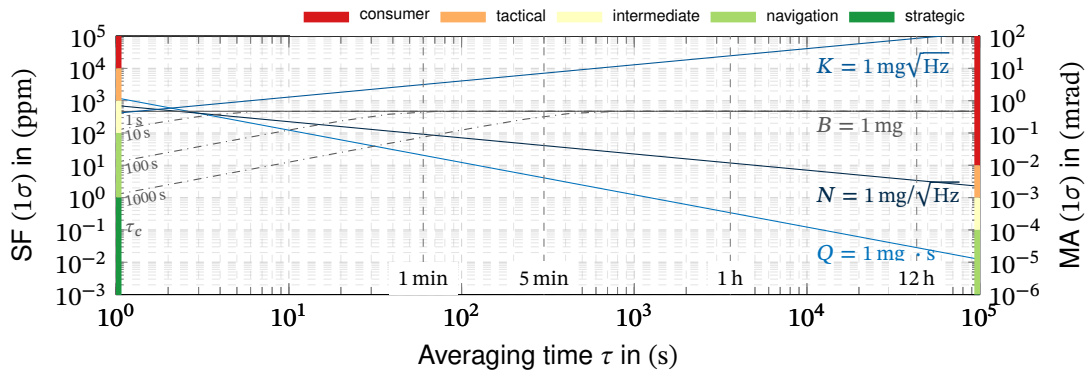
$$\begin{aligned} \delta\omega_{ib}^{(P)} = & \mathbf{R}_{\hat{b}u} \delta\omega_{vu} + \mathbf{R}_{\hat{b}u} \mathbf{R}_{\hat{u}v}^{(P)} \delta\omega_{wv} + \mathbf{R}_{\hat{b}u} \mathbf{R}_{\hat{u}v}^{(P)} \mathbf{R}_{\hat{v}w}^{(P)} \delta\omega_{pw} \\ & + \mathbf{R}_{\hat{b}u} \mathbf{R}_{\hat{u}v}^{(P)} \mathbf{R}_{\hat{v}w}^{(P)} \mathbf{R}_{\hat{w}p}(t) (\mathbf{R}_{\hat{p}n} \mathbf{R}_{ne} \delta\omega_{ie} + \delta\omega_{np}) \\ & - \left[\mathbf{R}_{\hat{b}u} \mathbf{R}_{\hat{u}v}^{(P)} \mathbf{R}_{\hat{v}w}^{(P)} (\mathbf{R}_{\hat{w}p}(t) \mathbf{R}_{\hat{p}n} \mathbf{R}_{ne} \hat{\omega}_{ie} + \hat{\omega}_{pw}) \right] \times \psi_{\hat{b}b} \\ & - \mathbf{R}_{\hat{b}u} \left[\mathbf{R}_{\hat{u}v}^{(P)} \mathbf{R}_{\hat{v}w}^{(P)} (\mathbf{R}_{\hat{w}p}(t) \mathbf{R}_{\hat{p}n} \mathbf{R}_{ne} \hat{\omega}_{ie} + \hat{\omega}_{pw}) \right] \times \psi_{\hat{u}u} \\ & - \mathbf{R}_{\hat{b}u} \mathbf{R}_{\hat{u}v}^{(P)} \left[\mathbf{R}_{\hat{v}w}^{(P)} (\mathbf{R}_{\hat{w}p}(t) \mathbf{R}_{\hat{p}n} \mathbf{R}_{ne} \hat{\omega}_{ie} + \hat{\omega}_{pw}) \right] \times \psi_{\hat{v}v} \\ & - \mathbf{R}_{\hat{b}u} \mathbf{R}_{\hat{u}v}^{(P)} \mathbf{R}_{\hat{v}w}^{(P)} \left[\mathbf{R}_{\hat{w}p}(t) \mathbf{R}_{\hat{p}n} \mathbf{R}_{ne} \hat{\omega}_{ie} + \hat{\omega}_{pw} \right] \times \psi_{\hat{w}w} \\ & - \mathbf{R}_{\hat{b}u} \mathbf{R}_{\hat{u}v}^{(P)} \mathbf{R}_{\hat{v}w}^{(P)} \mathbf{R}_{\hat{w}p}(t) \left[\mathbf{R}_{\hat{p}n} \mathbf{R}_{ne} \hat{\omega}_{ie} \right] \times \psi_{\hat{p}p} \\ & - \mathbf{R}_{\hat{b}u} \mathbf{R}_{\hat{u}v}^{(P)} \mathbf{R}_{\hat{v}w}^{(P)} \mathbf{R}_{\hat{w}p}(t) \mathbf{R}_{\hat{p}n} \left[\mathbf{R}_{ne} \hat{\omega}_{ie} \right] \times \psi_{\hat{n}n} \end{aligned} \quad (4.257)$$



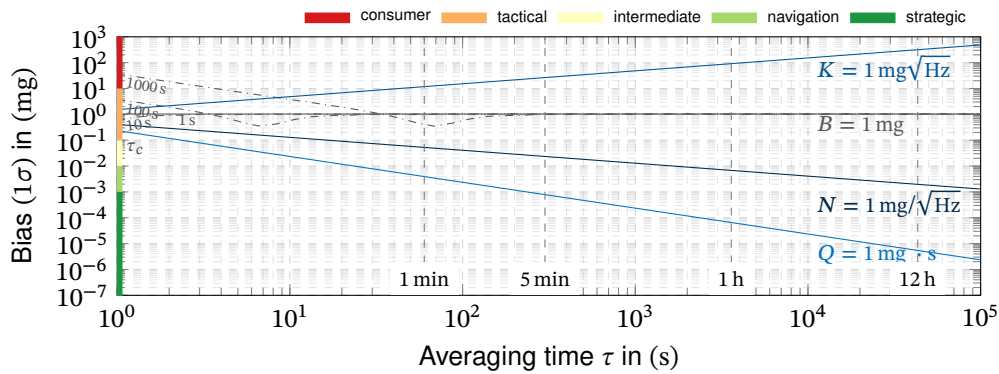
(a) Gyroscope scale factor and misalignment standard deviation for an applied angular rate of $1^\circ/\text{s}$. The plots are scaled for a geodetic latitude of $\phi = 45^\circ$.



(b) Gyroscope bias standard deviation.



(c) Accelerometer scale factor and misalignment standard deviation.



(d) Accelerometer bias standard deviation.

Figure 4.38.: Six position test sensor error variance from sensor noise over varying averaging time τ per pose.

The six different positions are defined by the constant rotation matrices \mathbf{R}_{vw} and \mathbf{R}_{uv} representing the middle and inner gimbals' orientation. The resulting linear sensitivities of each axis of the tested sensor triad are summarized in [Table H.1](#) to [Table H.3](#), given in the appendix. In general, the error terms for each two reversal positions are equal, but for some terms the sign is flipped between the positions. These terms modify the sign of the correlation between the averaged input errors of the two poses, which are often strongly correlated or even constant:

- The error sensitivities flipping their signs change the typically positive correlation to a negative correlation. Looking at (4.244), it can be seen that a negative correlation between the input errors of the positions increases the variance of the scale factor and misalignment estimates but decreases the variance of the bias estimate.
- Analogously, a positive correlation between the cluster averages decreases the scale factor and misalignment variance but increases the variance of the bias estimate.

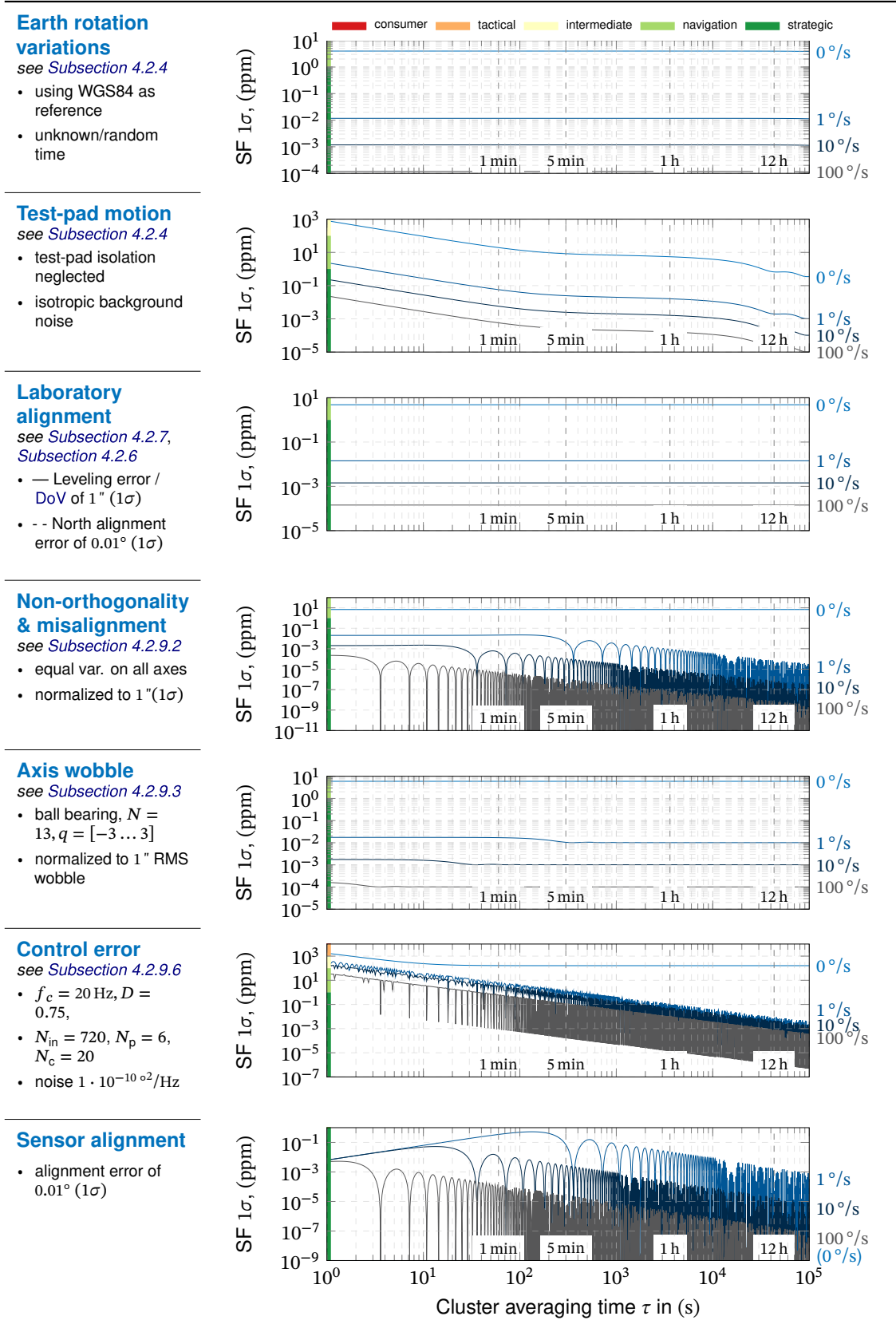
Comparing the error sensitivities of the three sensor axes, the general terms are very similar for each axis. However, the sensitivities to error inputs are permuted between the axes. Furthermore, the already described sign-flip between two reversal positions vanishes for some positions (e.g., the test pad orientation errors). This results from the selected test positions. Most of these sensitivities are based on the Earth's angular rate and are consequently very small.

4.4.5.4. Gyroscope Test Error Budget

In the following, the resulting variances of the estimated parameters are determined for typical or normalized error parameters. [Table 4.22](#) to [Table 4.24](#) illustrate how the effects of the error sources on the *SF*, *MA* and bias estimation depend on the averaging time of each position.

The *SF* error budget for the six-position test is depicted in [Table 4.22](#). Increasing the test's angular rate increases the signal-to-noise ratio and thus reduces the variance of the *SF* estimate, which can be observed in all plots. The effect of averaging, however, depends on the actual error source. No effect of averaging can be observed on the Earth's angular rate and the laboratory alignment errors. While the alignment errors are truly constant, the errors from the Earth's angular rate only appear quasi-constant for the considered averaging periods of up to $1 \cdot 10^5$ s (≈ 28 h). While the variance from test-pad motion and the control errors reduce at about two magnitudes per decade, the variance from axis non-orthogonality and wobble arises from periodic errors, which result in a periodic reduction of the variance. As the non-orthogonality errors are modeled as random constant, the resulting errors vanish for every complete revolution of the rate table. The same applies to the sensor alignment errors, which cancel out for whole revolutions. At zero rate, the symmetric poses also cancel out the sensor alignment errors.

Table 4.22.: Rate table six-position gyro test scale factor estimation error budget for varying rotation rate and averaging time. The laboratory is located at $\phi = 45^\circ$



Comparing the contributions of the error sources, the total resulting **SF** variance is dominated by the test-pad motion and the rate table's control errors. However, the plots indicate that even moderate averaging times of about 5 min are sufficient to reduce the **SF** standard deviation to the level of few **parts per million (ppm)** and thus towards the strategic grade.

The misalignment error budgets [Table 4.23](#) and [Table 4.24](#) display quite different sensitivities to the errors. First, the Earth's rotation is observed from a rotating view which introduces a dependency on the averaging time. The resulting variance increases towards the constant value of the **SF** case for the first half revolution of the rate table and decreases afterward. In the linearized error analysis, the laboratory alignment errors do not affect the misalignment estimates, while the axis non-orthogonality results in a constant error contribution. The same applies to the axis wobble, which reduces to a random constant axis orientation error and thus constant contribution to the misalignment variance. These two constant orientation errors are transferred directly into the axis misalignment. They cannot be reduced by averaging but only by increasing the rate table accuracy.

Regarding the control errors, there is an apparent difference between the two misalignment estimates that arises from the orientation of the sensor axes with respect to the actuated rate table axes. Errors of the sensor alignment with respect to the ideal rate table reference frames transfer directly into the misalignment estimates. The improved signal-to-noise ratio when rotating reduces the effects of sensor alignment errors compared to the static case. However, the differences between the non-zero rate cases are minimal.

Using the assumed laboratory setup and test procedure, the misalignment estimation cannot be driven to the levels achieved for the **SF** estimation. This is mainly due to the non-orthogonality, wobble, and position accuracy errors that are a property of the rate table. So, further improvement of the misalignment estimation requires even more accurate instrumentation (e.g., rate table or dividing head).

While the **SF** and **MA** estimates show a similar behavior, the bias estimate ([Table 4.25](#)) displays different dependency especially on the applied angular rates. Specifically, the constant axis non-orthogonality and wobble lead to a tilt of the sensor axes with respect to the rotating axis that is not canceled out by the reversal measurements. This manifests in a bias error that scales with the applied angular rate. The resulting variances and related sensor grades show that the bias estimation from six-position testing is worse than the **SF** and **MA** estimates. This is a result of the relatively high reference input rate, which amplifies the effect of rate table axis errors in the case of bias estimation and does not increase the signal-to-noise ratio in contrast to the **SF** and **MA** estimation. The same applies to the sensor alignment errors that scale linearly with the applied rate. An interesting observation is the variance increase from the test-pad motion with the applied angular rate at longer averaging times. This results from a resonance between the seismic reference noise and the applied angular rates.

The total bias variance is also dominated by the rate table errors, which results in bias variances that correspond to tactical or intermediate grade gyroscopes. The analyzed six-position gyro test procedure on a three-axis rate table is thus unable to calibrate the bias of

Table 4.23.: Rate table six-position gyro test axis misalignment M_{xy} estimation error budget for varying rotation rate and averaging time. The laboratory is located at $\phi = 45^\circ$

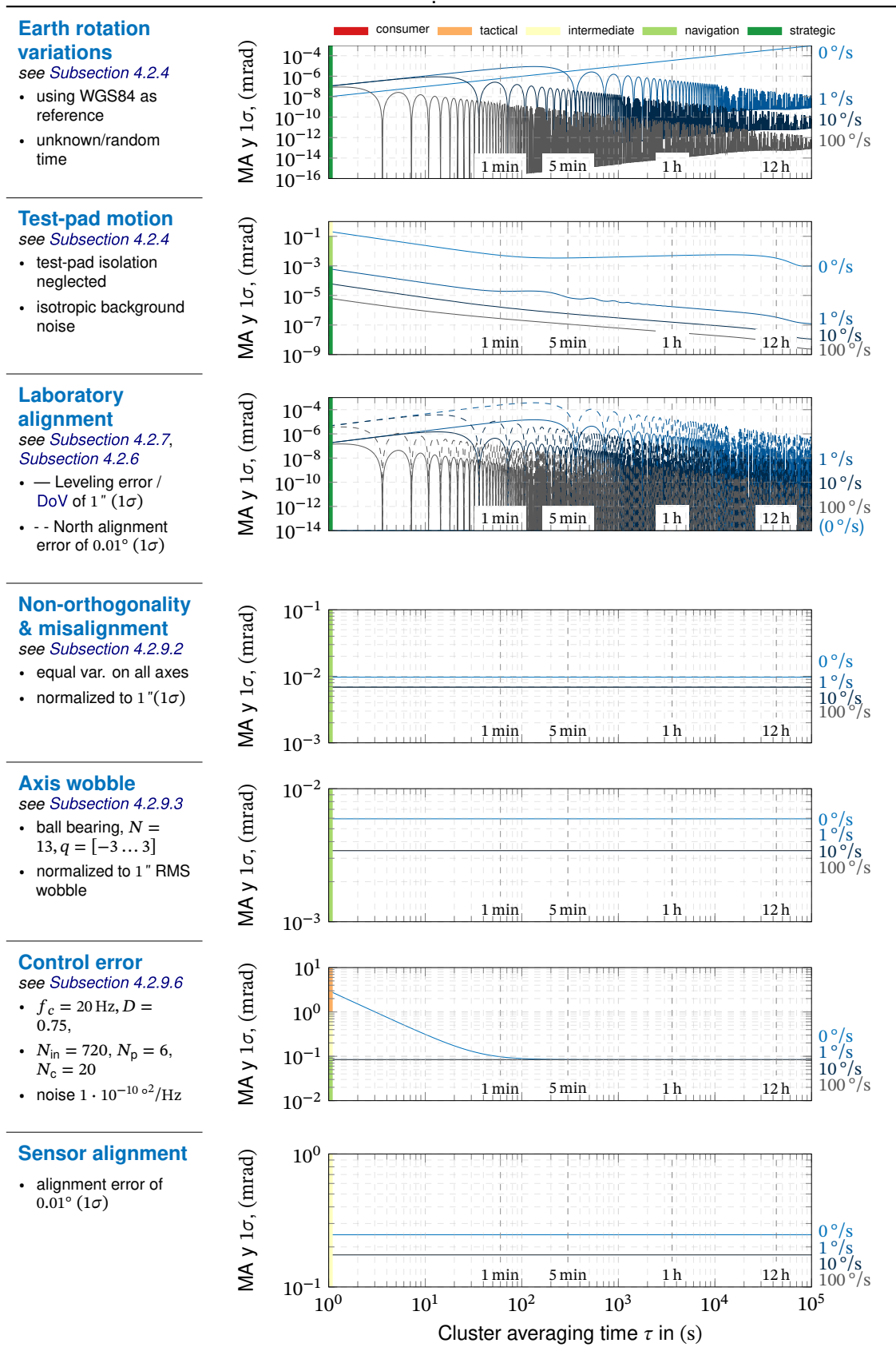
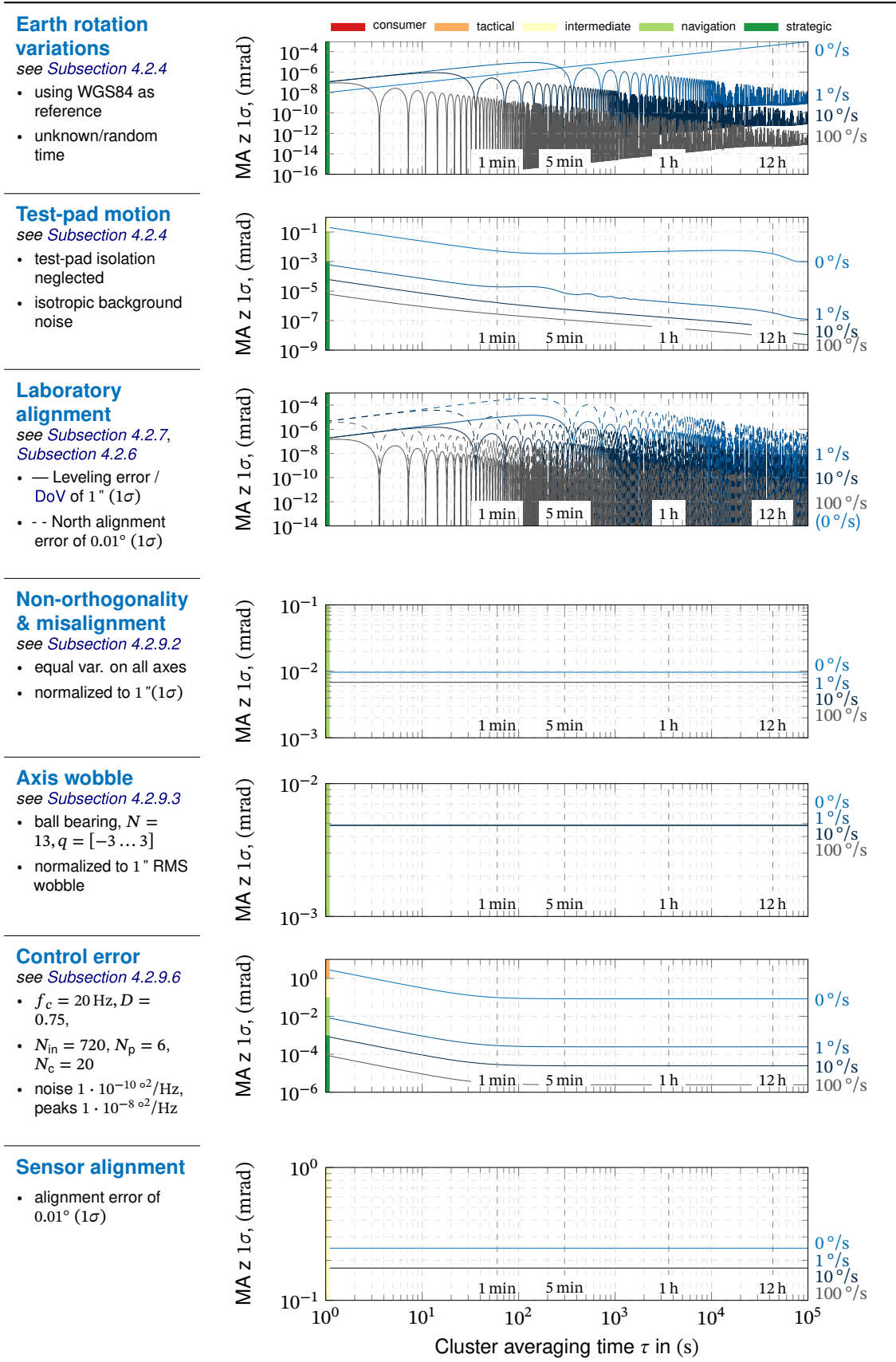


Table 4.24.: Rate table six-position gyro test axis misalignment M_{xz} estimation error budget for varying rotation rate and averaging time. The laboratory is located at $\phi = 45^\circ$



gyroscopes better than tactical grade. Instead, the bias should preferably be determined from static (reversal) tests. These results are confirmed by [Example 10](#).

Example 10: IMU 500 Six-Position Test

The six-position tests of the [FOG IMU](#) were performed at the inertial laboratory of the Institute of Flight System Dynamics. Each position is held for 1080 s at an input rate of 100 °/s. The laboratory is located at latitude $\phi = 48.2667^\circ$ and modeled in accordance with the error budgets. Alignment and axis errors are scaled to represent the real setup at the institute:

Laboratory parameters		Sensor noise	
Laboratory alignment	2.5 asec	Angular random walk N	$5 \cdot 10^{-3} \text{ }^\circ/\sqrt{\text{h}}$
Non-orthogonality	5.0 asec	Bias instability B	$2 \cdot 10^{-3} \text{ }^\circ/\text{h}$
Wobble RMS	2.5 asec	<i>determined from Example 4</i>	

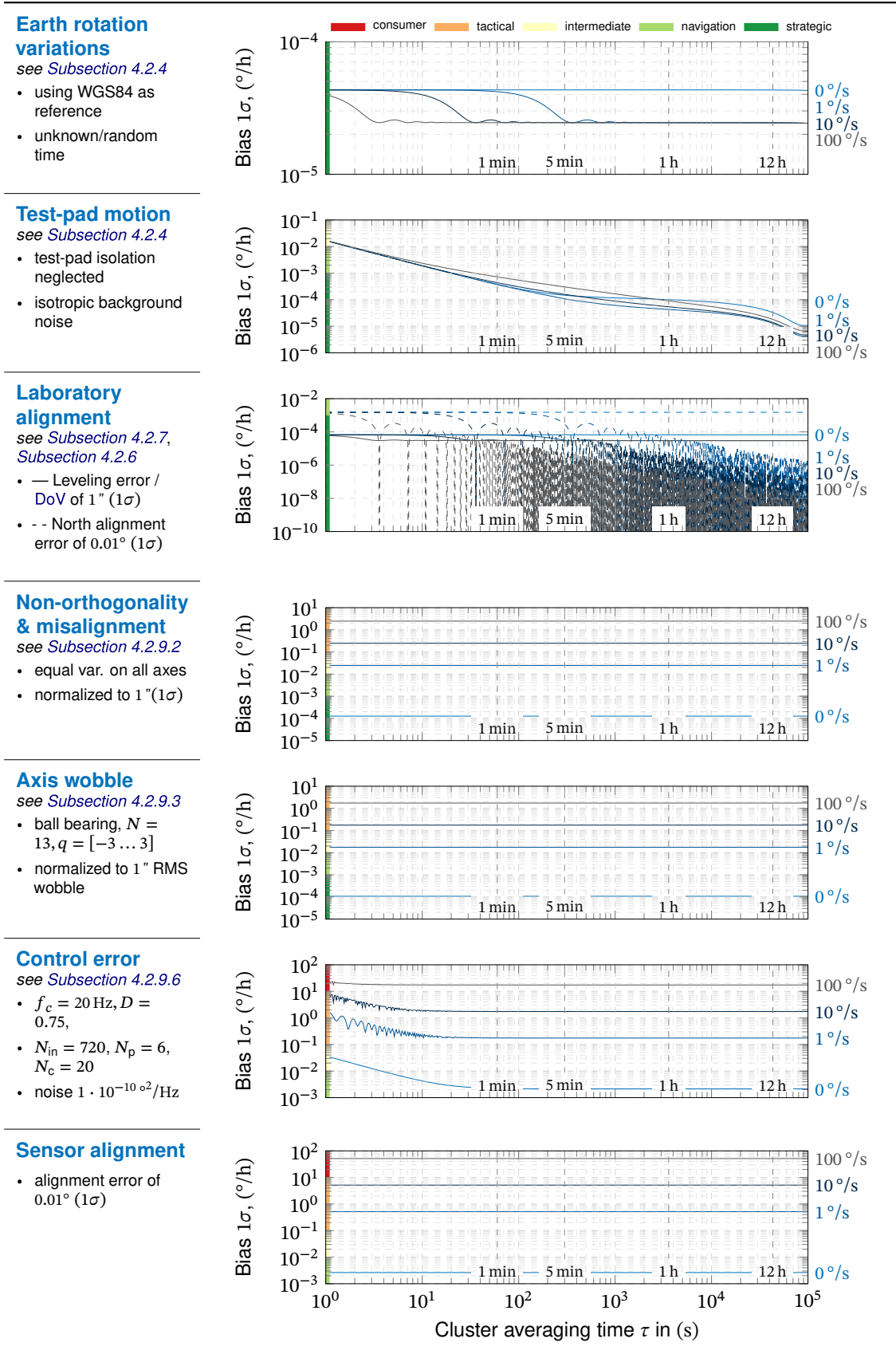
The estimated SF, misalignment and bias parameters and their uncertainty from both sensor noise and laboratory errors are summarized below:

	x	y	z	Sens. noise (1σ)	Laboratory* (1σ)
SF error (ppm)	-27.960	-16.950	-15.803	$1.811 \cdot 10^{-2}$	$3.636 \cdot 10^1$
MA 1 (mrad)	0.181	0.831	-0.821	$1.811 \cdot 10^{-5}$	$6.894 \cdot 10^{-2}$
MA 2 (mrad)	0.436	-1.027	1.209	$1.811 \cdot 10^{-5}$	$6.894 \cdot 10^{-2}$
Bias (°/h)	2.670	4.253	-6.529	$4.003 \cdot 10^{-3}$	6.084

* laboratory errors are determined for the sensor's z-axis. As depicted in the error budgets, the uncertainty of one of the misalignment angles can be much better, depending on axis orientation within the rate table.

For the analyzed test, the determined sensor scale factor errors and biases are in the same range as the errors caused by the environmental and laboratory errors. The sensor's noise would allow a more accurate estimation in this case. As expected from the error budgets, this laboratory setup does not provide sufficient accuracy to determine the scale factors and biases of this navigation grade [FOG](#) using a six-position test. For this level of accuracy, other test procedures should be preferred.

Table 4.25.: Rate table six-position gyro test bias estimation error budget for varying rotation rate and averaging time. The laboratory is located at $\phi = 45^\circ$



4.4.5.5. Accelerometer Test Error Model

During six-position testing, the ideal specific forces contain only the local gravity that is observed by the accelerometers under different orientations:

$$\hat{\mathbf{f}}_b^{(P)} = \mathbf{I}_{\hat{b}u} \mathbf{R}_{\hat{u}v}^{(P)} \mathbf{R}_{\hat{v}w}^{(P)} \mathbf{R}_{\hat{w}p}(t) \mathbf{I}_{\hat{p}n} \boldsymbol{\gamma}_n(P_b) \quad (4.258)$$

As the outer axis of an ideal rate table is aligned to the local gravity vector, its rotation has no effect on the reference signal. The reference input to the accelerometer axis is thus either zero or the local gravity at the tested sensor's position:

$$\overline{\hat{\mathbf{f}}_b} = \pm \boldsymbol{\gamma}_{n,z}(P_b) \quad (4.259)$$

The ideal rate table has no nominal lever arms, except the height of the intersection point of the three rotation axes above the test-pad:

$$\hat{\mathbf{r}}_p(P_w) = \begin{bmatrix} 0 & 0 & h \end{bmatrix}^T \quad (4.260)$$

All nominal angular rates are constant. Linearization of specific forces equation for the input errors about this ideal situation yields:

$$\begin{aligned} \delta \mathbf{f}_b^{(P)} = & \mathbf{R}_{\hat{b}n}^{(P)} \delta \boldsymbol{\gamma}_n \\ & + \left(\mathbf{R}_{\hat{b}n}^{(P)} \frac{\delta \delta \hat{\boldsymbol{\gamma}}_n(\mathbf{r}_e)}{\delta \mathbf{r}_e} \left([\mathbf{R}_{\hat{n}p} \hat{\mathbf{r}}_p(P_w)] \times \right) - \mathbf{R}_{\hat{b}n}^{(P)} (\hat{\boldsymbol{\gamma}}_n(P_b) \times) \right) \delta \boldsymbol{\Psi}_{n\hat{n}} \\ & - \mathbf{R}_{\hat{b}p}^{(P)} (\hat{\mathbf{r}}_p(P_w) \times) \mathbf{R}_{\hat{p}n} (\hat{\boldsymbol{\omega}}_{in} \times) \delta \boldsymbol{\omega}_{np} \\ & - \mathbf{R}_{\hat{b}p}^{(P)} (\hat{\mathbf{r}}_p(P_w) \times) \delta \boldsymbol{\omega}_{np} \\ & + \left(\mathbf{R}_{\hat{b}n}^{(P)} \frac{\delta \delta \hat{\boldsymbol{\gamma}}_n(\mathbf{r}_e)}{\delta \mathbf{r}_e} \left([\hat{\mathbf{r}}_p(P_w)] \times \right) - \mathbf{R}_{\hat{b}p}^{(P)} (\mathbf{R}_{\hat{p}n} \hat{\boldsymbol{\gamma}}_n(P_b) \times) \right) \delta \boldsymbol{\Psi}_{p\hat{p}} \\ & - \left(\mathbf{R}_{\hat{b}w}^{(P)} (\mathbf{R}_{\hat{w}n}^{(P)} \hat{\boldsymbol{\gamma}}_n(P_b) \times) \right) \delta \boldsymbol{\Psi}_{w\hat{w}} \\ & - \left(\mathbf{R}_{\hat{b}v}^{(P)} (\mathbf{R}_{\hat{v}n}^{(P)} \hat{\boldsymbol{\gamma}}_n(P_b) \times) \right) \delta \boldsymbol{\Psi}_{v\hat{v}} \\ & - \left(\mathbf{R}_{\hat{b}u} (\mathbf{R}_{\hat{u}n}^{(P)} \hat{\boldsymbol{\gamma}}_n(P_b) \times) \right) \delta \boldsymbol{\Psi}_{u\hat{u}} \\ & + \mathbf{R}_{\hat{b}n}^{(P)} \left(\hat{\boldsymbol{\Omega}}_{in}^2 + \dot{\hat{\boldsymbol{\Omega}}}_{in} \right) \delta \mathbf{r}_n(P_p) + \mathbf{R}_{\hat{b}n}^{(P)} \hat{\boldsymbol{\Omega}}_{in} \delta \dot{\mathbf{r}}_n(P_p) + \mathbf{R}_{\hat{b}n}^{(P)} \delta \ddot{\mathbf{r}}_n(P_p) \\ & + \mathbf{R}_{\hat{b}p}^{(P)} \left(\hat{\boldsymbol{\Omega}}_{ip}^2 + \dot{\hat{\boldsymbol{\Omega}}}_{ip} \right) \delta \mathbf{r}_p(P_w) + \mathbf{R}_{\hat{b}p}^{(P)} \hat{\boldsymbol{\Omega}}_{ip} \delta \dot{\mathbf{r}}_p(P_w) + \mathbf{R}_{\hat{b}p}^{(P)} \delta \ddot{\mathbf{r}}_p(P_w) \\ & + \mathbf{R}_{\hat{b}w}^{(P)} \left(\hat{\boldsymbol{\Omega}}_{iw}^2 + \dot{\hat{\boldsymbol{\Omega}}}_{iw} \right) \delta \mathbf{r}_w(P_v) + \mathbf{R}_{\hat{b}w}^{(P)} \hat{\boldsymbol{\Omega}}_{iw} \delta \dot{\mathbf{r}}_w(P_v) + \mathbf{R}_{\hat{b}w}^{(P)} \delta \ddot{\mathbf{r}}_w(P_v) \\ & + \mathbf{R}_{\hat{b}v}^{(P)} \left(\hat{\boldsymbol{\Omega}}_{iv}^2 + \dot{\hat{\boldsymbol{\Omega}}}_{iv} \right) \delta \mathbf{r}_v(P_u) + \mathbf{R}_{\hat{b}v}^{(P)} \hat{\boldsymbol{\Omega}}_{iv} \delta \dot{\mathbf{r}}_v(P_u) + \mathbf{R}_{\hat{b}v}^{(P)} \delta \ddot{\mathbf{r}}_v(P_u) \\ & + \mathbf{R}_{\hat{b}u} \left(\hat{\boldsymbol{\Omega}}_{iu}^2 + \dot{\hat{\boldsymbol{\Omega}}}_{iu} \right) \delta \mathbf{r}_u(P_b) + \mathbf{R}_{\hat{b}u} \hat{\boldsymbol{\Omega}}_{iu} \delta \dot{\mathbf{r}}_u(P_b) + \mathbf{R}_{\hat{b}u} \delta \ddot{\mathbf{r}}_u(P_b) \end{aligned} \quad (4.261)$$

The resulting linear sensitivities of the specific forces at the sensor are summarized in [Table H.4](#). Analogous to the gyro test, positions 1 to 4 have similar sensitivities, where some terms of the

middle and inner axes are permuted and flip signs between the reversal measurements. Again, only some (quasi-) constant errors are eliminated by the reversal measurements.

4.4.5.6. Accelerometer Test Error Budget

Table 4.26 to Table 4.29 illustrate the contributions of the different error sources to the estimated sensor parameters for a typical inertial laboratory setup. In contrast to the previously discussed gyro test, the reference-specific forces signal for the accelerometer test is affected by translational offsets of the axes and the sensors and linear accelerations, e.g., of the test pad. As the variances from geometrical rate table errors scale linearly, these are normalized to 1 asec respectively 1 mm. Note that the sensitivity to axis and sensor offsets depends on the rotation of the rate table. If the accelerometer test is performed independent of the gyro test (and thus without rotation), translational position errors only affect the local gravity. In addition, the specific forces are affected by the temporal variation of the local gravity, which was not the case for the gyroscope tests.

For the accelerometer tests, the applied angular rate does not affect the signal-to-noise ratio of the reference signals since the local gravity is used as a reference. However, a faster rotation rate yields a more immediate error reduction when observed under rotation. Of course, axis and sensor offsets act as lever-arms, and the resulting accelerations scale with the applied angular rates quadratically.

The accelerometer SF estimate is dominated by the test-pad motion, followed by the temporal variations of the local gravity. Significantly, the test-pad motion limits the SF estimation accuracy to the region of around 10 ppm. The effects of both test-pad motion and temporal gravity variations can be further reduced by very long averaging times of multiple hours per test position. While the SF variance from the laboratory alignment errors is not affected by averaging, the resulting levels of magnitude are already minimal for typical alignment errors. The SF variances from axis or sensor position offsets and the axis wobble can be reduced by averaging, and both reduce periodically with every revolution of the rate table. In the test discussed, at least in the linearized analysis, the control error does not affect the SF estimation of the sensor's x-axis. The same applies to the sensor alignment errors that cancel out due to the symmetric poses.

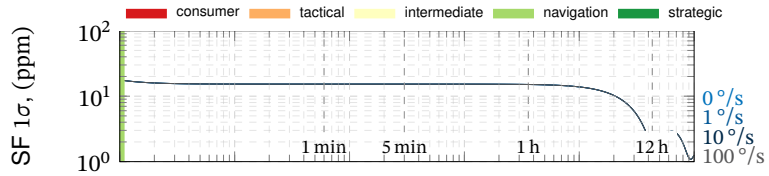
The error budgets for the misalignment are depicted in Table 4.26 and Table 4.24. In general, the two misalignment parameters are affected equally by the various errors. The only exception is the sensitivity to the rate table's position and rate errors, which can only be observed for one parameter. This is a result of the mechanization of this six-position test, and the orientation of the sensor's axes concerning the rate table's actuated axes. Just like for the gyroscopes, the rate table's axes non-orthogonality and sensor alignment errors transfer directly into the misalignment and cannot be reduced by averaging. For the misalignment estimation, gravity variations, the alignment errors, and the axis and sensor offsets are effectively reduced by increasing the averaging time and especially by averaging over complete revolutions of the rate

Table 4.26.: Rate table six-position accelerometer test scale factor estimation error budget for varying rotation rate and averaging time. The laboratory is located at $\phi = 45^\circ$

Test-pad motion

see Subsection 4.2.4

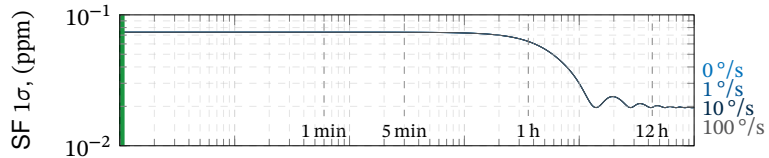
- test-pad isolation neglected
- isotropic background noise



Gravity variations

see Subsection 4.2.5

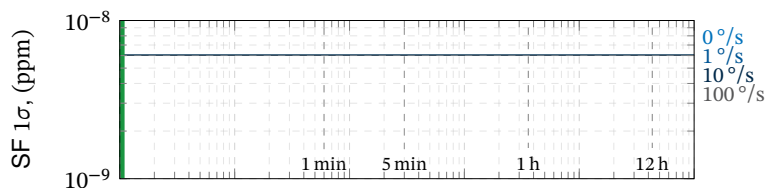
- tides from Sun and Moon
- other planets neglected



Laboratory alignment

see Subsection 4.2.7, Subsection 4.2.6

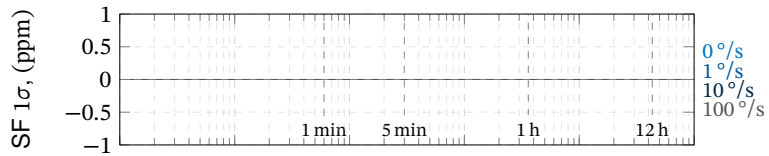
- — Leveling error / DoV of 1" (1σ)
- - - North alignment error of 0.01° (1σ)



Non-orthogonality & misalignment

see Subsection 4.2.9.2

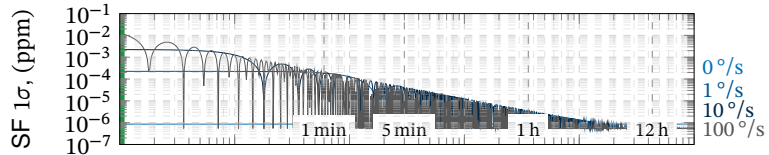
- equal var. on all axes
- normalized to 1" (1σ)



Axis and sensor offset

see Subsection 4.2.9.2

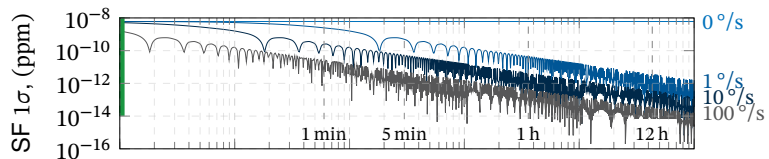
- equal var. on all axes
- normalized to 1 mm (1σ)



Axis wobble

see Subsection 4.2.9.3

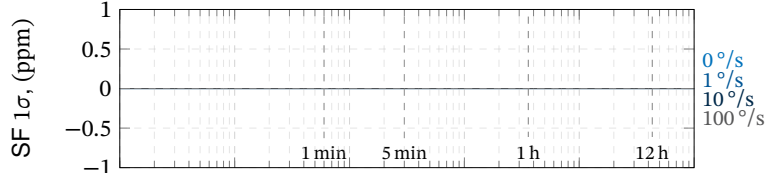
- ball bearing, $N = 13, q = [-3 \dots 3]$
- normalized to 1" RMS wobble



Control error

see Subsection 4.2.9.6

- $f_c = 20 \text{ Hz}, D = 0.75,$
- $N_{in} = 720, N_p = 6, N_c = 20$
- noise $1 \cdot 10^{-10} \text{ } \omega^2/\text{Hz}$



Sensor alignment

- alignment error of 0.01° (1σ)

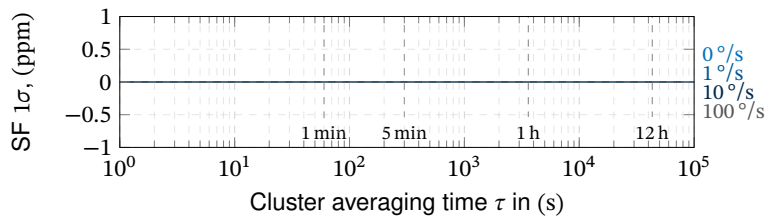


table. For the analyzed typical laboratory setup, the misalignment accuracy achieved during the six-position test is limited to the region of few ppm, typically associated with navigation grade sensors.

The error budget for the accelerometer bias estimation in the six-position test is presented in [Table 4.29](#). The bias estimation is dominated by the rate table's positioning errors and the test-pad motion. The effect of the test-pad motion can be reduced by averaging but reaches navigation grade levels only for very long averaging times of more than 10 h. However, the variance resulting from the table's position accuracy cannot be improved by averaging.

The bias variance from laboratory alignment errors is effectively reduced by averaging. It vanishes entirely for complete revolutions of the rate table. The errors from axis non-orthogonality and axis wobble, however, result reach a constant level after a few minutes and cannot be further reduced for the given configuration. The axis- and sensor offset together with the rate table's rotation create constant centrifugal forces that directly go into the sensor's bias estimate. Also, the sensor's alignment errors contribute to the bias estimate and are not affected by averaging.

All in all, the analyzed configuration allows the determination of the accelerometer bias during the six-position test at the navigation grade level. Higher accuracies require a more precise alignment and a calmer (e.g., actively stabilized) test pad.

4.4.5.7. Modification for Static Six Position Tests

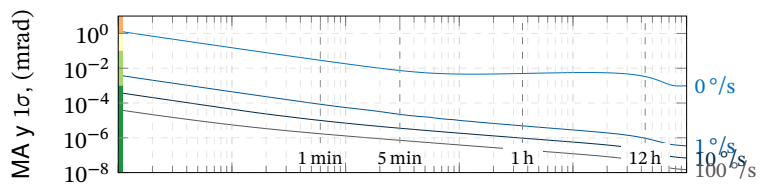
The presented error budgets can be easily modified to represent a static version of the six-position test that may be conducted, e.g., using a test cube. This can be easily represented by neglecting all rate-table errors and choosing the depicted graphs for zero applied rate. Due to the similar test structure, the results resemble the results of the static reversal measurements from [Subsection 4.4.3](#). However, the actual axes' orientations differ. Furthermore, in this six-position test, the bias estimate is based on all six measurements, adding additional errors, in contrast to the simple reversal measurements case.

Table 4.27.: Rate table six-position accelerometer test axis misalignment M_{xy} estimation error budget for varying rotation rate and averaging time. The laboratory is located at $\phi = 45^\circ$

Test-pad motion

see Subsection 4.2.4

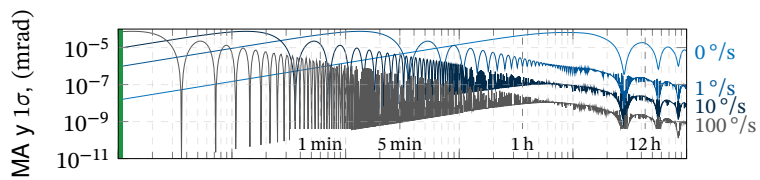
- test-pad isolation neglected
- isotropic background noise



Gravity variations

see Subsection 4.2.5

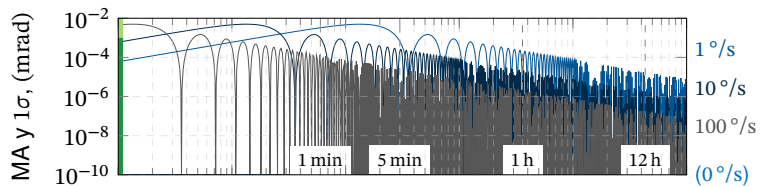
- tides from Sun and Moon
- other planets neglected



Laboratory alignment

see Subsection 4.2.7, Subsection 4.2.6

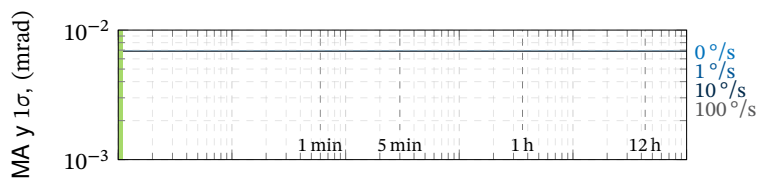
- — Leveling error / DoV of 1" (1σ)
- -- North alignment error of 0.01° (1σ)



Non-orthogonality & misalignment

see Subsection 4.2.9.2

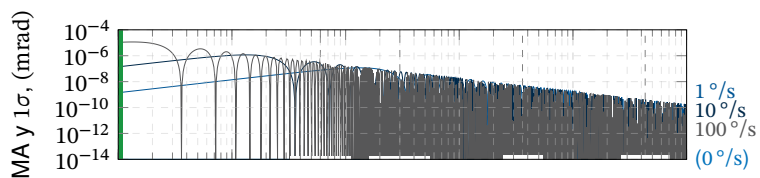
- equal var. on all axes
- normalized to 1" (1σ)



Axis and sensor offset

see Subsection 4.2.9.2

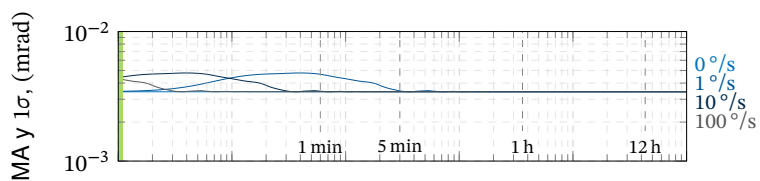
- equal var. on all axes
- normalized to 1 mm (1σ)



Axis wobble

see Subsection 4.2.9.3

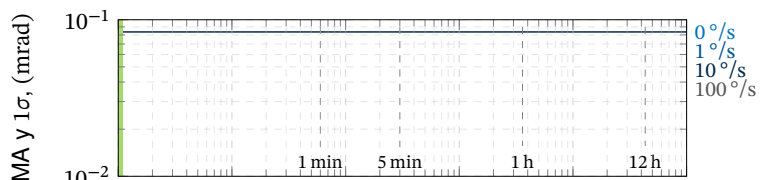
- ball bearing, $N = 13, q = [-3 \dots 3]$
- normalized to 1" RMS wobble



Control error

see Subsection 4.2.9.6

- $f_c = 20 \text{ Hz}, D = 0.75,$
- $N_{in} = 720, N_p = 6, N_c = 20$
- noise $1 \cdot 10^{-10} \text{ } \sigma^2/\text{Hz}$



Sensor alignment

- alignment error of 0.01° (1σ)

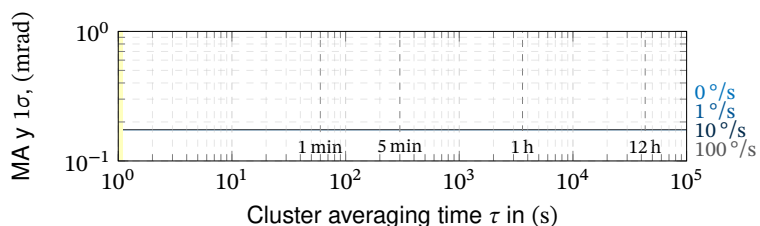


Table 4.28.: Rate table six-position accelerometer test axis misalignment M_{xz} estimation error budget for varying rotation rate and averaging time. The laboratory is located at $\phi = 45^\circ$

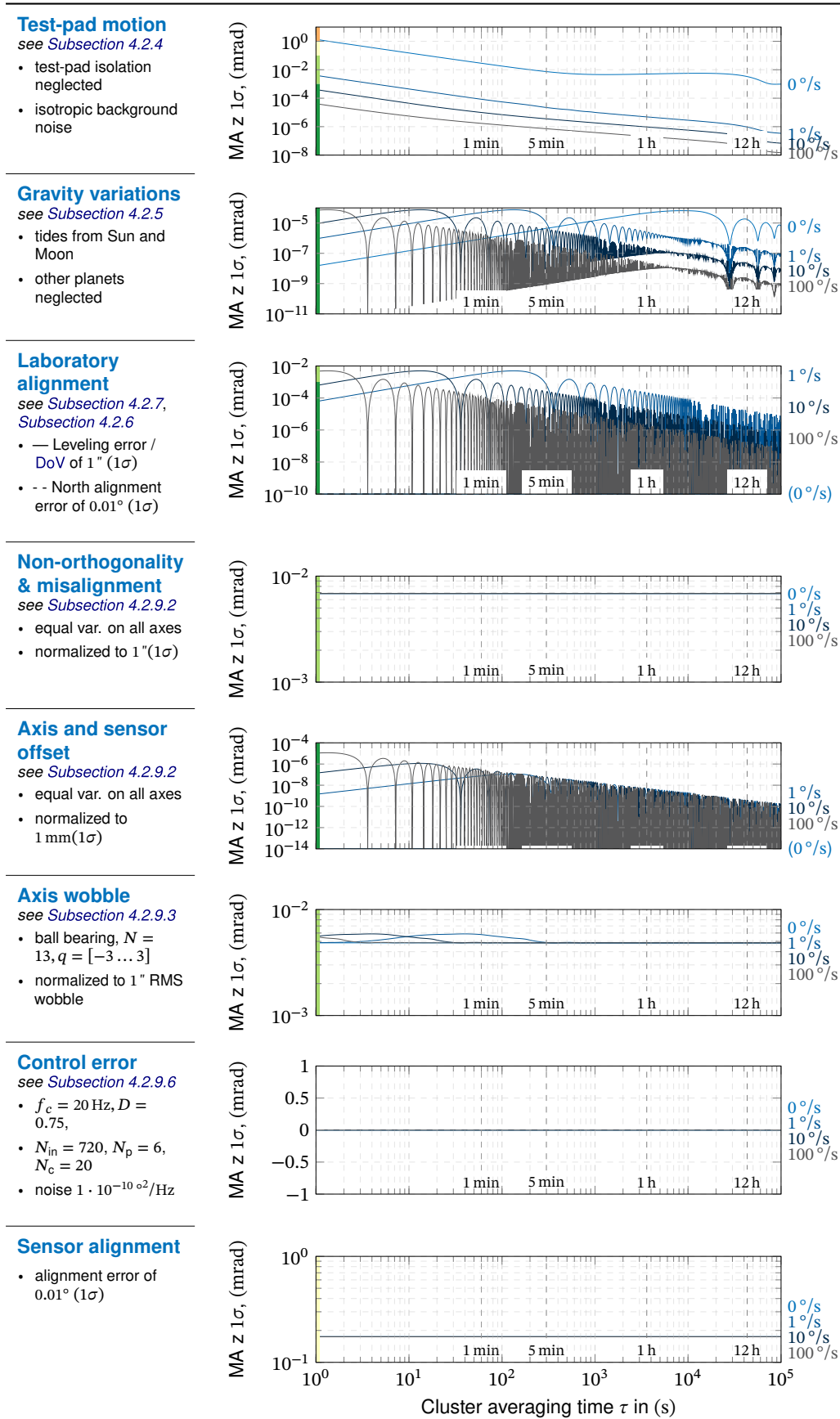


Table 4.29.: Rate table six-position accelerometer test bias estimation error budget for varying rotation rate and averaging time. The laboratory is located at $\phi = 45^\circ$

Test-pad motion

see Subsection 4.2.4

- test-pad isolation neglected
- isotropic background noise

Gravity variations

see Subsection 4.2.5

- tides from Sun and Moon
- other planets neglected

Laboratory alignment

see Subsection 4.2.7, Subsection 4.2.6

- — Leveling error / DoV of 1" (1σ)
- -- North alignment error of 0.01° (1σ)

Non-orthogonality & misalignment

see Subsection 4.2.9.2

- equal var. on all axes
- normalized to 1" (1σ)

Axis and sensor offset

see Subsection 4.2.9.2

- equal var. on all axes
- normalized to 1 mm (1σ)

Axis wobble

see Subsection 4.2.9.3

- ball bearing, $N = 13, q = [-3 \dots 3]$
- normalized to 1" RMS wobble

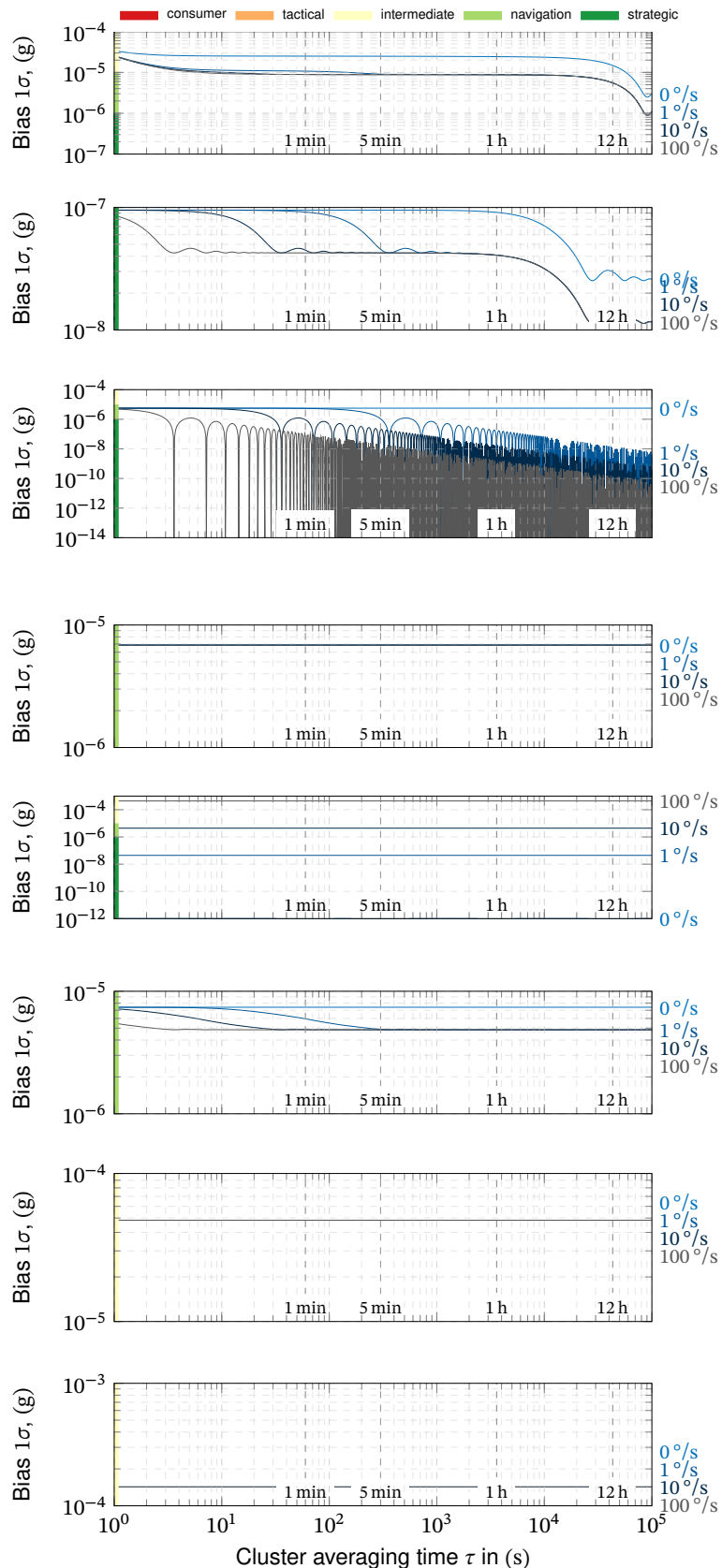
Control error

see Subsection 4.2.9.6

- $f_c = 20 \text{ Hz}, D = 0.75,$
- $N_{in} = 720, N_p = 6, N_c = 20$
- noise $1 \cdot 10^{-10} \text{ } \omega^2/\text{Hz}$

Sensor alignment

- alignment error of 0.01° (1σ)



Result 8: Six-Position Testing

The simple six-position error estimation is equivalent to reversal measurements for the scale factor and misalignment determination. However, here, the magnitude of the gyroscope input can be easily controlled by the rate table's applied rate. Independent of the test's degrees of freedom like the number of positions and applied rates, the following statements are valid:

- The linear scale factor estimate reaches the strategic grade quickly, as it can be improved by increasing the averaging time and the applied angular rate.
- The misalignment estimation accuracy is directly limited by the rate table's axis orientation errors, non-orthogonality, and wobble. Typical rate table accuracies allow the misalignment estimation at the navigation grade level.
- The bias estimation is dominated by rate table errors and limited to the level of tactical grade sensors. In contrast to the other sensor errors, the estimation accuracy worsens when the angular rate increases.
- Averaging over complete revolutions is always beneficial as it reduces periodical errors.

Similar statements can be made for the accelerometer testing:

- The (linear) scale factor estimate reaches only navigation grade and is limited by the test-pad motion.
- The misalignment estimation accuracy is directly limited by the rate table's axis orientation errors, non-orthogonality, and wobble. Typical rate table accuracies allow estimation of the misalignment at the level of navigation grade sensors.
- Also, the accelerometer's bias estimate is dominated by the rate table's control errors and limited to intermediate grade.

As the resulting accuracy levels for gyroscopes and accelerometers are similar, the multi-position test provides an effective tool for the simultaneous estimation of accelerometer and gyro errors. This is especially true when using a three-axis rate table that allows automated orientation changes of the IMU without manual handling. However, this efficiency comes with a reduced accuracy compared to the static, e.g., reversal position tests.

4.5. Kalman Filter Based Sensor Testing

Within the previous sections, the classical stationary calibration procedures have been discussed. These mainly relied on procedures designed to isolate and determine the sensor errors from averaging the sensor outputs determined at constant input signals.

Within this section, a different approach, based on **KF** will be presented. Here the sensor's model equations are transformed into state-space representation, and a **KF** is used to estimate the sensor errors from the sensor's output. The basic architecture of this calibration approach is illustrated in Figure 4.39. In contrast to the classical test procedures, the **KF** based estimation does not require specifically designed test procedures but runs independently of the applied sensor motion. This, however, requires knowledge of the rate table's angular positions and rates synchronized in time with the sensor's output. Using the kinematic models from Subsection 4.2.1, the ideal sensor input can be calculated from the measured rate table position and rates.

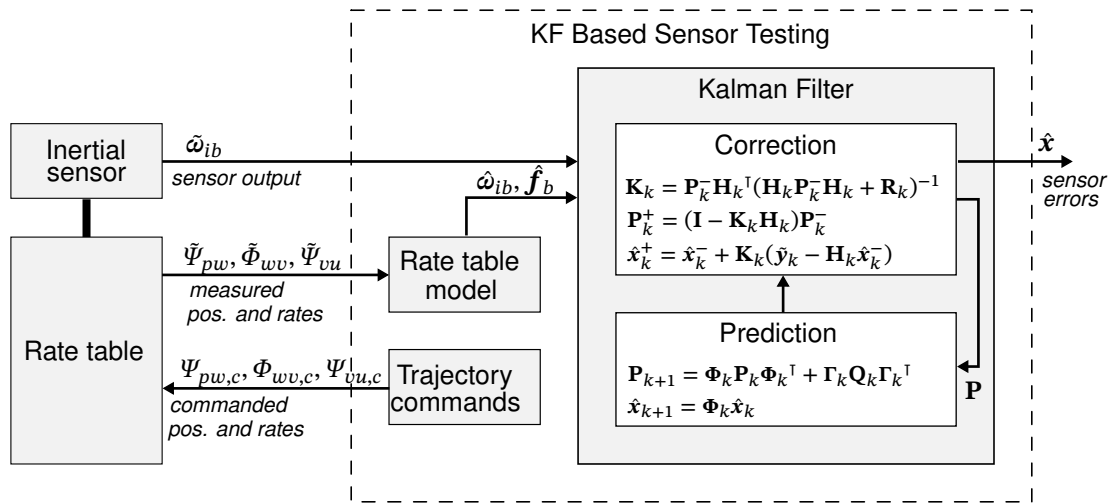


Figure 4.39.: General concept of Kalman Filter based laboratory calibration.

The **KF** approach inherently provides information on the accuracy of the estimation, represented by the covariance matrix. In case the input motion does not provide sufficient information to estimate the sensor parameters, this can be observed in the covariance matrix.

4.5.1. KF Design and Modeling

4.5.1.1. Estimation States and System

Just like for the previous test procedures, the goal is to determine the error terms of a sensor's model equation. The **KF** based laboratory testing will be demonstrated for the following model equation

$$\tilde{\omega}_{ib,x} = S_{1,x} \omega_{ib,x} + \dots + S_{s,x} \omega_{ib,x}^k + M_{xy} \omega_{ib,y} + M_{xz} \omega_{ib,z} + a_x f_{b,x} + a_y f_{b,y} + a_z f_{b,z} + b_x + v_x \quad (4.262)$$

which includes terms for a scale factor polynomial $S_{1,x}$ to $S_{s,x}$, linear misalignments M_{xy}, M_{xz} , acceleration sensitivities a_x, a_y, a_z , a bias b_x and sensor noise v_x . Ideally, the error parameters are constant, and the model equation is representative for a sufficiently long time to allow calibration and compensation of errors over the sensor's life. These errors are modeled as a random constant in the framework of a KF, which yields a straightforward state-space system without dynamics. A little dynamics is added, if a rate ramp error shall be considered. In this case, the sensor's bias changes at a constant rate r_x :

$$\dot{b}_x = r_x \quad (4.263)$$

Within this section, the analysis will focus on gyroscope testing respectively a gyroscope model equation. Since the model equation and the following analyses consider (high order) acceleration sensitivities, the results can be easily adopted to accelerometers with model equations of the form

$$\tilde{f}_{b,x} = a_{1,x} f_{b,x} + a_{2,x} f_{b,x}^2 + \dots + a_y f_{b,y} + a_z f_{b,z} + b_x + v_x \quad (4.264)$$

A model equation with high order and cross-axis sensitivity terms to angular rate and accelerations could be used for sensor testing/calibration independent of the actual sensor type.

For the model equation (4.262), the corresponding state space system can be written as

$$\underbrace{\frac{d}{dt} \begin{bmatrix} S_{1,x} \\ \vdots \\ S_{s,x} \\ M_{xy} \\ M_{xz} \\ a_x \\ a_y \\ a_z \\ b_x \\ r_x \end{bmatrix}}_{\dot{x}} = \underbrace{\begin{bmatrix} 0 & \dots & 0 & 0 & 0 & 0 & 0 & 0 & 0 & 0 \\ \vdots & \ddots & \vdots & \vdots & \vdots & \vdots & \vdots & \vdots & \vdots & \vdots \\ 0 & \dots & 0 & 0 & 0 & 0 & 0 & 0 & 0 & 0 \\ 0 & \dots & 0 & 0 & 0 & 0 & 0 & 0 & 0 & 0 \\ 0 & \dots & 0 & 0 & 0 & 0 & 0 & 0 & 0 & 0 \\ 0 & \dots & 0 & 0 & 0 & 0 & 0 & 0 & 0 & 0 \\ 0 & \dots & 0 & 0 & 0 & 0 & 0 & 0 & 0 & 0 \\ 0 & \dots & 0 & 0 & 0 & 0 & 0 & 0 & 0 & 1 \\ 0 & \dots & 0 & 0 & 0 & 0 & 0 & 0 & 0 & 0 \end{bmatrix}}_{\mathbf{A}} \underbrace{\begin{bmatrix} S_{1,x} \\ \vdots \\ S_{s,x} \\ M_{xy} \\ M_{xz} \\ a_x \\ a_y \\ a_z \\ b_x \\ r_x \end{bmatrix}}_x \quad (4.265)$$

For this model, there is no input to the system of the estimation states. The system matrix \mathbf{A}

can be easily time-discretized to the transition matrix Φ :

$$\Phi = \begin{bmatrix} 1 & \dots & 0 & 0 & 0 & 0 & 0 & 0 & 0 & 0 \\ \vdots & \ddots & \vdots & \vdots & \vdots & \vdots & \vdots & \vdots & \vdots & \vdots \\ 0 & \dots & 1 & 0 & 0 & 0 & 0 & 0 & 0 & 0 \\ 0 & \dots & 0 & 1 & 0 & 0 & 0 & 0 & 0 & 0 \\ 0 & \dots & 0 & 0 & 1 & 0 & 0 & 0 & 0 & 0 \\ 0 & \dots & 0 & 0 & 0 & 1 & 0 & 0 & 0 & 0 \\ 0 & \dots & 0 & 0 & 0 & 0 & 1 & 0 & 0 & 0 \\ 0 & \dots & 0 & 0 & 0 & 0 & 0 & 1 & 0 & 0 \\ 0 & \dots & 0 & 0 & 0 & 0 & 0 & 0 & 1 & \Delta t \\ 0 & \dots & 0 & 0 & 0 & 0 & 0 & 0 & 0 & 1 \end{bmatrix} \quad (4.266)$$

Based on the above state space model, the model equation (4.262) is transformed into the following measurement matrix

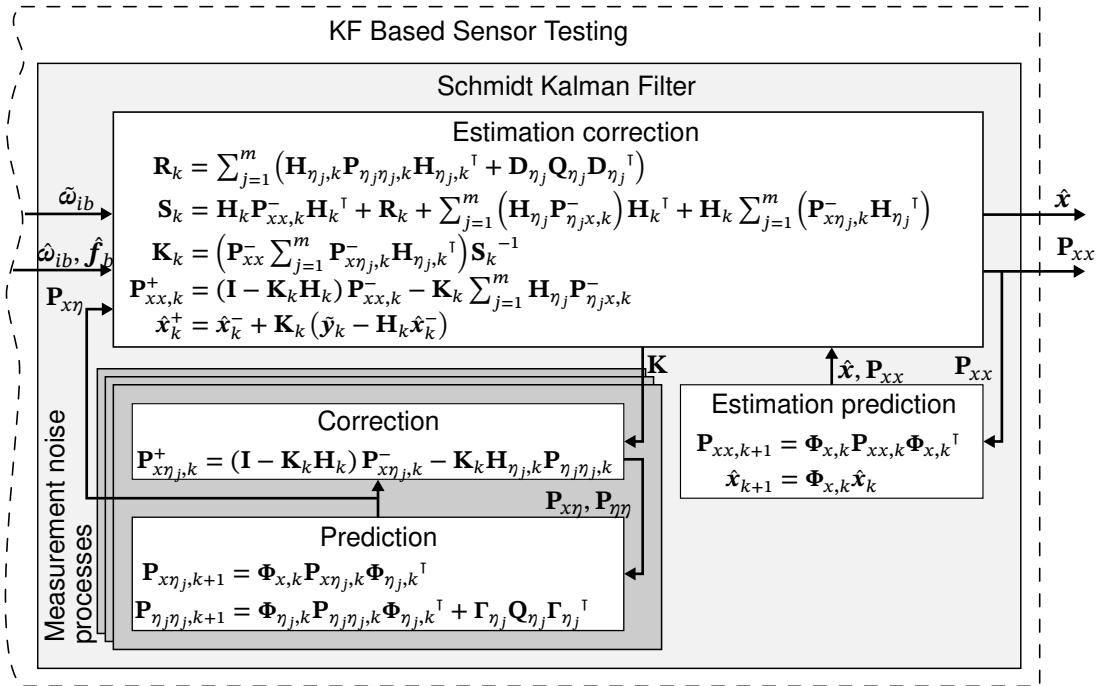
$$\mathbf{H}_k = \left[\hat{\omega}_{ib,x}, \dots, \hat{\omega}_{ib,x}^s, \hat{\omega}_{ib,y}, \hat{\omega}_{ib,z}, \hat{f}_{b,x}, \hat{f}_{b,y}, \hat{f}_{b,z}, 1, 0 \right]_k \quad (4.267)$$

with the ideal angular rates and specific forces as determined from the rate table's kinematic model at time k , see Subsection 4.2.1.

If the sensor noise ν_x were WGN, above system and measurement matrix would suffice to estimate the sensor parameters using the classical KF Algorithm 1. However, as widely discussed in this work, the sensor noise is correlated, which should be considered to achieve a consistent estimation of the sensor errors. The noise itself shall not be estimated, and only its stochastic shall be considered. Therefore a Schmidt-Kalman Filter, see Algorithm 3, is used. As depicted in Figure 4.40, the Schmidt-Kalman filter augments the KF based calibration from Figure 4.39 with measurement noise processes. These measurement noise processes can be used to incorporate both sensor noise as well as laboratory errors.

4.5.1.2. Sensor Noise Models

In the Kalman Filter framework, sensor noise is modeled as a stochastic process represented by a LTI system with WGN input. One option to determine such a system model is identifying an Auto-Regressive Moving-Average (ARMA) model from recorded sensor noise, e.g., as discussed in [57]. In this work, another approach is used: Each sensor noise process, as defined in Table 2.7 is modeled separately. The defining noise parameters for this approach are determined from static tests, see Subsection 4.4.2.3. In contrast to the ARMA approach, the separate noise models allow a simple analysis and tweaking of the different noise processes. The models for the sensor noise processes will be discussed in the following.



Quantization Noise

In Table 2.7 quantization noise is defined as the time derivative of white Gaussian noise, scaled by the factor Q . In the state space framework, this can be approximated by the difference quotient of the current and the previous noise sample. In the approximation model Model 11, the system's single state is used to store the previous noise sample.

Model 11: Quantization Noise

Transition matrix	Input matrix	Input covariance
$\Phi_Q = 0$	$\Gamma_Q = 1$	$Q_Q = \frac{Q^2}{\Delta t}$
Measurement matrix	Feedthrough	Initialization
$H_Q = -\frac{1}{\Delta t}$	$D_Q = \frac{1}{\Delta t}$	$P_{Q,0} = Q_Q$

Angular/Velocity Random Walk

As an angular, respectively velocity, random walk is just white Gaussian noise on the rates/acceleration (see Table 2.7), the state space noise model is reduced to the feedthrough D to the white-noise input with variance Q_N . There is no system dynamics and no states are required. The scaling is defined by the ARW coefficient N . The resulting state space representation is summarized in Model 12.

Model 12: Angular/Velocity Random Walk		
Transition matrix $\Phi_N = -$	Input matrix $\Gamma_N = -$	Input covariance $Q_N = \frac{N^2}{\Delta t}$
Measurement matrix $H_N = -$	Feedthrough $D_N = 1$	Initialization $R_{N,0} = 0$

Bias Instability

Bias instability is defined as a band-limited flicker noise (see Table 2.7). As discussed in Subsection 3.3.3, there is no LTI system that exactly reproduces bias instability from WGN input. In general, the bias instability noise process can be approximated by ARMA models as presented in [57]. This, however, required an identification of the ARMA models from a given signal.

Here, the bias instability noise process is modeled by a set of filters that approximate the $\sim 1/f$ PSD as proposed in [80]. A cascade of linear filters of the form

$$G(s) = \frac{\tau_2 \beta^i s + 1}{(\tau_2 + \tau_1) \beta^i s + 1} \quad \text{with } \beta = \left(\frac{\tau_2}{\tau_1 + \tau_2} \right)^2 \quad \text{for } i = 1, 2, \dots \quad (4.268)$$

is used to approximate the desired $\sim 1/f$ PSD over a specific frequency range. An example PSD of this approximation approach is given in Figure 4.41. In the filter design τ_2 and the number of filters should be chosen to approximate over the entire frequency range, from the Nyquist-frequency to the inverse of the relevant operation time.

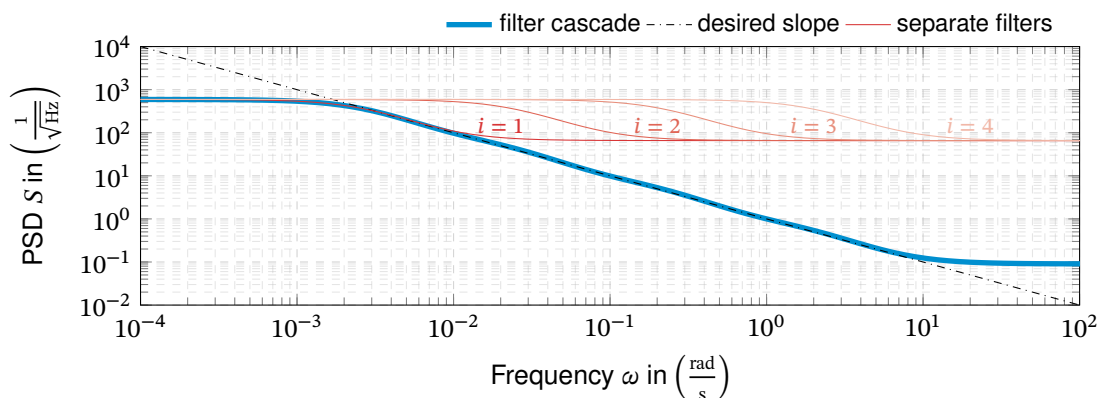


Figure 4.41.: Flicker noise approximation using filter cascade, $\beta = 1/9$, $\tau_2 = 1$ s.

The design process and derivation of a linear state-space system for use in a Kalman Filter is summarized in Model 13.

Model 13: Bias Instability

Using the approach of [80], an approximation for the bias instability noise process can be designed as follows:

1. Choose β , e.g., $\beta = \frac{1}{9}$.
2. Determine required number of filters n . The approximated frequency range is $\approx \beta^{-n}$.
3. Select time constant τ_2 , ideally so that τ_2^n is the inverse Nyquist-frequency $\tau_2^n \approx \frac{2}{f_s}$.
4. Determine $\tau_1 = (\beta^{-1/2} - 1) \tau_2$.
5. Determine the transfer function:

$$G(s) = \prod_{i=1}^n \left[\underbrace{\sqrt{\frac{(\tau_1 + \tau_2)^2 \beta^{2i} + 1}{\tau_2^2 \beta^{2i} + 1}} \frac{1 + s \tau_2 \beta^i}{1 + s (\tau_1 + \tau_2) \beta^i}}_{\text{flicker noise approx.}} \right] \underbrace{\frac{1}{1 + \tau_c s}}_{\text{cut-off approx.}} = \frac{b_n s^n + \dots b_1 s + b_0}{s^{n+1} + a_n s^n + \dots a_1 s + a_0}$$

6. The transfer function is transformed to the time-continuous state-space system

$$\mathbf{A} = \begin{bmatrix} 0 & 1 & 0 & \dots & 0 \\ 0 & 0 & 1 & \dots & 0 \\ \vdots & & & & \\ 0 & 0 & 0 & \dots & 1 \\ -a_0 & -a_1 & -a_2 & \dots & -a_n \end{bmatrix} \quad \mathbf{B} = \begin{bmatrix} 0 \\ 0 \\ \vdots \\ 0 \\ 1 \end{bmatrix} \quad \mathbf{H}_B = [b_0 \quad b_1 \quad \dots \quad b_{n-1}]$$

which can be discretized in time for the use in the Kalman Filter.

Transition matrix

$$\Phi_B = \mathbf{I} + \mathbf{A}\Delta t + \frac{1}{2}\mathbf{A}^2\Delta t^2 + \frac{1}{6}\mathbf{A}^3\Delta t^3$$

Input matrix

$$\Gamma_B = \left(\mathbf{I}\Delta t + \frac{1}{2}\mathbf{A}\Delta t^2 + \frac{1}{6}\mathbf{A}^2\Delta t^3 \right) \mathbf{B}$$

Input covariance

$$Q_B = \frac{B^2}{\Delta t}$$

Measurement matrix

$$\mathbf{H}_B = [b_0 \quad b_1 \quad \dots \quad b_{n-1}]$$

Feedthrough

$$\mathbf{D}_B = \mathbf{0}$$

Initialization

$$\mathbf{P}_{B,0} = \mathbf{0}$$

Rate/Acceleration Random Walk

As defined in Table 2.7, rate random walk is defined by its scaling factor K . The random walk is time-integrated white noise, as modeled in Model 14.

Model 14: Rate/Acceleration Random Walk		
Transition matrix $\Phi_K = 1$	Input matrix $\Gamma_K = \Delta t + \frac{1}{2}\Delta t^2 + \frac{1}{6}\Delta t^3$	Input covariance $Q_K = \frac{K^2}{\Delta t}$
Measurement matrix $H_K = 1$	Feedthrough $D_K = 0$	Initialization $P_{K,0} = 0$

4.5.1.3. Laboratory Error Models

Like the sensor errors, the effects of laboratory and environmental errors can also be considered using the Schmidt-Kalman Filter. Here, each error source of the laboratory model is modeled as a noise process. The corresponding measurement matrix for each of these processes \mathbf{H}_{η_j} consists of the linearized error sensitivity of the ideal angular rates/specific forces from Subsection 4.2.3, the sensor's sensitivity to these inputs and the measurement matrix of the noise process itself. As these sensitivities are just the sensor errors that shall be estimated, they are unknown. Similar to the Extended Kalman Filter, the current estimates of these errors may be used as sensitivity in the measurements matrix. For the error model (4.262), the measurement matrix H_{η_j} for each laboratory error source is given by

$$\mathbf{H}_{\eta_j} = \left(\hat{S}_x \frac{\partial \omega_{ib,x}}{\partial \eta_j} + \hat{M}_{xy} \frac{\partial \omega_{ib,y}}{\partial \eta_j} + \hat{M}_{xz} \frac{\partial \omega_{ib,z}}{\partial \eta_j} + \hat{a}_x \frac{\partial f_{b,x}}{\partial \eta_j} + \hat{a}_y \frac{\partial f_{b,y}}{\partial \eta_j} + \hat{a}_z \frac{\partial f_{b,z}}{\partial \eta_j} \right) \mathbf{L}_{\eta_j} \quad (4.269)$$

where \mathbf{L}_{η_j} is the measurement matrix that forms the scalar noise output from the noise process' states.

Variation of the Earth's Angular Rate

As described in Model 1, the Earth's angular rate variation may be modeled as a set of oscillations of known amplitude and frequency but an unknown phase. Like this, the uncertainty resulting from the neglect of the variations and the known time-correlation of these variations is considered. The corresponding state space model for the use in the Schmidt-Kalman filter (SKF) is presented in Model 15. Long-time variations of the Earth's angular rate may also be modeled as a random constant contribution, such as Model 16.

Model 15: Oscillating Errors

A oscillating error of known amplitude $\sqrt{2}\sigma_{\text{osc}}$ and frequency ω_{osc} with uniformly distributed random phase is modeled as the sum of a sine and a cosine wave. The result is a constant variance σ_{osc}^2 , but the time-correlation of the oscillation is properly considered in the (cross-) covariance matrices and thus in the KF estimation.

These oscillating processes are thus described by two uncoupled second-order systems:

$$\mathbf{A}_{\text{osc}} = \begin{bmatrix} 0 & 1 & 0 & 0 \\ -\omega_{\text{osc}}^2 & 0 & 0 & 0 \\ 0 & 0 & 0 & 1 \\ 0 & 0 & -\omega_{\text{osc}}^2 & 0 \end{bmatrix} \quad \mathbf{B}_{\text{osc}} = \begin{bmatrix} 0 \\ \omega_{\text{osc}}^2 \\ 0 \\ \omega_{\text{osc}}^2 \end{bmatrix}$$

which are then discretized for the use in the Schmidt-Kalman Filter.

Transition matrix

$$\Phi_{\text{osc}} = \mathbf{I} + \mathbf{A}\Delta t + \frac{1}{2}\mathbf{A}^2\Delta t^2 + \frac{1}{6}\mathbf{A}^3\Delta t^3$$

Input matrix

$$\Gamma_{\text{osc}} = \left(\mathbf{I}\Delta t + \frac{1}{2}\mathbf{A}\Delta t^2 + \frac{1}{6}\mathbf{A}^2\Delta t^3\right)\mathbf{B}$$

Input covariance

$$Q_{\text{osc}} = 0$$

Measurement matrix

$$\mathbf{L}_{\text{osc}} = [1 \quad 0 \quad 1 \quad 0], \text{ see (4.269)}$$

Feedthrough

$$D_{\text{osc}} = \mathbf{0}$$

Initialization

$$\mathbf{P}_{\text{osc},0} = \sigma_{\text{osc}}^2 \begin{bmatrix} 1 & 0 & 0 & 0 \\ 0 & 0 & 0 & 0 \\ 0 & 0 & 0 & 0 \\ 0 & 0 & 0 & \omega_{\text{osc}}^2 \end{bmatrix}$$

Uncertainty and Variation of the Local Gravity

Similar to the Earth’s angular rate variations, most local gravity variations (see [Model 2](#)) can be described by a set of oscillations. Measurement or model uncertainties of the local gravity are modeled as a random constant. In the *SKF* these are each modeled in as described in [Model 15](#) and [Model 16](#).

Testpad Alignment Errors

Test-pad alignment errors are modeled as random constant. In the context of the Schmidt-Kalman Filter, this is a single state without any dynamics and input. Since the noise states are not updated, the initial covariance of the random constant variable is kept throughout the entire operation. This simple model is summarized in [Model 16](#). This model is used for each alignment error angle as modeled in [Model 4](#). It is essential to create a separate instance of this model for each error source because the different measurement matrices result in different cross-covariances that must be tracked.

Model 16: Random Constant Errors		
Transition matrix $\Phi_{RC} = 1$	Input matrix $\Gamma_{RC} = -$	Input covariance $Q_{RC} = -$
Measurement matrix $L_{\eta_j} = 1$, see (4.269)	Feedthrough $D_{RC} = -$	Initialization $P_{RC,0} = \sigma_{RC}^2$

Test Pad Motion

If measurements of the local test-pad motion spectrum are available, an *ARMA* model for the use in the *SKF* can be identified for the specific laboratory location. If not, the reference spectra from [Model 5](#) may be used. Assuming the errors on each degree of freedom are mutually independent, a noise process instance is required for each degree of freedom. An approximation of the reference test-pad motion is presented in [Model 17](#).

Rate Table Non-Orthogonality and Static Errors

In accordance with [Model 6](#), the axis non-orthogonality is also modeled a simple random constant. Again, an instance of the random constant model [Model 16](#) is created for each constant error angle and offset from [Model 6](#).

Model 17: Testpad Motion Model

The testpad motion according to the seismic reference models from [Model 5](#) is created from [WGN](#) input to a shaping filter. The state space systems that approximate the reference [PSD](#) are given in:

- [Table J.2](#) for the tilt angles
- [Table J.1](#) for the angular
- [Table J.3](#) for the accelerations

Transition matrix $\Phi_{TP} = \mathbf{I} + \mathbf{A}\Delta t + \frac{1}{2}\mathbf{A}^2\Delta t^2 + \frac{1}{6}\mathbf{A}^3\Delta t^3$	Input matrix $\Gamma_{TP} = \left(\mathbf{I}\Delta t + \frac{1}{2}\mathbf{A}\Delta t^2 + \frac{1}{6}\mathbf{A}^2\Delta t^3\right)\mathbf{B}$	Input covariance $Q_{TP} = \frac{1}{\Delta t}$
Measurement matrix \mathbf{L}_{η_j} , see (4.269), Appendix J	Feedthrough $D_{TP} = 0$	Initialization $P_{TP,0} = \mathbf{0}$

Rate Table Axis Wobble

Following the wobble model from [Model 7](#), the axis wobble is modeled by the sum of multiple sines representing the waviness of the bearing's rings and balls. The frequencies of these waves are given by the waviness order and the rotation rate of the axes and the bearing's cage. While the frequencies are known, the amplitude of each wave is unknown and thus modeled as a random constant. For each waviness order, a random constant model like [Model 16](#) has to be added to the [SKF](#).

Model 18: Axis Wobble

Transition matrix $\Phi_{WOB} = 1$	Input matrix $\Gamma_{WOB} = -$	Input covariance $Q_{WOB} = -$
Measurement matrix $\mathbf{L}_{\eta_j} = \cos(qN_r(f_i - f_c) + pf_i t)$, see (4.269), Model 7	Feedthrough $D_{WOB} = -$	Initialization $P_{WOB,0} = \sigma_{WOB}^2$

Rate Table Control Errors

As pointed out in [Model 10](#), the modeling of the rate table's positioning and rate errors cannot be generalized as it depends on the implemented control laws and architecture. However, a typical servo-loop may be approximated by a second-order system as described in [Model 19](#). The sinusoidal errors from motor cogging and the measurement errors can be modeled similarly to the axis wobble. However, they have high frequencies at many multiples of the applied angular rates. They are averaged out very quickly on a rotating axis and may thus be neglected compared to other effects.

Model 19: Rate Table Positioning and Rate Error

A rough approximation of a rate-table's servo loop is given by a second order system defined by its natural frequency ω_c and damping ratio D :

$$\mathbf{A} = \begin{bmatrix} 0 & 1 \\ -\omega_c^2 & -2D\omega_c \end{bmatrix} \quad \mathbf{B} = \begin{bmatrix} 0 \\ \omega_c^2 \end{bmatrix}$$

This system is discretized for the use in the SKF. The WGN input to this system is scaled with q to match the rate table's position measurement noise.

Transition matrix	Input matrix	Input covariance
$\Phi_{\text{CTRL}} = \mathbf{I} + \mathbf{A}\Delta t + \frac{1}{2}\mathbf{A}^2\Delta t^2 + \frac{1}{6}\mathbf{A}^3\Delta t^3$	$\Gamma_{\text{CTRL}} = \left(\mathbf{I}\Delta t + \frac{1}{2}\mathbf{A}\Delta t^2 + \frac{1}{6}\mathbf{A}^2\Delta t^3\right)\mathbf{B}$	$Q_{\text{CTRL}} = \frac{q}{\Delta t}$
Measurement matrix	Feedthrough	Initialization
$\mathbf{L}_{\eta_j} = \begin{bmatrix} 1 & 0 \end{bmatrix}$ (position), see (4.269) $\mathbf{L}_{\eta_j} = \begin{bmatrix} 0 & 1 \end{bmatrix}$ (rate)	$D_{\text{CTRL}} = 0$	$P_{\text{CTRL},0} = \mathbf{0}$

4.5.2. Observability and Trajectory Design

4.5.2.1. General Remarks

The goal of inertial sensor calibration is the determination of all parameters of the sensor's error model. In the context of a Kalman Filter-based estimation, this requires complete observability of the system and thus of the estimation states.

The parameter estimation for the classical test procedures was based on the least-squares adjustment of averaged sensor outputs. These test procedures can also be performed using a KF for the parameter estimation. The rate table trajectories are the same, but the sensor signal is directly fed to the KF which inherently performs the averaging and estimation steps. The observability of the investigated sensor errors is always given for the classical tests since the test procedures have been explicitly designed to isolate and estimate them. However, this is only true if further sensor errors are neglected. Also for the classical test procedures, the tested parameters can often only be estimated in linear combination with other errors. The general observability of sensor sensitivities to kinematic inputs will be analyzed in the next section.

4.5.2.2. Observability

The classical test for observability of a (time-varying) time-discrete state space system as used in the Kalman Filter is based on the *observability Gramian* or *observability matrix* [173, p. 146]:

$$\mathbf{M}_{k_0,k_f} = \sum_{k=k_0}^{k_f} (\Phi_{k,k_0}^\top) \mathbf{H}_k^\top \mathbf{H}_k \Phi_{k,k_0} \quad (4.270)$$

with the cumulative transition matrix $\Phi_{k,0}$ from the time k_0 to the time k_f . The formal definition of observability is:

”The system is completely observable on the time interval T if for every $k_0 \in T$ there exists a $k_f \in T$ such that $k_f > k_0$ and \mathbf{M}_{k_0,k_f} has full rank, or is positive definite.” [173, p. 146]

While the observability Gramian provides a method to prove system observability for a given trajectory and time interval, it is hard to analyze or design a rate table trajectory from the above definition.

Here, an observability test for the time-continuous system is used to design a trajectory for complete system observability. For a time-varying linear state space system, with analytically given system matrix $\mathbf{A}(t)$ and $\mathbf{H}(t)$, the state observability can be tested using the another observability matrix [174, pp. 279–280]:

$$\text{rank} \underbrace{\begin{bmatrix} \mathbf{H}_0(t_0) \\ \mathbf{H}_1(t_0) \\ \vdots \\ \mathbf{H}_k(t_0) \end{bmatrix}}_{\mathbf{M}} = n \text{ for some } k \quad (4.271)$$

where

$$\mathbf{H}_0(t) = \mathbf{H}(t) \quad (4.272)$$

$$\mathbf{H}_{i+1}(t) = \mathbf{H}_i(t)\mathbf{A}(t) + \frac{d}{dt}\mathbf{H}_i(t) \quad (4.273)$$

For the example sensor error model (4.262), this yields the following observability matrix:

$$\mathbf{M} = \begin{bmatrix} \hat{\omega}_{ib,x}, & \dots & \hat{\omega}_{ib,x}^s & \hat{\omega}_{ib,y} & \hat{\omega}_{ib,z} & \hat{f}_{b,x} & \hat{f}_{b,y} & \hat{f}_{b,z} & 1 & 0 \\ \frac{d}{dt}\hat{\omega}_{ib,x}, & \dots & \frac{d}{dt}\hat{\omega}_{ib,x}^s & \frac{d}{dt}\hat{\omega}_{ib,y} & \frac{d}{dt}\hat{\omega}_{ib,z} & \frac{d}{dt}\hat{f}_{b,x} & \frac{d}{dt}\hat{f}_{b,y} & \frac{d}{dt}\hat{f}_{b,z} & 0 & 1 \\ \frac{d^2}{dt^2}\hat{\omega}_{ib,x}, & \dots & \frac{d^2}{dt^2}\hat{\omega}_{ib,x}^s & \frac{d^2}{dt^2}\hat{\omega}_{ib,y} & \frac{d^2}{dt^2}\hat{\omega}_{ib,z} & \frac{d^2}{dt^2}\hat{f}_{b,x} & \frac{d^2}{dt^2}\hat{f}_{b,y} & \frac{d^2}{dt^2}\hat{f}_{b,z} & 0 & 0 \\ \vdots & & \vdots & \vdots & \vdots & \vdots & \vdots & \vdots & \vdots & \vdots \\ \frac{d^k}{dt^k}\hat{\omega}_{ib,x}, & \dots & \frac{d^k}{dt^k}\hat{\omega}_{ib,x}^s & \frac{d^k}{dt^k}\hat{\omega}_{ib,y} & \frac{d^k}{dt^k}\hat{\omega}_{ib,z} & \frac{d^k}{dt^k}\hat{f}_{b,x} & \frac{d^k}{dt^k}\hat{f}_{b,y} & \frac{d^k}{dt^k}\hat{f}_{b,z} & 0 & 0 \end{bmatrix} \quad (4.274)$$

Based on above criteria, the observability of sensor errors during rate table testing can be analyzed for any analytically described rate table motion. Linearly independent columns correspond to sensor errors that can be estimated, while a linear dependency between columns means that the corresponding errors can only be estimated in combination, which does not allow the separation of these errors.

The ideal angular rates as a function of the rate table axes positions $\hat{\Psi}_{wp}(t)$, $\hat{\Phi}_{vw}(t)$, $\hat{\Psi}_{uv}(t)$

are given as:

$$\hat{\omega}_{ib,x} = \cos(\hat{\Psi}_{vu}(t)) \left(\hat{\Phi}_{vw}(t) + \hat{\omega}_{ie} \cos(\phi) \sin(\hat{\Psi}_{wp}(t)) \right) + \sin(\hat{\Psi}_{vu}(t)) \left(\sin(\hat{\Phi}_{vw}(t)) \left(\hat{\Psi}_{wp}(t) + \hat{\omega}_{ie} \sin(\phi) \right) + \hat{\omega}_{ie} \cos(\hat{\Psi}_{wp}(t)) \cos(\hat{\Phi}_{vw}(t)) \cos(\phi) \right) \quad (4.275)$$

$$\hat{\omega}_{ib,y} = -\sin(\hat{\Psi}_{vu}(t)) \left(\hat{\Phi}_{vw}(t) + \hat{\omega}_{ie} \cos(\phi) \sin(\hat{\Psi}_{wp}(t)) \right) + \cos(\hat{\Psi}_{vu}(t)) \left(\sin(\hat{\Phi}_{vw}(t)) \left(\hat{\Psi}_{wp}(t) + \hat{\omega}_{ie} \sin(\phi) \right) + \hat{\omega}_{ie} \cos(\hat{\Psi}_{wp}(t)) \cos(\hat{\Phi}_{vw}(t)) \cos(\phi) \right) \quad (4.276)$$

$$\hat{\omega}_{ib,z} = \hat{\Psi}_{uv}(t) + \cos(\hat{\Phi}_{vw}(t)) \left(\hat{\Psi}_{wp}(t) + \hat{\omega}_{ie} \sin(\phi) \right) - \hat{\omega}_{ie} \cos(\hat{\Psi}_{wp}(t)) \cos(\phi) \sin(\hat{\Phi}_{vw}(t)) \quad (4.277)$$

For a sensor placement without lever arm, the ideal specific forces are the local gravity observed from different orientations, written as:

$$\hat{f}_{b,x} = -g \sin(\hat{\Psi}_{uv}(t)) \sin(\hat{\Phi}_{vw}(t)) \quad (4.278)$$

$$\hat{f}_{b,y} = -g \cos(\hat{\Psi}_{uv}(t)) \sin(\hat{\Phi}_{vw}(t)) \quad (4.279)$$

$$\hat{f}_{b,z} = -g \cos(\hat{\Phi}_{vw}(t)) \quad (4.280)$$

Evaluating the observability matrix for the above equations is lengthy and best performed using a computer algebra system. The resulting observability of sensor errors during testing at different rate table motion profiles is summarized in [Table 4.30](#). The analysis augments the above error model with linear, quadratic, and higher-order sensitivities to all angular rates and specific forces components, as well as a sensor bias and rate/acceleration ramp.

Based on the observability matrix, some results of the presented table shall be explained in the following. To make the first columns that correspond to the scale factor polynomials independent from the bias, the input angular rate requires at least the first derivative to be non-zero. Vividly, it is impossible to distinguish between sensor bias and scale factors under a constant input rate. This can be observed for cases with single-axis rate table motion, as for the z axis in case I and the x axis in V. This can be easily changed by introducing a linearly increasing angular rate (II and VI). However, the linear scale factor cannot be distinguished from a rate ramp in these cases. Increasing the input rate at $\sim t^2$ allows independent observation of both the linear scale factor and the rate ramp. The same applies to sinusoidal rate table motion (IV). Sensitivities to specific forces about the horizontal axes cannot be observed for the rate table's vertical axis rotation. Due to the constant input, the sensitivity to the vertical specific forces cannot be distinguished from a bias.

Rotation about the rate table's outer axis (cases I to IV) results in oscillating input of the Earth's angular rate (outside the Earth's poles) on the sensors x and y axes. This allows an estimation of, e.g., the misalignment of these axes but requires sufficient sensor accuracy to use these small signals. For this motion, the sum of the quadratics $\omega_{ib,x}^2$ and $\omega_{ib,y}^2$ is constant, and the sum of the time-derivatives vanishes. Thus they cannot be distinguished from a bias.

Table 4.30.: Observability of sensor errors for different rate table motions.

Input		$\omega_{ib,x}$	$\omega_{ib,x}^2$	$\omega_{ib,x}^n$	$\omega_{ib,y}$	$\omega_{ib,y}^2$	$\omega_{ib,y}^n$	$\omega_{ib,z}$	$\omega_{ib,z}^2$	$\omega_{ib,z}^n$	$f_{b,x}$	$f_{b,x}^2$	$f_{b,x}^n$	$f_{b,y}$	$f_{b,y}^2$	$f_{b,y}^n$	$f_{b,z}$	$f_{b,z}^2$	$f_{b,z}^n$	1	0
Sensor errors	x axis	S_x	$S_{2,x}$	$S_{n,x}$	M_{xy}	$M_{2,xy}$	$M_{n,xy}$	M_{xz}	$M_{2,xz}$	$M_{n,xz}$	a_{xx}	$a_{2,xx}$	$a_{n,xx}$	a_{xy}	$a_{2,xy}$	$a_{n,xy}$	a_{xz}	$a_{2,xz}$	$a_{n,xz}$	b_x	r_x
	y axis	M_{yx}	$M_{2,yx}$	$M_{n,yx}$	S_y	$S_{2,y}$	$S_{n,y}$	M_{yz}	$M_{2,yz}$	$M_{n,yz}$	a_{yx}	$a_{2,yx}$	$a_{n,yx}$	a_{yy}	$a_{2,yy}$	$a_{n,yy}$	a_{yz}	$a_{2,yz}$	$a_{n,yz}$	b_y	r_y
	z axis	M_{zx}	$M_{2,zx}$	$M_{n,zx}$	M_{zy}	$M_{2,zy}$	$M_{n,zy}$	S_z	$S_{2,z}$	$S_{n,z}$	a_{zx}	$a_{2,zx}$	$a_{n,zx}$	a_{zy}	$a_{2,zy}$	$a_{n,zy}$	a_{zz}	$a_{2,zz}$	$a_{n,zz}$	b_z	r_z
Case	$\dot{\Psi}_{wp}$	Φ_{uv}	$\dot{\Psi}_{uv}$	<i>sensor mounted without lever arm</i>																	
I	const	0	0	[Color-coded grid for Case I]																	
II	$\sim t$	0	0	[Color-coded grid for Case II]																	
III	$\sim t^2$	0	0	[Color-coded grid for Case III]																	
IV	$\sim \sin(at)$	0	0	[Color-coded grid for Case IV]																	
V	0	const	0	[Color-coded grid for Case V]																	
VI	0	$\sim t$	0	[Color-coded grid for Case VI]																	
VII	0	$\sim t^2$	0	[Color-coded grid for Case VII]																	
VIII	0	$\sim \sin(at)$	0	[Color-coded grid for Case VIII]																	
IX	const	const	0	[Color-coded grid for Case IX]																	
X	0	const	const	[Color-coded grid for Case X]																	
XI	0	$\sim \sin(at)$	$\sim \sin(bt)$	[Color-coded grid for Case XI]																	
XII	const	const	const	[Color-coded grid for Case XII]																	
XIII	const	const	const	<i>sensor mounted with lever arm</i>																	

observable
 observable, but weak signal
 linear combination observable
 not observable

For a rotation about the horizontal middle axis of the rate table (cases V to VIII), there are no specific forces in the x direction, and the corresponding sensitivities can thus not be estimated. An interesting effect is the lack of observability of the misalignments and g -sensitivities about the y and z axis. For each axis, the angular rate sensitivities and specific forces sensitivities of a given order can only be estimated in linear combination. This can be explained by the fact that these axes pick up the Earth's angular rate and the local gravity under varying angles at the same phase. Again, the sum of quadratic inputs is constant and cannot be separated from the sensor's bias.

The observability of the sensitivities to angular rates can be improved by using multiple axes of the rate table. Such a multi-axis rotation results in varying angular rate inputs on all sensor axes. For a constant rotation of the rate table's outer and middle axis of the rate table (IX), there is no acceleration along the sensor's x axis, and the corresponding sensitivity cannot be observed. This can be easily changed by rotating the middle and inner axes instead (X). In both cases, the sensitivities to the squares of the specific forces cannot be distinguished from the bias. Also, the sensitivities to the squared angular rates cannot be separated in these scenarios. Furthermore, in each case, the angular rate along a sensor axis is mainly constant, with variations only in the size of the Earth's angular rate. The corresponding errors are thus only weakly observable.

This can be corrected by applying an oscillating motion to the middle and inner rate table axes (XI). In this case, the sensitivities to squared angular rates can also be observed. Still, the squared sensitivities to accelerations cannot be distinguished from a bias. The same observability can be achieved by applying constant rates to all three rate table axes (case XII). It should be noted that an oscillating motion allows the use of more simple test equipment, as, e.g., there are no expensive slip rings required.

However, if the sensor is mounted to the rate table without a lever arm, the sum of all squared specific forces input is still constant and cannot be separated from the bias. This problem can be compensated by mounting the sensor acentric to the rate table. The resulting centrifugal forces introduce additional non-space-fixed accelerations that yield full observability of all sensitivities to specific forces. On a typical rate table, both rates and possible lever arms limit the creation of centrifugal forces to the order of magnitude of $1g$. They thus do not allow testing for the effects of high accelerations.

Additionally, it should be noted that for multi-axis motion, the choice of the axes' angular rates impacts the observability. If the angular rates of the inner and middle gimbal match, this reduces the observability. The linear scale factor, the specific forces, and bias become intertwined and cannot be estimated independently. The outer gimbal's rate can be selected independently of the other rates. To achieve a similar calibration quality for each sensor axis, the rates should be chosen in a way that provides similar magnitudes of angular rates at each axes. An example of the resulting angular rates for multi-axis rotation is presented in [Figure 4.42](#).

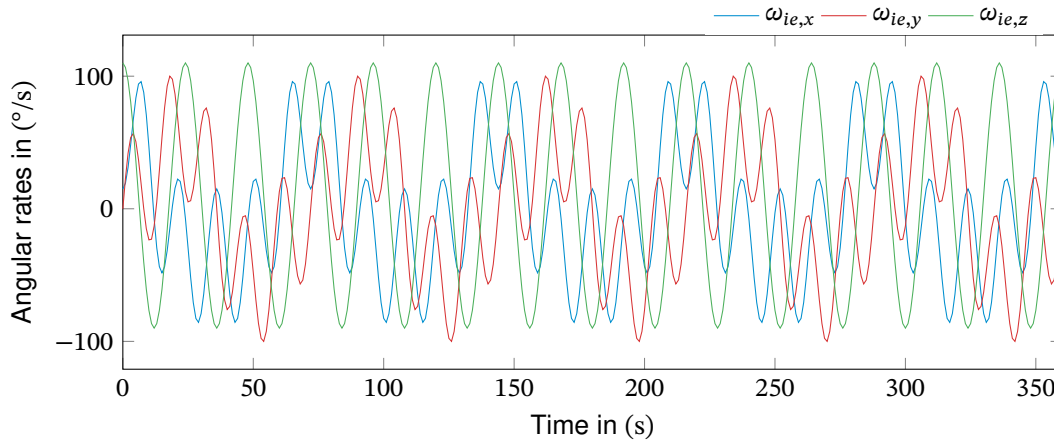


Figure 4.42.: Example of the sensor's input angular rates for a constant-rate multi-axes rate table motion. The axes rates are $\dot{\Psi}_{pw} = 100^\circ/\text{s}$, $\dot{\Phi}_{wv} = 15^\circ/\text{s}$, $\dot{\Psi}_{vu} = 10^\circ/\text{s}$.

4.5.3. Examples

Within this section, the properties of the **KF** based sensor calibration shall be demonstrated with the help of several examples. Since both the true sensor input and the actual sensor errors are unknown in reality, real-world experiments are not suitable to prove the feasibility of the **KF**-based testing approach. Here, the experiments are conducted using a numerical simulation of the laboratory testing setup. This includes numerical models of the environment (Earth's angular rate, gravity, test-pad motion) as well as the rate-table imperfections (geometric errors, bearings, controls) as modeled in [Section 4.2](#). The entire simulation and filtering are performed at a sample rate of 100 Hz.

Table 4.31.: Sensor noise parameters for the KF-based sensor testing examples.

Sensor Noise	
Quantization noise Q	0
Angular random walk N	$0.0035^\circ/\sqrt{\text{s}}$
Bias instability B	$0.01^\circ/\text{h}$
Rate random walk K	$1 \cdot 10^{-6}^\circ/(\text{s}\sqrt{\text{s}})$

To demonstrate the estimation's stochastic consistency, 120 Monte-Carlo runs are performed for each test case. All errors, except the sensor's deterministic errors to be estimated, are varied between each run. The true angular rates and specific forces are determined from the models presented in [Section 4.2](#). The selected model parameters are summarized in [Table 4.32](#).

The sensor's noise parameters are listed in [Table 4.31](#). The true sensor errors, as well as the filter's initialization values are summarized in [Table 4.33](#). The initial covariance matrix is a diagonal matrix with the given standard deviations squared as entries.

Table 4.32.: Laboratory model parameters for the Kalman Filter based sensor testing examples.

Error source	Model
Earth angular rate	IERS model (Subsection 4.2.4)
Local gravity	Sogmiliana gravity, Longman tide model (Subsection 4.2.5)
Test pad motion	Reference model (Subsection 4.2.8)
Test pad alignment	leveling 2.5 asec (1σ), north alignment 0.01 degree (1σ)
Axis non-orthogonality	2.5 asec (1σ) (Subsection 4.2.9.2)
Axis wobble	1.0 asec RMS, $N_r = 13, q = [0 \dots 4], p = [1 \dots 4]$, (Subsection 4.2.9.3)
Control errors	2nd order system $f_c = 25$ Hz, $Z = 0.75$, noise $S = 1 \cdot 10^{-5}$ rad/ $\sqrt{\text{Hz}}$, encoder $N = 720, A = 1 \cdot 10^{-6}$ rad (Subsection 4.2.9.6)

Table 4.33.: Initialisation for Kalman Filter based sensor testing examples.

Parameter	True	Initialization		
		State	σ	Unit
Linear scale factor $S_{1,*}$	1.01	1.0	0.1	—
Quadratic scale factor $S_{2,*}$	0.01	0.0	0.01	—
Misalignment M_*	0.05	0.0	0.1	—
Bias b_*	0.5	0.0	1.0	$^\circ/\text{s}$
Rate ramp r_*	0.01	0.0	0.1	$^\circ/\text{s}^2$
g -Sensitivity a_*	0.002	0.0	0.01	$^\circ/(\text{s g})$
g^2 -Sensitivity $a_{2,*}$	0.001	0.0	0.01	$^\circ/(\text{s g}^2)$

4.5.3.1. Observability

The observability of sensor errors for different rate table motions has been analytically derived in [Subsection 4.5.2](#). Here, these results shall be compared to numerical simulations. Compared to the purely mathematical analysis, this considers the different magnitudes of the input rates, e.g., rate table rates and the Earth's angular rate. Four different cases of constant rate table axes rates have been simulated.

The simulation results for a constant rate at the outer rate table axis are presented in [Figure 4.43](#). Just as analytically predicted in [Table 4.30](#) most states are not observable at all. While the rate ramp's slope states are fully observable and converge fast, the scale factor and misalignment states linked to the x and y axes converge rather slowly. As predicted, this results from the small input signal, which is a modulation of the Earth's angular rate. Higher-order scale factors and g -sensitivities cannot be estimated.

When switching to a constant rate about the rate table's middle axis, [Table 4.30](#) predicts that the only the rate ramp's slope can be observed independently. The simulation results in [Figure 4.44](#), however, display a convergence of the covariance of some of the g -sensitivities. However, this results from covariance initialization and the different magnitudes of the varying parts of the angular rate and specific forces input (ω_{ie} vs. g).

The simulation results for constant rotation angular rate about the outer and the middle rate table axes are presented in [Figure 4.45](#). In this case, the linear and quadratic scale factors and the misalignments linked to the sensor's y and z axis are entirely observable. The respective errors for the x axis are only weakly observable. The variable part of the input along this axis is again only in the magnitude of the Earth's angular rate. Also, the biases converge slowly, while the rate ramps slopes are quickly estimated.

As predicted analytically, the observability can be drastically improved by adding a simultaneous rotation about the rate table's inner axis (see [Figure 4.45](#)). In the simulation, all states except certain g -sensitivities are estimated. There is a slight difference in the convergence of the scale factor and misalignment estimated, where the states linked to the z -axis display a higher variance than the other axes. The analytical prediction state that by mounting the sensor to the rate table with a lever arm to the rotation axes, the resulting time-varying forces yield complete observability of all states. The simulation results confirmed this prediction. However, for the selected test case, the residual g -sensitivities could only be estimated for unrealistically high lever arms of more than 10 m. Thus, the full observability of all states is rather theoretical and often not achievable with typical rate table setups.

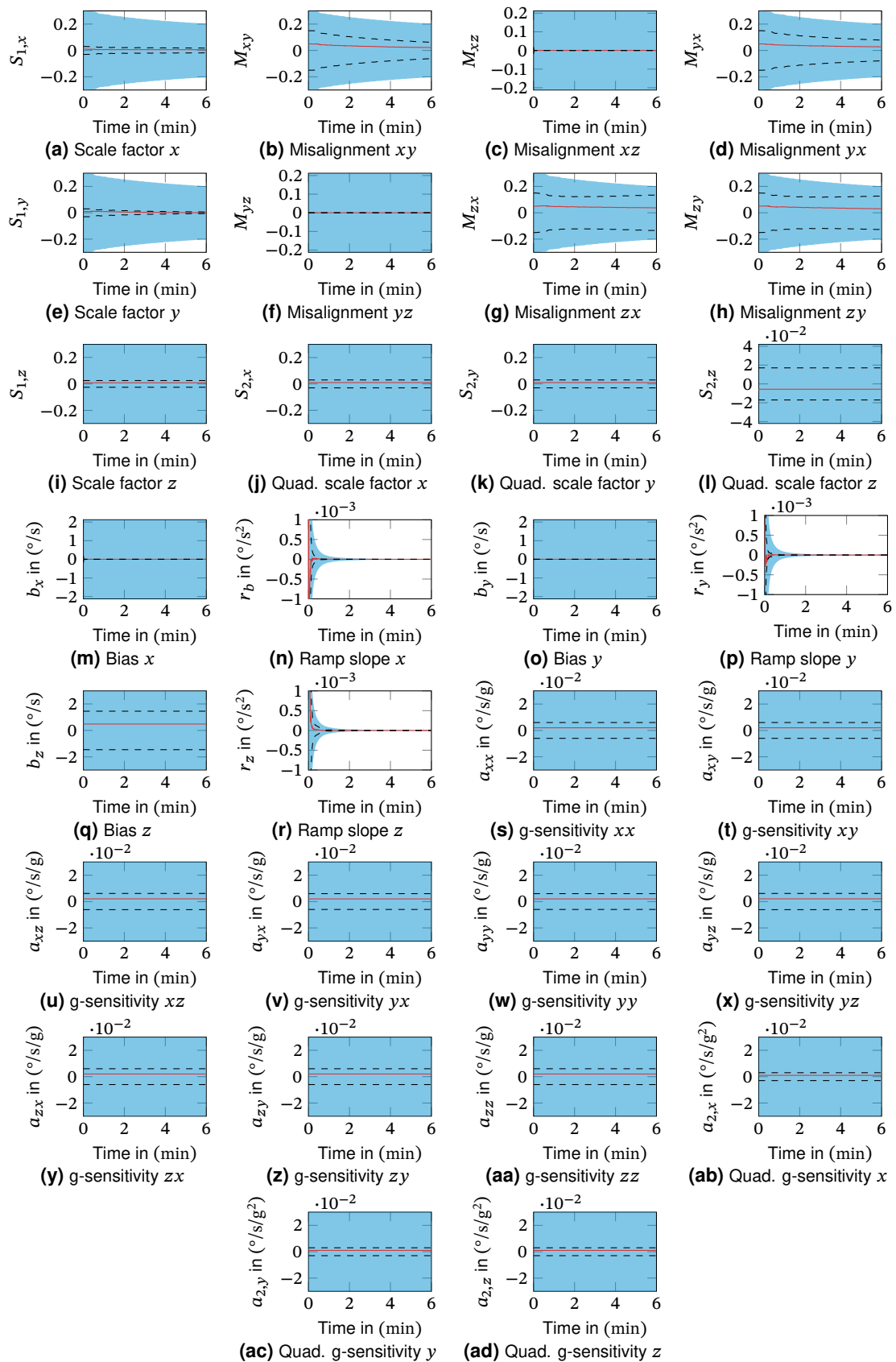


Figure 4.43.: Estimation results for the outer axis constant rate test case. An angular rate of $10^{\circ}/s$ is applied to the outer rate table axis. The graphs display a single simulation's state estimate (red), the estimated state variance ($\pm 3\sigma$, blue) and the variance obtained from 120 Monte Carlo runs ($\pm 3\sigma$, dashed).

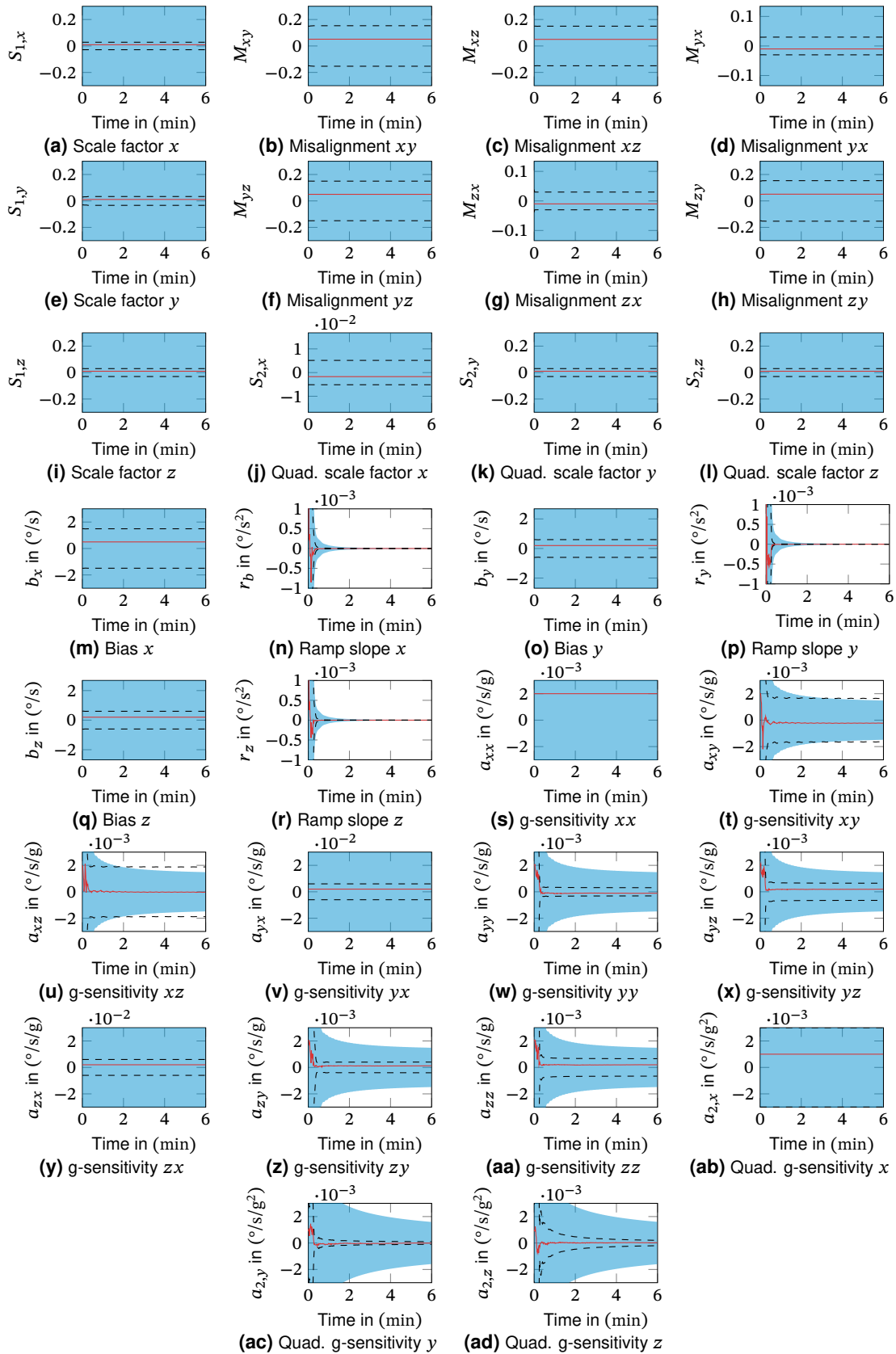


Figure 4.44.: Estimation results for the middle axis constant rate test case. An angular rate of $20^\circ/s$ is applied to the rate table's middle axis. The graphs display a single simulation's state estimate (red), the estimated state variance ($\pm 3\sigma$, blue) and the variance obtained from 120 Monte Carlo runs ($\pm 3\sigma$, dashed).

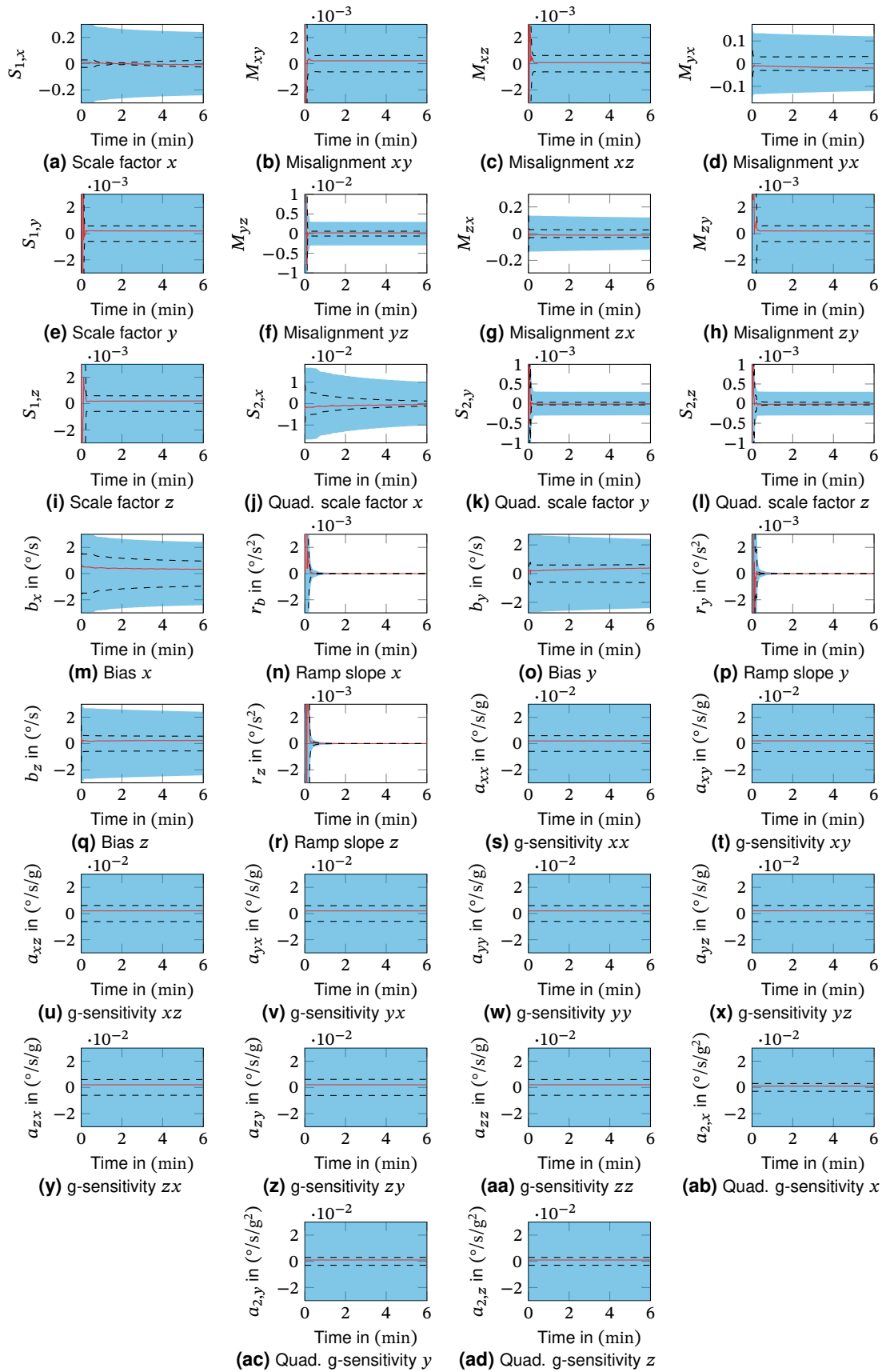


Figure 4.45.: Estimation results for the outer and middle axis constant rate test case. An angular rate of $10^{\circ}/s$ is applied to the rate table's outer axis, a rate of $20^{\circ}/s$ to the middle axis. The graphs display a single simulation's state estimate (red), the estimated state variance ($\pm 3\sigma$, blue) and the variance obtained from 120 Monte Carlo runs ($\pm 3\sigma$, dashed).

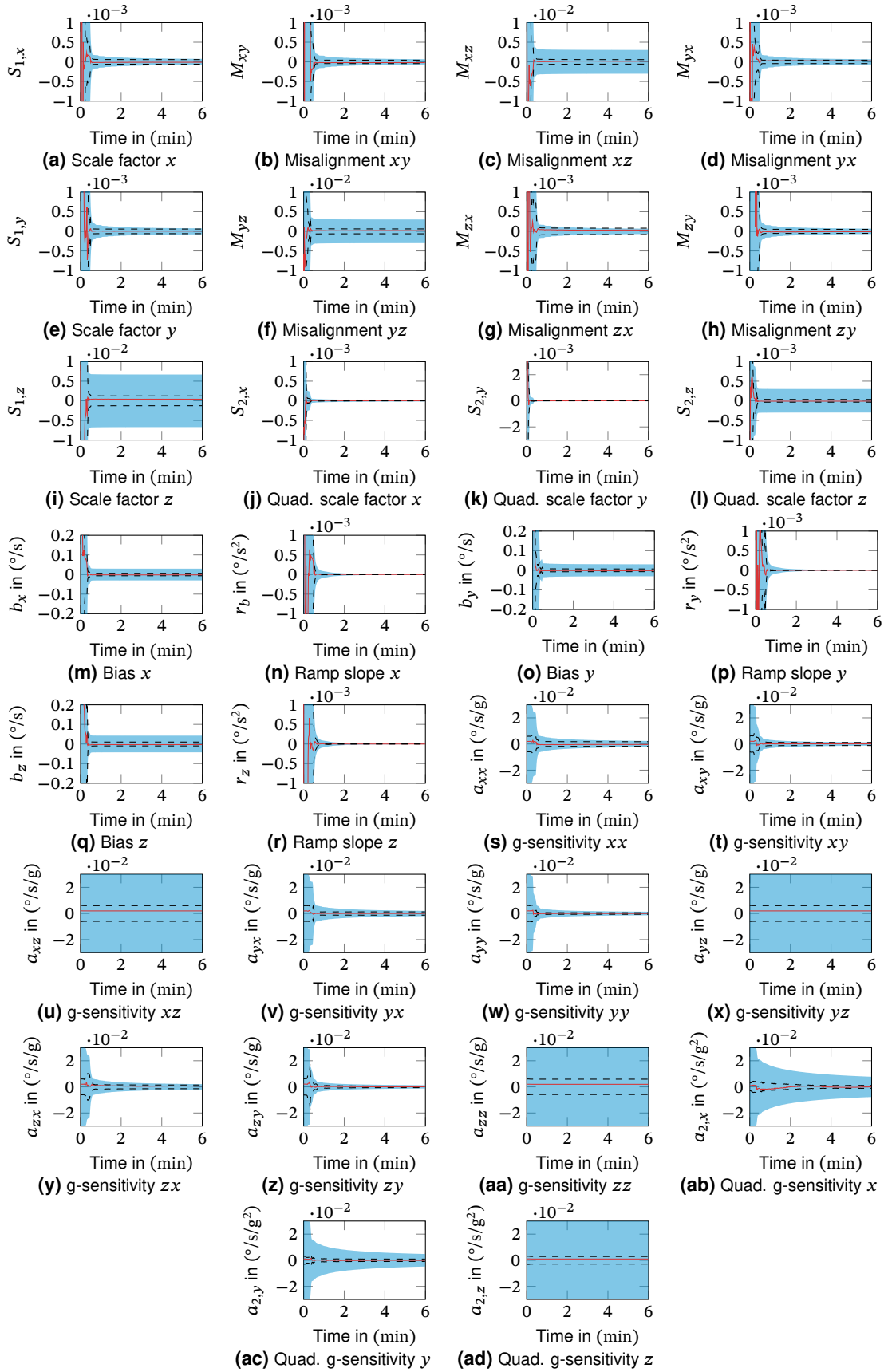


Figure 4.46.: Estimation results for the all axes constant rate test case. The applied angular rates are $10^\circ/\text{s}$ for the inner and outer rate table axis and $20^\circ/\text{s}$ for the middle axis. The graphs display a single simulation's state estimate (red), the estimated state variance ($\pm 3\sigma$, blue) and the variance obtained from 120 Monte Carlo runs ($\pm 3\sigma$, dashed).

4.5.3.2. Comparison with Classical Test Procedures and Error Budgets

The typically stationary test profiles of the classical test procedures from Section 4.4 can also be used for the KF based sensor testing.

The estimation results for a test series with angular rates of the outer rate table axis ramping from $-100^\circ/\text{s}$ to $+100^\circ/\text{s}$ are presented in Figure 4.47. This setup represents a scale factor test series of the sensor's z axis. As expected, the linear and higher-order scale factors for the z -axis are observable. However, due to the piece-wise constant rate, the estimates do not converge continuously but change step-wise at each rate change. Each new angular rate adds novel information to improve the estimation. Interestingly, the other axes' scale factors and misalignments are also observable. However, the input signal to these states is again only the Earth's angular rate which explains the slow convergence. Due to the single-axis motion, there is no possibility to estimate the g -sensitivities.

Another example is the simulation of a six-position test with a constant angular rate of $10^\circ/\text{s}$ applied to the rate table's outer axis. The estimation results are presented in Figure 4.48. As with the previous example, the piece-wise constant input results in a step-wise convergence of the estimation covariance. Again, each position adds information that is used to improve the estimation. The results also display the importance of the selected positions, as, e.g., the linear scale factor for the x -axis is practically only estimated at the beginning of the 6th position. Due to the static positions, the g -sensitivities cannot be estimated.

The classical test procedures are based on straightforward error models that neglect the effects of unmodeled sensor errors. In contrast, the previously presented simulation results consider the uncertainty introduced by the additional error terms, like g -sensitivities. A direct comparison with the analytical error budgets thus requires a simplified error model without sensor noise and the error terms not included in the classical test procedure. A comparison of the KF estimated variance and the analytically predicted values for such a test scenario are given in Table 4.34. The results for the classical scale factor test series and the six position test agree well with the inherently determined estimation variances of the KF based approach.

Table 4.34.: Comparison of KF-based testing with classical test procedures.

	Sensor error	Accuracy estimate 1σ	
		KF-based	Classical
Scale-factor test [1, 5, 10, 20, 100, 200] $^\circ/\text{s}$, 60 s <i>each</i>	Linear scale factor	1.8 ppm	1 ppm
	Bias	1.0 $^\circ/\text{h}$	0.1 $^\circ/\text{h}$
Six-position test <i>positions as in Figure 4.37</i> , 60 s <i>each</i> , $10^\circ/\text{s}$	Linear scale factor x	11.7 ppm	10 ppm
	Misalignment xy	0.18 mrad	0.1 mrad
	Misalignment xz	0.18 mrad	0.1 mrad
	Bias x	1.4 $^\circ/\text{h}$	4 $^\circ/\text{h}$

Nevertheless, it should be considered that the use of such a simplified sensor error model does, after all, undermine the rationale for using the KF approach.

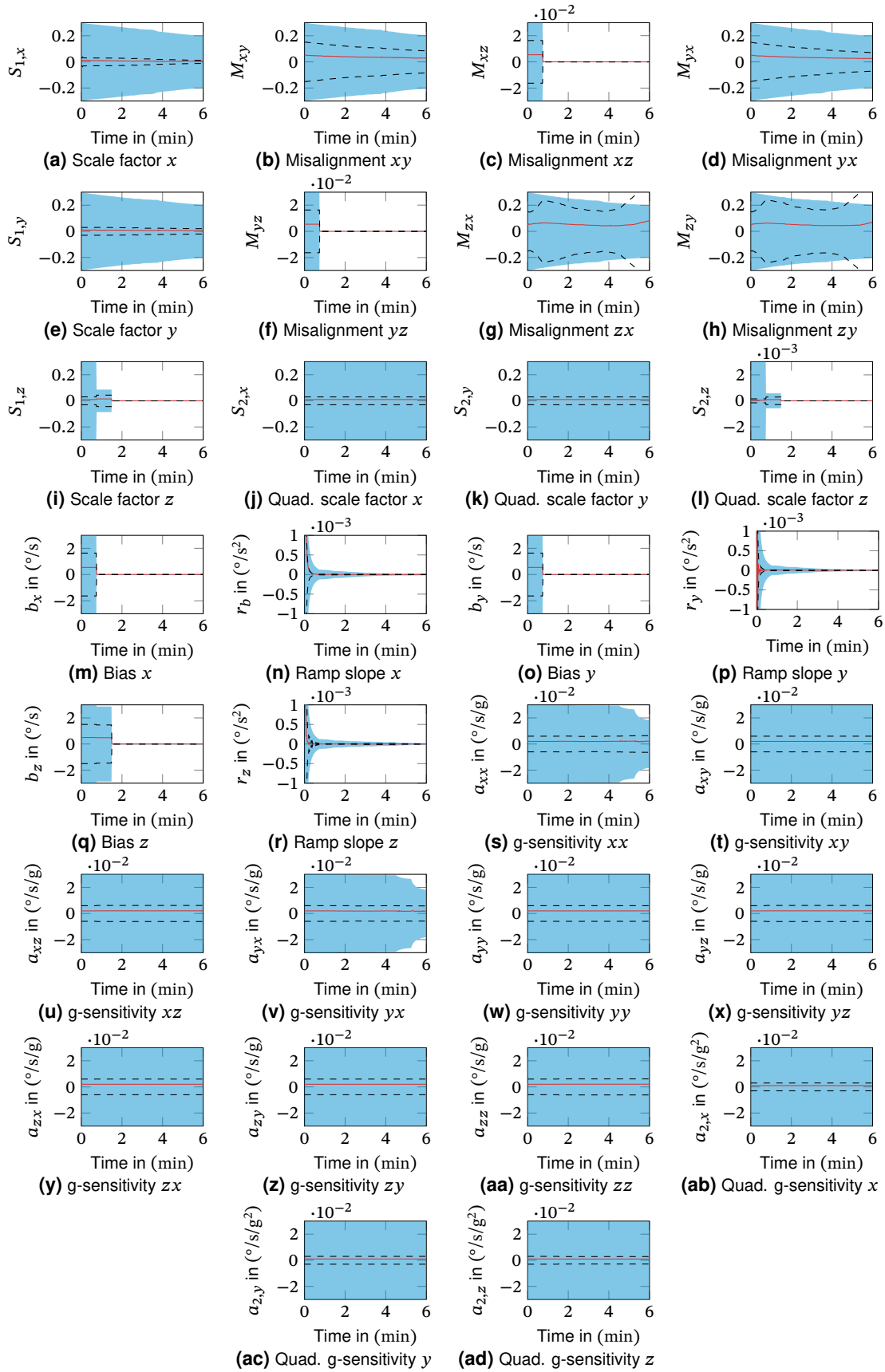


Figure 4.47.: Estimation results for the scale factor test series at rates of $[-100, -50, -20, -5, 5, 20, 50, 100]$ $^{\circ}/s$. The graphs display a single simulation's state estimate (red), the estimated state variance ($\pm 3\sigma$, blue) and the variance obtained from 120 Monte Carlo runs ($\pm 3\sigma$, dashed).

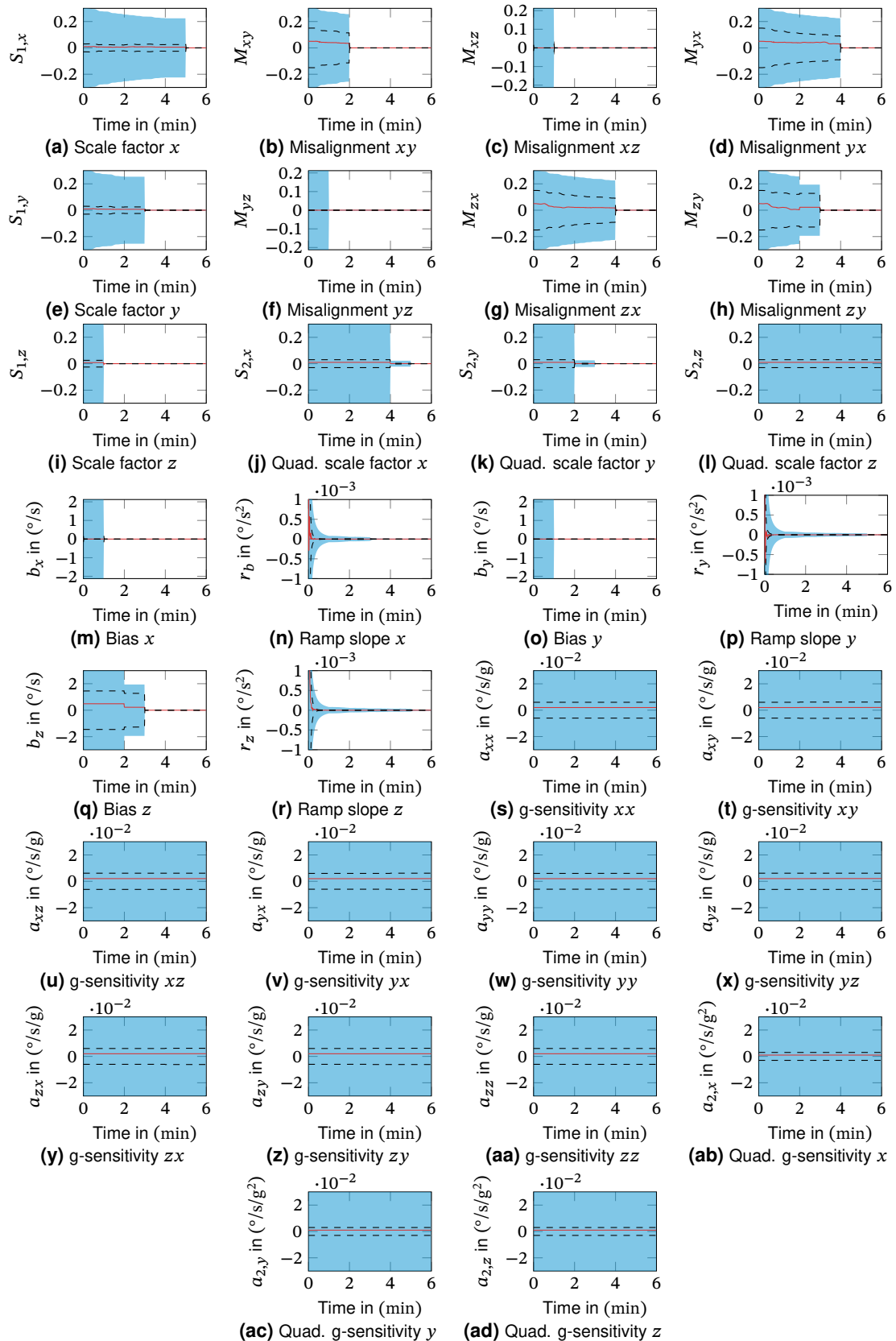


Figure 4.48.: Estimation results for the six-position test series. The graphs display a single simulation's state estimate (red), the estimated state variance ($\pm 3\sigma$, blue) and the variance obtained from 120 Monte Carlo runs ($\pm 3\sigma$, dashed).

4.5.3.3. Sensitivity to Dead-Times

In contrast to the classical test procedures, the KF based sensor testing does not rely on constant sensor input. However, sensor testing with time-variable inputs requires an accurate time-synchronization of the rate table's measured position and rates and the sensor output. A time delay between these two data streams leads to an erroneous ideal motion and thus to an erroneous measurement matrix. The actual effect of such an offset depends on the level of dynamics of the rate table profile.

Simulations with a variable delay between the true and the ideal inputs have been conducted for the example scenario of the three-axis rate table motion. The variation of the estimation error with the delay is exemplarily presented for the SF, MA and bias of the sensor's x -axis in Figure 4.49.

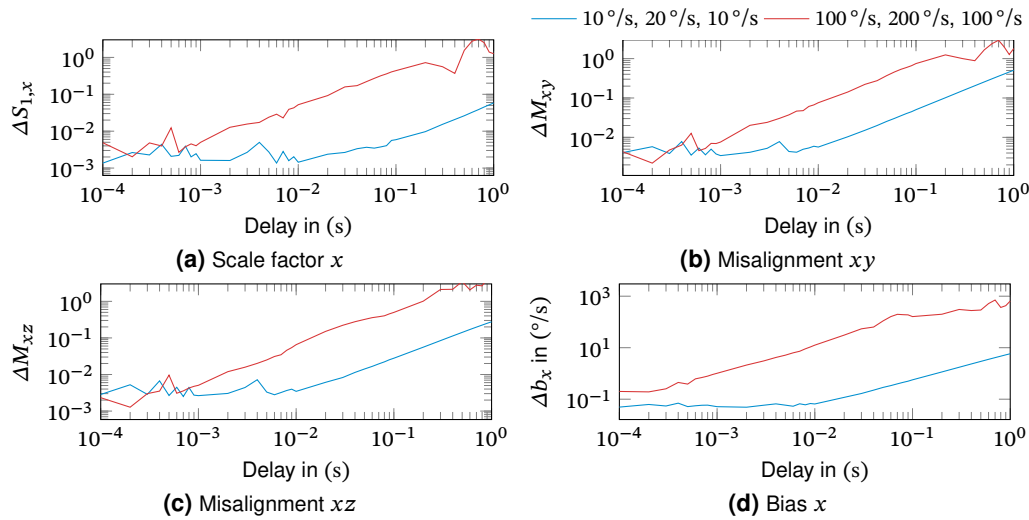


Figure 4.49.: Estimation errors for varying time delay between rate table and sensor signals. Simulation results for three axis constant rates of $10^\circ/s$ for the outer, $20^\circ/s$ the middle and $10^\circ/s$ for the inner axis respectively the tenfold rates.

For the given test case, the simulation results indicate that a delay of less than 10 ms has little effect on the estimation error, while the errors grow rapidly for higher delays. To demonstrate the effect of higher angular rates, the graphs also include the estimation errors for the tenfold angular rates. In this case, already very short delays of less than 1 ms increase the estimation error. This sensitivity to dead times poses rather strict requirements on the laboratory setup, like real-time systems and accurate time-synchronization, if a true online estimation shall be performed.

In principle, the time synchronization and subsequent estimation can also be performed offline by correlating the recorded sensor signals to the recorded rate table motion. However, this requires sufficiently small sensor errors and disturbances. A synchronized recording and time-stamping should be preferred, as this does not pose any requirements for sensor models and errors.

4.5.3.4. Numerical Stability

It is a well-known problem that the classical Kalman Filter and its variants suffer from numerical instability when the covariance matrix becomes small due to very accurate measurement updates [175]. As the covariance is a quadratic measure, small uncertainties are represented by even smaller covariance matrix entries that easily reach the limits of the typical machine precision of about 10^{-7} (*single precision*) respectively 10^{-16} (*double precision*) [176].

This problem can also be observed for the KF based sensor testing. Estimation with the combined laboratory error models is stable. However, this is caused by the dominating error sources, in this case, the test-pad motion and control errors. If these error sources are omitted, the residual error sources are small enough to cause numerical instabilities and filter divergences rapidly.

Since this problem has been known for a long time, modifications of the Kalman Filter have been suggested. Most of these approaches are based on the idea to replace the covariance matrix by a square-root representation $\mathbf{P} = \mathbf{A}\mathbf{A}^T$ [53, p. 107]. Like this, the distance of the matrix entries to the machine precision is increased, but also the positive-definiteness of the covariance matrix is enforced. However, the square-root Kalman Filters' formulations are incompatible with the Schmidt-Kalman filter. The implementation used in this example section alone has 162 independent systems used to model the sensor's noise and laboratory errors, resulting in a total of 247 states.

A test implementation of a square-root KF algorithm with a reduced error model showed better numerical stability. Still, it could not reach the levels of estimation covariance predicted in the classical test's error budgets. If this moderate improvement justifies the higher computational effort compared to the SKF may be questioned. However, if a sensor with extremely low sensor noise (better than navigation grade) shall be tested and calibrated, the presented algorithm is likely to fail, and another test design and procedure should be preferred. Still, for many sensor grades, the presented algorithm and models provide a simple to use test method with inherent uncertainty information.

Result 9: Kalman Filter-Based Testing

The here presented Kalman-filter-based sensor error estimation represents a proof of concept for a *one-click* sensor testing solution that also provides inherent uncertainty information for the estimates.

The following aspects of the Kalman-filter-based estimation shall be pointed out:

- Simultaneous rotation of all three rate-table axes provides observability of many potential sensor errors. Since the method allows very general error models, it may be used to check the validity of more specific error models that can be used for more accurate tests.
- A dynamic motion of the rate table introduces errors that limit the testing accuracy comparable with the multi-position tests.
- The number of states (247) needed to model the disturbances and the sensor noise motivate the use of a Schmidt-Kalman filter.
- Independent of the rate table motion, the filter's numerical instability for very small measurement covariances poses a problem for testing sensors better than navigation grade.

The presented simulation results demonstrate the feasibility of the proposed approach for, e.g., fully automated testing. However, the presented method is in a proof-of-concept state and requires further work (e.g., precise filter tuning and initialization) for productive use.

Chapter 5.

Conclusion

5.1. Summary

This work aimed to investigate the effects of inertial sensor errors on navigation performance and their testing and calibration in the laboratory.

Some prerequisites were presented in [Chapter 2](#) as a basis for the main chapters. The most crucial sensor error types and definitions were introduced, and a summary of typical sensor error models was given. Furthermore, an attempt was made to find the lowest common denominator in the literature's sensor grade definitions. After a recap of the aerospace reference frames, the basic strapdown inertial navigation algorithms were presented as a base for the error propagation analysis. This was supplemented by a brief recap of the Kalman filter and the idea of integrated navigation. The preliminaries section was concluded with an overview of the sensor noise processes and the signal analysis methods used to identify these processes.

Inertial Sensor Error Propagation

First, the stationary alignment of an inertial navigation system was analyzed. The resulting attitude initialization errors from inertial sensor errors were determined based on the linearized stationary alignment equations.

The differential equations for the strapdown navigation error dynamics were derived from the classical strapdown navigation equations in the local navigation frame. These equations were linearized around a straight and level flight condition, and further assumptions were taken to simplify the system further. It was demonstrated that the resulting system is still representative for many applications, including most aircraft.

The system's response to constant inputs was determined based on the linear error dynamics. The analytical equations representing the error growth for initialization errors of position, velocity, orientation, and bias-like sensor errors were presented. Subsequently, the linearized error system's response to white Gaussian noise input was derived. Shaping filters were introduced to form the typical sensor noise processes from white Gaussian noise and determine the navigation error growth from sensor noise represented by these processes. It was pointed out that the system's response to the sensor noise processes differs significantly from its response to white noise, which is typically used to approximate sensor noise. Charts for the error response

of each navigation state to normalized initialization and sensor errors were given to provide a simple to use prediction of the navigation errors. Furthermore, the correlation between the horizontal position, velocity, and orientation states was visualized over time. A summary of the figures that visualize the error growths for all errors and navigation states is given in Table 5.1.

Table 5.1.: Overview of the resulting navigation errors from initialization and sensor errors. The table lists the corresponding figures that illustrate the navigation state errors from a given error source.

Error Source	Error Term	Position Error		Velocity Error		Orientation Error		
		$\delta\phi$	$\delta\lambda$	δv_n	δv_e	$\delta\Phi$	$\delta\Theta$	$\delta\Psi$
Initialization Errors								
Initial Position	$\delta\phi_0, \delta\lambda_0, \delta h_0$	3.7a	3.7c	3.14a	3.15a	3.19a	3.19c	3.18a
Initial Velocity	$\delta v_{n,0}, \delta v_{e,0}, \delta v_{d,0}$	3.7b	3.7d	3.14b	3.15b	3.19b	3.19d	3.18b
Initial Orientation	$\delta\Phi_0, \delta\Theta_0, \delta\Psi_0$	3.9a	3.9b	3.16a	3.16b	3.20a	3.20b	3.20c
Accelerometer Errors								
Bias-like Sensor Errors	$b_{A,x}, b_{A,y}, b_{A,z}$	3.12a	3.12c	3.17a	3.17c	3.23a	3.23c	3.22a
Noise-like Sensor Errors								
Quantization Noise	$\nu_{Q_A,x}, \nu_{Q_A,y}, \nu_{Q_A,z}$	3.31a	3.31c	3.32a	3.32c	3.33a	3.33c	3.34a
Velocity Random Walk	$\nu_{N_A,x}, \nu_{N_A,y}, \nu_{N_A,z}$	3.25a	3.25c	3.27a	3.27c	3.29a	3.29c	3.28a
Bias Instability	$\nu_{B_A,x}, \nu_{B_A,y}, \nu_{B_A,z}$	3.36a	3.36c	3.37a	3.37c	3.38a	3.38c	3.39a
Acceleration RW	$\nu_{K_A,x}, \nu_{K_A,y}, \nu_{K_A,z}$	3.40a	3.40c	3.41a	3.41c	3.43a	3.43c	3.42a
Acceleration Ramp	$\nu_{R_A,x}, \nu_{R_A,y}, \nu_{R_A,z}$	3.44a	3.44c	3.45a	3.45c	3.46a	3.46c	3.47a
Gyroscope Errors								
Bias-like Sensor Errors	$b_{G,x}, b_{G,y}, b_{G,z}$	3.12b	3.12d	3.17b	3.17d	3.23b	3.23d	3.22b
Noise-like Sensor Errors								
Quantization Noise	$\nu_{Q_G,x}, \nu_{Q_G,y}, \nu_{Q_G,z}$	3.31b	3.31d	3.32b	3.32d	3.33b	3.33d	3.34b
Angular Random Walk	$\nu_{N_G,x}, \nu_{N_G,y}, \nu_{N_G,z}$	3.25b	3.25d	3.27b	3.27d	3.29b	3.29d	3.28b
Bias Instability	$\nu_{B_G,x}, \nu_{B_G,y}, \nu_{B_G,z}$	3.36b	3.36d	3.37b	3.37d	3.38b	3.38d	3.39b
Rate RW	$\nu_{K_G,x}, \nu_{K_G,y}, \nu_{K_G,z}$	3.40b	3.40d	3.41b	3.41d	3.43b	3.43d	3.42b
Rate Ramp	$\nu_{R_G,x}, \nu_{R_G,y}, \nu_{R_G,z}$	3.44b	3.44d	3.45b	3.45d	3.46b	3.46d	3.47b

The validity of the derived equations for the error growth is only limited by the error size itself, which should not violate the limits of the linearization. There is no limitation in time as the three known error dynamics, namely the Schuler-oscillation, the 24-hour oscillation, and the Foucault oscillation, are included in the analytical solutions. Further assumptions were applied to these lengthy equations to derive medium-term approximations for up to 4 hours and short-term approximations valid for about 10 minutes. The differences between these approximations were pointed out, and each approximation's validity period was demonstrated. A comprehensive summary of the short- and medium-term approximation equations for all navigation state errors from initialization and sensor errors was given in Table 3.14 respectively Table 3.12 and Table 3.13.

Within a brief review of the typical position error measures, like 2DRMS or CEP, used within the navigation community, the meaningfulness of the different definitions was discussed. It was demonstrated how these measures fail to represent the actual error distribution for the

correlated horizontal position errors observed in the error propagation visualization. Therefore, the handy single-valued position accuracy indicators should always be taken with a grain of salt.

A set of charts was created to support the selection of inertial sensors from navigation requirements. These charts relate gyroscope and accelerometer errors to navigation performance, e.g., the [2DRMS](#) position error after a given time. The graphs are not limited to the read-off of the allowed maximum sensor error for the desired navigation performance but also indicate the range of an equal contribution of gyroscope and accelerometer to the navigation errors. This supports the balanced selection of inertial sensors for a navigation system.

In addition to the charts, a template for a navigation performance error budget based on the derived propagation equations was presented. The validity and feasibility of the analytical performance prediction were assessed for two real-world examples, a commercial transatlantic flight, and a small aircraft round trip. It was demonstrated that the analytical error prediction gives additional insight into the respective contributions from each error source while providing a surprisingly good approximation of the true navigation errors determined from Monte Carlo simulations.

The presented methods thus allow a reasonably accurate prediction of the navigation errors independent of the actual trajectory. This allows a basic specification of the inertial sensor requirements and thus sensor selection already at an early stage of system design, as depicted in [Figure 1.2](#). The presented charts, e.g., [Figure 3.62](#) can be used by a sensor manufacturer to select a combination of gyroscope and accelerometer for an [IMU](#) without over-specifying any of the components.

After the acceptable sensor errors for the desired navigation performance were demonstrated in the first chapter, the second chapter aimed to assess how to test and assert these sensor errors in the laboratory.

Inertial Laboratory Sensor Testing and Calibration

As a first step, a kinematic model of an inertial laboratory with a three-axis rate table on an isolated test pier was created. This mathematical model provided the basis for the error propagation analysis. The model was linearized for the error sources and was later used for the error budget calculation and the Kalman filter-based testing.

Following the derived kinematic chain, a comprehensive discussion of the various error sources was presented. It was demonstrated how the variable Earth's angular rate differs from the idealized [WGS84](#) constant rate and also how the local gravity varies due to tides and atmospheric changes. The importance of an isolated test pad was pointed out, and a reference model for the test pad motion spectrum was derived from multiple seismic background noise models. The laboratory error models were concluded by discussing the three-axis rate table that can be easily adapted to similar test instruments. The axis wobble was discussed after reviewing the geometrical errors from manufacturing imperfections, thermal expansion, and

loads. It was demonstrated how axis wobble can be attributed to bearing imperfections and how mathematical bearing models can be used to model axis wobble. A comparison with real-world inertial sensor data showed the fundamental validity of the models. Models for a rate table's positioning and rate control errors were derived and validated similarly.

Since the traditional sensor test procedures rely on averaging over the sensor signal to reduce noise effects, the actual effects of averaging were analyzed for the different sensor noise processes. Analytical equations were derived to determine the variance of averages over signal segments of the sensor noise processes. While the variance of quantization noise and angular random walk is reduced by averaging over time, the opposite is true for bias instability, rate ramp, and rate random walk noise. The variance is undefined for the later noise processes, and it was pointed out how the Allan variance may be used as an alternative. It was concluded that the Allan variance graphs should be used to determine the optimal averaging time with the minimum variation of cluster averages due to sensor noise.

A review of the IEEE inertial sensor test and specification standards revealed a basis of a few test procedures that are used for virtually any sensor technology: single position and static reversal tests, scale factor test series, and multi-position tests. An error budget was created based on the previously derived models for each of these basic test procedures. The error budgets indicate the contribution of each sensor noise process and laboratory error source to the accuracy of the test results and how it is affected by the choice of the averaging time. It was demonstrated that single-position static tests allow bias testing to extreme accuracies but cannot distinguish between sensor bias and misalignments. In principle, the bias can only be determined for the test duration as it is subject to drift, e.g., bias instability. Static reversal position tests were shown to simultaneously allow the testing of linear scale factor, bias, and misalignment, but at a higher sensitivity to laboratory errors. For the scale factor test series, the rate table's rate errors proved to be the dominating error source, followed by the test-pad motion. A six-position test with a rotating vertical axis of the rate table was analyzed as an example for multi-position testing. Compared to the other tests, the accuracy of the test proved to be limited to intermediate or near navigation grade for the typical laboratory setup. The error budgets highlighted the benefits of averaging over complete revolutions, which can reduce or even eliminate the effects of several error sources.

An overview of how the test procedures analysed within this thesis correspond to the IEEE standard test procedures and error models is given in Figure 5.1 and Figure 5.2. The figures also indicate how further sensor errors, like environmental dependencies, are also based on the discussed basic tests. In general, the suggested procedures allow a determination of the sensor errors at an accuracy better than navigation grade. However, the procedures depend on the correctness of the assumed sensor error models for the tested sensor. Other procedures like multi-position tests may be more effective, e.g., require less handling.

Even more flexibility regarding the sensor error models can be achieved using a Kalman-filter-based test procedure. This Kalman-filter-based inertial sensor testing approach was introduced in the last section. The approach promised a *one-click* solution, where the modeled

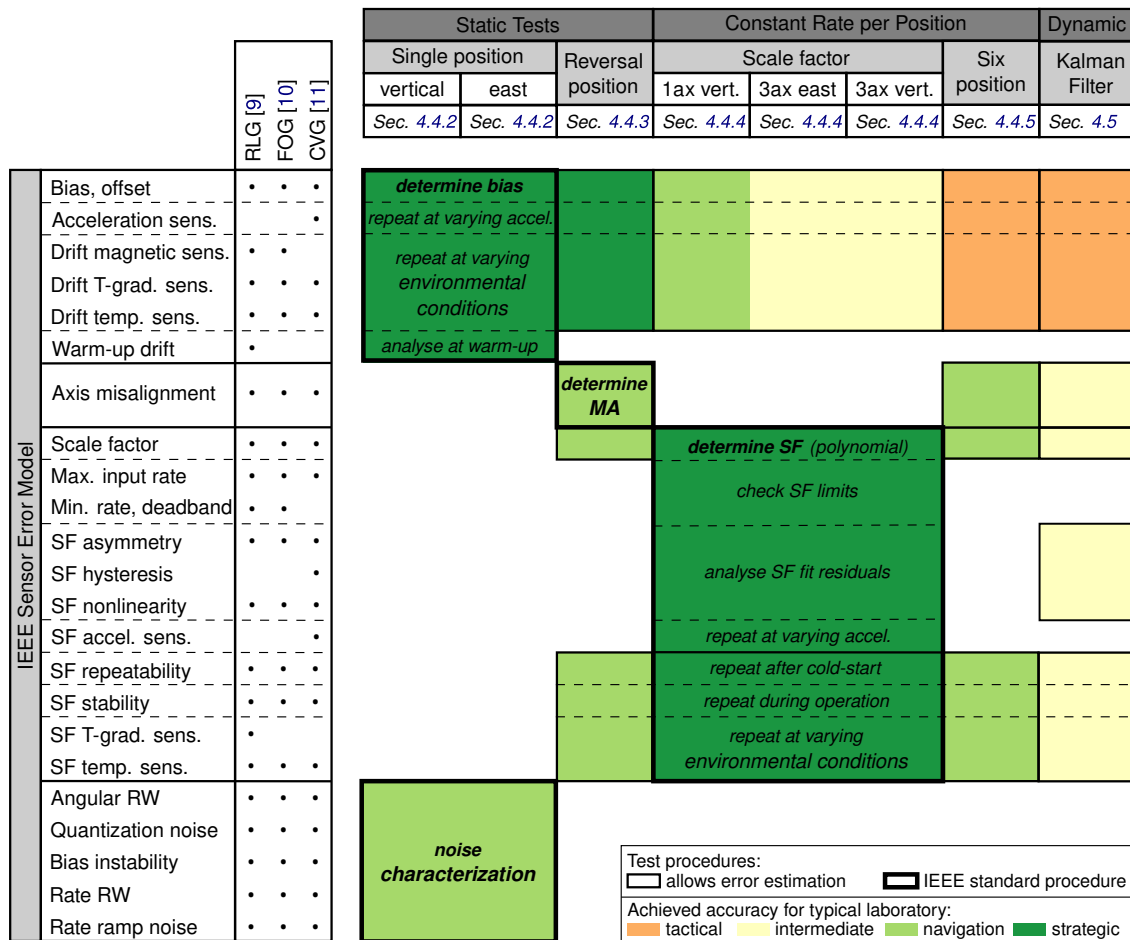


Figure 5.1.: Summary of gyroscope error model terms and test procedures covered in this thesis. The thick lines mark the test procedures that are suggested in the IEEE standards. The colors indicate the achievable accuracy grade for the typical laboratory setup analyzed in this thesis.

sensor errors are estimated with inherently included accuracy information while the rate table performs an appropriate motion without user interference. The filter’s measurement model included the sensor noise and laboratory errors to provide a consistent variance estimation of the test results. This was implemented as a Schmidt-Kalman filter to handle the high number of required model states.

An observability analysis demonstrated which rate table motion is required for each sensor error to be estimated during the testing. A constant angular rate applied to all three rate table axes proved sufficient to estimate nearly all deterministic sensor errors, including higher-order scale factors and g-sensitivities. Example simulations supported the analytically predicted observability of the sensor errors. Furthermore, the need for time-synchronization between sensor and rate table signals was highlighted. The chapter discussed the Kalman filter’s numerical instabilities that occur for inertial sensors better than navigation grade.

The dynamic motion of the rate table introduces additional errors so that the accuracy of the simple static tests cannot be reached. However, the filter can be designed with a general sensor

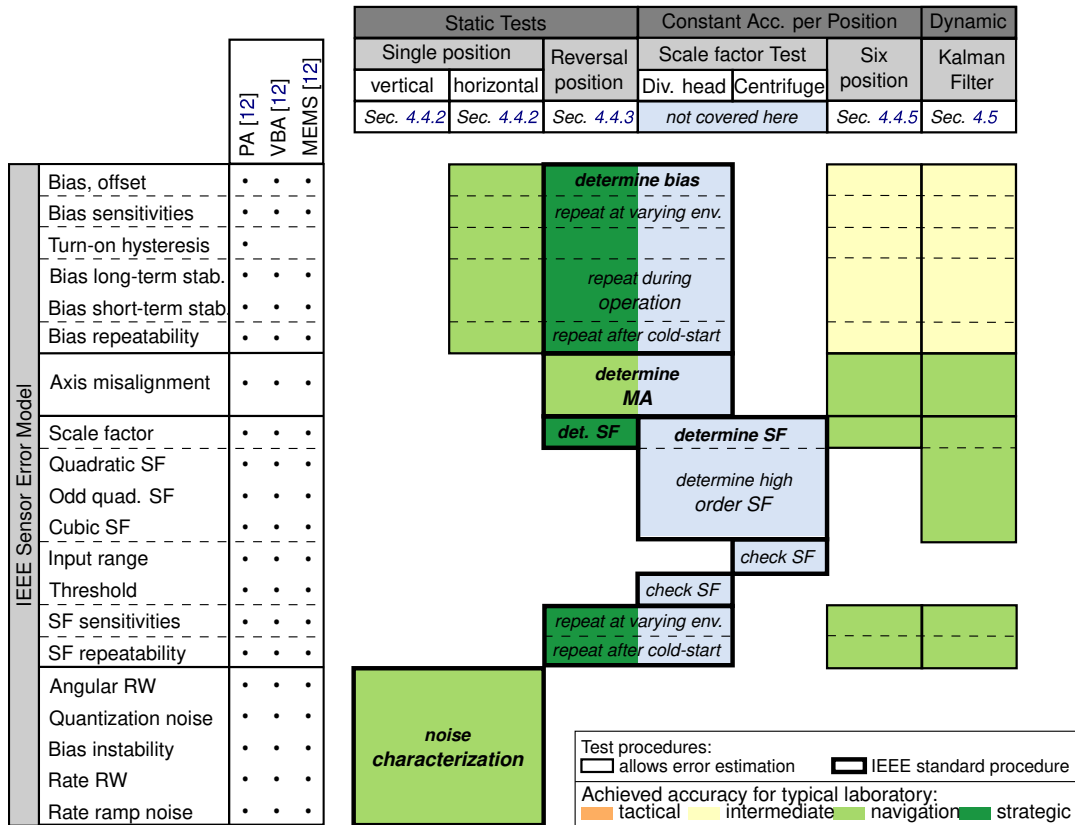


Figure 5.2.: Summary of accelerometer error model terms and test procedures covered in this thesis. The thick lines mark the test procedures that are suggested in the IEEE standards. The colors indicate the achievable accuracy grade for the typical laboratory setup analyzed in this thesis.

error model that does not require technology-specific knowledge. The proposed method is suitable for less accurate tests, especially if there is little information on the expected sensor errors. In the context of system development, see Figure 1.2, the Kalman-filter-based approach can thus be used as a time-effective test for quality assurance at both the sensor manufacturer and the system manufacturer. Furthermore, it may be used to ensure the validity of a less general sensor error model for subsequent high-accuracy tests.

5.2. Achievements beyond State-of-the-Art

The goal of this thesis was to revisit the field of inertial sensor selection and testing that spans between the sensor manufacturers and system manufacturers. The topic of sensor selection boils down to how the sensor accuracy requirements can be derived from the navigation requirements. Regarding sensor testing, the question is how to perform sensor tests at the desired accuracy level.

Within this work, both questions have been answered by analysis of the strapdown inertial navigation error propagation and the propagation of laboratory errors during sensor testing. In the following, the aspects in which the analyses carried out go beyond state-of-the-art are explained.

Inertial Navigation Error Propagation

The propagation of inertial sensor errors has been investigated since the early days of inertial navigation and is widely covered in the literature. Still, to the author's knowledge, this work added aspects that have not been covered at the given level of detail so far:

1. Within this work, a comprehensive set of analytical solutions to the long-term strapdown navigation error dynamics for all navigation states and sensor errors was given. Equations in literature were limited to the Schuler oscillations or approximations of the long-term solutions, valid for up to about 4 h. [Section 3.3]
2. In literature, sensor noise propagation has been addressed (if at all) only for white Gaussian noise. In contrast, the IEEE sensor inertial sensor noise processes were considered in this work, and the differences in the navigation errors for white and colored sensor noise were pointed out. [Subsection 3.3.3]
3. Within this work, also the correlation of the resulting navigation errors was considered and visualized. In general, the navigation errors cannot be considered *independently and identically distributed (i.i.d.)*, which reduces the meaningfulness of typical navigation performance indicators like 2DRMS or CEP. [Subsection 3.4.2]
4. The presented navigation performance charts provide simple-to-use support for the inertial sensor requirements definition from navigation requirements. They can be used at an early phase of navigation system design to determine the magnitude of acceptable inertial sensor errors without needing a detailed mission profile and simulations. [Subsection 3.4.3]
5. A systematic derivation of the medium- and short-term approximations for all navigation states was given. The given summary completes the set of well-known approximations by offering solutions for all navigation states and constant sensor errors and sensor noise. [Section 3.6]

The results of this chapter answer the original question of inertial sensor error propagation and, consequently, sensor requirement definition. Thus, they support the system manufacturer in selecting inertial sensors at an early development phase. Incorporating the long-term strapdown error dynamics also supports the design of navigation systems with the prospective accuracy of future technologies, like quantum inertial sensors. The thesis also pointed out the complexity of selecting the suitable sensor for a given application and the limits of analytical prediction methods. In doing so, the results presented provide a low-threshold approach to error propagation in inertial navigation, allowing, for example, a sensor manufacturer to develop and market its products for specific applications.

Inertial Sensor Laboratory Testing

The question of inertial sensor testing and the achievable test accuracy was answered with a systematic modeling approach and the derivation of error budgets for typical test procedures. Within this approach, the state of the art or literature was surpassed in the following aspects:

1. A systematic modeling of the entire kinematic chain of an inertial laboratory was presented. A comprehensive discussion of error sources along this chain was given. In addition, mathematical models of these error sources were derived for use in the error budgets. [Section 4.2]
2. The analytical determination of the variance of averaged sensor noise segments. Analytical methods were applied to the IEEE sensor noise processes to demonstrate the effect of sensor noise on the testing accuracy. [Section 4.3]
3. Systematic graphical error budgets for the most common test procedures were derived. Based on the derived models, the error budgets predict the contribution of the different error sources to the total error of the tested sensor error. Furthermore, the presented graphs indicate the time dependency and thus show how the accuracy is affected by increasing the averaging time. The test accuracy can be predicted from these, and the dominating error sources can be identified for the different test procedures. [Section 4.4]
4. An analysis of sensor error observability at inertial sensor testing on a three-axis rate table was performed. The results can be used to design test procedures and rate table trajectories for optimal estimation of sensor errors. [Subsection 4.5.2]
5. A Kalman-filter-based testing method that includes laboratory error and sensor noise models to inherently provide accuracy information for the sensor error estimates was developed. Combined with a suitable rate table trajectory, as determined from the observability analysis, this method offers a *one-click* solution that can identify various inertial sensor errors simultaneously with neither user interaction nor manual determination of an error budget. [Section 4.5]

This chapter demonstrated the complexity of sensor testing due to the vast number of error sources and degrees of freedom regarding the test procedures. Still, the presented error budgets support a sensor manufacturer in designing and using an inertial laboratory for development, production, and calibration. On the one side, this may be used to identify the limitations when testing extremely accurate future sensors and, on the other side, to reduce costs when testing low-cost sensors. From a system manufacturer's side, the results may also be used to assess the laboratory requirements for a typically less elaborate and accurate acceptance testing. The presented Kalman Filter approach goes in a similar direction by providing a simple-to-use but limited accuracy testing option. Figure 5.3 depicts the contributions in the context of the sensor and system development processes originally depicted in Figure 1.2.

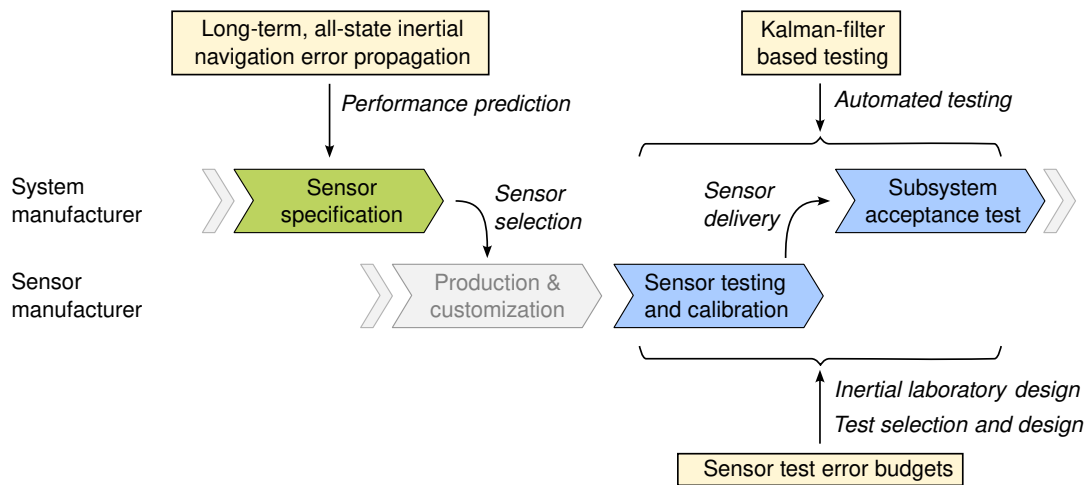


Figure 5.3.: This work's contributions in the context of the development processes from Figure 1.2.

In summary, the contributions presented in this work can lower the entry barrier for new market players by providing essential tools and knowledge required for both sensor and system manufacturers.

5.3. Outlook

The error propagation in inertial navigation has been analyzed for years, and this thesis was able to add only details to the already broad knowledge. To promote this thesis' results and increase the accessibility and applicability of this knowledge, creating an easy-to-use sensor error budget and navigation error prediction software seems helpful. In the author's opinion, options for follow-on works in this field arise if future sensor technologies display a different behavior than today's sensors, for example, quantum inertial sensors [6].

Although the chapter on laboratory calibration provides a comprehensive discussion of error sources and models, there is clear potential for refinement. The models presented within this work were created to represent a typical inertial laboratory. This provides valuable insight into inertial sensor laboratory testing error propagation and allows a fundamental prediction of the expectable test accuracy. However, refining and adapting the models to the actual test setup and environment would be beneficial for a laboratory operator. This requires creating locally representative test-pad motion spectra and refining and validating the instrument models, like rate table bearings and the servo control errors. The presented approach to derive the error budgets could also be applied to further, more specific test procedures. Many aspects require further investigation, e.g., the effects of the sensor's sampling or the test-pads reaction to rate table forces and moments.

Finally, the presented Kalman-filter-based testing approach offers space for further improvement. First, the approach shares the used models with the other error budgets and thus also benefits from refined models for a specific test setup. Second, the numerical instabilities of the Kalman filter for very low covariances need to be addressed. It should be investigated how the numerous approaches to increase the Kalman-filter stability can be applied to the Schmidt-Kalman filter used in this work. Furthermore, ways to automatically identify and incorporate the sensor noise should be investigated to create a real *one-click* solution. This could include adaptive Kalman filters or a priori automated noise identification.

In conclusion, future works should focus on bringing the theoretical results into practice by adapting them to specific laboratory setups and improving their accessibility and handling for both sensor and system manufacturers.

Appendices

Appendix A.

Mathematical and mechanical preliminaries

A.1. Cross-product building matrix

When calculating the time-derivatives of kinematic properties, the cross-product "×" of two three-dimensional vectors will occur at several occasions. By simple calculus it can be proven that there is a matrix $\mathbf{\Omega}$ that fulfills below equation for any vector \mathbf{r} :

$$\mathbf{\Omega}\mathbf{r} = \boldsymbol{\omega} \times \mathbf{r} \quad \text{where } \boldsymbol{\omega}, \mathbf{r} \in \mathbb{R}^3 \quad (\text{A.1})$$

where $\mathbf{\Omega}$ is the cross-product-building, skew-symmetric matrix as defined below:

$$\mathbf{\Omega} = [\boldsymbol{\omega}]_{\times} = \begin{bmatrix} 0 & -\omega_z & \omega_y \\ \omega_z & 0 & -\omega_x \\ -\omega_y & \omega_x & 0 \end{bmatrix} \in \mathbb{R}^{3 \times 3} \quad (\text{A.2})$$

A.2. Time derivative of rotation matrices

Using the relationship between rotation and linear velocity in classical mechanics, the formula for time-derivatives of rotation matrices can easily be determined. An arbitrary constant position vector \mathbf{r}_b , given in the rotating frame b , is expressed in the a -frame by the following transformation:

$$\mathbf{r}_a(P) = \mathbf{R}_{ab}\mathbf{r}_b(P) \quad (\text{A.3})$$

Time-derivation of both sides yields:

$$\dot{\mathbf{r}}_a(P) = \dot{\mathbf{R}}_{ab}\mathbf{r}_b(P) \quad (\text{A.4})$$

From classical mechanics, the velocity of P in the rotating b -frame is known to be:

$$\dot{\mathbf{r}}_b(P) = \boldsymbol{\omega}_{ab} \times \mathbf{r}_b(P) = \mathbf{\Omega}_{ab}\mathbf{r}_b(P) \quad (\text{A.5})$$

Transformation of equation (A.5) to the a -frame allows the identification of following well-known identity:

$$\frac{d}{dt}\mathbf{R}_{ab} = \mathbf{R}_{ab}\mathbf{\Omega}_{ab} \quad (\text{A.6})$$

In addition to this intuitively accessible method, also a mathematical proof without reference to classical mechanics can be found in literature, e.g. [177].

Appendix B.

Conversion of Random Walk Measures

Noise parameters, especially the random walk, are specified in a variety of different units. The units used in datasheets are up to the manufacturer's philosophy. To support the comparison of angular and velocity random walk measures, the conversion ratios are summarized in [Table B.1](#) and [Table B.2](#). The table gives the multipliers to get from one representation to the other. Additionally, the conversion of random walk coefficients to the corresponding standard deviation of a time-discrete white Gaussian noise time-series is given.

Table B.1.: Conversion of Angular Random Walk Measures.

conversion to		discrete time SD σ	ARW N			
from		$\frac{\text{deg}}{s}$	$\frac{\text{deg}}{\sqrt{s}}$	$\frac{\text{deg}}{s\sqrt{\text{Hz}}}$	$\frac{\text{deg}}{\sqrt{h}}$	$\frac{\text{deg}}{h\sqrt{\text{Hz}}}$
discrete time SD σ	$\frac{\text{deg}}{s}$	1	$\frac{1}{\sqrt{f_s}}$	$\frac{1}{\sqrt{f_s}}$	$\frac{60}{\sqrt{f_s}}$	$\frac{3600}{\sqrt{f_s}}$
ARW N	$\frac{\text{deg}}{\sqrt{s}}$	$\sqrt{f_s}$	1	1	60	3600
	$\frac{\text{deg}}{s\sqrt{\text{Hz}}}$	$\sqrt{f_s}$	1	1	60	3600
	$\frac{\text{deg}}{\sqrt{h}}$	$\frac{\sqrt{f_s}}{60}$	$\frac{1}{60}$	$\frac{1}{60}$	1	60
	$\frac{\text{deg}}{h\sqrt{\text{Hz}}}$	$\frac{\sqrt{f_s}}{3600}$	$\frac{1}{3600}$	$\frac{1}{3600}$	$\frac{1}{60}$	1

Table B.2.: Conversion of Velocity Random Walk Measures.

conversion		to	discrete time SD σ				
from			VRW N				
			$\frac{m}{s^2}$	$\frac{m}{s\sqrt{s}}$	$\frac{m}{s^2\sqrt{\text{Hz}}}$	$\frac{m}{s\sqrt{h}}$	$\frac{g}{\sqrt{\text{Hz}}}$
discrete time SD σ	$\frac{m}{s^2}$	1	1	$\frac{1}{\sqrt{f_s}}$	$\frac{1}{\sqrt{f_s}}$	$\frac{60}{\sqrt{f_s}}$	$\frac{1}{g_0\sqrt{f_s}}$
VRW N	$\frac{m}{s\sqrt{s}}$	$\sqrt{f_s}$	1	1	60	$\frac{1}{g_0}$	
	$\frac{m}{s^2\sqrt{\text{Hz}}}$	$\sqrt{f_s}$	1	1	60	$\frac{1}{g_0}$	
	$\frac{m}{s\sqrt{h}}$	$\frac{\sqrt{f_s}}{60}$	$\frac{1}{60}$	$\frac{1}{60}$	1	$\frac{1}{60g_0}$	
	$\frac{g}{\sqrt{\text{Hz}}}$	$g_0\sqrt{f_s}$	g_0	g_0	$60g_0$	1	

Appendix C.

Selected Laplace transformations

A set of selected transformations from the Laplace s -domain to time-domain is presented in the following table to support the determination of time-domain responses of the navigation error dynamics. The Laplace correspondences have been calculated using *Wolfram Alpha* [178].

Table C.1.: Selected Laplace transforms

Laplace s -domain	Time t -domain
1. $\frac{1}{(s^2 + \omega_1^2)(s^2 + \omega_2^2)}$	$-\frac{\sin \omega_1 t}{\omega_1 (\omega_1^2 - \omega_2^2)} - \frac{\sin \omega_2 t}{\omega_2 (\omega_2^2 - \omega_1^2)}$
2. $\frac{1}{s(s^2 + \omega_1^2)(s^2 + \omega_2^2)}$	$\frac{1}{\omega_1^2 \omega_2^2} + \frac{\cos \omega_1 t}{\omega_1^2 (\omega_1^2 - \omega_2^2)} + \frac{\cos \omega_2 t}{\omega_2^2 (\omega_2^2 - \omega_1^2)}$
3. $\frac{1}{s^2 (s^2 + \omega_1^2)(s^2 + \omega_2^2)}$	$\frac{t}{\omega_1^2 \omega_2^2} + \frac{\sin \omega_1 t}{\omega_1^3 (\omega_1^2 - \omega_2^2)} + \frac{\sin \omega_2 t}{\omega_2^3 (\omega_2^2 - \omega_1^2)}$
4. $\frac{s}{(s^2 + \omega_1^2)(s^2 + \omega_2^2)}$	$-\frac{\cos \omega_1 t}{(\omega_1^2 - \omega_2^2)} - \frac{\cos \omega_2 t}{(\omega_2^2 - \omega_1^2)}$
5. $\frac{s^2}{(s^2 + \omega_1^2)(s^2 + \omega_2^2)}$	$\frac{\omega_1 \sin \omega_1 t}{(\omega_1^2 - \omega_2^2)} + \frac{\omega_2 \sin \omega_2 t}{(\omega_2^2 - \omega_1^2)}$
6. $\frac{1}{(s^2 + \omega_1^2)(s^2 + \omega_2^2)(s^2 + \omega_3^2)}$	$\frac{\sin \omega_1 t}{\omega_1 (\omega_1^2 - \omega_2^2)(\omega_1^2 - \omega_3^2)} +$ $\frac{\sin \omega_2 t}{\omega_2 (\omega_2^2 - \omega_1^2)(\omega_2^2 - \omega_3^2)} + \frac{\sin \omega_3 t}{\omega_3 (\omega_3^2 - \omega_1^2)(\omega_3^2 - \omega_2^2)}$
7. $\frac{1}{s(s^2 + \omega_1^2)(s^2 + \omega_2^2)(s^2 + \omega_3^2)}$	$\frac{1}{\omega_1^2 \omega_2^2 \omega_3^2} - \frac{\cos \omega_1 t}{\omega_1^2 (\omega_1^2 - \omega_2^2)(\omega_1^2 - \omega_3^2)} -$ $\frac{\cos \omega_2 t}{\omega_2^2 (\omega_2^2 - \omega_1^2)(\omega_2^2 - \omega_3^2)} - \frac{\cos \omega_3 t}{\omega_3^2 (\omega_3^2 - \omega_1^2)(\omega_3^2 - \omega_2^2)}$

Laplace s -domain	Time t -domain
8. $\frac{1}{s^2(s^2 + \omega_1^2)(s^2 + \omega_2^2)(s^2 + \omega_3^2)}$	$\frac{1}{\omega_1^2\omega_2^2\omega_3^2} - \frac{\sin \omega_1 t}{\omega_1^2(\omega_1^2 - \omega_2^2)(\omega_1^2 - \omega_3^2)} - \frac{\sin \omega_2 t}{\omega_2^2(\omega_2^2 - \omega_1^2)(\omega_2^2 - \omega_3^2)} - \frac{\sin \omega_3 t}{\omega_3^2(\omega_3^2 - \omega_1^2)(\omega_3^2 - \omega_2^2)}$
9. $\frac{s}{(s^2 + \omega_1^2)(s^2 + \omega_2^2)(s^2 + \omega_3^2)}$	$\frac{\cos \omega_1 t}{(\omega_1^2 - \omega_2^2)(\omega_1^2 - \omega_3^2)} + \frac{\cos \omega_2 t}{(\omega_2^2 - \omega_1^2)(\omega_2^2 - \omega_3^2)} + \frac{\cos \omega_3 t}{(\omega_3^2 - \omega_1^2)(\omega_3^2 - \omega_2^2)}$
10. $\frac{s^2}{(s^2 + \omega_1^2)(s^2 + \omega_2^2)(s^2 + \omega_3^2)}$	$-\frac{\omega_1 \sin \omega_1 t}{(\omega_1^2 - \omega_2^2)(\omega_1^2 - \omega_3^2)} - \frac{\omega_2 \sin \omega_2 t}{(\omega_2^2 - \omega_1^2)(\omega_2^2 - \omega_3^2)} - \frac{\omega_3 \sin \omega_3 t}{(\omega_3^2 - \omega_1^2)(\omega_3^2 - \omega_2^2)}$
11. $\frac{s^3}{(s^2 + \omega_1^2)(s^2 + \omega_2^2)(s^2 + \omega_3^2)}$	$-\frac{\omega_1^2 \cos \omega_1 t}{(\omega_1^2 - \omega_2^2)(\omega_1^2 - \omega_3^2)} - \frac{\omega_2^2 \cos \omega_2 t}{(\omega_2^2 - \omega_1^2)(\omega_2^2 - \omega_3^2)} - \frac{\omega_3^2 \cos \omega_3 t}{(\omega_3^2 - \omega_1^2)(\omega_3^2 - \omega_2^2)}$
12. $\frac{(s^2 + \omega_4^2)}{(s^2 + \omega_1^2)(s^2 + \omega_2^2)(s^2 + \omega_3^2)}$	$-\frac{(\omega_1^2 - \omega_4^2) \sin \omega_1 t}{\omega_1(\omega_1^2 - \omega_2^2)(\omega_1^2 - \omega_3^2)} - \frac{(\omega_2^2 - \omega_4^2) \sin \omega_2 t}{\omega_2(\omega_2^2 - \omega_1^2)(\omega_2^2 - \omega_3^2)} - \frac{(\omega_3^2 - \omega_4^2) \sin \omega_3 t}{\omega_3(\omega_3^2 - \omega_1^2)(\omega_3^2 - \omega_2^2)}$
13. $\frac{(s^2 + \omega_4^2)(s^2 + \omega_5^2)}{(s^2 + \omega_1^2)(s^2 + \omega_2^2)(s^2 + \omega_3^2)}$	$\frac{(\omega_1^4 - \omega_1^2(\omega_4^2 + \omega_5^2) + \omega_4^2\omega_5^2) \sin \omega_1 t}{\omega_1(\omega_1^2 - \omega_2^2)(\omega_1^2 - \omega_3^2)} + \frac{(\omega_2^4 - \omega_2^2(\omega_4^2 + \omega_5^2) + \omega_4^2\omega_5^2) \sin \omega_2 t}{\omega_2(\omega_2^2 - \omega_1^2)(\omega_2^2 - \omega_3^2)} + \frac{(\omega_3^4 - \omega_3^2(\omega_4^2 + \omega_5^2) + \omega_4^2\omega_5^2) \sin \omega_3 t}{\omega_3(\omega_3^2 - \omega_1^2)(\omega_3^2 - \omega_2^2)}$
14. $\frac{(s^2 + \omega_4^2)}{s(s^2 + \omega_1^2)(s^2 + \omega_2^2)(s^2 + \omega_3^2)}$	$\frac{\omega_4^2}{\omega_1^2\omega_2^2\omega_3^2} + \frac{(\omega_1^2 - \omega_4^2) \cos \omega_1 t}{\omega_1^2(\omega_1^2 - \omega_2^2)(\omega_1^2 - \omega_3^2)} + \frac{(\omega_2^2 - \omega_4^2) \cos \omega_2 t}{\omega_2^2(\omega_2^2 - \omega_1^2)(\omega_2^2 - \omega_3^2)} + \frac{(\omega_3^2 - \omega_4^2) \cos \omega_3 t}{\omega_3^2(\omega_3^2 - \omega_1^2)(\omega_3^2 - \omega_2^2)}$

Laplace s -domain	Time t -domain
15. $\frac{(s^2 + \omega_4^2)(s^2 + \omega_5^2)}{s(s^2 + \omega_1^2)(s^2 + \omega_2^2)(s^2 + \omega_3^2)}$	$\frac{\omega_4^2 \omega_5^2}{\omega_1^2 \omega_2^2 \omega_3^2} t - \frac{(\omega_1^4 - \omega_1^2(\omega_4^2 + \omega_5^2) + \omega_4^2 \omega_5^2) \cos \omega_1 t}{\omega_1^2 (\omega_1^2 - \omega_2^2)(\omega_1^2 - \omega_3^2)} -$ $\frac{(\omega_2^4 - \omega_2^2(\omega_4^2 + \omega_5^2) + \omega_4^2 \omega_5^2) \cos \omega_2 t}{\omega_2^2 (\omega_2^2 - \omega_1^2)(\omega_2^2 - \omega_3^2)} -$ $\frac{(\omega_3^4 - \omega_3^2(\omega_4^2 + \omega_5^2) + \omega_4^2 \omega_5^2) \cos \omega_3 t}{\omega_3^2 (\omega_3^2 - \omega_1^2)(\omega_3^2 - \omega_2^2)}$
16. $\frac{(s^2 + \omega_4^2)(s^2 + \omega_5^2)}{s^2(s^2 + \omega_1^2)(s^2 + \omega_2^2)(s^2 + \omega_3^2)}$	$\frac{\omega_4^2 \omega_5^2}{\omega_1^2 \omega_2^2 \omega_3^2} t - \frac{(\omega_1^4 - \omega_1^2(\omega_4^2 + \omega_5^2) + \omega_4^2 \omega_5^2) \sin \omega_1 t}{\omega_1^3 (\omega_1^2 - \omega_2^2)(\omega_1^2 - \omega_3^2)} -$ $\frac{(\omega_2^4 - \omega_2^2(\omega_4^2 + \omega_5^2) + \omega_4^2 \omega_5^2) \sin \omega_2 t}{\omega_2^3 (\omega_2^2 - \omega_1^2)(\omega_2^2 - \omega_3^2)} -$ $\frac{(\omega_3^4 - \omega_3^2(\omega_4^2 + \omega_5^2) + \omega_4^2 \omega_5^2) \sin \omega_3 t}{\omega_3^3 (\omega_3^2 - \omega_1^2)(\omega_3^2 - \omega_2^2)}$
17. $\frac{1}{(s^2 + \omega_1^2)(s^2 + \omega_2^2)(s^2 + \omega_3^2)(s^2 + \omega_4^2)}$	$\frac{\sin \omega_1 t}{\omega_1 (\omega_1^2 - \omega_2^2)(\omega_1^2 - \omega_3^2)(\omega_1^2 - \omega_4^2)} -$ $\frac{\sin \omega_2 t}{\omega_2 (\omega_2^2 - \omega_1^2)(\omega_2^2 - \omega_3^2)(\omega_2^2 - \omega_4^2)} -$ $\frac{\sin \omega_3 t}{\omega_3 (\omega_3^2 - \omega_1^2)(\omega_3^2 - \omega_2^2)(\omega_3^2 - \omega_4^2)} -$ $\frac{\sin \omega_4 t}{\omega_4 (\omega_4^2 - \omega_1^2)(\omega_4^2 - \omega_2^2)(\omega_4^2 - \omega_3^2)}$

Appendix D.

Solutions to the Linearized Error Dynamics

D.1. Step Responses

D.1.1. Position Errors from Initialization Errors

Table D.1.: Latitude error step responses to position and velocity initialization errors.

Input	Step response
$\delta\phi_0$	$H_{1,1}(s) = -\frac{\omega_s^2 \omega_{ie}^2 (2 \sin^2 \phi + 1)s}{(s^2 + \omega_{s-}^2)(s^2 + \omega_{s+}^2)(s^2 + \omega_{ie}^2)} - \frac{\omega_s^4 \omega_{ie}^2}{s(s^2 + \omega_{s-}^2)(s^2 + \omega_{s+}^2)(s^2 + \omega_{ie}^2)}$ $h_{1,1}(t) = \left(-\frac{\omega_s^2}{\omega_{s-}^2 \omega_{s+}^2 \omega_{ie}^2} + \frac{\omega_s^2 - \omega_{s-}^2 (2 \sin^2 \phi + 1)}{\omega_{s-}^2 (\omega_{s-}^2 - \omega_{s+}^2) (\omega_{s-}^2 - \omega_{ie}^2)} \cos(\omega_{s-} t) \right. \\ \left. + \frac{\omega_s^2 - \omega_{s+}^2 (2 \sin^2 \phi + 1)}{\omega_{s+}^2 (\omega_{s+}^2 - \omega_{s-}^2) (\omega_{s+}^2 - \omega_{ie}^2)} \cos(\omega_{s+} t) \right. \\ \left. + \frac{\omega_s^2 - \omega_{ie}^2 (2 \sin^2 \phi + 1)}{\omega_{ie}^2 (\omega_{ie}^2 - \omega_{s-}^2) (\omega_{ie}^2 - \omega_{s+}^2)} \cos(\omega_{ie} t) \right) \omega_s^2 \omega_{ie}^2 + 1$
$\delta\lambda_0$	$H_{1,2}(s) = 0$ $h_{1,2}(t) = 0$
$\delta v_{n,0}$	$H_{1,3}(s) = \frac{\frac{1}{R} s^2}{(s^2 + \omega_{s-}^2)(s^2 + \omega_{s+}^2)} + \frac{\frac{\omega_s^2}{R}}{(s^2 + \omega_{s-}^2)(s^2 + \omega_{s+}^2)}$ $h_{1,3}(t) = \left(\frac{\omega_{s-}^2 - \omega_s^2}{\omega_{s-}^2 (\omega_{s-}^2 - \omega_{s+}^2)} \sin(\omega_{s-} t) + \frac{\omega_{s+}^2 - \omega_s^2}{\omega_{s+}^2 (\omega_{s+}^2 - \omega_{s-}^2)} \sin(\omega_{s+} t) \right) \frac{1}{R}$
$\delta v_{e,0}$	$H_{1,4}(s) = -\frac{\frac{2}{R} \omega_{ie} \sin \phi s}{(s^2 + \omega_{s-}^2)(s^2 + \omega_{s+}^2)}$ $h_{1,4}(t) = \left(\frac{1}{(\omega_{s-}^2 - \omega_{s+}^2)} \cos(\omega_{s-} t) + \frac{1}{(\omega_{s+}^2 - \omega_{s-}^2)} \cos(\omega_{s+} t) \right) \frac{2}{R} \omega_{ie} \sin \phi$
$\delta v_{d,0}$	$H_{1,14}(s) = -\frac{\frac{4}{R} \omega_{ie}^2 \cos \phi \sin \phi}{(s^2 + \omega_{s-}^2)(s^2 + \omega_{s+}^2)}$ $h_{1,14}(t) = \left(\frac{1}{\omega_{s-}^2 (\omega_{s-}^2 - \omega_{s+}^2)} \sin(\omega_{s-} t) + \frac{1}{\omega_{s+}^2 (\omega_{s+}^2 - \omega_{s-}^2)} \sin(\omega_{s+} t) \right) \frac{4}{R} \omega_{ie}^2 \cos \phi \sin \phi$

Table D.2.: Longitude error step responses to position and velocity initialization errors.

Input	Step response
$\delta\phi_0$	$H_{2,1}(s) = \frac{\omega_s^2 \omega_{ie} \tan \phi s^2}{(s^2 + \omega_{s-}^2)(s^2 + \omega_{s+}^2)(s^2 + \omega_{ie}^2)} + \frac{\omega_s^2 \omega_{ie} \tan \phi (\omega_s^2 - 2\omega_{ie}^2)}{s(s^2 + \omega_{s-}^2)(s^2 + \omega_{s+}^2)(s^2 + \omega_{ie}^2)}$ $h_{2,1}(t) = \left(\frac{\omega_s^2 - 2\omega_{ie}^2 - \omega_1^2}{\omega_{s-}(\omega_{s-}^2 - \omega_{s+}^2)(\omega_{s-}^2 - \omega_{ie}^2)} \sin(\omega_{s-} t) \right. \\ \left. + \frac{\omega_s^2 - 2\omega_{ie}^2 - \omega_2^2}{\omega_{s+}(\omega_{s+}^2 - \omega_{s-}^2)(\omega_{s+}^2 - \omega_{ie}^2)} \sin(\omega_{s+} t) + \frac{\omega_s^2 - 2\omega_{ie}^2 - \omega_{ie}^2}{\omega_{ie}(\omega_{ie}^2 - \omega_{s-}^2)(\omega_{ie}^2 - \omega_{s+}^2)} \sin(\omega_{ie} t) \right) \omega_s^2 \omega_{ie} \tan \phi$
$\delta\lambda_0$	$H_{2,2}(s) = 0$ $h_{2,2}(t) = 0$
$\delta v_{n,0}$	$H_{2,3}(s) = \frac{\frac{2}{R} \omega_{ie} \tan \phi s}{(s^2 + \omega_{s-}^2)(s^2 + \omega_{s+}^2)}$ $h_{2,3}(t) = - \left(\frac{1}{(\omega_{s-}^2 - \omega_{s+}^2)} \cos(\omega_{s-} t) + \frac{1}{(\omega_{s+}^2 - \omega_{s-}^2)} \cos(\omega_{s+} t) \right) \frac{2}{R} \omega_{ie} \tan \phi$
$\delta v_{e,0}$	$H_{2,4}(s) = \frac{\frac{1}{R \cos \phi} s^2}{(s^2 + \omega_{s-}^2)(s^2 + \omega_{s+}^2)} + \frac{\frac{\omega_s^2}{R \cos \phi}}{(s^2 + \omega_{s-}^2)(s^2 + \omega_{s+}^2)}$ $h_{2,4}(t) = \left(\frac{\omega_{s-}^2 - \omega_s^2}{\omega_{s-}(\omega_{s-}^2 - \omega_{s+}^2)} \sin(\omega_{s-} t) + \frac{\omega_{s+}^2 - \omega_s^2}{\omega_{s+}(\omega_{s+}^2 - \omega_{s-}^2)} \sin(\omega_{s+} t) \right) \frac{1}{R \cos \phi}$
$\delta v_{d,0}$	$H_{2,14}(s) = \frac{\frac{2}{R} \omega_{ie} s}{(s^2 + \omega_{s-}^2)(s^2 + \omega_{s+}^2)} + \frac{\frac{2}{R} \omega_s^2 \omega_{ie}}{s(s^2 + \omega_{s-}^2)(s^2 + \omega_{s+}^2)}$ $h_{2,14}(t) = \left(\frac{\omega_s^2}{\omega_{s-}^2 \omega_{s+}^2} + \frac{\omega_s^2 - \omega_{s-}^2}{\omega_{s-}(\omega_{s-}^2 - \omega_{s+}^2)} \cos(\omega_{s-} t) + \frac{\omega_s^2 - \omega_{s+}^2}{\omega_{s+}(\omega_{s+}^2 - \omega_{s-}^2)} \cos(\omega_{s+} t) \right) \frac{2}{R} \omega_{ie}$

D.1.2. Position Errors from Initial Alignment Errors

Table D.3.: Latitude error step responses to initial alignment errors.

Input	Step response
$\delta\Phi_0$	$H_{1,5}(s) = -\frac{3\omega_s^2\omega_{ie}\sin\phi s^2}{(s^2 + \omega_{s-}^2)(s^2 + \omega_{s+}^2)(s^2 + \omega_{ie}^2)} - \frac{\omega_s^2\omega_{ie}\sin\phi(2\omega_{ie}^2\cos^2\phi + \omega_s^2)}{(s^2 + \omega_{s-}^2)(s^2 + \omega_{s+}^2)(s^2 + \omega_{ie}^2)}$ $h_{1,5}(t) = \left(\frac{3\omega_{s-}^2 - 2\omega_{ie}\cos^2\phi - \omega_s^2}{\omega_{s-}(\omega_{s-}^2 - \omega_{s+}^2)(\omega_{s-}^2 - \omega_{ie}^2)} \sin(\omega_{s-}t) \right.$ $+ \frac{3\omega_{s+}^2 - 2\omega_{ie}\cos^2\phi - \omega_s^2}{\omega_{s+}(\omega_{s+}^2 - \omega_{s-}^2)(\omega_{s+}^2 - \omega_{ie}^2)} \sin(\omega_{s+}t) +$ $\left. + \frac{3\omega_{ie}^2 - 2\omega_{ie}\cos^2\phi - \omega_s^2}{\omega_{ie}(\omega_{ie}^2 - \omega_{s-}^2)(\omega_{ie}^2 - \omega_{s+}^2)} \sin(\omega_{ie}t) \right) \omega_s^2\omega_{ie}\sin\phi$
$\delta\Theta_0$	$H_{1,6}(s) = -\frac{\omega_s^2 s^3}{(s^2 + \omega_{s-}^2)(s^2 + \omega_{s+}^2)(s^2 + \omega_{ie}^2)} - \frac{\omega_s^2(\omega_s^2 - 2\omega_{ie}^2\sin^2\phi)s}{(s^2 + \omega_{s-}^2)(s^2 + \omega_{s+}^2)(s^2 + \omega_{ie}^2)}$ $h_{1,6}(t) = \left(\frac{\omega_{s-}^2 + 2\omega_{ie}^2\sin^2\phi - \omega_s^2}{(\omega_{s-}^2 - \omega_{s+}^2)(\omega_{s-}^2 - \omega_{ie}^2)} \cos(\omega_{s-}t) \right.$ $+ \frac{\omega_{s+}^2 + 2\omega_{ie}^2\sin^2\phi - \omega_s^2}{(\omega_{s+}^2 - \omega_{s-}^2)(\omega_{s+}^2 - \omega_{ie}^2)} \cos(\omega_{s+}t) +$ $\left. + \frac{\omega_{ie}^2 + 2\omega_{ie}^2\sin^2\phi - \omega_s^2}{(\omega_{ie}^2 - \omega_{s-}^2)(\omega_{ie}^2 - \omega_{s+}^2)} \cos(\omega_{ie}t) \right) \omega_s^2$
$\delta\Psi_0$	$H_{1,7}(s) = -\frac{\omega_s^2\omega_{ie}\cos\phi s^2}{(s^2 + \omega_{s-}^2)(s^2 + \omega_{s+}^2)(s^2 + \omega_{ie}^2)} - \frac{\omega_s^2\omega_{ie}\cos\phi(\omega_s^2 - 2\omega_{ie}^2\sin^2\phi)}{(s^2 + \omega_{s-}^2)(s^2 + \omega_{s+}^2)(s^2 + \omega_{ie}^2)}$ $h_{1,7}(t) = \left(\frac{\omega_{s-}^2 + 2\omega_{ie}\sin^2\phi - \omega_s^2}{\omega_{s-}(\omega_{s-}^2 - \omega_{s+}^2)(\omega_{s-}^2 - \omega_{ie}^2)} \sin(\omega_{s-}t) \right.$ $+ \frac{\omega_{s+}^2 + 2\omega_{ie}\sin^2\phi - \omega_s^2}{\omega_{s+}(\omega_{s+}^2 - \omega_{s-}^2)(\omega_{s+}^2 - \omega_{ie}^2)} \sin(\omega_{s+}t) +$ $\left. + \frac{\omega_{ie}^2 + 2\omega_{ie}\sin^2\phi - \omega_s^2}{\omega_{ie}(\omega_{ie}^2 - \omega_{s-}^2)(\omega_{ie}^2 - \omega_{s+}^2)} \sin(\omega_{ie}t) \right) \omega_s^2\omega_{ie}\cos\phi$

Table D.4.: Longitude error step responses to initial alignment errors.

Input	Step response
$\delta\Phi_0$	$H_{2,5}(s) = -\frac{\omega_s^2 (s^2 + \omega_{2,5+}^2)(s^2 + \omega_{2,5-}^2)}{s \cos \phi (s^2 + \omega_{s-}^2)(s^2 + \omega_{s+}^2)(s^2 + \omega_{ie}^2)}$ $h_{2,5}(t) = \left(\frac{\omega_{s-}^4 - \omega_{s-}^2 (\omega_{2,5+}^2 + \omega_{2,5-}^2) + \omega_{2,5+}^2 \omega_{2,5-}^2}{\omega_{s-}^2 (\omega_{s-}^2 - \omega_{s+}^2)(\omega_{s-}^2 - \omega_{ie}^2)} \cos(\omega_{s-} t) \right.$ $+ \frac{\omega_{s+}^4 - \omega_{s+}^2 (\omega_{2,5+}^2 + \omega_{2,5-}^2) + \omega_{2,5+}^2 \omega_{2,5-}^2}{\omega_{s+}^2 (\omega_{s+}^2 - \omega_{s-}^2)(\omega_{s+}^2 - \omega_{ie}^2)} \cos(\omega_{s+} t) +$ $\left. + \frac{\omega_{ie}^4 - \omega_{ie}^2 (\omega_{2,5+}^2 + \omega_{2,5-}^2) + \omega_{2,5+}^2 \omega_{2,5-}^2}{\omega_{ie}^2 (\omega_{ie}^2 - \omega_{s-}^2)(\omega_{ie}^2 - \omega_{s+}^2)} \cos(\omega_{ie} t) \right) \frac{\omega_s^2}{\cos \phi}$ $\omega_{2,5\pm}^2 = \frac{\omega_s^2 + 3\omega_{ie}^2 \cos^2 \phi}{2} - \omega_{ie}^2 \pm \frac{1}{2} \sqrt{(\omega_{ie}^2 \cos^2 \phi - 2\omega_{ie}^2 + \omega_s^2)^2 - 4\omega_s^2 \omega_{ie}^2 \cos^2 \phi}$
$\delta\Theta_0$	$H_{2,6}(s) = -\frac{3\omega_s^2 \omega_{ie} \tan \phi s}{(s^2 + \omega_{s-}^2)(s^2 + \omega_{s+}^2)(s^2 + \omega_{ie}^2)} - \frac{\omega_s^4 \omega_{ie} \tan \phi}{(s^2 + \omega_{s-}^2)(s^2 + \omega_{s+}^2)(s^2 + \omega_{ie}^2)}$ $h_{2,6}(t) = \left(\frac{3\omega_{s-}^2 - \omega_s^2}{\omega_{s-} (\omega_{s-}^2 - \omega_{s+}^2)(\omega_{s-}^2 - \omega_{ie}^2)} \sin(\omega_{s-} t) \right.$ $+ \frac{3\omega_{s+}^2 - \omega_s^2}{\omega_{s+} (\omega_{s+}^2 - \omega_{s-}^2)(\omega_{s+}^2 - \omega_{ie}^2)} \sin(\omega_{s+} t) +$ $\left. + \frac{3\omega_{ie}^2 - \omega_s^2}{\omega_{ie} (\omega_{ie}^2 - \omega_{s-}^2)(\omega_{ie}^2 - \omega_{s+}^2)} \sin(\omega_{ie} t) \right) \omega_s^2 \omega_{ie} \tan \phi$
$\delta\Psi_0$	$H_{2,7}(s) = -\frac{3\omega_s^2 \omega_{ie}^2 \sin \phi s}{(s^2 + \omega_{s-}^2)(s^2 + \omega_{s+}^2)(s^2 + \omega_{ie}^2)} - \frac{\omega_s^4 \omega_{ie}^2 \sin \phi}{s (s^2 + \omega_{s-}^2)(s^2 + \omega_{s+}^2)(s^2 + \omega_{ie}^2)}$ $h_{2,7}(t) = \left(-\frac{\omega_s^2}{\omega_{s-}^2 \omega_{s+}^2 \omega_{ie}^2} + \frac{\omega_s^2 - 3\omega_{s-}^2}{\omega_{s-}^2 (\omega_{s-}^2 - \omega_{s+}^2)(\omega_{s-}^2 - \omega_{ie}^2)} \cos(\omega_{s-} t) \right.$ $+ \frac{\omega_s^2 - 3\omega_{s+}^2}{\omega_{s+}^2 (\omega_{s+}^2 - \omega_{s-}^2)(\omega_{s+}^2 - \omega_{ie}^2)} \cos(\omega_{s+} t) +$ $\left. + \frac{\omega_s^2 - 3\omega_{ie}^2}{\omega_{ie}^2 (\omega_{ie}^2 - \omega_{s-}^2)(\omega_{ie}^2 - \omega_{s+}^2)} \cos(\omega_{ie} t) \right) \omega_s^2 \omega_{ie}^2 \sin \phi$

D.1.3. Position Errors from Sensor Biases

Table D.5.: Latitude error step responses to IMU biases.

Input	Step response
$\delta f_{b,n}$	$H_{1,8}(s) = \frac{\frac{1}{R}s}{(s^2 + \omega_{s-}^2)(s^2 + \omega_{s+}^2)} + \frac{\frac{\omega_s^2}{R}}{s(s^2 + \omega_{s-}^2)(s^2 + \omega_{s+}^2)}$ $h_{1,8}(t) = \left(\frac{\omega_s^2}{\omega_{s-}^2 \omega_{s+}^2} + \frac{\omega_s^2 - \omega_{s-}^2}{\omega_{s-}^2 (\omega_{s-}^2 - \omega_{s+}^2)} \cos(\omega_{s-} t) + \frac{\omega_s^2 - \omega_{s+}^2}{\omega_{s+}^2 (\omega_{s+}^2 - \omega_{s-}^2)} \cos(\omega_{s+} t) \right) \frac{1}{R}$
$\delta f_{b,e}$	$H_{1,9}(s) = \frac{\frac{2}{R} \omega_{ie} \sin \tilde{\phi}}{(s^2 + \omega_{s-}^2)(s^2 + \omega_{s+}^2)}$ $h_{1,9}(t) = \left(\frac{1}{\omega_{s-} (\omega_{s-}^2 - \omega_{s+}^2)} \sin(\omega_{s-} t) + \frac{1}{\omega_{s+} (\omega_{s+}^2 - \omega_{s-}^2)} \sin(\omega_{s+} t) \right) \frac{2}{R} \omega_{ie} \sin \tilde{\phi}$
$\delta f_{b,d}$	$H_{1,10}(s) = 0$ $h_{1,10}(t) = 0$
$\delta \omega_{ib,n}$	$H_{1,11}(s) = -\frac{3\omega_s^2 \omega_{ie} \sin \tilde{\phi} s}{(s^2 + \omega_{ie}^2)(s^2 + \omega_{s-}^2)(s^2 + \omega_{s+}^2)} - \frac{\omega_s^2 \omega_{ie} \sin \phi (2\omega_{ie}^2 \cos^2 \phi + \omega_s^2)}{s(s^2 + \omega_{ie}^2)(s^2 + \omega_{s-}^2)(s^2 + \omega_{s+}^2)}$ $h_{1,11}(t) = \left(\frac{2\omega_{ie} \cos^2 \phi + \omega_s^2}{\omega_{s-}^2 \omega_{s+}^2 \omega_s^2} - \frac{2\omega_{ie}^2 \cos \tilde{\phi} + \omega_s^2 - 3\omega_{s-}^2}{\omega_{s-}^2 (\omega_{s-}^2 - \omega_{s+}^2) (\omega_{s-}^2 - \omega_{ie}^2)} \cos(\omega_{s-} t) \right. \\ \left. - \frac{2\omega_{ie}^2 \cos \tilde{\phi} + \omega_s^2 - 3\omega_{s+}^2}{\omega_{s+}^2 (\omega_{s+}^2 - \omega_{s-}^2) (\omega_{s+}^2 - \omega_{ie}^2)} \cos(\omega_{s+} t) \right. \\ \left. - \frac{2\omega_{ie}^2 \cos \tilde{\phi} + \omega_s^2 - 3\omega_{ie}^2}{\omega_{ie}^2 (\omega_{ie}^2 - \omega_{s-}^2) (\omega_{ie}^2 - \omega_{s+}^2)} \cos(\omega_{ie} t) \right) \omega_s^2 \omega_{ie} \sin \tilde{\phi}$
$\delta \omega_{ib,e}$	$H_{1,12}(s) = -\frac{\omega_s^2 \omega_{ie} \cos \tilde{\phi} s}{(s^2 + \omega_{ie}^2)(s^2 + \omega_{s-}^2)(s^2 + \omega_{s+}^2)} - \frac{\omega_s^2 (\omega_s^2 - 2\omega_{ie}^2 \sin^2 \tilde{\phi})}{(s^2 + \omega_{ie}^2)(s^2 + \omega_{s-}^2)(s^2 + \omega_{s+}^2)}$ $h_{1,12}(t) = \left(\frac{\omega_{s-}^2 + 2\omega_{ie}^2 \cos \tilde{\phi} - \omega_s^2}{\omega_{s-} (\omega_{s-}^2 - \omega_{s+}^2) (\omega_{s-}^2 - \omega_{ie}^2)} \sin(\omega_{s-} t) + \frac{\omega_{s+}^2 + 2\omega_{ie}^2 \cos \tilde{\phi} - \omega_s^2}{\omega_{s+} (\omega_{s+}^2 - \omega_{s-}^2) (\omega_{s+}^2 - \omega_{ie}^2)} \sin(\omega_{s+} t) \right. \\ \left. + \frac{\omega_{ie}^2 + 2\omega_{ie}^2 \cos \tilde{\phi} - \omega_s^2}{\omega_{ie} (\omega_{ie}^2 - \omega_{s-}^2) (\omega_{ie}^2 - \omega_{s+}^2)} \sin(\omega_{ie} t) \right) \omega_s^2$
$\delta \omega_{ib,d}$	$H_{1,13}(s) = -\frac{\omega_s^2 \omega_{ie} \cos \tilde{\phi} s}{(s^2 + \omega_{ie}^2)(s^2 + \omega_{s-}^2)(s^2 + \omega_{s+}^2)} - \frac{\omega_s^2 \omega_{ie} \cos \tilde{\phi} (\omega_s^2 - 2\omega_{ie}^2 \sin^2 \tilde{\phi})}{s(s^2 + \omega_{ie}^2)(s^2 + \omega_{s-}^2)(s^2 + \omega_{s+}^2)}$ $h_{1,13}(t) = -\left(\frac{2\omega_{ie}^2 \sin^2 \phi + \omega_s^2}{\omega_{s-}^2 \omega_{s+}^2 \omega_s^2} + \frac{2\omega_{ie}^2 \cos \tilde{\phi} + \omega_s^2 - \omega_{s-}^2}{\omega_{s-}^2 (\omega_{s-}^2 - \omega_{s+}^2) (\omega_{s-}^2 - \omega_{ie}^2)} \cos(\omega_{s-} t) \right. \\ \left. + \frac{2\omega_{ie}^2 \cos \tilde{\phi} + \omega_s^2 - \omega_{s+}^2}{\omega_{s+}^2 (\omega_{s+}^2 - \omega_{s-}^2) (\omega_{s+}^2 - \omega_{ie}^2)} \cos(\omega_{s+} t) \right. \\ \left. + \frac{2\omega_{ie}^2 \cos \tilde{\phi} + \omega_s^2 - \omega_{ie}^2}{\omega_{ie}^2 (\omega_{ie}^2 - \omega_{s-}^2) (\omega_{ie}^2 - \omega_{s+}^2)} \cos(\omega_{ie} t) \right) \omega_s^2 \omega_{ie} \cos \tilde{\phi}$

Table D.6.: Longitude error step responses to IMU biases.

Input	Step response
$\delta f_{b,n}$	$H_{2,8}(s) = -\frac{\frac{2}{R}\omega_{ie} \tan \tilde{\phi}}{(s^2 + \omega_{s-}^2)(s^2 + \omega_{s+}^2)}$ $h_{2,8}(t) = \left(\frac{1}{\omega_{s-}(\omega_{s-}^2 - \omega_{s+}^2)} \sin(\omega_{s-}t) + \frac{1}{\omega_{s+}(\omega_{s+}^2 - \omega_{s-}^2)} \sin(\omega_{s+}t) \right) \frac{2}{R}\omega_{ie} \tan \tilde{\phi}$
$\delta f_{b,e}$	$H_{2,9}(s) = \frac{\frac{1}{R \cos \tilde{\phi}} s}{(s^2 + \omega_{s-}^2)(s^2 + \omega_{s+}^2)} + \frac{\frac{\omega_s^2}{R \cos \tilde{\phi}}}{s(s^2 + \omega_{s-}^2)(s^2 + \omega_{s+}^2)}$ $h_{2,9}(t) = \left(\frac{\omega_s^2}{\omega_{s-}^2 \omega_{s+}^2} + \frac{\omega_s^2 - \omega_{s-}^2}{\omega_{s-}(\omega_{s-}^2 - \omega_{s+}^2)} \cos(\omega_{s-}t) + \frac{\omega_s^2 - \omega_{s+}^2}{\omega_{s+}(\omega_{s+}^2 - \omega_{s-}^2)} \cos(\omega_{s+}t) \right) \frac{1}{R \cos \tilde{\phi}}$
$\delta f_{b,d}$	$H_{2,10}(s) = 0$ $h_{2,10}(t) = 0$
$\delta \omega_{ib,n}$	$H_{2,11}(s) = \frac{\omega_s^2(s^2 + \omega_{2,11+}^2)(s^2 + \omega_{2,11-}^2)}{s^2(s^2 + \omega_{ie}^2)(s^2 + \omega_{s-}^2)(s^2 + \omega_{s+}^2)} \frac{1}{\cos \tilde{\phi}}$ $h_{2,11}(t) = \left(\frac{\omega_{2,11+}^2 \omega_{2,11-}^2}{\omega_{s-}^2 \omega_{s+}^2 \omega_{ie}^2} t - \frac{\omega_{s-}^4 - \omega_{s-}^2(\omega_{2,11+}^2 + \omega_{2,11-}^2) + \omega_{2,11+}^2 \omega_{2,11-}^2}{\omega_{s-}^3(\omega_{s-}^2 - \omega_{s+}^2)(\omega_{s-}^2 - \omega_{ie}^2)} \sin(\omega_{s-}t) \right. \\ \left. - \frac{\omega_{s+}^4 - \omega_{s+}^2(\omega_{2,11+}^2 + \omega_{2,11-}^2) + \omega_{2,11+}^2 \omega_{2,11-}^2}{\omega_{s+}^3(\omega_{s+}^2 - \omega_{s-}^2)(\omega_{s+}^2 - \omega_{ie}^2)} \sin(\omega_{s+}t) \right. \\ \left. - \frac{\omega_{ie}^4 - \omega_{ie}^2(\omega_{2,11+}^2 + \omega_{2,11-}^2) + \omega_{2,11+}^2 \omega_{2,11-}^2}{\omega_{ie}^3(\omega_{ie}^2 - \omega_{s-}^2)(\omega_{ie}^2 - \omega_{s-}^2)} \sin(\omega_{ie}t) \right) \frac{\omega_s^2}{\cos \tilde{\phi}}$ $\omega_{2,11\pm}^2 = \frac{\omega_s^2 + 3\omega_{ie}^2 \cos^2 \tilde{\phi}}{2} - \omega_{ie}^2 \pm \frac{1}{2} \sqrt{(\omega_{ie}^2 \cos^2 \tilde{\phi} - 3\omega_{ie}^2 + \omega_s^2)^2 - 4\omega_s^2 \omega_{ie}^2 \cos^2 \tilde{\phi}}$
$\delta \omega_{ib,e}$	$H_{2,12}(s) = -\frac{3\omega_s \omega_{ie} \tan \tilde{\phi} s}{(s^2 + \omega_{ie}^2)(s^2 + \omega_{s-}^2)(s^2 + \omega_{s+}^2)} - \frac{\omega_s^4 \omega_{ie} \tan \tilde{\phi}}{s(s^2 + \omega_{ie}^2)(s^2 + \omega_{s-}^2)(s^2 + \omega_{s+}^2)}$ $h_{2,12}(t) = \left(-\frac{\omega_s^2}{\omega_{s-}^2 \omega_{s+}^2 \omega_{ie}^2} + \frac{\omega_s^2 - 3\omega_{s-}^2}{\omega_{s-}^2(\omega_{s-}^2 - \omega_{s+}^2)(\omega_{s-}^2 - \omega_{ie}^2)} \cos(\omega_{s-}t) \right. \\ \left. + \frac{\omega_s^2 - 3\omega_{s+}^2}{\omega_{s+}^2(\omega_{s+}^2 - \omega_{s-}^2)(\omega_{s+}^2 - \omega_{ie}^2)} \cos(\omega_{s+}t) + \frac{\omega_s^2 - 3\omega_{ie}^2}{\omega_{ie}^2(\omega_{ie}^2 - \omega_{s-}^2)(\omega_{ie}^2 - \omega_{s+}^2)} \cos(\omega_{ie}t) \right) \omega_s^2 \omega_{ie} \tan \tilde{\phi}$
$\delta \omega_{ib,d}$	$H_{2,13}(s) = -\frac{3\omega_s \omega_{ie}^2 \sin \tilde{\phi}}{(s^2 + \omega_{ie}^2)(s^2 + \omega_{s-}^2)(s^2 + \omega_{s+}^2)} - \frac{\omega_s^4 \omega_{ie}^2 \sin \tilde{\phi}}{s^2(s^2 + \omega_{ie}^2)(s^2 + \omega_{s-}^2)(s^2 + \omega_{s+}^2)}$ $h_{2,13}(t) = \left(-\frac{\omega_s^2}{\omega_{s-}^2 \omega_{s+}^2 \omega_{ie}^2} t + \frac{\omega_s^2 - 3\omega_{s-}^2}{\omega_{s-}^3(\omega_{s-}^2 - \omega_{s+}^2)(\omega_{s-}^2 - \omega_{ie}^2)} \sin(\omega_{s-}t) \right. \\ \left. + \frac{\omega_s^2 - 3\omega_{s+}^2}{\omega_{s+}^3(\omega_{s+}^2 - \omega_{s-}^2)(\omega_{s+}^2 - \omega_{ie}^2)} \sin(\omega_{s+}t) + \frac{\omega_s^2 - 3\omega_{ie}^2}{\omega_{ie}^3(\omega_{ie}^2 - \omega_{s-}^2)(\omega_{ie}^2 - \omega_{s+}^2)} \sin(\omega_{ie}t) \right) \omega_s^2 \omega_{ie}^2 \sin \tilde{\phi}$

D.1.4. Velocity Errors from Initialization Errors

Table D.7.: North velocity error step responses to position and velocity initialization errors.

Input	Step response
$\delta\phi_0$	$H_{3,1}(s) = -\frac{\omega_s^2 \omega_{ie}^2 (2 \sin^2 \phi + 1) s^2 R}{(s^2 + \omega_{s-}^2)(s^2 + \omega_{s+}^2)(s^2 + \omega_{ie}^2)} - \frac{\omega_s^4 \omega_{ie}^2 R}{(s^2 + \omega_{s-}^2)(s^2 + \omega_{s+}^2)(s^2 + \omega_{ie}^2)}$ $h_{3,1}(t) = -\left(\frac{\omega_s^2 - \omega_{s-}^2 (2 \sin^2 \phi + 1)}{\omega_{s-} (\omega_{s-}^2 - \omega_{s+}^2) (\omega_{s-}^2 - \omega_{ie}^2)} \sin(\omega_{s-} t) \right.$ $+ \frac{\omega_s^2 - \omega_{s+}^2 (2 \sin^2 \phi + 1)}{\omega_{s+} (\omega_{s+}^2 - \omega_{s-}^2) (\omega_{s+}^2 - \omega_{ie}^2)} \sin(\omega_{s+} t)$ $\left. + \frac{\omega_s^2 - \omega_{ie}^2 (2 \sin^2 \phi + 1)}{\omega_{ie} (\omega_{ie}^2 - \omega_{s-}^2) (\omega_{ie}^2 - \omega_{s+}^2)} \sin(\omega_{ie} t) \right) \omega_s^2 \omega_{ie}^2 R$
$\delta\lambda_0$	$H_{3,2}(s) = 0$ $h_{3,2}(t) = 0$
$\delta v_{n,0}$	$H_{3,3}(s) = \frac{s^3}{(s^2 + \omega_{s-}^2)(s^2 + \omega_{s+}^2)} + \frac{\omega_s^2 s}{(s^2 + \omega_{s-}^2)(s^2 + \omega_{s+}^2)}$ $h_{3,3}(t) = \left(\frac{\omega_{s-}^2 - \omega_s^2}{(\omega_{s-}^2 - \omega_{s+}^2)} \cos(\omega_{s-} t) + \frac{\omega_{s+}^2 - \omega_s^2}{(\omega_{s+}^2 - \omega_{s-}^2)} \cos(\omega_{s+} t) \right)$
$\delta v_{e,0}$	$H_{3,4}(s) = -\frac{2\omega_{ie} \sin \phi s^2}{(s^2 + \omega_{s-}^2)(s^2 + \omega_{s+}^2)}$ $h_{3,4}(t) = -\left(\frac{\omega_{s-}}{(\omega_{s-}^2 - \omega_{s+}^2)} \sin(\omega_{s-} t) + \frac{\omega_{s+}}{(\omega_{s+}^2 - \omega_{s-}^2)} \sin(\omega_{s+} t) \right) 2\omega_{ie} \sin \phi$
$\delta v_{d,0}$	$H_{3,14}(s) = -\frac{4\omega_{ie}^2 \cos \phi \sin \phi s}{(s^2 + \omega_{s-}^2)(s^2 + \omega_{s+}^2)}$ $h_{3,14}(t) = \left(\frac{1}{(\omega_{s-}^2 - \omega_{s+}^2)} \cos(\omega_{s-} t) + \frac{1}{(\omega_{s+}^2 - \omega_{s-}^2)} \cos(\omega_{s+} t) \right) 4\omega_{ie}^2 \cos \phi \sin \phi$

Table D.8.: East velocity error step responses to position and velocity initialization errors.

Input	Step response
$\delta\phi_0$	$H_{4,1}(s) = \frac{\omega_s^2 \omega_{ie} \sin \phi R s^3}{(s^2 + \omega_{s-}^2)(s^2 + \omega_{s+}^2)(s^2 + \omega_{ie}^2)} + \frac{\omega_s^2 \omega_{ie} \sin \phi (\omega_s^2 - 2\omega_{ie}^2) R}{(s^2 + \omega_{s-}^2)(s^2 + \omega_{s+}^2)(s^2 + \omega_{ie}^2)}$ $h_{4,1}(t) = \left(\frac{\omega_s^2 - 2\omega_{ie}^2 - \omega_{s-}^2}{(\omega_{s-}^2 - \omega_{s+}^2)(\omega_{s-}^2 - \omega_{ie}^2)} \cos(\omega_{s-} t) \right.$ $+ \frac{\omega_s^2 - 2\omega_{ie}^2 - \omega_{s+}^2}{(\omega_{s+}^2 - \omega_{s-}^2)(\omega_{s+}^2 - \omega_{ie}^2)} \cos(\omega_{s+} t) +$ $\left. + \frac{\omega_s^2 - 2\omega_{ie}^2 - \omega_{ie}^2}{(\omega_{ie}^2 - \omega_{s-}^2)(\omega_{ie}^2 - \omega_{s+}^2)} \cos(\omega_{ie} t) \right) \omega_s^2 \omega_{ie} R \sin \phi$
$\delta\lambda_0$	$H_{4,2}(s) = 0$ $h_{4,2}(t) = 0$
$\delta v_{n,0}$	$H_{4,3}(s) = \frac{2\omega_{ie} \sin \phi s^2}{(s^2 + \omega_{s-}^2)(s^2 + \omega_{s+}^2)}$ $h_{4,3}(t) = \left(\frac{\omega_{s-}}{(\omega_{s-}^2 - \omega_{s+}^2)} \sin(\omega_{s-} t) + \frac{\omega_{s+}}{(\omega_{s+}^2 - \omega_{s-}^2)} \sin(\omega_{s+} t) \right) 2\omega_{ie} \sin \phi$
$\delta v_{e,0}$	$H_{4,4}(s) = \frac{s^3}{(s^2 + \omega_{s-}^2)(s^2 + \omega_{s+}^2)} + \frac{\frac{\omega_s^2}{\cos \phi} s}{(s^2 + \omega_{s-}^2)(s^2 + \omega_{s+}^2)}$ $h_{4,4}(t) = \left(\frac{\omega_{s-}^2 - \omega_s^2}{(\omega_{s-}^2 - \omega_{s+}^2)} \cos(\omega_{s-} t) + \frac{\omega_{s+}^2 - \omega_s^2}{(\omega_{s+}^2 - \omega_{s-}^2)} \cos(\omega_{s+} t) \right)$
$\delta v_{d,0}$	$H_{4,14}(s) = \frac{2\omega_{ie} \cos \phi s^2}{(s^2 + \omega_{s-}^2)(s^2 + \omega_{s+}^2)} + \frac{2\omega_s^2 \omega_{ie} \cos \phi}{(s^2 + \omega_{s-}^2)(s^2 + \omega_{s+}^2)}$ $h_{4,14}(t) = \left(\frac{\omega_s^2 - \omega_{s-}^2}{\omega_{s-}(\omega_{s-}^2 - \omega_{s+}^2)} \sin(\omega_{s-} t) + \frac{\omega_s^2 - \omega_{s+}^2}{\omega_{s+}(\omega_{s+}^2 - \omega_{s-}^2)} \sin(\omega_{s+} t) \right) 2\omega_{ie} \cos \phi$

D.1.5. Velocity Errors from Initial Alignment Errors

Table D.9.: North velocity error step responses to initial alignment errors.

Input	Step response
$\delta\Phi_0$	$H_{3,5}(s) = -\frac{3\omega_s^2\omega_{ie}^2 \sin\phi R s^3}{(s^2 + \omega_{s-}^2)(s^2 + \omega_{s+}^2)(s^2 + \omega_{ie}^2)} - \frac{\omega_s^2\omega_{ie}^2 \sin\phi(2\omega_{ie}^2 \cos^2\phi + \omega_s^2)Rs}{(s^2 + \omega_{s-}^2)(s^2 + \omega_{s+}^2)(s^2 + \omega_{ie}^2)}$ $h_{3,5}(t) = -\left(\frac{3\omega_{s-}^2 - 2\omega_{ie}^2 \cos^2\phi - \omega_s^2}{(\omega_{s-}^2 - \omega_{s+}^2)(\omega_{s-}^2 - \omega_{ie}^2)} \cos(\omega_{s-}t) + \frac{3\omega_{s+}^2 - 2\omega_{ie}^2 \cos^2\phi - \omega_s^2}{(\omega_{s+}^2 - \omega_{s-}^2)(\omega_{s+}^2 - \omega_{ie}^2)} \cos(\omega_{s+}t) + \frac{3\omega_{ie}^2 - 2\omega_{ie}^2 \cos^2\phi - \omega_s^2}{(\omega_{ie}^2 - \omega_{s-}^2)(\omega_{ie}^2 - \omega_{s+}^2)} \cos(\omega_{ie}t)\right) \omega_s^2\omega_{ie}R \sin\phi$
$\delta\Theta_0$	$H_{3,6}(s) = -\frac{\omega_s^2 R s^4}{(s^2 + \omega_{s-}^2)(s^2 + \omega_{s+}^2)(s^2 + \omega_{ie}^2)} - \frac{\omega_s^2(\omega_s^2 - 2\omega_{ie}^2 \sin^2\phi)R s^2}{(s^2 + \omega_{s-}^2)(s^2 + \omega_{s+}^2)(s^2 + \omega_{ie}^2)}$ $h_{3,6}(t) = -\left(\frac{\omega_{s-}(\omega_{s-}^2 + 2\omega_{ie}^2 \sin^2\phi - \omega_s^2)}{(\omega_{s-}^2 - \omega_{s+}^2)(\omega_{s-}^2 - \omega_{ie}^2)} \sin(\omega_{s-}t) + \frac{\omega_{s+}(\omega_{s+}^2 + 2\omega_{ie}^2 \sin^2\phi - \omega_s^2)}{(\omega_{s+}^2 - \omega_{s-}^2)(\omega_{s+}^2 - \omega_{ie}^2)} \sin(\omega_{s+}t) + \frac{\omega_{ie}(\omega_{ie}^2 + 2\omega_{ie}^2 \sin^2\phi - \omega_s^2)}{(\omega_{ie}^2 - \omega_{s-}^2)(\omega_{ie}^2 - \omega_{s+}^2)} \sin(\omega_{ie}t)\right) \omega_s^2 R$
$\delta\Psi_0$	$H_{3,7}(s) = -\frac{\omega_s^2\omega_{ie}^2 \cos\phi R s^3}{(s^2 + \omega_{s-}^2)(s^2 + \omega_{s+}^2)(s^2 + \omega_{ie}^2)} - \frac{\omega_s^2\omega_{ie}^2 \cos\phi(\omega_s^2 - 2\omega_{ie}^2 \sin^2\phi)Rs}{(s^2 + \omega_{s-}^2)(s^2 + \omega_{s+}^2)(s^2 + \omega_{ie}^2)}$ $h_{3,7}(t) = \left(\frac{\omega_{s-}^2 + 2\omega_{ie}^2 \sin^2\phi - \omega_s^2}{(\omega_{s-}^2 - \omega_{s+}^2)(\omega_{s-}^2 - \omega_{ie}^2)} \cos(\omega_{s-}t) + \frac{\omega_{s+}^2 + 2\omega_{ie}^2 \sin^2\phi - \omega_s^2}{(\omega_{s+}^2 - \omega_{s-}^2)(\omega_{s+}^2 - \omega_{ie}^2)} \cos(\omega_{s+}t) + \frac{\omega_{ie}^2 + 2\omega_{ie}^2 \sin^2\phi - \omega_s^2}{(\omega_{ie}^2 - \omega_{s-}^2)(\omega_{ie}^2 - \omega_{s+}^2)} \cos(\omega_{ie}t)\right) \omega_s^2\omega_{ie}R \cos\phi$

Table D.10.: East velocity error step responses to initial alignment errors.

Input	Step response
$\delta\Phi_0$	$H_{4,5}(s) = -\frac{\omega_s^2 (s^2 + \omega_{2,5+}^2)(s^2 + \omega_{2,5-}^2)R}{(s^2 + \omega_{s-}^2)(s^2 + \omega_{s+}^2)(s^2 + \omega_{ie}^2)}$ $h_{4,5}(t) = \left(\frac{\omega_{s-}^4 - \omega_{s-}^2(\omega_{2,5+}^2 + \omega_{2,5-}^2) + \omega_{2,5+}^2\omega_{2,5-}^2}{\omega_{s-}(\omega_{s-}^2 - \omega_{s+}^2)(\omega_{s-}^2 - \omega_{ie}^2)} \sin(\omega_{s-}t) \right. \\ \left. + \frac{\omega_{s+}^4 - \omega_{s+}^2(\omega_{2,5+}^2 + \omega_{2,5-}^2) + \omega_{2,5+}^2\omega_{2,5-}^2}{\omega_{s+}(\omega_{s+}^2 - \omega_{s-}^2)(\omega_{s+}^2 - \omega_{ie}^2)} \sin(\omega_{s+}t) + \right. \\ \left. + \frac{\omega_{ie}^4 - \omega_{ie}^2(\omega_{2,5+}^2 + \omega_{2,5-}^2) + \omega_{2,5+}^2\omega_{2,5-}^2}{\omega_{ie}(\omega_{ie}^2 - \omega_{s-}^2)(\omega_{ie}^2 - \omega_{s+}^2)} \sin(\omega_{ie}t) \right) \omega_s^2 R$ $\omega_{2,5\pm}^2 = \frac{\omega_s^2 + 3\omega_{ie}^2 \cos^2 \check{\phi}}{2} - \omega_{ie}^2 \pm \frac{1}{2} \sqrt{(\omega_{ie}^2 \cos^2 \check{\phi} - 2\omega_{ie}^2 + \omega_s^2)^2 - 4\omega_s^2\omega_{ie}^2 \cos^2 \check{\phi}}$
$\delta\Theta_0$	$H_{4,6}(s) = -\frac{3\omega_s^2\omega_{ie} \sin \phi R s^2}{(s^2 + \omega_{s-}^2)(s^2 + \omega_{s+}^2)(s^2 + \omega_{ie}^2)} - \frac{\omega_s^4\omega_{ie} R \sin \phi s}{(s^2 + \omega_{s-}^2)(s^2 + \omega_{s+}^2)(s^2 + \omega_{ie}^2)}$ $h_{4,6}(t) = \left(\frac{3\omega_{s-}^2 - \omega_s^2}{(\omega_{s-}^2 - \omega_{s+}^2)(\omega_{s-}^2 - \omega_{ie}^2)} \cos(\omega_{s-}t) \right. \\ \left. + \frac{3\omega_{s+}^2 - \omega_s^2}{(\omega_{s+}^2 - \omega_{s-}^2)(\omega_{s+}^2 - \omega_{ie}^2)} \cos(\omega_{s+}t) + \right. \\ \left. + \frac{3\omega_{ie}^2 - \omega_s^2}{(\omega_{ie}^2 - \omega_{s-}^2)(\omega_{ie}^2 - \omega_{s+}^2)} \cos(\omega_{ie}t) \right) \omega_s^2\omega_{ie} R \sin \phi$
$\delta\Psi_0$	$H_{4,7}(s) = -\frac{3\omega_s^2\omega_{ie}^2 \sin \phi \cos \phi R s^2}{(s^2 + \omega_{s-}^2)(s^2 + \omega_{s+}^2)(s^2 + \omega_{ie}^2)} - \frac{\omega_s^4\omega_{ie}^2 \sin \phi \cos \phi R}{(s^2 + \omega_{s-}^2)(s^2 + \omega_{s+}^2)(s^2 + \omega_{ie}^2)}$ $h_{4,7}(t) = \left(\frac{3\omega_{s-}^2 - \omega_s^2}{\omega_{s-}(\omega_{s-}^2 - \omega_{s+}^2)(\omega_{s-}^2 - \omega_{ie}^2)} \sin(\omega_{s-}t) \right. \\ \left. + \frac{3\omega_{s+}^2 - \omega_s^2}{\omega_{s+}(\omega_{s+}^2 - \omega_{s-}^2)(\omega_{s+}^2 - \omega_{ie}^2)} \sin(\omega_{s+}t) + \right. \\ \left. + \frac{3\omega_{ie}^2 - \omega_s^2}{\omega_{ie}(\omega_{ie}^2 - \omega_{s-}^2)(\omega_{ie}^2 - \omega_{s+}^2)} \sin(\omega_{ie}t) \right) \omega_s^2\omega_{ie}^2 R \sin \phi \cos \phi$

D.1.6. Velocity Errors from Sensor Biases

Table D.11.: North velocity error step responses to IMU biases.

Input	Step response
$\delta f_{b,n}$	$H_{3,8}(s) = \frac{s^2}{(s^2 + \omega_{s-}^2)(s^2 + \omega_{s+}^2)} + \frac{\omega_s^2}{(s^2 + \omega_{s-}^2)(s^2 + \omega_{s+}^2)}$ $h_{3,8}(t) = \left(\frac{\omega_{s-}^2 - \omega_s^2}{\omega_{s-}(\omega_{s-}^2 - \omega_{s+}^2)} \sin(\omega_{s-}t) + \frac{\omega_{s+}^2 - \omega_s^2}{\omega_{s+}(\omega_{s+}^2 - \omega_{s-}^2)} \sin(\omega_{s+}t) \right)$
$\delta f_{b,e}$	$H_{3,9}(s) = \frac{2\omega_{ie} \sin \tilde{\phi} s}{(s^2 + \omega_{s-}^2)(s^2 + \omega_{s+}^2)}$ $h_{3,9}(t) = \left(\frac{1}{(\omega_{s-}^2 - \omega_{s+}^2)} \cos(\omega_{s-}t) + \frac{1}{(\omega_{s+}^2 - \omega_{s-}^2)} \cos(\omega_{s+}t) \right) 2\omega_{ie} \sin \tilde{\phi}$
$\delta f_{b,d}$	$H_{3,10}(s) = 0$ $h_{3,10}(t) = 0$
$\delta \omega_{ib,n}$	$H_{3,11}(s) = -\frac{3\omega_s^2 \omega_{ie} \sin \tilde{\phi} R s^2}{(s^2 + \omega_{ie}^2)(s^2 + \omega_{s-}^2)(s^2 + \omega_{s+}^2)} - \frac{\omega_s^2 \omega_{ie} \sin \phi (2\omega_{ie}^2 \cos^2 \phi + \omega_s^2) R}{(s^2 + \omega_{ie}^2)(s^2 + \omega_{s-}^2)(s^2 + \omega_{s+}^2)}$ $h_{3,11}(t) = -\left(\frac{2\omega_{ie}^2 \cos \tilde{\phi} + \omega_s^2 - 3\omega_{s-}^2}{\omega_{s-}(\omega_{s-}^2 - \omega_{s+}^2)(\omega_{s-}^2 - \omega_{ie}^2)} \sin(\omega_{s-}t) \right.$ $+ \frac{2\omega_{ie}^2 \cos \tilde{\phi} + \omega_s^2 - 3\omega_{s+}^2}{\omega_{s+}(\omega_{s+}^2 - \omega_{s-}^2)(\omega_{s+}^2 - \omega_{ie}^2)} \sin(\omega_{s+}t)$ $\left. + \frac{2\omega_{ie}^2 \cos \tilde{\phi} + \omega_s^2 - 3\omega_{ie}^2}{\omega_{ie}(\omega_{ie}^2 - \omega_{s-}^2)(\omega_{ie}^2 - \omega_{s+}^2)} \sin(\omega_{ie}t) \right) \omega_s^2 \omega_{ie} R \sin \tilde{\phi}$
$\delta \omega_{ib,e}$	$H_{3,12}(s) = -\frac{\omega_s R s^3}{(s^2 + \omega_{ie}^2)(s^2 + \omega_{s-}^2)(s^2 + \omega_{s+}^2)} - \frac{\omega_s^2 (\omega_s^2 - 2\omega_{ie}^2 \sin^2 \tilde{\phi}) R s}{(s^2 + \omega_{ie}^2)(s^2 + \omega_{s-}^2)(s^2 + \omega_{s+}^2)}$ $h_{3,12}(t) = \left(\frac{\omega_{s-}^2 + 2\omega_{ie}^2 \cos^2 \tilde{\phi} - \omega_s^2}{(\omega_{s-}^2 - \omega_{s+}^2)(\omega_{s-}^2 - \omega_{ie}^2)} \cos(\omega_{s-}t) + \frac{\omega_{s+}^2 + 2\omega_{ie}^2 \cos^2 \tilde{\phi} - \omega_s^2}{(\omega_{s+}^2 - \omega_{s-}^2)(\omega_{s+}^2 - \omega_{ie}^2)} \cos(\omega_{s+}t) \right.$ $\left. + \frac{\omega_{ie}^2 + 2\omega_{ie}^2 \cos^2 \tilde{\phi} - \omega_s^2}{(\omega_{ie}^2 - \omega_{s-}^2)(\omega_{ie}^2 - \omega_{s+}^2)} \cos(\omega_{ie}t) \right) \omega_s^2 R$
$\delta \omega_{ib,d}$	$H_{3,13}(s) = -\frac{\omega_s^2 \omega_{ie} \cos \tilde{\phi} R s^2}{(s^2 + \omega_{ie}^2)(s^2 + \omega_{s-}^2)(s^2 + \omega_{s+}^2)} - \frac{\omega_s^2 \omega_{ie} \cos \tilde{\phi} (\omega_s^2 - 2\omega_{ie}^2 \sin^2 \tilde{\phi}) R}{(s^2 + \omega_{ie}^2)(s^2 + \omega_{s-}^2)(s^2 + \omega_{s+}^2)}$ $h_{3,13}(t) = -\left(\frac{2\omega_{ie}^2 \cos \tilde{\phi} + \omega_s^2 - \omega_{s-}^2}{\omega_{s-}(\omega_{s-}^2 - \omega_{s+}^2)(\omega_{s-}^2 - \omega_{ie}^2)} \sin(\omega_{s-}t) \right.$ $+ \frac{2\omega_{ie}^2 \cos \tilde{\phi} + \omega_s^2 - \omega_{s+}^2}{\omega_{s+}(\omega_{s+}^2 - \omega_{s-}^2)(\omega_{s+}^2 - \omega_{ie}^2)} \sin(\omega_{s+}t)$ $\left. + \frac{2\omega_{ie}^2 \cos \tilde{\phi} + \omega_s^2 - \omega_{ie}^2}{\omega_{ie}(\omega_{ie}^2 - \omega_{s-}^2)(\omega_{ie}^2 - \omega_{s+}^2)} \sin(\omega_{ie}t) \right) \omega_s^2 \omega_{ie} R \cos \tilde{\phi}$

Table D.12.: East velocity error step responses to IMU biases.

Input	Step response
$\delta f_{b,n}$	$H_{4,8}(s) = -\frac{2\omega_{ie} \sin \tilde{\phi} s}{(s^2 + \omega_{s-}^2)(s^2 + \omega_{s+}^2)}$ $h_{4,8}(t) = -\left(\frac{1}{(\omega_{s-}^2 - \omega_{s+}^2)} \cos(\omega_{s-} t) + \frac{1}{(\omega_{s+}^2 - \omega_{s-}^2)} \cos(\omega_{s+} t)\right) 2\omega_{ie} \sin \tilde{\phi}$
$\delta f_{b,e}$	$H_{4,9}(s) = \frac{s^2}{(s^2 + \omega_{s-}^2)(s^2 + \omega_{s+}^2)} + \frac{\omega_s^2}{(s^2 + \omega_{s-}^2)(s^2 + \omega_{s+}^2)}$ $h_{4,9}(t) = -\left(\frac{\omega_s^2 - \omega_{s-}^2}{\omega_{s-}(\omega_{s-}^2 - \omega_{s+}^2)} \sin(\omega_{s-} t) + \frac{\omega_s^2 - \omega_{s+}^2}{\omega_{s+}(\omega_{s+}^2 - \omega_{s-}^2)} \sin(\omega_{s+} t)\right)$
$\delta f_{b,d}$	$H_{4,10}(s) = 0$ $h_{4,10}(t) = 0$
$\delta \omega_{ib,n}$	$H_{4,11}(s) = \frac{\omega_s^2(s^2 + \omega_{2,11+}^2)(s^2 + \omega_{2,11-}^2)R}{s(s^2 + \omega_{ie}^2)(s^2 + \omega_{s-}^2)(s^2 + \omega_{s+}^2)}$ $h_{4,11}(t) = \left(\frac{\omega_{2,11+}^2 \omega_{2,11-}^2}{\omega_{s-}^2 \omega_{s+}^2 \omega_{ie}^2} - \frac{\omega_{s-}^4 - \omega_{s-}^2(\omega_{2,11+}^2 + \omega_{2,11-}^2) + \omega_{2,11+}^2 \omega_{2,11-}^2}{\omega_{s-}^2(\omega_{s-}^2 - \omega_{s+}^2)(\omega_{s-}^2 - \omega_{ie}^2)} \cos(\omega_{s-} t)\right. \\ \left. - \frac{\omega_{s+}^4 - \omega_{s+}^2(\omega_{2,11+}^2 + \omega_{2,11-}^2) + \omega_{2,11+}^2 \omega_{2,11-}^2}{\omega_{s+}^2(\omega_{s+}^2 - \omega_{s-}^2)(\omega_{s+}^2 - \omega_{ie}^2)} \cos(\omega_{s+} t)\right. \\ \left. - \frac{\omega_{ie}^4 - \omega_{ie}^2(\omega_{2,11+}^2 + \omega_{2,11-}^2) + \omega_{2,11+}^2 \omega_{2,11-}^2}{\omega_{ie}^2(\omega_{ie}^2 - \omega_{s-}^2)(\omega_{ie}^2 - \omega_{s+}^2)} \cos(\omega_{ie} t)\right) \omega_s^2 R$ $\omega_{2,11\pm}^2 = \frac{\omega_s^2 + 3\omega_{ie}^2 \cos^2 \tilde{\phi}}{2} + \omega_{ie}^2 \pm \frac{1}{2} \sqrt{(3\omega_{ie}^2 \cos^2 \tilde{\phi} - 2\omega_{ie}^2 + \omega_s^2)^2 - 4\omega_s^2 \omega_{ie}^2 \cos^2 \tilde{\phi}}$
$\delta \omega_{ib,e}$	$H_{4,12}(s) = -\frac{3\omega_s \omega_{ie} R \sin \tilde{\phi} s^2}{(s^2 + \omega_{ie}^2)(s^2 + \omega_{s-}^2)(s^2 + \omega_{s+}^2)} - \frac{\omega_s^4 \omega_{ie} R \sin \tilde{\phi}}{(s^2 + \omega_{ie}^2)(s^2 + \omega_{s-}^2)(s^2 + \omega_{s+}^2)}$ $h_{4,12}(t) = -\left(\frac{\omega_s^2 - 3\omega_{s-}^2}{\omega_{s-}(\omega_{s-}^2 - \omega_{s+}^2)(\omega_{s-}^2 - \omega_{ie}^2)} \sin(\omega_{s-} t) + \frac{\omega_s^2 - 3\omega_{s+}^2}{\omega_{s+}(\omega_{s+}^2 - \omega_{s-}^2)(\omega_{s+}^2 - \omega_{ie}^2)} \sin(\omega_{s+} t)\right. \\ \left. + \frac{\omega_s^2 - 3\omega_{ie}^2}{\omega_{ie}(\omega_{ie}^2 - \omega_{s-}^2)(\omega_{ie}^2 - \omega_{s+}^2)} \sin(\omega_{ie} t)\right) \omega_s^2 \omega_{ie} R \sin \tilde{\phi}$
$\delta \omega_{ib,d}$	$H_{4,13}(s) = -\frac{3\omega_s \omega_{ie}^2 R \sin \tilde{\phi} \cos \tilde{\phi} s}{(s^2 + \omega_{ie}^2)(s^2 + \omega_{s-}^2)(s^2 + \omega_{s+}^2)} - \frac{\omega_s^4 \omega_{ie}^2 R \sin \tilde{\phi} \cos \tilde{\phi}}{s(s^2 + \omega_{ie}^2)(s^2 + \omega_{s-}^2)(s^2 + \omega_{s+}^2)}$ $h_{4,13}(t) = \left(-\frac{\omega_s^2}{\omega_{s-}^2 \omega_{s+}^2 \omega_{ie}^2} + \frac{\omega_s^2 - 3\omega_{s-}^2}{\omega_{s-}^2(\omega_{s-}^2 - \omega_{s+}^2)(\omega_{s-}^2 - \omega_{ie}^2)} \cos(\omega_{s-} t)\right. \\ \left. + \frac{\omega_s^2 - 3\omega_{s+}^2}{\omega_{s+}^2(\omega_{s+}^2 - \omega_{s-}^2)(\omega_{s+}^2 - \omega_{ie}^2)} \cos(\omega_{s+} t) + \frac{\omega_s^2 - 3\omega_{ie}^2}{\omega_{ie}^2(\omega_{ie}^2 - \omega_{s-}^2)(\omega_{ie}^2 - \omega_{s+}^2)} \cos(\omega_{ie} t)\right) \\ \omega_s^2 \omega_{ie}^2 R \sin \tilde{\phi} \cos \tilde{\phi}$

D.1.7. Orientation Errors from Initialization Errors

Table D.13.: Roll angle error step responses to position and velocity initialization errors.

Input	Step response
$\delta\phi_0$	$H_{5,1}(s) = \frac{\omega_{ie} \sin \phi (s^2 + \omega_{5,1+}^2)(s^2 + \omega_{5,1-}^2)}{(s^2 + \omega_{s-}^2)(s^2 + \omega_{s+}^2)(s^2 + \omega_{ie}^2)}$ $h_{5,1}(t) = \left(\frac{\omega_{s+}^4 + \omega_{s+}^2 (\omega_{5,1+}^2 + \omega_{5,1-}^2) + \omega_{5,1+}^2 \omega_{5,1-}^2}{\omega_{s+} (\omega_{s+}^2 - \omega_{s-}^2) (\omega_{s+}^2 - \omega_{ie}^2)} \sin(\omega_{s+} t) \right. \\ \left. + \frac{\omega_{s-}^4 + \omega_{s-}^2 (\omega_{5,1+}^2 + \omega_{5,1-}^2) + \omega_{5,1+}^2 \omega_{5,1-}^2}{\omega_{s-} (\omega_{s-}^2 - \omega_{s+}^2) (\omega_{s-}^2 - \omega_{ie}^2)} \sin(\omega_{s-} t) \right. \\ \left. + \frac{\omega_{ie}^4 + \omega_{ie}^2 (\omega_{5,1+}^2 + \omega_{5,1-}^2) + \omega_{5,1+}^2 \omega_{5,1-}^2}{\omega_{ie} (\omega_{ie}^2 - \omega_{s-}^2) (\omega_{ie}^2 - \omega_{s+}^2)} \sin(\omega_{ie} t) \right) \omega_{ie} \sin \phi$ $\omega_{5,1\pm}^2 = \frac{1}{2} (4\omega_{ie}^2 \sin^2 \phi + \omega_s^2) \pm \frac{1}{2} \sqrt{(4\omega_{ie}^2 \sin^2 \phi + \omega_s^2)^2 - 8\omega_{ie}^2 \omega_s^2}$
$\delta\lambda_0$	$h_{5,2}(t) = 0$
$\delta v_{n,0}$	$H_{5,3}(s) = -\frac{\frac{2}{R} \omega_{ie} \sin \phi s}{(s^2 + \omega_{s-}^2)(s^2 + \omega_{s+}^2)}$ $h_{5,3}(t) = \left(\frac{1}{(\omega_{s+}^2 - \omega_{s-}^2)} \cos(\omega_{s+} t) + \frac{1}{(\omega_{s-}^2 - \omega_{s+}^2)} \cos(\omega_{s-} t) \right) \frac{2}{R} \omega_{ie} \sin \phi$
$\delta v_{e,0}$	$H_{5,4}(s) = -\frac{\frac{1}{R} s^2}{(s^2 + \omega_{s-}^2)(s^2 + \omega_{s+}^2)} - \frac{\frac{1}{R} \omega_s^2}{\omega_{s-} (s^2 + \omega_{s-}^2) (s^2 + \omega_{s+}^2)}$ $h_{5,4}(t) = -\left(\frac{\omega_{s-}^2 - \omega_s^2}{(\omega_{s-}^2 - \omega_{s+}^2)} \sin(\omega_{s-} t) + \frac{\omega_{s+}^2 - \omega_s^2}{\omega_{s+} (\omega_{s+}^2 - \omega_{s-}^2)} \sin(\omega_{s+} t) \right) \frac{1}{R}$
$\delta v_{d,0}$	$H_{5,14}(s) = -\frac{\frac{2}{R} \omega_{ie} \cos \phi s}{(s^2 + \omega_{s-}^2)(s^2 + \omega_{s+}^2)} - \frac{\frac{2}{R} \omega_s^2 \omega_{ie} \cos \phi}{s (s^2 + \omega_{s-}^2) (s^2 + \omega_{s+}^2)}$ $h_{5,14}(t) = \left(-\frac{\omega_s^2}{\omega_{s-}^2 \omega_{s+}^2} + \frac{\omega_s^2 - \omega_{s-}^2}{\omega_{s-}^2 (\omega_{s-}^2 - \omega_{s+}^2)} \cos(\omega_{s-} t) \right. \\ \left. + \frac{\omega_s^2 - \omega_{s+}^2}{\omega_{s+}^2 (\omega_{s+}^2 - \omega_{s-}^2)} \cos(\omega_{s+} t) \right) \frac{2}{R} \omega_{ie} \cos \phi$

Table D.14.: Pitch angle error step responses to position and velocity initialization errors.

Input	Step response
$\delta\phi_0$	$H_{6,1}(s) = \frac{\omega_{ie}^2 s^3}{(s^2 + \omega_{s-}^2)(s^2 + \omega_{s+}^2)(s^2 + \omega_{ie}^2)} + \frac{(4\omega_{ie}^2 \sin^2 \phi - 2\omega_s^2 \sin^2 \phi + \omega_s^2) \omega_{ie}^2 s}{(s^2 + \omega_{s-}^2)(s^2 + \omega_{s+}^2)(s^2 + \omega_{ie}^2)}$ $h_{6,1}(t) = \left(\frac{4\omega_{ie}^2 \sin^2 \phi - 2\omega_s^2 \sin^2 \phi + \omega_s^2 - \omega_{s+}^2}{(\omega_{s+}^2 - \omega_{s-}^2)(\omega_{s+}^2 - \omega_{ie}^2)} \cos(\omega_{s+} t) \right. \\ \left. + \frac{4\omega_{ie}^2 \sin^2 \phi - 2\omega_s^2 \sin^2 \phi + \omega_s^2 - \omega_{s-}^2}{(\omega_{s-}^2 - \omega_{s+}^2)(\omega_{s-}^2 - \omega_{ie}^2)} \cos(\omega_{s-} t) \right. \\ \left. + \frac{4\omega_{ie}^2 \sin^2 \phi - 2\omega_s^2 \sin^2 \phi + \omega_s^2 - \omega_{ie}^2}{(\omega_{ie}^2 - \omega_{s+}^2)(\omega_{ie}^2 - \omega_{s-}^2)} \cos(\omega_{ie} t) \right) \omega_{ie}^2$
$\delta\lambda_0$	$H_{6,2}(s) = 0$ $h_{6,2}(t) = 0$
$\delta v_{n,0}$	$H_{6,3}(s) = \frac{\frac{1}{R} s^2}{(s^2 + \omega_{s-}^2)(s^2 + \omega_{s+}^2)} + \frac{\frac{\omega_s^2}{R}}{(s^2 + \omega_{s-}^2)(s^2 + \omega_{s+}^2)}$ $h_{6,3}(t) = \left(\frac{\omega_{s-}^2 - \omega_s^2}{\omega_{s-} (\omega_{s-}^2 - \omega_{s+}^2)} \sin(\omega_{s-} t) + \frac{\omega_{s+}^2 - \omega_s^2}{\omega_{s+} (\omega_{s+}^2 - \omega_{s-}^2)} \sin(\omega_{s+} t) \right) \frac{1}{R}$
$\delta v_{e,0}$	$H_{6,4}(s) = -\frac{\frac{2}{R} \omega_{ie} \sin \phi s}{(s^2 + \omega_{s-}^2)(s^2 + \omega_{s+}^2)}$ $h_{6,4}(t) = \left(\frac{1}{(\omega_{s-}^2 - \omega_{s+}^2)} \cos(\omega_{s-} t) + \frac{1}{(\omega_{s+}^2 - \omega_{s-}^2)} \cos(\omega_{s+} t) \right) \frac{2}{R} \omega_{ie} \sin \phi$
$\delta v_{d,0}$	$H_{6,14}(s) = -\frac{\frac{4}{R} \omega_{ie}^2 \sin \phi \cos \phi}{(s^2 + \omega_{s-}^2)(s^2 + \omega_{s+}^2)}$ $h_{6,14}(t) = \left(\frac{1}{\omega_{s-} (\omega_{s-}^2 - \omega_{s+}^2)} \sin(\omega_{s-} t) + \frac{1}{\omega_{s+} (\omega_{s+}^2 - \omega_{s-}^2)} \sin(\omega_{s+} t) \right) \frac{4}{R} \omega_{ie}^2 \cos \phi \sin \phi$

Table D.15.: Yaw angle error step responses to position and velocity initialization errors.

Input	Step response
$\delta\phi_0$	$H_{7,1}(s) = \frac{\omega_{ie} \cos \phi (s^2 + \omega_{7,1+}^2)(s^2 + \omega_{7,1-}^2)}{(s^2 + \omega_{s-}^2)(s^2 + \omega_{s+}^2)(s^2 + \omega_{ie}^2)}$ $h_{7,1}(t) = \left(\frac{\omega_{s+}^4 - \omega_{s+}^2 (\omega_{7,1+}^2 + \omega_{7,1-}^2) + \omega_{7,1+}^2 \omega_{7,1-}^2}{\omega_{s+} (\omega_{s+}^2 - \omega_{s-}^2)(\omega_{s+}^2 - \omega_{ie}^2)} \sin(\omega_{s+} t) \right. \\ \left. + \frac{\omega_{s-}^4 - \omega_{s-}^2 (\omega_{7,1+}^2 + \omega_{7,1-}^2) + \omega_{7,1+}^2 \omega_{7,1-}^2}{\omega_{s-} (\omega_{s-}^2 - \omega_{s+}^2)(\omega_{s-}^2 - \omega_{ie}^2)} \sin(\omega_{s-} t) \right. \\ \left. + \frac{\omega_{ie}^4 - \omega_{ie}^2 (\omega_{7,1+}^2 + \omega_{7,1-}^2) + \omega_{7,1+}^2 \omega_{7,1-}^2}{\omega_{ie} (\omega_{ie}^2 - \omega_{s-}^2)(\omega_{ie}^2 - \omega_{s+}^2)} \sin(\omega_{ie} t) \right) \omega_{ie} \cos \phi$ $\omega_{7,1\pm}^2 = \frac{1}{2} (4\omega_{ie}^2 \sin^2 \phi + \omega_s^2 (1 + \sec^2 \phi))$ $\pm \frac{1}{2} \sqrt{(4\omega_{ie}^2 \sin^2 \phi + \omega_s^2 (1 + \sec^2 \phi))^2 - 4 \left(\omega_s^4 \frac{1}{\cos^2 \phi} - 2\omega_s^2 \omega_{ie}^2 \tan^2 \phi \right)}$
$\delta\lambda_0$	$H_{7,2}(s) = 0$ $h_{7,2}(t) = 0$
$\delta v_{n,0}$	$H_{7,3}(s) = \frac{\frac{2}{R} \omega_{ie} \tan \phi \sin \phi s}{(s^2 + \omega_{s-}^2)(s^2 + \omega_{s+}^2)}$ $h_{7,3}(t) = - \left(\frac{1}{(\omega_{s-}^2 - \omega_{s+}^2)} \cos(\omega_{s-} t) + \frac{1}{(\omega_{s+}^2 - \omega_{s-}^2)} \cos(\omega_{s+} t) \right) \frac{2}{R} \omega_{ie} \tan \phi \sin \phi$
$\delta v_{e,0}$	$H_{7,4}(s) = \frac{\frac{1}{R} \tan \phi s^2}{(s^2 + \omega_{s-}^2)(s^2 + \omega_{s+}^2)} + \frac{\frac{1}{R} \tan \phi \omega_s^2}{(s^2 + \omega_{s-}^2)(s^2 + \omega_{s+}^2)}$ $h_{7,4}(t) = \left(\frac{\omega_{s-}^2 - \omega_s^2}{(\omega_{s-}^2 - \omega_{s+}^2)} \sin(\omega_{s-} t) + \frac{\omega_{s+}^2 - \omega_s^2}{(\omega_{s+}^2 - \omega_{s-}^2)} \sin(\omega_{s+} t) \right) \frac{1}{R} \tan \phi$
$\delta v_{d,0}$	$H_{7,14}(s) = \frac{\frac{2}{R} \omega_{ie} \sin \phi s}{(s^2 + \omega_{s-}^2)(s^2 + \omega_{s+}^2)} + \frac{\frac{2}{R} \sin \phi \omega_{ie} \omega_s^2}{s (s^2 + \omega_{s-}^2)(s^2 + \omega_{s+}^2)}$ $h_{7,14}(t) = \left(\frac{\omega_s^2}{\omega_{s-}^2 \omega_{s+}^2} - \frac{\omega_{s-}^- \omega_s^2 2}{\omega_{s-}^2 (\omega_{s-}^2 - \omega_{s+}^2)} \cos(\omega_{s-} t) - \frac{\omega_{s+}^2 - \omega_s^2}{\omega_{s+}^2 (\omega_{s+}^2 - \omega_{s-}^2)} \cos(\omega_{s+} t) \right) \frac{2}{R} \omega_{ie} \sin \phi$

D.1.8. Orientation Errors from Initial Alignment Errors
Table D.16.: Roll angle error step responses to initial alignment errors.

Input	Step response
$\delta\Phi_0$	$H_{5,5}(s) = -\frac{(s^2 + \omega_{5,5+}^2)(s^2 + \omega_{5,5-}^2)(\omega_{ie}^2 \sin^2 \phi + \omega_s^2)}{s(s^2 + \omega_{s-}^2)(s^2 + \omega_{s+}^2)(s^2 + \omega_{ie}^2)}$ $h_{5,5}(t) = -\frac{\omega_{5,5+}^2 \omega_{5,5-}^2}{\omega_{s+}^2 \omega_{s-}^2 \omega_{ie}^2} + \left(\frac{\omega_{s-}^4 - \omega_{s-}^2 (\omega_{5,5+}^2 + \omega_{5,5-}^2) + \omega_{5,5+}^2 \omega_{5,5-}^2}{\omega_{s-}^2 (\omega_{s-}^2 - \omega_{s+}^2) (\omega_{s-}^2 - \omega_{ie}^2)} \cos(\omega_{s-} t) \right.$ $+ \frac{\omega_{s+}^4 - \omega_{s+}^2 (\omega_{5,5+}^2 + \omega_{5,5-}^2) + \omega_{5,5+}^2 \omega_{5,5-}^2}{\omega_{s+}^2 (\omega_{s+}^2 - \omega_{s-}^2) (\omega_{s+}^2 - \omega_{ie}^2)} \cos(\omega_{s+} t) +$ $\left. + \frac{\omega_{ie}^4 - \omega_{ie}^2 (\omega_{5,5+}^2 + \omega_{5,5-}^2) + \omega_{5,5+}^2 \omega_{5,5-}^2}{\omega_{ie}^2 (\omega_{ie}^2 - \omega_{s-}^2) (\omega_{ie}^2 - \omega_{s+}^2)} \cos(\omega_{ie} t) \right) (\omega_{ie}^2 \sin^2 \phi + \omega_s^2)$ $\omega_{5,5\pm}^2 = \frac{4\omega_{ie}^4 \sin^4 \phi + \omega_s^2 \omega_{ie}^2 \cos^2 \phi + \omega_s^4}{2(\omega_{ie}^2 \sin^2 \phi + \omega_s^2)}$ $\pm \frac{\sqrt{(4\omega_{ie}^4 \sin^4 \phi + \omega_s^2 \omega_{ie}^2 \cos^2 \phi + \omega_s^4)^2 - 4(\omega_{ie}^2 \sin^2 \phi + \omega_s^2) \omega_s^4 \omega_{ie}^2}}{2(\omega_{ie}^2 \sin^2 \phi + \omega_s^2)}$
$\delta\Theta_0$	$H_{5,6}(s) = -\frac{\omega_{ie} \sin \phi s^4}{(s^2 + \omega_{s-}^2)(s^2 + \omega_{s+}^2)(s^2 + \omega_{ie}^2)} - \frac{(4\omega_{ie}^2 \sin^2 \phi - \omega_s^2) \omega_{ie} \sin \phi s^2}{(s^2 + \omega_{s-}^2)(s^2 + \omega_{s+}^2)(s^2 + \omega_{ie}^2)}$ $h_{5,6}(t) = \left(\frac{(4\omega_{ie}^2 \sin^2 \phi - \omega_s^2 - \omega_{s+}^2) \omega_{s+}}{(\omega_{s+}^2 - \omega_{s-}^2) (\omega_{s+}^2 - \omega_{ie}^2)} \sin(\omega_{s+} t) \right.$ $+ \frac{(4\omega_{ie}^2 \sin^2 \phi - \omega_s^2 - \omega_{s-}^2) \omega_{s-}}{(\omega_{s-}^2 - \omega_{s+}^2) (\omega_{s-}^2 - \omega_{ie}^2)} \sin(\omega_{s-} t)$ $\left. + \frac{(4\omega_{ie}^2 \sin^2 \phi - \omega_s^2 - \omega_{ie}^2) \omega_{ie}}{(\omega_{ie}^2 - \omega_{s+}^2) (\omega_{ie}^2 - \omega_{s-}^2)} \sin(\omega_{ie} t) \right) \omega_{ie} \sin \phi$
$\delta\Psi_0$	$H_{5,7}(s) = -\frac{\omega_{ie}^2 \sin \phi \cos \phi s^3}{(s^2 + \omega_{s-}^2)(s^2 + \omega_{s+}^2)(s^2 + \omega_{ie}^2)} - \frac{(4\omega_{ie}^2 \sin^3 \phi \cos \phi - \omega_s^2 \sin \phi \cos \phi) \omega_{ie}^2 s}{(s^2 + \omega_{s-}^2)(s^2 + \omega_{s+}^2)(s^2 + \omega_{ie}^2)}$ $h_{5,7}(t) = -\left(\frac{4\omega_{ie}^2 \sin^2 \phi - \omega_s^2 - \omega_{s+}^2}{(\omega_{s+}^2 - \omega_{s-}^2) (\omega_{s+}^2 - \omega_{ie}^2)} \sin(\omega_{s+} t) \right.$ $+ \frac{4\omega_{ie}^2 \sin^2 \phi - \omega_s^2 - \omega_{s-}^2}{(\omega_{s-}^2 - \omega_{s+}^2) (\omega_{s-}^2 - \omega_{ie}^2)} \sin(\omega_{s-} t)$ $\left. + \frac{4\omega_{ie}^2 \sin^2 \phi - \omega_s^2 - \omega_{ie}^2}{(\omega_{ie}^2 - \omega_{s+}^2) (\omega_{ie}^2 - \omega_{s-}^2)} \sin(\omega_{ie} t) \right) \omega_{ie}^2 \sin \phi \cos \phi$

Table D.17.: Pitch angle error step responses to initial alignment errors.

Input	Step response
$\delta\Phi_0$	$H_{6,5}(s) = \frac{(s^2 + \omega_{6,5+}^2)(s^2 + \omega_{6,5-}^2) \omega_{ie} \sin \phi}{(s^2 + \omega_{s-}^2)(s^2 + \omega_{s+}^2)(s^2 + \omega_{ie}^2)}$ $h_{6,5}(t) = \left(\frac{\omega_{s-}^4 - \omega_{s-}^2(\omega_{6,5+}^2 + \omega_{6,5-}^2) + \omega_{6,5+}^2 \omega_{6,5-}^2}{\omega_{s-}(\omega_{s-}^2 - \omega_{s+}^2)(\omega_{s-}^2 - \omega_{ie}^2)} \sin(\omega_{s-} t) \right. \\ \left. + \frac{\omega_{s+}^4 - \omega_{s+}^2(\omega_{6,5+}^2 + \omega_{6,5-}^2) + \omega_{6,5+}^2 \omega_{6,5-}^2}{\omega_{s+}(\omega_{s+}^2 - \omega_{s-}^2)(\omega_{s+}^2 - \omega_{ie}^2)} \sin(\omega_{s+} t) + \right. \\ \left. + \frac{\omega_{ie}^4 - \omega_{ie}^2(\omega_{6,5+}^2 + \omega_{6,5-}^2) + \omega_{6,5+}^2 \omega_{6,5-}^2}{\omega_{ie}(\omega_{ie}^2 - \omega_{s-}^2)(\omega_{ie}^2 - \omega_{s+}^2)} \sin(\omega_{ie} t) \right) \omega_{ie} \sin \phi$ $\omega_{6,5\pm}^2 = -\frac{1}{2}(\omega_s^2 - \omega_{ie}^2 \sin^2 \phi) \pm \frac{1}{2} \sqrt{(\omega_s^2 - \omega_{ie}^2 \sin^2 \phi)^2 + 8\omega_s^2 \omega_{ie}^2 \cos^2 \phi}$
$\delta\Theta_0$	$H_{6,6}(s) = -\frac{(s^2 + \omega_{6,6+}^2)(s^2 + \omega_{6,6-}^2)(\omega_{ie}^2 + \omega_s^2)}{s(s^2 + \omega_{s-}^2)(s^2 + \omega_{s+}^2)(s^2 + \omega_{ie}^2)}$ $h_{6,6}(t) = \left(-\frac{\omega_{6,6-}^2 \omega_{6,6+}^2}{\omega_{s+}^2 \omega_{s-}^2 \omega_{ie}^2} + \frac{\omega_{s-}^4 - \omega_{s-}^2(\omega_{6,6+}^2 + \omega_{6,6-}^2) + \omega_{6,6+}^2 \omega_{6,6-}^2}{\omega_{s-}(\omega_{s-}^2 - \omega_{s+}^2)(\omega_{s-}^2 - \omega_{ie}^2)} \cos(\omega_{s-} t) \right. \\ \left. + \frac{\omega_{s+}^4 - \omega_{s+}^2(\omega_{6,6+}^2 + \omega_{6,6-}^2) + \omega_{6,6+}^2 \omega_{6,6-}^2}{\omega_{s+}(\omega_{s+}^2 - \omega_{s-}^2)(\omega_{s+}^2 - \omega_{ie}^2)} \cos(\omega_{s+} t) + \right. \\ \left. + \frac{\omega_{ie}^4 - \omega_{ie}^2(\omega_{6,6+}^2 + \omega_{6,6-}^2) + \omega_{6,6+}^2 \omega_{6,6-}^2}{\omega_{ie}(\omega_{ie}^2 - \omega_{s-}^2)(\omega_{ie}^2 - \omega_{s+}^2)} \cos(\omega_{ie} t) \right) (\omega_{ie}^2 + \omega_s^2)$ $\omega_{6,6\pm}^2 = \frac{4\omega_{ie}^4 \sin^2 \phi + 2\omega_s^2 \omega_{ie}^2 \cos^2 \phi + \omega_s^4}{2(\omega_{ie}^2 + \omega_s^2)} \\ \pm \frac{\sqrt{(4\omega_{ie}^4 \sin^2 \phi + 2\omega_s^2 \omega_{ie}^2 \cos^2 \phi + \omega_s^4)^2 + 4\omega_s^4 \omega_{ie}^2 (\omega_{ie}^2 + \omega_s^2)}}{2(\omega_{ie}^2 + \omega_s^2)}$
$\delta\Psi_0$	$H_{6,7}(s) = \frac{(s^2 + \omega_{6,7+}^2)(s^2 + \omega_{6,7-}^2) \omega_{ie} \cos \phi}{(s^2 + \omega_{s-}^2)(s^2 + \omega_{s+}^2)(s^2 + \omega_{ie}^2)}$ $h_{6,7}(t) = \left(\frac{\omega_{s-}^4 - \omega_{s-}^2(\omega_{6,7+}^2 + \omega_{6,7-}^2) + \omega_{6,7+}^2 \omega_{6,7-}^2}{\omega_{s-}(\omega_{s-}^2 - \omega_{s+}^2)(\omega_{s-}^2 - \omega_{ie}^2)} \sin(\omega_{s-} t) \right. \\ \left. + \frac{\omega_{s+}^4 - \omega_{s+}^2(\omega_{6,7+}^2 + \omega_{6,7-}^2) + \omega_{6,7+}^2 \omega_{6,7-}^2}{\omega_{s+}(\omega_{s+}^2 - \omega_{s-}^2)(\omega_{s+}^2 - \omega_{ie}^2)} \sin(\omega_{s+} t) + \right. \\ \left. + \frac{\omega_{ie}^4 - \omega_{ie}^2(\omega_{6,7+}^2 + \omega_{6,7-}^2) + \omega_{6,7+}^2 \omega_{6,7-}^2}{\omega_{ie}(\omega_{ie}^2 - \omega_{s-}^2)(\omega_{ie}^2 - \omega_{s+}^2)} \sin(\omega_{ie} t) \right) \omega_{ie} \cos \phi$ $\omega_{6,7\pm}^2 = \frac{1}{2}(\omega_s^2 + 4\omega_{ie}^2 \sin^2 \phi) \pm \frac{1}{2} \sqrt{(\omega_s^2 + 4\omega_{ie}^2 \sin^2 \phi)^2 - 8\omega_s^2 \omega_{ie}^2 \sin^2 \phi}$

Table D.18.: Yaw angle error step responses to initial alignment errors.

Input	Step response
$\delta\Phi_0$	$H_{7,5}(s) = \frac{\tan \phi (\omega_s^2 - \omega_{ie}^2 \cos^2 \phi) s^3}{(s^2 + \omega_{s-}^2)(s^2 + \omega_{s+}^2)(s^2 + \omega_{ie}^2)}$ $+ \frac{\tan \phi (\omega_s^4 - 4\omega_{ie}^4 \sin^2 \phi \cos^2 \phi - \omega_s^2 \omega_{ie}^2 \sin^2 \phi - \omega_s^2 \omega_{ie}^2) s}{(s^2 + \omega_{s-}^2)(s^2 + \omega_{s+}^2)(s^2 + \omega_{ie}^2)}$ $h_{7,5}(t) = \left(\frac{\omega_{s+}^2 (\omega_{ie}^2 \cos^2 \phi - \omega_s^2) - \omega_s^4 - 4\omega_{ie}^4 \sin^2 \phi \cos^2 \phi - \omega_s^2 \omega_{ie}^2 (\sin^2 \phi + 1)}{(\omega_{s+}^2 - \omega_{s-}^2)(\omega_{s+}^2 - \omega_{ie}^2)} \cos(\omega_{s+} t) \right.$ $+ \frac{\omega_{s-}^2 (\omega_{ie}^2 \cos^2 \phi - \omega_s^2) - \omega_s^4 - 4\omega_{ie}^4 \sin^2 \phi \cos^2 \phi - \omega_s^2 \omega_{ie}^2 (\sin^2 \phi + 1)}{(\omega_{s-}^2 - \omega_{s+}^2)(\omega_{s-}^2 - \omega_{ie}^2)} \cos(\omega_{s-} t)$ $\left. + \frac{\omega_{ie}^2 (\omega_{ie}^2 \cos^2 \phi - \omega_s^2) - \omega_s^4 - 4\omega_{ie}^4 \sin^2 \phi \cos^2 \phi - \omega_s^2 \omega_{ie}^2 (\sin^2 \phi + 1)}{(\omega_{ie}^2 - \omega_{s+}^2)(\omega_{ie}^2 - \omega_{s-}^2)} \cos(\omega_{ie} t) \right) \tan \phi$
$\delta\Theta_0$	$H_{7,6}(s) = \frac{\omega_{ie} \cos \phi (s^2 + \omega_{7,6+}^2)(s^2 + \omega_{7,6-}^2)}{(s^2 + \omega_{s-}^2)(s^2 + \omega_{s+}^2)(s^2 + \omega_{ie}^2)}$ $h_{7,6}(t) = - \left(\frac{\omega_{s-}^4 - \omega_{s-}^2 (\omega_{7,6+}^2 + \omega_{7,6-}^2) + \omega_{7,6+}^2 \omega_{7,6-}^2}{\omega_{s-}^2 (\omega_{s-}^2 - \omega_{s+}^2)(\omega_{s-}^2 - \omega_{ie}^2)} \sin(\omega_{s-} t) \right.$ $+ \frac{\omega_{s+}^4 - \omega_{s+}^2 (\omega_{7,6+}^2 + \omega_{7,6-}^2) + \omega_{7,6+}^2 \omega_{7,6-}^2}{\omega_{s+}^2 (\omega_{s+}^2 - \omega_{s-}^2)(\omega_{s+}^2 - \omega_{ie}^2)} \sin(\omega_{s+} t) +$ $\left. + \frac{\omega_{ie}^4 - \omega_{ie}^2 (\omega_{7,6+}^2 + \omega_{7,6-}^2) + \omega_{7,6+}^2 \omega_{7,6-}^2}{\omega_{ie}^2 (\omega_{ie}^2 - \omega_{s-}^2)(\omega_{ie}^2 - \omega_{s+}^2)} \sin(\omega_{ie} t) \right) \omega_{ie} \cos \phi$ $\omega_{7,6\pm}^2 = \frac{1}{2} (4\omega_{ie}^2 \sin^2 \phi + 3\omega_s^2 \sec^2 \phi - \omega_s^2) \pm \frac{1}{2} \sqrt{(4\omega_{ie}^2 \sin^2 \phi + 3\omega_s^2 \sec^2 \phi - \omega_s^2)^2 - 4\omega_s^4 \sec^2 \phi}$
$\delta\Psi_0$	$H_{7,7}(s) = \frac{(s^2 + \omega_{7,7+}^2)(s^2 + \omega_{7,7-}^2) \omega_{ie}^2 \cos^2 \phi}{s(s^2 + \omega_{s-}^2)(s^2 + \omega_{s+}^2)(s^2 + \omega_{ie}^2)}$ $h_{7,7}(t) = \left(\frac{\omega_{7,7-}^2 \omega_{6,6+}^2 - \omega_{s-}^4 - \omega_{s-}^2 (\omega_{7,7+}^2 + \omega_{7,7-}^2) + \omega_{7,7+}^2 \omega_{7,7-}^2}{\omega_{s+}^2 \omega_{s-}^2 \omega_{ie}^2} \cos(\omega_{s-} t) \right.$ $- \frac{\omega_{s+}^4 - \omega_{s+}^2 (\omega_{7,7+}^2 + \omega_{7,7-}^2) + \omega_{7,7+}^2 \omega_{7,7-}^2}{\omega_{s+}^2 (\omega_{s+}^2 - \omega_{s-}^2)(\omega_{s+}^2 - \omega_{ie}^2)} \cos(\omega_{s+} t) +$ $\left. - \frac{\omega_{ie}^4 - \omega_{ie}^2 (\omega_{7,7+}^2 + \omega_{7,7-}^2) + \omega_{7,7+}^2 \omega_{7,7-}^2}{\omega_{ie}^2 (\omega_{ie}^2 - \omega_{s-}^2)(\omega_{ie}^2 - \omega_{s+}^2)} \cos(\omega_{ie} t) \right) \omega_{ie}^2 \cos^2 \phi$ $\omega_{7,7\pm}^2 = \frac{4\omega_{ie}^2 \sin^4 \phi - 4\omega_{ie}^2 \sin^2 \phi + \omega_s^2 \omega_{ie}^2 \sin^2 \phi - 2\omega_s^2}{2 \cos^2 \phi}$ $\pm \frac{\sqrt{(4\omega_{ie}^2 \sin^4 \phi - 4\omega_{ie}^2 \sin^2 \phi + \omega_s^2 \omega_{ie}^2 \sin^2 \phi - 2\omega_s^2)^2 + 4\omega_s^4 \cos^2 \phi}}{2 \cos^2 \phi}$

D.1.9. Orientation Errors from Sensor Biases

Table D.19.: Roll angle error step responses to accelerometer biases.

Input	Step response
$\delta f_{b,n}$	$H_{5,8}(s) = -\frac{\frac{2}{R}\omega_{ie} \sin \phi}{(s^2 + \omega_{s-}^2)(s^2 + \omega_{s+}^2)}$ $h_{5,8}(t) = \left(\frac{1}{\omega_{s-}(\omega_{s-}^2 - \omega_{s+}^2)} \sin(\omega_{s-}t) + \frac{1}{\omega_{s+}(\omega_{s+}^2 - \omega_{s-}^2)} \sin(\omega_{s+}t) \right) \frac{2}{R}\omega_{ie} \sin \phi$
$\delta f_{b,e}$	$H_{5,9}(s) = -\frac{\frac{1}{R}s}{(s^2 + \omega_{s-}^2)(s^2 + \omega_{s+}^2)} - \frac{\frac{1}{R}\omega_s^2}{s(s^2 + \omega_{s-}^2)(s^2 + \omega_{s+}^2)}$ $h_{5,9}(t) = \left(-\frac{\omega_s^2}{\omega_{s-}^2\omega_{s+}^2} + \frac{\omega_s^2 - \omega_{s-}^2}{\omega_{s-}^2(\omega_{s-}^2 - \omega_{s+}^2)} \cos(\omega_{s-}t) + \frac{\omega_s^2 - \omega_{s+}^2}{\omega_{s+}^2(\omega_{s+}^2 - \omega_{s-}^2)} \cos(\omega_{s+}t) \right) \frac{1}{R}$
$\delta f_{b,d}$	$H_{5,10}(s) = 0$ $h_{5,10}(t) = 0$

Table D.20.: Roll angle error step responses to gyroscope biases.

Input	Step response
$\delta\omega_{ib,n}$	$H_{5,11}(s) = \frac{(s^2 + \omega_{5,11+}^2)(s^2 + \omega_{5,11-}^2)}{(s^2 + \omega_{s-}^2)(s^2 + \omega_{s+}^2)(s^2 + \omega_{ie}^2)}$ $h_{5,11}(t) = \left(\frac{\omega_{s-}^4 - \omega_{s-}^2(\omega_{5,11+}^2 + \omega_{5,11-}^2) + \omega_{5,11+}^2\omega_{5,11-}^2}{\omega_{s-}^2(\omega_{s-}^2 - \omega_{s+}^2)(\omega_{s-}^2 - \omega_{ie}^2)} \sin(\omega_{s-}t) \right.$ $+ \frac{\omega_{s+}^4 - \omega_{s+}^2(\omega_{5,11+}^2 + \omega_{5,11-}^2) + \omega_{5,11+}^2\omega_{5,11-}^2}{\omega_{s+}^2(\omega_{s+}^2 - \omega_{s-}^2)(\omega_{s+}^2 - \omega_{ie}^2)} \sin(\omega_{s+}t) +$ $\left. + \frac{\omega_{ie}^4 - \omega_{ie}^2(\omega_{5,11+}^2 + \omega_{5,11-}^2) + \omega_{5,11+}^2\omega_{5,11-}^2}{\omega_{ie}^2(\omega_{ie}^2 - \omega_{s-}^2)(\omega_{ie}^2 - \omega_{s+}^2)} \sin(\omega_{ie}t) \right)$ $\omega_{5,11\pm}^2 = \frac{1}{2} (3\omega_{ie}^2 \sin^2 \phi + \omega_{ie}^2 + \omega_s^2)$ $\pm \frac{1}{2} \sqrt{(3\omega_{ie}^2 \sin^2 \phi + \omega_{ie}^2 + \omega_s^2)^2 - 4\omega_{ie}^2 (4\omega_{ie}^2 \sin^2 \phi - 4\omega_{ie}^2 \sin^4 \phi + \omega_s^2 \sin^2 \phi + \omega_s^2)}$
$\delta\omega_{ib,e}$	$H_{5,12}(s) = -\frac{\omega_{ie} \sin \phi s^3}{(s^2 + \omega_{s-}^2)(s^2 + \omega_{s+}^2)(s^2 + \omega_{ie}^2)} - \frac{(\omega_{ie}^2 \sin^2 \phi - \omega_s^2) \omega_{ie} \sin \phi s}{(s^2 + \omega_{s-}^2)(s^2 + \omega_{s+}^2)(s^2 + \omega_{ie}^2)}$ $h_{5,12}(t) = \left(\frac{\omega_{s-}^2 - \omega_{ie}^2 \sin^2 \phi + \omega_s^2}{(\omega_{s-}^2 - \omega_{s+}^2)(\omega_{s-}^2 - \omega_{ie}^2)} \cos(\omega_{s-}t) + \frac{\omega_{s+}^2 - \omega_{ie}^2 \sin^2 \phi + \omega_s^2}{(\omega_{s+}^2 - \omega_{s-}^2)(\omega_{s+}^2 - \omega_{ie}^2)} \cos(\omega_{s+}t) \right.$ $\left. + \frac{\omega_{ie}^2 - \omega_{ie}^2 \sin^2 \phi + \omega_s^2}{(\omega_{ie}^2 - \omega_{s-}^2)(\omega_{ie}^2 - \omega_{s+}^2)} \cos(\omega_{ie}t) \right) \omega_{ie} \sin \phi$
$\delta\omega_{ib,d}$	$H_{5,13}(s) = \frac{\omega_{ie}^2 \sin \phi \cos \phi s^2}{(s^2 + \omega_{s-}^2)(s^2 + \omega_{s+}^2)(s^2 + \omega_{ie}^2)} - \frac{(4\omega_{ie}^2 \sin^3 \phi \cos \phi - \omega_s^2 \sin \phi \cos \phi) \omega_{ie}^2}{(s^2 + \omega_{s-}^2)(s^2 + \omega_{s+}^2)(s^2 + \omega_{ie}^2)}$ $h_{5,13}(t) = \left(\frac{\omega_s^2 - 4\omega_{ie}^2 \sin^2 \phi + \omega_{s-}^2 \omega_s^2}{\omega_{s-}(\omega_{s-}^2 - \omega_{s+}^2)(\omega_{s-}^2 - \omega_{ie}^2)} \sin(\omega_{s-}t) + \frac{\omega_s^2 - 4\omega_{ie}^2 \sin^2 \phi + \omega_{s+}^2 \omega_s^2}{\omega_{s+}(\omega_{s+}^2 - \omega_{s-}^2)(\omega_{s+}^2 - \omega_{ie}^2)} \sin(\omega_{s+}t) \right.$ $\left. + \frac{\omega_s^2 - 4\omega_{ie}^2 \sin^2 \phi + \omega_{ie}^2 \omega_s^2}{\omega_{ie}(\omega_{ie}^2 - \omega_{s-}^2)(\omega_{ie}^2 - \omega_{s+}^2)} \sin(\omega_{ie}t) \right) \omega_{ie}^2 \sin \phi \cos \phi$

Table D.21.: Pitch angle error step responses to accelerometer biases.

Input	Step response
$\delta f_{b,n}$	$H_{6,8}(s) = \frac{\frac{1}{R}s}{(s^2 + \omega_{s-}^2)(s^2 + \omega_{s+}^2)} + \frac{\frac{1}{R}\omega_s^2}{s(s^2 + \omega_{s-}^2)(s^2 + \omega_{s+}^2)}$ $h_{6,8}(t) = \left(\frac{\omega_s^2}{\omega_{s-}^2 \omega_{s+}^2} - \frac{\omega_{s-}^2 - \omega_s^2}{\omega_{s-}^2 (\omega_{s-}^2 - \omega_{s+}^2)} \cos(\omega_{s-} t) - \frac{\omega_{s+}^2 - \omega_s^2}{\omega_{s+}^2 (\omega_{s+}^2 - \omega_{s-}^2)} \cos(\omega_{s+} t) \right) \frac{1}{R}$
$\delta f_{b,e}$	$H_{6,9}(s) = -\frac{\frac{2}{R}\omega_{ie} \sin \phi}{(s^2 + \omega_{s-}^2)(s^2 + \omega_{s+}^2)}$ $h_{6,9}(t) = \left(\frac{1}{\omega_{s-} (\omega_{s-}^2 - \omega_{s+}^2)} \sin(\omega_{s-} t) + \frac{1}{\omega_{s+} (\omega_{s+}^2 - \omega_{s-}^2)} \sin(\omega_{s+} t) \right) \frac{2}{R}\omega_{ie} \sin \phi$
$\delta f_{b,d}$	$H_{6,10}(s) = 0$ $h_{6,10}(t) = 0$

Table D.22.: Pitch angle error step responses to gyroscope biases.

Input	Step response
$\delta\omega_{ib,n}$	$H_{6,11}(s) = \frac{(s^2 + \omega_{6,11+}^2)(s^2 + \omega_{6,11-}^2) \omega_{ie} \sin \phi}{s(s^2 + \omega_{s-}^2)(s^2 + \omega_{s+}^2)(s^2 + \omega_{ie}^2)}$ $h_{6,11}(t) = \left(\frac{\omega_{6,11+}^2 \omega_{6,11-}^2}{\omega_{s-}^2 \omega_{s+}^2 \omega_{ie}^2} - \frac{\omega_{s-}^4 - \omega_{s-}^2 (\omega_{6,11+}^2 + \omega_{6,11-}^2) + \omega_{6,11+}^2 \omega_{6,11-}^2}{\omega_{s-}^2 (\omega_{s-}^2 - \omega_{s+}^2) (\omega_{s-}^2 - \omega_{ie}^2)} \cos(\omega_{s-} t) \right. \\ \left. - \frac{\omega_{s+}^4 - \omega_{s+}^2 (\omega_{6,11+}^2 + \omega_{6,11-}^2) + \omega_{6,11+}^2 \omega_{6,11-}^2}{\omega_{s+}^2 (\omega_{s+}^2 - \omega_{s-}^2) (\omega_{s+}^2 - \omega_{ie}^2)} \cos(\omega_{s+} t) + \right. \\ \left. - \frac{\omega_{ie}^4 - \omega_{ie}^2 (\omega_{6,11+}^2 + \omega_{6,11-}^2) + \omega_{6,11+}^2 \omega_{6,11-}^2}{\omega_{ie}^2 (\omega_{ie}^2 - \omega_{s-}^2) (\omega_{ie}^2 - \omega_{s+}^2)} \cos(\omega_{ie} t) \right) \omega_{ie} \sin \phi$ $\omega_{6,11\pm}^2 = \frac{1}{2} (4\omega_{ie}^2 \sin^2 \phi - \omega_s^2) \pm \frac{1}{2} \sqrt{(4\omega_{ie}^2 \sin^2 \phi + \omega_s^2)^2 + 8\omega_s^2 \omega_{ie}^2 \cos^2 \phi}$
$\delta\omega_{ib,e}$	$H_{6,12}(s) = \frac{(s^2 + \omega_{6,12+}^2)(s^2 + \omega_{6,12-}^2)}{(s^2 + \omega_{s-}^2)(s^2 + \omega_{s+}^2)(s^2 + \omega_{ie}^2)}$ $h_{6,12}(t) = \left(\frac{\omega_{s-}^4 - \omega_{s-}^2 (\omega_{6,12+}^2 + \omega_{6,12-}^2) + \omega_{6,12+}^2 \omega_{6,12-}^2}{\omega_{s-}^2 (\omega_{s-}^2 - \omega_{s+}^2) (\omega_{s-}^2 - \omega_{ie}^2)} \sin(\omega_{s-} t) \right. \\ \left. + \frac{\omega_{s+}^4 - \omega_{s+}^2 (\omega_{6,12+}^2 + \omega_{6,12-}^2) + \omega_{6,12+}^2 \omega_{6,12-}^2}{\omega_{s+}^2 (\omega_{s+}^2 - \omega_{s-}^2) (\omega_{s+}^2 - \omega_{ie}^2)} \sin(\omega_{s+} t) + \right. \\ \left. + \frac{\omega_{ie}^4 - \omega_{ie}^2 (\omega_{6,12+}^2 + \omega_{6,12-}^2) + \omega_{6,12+}^2 \omega_{6,12-}^2}{\omega_{ie}^2 (\omega_{ie}^2 - \omega_{s-}^2) (\omega_{ie}^2 - \omega_{s+}^2)} \sin(\omega_{ie} t) \right)$ $\omega_{6,12\pm}^2 = \frac{1}{2} (4\omega_{ie}^2 \sin^2 \phi + \omega_s^2) \pm \frac{1}{2} \sqrt{(4\omega_{ie}^2 \sin^2 \phi + \omega_s^2)^2 - 8\omega_s^2 \omega_{ie}^2 \sin^2 \phi}$
$\delta\omega_{ib,d}$	$H_{6,13}(s) = \frac{(s^2 + \omega_{6,13+}^2)(s^2 + \omega_{6,13-}^2) \omega_{ie} \cos \phi}{s(s^2 + \omega_{s-}^2)(s^2 + \omega_{s+}^2)(s^2 + \omega_{ie}^2)}$ $h_{6,13}(t) = \left(\frac{\omega_{6,13-}^2 \omega_{6,13+}^2}{\omega_{s+}^2 \omega_{s-}^2 \omega_{ie}^2} - \frac{\omega_{s-}^4 - \omega_{s-}^2 (\omega_{6,13+}^2 + \omega_{6,13-}^2) + \omega_{6,13+}^2 \omega_{6,13-}^2}{\omega_{s-}^2 (\omega_{s-}^2 - \omega_{s+}^2) (\omega_{s-}^2 - \omega_{ie}^2)} \cos(\omega_{s-} t) \right. \\ \left. - \frac{\omega_{s+}^4 - \omega_{s+}^2 (\omega_{6,13+}^2 + \omega_{6,13-}^2) + \omega_{6,13+}^2 \omega_{6,13-}^2}{\omega_{s+}^2 (\omega_{s+}^2 - \omega_{s-}^2) (\omega_{s+}^2 - \omega_{ie}^2)} \cos(\omega_{s+} t) + \right. \\ \left. - \frac{\omega_{ie}^4 - \omega_{ie}^2 (\omega_{6,13+}^2 + \omega_{6,13-}^2) + \omega_{6,13+}^2 \omega_{6,13-}^2}{\omega_{ie}^2 (\omega_{ie}^2 - \omega_{s-}^2) (\omega_{ie}^2 - \omega_{s+}^2)} \cos(\omega_{ie} t) \right) \omega_{ie} \cos \phi$ $\omega_{6,13\pm}^2 = \frac{1}{2} (4\omega_{ie}^2 \sin^2 \phi + \omega_s^2) \pm \frac{1}{2} \sqrt{(4\omega_{ie}^2 \sin^2 \phi + \omega_s^2)^2 + 8\omega_s^2 \omega_{ie}^2 \sin^2 \phi}$

Table D.23.: Yaw angle error step responses to accelerometer biases.

Input	Step response
$\delta f_{b,n}$	$H_{7,8}(s) = \frac{\frac{2}{R}\omega_{ie} \tan \phi \sin \phi}{(s^2 + \omega_{s_-}^2)(s^2 + \omega_{s_+}^2)}$ $h_{7,8}(t) = -\left(\frac{1}{\omega_{s_-}(\omega_{s_-}^2 - \omega_{s_+}^2)} \sin(\omega_{s_-} t) + \frac{1}{\omega_{s_+}(\omega_{s_+}^2 - \omega_{s_-}^2)} \sin(\omega_{s_+} t)\right) \frac{2}{R}\omega_{ie} \sin \phi \tan \phi$
$\delta f_{b,e}$	$H_{7,9}(s) = \frac{\frac{1}{R} \tan \phi s}{(s^2 + \omega_{s_-}^2)(s^2 + \omega_{s_+}^2)} + \frac{\frac{1}{R}\omega_s^2 \tan \phi}{s(s^2 + \omega_{s_-}^2)(s^2 + \omega_{s_+}^2)}$ $h_{7,9}(t) = \left(\frac{\omega_s^2}{\omega_{s_-}^2 \omega_{s_+}^2} - \frac{\omega_{s_-}^2 - \omega_s^2}{\omega_{s_-}^2(\omega_{s_-}^2 - \omega_{s_+}^2)} \cos(\omega_{s_-} t) - \frac{\omega_{s_+}^2 - \omega_s^2}{\omega_{s_+}^2(\omega_{s_+}^2 - \omega_{s_-}^2)} \cos(\omega_{s_+} t)\right) \frac{1}{R} \tan \phi$
$\delta f_{b,d}$	$H_{7,10}(s) = 0$ $h_{7,10}(t) = 0$

Table D.24.: Yaw angle error step responses to gyroscope biases.

Input	Step response
$\delta\omega_{ib,n}$	$H_{7,11}(s) = \frac{(\omega_s^2 - \omega_{ie}^2 \cos^2 \phi) \tan \phi s^2}{(s^2 + \omega_{s-}^2)(s^2 + \omega_{s+}^2)(s^2 + \omega_{ie}^2)}$ $+ \frac{(4\omega_{ie}^4 \sin^2 \phi \cos^2 \phi - \omega_s^2 \omega_{ie}^2 (\sin^2 \phi + 1) + \omega_s^4) \tan \phi}{(s^2 + \omega_{s-}^2)(s^2 + \omega_{s+}^2)(s^2 + \omega_{ie}^2)}$ $h_{7,11}(t) = \left(\frac{4\omega_{ie}^4 \sin^2 \phi \cos^2 \phi - \omega_s^2 \omega_{ie}^2 (\sin^2 \phi + 1) + \omega_s^4 - (\omega_s^2 - \omega_{ie}^2 \cos^2 \phi) \omega_{s+}^2}{\omega_{s-} (\omega_{s-}^2 - \omega_{s+}^2) (\omega_{s-}^2 - \omega_{ie}^2)} \sin(\omega_{s-} t) \right.$ $+ \frac{4\omega_{ie}^4 \sin^2 \phi \cos^2 \phi - \omega_s^2 \omega_{ie}^2 (\sin^2 \phi + 1) + \omega_s^4 - (\omega_s^2 - \omega_{ie}^2 \cos^2 \phi) \omega_{s-}^2}{\omega_{s+} (\omega_{s+}^2 - \omega_{s-}^2) (\omega_{s+}^2 - \omega_{ie}^2)} \sin(\omega_{s+} t) +$ $\left. + \frac{4\omega_{ie}^4 \sin^2 \phi \cos^2 \phi - \omega_s^2 \omega_{ie}^2 (\sin^2 \phi + 1) + \omega_s^4 - (\omega_s^2 - \omega_{ie}^2 \cos^2 \phi) \omega_{ie}^2}{\omega_{ie} (\omega_{ie}^2 - \omega_{s-}^2) (\omega_{ie}^2 - \omega_{s+}^2)} \sin(\omega_{ie} t) \right) \tan \phi$
$\delta\omega_{ib,e}$	$H_{7,12}(s) = -\frac{(s^2 + \omega_{7,12+}^2)(s^2 + \omega_{7,12-}^2) \omega_{ie} \cos \phi}{s(s^2 + \omega_{s-}^2)(s^2 + \omega_{s+}^2)(s^2 + \omega_{ie}^2)}$ $h_{7,12}(t) = \left(-\frac{\omega_{7,12-}^2 \omega_{7,12+}^2}{\omega_{s+}^2 \omega_{s-}^2 \omega_{ie}^2} + \frac{\omega_{s-}^4 - \omega_{s-}^2 (\omega_{7,12+}^2 + \omega_{6,13-}^2) + \omega_{7,12+}^2 \omega_{7,12-}^2}{\omega_{s-}^2 (\omega_{s-}^2 - \omega_{s+}^2) (\omega_{s-}^2 - \omega_{ie}^2)} \cos(\omega_{s-} t) \right.$ $+ \frac{\omega_{s+}^4 - \omega_{s+}^2 (\omega_{7,12+}^2 + \omega_{7,12-}^2) + \omega_{7,12+}^2 \omega_{7,12-}^2}{\omega_{s+}^2 (\omega_{s+}^2 - \omega_{s-}^2) (\omega_{s+}^2 - \omega_{ie}^2)} \cos(\omega_{s+} t) +$ $\left. + \frac{\omega_{ie}^4 - \omega_{ie}^2 (\omega_{7,12+}^2 + \omega_{7,12-}^2) + \omega_{7,12+}^2 \omega_{7,12-}^2}{\omega_{ie}^2 (\omega_{ie}^2 - \omega_{s-}^2) (\omega_{ie}^2 - \omega_{s+}^2)} \cos(\omega_{ie} t) \right) \omega_{ie} \cos \phi$ $\omega_{7,12\pm}^2 = \frac{1}{2} \left(4\omega_{ie}^2 \sin^2 \phi - \omega_s^2 + \frac{3\omega_s^2}{\cos^2 \phi} \right) \pm \frac{1}{2} \sqrt{\left(4\omega_{ie}^2 \sin^2 \phi - \omega_s^2 + \frac{3\omega_s^2}{\cos^2 \phi} \right)^2 - 4\omega_s^4}$
$\delta\omega_{ib,d}$	$H_{7,13}(s) = \frac{(s^2 + \omega_{7,13+}^2)(s^2 + \omega_{7,13-}^2)}{(s^2 + \omega_{s-}^2)(s^2 + \omega_{s+}^2)(s^2 + \omega_{ie}^2)}$ $h_{7,13}(t) = \left(\frac{\omega_{s-}^4 - \omega_{s-}^2 (\omega_{7,13+}^2 + \omega_{7,13-}^2) + \omega_{7,13+}^2 \omega_{7,13-}^2}{\omega_{s-} (\omega_{s-}^2 - \omega_{s+}^2) (\omega_{s-}^2 - \omega_{ie}^2)} \sin(\omega_{s-} t) \right.$ $+ \frac{\omega_{s+}^4 - \omega_{s+}^2 (\omega_{7,13+}^2 + \omega_{7,13-}^2) + \omega_{7,13+}^2 \omega_{7,13-}^2}{\omega_{s+} (\omega_{s+}^2 - \omega_{s-}^2) (\omega_{s+}^2 - \omega_{ie}^2)} \sin(\omega_{s+} t) +$ $\left. + \frac{\omega_{ie}^4 - \omega_{ie}^2 (\omega_{7,13+}^2 + \omega_{7,13-}^2) + \omega_{7,13+}^2 \omega_{7,13-}^2}{\omega_{ie} (\omega_{ie}^2 - \omega_{s-}^2) (\omega_{ie}^2 - \omega_{s+}^2)} \sin(\omega_{ie} t) \right)$ $\omega_{7,13\pm}^2 = \frac{1}{2} (5\omega_{ie}^2 \sin^2 \phi + 2\omega_s^2)$ $\pm \frac{1}{2} \sqrt{(5\omega_{ie}^2 \sin^2 \phi + 2\omega_s^2)^2 - 4(4\omega_{ie}^4 \sin^2 \phi - \omega_s^2 \omega_{ie}^2 \sin^2 \phi + \omega_s^4)}$

D.2. Impulse Responses

D.2.1. Position Errors Impulse Responses to Sensor Errors

Table D.25.: Latitude error pulse responses to accelerometer errors.

Input	Transfer function / impulse response
$\delta f_{b,n}$	$G_{1,8}(s) = \frac{\frac{1}{R}s^2}{(s^2 + \omega_{s-}^2)(s^2 + \omega_{s+}^2)} + \frac{\frac{\omega_s^2}{R}}{(s^2 + \omega_{s-}^2)(s^2 + \omega_{s+}^2)}$ $g_{1,8}(t) = \left(\frac{\omega_{s-}^2 - \omega_s^2}{\omega_{s-}(\omega_{s-}^2 - \omega_{s+}^2)} \sin(\omega_{s-}t) + \frac{\omega_{s+}^2 - \omega_s^2}{\omega_{s+}(\omega_{s+}^2 - \omega_{s-}^2)} \sin(\omega_{s+}t) \right) \frac{1}{R}$
$\delta f_{b,e}$	$G_{1,9}(s) = \frac{\frac{2}{R}\omega_{ie} \sin \tilde{\phi} s}{(s^2 + \omega_{s-}^2)(s^2 + \omega_{s+}^2)}$ $g_{1,9}(t) = \left(\frac{1}{(\omega_{s-}^2 - \omega_{s+}^2)} \sin(\omega_{s-}t) + \frac{1}{(\omega_{s+}^2 - \omega_{s-}^2)} \sin(\omega_{s+}t) \right) \frac{2}{R}\omega_{ie} \sin \tilde{\phi}$
$\delta f_{b,d}$	$G_{1,10}(s) = 0$ $g_{1,10}(t) = 0$

Table D.26.: Latitude error impulse responses to gyroscope errors.

Input	Transfer function / impulse response
$\delta\omega_{ib,n}$	$G_{1,11}(s) = -\frac{3\omega_s^2\omega_{ie}\sin\tilde{\phi}s}{(s^2 + \omega_{ie}^2)(s^2 + \omega_{s-}^2)(s^2 + \omega_{s+}^2)} - \frac{\omega_s^2\omega_{ie}\sin\tilde{\phi}(\omega_s^2 - 2\omega_{ie}\cos^2\tilde{\phi})}{(s^2 + \omega_{ie}^2)(s^2 + \omega_{s-}^2)(s^2 + \omega_{s+}^2)}$ $g_{1,11}(t) = \left(\frac{3\omega_{s-}^2 - 2\omega_{ie}^2\cos\tilde{\phi} - \omega_s^2}{\omega_{s-}(\omega_{s-}^2 - \omega_{s+}^2)(\omega_{s-}^2 - \omega_{ie}^2)} \sin(\omega_{s-}t) + \frac{3\omega_{s+}^2 - 2\omega_{ie}^2\cos\tilde{\phi} - \omega_s^2}{\omega_{s+}(\omega_{s+}^2 - \omega_{s-}^2)(\omega_{s+}^2 - \omega_{ie}^2)} \sin(\omega_{s+}t) \right. \\ \left. + \frac{3\omega_{ie}^2 - 2\omega_{ie}^2\cos\tilde{\phi} - \omega_s^2}{\omega_{ie}(\omega_{ie}^2 - \omega_{s-}^2)(\omega_{ie}^2 - \omega_{s+}^2)} \sin(\omega_{ie}t) \right) \omega_s^2\omega_{ie}\sin\tilde{\phi}$
$\delta\omega_{ib,e}$	$G_{1,12}(s) = -\frac{\omega_s s^3}{(s^2 + \omega_{ie}^2)(s^2 + \omega_{s-}^2)(s^2 + \omega_{s+}^2)} - \frac{\omega_s^2(\omega_s^2 - 2\omega_{ie}^2\sin^2\tilde{\phi})s}{(s^2 + \omega_{ie}^2)(s^2 + \omega_{s-}^2)(s^2 + \omega_{s+}^2)}$ $g_{1,12}(t) = \left(\frac{\omega_{s-}^2 + 2\omega_{ie}^2\cos\tilde{\phi} - \omega_s^2}{(\omega_{s-}^2 - \omega_{s+}^2)(\omega_{s-}^2 - \omega_{ie}^2)} \cos(\omega_{s-}t) + \frac{\omega_{s+}^2 + 2\omega_{ie}^2\cos\tilde{\phi} - \omega_s^2}{(\omega_{s+}^2 - \omega_{s-}^2)(\omega_{s+}^2 - \omega_{ie}^2)} \cos(\omega_{s+}t) \right. \\ \left. + \frac{\omega_{ie}^2 + 2\omega_{ie}^2\cos\tilde{\phi} - \omega_s^2}{(\omega_{ie}^2 - \omega_{s-}^2)(\omega_{ie}^2 - \omega_{s+}^2)} \cos(\omega_{ie}t) \right) \omega_s^2$
$\delta\omega_{ib,d}$	$G_{1,13}(s) = -\frac{\omega_s^2\omega_{ie}\cos\tilde{\phi}s^2}{(s^2 + \omega_{ie}^2)(s^2 + \omega_{s-}^2)(s^2 + \omega_{s+}^2)} - \frac{\omega_s^2\omega_{ie}\cos\tilde{\phi}(\omega_s^2 - 2\omega_{ie}^2\sin^2\tilde{\phi})}{(s^2 + \omega_{ie}^2)(s^2 + \omega_{s-}^2)(s^2 + \omega_{s+}^2)}$ $g_{1,13}(t) = \left(\frac{3\omega_{s-}^2 - 2\omega_{ie}^2\cos\tilde{\phi} - \omega_s^2}{\omega_{s-}(\omega_{s-}^2 - \omega_{s+}^2)(\omega_{s-}^2 - \omega_{ie}^2)} \sin(\omega_{s-}t) + \frac{3\omega_{s+}^2 - 2\omega_{ie}^2\cos\tilde{\phi} - \omega_s^2}{\omega_{s+}(\omega_{s+}^2 - \omega_{s-}^2)(\omega_{s+}^2 - \omega_{ie}^2)} \sin(\omega_{s+}t) \right. \\ \left. + \frac{3\omega_{ie}^2 - 2\omega_{ie}^2\cos\tilde{\phi} - \omega_s^2}{\omega_{ie}(\omega_{ie}^2 - \omega_{s-}^2)(\omega_{ie}^2 - \omega_{s+}^2)} \sin(\omega_{ie}t) \right) \omega_s^2\omega_{ie}\sin\tilde{\phi}$

Table D.27.: Longitude error impulse responses to accelerometer errors.

Input	Transfer function / impulse response
$\delta f_{b,n}$	$G_{2,8}(s) = \frac{\frac{2}{R}\omega_{ie}\tan\tilde{\phi}s}{(s^2 + \omega_{s-}^2)(s^2 + \omega_{s+}^2)}$ $g_{2,8}(t) = \left(\frac{1}{(\omega_{s-}^2 - \omega_{s+}^2)} \cos(\omega_{s-}t) + \frac{1}{(\omega_{s+}^2 - \omega_{s-}^2)} \cos(\omega_{s+}t) \right) \frac{2}{R}\omega_{ie}\tan\tilde{\phi}$
$\delta f_{b,e}$	$G_{2,9}(s) = \frac{\frac{1}{R\cos\tilde{\phi}}s^2}{(s^2 + \omega_{s-}^2)(s^2 + \omega_{s+}^2)} + \frac{\frac{\omega_s^2}{R\cos\tilde{\phi}}}{(s^2 + \omega_{s-}^2)(s^2 + \omega_{s+}^2)}$ $g_{2,9}(t) = \left(\frac{\omega_{s-}^2 - \omega_s^2}{\omega_{s-}(\omega_{s-}^2 - \omega_{s+}^2)} \sin(\omega_{s-}t) + \frac{\omega_{s+}^2 - \omega_s^2}{\omega_{s+}(\omega_{s+}^2 - \omega_{s-}^2)} \sin(\omega_{s+}t) \right) \frac{1}{R\cos\tilde{\phi}}$
$\delta f_{b,d}$	$G_{2,10}(s) = 0$ $g_{2,10}(t) = 0$

Table D.28.: Longitude error impulse responses to gyroscope errors.

Input	Transfer function / impulse response
$\delta\omega_{ib,n}$	$G_{2,11}(s) = \frac{\omega_s^2(s^2 + \omega_3^2)(s^2 + \omega_4^2)}{s(s^2 + \omega_{ie}^2)(s^2 + \omega_{s-}^2)(s^2 + \omega_{s+}^2)} \frac{1}{\cos \tilde{\phi}}$ $g_{2,11}(t) = \left(\frac{\omega_3^2 \omega_4^2}{\omega_{s-}^2 \omega_{s+}^2 \omega_{ie}^2} - \frac{\omega_{s-}^4 - \omega_{s-}^2(\omega_3^2 + \omega_4^2) + \omega_3^2 \omega_4^2}{\omega_{s-}^2(\omega_{s-}^2 - \omega_{s+}^2)(\omega_{s-}^2 - \omega_{ie}^2)} \cos(\omega_{s-} t) \right. \\ \left. - \frac{\omega_{s+}^4 - \omega_{s+}^2(\omega_3^2 + \omega_4^2) + \omega_3^2 \omega_4^2}{\omega_{s+}^2(\omega_{s+}^2 - \omega_{s-}^2)(\omega_{s+}^2 - \omega_{ie}^2)} \cos(\omega_{s+} t) \right. \\ \left. - \frac{\omega_{ie}^4 - \omega_{ie}^2(\omega_3^2 + \omega_4^2) + \omega_3^2 \omega_4^2}{\omega_{ie}^2(\omega_{ie}^2 - \omega_{s-}^2)(\omega_{ie}^2 - \omega_{s+}^2)} \cos(\omega_{ie} t) \right) \frac{\omega_s^2}{\cos \tilde{\phi}}$
$\delta\omega_{ib,e}$	$G_{2,12}(s) = -\frac{3\omega_s \omega_{ie} \tan \tilde{\phi} s^2}{(s^2 + \omega_{ie}^2)(s^2 + \omega_{s-}^2)(s^2 + \omega_{s+}^2)} - \frac{\omega_s^4 \omega_{ie} \tan \tilde{\phi}}{(s^2 + \omega_{ie}^2)(s^2 + \omega_{s-}^2)(s^2 + \omega_{s+}^2)}$ $g_{2,12}(t) = \left(\frac{3\omega_{s-}^2 - \omega_s^2}{\omega_{s-}(\omega_{s-}^2 - \omega_{s+}^2)(\omega_{s-}^2 - \omega_{ie}^2)} \sin(\omega_{s-} t) + \frac{3\omega_{s+}^2 - \omega_s^2}{\omega_{s+}(\omega_{s+}^2 - \omega_{s-}^2)(\omega_{s+}^2 - \omega_{ie}^2)} \sin(\omega_{s+} t) \right. \\ \left. + \frac{3\omega_{ie}^2 - \omega_s^2}{\omega_{ie}(\omega_{ie}^2 - \omega_{s-}^2)(\omega_{ie}^2 - \omega_{s+}^2)} \sin(\omega_{ie} t) \right) \omega_s^2 \omega_{ie} \tan \tilde{\phi}$
$\delta\omega_{ib,d}$	$G_{2,13}(s) = -\frac{3\omega_s \omega_{ie}^2 \sin \tilde{\phi} s}{(s^2 + \omega_{ie}^2)(s^2 + \omega_{s-}^2)(s^2 + \omega_{s+}^2)} - \frac{\omega_s^4 \omega_{ie}^2 \sin \tilde{\phi}}{(s^2 + \omega_{ie}^2)(s^2 + \omega_{s-}^2)(s^2 + \omega_{s+}^2)}$ $g_{2,13}(t) = \left(-\frac{\omega_s^2}{\omega_{s-}^2 \omega_{s+}^2 \omega_{ie}^2} + \frac{\omega_s^2 - 3\omega_{s-}^2}{\omega_{s-}^2(\omega_{s-}^2 - \omega_{s+}^2)(\omega_{s-}^2 - \omega_{ie}^2)} \cos(\omega_{s-} t) \right. \\ \left. + \frac{\omega_s^2 - 3\omega_{s+}^2}{\omega_{s+}^2(\omega_{s+}^2 - \omega_{s-}^2)(\omega_{s+}^2 - \omega_{ie}^2)} \cos(\omega_{s+} t) \right. \\ \left. + \frac{\omega_s^2 - 3\omega_{ie}^2}{\omega_{ie}^2(\omega_{ie}^2 - \omega_{s-}^2)(\omega_{ie}^2 - \omega_{s+}^2)} \cos(\omega_{ie} t) \right) \omega_s^2 \omega_{ie}^2 \sin \tilde{\phi}$

D.2.2. Velocity Errors Impulse Responses to Sensor Errors

Table D.29.: North velocity error impulse responses to accelerometer errors.

Input	Transfer function / impulse response
$\delta f_{b,n}$	$G_{3,8}(s) = \frac{s^2}{(s^2 + \omega_{s-}^2)(s^2 + \omega_{s+}^2)} + \frac{\omega_{s-}^2 s}{(s^2 + \omega_{s-}^2)(s^2 + \omega_{s+}^2)}$ $g_{3,8}(t) = \left(\frac{\omega_{s-}^2 - \omega_{s+}^2}{(\omega_{s-}^2 - \omega_{s+}^2)} \cos(\omega_{s-} t) + \frac{\omega_{s-}^2 - \omega_{s+}^2}{(\omega_{s+}^2 - \omega_{s-}^2)} \cos(\omega_{s+} t) \right)$
$\delta f_{b,e}$	$G_{3,9}(s) = \frac{2\omega_{ie} \sin \tilde{\phi} s^2}{(s^2 + \omega_{s-}^2)(s^2 + \omega_{s+}^2)}$ $g_{3,9}(t) = \left(\frac{\omega_{s-}}{(\omega_{s-}^2 - \omega_{s+}^2)} \sin(\omega_{s-} t) + \frac{\omega_{s+}}{(\omega_{s+}^2 - \omega_{s-}^2)} \sin(\omega_{s+} t) \right) 2\omega_{ie} \sin \tilde{\phi}$
$\delta f_{b,d}$	$G_{3,10}(s) = 0$ $g_{3,10}(t) = 0$

Table D.30.: North velocity error impulse responses to gyroscope errors.

Input	Transfer function / impulse response
$\delta\omega_{ib,n}$	$G_{3,11}(s) = -\frac{3\omega_s^2\omega_{ie}\sin\tilde{\phi}Rs^3}{(s^2 + \omega_{ie}^2)(s^2 + \omega_{s-}^2)(s^2 + \omega_{s+}^2)} - \frac{\omega_s^2\omega_{ie}\sin\phi(2\omega_{ie}^2\cos^2\phi + \omega_s^2)Rs}{(s^2 + \omega_{ie}^2)(s^2 + \omega_{s-}^2)(s^2 + \omega_{s+}^2)}$ $g_{3,11}(t) = \left(\frac{2\omega_{ie}^2\cos^2\tilde{\phi} + \omega_s^2 - 3\omega_{s-}^2}{(\omega_{s-}^2 - \omega_{s+}^2)(\omega_{s-}^2 - \omega_{ie}^2)} \cos(\omega_{s-}t) \right. \\ \left. + \frac{2\omega_{ie}^2\cos^2\tilde{\phi} + \omega_s^2 - 3\omega_{s+}^2}{(\omega_{s+}^2 - \omega_{s-}^2)(\omega_{s+}^2 - \omega_{ie}^2)} \cos(\omega_{s+}t) \right. \\ \left. + \frac{2\omega_{ie}^2\cos^2\tilde{\phi} + \omega_s^2 - 3\omega_{ie}^2}{(\omega_{ie}^2 - \omega_{s-}^2)(\omega_{ie}^2 - \omega_{s+}^2)} \cos(\omega_{ie}t) \right) \omega_s^2\omega_{ie}R\sin\tilde{\phi}$
$\delta\omega_{ib,e}$	$G_{3,12}(s) = -\frac{\omega_sRs^4}{(s^2 + \omega_{ie}^2)(s^2 + \omega_{s-}^2)(s^2 + \omega_{s+}^2)} - \frac{\omega_s^2(\omega_s^2 - 2\omega_{ie}^2\sin^2\tilde{\phi})Rs^2}{(s^2 + \omega_{ie}^2)(s^2 + \omega_{s-}^2)(s^2 + \omega_{s+}^2)}$ $g_{3,12}(t) = -\left(\frac{\omega_{s-}^2 - 2\omega_{ie}^2\cos^2\tilde{\phi} - \omega_s^2}{(\omega_{s-}^2 - \omega_{s+}^2)(\omega_{s-}^2 - \omega_{ie}^2)} \sin(\omega_{s-}t) + \frac{\omega_{s+}^2 - 2\omega_{ie}^2\cos^2\tilde{\phi} - \omega_s^2}{(\omega_{s+}^2 - \omega_{s-}^2)(\omega_{s+}^2 - \omega_{ie}^2)} \sin(\omega_{s+}t) \right. \\ \left. + \frac{\omega_{ie}^2 - 2\omega_{ie}^2\cos^2\tilde{\phi} - \omega_s^2}{(\omega_{ie}^2 - \omega_{s-}^2)(\omega_{ie}^2 - \omega_{s+}^2)} \sin(\omega_{ie}t) \right) \omega_s^2R$
$\delta\omega_{ib,d}$	$G_{3,13}(s) = -\frac{\omega_s^2\omega_{ie}\cos^2\tilde{\phi}Rs^3}{(s^2 + \omega_{ie}^2)(s^2 + \omega_{s-}^2)(s^2 + \omega_{s+}^2)} - \frac{\omega_s^2\omega_{ie}\cos^2\tilde{\phi}(\omega_s^2 - 2\omega_{ie}^2\sin^2\tilde{\phi})Rs}{(s^2 + \omega_{ie}^2)(s^2 + \omega_{s-}^2)(s^2 + \omega_{s+}^2)}$ $g_{3,13}(t) = \left(\frac{2\omega_{ie}^2\cos^2\tilde{\phi} + \omega_s^2 - \omega_{s-}^2}{(\omega_{s-}^2 - \omega_{s+}^2)(\omega_{s-}^2 - \omega_{ie}^2)} \cos(\omega_{s-}t) \right. \\ \left. + \frac{2\omega_{ie}^2\cos^2\tilde{\phi} + \omega_s^2 - \omega_{s+}^2}{(\omega_{s+}^2 - \omega_{s-}^2)(\omega_{s+}^2 - \omega_{ie}^2)} \cos(\omega_{s+}t) \right. \\ \left. + \frac{2\omega_{ie}^2\cos\tilde{\phi} + \omega_s^2 - \omega_{ie}^2}{(\omega_{ie}^2 - \omega_{s-}^2)(\omega_{ie}^2 - \omega_{s+}^2)} \cos(\omega_{ie}t) \right) \omega_s^2\omega_{ie}R\cos\tilde{\phi}$

Table D.31.: East velocity error impulse responses to accelerometer errors.

Input	Transfer function / impulse response
$\delta f_{b,n}$	$G_{4,8}(s) = -\frac{2\omega_{ie}\sin\tilde{\phi}s^2}{(s^2 + \omega_{s-}^2)(s^2 + \omega_{s+}^2)}$ $g_{4,8}(t) = \left(\frac{\omega_{s-}}{(\omega_{s-}^2 - \omega_{s+}^2)} \sin(\omega_{s-}t) + \frac{\omega_{s+}}{(\omega_{s+}^2 - \omega_{s-}^2)} \sin(\omega_{s+}t) \right) 2\omega_{ie}\sin\tilde{\phi}$
$\delta f_{b,e}$	$G_{4,9}(s) = \frac{s^3}{(s^2 + \omega_{s-}^2)(s^2 + \omega_{s+}^2)} + \frac{\omega_s^2s}{(s^2 + \omega_{s-}^2)(s^2 + \omega_{s+}^2)}$ $g_{4,9}(t) = -\left(\frac{\omega_s^2 - \omega_{s-}^2}{(\omega_{s-}^2 - \omega_{s+}^2)} \cos(\omega_{s-}t) + \frac{\omega_s^2 - \omega_{s+}^2}{(\omega_{s+}^2 - \omega_{s-}^2)} \cos(\omega_{s+}t) \right)$
$\delta f_{b,d}$	$G_{4,10}(s) = 0$ $g_{4,10}(t) = 0$

Table D.32.: East velocity error impulse responses to gyroscope errors.

Input	Transfer function / impulse response
$\delta\omega_{ib,n}$	$G_{4,11}(s) = \frac{\omega_s^2(s^2 + \omega_{2,11+}^2)(s^2 + \omega_{2,11-}^2)R}{(s^2 + \omega_{ie}^2)(s^2 + \omega_{s-}^2)(s^2 + \omega_{s+}^2)}$ $g_{4,11}(t) = \left(\frac{\omega_{s-}^4 - \omega_{s-}^2(\omega_{2,11+}^2 + \omega_{2,11-}^2) + \omega_{2,11+}^2\omega_{2,11-}^2}{\omega_{s-}(\omega_{s-}^2 - \omega_{s+}^2)(\omega_{s-}^2 - \omega_{ie}^2)} \sin(\omega_{s-}t) \right. \\ \left. + \frac{\omega_{s+}^4 - \omega_{s+}^2(\omega_{2,11+}^2 + \omega_{2,11-}^2) + \omega_{2,11+}^2\omega_{2,11-}^2}{\omega_{s+}(\omega_{s+}^2 - \omega_{s-}^2)(\omega_{s+}^2 - \omega_{ie}^2)} \sin(\omega_{s+}t) \right. \\ \left. + \frac{\omega_{ie}^4 - \omega_{ie}^2(\omega_{2,11+}^2 + \omega_{2,11-}^2) + \omega_{2,11+}^2\omega_{2,11-}^2}{\omega_{ie}(\omega_{ie}^2 - \omega_{s-}^2)(\omega_{ie}^2 - \omega_{s+}^2)} \sin(\omega_{ie}t) \right) \omega_s^2 R$ $\omega_{2,11\pm}^2 = \frac{\omega_s^2 + 3\omega_{ie}^2 \cos^2 \tilde{\phi}}{2} + \omega_{ie}^2 \pm \frac{1}{2} \sqrt{(3\omega_{ie}^2 \cos^2 \tilde{\phi} + 2\omega_{ie}^2 + \omega_s^2)^2 - 4\omega_s^2\omega_{ie}^2 \cos^2 \tilde{\phi}}$
$\delta\omega_{ib,e}$	$G_{4,12}(s) = -\frac{3\omega_s\omega_{ie}R \sin \tilde{\phi} s^3}{(s^2 + \omega_{ie}^2)(s^2 + \omega_{s-}^2)(s^2 + \omega_{s+}^2)} - \frac{\omega_s^4\omega_{ie}R \sin \tilde{\phi} s}{(s^2 + \omega_{ie}^2)(s^2 + \omega_{s-}^2)(s^2 + \omega_{s+}^2)}$ $g_{4,12}(t) = -\left(\frac{\omega_s^2 - 3\omega_{s-}^2}{(\omega_{s-}^2 - \omega_{s+}^2)(\omega_{s-}^2 - \omega_{ie}^2)} \cos(\omega_{s-}t) + \frac{\omega_s^2 - 3\omega_{s+}^2}{(\omega_{s+}^2 - \omega_{s-}^2)(\omega_{s+}^2 - \omega_{ie}^2)} \cos(\omega_{s+}t) \right. \\ \left. + \frac{\omega_s^2 - 3\omega_{ie}^2}{(\omega_{ie}^2 - \omega_{s-}^2)(\omega_{ie}^2 - \omega_{s+}^2)} \cos(\omega_{ie}t) \right) \omega_s^2\omega_{ie}R \sin \tilde{\phi}$
$\delta\omega_{ib,d}$	$G_{4,13}(s) = -\frac{3\omega_s\omega_{ie}^2R \sin \tilde{\phi} \cos \tilde{\phi} s^2}{(s^2 + \omega_{ie}^2)(s^2 + \omega_{s-}^2)(s^2 + \omega_{s+}^2)} - \frac{\omega_s^4\omega_{ie}^2R \sin \tilde{\phi} \sin \tilde{\phi}}{(s^2 + \omega_{ie}^2)(s^2 + \omega_{s-}^2)(s^2 + \omega_{s+}^2)}$ $g_{4,13}(t) = -\left(\frac{\omega_s^2 - 3\omega_{s-}^2}{\omega_{s-}(\omega_{s-}^2 - \omega_{s+}^2)(\omega_{s-}^2 - \omega_{ie}^2)} \sin(\omega_{s-}t) + \frac{\omega_s^2 - 3\omega_{s+}^2}{\omega_{s+}(\omega_{s+}^2 - \omega_{s-}^2)(\omega_{s+}^2 - \omega_{ie}^2)} \sin(\omega_{s+}t) \right. \\ \left. + \frac{\omega_s^2 - 3\omega_{ie}^2}{\omega_{ie}(\omega_{ie}^2 - \omega_{s-}^2)(\omega_{ie}^2 - \omega_{s+}^2)} \sin(\omega_{ie}t) \right) \omega_s^2\omega_{ie}^2R \sin \tilde{\phi} \cos \tilde{\phi}$

D.2.3. Orientation Errors Impulse Responses to Sensor Errors

Table D.33.: Roll angle error impulse responses to accelerometer errors.

Input	Transfer function / impulse response
$\delta f_{b,n}$	$G_{5,8}(s) = -\frac{\frac{2}{R}\omega_{ie} \sin \phi s}{(s^2 + \omega_{s-}^2)(s^2 + \omega_{s+}^2)}$ $g_{5,8}(t) = \left(\frac{1}{(\omega_{s-}^2 - \omega_{s+}^2)} \cos(\omega_{s-} t) + \frac{1}{(\omega_{s+}^2 - \omega_{s-}^2)} \cos(\omega_{s+} t) \right) \frac{2}{R}\omega_{ie} \sin \tilde{\phi}$
$\delta f_{b,e}$	$G_{5,9}(s) = -\frac{\frac{1}{R}s^2}{(s^2 + \omega_{s-}^2)(s^2 + \omega_{s+}^2)} - \frac{\frac{1}{R}\omega_s^2}{(s^2 + \omega_{s-}^2)(s^2 + \omega_{s+}^2)}$ $g_{5,9}(t) = \left(-\frac{\omega_s^2 - \omega_{s-}^2}{\omega_{s-}(\omega_{s-}^2 - \omega_{s+}^2)} \sin(\omega_{s-} t) - \frac{\omega_s^2 - \omega_{s+}^2}{\omega_{s+}(\omega_{s+}^2 - \omega_{s-}^2)} \sin(\omega_{s+} t) \right) \frac{1}{R}$
$\delta f_{b,d}$	$G_{5,10}(s) = 0$ $g_{5,10}(t) = 0$

Table D.34.: Roll angle error impulse responses to gyroscope errors.

Input	Transfer function / impulse response
$\delta\omega_{ib,n}$	$G_{5,11}(s) = \frac{(s^2 + \omega_{s,11+}^2)(s^2 + \omega_{s,11-}^2)s}{(s^2 + \omega_{s-}^2)(s^2 + \omega_{s+}^2)(s^2 + \omega_{ie}^2)}$ $g_{5,11}(t) = \left(\frac{\omega_{s-}^4 - \omega_{s-}^2(\omega_{s,11+}^2 + \omega_{s,11-}^2) + \omega_{s,11+}^2\omega_{s,11-}^2}{\omega_{s-}(\omega_{s-}^2 - \omega_{s+}^2)(\omega_{s-}^2 - \omega_{ie}^2)} \cos(\omega_{s-}t) \right. \\ \left. + \frac{\omega_{s+}^4 - \omega_{s+}^2(\omega_{s,11+}^2 + \omega_{s,11-}^2) + \omega_{s,11+}^2\omega_{s,11-}^2}{\omega_{s+}(\omega_{s+}^2 - \omega_{s-}^2)(\omega_{s+}^2 - \omega_{ie}^2)} \cos(\omega_{s+}t) + \right. \\ \left. + \frac{\omega_{ie}^4 - \omega_{ie}^2(\omega_{s,11+}^2 + \omega_{s,11-}^2) + \omega_{s,11+}^2\omega_{s,11-}^2}{\omega_{ie}(\omega_{ie}^2 - \omega_{s-}^2)(\omega_{ie}^2 - \omega_{s+}^2)} \cos(\omega_{ie}t) \right)$ $\omega_{s,11\pm}^2 = \frac{1}{2} (3\omega_{ie}^2 \sin^2 \phi + \omega_{ie}^2 + \omega_s^2) \\ \pm \frac{1}{2} \sqrt{(3\omega_{ie}^2 \sin^2 \phi + \omega_{ie}^2 + \omega_s^2)^2 - 4\omega_{ie}^2 (4\omega_{ie}^2 \sin^2 \phi - 4\omega_{ie}^2 \sin^4 \phi + \omega_s^2 \sin^2 \phi + \omega_s^2)}$
$\delta\omega_{ib,e}$	$G_{5,12}(s) = -\frac{\omega_{ie} \sin \phi s^4}{(s^2 + \omega_{s-}^2)(s^2 + \omega_{s+}^2)(s^2 + \omega_{ie}^2)} - \frac{(\omega_{ie}^2 \sin^2 \phi - \omega_s^2) \omega_{ie} \sin \phi s^2}{(s^2 + \omega_{s-}^2)(s^2 + \omega_{s+}^2)(s^2 + \omega_{ie}^2)}$ $g_{5,12}(t) = -\left(\frac{(\omega_{s-}^2 - \omega_{ie}^2 \sin^2 \phi + \omega_s^2) \omega_{s-}}{(\omega_{s-}^2 - \omega_{s+}^2)(\omega_{s-}^2 - \omega_{ie}^2)} \sin(\omega_{s-}t) + \frac{(\omega_{s+}^2 - \omega_{ie}^2 \sin^2 \phi + \omega_s^2) \omega_{s+}}{(\omega_{s+}^2 - \omega_{s-}^2)(\omega_{s+}^2 - \omega_{ie}^2)} \sin(\omega_{s+}t) + \right. \\ \left. + \frac{(\omega_{ie}^2 - \omega_{ie}^2 \sin^2 \phi + \omega_s^2) \omega_{ie}}{(\omega_{ie}^2 - \omega_{s-}^2)(\omega_{ie}^2 - \omega_{s+}^2)} \sin(\omega_{ie}t) \right) \omega_{ie} \sin \phi$
$\delta\omega_{ib,d}$	$G_{5,13}(s) = \frac{\omega_{ie}^2 \sin \phi \cos \phi s^3}{(s^2 + \omega_{s-}^2)(s^2 + \omega_{s+}^2)(s^2 + \omega_{ie}^2)} - \frac{(4\omega_{ie}^2 \sin^3 \phi \cos \phi - \omega_s^2 \sin \phi \cos \phi) \omega_{ie}^2 s}{(s^2 + \omega_{s-}^2)(s^2 + \omega_{s+}^2)(s^2 + \omega_{ie}^2)}$ $g_{5,13}(t) = \left(\frac{\omega_s^2 - 4\omega_{ie}^2 \sin^2 \phi + \omega_{s-}^2 \omega_s^2}{(\omega_{s-}^2 - \omega_{s+}^2)(\omega_{s-}^2 - \omega_{ie}^2)} \cos(\omega_{s-}t) + \frac{\omega_s^2 - 4\omega_{ie}^2 \sin^2 \phi + \omega_{s+}^2 \omega_s^2}{(\omega_{s+}^2 - \omega_{s-}^2)(\omega_{s+}^2 - \omega_{ie}^2)} \cos(\omega_{s+}t) + \right. \\ \left. + \frac{\omega_s^2 - 4\omega_{ie}^2 \sin^2 \phi + \omega_{ie}^2 \omega_s^2}{(\omega_{ie}^2 - \omega_{s-}^2)(\omega_{ie}^2 - \omega_{s+}^2)} \cos(\omega_{ie}t) \right) \omega_{ie}^2 \sin \phi \cos \phi$

Table D.35.: Pitch angle error impulse responses to accelerometer errors.

Input	Transfer function / impulse response
$\delta f_{b,n}$	$G_{6,8}(s) = \frac{\frac{1}{R}s^2}{(s^2 + \omega_{s-}^2)(s^2 + \omega_{s+}^2)} + \frac{\frac{1}{R}\omega_s^2}{(s^2 + \omega_{s-}^2)(s^2 + \omega_{s+}^2)}$ $g_{6,8}(t) = \left(\frac{\omega_{s-}^2 - \omega_s^2}{\omega_{s-}(\omega_{s-}^2 - \omega_{s+}^2)} \sin(\omega_{s-}t) + \frac{\omega_{s+}^2 - \omega_s^2}{\omega_{s+}(\omega_{s+}^2 - \omega_{s-}^2)} \sin(\omega_{s+}t) \right) \frac{1}{R}$
$\delta f_{b,e}$	$G_{6,9}(s) = -\frac{\frac{2}{R}\omega_{ie} \sin \phi s}{(s^2 + \omega_{s-}^2)(s^2 + \omega_{s+}^2)}$ $g_{6,9}(t) = \left(\frac{1}{\omega_{s-}(\omega_{s-}^2 - \omega_{s+}^2)} \sin(\omega_{s-}t) + \frac{1}{\omega_{s+}(\omega_{s+}^2 - \omega_{s-}^2)} \sin(\omega_{s+}t) \right) \frac{2}{R}\omega_{ie} \sin \phi$
$\delta f_{b,d}$	$G_{6,10}(s) = 0$ $g_{6,10}(t) = 0$

Table D.36.: Pitch angle error impulse responses to gyroscope errors.

Input	Transfer function / impulse response
$\delta\omega_{ib,n}$	$G_{6,11}(s) = \frac{(s^2 + \omega_{6,11+}^2)(s^2 + \omega_{6,11-}^2) \omega_{ie} \sin \phi}{(s^2 + \omega_{s-}^2)(s^2 + \omega_{s+}^2)(s^2 + \omega_{ie}^2)}$ $g_{6,11}(t) = \left(\frac{\omega_{s-}^4 - \omega_{s-}^2 (\omega_{6,11+}^2 + \omega_{6,11-}^2) + \omega_{6,11+}^2 \omega_{6,11-}^2}{\omega_{s-} (\omega_{s-}^2 - \omega_{s+}^2) (\omega_{s-}^2 - \omega_{ie}^2)} \sin(\omega_{s-} t) \right. \\ \left. + \frac{\omega_{s+}^4 - \omega_{s+}^2 (\omega_{6,11+}^2 + \omega_{6,11-}^2) + \omega_{6,11+}^2 \omega_{6,11-}^2}{\omega_{s+} (\omega_{s+}^2 - \omega_{s-}^2) (\omega_{s+}^2 - \omega_{ie}^2)} \sin(\omega_{s+} t) + \right. \\ \left. + \frac{\omega_{ie}^4 - \omega_{ie}^2 (\omega_{6,11+}^2 + \omega_{6,11-}^2) + \omega_{6,11+}^2 \omega_{6,11-}^2}{\omega_{ie} (\omega_{ie}^2 - \omega_{s-}^2) (\omega_{ie}^2 - \omega_{s+}^2)} \sin(\omega_{ie} t) \right) \omega_{ie} \sin \phi$ $\omega_{6,11\pm}^2 = \frac{1}{2} (4\omega_{ie}^2 \sin^2 \phi - \omega_s^2) \pm \frac{1}{2} \sqrt{(4\omega_{ie}^2 \sin^2 \phi + \omega_s^2)^2 + 8\omega_s^2 \omega_{ie}^2 \cos^2 \phi}$
$\delta\omega_{ib,e}$	$G_{6,12}(s) = \frac{(s^2 + \omega_{6,12+}^2)(s^2 + \omega_{6,12-}^2)}{(s^2 + \omega_{s-}^2)(s^2 + \omega_{s+}^2)(s^2 + \omega_{ie}^2)}$ $g_{6,12}(t) = \left(\frac{\omega_{s-}^4 - \omega_{s-}^2 (\omega_{6,12+}^2 + \omega_{6,12-}^2) + \omega_{6,12+}^2 \omega_{6,12-}^2 s}{\omega_{s-} (\omega_{s-}^2 - \omega_{s+}^2) (\omega_{s-}^2 - \omega_{ie}^2)} \cos(\omega_{s-} t) \right. \\ \left. + \frac{\omega_{s+}^4 - \omega_{s+}^2 (\omega_{6,12+}^2 + \omega_{6,12-}^2) + \omega_{6,12+}^2 \omega_{6,12-}^2}{\omega_{s+} (\omega_{s+}^2 - \omega_{s-}^2) (\omega_{s+}^2 - \omega_{ie}^2)} \cos(\omega_{s+} t) + \right. \\ \left. + \frac{\omega_{ie}^4 - \omega_{ie}^2 (\omega_{6,12+}^2 + \omega_{6,12-}^2) + \omega_{6,12+}^2 \omega_{6,12-}^2}{\omega_{ie} (\omega_{ie}^2 - \omega_{s-}^2) (\omega_{ie}^2 - \omega_{s+}^2)} \cos(\omega_{ie} t) \right)$ $\omega_{6,12\pm}^2 = \frac{1}{2} (4\omega_{ie}^2 \sin^2 \phi + \omega_s^2) \pm \frac{1}{2} \sqrt{(4\omega_{ie}^2 \sin^2 \phi + \omega_s^2)^2 - 8\omega_s^2 \omega_{ie}^2 \sin^2 \phi}$
$\delta\omega_{ib,d}$	$G_{6,13}(s) = \frac{(s^2 + \omega_{6,13+}^2)(s^2 + \omega_{6,13-}^2) \omega_{ie} \cos \phi}{(s^2 + \omega_{s-}^2)(s^2 + \omega_{s+}^2)(s^2 + \omega_{ie}^2)}$ $g_{6,13}(t) = \left(\frac{\omega_{s-}^4 - \omega_{s-}^2 (\omega_{6,13+}^2 + \omega_{6,13-}^2) + \omega_{6,13+}^2 \omega_{6,13-}^2}{\omega_{s-} (\omega_{s-}^2 - \omega_{s+}^2) (\omega_{s-}^2 - \omega_{ie}^2)} \sin(\omega_{s-} t) \right. \\ \left. + \frac{\omega_{s+}^4 - \omega_{s+}^2 (\omega_{6,13+}^2 + \omega_{6,13-}^2) + \omega_{6,13+}^2 \omega_{6,13-}^2}{\omega_{s+} (\omega_{s+}^2 - \omega_{s-}^2) (\omega_{s+}^2 - \omega_{ie}^2)} \sin(\omega_{s+} t) + \right. \\ \left. + \frac{\omega_{ie}^4 - \omega_{ie}^2 (\omega_{6,13+}^2 + \omega_{6,13-}^2) + \omega_{6,13+}^2 \omega_{6,13-}^2}{\omega_{ie} (\omega_{ie}^2 - \omega_{s-}^2) (\omega_{ie}^2 - \omega_{s+}^2)} \sin(\omega_{ie} t) \right) \omega_{ie} \cos \phi$ $\omega_{6,13\pm}^2 = \frac{1}{2} (4\omega_{ie}^2 \sin^2 \phi + \omega_s^2) \pm \frac{1}{2} \sqrt{(4\omega_{ie}^2 \sin^2 \phi + \omega_s^2)^2 + 8\omega_s^2 \omega_{ie}^2 \sin^2 \phi}$

Table D.37.: Yaw angle error pulse responses to accelerometer errors.

Input	Transfer function / impulse response
$\delta f_{b,n}$	$G_{7,8}(s) = \frac{\frac{2}{R} \omega_{ie} \tan \phi \sin \phi s}{(s^2 + \omega_{s-}^2)(s^2 + \omega_{s+}^2)}$ $g_{7,8}(t) = - \left(\frac{1}{(\omega_{s-}^2 - \omega_{s+}^2)} \cos(\omega_{s-} t) + \frac{1}{(\omega_{s+}^2 - \omega_{s-}^2)} \cos(\omega_{s+} t) \right) \frac{2}{R} \omega_{ie} \sin \phi \tan \phi$
$\delta f_{b,e}$	$G_{7,9}(s) = \frac{\frac{1}{R} \tan \phi s^2}{(s^2 + \omega_{s-}^2)(s^2 + \omega_{s+}^2)} + \frac{\frac{1}{R} \omega_s^2 \tan \phi}{(s^2 + \omega_{s-}^2)(s^2 + \omega_{s+}^2)}$ $g_{7,9}(t) = \left(\frac{\omega_{s-}^2 - \omega_s^2}{\omega_{s-}^2 (\omega_{s-}^2 - \omega_{s+}^2)} \sin(\omega_{s-} t) + \frac{\omega_{s+}^2 - \omega_s^2}{\omega_{s+}^2 (\omega_{s+}^2 - \omega_{s-}^2)} \sin(\omega_{s+} t) \right) \frac{1}{R} \tan \phi$
$\delta f_{b,d}$	$G_{7,10}(s) = 0$ $g_{7,10}(t) = 0$

Table D.38.: Yaw angle error pulse responses to gyroscope errors.

Input	Transfer function / impulse response
$\delta\omega_{ib,n}$	$G_{7,11}(s) = \frac{(\omega_s^2 - \omega_{ie}^2 \cos^2 \phi) \tan \phi s^3}{(s^2 + \omega_{s-}^2)(s^2 + \omega_{s+}^2)(s^2 + \omega_{ie}^2)}$ $+ \frac{(4\omega_{ie}^4 \sin^2 \phi \cos^2 \phi - \omega_s^2 \omega_{ie}^2 (\sin^2 \phi + 1) + \omega_s^4) \tan \phi s}{(s^2 + \omega_{s-}^2)(s^2 + \omega_{s+}^2)(s^2 + \omega_{ie}^2)}$ $g_{7,11}(t) = \left(\frac{4\omega_{ie}^4 \sin^2 \phi \cos^2 \phi - \omega_s^2 \omega_{ie}^2 (\sin^2 \phi + 1) + \omega_s^4 - (\omega_s^2 - \omega_{ie}^2 \cos^2 \phi) \omega_{s+}^2}{(\omega_{s-}^2 - \omega_{s+}^2)(\omega_{s-}^2 - \omega_{ie}^2)} \cos(\omega_{s-} t) \right.$ $+ \frac{4\omega_{ie}^4 \sin^2 \phi \cos^2 \phi - \omega_s^2 \omega_{ie}^2 (\sin^2 \phi + 1) + \omega_s^4 - (\omega_s^2 - \omega_{ie}^2 \cos^2 \phi) \omega_{s-}^2}{(\omega_{s+}^2 - \omega_{s-}^2)(\omega_{s+}^2 - \omega_{ie}^2)} \cos(\omega_{s+} t) +$ $\left. + \frac{4\omega_{ie}^4 \sin^2 \phi \cos^2 \phi - \omega_s^2 \omega_{ie}^2 (\sin^2 \phi + 1) + \omega_s^4 - (\omega_s^2 - \omega_{ie}^2 \cos^2 \phi) \omega_{ie}^2}{(\omega_{ie}^2 - \omega_{s-}^2)(\omega_{ie}^2 - \omega_{s+}^2)} \cos(\omega_{ie} t) \right) \tan \phi$
$\delta\omega_{ib,e}$	$G_{7,12}(s) = -\frac{(s^2 + \omega_{7,12+}^2)(s^2 + \omega_{7,12-}^2) \omega_{ie} \cos \phi}{(s^2 + \omega_{s-}^2)(s^2 + \omega_{s+}^2)(s^2 + \omega_{ie}^2)}$ $g_{7,12}(t) = \left(-\frac{\omega_{s-}^4 - \omega_{s-}^2 (\omega_{7,12+}^2 + \omega_{6,13-}^2) + \omega_{7,12+}^2 \omega_{7,12-}^2}{\omega_{s-} (\omega_{s-}^2 - \omega_{s+}^2)(\omega_{s-}^2 - \omega_{ie}^2)} \sin(\omega_{s-} t) \right.$ $- \frac{\omega_{s+}^4 - \omega_{s+}^2 (\omega_{7,12+}^2 + \omega_{7,12-}^2) + \omega_{7,12+}^2 \omega_{7,12-}^2}{\omega_{s+} (\omega_{s+}^2 - \omega_{s-}^2)(\omega_{s+}^2 - \omega_{ie}^2)} \sin(\omega_{s+} t) +$ $\left. - \frac{\omega_{ie}^4 - \omega_{ie} (\omega_{7,12+}^2 + \omega_{7,12-}^2) + \omega_{7,12+}^2 \omega_{7,12-}^2}{\omega_{ie}^2 (\omega_{ie}^2 - \omega_{s-}^2)(\omega_{ie}^2 - \omega_{s+}^2)} \sin(\omega_{ie} t) \right) \omega_{ie} \cos \phi$ $\omega_{7,12\pm}^2 = \frac{1}{2} \left(4\omega_{ie}^2 \sin^2 \phi - \omega_s^2 + \frac{3\omega_s^2}{\cos^2 \phi} \right) \pm \frac{1}{2} \sqrt{\left(4\omega_{ie}^2 \sin^2 \phi - \omega_s^2 + \frac{3\omega_s^2}{\cos^2 \phi} \right)^2 - 4\omega_s^4}$
$\delta\omega_{ib,d}$	$G_{7,13}(s) = \frac{(s^2 + \omega_{7,13+}^2)(s^2 + \omega_{7,13-}^2) s}{(s^2 + \omega_{s-}^2)(s^2 + \omega_{s+}^2)(s^2 + \omega_{ie}^2)}$ $g_{7,13}(t) = \left(\frac{\omega_{s-}^4 - \omega_{s-}^2 (\omega_{7,13+}^2 + \omega_{7,13-}^2) + \omega_{7,13+}^2 \omega_{7,13-}^2}{(\omega_{s-}^2 - \omega_{s+}^2)(\omega_{s-}^2 - \omega_{ie}^2)} \cos(\omega_{s-} t) \right.$ $+ \frac{\omega_{s+}^4 - \omega_{s+}^2 (\omega_{7,13+}^2 + \omega_{7,13-}^2) + \omega_{7,13+}^2 \omega_{7,13-}^2}{(\omega_{s+}^2 - \omega_{s-}^2)(\omega_{s+}^2 - \omega_{ie}^2)} \cos(\omega_{s+} t) +$ $\left. + \frac{\omega_{ie}^4 - \omega_{ie}^2 (\omega_{7,13+}^2 + \omega_{7,13-}^2) + \omega_{7,13+}^2 \omega_{7,13-}^2}{(\omega_{ie}^2 - \omega_{s-}^2)(\omega_{ie}^2 - \omega_{s+}^2)} \cos(\omega_{ie} t) \right)$ $\omega_{7,13\pm}^2 = \frac{1}{2} (5\omega_{ie}^2 \sin^2 \phi + 2\omega_s^2)$ $\pm \frac{1}{2} \sqrt{(5\omega_{ie}^2 \sin^2 \phi + 2\omega_s^2)^2 - 4(4\omega_{ie}^4 \sin^2 \phi - \omega_s^2 \omega_{ie}^2 \sin^2 \phi + \omega_s^4)}$

Appendix E.

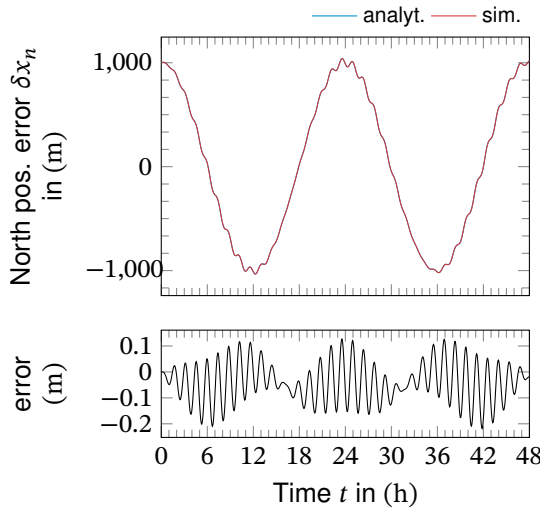
Validation of the Linearized Error Dynamics

E.1. System Response to Initialization Errors

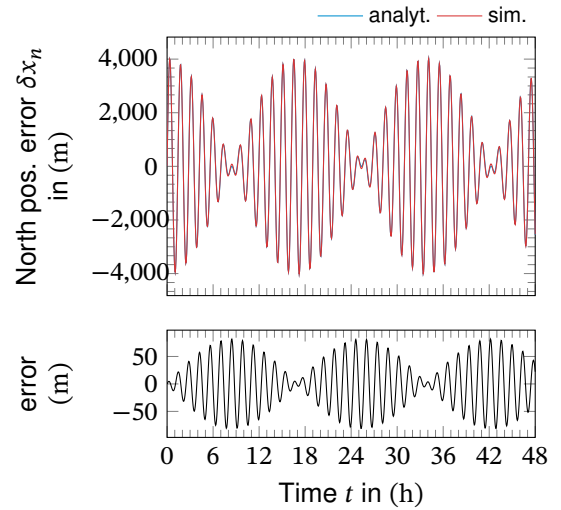
To evaluate the validity of the linearized error dynamics, the step responses of the latter are compared to the nonlinear simulation results. Therefore, the strapdown calculations are performed for a stationary vehicle at latitude of $\phi = 45^\circ$. The simulation is performed for different initialization errors and inertial measurement biases. The resulting graphs are presented in [Figure E.1](#) and [Figure E.2](#). Each graph is accompanied by a graph of the error between the two approaches. The absolute error is chosen here, as the relative error would provide misleading information in the vicinity of the zero-crossings.

The linearized step responses clearly show the same shape as the nonlinear references for all inputs. Still, a difference that grows with time can be observed. This growing difference arises from a difference in the frequencies between the linearized and the nonlinear system. In consequence, there is only little difference in the maximum amplitudes. Additionally, there must be differences in the three frequencies of the underlying oscillations that cause a slightly different shape of the modulations. This can be especially observed at the zero-crossings.

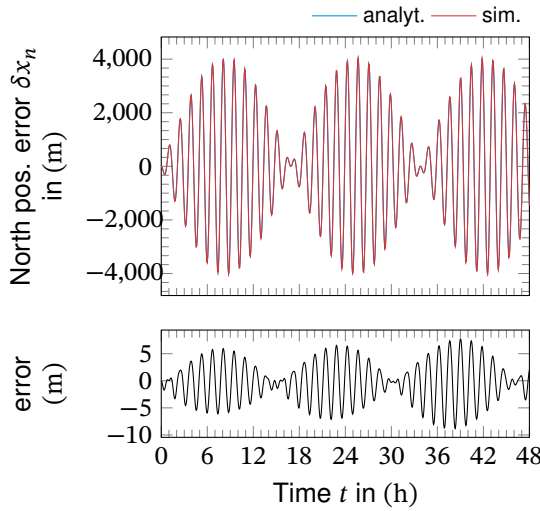
The good coverage of the nonlinear dynamics justifies the use of the linearized system for further analysis of the error propagation and prediction.



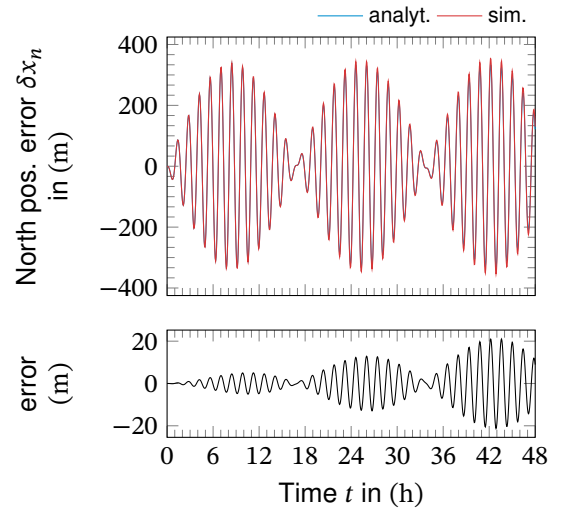
(a) North position error from $1000\text{ m } \delta\phi_0$.



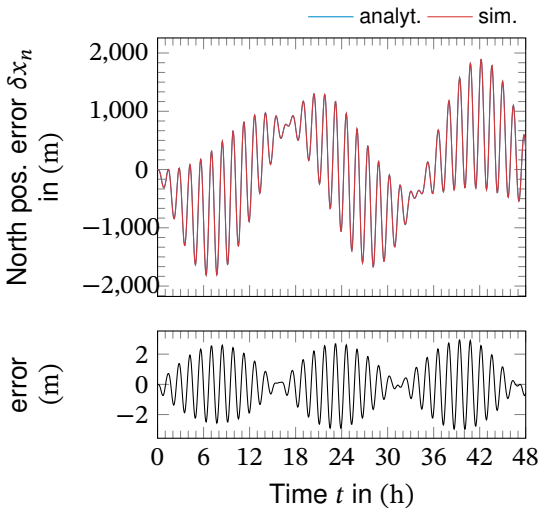
(b) North position error from $5\text{ m/s } \delta v_{n,0}$.



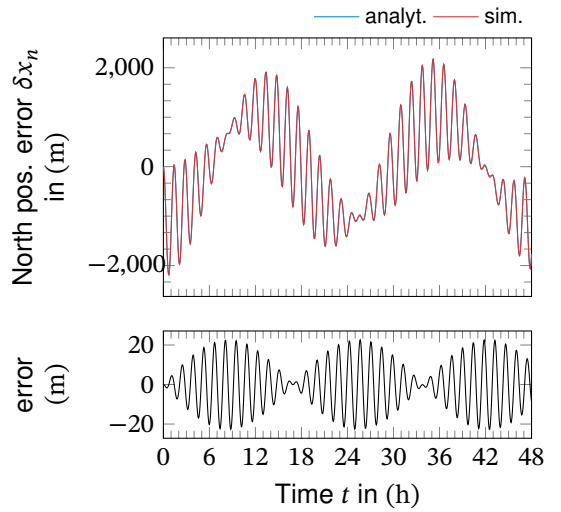
(c) North position error from $5\text{ m/s } \delta v_{e,0}$.



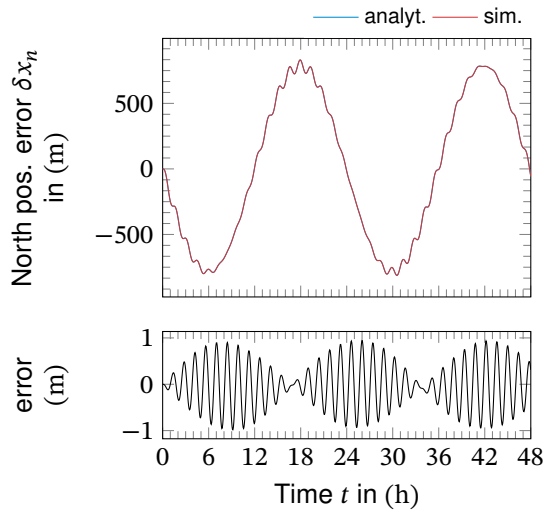
(d) North position error from $5\text{ m/s } \delta v_{d,0}$.



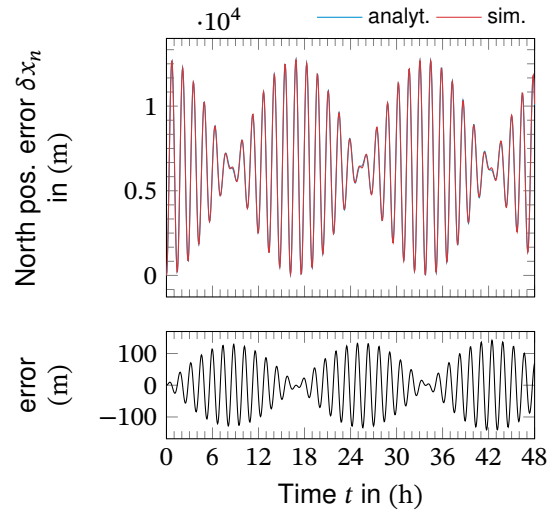
(e) North position error from $0.01^\circ \delta\Phi_0$.



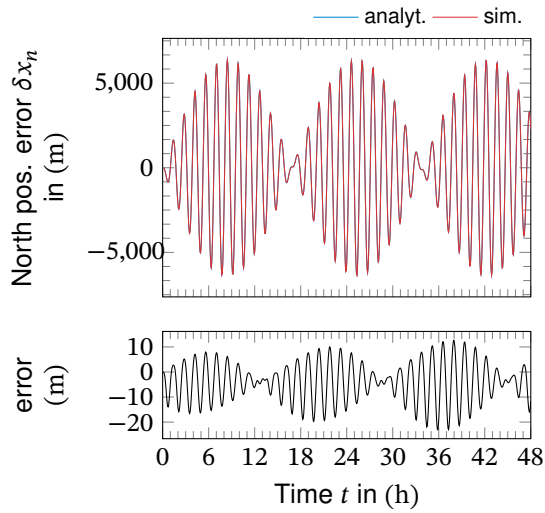
(f) North position error from $0.01^\circ \delta\Theta_0$.



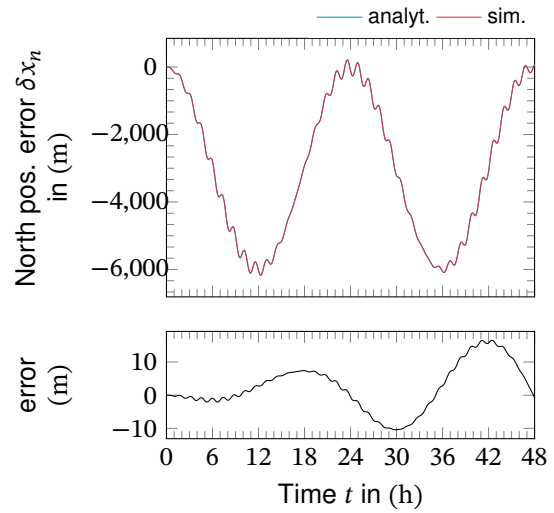
(g) North position error from $0.01^\circ \delta\Psi_0$.



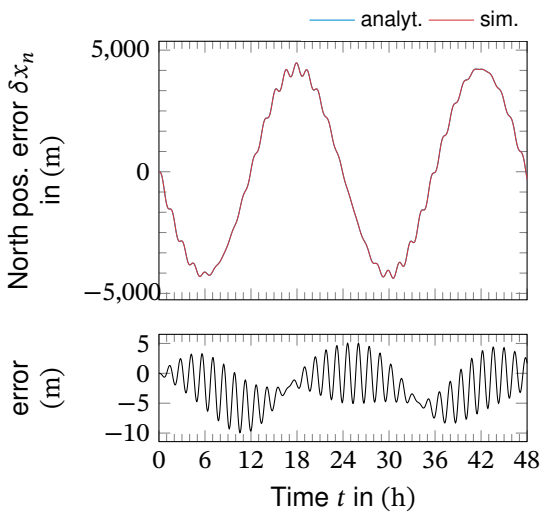
(h) North position error from $1 \text{ mg } f_{b,n}$ bias.



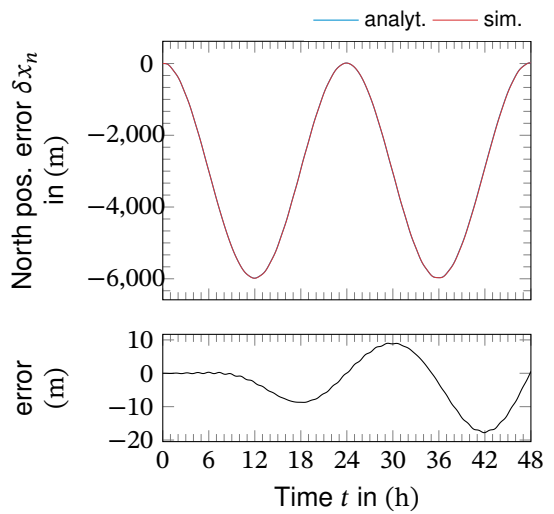
(i) North position error from $1 \text{ mg } f_{b,e}$ bias.



(j) North pos. error from $0.01^\circ/\text{h } \omega_{ib,n}$ bias.

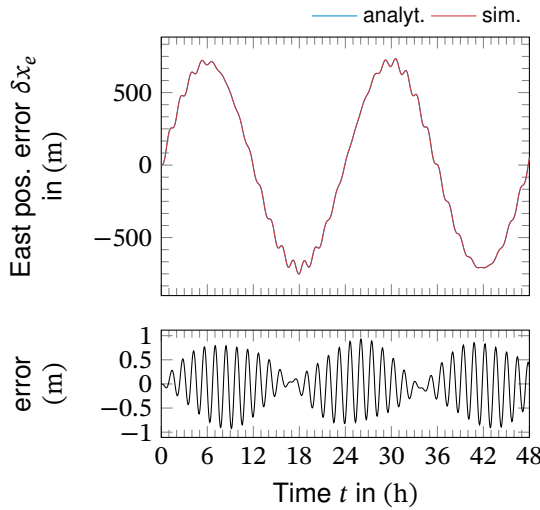


(k) North pos. error from $0.01^\circ/\text{h } \omega_{ib,e}$ bias.

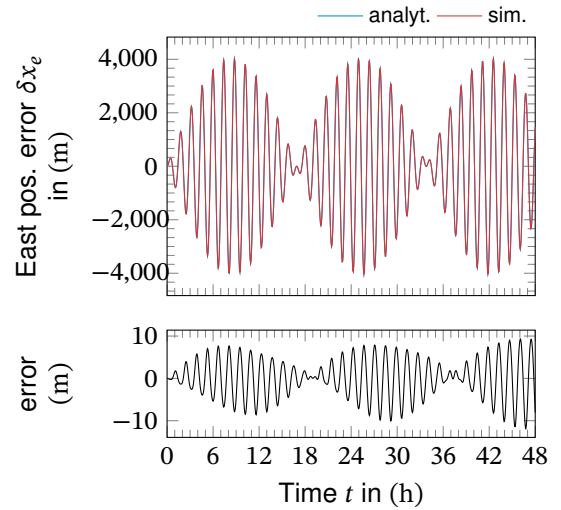


(l) North pos. error from $0.01^\circ/\text{h } \omega_{ib,d}$ bias.

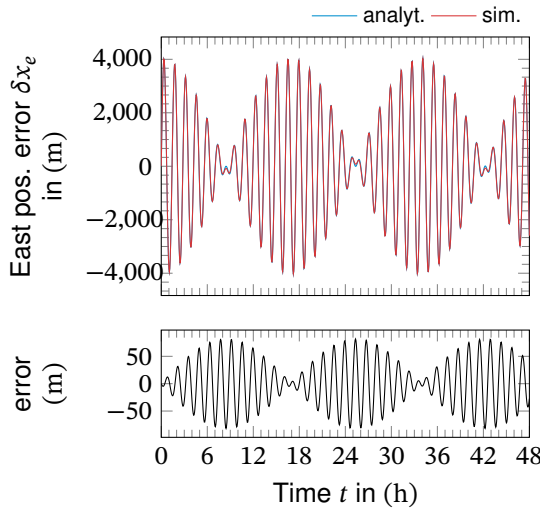
Figure E.1.: North position errors of linearized step response and numerical simulation.



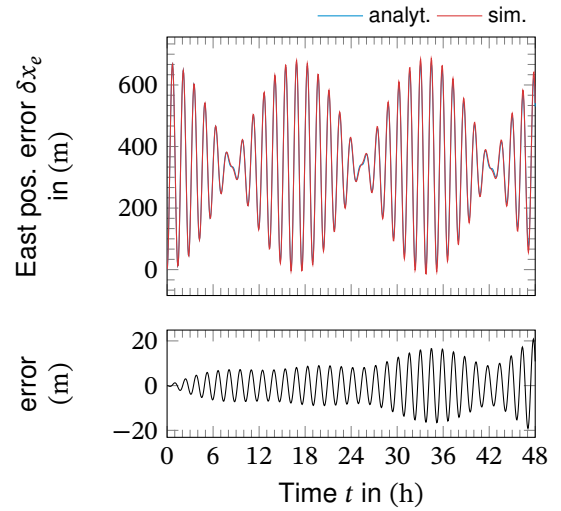
(a) East pos. error from 1000 m $\delta\phi_0$.



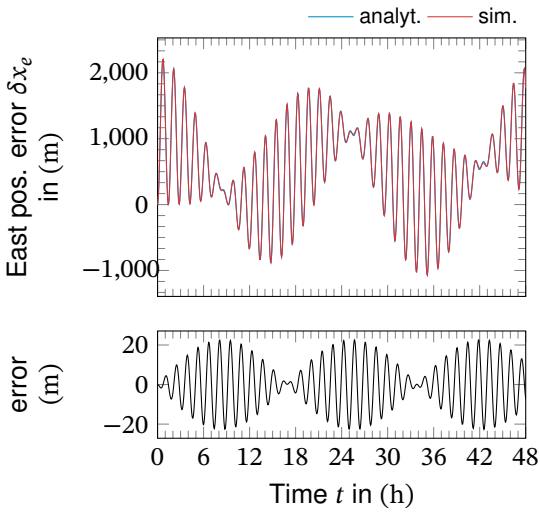
(b) East pos. error from 5 m/s $\delta v_{n,0}$.



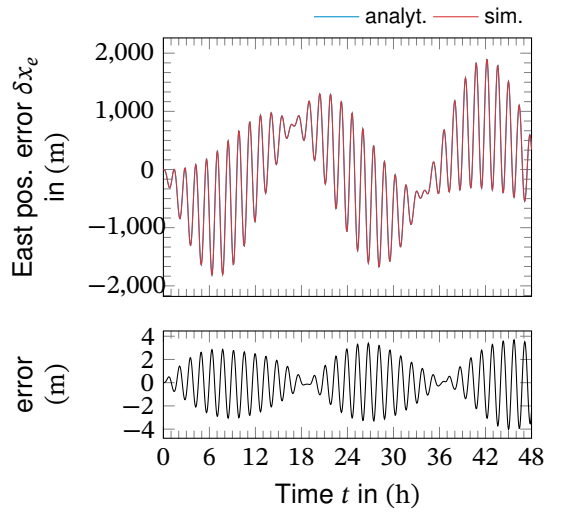
(c) East pos. error from 5 m/s $\delta v_{e,0}$.



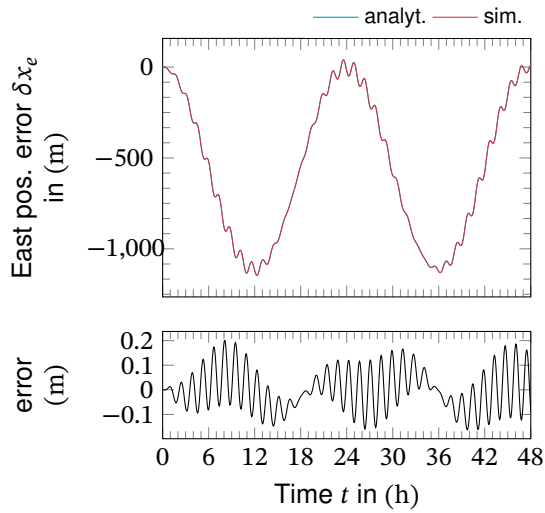
(d) East pos. error from 5 m/s $\delta v_{d,0}$.



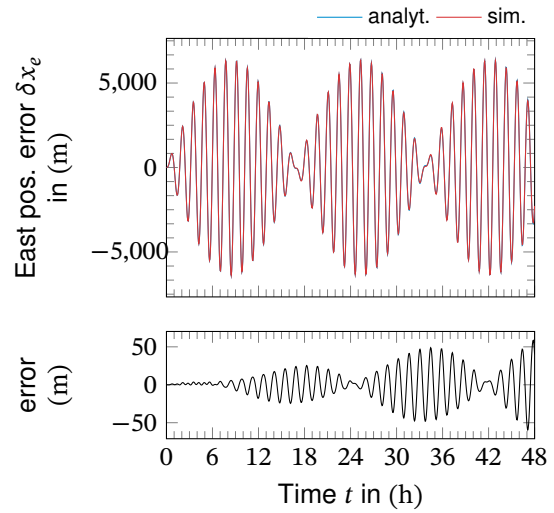
(e) East pos. error from $0.01^\circ \delta\Phi_0$.



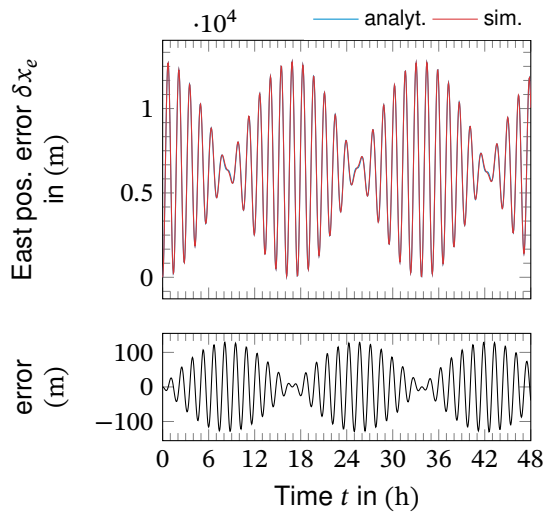
(f) East pos. error from $0.01^\circ \delta\Theta_0$.



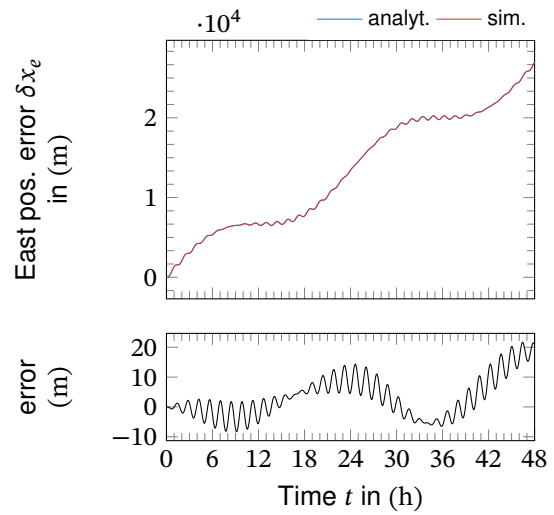
(g) East pos. error from $0.01^\circ \delta\Psi_0$.



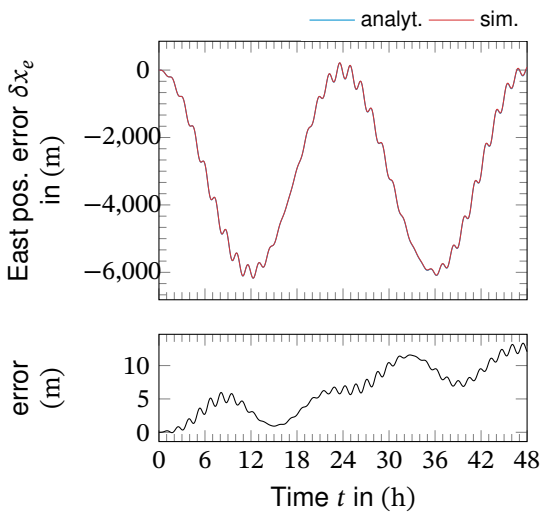
(h) East pos. error from $1 \text{ mg } f_{b,n}$ bias.



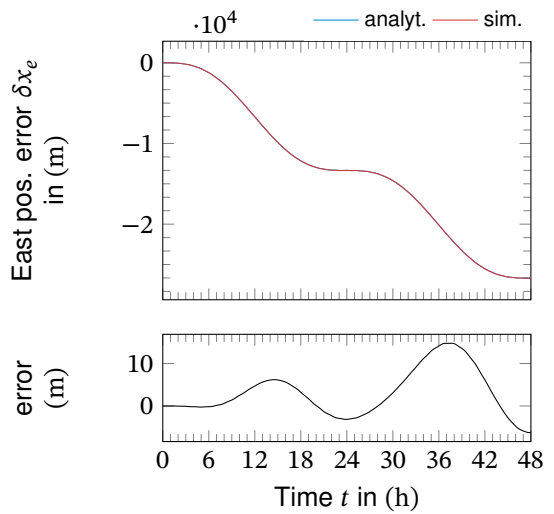
(i) East pos. error from $1 \text{ mg } f_{b,e}$ bias.



(j) East pos. error from $0.01^\circ/\text{h } \omega_{ib,n}$ bias.

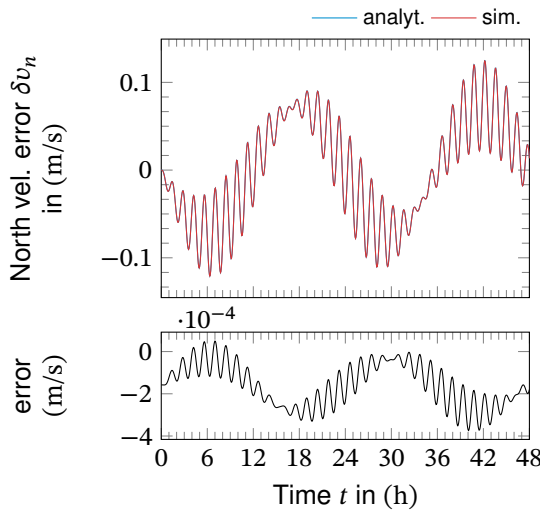


(k) East pos. error from $0.01^\circ/\text{h } \omega_{ib,e}$ bias.

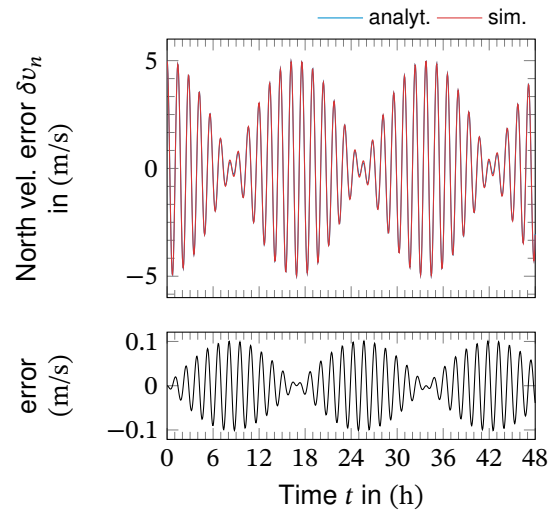


(l) East pos. error from $0.01^\circ/\text{h } \omega_{ib,d}$ bias.

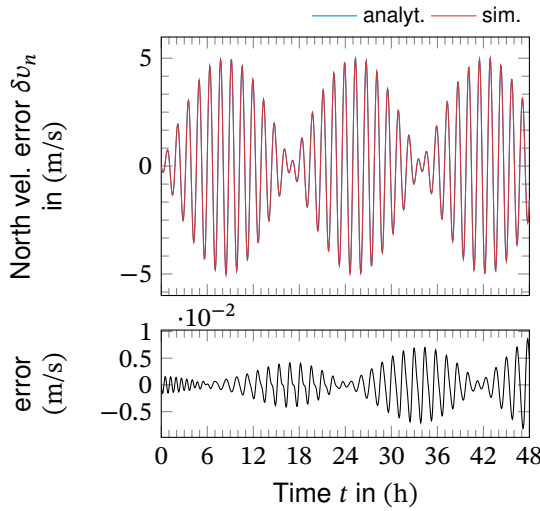
Figure E.2.: East position errors of linearized step response and numerical simulation.



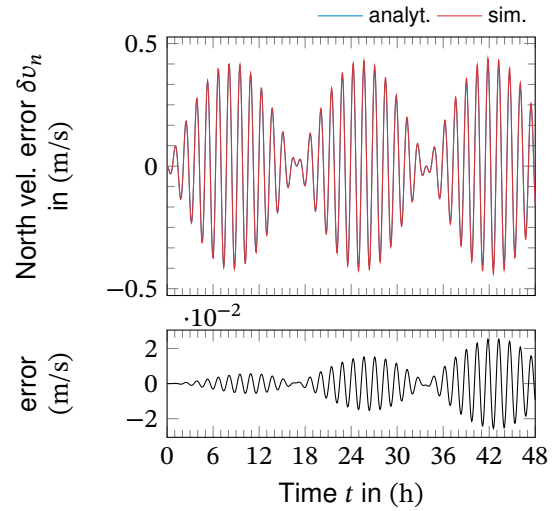
(a) North velocity error from $1000 \text{ m } \delta \phi_0$.



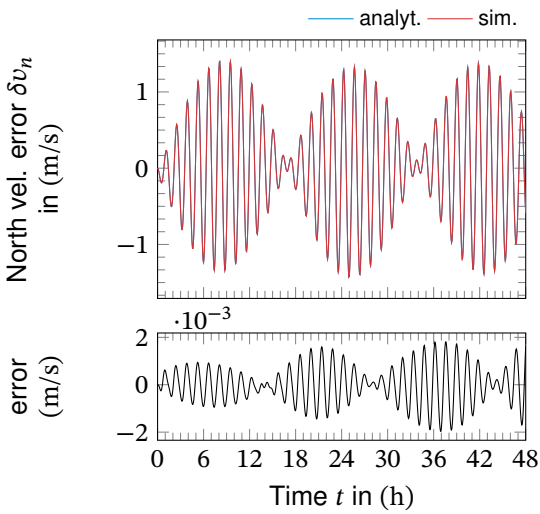
(b) North velocity error from $5 \text{ m/s } \delta v_{n,0}$.



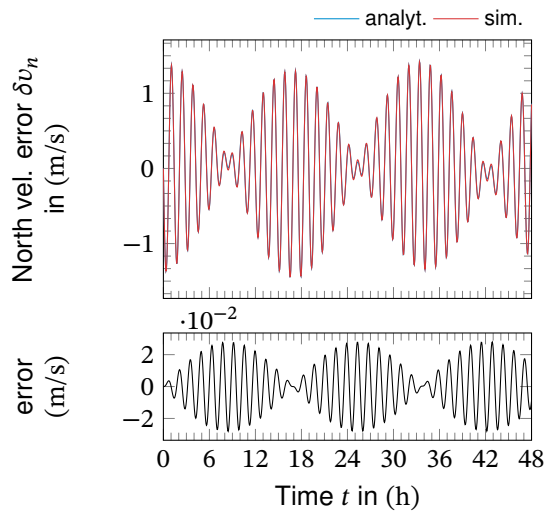
(c) North velocity error from $5 \text{ m/s } \delta v_{e,0}$.



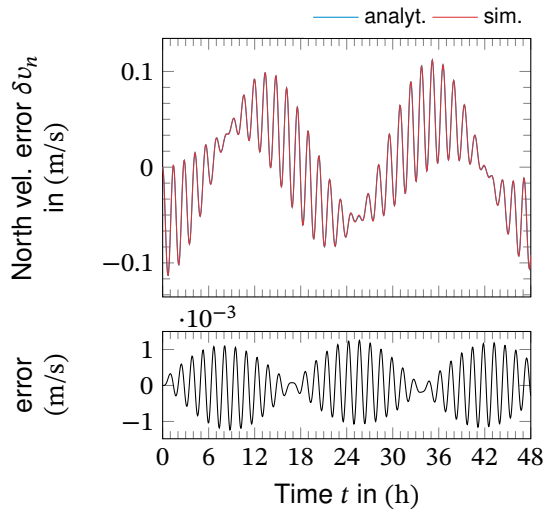
(d) North velocity error from initial $5 \text{ m/s } \delta v_{d,0}$.



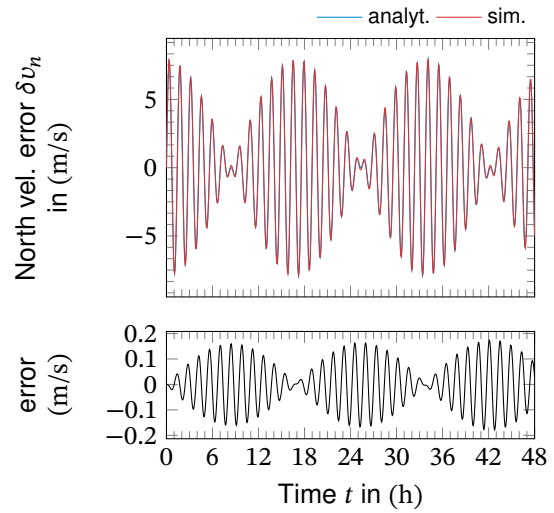
(e) North velocity error from $0.01^\circ \delta \Phi_0$.



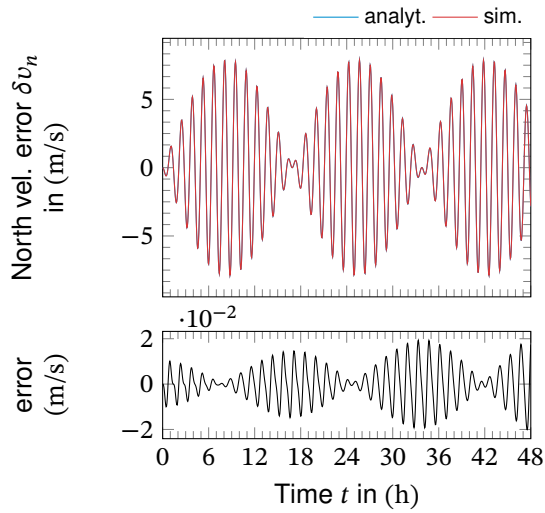
(f) North velocity error from $0.01^\circ \delta \Theta_0$.



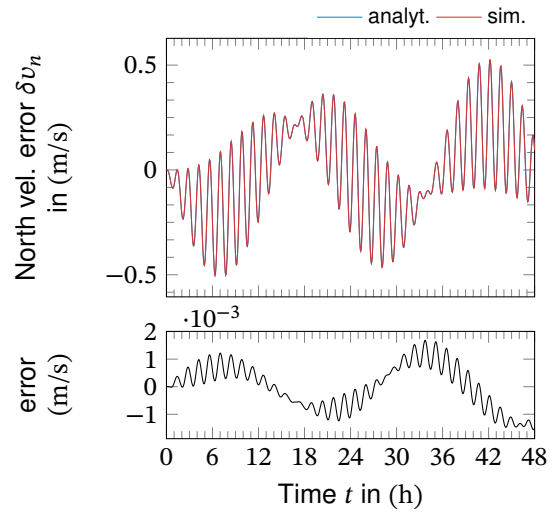
(g) North velocity error from $0.01^\circ \delta \Psi_0$.



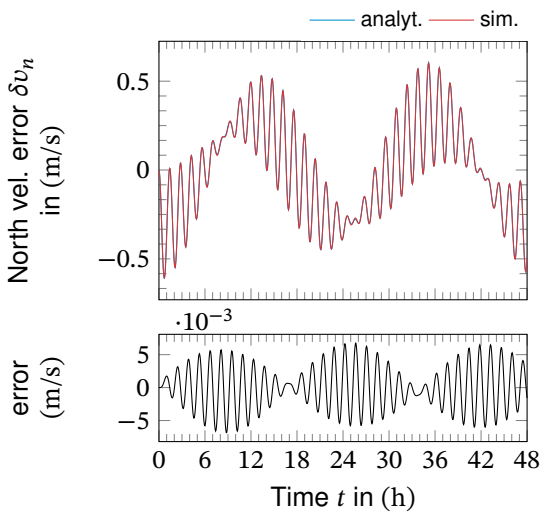
(h) North velocity error from 1 mg $f_{b,n}$ bias.



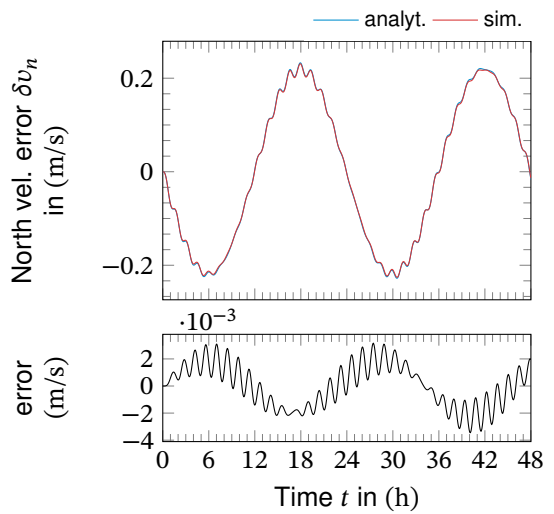
(i) North velocity error from 1 mg $f_{b,e}$ bias.



(j) North vel. error from $0.01^\circ/\text{h} \omega_{ib,n}$ bias.

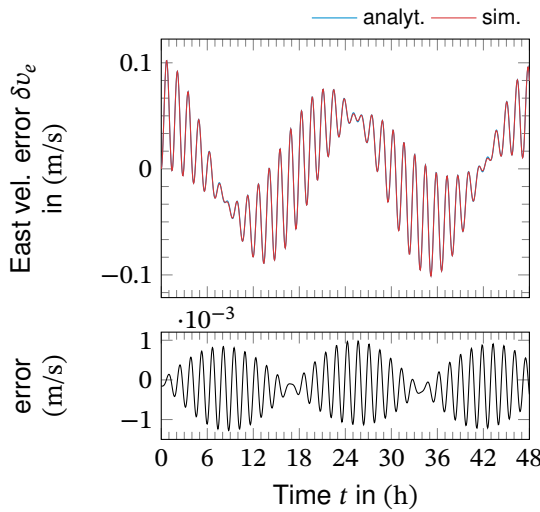


(k) North vel. error from $0.01^\circ/\text{h} \omega_{ib,e}$ bias.

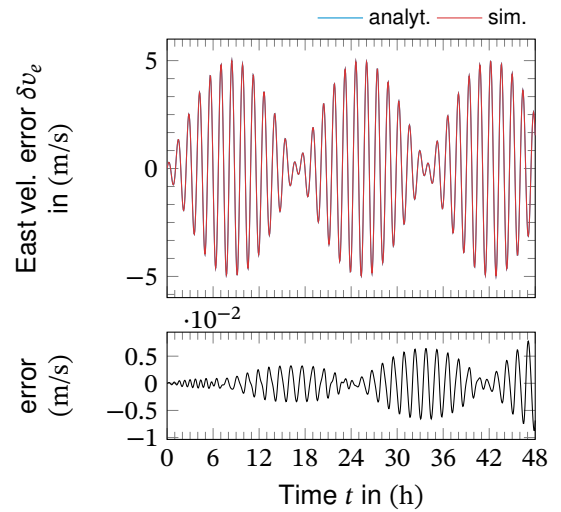


(l) North vel. error from $0.01^\circ/\text{h} \omega_{ib,d}$ bias.

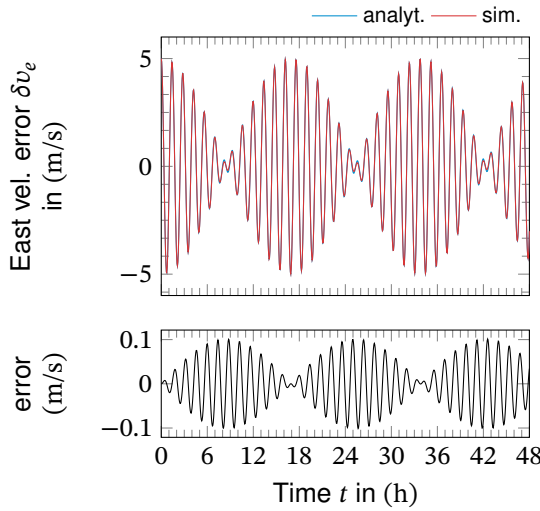
Figure E.3.: North velocity errors of linearized step response and numerical simulation.



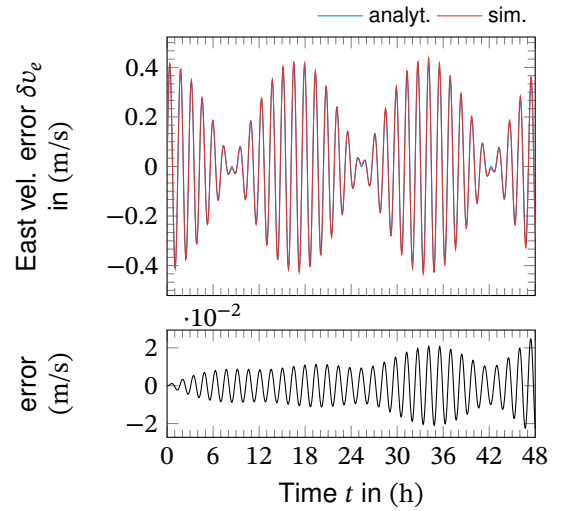
(a) East velocity error from 1000 m $\delta\phi_0$.



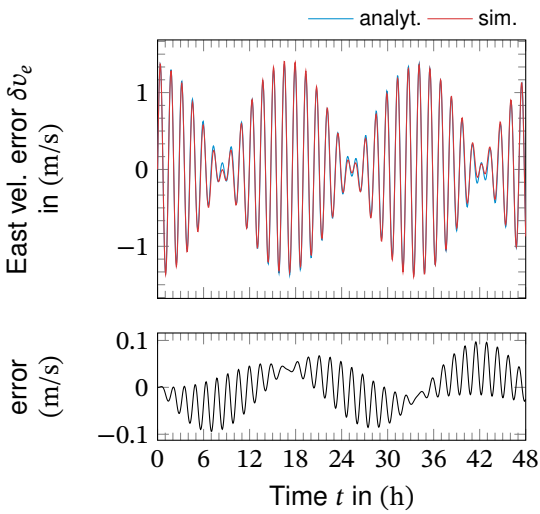
(b) East velocity error from 5 m/s $\delta v_{n,0}$.



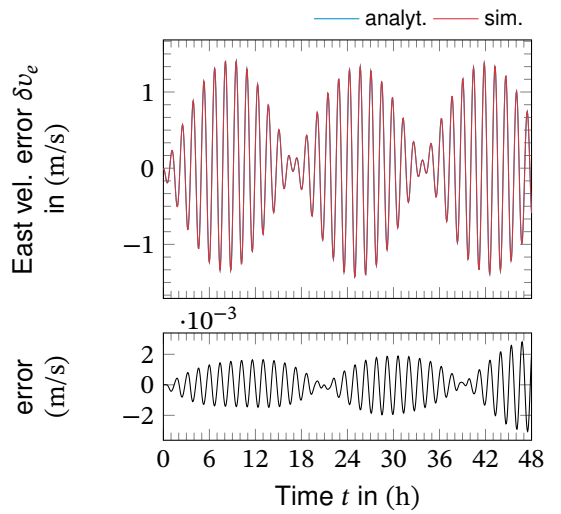
(c) East velocity error from 5 m/s $\delta v_{e,0}$.



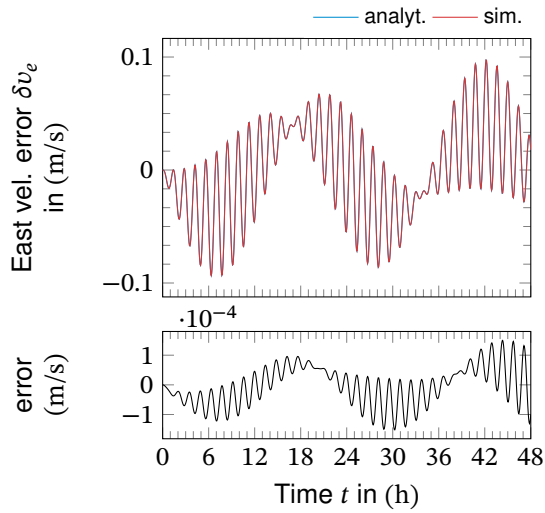
(d) East velocity error from 5 m/s $\delta v_{d,0}$.



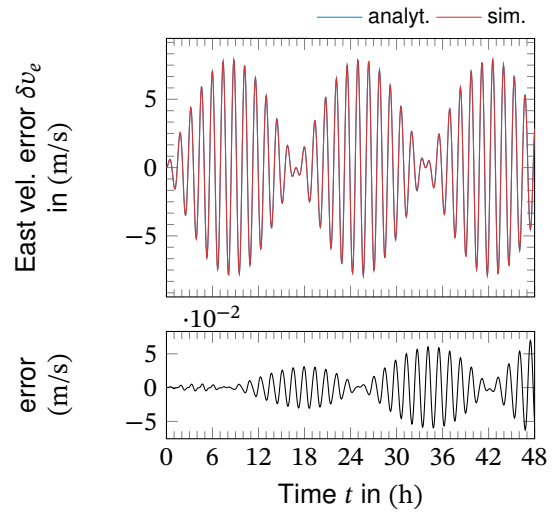
(e) East velocity error from $0.01^\circ \delta\Phi_0$.



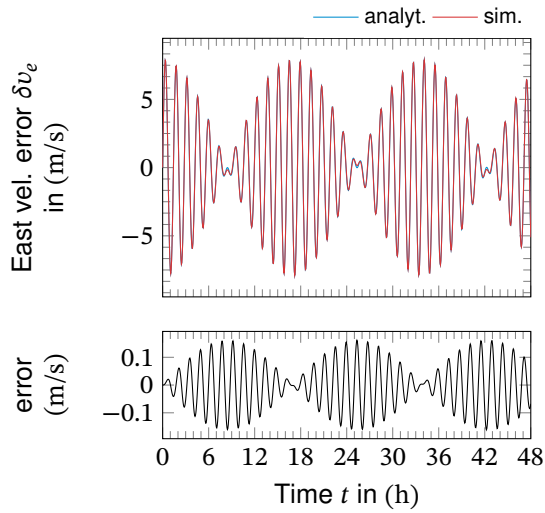
(f) East velocity error from $0.01^\circ \delta\Theta_0$.



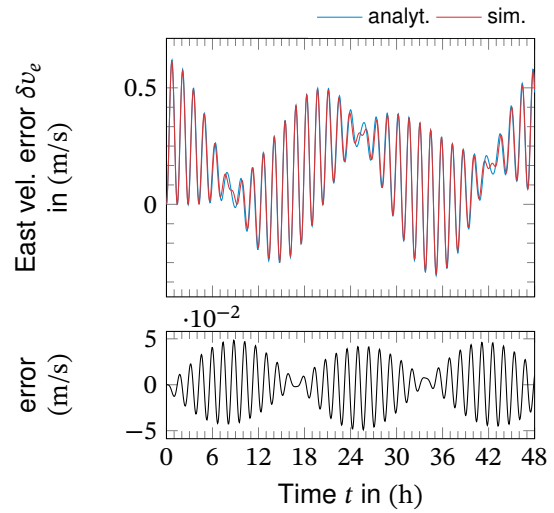
(g) East velocity error from $0.01^\circ \delta\Psi_0$.



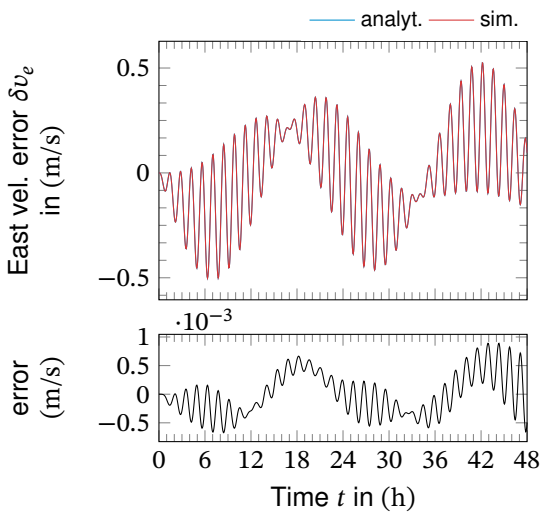
(h) East velocity error from $1 \text{ mg } f_{b,n}$ bias.



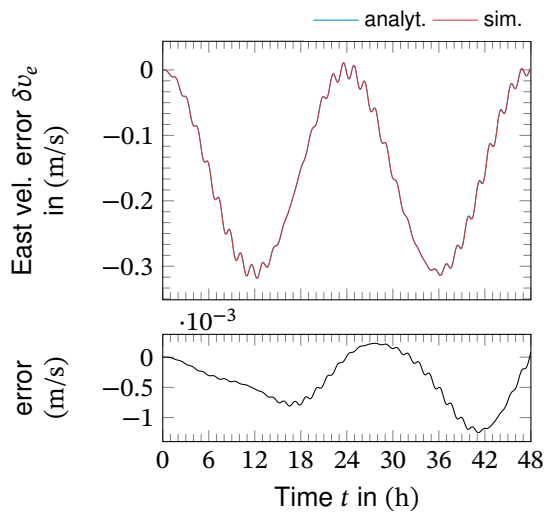
(i) East velocity error from $1 \text{ mg } f_{b,e}$ bias.



(j) East velocity error from $0.1^\circ/\text{h } \omega_{ib,n}$ bias.

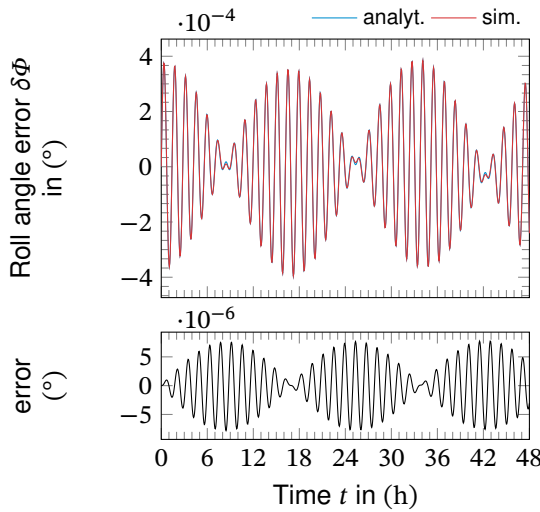


(k) East velocity error from $0.1^\circ/\text{h } \omega_{ib,e}$ bias.

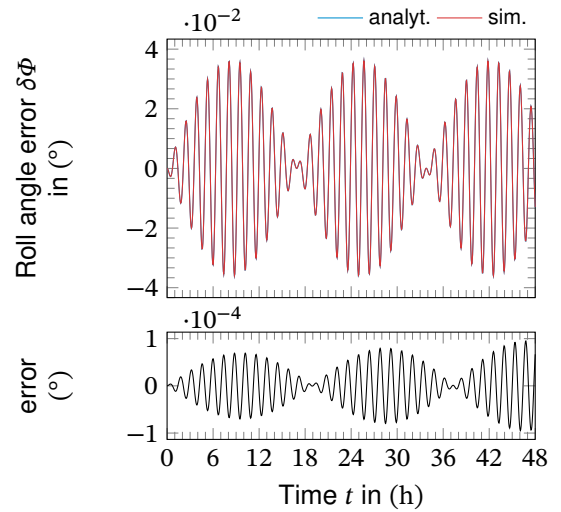


(l) East velocity error from $0.1^\circ/\text{h } \omega_{ib,d}$ bias.

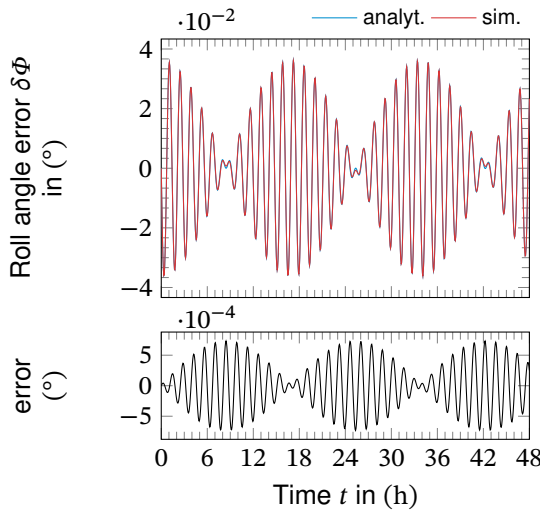
Figure E.4.: East velocity errors of linearized step response and numerical simulation.



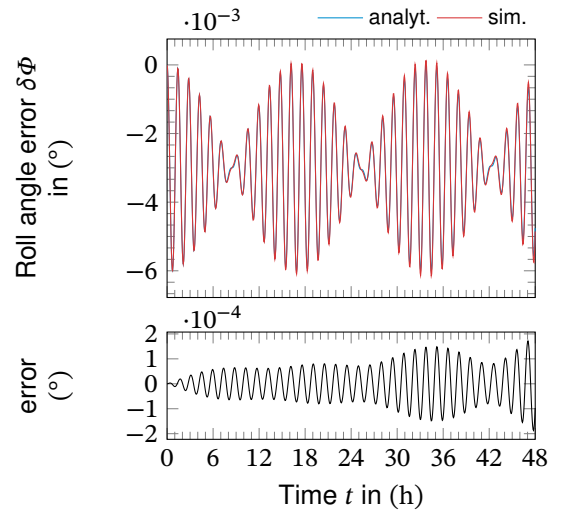
(a) Roll error from 1000 m $\delta\phi_0$.



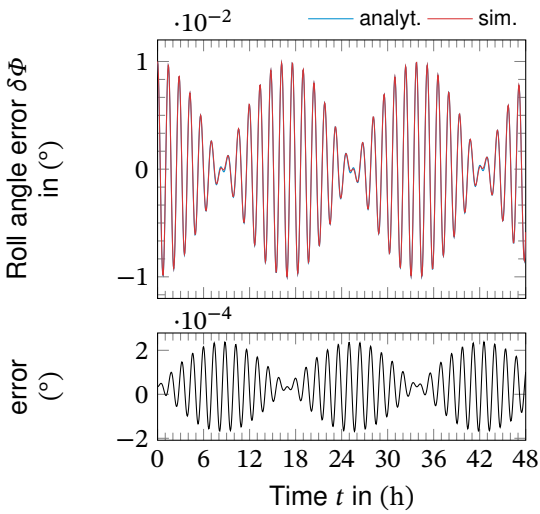
(b) Roll error from 5 m/s $\delta v_{n,0}$.



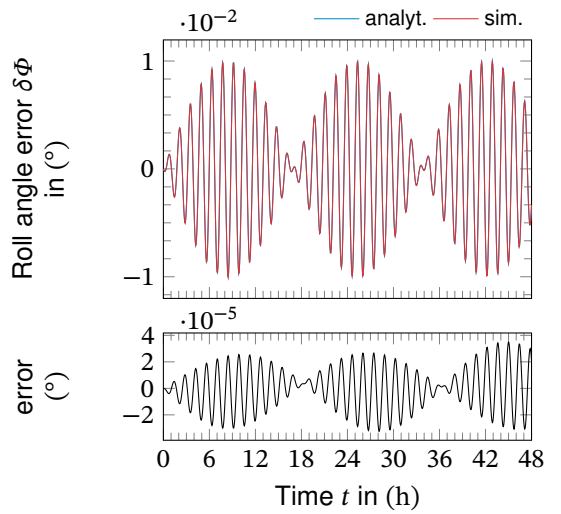
(c) Roll error from 5 m/s $\delta v_{e,0}$.



(d) Roll error from 5 m/s $\delta v_{d,0}$.



(e) Roll error from $0.01^\circ \delta\Phi_0$.



(f) Roll error from $0.01^\circ \delta\Theta_0$.

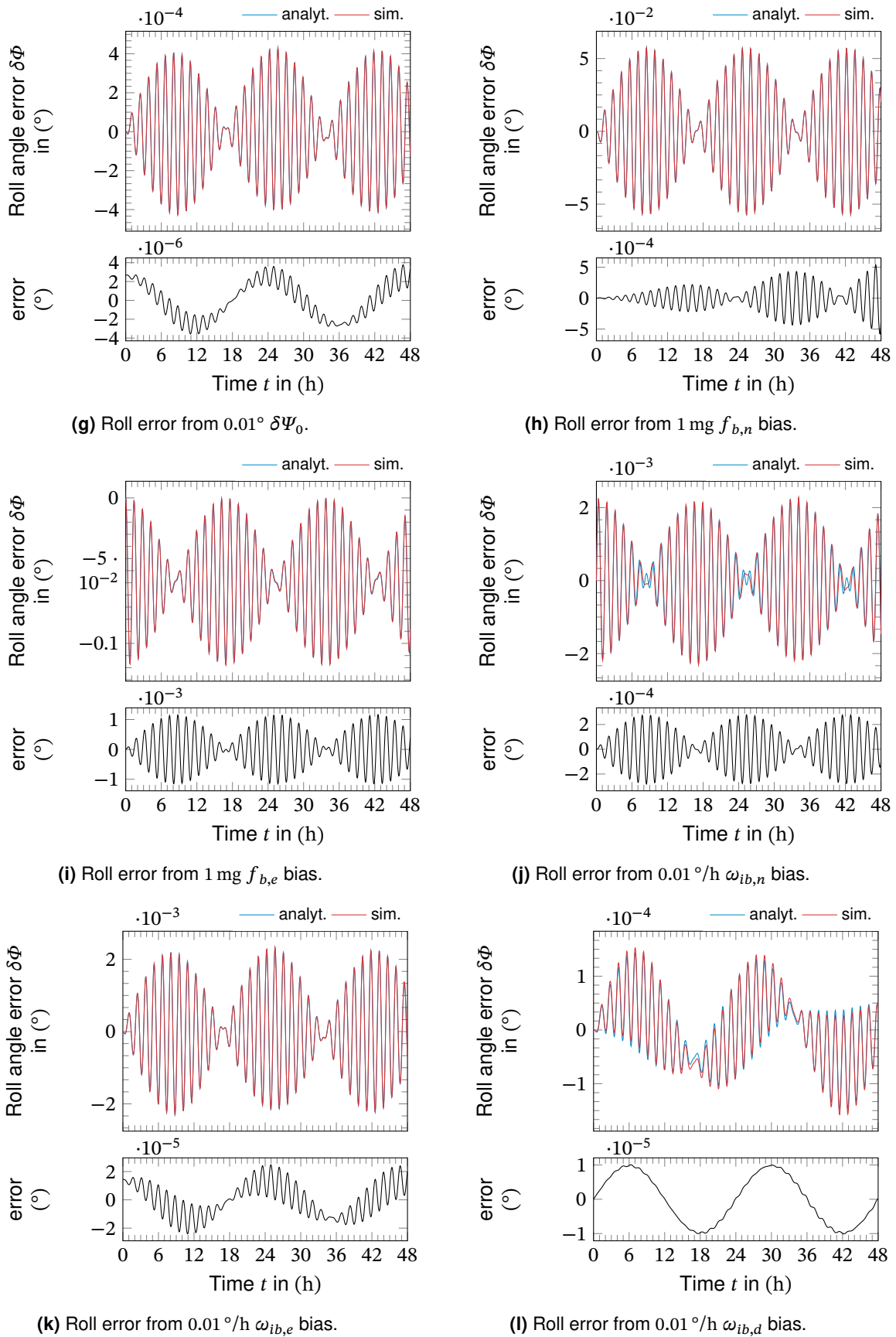
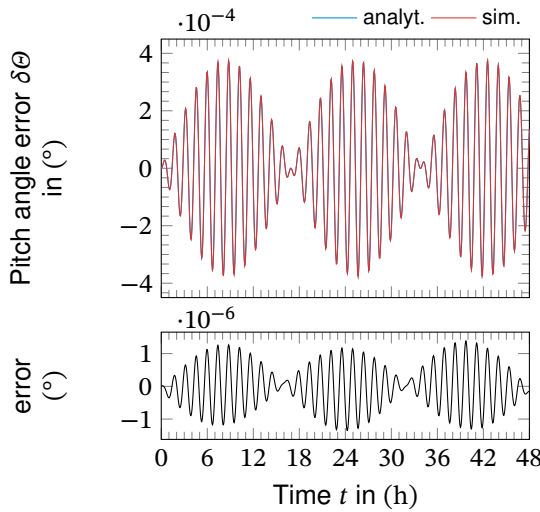
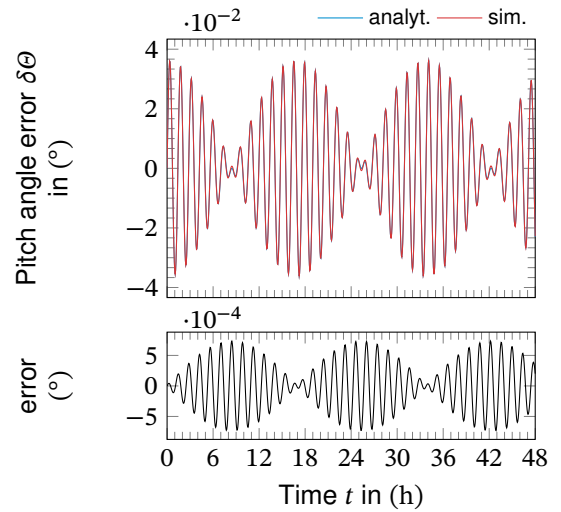


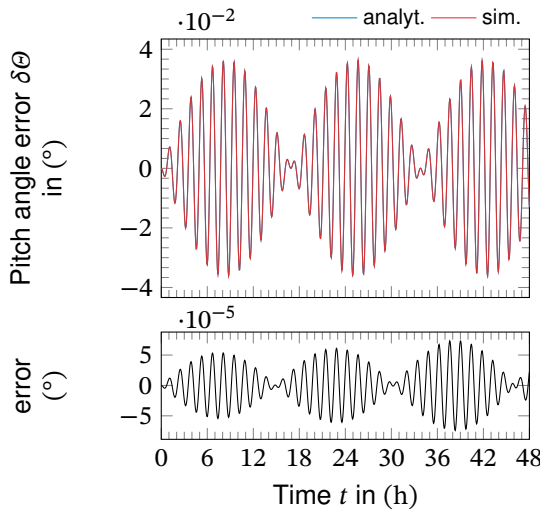
Figure E.5.: Roll angle errors of linearized step response and numerical simulation.



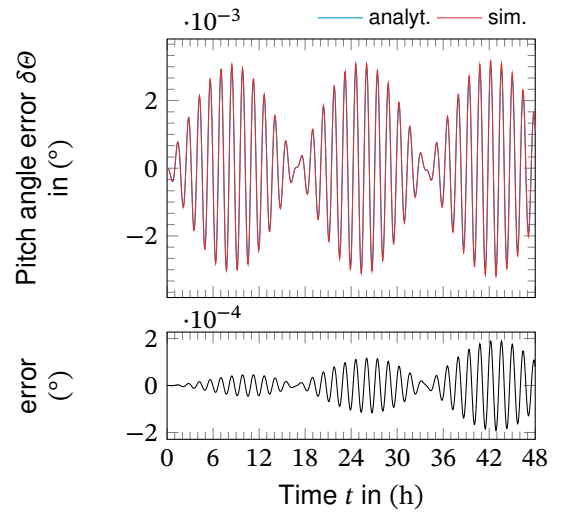
(a) Pitch error from 1000 m $\delta\phi_0$.



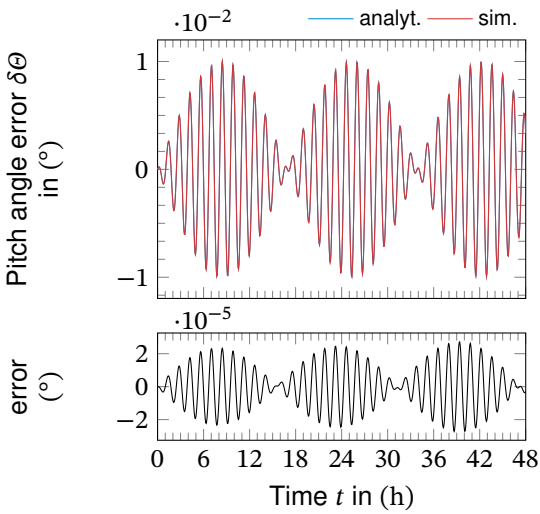
(b) Pitch error from 5 m/s $\delta v_{n,0}$.



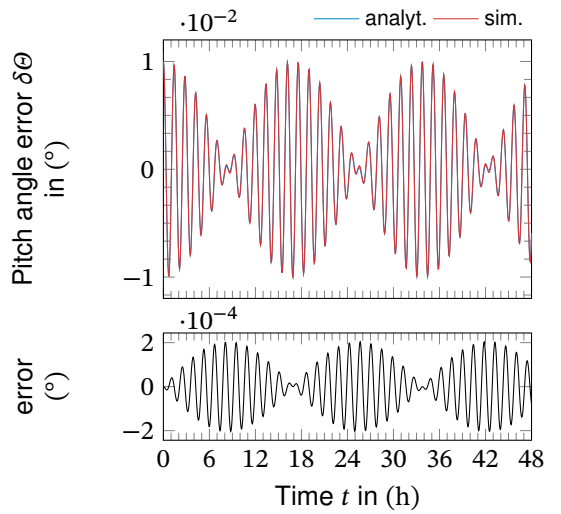
(c) Pitch error from 5 m/s $\delta v_{e,0}$.



(d) Pitch error from 5 m/s $\delta v_{d,0}$.



(e) Pitch error from $0.01^\circ \delta\Phi_0$.



(f) Pitch error from $0.01^\circ \delta\Theta_0$.

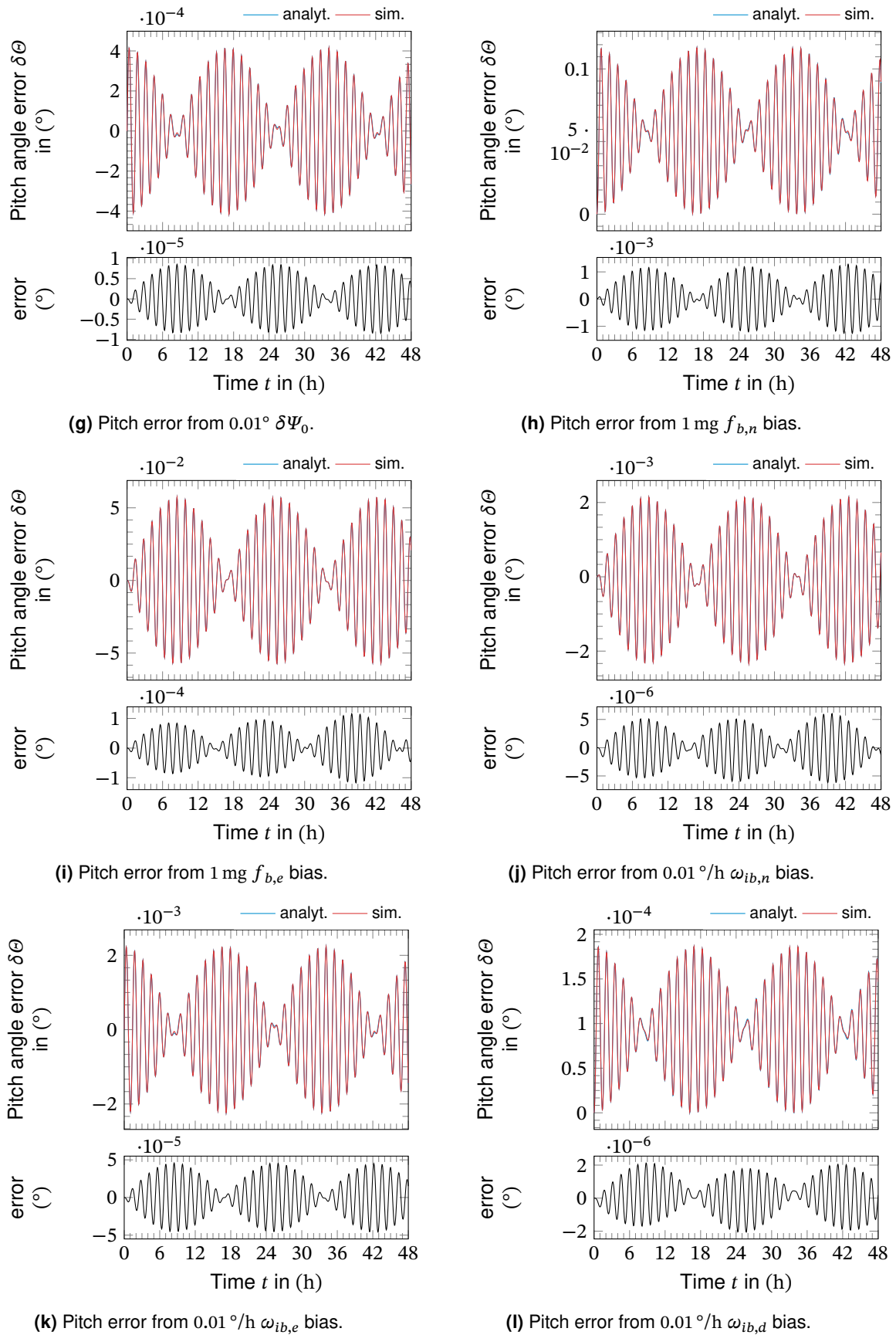
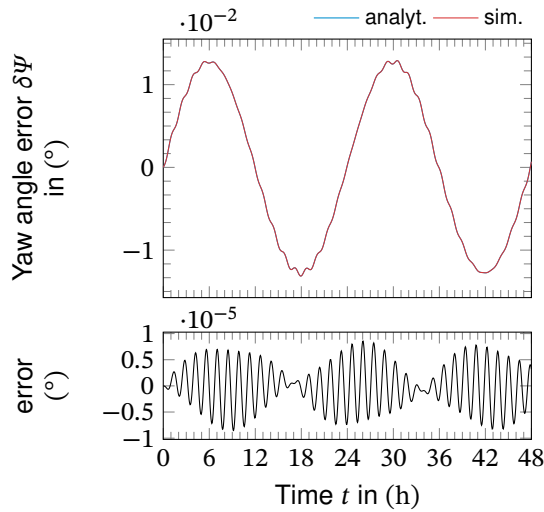
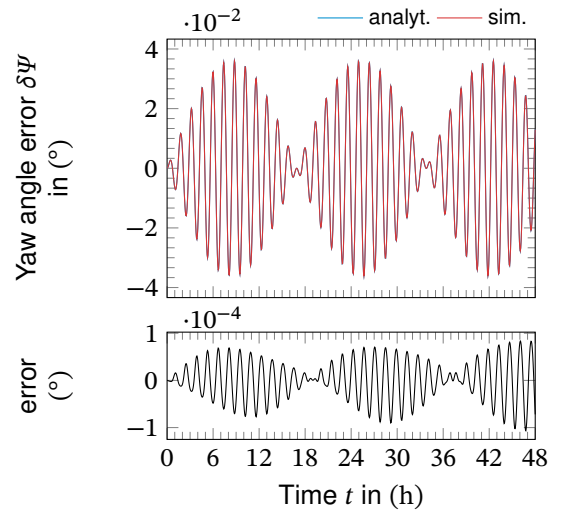


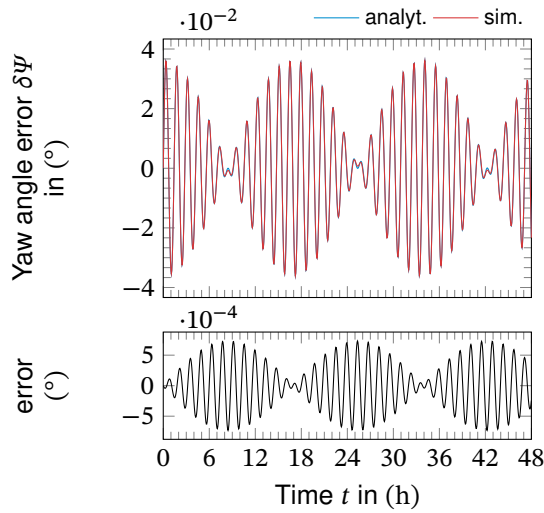
Figure E.6.: Pitch angle errors of linearized step response and numerical simulation.



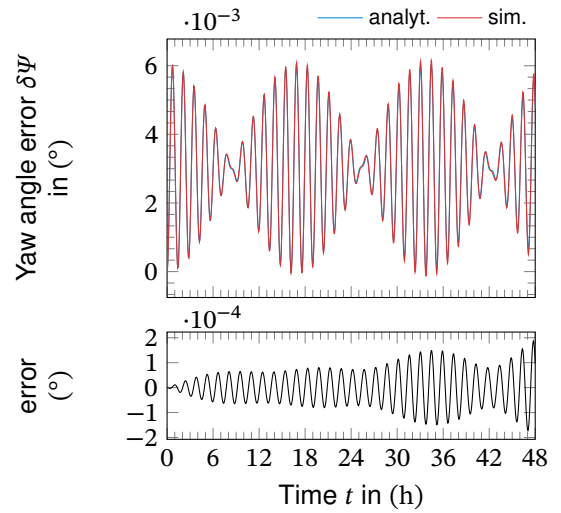
(a) Yaw error from 1000 m $\delta\phi_0$.



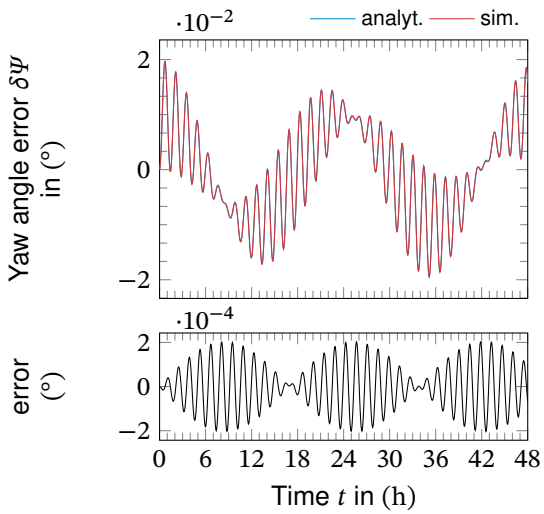
(b) Yaw error from 5 m/s $\delta v_{n,0}$.



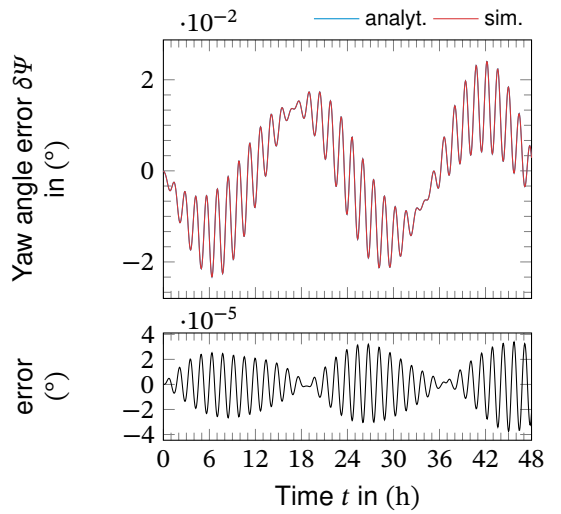
(c) Yaw error from 5 m/s $\delta v_{e,0}$.



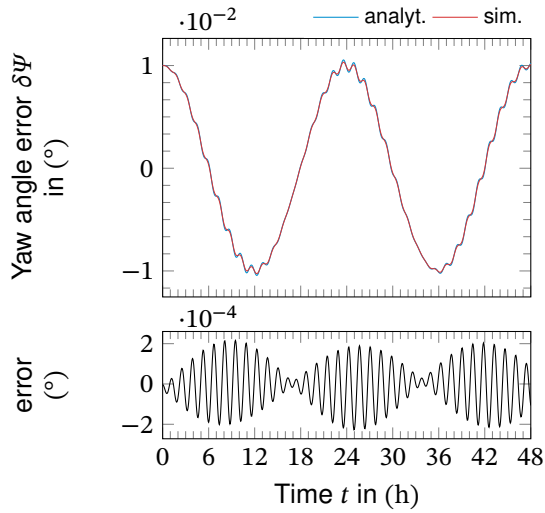
(d) Yaw error from 5 m/s $\delta v_{d,0}$.



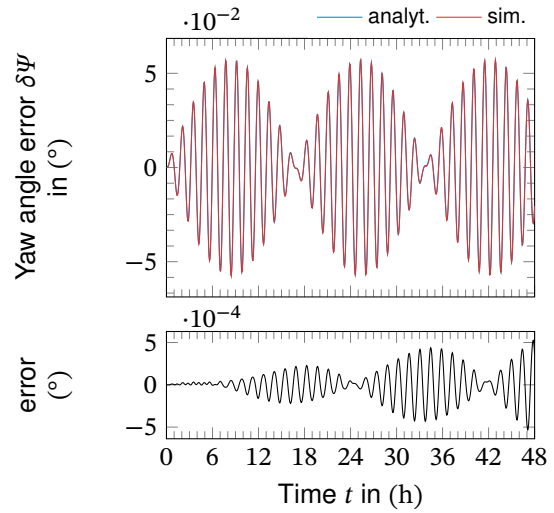
(e) Yaw error from $0.01^\circ \delta\Phi_0$.



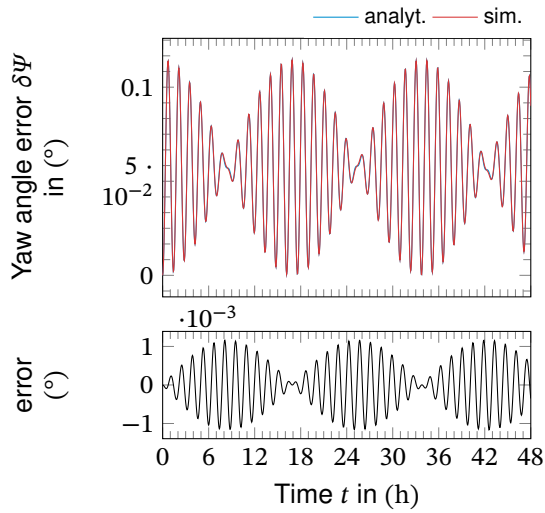
(f) Yaw error from $0.01^\circ \delta\Theta_0$.



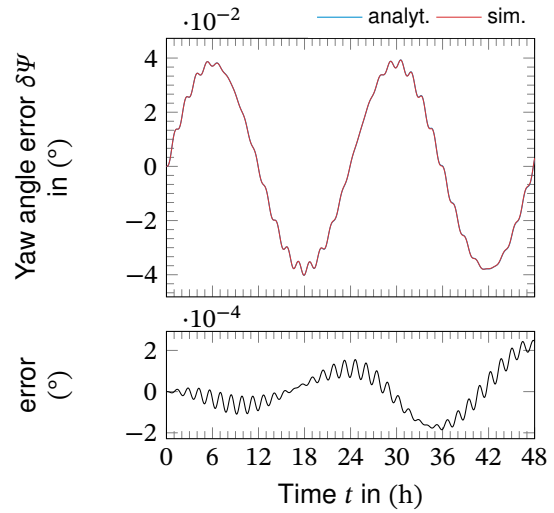
(g) Yaw error from $0.01^\circ \delta\Psi_0$.



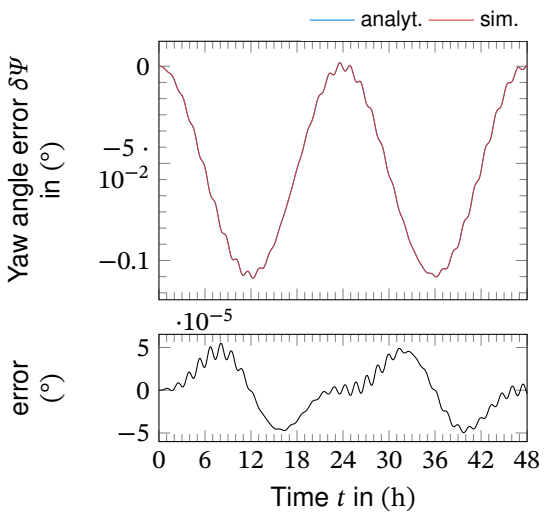
(h) Yaw error from $1 \text{ mg } f_{b,n}$ bias.



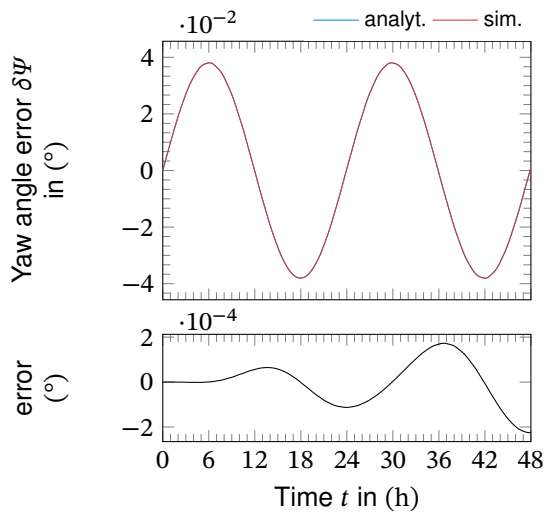
(i) Yaw error from $1 \text{ mg } f_{b,e}$ bias.



(j) Yaw error from $0.01^\circ/\text{h } \omega_{ib,n}$ bias.



(k) Yaw error from $0.01^\circ/\text{h } \omega_{ib,e}$ bias.



(l) Yaw error from $0.01^\circ/\text{h } \omega_{ib,d}$ bias.

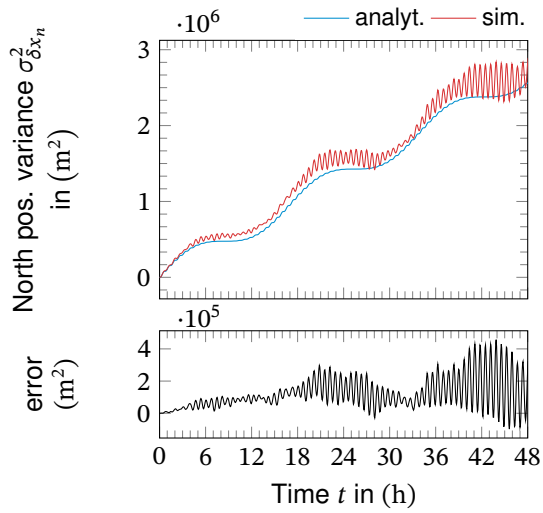
Figure E.7.: Yaw angle errors of linearized step response and numerical simulation.

E.2. Position Uncertainty from Sensor Noise

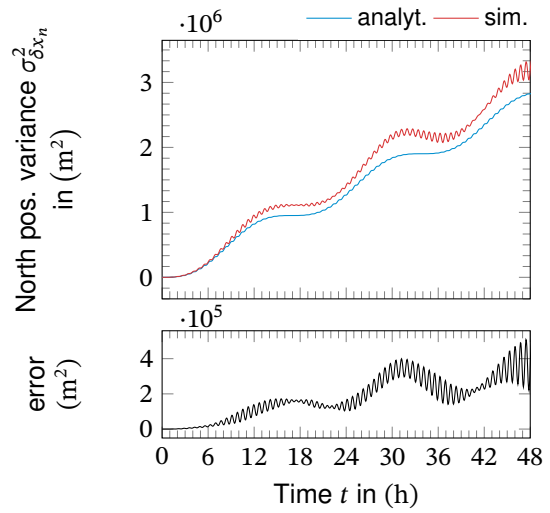
Analog to [Section E.1](#), the validity of the analytic noise propagation through the linearized error dynamics is evaluated by comparison to the nonlinear simulation. Again, the strapdown algorithm is simulated for a stationary vehicle at $\phi = 45^\circ$. The variance of the resulting position errors is calculated from 1000 Monte Carlo runs of [WGN](#) input, for each sensor axis.

In general, the curve's shapes of the simulation and the analytical solution coincide but the two curves diverge over time. Partly, this can be attributed to the differences between the linear and nonlinear model, as has been observed in [E](#). The major differences arise from growing variance of the Monte Carlo sample variance.

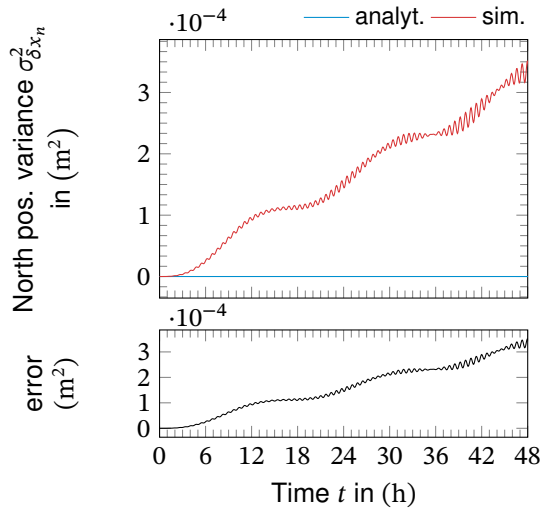
Considering the extreme long simulation times of 48 h, the analytical solution matches the Monte Carlo results sufficiently good to justify its use for performance analysis and prediction.



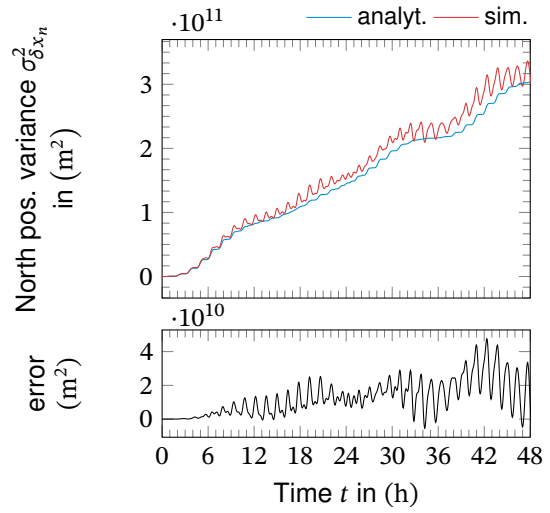
(a) North pos. variance from WGN $f_{b,x}$.



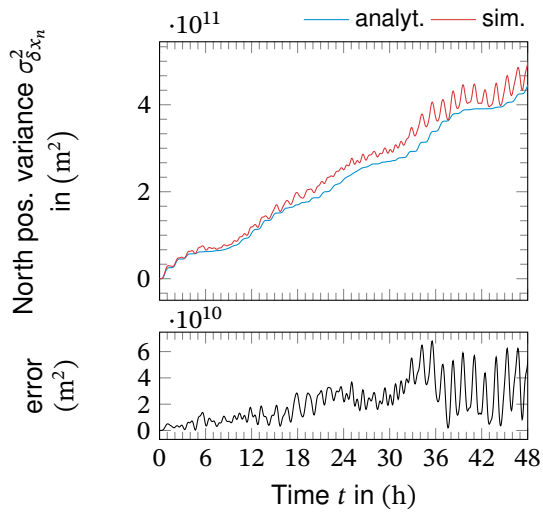
(b) North pos. variance from WGN $f_{b,y}$.



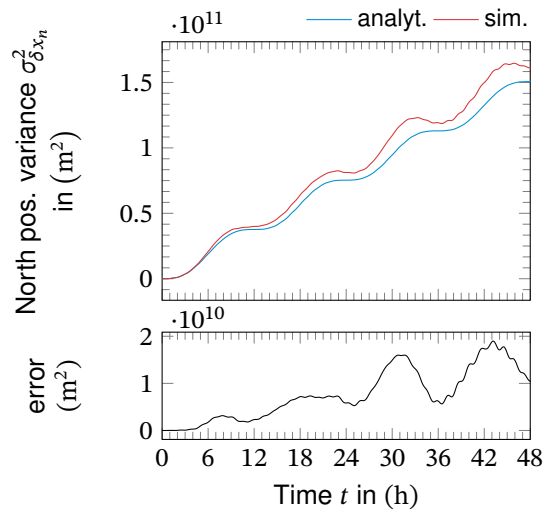
(c) North pos. variance from WGN $f_{b,z}$.



(d) North pos. variance from WGN $\omega_{ib,x}$.



(e) North pos. variance from WGN $\omega_{ib,y}$.



(f) North pos. variance from WGN $\omega_{ib,z}$.

Figure E.8.: Analytical north position error variance for WGN compared to Monte Carlo simulation. Velocity random walk $N_{acc} = 1 \frac{\text{mg}}{\sqrt{\text{Hz}}}$, angular random walk $N_{gyr} = 1 \frac{\circ}{\sqrt{\text{h}}}$.

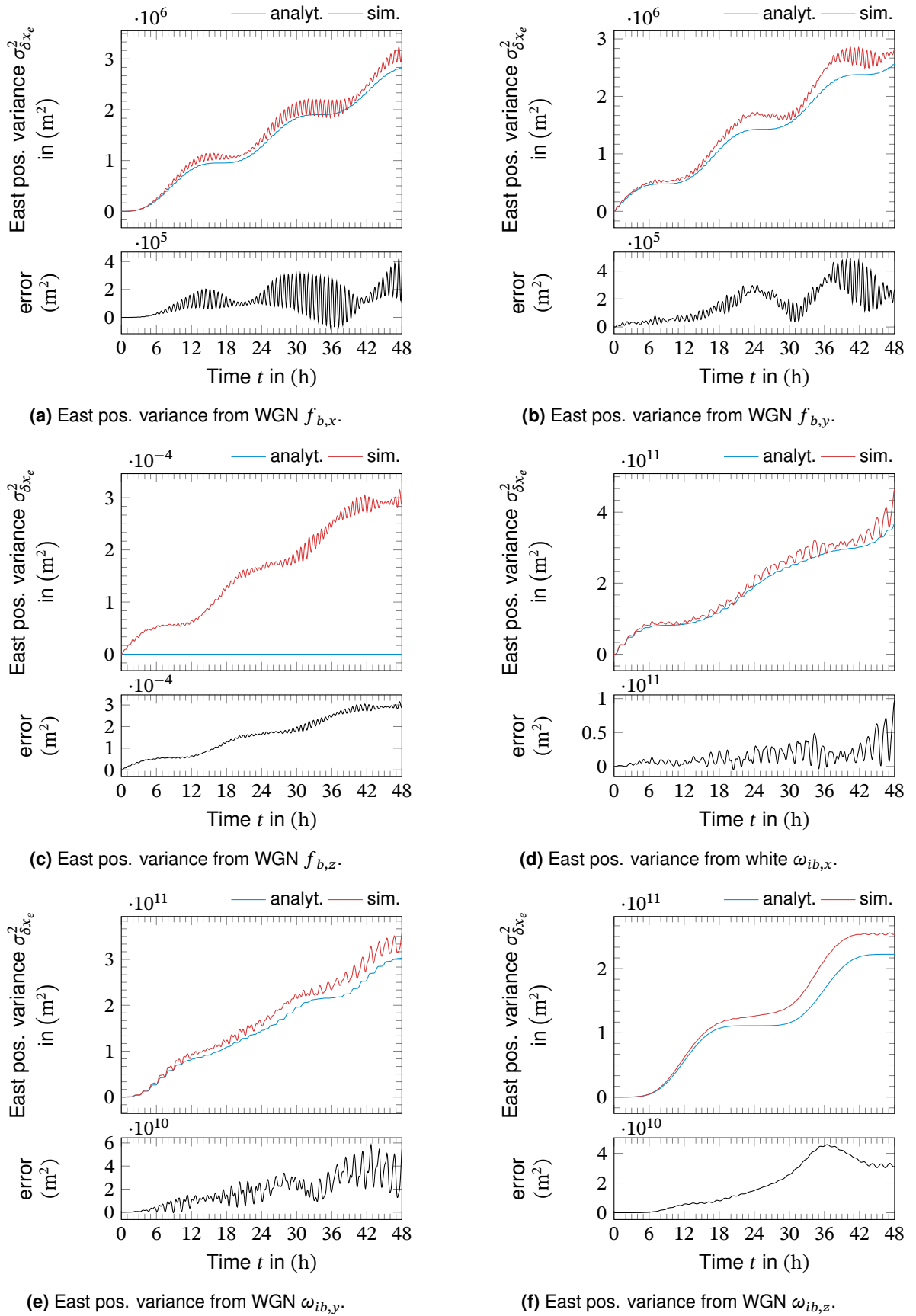
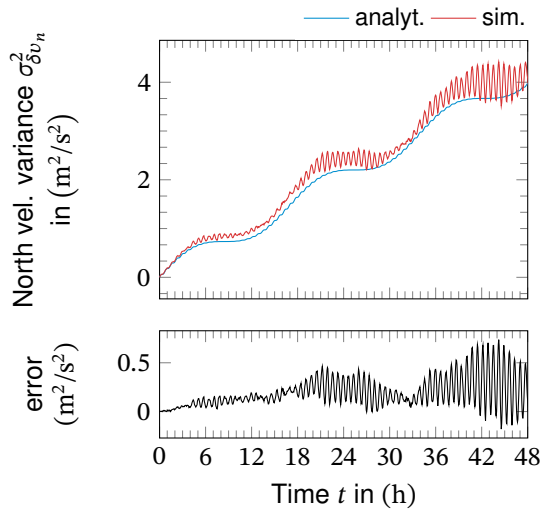
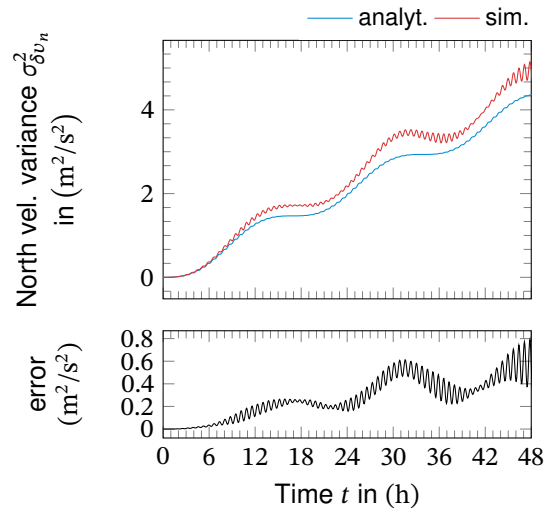


Figure E.9.: Analytical east position error variance for WGN compared to Monte Carlo simulation.

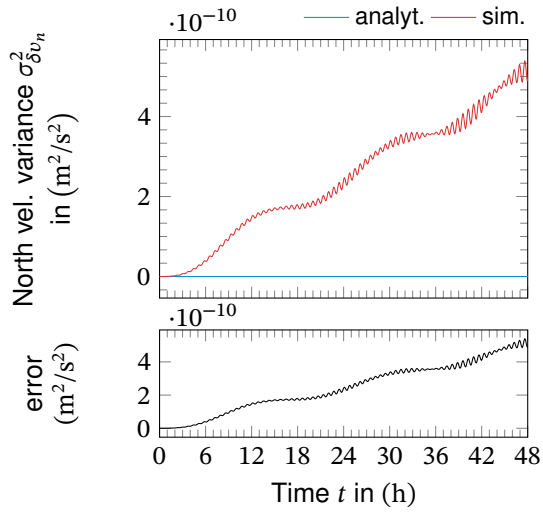
Velocity random walk $N_{acc} = 1 \frac{\text{mg}}{\sqrt{\text{Hz}}}$, angular random walk $N_{gyr} = 1 \frac{\circ}{\sqrt{\text{h}}}$.



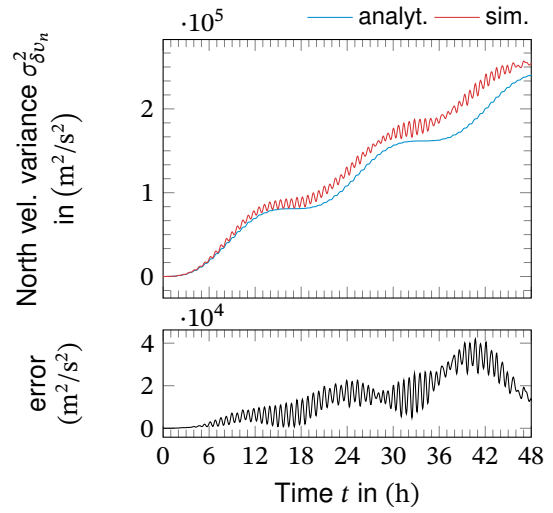
(a) North vel. variance from WGN $f_{b,x}$.



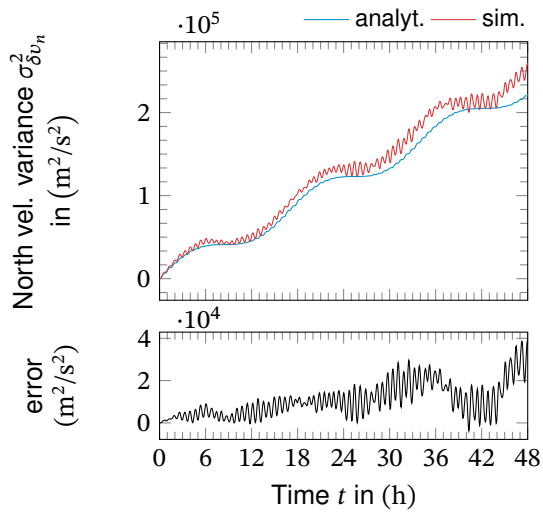
(b) North vel. variance from WGN $f_{b,y}$.



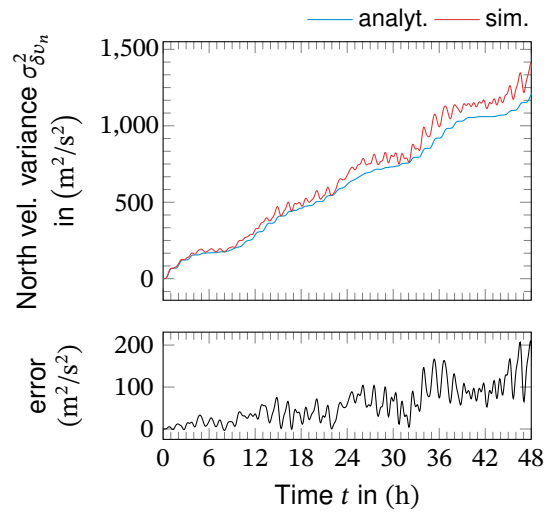
(c) North vel. variance from WGN $f_{b,z}$.



(d) North vel. variance from WGN $\omega_{ib,x}$.



(e) North vel. variance from WGN $\omega_{ib,y}$.



(f) North vel. variance from WGN $\omega_{ib,z}$.

Figure E.10.: Analytical north velocity error variance for WGN compared to Monte Carlo simulation.

Velocity random walk $N_{acc} = 1 \frac{\text{mg}}{\sqrt{\text{Hz}}}$, angular random walk $N_{gyr} = 1 \frac{\circ}{\sqrt{\text{h}}}$.

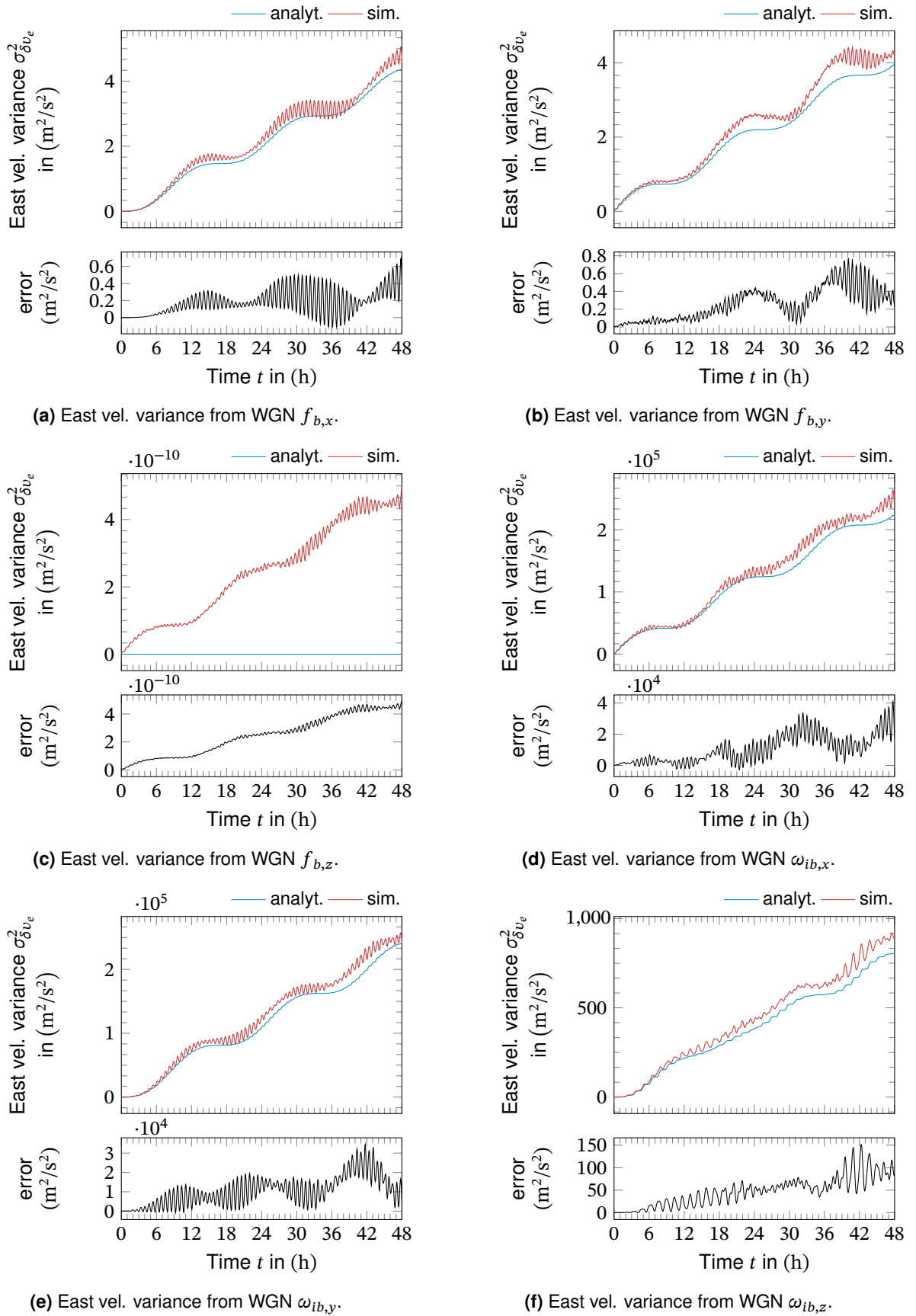
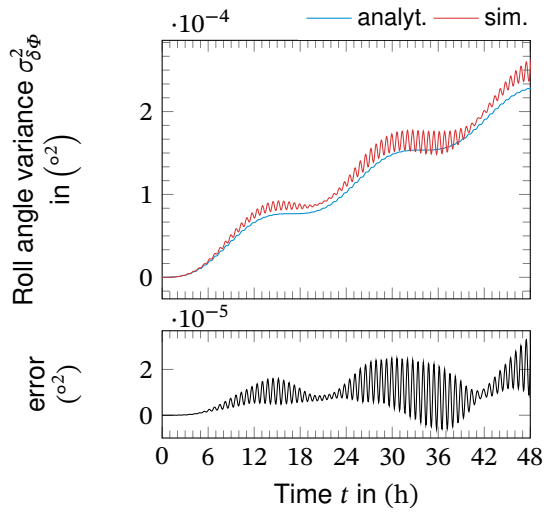
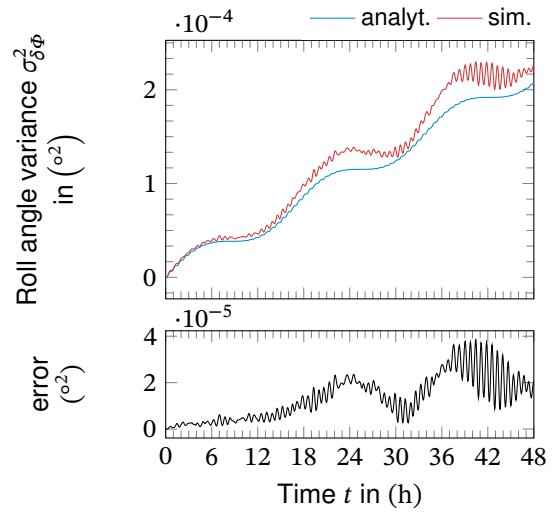


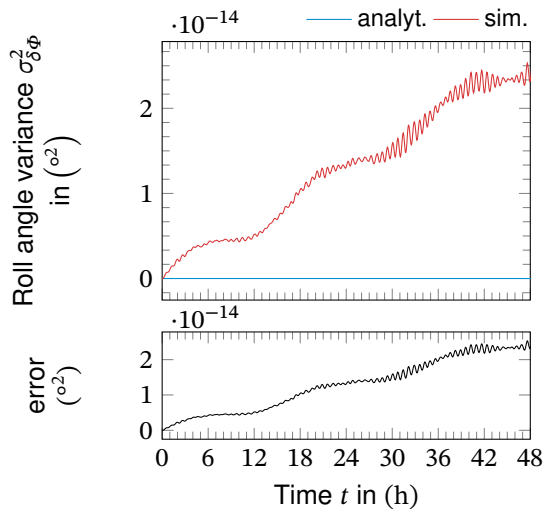
Figure E.11.: Analytical east velocity error variance for WGN compared to Monte Carlo simulation. Velocity random walk $N_{acc} = 1 \frac{\text{mg}}{\sqrt{\text{Hz}}}$, angular random walk $N_{gyr} = 1 \frac{\circ}{\sqrt{\text{h}}}$.



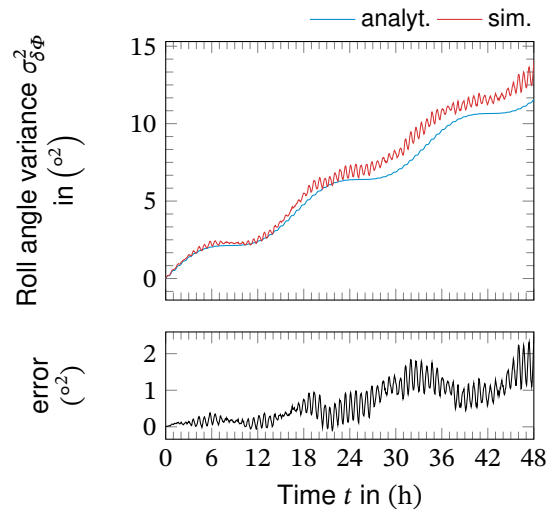
(a) Roll angle variance from WGN $f_{b,x}$.



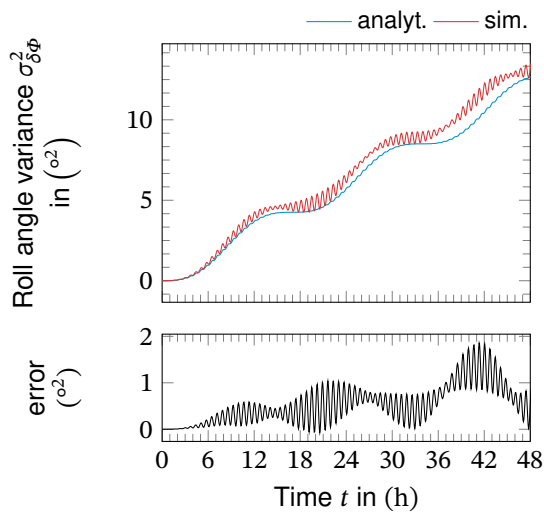
(b) Roll angle variance from WGN $f_{b,y}$.



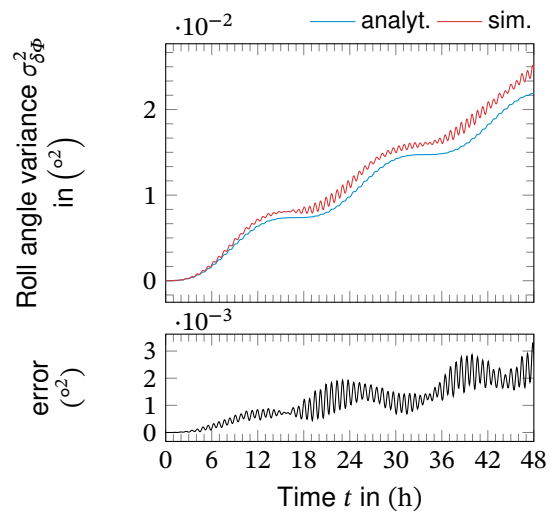
(c) Roll angle variance from WGN $f_{b,z}$.



(d) Roll angle variance from WGN $\omega_{ib,x}$.



(e) Roll angle variance from WGN $\omega_{ib,y}$.



(f) Roll angle variance from WGN $\omega_{ib,z}$.

Figure E.12.: Roll angle error variance for WGN compared to Monte Carlo simulation. Velocity random walk $N_{acc} = 1 \frac{\text{mg}}{\sqrt{\text{Hz}}}$, angular random walk $N_{gyr} = 1 \frac{\circ}{\sqrt{\text{h}}}$.

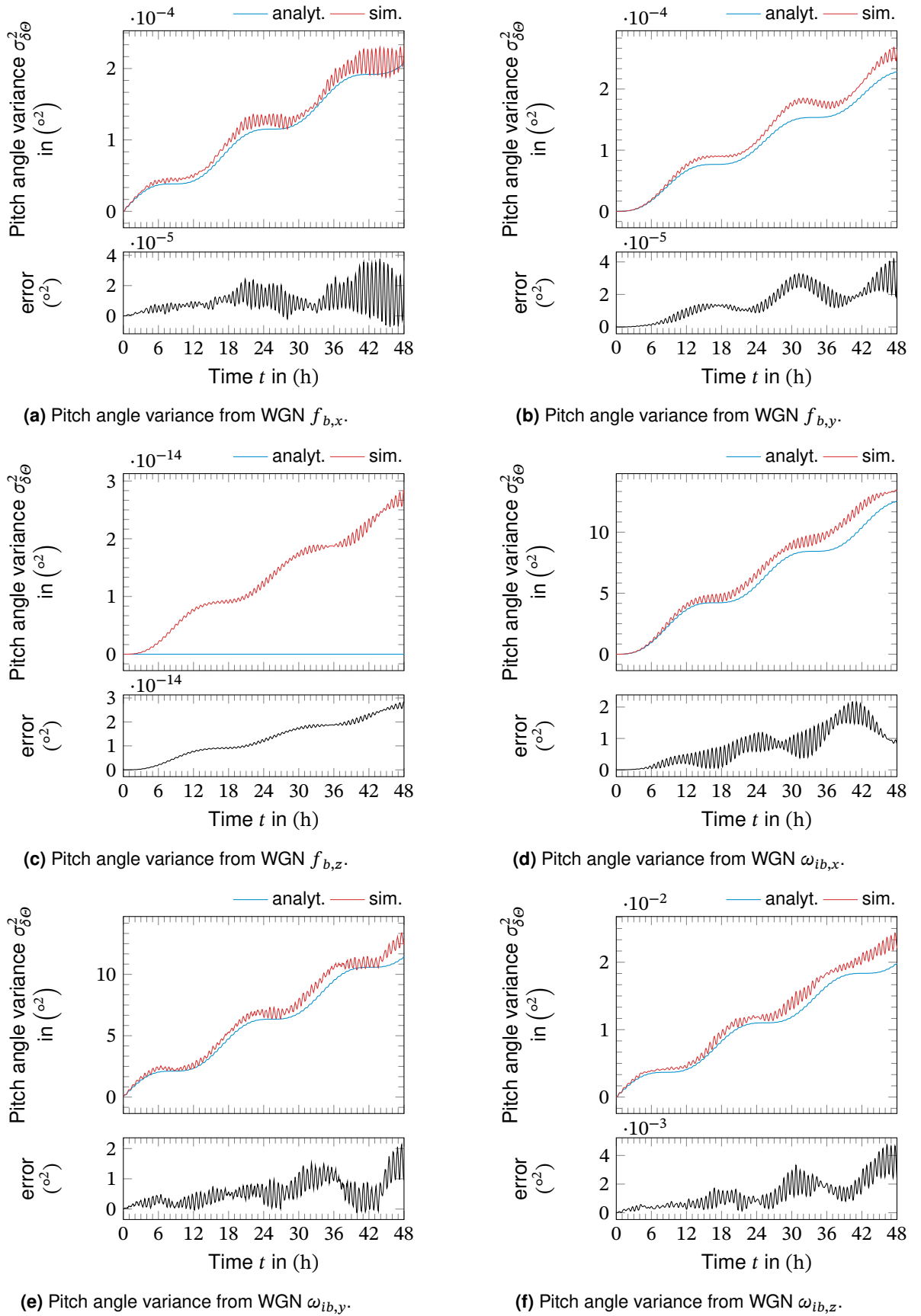
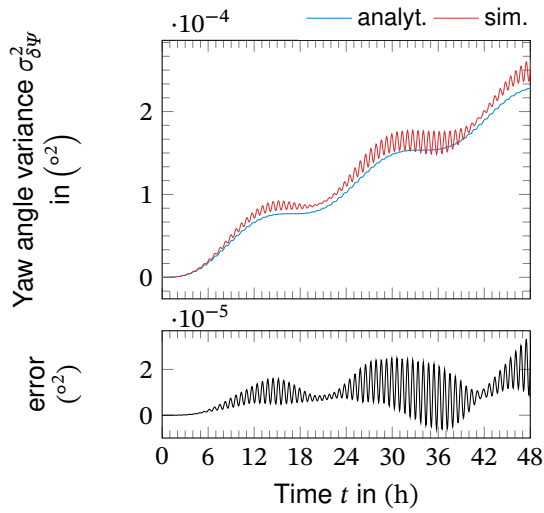
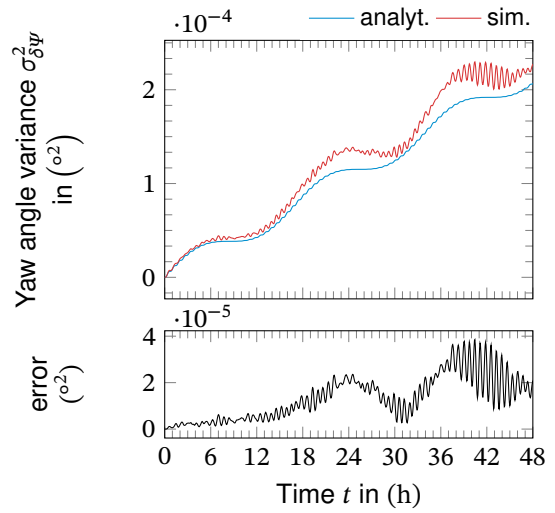


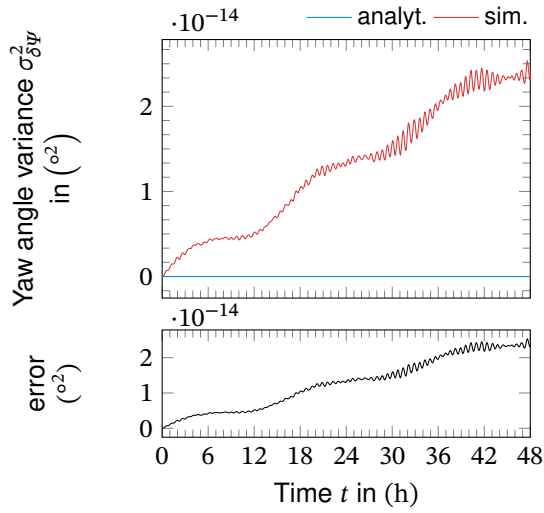
Figure E.13.: Pitch angle error variance for WGN compared to Monte Carlo simulation. Velocity random walk $N_{acc} = 1 \frac{\text{mg}}{\sqrt{\text{Hz}}}$, angular random walk $N_{gyr} = 1 \frac{^\circ}{\sqrt{\text{h}}}$.



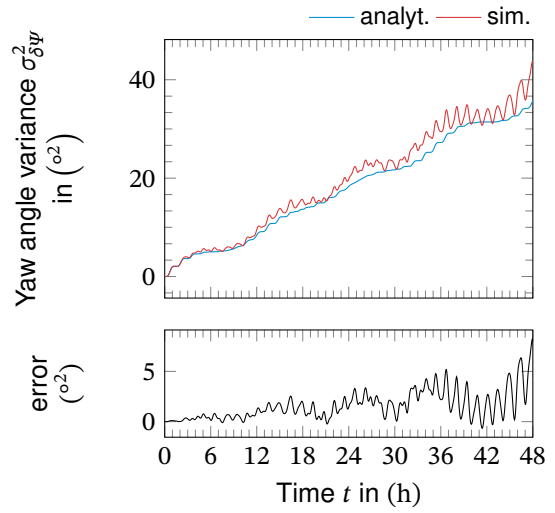
(a) Yaw angle variance from WGN $f_{b,x}$.



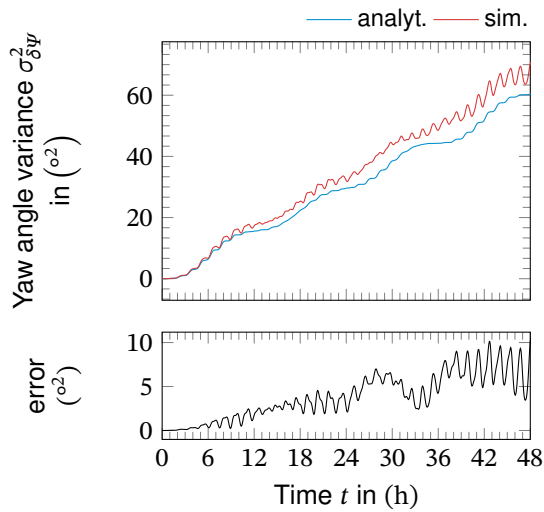
(b) Yaw angle variance from WGN $f_{b,y}$.



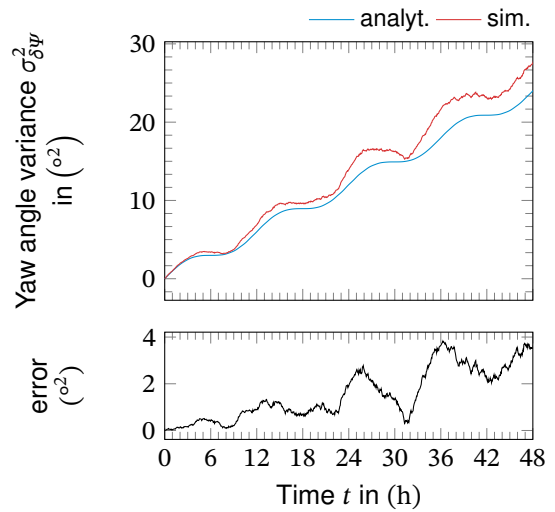
(c) Yaw angle variance from WGN $f_{b,z}$.



(d) Yaw angle variance from WGN $\omega_{ib,x}$.



(e) Yaw angle variance from WGN $\omega_{ib,y}$.



(f) Yaw angle variance from WGN $\omega_{ib,z}$.

Figure E.14.: Yaw angle error variance for WGN compared to Monte Carlo simulation. Velocity random walk $N_{acc} = 1 \frac{mg}{\sqrt{Hz}}$, angular random walk $N_{gyr} = 1 \frac{\circ}{\sqrt{h}}$.

Appendix F.

Inertial Laboratory Error Sensitivities

Table F.1.: Earth angular rate.

Error	Sensitivity of IMU kinematic errors
$\delta\omega_{ie}$	$\frac{\partial\delta\omega_{ib}}{\partial\delta\omega_{ie}^T} = \mathbf{R}_{\hat{b}e}$ $\frac{\partial\delta\dot{\omega}_{ib}}{\partial\delta\omega_{ie}^T} = -\mathbf{R}_{\hat{b}n}(\hat{\omega}_{np}\times)\mathbf{R}_{\hat{n}e} - \mathbf{R}_{\hat{b}p}(\hat{\omega}_{pw}\times)\mathbf{R}_{\hat{p}e} - \mathbf{R}_{\hat{b}w}(\hat{\omega}_{wv}\times)\mathbf{R}_{\hat{v}e}$ $- \mathbf{R}_{\hat{b}v}(\hat{\omega}_{vu}\times)\mathbf{R}_{\hat{v}e} - \mathbf{R}_{\hat{b}u}(\hat{\omega}_{ub}\times)\mathbf{R}_{\hat{u}e}$ $\frac{\partial\delta\mathbf{f}_b}{\partial\delta\omega_{ie}^T} = \mathbf{0}$ <p>Effect of Earth's angular rate on the specific forces is covered by gravity and gravity errors.</p>
$\delta\dot{\omega}_{ie}$	$\frac{\partial\delta\omega_{ib}}{\partial\delta\dot{\omega}_{ie}^T} = \mathbf{0}$ $\frac{\partial\delta\dot{\omega}_{ib}}{\partial\delta\dot{\omega}_{ie}^T} = \mathbf{R}_{\hat{b}e}$ $\frac{\partial\delta\mathbf{f}_b}{\partial\delta\dot{\omega}_{ie}^T} = \mathbf{0}$ <p>Effect of Earth's angular rate on the specific forces is covered by gravity and gravity errors.</p>

Table F.2.: Local gravity.

Error	Sensitivity of IMU kinematic errors
$\delta\gamma_n$	$\frac{\partial\delta\omega_{ib}}{\partial\delta\gamma_n^T} = \mathbf{0}$ $\frac{\partial\delta\dot{\omega}_{ib}}{\partial\delta\gamma_n^T} = \mathbf{0}$ $\frac{\partial\delta\mathbf{f}_b}{\partial\delta\gamma_n^T} = \mathbf{R}_{\hat{b}n}$

Table F.3.: Rotation of the local NED reference frame with respect to the ECEF frame.

Error	Sensitivity of IMU kinematic errors
$\Psi_{n\hat{n}}$	$\begin{aligned} \frac{\partial \delta \mathbf{f}_b}{\partial \Psi_{n\hat{n}^T}} = & -2\mathbf{R}_{\hat{b}n} [(\hat{\mathbf{r}}_n(P_p) \times) + \hat{\mathbf{\Omega}}_{en}(\hat{\mathbf{r}}_n(P_p) \times)] ((\mathbf{R}_{\hat{n}e} \hat{\boldsymbol{\omega}}_{ie}) \times) \\ & - 2\mathbf{R}_{\hat{b}p} [(\hat{\mathbf{r}}_p(P_w) \times) + \hat{\mathbf{\Omega}}_{ep}(\hat{\mathbf{r}}_p(P_w) \times)] \mathbf{R}_{\hat{p}n} ((\mathbf{R}_{\hat{n}e} \hat{\boldsymbol{\omega}}_{ie}) \times) \\ & - 2\mathbf{R}_{\hat{b}w} [(\hat{\mathbf{r}}_w(P_v) \times) + \hat{\mathbf{\Omega}}_{ew}(\hat{\mathbf{r}}_w(P_v) \times)] \mathbf{R}_{\hat{w}n} ((\mathbf{R}_{\hat{n}e} \hat{\boldsymbol{\omega}}_{ie}) \times) \\ & - 2\mathbf{R}_{\hat{b}v} [(\hat{\mathbf{r}}_v(P_u) \times) + \hat{\mathbf{\Omega}}_{ev}(\hat{\mathbf{r}}_v(P_u) \times)] \mathbf{R}_{\hat{v}n} ((\mathbf{R}_{\hat{n}e} \hat{\boldsymbol{\omega}}_{ie}) \times) \\ & - 2\mathbf{R}_{\hat{b}u} [(\hat{\mathbf{r}}_u(P_b) \times) + \hat{\mathbf{\Omega}}_{eu}(\hat{\mathbf{r}}_u(P_b) \times)] \mathbf{R}_{\hat{u}n} ((\mathbf{R}_{\hat{n}e} \hat{\boldsymbol{\omega}}_{ie}) \times) \\ & + \mathbf{R}_{\hat{b}n}(\hat{\mathbf{r}}_n(P_p) \times) ((\mathbf{R}_{\hat{n}e} \hat{\boldsymbol{\omega}}_{ie}) \times) \\ & + \mathbf{R}_{\hat{b}p}(\hat{\mathbf{r}}_p(P_w) \times) \mathbf{R}_{\hat{p}n} ((\mathbf{R}_{\hat{n}e} \hat{\boldsymbol{\omega}}_{ie}) \times) \\ & + \mathbf{R}_{\hat{b}w}(\hat{\mathbf{r}}_w(P_v) \times) \mathbf{R}_{\hat{w}n} ((\mathbf{R}_{\hat{n}e} \hat{\boldsymbol{\omega}}_{ie}) \times) \\ & + \mathbf{R}_{\hat{b}v}(\hat{\mathbf{r}}_v(P_u) \times) \mathbf{R}_{\hat{v}n} ((\mathbf{R}_{\hat{n}e} \hat{\boldsymbol{\omega}}_{ie}) \times) \\ & + \mathbf{R}_{\hat{b}u}(\hat{\mathbf{r}}_u(P_b) \times) \mathbf{R}_{\hat{u}n} ((\mathbf{R}_{\hat{n}e} \hat{\boldsymbol{\omega}}_{ie}) \times) \\ & + \mathbf{R}_{\hat{b}n} \frac{\partial \hat{\boldsymbol{\gamma}}_n(\mathbf{r}_e)}{\partial \mathbf{r}_e} ([\hat{\mathbf{r}}_n(P_p) + \mathbf{R}_{\hat{n}p}[\hat{\mathbf{r}}_p(P_w) + \mathbf{R}_{\hat{p}w}[\hat{\mathbf{r}}_w(P_v) + \mathbf{R}_{\hat{w}v}[\hat{\mathbf{r}}_v(P_u) + \mathbf{R}_{\hat{v}u}\hat{\mathbf{r}}_u(P_b)]]]] \times) \\ & - \mathbf{R}_{\hat{b}n}((\hat{\boldsymbol{\gamma}}_n(P_b)) \times) \end{aligned}$

Table F.4.: Rotation of the test pad with respect to the local reference frame.

Error	Sensitivity of IMU kinematic errors
$\delta\omega_{np}$	$\frac{\partial\delta\omega_{ib}}{\partial\delta\omega_{np}^\top} = \mathbf{R}_{\hat{b}p}$ $\frac{\partial\delta\dot{\omega}_{ib}}{\partial\delta\omega_{np}^\top} = -\mathbf{R}_{\hat{b}p}(\hat{\omega}_{pw}\times) - \mathbf{R}_{\hat{b}w}(\hat{\omega}_{wv}\times)\mathbf{R}_{\hat{w}p} - \mathbf{R}_{\hat{b}v}(\hat{\omega}_{vu}\times)\mathbf{R}_{\hat{v}p} - \mathbf{R}_{\hat{b}u}(\hat{\omega}_{ub}\times)\mathbf{R}_{\hat{u}p}$ $\begin{aligned} \frac{\partial\delta\mathbf{f}_b}{\partial\delta\omega_{np}^\top} = & -2\mathbf{R}_{\hat{b}p}[(\dot{\hat{\mathbf{r}}}_p(P_w)\times) + \hat{\mathbf{\Omega}}_{ep}(\hat{\mathbf{r}}_p(P_w)\times)] \\ & - 2\mathbf{R}_{\hat{b}w}[(\dot{\hat{\mathbf{r}}}_w(P_v)\times) + \hat{\mathbf{\Omega}}_{ew}(\hat{\mathbf{r}}_w(P_v)\times)]\mathbf{R}_{\hat{w}p} \\ & - 2\mathbf{R}_{\hat{b}v}[(\dot{\hat{\mathbf{r}}}_v(P_u)\times) + \hat{\mathbf{\Omega}}_{ev}(\hat{\mathbf{r}}_v(P_u)\times)]\mathbf{R}_{\hat{v}p} \\ & - 2\mathbf{R}_{\hat{b}u}[(\dot{\hat{\mathbf{r}}}_u(P_b)\times) + \hat{\mathbf{\Omega}}_{eu}(\hat{\mathbf{r}}_u(P_b)\times)]\mathbf{R}_{\hat{u}p} \\ & - \mathbf{R}_{\hat{b}p}(\hat{\mathbf{r}}_p(P_w)\times)\mathbf{R}_{\hat{p}n}(\hat{\omega}_{in}\times) \\ & - \mathbf{R}_{\hat{b}w}(\hat{\mathbf{r}}_w(P_v)\times)(\mathbf{R}_{\hat{w}p}(\hat{\omega}_{pw}\times) + \mathbf{R}_{\hat{w}n}(\hat{\omega}_{in}\times)) \\ & - \mathbf{R}_{\hat{b}v}(\hat{\mathbf{r}}_v(P_u)\times)(\mathbf{R}_{\hat{v}w}(\hat{\omega}_{wv}\times)\mathbf{R}_{\hat{w}p} + \mathbf{R}_{\hat{v}p}(\hat{\omega}_{pw}\times) + \mathbf{R}_{\hat{v}n}(\hat{\omega}_{in}\times)) \\ & - \mathbf{R}_{\hat{b}u}(\hat{\mathbf{r}}_u(P_b)\times)(\mathbf{R}_{\hat{u}v}(\hat{\omega}_{vu}\times)\mathbf{R}_{\hat{v}p} + \mathbf{R}_{\hat{u}w}(\hat{\omega}_{wv}\times)\mathbf{R}_{\hat{w}p} + \mathbf{R}_{\hat{u}p}(\hat{\omega}_{pw}\times) + \mathbf{R}_{\hat{u}n}(\hat{\omega}_{in}\times)) \end{aligned}$
$\delta\dot{\omega}_{np}$	$\frac{\partial\delta\omega_{ib}}{\partial\delta\dot{\omega}_{np}^\top} = \mathbf{0}$ $\frac{\partial\delta\dot{\omega}_{ib}}{\partial\delta\dot{\omega}_{np}^\top} = \mathbf{R}_{\hat{b}p}$ $\begin{aligned} \frac{\partial\delta\mathbf{f}_b}{\partial\delta\dot{\omega}_{np}^\top} = & -\mathbf{R}_{\hat{b}p}(\dot{\hat{\mathbf{r}}}_p(P_w)\times) - \mathbf{R}_{\hat{b}w}(\dot{\hat{\mathbf{r}}}_w(P_v)\times)\mathbf{R}_{\hat{w}p} \\ & - \mathbf{R}_{\hat{b}v}(\dot{\hat{\mathbf{r}}}_v(P_u)\times)\mathbf{R}_{\hat{v}p} - \mathbf{R}_{\hat{b}u}(\dot{\hat{\mathbf{r}}}_u(P_b)\times)\mathbf{R}_{\hat{u}p} \end{aligned}$
Ψ_{pp}	$\frac{\partial\delta\omega_{ib}}{\partial\Psi_{pp}^\top} = -\mathbf{R}_{\hat{b}p}((\hat{\omega}_{np} + \mathbf{R}_{\hat{p}n}\mathbf{R}_{\hat{n}e}\hat{\omega}_{ie})\times)$ $\begin{aligned} \frac{\partial\delta\dot{\omega}_{ib}}{\partial\Psi_{pp}^\top} = & -\mathbf{R}_{\hat{b}p}((\dot{\hat{\omega}}_{np} + \mathbf{R}_{\hat{p}n}\mathbf{R}_{\hat{n}e}\dot{\hat{\omega}}_{ie})\times) \\ & + \mathbf{R}_{\hat{b}p}(\hat{\omega}_{pw}\times)((\hat{\omega}_{np} + \mathbf{R}_{\hat{p}n}\mathbf{R}_{\hat{n}e}\hat{\omega}_{ie})\times) \\ & + \mathbf{R}_{\hat{b}w}(\hat{\omega}_{wv}\times)\mathbf{R}_{\hat{w}p}((\hat{\omega}_{np} + \mathbf{R}_{\hat{p}n}\mathbf{R}_{\hat{n}e}\hat{\omega}_{ie})\times) \\ & + \mathbf{R}_{\hat{b}v}(\hat{\omega}_{vu}\times)\mathbf{R}_{\hat{v}p}((\hat{\omega}_{np} + \mathbf{R}_{\hat{p}n}\mathbf{R}_{\hat{n}e}\hat{\omega}_{ie})\times) \\ & + \mathbf{R}_{\hat{b}u}(\hat{\omega}_{ub}\times)\mathbf{R}_{\hat{u}p}((\hat{\omega}_{np} + \mathbf{R}_{\hat{p}n}\mathbf{R}_{\hat{n}e}\hat{\omega}_{ie})\times) \\ & + (\hat{\omega}_{ub}\times)\mathbf{R}_{\hat{b}p}((\hat{\omega}_{np} + \mathbf{R}_{\hat{p}n}\mathbf{R}_{\hat{n}e}\hat{\omega}_{ie})\times) \end{aligned}$ $\begin{aligned} \frac{\partial\delta\mathbf{f}_b}{\partial\Psi_{pp}^\top} = & -2\mathbf{R}_{\hat{b}p}[(\dot{\hat{\mathbf{r}}}_p(P_w)\times) + \hat{\mathbf{\Omega}}_{ep}(\hat{\mathbf{r}}_p(P_w)\times)]((\hat{\omega}_{np} + \mathbf{R}_{\hat{p}n}\mathbf{R}_{\hat{n}e}\hat{\omega}_{ie})\times) \\ & - 2\mathbf{R}_{\hat{b}w}[(\dot{\hat{\mathbf{r}}}_w(P_v)\times) + \hat{\mathbf{\Omega}}_{ew}(\hat{\mathbf{r}}_w(P_v)\times)]\mathbf{R}_{\hat{w}p}((\hat{\omega}_{np} + \mathbf{R}_{\hat{p}n}\mathbf{R}_{\hat{n}e}\hat{\omega}_{ie})\times) \\ & - 2\mathbf{R}_{\hat{b}v}[(\dot{\hat{\mathbf{r}}}_v(P_u)\times) + \hat{\mathbf{\Omega}}_{ev}(\hat{\mathbf{r}}_v(P_u)\times)]\mathbf{R}_{\hat{v}p}((\hat{\omega}_{np} + \mathbf{R}_{\hat{p}n}\mathbf{R}_{\hat{n}e}\hat{\omega}_{ie})\times) \\ & - 2\mathbf{R}_{\hat{b}u}[(\dot{\hat{\mathbf{r}}}_u(P_b)\times) + \hat{\mathbf{\Omega}}_{eu}(\hat{\mathbf{r}}_u(P_b)\times)]\mathbf{R}_{\hat{u}p}((\hat{\omega}_{np} + \mathbf{R}_{\hat{p}n}\mathbf{R}_{\hat{n}e}\hat{\omega}_{ie})\times) \\ & + \mathbf{R}_{\hat{b}p}(\dot{\hat{\mathbf{r}}}_p(P_w)\times)((\dot{\hat{\omega}}_{np} + \mathbf{R}_{\hat{p}n}\mathbf{R}_{\hat{n}e}\dot{\hat{\omega}}_{ie})\times) \\ & + \mathbf{R}_{\hat{b}w}(\dot{\hat{\mathbf{r}}}_w(P_v)\times)\mathbf{R}_{\hat{w}p}((\dot{\hat{\omega}}_{np} + \mathbf{R}_{\hat{p}n}\mathbf{R}_{\hat{n}e}\dot{\hat{\omega}}_{ie})\times) \\ & + \mathbf{R}_{\hat{b}v}(\dot{\hat{\mathbf{r}}}_v(P_u)\times)\mathbf{R}_{\hat{v}p}((\dot{\hat{\omega}}_{np} + \mathbf{R}_{\hat{p}n}\mathbf{R}_{\hat{n}e}\dot{\hat{\omega}}_{ie})\times) \\ & + \mathbf{R}_{\hat{b}u}(\dot{\hat{\mathbf{r}}}_u(P_b)\times)\mathbf{R}_{\hat{u}p}((\dot{\hat{\omega}}_{np} + \mathbf{R}_{\hat{p}n}\mathbf{R}_{\hat{n}e}\dot{\hat{\omega}}_{ie})\times) \\ & + \mathbf{R}_{\hat{b}n}\frac{\partial\hat{\gamma}_n(\mathbf{r}_e)}{\partial\mathbf{r}_e}([\hat{\mathbf{r}}_p(P_w) + \mathbf{R}_{\hat{p}w}[\hat{\mathbf{r}}_w(P_v) + \mathbf{R}_{\hat{w}v}[\hat{\mathbf{r}}_v(P_u) + \mathbf{R}_{\hat{v}u}\hat{\mathbf{r}}_u(P_b)]]])\times) \\ & - \mathbf{R}_{\hat{b}p}((\mathbf{R}_{\hat{p}n}\hat{\gamma}_n(P_b))\times) \end{aligned}$

Table F.5.: Position of the test pad with respect to the local reference frame.

Error	Sensitivity of IMU kinematic errors
$\delta \mathbf{r}_n(P_p)$	$\frac{\partial \delta \boldsymbol{\omega}_{ib}}{\partial \delta \mathbf{r}_n(P_p)^\top} = \mathbf{0}$ $\frac{\partial \delta \dot{\boldsymbol{\omega}}_{ib}}{\partial \delta \mathbf{r}_n(P_p)^\top} = \mathbf{0}$ $\frac{\partial \delta \mathbf{f}_b}{\partial \delta \mathbf{r}_n(P_p)^\top} = \mathbf{R}_{bn} (\hat{\boldsymbol{\Omega}}_{in}^2 + \dot{\hat{\boldsymbol{\Omega}}}_{in})$
$\delta \dot{\mathbf{r}}_n(P_p)$	$\frac{\partial \delta \boldsymbol{\omega}_{ib}}{\partial \delta \dot{\mathbf{r}}_n(P_p)^\top} = \mathbf{0}$ $\frac{\partial \delta \dot{\boldsymbol{\omega}}_{ib}}{\partial \delta \dot{\mathbf{r}}_n(P_p)^\top} = \mathbf{0}$ $\frac{\partial \delta \mathbf{f}_b}{\partial \delta \dot{\mathbf{r}}_n(P_p)^\top} = \mathbf{R}_{bn} \hat{\boldsymbol{\Omega}}_{in}$
$\delta \ddot{\mathbf{r}}_n(P_p)$	$\frac{\partial \delta \boldsymbol{\omega}_{ib}}{\partial \delta \ddot{\mathbf{r}}_n(P_p)^\top} = \mathbf{0}$ $\frac{\partial \delta \dot{\boldsymbol{\omega}}_{ib}}{\partial \delta \ddot{\mathbf{r}}_n(P_p)^\top} = \mathbf{0}$ $\frac{\partial \delta \mathbf{f}_b}{\partial \delta \ddot{\mathbf{r}}_n(P_p)^\top} = \mathbf{R}_{bn}$

Table F.6.: Rotation of the outer gimbal with respect to the test pad.

Error	Sensitivity of IMU kinematic errors
$\delta\omega_{pw}$	$\frac{\partial\delta\omega_{ib}}{\partial\delta\omega_{pw}^\top} = \mathbf{R}_{\hat{b}w}$ $\frac{\partial\delta\dot{\omega}_{ib}}{\partial\delta\omega_{pw}^\top} = -\mathbf{R}_{\hat{b}w}(\dot{\omega}_{wv}\times) - \mathbf{R}_{\hat{b}v}(\dot{\omega}_{vu}\times)\mathbf{R}_{\hat{v}w} - \mathbf{R}_{\hat{b}u}(\dot{\omega}_{ub}\times)\mathbf{R}_{\hat{u}w}$ $\begin{aligned} \frac{\partial\delta\mathbf{f}_b}{\partial\delta\omega_{pw}^\top} = & -2\mathbf{R}_{\hat{b}w}[(\hat{\mathbf{r}}_w(P_v)\times) + \hat{\mathbf{\Omega}}_{ew}(\hat{\mathbf{r}}_w(P_v)\times)] \\ & - 2\mathbf{R}_{\hat{b}v}[(\hat{\mathbf{r}}_v(P_u)\times) + \hat{\mathbf{\Omega}}_{ev}(\hat{\mathbf{r}}_v(P_u)\times)]\mathbf{R}_{\hat{v}w} \\ & - 2\mathbf{R}_{\hat{b}u}[(\hat{\mathbf{r}}_u(P_b)\times) + \hat{\mathbf{\Omega}}_{eu}(\hat{\mathbf{r}}_u(P_b)\times)]\mathbf{R}_{\hat{u}w} \\ & - \mathbf{R}_{\hat{b}w}(\hat{\mathbf{r}}_w(P_v)\times)(\mathbf{R}_{\hat{w}p}(\dot{\omega}_{ip}\times)) \\ & - \mathbf{R}_{\hat{b}v}(\hat{\mathbf{r}}_v(P_u)\times)(\mathbf{R}_{\hat{v}w}(\dot{\omega}_{wv}\times) + \mathbf{R}_{\hat{v}p}(\dot{\omega}_{ip}\times)) \\ & - \mathbf{R}_{\hat{b}u}(\hat{\mathbf{r}}_u(P_b)\times)(\mathbf{R}_{\hat{u}v}(\dot{\omega}_{vu}\times)\mathbf{R}_{\hat{v}w} + \mathbf{R}_{\hat{u}w}(\dot{\omega}_{wv}\times) + \mathbf{R}_{\hat{u}p}(\dot{\omega}_{ip}\times)) \end{aligned}$
$\delta\dot{\omega}_{pw}$	$\frac{\partial\delta\omega_{ib}}{\partial\delta\dot{\omega}_{pw}^\top} = \mathbf{0}$ $\frac{\partial\delta\dot{\omega}_{ib}}{\partial\delta\dot{\omega}_{pw}^\top} = \mathbf{R}_{\hat{b}w}$ $\begin{aligned} \frac{\partial\delta\mathbf{f}_b}{\partial\delta\dot{\omega}_{pw}^\top} = & -\mathbf{R}_{\hat{b}w}(\hat{\mathbf{r}}_w(P_v)\times) \\ & - \mathbf{R}_{\hat{b}v}(\hat{\mathbf{r}}_v(P_u)\times)\mathbf{R}_{\hat{v}w} - \mathbf{R}_{\hat{b}u}(\hat{\mathbf{r}}_u(P_b)\times)\mathbf{R}_{\hat{u}w} \end{aligned}$
$\Psi_{w\dot{w}}$	$\frac{\partial\delta\omega_{ib}}{\partial\Psi_{w\dot{w}}^\top} = -\mathbf{R}_{\hat{b}w}((\dot{\omega}_{pw} + \mathbf{R}_{\hat{w}p}(\dot{\omega}_{np} + \mathbf{R}_{\hat{p}n}\mathbf{R}_{\hat{n}e}\dot{\omega}_{ie}))\times)$ $\begin{aligned} \frac{\partial\delta\dot{\omega}_{ib}}{\partial\Psi_{w\dot{w}}^\top} = & -\mathbf{R}_{\hat{b}w}((\dot{\omega}_{pw} + \mathbf{R}_{\hat{w}p}(\dot{\omega}_{np} + \mathbf{R}_{\hat{p}n}\mathbf{R}_{\hat{n}e}\dot{\omega}_{ie}))\times) \\ & + \mathbf{R}_{\hat{b}w}(\dot{\omega}_{wv}\times)((\dot{\omega}_{pw} + \mathbf{R}_{\hat{w}p}(\dot{\omega}_{np} + \mathbf{R}_{\hat{p}n}\mathbf{R}_{\hat{n}e}\dot{\omega}_{ie}))\times) \\ & + \mathbf{R}_{\hat{b}v}(\dot{\omega}_{wv}\times)\mathbf{R}_{\hat{v}w}((\dot{\omega}_{pw} + \mathbf{R}_{\hat{w}p}(\dot{\omega}_{np} + \mathbf{R}_{\hat{p}n}\mathbf{R}_{\hat{n}e}\dot{\omega}_{ie}))\times) \\ & + \mathbf{R}_{\hat{b}u}(\dot{\omega}_{vu}\times)\mathbf{R}_{\hat{u}w}((\dot{\omega}_{pw} + \mathbf{R}_{\hat{w}p}(\dot{\omega}_{np} + \mathbf{R}_{\hat{p}n}\mathbf{R}_{\hat{n}e}\dot{\omega}_{ie}))\times) \\ & + (\dot{\omega}_{ub}\times)\mathbf{R}_{\hat{b}w}((\dot{\omega}_{pw} + \mathbf{R}_{\hat{w}p}(\dot{\omega}_{np} + \mathbf{R}_{\hat{p}n}\mathbf{R}_{\hat{n}e}\dot{\omega}_{ie}))\times) \end{aligned}$ $\begin{aligned} \frac{\partial\delta\mathbf{f}_b}{\partial\Psi_{w\dot{w}}^\top} = & -2\mathbf{R}_{\hat{b}w}[(\hat{\mathbf{r}}_w(P_v)\times) + \hat{\mathbf{\Omega}}_{ew}(\hat{\mathbf{r}}_w(P_v)\times)]((\dot{\omega}_{pw} + \mathbf{R}_{\hat{w}p}(\dot{\omega}_{np} + \mathbf{R}_{\hat{p}n}\mathbf{R}_{\hat{n}e}\dot{\omega}_{ie}))\times) \\ & - 2\mathbf{R}_{\hat{b}v}[(\hat{\mathbf{r}}_v(P_u)\times) + \hat{\mathbf{\Omega}}_{ev}(\hat{\mathbf{r}}_v(P_u)\times)]\mathbf{R}_{\hat{v}w}((\dot{\omega}_{pw} + \mathbf{R}_{\hat{w}p}(\dot{\omega}_{np} + \mathbf{R}_{\hat{p}n}\mathbf{R}_{\hat{n}e}\dot{\omega}_{ie}))\times) \\ & - 2\mathbf{R}_{\hat{b}u}[(\hat{\mathbf{r}}_u(P_b)\times) + \hat{\mathbf{\Omega}}_{eu}(\hat{\mathbf{r}}_u(P_b)\times)]\mathbf{R}_{\hat{u}w}((\dot{\omega}_{pw} + \mathbf{R}_{\hat{w}p}(\dot{\omega}_{np} + \mathbf{R}_{\hat{p}n}\mathbf{R}_{\hat{n}e}\dot{\omega}_{ie}))\times) \\ & + \mathbf{R}_{\hat{b}w}(\hat{\mathbf{r}}_w(P_v)\times)((\dot{\omega}_{pw} + \mathbf{R}_{\hat{w}p}(\dot{\omega}_{np} + \mathbf{R}_{\hat{p}n}\mathbf{R}_{\hat{n}e}\dot{\omega}_{ie}))\times) \\ & + \mathbf{R}_{\hat{b}v}(\hat{\mathbf{r}}_v(P_u)\times)\mathbf{R}_{\hat{v}w}((\dot{\omega}_{pw} + \mathbf{R}_{\hat{w}p}(\dot{\omega}_{np} + \mathbf{R}_{\hat{p}n}\mathbf{R}_{\hat{n}e}\dot{\omega}_{ie}))\times) \\ & + \mathbf{R}_{\hat{b}u}(\hat{\mathbf{r}}_u(P_b)\times)\mathbf{R}_{\hat{u}w}((\dot{\omega}_{pw} + \mathbf{R}_{\hat{w}p}(\dot{\omega}_{np} + \mathbf{R}_{\hat{p}n}\mathbf{R}_{\hat{n}e}\dot{\omega}_{ie}))\times) \\ & + \mathbf{R}_{\hat{b}n}\frac{\partial\hat{\mathbf{r}}_n(\mathbf{r}_e)}{\partial\mathbf{r}_e}([\hat{\mathbf{r}}_w(P_v) + \mathbf{R}_{\hat{w}v}[\hat{\mathbf{r}}_v(P_u) + \mathbf{R}_{\hat{v}u}\hat{\mathbf{r}}_u(P_b)])\times) - \mathbf{R}_{\hat{b}w}((\mathbf{R}_{\hat{w}n}\hat{\mathbf{r}}_n(P_b))\times) \\ & - \mathbf{R}_{\hat{b}u}\mathbf{R}_{\hat{u}v}\mathbf{R}_{\hat{v}w}(\hat{\mathbf{a}}_p\times) \end{aligned}$

Table F.7.: Position of the outer gimbal with respect to the test pad.

Error	Sensitivity of IMU kinematic errors
$\delta \mathbf{r}_p(P_w)$	$\frac{\partial \delta \boldsymbol{\omega}_{ib}}{\partial \delta \mathbf{r}_p(P_w)^\top} = \mathbf{0}$ $\frac{\partial \delta \dot{\boldsymbol{\omega}}_{ib}}{\partial \delta \mathbf{r}_p(P_w)^\top} = \mathbf{0}$ $\frac{\partial \delta \mathbf{f}_b}{\partial \delta \mathbf{r}_p(P_w)^\top} = \mathbf{R}_{\hat{b}p} (\hat{\boldsymbol{\Omega}}_{ip}^2 + \dot{\hat{\boldsymbol{\Omega}}}_{ip})$
$\delta \dot{\mathbf{r}}_p(P_w)$	$\frac{\partial \delta \boldsymbol{\omega}_{ib}}{\partial \delta \dot{\mathbf{r}}_p(P_w)^\top} = \mathbf{0}$ $\frac{\partial \delta \dot{\boldsymbol{\omega}}_{ib}}{\partial \delta \dot{\mathbf{r}}_p(P_w)^\top} = \mathbf{0}$ $\frac{\partial \delta \mathbf{f}_b}{\partial \delta \dot{\mathbf{r}}_p(P_w)^\top} = \mathbf{R}_{\hat{b}n} \hat{\boldsymbol{\Omega}}_{ip}$
$\delta \ddot{\mathbf{r}}_p(P_w)$	$\frac{\partial \delta \boldsymbol{\omega}_{ib}}{\partial \delta \ddot{\mathbf{r}}_p(P_w)^\top} = \mathbf{0}$ $\frac{\partial \delta \dot{\boldsymbol{\omega}}_{ib}}{\partial \delta \ddot{\mathbf{r}}_p(P_w)^\top} = \mathbf{0}$ $\frac{\partial \delta \mathbf{f}_b}{\partial \delta \ddot{\mathbf{r}}_p(P_w)^\top} = \mathbf{R}_{\hat{b}p}$

Table F.8.: Rotation of the middle gimbal with respect to the outer gimbal.

Error	Sensitivity of IMU kinematic errors
$\delta\omega_{wv}$	$\frac{\partial\delta\omega_{ib}}{\partial\delta\omega_{wv}^\top} = \mathbf{R}_{bv}$ $\frac{\partial\delta\dot{\omega}_{ib}}{\partial\delta\omega_{wv}^\top} = -\mathbf{R}_{bv}(\hat{\omega}_{vu}\times) - \mathbf{R}_{bu}(\hat{\omega}_{ub}\times)\mathbf{R}_{uv}$ $\frac{\partial\delta\mathbf{f}_b}{\partial\delta\omega_{wv}^\top} = -2\mathbf{R}_{bv}[(\dot{\hat{\mathbf{r}}}_v(P_u)\times) + \hat{\mathbf{\Omega}}_{ev}(\hat{\mathbf{r}}_v(P_u)\times)]$ $- 2\mathbf{R}_{bu}[(\dot{\hat{\mathbf{r}}}_u(P_b)\times) + \hat{\mathbf{\Omega}}_{eu}(\hat{\mathbf{r}}_u(P_b)\times)]\mathbf{R}_{uv}$ $- \mathbf{R}_{bv}(\hat{\mathbf{r}}_v(P_u)\times)(\mathbf{R}_{vw}(\hat{\omega}_{iw}\times))$ $- \mathbf{R}_{bu}(\hat{\mathbf{r}}_u(P_b)\times)(\mathbf{R}_{uv}(\hat{\omega}_{vu}\times) + \mathbf{R}_{uw}(\hat{\omega}_{iw}\times))$
$\delta\dot{\omega}_{wv}$	$\frac{\partial\delta\omega_{ib}}{\partial\delta\dot{\omega}_{wv}^\top} = \mathbf{0}$ $\frac{\partial\delta\dot{\omega}_{ib}}{\partial\delta\dot{\omega}_{wv}^\top} = \mathbf{R}_{bv}$ $\frac{\partial\delta\mathbf{f}_b}{\partial\delta\dot{\omega}_{wv}^\top} = -\mathbf{R}_{bv}(\hat{\mathbf{r}}_v(P_u)\times) - \mathbf{R}_{bu}(\hat{\mathbf{r}}_u(P_b)\times)\mathbf{R}_{uv}$
$\Psi_{v\hat{v}}$	$\frac{\partial\delta\omega_{ib}}{\partial\Psi_{v\hat{v}}^\top} = -\mathbf{R}_{bv}((\hat{\omega}_{wv} + \mathbf{R}_{vw}(\hat{\omega}_{pw} + \mathbf{R}_{wp}(\hat{\omega}_{np} + \mathbf{R}_{pn}\mathbf{R}_{ne}\hat{\omega}_{ie})))\times)$ $\frac{\partial\delta\dot{\omega}_{ib}}{\partial\Psi_{v\hat{v}}^\top} = -\mathbf{R}_{bv}((\dot{\hat{\omega}}_{wv} + \mathbf{R}_{vw}(\dot{\hat{\omega}}_{pw} + \mathbf{R}_{wp}(\dot{\hat{\omega}}_{np} + \mathbf{R}_{pn}\mathbf{R}_{ne}\dot{\hat{\omega}}_{ie})))\times)$ $+ \mathbf{R}_{bv}(\hat{\omega}_{wv}\times)((\hat{\omega}_{wv} + \mathbf{R}_{vw}(\hat{\omega}_{pw} + \mathbf{R}_{wp}(\hat{\omega}_{np} + \mathbf{R}_{pn}\mathbf{R}_{ne}\hat{\omega}_{ie})))\times)$ $+ \mathbf{R}_{bu}(\hat{\omega}_{vu}\times)\mathbf{R}_{uv}((\hat{\omega}_{wv} + \mathbf{R}_{vw}(\hat{\omega}_{pw} + \mathbf{R}_{wp}(\hat{\omega}_{np} + \mathbf{R}_{pn}\mathbf{R}_{ne}\hat{\omega}_{ie})))\times)$ $+ (\hat{\omega}_{ub}\times)\mathbf{R}_{bv}((\hat{\omega}_{wv} + \mathbf{R}_{vw}(\hat{\omega}_{pw} + \mathbf{R}_{wp}(\hat{\omega}_{np} + \mathbf{R}_{pn}\mathbf{R}_{ne}\hat{\omega}_{ie})))\times)$ $\frac{\partial\delta\mathbf{f}_b}{\partial\Psi_{v\hat{v}}^\top} = -2\mathbf{R}_{bv}[(\dot{\hat{\mathbf{r}}}_v(P_u)\times) + \hat{\mathbf{\Omega}}_{ev}(\hat{\mathbf{r}}_v(P_u)\times)]((\hat{\omega}_{wv} + \mathbf{R}_{vw}(\hat{\omega}_{pw} + \mathbf{R}_{wp}(\hat{\omega}_{np} + \mathbf{R}_{pn}\mathbf{R}_{ne}\hat{\omega}_{ie})))\times)$ $- 2\mathbf{R}_{bu}[(\dot{\hat{\mathbf{r}}}_u(P_b)\times) + \hat{\mathbf{\Omega}}_{eu}(\hat{\mathbf{r}}_u(P_b)\times)]\mathbf{R}_{uv}((\hat{\omega}_{wv} + \mathbf{R}_{vw}(\hat{\omega}_{pw} + \mathbf{R}_{wp}(\hat{\omega}_{np} + \mathbf{R}_{pn}\mathbf{R}_{ne}\hat{\omega}_{ie})))\times)$ $+ \mathbf{R}_{bv}(\hat{\mathbf{r}}_v(P_u)\times)((\dot{\hat{\omega}}_{wv} + \mathbf{R}_{vw}(\dot{\hat{\omega}}_{pw} + \mathbf{R}_{wp}(\dot{\hat{\omega}}_{np} + \mathbf{R}_{pn}\mathbf{R}_{ne}\dot{\hat{\omega}}_{ie})))\times)$ $+ \mathbf{R}_{bu}(\hat{\mathbf{r}}_u(P_b)\times)\mathbf{R}_{uv}((\dot{\hat{\omega}}_{wv} + \mathbf{R}_{vw}(\dot{\hat{\omega}}_{pw} + \mathbf{R}_{wp}(\dot{\hat{\omega}}_{np} + \mathbf{R}_{pn}\mathbf{R}_{ne}\dot{\hat{\omega}}_{ie})))\times)$ $+ \mathbf{R}_{bn}\frac{\partial\hat{\gamma}_n(\mathbf{r}_e)}{\partial\mathbf{r}_e}([\hat{\mathbf{r}}_v(P_u) + \mathbf{R}_{vu}\hat{\mathbf{r}}_u(P_b)]\times) - \mathbf{R}_{bv}((\mathbf{R}_{vn}\hat{\gamma}_n(P_b))\times)$ $- \mathbf{R}_{bu}\mathbf{R}_{uv}(\hat{\mathbf{a}}_w\times)$

Table F.9.: Position of the middle gimbal with respect to the outer gimbal.

Error	Sensitivity of IMU kinematic errors
$\delta \mathbf{r}_w(P_v)$	$\frac{\partial \delta \boldsymbol{\omega}_{ib}}{\partial \delta \mathbf{r}_w(P_v)^T} = \mathbf{0}$ $\frac{\partial \delta \dot{\boldsymbol{\omega}}_{ib}}{\partial \delta \mathbf{r}_w(P_v)^T} = \mathbf{0}$ $\frac{\partial \delta \mathbf{f}_b}{\partial \delta \mathbf{r}_w(P_v)^T} = \mathbf{R}_{bw} (\hat{\boldsymbol{\Omega}}_{iw}^2 + \dot{\hat{\boldsymbol{\Omega}}}_{iw})$
$\delta \dot{\mathbf{r}}_w(P_v)$	$\frac{\partial \delta \boldsymbol{\omega}_{ib}}{\partial \delta \dot{\mathbf{r}}_w(P_v)^T} = \mathbf{0}$ $\frac{\partial \delta \dot{\boldsymbol{\omega}}_{ib}}{\partial \delta \dot{\mathbf{r}}_w(P_v)^T} = \mathbf{0}$ $\frac{\partial \delta \mathbf{f}_b}{\partial \delta \dot{\mathbf{r}}_w(P_v)^T} = \mathbf{R}_{bw} \hat{\boldsymbol{\Omega}}_{iw}$
$\delta \ddot{\mathbf{r}}_w(P_v)$	$\frac{\partial \delta \boldsymbol{\omega}_{ib}}{\partial \delta \ddot{\mathbf{r}}_w(P_v)^T} = \mathbf{0}$ $\frac{\partial \delta \dot{\boldsymbol{\omega}}_{ib}}{\partial \delta \ddot{\mathbf{r}}_w(P_v)^T} = \mathbf{0}$ $\frac{\partial \delta \mathbf{f}_b}{\partial \delta \ddot{\mathbf{r}}_w(P_v)^T} = \mathbf{R}_{bw}$

Table F.10.: Rotation of the inner gimbal with respect to the middle gimbal.

Error	Sensitivity of IMU kinematic errors
$\delta\omega_{vu}$	$\frac{\partial\delta\omega_{ib}}{\partial\delta\omega_{vu}^\top} = \mathbf{R}_{\hat{b}u}$ $\frac{\partial\delta\dot{\omega}_{ib}}{\partial\delta\omega_{vu}^\top} = -\mathbf{R}_{\hat{b}u}(\dot{\omega}_{ub}\times)$ $\frac{\partial\delta\mathbf{f}_b}{\partial\delta\omega_{vu}^\top} = -2\mathbf{R}_{\hat{b}u}[(\dot{\mathbf{r}}_u(P_b)\times) + \hat{\mathbf{\Omega}}_{eu}(\dot{\mathbf{r}}_u(P_b)\times)]$ $- \mathbf{R}_{\hat{b}u}(\dot{\mathbf{r}}_u(P_b)\times)(\mathbf{R}_{\hat{u}v}(\dot{\omega}_{iv}\times))$
$\delta\dot{\omega}_{vu}$	$\frac{\partial\delta\omega_{ib}}{\partial\delta\dot{\omega}_{vu}^\top} = \mathbf{0}$ $\frac{\partial\delta\dot{\omega}_{ib}}{\partial\delta\dot{\omega}_{vu}^\top} = \mathbf{R}_{\hat{b}u}$ $\frac{\partial\delta\mathbf{f}_b}{\partial\delta\dot{\omega}_{vu}^\top} = -\mathbf{R}_{\hat{b}u}(\dot{\mathbf{r}}_u(P_b)\times)$
Ψ_{uu}	$\frac{\partial\delta\omega_{ib}}{\partial\Psi_{uu}^\top} = -\mathbf{R}_{\hat{b}u}((\dot{\omega}_{vu} + \mathbf{R}_{\hat{u}v}(\dot{\omega}_{wv} + \mathbf{R}_{\hat{v}w}(\dot{\omega}_{pw} + \mathbf{R}_{\hat{w}p}(\dot{\omega}_{np} + \mathbf{R}_{\hat{p}n}\mathbf{R}_{\hat{n}e}\dot{\omega}_{ie}))))\times)$ $\frac{\partial\delta\dot{\omega}_{ib}}{\partial\Psi_{uu}^\top} = -\mathbf{R}_{\hat{b}u}((\dot{\omega}_{vu} + \mathbf{R}_{\hat{u}v}(\dot{\omega}_{wv} + \mathbf{R}_{\hat{v}w}(\dot{\omega}_{pw} + \mathbf{R}_{\hat{w}p}(\dot{\omega}_{np} + \mathbf{R}_{\hat{p}n}\mathbf{R}_{\hat{n}e}\dot{\omega}_{ie}))))\times)$ $+ \mathbf{R}_{\hat{b}u}(\dot{\omega}_{vu}\times)((\dot{\omega}_{vu} + \mathbf{R}_{\hat{u}v}(\dot{\omega}_{wv} + \mathbf{R}_{\hat{v}w}(\dot{\omega}_{pw} + \mathbf{R}_{\hat{w}p}(\dot{\omega}_{np} + \mathbf{R}_{\hat{p}n}\mathbf{R}_{\hat{n}e}\dot{\omega}_{ie}))))\times)$ $+ (\dot{\omega}_{ub}\times)\mathbf{R}_{\hat{b}u}((\dot{\omega}_{vu} + \mathbf{R}_{\hat{u}v}(\dot{\omega}_{wv} + \mathbf{R}_{\hat{v}w}(\dot{\omega}_{pw} + \mathbf{R}_{\hat{w}p}(\dot{\omega}_{np} + \mathbf{R}_{\hat{p}n}\mathbf{R}_{\hat{n}e}\dot{\omega}_{ie}))))\times)$ $\frac{\partial\delta\mathbf{f}_b}{\partial\Psi_{uu}^\top} = -2\mathbf{R}_{\hat{b}u}[(\dot{\mathbf{r}}_u(P_b)\times) + \hat{\mathbf{\Omega}}_{eu}(\dot{\mathbf{r}}_u(P_b)\times)]$ $\cdot ((\dot{\omega}_{vu} + \mathbf{R}_{\hat{u}v}(\dot{\omega}_{wv} + \mathbf{R}_{\hat{v}w}(\dot{\omega}_{pw} + \mathbf{R}_{\hat{w}p}(\dot{\omega}_{np} + \mathbf{R}_{\hat{p}n}\mathbf{R}_{\hat{n}e}\dot{\omega}_{ie}))))\times)$ $+ \mathbf{R}_{\hat{b}u}(\dot{\mathbf{r}}_u(P_b)\times)((\dot{\omega}_{vu} + \mathbf{R}_{\hat{u}v}(\dot{\omega}_{wv} + \mathbf{R}_{\hat{v}w}(\dot{\omega}_{pw} + \mathbf{R}_{\hat{w}p}(\dot{\omega}_{np} + \mathbf{R}_{\hat{p}n}\mathbf{R}_{\hat{n}e}\dot{\omega}_{ie}))))\times)$ $+ \mathbf{R}_{\hat{b}n}\frac{\partial\hat{\gamma}_n(\mathbf{r}_e)}{\partial\mathbf{r}_e}(\dot{\mathbf{r}}_u(P_b)\times) - \mathbf{R}_{\hat{b}u}((\mathbf{R}_{\hat{u}n}\hat{\gamma}_n(P_b))\times)$ $- \mathbf{R}_{\hat{b}u}(\hat{\mathbf{a}}_v\times)$

Table F.11.: Position of the inner gimbal with respect to the middle gimbal.

Error	Sensitivity of IMU kinematic errors
$\delta \mathbf{r}_v(P_u)$	$\frac{\partial \delta \boldsymbol{\omega}_{ib}}{\partial \delta \mathbf{r}_v(P_u)^\top} = \mathbf{0}$ $\frac{\partial \delta \dot{\boldsymbol{\omega}}_{ib}}{\partial \delta \mathbf{r}_v(P_u)^\top} = \mathbf{0}$ $\frac{\partial \delta \mathbf{f}_b}{\partial \delta \mathbf{r}_v(P_u)^\top} = \mathbf{R}_{bv} (\hat{\boldsymbol{\Omega}}_{iv}^2 + \dot{\hat{\boldsymbol{\Omega}}}_{iv})$
$\delta \dot{\mathbf{r}}_v(P_u)$	$\frac{\partial \delta \boldsymbol{\omega}_{ib}}{\partial \delta \dot{\mathbf{r}}_v(P_u)^\top} = \mathbf{0}$ $\frac{\partial \delta \dot{\boldsymbol{\omega}}_{ib}}{\partial \delta \dot{\mathbf{r}}_v(P_u)^\top} = \mathbf{0}$ $\frac{\partial \delta \mathbf{f}_b}{\partial \delta \dot{\mathbf{r}}_v(P_u)^\top} = \mathbf{R}_{bv} \hat{\boldsymbol{\Omega}}_{iv}$
$\delta \ddot{\mathbf{r}}_v(P_u)$	$\frac{\partial \delta \boldsymbol{\omega}_{ib}}{\partial \delta \ddot{\mathbf{r}}_v(P_u)^\top} = \mathbf{0}$ $\frac{\partial \delta \dot{\boldsymbol{\omega}}_{ib}}{\partial \delta \ddot{\mathbf{r}}_v(P_u)^\top} = \mathbf{0}$ $\frac{\partial \delta \mathbf{f}_b}{\partial \delta \ddot{\mathbf{r}}_v(P_u)^\top} = \mathbf{R}_{bv}$

Table F.12.: Rotation and orientation of the UUT.

Error	Sensitivity of IMU kinematic errors
$\delta\omega_{ub}$	$\frac{\partial\delta\omega_{ib}}{\partial\delta\omega_{ub}^T} = \mathbf{I}$ $\frac{\partial\delta\dot{\omega}_{ib}}{\partial\delta\omega_{ub}^T} = \mathbf{0}$ $\frac{\partial\delta\mathbf{f}_b}{\partial\delta\omega_{ub}^T} = \mathbf{0}$
$\delta\dot{\omega}_{ub}$	$\frac{\partial\delta\omega_{ib}}{\partial\delta\dot{\omega}_{ub}^T} = \mathbf{0}$ $\frac{\partial\delta\dot{\omega}_{ib}}{\partial\delta\dot{\omega}_{ub}^T} = \mathbf{I}$ $\frac{\partial\delta\mathbf{f}_b}{\partial\delta\dot{\omega}_{ub}^T} = \mathbf{0}$
$\Psi_{b\hat{b}}$	$\frac{\partial\delta\omega_{ib}}{\partial\Psi_{b\hat{b}}^T} = -((\dot{\omega}_{ub} + \mathbf{R}_{\hat{b}u}(\dot{\omega}_{vu} + \mathbf{R}_{\hat{a}v}(\dot{\omega}_{wv} + \mathbf{R}_{\hat{o}w}(\dot{\omega}_{pw} + \mathbf{R}_{\hat{w}p}(\dot{\omega}_{np} + \mathbf{R}_{\hat{p}n}\mathbf{R}_{\hat{n}e}\dot{\omega}_{ie})))))) \times)$ $\frac{\partial\delta\dot{\omega}_{ib}}{\partial\Psi_{b\hat{b}}^T} = -((\dot{\omega}_{ub} + \mathbf{R}_{\hat{b}u}(\dot{\omega}_{vu} + \mathbf{R}_{\hat{a}v}(\dot{\omega}_{wv} + \mathbf{R}_{\hat{o}w}(\dot{\omega}_{pw} + \mathbf{R}_{\hat{w}p}(\dot{\omega}_{np} + \mathbf{R}_{\hat{p}n}\mathbf{R}_{\hat{n}e}\dot{\omega}_{ie})))))) \times)$ $+ (\dot{\omega}_{ub} \times) \mathbf{R}_{\hat{b}u} ((\dot{\omega}_{ub} + \mathbf{R}_{\hat{b}u}(\dot{\omega}_{vu} + \mathbf{R}_{\hat{a}v}(\dot{\omega}_{wv} + \mathbf{R}_{\hat{o}w}(\dot{\omega}_{pw} + \mathbf{R}_{\hat{w}p}(\dot{\omega}_{np} + \mathbf{R}_{\hat{p}n}\mathbf{R}_{\hat{n}e}\dot{\omega}_{ie})))))) \times)$ $\frac{\partial\delta\mathbf{f}_b}{\partial\Psi_{b\hat{b}}^T} = -((\mathbf{R}_{\hat{b}n}\hat{\gamma}_n(P_{\hat{b}})) \times) - (\hat{\mathbf{a}}_u \times)$

Table F.13.: Position of the UUT with respect to the inner gimbal.

Error	Sensitivity of IMU kinematic errors
$\delta \mathbf{r}_u(P_b)$	$\frac{\partial \delta \boldsymbol{\omega}_{ib}}{\partial \delta \mathbf{r}_u(P_b)^T} = \mathbf{0}$ $\frac{\partial \delta \dot{\boldsymbol{\omega}}_{ib}}{\partial \delta \mathbf{r}_u(P_b)^T} = \mathbf{0}$ $\frac{\partial \delta \mathbf{f}_b}{\partial \delta \mathbf{r}_u(P_b)^T} = \mathbf{R}_{bu} (\hat{\boldsymbol{\Omega}}_{iu}^2 + \dot{\hat{\boldsymbol{\Omega}}}_{iu})$
$\delta \dot{\mathbf{r}}_u(P_b)$	$\frac{\partial \delta \boldsymbol{\omega}_{ib}}{\partial \delta \dot{\mathbf{r}}_u(P_b)^T} = \mathbf{0}$ $\frac{\partial \delta \dot{\boldsymbol{\omega}}_{ib}}{\partial \delta \dot{\mathbf{r}}_u(P_b)^T} = \mathbf{0}$ $\frac{\partial \delta \mathbf{f}_b}{\partial \delta \dot{\mathbf{r}}_u(P_b)^T} = \mathbf{R}_{bu} \dot{\hat{\boldsymbol{\Omega}}}_{iu}$
$\delta \ddot{\mathbf{r}}_u(P_b)$	$\frac{\partial \delta \boldsymbol{\omega}_{ib}}{\partial \delta \ddot{\mathbf{r}}_u(P_b)^T} = \mathbf{0}$ $\frac{\partial \delta \dot{\boldsymbol{\omega}}_{ib}}{\partial \delta \ddot{\mathbf{r}}_u(P_b)^T} = \mathbf{0}$ $\frac{\partial \delta \mathbf{f}_b}{\partial \delta \ddot{\mathbf{r}}_u(P_b)^T} = \mathbf{R}_{bu}$

Appendix G.

Overview of IEEE Test Procedures

The IEEE provides specification standards and test procedures for all typical inertial sensor technologies. These standards share a lot of general test procedures that can be applied independent of the actual sensor. [Table G.1](#) and [Table G.2](#) list the relevant IEEE standards and covered test procedures for gyroscopes respectively accelerometers. For each test case, the corresponding section in the respective IEEE standard is given, where applicable. Additionally, the test cases are color coded to the general test concept that represents each test case best.

Table G.1.: IEEE test procedures related to the gyroscope accuracy. The different tests are grouped to the general test type that best represents the respective test procedure.

IEEE Std.	647 RLG	952 FOG	1431 CVG	813 DTG	517 SDFIG	293 SDFRG
Rate Transfer Tests						
Maximum input rate	12.10.4	12.10.4	12.10	10.7.3	10.7.3.1	4.14
Min. input rate, dead band, threshold	12.10.4	12.10.4		10.7.3	10.7.3.1	4.13.2
Scale factor	12.9.3	12.9.3	12.9.4	10.6.4.1	10.12.4	4.13.3
Scale factor acceleration sensitivity			12.9.4			
Scale factor asymmetry	12.9.4	12.9.4.2	12.9.4	10.7.3		
Scale factor hysteresis			12.9.4			4.13.3
Scale factor nonlinearity	12.9.4	12.9.4.2	12.9.4	10.7.3		4.13.3
Scale factor repeatability	12.9.4	12.9.4.2	12.9.4	10.7.3		
Scale factor stability	12.9.4	12.9.4.2	12.9.4	10.7.3		
Scale factor temperature gradient	12.9.3					
Scale factor temperature sensitivity	12.9.3	12.9.3.2	12.9.4	10.7.3		
Multi-Pose Tests						
Axis misalignment	12.13.3	12.12.3	12.12.3	10.10	10.10	4.19
Bias hysteresis				10.14.3		
Drift from acceleration					10.13.3	4.18
Static Tests						
Angular Random Walk	12.12.4	12.11.4	12.11.4	10.14.4	10.13.3	
Bias Instability	12.12.4	12.11.4	12.11.4			
Bias, offset	12.12.4	12.11.4	12.11.4	10.6.3		4.13.3
Drift magnetic sensitivity	12.12.3	12.11.3				
Drift temperature gradient	12.12.3	12.11.3	12.11.4			
Drift temperature sensitivity	12.12.3	12.11.3	12.11.4	10.14.3		
Electric null				10.6.3	10.6.4.2	4.7
Output noise peak to peak						4.8
Quantization Noise	12.11	12.11.4	12.11.4			
Rate Ramp Noise	12.12.4	12.11.4	12.11.4			
Rate Random Walk	12.12.4	12.11.4	12.11.4			
Warm-up drift	12.12.4					
Vibration Tests						
Drift from acceleration squared				10.14.3	10.13.3	
Drift from angular acceleration					10.16	4.21
Drift from anisoinertia				10.14.3		
Drift from cross-coupling				10.14.3		
Drift from synchronous vibration				10.14.4		
Dynamic time constant				10.13	10.12.4	
Transfer function			12.15	10.16	10.5.3	4.22
Other Tests						
Drift from rotor speed variations				10.14.3		
Drift from torquer current rectification				10.14.3		
Elastic restraint drift rate					10.13.3	
Gimbal retardation					10.13.3	
Pickup phase shift				10.6.3	10.6.4	4.15
Spring rate drift rate				10.15		

Table G.2.: IEEE accelerometer test procedures related to the accelerometer sensor accuracy. The different tests are grouped to the general test type that best represents the respective test procedure.

IEEE Std.	1293		
	PA	VBA	MEMS
Transfer Tests			
Centrifuge input range	12.3.14	12.3.14	12.3.14
Cubic scalefactor nonlinearity	12.3.5, 12.3.15	12.3.5, 12.3.15	12.3.5, 12.3.15
Odd quadratic scale factor nonlinearity	12.3.15	12.3.15	12.3.15
Quadratic scale factor nonlinearity	12.3.5, 12.3.15	12.3.5, 12.3.15	12.3.5, 12.3.15
Threshold	12.3.6	12.3.6	12.3.6
Multi-Pose Tests			
Axis misalignment	12.3.4	12.3.4	12.3.4
Bias	12.3.4	12.3.4	12.3.4
Bias sensitivities	12.3.11	12.3.11	12.3.11
Bias long-term stability	12.3.9	12.3.9	12.3.9
Bias short-term stability	12.3.8	12.3.8	12.3.8
Inversion transient	12.3.3	12.3.3	12.3.3
Scale factor	12.3.4	12.3.4	12.3.4
Scale factor high g vibration calibration	12.3.18	12.3.18	12.3.18
Scale factor sensitivity	12.3.11	12.3.11	12.3.11
Slew calibration	12.3.21	12.3.21	12.3.21
Static Tests			
Electrical null	12.4.1		
Noise	12.3.2	12.3.2	12.3.2
Turn-on hysteresis	12.4.5		
Vibration Tests			
Bias high g vibration calibration	12.3.18	12.3.18	12.3.18
Frequency response	12.3.16	12.3.16	12.3.16
Open-loop frequency response	12.4.3		
Performance though and across environment	12.3.19	12.3.19	12.3.19
Other Tests			
Frequency lock		12.5.1	
Pendulum elastic restraint	12.4.4		12.6.6
Pickoff phase shift	12.4.1		
Pickoff scale factor	12.4.4		12.6.5
Repeatability	12.3.10	12.3.10	12.3.10
Temperature model calibration	12.3.12	12.3.12	12.3.12
Torquer scale factor	12.4.6		

Appendix H.

Error Sensitivities in Sensor Testing

Table H.1.: Error sensitivities of the gyroscope x-axis input during the six-position test.

Position	1 and 2	3 and 4	5 and 6
$\delta\omega_{ie,x}$	$-\cos\hat{\Psi}_{pw}\sin\lambda - \sin\hat{\Psi}_{pw}\cos\lambda\sin\phi$	$-\cos\hat{\Psi}_{pw}\sin\lambda - \sin\hat{\Psi}_{pw}\cos\lambda\sin\phi$	$\mp\cos\phi\cos\lambda$
$\delta\omega_{ie,y}$	$\cos\hat{\Psi}_{pw}\cos\lambda - \sin\hat{\Psi}_{pw}\sin\phi\sin\lambda$	$\cos\hat{\Psi}_{pw}\cos\lambda - \sin\hat{\Psi}_{pw}\sin\phi\sin\lambda$	$\mp\cos\phi\sin\lambda$
$\delta\omega_{ie,z}$	$\sin\hat{\Psi}_{pw}\cos\phi$	$\sin\hat{\Psi}_{pw}\cos\phi$	$\mp\sin\phi$
$\Phi_{\hat{nn}}$	$\cos\hat{\Psi}_{pw}\hat{\omega}_{ie}\sin\phi$	$-\cos\hat{\Psi}_{pw}\hat{\omega}_{ie}\sin\phi$	0
$\Theta_{\hat{nn}}$	$-\sin\hat{\Psi}_{pw}\hat{\omega}_{ie}\sin\phi$	$\sin\hat{\Psi}_{pw}\hat{\omega}_{ie}\sin\phi$	$\pm\hat{\omega}_{ie}\cos\phi$
$\Psi_{\hat{nn}}$	$\cos\hat{\Psi}_{pw}\hat{\omega}_{ie}\cos\phi$	$-\cos\hat{\Psi}_{pw}\hat{\omega}_{ie}\cos\phi$	0
$\delta\omega_{np,x}$	$\cos\hat{\Psi}_{pw}$	$\cos\hat{\Psi}_{pw}$	0
$\delta\omega_{np,y}$	$\sin\hat{\Psi}_{pw}$	$\sin\hat{\Psi}_{pw}$	0
$\delta\omega_{np,z}$	0	0	∓ 1
$\Phi_{\hat{pp}}$	$\sin\hat{\Psi}_{pw}\hat{\omega}_{ie}\sin\phi$	$\sin\hat{\Psi}_{pw}\hat{\omega}_{ie}\sin\phi$	$\pm\hat{\omega}_{ie}\cos\phi$
$\Theta_{\hat{pp}}$	$-\cos\hat{\Psi}_{pw}\hat{\omega}_{ie}\sin\phi$	$-\cos\hat{\Psi}_{pw}\hat{\omega}_{ie}\sin\phi$	0
$\Psi_{\hat{pp}}$	$\cos\hat{\Psi}_{pw}\hat{\omega}_{ie}\cos\phi$	$\cos\hat{\Psi}_{pw}\hat{\omega}_{ie}\cos\phi$	0
$\delta\omega_{pw,x}$	1	1	0
$\delta\omega_{pw,y}$	0	0	0
$\delta\omega_{pw,z}$	0	0	∓ 1
$\Phi_{\hat{ww}}$	0	0	$\pm\cos\hat{\Psi}_{pw}\hat{\omega}_{ie}\cos\phi$
$\Theta_{\hat{ww}}$	$-\hat{\omega}_{ie}\sin\phi - \hat{\omega}_{pw}$	$-\hat{\omega}_{ie}\sin\phi - \hat{\omega}_{pw}$	$\mp\sin\hat{\Psi}_{pw}\hat{\omega}_{ie}\cos\phi$
$\Psi_{\hat{ww}}$	$\cos\hat{\Psi}_{pw}\hat{\omega}_{ie}\cos\phi$	$\cos\hat{\Psi}_{pw}\hat{\omega}_{ie}\cos\phi$	0
$\delta\omega_{wv,x}$	1	1	0
$\delta\omega_{wv,y}$	0	0	1
$\delta\omega_{wv,z}$	0	0	0
$\Phi_{\hat{vv}}$	0	0	$\cos\hat{\Psi}_{pw}\hat{\omega}_{ie}\cos\phi$
$\Theta_{\hat{vv}}$	$\pm(\hat{\omega}_{ie}\sin\phi + \hat{\omega}_{pw})$	$\pm\cos\hat{\Psi}_{pw}\hat{\omega}_{ie}\cos\phi$	0
$\Psi_{\hat{vv}}$	$\mp\cos\hat{\Psi}_{pw}\hat{\omega}_{ie}\cos\phi$	$\pm(\hat{\omega}_{ie}\sin\phi + \hat{\omega}_{pw})$	$-\sin\hat{\Psi}_{pw}\hat{\omega}_{ie}\cos\phi$
$\delta\omega_{vu,x}$	1	1	1
$\delta\omega_{vu,y}$	0	0	0
$\delta\omega_{vu,z}$	0	0	0
$\Phi_{\hat{uu}}$	0	0	0
$\Theta_{\hat{uu}}$	$\pm(\hat{\omega}_{ie}\sin\phi + \hat{\omega}_{pw})$	$\pm\cos\hat{\Psi}_{pw}\hat{\omega}_{ie}\cos\phi$	$-\cos\hat{\Psi}_{pw}\hat{\omega}_{ie}\cos\phi$
$\Psi_{\hat{uu}}$	$\mp\cos\hat{\Psi}_{pw}\hat{\omega}_{ie}\cos\phi$	$\pm(\hat{\omega}_{ie}\sin\phi + \hat{\omega}_{pw})$	$-\sin\hat{\Psi}_{pw}\hat{\omega}_{ie}\cos\phi$
$\Phi_{\hat{bb}}$	0	0	0
$\Theta_{\hat{bb}}$	$\pm(\hat{\omega}_{ie}\sin\phi + \hat{\omega}_{pw})$	$\pm\cos\hat{\Psi}_{pw}\hat{\omega}_{ie}\cos\phi$	$-\cos\hat{\Psi}_{pw}\hat{\omega}_{ie}\cos\phi$
$\Psi_{\hat{bb}}$	$\mp\cos\hat{\Psi}_{pw}\hat{\omega}_{ie}\cos\phi$	$\pm(\hat{\omega}_{ie}\sin\phi + \hat{\omega}_{pw})$	$-\sin\hat{\Psi}_{pw}\hat{\omega}_{ie}\cos\phi$

Table H.2.: Error sensitivities of the gyroscope y-axis input during the six-position test.

Position	1 and 2	3 and 4	5 and 6
$\delta\omega_{ie,x}$	$-\sin \hat{\Psi}_{pw} \sin \lambda + \cos \hat{\Psi}_{pw} \cos \lambda \sin \phi$	$\pm \cos \phi \cos \lambda$	$\cos \hat{\Psi}_{pw} \sin \lambda + \sin \hat{\Psi}_{pw} \cos \lambda \sin \phi$
$\delta\omega_{ie,y}$	$\sin \hat{\Psi}_{pw} \cos \lambda + \cos \hat{\Psi}_{pw} \sin \phi \sin \lambda$	$\pm \cos \phi \sin \lambda$	$-\cos \hat{\Psi}_{pw} \cos \lambda \sin \hat{\Psi}_{pw} \sin \phi \sin \lambda$
$\delta\omega_{ie,z}$	$-\cos \hat{\Psi}_{pw} \cos \phi$	$\pm \sin \phi$	$-\sin \hat{\Psi}_{pw} \cos \phi$
Φ_{nn}	$\mp \sin \hat{\Psi}_{pw} \hat{\omega}_{ie} \sin \phi$	0	$\mp \cos \hat{\Psi}_{pw} \hat{\omega}_{ie} \sin \phi$
Θ_{nn}	$\mp \cos \hat{\Psi}_{pw} \hat{\omega}_{ie} \sin \phi$	$\mp \hat{\omega}_{ie} \cos \phi$	$\pm \sin \hat{\Psi}_{pw} \hat{\omega}_{ie} \sin \phi$
Ψ_{nn}	$\mp \sin \hat{\Psi}_{pw} \hat{\omega}_{ie} \cos \phi$	0	$\mp \cos \hat{\Psi}_{pw} \hat{\omega}_{ie} \cos \phi$
$\delta\omega_{np,x}$	$\pm \sin \hat{\Psi}_{pw}$	0	$-\cos \hat{\Psi}_{pw}$
$\delta\omega_{np,y}$	$\mp \cos \hat{\Psi}_{pw}$	0	$-\sin \hat{\Psi}_{pw}$
$\delta\omega_{np,z}$	0	± 1	0
Φ_{pp}	$\mp \cos \hat{\Psi}_{pw} \hat{\omega}_{ie} \sin \phi$	$\mp \hat{\omega}_{ie} \cos \phi$	$-\sin \hat{\Psi}_{pw} \hat{\omega}_{ie} \sin \phi$
Θ_{pp}	$\mp \sin \hat{\Psi}_{pw} \hat{\omega}_{ie} \sin \phi$	0	$\cos \hat{\Psi}_{pw} \hat{\omega}_{ie} \sin \phi$
Ψ_{pp}	$\pm \sin \hat{\Psi}_{pw} \hat{\omega}_{ie} \cos \phi$	0	$-\cos \hat{\Psi}_{pw} \hat{\omega}_{ie} \cos \phi$
$\delta\omega_{pw,x}$	0	0	-1
$\delta\omega_{pw,y}$	∓ 1	0	0
$\delta\omega_{pw,z}$	0	± 1	0
Φ_{ww}	$\mp(\hat{\omega}_{ie} \sin \phi + \hat{\omega}_{pw})$	$\mp \cos \hat{\Psi}_{pw} \hat{\omega}_{ie} \cos \phi$	0
Θ_{ww}	0	$\pm \sin \hat{\Psi}_{pw} \hat{\omega}_{ie} \cos \phi$	$(\hat{\omega}_{ie} \sin \phi + \hat{\omega}_{pw})$
Ψ_{ww}	$\pm \sin \hat{\Psi}_{pw} \hat{\omega}_{ie} \cos \phi$	0	$-\cos \hat{\Psi}_{pw} \hat{\omega}_{ie} \cos \phi$
$\delta\omega_{wv,x}$	0	0	-1
$\delta\omega_{wv,y}$	1	1	0
$\delta\omega_{wv,z}$	0	0	0
Φ_{vv}	$\mp(\hat{\omega}_{ie} \sin \phi + \hat{\omega}_{pw})$	$\mp \cos \hat{\Psi}_{pw} \hat{\omega}_{ie} \cos \phi$	0
Θ_{vv}	0	0	$\cos \hat{\Psi}_{pw} \hat{\omega}_{ie} \cos \phi$
Ψ_{vv}	$\pm \sin \hat{\Psi}_{pw} \hat{\omega}_{ie} \cos \phi$	$-\sin \hat{\Psi}_{pw} \hat{\omega}_{ie} \cos \phi$	$\pm(\hat{\omega}_{ie} \sin \phi + \hat{\omega}_{pw})$
$\delta\omega_{vu,x}$	0	0	0
$\delta\omega_{vu,y}$	1	1	1
$\delta\omega_{vu,z}$	0	0	0
Φ_{uu}	$\mp(\hat{\omega}_{ie} \sin \phi + \hat{\omega}_{pw})$	$\mp \cos \hat{\Psi}_{pw} \hat{\omega}_{ie} \cos \phi$	$\cos \hat{\Psi}_{pw} \hat{\omega}_{ie} \cos \phi$
Θ_{uu}	0	0	0
Ψ_{uu}	$\pm \cos \hat{\Psi}_{pw} \hat{\omega}_{ie} \cos \phi$	$-\sin \hat{\Psi}_{pw} \hat{\omega}_{ie} \cos \phi$	$\pm(\hat{\omega}_{ie} \sin \phi + \hat{\omega}_{pw})$
Φ_{bb}	$\mp(\hat{\omega}_{ie} \sin \phi + \hat{\omega}_{pw})$	$\mp \cos \hat{\Psi}_{pw} \hat{\omega}_{ie} \cos \phi$	$\cos \hat{\Psi}_{pw} \hat{\omega}_{ie} \cos \phi$
Θ_{bb}	0	0	0
Ψ_{bb}	$\pm \cos \hat{\Psi}_{pw} \hat{\omega}_{ie} \cos \phi$	$-\sin \hat{\Psi}_{pw} \hat{\omega}_{ie} \cos \phi$	$\pm(\hat{\omega}_{ie} \sin \phi + \hat{\omega}_{pw})$

Table H.3.: Error sensitivities of the gyroscope z-axis input during the six-position test.

Position	1 and 2	3 and 4	5 and 6
$\delta\omega_{ie,x}$	$\mp \cos \phi \cos \lambda$	$\mp \sin \hat{\Psi}_{pw} \sin \lambda \pm \cos \hat{\Psi}_{pw} \cos \lambda \sin \phi$	$-\cos \hat{\Psi}_{pw} \sin \lambda + \sin \hat{\Psi}_{pw} \cos \lambda \sin \phi$
$\delta\omega_{ie,y}$	$\mp \cos \phi \sin \lambda$	$\pm \sin \hat{\Psi}_{pw} \cos \lambda \pm \cos \hat{\Psi}_{pw} \sin \phi \sin \lambda$	$-\cos \hat{\Psi}_{pw} \cos \lambda - \sin \hat{\Psi}_{pw} \sin \phi \sin \lambda$
$\delta\omega_{ie,z}$	$\mp \sin \phi$	$\mp \cos \hat{\Psi}_{pw} \cos \phi$	$\cos \hat{\Psi}_{pw} \cos \phi$
$\Phi_{\hat{n}n}$	0	$\mp \sin \hat{\Psi}_{pw} \hat{\omega}_{ie} \sin \phi$	$\sin \hat{\Psi}_{pw} \hat{\omega}_{ie} \sin \phi$
$\Theta_{\hat{n}n}$	$\pm \hat{\omega}_{ie} \cos \phi$	$\mp \cos \hat{\Psi}_{pw} \hat{\omega}_{ie} \sin \phi$	$\cos \hat{\Psi}_{pw} \hat{\omega}_{ie} \sin \phi$
$\Psi_{\hat{n}n}$	0	$\mp \sin \hat{\Psi}_{pw} \hat{\omega}_{ie} \cos \phi$	$\sin \hat{\Psi}_{pw} \hat{\omega}_{ie} \cos \phi$
$\delta\omega_{np,x}$	0	$\pm \sin \hat{\Psi}_{pw}$	$-\sin \hat{\Psi}_{pw}$
$\delta\omega_{np,y}$	0	$\mp \cos \hat{\Psi}_{pw}$	$\cos \hat{\Psi}_{pw}$
$\delta\omega_{np,z}$	∓ 1	0	0
$\Phi_{\hat{p}p}$	$\pm \hat{\omega}_{ie} \cos \phi$	$\mp \cos \hat{\Psi}_{pw} \hat{\omega}_{ie} \sin \phi$	$\cos \hat{\Psi}_{pw} \hat{\omega}_{ie} \sin \phi$
$\Theta_{\hat{p}p}$	0	$\mp \sin \hat{\Psi}_{pw} \hat{\omega}_{ie} \sin \phi$	$\sin \hat{\Psi}_{pw} \hat{\omega}_{ie} \sin \phi$
$\Psi_{\hat{p}p}$	0	$\pm \sin \hat{\Psi}_{pw} \hat{\omega}_{ie} \cos \phi$	$-\sin \hat{\Psi}_{pw} \hat{\omega}_{ie} \cos \phi$
$\delta\omega_{pw,x}$	0	0	0
$\delta\omega_{pw,y}$	0	∓ 1	1
$\delta\omega_{pw,z}$	∓ 1	0	0
$\Phi_{\hat{w}w}$	$\pm \cos \hat{\Psi}_{pw} \hat{\omega}_{ie} \cos \phi$	$\mp (\hat{\omega}_{ie} \sin \phi + \hat{\omega}_{pw})$	0
$\Theta_{\hat{w}w}$	$\mp \sin \hat{\Psi}_{pw} \hat{\omega}_{ie} \cos \phi$	0	$(\hat{\omega}_{ie} \sin \phi + \hat{\omega}_{pw})$
$\Psi_{\hat{w}w}$	0	$\pm \sin \hat{\Psi}_{pw} \hat{\omega}_{ie} \cos \phi$	0
$\delta\omega_{wv,x}$	0	0	$-\sin \hat{\Psi}_{pw} \hat{\omega}_{ie} \cos \phi$
$\delta\omega_{wv,y}$	0	0	0
$\delta\omega_{wv,z}$	1	1	1
$\Phi_{\hat{v}v}$	$\pm \cos \hat{\Psi}_{pw} \hat{\omega}_{ie} \cos \phi$	$\mp (\hat{\omega}_{ie} \sin \phi + \hat{\omega}_{pw})$	$\pm (\hat{\omega}_{ie} \sin \phi + \hat{\omega}_{pw})$
$\Theta_{\hat{v}v}$	$\sin \hat{\Psi}_{pw} \hat{\omega}_{ie} \cos \phi$	$\sin \hat{\Psi}_{pw} \hat{\omega}_{ie} \cos \phi$	$\sin \hat{\Psi}_{pw} \hat{\omega}_{ie} \cos \phi$
$\Psi_{\hat{v}v}$	0	0	0
$\delta\omega_{vu,x}$	0	0	0
$\delta\omega_{vu,y}$	0	0	0
$\delta\omega_{vu,z}$	1	1	1
$\Phi_{\hat{u}u}$	$\pm \cos \hat{\Psi}_{pw} \hat{\omega}_{ie} \cos \phi$	$\mp (\hat{\omega}_{ie} \sin \phi + \hat{\omega}_{pw})$	$\sin \hat{\Psi}_{pw} \hat{\omega}_{ie} \cos \phi$
$\Theta_{\hat{u}u}$	$\sin \hat{\Psi}_{pw} \hat{\omega}_{ie} \cos \phi$	$\sin \hat{\Psi}_{pw} \hat{\omega}_{ie} \cos \phi$	$\mp (\hat{\omega}_{ie} \sin \phi + \hat{\omega}_{pw})$
$\Psi_{\hat{u}u}$	0	0	0
$\Phi_{\hat{b}b}$	$\pm \cos \hat{\Psi}_{pw} \hat{\omega}_{ie} \cos \phi$	$\mp (\hat{\omega}_{ie} \sin \phi + \hat{\omega}_{pw})$	$\sin \hat{\Psi}_{pw} \hat{\omega}_{ie} \cos \phi$
$\Theta_{\hat{b}b}$	$\sin \hat{\Psi}_{pw} \hat{\omega}_{ie} \cos \phi$	$\sin \hat{\Psi}_{pw} \hat{\omega}_{ie} \cos \phi$	$\mp (\hat{\omega}_{ie} \sin \phi + \hat{\omega}_{pw})$
$\Psi_{\hat{b}b}$	0	0	0

Table H.4.: Error sensitivities of the accelerometer x-axis input during the six-position test.

Position	1 and 2	3 and 4	5 and 6
$\delta\gamma_{n,x}$	$\sin \Psi(t)$	$\sin \Psi(t)$	0
$\delta\gamma_{n,y}$	$\cos \Psi(t)$	$\cos \Psi(t)$	0
$\delta\gamma_{n,z}$	0	0	± 1
$\delta\omega_{ie,x}$	0	0	0
$\delta\omega_{ie,y}$	0	0	0
$\delta\omega_{ie,z}$	0	0	0
$\Phi_{\hat{n}n}$	$-g \cos \Psi(t) - h \left(\frac{\partial \gamma_{n,e}(P_b)}{\partial r_{n,e}} \cos \Psi(t) + \frac{\partial \gamma_{n,n}(P_b)}{\partial r_{n,e}} \sin \Psi(t) \right)$	$-g \cos \Psi(t) - h \left(\frac{\partial \gamma_{n,e}(P_b)}{\partial r_{n,e}} \cos \Psi(t) + \frac{\partial \gamma_{n,n}(P_b)}{\partial r_{n,e}} \sin \Psi(t) \right)$	$\mp h \frac{\partial \gamma_{n,d}(P_b)}{\partial r_{n,e}}$
$\Theta_{\hat{n}n}$	$+g \sin \Psi(t) + h \left(\frac{\partial \gamma_{n,e}(P_b)}{\partial r_{n,n}} \cos \Psi(t) + \frac{\partial \gamma_{n,n}(P_b)}{\partial r_{n,n}} \sin \Psi(t) \right)$	$+g \sin \Psi(t) + h \left(\frac{\partial \gamma_{n,e}(P_b)}{\partial r_{n,n}} \cos \Psi(t) + \frac{\partial \gamma_{n,n}(P_b)}{\partial r_{n,n}} \sin \Psi(t) \right)$	$\pm h \frac{\partial \gamma_{n,d}(P_b)}{\partial r_{n,n}}$
$\Psi_{\hat{n}n}$	0	0	0
$\delta\omega_{np,x}$	$-\omega_{ie}(h \sin \Psi(t) \cos \lambda + h \cos \Psi(t) \sin \phi \sin \lambda)$	$-\omega_{ie}(h \sin \Psi(t) \cos \lambda + h \cos \Psi(t) \sin \phi \sin \lambda)$	0
$\delta\omega_{np,y}$	$-\omega_{ie}(h \sin \Psi(t) \sin \lambda - h \cos \Psi(t) \cos \lambda \sin \phi)$	$-\omega_{ie}(h \sin \Psi(t) \sin \lambda - h \cos \Psi(t) \cos \lambda \sin \phi)$	0
$\delta\omega_{np,z}$	0	0	0
$\delta\dot{\omega}_{np,x}$	$-h \sin \Psi(t)$	$-h \sin \Psi(t)$	0
$\delta\dot{\omega}_{np,y}$	$h \cos \Psi(t)$	$h \cos \Psi(t)$	0
$\delta\dot{\omega}_{np,z}$	0	0	0
$\delta r_{n,x}(P_p)$	$-\omega_{ie}^2 \sin \Psi(t) \sin^2 \phi$	$-\omega_{ie}^2 \sin \Psi(t) \sin^2 \phi$	$\mp \omega_{ie}^2 \cos \phi \sin \phi$
$\delta r_{n,y}(P_p)$	$-\omega_{ie}^2 \cos \Psi(t)$	$-\omega_{ie}^2 \cos \Psi(t)$	0
$\delta r_{n,z}(P_p)$	$-\omega_{ie}^2 \sin \Psi(t) \cos \phi \sin \phi$	$-\omega_{ie}^2 \sin \Psi(t) \cos \phi \sin \phi$	$\mp \omega_{ie}^2 \cos^2 \phi$
$\delta \hat{r}_{n,x}(P_p)$	$-\omega_{ie} \cos \Psi(t) \sin \phi$	$-\omega_{ie} \cos \Psi(t) \sin \phi$	0
$\delta \hat{r}_{n,y}(P_p)$	$\omega_{ie} \sin \Psi(t) \sin \phi$	$\omega_{ie} \sin \Psi(t) \sin \phi$	$\pm \omega_{ie} \cos \phi$
$\delta \hat{r}_{n,z}(P_p)$	$-\omega_{ie} \cos \Psi(t) \cos \phi$	$-\omega_{ie} \cos \Psi(t) \cos \phi$	0
$\delta \hat{r}_{n,x}(P_p)$	$\sin \Psi(t)$	$\sin \Psi(t)$	0
$\delta \hat{r}_{n,y}(P_p)$	$\cos \Psi(t)$	$\cos \Psi(t)$	0
$\delta \hat{r}_{n,z}(P_p)$	0	0	± 1
$\Phi_{\hat{p}p}$	$g \sin \Psi(t) + h \left(\frac{\partial \gamma_{n,e}(P_b)}{\partial r_{n,e}} \cos \Psi(t) + \frac{\partial \gamma_{n,n}(P_b)}{\partial r_{n,e}} \sin \Psi(t) \right)$	$g \sin \Psi(t) + h \left(\frac{\partial \gamma_{n,e}(P_b)}{\partial r_{n,e}} \cos \Psi(t) + \frac{\partial \gamma_{n,n}(P_b)}{\partial r_{n,e}} \sin \Psi(t) \right)$	$\pm h \frac{\partial \gamma_{n,d}(P_b)}{\partial r_{n,e}}$
$\Theta_{\hat{p}p}$	$-g \sin \Psi(t) - h \left(\frac{\partial \gamma_{n,e}(P_b)}{\partial r_{n,n}} \cos \Psi(t) + \frac{\partial \gamma_{n,n}(P_b)}{\partial r_{n,n}} \sin \Psi(t) \right)$	$-g \sin \Psi(t) - h \left(\frac{\partial \gamma_{n,e}(P_b)}{\partial r_{n,n}} \cos \Psi(t) + \frac{\partial \gamma_{n,n}(P_b)}{\partial r_{n,n}} \sin \Psi(t) \right)$	$\mp h \frac{\partial \gamma_{n,d}(P_b)}{\partial r_{n,n}}$
$\Psi_{\hat{p}p}$	0	0	0
$\delta\omega_{pw,x}$	0	0	0
$\delta\omega_{pw,y}$	0	0	0
$\delta\omega_{pw,z}$	0	0	0
$\delta r_{p,x}(P_w)$	$-\omega_{ie}^2 \cos \Psi(t)$	$-\omega_{ie}^2 \cos \Psi(t)$	0
$\delta r_{p,y}(P_w)$	$-\omega_{ie}^2 \sin \Psi(t) \sin^2 \phi$	$-\omega_{ie}^2 \sin \Psi(t) \sin^2 \phi$	$\mp \omega_{ie}^2 \cos \phi \sin \phi$
$\delta r_{p,z}(P_w)$	$\omega_{ie}^2 \sin \Psi(t) \cos \phi \sin \phi$	$\omega_{ie}^2 \sin \Psi(t) \cos \phi \sin \phi$	$\pm \omega_{ie}^2 \cos^2 \phi$
$\delta \hat{r}_{p,x}(P_w)$	$\omega_{ie} \sin \Psi(t) \sin \phi$	$\omega_{ie} \sin \Psi(t) \sin \phi$	$\pm \omega_{ie} \cos \phi$
$\delta \hat{r}_{p,y}(P_w)$	$-\omega_{ie} \cos \Psi(t) \sin \phi$	$-\omega_{ie} \cos \Psi(t) \sin \phi$	0
$\delta \hat{r}_{p,z}(P_w)$	$\omega_{ie} \cos \Psi(t) \cos \phi$	$\omega_{ie} \cos \Psi(t) \cos \phi$	0
$\delta \hat{r}_{p,x}(P_w)$	$\cos \Psi(t)$	$\cos \Psi(t)$	0
$\delta \hat{r}_{p,y}(P_w)$	$\sin \Psi(t)$	$\sin \Psi(t)$	0
$\delta \hat{r}_{p,z}(P_w)$	0	0	∓ 1

Table H.4.: Error sensitivities of the accelerometer x-axis input during the six-position test, continued.

Position	1 and 2	3 and 4	5 and 6
Φ_{ww}	0	0	0
Θ_{ww}	$-g$	$-g$	0
Ψ_{ww}	0	0	0
$\delta\omega_{wv,x}$	0	0	0
$\delta\omega_{wv,y}$	0	0	0
$\delta\omega_{wv,z}$	0	0	0
$\delta r_{w,x}(P_v)$	$-(\omega_{pw} + \omega_{ie} \sin \phi)^2 - \omega_{ie}^2 \cos^2 \Psi(t) \cos^2 \phi$	$-(\omega_{pw} + \omega_{ie} \sin \phi)^2 - \omega_{ie}^2 \cos^2 \Psi(t) \cos^2 \phi$	$\mp \omega_{ie} \sin \Psi(t) \cos \phi (\omega_{pw} + \omega_{ie} \sin \phi)$
$\delta r_{w,y}(P_v)$	$\omega_{ie}^2 \cos \Psi(t) \sin \Psi(t) \cos^2 \phi$	$\omega_{ie}^2 \cos \Psi(t) \sin \Psi(t) \cos^2 \phi$	$\mp \omega_{ie} \cos \Psi(t) \cos \phi (\omega_{pw} + \omega_{ie} \sin \phi)$
$\delta r_{w,z}(P_v)$	$\omega_{ie} \sin \Psi(t) \cos \phi (\omega_{pw} + \omega_{ie} \sin \phi)$	$\omega_{ie} \sin \Psi(t) \cos \phi (\omega_{pw} + \omega_{ie} \sin \phi)$	$\pm \omega_{ie}^2 (1 - \sin^2 \phi)$
$\delta \dot{r}_{w,x}(P_v)$	0	0	$\mp \omega_{ie} \cos \Psi(t) \cos \phi$
$\delta \dot{r}_{w,y}(P_v)$	$-\omega_{pw} - \omega_{ie} \sin \phi$	$-\omega_{pw} - \omega_{ie} \sin \phi$	$\pm \omega_{ie} \sin \Psi(t) \cos \phi$
$\delta \dot{r}_{w,z}(P_v)$	$\omega_{ie} \cos \Psi(t) \cos \phi$	$\omega_{ie} \cos \Psi(t) \cos \phi$	0
$\delta \ddot{r}_{w,x}(P_v)$	1	1	0
$\delta \ddot{r}_{w,y}(P_v)$	0	0	0
$\delta \ddot{r}_{w,z}(P_v)$	0	0	1
Φ_{vv}	0	0	0
Θ_{vv}	$\pm g$	0	0
Ψ_{vv}	0	$\pm g$	0
$\delta\omega_{vu,x}$	0	0	0
$\delta\omega_{vu,y}$	0	0	0
$\delta\omega_{vu,z}$	0	0	0
$\delta r_{v,x}(P_u)$	$-(\omega_{pw} + \omega_{ie} \sin \phi)^2 - \omega_{ie}^2 \cos^2 \Psi(t) \cos^2 \phi$	$-(\omega_{pw} + \omega_{ie} \sin \phi)^2 - \omega_{ie}^2 \cos^2 \Psi(t) \cos^2 \phi$	$\mp \omega_{ie} \sin \Psi(t) \cos \phi (\omega_{pw} + \omega_{ie} \sin \phi)$
$\delta r_{v,y}(P_u)$	$-\omega_{ie}^2 \cos \Psi(t) \sin \Psi(t) \cos^2 \phi$	$\omega_{ie} \sin \Psi(t) \cos \phi (\omega_{pw} + \omega_{ie} \sin \phi)$	$\pm \omega_{ie}^2 (\sin^2 \phi - 1)$
$\delta r_{v,z}(P_u)$	$-\omega_{ie} \sin \Psi(t) \cos \phi (\omega_{pw} + \omega_{ie} \sin \phi)$	$-\omega_{ie}^2 \cos \Psi(t) \sin \Psi(t) \cos^2 \phi$	$\mp \omega_{ie} \cos \Psi(t) \cos \phi (\omega_{pw} + \omega_{ie} \sin \phi)$
$\delta \dot{r}_{v,x}(P_u)$	0	0	$\omega_{ie} \cos \Psi(t) \cos \phi$
$\delta \dot{r}_{v,y}(P_u)$	$\pm (\omega_{pw} + \omega_{ie} \sin \phi)$	$\pm \omega_{ie} \cos \Psi(t) \cos \phi$	0
$\delta \dot{r}_{v,z}(P_u)$	$\mp \omega_{ie} \cos \Psi(t) \cos \phi$	$\pm (\omega_{pw} + \omega_{ie} \sin \phi)$	$-\omega_{ie} \sin \Psi(t) \cos \phi$
$\delta \ddot{r}_{v,x}(P_u)$	1	1	0
$\delta \ddot{r}_{v,y}(P_u)$	0	0	1
$\delta \ddot{r}_{v,z}(P_u)$	0	0	0
Φ_{uu}	0	0	0
Θ_{uu}	$\pm g$	0	0
Ψ_{uu}	0	$\pm g$	0
$\delta r_{u,x}(P_b)$	$-(\omega_{pw} + \omega_{ie} \sin \phi)^2 - \omega_{ie}^2 \cos^2 \Psi(t) \cos^2 \phi$	$-(\omega_{pw} + \omega_{ie} \sin \phi)^2 - \omega_{ie}^2 \cos^2 \Psi(t) \cos^2 \phi$	$\omega_{ie}^2 (\sin^2 \phi - 1)$
$\delta r_{u,y}(P_b)$	$-\omega_{ie}^2 \cos \Psi(t) \sin \Psi(t) \cos^2 \phi$	$\omega_{ie} \sin \Psi(t) \cos \phi (\omega_{pw} + \omega_{ie} \sin \phi)$	$\pm \omega_{ie} \sin \Psi(t) \cos \phi (\omega_{pw} + \omega_{ie} \sin \phi)$
$\delta r_{u,z}(P_b)$	$-\omega_{ie} \sin \Psi(t) \cos \phi (\omega_{pw} + \omega_{ie} \sin \phi)$	$-\omega_{ie}^2 \cos \Psi(t) \sin \Psi(t) \cos^2 \phi$	$\mp \omega_{ie} \cos \Psi(t) \cos \phi (\omega_{pw} + \omega_{ie} \sin \phi)$
$\delta \dot{r}_{u,x}(P_b)$	0	0	0
$\delta \dot{r}_{u,y}(P_b)$	$\pm (\omega_{pw} + \omega_{ie} \sin \phi)$	$\pm \omega_{ie} \cos \Psi(t) \cos \phi$	$-\omega_{ie} \cos \Psi(t) \cos \phi$
$\delta \dot{r}_{u,z}(P_b)$	$\mp \omega_{ie} \cos \Psi(t) \cos \phi$	$\pm (\omega_{pw} + \omega_{ie} \sin \phi)$	$-\omega_{ie} \sin \Psi(t) \cos \phi$
$\delta \ddot{r}_{u,x}(P_b)$	1	1	1
$\delta \ddot{r}_{u,y}(P_b)$	0	0	0
$\delta \ddot{r}_{u,z}(P_b)$	0	0	0
Φ_{bb}	0	0	0
Θ_{bb}	$\pm g$	0	0
Ψ_{bb}	0	$\pm g$	0

Table H.5.: Error sensitivities of the accelerometer y-axis input during the six-position test.

Position	1 and 2	3 and 4	5 and 6
$\delta\gamma_{n,x}$	$\mp \cos \Psi(t)$	0	$-\sin \Psi(t)$
$\delta\gamma_{n,y}$	$\pm \sin \Psi(t)$	0	$-\cos \Psi(t)$
$\delta\gamma_{n,z}$	0	∓ 1	0
$\delta\omega_{ie,x}$	0	0	0
$\delta\omega_{ie,y}$	0	0	0
$\delta\omega_{ie,z}$	0	0	0
$\Phi_{\hat{n}n}$	$\mp g \sin \Psi(t) \pm h \left(\frac{\partial \gamma_{n,n}(P_b)}{\partial r_{n,e}} \cos \Psi(t) - \frac{\partial \gamma_{n,e}(P_b)}{\partial r_{n,e}} \sin \Psi(t) \right)$	$\pm h \frac{\partial \gamma_{n,d}(P_b)}{\partial r_{n,e}}$	$g \cos \Psi(t) + h \left(\frac{\partial \gamma_{n,e}(P_b)}{\partial r_{n,e}} \cos \Psi(t) + \frac{\partial \gamma_{n,n}(P_b)}{\partial r_{n,e}} \sin \Psi(t) \right)$
$\Theta_{\hat{n}n}$	$\mp g \cos \Psi(t) \pm h \left(\frac{\partial \gamma_{n,n}(P_b)}{\partial r_{n,n}} \cos \Psi(t) - \frac{\partial \gamma_{n,e}(P_b)}{\partial r_{n,n}} \sin \Psi(t) \right)$	$\mp h \frac{\partial \gamma_{n,d}(P_b)}{\partial r_{n,n}}$	$-g \cos \Psi(t) - h \left(\frac{\partial \gamma_{n,n}(P_b)}{\partial r_{n,n}} \cos \Psi(t) + \frac{\partial \gamma_{n,e}(P_b)}{\partial r_{n,n}} \sin \Psi(t) \right)$
$\Psi_{\hat{n}n}$	0	0	0
$\delta\omega_{np,x}$	$\pm \omega_{ie} (h \cos \Psi(t) \cos \lambda - h \sin \Psi(t) \sin \phi \sin \lambda)$	0	$\omega_{ie} (h \sin \Psi(t) \cos \lambda + h \cos \Psi(t) \sin \lambda \sin \phi)$
$\delta\omega_{np,y}$	$\pm \omega_{ie} (h \cos \Psi(t) \sin \lambda + h \sin \Psi(t) \cos \lambda \sin \phi)$	0	$\omega_{ie} (h \sin \Psi(t) \sin \lambda - h \cos \Psi(t) \cos \lambda \sin \phi)$
$\delta\omega_{np,z}$	0	0	0
$\delta\dot{\omega}_{np,x}$	$\pm h \cos \Psi(t)$	0	$h \sin \Psi(t)$
$\delta\dot{\omega}_{np,y}$	$\pm h \sin \Psi(t)$	0	$-h \cos \Psi(t)$
$\delta\dot{\omega}_{np,z}$	0	0	0
$\delta r_{n,x}(P_p)$	$\pm \omega_{ie}^2 \cos \Psi(t) \sin^2 \phi$	$\pm \omega_{ie}^2 \cos \phi \sin \phi$	$\omega_{ie}^2 \sin \Psi(t) \sin^2 \phi$
$\delta r_{n,y}(P_p)$	$\mp \omega_{ie}^2 \sin \Psi(t)$	0	$\omega_{ie}^2 \cos \Psi(t)$
$\delta r_{n,z}(P_p)$	$\pm \omega_{ie}^2 \cos \Psi(t) \cos \phi \sin \phi$	$\pm \omega_{ie}^2 \cos^2 \phi$	$\omega_{ie}^2 \sin \Psi(t) \sin \phi \cos \phi$
$\delta \dot{r}_{n,x}(P_p)$	$\mp \omega_{ie} \sin \Psi(t) \sin \phi$	0	$\omega_{ie} \cos \Psi(t) \sin \phi$
$\delta \dot{r}_{n,y}(P_p)$	$\mp \omega_{ie} \cos \Psi(t) \sin \phi$	$\mp \omega_{ie} \cos \phi$	$-\omega_{ie} \sin \Psi(t) \sin \phi$
$\delta \dot{r}_{n,z}(P_p)$	$\mp \omega_{ie} \sin \Psi(t) \cos \phi$	0	$\omega_{ie} \cos \Psi(t) \cos \phi$
$\delta \ddot{r}_{n,x}(P_p)$	$\mp \cos \Psi(t)$	0	$-\sin \Psi(t)$
$\delta \ddot{r}_{n,y}(P_p)$	$\pm \sin \Psi(t)$	0	$-\cos \Psi(t)$
$\delta \ddot{r}_{n,z}(P_p)$	0	∓ 1	0
$\Phi_{\hat{p}p}$	$\mp g \sin \Psi(t) \pm h \left(\frac{\partial \gamma_{n,n}(P_b)}{\partial r_{n,e}} \cos \Psi(t) - \frac{\partial \gamma_{n,e}(P_b)}{\partial r_{n,e}} \sin \Psi(t) \right)$	$\pm h \frac{\partial \gamma_{n,d}(P_b)}{\partial r_{n,e}}$	$-g \sin \Psi(t) - h \left(\frac{\partial \gamma_{n,e}(P_b)}{\partial r_{n,e}} \cos \Psi(t) + \frac{\partial \gamma_{n,n}(P_b)}{\partial r_{n,e}} \sin \Psi(t) \right)$
$\Theta_{\hat{p}p}$	$\mp g \cos \Psi(t) \pm h \left(\frac{\partial \gamma_{n,n}(P_b)}{\partial r_{n,n}} \cos \Psi(t) - \frac{\partial \gamma_{n,e}(P_b)}{\partial r_{n,n}} \sin \Psi(t) \right)$	$\mp h \frac{\partial \gamma_{n,d}(P_b)}{\partial r_{n,n}}$	$g \cos \Psi(t) + h \left(\frac{\partial \gamma_{n,e}(P_b)}{\partial r_{n,n}} \cos \Psi(t) + \frac{\partial \gamma_{n,n}(P_b)}{\partial r_{n,n}} \sin \Psi(t) \right)$
$\Psi_{\hat{p}p}$	0	0	0
$\delta\omega_{pw,x}$	0	0	0
$\delta\omega_{pw,y}$	0	0	0
$\delta\omega_{pw,z}$	0	0	0
$\delta r_{p,x}(P_w)$	$\mp \omega_{ie}^2 \sin \Psi(t)$	0	$\omega_{ie}^2 \cos \Psi(t)$
$\delta r_{p,y}(P_w)$	$\pm \omega_{ie}^2 \cos \Psi(t) \sin^2 \phi$	$\pm \omega_{ie}^2 \cos \phi \sin \phi$	$\omega_{ie}^2 \sin \Psi(t) \sin^2 \phi$
$\delta r_{p,z}(P_w)$	$\mp \omega_{ie}^2 \cos \Psi(t) \cos \phi \sin \phi$	$\mp \omega_{ie}^2 \cos^2 \phi$	$-\omega_{ie}^2 \sin \Psi(t) \cos \phi \sin \phi$
$\delta \dot{r}_{p,x}(P_w)$	$\mp \omega_{ie} \cos \Psi(t) \sin \phi$	$\mp \omega_{ie} \cos \phi$	$-\omega_{ie} \sin \Psi(t) \sin \phi$
$\delta \dot{r}_{p,y}(P_w)$	$\mp \omega_{ie} \sin \Psi(t) \sin \phi$	0	$\omega_{ie} \cos \Psi(t) \sin \phi$
$\delta \dot{r}_{p,z}(P_w)$	$\pm \omega_{ie} \sin \Psi(t) \cos \phi$	0	$-\omega_{ie} \cos \Psi(t) \cos \phi$
$\delta \ddot{r}_{p,x}(P_w)$	$\pm \sin \Psi(t)$	0	$-\cos \Psi(t)$
$\delta \ddot{r}_{p,y}(P_w)$	$\mp \cos \Psi(t)$	0	$-\cos \Psi(t)$
$\delta \ddot{r}_{p,z}(P_w)$	0	± 1	0

Table H.5.: Error sensitivities of the accelerometer y-axis input during the six-position test, continued.

Position	1 and 2	3 and 4	5 and 6
Φ_{ww}	$\mp g$	0	0
Θ_{ww}	0	0	g
Ψ_{ww}	0	0	0
$\delta\omega_{wv,x}$	0	0	0
$\delta\omega_{wv,y}$	0	0	0
$\delta\omega_{wv,z}$	0	0	0
$\delta\dot{r}_{w,x}(P_v)$	$\mp\omega_{ie}^2 \cos \Psi(t) \sin \Psi(t) \cos^2 \phi$	$\pm\omega_{ie} \sin \Psi(t) \cos \phi(\omega_{pw} + \omega_{ie} \sin \phi)$	$(\omega_{pw} + \omega_{ie} \sin \phi)^2 + \omega_{ie}^2 \cos^2 \Psi(t) \cos^2 \phi$
$\delta\dot{r}_{w,y}(P_v)$	$\pm(\omega_{pw} + \omega_{ie} \sin \phi)^2 + \omega_{ie}^2 \sin^2 \Psi(t) \cos^2 \phi$	$\pm\omega_{ie} \cos \Psi(t) \cos \phi(\omega_{pw} + \omega_{ie} \sin \phi)$	$-\omega_{ie}^2 \cos \Psi(t) \sin \Psi(t) \cos^2 \phi$
$\delta\dot{r}_{w,z}(P_v)$	$\mp\omega_{ie} \cos \Psi(t) \cos \phi(\omega_{pw} + \omega_{ie} \sin \phi)$	$\pm\omega_{ie}^2(\sin^2 \phi - 1)$	$-\omega_{ie} \sin \Psi(t) \cos \phi(\omega_{pw} + \omega_{ie} \sin \phi)$
$\delta\ddot{r}_{w,x}(P_v)$	$\mp\omega_{pw} - \omega_{ie} \sin \phi$	$\omega_{ie} \sin \Psi(t) \cos \phi$	0
$\delta\ddot{r}_{w,y}(P_v)$	0	$-\omega_{ie} \sin \Psi(t) \cos \phi$	$\omega_{pw} + \omega_{ie} \sin \phi$
$\delta\ddot{r}_{w,z}(P_v)$	$\pm\omega_{ie} \sin \Psi(t) \cos \phi$	0	$-\omega_{ie} \cos \Psi(t) \sin \phi$
$\delta\ddot{r}_{w,x}(P_v)$	0	0	-1
$\delta\ddot{r}_{w,y}(P_v)$	∓ 1	0	0
$\delta\ddot{r}_{w,z}(P_v)$	0	± 1	0
Φ_{vv}	$\mp g$	0	0
Θ_{vv}	0	0	0
Ψ_{vv}	0	0	$\pm g$
$\delta\omega_{vu,x}$	0	0	0
$\delta\omega_{vu,y}$	0	0	0
$\delta\omega_{vu,z}$	0	0	0
$\delta\dot{r}_{v,x}(P_u)$	$\mp\omega_{ie}^2 \cos \Psi(t) \sin \Psi(t) \cos^2 \phi$	$\pm\omega_{ie} \sin \Psi(t) \cos \phi(\omega_{pw} + \omega_{ie} \sin \phi)$	$(\omega_{pw} + \omega_{ie} \sin \phi)^2 \mp \omega_{ie}^2 \cos^2 \Psi(t) \cos^2 \phi$
$\delta\dot{r}_{v,y}(P_u)$	$\mp(\omega_{pw} + \omega_{ie} \sin \phi)^2 - \omega_{ie}^2 \sin^2 \Psi(t) \cos^2 \phi$	$\omega_{ie}^2(\sin^2 \phi - 1)$	$\pm\omega_{ie} \sin \Psi(t) \cos \phi(\omega_{pw} + \omega_{ie} \sin \phi)$
$\delta\dot{r}_{v,z}(P_u)$	$\pm\omega_{ie} \cos \Psi(t) \cos \phi(\omega_{pw} + \omega_{ie} \sin \phi)$	$-\omega_{ie} \cos \Psi(t) \cos \phi(\omega_{pw} + \omega_{ie} \sin \phi)$	$-\omega_{ie}^2 \cos \Psi(t) \sin \Psi(t) \cos^2 \phi$
$\delta\ddot{r}_{v,x}(P_u)$	$\mp(\omega_{pw} + \omega_{ie} \sin \phi)$	$\omega_{ie} \cos \Psi(t) \cos \phi$	0
$\delta\ddot{r}_{v,y}(P_u)$	0	0	$\omega_{ie} \cos \Psi(t) \cos \phi$
$\delta\ddot{r}_{v,z}(P_u)$	$\mp\omega_{ie} \sin \Psi(t) \cos \phi$	$-\omega_{ie} \sin \Psi(t) \cos \phi$	$(\omega_{pw} + \omega_{ie} \sin \phi)$
$\delta\ddot{r}_{v,x}(P_u)$	0	0	-1
$\delta\ddot{r}_{v,y}(P_u)$	1	1	0
$\delta\ddot{r}_{v,z}(P_u)$	0	0	0
Φ_{uu}	$\mp g$	0	0
Θ_{uu}	0	0	0
Ψ_{uu}	0	0	$\pm g$
$\delta\dot{r}_{u,x}(P_b)$	$\mp\omega_{ie}^2 \cos \Psi(t) \sin \Psi(t) \cos^2 \phi$	$\omega_{ie} \sin \Psi(t) \cos \phi(\omega_{pw} + \omega_{ie} \sin \phi)$	$\pm\omega_{ie} \cos \Psi(t) \cos \phi(\omega_{pw} + \omega_{ie} \sin \phi)$
$\delta\dot{r}_{u,y}(P_b)$	$\mp(\omega_{pw} + \omega_{ie} \sin \phi)^2 - \omega_{ie}^2 \sin^2 \Psi(t) \cos^2 \phi$	$\omega_{ie}^2(\sin^2 \phi - 1)$	$-(\omega_{pw} + \omega_{ie} \sin \phi)^2 - \omega_{ie}^2 \cos^2 \Psi(t) \cos^2 \phi$
$\delta\dot{r}_{u,z}(P_b)$	$\pm\omega_{ie} \cos \Psi(t) \cos \phi(\omega_{pw} + \omega_{ie} \sin \phi)$	$-\omega_{ie} \cos \Psi(t) \cos \phi(\omega_{pw} + \omega_{ie} \sin \phi)$	$-\omega_{ie}^2 \cos \Psi(t) \sin \Psi(t) \cos^2 \phi$
$\delta\ddot{r}_{u,x}(P_b)$	$\mp(\omega_{pw} + \omega_{ie} \sin \phi)$	$-\omega_{ie} \cos \Psi(t) \cos \phi$	$\omega_{ie} \sin \Psi(t) \cos \phi$
$\delta\ddot{r}_{u,y}(P_b)$	0	0	0
$\delta\ddot{r}_{u,z}(P_b)$	$\mp\omega_{ie} \sin \Psi(t) \cos \phi$	$-\omega_{ie} \sin \Psi(t) \cos \phi$	$\pm(\omega_{pw} + \omega_{ie} \sin \phi)$
$\delta\ddot{r}_{u,x}(P_b)$	0	0	0
$\delta\ddot{r}_{u,y}(P_b)$	1	1	1
$\delta\ddot{r}_{u,z}(P_b)$	0	0	0
Φ_{bb}	$\mp g$	0	0
Θ_{bb}	0	0	0
Ψ_{bb}	0	0	$\pm g$

Table H.6.: Error sensitivities of the accelerometer z-axis input during the six-position test.

Position	1 and 2	3 and 4	5 and 6
$\delta\gamma_{n,x}$	0	$\mp \cos \Psi(t)$	$\cos \Psi(t)$
$\delta\gamma_{n,y}$	0	$\pm \sin \Psi(t)$	$-\sin \Psi(t)$
$\delta\gamma_{n,z}$	± 1	0	0
$\delta\omega_{ie,x}$	0	0	0
$\delta\omega_{ie,y}$	0	0	0
$\delta\omega_{ie,z}$	0	0	0
$\Phi_{\dot{n}n}$	$\mp h \frac{\partial \gamma_{n,d}(P_b)}{\partial r_{n,e}}$	$\mp g \sin \Psi(t) \pm h \left(\frac{\partial \gamma_{n,n}(P_b)}{\partial r_{n,e}} \cos \Psi(t) - \frac{\partial \gamma_{n,e}(P_b)}{\partial r_{n,e}} \sin \Psi(t) \right)$	$g \sin \Psi(t) - h \left(\frac{\partial \gamma_{n,n}(P_b)}{\partial r_{n,e}} \cos \Psi(t) - \frac{\partial \gamma_{n,e}(P_b)}{\partial r_{n,e}} \sin \Psi(t) \right)$
$\Theta_{\dot{n}n}$	$\pm h \frac{\partial \gamma_{n,d}(P_b)}{\partial r_{n,n}}$	$\mp g \cos \Psi(t) \mp h \left(\frac{\partial \gamma_{n,n}(P_b)}{\partial r_{n,n}} \cos \Psi(t) - \frac{\partial \gamma_{n,e}(P_b)}{\partial r_{n,n}} \sin \Psi(t) \right)$	$g \cos \Psi(t) + h \left(\frac{\partial \gamma_{n,n}(P_b)}{\partial r_{n,n}} \cos \Psi(t) + \frac{\partial \gamma_{n,e}(P_b)}{\partial r_{n,n}} \sin \Psi(t) \right)$
$\Psi_{\dot{n}n}$	0	0	0
$\delta\omega_{np,x}$	0	$\pm \omega_{ie} (h \cos \Psi(t) \cos \lambda - h \sin \Psi(t) \sin \phi \sin \lambda)$	$-\omega_{ie} (h \sin \Psi(t) \cos \lambda - h \cos \Psi(t) \sin \lambda \sin \phi)$
$\delta\omega_{np,y}$	0	$\pm \omega_{ie} (h \cos \Psi(t) \sin \lambda + h \sin \Psi(t) \cos \lambda \sin \phi)$	$-\omega_{ie} (h \sin \Psi(t) \sin \lambda + h \cos \Psi(t) \cos \lambda \sin \phi)$
$\delta\omega_{np,z}$	0	0	0
$\delta\dot{\omega}_{np,x}$	0	$\pm h \cos \Psi(t)$	$-h \cos \Psi(t)$
$\delta\dot{\omega}_{np,y}$	0	$\pm h \sin \Psi(t)$	$-h \sin \Psi(t)$
$\delta\dot{\omega}_{np,z}$	0	0	0
$\delta r_{n,x}(P_p)$	$\mp \omega_{ie}^2 \cos \phi \sin \phi$	$\pm \omega_{ie}^2 \cos \Psi(t) \sin^2 \phi$	$-\omega_{ie}^2 \sin \Psi(t) \sin^2 \phi$
$\delta r_{n,y}(P_p)$	0	$\mp \omega_{ie}^2 \sin \Psi(t)$	$\omega_{ie}^2 \cos \Psi(t)$
$\delta r_{n,z}(P_p)$	$\pm \omega_{ie}^2 \cos^2 \phi$	$\pm \omega_{ie}^2 \cos \Psi(t) \cos \phi \sin \phi$	$-\omega_{ie}^2 \sin \Psi(t) \sin \phi \cos \phi$
$\delta \dot{r}_{n,x}(P_p)$	0	$\mp \omega_{ie} \sin \Psi(t) \sin \phi$	$\omega_{ie} \sin \Psi(t) \sin \phi$
$\delta \dot{r}_{n,y}(P_p)$	$\pm \omega_{ie} \cos \phi$	$\mp \omega_{ie} \cos \Psi(t) \sin \phi$	$\omega_{ie} \cos \Psi(t) \sin \phi$
$\delta \dot{r}_{n,z}(P_p)$	0	$\mp \omega_{ie} \sin \Psi(t) \cos \phi$	$\omega_{ie} \sin \Psi(t) \cos \phi$
$\delta \ddot{r}_{n,x}(P_p)$	0	$\mp \cos \Psi(t)$	$\cos \Psi(t)$
$\delta \ddot{r}_{n,y}(P_p)$	0	$\pm \sin \Psi(t)$	$-\sin \Psi(t)$
$\delta \ddot{r}_{n,z}(P_p)$	± 1	0	0
$\Phi_{\dot{p}p}$	$\pm h \frac{\partial \gamma_{n,d}(P_b)}{\partial r_{n,e}}$	$\mp g \sin \Psi(t) \mp h \left(\frac{\partial \gamma_{n,n}(P_b)}{\partial r_{n,e}} \cos \Psi(t) - \frac{\partial \gamma_{n,e}(P_b)}{\partial r_{n,e}} \sin \Psi(t) \right)$	$g \cos \Psi(t) + h \left(\frac{\partial \gamma_{n,n}(P_b)}{\partial r_{n,e}} \cos \Psi(t) - \frac{\partial \gamma_{n,e}(P_b)}{\partial r_{n,e}} \sin \Psi(t) \right)$
$\Theta_{\dot{p}p}$	$\mp h \frac{\partial \gamma_{n,d}(P_b)}{\partial r_{n,n}}$	$\mp g \cos \Psi(t) \pm h \left(\frac{\partial \gamma_{n,n}(P_b)}{\partial r_{n,n}} \cos \Psi(t) - \frac{\partial \gamma_{n,e}(P_b)}{\partial r_{n,n}} \sin \Psi(t) \right)$	$g \sin \Psi(t) - h \left(\frac{\partial \gamma_{n,n}(P_b)}{\partial r_{n,n}} \cos \Psi(t) - \frac{\partial \gamma_{n,e}(P_b)}{\partial r_{n,n}} \sin \Psi(t) \right)$
$\Psi_{\dot{p}p}$	0	0	0
$\delta\omega_{pw,x}$	0	0	0
$\delta\omega_{pw,y}$	0	0	0
$\delta\omega_{pw,z}$	0	0	0
$\delta r_{p,x}(P_w)$	0	$\mp \omega_{ie}^2 \sin \Psi(t)$	$\omega_{ie}^2 \sin \Psi(t)$
$\delta r_{p,y}(P_w)$	$\mp \omega_{ie}^2 \cos \phi \sin \phi$	$\pm \omega_{ie}^2 \cos \Psi(t) \sin^2 \phi$	$-\omega_{ie}^2 \cos \Psi(t) \sin^2 \phi$
$\delta r_{p,z}(P_w)$	$\pm \omega_{ie}^2 \cos^2 \phi$	$\mp \omega_{ie}^2 \cos \Psi(t) \cos \phi \sin \phi$	$\omega_{ie}^2 \cos \Psi(t) \cos \phi \sin \phi$
$\delta \dot{r}_{p,x}(P_w)$	$\pm \omega_{ie} \cos \phi$	$\mp \omega_{ie} \cos \Psi(t) \sin \phi$	$\omega_{ie} \cos \Psi(t) \sin \phi$
$\delta \dot{r}_{p,y}(P_w)$	0	$\mp \omega_{ie} \sin \Psi(t) \sin \phi$	$\omega_{ie} \sin \Psi(t) \sin \phi$
$\delta \dot{r}_{p,z}(P_w)$	0	$\pm \omega_{ie} \sin \Psi(t) \cos \phi$	$-\omega_{ie} \sin \Psi(t) \cos \phi$
$\delta \ddot{r}_{p,x}(P_w)$	0	$\pm \sin \Psi(t)$	$-\sin \Psi(t)$
$\delta \ddot{r}_{p,y}(P_w)$	0	$\mp \cos \Psi(t)$	$\cos \Psi(t)$
$\delta \ddot{r}_{p,z}(P_w)$	∓ 1	0	0

Table H.6.: Error sensitivities of the accelerometer z-axis input during the six-position test, continued.

Position	1 and 2	3 and 4	5 and 6
Φ_{ww}	0	$\mp g$	g
Θ_{ww}	0	0	0
Ψ_{ww}	0	0	0
$\delta\omega_{wv,x}$	0	0	0
$\delta\omega_{wv,y}$	0	0	0
$\delta\omega_{wv,z}$	0	0	0
$\delta\dot{r}_{w,x}(P_v)$	$\mp\omega_{ie} \sin \Psi(t) \cos \phi(\omega_{pw} + \omega_{ie} \sin \phi)$	$\mp\omega_{ie}^2 \cos \Psi(t) \sin \Psi(t) \cos^2 \phi$	$\omega_{ie}^2 \cos \Psi(t) \sin \Psi(t) \cos^2 \phi$
$\delta\dot{r}_{w,y}(P_v)$	$\mp\omega_{ie} \cos \Psi(t) \cos \phi(\omega_{pw} + \omega_{ie} \sin \phi)$	$\pm(\omega_{pw} + \omega_{ie} \sin \phi)^2 + \omega_{ie}^2 \sin^2 \Psi(t) \cos^2 \phi$	$-(\omega_{pw} + \omega_{ie} \sin \phi)^2 - \omega_{ie}^2 \cos^2 \Psi(t) \cos^2 \phi$
$\delta\dot{r}_{w,z}(P_v)$	$\mp\omega_{ie}^2 (\sin^2 \phi - 1)$	$\mp\omega_{ie} \cos \Psi(t) \cos \phi(\omega_{pw} + \omega_{ie} \sin \phi)$	$\omega_{ie} \cos \Psi(t) \cos \phi(\omega_{pw} + \omega_{ie} \sin \phi)$
$\delta\ddot{r}_{w,x}(P_v)$	$\pm\omega_{ie} \sin \Psi(t) \cos \phi$	$\mp\omega_{pw} - \omega_{ie} \sin \phi$	$\pm(\omega_{pw} + \omega_{ie} \sin \phi)$
$\delta\ddot{r}_{w,y}(P_v)$	$\mp\omega_{ie} \sin \Psi(t) \cos \phi$	0	0
$\delta\ddot{r}_{w,z}(P_v)$	0	$\pm\omega_{ie} \sin \Psi(t) \cos \phi$	$-\omega_{ie} \sin \Psi(t) \cos \phi$
$\delta\ddot{r}_{w,x}(P_v)$	0	0	0
$\delta\ddot{r}_{w,y}(P_v)$	0	∓ 1	1
$\delta\ddot{r}_{w,z}(P_v)$	∓ 1	0	0
Φ_{vv}	0	$\mp g$	$\pm g$
Θ_{vv}	0	0	0
Ψ_{vv}	0	0	0
$\delta\omega_{vu,x}$	0	0	0
$\delta\omega_{vu,y}$	0	0	0
$\delta\omega_{vu,z}$	0	0	0
$\delta\dot{r}_{v,x}(P_u)$	$\mp\omega_{ie} \sin \Psi(t) \cos \phi(\omega_{pw} + \omega_{ie} \sin \phi)$	$\mp\omega_{ie}^2 \cos \Psi(t) \sin \Psi(t) \cos^2 \phi$	$\omega_{ie}^2 \cos \Psi(t) \sin \Psi(t) \cos^2 \phi$
$\delta\dot{r}_{v,y}(P_u)$	$\omega_{ie}^2 (\sin^2 \phi - 1)$	$(\omega_{pw} + \omega_{ie} \sin \phi)^2 - \omega_{ie}^2 \sin^2 \Psi(t) \cos^2 \phi$	$\mp\omega_{ie} \cos \Psi(t) \cos \phi(\omega_{pw} + \omega_{ie} \sin \phi)$
$\delta\dot{r}_{v,z}(P_u)$	$\omega_{ie} \cos \Psi(t) \cos \phi(\omega_{pw} + \omega_{ie} \sin \phi)$	$\omega_{ie} \cos \Psi(t) \cos \phi(\omega_{pw} + \omega_{ie} \sin \phi)$	$-(\omega_{pw} + \omega_{ie} \sin \phi)^2 - \omega_{ie}^2 \sin^2 \Psi(t) \cos^2 \phi$
$\delta\ddot{r}_{v,x}(P_u)$	$\pm(\omega_{pw} + \omega_{ie} \sin \phi)$	$\mp(\omega_{pw} + \omega_{ie} \sin \phi)$	$\omega_{ie} \sin \Psi(t) \cos \phi$
$\delta\ddot{r}_{v,y}(P_u)$	$\omega_{ie} \cos \Psi(t) \cos \phi$	$\omega_{ie} \sin \Psi(t) \cos \phi$	$\mp(\omega_{pw} + \omega_{ie} \sin \phi)$
$\delta\ddot{r}_{v,z}(P_u)$	0	0	0
$\delta\ddot{r}_{v,x}(P_u)$	0	0	0
$\delta\ddot{r}_{v,y}(P_u)$	1	0	0
$\delta\ddot{r}_{v,z}(P_u)$	0	1	1
Φ_{uu}	0	$\mp g$	0
Θ_{uu}	0	0	$\mp g$
Ψ_{uu}	0	0	0
$\delta\dot{r}_{u,x}(P_b)$	$\mp\omega_{ie} \sin \Psi(t) \cos \phi(\omega_{pw} + \omega_{ie} \sin \phi)$	$\mp\omega_{ie}^2 \cos \Psi(t) \sin \Psi(t) \cos^2 \phi$	$\mp\omega_{ie} \cos \Psi(t) \cos \phi(\omega_{pw} + \omega_{ie} \sin \phi)$
$\delta\dot{r}_{u,y}(P_b)$	$\omega_{ie}^2 (\sin^2 \phi - 1)$	$(\omega_{pw} + \omega_{ie} \sin \phi)^2 - \omega_{ie}^2 \sin^2 \Psi(t) \cos^2 \phi$	$-(\omega_{pw} + \omega_{ie} \sin \phi)^2 - \omega_{ie}^2 \cos^2 \Psi(t) \cos^2 \phi$
$\delta\dot{r}_{u,z}(P_b)$	$\omega_{ie} \cos \Psi(t) \cos \phi(\omega_{pw} + \omega_{ie} \sin \phi)$	$\omega_{ie} \cos \Psi(t) \cos \phi(\omega_{pw} + \omega_{ie} \sin \phi)$	$-\omega_{ie}^2 \cos \Psi(t) \sin \Psi(t) \cos^2 \phi$
$\delta\ddot{r}_{u,x}(P_b)$	$\pm\omega_{ie} \cos \Psi(t) \cos \phi$	$\mp(\omega_{pw} + \omega_{ie} \sin \phi)$	$\omega_{ie} \sin \Psi(t) \cos \phi$
$\delta\ddot{r}_{u,y}(P_b)$	$\omega_{ie} \sin \Psi(t) \cos \phi$	$\omega_{ie} \sin \Psi(t) \cos \phi$	$\mp(\omega_{pw} + \omega_{ie} \sin \phi)$
$\delta\ddot{r}_{u,z}(P_b)$	0	0	0
$\delta\ddot{r}_{u,x}(P_b)$	0	0	0
$\delta\ddot{r}_{u,y}(P_b)$	0	0	0
$\delta\ddot{r}_{u,z}(P_b)$	1	1	1
Φ_{bb}	0	$\mp g$	0
Θ_{bb}	0	0	$\mp g$
Ψ_{bb}	0	0	0

Appendix I.

Scale Factor Test Series Error Budgets

This section provides the remaining error budgets for the scale factor test series estimation of section [Subsection 4.4.4](#). The three different test mechanizations are illustrated in [Figure 4.35](#).

Scenario	Test device	Sensor orientation	Error budget
I	single-axis rate table	vertical	Table I.1 , Table I.2
II	three-axis rate table	horizontal	Table I.3 , Table I.4
III	three-axis rate table	vertical	Table 4.20 , Table 4.21

While test-case III is discussed and presented in [Subsection 4.4.4](#), the error budgets for test cases I and II will be presented in the following.

I.1. Test Scenario I

Table I.1.: Gyro scale factor test series scale factor error for scenario I. The laboratory is located at $\phi = 45^\circ$. The applied rate series *a* to *d* are summarized in Table 4.19.

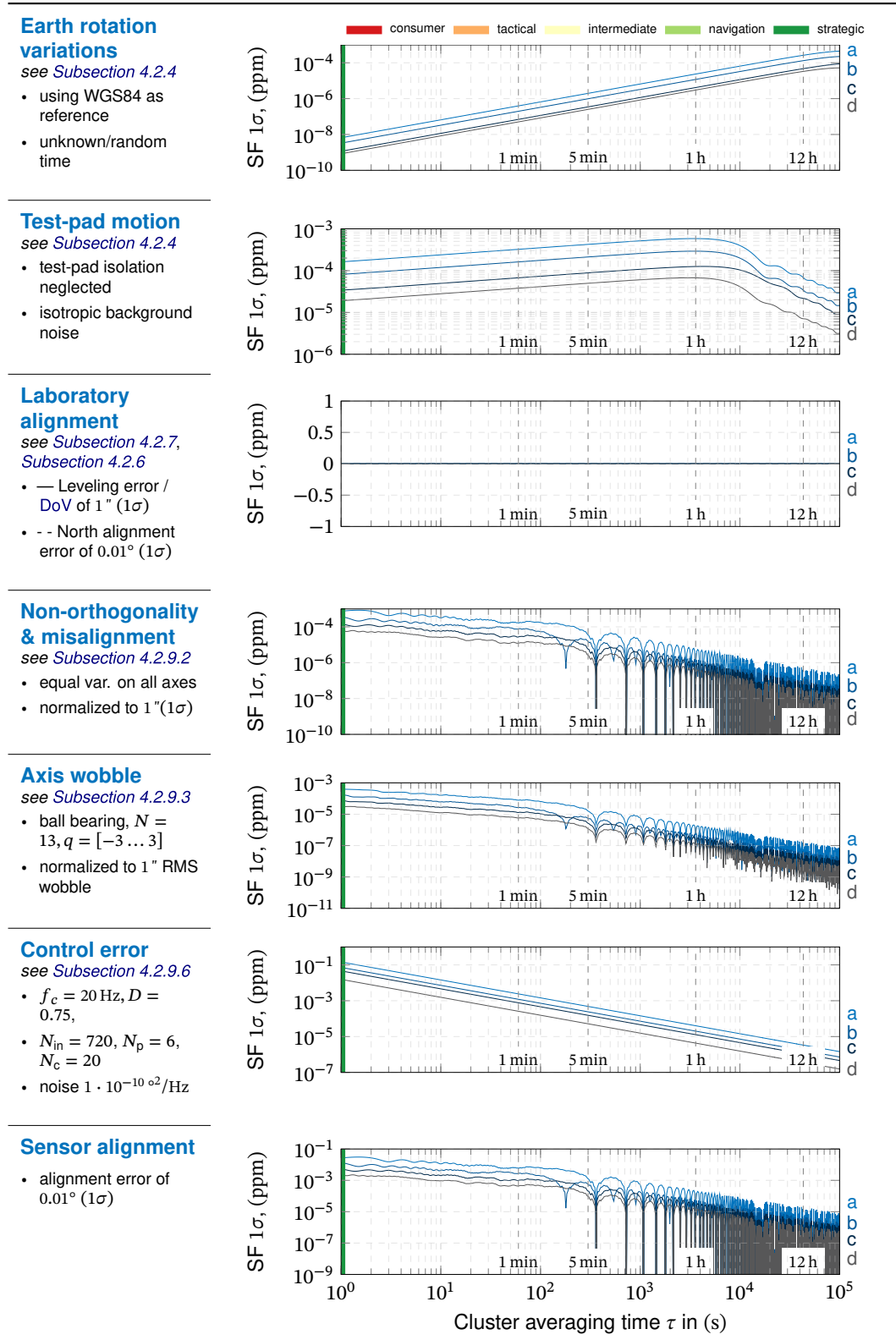
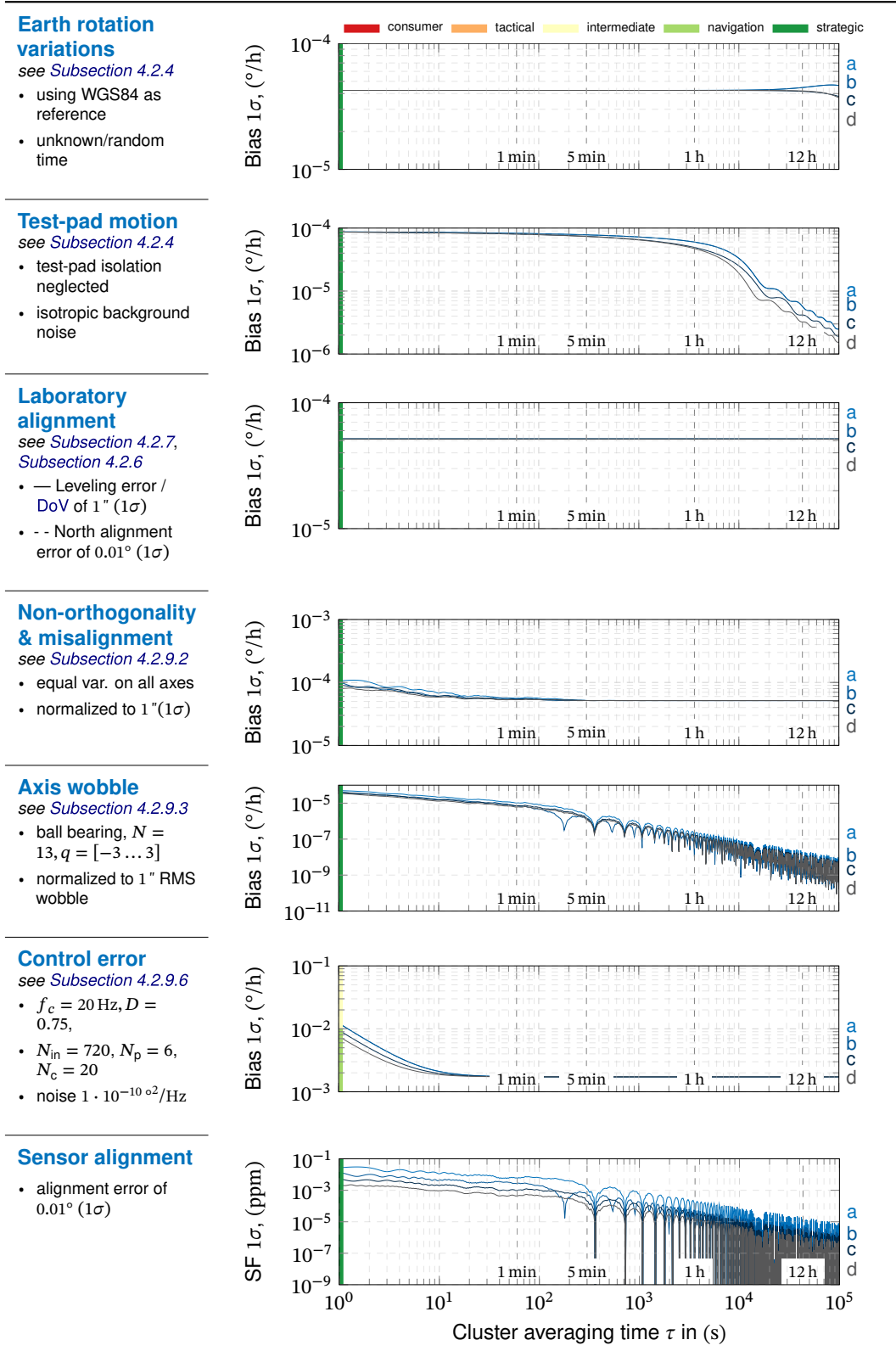


Table I.2.: Gyro scale factor test series bias error for scenario I. The laboratory is located at $\phi = 45^\circ$. The applied rate series *a* to *d* are summarized in Table 4.19.



I.2. Test Scenario II

Table I.3.: Gyro scale factor test series scale factor error for scenario II. The laboratory is located at $\phi = 45^\circ$. The applied rate series *a* to *d* are summarized in Table 4.19.

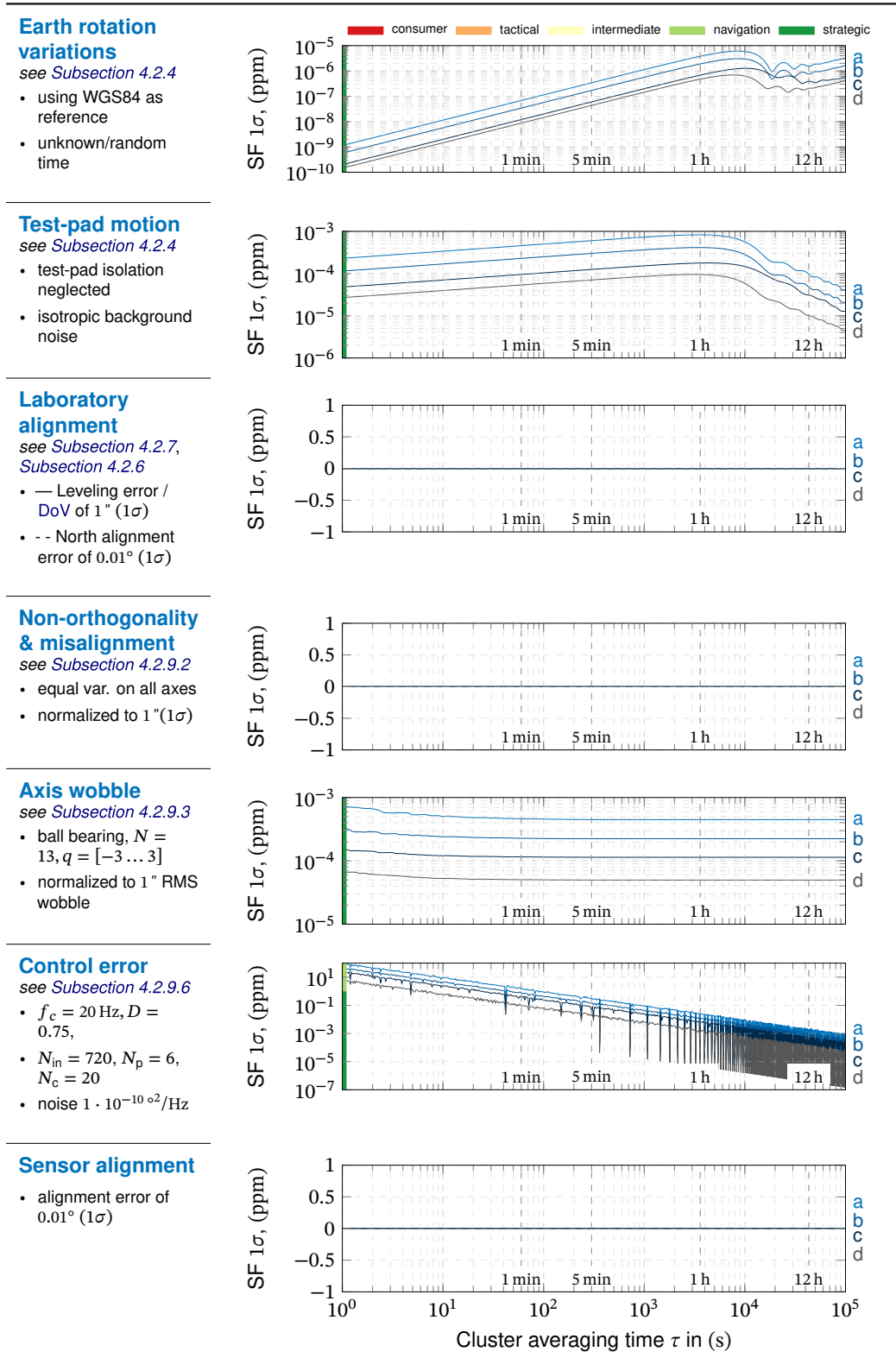
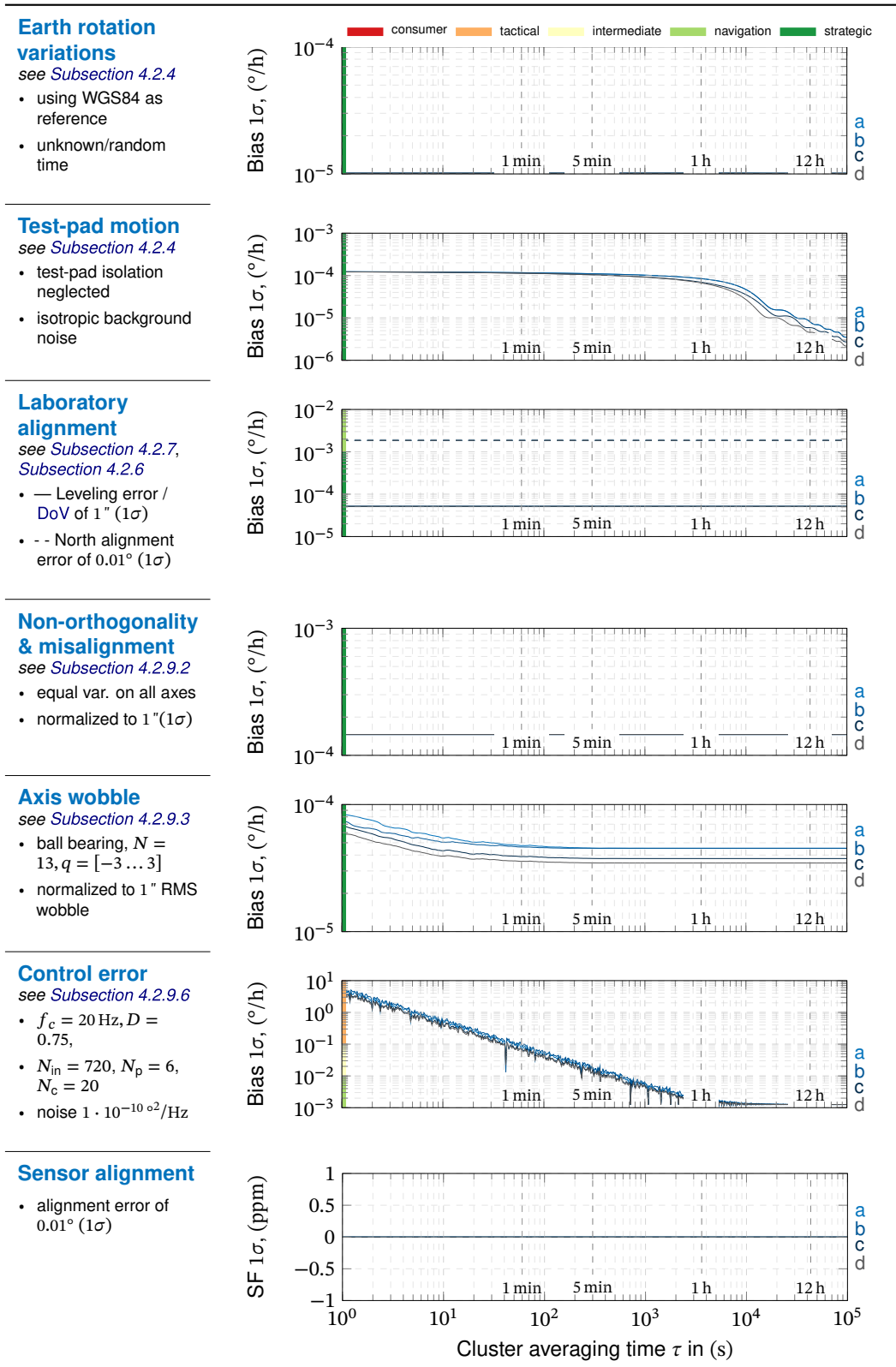


Table I.4.: Gyro scale factor test series bias error for scenario II. The laboratory is located at $\phi = 45^\circ$. The applied rate series *a* to *d* are summarized in Table 4.19.



Appendix J.

Kalman Filter Noise Models

Table J.1.: Test pad angular rates reference model approximation. Output is scaled to °/s for normalized input.

$$\mathbf{A} = \begin{bmatrix}
 -1.27 \cdot 10^2 & -6.44 \cdot 10^1 & -1.09 \cdot 10^1 & -2.23 & -4.82 \cdot 10^{-1} & -1.45 \cdot 10^{-1} & -2.46 \cdot 10^{-2} & -5.88 \cdot 10^{-3} & -1.59 \cdot 10^{-3} & -6.07 \cdot 10^{-4} & -2.60 \cdot 10^{-4} & -7.77 \cdot 10^{-5} & -2.44 \cdot 10^{-5} & -9.03 \cdot 10^{-6} \\
 64 & 0 & 0 & 0 & 0 & 0 & 0 & 0 & 0 & 0 & 0 & 0 & 0 & 0 \\
 0 & 8 & 0 & 0 & 0 & 0 & 0 & 0 & 0 & 0 & 0 & 0 & 0 & 0 \\
 0 & 0 & 2 & 0 & 0 & 0 & 0 & 0 & 0 & 0 & 0 & 0 & 0 & 0 \\
 0 & 0 & 0 & 5.00 \cdot 10^{-1} & 0 & 0 & 0 & 0 & 0 & 0 & 0 & 0 & 0 & 0 \\
 0 & 0 & 0 & 0 & 1.25 \cdot 10^{-1} & 0 & 0 & 0 & 0 & 0 & 0 & 0 & 0 & 0 \\
 0 & 0 & 0 & 0 & 0 & 6.25 \cdot 10^{-2} & 0 & 0 & 0 & 0 & 0 & 0 & 0 & 0 \\
 0 & 0 & 0 & 0 & 0 & 0 & 1.56 \cdot 10^{-2} & 0 & 0 & 0 & 0 & 0 & 0 & 0 \\
 0 & 0 & 0 & 0 & 0 & 0 & 0 & 3.91 \cdot 10^{-3} & 0 & 0 & 0 & 0 & 0 & 0 \\
 0 & 0 & 0 & 0 & 0 & 0 & 0 & 0 & 9.77 \cdot 10^{-4} & 0 & 0 & 0 & 0 & 0 \\
 0 & 0 & 0 & 0 & 0 & 0 & 0 & 0 & 0 & 2.44 \cdot 10^{-4} & 0 & 0 & 0 & 0 \\
 0 & 0 & 0 & 0 & 0 & 0 & 0 & 0 & 0 & 0 & 1.22 \cdot 10^{-4} & 0 & 0 & 0 \\
 0 & 0 & 0 & 0 & 0 & 0 & 0 & 0 & 0 & 0 & 0 & 3.05 \cdot 10^{-5} & 0 & 0 \\
 0 & 0 & 0 & 0 & 0 & 0 & 0 & 0 & 0 & 0 & 0 & 0 & 7.63 \cdot 10^{-6} & 0
 \end{bmatrix}$$

$$\mathbf{B}^T = [8 \ 0 \ 0 \ 0 \ 0 \ 0 \ 0 \ 0 \ 0 \ 0 \ 0 \ 0 \ 0 \ 0]$$

$$\mathbf{L} = [1.13 \cdot 10^{-2} \ 4.92 \cdot 10^{-4} \ 5.08 \cdot 10^{-5} \ 5.50 \cdot 10^{-6} \ 8.30 \cdot 10^{-7} \ 1.41 \cdot 10^{-7} \ 1.68 \cdot 10^{-8} \ 2.28 \cdot 10^{-9} \ 4.34 \cdot 10^{-10} \ 9.31 \cdot 10^{-11} \ 2.78 \cdot 10^{-11} \ 4.36 \cdot 10^{-12} \ 8.07 \cdot 10^{-13} \ 0]$$

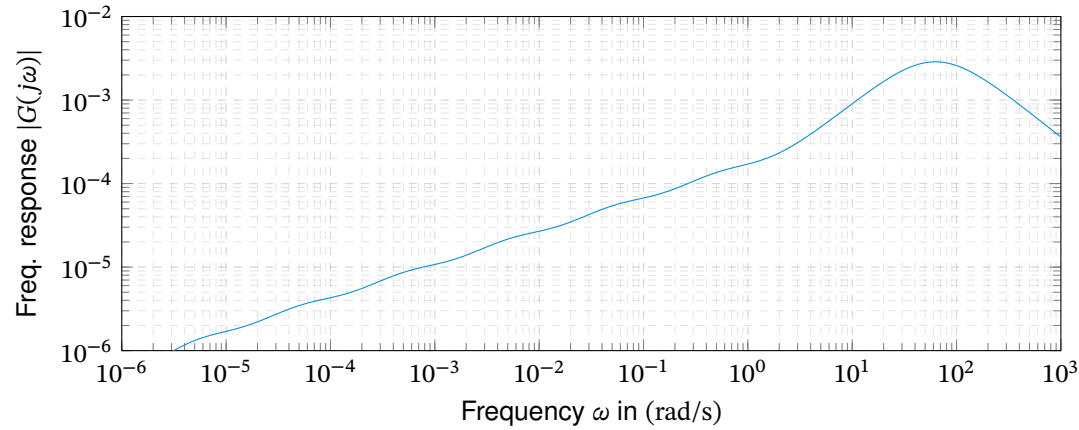
$$\mathbf{D} = 0$$


Table J.2.: Test pad tilt angles reference model approximation. Output is scaled to ° for normalized input.

$$\mathbf{A} = \begin{bmatrix}
 -1.27 \cdot 10^2 & -6.44 \cdot 10^1 & -1.09 \cdot 10^1 & -2.23 & -4.82 \cdot 10^{-1} & -1.45 \cdot 10^{-1} & -2.46 \cdot 10^{-2} & -5.88 \cdot 10^{-3} & -1.59 \cdot 10^{-3} & -6.07 \cdot 10^{-4} & -2.60 \cdot 10^{-4} & -7.77 \cdot 10^{-5} & -2.44 \cdot 10^{-5} & -9.03 \cdot 10^{-6} \\
 64 & 0 & 0 & 0 & 0 & 0 & 0 & 0 & 0 & 0 & 0 & 0 & 0 & 0 \\
 0 & 8 & 0 & 0 & 0 & 0 & 0 & 0 & 0 & 0 & 0 & 0 & 0 & 0 \\
 0 & 0 & 2 & 0 & 0 & 0 & 0 & 0 & 0 & 0 & 0 & 0 & 0 & 0 \\
 0 & 0 & 0 & 5.00 \cdot 10^{-1} & 0 & 0 & 0 & 0 & 0 & 0 & 0 & 0 & 0 & 0 \\
 0 & 0 & 0 & 0 & 1.25 \cdot 10^{-1} & 0 & 0 & 0 & 0 & 0 & 0 & 0 & 0 & 0 \\
 0 & 0 & 0 & 0 & 0 & 6.25 \cdot 10^{-2} & 0 & 0 & 0 & 0 & 0 & 0 & 0 & 0 \\
 0 & 0 & 0 & 0 & 0 & 0 & 1.56 \cdot 10^{-2} & 0 & 0 & 0 & 0 & 0 & 0 & 0 \\
 0 & 0 & 0 & 0 & 0 & 0 & 0 & 3.91 \cdot 10^{-3} & 0 & 0 & 0 & 0 & 0 & 0 \\
 0 & 0 & 0 & 0 & 0 & 0 & 0 & 0 & 9.77 \cdot 10^{-4} & 0 & 0 & 0 & 0 & 0 \\
 0 & 0 & 0 & 0 & 0 & 0 & 0 & 0 & 0 & 2.44 \cdot 10^{-4} & 0 & 0 & 0 & 0 \\
 0 & 0 & 0 & 0 & 0 & 0 & 0 & 0 & 0 & 0 & 1.22 \cdot 10^{-4} & 0 & 0 & 0 \\
 0 & 0 & 0 & 0 & 0 & 0 & 0 & 0 & 0 & 0 & 0 & 3.05 \cdot 10^{-5} & 0 & 0 \\
 0 & 0 & 0 & 0 & 0 & 0 & 0 & 0 & 0 & 0 & 0 & 0 & 7.63 \cdot 10^{-6} & 0
 \end{bmatrix}$$

$$\mathbf{B}^T = [8 \ 0 \ 0 \ 0 \ 0 \ 0 \ 0 \ 0 \ 0 \ 0 \ 0 \ 0 \ 0 \ 0]$$

$$\mathbf{L} = [0 \ 7.05 \cdot 10^{-4} \ 2.46 \cdot 10^{-4} \ 1.02 \cdot 10^{-4} \ 4.40 \cdot 10^{-5} \ 2.65 \cdot 10^{-5} \ 9.00 \cdot 10^{-6} \ 4.31 \cdot 10^{-6} \ 2.33 \cdot 10^{-6} \ 1.78 \cdot 10^{-6} \ 1.52 \cdot 10^{-6} \ 9.10 \cdot 10^{-7} \ 5.71 \cdot 10^{-7} \ 4.23 \cdot 10^{-7}]$$

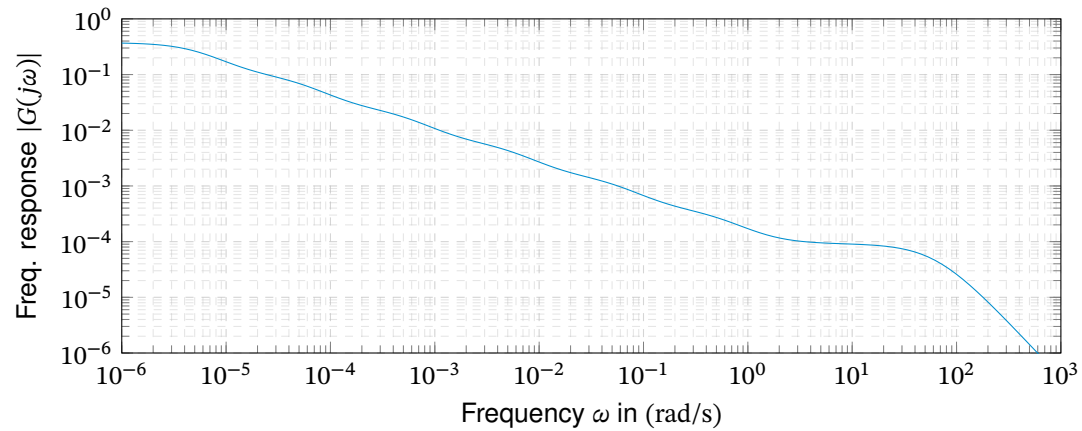
$$\mathbf{D} = 0$$


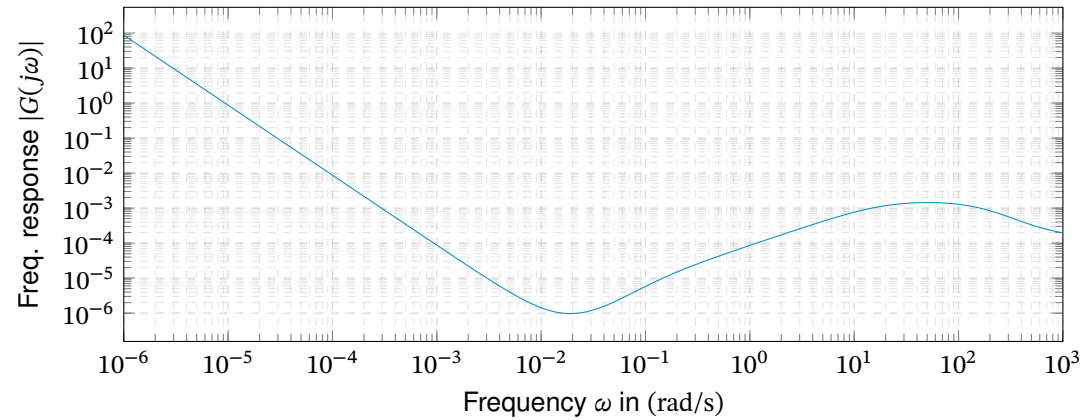
Table J.3.: Test pad acceleration reference model approximation. Output is scaled to m/s^2 for normalized input.

$$\mathbf{A} = \begin{bmatrix} -3.96 \cdot 10^2 & -1.67 \cdot 10^2 & -4.12 \cdot 10^1 & -2.57 & 0 & 0 \\ 256 & 0 & 0 & 0 & 0 & 0 \\ 0 & 64 & 0 & 0 & 0 & 0 \\ 0 & 0 & 2 & 0 & 0 & 0 \\ 0 & 0 & 0 & 3.13 \cdot 10^{-2} & 0 & 0 \\ 0 & 0 & 0 & 0 & 3.13 \cdot 10^{-2} & 0 \end{bmatrix}$$

$$\mathbf{B}^T = \begin{bmatrix} 0.25 & 0 & 0 & 0 & 0 & 0 \end{bmatrix}$$

$$\mathbf{L} = \begin{bmatrix} 5.06 \cdot 10^{-1} & 8.09 \cdot 10^{-1} & -2.32 \cdot 10^{-2} & -1.50 \cdot 10^{-3} & 6.08 \cdot 10^{-6} & 9.16 \cdot 10^{-7} \end{bmatrix}$$

$$\mathbf{D} = 0$$



References

- [1] Courtney Kube. “Russia has figured out how to jam U.S. drones in Syria, officials say, Four U.S. officials said Russia’s signal scrambling has seriously affected military operations.” (2018), [Online]. Available: <https://www.nbcnews.com/news/military/russia-has-figured-out-how-jam-u-s-drones-syria-n863931>.
- [2] “Beyond GPS, 5 Next-Generation Technologies for Positioning, Navigation & Timing (PNT),” Defense Advanced Research Projects Agency. (2014), [Online]. Available: <https://www.darpa.mil/news-events/2014-07-24> (visited on 08/03/2018).
- [3] UK National Quantum Technologies Programme 2018. “UKNQT Hubs.” (), [Online]. Available: <http://uknqt.epsrc.ac.uk/about/uknqt-hubs/> (visited on 08/03/2018).
- [4] European Comission. “Quantum Manifesto, A New Era of Technology.” (2016), [Online]. Available: http://querope.eu/system/files/u7/93056_Quantum%20Manifesto_WEB.pdf.
- [5] Elsa Kania and Stephen Armitage. “Disruption Under the Radar: Chinese Advances in Quantum Sensing.” (2017), [Online]. Available: <https://jamestown.org/program/disruption-under-the-radar-chinese-advances-in-quantum-sensing/>.
- [6] C. Jekeli, “Navigation Error Analysis of Atom Interferometer Inertial Sensor,” *Navigation*, vol. 52, no. 1, pp. 1–14, 2005, ISSN: 00281522. DOI: 10.1002/j.2161-4296.2005.tb01726.x.
- [7] Levitate Capital. “Drone Market Size Worldwide from 2020 to 2030, by Segment (in Billion U.S. Dollars).” Statista, Statista Inc., Ed. (2020), [Online]. Available: <https://www.statista.com/statistics/1234538/worldwide-drone-market-by-segment/>.
- [8] Teal Group, “Estimated worldwide production volume for unmanned aerial vehicles (military drones) from 2013 to 2022,” in *Statista - The Statistics Portal*. [Online]. Available: <https://statista.com/statistics/428911/global-production-volume-forecast-for-unmanned-aerial-systems-or-drones/>.
- [9] IEEE Aerospace Electronics Systems Society, Ed., *IEEE Standard Specification Format Guide and Test Procedure for Single-Axis Laser Gyros*, IEEE Std. 1995.
- [10] IEEE Aerospace Electronics Systems Society, Ed., *IEEE standard specification format guide and test procedure for single-axis interferometric fiber optic gyros*, IEEE Std. New York, N.Y., USA: Institute of Electrical and Electronics Engineers, 2008.

- [11] IEEE Aerospace Electronics Systems Society, Ed., *IEEE standard specification format guide and test procedure for coriolis vibratory gyros*, IEEE Std. New York, N.Y: Institute of Electrical and Electronics Engineers, 2004.
- [12] IEEE Aerospace Electronics Systems Society, Ed., *IEEE standard specification format guide and test procedure for single-axis laser gyros*, IEEE Std. New York, N.Y., USA: Institute of Electrical and Electronics Engineers, 2008.
- [13] P. D. Groves, *Principles of GNSS, inertial, and multisensor integrated navigation systems* (GNSS technology and application series), eng, Second edition. Boston: Artech House, 2013, 776 pp., ISBN: 9781608070053. [Online]. Available: <http://search.ebscohost.com/login.aspx?direct=true&scope=site&db=nlebk&db=nlabk&AN=753597>.
- [14] D. H. Titterton and J. L. Weston, *Strapdown inertial navigation technology* (IET radar, sonar, navigation and avionics series), 2. ed. Stevenage: The Inst. of Engineering and Technology, 2009, vol. 17, XVII, 558 S, Weston, John L (Author), ISBN: 9780863413582.
- [15] C. Jekeli, *Inertial Navigation Systems with Geodetic Applications*, eng. Berlin/Boston: De Gruyter, 2001, Online-Ressource, Jekeli, Christopher (Verfasser), ISBN: 3110800233.
- [16] O. S. Salychev, *Inertial systems in navigation and geophysics*. Moscow: Bauman, 1998, 352 blz. ; ISBN: 5-7038-1346-8.
- [17] K. R. Britting, *Inertial navigation systems analysis*. New York and (Chichester): Wiley-Interscience, 1971, xvii, 249, ISBN: 0-471-10485-X.
- [18] C. F. O'Donnell, Ed., *Inertial navigation, Analysis and design*, eng, O'Donnell, Cedric F. (Hrsg.), New York: McGraw-Hill, 1964, 442 pp.
- [19] C. Broxmeyer, *Inertial navigation systems* (McGraw-Hill electronic science series), eng. New York, NY: McGraw-Hill, 1964, 254 pp., Broxmeyer, Charles (VerfasserIn).
- [20] P. G. Savage, *Strapdown analytics*, 2nd ed. Maple Plain, Minn.: Strapdown Associates, 2007, 2 volumes.
- [21] A. B. Chatfield, *Fundamentals on high accuracy inertial navigation* (Progress in astronautics and aeronautics). Reston, Va.: American Inst. of Aeronautics and Astronautics, 1997, vol. 174, 339 pp., Chatfield, Averil B. (VerfasserIn), ISBN: 1563472430.
- [22] A. Lawrence, *Modern inertial technology, Navigation, guidance, and control* (Mechanical engineering series), eng, 2. ed., corr. 3 print. New York, NY: Springer, 2001, 278 pp., ISBN: 9780387985077.
- [23] IEEE Aerospace and Electronics Systems Society, Ed., *IEEE Standard for Inertial Systems Terminology*, IEEE Std, 2009.
- [24] IEEE Aerospace Electronics Systems Society, Ed., *IEEE standard specification format guide and test procedure for single-degree-of-freedom rate-integrating gyros*, IEEE Std. New York, N.Y: Institute of Electrical and Electronics Engineers, 2010.

-
- [25] IEEE Aerospace and Electronics Systems Society, Ed., *IEEE Standard Specification Format Guide and Test Procedure for Coriolis Vibratory Gyros*, IEEE Std. 2004.
- [26] IEEE Aerospace Electronics Systems Society, Ed., *IEEE recommended practice for inertial sensor test equipment, instrumentation, data acquisition, and analysis*, IEEE Std, New York, N.Y: Institute of Electrical and Electronics Engineers, 2005.
- [27] X. Ru, N. Gu, H. Shang, and H. Zhang, "MEMS Inertial Sensor Calibration Technology: Current Status and Future Trends," *Micromachines*, vol. 13, no. 6, p. 879, 2022, PII: mi13060879. DOI: [10.3390/mi13060879](https://doi.org/10.3390/mi13060879).
- [28] L. DeMore *et al.*, "Design study for a high accuracy three-axis test table," in *Guidance, Navigation and Control Conference*, (Snowmass,CO,U.S.A), Reston, Virginia: American Institute of Aeronautics and Astronautics, 8191985. DOI: [10.2514/6.1985-1893](https://doi.org/10.2514/6.1985-1893).
- [29] J. Wittry, "Description of an inertial test facility incorporating a passively isolated and actively stabilized platform," in *AIAA Guidance Control and Flight Mechanics Conference*, (Princeton), American Institute of Aeronautics and Astronautics, 1969. DOI: [10.2514/6.1969-863](https://doi.org/10.2514/6.1969-863).
- [30] L. Mathis, J. Stephens, and S. Wright, "The Design and Construction of an Inertial Test Facility," in *AIAA Guidance Control Conference*, American Institute of Aeronautics and Astronautics, 1967, pp. 376-390. DOI: [10.2514/6.1965-1240](https://doi.org/10.2514/6.1965-1240).
- [31] L. Keller and A. Abernathy, "Stable test platform - Passive type," in *AIAA Guidance Control and Flight Mechanics Conference*, American Institute of Aeronautics and Astronautics, Santa Barabara, 1970. DOI: [10.2514/6.1970-960](https://doi.org/10.2514/6.1970-960).
- [32] W. M. Weil, W. E. Srode, and R. M. Burrows, "Description of an inertial test facility located 1,100 feet below the surface of the earth," in *AIAA Guidance Control and Flight Dynamics Conference*, (Huntsville), American Institute of Aeronautics and Astronautics, 1967. DOI: [10.2514/6.1967-538](https://doi.org/10.2514/6.1967-538).
- [33] M. Flack and R. Dickie, "Building a dynamic test complex near an inertial test facility and general test pad considerations," in *AIAA Guidance and Control Conference*, American Institute of Aeronautics and Astronautics, Key Biscayne, 1973. DOI: [10.2514/6.1973-827](https://doi.org/10.2514/6.1973-827).
- [34] D. Blackstone and W. Whitesell, "Test pad motions at the Celestial Inertial Laboratory, Holloman AFB,NM," in *AIAA Guidance and Control Conference*, (Boston, MA), American Institute of Aeronautics and Astronautics, 1975. DOI: [10.2514/6.1975-1103](https://doi.org/10.2514/6.1975-1103).
- [35] G. Evans, B. Simmons, and D. Stevens, "A vibration analysis of a third generation inertial instrument test table," in *AIAA Guidance and Control Conference*, American Institute of Aeronautics and Astronautics, 1978. DOI: [10.2514/6.1978-1256](https://doi.org/10.2514/6.1978-1256).
- [36] R. L. McNeill, B. E. Margason, and F. M. Babcock, "The Role of Soil Dynamics in the Design of Stable Test Pads," in *AIAA Guidance and Control Conference*, American Institute of Aeronautics and Astronautics, 1965.

- [37] K. Tsutsumi, "Geokinetics - Its background, requirements and development," in *AIAA Guidance Control and Flight Mechanics Conference*, American Institute of Aeronautics and Astronautics, Santa Barbara, 1970. DOI: [10.2514/6.1970-958](https://doi.org/10.2514/6.1970-958).
- [38] R. T. Berg, "Inertial Test Slab Stability Study," in *AIAA Guidance and Control Conference*, (Minneapolis), American Institute of Aeronautics and Astronautics, Minneapolis, 1965.
- [39] T. Weiher, "Progress in Test Pad Stability," in *AIAA Guidance and Control Conference*, American Institute of Aeronautics and Astronautics, 1965. DOI: [10.2514/6.1965-1229](https://doi.org/10.2514/6.1965-1229).
- [40] H. Weinstock, *Limitations On Inertial Sensor Testing Produced by Test Platform Vibrations*, Electronics Research Center Cambridge, MA, 1966.
- [41] IEEE Aerospace Electronics Systems Society, Ed., *IEEE standard specification format guide and test procedure for linear, single-axis, nongyroscopic accelerometers corrigendum 1: changes to annex K and annex L*, IEEE Std. New York: Institute of Electrical and Electronics Engineers, 2008.
- [42] G. T. Schmidt, *INS/GPS Technology Trends, RTO-EN-SET-116*, 2009. [Online]. Available: [https://www.sto.nato.int/publications/STO%20Educational%20Notes/RTO-EN-SET-116-2009/EN-SET-116\(2009\)-01.pdf](https://www.sto.nato.int/publications/STO%20Educational%20Notes/RTO-EN-SET-116-2009/EN-SET-116(2009)-01.pdf).
- [43] M. Grewal, "How Good Is Your Gyro [Ask the Experts]," *IEEE Control Systems*, vol. 30, no. 1, pp. 12–86, 2010, ISSN: 1066-033X. DOI: [10.1109/MCS.2009.935122](https://doi.org/10.1109/MCS.2009.935122).
- [44] G. T. Schmidt, "Navigation sensors and systems in GNSS degraded and denied environments 2018, (Or how i learned to stop worrying about GPS)," in *2018 25th Saint Petersburg International Conference on Integrated Navigation Systems (ICINS)*, (St. Petersburg), IEEE, 52018, pp. 1–12, ISBN: 978-5-91995-057-8. DOI: [10.23919/ICINS.2018.8405890](https://doi.org/10.23919/ICINS.2018.8405890).
- [45] IEEE Aerospace Electronics Systems Society, Ed., *IEEE Specification Format Guide and Test Procedure for Two-Degree-Of-Freedom Dynamically Tuned Gyros*, IEEE Std. Piscataway, NJ, USA: IEEE, 1988. DOI: [10.1109/IEEESTD.1989.94579](https://doi.org/10.1109/IEEESTD.1989.94579).
- [46] International Organization for Standardization, Ed., *Flight dynamics — Concepts, quantities and symbols — Part 1: Aircraft motion relative to the air*, ISO, 1998.
- [47] American National Standards Institute, Ed., *Recommended Practice for Atmospheric and Space Flight Vehicle Coordinate Systems*, ANSI/AIAA, 1992.
- [48] D. D. McCarthy and G. Petit, Eds., *IERS Conventions (2003), IERS Technical Note 32*, International Earth Rotation and Reference Systems Service, 2004.
- [49] *The Second Realization of the International Celestial Reference Frame by Very Long Baseline Interferometry, IERS Technical Note 35*, International Earth Rotation and Reference Systems Service.
- [50] *Department of Defense World Geodetic System 1984, Its Definition and Relationships with Local Geodetic Systems*, National Imagery and Mapping Agency.

-
- [51] J. Dambeck and B. Braun, "A Single Frequency Strapdown Algorithm for Integrating IMUs in ECEF-Frame," in *Advances in Aerospace Guidance, Navigation and Control*, F. Holzapfel and S. Theil, Eds., Berlin, Heidelberg: Springer Berlin Heidelberg, 2011, pp. 305–319, ISBN: 978-3-642-19816-8. DOI: [10.1007/978-3-642-19817-5_24](https://doi.org/10.1007/978-3-642-19817-5_24).
- [52] W. A. Poor, "A Geometric Description of Wander Azimuth Frames," *Navigation*, vol. 36, no. 3, pp. 303–318, 1989, ISSN: 00281522. DOI: [10.1002/j.2161-4296.1989.tb01519.x](https://doi.org/10.1002/j.2161-4296.1989.tb01519.x).
- [53] C. K. Chui and G. Chen, *Kalman Filtering, With Real-Time Applications*, eng, Softcover reprint of the original 5th edition 2017. Cham: Springer International Publishing and Springer, 2018, XVIII, 247 Seiten in 1 Teil, ISBN: 9783319837802.
- [54] R. E. Kalman and R. S. Bucy, "New Results in Linear Filtering and Prediction Theory," *Journal of Basic Engineering*, vol. 83, no. 1, pp. 95–108, 1961, ISSN: 0021-9223. DOI: [10.1115/1.3658902](https://doi.org/10.1115/1.3658902).
- [55] G. L. Smith, S. F. Schmidt, and L. A. McGee, *Application of Statistical Filter Theory to the Optimal Estimation of Position and Velocity on Board a Circumlunar Vehicle*, National Aeronautics and Space Administration, 1962.
- [56] S. F. Schmidt, "Applications of State-space Methods to Navigation Problems," in *Advances in Control Systems*, L. T. Cornelius, Ed., vol. 3, Academic Press, 1966, pp. 293–340.
- [57] B. Braun, "High Performance Kalman Filter Tuning for Integrated Navigation Systems," Dissertation, Technical University of Munich, Munich, 2016.
- [58] K. D. Rao and M. Swamy, *Digital Signal Processing*. Singapore: Springer Singapore, 2018, ISBN: 978-981-10-8080-7. DOI: [10.1007/978-981-10-8081-4](https://doi.org/10.1007/978-981-10-8081-4).
- [59] J. A. Gubner, *Probability and Random Processes for Electrical and Computer Engineers*. Cambridge University Press, 2012, ISBN: 9780521864701. DOI: [10.1017/CB09780521864701](https://doi.org/10.1017/CB09780521864701).
- [60] P. Welch, "The use of fast Fourier transform for the estimation of power spectra: A method based on time averaging over short, modified periodograms," *IEEE Transactions on Audio and Electroacoustics*, vol. 15, no. 2, pp. 70–73, 1967, ISSN: 0018-9278. DOI: [10.1109/TAU.1967.1161901](https://doi.org/10.1109/TAU.1967.1161901).
- [61] D. W. Allan, "Statistics of atomic frequency standards," *Proceedings of the IEEE*, vol. 54, no. 2, pp. 221–230, 1966, ISSN: 0018-9219. DOI: [10.1109/PROC.1966.4634](https://doi.org/10.1109/PROC.1966.4634).
- [62] National Institute of Standards and Technology, Ed., *Handbook of Frequency Stability Analysis*, NIST Special Publication, Jul. 1, 2008.

- [63] T. Marusenkova and I. Yurchak, "A Dynamic Programming Method of Calculating the Overlapping Allan Variance," in *2019 IEEE 15th International Conference on the Experience of Designing and Application of CAD Systems (CADSM)*, (Polyana, Ukraine), IEEE, 26.02.2019 - 02.03.2019, pp. 1–4, ISBN: 978-1-7281-0053-1. DOI: [10.1109/CADSM.2019.8779282](https://doi.org/10.1109/CADSM.2019.8779282).
- [64] S. M. Yadav, S. K. Shastri, G. B. Chakravarthi, V. Kumar, and D. R. A., "A Fast, Parallel Algorithm for Fully Overlapped Allan Variance and Total Variance for Analysis and Modeling of Noise in Inertial Sensors," *IEEE Sensors Letters*, vol. 2, no. 2, pp. 1–4, 2018. DOI: [10.1109/LSSENS.2018.2829799](https://doi.org/10.1109/LSSENS.2018.2829799).
- [65] L. Galleani and P. Tavella, "The dynamic Allan variance," eng. *IEEE transactions on ultrasonics, ferroelectrics, and frequency control*, vol. 56, no. 3, pp. 450–464, 2009, Journal Article. DOI: [10.1109/TUFFC.2009.1064](https://doi.org/10.1109/TUFFC.2009.1064). eprint: [19411206](https://arxiv.org/abs/19411206).
- [66] P. Lv, J. Liu, J. Lai, and K. Huang, "Allan variance method for gyro noise analysis using weighted least square algorithm," *Optik*, vol. 126, no. 20, pp. 2529–2534, 2015, PII: S0030402615005161, ISSN: 00304026. DOI: [10.1016/j.ijleo.2015.06.044](https://doi.org/10.1016/j.ijleo.2015.06.044).
- [67] C. A. Greenhall, "Estimating the modified Allan variance," in *Proceedings of the 1995 IEEE International Frequency Control Symposium (49th Annual Symposium)*, (San Francisco, CA, USA), IEEE, 31 May-2 June 1995, pp. 346–353, ISBN: 0-7803-2500-1. DOI: [10.1109/FREQ.1995.483920](https://doi.org/10.1109/FREQ.1995.483920).
- [68] D. A. Howe, D. U. Allan, and J. A. Barnes, "Properties of Signal Sources and Measurement Methods," in *Thirty Fifth Annual Frequency Control Symposium*, IEEE, 27.05.1981 - 29.05.1981, pp. 669–716. DOI: [10.1109/FREQ.1981.200541](https://doi.org/10.1109/FREQ.1981.200541).
- [69] L. Goercke, F. Holzapfel, and J. Dambeck, "Aerodynamic Flight Simulation in Inertial Quality," in *Proceedings of the 2013 International Technical Meeting of The Institute of Navigation*, (San Diego, California), 2013, pp. 415–425.
- [70] Institute of Flight System Dynamics, *FDM recordings of a transatlantic Boeing 747 cargo flight. Retrieved from a research cooperation, anonymized publication only*. 2018.
- [71] J. Lunze, *Regelungstechnik 2*. Berlin, Heidelberg: Springer Berlin Heidelberg, 2014, ISBN: 978-3-642-53943-5. DOI: [10.1007/978-3-642-53944-2](https://doi.org/10.1007/978-3-642-53944-2).
- [72] I. N. Bronshtein, H. Muehlig, G. Musiol, and K. A. Semendyayev, *Handbook of Mathematics*, 5th Ed. Berlin, Heidelberg: Springer-Verlag Berlin Heidelberg, 2007, Online-Ressource, ISBN: 978-3-540-72121-5.
- [73] M. Schuler, "Die Störung von Pendel- und Kreiselapparaten durch die Beschleunigung des Fahrzeuges.," *Physikalische Zeitschrift*, vol. 24, no. 344, 1923, Translated by W. E. Frye. [Online]. Available: <https://apps.dtic.mil/dtic/tr/fulltext/u2/b806120.pdf>.

-
- [74] C. Blum and J. Dambeck, "Analytical Assessment of the Propagation of Colored Sensor Noise in Strapdown Inertial Navigation," eng, *Sensors (Basel, Switzerland)*, vol. 20, no. 23, 2020, Journal Article. DOI: [10.3390/s20236914](https://doi.org/10.3390/s20236914). eprint: [33287275](https://arxiv.org/abs/33287275).
- [75] S. Engelberg, *Random signals and noise: A mathematical introduction*. CRC Press, 2007.
- [76] P. G. Savage, "Analytical Modeling of Sensor Quantization in Strapdown Inertial Navigation Error Equations," *Journal of Guidance, Control, and Dynamics*, vol. 25, no. 5, pp. 833–842, 2002, ISSN: 0731-5090. DOI: [10.2514/2.4963](https://doi.org/10.2514/2.4963).
- [77] C. F. Chen and R. F. Chiu, "Evaluation of irrational and transcendental transfer functions via the fast Fourier transform†," *International Journal of Electronics*, vol. 35, no. 2, pp. 267–276, 1973, ISSN: 0020-7217. DOI: [10.1080/00207217308938541](https://doi.org/10.1080/00207217308938541).
- [78] J. N. Kasdin, "Discrete Simulation of Stochastic Processes and Power Law Noise Generation," *Proceedings of the IEEE*, vol. 83, pp. 802–827, 1995.
- [79] M. S. Keshner, "1/f noise," *Proceedings of the IEEE*, vol. 70, no. 3, pp. 212–218, 1982, ISSN: 0018-9219. DOI: [10.1109/PROC.1982.12282](https://doi.org/10.1109/PROC.1982.12282).
- [80] J. A. Barnes and S. Jarvis, *Efficient Numerical and Analog Modeling of Flicker Noise Processes*, United States Department of Commerce, National Bureau of Standards, 1971.
- [81] Sensoror AS. "STIM300 Inertia Measurement Unit, Datasheet." (2013), [Online]. Available: <https://www.sensoror.com/media/1132/ts1524r9-datasheet-stim300.pdf>.
- [82] Silicon Sensing Systems Limited, *DMU10 Technical Datasheet, Six Degrees of Freedom Precision MEMS Inertial Measurement Unit*, version 6, Plymouth Devon, UK, 2016. [Online]. Available: <https://www.siliconsensing.com/media/30805/dmu10-00-0100-132-rev-6.pdf>.
- [83] Y. N. Korkishko *et al.*, "Highest bias stability fiber-optic gyroscope SRS-5000," in *2017 DGON Inertial Sensors and Systems (ISS)*, (Karlsruhe), IEEE, 19.09.2017 - 20.09.2017, pp. 1–23, ISBN: 978-1-5386-3962-7. DOI: [10.1109/InertialSensors.2017.8171490](https://doi.org/10.1109/InertialSensors.2017.8171490).
- [84] V. V. Chikovani, "Performance parameters comparison of ring laser, coriolis vibratory and fiber-optic gyros based on Allan variance analysis," in *2013 IEEE 2nd International Conference Actual Problems of Unmanned Air Vehicles Developments Proceedings (APUAVD)*, (Kiev, Ukraine), IEEE, 15.10.2013 - 17.10.2013, pp. 153–156, ISBN: 978-1-4799-3306-8. DOI: [10.1109/APUAVD.2013.6705312](https://doi.org/10.1109/APUAVD.2013.6705312).
- [85] J. Rohac, M. Sipos, J. Simanek, and O. Teren, "Inertial reference unit in a directional gyro mode of operation," in *2012 IEEE Sensors*, (Taipei, Taiwan), IEEE, 102012, pp. 1–4, ISBN: 978-1-4577-1767-3. DOI: [10.1109/ICSENS.2012.6411226](https://doi.org/10.1109/ICSENS.2012.6411226).
- [86] R. Dorobantu, *Investigation of a navigation-grade RLG SIMU type iNAV-RQH (IAPG-FESG)*. München: Institut für Astronomische und Physikalische Geodäsie, Forschungsseinrichtung Satellitengeodäsie, 2004, vol. 16.

- [87] D. Y. Hsu, *Spatial error analysis, A unified, application-oriented treatment*. New York: IEEE Press, op. 1999, XVII-217, ISBN: 0-7803-3453-1.
- [88] F. van Diggelen. "Update: GNSS Accuracy: Lies, Damn Lies, and Statistics." GPS World, Ed. (2007), [Online]. Available: <https://www.gpsworld.com/gpsgnss-accuracy-lies-damn-lies-and-statistics-1134/>.
- [89] F. van Diggelen. "GPS Accuracy: Lies, Damn Lies, and Statistics." GPS World, Ed. (1998), [Online]. Available: <https://www.gpsworld.com/gps-accuracy-lies-damn-lies-and-statistics/>.
- [90] Federal Aviation Administration, *Required Navigation Performance 10 (RNP 10) Operational Authorization*, Order 8400.12C, 2011. [Online]. Available: <https://www.faa.gov/documentLibrary/media/Order/8400.12.pdf>.
- [91] United States Department of Defence, *Global Positioning System Standard Positioning Service Performance Standard*, GPS SPS PS, 2008. [Online]. Available: <https://www.gps.gov/technical/ps/2008-SPS-performance-standard.pdf>.
- [92] N. K. Pavlis, S. A. Holmes, S. C. Kenyon, and J. K. Factor, "The development and evaluation of the Earth Gravitational Model 2008 (EGM2008)," *Journal of Geophysical Research: Solid Earth*, vol. 117, no. B4, n/a-n/a, 2012, ISSN: 01480227. DOI: [10.1029/2011JB008916](https://doi.org/10.1029/2011JB008916).
- [93] N. Beverini *et al.*, "High-Accuracy Ring Laser Gyroscopes: Earth Rotation Rate and Relativistic Effects," *Journal of Physics: Conference Series*, vol. 723, p. 012 061, 2016, ISSN: 1593-5213. DOI: [10.1088/1742-6596/723/1/012061](https://doi.org/10.1088/1742-6596/723/1/012061).
- [94] W. Torge, *Geodesy*, 2. ed. Berlin and New York: Walter de Gruyter, 1991, x, 264 s. ISBN: 3-11-012408-4.
- [95] W. J. Hinze, A. H. Saad, and R. von Frese, *Gravity and magnetic exploration, Principles, practices, and applications*, 1st publised, reprinted. New York: Cambridge University Press, 2013, xii, 512, ISBN: 978-0-521-87101-3.
- [96] F. Guattari *et al.*, "Touching the limit of FOG angular random walk: Challenges and applications," in *2016 DGON Inertial Sensors and Systems (ISS)*, (Karlsruhe, Germany), IEEE, 20.09.2016 - 21.09.2016, pp. 1-13, ISBN: 978-1-5090-2515-2. DOI: [10.1109/InertialSensors.2016.7745662](https://doi.org/10.1109/InertialSensors.2016.7745662).
- [97] "Earth orientation Data," Federal Agency for Cartography and Geodesy. (2013), [Online]. Available: <https://www.iers.org/IERS/EN/DataProducts/EarthOrientationData/eop.html> (visited on 02/26/2020).
- [98] K. U. Schreiber, T. Klügel, J.-P. R. Wells, R. B. Hurst, and A. Gebauer, "How to detect the Chandler and the annual wobble of the Earth with a large ring laser gyroscope," *Physical review letters*, vol. 107, no. 17, p. 173 904, 2011, Journal Article. DOI: [10.1103/PhysRevLett.107.173904](https://doi.org/10.1103/PhysRevLett.107.173904). eprint: [22107520](https://arxiv.org/abs/22107520).

-
- [99] J. M. Wahr, “The Earth’s Rotation,” *Annual Review of Earth and Planetary Sciences*, vol. 16, no. 1, pp. 231–249, 1988, ISSN: 0084-6597. DOI: [10.1146/annurev.ea.16.050188.001311](https://doi.org/10.1146/annurev.ea.16.050188.001311).
- [100] R. S. Gross, “The excitation of the Chandler wobble,” *Geophysical Research Letters*, vol. 27, no. 15, pp. 2329–2332, 2000, ISSN: 00948276. DOI: [10.1029/2000GL011450](https://doi.org/10.1029/2000GL011450).
- [101] S.-H. Na, “Earth Rotation – Basic Theory and Features,” in *Geodetic Sciences - Observations, Modeling and Applications*, S. Jin, Ed., InTech, 2013, ISBN: 978-953-51-1144-3. DOI: [10.5772/54584](https://doi.org/10.5772/54584).
- [102] B. W. Levin, E. V. Sasorova, G. M. Steblov, A. V. Domanski, A. S. Prytkov, and E. N. Tsyba, “Variations of the Earth’s rotation rate and cyclic processes in geodynamics,” *Geodesy and Geodynamics*, vol. 8, no. 3, pp. 206–212, 2017, PII: S1674984717300666, ISSN: 16749847. DOI: [10.1016/j.geog.2017.03.007](https://doi.org/10.1016/j.geog.2017.03.007).
- [103] J. G. Williams, “Contributions to the Earth’s obliquity rate, precession, and nutation,” *The Astronomical Journal*, vol. 108, p. 711, 1994, PII: 117108. DOI: [10.1086/117108](https://doi.org/10.1086/117108).
- [104] “International Earth Rotation and Reference Systems Service, Measuring the irregularities of the Earth’s rotation,” Federal Agency for Cartography and Geodesy. (2013), [Online]. Available: <https://www.iers.org/IERS/EN/Science/EarthRotation/EarthRotation.html> (visited on 02/19/2020).
- [105] K. U. Schreiber and J.-P. R. Wells, “Invited review article: Large ring lasers for rotation sensing,” eng, *The Review of scientific instruments*, vol. 84, no. 4, p. 041 101, 2013, Journal Article. DOI: [10.1063/1.4798216](https://doi.org/10.1063/1.4798216). eprint: 23635174.
- [106] “Measuring the irregularities of the Earth’s rotation,” International Earth Rotation and Reference Systems Service. (2013), [Online]. Available: <https://www.iers.org/IERS/EN/Science/EarthRotation/EarthRotation.html> (visited on 10/15/2020).
- [107] C. Förste *et al.*, *EIGEN-6C4 The latest combined global gravity field model including GOCE data up to degree and order 2190 of GFZ Potsdam and GRGS Toulouse*, eng, 2014. DOI: [10.5880/icgem.2015.1](https://doi.org/10.5880/icgem.2015.1).
- [108] C. Hirt, B. Bürki, A. Somieski, and G. Seeber, “Modern Determination of Vertical Deflections Using Digital Zenith Cameras,” *Journal of Surveying Engineering*, vol. 136, no. 1, pp. 1–12, 2010, ISSN: 0733-9453. DOI: [10.1061/\(ASCE\)SU.1943-5428.0000009](https://doi.org/10.1061/(ASCE)SU.1943-5428.0000009).
- [109] J. B. Merriam, “Atmospheric pressure and gravity,” *Geophysical Journal International*, vol. 109, no. 3, pp. 488–500, 1992, ISSN: 0956-540X. DOI: [10.1111/j.1365-246X.1992.tb00112.x](https://doi.org/10.1111/j.1365-246X.1992.tb00112.x).
- [110] J. Neumeyer, J. Hagedoorn, J. Leitloff, and T. Schmidt, “Gravity reduction with three-dimensional atmospheric pressure data for precise ground gravity measurements,” *Journal of Geodynamics*, vol. 38, no. 3-5, pp. 437–450, 2004, PII: S0264370704000821, ISSN: 02643707. DOI: [10.1016/j.jog.2004.07.006](https://doi.org/10.1016/j.jog.2004.07.006).

- [111] K. Matsuo, B. F. Chao, T. Otsubo, and K. Heki, “Accelerated ice mass depletion revealed by low-degree gravity field from satellite laser ranging: Greenland, 1991-2011,” *Geophysical Research Letters*, vol. 40, no. 17, pp. 4662–4667, 2013, ISSN: 00948276. DOI: [10.1002/grl.50900](https://doi.org/10.1002/grl.50900).
- [112] H.-G. Wenzel, “Tide-generating potential for the earth,” in *Tidal Phenomena*, ser. Lecture Notes in Earth Sciences, H. Wilhelm, W. Zürn, and H.-G. Wenzel, Eds., vol. 66, Berlin/Heidelberg: Springer-Verlag, 1997, pp. 9–26, ISBN: 3-540-62833-9. DOI: [10.1007/BFb0011455](https://doi.org/10.1007/BFb0011455).
- [113] I. M. Longman, “Formulas for computing the tidal accelerations due to the moon and the sun,” *Journal of Geophysical Research: Solid Earth*, vol. 64, no. 12, pp. 2351–2355, 1959, ISSN: 01480227. DOI: [10.1029/JZ064i012p02351](https://doi.org/10.1029/JZ064i012p02351).
- [114] J. R. Leeman. “LongmanTide, Gravitational tide computation based on Longman 1959.” (2018), [Online]. Available: <https://github.com/jrleeman/LongmanTide> (visited on 03/06/2020).
- [115] T. F. Baker and M. S. Bos, “Validating Earth and ocean tide models using tidal gravity measurements,” *Geophysical Journal International*, vol. 152, no. 2, pp. 468–485, 2003, ISSN: 0956-540X. DOI: [10.1046/j.1365-246X.2003.01863.x](https://doi.org/10.1046/j.1365-246X.2003.01863.x).
- [116] Bundesamt für Kartographie und Geodäsie. “ETERNA-X, Enhanced Earth and ocean tide analysis and prediction program system ETERNA-x.” (), [Online]. Available: <http://ggp.bkg.bund.de/eterna/> (visited on 10/30/2020).
- [117] F. van Diggelen and P. Enge, “The world’s first GPS MOOC and worldwide laboratory using smartphones,” in *28th International Technical Meeting of the Satellite Division of the Institute of Navigation, ION GNSS 2015*, vol. 1, 2015, pp. 361–369, ISBN: 9781510817258.
- [118] B. A. Renfro, M. Stein, N. Boeker, E. Reed, and E. Villalba, *An Analysis of Global Positioning System (GPS) Standard Positioning Service (SPS) Performance for 2018, TR-SGL-19-02*, Space and Geophysics Laboratory, University of Texas at Austin, 13.03.2019. [Online]. Available: <https://www.gps.gov/systems/gps/performance/2018-GPS-SPS-performance-analysis.pdf>.
- [119] B. Hofmann-Wellenhof, H. Lichtenegger, and E. Wasle, *GNSS – Global Navigation Satellite Systems, GPS, GLONASS, Galileo, and more*. Vienna: Springer Vienna, 2008, 516 pp., ISBN: 978-3-211-73012-6.
- [120] Wyler AG. “BlueSYSTEM SIGMA, The latest generation of inclination measuring instruments and systems.” (2019), [Online]. Available: https://www.wylerag.com/fileadmin/pdf/catalogue2019/bluelevel_SIGMA%202019.pdf.
- [121] E. Lambrou and G. Pantazis, “Astronomical azimuth determination by the hour angle of Polaris using ordinary total stations,” *Survey Review*, vol. 40, no. 308, pp. 164–172, 2008, ISSN: 0039-6265. DOI: [10.1179/003962608X290951](https://doi.org/10.1179/003962608X290951).

-
- [122] K. Jaskólski, A. Felski, and P. Piskur, “The Compass Error Comparison of an On-board Standard Gyrocompass, Fiber-Optic Gyrocompass (FOG) and Satellite Compass,” eng, *Sensors (Basel, Switzerland)*, vol. 19, no. 8, 2019, Journal Article. DOI: [10.3390/s19081942](https://doi.org/10.3390/s19081942). eprint: [31027224](https://arxiv.org/abs/31027224).
- [123] National Geospatial-Intelligence Agency. “The World Magnetic Model - Accuracy, limitations, magnetic poles and error model.” (2020), [Online]. Available: <https://www.ngdc.noaa.gov/geomag/WMM/limit.shtml>.
- [124] H. Igel, *Computational Seismology, A Practical Introduction*, eng. Oxford: OUP Oxford, 2016, 341 pp., ISBN: 978-0-19-871740-9. DOI: [10.1093/acprof:oso/9780198717409.001.0001](https://doi.org/10.1093/acprof:oso/9780198717409.001.0001). [Online]. Available: <http://search.ebscohost.com/login.aspx?direct=true&scope=site&db=nlebk&AN=1433934>.
- [125] J. N. Brune and J. Oliver, “The seismic noise of the Earth’s surface,” *Bulletin of the Seismological Society of America*, vol. 49, no. 4, pp. 349–353, 1959.
- [126] P. Bormann, *Seismic Signals and Noise*, eng. Deutsches GeoForschungsZentrum GFZ, 2009. DOI: [10.2312/GFZ.NMSOP_r1_ch4](https://doi.org/10.2312/GFZ.NMSOP_r1_ch4).
- [127] J. Peterson, *Observations and Modeling of Seismic Background Noise, Open-File Report 93-322*, Albuquerque, NM: U.S. Department of Interior Geological Survey, 1993.
- [128] K. Venkateswara *et al.*, *Windproofing LIGO: Improving low-frequency active seismic isolation using rotation sensors*, LIGO, 2018. [Online]. Available: <https://dcc-llo.ligo.org/LIGO-P1800038/public>.
- [129] “IRIS DMC MUSTANG Noise-psd Web Service,” Incorporated Research Institutions for Seismology. (2020), [Online]. Available: <https://service.iris.edu/mustang/noise-psd/1/> (visited on 03/22/2020).
- [130] G. W. Kamperman, “Vibration isolation effectiveness of inertia pads resting on soil,” *Journal of Spacecraft and Rockets*, vol. 2, no. 2, pp. 182–186, 1965, ISSN: 0022-4650. DOI: [10.2514/3.28148](https://doi.org/10.2514/3.28148).
- [131] D. G. Albert and S. N. Decato, “Acoustic and seismic ambient noise measurements in urban and rural areas,” *Applied Acoustics*, vol. 119, pp. 135–143, 2017, PII: S0003682X16306120, ISSN: 0003682X. DOI: [10.1016/j.apacoust.2016.12.015](https://doi.org/10.1016/j.apacoust.2016.12.015).
- [132] Y. Zhao, “Research on background noise level of vertical pendulum tiltmeter in China,” *Geodesy and Geodynamics*, 2020, PII: S1674984720300124, ISSN: 16749847. DOI: [10.1016/j.geog.2020.01.002](https://doi.org/10.1016/j.geog.2020.01.002).
- [133] Lang *et al.*, *Bodenmechanik und Grundbau*. Springer Berlin Heidelberg, 2011.
- [134] S. A. Savidis, “Recommendation of the Committee on „Soil Dynamics“ (Baugrund-dynamik) of the German Geotechnical Society (DGGT),” *Bautechnik*, vol. 75, no. 10, pp. 792–798, 1998.

- [135] H. Kramer, "Kippschwingungen eines indirekt durch Oberflächenwellen erregten Fundaments," *Bautechnik*, vol. 76, no. 1, pp. 970–975, 1999.
- [136] "Three Axis Motion Simulator Model AC3350-140," Acutronic Switzerland Ltd. (2015), [Online]. Available: http://www.acutronic.com/uploads/tx_AcutronicProducts/DS-3-Axis-Rate-Table-AC3350-140_b.pdf (visited on 03/25/2020).
- [137] "1573P Series Three Axis Positioning and Rate Table Systems," Ideal Aerosmith Inc. (2018), [Online]. Available: https://www.ideal-aerosmith.com/wp-content/uploads/2018/08/IdealAerosmith_Model1573P_rev.pdf.
- [138] Deutschen Instituts für Normung, Ed., *Allgemeintoleranzen, Toleranzen für Längen- und Winkelmaße ohne einzelne Toleranzeintragung*, DIN ISO, Berlin: Beuth Verlag GmbH, 1991. DOI: [10.31030/2458559](https://doi.org/10.31030/2458559).
- [139] T. A. Harris, *Rolling bearing analysis*, eng, 4. ed. New York, NY: Wiley, 2001, 1086 pp., ISBN: 0-471-35457-0. [Online]. Available: <http://www.loc.gov/catdir/description/wiley035/00038171.html>.
- [140] M. Qiu, L. Chen, Y. Li, and J. Yan, *Bearing Tribology*. Berlin, Heidelberg: Springer Berlin Heidelberg, 2017, ISBN: 978-3-662-53095-5. DOI: [10.1007/978-3-662-53097-9](https://doi.org/10.1007/978-3-662-53097-9).
- [141] K. M. Ragulskis, A. Y. Jurkauskas, V. V. Atstupenas, A. Y. Vitkute, and A. P. Kulvec, *Vibration of Bearings, Translated from Russian*, NASA TT F-679. New Delhi: Amerind Publishing Co. Pvt. Ltd., 1979.
- [142] H. Yabe, "A Study on Run-Out Characteristics of Externally Pressurized Gas Journal Bearing : Rotor Run-Out Characteristics," *JSME international journal. Ser. C, Dynamics, control, robotics, design and manufacturing*, vol. 37, no. 2, pp. 355–361, 1994, ISSN: 1340-8062. DOI: [10.1299/jsmec1993.37.355](https://doi.org/10.1299/jsmec1993.37.355).
- [143] S. Cappa, D. Reynaerts, and F. Al-Bender, "Reducing the Radial Error Motion of an Aerostatic Journal Bearing to a Nanometre Level: Theoretical Modelling," *Tribology Letters*, vol. 53, no. 1, pp. 27–41, 2014, PII: 241, ISSN: 1023-8883. DOI: [10.1007/s11249-013-0241-8](https://doi.org/10.1007/s11249-013-0241-8).
- [144] J. Sopenan and A. Mikkola, "Dynamic model of a deep-groove ball bearing including localized and distributed defects. Part 1: Theory," *Proceedings of the Institution of Mechanical Engineers, Part K: Journal of Multi-body Dynamics*, vol. 217, no. 3, pp. 201–211, 2003, ISSN: 1464-4193. DOI: [10.1243/14644190360713551](https://doi.org/10.1243/14644190360713551).
- [145] F. P. Wardle, "Vibration Forces Produced by Waviness of the Rolling Surfaces of Thrust Loaded Ball Bearings Part 1: Theory," *Proceedings of the Institution of Mechanical Engineers, Part C: Journal of Mechanical Engineering Science*, vol. 202, no. 5, pp. 305–312, 1988, ISSN: 0954-4062. DOI: [10.1243/PIME_PROC_1988_202_127_02](https://doi.org/10.1243/PIME_PROC_1988_202_127_02).
- [146] D. Gross, W. Hauger, J. Schröder, W. A. Wall, and J. Bonet, *Engineering Mechanics 2*. Berlin, Heidelberg: Springer Berlin Heidelberg, 2018, ISBN: 978-3-662-56271-0. DOI: [10.1007/978-3-662-56272-7](https://doi.org/10.1007/978-3-662-56272-7).

-
- [147] H. Dresig and F. Holzweißig, *Maschinendynamik*. Berlin, Heidelberg: Springer Berlin Heidelberg, 2016, ISBN: 978-3-662-52712-2. DOI: [10.1007/978-3-662-52713-9](https://doi.org/10.1007/978-3-662-52713-9).
- [148] K.-H. Grote, J. Feldhusen, and H. Dubbel, *Dubbel, Taschenbuch für den Maschinenbau*, ger, 24., aktualisierte Aufl. Berlin: Springer Vieweg, 2014, 2072 pp., ISBN: 978-3-642-38890-3. DOI: [10.1007/978-3-642-38891-0](https://doi.org/10.1007/978-3-642-38891-0).
- [149] *Precision Inductosyn Position Transducers, For industrial automation, aerospace and military applications*, Ruhle Companies Inc. [Online]. Available: <http://www.inductosyn.com/PDF%20Files/Farrand%20Controls%20Brochure.pdf>.
- [150] *Modulare Winkelmessgeräte mit magnetischer Abtastung*, Dr. Johannes Heidenhain GmbH, 9/2018. [Online]. Available: https://www.heidenhain.de/fileadmin/pdb/media/img/745168-14_Modulare_WMG_magnetisch_de_01.pdf (visited on 03/25/2020).
- [151] *Modulare Winkelmessgeräte mit optischer Abtastung*, Dr. Johannes Heidenhain GmbH, 9/2017. [Online]. Available: https://www.heidenhain.dehttps://www.heidenhain.de/fileadmin/pdb/media/img/1222041-10_Modulare_WMG_optisch_de.pdf
[fileadmin/pdb/media/img/745168-14_Modulare_WMG_magnetisch_de_01.pdf](https://www.heidenhain.de/fileadmin/pdb/media/img/745168-14_Modulare_WMG_magnetisch_de_01.pdf) (visited on 03/25/2020).
- [152] Y. A. Wu, “On-orbit calibration of inductosyn error,” in *Proceedings of 1994 American Control Conference - ACC '94*, (Baltimore, MD, USA), IEEE, 29 June-1 July 1994, pp. 2887–2891, ISBN: 0-7803-1783-1. DOI: [10.1109/ACC.1994.735096](https://doi.org/10.1109/ACC.1994.735096).
- [153] A. Zou, H. Zhao, Y. Ma, and D. Li, “Analysis calculation and testing of rotary inductosyn angle measuring errors,” in *Proceedings of the 33rd Chinese Control Conference*, (Nanjing, China), IEEE, 28.07.2014 - 30.07.2014, pp. 8091–8096, ISBN: 978-9-8815-6387-3. DOI: [10.1109/ChiCC.2014.6896354](https://doi.org/10.1109/ChiCC.2014.6896354).
- [154] Wu, “Calibration of inductosyn cyclic error,” in *Proceedings of IEEE International Conference on Control and Applications CCA-94*, (Glasgow, UK), IEEE, 13.09.1993 - 16.09.1993, 187–192 vol.1, ISBN: 0-7803-1872-2. DOI: [10.1109/CCA.1994.381229](https://doi.org/10.1109/CCA.1994.381229).
- [155] Acutronic Switzerland Ltd. “Motion Simulators.” (), [Online]. Available: <http://www.acutronic.com/ch/products.html> (visited on 06/03/2020).
- [156] Ideal Aerosmith, Inc. “Product Solutions.” (), [Online]. Available: <https://www.ideal-aerosmith.com/products/>.
- [157] iXblue SAS. “Rate Tables.” (), [Online]. Available: <https://motion.ixblue.com/> (visited on 06/03/2020).
- [158] acuitas AG. “Motion Simulators.” (), [Online]. Available: <https://www.acuitas.ch/products/motion-simulators> (visited on 06/03/2020).

- [159] W. Drury, *Electric Motors and Drives, Fundamentals, Types and Applications : Fundamentals, Types and Applications*, 5th ed. San Diego, UNITED KINGDOM: Newnes, 2019, 1 online resource (514), ISBN: 9780128189252.
- [160] Z. Q. Zhu, S. Ruangsinchaiwanich, Y. Chen, and D. Howe, "Evaluation of superposition technique for calculating cogging torque in permanent-magnet brushless machines," *IEEE Transactions on Magnetics*, vol. 42, no. 5, pp. 1597–1603, 2006, ISSN: 0018-9464. DOI: [10.1109/TMAG.2005.861831](https://doi.org/10.1109/TMAG.2005.861831).
- [161] L. Zhu, S. Z. Jiang, Z. Q. Zhu, and C. C. Chan, "Comparison of alternate analytical models for predicting cogging torque in surface-mounted permanent magnet machines," in *2008 IEEE Vehicle Power and Propulsion Conference*, (Harbin, Hei Longjiang, China), IEEE, 3.09.2008 - 05.09.2008, pp. 1–6, ISBN: 978-1-4244-1848-0. DOI: [10.1109/VPPC.2008.4677557](https://doi.org/10.1109/VPPC.2008.4677557).
- [162] J. A. Barnes, "Atomic timekeeping and the statistics of precision signal generators," *Proceedings of the IEEE*, vol. 54, no. 2, pp. 207–220, 1966, ISSN: 0018-9219. DOI: [10.1109/PROC.1966.4633](https://doi.org/10.1109/PROC.1966.4633).
- [163] L. S. Cutler and C. L. Searle, "Some aspects of the theory and measurement of frequency fluctuations in frequency standards," *Proceedings of the IEEE*, vol. 54, no. 2, pp. 136–154, 1966, ISSN: 0018-9219. DOI: [10.1109/PROC.1966.4627](https://doi.org/10.1109/PROC.1966.4627).
- [164] J. Rutman, "Comment on "Characterization of Frequency Stability";" *IEEE Transactions on Instrumentation and Measurement*, vol. 21, no. 1, p. 85, 1972, ISSN: 0018-9456. DOI: [10.1109/TIM.1972.4313968](https://doi.org/10.1109/TIM.1972.4313968).
- [165] J. A. Barnes, *Tables of bias functions, B_1 and B_2 for variances based on finite samples of processes with power law spectral densities* (NBS Technical Note). Washington: U.S. G.P.O, 1969, vol. 375, 37 pp.
- [166] Wolfram Research, Inc., *Mathematica*, version 11.2, Champaign, Illinois: Wolfram Research, Inc., 2020. [Online]. Available: <https://www.wolfram.com/mathematica>.
- [167] R. Bhardwaj, N. Kumar, and V. Kumar, "Errors in micro-electro-mechanical systems inertial measurement and a review on present practices of error modelling," *Transactions of the Institute of Measurement and Control*, vol. 40, no. 9, pp. 2843–2854, 2018, ISSN: 0142-3312. DOI: [10.1177/0142331217708237](https://doi.org/10.1177/0142331217708237).
- [168] S. Poddar, V. Kumar, and A. Kumar, "A Comprehensive Overview of Inertial Sensor Calibration Techniques," *Journal of Dynamic Systems, Measurement, and Control*, vol. 139, no. 1, 2017, ISSN: 0022-0434. DOI: [10.1115/1.4034419](https://doi.org/10.1115/1.4034419).
- [169] Fiber Optical Solution. "Catalogue 2019." (2019), [Online]. Available: <http://opticalsolution.lv/wp-content/uploads/2019/08/FOS-Catalogue-2019.pdf>.
- [170] R. Isermann and M. Münchhof, *Identification of Dynamic Systems, An Introduction with Applications*, eng. Berlin: Springer, 2014, 705 pp., ISBN: 978-3-642-42267-6.

-
- [171] I. Markovsky and S. van Huffel, "Overview of total least-squares methods," *Signal Processing*, vol. 87, no. 10, pp. 2283–2302, 2007, PII: S0165168407001405, ISSN: 01651684. DOI: [10.1016/j.sigpro.2007.04.004](https://doi.org/10.1016/j.sigpro.2007.04.004).
- [172] IEEE Aerospace Electronics Systems Society, Ed., *IEEE Recommended Practice for Precision Centrifuge Testing of Linear Accelerometers*, IEEE Std. New York, N.Y., USA: Institute of Electrical and Electronics Engineers, 2009.
- [173] G. Minkler and J. Minkler, *Theory and application of Kalman filtering*, eng. Palm Bay, FL: Magellan Book Company, 1993, 608 pp., ISBN: 9780962161827.
- [174] E. D. Sontag, *Mathematical control theory, Deterministic finite dimensional systems* (Texts in applied mathematics), eng, 2. ed. New York and Heidelberg: Springer, 1998, vol. 6, 531 pp., ISBN: 978-0-387-98489-6.
- [175] J. F. Bellantoni and K. W. Dodge, "A square root formulation of the Kalman- Schmidt filter," *AIAA Journal*, vol. 5, no. 7, pp. 1309–1314, 1967, ISSN: 0001-1452. DOI: [10.2514/3.4189](https://doi.org/10.2514/3.4189).
- [176] IEEE, Ed., *IEEE Standard for Floating-Point Arithmetic*, IEEE Std, Piscataway, NJ, USA: IEEE, 2008. DOI: [10.1109/IEEESTD.2019.8766229](https://doi.org/10.1109/IEEESTD.2019.8766229).
- [177] F. Hamano, "Derivative of Rotation Matrix - Direct Matrix Derivation of Well Known Formula," in *Proceedings of Green Energy and Systems Conference 2013*, (Long Beach, CA, USA), 2013. [Online]. Available: <http://arxiv.org/pdf/1311.6010v1>.
- [178] Wolfram Alpha LLC. "Wolfram|Alpha." (2009), [Online]. Available: <http://www.wolframalpha.com>.